T. Pradeep

Publications 2013

Contents

1. Journal Covers

Vol. 30 · No. 12 · December 2013

Particle & Particle Systems Characterization

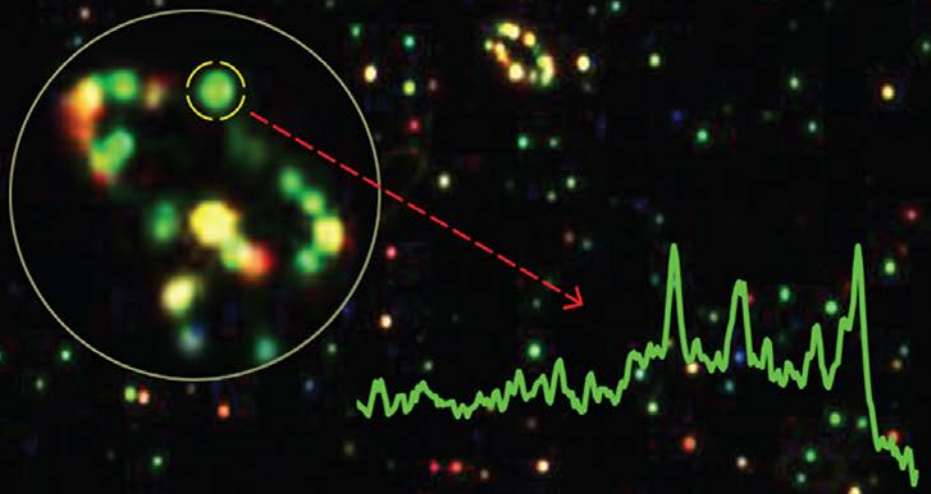

www.particle-journal.com

WILEY-VCH

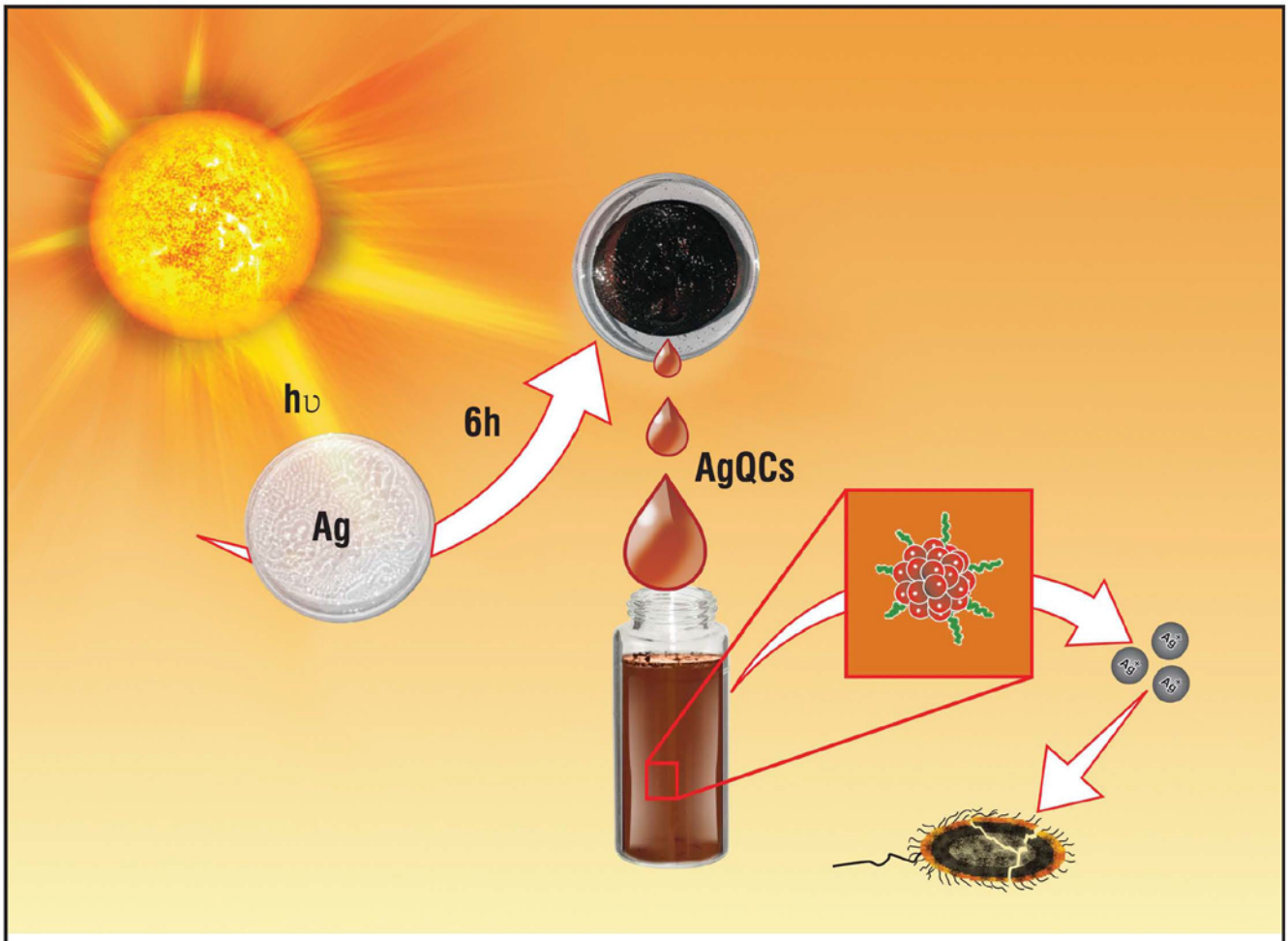

Showcasing research from Prof. T. Pradeep's laboratory at IIT Madras, Chennai, India.

Title: Sunlight mediated synthesis and antibacterial properties of monolayer protected silver clusters

Details of the research undertaken in our laboratory can be found at http://www.dstuns.iitm.ac.in/pradeep-research-group.php. A green route to synthesise glutathione protected atomically precise silver clusters by sunlight irradiation of silver thiolates confined in gel cavities, and the antibacterial properties of the as-synthesized clusters against gram-negative and gram-positive bacteria.

As featured in:

See I. Chakraborty *et al.*, *J. Mater. Chem. B*, 2013, **1**, 4059.

RSC Publishing

www.rsc.org/MaterialsB

Registered Charity Number 207890

2. Book

Only cover page is attached

Noble metal nanoparticles, T. S. Sreeprasad and T. Pradeep, Springer Handbook of Nanomaterials, R. Vajtai (Ed.), Springer, Heidelberg, 2013.

(A comprehensive summary of noble metal nanoparticles in 86 pages)

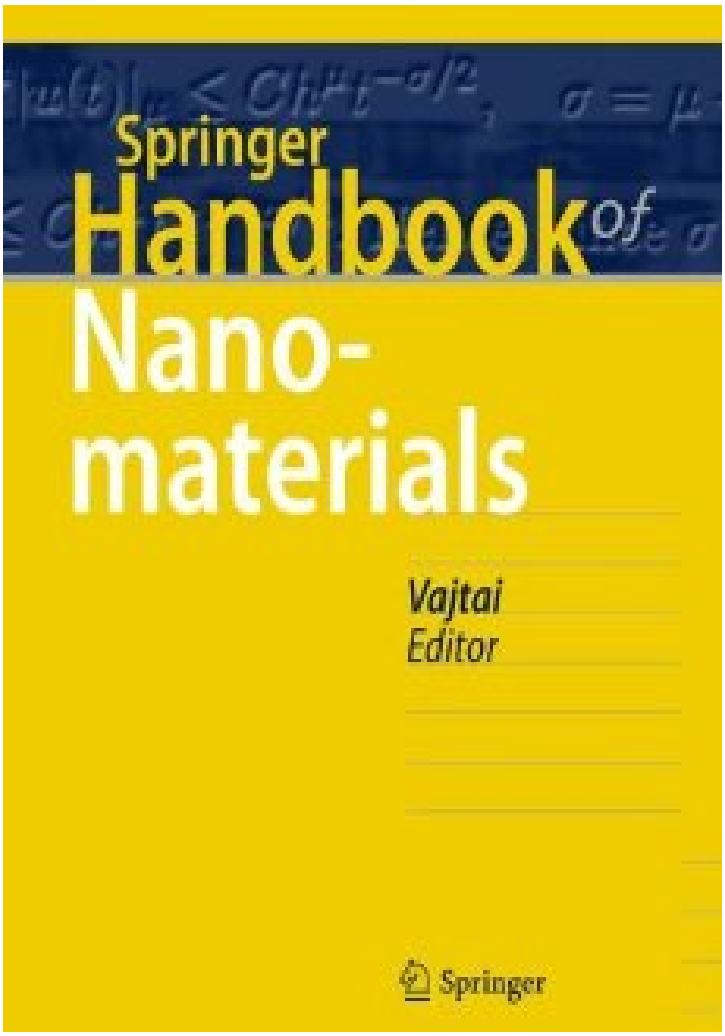
Springer
Handbook of
Nano-
materials
Vajtai
Editor
Springer

3. Journal Papers

2013

1. Electrical conductivity of ceramic and metallic nanofluids, K. G. Kalpana Sarojini , Siva V. Manoj, Pawan K. Singh, T. Pradeep, Sarit K. Das, Colloids and Surfaces A: Physicochem. Eng. Aspects, 417 (2013) 39-46 (DOI: 10.1016/j.colsurfa.2012.10.010).

2. Ultrafast photoinduced enhancement of nonlinear optical response in 15-atom gold clusters on indium tin oxide conducting film, Sunil Kumar, E. S. Shibu, T. Pradeep and A. K. Sood, Optics Express, 21(2013) 8483-8492 (DOI: 10.1364/OE.21.008483).

3. Atomically precise silver clusters for efficient chlorocarbon degradation, M. S. Bootharaju, G. K. Deepesh, T. Udayabhaskararao and T. Pradeep, J. Mater. Chem. A, 1 (2013) 611-620 (DOI:10.1039/C2TA00254J).

4. Immobilized graphene-based composite from asphalt: Facile synthesis and application in water purification, T. S. Sreeprasad, Soujit Sen Gupta, Shihabudheen M. Maliyekkal and T. Pradeep, J. Haz. Mat., 246-247 (2013) 213-220.

5. Evolution of atomically precise silver clusters to superlattice crystals, K. S. Sugi, Indranath Chakraborty, T. Udayabhaskararao, Jyoti Sarita Mohanty and T. Pradeep, Particle, 30 (2013) 241-243.

6. Protein-encapsulated gold cluster aggregates: The case of lysozyme, Ananya Baksi, Paulrajpillai Lourdu Xavier, Kamalesh Chaudhari, Nirmal Goswami, Samir Kumar Pal and T. Pradeep, Nanoscale, 5 (2013) 2009-2016.

7. Bare clusters derived from protein templates: Au_{25}^{+}, Au_{38}^{+} and Au_{102}^{+}, Ananya Baksi, T. Pradeep, Bokwon Yoon, Constantine Yannouleas and Uzi Landman, ChemPhysChem, 14 (2013) 1272-1282. (DOI: 10.1002/cphc.201200927)

8. Probing molecular solids with low energy ions, Soumabha Bag, Radha Gobinda Bhuin, Ganapati Natarajan and T. Pradeep, Ann. Rev. Anal. Chem., 6 (2013) 97-118. (DOI: 10.1146/annurev-anchem-062012-092547

9. A copper cluster protected with phenylethanethiol, Anindya Ganguly, Indranath Chakraborty, T. Udayabhaskararao and T. Pradeep, Journal of Nanoparticle Research, (2013) 15:1522 (DOI: 10.1007/s11051-013-1522-8)

10. Unprecedented inhibition of tubulin polymerization directed by gold nanoparticles inducing cell cycle arrest and apoptosis, Diptiman Choudhury, Paulrajpillai Lourdu Xavier, Kamalesh Chaudhari, Robin John, Anjan Kumar Dasgupta, T. Pradeep and G. Chakrabarti, Nanoscale, 5 (2013) 4476-4489 (DOI: 10.1039/c3nr33891f).

11. Separation of precise compositions of noble metal clusters protected with mixed ligands Yoshiki Niihori, Miku Matsuzaki, T. Pradeep and Yuichi Negishi, J. Am. Chem. Soc., 135 (2013) 4946-4949 (DOI: 10.1021/ja4009369).

12. New protocols for the synthesis of stable Ag and Au nanocluster molecules, T. Udayabhaskararao and T. Pradeep, J. Phys. Chem. Lett. 4 (2013) 1553–1564 (DOI: 10.1021/jz400332g).

13. Biopolymer reinforced synthetic granular nanocomposites for affordable point-of-use water purification, M. Udhaya Sankar, Sahaja Aigal, Amrita Chaudhary, Anshup, Shihabudheen M. Maliyekkal, A. Anil Kumar, Kamalesh Chaudhari and T. Pradeep, PNAS 110 (2013) 8459–8464 (doi: 10.1073/pnas.1220222110).

14. Anomalous subsurface thermal behavior in tissue mimics upon NIR irradiation mediated photothermal therapy, Soham Ghosh, P. R. Sajanlal, Nilmoni Sahoo, Tapobrata Panda, T. Pradeep, Sarit Kumar Das, J. Biomed. Nanotechnol. (2013) In Press.

15. Distinguishing amorphous and crystalline ices by ultra-low energy collisions of reactive ions, Soumabha Bag, Radha Gobinda Bhuin and T. Pradeep, J. Phys. Chem. C., (2013) (DOI: 10.1021/jp4016432).

16. Single cell investigations of silver nanoparticle-bacteria interactions, Vishnupriya Sudarsan, Kamalesh Chaudhari, Ramya Jagannathan, T. Pradeep, Particle, (2013) In press. **Highlighted on the inside cover**

17. Facile and rapid synthesis of dithiol-protected Ag7 quantum cluster for selective adsorption of cationic dyes, M. S. Bootharaju and T. Pradeep, Langmuir, (2013) (DOI: 10.1021/la401180r).

18. Sunlight mediated synthesis and antibacterial properties of monolayer protected silver clusters, Indranath Chakraborty, T. Udayabhaskararao, G. K. Deepesh and T. Pradeep, J. Mater. Chem. B, 1 (2013) 4059-4064. (DOI:10.1039/C3TB20603C). **Highlighted on the back cover**

19. Understanding the molecular signatures in leaves and flowers by desorption electrospray ionization mass spectrometry (DESI MS) imaging Hemalatha, Rani and T. Pradeep, Journal of Agricultural and Food Chemistry, (2013) (DOI:10.1021/jf4011998).

20. Thiolate-protected Ag32 clusters: Mass spectral studies of composition and insights into the Ag-thiolate structure from NMR, T. Udayabhaskararao, M. S. Bootharaju and T. Pradeep, Nanoscale, 5, (2013), 9404-9411 (Manuscript ID: NR-ART-07-2013-003463.R1).

21. Atomically Precise Silver Clusters as New SERS Substrates, Indranath Chakraborty, Soumabha Bag, Uzi Landman, and T. Pradeep, J. Phys. Chem. Lett., 4, (2013), pp 2769–2773 (DOI: 10.1021/jz4014097).

22. Ag44(SeR)30: A Hollow Cage Silver Cluster with Selenolate Protection, Indranath Chakraborty, Wataru Kurashige, Keita Kanehira, Lars Gell, Hannu Häkkinen, Yuichi Negishi and Thalappil Pradeep, J. Phys. Chem. Lett., 4, (2013), pp 3351–3355, (DOI: 10.1021/jz401879c).

23. Noble metal alloy clusters in the gas phase derived from protein templates: Unusual recognition of palladium by gold, Ananya Baksi and T. Pradeep, Nanoscale, (2013), Just Accepted (DOI: 10.1039/C3NR04257J).

24. Percolation network dynamicity and sheet dynamics governed viscous behavior of poly-dispersed Graphene nano-sheet suspensions, Purbarun Dhar, Hasan Ansari, Soujit Sen Gupta, V. Manoj Siva, T. Pradeep, Arvind Pattamatta and Sarit K. Das, Journal of Nanoparticle Research, (2013), Just Accepted (DOI: 10.1007/s11051-013-2095-2)

25. Studying reaction intermediates formed at graphenic surfaces, Depanjan Sarkar, Soujit Sen Gupta, Rahul Narayanan and T. Pradeep, Journal of The American Society for Mass Spectrometry, (2013), In Press. (As proof)

26. Luminescent AgAu alloy clusters derived from Ag nanoparticles: Manifestations of tunable AuI-CuI metallophilic interactions, Kumaranchira R. Krishnadas, Thumu Udayabhaskararao, Susobhan Choudhury, Nirmal Goswami, Samir Kumar Pal and Thalappil Pradeep, Eur. J. Inorg. Chem., (2013) (DOI: 10.1002/ejic.201301424).

27. Development of ultralow energy (1-10 eV) ion scattering spectrometry coupled with reflection absorption infrared spectroscopy and temperature programmed desorption for the investigation of molecular solids, Soumabha Bag, Radha Gobinda Bhuin, Rabin Rajan J. Methikkalam, Luke Kephart, Jeff Walker, Kevin Kuchta, Dave Martin, Jian Wei and T. Pradeep, Rev. Sci. Instrum. (2013), Just Accepted.

28. Sequential Electrochemical Unzipping of Single Walled Carbon Nanotube to Graphene Ribbons Revealed by in-situ Raman Spectroscopy and Imaging, Robin John, Dhanraj Shinde, Lili Liu, Feng Ding, Zhiping Xu, Cherianath Vijayan, Vijayamohanan Pillai, T. Pradeep, ACS Nano (2013)(DOI: 10.1021/nn403289g).

29. Supramolecular Functionalization and Concomitant Enhancement in Properties of Au25 Clusters, Ammu Mathew, Ganapati Natarajan, Lauri Lehtovaara, Hannu Hakkinen, Ravva Kumar, Venkatesan Subramanian, Abdul Jaleel, T. Pradeep, ACS Nano (2013) (DOI: 10.1021/nn406219x).

Papers with T. Pradeep as the/a corresponding author are reproduced in the following pages.

Journal of Materials Chemistry A

RSC Publishing

PAPER

View Article Online
View Journal | View Issue

Atomically precise silver clusters for efficient chlorocarbon degradation†

Cite this: *J. Mater. Chem. A*, 2013, **1**, 611

M. S. Bootharaju,‡ G. K. Deepesh,‡ T. Udayabhaskararao and T. Pradeep*

We describe the degradation of chlorocarbons (CCl_4, $C_6H_5CH_2Cl$ and $CHCl_3$) in solution at room temperature (27 ± 4 °C) by the monolayer-protected silver quantum cluster, Ag_9MSA_7 (MSA: mercaptosuccinic acid) in the presence of isopropyl alcohol (IPA). The main degradation products were silver chloride and amorphous carbon. Benzyl chloride was less reactive towards clusters than CCl_4 and $CHCl_3$. Materials used in the reactions and the reaction products were characterized using several spectroscopic and microscopic tools such as ultraviolet-visible (UV/Vis) absorption spectroscopy, Fourier transform infrared spectroscopy (FTIR), photoluminescence spectroscopy, X-ray diffraction (XRD), Raman spectroscopy, X-ray photoelectron spectroscopy (XPS), energy dispersive analysis of X-rays (EDAX) and scanning electron microscopy (SEM). We have shown that clusters are more efficient for the degradation of halocarbons than the corresponding monolayer-protected nanoparticles (Ag@MSA, particle diameter 15 ± 5 nm) at a given time and temperature. The higher reactivity of clusters is attributed to their small size and large surface area. Clusters and nanoparticles were used for reactions in supported (on neutral alumina) and unsupported forms. A possible mechanism for the reaction has been postulated on the basis of experimental results.

Received 10th September 2012
Accepted 12th October 2012

DOI: 10.1039/c2ta00254j

www.rsc.org/MaterialsA

Introduction

Research on noble metal (silver and gold) quantum clusters[1,2] has become increasingly fascinating in the last two decades. Quantum clusters, composed of a few tens to hundreds of atoms at the core and protected with ligands, are the connecting link between nanoparticles and molecules which exhibit molecular optical properties like absorption,[3,4] emission,[5,6] chirality,[7] *etc.* These nanosystems are very interesting because they show several applications in various fields such as catalysis,[8,9] biology,[10] environmental remediation,[11] *etc.* They are highly reactive due to their extremely small size and large surface area. They show unusual reactivity with salts.[12] Metal clusters exhibit the property of alloying with other metals.[13,14] Clusters have been used for sensing metal ions[15–17] and anions[18] by using their luminescence property.

The environment has been contaminated by a large number of pollutants like organic halides[19] (chloroflurocarbons (CFC), C_2Cl_4, C_2ClF_3, CCl_4, *etc.*), heavy metals[20] (Hg, Pb, Cd, Cr, *etc.* in various forms), energetic materials[21] (hexahydro-1,3,5-trinitro-1,3,5-triazine (RDX) and 2,4,6-trinitrotoluene (TNT)), and many others. Halocarbons are harmful trace components in water and air, either in the context of biological toxicity or due to their global warming potential or undesirable atmospheric chemistry.[22] The main sources of these are cleaning solvents, lubricants, plasticizers and refrigerants. Several of these have been replaced by less harmful chemicals. However, many of them continue to be used due to economic considerations or the lack of suitable replacements. CCl_4 is a widely used solvent in industry, research laboratories, dry cleaning, *etc.*[23] It is carcinogenic and it can persist in ground and surface waters. Due to this, it is one of the complex contaminants. The maximum allowed level of CCl_4 in surface water is 5 μg L^{-1}.[24] CFCs cause depletion of the ozone layer.[25] Various methods such as photodecomposition,[26] incineration,[27] photocatalysis[28,29] and adsorption[30] are developed to eliminate halocarbons from the environment. Chlorinated halocarbons are degraded by reductive mechanisms.[31] There are four types of reductive mechanisms: hydrogenolysis, elimination, dehydrohalogenation and hydrogenation.

Nanoparticles are increasingly used for environmental applications due to increased amount of contaminants in soil and groundwater.[32] Common nanoparticles used for halocarbon degradation in the literature are iron in oxide and zero-valent forms,[31] MgO[33] and ZnO.[34] In most of the above studies, nanoparticles form corresponding metal halides as principal products at high temperatures. Recently, noble metal and oxide nanoparticles have been studied in the degradation of

DST Unit of Nanoscience (DST UNS), Department of Chemistry, Indian Institute of Technology Madras, Chennai - 600 036, India. E-mail: pradeep@iitm.ac.in

† Electronic supplementary information (ESI) available: SEM elemental analysis and photograph of supported silver clusters, UV/Vis absorption spectrum and TEM image of Ag@MSA nanoparticles, XPS, XRD, Raman and EDAX data of the products of the reaction between supported clusters and CCl_4. See DOI: 10.1039/c2ta00254j

‡ These authors have contributed equally.

halocarbons.[35] Our research group has pioneered the use of noble metal nanoparticles for the removal of pesticides and halocarbons from drinking water.[36–40]

The standard Gibbs free energy change of formation ($\Delta_f G^0$) of AgCl(s) and CCl_4(l) are −109.8 and −65.2 kJ mol^{-1}, respectively. The net free energy change for the reaction 4Ag(s) + CCl_4(l) → 4AgCl(s) + C (graphite) is −374.0 kJ mol^{-1}. This indicates that the above reaction is feasible at 298 K and 1 atm pressure. The cell electromotive force (emf), E^0_{cell}, for the reduction of CCl_4 by silver (in the above reaction) is calculated to be 0.97 V using the equation $\Delta_f G^0 = -4FE^0_{cell}$, where F is Faraday's constant (96 500 C or J/V). The reaction may be slow but it is feasible. However, by using materials at the nanoscale, particularly silver at the nano/cluster length scale, the reduction potential is expected to reduce significantly as nanoscale silver is metastable with respect to the bulk. Due to the reduced dimension, the reaction is likely to be kinetically more favorable. Therefore, we may see interesting reactivity. This motivated us to study the reaction of CCl_4 with silver quantum clusters.

In the context of environmental applications, there are only a few studies on metal clusters. A study of sensitivity of Au_{25} clusters, one of the most studied clusters, to various metal ions was performed by Habeeb Muhammed and Pradeep.[12] Subsequently, a number of studies have shown the effect of metal ions on monolayer-protected as well as protein-protected gold clusters.[10,15,41] Sensing experiments have been performed with silver clusters as well.[16,17] There is a large need to develop techniques to use such materials as commercial products. Here, we utilized Ag_9 clusters protected with mercaptosuccinic acid (MSA) for the complete catalytic degradation of CCl_4, $CHCl_3$ and $C_6H_5CH_2Cl$ at room temperature. The reaction products were AgCl, CCl_3COOH, amorphous carbon and acetone. We found that isopropyl alcohol (IPA), used to increase the solubility of halocarbons in water, is very important in the reaction. Mechanistic aspects of the reaction are discussed based on experimental results. We propose that Cl^- ions, which are formed due to the cleavage of Cl_3C–Cl, replace the thiolates on the surface of the cluster. As a result, stability of the cluster is lost which causes the interaction of silver with Cl^-, leading to the formation of AgCl. The detached thiolates are converted to stable sulphites/sulphates in solution, the presence of which was confirmed by XPS. We demonstrate the increased efficiency of clusters for halocarbon degradation compared to analogous MSA protected silver nanoparticles. Reactions were carried out with clusters supported on alumina also, in which observations similar to unsupported clusters were noted.

Experimental section

Materials

Silver nitrate (CDH, India), mercaptosuccinic acid (MSA), sodium borohydride (Sigma Aldrich), methanol, ethanol, isopropyl alcohol (IPA), carbon tetrachloride (CCl_4), benzyl chloride ($C_6H_5CH_2Cl$) and chloroform ($CHCl_3$) (SRL Chemical Co. Ltd., India) were purchased from various sources and used as such without further purification. Neutral alumina was supplied by SRL, India. The surface area and the mean particle size were 900 ± 50 cm^2 g^{-1} and 0.13 mm, respectively.

Synthesis of silver clusters

The Ag_9MSA_7 cluster was synthesized according to the reported protocol.[42] Briefly, 47 mg of $AgNO_3$(s) and 187 mg of MSA(s) were ground until the mixture turned orange due to the formation of Ag-thiolates. After that, about 50 mg of $NaBH_4$(s) was added to it and grinding was continued for 2–3 minutes. To this, 10 mL of distilled water was added which led to the formation of clusters. The cluster was precipitated by the addition of ethanol. The precipitate was washed several times with pure methanol to remove excess $NaBH_4$, MSA and thiolates. Finally, a reddish brown powder of the clusters was obtained after evaporation of methanol using a rotavapor.

Synthesis of Ag@MSA nanoparticles

Ag@MSA nanoparticles were prepared as per the previous report.[20] Nearly 1.7 mL of distilled water containing 85 mg of $AgNO_3$ was added to 100 mL of methanol containing 448.9 mg of MSA which was kept at 0–5 °C. The resulting solution was stirred at 4000 rpm. 25 mL of freshly prepared 0.2 M $NaBH_4$ solution was added to the above solution drop-wise. Stirring was continued for 45 minutes at 0–5 °C. The mixture containing the precipitate of nanoparticles was centrifuged and the residue was washed with methanol to remove excess MSA and $NaBH_4$. Finally, a black powder of nanoparticles was obtained by evaporating methanol using a rotavapor.

Preparation of supported clusters and nanoparticles on neutral alumina

Loading of clusters was done by the addition of cluster solution (known amount) to a calculated amount of alumina followed by shaking with a mechanical shaker. The color of the solution disappeared immediately, indicating adsorption of clusters on alumina. The addition of cluster solution and shaking were continued until the supernatant retained the color of the cluster solution, indicating saturation loading. The supernatant at this stage showed the absorption features of the clusters, indicating the saturation of the alumina surface with adsorbed clusters. The saturation limit was found to be 10 mg per gram of alumina. After surface saturation, the supernatant was removed by centrifugation. Supported clusters were washed with water followed by methanol to remove the excess cluster. A solvent-free material was obtained by evaporation using a rotavapor. The same method was followed to prepare Ag@MSA nanoparticles supported on neutral alumina.

Reaction of halocarbons with clusters and nanoparticles

Nearly 5 mL of CCl_4 was added to the cluster solution (25 mg in 30 mL water). To this, 10 mL of isopropyl alcohol (IPA) was added. Here, the importance of IPA was to increase the miscibility of CCl_4 in the reaction mixture (solubility of CCl_4 = 800 mg L^{-1} in water at 298 K). The above mixture (orange red color) was stirred at 4000 rpm for 24 h at room temperature. The CCl_4 layer

disappeared and a grey colored precipitate was formed after 1.5 h. These observations indicate the occurrence of reaction between clusters and CCl_4. Reactions were carried out in methanol and ethanol as well in place of IPA. In these cases, no reaction was seen. A probable reason is that oxidation of IPA is more facile than other alcohols (methanol and ethanol). Other halocarbons, $CHCl_3$ and $C_6H_5CH_2Cl$, were used in place of CCl_4 under identical experimental conditions. A precipitate was formed after 24 h in the case of benzyl chloride, indicating less reactivity. In the case of supported clusters, 500 mg of the material was used under the above experimental conditions. Similar quantities of Ag@MSA nanoparticles (both unsupported and supported) were also used for the reaction of halocarbons.

Instrumentation

UV/Vis absorption spectra were recorded with a PerkinElmer Lambda 25 instrument in the spectral range of 200 to 1100 nm. FTIR spectra were recorded with a PerkinElmer Spectrum One instrument. KBr crystals were used as the matrix for preparing the samples. X-ray photoelectron spectroscopy (XPS) measurements were done using an Omicron ESCA Probe spectrometer with polychromatic Mg Kα X-rays ($h\nu = 1253.6$ eV). Experiments were carried out at an X-ray power of 300 W and pass energies of 50 eV for survey scans and 20 eV for specific regions. The base pressure of the instrument was 5.0×10^{-10} mbar. The binding energy was calibrated with respect to the adventitious C 1s feature at 285.0 eV. Most of the spectra were deconvoluted to their component peaks using the software CASA XPS. Scanning electron microscopy (SEM) and energy dispersive analysis of X-rays (EDAX) were performed using a FEI QUANTA-200 SEM. For the SEM measurements, samples were spotted on an indium tin oxide (ITO)-coated conducting glass and dried in ambience. X-ray diffraction (XRD) data were collected with a Shimadzu XD-D1 diffractometer using Cu Kα ($\lambda = 1.54$ Å) radiation. The samples were scanned in the 2θ range of 10 to 90°. The electrospray ionization mass spectrometry (ESI MS) measurements were done in the negative and positive modes using a MDX Sciex 3200 QTRAP MS/MS instrument having a mass range of m/z 50–1700, in which the spray and the extraction are orthogonal to each other. The samples were electrosprayed at a flow rate of 10 μL min^{-1} and an ion spray voltage of 5 kV. The spectra were averaged for 100 scans. MS/MS spectra were collected at optimized collision energies in the range of 25–45 eV.

Results and discussion

Starting materials: clusters, nanoparticles and supported materials

Silver nanoclusters (Ag_9MSA_7) and Ag@MSA nanoparticles have been well characterized as per other reports[20,42] and we present here only the essential data. As-synthesized silver clusters show characteristic UV/Vis absorption features at 450, 490, 626 and 886 nm (Fig. 1A). These clusters showed red emission at 726 nm when excited at 590 nm in a water–methanol mixture at 5 °C (inset of Fig. 1A). These two data prove the formation of clusters. The evidence for the binding of MSA to the cluster core was obtained by FTIR analysis (Fig. 1B). Pure MSA shows a characteristic –CO– of free carboxylate and S–H stretching peaks at 1700 and 2566 cm^{-1}, respectively (trace (a)). In the cluster sample, carboxylate stretching mode got shifted to 1576 cm^{-1} and the S–H stretching peak was absent (trace (b)). The presence of characteristic peaks of MSA in clusters (trace (b)) with a characteristic shift in peak positions in comparison to parent MSA (trace (a)) confirms the binding of MSA. The absence of the S–H feature (marked in trace (a)) in the cluster sample shows the binding of MSA with the cluster through an Ag–S linkage.[42] The chemical nature of silver and sulphur was confirmed by XPS (discussed later).

Supported clusters on alumina were characterized by SEM EDAX and the data are shown in Fig. S1 of ESI.† The spectrum

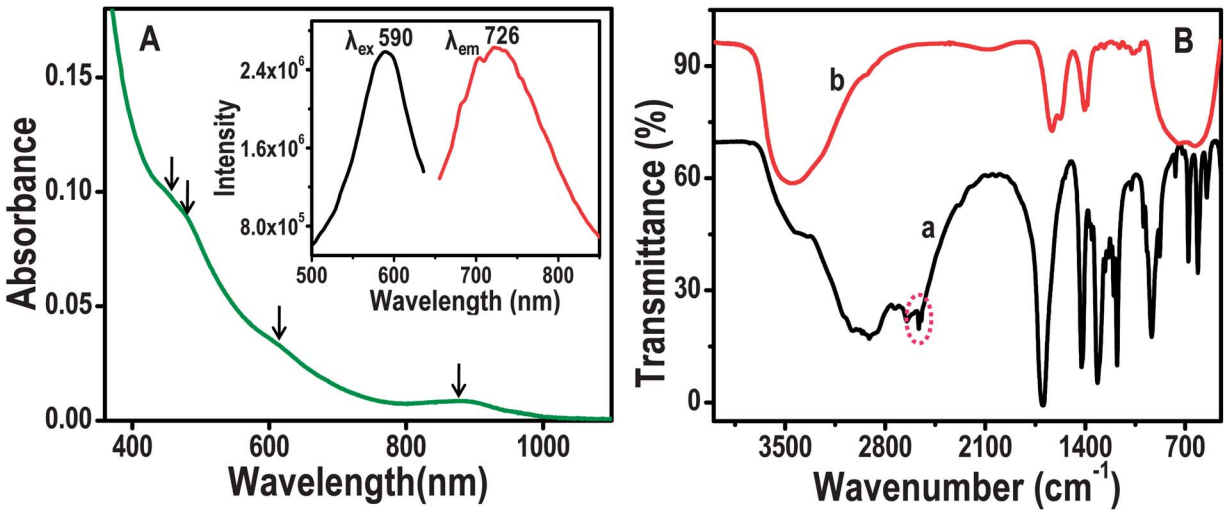

Fig. 1 (A) UV/Vis absorption spectrum of as-synthesized Ag_9MSA_7 clusters. Inset of (A) is the photoluminescence excitation and emission spectra of the clusters. They show emission at 726 nm when excited at 590 nm, at 5 °C. (B) Comparison of the FTIR spectra of MSA and Ag_9MSA_7 (traces (a) and (b), respectively); the latter shows the absence of S–H stretching in (b).

shows the presence of elements silver and sulphur which confirms the adsorption of clusters. Important evidence to show the presence of clusters on alumina is the red luminescence of the supported cluster kept under a UV lamp at liquid nitrogen temperature (inset of Fig. S1†). Bare alumina does not show any luminescence under UV lamp. The Ag@MSA nanoparticles were characterized by absorption spectroscopy. Silver nanoparticles show a surface plasmon resonance band at 392 nm which proves the formation of nanoparticles (Fig. S2†). TEM analysis of nanoparticles shows the average size to be 15 ± 5 nm (inset of Fig. S2†).

Reaction with CCl_4

We performed reactions with unsupported and supported clusters (on alumina) which are presented separately.

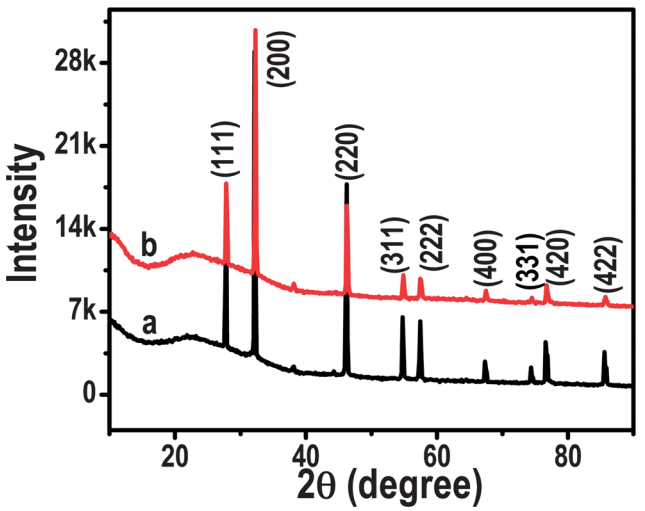

Fig. 2 XRD of as-prepared AgCl (a) and the product (b) obtained due to the reaction of Ag_9MSA_7 with CCl_4. The data have not been corrected for the background.

A. Unsupported clusters. The reactions were performed as described in the Experimental section. We have products in the solid state and products in solution. While the former are studied by XRD, Raman, IR, *etc.*, the latter are studied by mass spectrometry. The grey colored precipitate and colorless supernatant obtained after the reaction of CCl_4 and clusters were characterized with various analytical tools. The XRD pattern of the precipitate is shown in Fig. 2. It matches exactly with as-prepared AgCl (a precipitate obtained after mixing solutions of $AgNO_3$ and NaCl). This observation confirms the formation of AgCl as the reaction product.

The precipitate was used for Raman analysis before and after washing with ammonia solution (Fig. 3A). The purpose of washing with ammonia was to remove AgCl as a soluble complex, $[Ag(NH_3)_2]^+Cl^-$. After that, the solution was centrifuged at 10 000 rpm. A black residue was obtained which was analyzed by Raman spectroscopy. The unwashed precipitate (trace (a)) shows the presence of peaks at ~1408 and ~1575 cm^{-1}. These are attributed to D and G bands of carbonaceous species which is due to the formation of carbon from degradation of CCl_4.[43] After washing with ammonia, the peaks got shifted to ~1357 and ~1590 cm^{-1} (trace (b)). This shift may be due to the removal of impurities like AgCl which are soluble in ammonia. The red shift of the D band may be due to variation in defects (due to washing with NH_3 solution) of the graphitic structure and the blue shift of the G band is due to further amorphization of carbon due to removal of impurities.[44] Comparison of FTIR data of the reaction product (Fig. 3B) and the parent cluster (trace (a) in the inset of Fig. 3B) further supports the formation of the carbonaceous material. The stretching modes of the carboxylate group at 1576 and 1407 cm^{-1} are completely absent in the reaction product (trace (b) in the inset of Fig. 3B). This confirms the removal of a monolayer of MSA from the cluster. The peak at 1625 cm^{-1} in traces (a) and (b) is due to adsorbed water. A strong peak at 1384 cm^{-1} has emerged due to the presence of carbonaceous

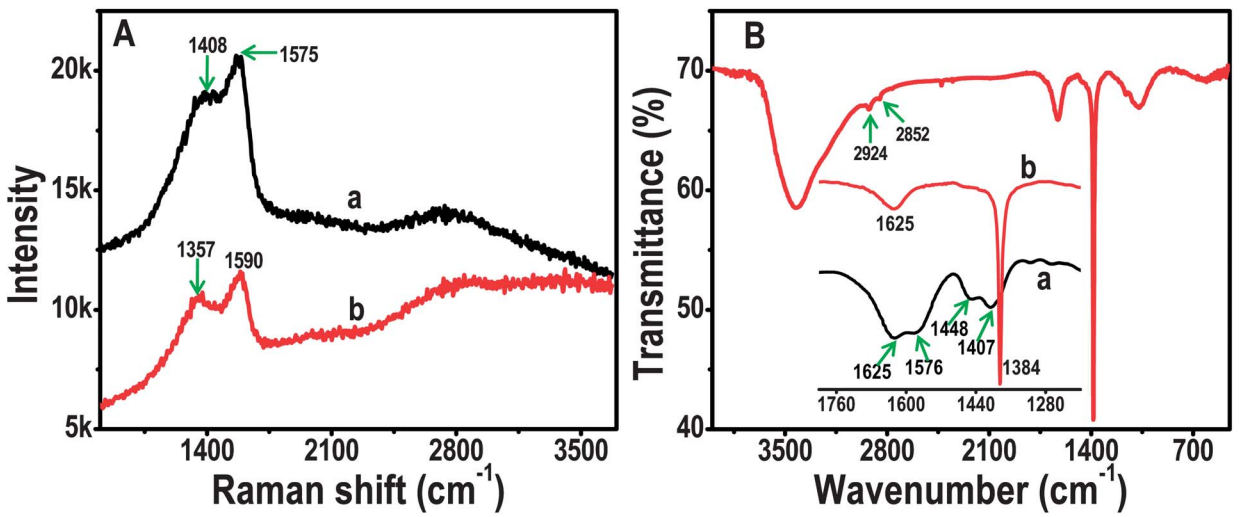

Fig. 3 (A) Raman spectra of the reaction product of Ag_9MSA_7 and CCl_4 before and after washing ((a) and (b), respectively) with aqueous ammonia. (B) FTIR spectrum of the reaction product before washing. Inset of (B) is the FTIR spectra of parent clusters (a) and the reaction product (b) in a specific region.

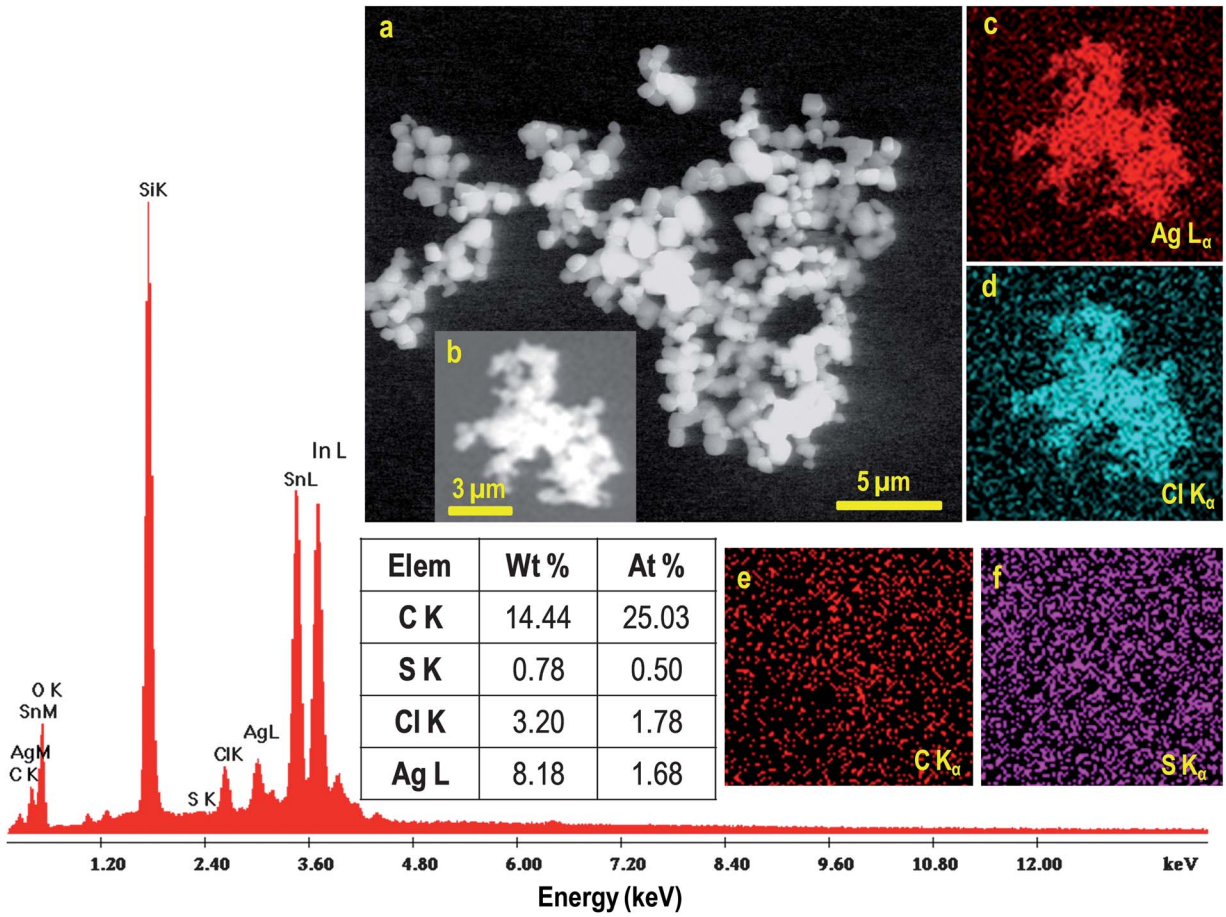

Elem	Wt %	At %
C K	14.44	25.03
S K	0.78	0.50
Cl K	3.20	1.78
Ag L	8.18	1.68

Fig. 4 EDAX spectrum of the product obtained after the reaction of the Ag_9MSA_7 cluster with CCl_4. The quantification table of elements in the EDAX spectrum is also shown. Si, In and Sn are due to the indium tin oxide substrate used. (a) and (b) are SEM images of the above sample. Elements Ag, Cl, C and S of the region shown in (b) are mapped in (c)–(f), respectively using X-ray energies of Ag L_α, Cl K_α, C K_α and S K_α.

species which confirms the formation of carbon, possibly as a graphitic product.[45] The other peaks at 2924 and 2852 cm^{-1} in Fig. 3B are due to the C–H stretching mode in graphitic carbon. The presence of chemically transformed sulphur species (sulphite/suphate) which are adsorbed on the reaction product and the absence of carboxylate features were confirmed by XPS (discussed later). From all these, it is evident that a monolayer of the cluster has been transformed chemically. However, the mechanism is complex and is not understood well.

SEM analysis of the precipitate is given in Fig. 4. Fig. 4a is a large area SEM image. It shows the presence of AgCl crystals. The elemental maps of the area shown in (b) are presented in (c)–(f). They clearly show the presence of elements Ag, Cl and a little amount of C. The EDAX spectrum collected from a portion of the sample is shown in Fig. 4. It shows the presence of elements Ag, Cl and trace amounts of S. The quantification table of elements of the same area (in Fig. 4) shows the presence of Ag and Cl in 1 : 1 atomic ratio which matches with AgCl composition. Also it shows the atomic percent of C and S in which sulphur was seen less in quantity.

In Fig. 5, XPS data of the precipitate (traces (b)) are compared with parent silver clusters (traces (a)). In the survey spectra of both the samples, carbon, silver, sulphur and oxygen were present (Fig. 5A). After the reaction, a new peak around 200.0 eV appears due to the presence of chlorine. The C 1s regions of the cluster and the reaction product clearly indicate the almost complete disappearance of the peak at 288.9 eV due to the carboxylate[46] groups in the product (Fig. S3†). This observation is also supported by FTIR analysis which confirms the replacement of the ligand MSA on the cluster. The intensity of the peak at 286.5 eV (due to carbon in C–O) increased compared to the parent clusters. The Ag 3d regions of both the samples are compared in Fig. 5B. Before the reaction, Ag $3d_{5/2}$ appeared at 368.1 eV whereas it is at 367.6 eV after the reaction. This clearly reveals the oxidation of silver from Ag^0 to Ag^+ state.[16] Note that in Ag, oxidation leads to shifting of binding energy to lower values.[16] The S 2p region due to the monolayer of the cluster is shown in Fig. 5C. Before the reaction, S $2p_{3/2}$ was at 162.1 eV assigned to sulphur bound to the cluster in the thiolate form. After the reaction, it shifted to 168.5 eV. This suggests the chemical change of the monolayer due to the reaction of the cluster core. This peak is assigned to sulphate/sulphite species.[47] The Cl 2p feature (Fig. 5D) is quite broad and it is fitted into two components corresponding to two types of Cl moieties. The Cl $2p_{3/2}$ positions are at 198.9 and 201.1 eV. The former peak may be due to chemisorbed chloride[48] possibly

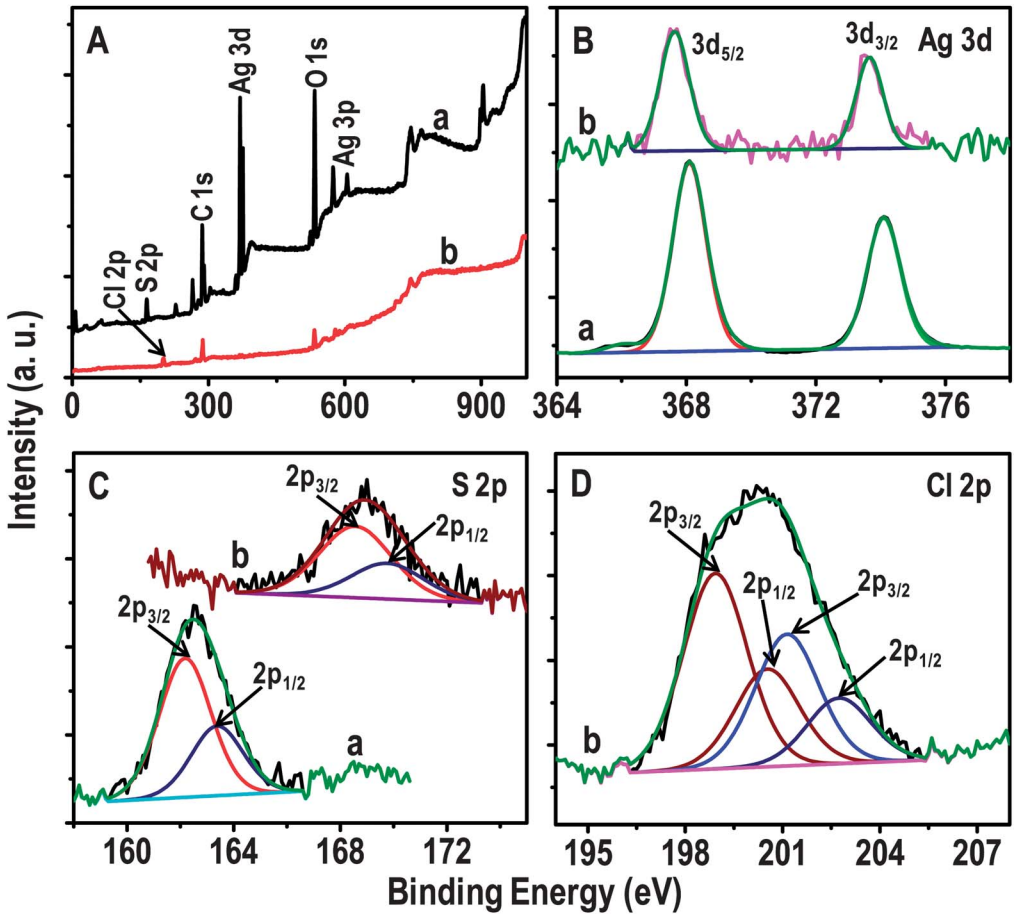

Fig. 5 XPS of parent Ag_9MSA_7 clusters (a) and the product obtained after the reaction of clusters with CCl_4 (b). (A–D) survey spectra, Ag 3d, S 2p and Cl 2p regions, respectively.

from AgCl and the latter may be due to adsorbed organic chlorine, possibly from CCl_4.[39,49] While all the silver got reacted in this sample, there could be some CCl_4 left behind.

During the progress of the reaction, we have followed the variation in pH of the solution with time (Fig. 6A). Initially, the pH of the reaction mixture was 5.7. The pH after 1.0, 2.0, 3.0 and

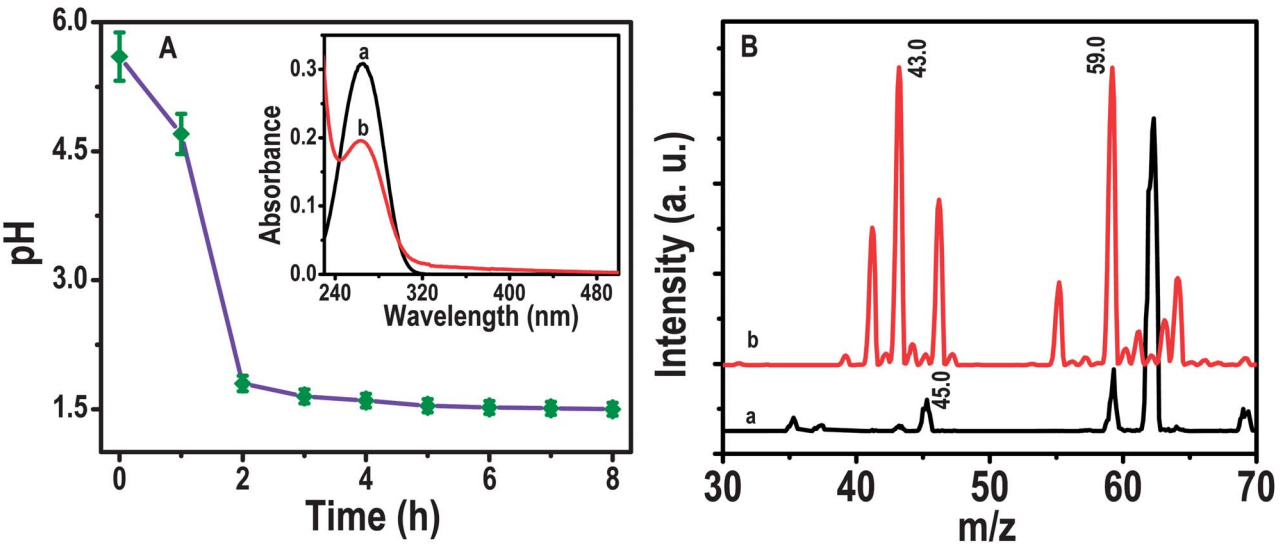

Fig. 6 (A) Plot of pH of the reaction product of Ag_9MSA_7 + CCl_4 with time. The estimated error is 5%. Inset is the absorption spectra of pure acetone (a) and that of the supernatant (b) of the above reaction, after 8.0 h. (B) Comparison of positive mode ESI MS of IPA and the reaction mixture (traces (a) and (b), respectively).

4.0 h of the reaction was 4.7, 1.8, 1.6 and 1.5, respectively. This clearly indicates the increase in the acidity of the reaction mixture. The release of H^+ can be due to the oxidation of IPA to acetone during the reaction. The UV/Vis absorption spectra of the supernatant of the reaction mixture and of acetone are compared in the inset of Fig. 6A. Pure acetone (trace (a)) shows an absorption maximum in water at 265 nm due to n–π* transition of the carbonyl group. The presence of an identical peak at 265 nm (trace (b)) in the reaction mixture confirms the formation of acetone from IPA.[50] Formation of acetone was further confirmed by comparison of ESI MS of IPA and reaction products in solution (Fig. 6B). IPA (trace (a)) shows an intense peak at *m*/*z* 45.0 which is assigned to $CH_3C(OH)H^+$. The reaction product (trace (b)) shows the disappearance of the peak at *m*/*z* 45.0 (due to IPA) with the appearance of a new peak at *m*/*z* 43.0 assigned to CH_3CO^+. The molecular ion peak of acetone was also seen at *m*/*z* 59.0. Interestingly, ESI MS data (Fig. S4†) of the reaction product show the formation of CCl_3COO^- which was tentatively assigned using mass spectrometry/mass spectrometry (MS/MS) analysis. In Fig. S4A,† trace (a) is the positive mode ESI MS of the reaction mixture in which no MSA peak at *m*/*z* 151.0 was noticed. Trace (b) is in negative mode where the peaks at *m*/*z* 196.0 and 161.0 are seen. The MSA peak at *m*/*z* 149.0 was not noticed here as well. The absence of parent MSA peaks after the reaction indicates the chemical transformation of detached ligands. The peak at *m*/*z* 196.0 is assigned to CCl_4COO^-. MS/MS of *m*/*z* 196.0 gives the peak *m*/*z* 161.0 due to the loss of ^{35}Cl (Fig. S4B†). MS^2 of *m*/*z* 198.0 gives 161.0 and 163.0 due to the loss of ^{37}Cl and ^{35}Cl, respectively. Similar losses were seen in MS^2 of *m*/*z* 200.0 and 202.0. The species CCl_4COO^- (or $[CCl_3COO]Cl^-$) may be formed by halogen attachment to CCl_3COO^-. Above assignments were again checked by comparing the calculated and experimental mass spectra for the above species which show an exact match (Fig. S4C and D†). Formation of CCl_3COO^- may be explained as follows. Oxidation of acetone may be continued to form CH_3COOH by active Cl species formed in the reaction (active Cl species can act as oxidizing agents) followed by the formation of chlorinated acid. However, more studies are essential to understand the formation mechanism of such species. A possible chemical equation for the above reaction can be written as follows. The changes observed in the monolayer are not included in the reaction as we do not know the exact mechanism of the chemical transformation of the ligand.

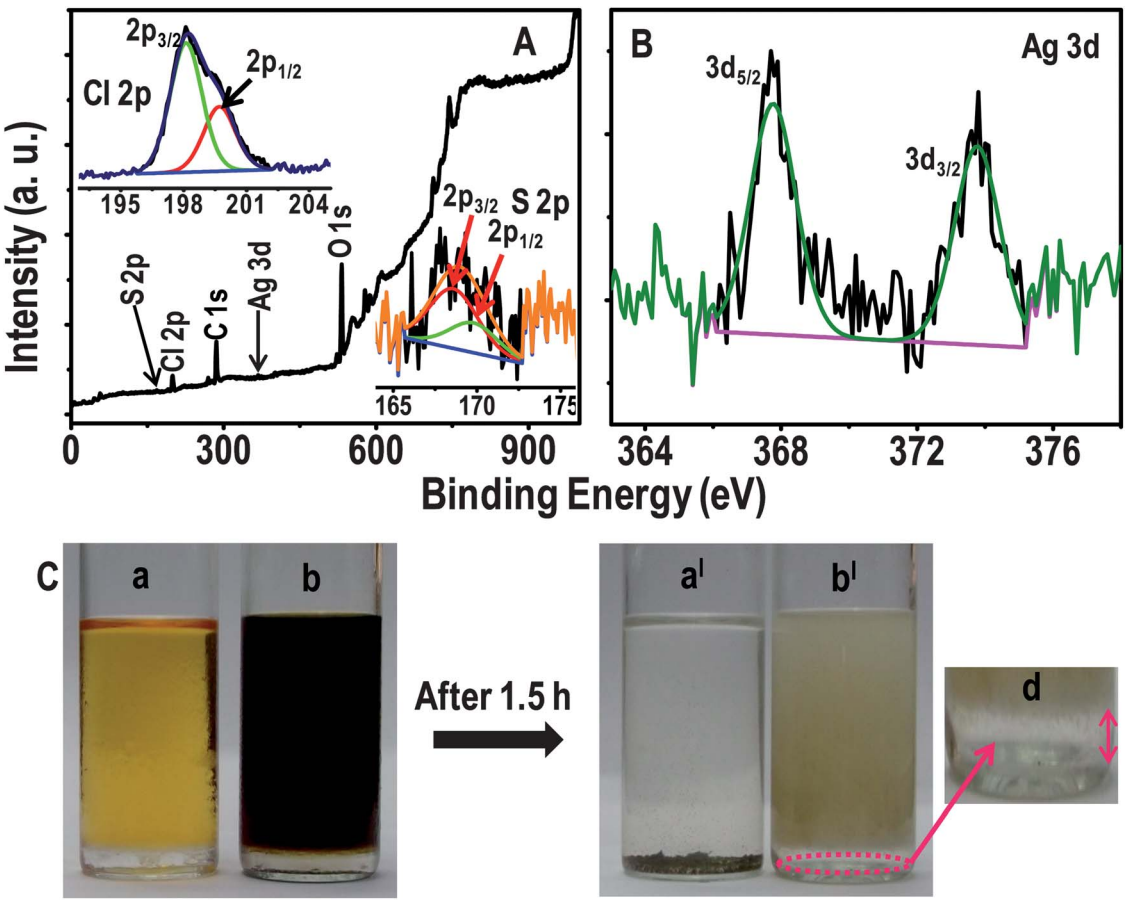

Fig. 7 (A) and (B) XPS survey spectrum and expanded Ag 3d region, respectively of the product of the reaction between Ag_9MSA_7 and benzyl chloride. Insets of (A) are Cl 2p and S 2p regions in the XPS of the same sample. (C) Photographs of the reaction mixtures of (a) Ag_9MSA_7 + CCl_4 and (b) Ag@MSA nanoparticles + CCl_4 initially (0.0 h). The CCl_4 layer is seen separately at the bottom. Photographs (a^I) and (b^I) are of corresponding mixtures after the reaction for 1.5 h. Unreacted CCl_4 is marked in (b^I). An enlarged photograph of the marked area of (b^I) is shown in (d).

Table 1 Comparison of various nanomaterials used for the degradation of chlorocarbons

Nanomaterials	Halocarbons	Process	Conditions	Products	Remarks	Ref.
Elemental iron and zinc	CCl_4	Reductive dechlorination	Ambient conditions	Free metal ions, $CHCl_3$ and H_2	Kinetics depends on pH, surface area, *etc.*	51
Pd/C, Rh/C, Ru/C and Pt/C	Polychlorinated biphenyls (PCBs)	Catalytic dechlorination	2-Propanol, aq. NaOH, 82 °C	Biphenyl and phenylcyclohexane	Complete dechlorination in ~2–3 h	52
TiO_2 (30 nm) suspension	$CHCl_3$, $CHBr_3$, and CCl_3COO^-	Photocatalysis	pH > 11, H_2O + CH_3OH	CO, CO_2 and Cl^-	Xe arc lamp at 910 W, 2 h irradiation	53
Subcolloidal Fe/Ag particles (<0.1 μm size)	Hexachlorobenzene (HCB)	Reductive dehalogenation	Room temperature, in water	Tetra-, tri-, and dichlorobenzenes	Complete dehalogenation in 24 h	54
Charge stabilized Ag and Au NPs (10–150 nm)	CCl_4, $C_6H_5CH_2Cl$, $CHCl_3$, CH_2Cl_2, *etc.*	Catalytic degradation	2-Propanol + water, 28 °C	AgCl, C and acetone	Complete destruction in 12 h	35
TiO_2 (40 and 80 nm)	CCl_4	Thermal decomposition	<550 °C, gaseous CCl_4	CO, CO_2, $COCl_2$, Cl_2, C, $TiCl_4$, HCl and titanium oxychloride	Particles of size 40 nm are more reactive than 80 nm	55
Monolayer-protected Ag clusters (<1 nm size)	CCl_4, $C_6H_5CH_2Cl$ and $CHCl_3$	Catalytic degradation	2-Propanol + water, 28 °C	AgCl, C, acetone and CCl_3COOH	Complete destruction within 3 h	Present study

$$Ag_9MSA_7(aq.) + (CH_3)_2CHOH + CCl_4 \rightarrow C + AgCl\downarrow + (CH_3)_2CO + 2H^+$$

B. Supported clusters. Clusters supported on neutral alumina were also used for the study of degradation of CCl_4. Reaction products were characterized by XRD, Raman and SEM EDAX. XRD (Fig. S5A†) confirms the formation of AgCl and Raman analysis (Fig. S5B†) reveals the presence of the carbonaceous material due to the degradation of halocarbon. EDAX analysis shows clearly the presence of Cl, Ag and S (Fig. S6†). The quantification table of elements also supports the formation of AgCl which shows the silver to chlorine atomic ratio as 1 : 1 (inset of Fig. S6†). Other halocarbons like $CHCl_3$ and $C_6H_5CH_2Cl$ were also degraded by unsupported and supported clusters giving silver chloride and amorphous carbon as the products (data are not shown). Time taken for complete destruction of $CHCl_3$ is comparable to the CCl_4 case, whereas for benzyl chloride, it was more. The possible reason is its complete immiscibility in the reaction mixture. XPS data of the reaction products of benzyl chloride and clusters are shown in Fig. 7A and B. A survey spectrum indicates the presence of elements C, O, Ag, S and Cl (Fig. 7A). The peak of Ag $3d_{5/2}$ at 367.7 eV confirms the presence of silver in the +1 oxidation state formed due to the reaction (Fig. 7B). The chemical change of the monolayer has been confirmed by the presence of S $2p_{3/2}$ at

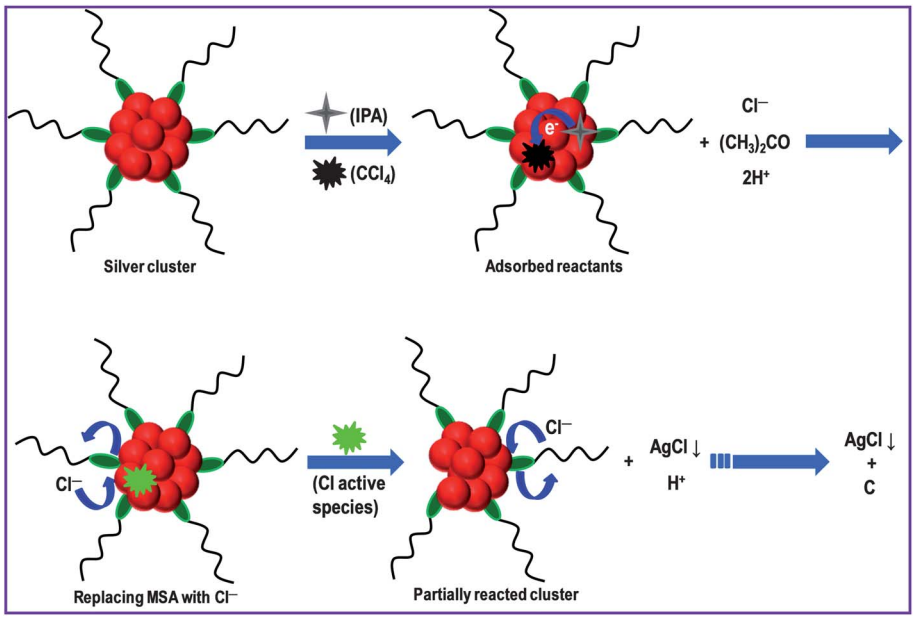

Scheme 1 Schematic representation of the degradation of halocarbon, CCl_4, by silver clusters along with other chemical transformations. All the chemical species detected are not marked.

168.5 eV (inset of Fig. 7A). The nature of Cl has been understood from the peak of Cl $2p_{3/2}$ at 198.2 (inset of Fig. 7A). This is due to Cl^- from AgCl. It is important to recall that as the reaction was complete in this case, no unreacted chlorine feature was detected.

It is good to compare the efficiency of degradation of halocarbons by quantum clusters with the corresponding nanoparticles. For that, the same quantities (25 mg) of clusters and nanoparticles were used for the degradation of 5 mL of CCl_4 under the same experimental conditions. Surprisingly, in the case of clusters, the color of the mixture disappeared after 1.5 h accompanied by the formation of a grey colored precipitate (Fig. 7C). But, in the case of nanoparticles, reddish black color turned to pale brown. No precipitate of AgCl was seen after 1.5 h, and CCl_4 remained at the bottom, as marked in Fig. 7b[1]. The color change reflects progress in the reaction. The color change and the presence of CCl_4 confirm that clusters are more efficient for the degradation reaction. Degradation of chlorocarbons by other relevant nanomaterials is compared in Table 1. This suggests that quantum clusters of silver are good candidates for efficient degradation of chlorocarbons. Other materials need light, high temperatures, *etc.* whereas in our study we show the possibility of degradation at room temperature by simple mixing.

Mechanism

We propose the following mechanism on the basis of experimental observations. After addition of IPA and CCl_4 to the cluster solution, adsorption of both would occur on the surface of the cluster. Clusters play two important roles: one in catalyzing the oxidation of IPA and the other in activating the halocarbon. Formation of acetone from IPA due to catalytic oxidation (on the surface of the cluster) has been confirmed by UV/Vis spectroscopic analysis during the reaction. The control experiment, *i.e.*, a mixture of clusters (in water) and IPA, reveals that there is no formation of acetone. Mixture of IPA and CCl_4 also does not lead to the formation of acetone with time. These observations clearly indicate the necessity of an electron acceptor for the facile formation of H^+ as indicated by the decrease in pH of the solution. Activation of the C–Cl bond of chlorocarbon may occur on the surface of the cluster as reported previously in the case of noble metals.[56] The electrons released in the oxidation of IPA are abstracted by activated CCl_4 on the surface leading to the formation of Cl^- and other active Cl species which may act as oxidizing agents. The Cl^- formed may replace some of the MSA ligands similar to a report wherein phenylethane thiolate on Au cluster was replaced by the halide ion.[57] As MSA is replaced by Cl^-, stability of the cluster is lost which makes silver to react to form crystalline AgCl. Once one Ag atom from a cluster is removed to form AgCl, the other silver atoms also take part in the reaction. The final pH of the reaction mixture is acidic which may also facilitate the mineralization of CCl_4. The molecules of the monolayer which are detached from the cluster surface will be oxidized in the solution to form stable sulphate/sulphite species (confirmed by XPS). The process is schematically represented in Scheme 1.

Summary and conclusions

In summary, we have studied the reaction of monolayer-protected atomically precise silver clusters and nanoparticles with halocarbons at room temperature. The presence of reaction products, silver chloride, CCl_3COO^- and amorphous carbon, was confirmed by various spectroscopic and microscopic tools. A possible mechanism for the reaction is proposed accounting for the observed products. The efficiency of clusters in degrading halocarbons is considerably higher than the corresponding nanoparticles. This was attributed to the smaller size and reduced nobility of silver. Control experiments and the measurement of pH were carried out to validate the proposed mechanism. A limitation of this material is the non-reusability. But the reaction product AgCl can be recovered and used to make metallic silver or silver clusters back again.

Acknowledgements

We thank the Department of Science and Technology (DST), Government of India, for constantly supporting our research program on nanomaterials. M.S.B. thanks the CSIR for a senior research fellowship.

References

1 R. Jin, *Nanoscale*, 2010, **2**, 343–362.
2 P. L. Xavier, K. Chaudhari, A. Baksi and T. Pradeep, *Nano Rev.*, 2012, **3**, 14767.
3 O. M. Bakr, V. Amendola, C. M. Aikens, W. Wenseleers, R. Li, N. L. Dal, G. C. Schatz and F. Stellacci, *Angew. Chem., Int. Ed.*, 2009, **48**, 5921–5926.
4 S. Kumar, M. D. Bolan and T. P. Bigioni, *J. Am. Chem. Soc.*, 2010, **132**, 13141–13143.
5 T. U. B. Rao and T. Pradeep, *Angew. Chem., Int. Ed.*, 2010, **49**, 3925–3929.
6 A. George, E. S. Shibu, S. M. Maliyekkal, M. S. Bootharaju and T. Pradeep, *ACS Appl. Mater. Interfaces*, 2012, **4**, 639–644.
7 M. Zhu, H. Qian, X. Meng, S. Jin, Z. Wu and R. Jin, *Nano Lett.*, 2011, **11**, 3963–3969.
8 Y. Lei, F. Mehmood, S. Lee, J. Greeley, B. Lee, S. Seifert, R. E. Winans, J. W. Elam, R. J. Meyer, P. C. Redfern, D. Teschner, R. Schloegl, M. J. Pellin, L. A. Curtiss and S. Vajda, *Science*, 2010, **328**, 224–228.
9 K.-I. Shimizu, R. Sato and A. Satsuma, *Angew. Chem., Int. Ed.*, 2009, **48**, 3982–3986.
10 M. M. A. Habeeb, P. K. Verma, S. K. Pal, A. Retnakumari, M. Koyakutty, S. Nair and T. Pradeep, *Chem.–Eur. J.*, 2010, **16**, 10103–10112.
11 Y. Lu and W. Chen, *Chem. Soc. Rev.*, 2012, **41**, 3594–3623.
12 M. M. A. Habeeb and T. Pradeep, *Chem. Phys. Lett.*, 2007, **449**, 186–190.
13 T. Udayabhaskararao, Y. Sun, N. Goswami, S. K. Pal, K. Balasubramanian and T. Pradeep, *Angew. Chem., Int. Ed.*, 2012, **51**, 2155–2159.
14 C. Kumara and A. Dass, *Nanoscale*, 2011, **3**, 3064–3067.

15 M. A. H. Muhammed, P. K. Verma, S. K. Pal, R. C. A. Kumar, S. Paul, R. V. Omkumar and T. Pradeep, *Chem.–Eur. J.*, 2009, **15**, 10110–10120.
16 M. S. Bootharaju and T. Pradeep, *Langmuir*, 2011, **27**, 8134–8143.
17 I. Chakraborty, T. Udayabhaskararao and T. Pradeep, *J. Hazard. Mater.*, 2012, **211–212**, 396–403.
18 Y. Liu, K. Ai, X. Cheng, L. Huo and L. Lu, *Adv. Funct. Mater.*, 2010, **20**, 951–956.
19 B. Schrick, J. L. Blough, A. D. Jones and T. E. Mallouk, *Chem. Mater.*, 2002, **14**, 5140–5147.
20 E. Sumesh, M. S. Bootharaju, Anshup and T. Pradeep, *J. Hazard. Mater.*, 2011, **189**, 450–457.
21 W. Zheng, J. Lichwa, M. D'Alessio and C. Ray, *Chemosphere*, 2009, **76**, 1167–1177.
22 C. Kroeze and L. Reijnders, *Sci. Total Environ.*, 1992, **112**, 269–290.
23 W.-Y. Xu and T.-Y. Gao, *J. Environ. Sci.*, 2007, **19**, 792–799.
24 G. W. Reynolds, J. T. Hoff and R. W. Gillham, *Environ. Sci. Technol.*, 1990, **24**, 135–142.
25 C. A. Keller, M. Hill, M. K. Vollmer, S. Henne, D. Brunner, S. Reimann, S. O'Doherty, J. Arduini, M. Maione, Z. Ferenczi, L. Haszpra, A. J. Manning and T. Peter, *Environ. Sci. Technol.*, 2011, **46**, 217–225.
26 C. E. Jones and L. J. Carpenter, *Environ. Sci. Technol.*, 2005, **39**, 6130–6137.
27 T.-K. Tseng, H. Chu and H.-H. Hsu, *Environ. Sci. Technol.*, 2002, **37**, 171–176.
28 Q. Xiang, J. Yu, B. Cheng and H. C. Ong, *Chem.–Asian J.*, 2010, **5**, 1466–1474.
29 X. Zhou, G. Liu, J. Yu and W. Fan, *J. Mater. Chem.*, 2012, **22**, 21337–21354.
30 O. Koper, I. Lagadic and K. J. Klabunde, *Chem. Mater.*, 1997, **9**, 838–848.
31 J. Farrell, M. Kason, N. Melitas and T. Li, *Environ. Sci. Technol.*, 1999, **34**, 514–521.
32 M. I. Litter, W. Choi, D. D. Dionysiou, P. Falaras, A. Hiskia, G. Li Puma, T. Pradeep and J. Zhao, *J. Hazard. Mater.*, 2012, **211–212**, 1–2.
33 I. V. Mishakov, V. I. Zaikovskii, D. S. Heroux, A. F. Bedilo, V. V. Chesnokov, A. M. Volodin, I. N. Martyanov, S. V. Filimonova, V. N. Parmon and K. J. Klabunde, *J. Phys. Chem. B*, 2005, **109**, 6982–6989.
34 C. L. Carnes and K. J. Klabunde, *Langmuir*, 2000, **16**, 3764–3772.
35 A. S. Nair and T. Pradeep, *Curr. Sci.*, 2003, **84**, 1560–1564.
36 A. S. Nair and T. Pradeep, *Indian Pat.*, 200767, 2006.
37 A. S. Nair and T. Pradeep, *U. S. Pat.*, 7,968,493B962, 2011.
38 A. S. Nair and T. Pradeep, *J. Nanosci. Nanotechnol.*, 2007, **7**, 1871–1877.
39 M. S. Bootharaju and T. Pradeep, *Langmuir*, 2012, **28**, 2671–2679.
40 T. Pradeep and Anshup, *Thin Solid Films*, 2009, **517**, 6441–6478.
41 E. S. Shibu and T. Pradeep, *Chem. Mater.*, 2011, **23**, 989–999.
42 T. U. B. Rao, B. Nataraju and T. Pradeep, *J. Am. Chem. Soc.*, 2010, **132**, 16304–16307.
43 R. John, A. Ashokreddy, C. Vijayan and T. Pradeep, *Nanotechnology*, 2011, **22**, 165701.
44 K. N. Kudin, B. Ozbas, H. C. Schniepp, R. K. Prud'homme, I. A. Aksay and R. Car, *Nano Lett.*, 2007, **8**, 36–41.
45 V. Palshin, E. I. Meletis, S. Ves and S. Logothetidis, *Thin Solid Films*, 1995, **270**, 165–172.
46 D. Fan, C. Zhang, J. He, R. Hua, Y. Zhang and Y. Yang, *J. Mater. Chem.*, 2012, **22**, 18564–18571.
47 M. S. Bootharaju and T. Pradeep, *J. Phys. Chem. C*, 2010, **114**, 8328–8336.
48 H. Zhang, Q. Fu, Y. Yao, Z. Zhang, T. Ma, D. Tan and X. Bao, *Langmuir*, 2008, **24**, 10874–10878.
49 H. Piao, K. Adib, Z. Chang, J. Hrbek, M. Enever, M. A. Barteau and D. R. Mullins, *J. Phys. Chem. B*, 2003, **107**, 13976–13985.
50 A. Henglein, B. G. Ershov and M. Malow, *J. Phys. Chem.*, 1995, **99**, 14129–14136.
51 K. D. Warren, R. G. Arnold, T. L. Bishop, L. C. Lindholm and E. A. Betterton, *J. Hazard. Mater.*, 1995, **41**, 217–227.
52 Y. Ukisu, S. Iimura and R. Uchida, *Chemosphere*, 1996, **33**, 1523–1530.
53 W. Choi and M. R. Hoffmann, *Environ. Sci. Technol.*, 1996, **31**, 89–95.
54 Y. Xu and W.-X. Zhang, *Ind. Eng. Chem. Res.*, 2000, **39**, 2238–2244.
55 G. Liu, J. Wang, Y. Zhu and X. Zhang, *Phys. Chem. Chem. Phys.*, 2004, **6**, 985–991.
56 H. Imai, T. Nishiguchi, M. Tanaka and K. Fukuzumi, *J. Org. Chem.*, 1977, **42**, 2309–2313.
57 M. Zhu, G. Chan, H. Qian and R. Jin, *Nanoscale*, 2011, **3**, 1703–1707.

Electronic Supplementary Material (ESI) for Journal of Materials Chemistry A

Electronic supplementary information

Atomically precise silver clusters for efficient chlorocarbon degradation

M. S. Bootharaju,[a] G. K. Deepesh,[a] T. Udayabhaskararao and T. Pradeep*

DST Unit of Nanoscience (DST UNS), Department of Chemistry,

Indian Institute of Technology Madras, Chennai - 600 036, India

***E-mail: pradeep@iitm.ac.in**

[a]These authors have contributed equally

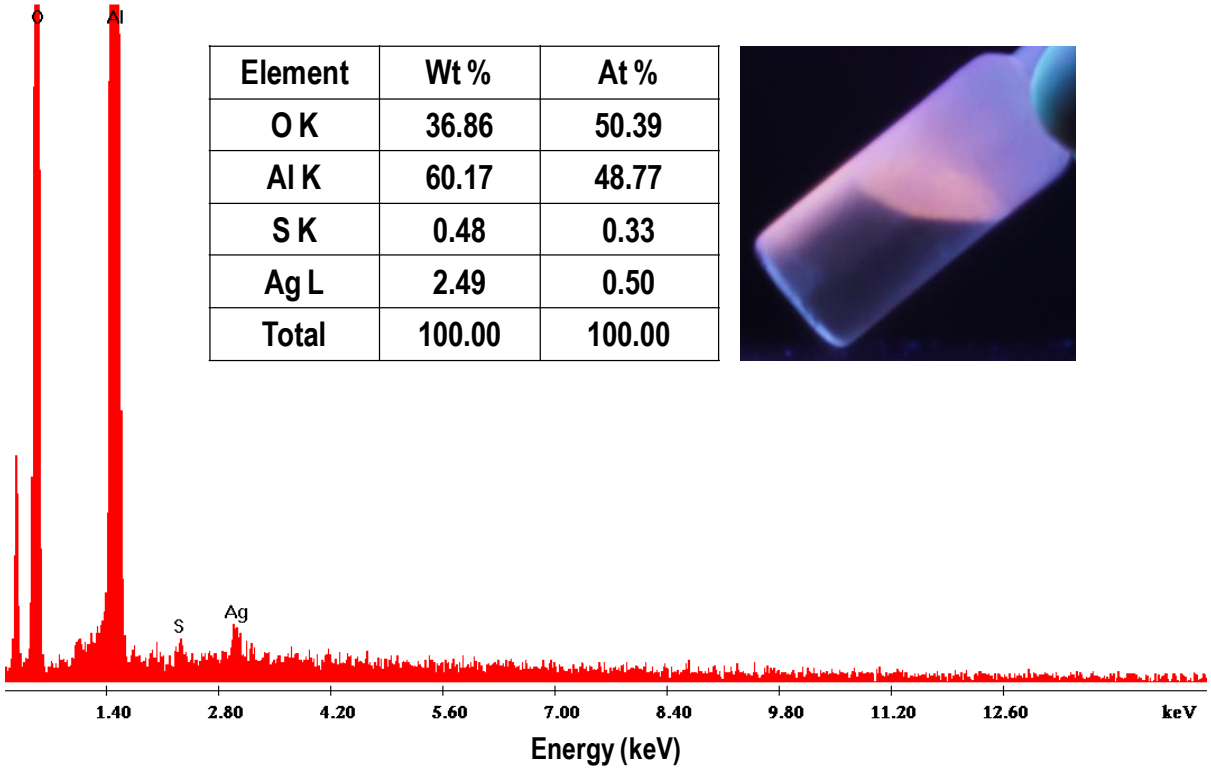

Element	Wt %	At %
O K	36.86	50.39
Al K	60.17	48.77
S K	0.48	0.33
Ag L	2.49	0.50
Total	100.00	100.00

Fig. S1 EDAX spectrum of supported Ag_9MSA_7 clusters which confirms the presence of Ag and S from the cluster on alumina. Insets are the quantification table of elements and a photograph of supported Ag_9MSA_7 clusters under UV lamp. Photograph was taken after dipping the sample bottle in liquid nitrogen. The blue scattered light around the glass bottle is due to scattering from condensed moisture. The emission of the cluster is red.

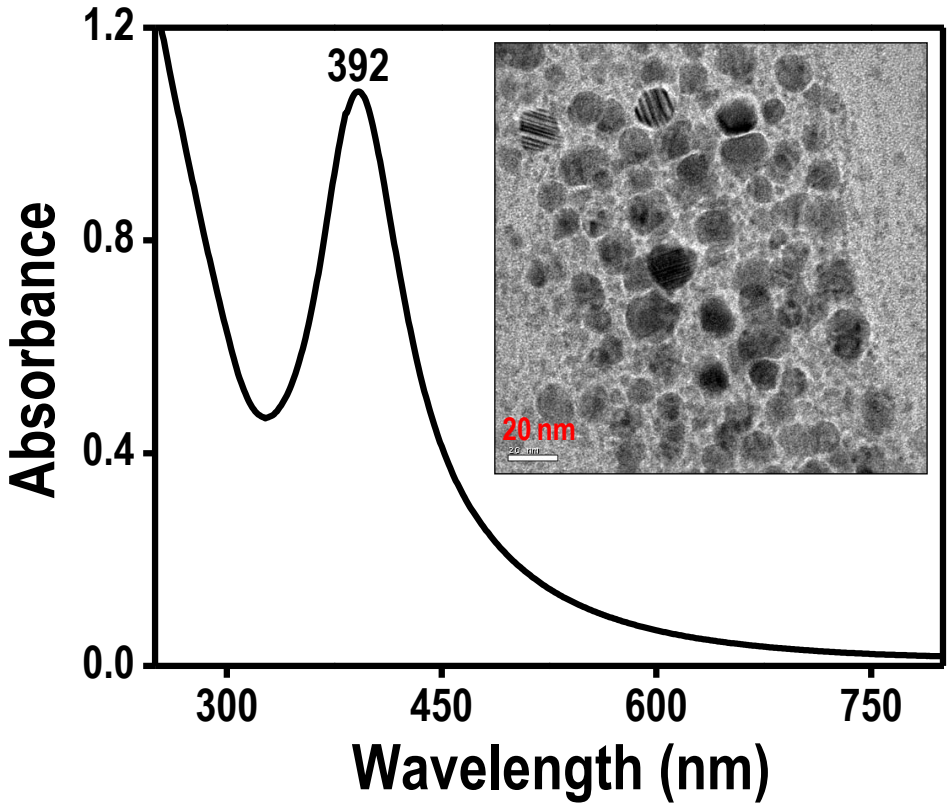

Fig. S2 UV/Vis absorption spectrum of as-synthesized Ag@MSA nanoparticles. Inset is a TEM image of Ag@MSA nanoparticles.

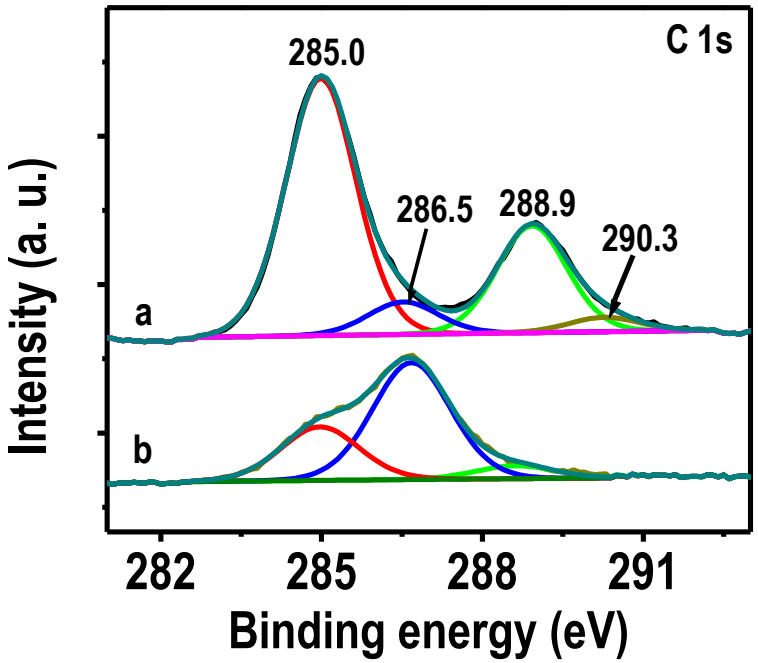

Fig. S3 C 1s region of the XPS of parent Ag_9MSA_7 clusters (a) and the product (b) obtained after the reaction of clusters with CCl_4.

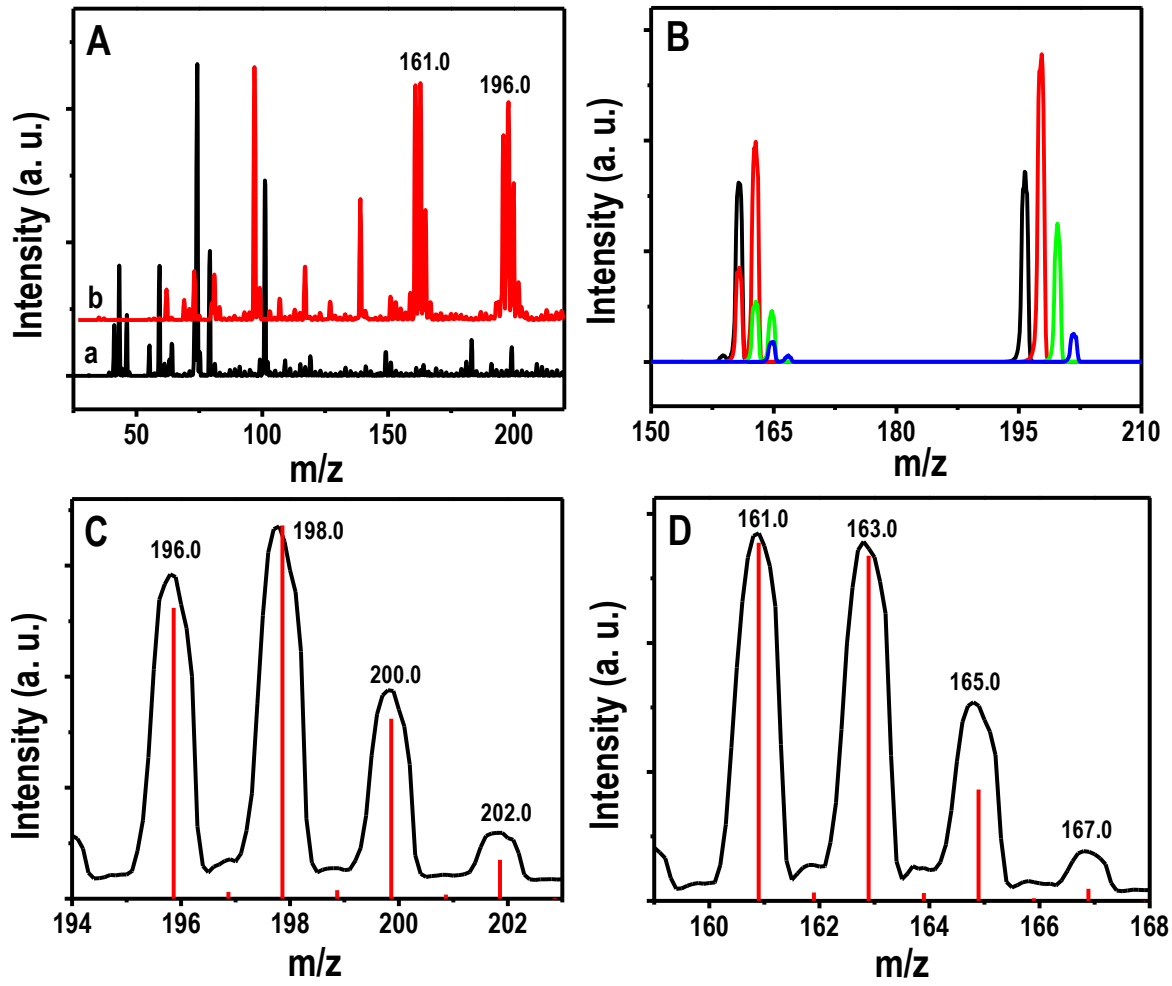

Fig. S4 A) ESI MS of reaction mixture of Ag_9MSA_7 and CCl_4 in positive and negative modes (traces a and b, respectively). B is MS/MS of m/z 196.0, 198.0, 200.0 and 202.0 in negative mode. C and D are comparisons of experimental (black traces) and calculated spectra (red traces) for species CCl_4COO^- and CCl_3COO^-, respectively.

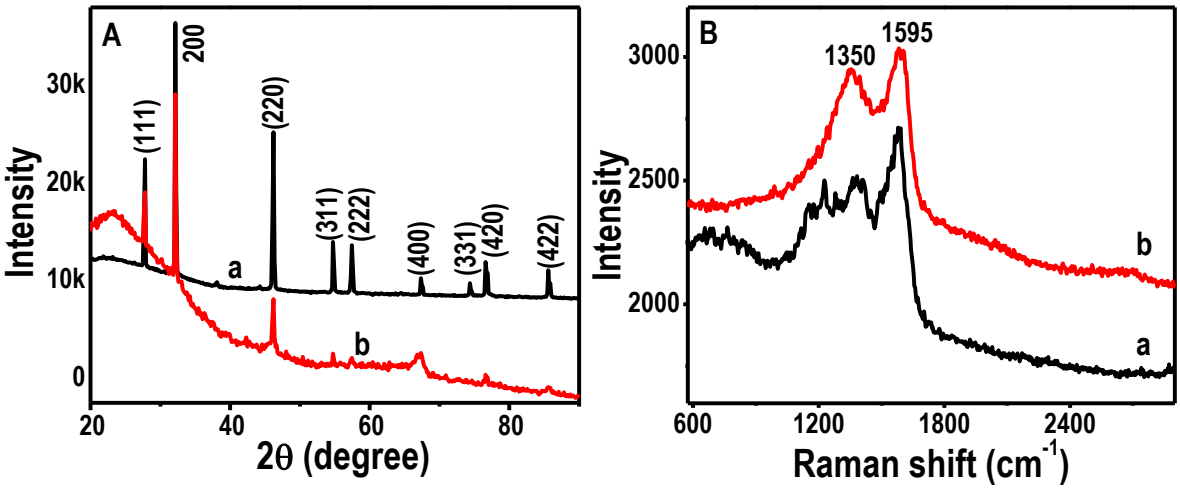

Fig. S5 A) Comparison of XRD patterns of as-prepared AgCl (a) and reaction product (b) of CCl_4 and supported clusters. B) Raman spectra of the reaction product of CCl_4 and supported clusters before (a) and after (b) washing with ammonia solution.

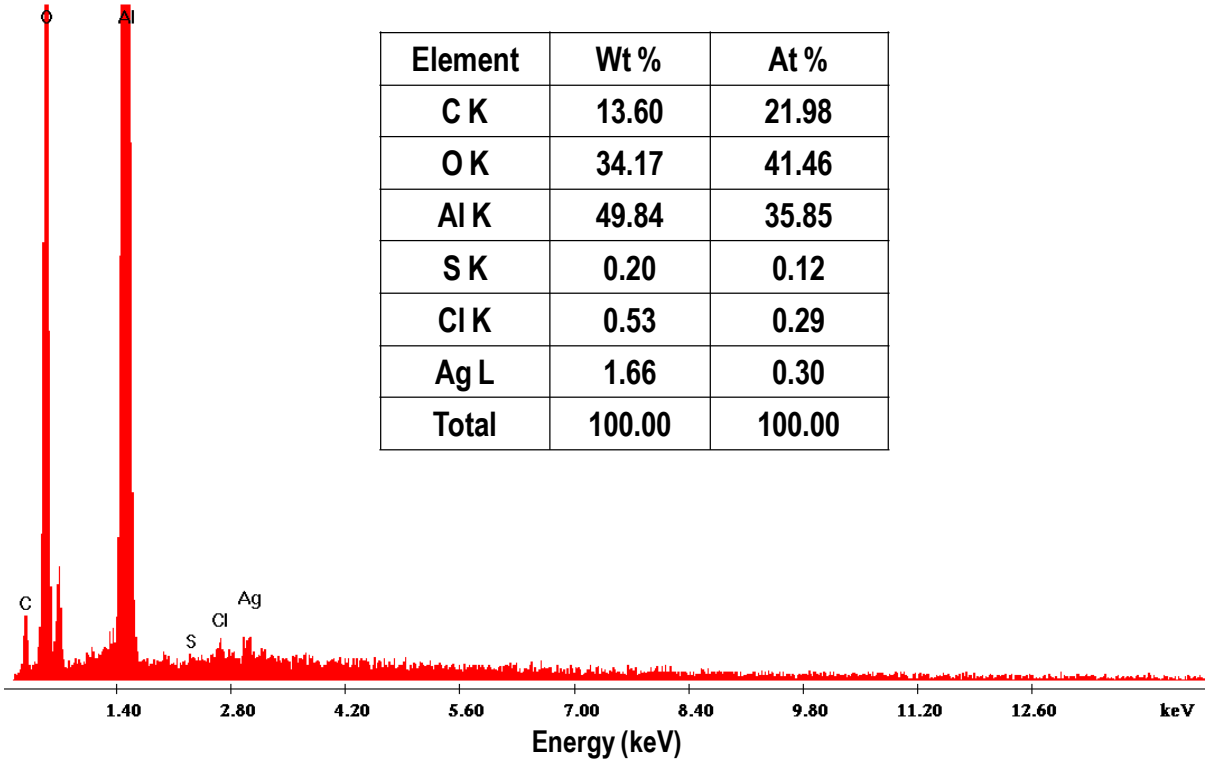

Element	Wt %	At %
C K	13.60	21.98
O K	34.17	41.46
Al K	49.84	35.85
S K	0.20	0.12
Cl K	0.53	0.29
Ag L	1.66	0.30
Total	100.00	100.00

Fig. S6 EDAX spectrum of the reaction product of CCl_4 and supported clusters showing the presence of Cl, Ag and S. Inset is a quantification table of elements which shows that the atomic ratio of Ag to S is 1:1.

Journal of Hazardous Materials 246–247 (2013) 213–220

Contents lists available at SciVerse ScienceDirect

Journal of Hazardous Materials

journal homepage: www.elsevier.com/locate/jhazmat

Immobilized graphene-based composite from asphalt: Facile synthesis and application in water purification

Theruvakkattil Sreenivasan Sreeprasad[a], Soujit Sen Gupta[a], Shihabudheen Mundampra Maliyekkal[b], Thalappil Pradeep[a,*]

[a] DST Unit on Nanoscience, Department of Chemistry, Indian Institute of Technology Madras, Chennai 600036, India
[b] School of Mechanical and Building Sciences, VIT University, Chennai Campus, Chennai 600048, India

HIGHLIGHTS

- Facile strategy to make graphenic materials from cheaper precursor such as asphalt.
- Material can be made in solution; also as anchored on solid substrates.
- The synthesized material, GSC, was found to be excellent for water purification.
- The applicability was demonstrated through batch and laboratory columns experiments.
- The capacity was compared to other similar adsorbents and was found to be superior.

GRAPHICAL ABSTRACT

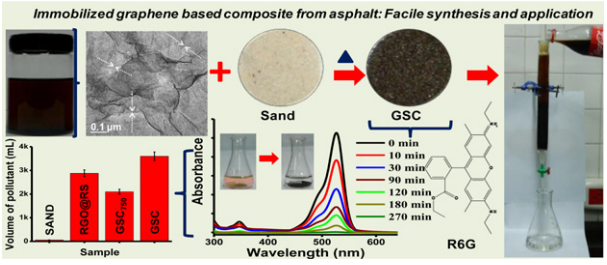

ARTICLE INFO

Article history:
Received 12 October 2012
Received in revised form 4 December 2012
Accepted 11 December 2012
Available online 20 December 2012

Keywords:
Adsorption
Graphene-sand composite
Pesticide removal
Water purification
Asphalt

ABSTRACT

An in situ strategy for the preparation of graphene immobilized on sand using asphalt, a cheap carbon precursor is presented. The as-synthesized material was characterized in detail using various spectroscopic and microscopic techniques. The presence of G and D bands at 1578 cm^{-1} and 1345 cm^{-1} in Raman spectroscopy and the 2D sheet-like structure with wrinkles in transmission electron microscopy confirmed the formation of graphenic materials. In view of the potential applicability of supported graphenic materials in environmental application, the as-synthesized material was tested for purifying water. Removal of a dye (rhodamine-6G) and a pesticide (chlorpyrifos), two of the important types of pollutants of concern in water, were investigated in this study. Adsorption studies were conducted in batch mode as a function of time, particle size, and adsorbent dose. The continuous mode experiments were conducted in multiple cycles and they confirmed that the material can be used for water purification applications. The adsorption efficacy of the present adsorbent system was compared to other reported similar adsorbent systems and the results illustrated that the present materials are superior. The adsorbents were analyzed for post treatment and their reusability was evaluated.

1. Introduction

Graphene, a 2D sheet made up of extended carbon network, or their chemical analogs are promising adsorbents [1–7] and have great potential in water purification due to their unique physical and chemical properties including high surface area [8], antibacterial properties [9,10] and lesser cytotoxicity compared to carbon nanotubes [11,12]. However, the immediate use of graphenic materials for down-to-earth applications such as water purification is limited mainly due to the difficulty in large-scale synthesis and post treatment-handling, including solid–liquid separation [6,13].

* Corresponding author. Tel.: +91 44 2257 4208; fax: +91 44 2257 0545/0509.
E-mail address: pradeep@iitm.ac.in (T. Pradeep).

0304-3894/$ – see front matter © 2012 Elsevier B.V. All rights reserved.
http://dx.doi.org/10.1016/j.jhazmat.2012.12.022

Discovery of chemical routes to produce graphenic materials by the oxidation of graphite to graphite oxide (GO) [14] and subsequent reduction to reduced graphene oxide (RGO), closely resembling graphene with extended double bonded sp^2 carbon network with edge carboxylic acid moieties [15–19] opened up the pathway for mass production of RGO. Recently, we have shown that RGO and chemically reduced graphene can be bound on cheap substrate such as river sand and such substrates are effective in contaminant removal [6]. In another effort, Gao and coworkers have demonstrated that GO-coated sand, termed as 'super sand', could be used as a low-cost water purification material for the developing economies [20]. The use of GO/RGO supported on silica as adsorbent for solid phase extraction was also reported recently [13]. These materials got wide publicity in the world news due to their likely utility in water purification. These composites were prepared through two-step processes that involve the preparation of graphene through relatively laborious chemical conversion of graphite to graphite oxide [14,21] and subsequent reduction of GO by hydrazine to RGO [15]. In the second step, the GO/RGO was immobilized onto sand via heat treatment [20] or by directly binding them covalently onto silica [13] or by using molecular binders [6]. However, the preparation of RGO involves the use of a variety of chemicals including hydrazine, P_2O_5 and $K_2S_2O_8$ which produces undesirable hazardous products like, P_2O_3, SO_2, etc. This necessitates laborious steps including post-synthesis cleaning. Developing an efficient and eco-friendly graphenic adsorbent generated from a cheaper source is desirable for water purification. Several graphene based composites with metals and metal oxides have also been demonstrated to be useful for this application. As cost is an important criterion in the success of such materials, new approaches for their production are necessary. Efforts have been made to grow graphene from diverse sources. Recent studies show that graphenic material can be synthesized from cheaper sources of carbon, like sugar [7,22] using a modified CVD process [23]. Graphene was also prepared from food, insects, and waste using a similar methodology [24]. This is necessary as chemically different carbon sources are available in different parts of the world. Among these, asphalt and various petroleum products are important to consider. A simple synthetic route is always preferable when it comes to applications such as water purification, where the use of chemicals should be avoided as much as possible.

Here, a method for the in situ preparation of graphenic material anchored on a solid substrate starting from a cheap and locally available material, asphalt, is discussed. A single-step strategy was used to immobilize the graphenic material on sand surface. Application of the as-synthesized material as a water purifying medium is reported using a pesticide and a dye as examples. Synthetic dyes mostly being non-biodegradable can have acute effects on exposed organisms and aquatic life. Exposure to such dyes can cause abnormal coloration and resultant reduction in photosynthetic efficiency. Pesticides, designed to induce acute effects or kill living organisms, are highly toxic to the environment and to all living forms including humans. We have used rhodamine-6G (R6G), a rhodamine dye and chlorpyrifos (CP), an organo-phosphorus pesticide in our studies. The adsorption capacity of the reported adsorbent was compared to several other adsorbents reported and the superiority of the present system is demonstrated. The simple and cost effective methodology adopted here facilitates the preparation of large-scale graphenic material and immobilization of the material on sand surface without any external chemical agents, in a single step. This may open up the practical use of graphenic materials. The solution based processability of the sample has also been demonstrated. However, additional experiments are needed to validate the applications of the material.

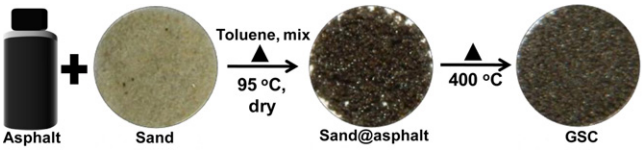

Scheme 1. Schematic illustration of the formation of GSC.

2. Materials and methods

Materials, in situ synthesis of graphene-sand composite (GSC), batch adsorption experiments, fixed-bed column experiments, instrumentation and the mechanism for the formation of graphene are given in supplementary data 1. The process of preparation of GSC starting from asphalt and sand is shown in Scheme 1.

3. Results and discussion

3.1. Characterization of the graphene-sand composite (GSC)

GSC was characterized using different microscopic techniques. Fig. 1A and B shows the SEM image of the prepared composite. The sheet-like structure covering the surface of the sand particles indicate the formation of graphenic material. Asphalt coated samples before heating had a sticky coating over the surface and formed aggregated clusters (insets in Fig. 1A and B). To understand the elemental composition of the material, the composite was analyzed using EDAX (Fig. 1C), where, we can see that the major elements present are carbon, silicon and oxygen. Inset in Fig. 1C shows the SEM image of a GSC particle and the corresponding elemental maps. Si and O features are due to sand (SiO_2). The large C feature points to the presence of graphenic material formed over the sand surface.

The (0 0 2) diffraction of graphite (0 0 2) appears at ~26° (2θ) in CuKα powder X-ray diffraction (XRD) and as it is getting exfoliated, due to the increase in inter-layer spacing, this feature is known to occur at lower values. Fully exfoliated graphite oxide is known to show this feature around 11°. River sand, used as a substrate in this study, also showed a feature in the same region and at lower carbon contents, no feature corresponding to graphene was observed. Graphenic material formed in the study was treated with

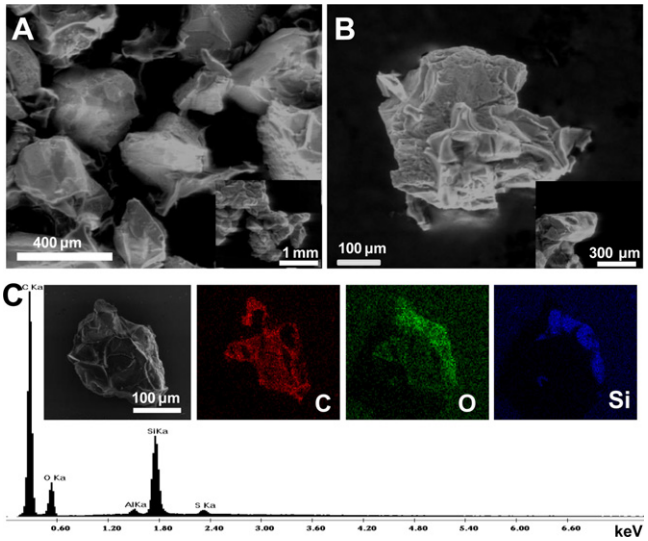

Fig. 1. (A and B) SEM images and (C) EDAX spectrum and the corresponding elemental maps of GSC (5% loading). A higher loading was used for getting a more clear observation of the film in SEM and EDAX mapping. Insets in (A) and (B) show the corresponding asphalt coated samples before heating. Clustered particles can be seen in the expanded figure.

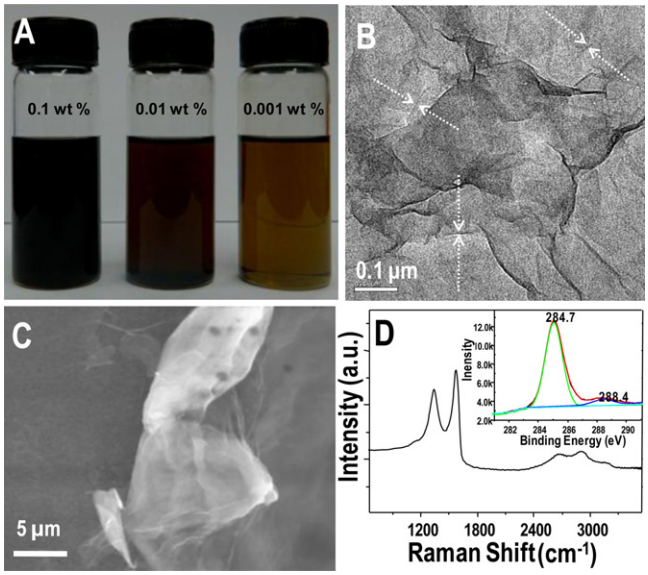

Fig. 2. (A) Photographs of the prepared graphenic material dispersed in toluene at different wt% of initial asphalt. (B) TEM and (C) SEM images of a graphene sheet and (D) Raman spectra taken from the sample showing the D and G band. Inset shows the XPS spectrum in the C 1s region. The TEM image shows foldings of 2 nm thickness (marked).

acid and has undergone heat treatment as well. Hence, the multilayer structures getting formed in the study are expected to have higher d-spacing compared pristine graphite. Our observations are consistent with these. A new peak was seen around 22° for GSC of 2% loading and at 24° for GSC having 5% loading. This was attributed to (0 0 2) diffraction of multilayer graphenic structures. XRD data of GSC at these two carbon loadings and a comparison with bare river sand is included in supplementary data, Fig. S2.

The possibility of producing graphenic material in dispersed phase was also investigated. The procedure employed for the preparation of GSC was carried without the presence of sand. The material obtained was suspended in N-Methyl-2-pyrrolidone (NMPs) by mild sonication, which points to the non-polar nature of the material. Hence, the presence of oxygen functionalities can be neglected [25]. This material was analyzed using microscopic and spectroscopic techniques. Fig. 2A shows the dispersibility of the material in NMP. Near perfect colloidal dispersions of the material at different weight percentages can be seen in the figure. Fig. 2B shows the TEM taken from such a sample (0.0005 wt%). We can see large sheets spread over μm^2 area. Large number of wrinkles, which characterize graphene, can be seen on the surface confirming that the material prepared is graphenic, comprising of thin sheets. However, in some areas of the grid thicker sheets were also seen. Fig. 2C shows the SEM image of such a thick film spread over μm^2 area. Hence, we can conclude that the present methodology predominantly gives multi-layer graphenic structures. The sample was analyzed using Raman and XPS as well (Fig. 2D). Raman spectrum clearly showed a prominent G band and a less intense D band at 1578 and 1345 cm^{-1}, respectively. The presence of such a peak again points to the material being graphenic in nature. The presence of D band points toward the presence of defects. We attribute these defects to structural defects other than those arising from the presence of oxygen functionalities. Moreover, most of the functionalities are unstable at 400 °C. In the present methodology, due to the presence of multilayers, a larger number of grains can be present, giving rise to the D-band observed. The 2D region had a broad feature similar to chemically prepared graphene (RGO). Presence of the D-band (and the associated D + D′ band) and the presence multi-layer structure might be reducing the intensity of 2D band. To confirm the absence of oxygen functionalities, the sample was analyzed using XPS. The inset of Fig. 2D, shows the deconvoluted XPS spectrum in the carbon 1s region of the prepared material. We can clearly see that the carbon is unfunctionalized, nearly completely.

As the main theme of this work being the creation of a cheap graphenic adsorbent for water purification, the supported composite was analyzed in more detail. The material was characterized using Raman and XPS extensively. Fig. 3A shows the Raman spectra at different stages of GSC preparation. Initial sand showed a prominent feature at 470 cm^{-1} (due to SiO_2). However, upon coating with asphalt, all the features disappeared (curve ii in Fig. 3A). Only a large fluorescence background due to asphalt was seen. Upon heating the particle at 250 °C (curve iii), a small G-band started to appear. Still, the large fluorescence background was persistent. Curve iv shows the Raman spectrum of the final GSC sample. The sample clearly showed a prominent G-band centered at 1578 cm^{-1} and a less prominent D-band at 1345 cm^{-1} pointing to the formation of graphenic material. The peak at 470 cm^{-1} confirmed the presence of sand. The resulting sample was compared with RGO supported on river-sand sample (RGO@RS) prepared through the methodology reported earlier [6]. Curve v shows the Raman spectra collected from RGO@RS. We can see that there are close similarities between the samples, indicating that the GSC prepared is closely related to the graphenic adsorbent in the literature [6,19]. On closer examination we can see that the intensity of the D band is much lesser in GSC, indicating the lesser extent of defects in the sample compared to RGO@RS. It is proposed that this may be due to the absence of oxygen functionalities in GSC. We can also see that the 2D region is more prominent in GSC compared to RGO@RS. Hence, it might be proposed that graphene formed in the present case is of better quality than RGO.

Panel B in Fig. 3 shows the XPS of GSC at different stages of synthesis. Fig. 3B a1 shows the survey spectrum of the asphalt coated sand sample. The C 1s region of the same sample is given in a2. We can see that the carbon is highly functionalized with several components other than the most prominent peak at 284.5 eV (a2). The survey spectra (b1 and c1) show that as the heating and acid treatment is done to the sample, most of the oxygen is getting removed from the sample. This is expected since the thermal stability of most of the functional groups is lesser than the temperature used and due to the use of strong dehydrating agent (H_2SO_4). Upon heating at 400 °C, these extra features disappeared to give a single component (b2). After acid wash also only one component was seen for C 1s (c2) showing that the carbon is mostly unfunctionalized.

Carbon loading on GSC was calculated using TGA (supplementary data Fig. S3). Pristine sand did not show any weight loss when subjected to heat treatment. However, for 2 wt% asphalt loaded sand, there was a weight loss of about 0.8% indicating the removal of functional groups in asphalt leaving behind pure carbon. Using this, the exact carbon content on GSC was calculated and different sets of composites with varying loading (wt% loading) and varying sand particle size were prepared. Fig. 4 shows the SEM images of GSC having different carbon loading. The sand particles to begin with were pretty clean and had no covering on the surface (supplementary data Fig. S4). As the loading of graphene was increased, a layer was progressively visible on the surface (details are given in supplementary data 5). Similarly, GSC with different sand particle size having the same loading was also prepared (supplementary data Fig. S6).

3.2. Batch adsorption experiments

3.2.1. Parameter optimization

In this study, the R6G removal performance of the material synthesized at various conditions were tested. The variables in

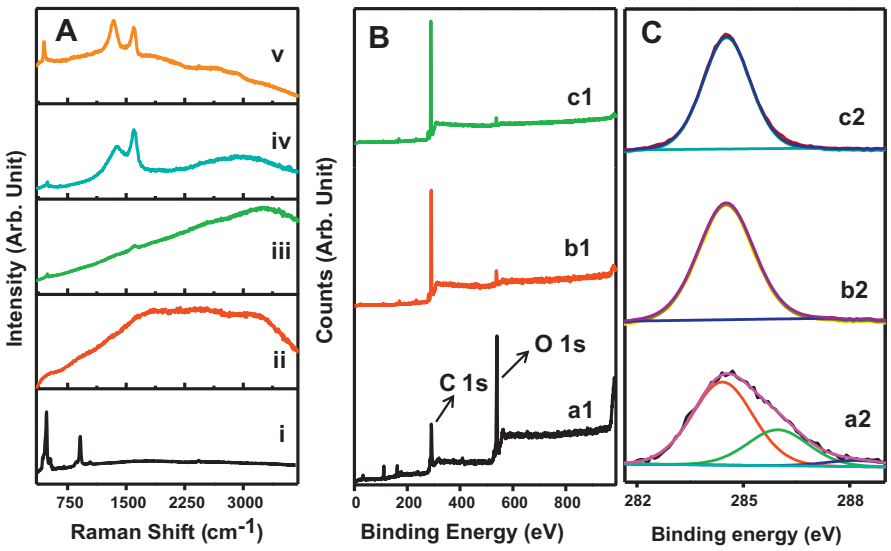

Fig. 3. (A) Raman spectra at different stages of preparation of GSC. (i) Sand, (ii) asphalt coated sand, (iii) heated at 250 °C, (iv) GSC and (v) RGO@RS. (B and C) XPS analysis of GSC at different stages. a1, b1 and c1 are the survey spectra and a2, b2, and c2 are the corresponding C 1s spectra: (a1 and a2) asphalt coated sand, (b1 and b2) asphalt coated sand particles heated at 400 °C before acid wash and (c1 and c2) after acid wash (GSC).

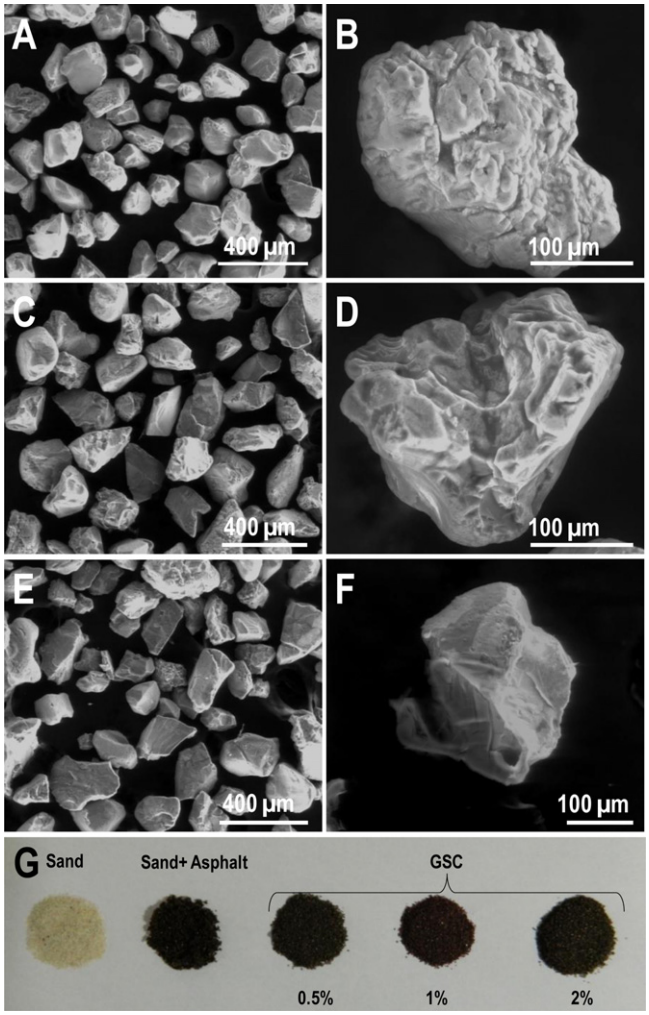

Fig. 4. SEM images (larger and small area) of GSC having different carbon loading (A and B) 0.2, (C and D) 0.5 and (E and F) 1 wt% of graphenic carbon. (G) Photographs of pristine sand, sand coated asphalt and GSC of different loading.

synthesis were carbon loading, particle size and process temperature. Fig. 5A shows a direct correlation between the carbon content and adsorption capacity. The maximum uptake was observed at a loading of 1 wt% and further loading did not affect the adsorption capacity greatly. The plausible reason might be that, as the loading increases from 0.2 to 1 wt%, sand surface is progressively getting covered by graphene resulting in large increase in the effective surface area and at 1 wt%, a complete coverage occurs. Upon further increase in loading, only multi-layers are getting formed which do not increase the effective surface area significantly. Hence, no appreciable increase in uptake capacity was observed further.

The effect of sand particle size on the adsorption capacity was also tested (Fig. 5B). As expected, the data show an increase in the uptake with decrease in sand size due to the increase in effective surface area. The synthesis temperature was also optimized through several iterations and the optimum performance was achieved at 400 °C. The auto-ignition temperature of the material is above 400 °C, so further increase in temperature beyond 400 °C in the presence of oxygen was not possible. The temperature was increased to 500 °C under nitrogen atmosphere but it did not show any appreciable increase in graphene quality or adsorption efficiency. Fig. 5C shows the effect of heat treatment as a function of time. The data show an optimum heating time of 4 h and further heating did not change the uptake much. The adsorbent dose was also optimized as a function of pollutant uptake. The percentage capacities increased with increasing dose. This can be attributed to increase in adsorption sites with increasing dose. 100% removal efficiency (for the used pollutant concentration) was observed with an adsorbent dose above 50 g/L (Fig. 5D). With acid treatment, the adsorption capacity of the sample increases significantly (about 12%, supplementary data S7) possibly due to increase in the number of adsorption sites of the composite or due to some electrostatic interaction between GSC and the pollutant [27]. Our recent ab initio calculations have shown that adsorption is likely to be mediated by adsorbed water itself [28]. Still the adsorption mechanism is unclear as far as graphene is concerned.

The CP removal capacity of the adsorbent was also tested. CP had a prominent adsorption peak at 297 nm in the UV/vis spectrum. The change in the spectrum during exposure is shown in Fig. 6A. The kinetics was observed to be faster for the initial stages (up to 120 min) but then slows down significantly. Complete removal (below the detection limit) of CP was assumed when no peak was

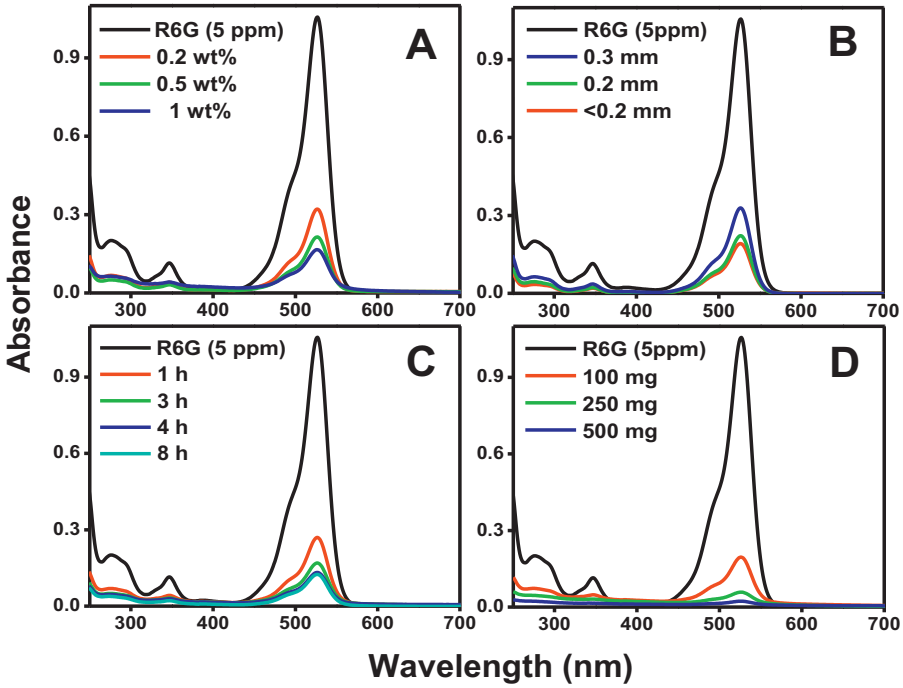

Fig. 5. Effect on adsorption capacity of the composite with change in (A) carbon loading, (B) sand size, (C) heating time and (D) adsorbent dose. The capacity is manifested in terms of the decrease in the absorbance of R6G upon exposure to GSC after an exposure of 1 h.

observed at 297 nm. About 250 mg of GSC (0.5 wt%) removes 4 ppm of CP (10 mL) completely.

The versatility of the adsorbent in removing pollutants/colored materials was further explored with the experiments conducted with Coca-cola. The original Coca-cola after dilution with water (1:20) has an adsorption peak at 274 nm. The decrease in peak height with respect to time confirms that GSC can decolorize Coca-cola as shown in Fig. 6B. Column experiments were also done to confirm the results (supplementary data video1 in S8). It was seen that the adsorption is very fast and 50 cm column of 8 cm length filled with GSC of 1% loading efficiently decolorized 200 mL Coca-cola in 20 min.

3.2.2. Kinetic study

Adsorption rate is an important parameter in designing batch or continuous adsorption process. The pollutant removal was tested as a function of time and the data are shown in Fig. 7. Here, we used R6G as the model pollutant (10 mL) and 500 mg of 1 wt% (loading) of GSC as the adsorbent. As we can see, the kinetic data exhibited rapid removal of R6G. More than 65% of the pollutant was removed in the first 60 min and the system reached pseudo equilibrium in 240 min and further contact did not make noticeable change in the uptake. Control samples were also run to account for any possible natural attenuation and the data showed insignificant effect. Estimation of adsorption rate constants was done by fitting the experimental data with well-known adsorption kinetic models, viz. Langergren pseudo first-order kinetic model [29], and Ho's pseudo-second-order kinetic model [30–32]. The mathematical representations of these models are given in supplementary data 9. The inset in Fig. 7 shows the pseudo first and second order model fitted data along with experimental data. The data analysis and associated error measurements show that pseudo second-order model is more appropriate to describe the system and the data fitted well with more than 99% confidence level.

3.3. Fixed-bed column experiment

Laboratory based fixed bed adsorption studies are important in order to obtain basic engineering data for the design of any

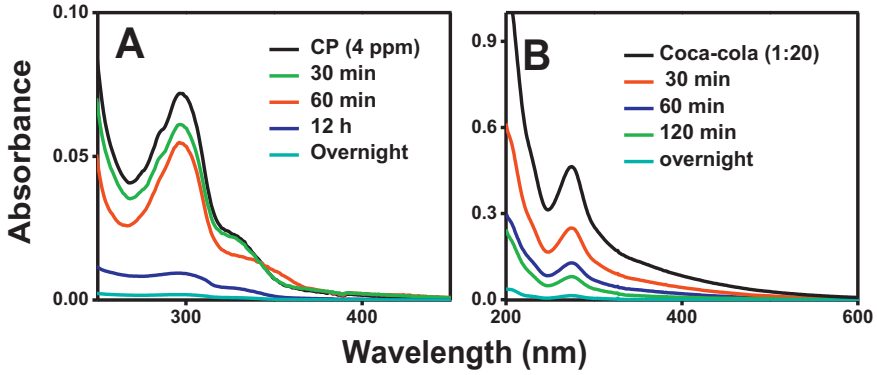

Fig. 6. (A and B) Adsorption experiments using GSC. The adsorbents were CP and Coca-cola, respectively for A and B. A standard Coca-cola sample was diluted 20 times with deionized water.

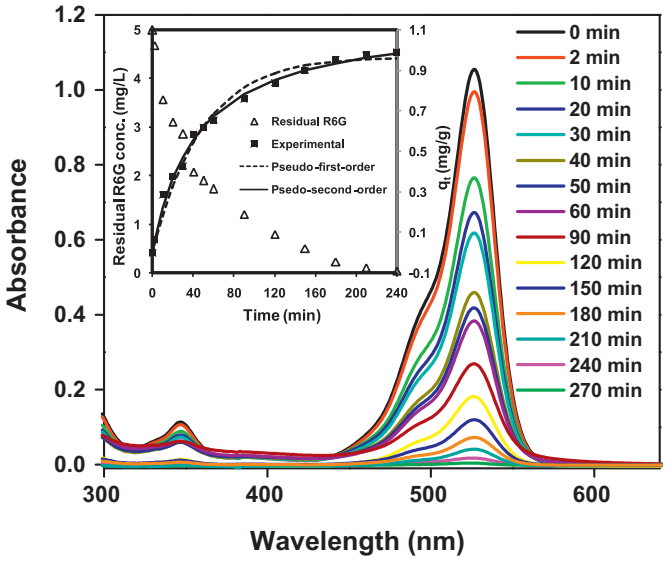

Fig. 7. UV/vis data showing time dependant removal of R6G. The inset shows the removal of R6G as function of time (primary axis). The pseudo and second order model fits are shown in secondary axis. Initial R6G concentration = 1/mg/L; flow rate = 2.3 mL/min.

adsorption column. In this study, removal of R6G from contaminated water using columns packed with GSC was examined. The ratio of column diameter to the diameter of the particles was approximately 100, which is much above the ratio reported to overcome the premature leakage with wall effect [33,34]. Three successive cycles of adsorption and desorption were carried out in situ to test the reusability. After the first adsorption cycle, the bed was regenerated in situ by backwashing with 42 bed volume of acetone at flow rate of 2.3 mL/min followed by purging with hot air to remove the entrapped/adsorbed acetone. Fig. 8A shows the adsorption and desorption breakthrough curves and the data are summarized in Table 1. From the data it is clear that the material can be used in multiple cycles without affecting the adsorption capacity significantly. The reduction in adsorption was found to be less than 5% at the end of the third cycle (Fig. 8B).

3.4. Comparison study

The superiority of our material over other similar absorbents was investigated. We compared the adsorption capacity (q) of the as-synthesized material with RGO@RS, GSC_{750}, GO_{SAND} (also called super-sand). While the performance of RGO@RS and GSC_{750} was evaluated in the lab; that of GO_{SAND} was taken from the literature [20]. RGO@RS was prepared as reported by Sreeprasad et al. [6] and GSC_{750} was prepared from sugar [7], where carbon loading was fixed as 0.5 wt% in both cases. A comparison of q of GSC, GSC_{750}, and RGO@RS was made based on batch experiments. 100 mg of sand-composites having 0.5 wt% of carbon content were taken separately and their adsorption efficiencies were evaluated with 10 mL of 5 ppm R6G. The adsorption experiment was performed as mentioned previously and the sample was allowed to stir for a day to ensure saturation adsorption. The q value was determined from UV/Vis data (supplementary data S10A). From the standard curve, the q was calculated. The q value of RGO@RS and GSC_{750} was 60 and 50–55 mg/g of carbon content, respectively. The q of our material (GSC) is 75.4 mg/g in terms of carbon content. The q of AC for R6G reported in batch experiments is 44.7 mg/g [35] which is much lower than that observed for GSC. For CP, GSC exhibited a q of 52.6 mg/g of carbon under identical conditions (supplementary data Fig. S10B).

Table 1
Breakthrough parameters obtained during three consecutive cycles of adsorption.

Cycle number	Bed height (cm)	Breakthrough volume (mL)	Adsorption capacity (mg/g) of carbon
1	3	3547	44.5
2	3	3260	42.3
3	3	3146	40.4

Fixed-bed experiments were also conducted to compare adsorption efficiency. Columns of equal diameter were taken and packed with adsorbents (GSC, GSC_{750}, RGO@RS and sand) with equal bed height of 3 cm. Graphenic content in all the adsorbents were 0.5 wt%. R6G (1 ppm) was passed through the columns packed with the adsorbent at the flow rate of 2.3 mL/min. It was observed that while the sand got exhausted after passing 60 mL of R6G, whereas the other adsorbents had higher capacity. The column packed with GSC_{750} and RGO@RS showed 35 (2.1 L) and 48-fold (2.9 L) increase in q than regular sand. GSC showed the highest q among all the adsorbents, the column got exhausted after passing 3.6 L of R6G solution, which shows a 60-fold increase in q than sand itself. Recently, Gao et al. claimed a 5-fold higher q than regular sand for 'super sand' [20]. A comparison of different adsorbents is shown in Fig. 9. These results clearly indicate that our material is superior to other adsorbents in terms of q and it has about 12 times more adsorption efficacy compared to 'super sand' and can function as

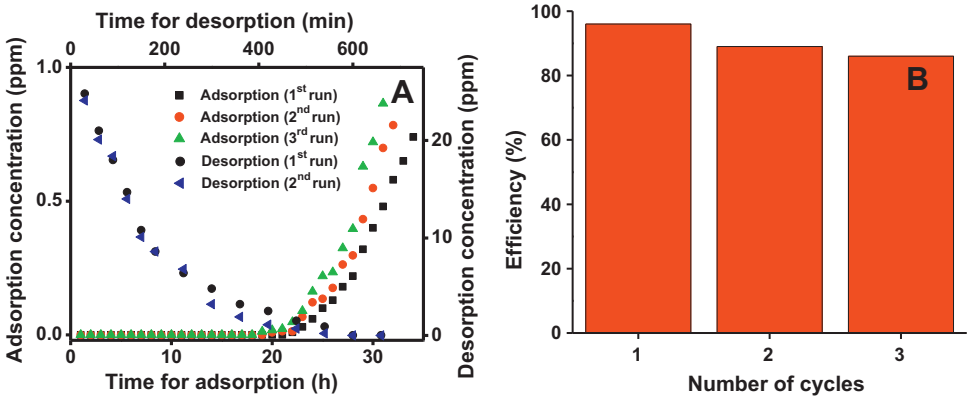

Fig. 8. (A) Breakthrough curves showing the performance of the adsorbent composite in removing R6G from water for three consecutive adsorption cycles and (B) efficiency bar (initial R6G concentration = 1.0 mg/L; pH = 7 ± 0.2; bed depth = 3 cm; loading = 0.6 wt% (carbon content), particle size = 0.2 mm and flow rate = 2.3 mL/min). (B) The amount of R6G desorbed in three consecutive cycles of desorption using acetone as the eluent.

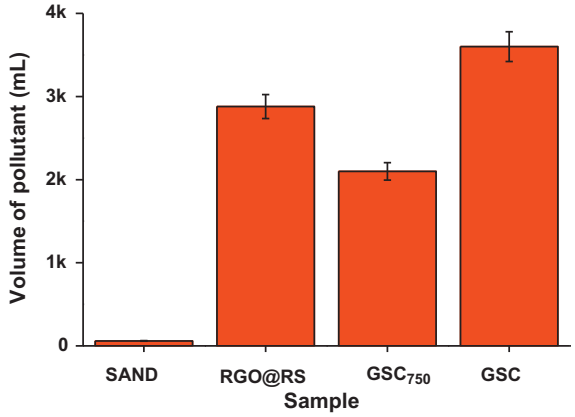

Fig. 9. Comparison of adsorption capacity with different graphenic adsorbents. Estimated error bar is 5%.

a cheaper and superior substitute. For want of a better word, we name this as 'wonder sand'.

4. Post-adsorption analysis of the adsorbent

The adsorbent was analyzed after the adsorption process to check the presence of the contaminants. Fig. 10A shows the SEM and EDAX characterization of GSC after the adsorption of chlorpyrifos. We can clearly see that the morphology of the GSC does not change during the adsorption process. However, EDAX identified signatures of P, S and Cl which was not present in the parent sample (data given earlier), which points to the presence of chlorpyrifos adsorbed on the particle. After regeneration, the sample was again analyzed using SEM and EDAX. The absence of P or Cl indicates the removal of chlorpyrifos (supplementary data S11).

In Fig. 10B, the LDI data confirms that the adsorption has taken place on the surface of GSC. There is no peak corresponding to GSC either in positive or negative mode (the data presented here is in positive mode, trace i). After the complete exhaustion of the adsorbent (R6G and CP adsorption in batch), the material was filtered and dried under N_2 atmosphere. The sample was spotted on the LDI plate. The LDI MS in positive mode of the R6G sample (Fig. 10B (ii)) shows a peak at m/z 444 corresponding to $C_{28}H_{31}N_2O_3^+$ (R6G) and the fragmented peaks at m/z 415 and 386 due to the elimination of ethyl groups from the side chain. The LDI of GSC adsorbed CP was taken in negative mode, Fig. 10B (iii) showing fragmented peaks at m/z 181, 79 and 228 corresponding to $C_5HCl_3N^-$, $(SPO_2)^-$ and $(C_5HCl_3NPO)^-$. The fragmented structures are shown in supplementary data of Fig. S12. The inset shows the isotopic distribution due the presence of three Cl groups at a mass difference of two (the peak at m/z 181 is enlarged). This categorically proved the adsorption of targeted pollutants on GSC.

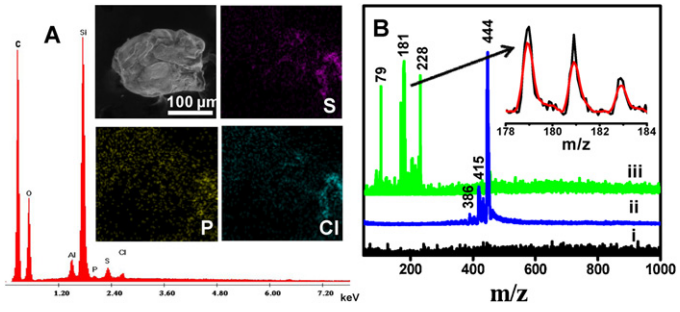

Fig. 10. (A) SEM and EDAX characterization of adsorbent after adsorption of chlorpyrifos. (B) LDI of (i) GSC, (ii) R6G adsorbed on GSC and (iii) CP adsorbed on GSC. Inset shows an expanded view of the peak at m/z 181.

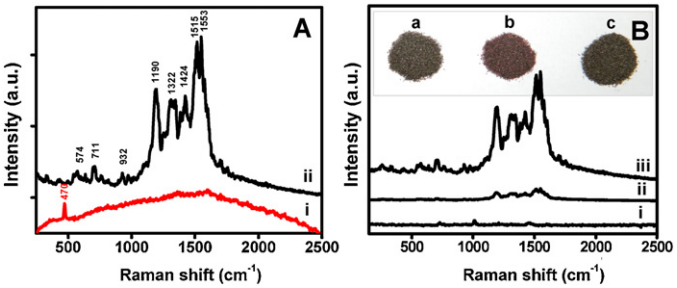

Fig. 11. (A) Raman spectrum of (i) R6G adsorbed on GSC and (ii) SERS of R6G. (B) Evaluation of the capacity of the column. SERS collected from the R6G spiked water sample after passing (i) 2 L, (ii) 3.6 L and (iii) 4.8 L through the column. The inset shows the photograph of (a) GSC, (b) R6G adsorbed GSC and (c) GSC after regeneration. (Inset of B is in color and this can be viewed in the Web version of the article.)

Unlike pesticides, the characteristic colors of the dyes can be used to identify the adsorption or desorption of these substances. The adsorption of R6G was evident from the color change (black to reddish) of the adsorbent particle (photograph in the inset of Fig. 11B). After regeneration, the adsorbent completely regained the initial color (black). Expanded photographs of the materials are presented in supplementary data S13 so that the color changes are appreciated.

However, trace amounts of R6G can be present on the adsorbent even without giving visual color. R6G being a Raman active molecule, Raman spectroscopy was employed for this analysis. Due to the inherent fluorescence of R6G, normal Raman spectrum was not able to show the characteristic features. In such cases, surface enhanced Raman spectroscopy (SERS) can be a useful technique to identify the sample. Hence, we used silver nanoparticles, which are known to be highly active SERS substrates [36,37]. We can see that the normal Raman spectrum does not have prominent features of R6G as in Fig. 11A (red trace) whereas the SERS spectrum obtained using silver nanoparticles showed all the characteristic features of R6G (Fig. 11A (black trace)). GSC before adsorption of R6G does not have the fluorescence background and the presence of this background (which masks other features) confirms the presence of R6G on GSC.

To assure complete regeneration of the adsorbent, the adsorbent was washed with acetone at a flow rate of 2.3 mL/min. The acetone extract after different wash cycles were analyzed. It was found that after 42 bed-volume of washing, no trace of R6G remained in the SERS spectra (supplementary data S14) pointing to the complete removal of R6G from the adsorbent surface. A similar strategy was used to calculate the capacity of the column. The bed height of the column was 3 cm (containing silica particle of size 0.3 μm and graphenic carbon loading of 0.6%). The filtrate was collected after different time (volume passed through the column) and was analyzed using SERS. Fig. 11B shows the SERS spectra taken from filtrate collected after passing 1 ppm of R6G solution through the column at different times (different volumes passed through the column). We can see that the evolution of peaks started after the passage of 3.6 L (1 ppm) of R6G solution through the column and appreciable features were seen when the volume passed through the column reached 4.8 L.

5. Conclusions

A facile in situ strategy for the synthesis of graphene-sand composite (GSC) is reported. A cheap and abundant material, asphalt was used as the carbon precursor. The synthetic strategy used here is useful to produce graphenic materials in solution phase as well as on solid substrates. The formation of graphenic materials was

confirmed by different spectroscopic and microscopic techniques. Characteristic G and D bands were observed at 1578 cm^{-1} and 1345 cm^{-1}, respectively, in the Raman spectrum. The 2D sheet-like structure with wrinkles observed in TEM and SEM confirmed the formation of graphenic materials. The as-synthesized composite, GSC, was tested for its applicability in decontaminating water. Rhodamine-6G and chlorpyrifos, a dye and a pesticide, respectively, were taken as the model pollutants. Batch experiments indicated that adsorption is highly dependent on the particle size, and carbon loading on sand particles. The suitability of the adsorbent in real time application was demonstrated through laboratory column experiments. The performance of GSC was compared to some other reported graphenic adsorbents and the results illustrated that GSC is superior in terms of strength and adsorption capacity for the contaminant tested. The adsorption capacity of GSC is 75.4 mg/g while it is 44.7 mg/g for AC in the case of R6G. The reusability of the adsorbent was demonstrated and found that the material is reusable and hence economically viable. The present study illustrates the possibility of making large quantity of graphenic materials in a cost effective manner and it is likely to be used in water purification industry.

Acknowledgements

We thank the Nanoscience and Nano Mission of the Department of Science and Technology (DST), Government of India, for supporting our research program and Anirban Som for helping in taking the TEM images. SSG also thank UGC for the fellowship.

Appendix A. Supplementary data

Supplementary data associated with this article can be found, in the online version, at http://dx.doi.org/10.1016/j.jhazmat.2012.12.022.

References

[1] V. Chandra, K.S. Kim, Highly selective adsorption of Hg^{2+} by a polypyrrole-reduced graphene oxide composite, Chem. Commun. 47 (2011) 3942–3944.
[2] V. Chandra, J. Park, Y. Chun, J.W. Lee, I.C. Hwang, K.S. Kim, Water-dispersible magnetite-reduced graphene oxide composites for arsenic removal, ACS Nano 4 (2010) 3979–3986.
[3] D. Cohen-Tanugi, J.C. Grossman, Water desalination across nanoporous graphene, Nano Lett. 12 (2012) 3602–3608.
[4] F. Liu, S. Chung, G. Oh, T.S. Seo, Three-dimensional graphene oxide nanostructure for fast and efficient water-soluble dye removal, ACS Appl. Mater. Interfaces 4 (2011) 922–927.
[5] A.K. Mishra, S. Ramaprabhu, Functionalized graphene sheets for arsenic removal and desalination of sea water, Desalination 282 (2011) 39–45.
[6] T.S. Sreeprasad, S.M. Maliyekkal, K.P. Lisha, T. Pradeep, Reduced graphene oxide–metal/metal oxide composites: facile synthesis and application in water purification, J. Hazard. Mater. 186 (2011) 921–931.
[7] S.S. Gupta, T.S. Sreeprasad, S.M. Maliyekkal, S.K. Das, T. Pradeep, Graphene from sugar and its application in water purification, ACS Appl. Mater. Interfaces 4 (2012) 4156–4163.
[8] Y.W. Zhu, S. Murali, W.W. Cai, X.S. Li, J.W. Suk, J.R. Potts, R.S. Ruoff, Graphene and graphene oxide: synthesis, properties, and applications, Adv. Mater. 22 (2010) 5226.
[9] W. Hu, C. Peng, W. Luo, M. Lv, X. Li, D. Li, Q. Huang, C. Fan, Graphene-based antibacterial paper, ACS Nano 4 (2010) 4317–4323.
[10] T.S. Sreeprasad, M.S. Maliyekkal, K. Deepti, K. Chaudhari, P.L. Xavier, T. Pradeep, Transparent, luminescent, antibacterial and patternable film forming composites of graphene oxide/reduced graphene oxide, ACS Appl. Mater. Interfaces 3 (2011) 2643–2654.
[11] M.L. Schipper, N. Nakayama-Ratchford, C.R. Davis, N.W.S. Kam, P. Chu, Z. Liu, X. Sun, H. Dai, S.S. Gambhir, A pilot toxicology study of single-walled carbon nanotubes in a small sample of mice, Nat. Nanotechnol. 3 (2008) 216–221.
[12] J.W. Seo, A. Magrez, M. Milas, K. Lee, V. Lukovac, L. Forró, Catalytically grown carbon nanotubes: from synthesis to toxicity, J. Phys. D: Appl. Phys. 40 (2007) R109.
[13] Q. Liu, J. Shi, J. Sun, T. Wang, L. Zeng, G. Jiang, Graphene and graphene oxide sheets supported on silica as versatile and high-performance adsorbents for solid-phase extraction, Angew. Chem. Int. Ed. 50 (2011) 5913–5917.
[14] W.S. Hummers, R.E. Offeman, Preparation of graphitic oxide, J. Am. Chem. Soc. 80 (1958) 1339.
[15] D. Li, M.B. Muller, S. Gilje, R.B. Kaner, G.G. Wallace, Processable aqueous dispersions of graphene nanosheets, Nat. Nanotechnol. 3 (2008) 101–105.
[16] M.J. McAllister, J.L. Li, D.H. Adamson, H.C. Schniepp, A.A. Abdala, J. Liu, M. Herrera-Alonso, D.L. Milius, R. Car, R.K. Prud'homme, I.A. Aksay, Single sheet functionalized graphene by oxidation and thermal expansion of graphite, Chem. Mater. 19 (2007) 4396–4404.
[17] S. Stankovich, D.A. Dikin, G.H.B. Dommett, K.M. Kohlhaas, E.J. Zimney, E.A. Stach, R.D. Piner, S.T. Nguyen, R.S. Ruoff, Graphene-based composite materials, Nature 442 (2006) 282–286.
[18] S. Stankovich, D.A. Dikin, R.D. Piner, K.A. Kohlhaas, A. Kleinhammes, Y. Jia, Y. Wu, S.T. Nguyen, R.S. Ruoff, Synthesis of graphene-based nanosheets via chemical reduction of exfoliated graphite oxide, Carbon 45 (2007) 1558–1565.
[19] T.S. Sreeprasad, A.K. Samal, T. Pradeep, Tellurium nanowire-induced room temperature conversion of graphite oxide to leaf-like graphenic structures, J. Phys. Chem. C 113 (2009) 1727–1737.
[20] W. Gao, M. Majumder, L.B. Alemany, T.N. Narayanan, M.A. Ibarra, B.K. Pradhan, P.M. Ajayan, Engineered graphite oxide materials for application in water purification, ACS Appl. Mater. Interfaces 3 (2011) 1821–1826.
[21] N.I. Kovtyukhova, P.J. Ollivier, B.R. Martin, T.E. Mallouk, S.A. Chizhik, E.V. Buzaneva, A.D. Gorchinskiy, Layer-by-layer assembly of ultrathin composite films from micron-sized graphite oxide sheets and polycations, Chem. Mater. 11 (1999) 771–778.
[22] E. Ruiz-Hitzky, M. Darder, F.M. Fernandes, E. Zatile, F.J. Palomares, P. Aranda, Supported graphene from natural resources: easy preparation and applications, Adv. Mater. 23 (2011) 5250–5255.
[23] Z. Sun, Z. Yan, J. Yao, E. Beitler, Y. Zhu, J.M. Tour, Growth of graphene from solid carbon sources, Nature 468 (2010) 549–552.
[24] G. Ruan, Z. Sun, Z. Peng, J.M. Tour, Growth of graphene from food, insects and waste, ACS Nano 5 (2011) 7601–7607.
[25] Y. Hernandez, V. Nicolosi, M. Lotya, F.M. Blighe, Z. Sun, S. De, I.T. McGovern, B. Holland, M. Byrne, Y.K. Gun'Ko, J.J. Boland, P. Niraj, G. Duesberg, S. Krishnamurthy, R. Goodhue, J. Hutchison, V. Scardaci, A.C. Ferrari, J.N. Coleman, High-yield production of graphene by liquid-phase exfoliation of graphite, Nat. Nanotechnol. 3 (2008) 563–568.
[27] R. Sariri, M.S. Zakerhamidi, K. Baharpaima, A. Ghanadzadeh, The anion effect and molecular association of rhodamine dyes in isotropic and anisotropic solvents, J. Mol. Liq. 115 (2004) 55–61.
[28] S.M. Maliyekkal, T.S. Sreeprasad, D. Krishnan, S. Kouser, A.K. Mishra, U.V. Waghmare, T. Pradeep, Graphene, A reusable substrate for unprecedented adsorption of pesticides, Small (2012), http://dx.doi.org/10.1002/smll.201201125.
[29] S. Lagergren, Zur theorie der sogenannten adsorption gelöster stoffe, K Sven Ventenskapsakad Handl. 24 (1898) 1–39.
[30] Y.S. Ho, G. McKay, The kinetics of sorption of divalent metal ions onto sphagnum moss peat, Water Res. 34 (2000) 735–742.
[31] Y.S. Ho, C.C. Chiang, Y.C. Hsu, Sorption kinetics for dye removal from aqueous solution using activated clay, Sep. Purif. Technol. 36 (2001) 2473–2488.
[32] K.P. Lisha, S.M. Maliyekkal, T. Pradeep, Manganese dioxide nanowhiskers: a potential adsorbent for the removal of Hg(II) from water, Chem. Eng. J. 160 (2010) 432–439.
[33] S. Kuriakose, T.S. Singh, K.K. Pant, Adsorption of As(III) from aqueous solution onto iron oxide impregnated activated alumina, Water Qual. Res. J. Can. 39 (2004) 258–266.
[34] T.S. Singh, K.K. Pant, Experimental and modelling studies on fixed bed adsorption of As(III) ions from aqueous solution, Sep. Purif. Technol. 48 (2006) 288–296.
[35] G. Annadurai, R.S. Juang, D.J. Lee, Adsorption of rhodamine 6G from aqueous solutions on activated carbon, J. Environ. Sci. Health A 36 (2001) 715–725.
[36] P. Hildebrandt, M. Stockburger, Surface-enhanced resonance Raman spectroscopy of rhodamine 6G adsorbed on colloidal silver, J. Phys. Chem. 88 (1984) 5935–5944.
[37] A.M. Michaels, M. Nirmal, L.E. Brus, Surface enhanced Raman spectroscopy of individual rhodamine 6G molecules on large Ag nanocrystals, J. Am. Chem. Soc. 121 (1999) 9932–9939.

Supplementary data

Immobilized graphene-based composite from asphalt: Facile synthesis and application in water purification

T. S. Sreeprasad[1], Soujit Sen Gupta[1], Shihabudheen M. Maliyekkal[2], and T. Pradeep[1]*

[1]DST Unit on Nanoscience, Department of Chemistry,
Indian Institute of Technology Madras, Chennai - 600 036, India

[2]School of Mechanical and Building Sciences,
VIT University, Chennai Campus, Chennai-600 048, India

**Email: pradeep@iitm.ac.in; Fax: 91-44-2257-0545/ 0509*

Supplementary data 1

Methods and Materials

Materials

The carbon source used for the preparation of graphene, asphalt, was procured from the local market of Chennai, India. Toluene (industrial grade) was purchased from Rankem Chemicals Pvt. Ltd., India. CP (HPLC assay 99.9%) and Rhodamine 6G chloride (R6G, $C_{27}H_{29}ClN_2O_3$) were obtained from Sigma Aldrich. Standard sand collected from Ennore, Tamilnadu was initially treated with 0.1 M nitric acid to remove impurities. Subsequently the sand was washed extensively with deionized water and dried at 100±3 ^{o}C. This purified sand was sieved to obtain particles of desired size. All chemicals were used as received without additional purification. All solutions and suspensions were prepared using deionized water, unless otherwise mentioned.

In-situ synthesis of graphene-sand composite (GSC)

Asphalt was initially dissolved in toluene at a solid to solvent ratio of 1:10. The dispersed asphalt was then mixed with sand particles of size ranging from 200-500 micrometers. The carbon loading on the sand particles was varied by changing the sand to asphalt ratio. The samples were then dried in a hot air oven at 90±3 ^{o}C under constant stirring for about 5 h. The dried sample was then transferred to a muffle furnace and subjected to heat treatment. The furnace was programmed as follows: a) temperature was increased from 30 to 250 ^{o}C in 30 min. b) held at 250 ^{o}C for an hour, c) again increased to 400 ^{o}C in next 1 h and d) finally held at 400 ^{o}C for next 4 h. It was then cooled to room temperature, just by switching off the power and without any control on the cooling rate. The optimum temperature was 400±5 ^{o}C, which was established after several iterations. The stable carbon coating on the sand surface was evident from the characteristic black color of the sample. The pre-weighed material was then soaked in concentrated sulfuric

acid for about 30 min and filtered, washed several times with deionized water until the pH of the wash-water reaches that of the input water. The composite was then dried at 110 ^{o}C for further use. The sample was again weighed to check any weight gain or loss. This material is termed as graphene sand composite (GSC). The carbon loading (wt%) was calculated from thermo-gravimetric analysis (TGA) (Supplementary data Fig. S2).

Batch adsorption experiments

Batch experiments were carried out to evaluate the pollutant uptake capacity of the composite in 25 mL conical flasks. Calculated amount of adsorbent was added to 10 mL of the water spiked with the target pollutant (R6G or CP) and placed on a shaker at room temperature (30±2 ^{o}C). The solid-liquid separation was done by filtration. The filtrate was analyzed to quantify the target molecule R6G in the aqueous phase by UV/Vis spectrophotometer based on the absorbance at 527 nm. Analysis of CP was carried out at a wavelength of 297 nm. The effect of particle size, contact time, and adsorbent dose were evaluated by varying the parameters in the appropriate window. Except kinetics, all other studies were conducted by batch equilibration method. Control samples were kept in all the cases to assess the natural attenuation of the target molecule. All the experiments were conducted in duplicate and the average values are reported.

Fixed-bed column experiments

Continuous removal of the R6G was studied in fixed-bed columns made of transparent glass with a length of 500 mm and an internal diameter of 18 mm. The columns were packed with the adsorbent to a depth of 3 cm and operated in down-flow mode at a feed flow rate of 2.3 mL/min. The performance of the column was evaluated as a function of time at room temperature. The initial R6G concentration was maintained at 1 mg/L. The residual concentration of the effluent samples were analysed as a function of time.

The R6G loaded adsorbents were regenerated *in-situ* in the columns using acetone as the eluent. The regenerant was passed through the column bed with the same flow rate of adsorption cycle. Nearly 42 bed

volumes of acetone were passed through the column in down-flow mode and followed by purging with hot air. The column was then washed to check the pollutant concentration in the wash-water. The spent regenerant and back washed water were collected and analysed for eluted concentrations of the pollutant as function of time.

Instrumentation

UV/Vis spectra were measured using a Perkin-Elmer Lambda 25 UV/Vis spectrophotometer. Raman spectra were collected using a confocal Raman spectroscope (WiTec GmbH CRM 200). High-resolution transmission electron microscopy (HRTEM) of the samples was carried out using a JEOL 3010 microscope with a UHR pole piece. X-ray photoelectron spectroscopy (XPS) measurements were done with Omicron ESCA Probe spectrometer with unmonochromatized Mg K_α X-rays (h_γ = 1253.6 eV). The energy resolution of the spectrometer was set at 0.1 eV at pass energy of 20 eV. Binding energy was corrected with respect to C 1s at 284.5 eV. Surface morphology, elemental analysis and elemental mapping studies were carried out using scanning electron microscopy (SEM) equipped with energy dispersive analysis of X-rays (EDAX). SEM measurements used indium doped tin oxide (ITO plate), presence of Si and Sn in the images is expected. For mass analyses, an Applied Biosystems Voyager DE Pro LDI-MS instrument was used. A pulsed nitrogen laser of 337 nm was used for desorption/ionization.

Mechanism of formation of graphenic material from asphalt

The mechanism behind the formation of graphenic material is not fully understood. However, Raman and XPS evaluation suggested the loss of organic functionalities from asphalt during the process. TGA also indicated a weight loss during the process. Asphalt mainly consists of highly condensed polycyclic aromatic hydrocarbons. It is considered as a colloidal mixture with the chief component being asphaltene. Asphaltene is composed of nitrogen, oxygen and sulfur (as functional groups or adsorbates) in addition to carbon and hydrogen. Asphaltene is highly soluble in toluene. In our process, asphalt was first dissolved in toluene and hence chief fraction in the solution is asphaltene. The carbon functionalities are highly

susceptible to thermal decomposition above 300 ^{0}C [1, 2]. Hence, based on the prevailing knowledge and Raman, XPS and TGA results obtained in the study, it is proposed that at elevated temperatures, asphaltene will lose the impurities (the functional groups) and will form unfunctionalized carbon. This carbon, in presence of a solid substrate (sand particle), is believed to combine and form the graphenic materials. The substrate not being single crystalline, the formation can start from different places in different orientation. This leads to the formation of large number of structural defects in the films formed.

Supplementary data 2

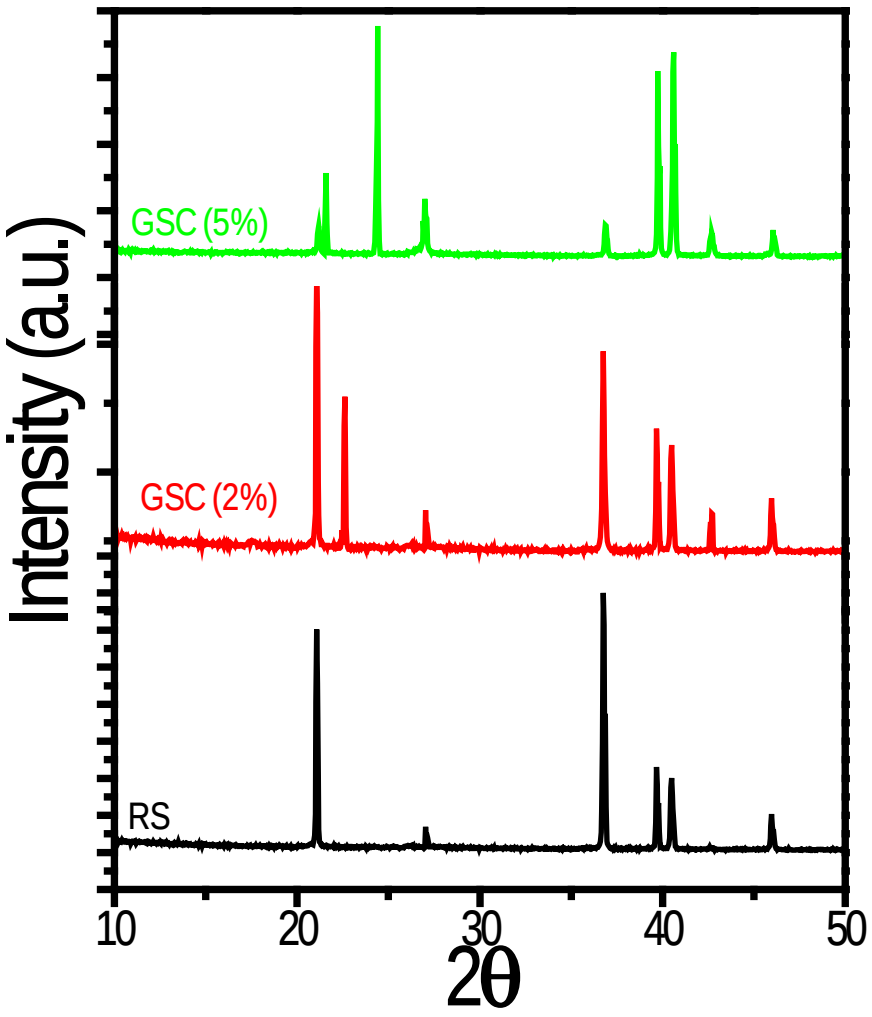

Fig S2: XRD data of bare sand (silica) and GSC at different graphenic carbon loading (2 and 5 wt%).

Supplementary data 3

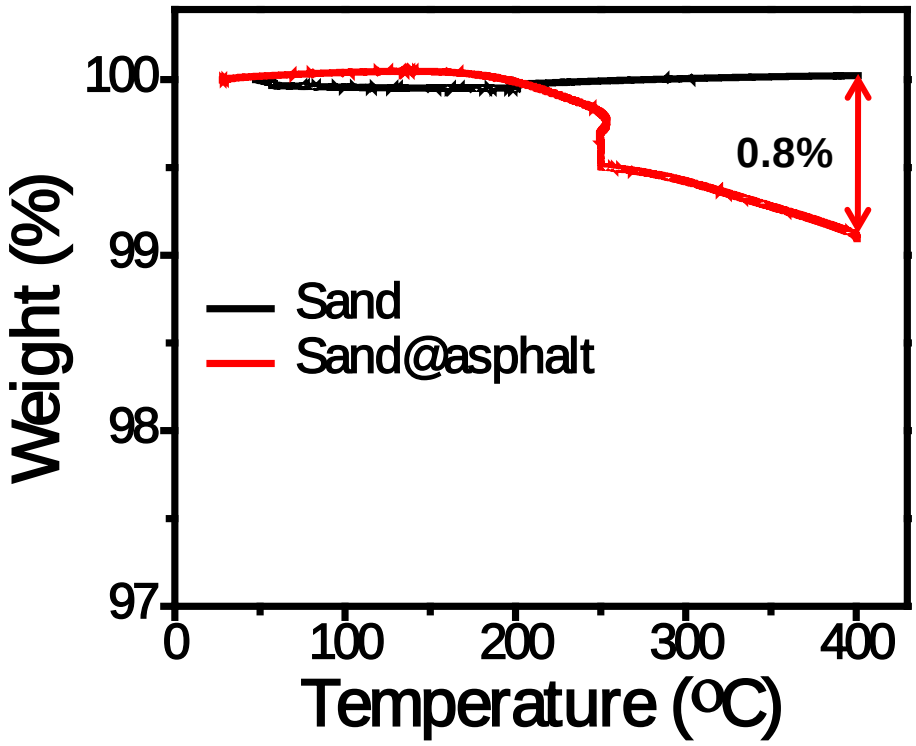

Fig. S3: TGA of sand and asphalt coated sand (2 wt%), showing weight loss of 0.8 wt%. Temperature was programmed as given in text. The initial loading is based on calculation. The temperature was not ramped above 400 ^{0}C as the auto-ignition temperature in air is above this value. However, heating up to 750 ^{o}C in N_2 atmosphere did not increase the adsorption capacity.

Supplementary data 4

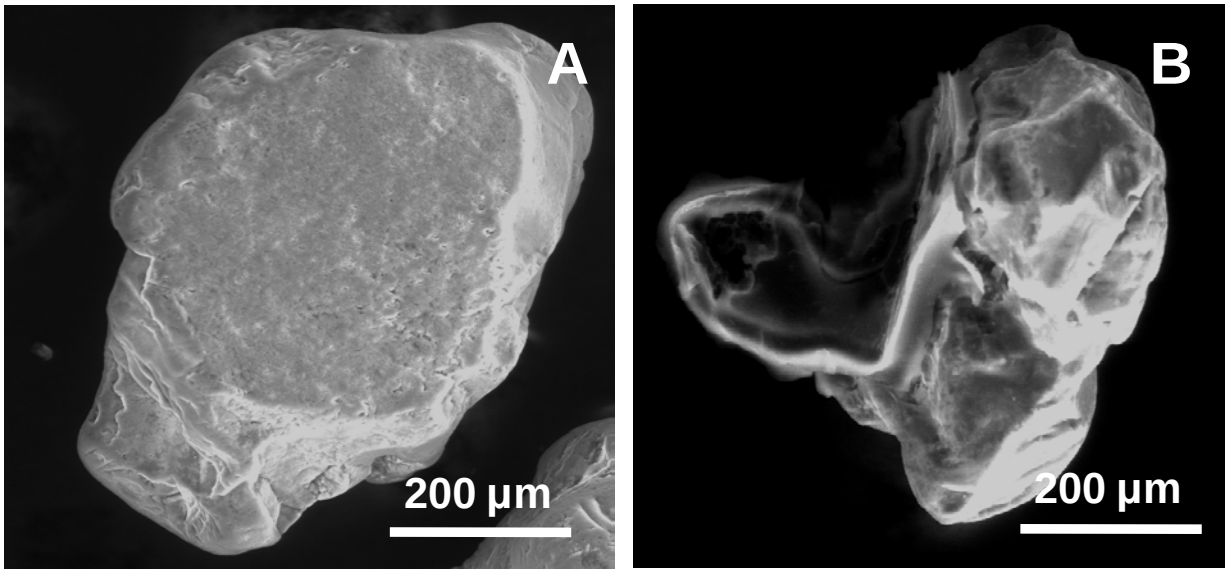

Fig. S4: SEM images of A) virgin-sand showing that the surface is plain and B) sand coated with graphene, where the surface is rougher and sheet-like structures can be seen.

Supplementary data 5

Fig. 4A and B show the SEM images of GSC with 0.2 % loading, where the surface is rougher than the pristine sand. When the loading reached 0.5%, careful observation showed more prominent surface changes. The surface looked rougher compared 0.2% loading (Fig. 4C and D). At 1% loading, a clear sheet-like structure was visible (Fig. 4E and F). Fig. 4F shows a closer view (higher magnification) of a GSC particle with 1% loading. We can see a sheet covering the surface of sand. The outward appearance (color) of the sand also changed as the loading increased. The color turned more intense as the loading increased (Fig. 4G).

Supplementary data 6

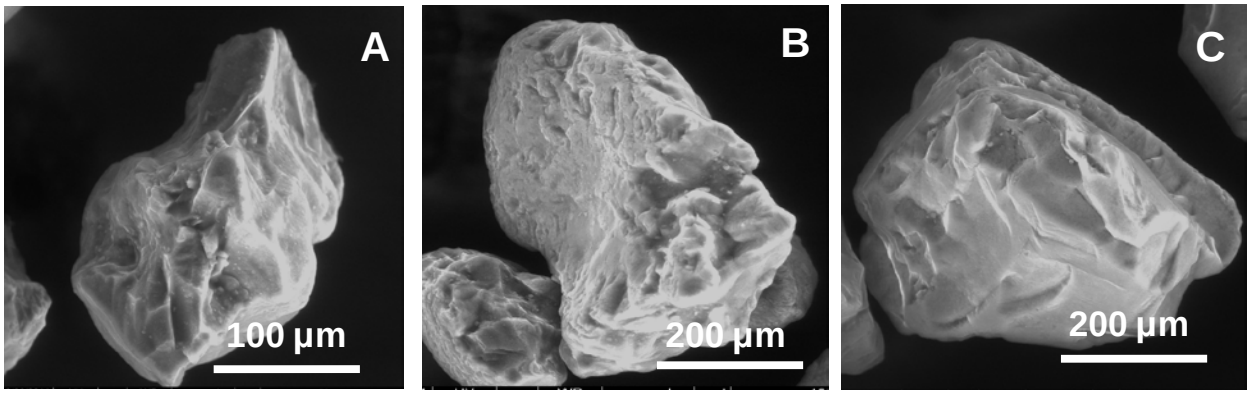

Fig. S6: SEM images of GSC with different sand particle sizes. A) Less than 0.2 mm, B) between 0.2-0.3 mm and C) more than 0.3 mm having 0.5% carbon loading.

Supplementary data 7

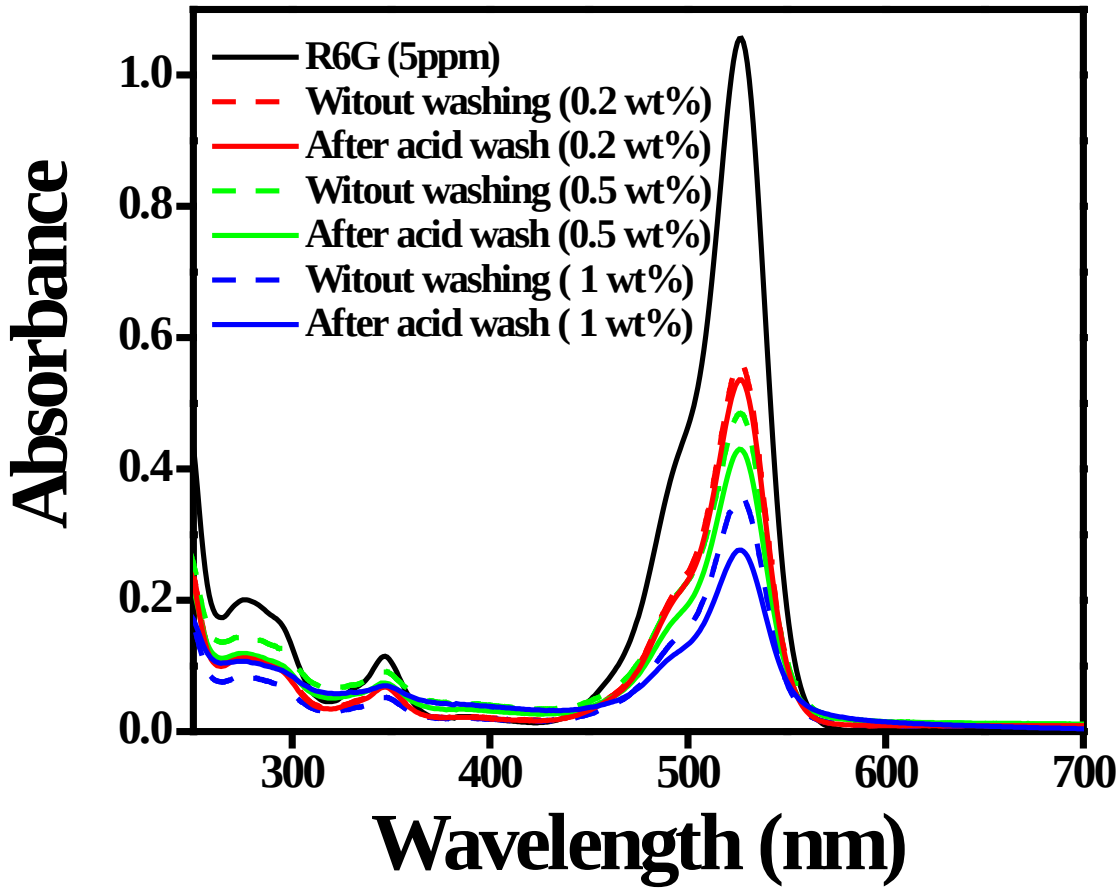

Fig. S7: UV/Vis spectrum showing an increase in efficiency of GSC after acid wash for different carbon loading.

Supplementary data 8

Video 1: Removal of Coca-cola. Bed depth was 6 cm and no special care was taken for controlling the flow-rate in this clip.

Supplementary data 9

Pseudo-first-order equation: $q_t = q_e\left(1 - e^{-k_1 t}\right)$ (1)

Pseudo- second-order equation: $\frac{q_e^2 k_2 t}{1 + q_e k_2 t}$ (2)

Where q_e and q_t are the adsorption capacities at equilibrium and at time t, respectively (mg/g). k_1 is the rate constant of pseudo-first-order adsorption (L/min) and k_2 is the rate constant of pseudo-second order adsorption (g/mg min). The estimated value of k_1 and k_2 are 0.02 /min and 0.019 mg/g min, respectively.

Supplementary data 10

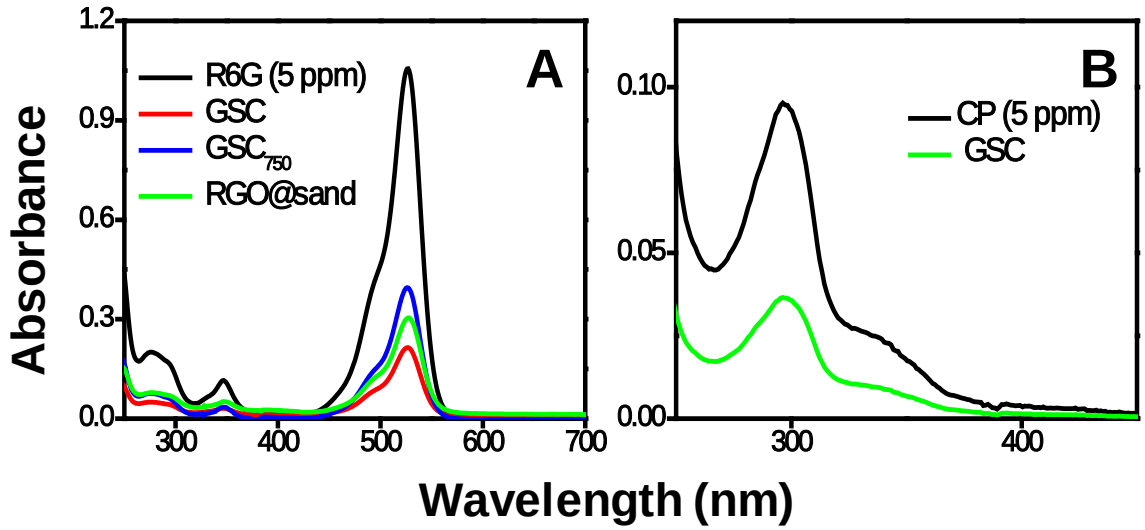

Fig. S10: UV/Vis spectrum showing A) removal of R6G with different graphenic materials as the adsorbent. B) Removal of CP with GSC.

Supplementary data 11

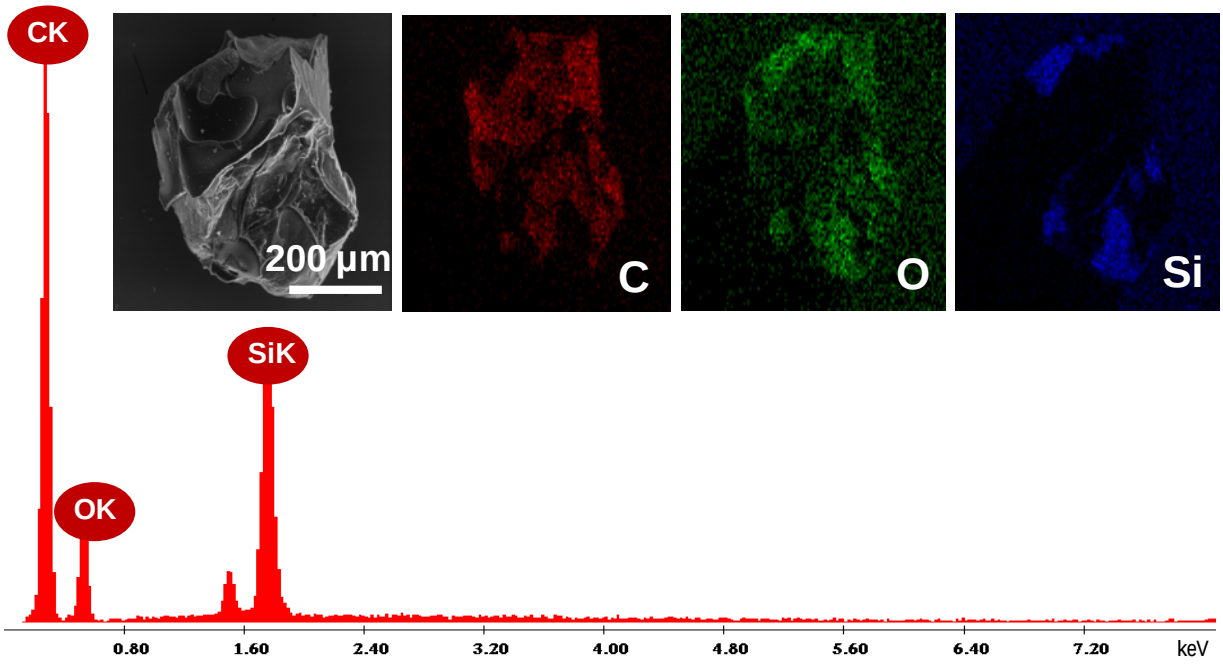

Fig. S11: SEM-EDAX of CP adsorbed GSC after regeneration. P, Cl and S are absent.

Supplementary data 12

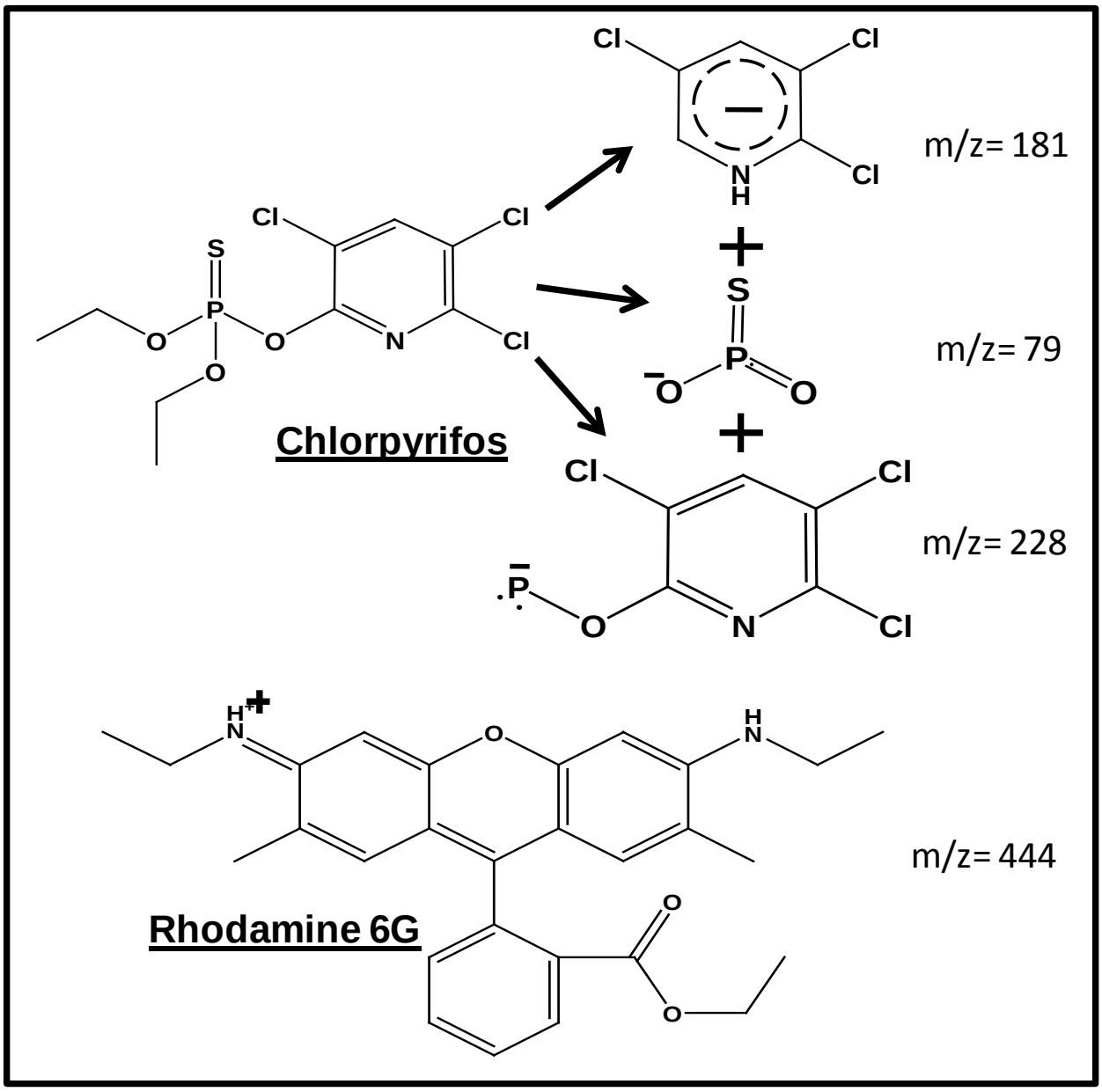

Fig. S12: Common fragments of CP and the molecular ion of R6G.

Supplementary data 13

Fig. S13: Photographs of a) initial material (GSC), b) R6G adsorbed GSC and c) GSC after regeneration. The color change of the material after adsorption of R6G, from black (a) to reddish (b) can be clearly seen.

Supplementary data 14

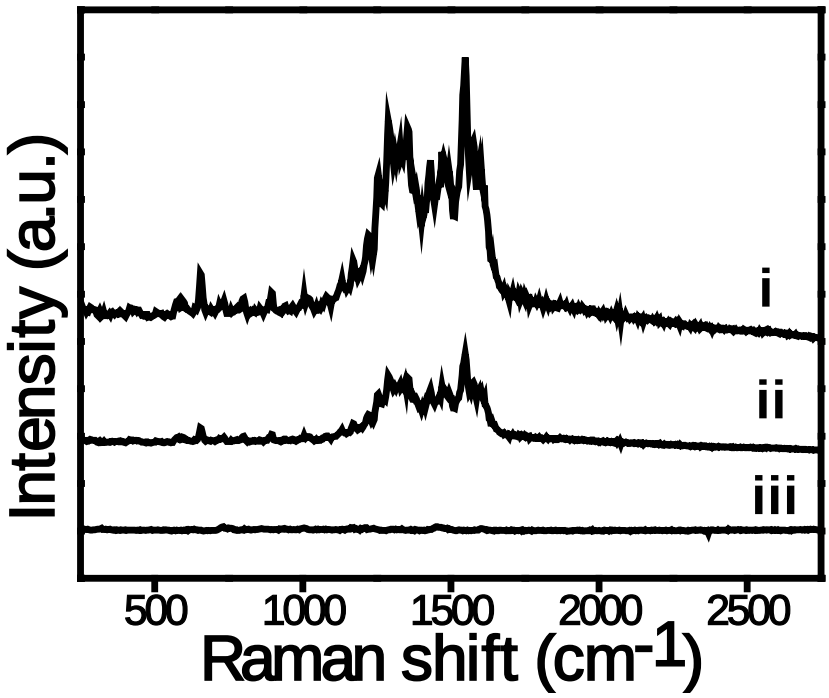

Fig. S14: SERS of the filtrate after passing different volumes of acetone during regeneration, i) after 10 bed volume, ii) after 20 bed volume and iii) 30 bed volume.

References:

[1] G. de la Puente, J. J. Pis, J. A. Menendez, P. Grange, Thermal stability of oxygenated functions in activated carbons, J. Anal. Appl. Pyrol. 43 (1997), 125–138.

[2] A. G. Vandeputte, M. F. Reyniers, G. B. Marin, Theoretical study of the thermal decomposition of dimethyl disulfide, J. Phys. Chem. A 114 (2010), 10531-10549.

Particle & Particle Systems Characterization
www.particle-journal.com

Evolution of Atomically Precise Silver Clusters to Superlattice Crystals

*Korath Shivan Sugi, Indranath Chakraborty, Thumu Udayabhaskararao, Jyoti Sarita Mohanty, and Thalappil Pradeep**

We report the systematic size evolution of an organic-soluble, atomically precise silver cluster (product **1**) of ≈0.9 nm diameter to superlattices (SLs). Product **1** converts gradually to more stable plasmonic particles of ≈2.9 nm diameter (product **2**) and constant heating of the latter at 100 °C leads to crystals composed of self organized nanoparticles or SLs (product **3**). Evolution of product **1** to larger nanoparticles was observed by mass spectrometry, while the formation of nanoparticles and crystals was investigated by electron microscopy. The constituent units of products, **1** (m/z of 13.5 k), **2** (mixture of m/z 70 k and 80 k), and **3** (m/z of 148 k) are tentatively assigned to $Ag_{75}(PET)_{40}$, $Ag_{\sim 530}(PET)_{\sim 100}$ (with $Ag_{\sim 561}(PET)_{\sim 150}$), and $Ag_{\sim 923}(PET)_{\sim 351}$, respectively, where PET refers to 2-phenylethanethiol, the ligand used for protecting the cluster core. Creation of nanoparticle crystals starting from atomically precise clusters points to the synthesis of nanoparticle solids with tunable properties.

Atomically precise clusters of noble metals exhibiting intense luminescence and having distinct absorption characteristics[1] are said to be the missing link between the atomic and nanoparticle (NP) regimes of matter. Metallic NPs[2,3] possessing characteristic optical absorption due to plasmon resonance[4,5] can be converted to clusters exhibiting distinct optical absorption and emission in the visible region, by appropriate chemistry.[6] NPs having varying morphologies can be annealed to definite, uniform shapes by digestive ripening[7–11] and such monodisperse particles can self-organize to yield particle crystals or SLs.[12–17] Refined synthetic methods yielding monodisperse particles can also form self-organized structures directly.[18] Stacking of NPs into 2D and 3D superstructures and investigating their collective properties are receiving much attention among nanochemists due to diverse applications for the latter.[19,20]

We show here that atomically precise clusters, consisting of a few tens of atoms can be grown systematically to plasmonic particles, which subsequently yield particle crystals. This methodology can possibly create SLs from particles of any desired size, enabling the creation of designer crystals and consequently varying properties. We show that crystals of plasmonic nanoparticles are better formed starting from sub-nanometer clusters.

A solid-state route[21] was used to synthesize atomically precise clusters. Briefly, the method involves grinding the precursors ($AgNO_3$ and PET) in a mortar and pestle to form silver thiolates. Addition of sodium borohydride in the solid state to this mixture with continued grinding produces well-defined clusters that can be extracted with suitable solvents (details of experimental procedure are outlined in Figure S2, Supporting Information). First, a mixture of $AgNO_3$ and tetraoctyl ammonium bromide (TOABr) was taken in an agate mortar and ground uniformly. To that, PET was added and ground till the initial yellow color changed to orange (due to the formation of silver thiolate). Reduction was achieved by adding solid $NaBH_4$ and by constant grinding in ambient air so that the mixture became blackish brown. The product was extracted in ethanol and centrifuged to remove extra thiol in the supernatant and finally the residue was extracted in toluene, which gives a reddish-brown solution. A crucial aspect of the synthesis is the limited supply of water required for the reduction. This was made available from the laboratory air (as $NaBH_4$ is hygroscopic) and ethanol used for extraction.

Initial extract of the solid state reaction product with ethanol was discarded as it contains excess thiol[22,23] used in the synthesis along with some clusters. Excess thiol makes smaller clusters unstable and gradually thiolates are formed. Matrix-assisted laser desorption mass spectrum (MALDI MS) of the ethanol extract shows a sharp peak at m/z of 11.8 k (that is, 11 800) and the optical spectrum (corrected by Jacobian factor[24] shows step-like multiple features at 351 nm, 506 nm and 593 nm, mainly due to the formation of clusters, which is further confirmed by transmission electron microscopy (TEM) (Figure S3, Supporting Information)). The residue upon extraction with toluene (labeled as product **1**) yields a characteristic feature at 13.5 k in MALDI MS, along with its dimer at 27 k, with no other features in the entire mass spectrum measured up to 400 k. It is important to note that the mass spectra are measured at threshold laser intensities. A sharp rise and quick fall of the mass spectral features at threshold laser fluence is a characteristic signature of atomically precise clusters.[25,26] Upon increasing the laser intensity, another threshold is reached where fragmentation commenced yielding lower mass features. Fragmentation increases with increase in fluence and subsequently another threshold is reached beyond which no further fragmentation was observed[27] (Figure S4, Supporting Information). A small hump arises with increase in fluence at m/z of 78 k along with the 13.5 k peak which suggests the fact that product **1** may be co-existing with another cluster at smaller

K. S. Sugi, I. Chakraborty, T. Udayabhaskararao, J. S. Mohanty, T. Pradeep
DST Unit of Nanoscience (DST UNS)
Department of Chemistry
Indian Institute of Technology Madras
Chennai, 600036, India
E-mail: pradeep@iitm.ac.in

DOI: 10.1002/ppsc.201200102

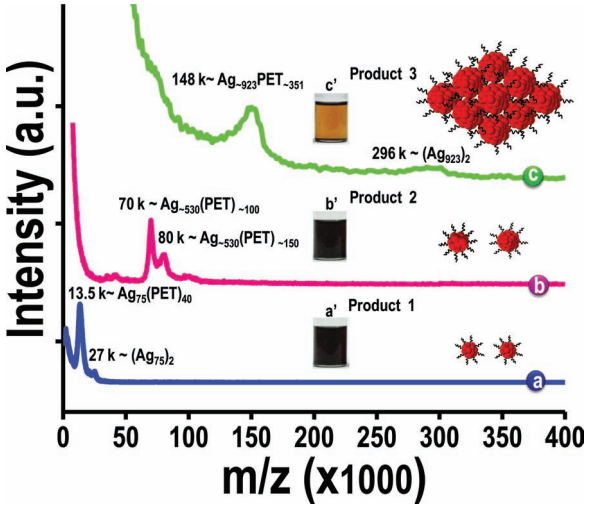

Figure 1. MALDI mass spectra showing the systematic size evolution of product **1** to particle crystals. A sharp peak centered at *m*/*z* of 13.5 k (a) obtained by operating at the threshold laser fluence is assigned as ~$Ag_{75}(PET)_{40}$ (product **1**) with a hump at *m*/*z* of 27 k, probably due to the dimer. Product **1** converts to a new plasmonic product **2** (b) with mass of 70 k and a weaker feature at 80 k (tentatively assigned as $Ag_{\sim 530}(PET)_{\sim 100}$ and $Ag_{\sim 561}(PET)_{\sim 150}$, respectively). Gradual heating makes assembly of plasmonic product **2** to form SLs with definite periodicity (c) composed of ≈923 Ag atoms ($Ag_{\sim 923}(PET)_{\sim 351}$). Dimer at 296 k is also observed (c). Insets of mass spectra show the corresponding photographs and cartoon representations of the size evolution. In photograph (c'), a black precipitate can be seen, which corresponds to the SL.

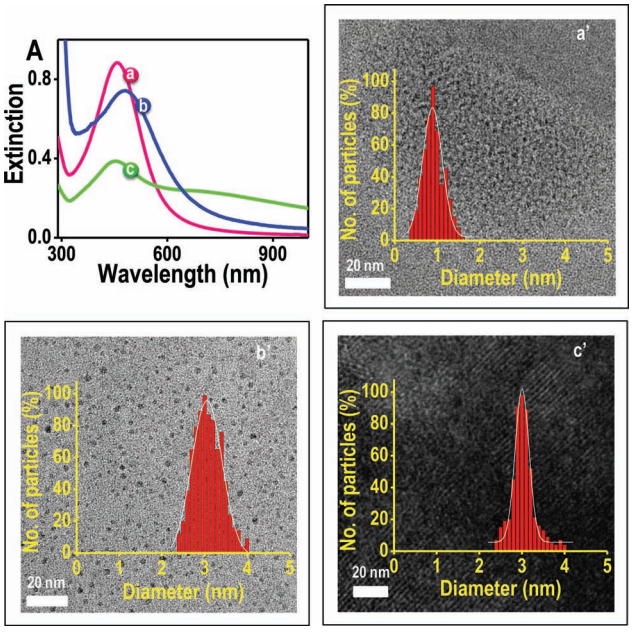

Figure 2. A) UV/Vis spectrum of product **1** showing a band at 480 nm along with a small hump at 425 nm (a), which gradually evolves to plasmonic product, **2** (b). After 2 h of heating of product **2** we obtained a residue that was dispersed in toluene and gives a less intense 455 nm peak with a broad peak around 700 nm (c). This is due to the gradual assembly of product **2** to form SLs. Broad background is in agreement with this. The TEM images and the corresponding size distribution of product **1**, product **2** and product **3** (a',b',c') and their Gaussian fits further confirm evolution of clusters.

concentration, which needs a higher threshold fluence for desorption-ionization. The tentative assignment of 13.5 k would be $Ag_{75}(PET)_{40}$ which was originally observed by Indranath et al.[28] and that at 27 k is the dimer of 13.5 k (2 × 13.5). The clusters kept for one day in refrigerator show a gradual increase in mass. The 13.5 k mass feature disappeared completely after a day. Subsequently two characteristic mass features (**Figure 1**a) were seen at 70 and 80 k (product **2**) suggesting slow size evolution of clusters, which is in agreement with the laser threshold dependence of the 13.5 k feature. These two peaks are tentatively assigned as $Ag_{\sim 530}(PET)_{\sim 100}$ (similar to the recently reported Au_{530} clusters[27] and $Ag_{\sim 561}(PET)_{\sim 150}$. Product **2** upon annealing at 100 °C for 2 h yields a black residue (product **3**) and a dark yellow supernatant. Mass spectrum of the residue shows a broad feature centered at 148 k (Figure **1**c) with its dimer at 296 k. Further increasing the annealing time, the supernatant becomes colorless indicating complete precipitation. As the cluster size increased, the threshold laser intensity also increases: 1311 for 13.5 k, 1498 for 70 and 80 k and 2000 for 148 k (numbers refer to laser intensity measured in a unitless instrument setting).

Along with this gradual mass evolution, systematic change is observed in the optical absorption spectra (as seen in **Figure 2**). Characteristic absorption in the higher wavelength region is observed for nanoclusters. Product **1** shows a band at 480 nm along with a hump at 425 nm (Figure 2a) which closely resembles the Ag_{75} cluster feature, reported from our group.[25] At smaller core sizes, the spectrum shows distinct features in the higher wavelength region as in $Ag_{7,8}$, Ag_9, etc. The spectrum of Ag_{75} evolves to a single plasmonic feature at 458 nm (Figure 2b) which is further confirmed from TEM images. This implies the formation of bigger NPs. The spectrum of a dispersion of product **3** shows the plasmonic feature at 455 nm but with a higher wavelength band, characteristic of aggregates and is attributed to interplasmon coupling.[29] The characteristic 458 nm feature is identical to the plasmon absorption spectrum of PET protected NPs (Figure S5, Supporting Information). The TEM image of product **1** shows uniform size distribution (0.9 nm ± 0.2 nm) but, product **2** shows a broad size distribution (2.9 nm ± 0.4 nm) and product **3** shows uniform size distribution (3.4 nm ± 0.2 nm), which is a requirement of SL formation.

The residue upon closer examination in TEM shows a periodic array of NPs of 3.4 nm core size (**Figure 3**A). The average size of these particles increased from product **2** (2.9 nm) to product **3** (3.4 nm). The improved monodispersity is suggested to be due to core size growth in clusters, similar to digestive ripening upon heating. In the TEM image presented, the (110) plane of the SL crystal is projecting towards the viewer. The image reveals that no further growth of the NPs occurs in the SL crystal. The constituent silver NPs are stacked in a *fcc* pattern rather than *hcp* in the 3D array. The crystals show preferential (111) (Figure 3A,a') orientation as expected from a majority of hexagonal or diamond-like morphologies (Figure 3B,C).

The (111) plane of the SL yields a characteristic hexagonal Fourier transform indicating extended periodicity in the

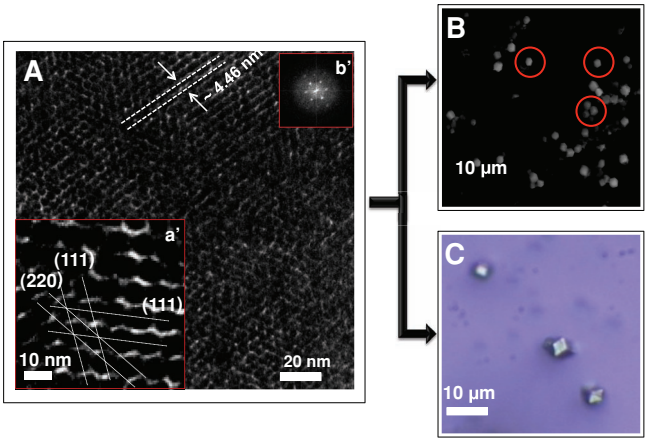

Figure 3. A) TEM image of superlattice formed after 2 h of heating of the plasmonic product **2**. Inset (a') shows an expanded view of the hexagonal array of the NPs with (111) and (220) facets which confirms the periodic arrangement of superlattices (SLs). Inset (b') shows the characteristic hexagonal FFT pattern from the same area emphasizing periodic arrangement of NPs. The SEM image (B) shows that they are hexagonal crystals with sharp edges and C) shows the optical image of the same which further confirms the formation of SL crystals.

material (Figure 3A,b'). This core size of 3.4 nm is in agreement with a cluster of ≈923 atoms, suggested by the mass spectrum. As expected, the crystals in SEM show well-defined facets (Figure 3B). It suggests that each facet has hexagonal plate-like morphologies which confirm the periodic arrangement of the NPs. The residue gave shiny crystals under an optical microscope (Figure 3C). The corresponding TEM image of dark yellow supernatant (obtained after 2 h heating of product **2**) shows a uniform size distribution with a size of 2.4 ± 0.4 nm (Figure S6, Supporting Information) and optical absorption spectrum shows a broad SPR band at 455 nm.

Elemental analysis of the SL by EDAX shows Ag and S at 2.5:1 ratio in agreement with the composition (Figure S7, Supporting Information), $Ag_{\sim 923}(PET)_{\sim 351}$. No other elements (other than C) were seen in significant concentration. These support the formation of particle crystals of atomically precise NPs. The inter-particle distance observed is 5.48 nm (Figure S8, Supporting Information), which is smaller than twice the distance of the clusters (including PET shell and the core, i.e., 5.82 nm). This suggests interdigitation of the monolayers during the formation of SLs.[30]

In summary, we have demonstrated the transformation of atomically precise clusters to NPs and the latter's subsequent conversion to SLs. Although systematic size evolution is studied here with MALDI MS, experiments with electrospray ionization mass spectrometry (ESI MS), small-angle X-ray scattering (SAXS), and dynamic light scattering (DLS) can reveal the dynamics of size evolution in solution and such studies are important to understand the events in solution. The present study, in conjunction with other reports of clusters suggests the possibility of creating SLs of varying core sizes starting from well-defined clusters. This will enable the creation of designer crystals of metals with varying properties as particle growth can be controlled at various stages.

Supporting Information

Supporting Information is available from the Wiley Online Library or from the author.

Acknowledgements

I.C. and T.U. contributed equally to this work. The authors thank the Department of Science and Technology, Government of India and IIT Madras for financial support.

Received: October 16, 2012
Revised: November 22, 2012

[1] H. Qian, M. Zhu, Z. Wu, R. Jin, *Acc. Chem. Res.* **2012**, *45*, 1470.
[2] C. Burda, X. Chen, R. Narayanan, M. A. El-Sayed, *Chem.Rev* **2005**, *105*, 1025.
[3] C. N. R. Rao, G. U. Kulkarni, P. J. Thomas, P. P. Edwards, *Chem. Soc. Rev.* **2000**, *29*, 27.
[4] M. A. Garcia, *J. Phys. D* **2011**, *44*, 283001.
[5] J. A. Scholl, A. L. Koh, J. A. Dionne, *Nature* **2012**, *483*, 421.
[6] L. Dhanalakshmi, T. Udayabhaskararao, T. Pradeep, *Chem. Commun.* **2012**, *48*, 859.
[7] B. L. V. Prasad, S. I. Stoeva, C. M. Sorensen, K. J. Klabunde, *Langmuir* **2002**, *18*, 7515.
[8] B. L. V. Prasad, S. I. Stoeva, C. M. Sorensen, K. J. Klabunde, *Chem. Mater.* **2003**, *15*, 935.
[9] P. Sahu, B. L. V. Prasad, *Chem. Phys. Lett.* **2012**, *525–526*, 101.
[10] D. S. Sidhaye, B. L. V. Prasad, *New J. Chem.* **2011**, *35*, 755.
[11] A. B. Smetana, K. J. Klabunde, C. M. Sorensen, *J. Colloid Interface Sci.* **2005**, *284*, 521.
[12] C. P. Collier, T. Vossmeyer, J. R. Heath, *Annu. Rev. Phys. Chem.* **1998**, *49*, 371.
[13] M. P. Pileni, *J. Phys. Chem. B* **2001**, *105*, 3358.
[14] N. Pinna, M. Maillard, A. Courty, V. Russier, M. P. Pileni, *Phys. Rev. B* **2002**, *66*, 045415.
[15] H. Yao, T. Minami, A. Hori, M. Koma, K. Kimura, *J. Phys. Chem. B* **2006**, *110*, 14040.
[16] W. Cheng, M. J. Campolongo, J. J. Cha, S. J. Tan, C. C. Umbach, D. A. Muller, D. Luo, *Nat. Mater.* **2009**, *8*, 519.
[17] E. V. Shevchenko, D. V. Talapin, N. A. Kotov, S. O'Brien, C. B. Murray, *Nature* **2006**, *439*, 55.
[18] K. Kimura, T. Pradeep, *Phys. Chem. Chem. Phys.* **2011**, *13*, 19214.
[19] E. S. Shibu, J. Cyriac, T. Pradeep, J. Chakrabarti, *Nanoscale* **2011**, *3*, 1066.
[20] E. S. Shibu, K. Kimura, T. Pradeep, *Chem. Mater.* **2009**, *21*, 3773.
[21] T. Udaya Bhaskara Rao, T. Pradeep, *Angew. Chem. Int. Ed.* **2010**, *122*, 4017.
[22] M. Brust, M. Walker, D. Bethell, D. J. Schiffrin, R. Whyman, *Chem. Commun.* **1994**, 801.
[23] H. Tsunoyama, P. Nickut, Y. Negishi, K. Al-Shamery, Y. Matsumoto, T. Tsukuda, *J. Phys. Chem. C* **2007**, *111*, 4153.
[24] E. S. Shibu, T. Pradeep, *Chem. Mater.* **2011**, *23*, 989.
[25] H. Qian, Y. Zhu, R. Jin, *Proc. Natl. Acad. Sci. USA* **2012**.
[26] I. Chakraborty, A. Govindarajan, J. Erusappan, A. Ghosh, T. Pradeep, B. Yoon, R. L. Whetten, U. Landman, *Nano Lett.* **2012**, *12*, 5861.
[27] A. Dass, A. Stevenson, G. R. Dubay, J. B. Tracy, R. W. Murray, *J. Am. Chem. Soc.* **2008**, *130*, 5940.
[28] I. Chakraborty, T. Udayabhaskararao, T. Pradeep, *Chem. Commun.* **2012**, *48*, 6788.
[29] P. K. Jain, M. A. El-Sayed, *Chem. Phys. Lett.* **2010**, *487*, 153.
[30] N. Sandhyarani, T. Pradeep, *Int. Rev. Phys. Chem.* **2003**, *22*, 221.

Submitted to Particle & Particle Systems Characterization

Supporting Information

for *Part. Part. Sys. Charact.*, DOI: 10.1002/ppsc.((please add manuscript number))

Evolution of atomically precise silver clusters to superlattices

*K.S.Sugi, Indranath Chakraborthy[#], T.Udaya Bhaskara Rao[#], Jyoti Sarita Mohanty and T.Pradeep**

S1.Supplementary information 1

Experimental section

Materials

All the chemicals were commercially available and were used without further purification. Silver nitrate ($AgNO_3$, 99%), 2-phenylethanethiol (PET, 97%), tetraoctylammonium bromide (TOABr, 99%), sodium borohydride ($NaBH_4$) and trans-2-[3-(4-tert-Butylphenyl)-2-methyl-2-propenylidene]malononitrile (DCTB) were purchased from Aldrich.

Instrumentation

UV/Vis spectra were measured with a Perkin Elmer Lambda 25 instrument in the range of 200-1100 nm. High resolution transmission electron microscopy of clusters was carried out with a JEOL 3010 instrument. The samples were drop casted on carbon-coated copper grids and allowed to dry under ambient conditions. Matrix-assisted laser desorption ionization mass spectrometry (MALDI MS) studies were conducted using a Voyager-DE PRO Bio-spectrometry Workstation from Applied Bio-systems. A pulsed nitrogen laser of 337 nm was used for the MALDI MS studies. The samples are mixed with DCTB matrix in 1:1 ratio and spotted on target plate and allowed to dry under ambient conditions. Mass spectra were collected in the negative ion mode and were averaged for 200 shots. Scanning electron microscopy (SEM) and energy dispersive X-ray (EDAX) analysis were done in a FEI QUANTA-200 SEM. For measurements, samples were drop casted on an indium tin oxide coated conducting glass and dried in ambient conditions.

Method of Jacobian correction

To amplify the less-intense absorption features, the data have been corrected with the Jacobian factor. For this, the experimentally obtained absorbance values as a function of wavelength [I(ω)], were converted to energy-dependent numbers [I(E)], using the expression,

$I(E) = I(\omega)/ \partial E/\partial \omega \propto I(\omega) * \omega^2$

where $\partial E/\partial \omega$ represents the Jacobian factor.

S2. Supplementary information 2

Photographs during synthesis

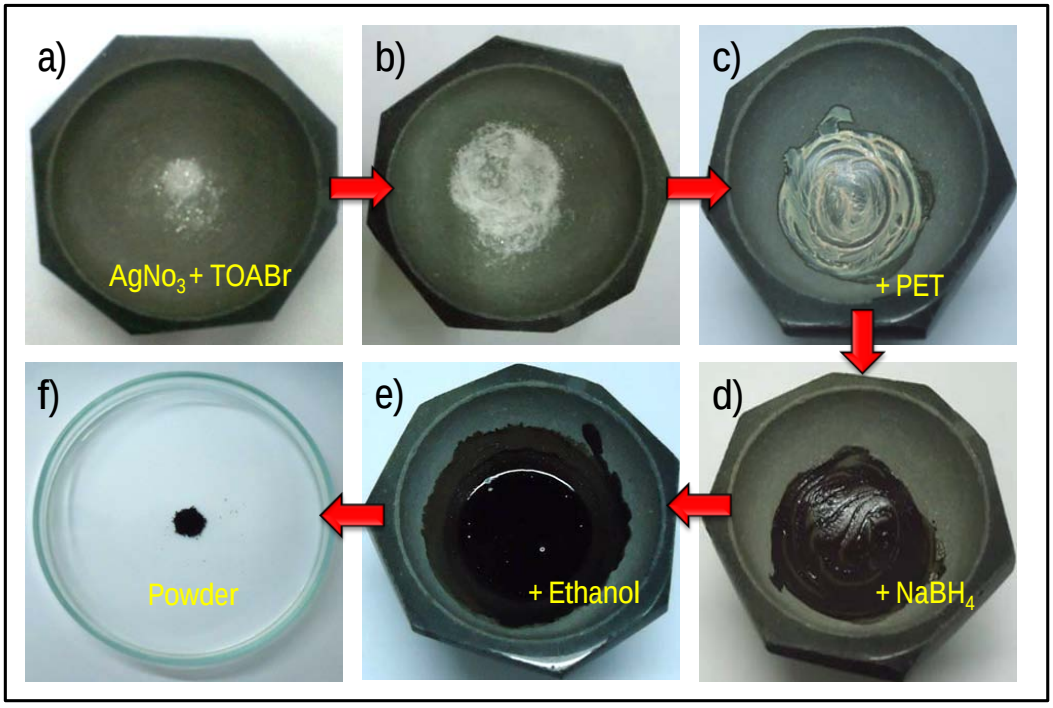

Figure S2. Photographs representing various stages during the synthesis of Ag@PET clusters. The mixture of silver nitrate and TOABr (a) was ground for 5 mins to obtain fine powder of uniform size (b). To that mixture, PET was added and ground well which shows a pale orange color, may be due to the formation of Ag (I) PET thiolate (c). Finally, $NaBH_4$(s) was added and ground uniformly (d). The final mixture was extracted with ethanol (e). This solution contains small clusters which show distinct peaks. After purification these clusters are extracted in toluene. Toluene was removed from the extract and a fine powder was obtained (f).

S3. Supplementary information 3

MALDI mass spectrum, UV/Vis spectrum and TEM of ethanol extracted clusters

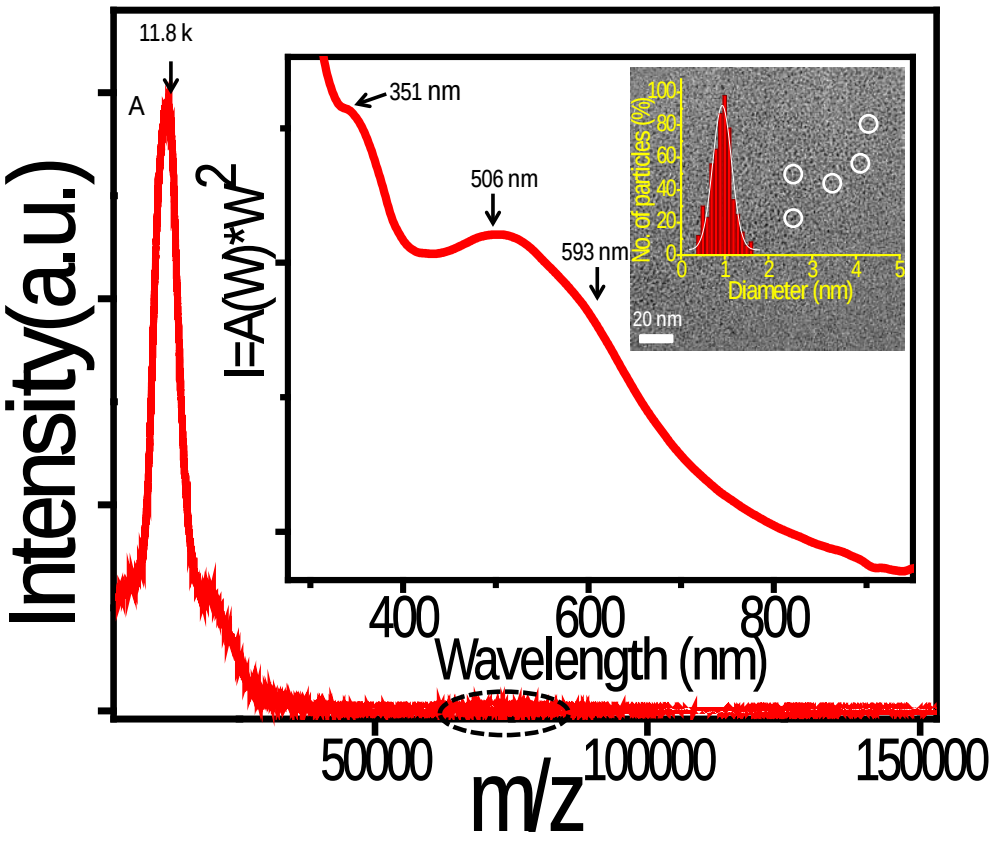

Figure S3. MALDI mass spectrum of Ag@PET clusters extracted in ethanol. Two small humps are arising at 62 and 72 k which are marked by a dotted line. Inset shows the corresponding optical absorption spectrum (corrected by the Jacobian factor). Inset of inset is TEM image and size distribution of the corresponding clusters. Some of the clusters seen are marked by white circles.

S4. Supplementary information 4

Laser dependent MALDI mass spectra of product 1

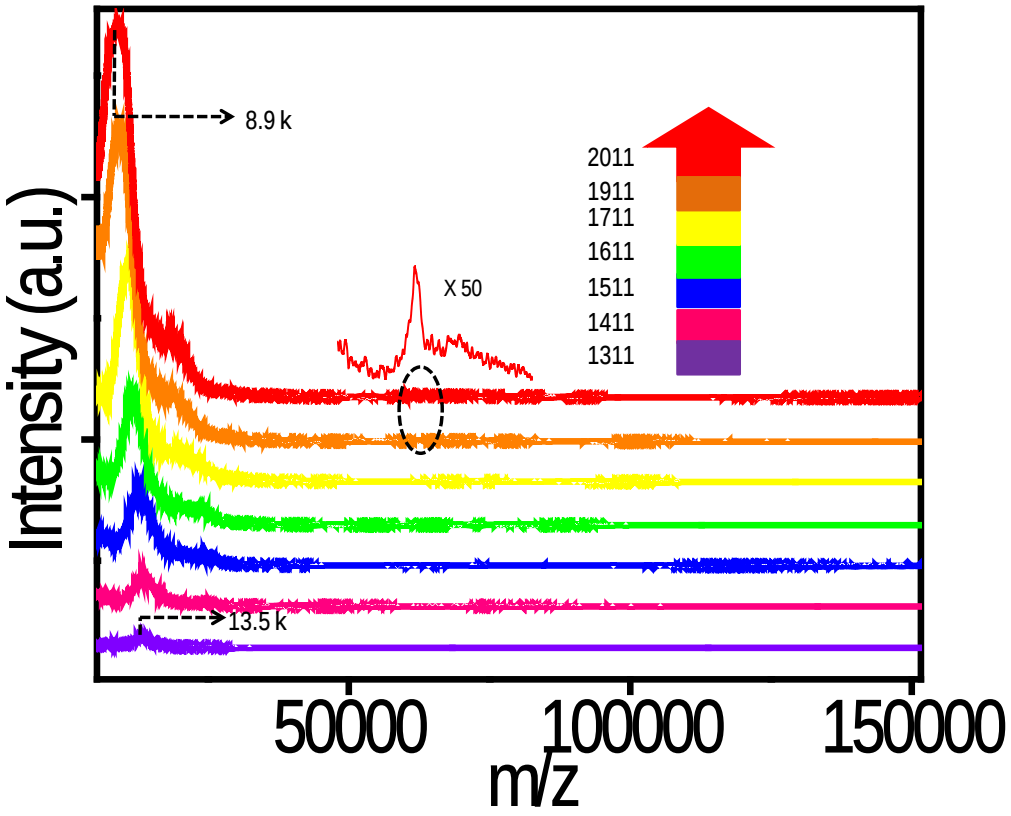

Figure S4. Laser dependent MALDI mass spectra of product **1** extracted in toluene. It shows a shift from 13.5 kDa to 8.9 kDa. This could be attributed to gradual fragmentation arising because of high laser power. The 27 k feature is due to the dimer of product **1**. A small hump near 78 k is seen at high laser power (Inset) which confirms the growth of clusters to form a stable plasmonic product **2**. This requires a higher laser power to desorb.

S5. Supplementary information 5

UV-Vis spectrum and TEM image of PET protected silver NPs

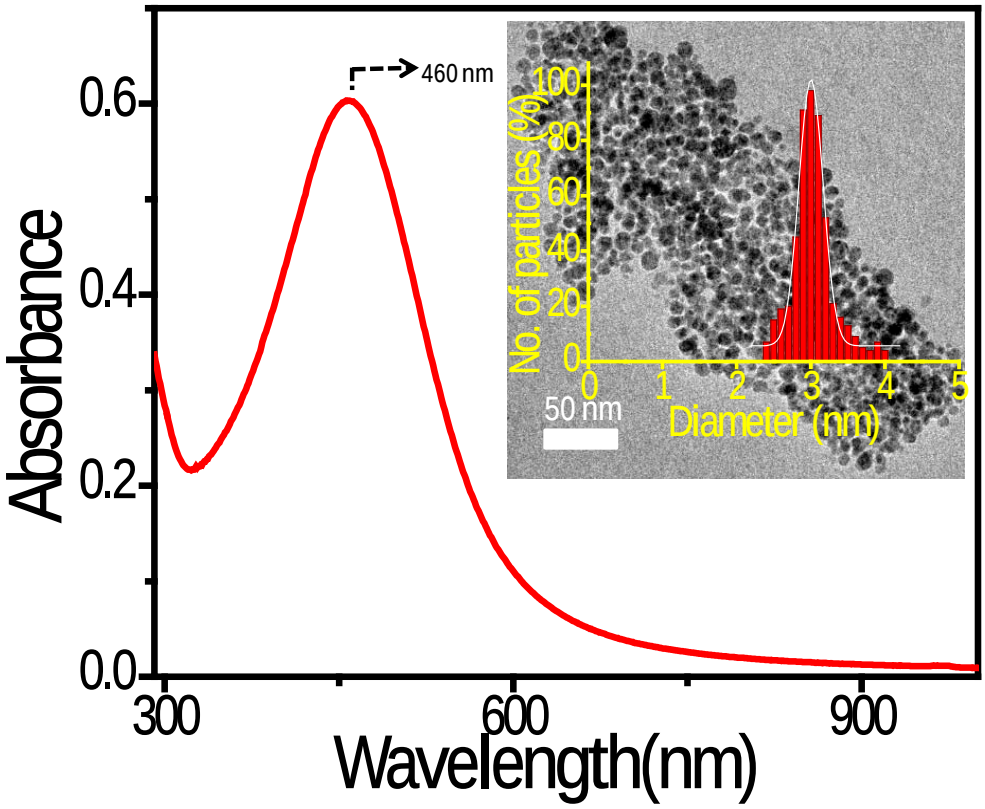

Figure S5. The UV-Vis spectrum of PET protected silver NPs showing a sharp SPR band at 460 nm. Inset shows the corresponding TEM image and size distribution.

S6. Supplementary information 6

UV/Vis spectrum and TEM image of dark yellow supernatant after 2 h heating.

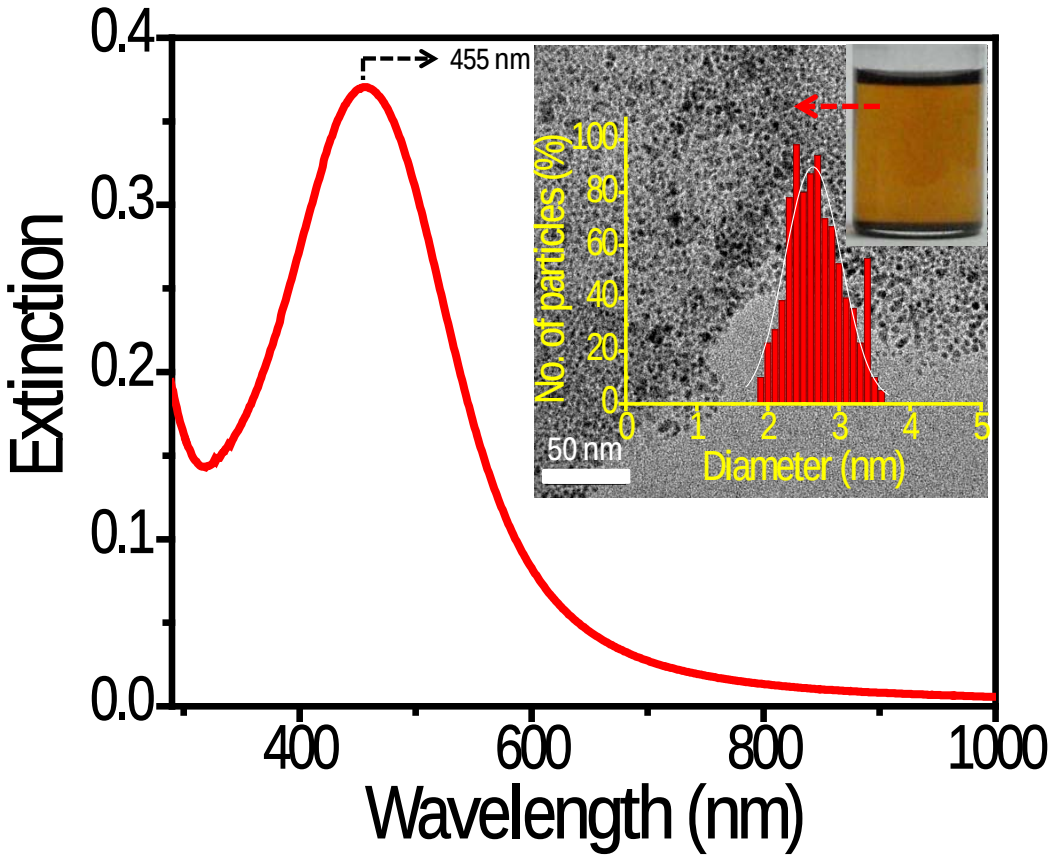

Figure S6. UV/Vis spectrum of the supernatant obtained after 2 h constant heating of product **2**. It shows a SPR band at 455 nm. Inset shows the corresponding TEM image, size distribution and photograph of the solution.

S7. Supplementary information 7

SEM/EDAX of product 3.

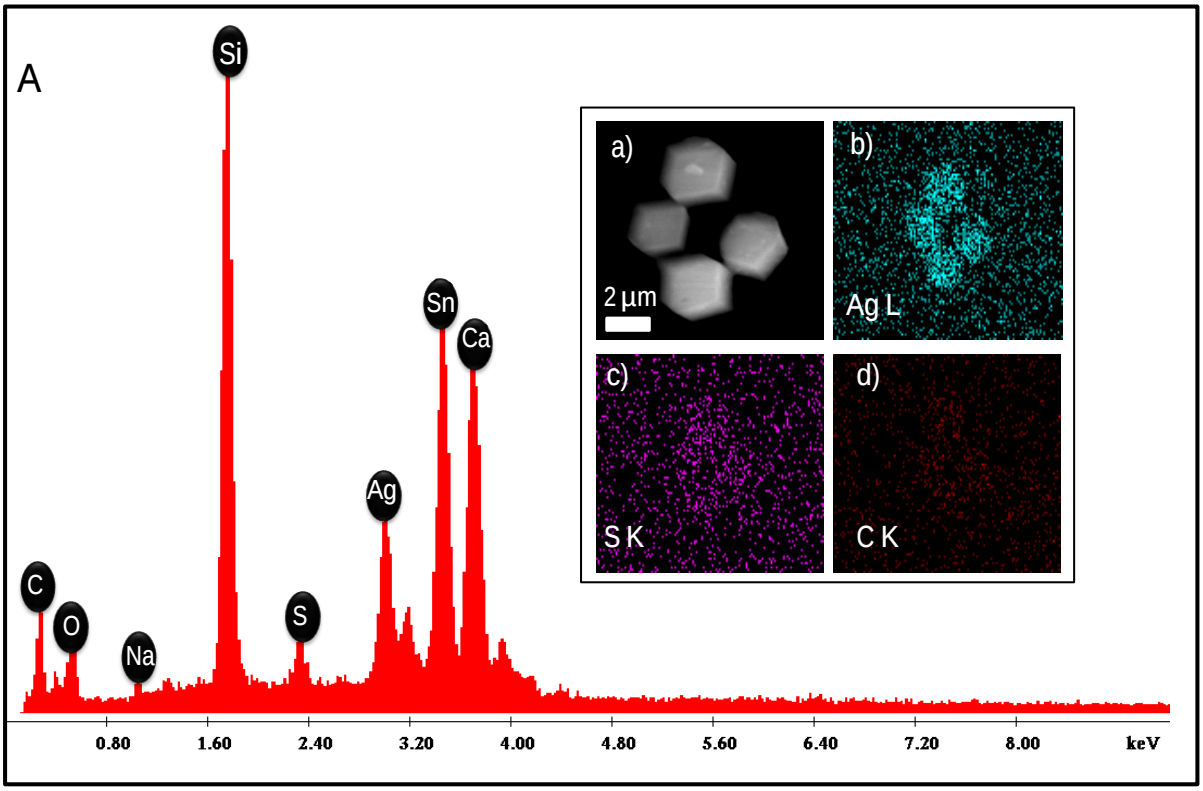

Figure S7. (A) SEM/EDAX spectrum of the SLs (taken on an ITO plate) which shows the presence of silver and sulphur with a ratio of 2.5:1 (Sn Kα, Ca Lα, Si Kα and O Kα are coming from the ITO sample plate). Insets: (a) The corresponding SEM image that shows crystals with sharp edges; (b), (c) and (d) are the elemental maps of Ag, S and C, respectively.

S8. Supplementary information 8

TEM image of product 3.

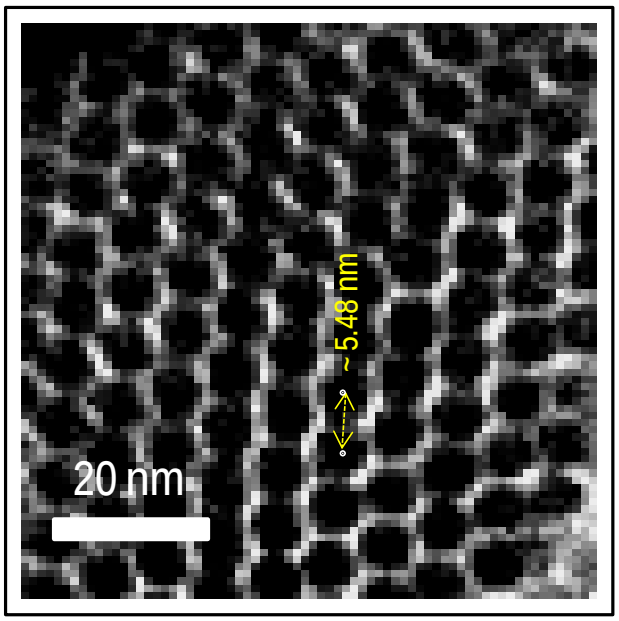

Figure S8. TEM image of product **3** showing definite periodicity and the interparticle distance is ~5.48 nm which is smaller than twice the distance of core+shell which confirms the interdigitation of monolayers. Details of the calculation of distances is below.

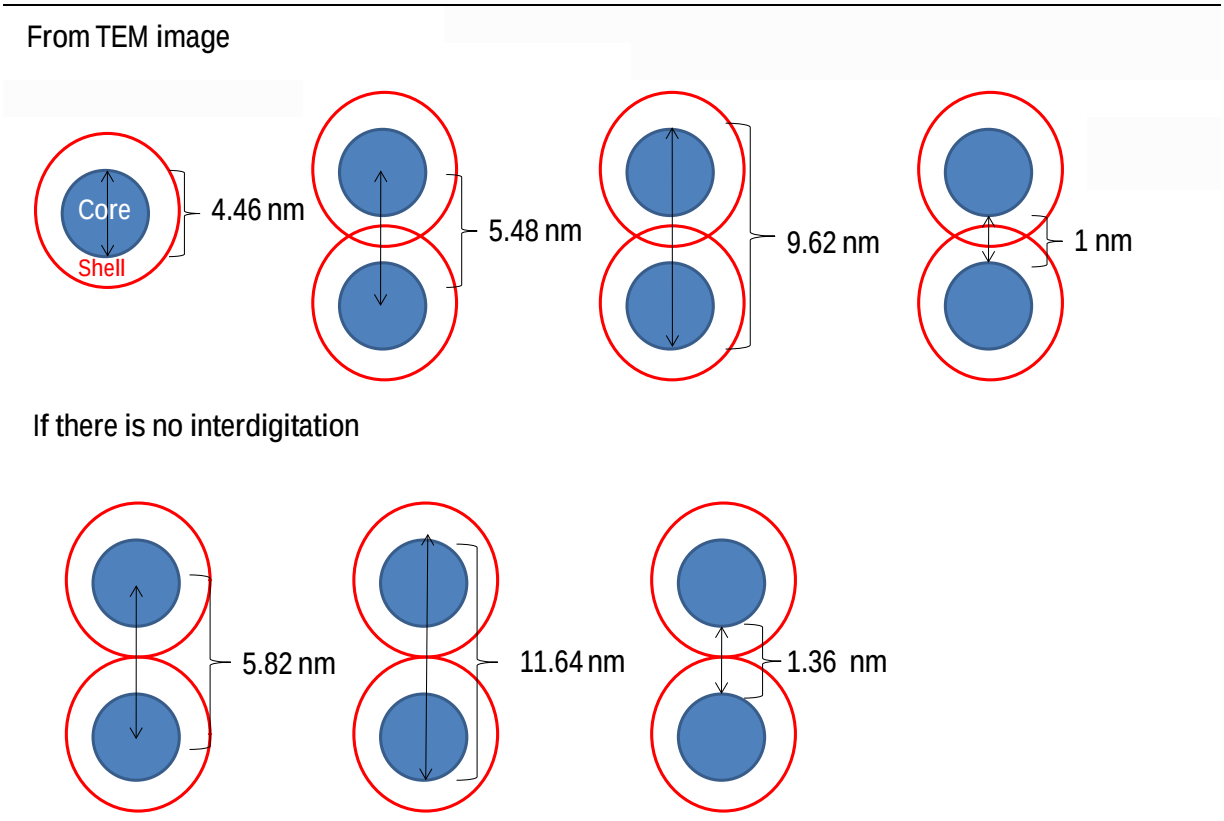

Here metal is considered as core and protecting ligand (PET) is considered as shell.
Chain length of PET is 0.68 nm or 6.8 A°.
Core diameter = 4.46 nm.
Core radius = 2.23 nm.
Chain length of PET = 0.68 nm.
So theoretically interparticle distance = 2 * core radius + 2 * PET chain length = 4.46 nm + 1.36 nm = 5.82 nm.
From TEM image the interparticle distance is 5.48 nm < 5.82 nm, this confirms the interdigitation of monolayers.
If there is no interdigitation, this distance between core of two particles will be twice the length of PET.

Nanoscale

RSC Publishing

PAPER

Protein-encapsulated gold cluster aggregates: the case of lysozyme†

Cite this: *Nanoscale*, 2013, **5**, 2009

Ananya Baksi,[a] Paulrajpillai Lourdu Xavier,[a] Kamalesh Chaudhari,[ab] N. Goswami,[c] S. K. Pal[c] and T. Pradeep*[a]

Received 15th October 2012
Accepted 26th December 2012

DOI: 10.1039/c2nr33180b

www.rsc.org/nanoscale

We report the evolution and confinement of atomically precise and luminescent gold clusters in a small protein, lysozyme (Lyz) using detailed mass spectrometric (MS) and other spectroscopic investigations. A maximum of 12 Au^0 species could be bound to a single Lyz molecule irrespective of the molar ratio of Lyz : Au^{3+} used for cluster growth. The cluster-encapsulated protein also forms aggregates similar to the parent protein. Time dependent studies reveal the emergence of free protein and the redistribution of detached Au atoms, at specific Lyz to Au^{3+} molar ratios, as a function of incubation time, proposing inter-protein metal ion transfer. The results are in agreement with the studies of inter-protein metal transfer during cluster growth in similar systems. We believe that this study provides new insights into the growth of clusters in smaller proteins.

1 Introduction

One of the emerging categories of noble metal nanosystems is their ligand protected, atomically precise, quantum confined analogues, with a core size less than 2 nm. They are referred to as quantum clusters[1–4] (QCs) (also referred to as clusters, quantum confined/sized clusters, metal quantum dots, nanoclusters and superatoms). They exhibit intense luminescence besides distinct optical absorption features due to inter-band and intra-band transitions. Several monolayer protected clusters of this family have been investigated in detail[5–15] and in some cases, crystal structures are also known. For example, the total structures of monolayer protected gold clusters such as $Au_{25}(SR)_{18}$, Au_{38} $(SC_2H_4Ph)_{24}$, $Au_{102}(p\text{-MBA})_{44}$ and more recently, $Au_{36}(SPh\text{-}tBu)_{24}$ have been determined by X-ray crystallography.[13–17] A new window of opportunity has opened up with the creation of quantum clusters using macromolecular templates, where bigger molecules such as DNA,[18] dendrimers,[19,20] *etc.* have been used for cluster growth. New entrants to this fascinating family are protein-protected clusters.[1,21–35] Although they have well-defined molecular compositions and distinct luminescence characteristics, their optical absorption features are ill-defined in comparison to their ligand-protected analogues.[5–17] Both gold and silver clusters, protected with large proteins such as bovine serum albumin (BSA, 66.7 kDa),[21–25] lactotransferrin (Lf, 83.3 kDa),[26,27] and small proteins such as lysozyme (Lyz, 14.3 kDa),[28–32] insulin,[33] (5.8 kDa) horse radish peroxidase[34] and pepsin,[35] have been reported. Recently, AuAg alloy clusters have been synthesized in BSA.[25] Inter-cluster interaction between such clusters produces alloy systems whose compositions are tunable.[25] The luminescence of these protein-protected clusters has been used for biolabeling.[1,22,33,36,37] While functional proteins are fragile in general, a few reports indicating the retention of chemical reactivity and protein's bio-activity are available, however whether this robustness is applicable to many other cluster forming proteins is yet to be known.[33]

Myriad efforts have been made to understand the biomineralization process in the recent past, especially, biomineralization by proteins. Wei *et al.*[31] designed an experiment in which they grew plasmonic nanoparticles inside single lysozyme crystals. They could identify gold (in the ionic form)-bound amino acids by determining crystal structures as a function of time. MS has been the most suitable method to characterize metal clusters, though X-ray crystallography is ideal. We attempted to understand the growth of Au_{QCs} in Lf by time-dependent MS.[27] In these systems, evolution of the cluster core occurs gradually through an Au^{1+} intermediate in solution. Lf forms a thiolate-type of intermediate characterized by a well-defined Au^{1+} feature in the photoemission spectra.[27] Chemical reduction of this intermediate in alkaline pH gradually nucleates the Au cluster. Along with the cluster evolution, the protein is regenerated from the Au^{1+} complex. One of the important questions in such clusters is whether the cluster is generated inside the protein or it grows in-between a few protein molecules.

[a]*DST Unit of Nanoscience, Department of Chemistry, Indian Institute of Technology Madras, Chennai-600036, India. E-mail: pradeep@iitm.ac.in*

[b]*Department of Biotechnology, Indian Institute of Technology Madras, Chennai-600036, India*

[c]*Unit of Nanoscience and Technology, Department of Chemical, Biological and Macromolecular Sciences, Satyendra Nath Bose National Centre for Basic Sciences, Block JD, Sector III, Salt Lake, Kolkata 700 098, India*

† Electronic supplementary information (ESI) available. See DOI: 10.1039/c2nr33180b

A detailed investigation of the growth processes and distinction between these two possibilities require detailed mass spectrometric studies at different stages of growth. The reduction in instrumental resolution and ion transmission at large masses makes it difficult to explore the details of molecular changes in every system, especially in larger proteins. In the present study, instead of Lf or BSA, which are bulky in nature, we have chosen a small protein, Lyz, and probed how different it is from the larger protein analogues. It is important to emphasize that computations have shown that cluster growth within proteins is feasible. Large organic molecules such as dendrimers containing multiple thiol groups can completely wrap an Au_{55} cluster through gold–thiol interactions.[20] Ackerson and Sexton studied the binding of Au_{144} with neuro-proteins through thiol linkers and estimated the rigidity and positional displacement of the cluster using single particle cryo-electron microscopy.[38]

In this paper, we examine the growth of Au clusters in Lyz, a fairly small protein, which allows detailed examination by mass spectrometry. Lyz has a molecular weight of 14.3 kDa. It has 129 amino acid residues including 8 cysteines. These cysteine residues form 4 disulphide bonds located between the positions, 6–127, 30–115, 64–80 and 76–94. Unlike in proteins such as Lf, the mass spectrum of Lyz is characterized by intense features due to dimer, trimer and other higher oligomers. Previously, a few groups have used Lyz for gold cluster synthesis,[28–32] however, the size and growth of gold clusters synthesized in Lyz have not been ascertained through MS. Our study, presented in this paper, conclusively established that the cluster growth happens under the strong influence of cysteines. The chemistry of the cluster encapsulated protein seems to be similar to that of free protein as both of them form similar kinds of aggregates. In monolayer-protected clusters, multiple ligands bind to the cluster surface, while in the case of large proteins, a single molecule of protein acts as a wrapping entity. In the case of BSA or Lf, with high molecular weight, the large number of thiol groups (34 and 36 cysteine residues) and bulky nature may facilitate the formation of clusters within a single protein molecule.[21–27] The small protein used here is intermediate between small ligands and larger proteins with a relatively less number of available S–S groups.[28–33] This investigation will rationally establish the relationship between the protein (ligand) size and the cluster formed and also the number of stabilizing groups binding the cluster surface in encapsulated clusters of this kind. The associated properties of the clusters such as luminescence are discussed only to a limited extent as these aspects have been discussed earlier.[1,21–33]

2 Experimental

2.1 Reagents and materials

Tetrachloroauric acid trihydrate ($HAuCl_4 \cdot 3H_2O$) was prepared in our lab starting from elemental gold. Sodium hydroxide (Rankem, India) was purchased from the local supplier. Lysozyme (>90% purity) and sinapic acid (~99% purity) were purchased from Sigma-Aldrich. All the chemicals were used without further purification. Deionized water was used in all the experiments.

2.2 Instrumentation

For MALDI TOF MS analysis, an Applied Biosystems Voyager De Pro instrument was used with sinapic acid as the matrix. A pulsed nitrogen laser of 337 nm was used for ionizing the sample. Spectra were collected in the positive mode and an average of 250 shots was used for each spectrum. The matrix was prepared by dissolving 10 mg of sinapic acid in a 1 : 3 mixture of acetonitrile: 0.1% trifluoroacetic acid (overall volume of 1 mL). While preparing samples for analysis, 5 μL of the cluster solution, without dilution, was mixed thoroughly with 100 μL of the matrix mixture. 2.5 μL of the resulting mixture was used for spotting. For ESI MS analysis, 10 μL of the sample was taken and diluted to 2 mL with DI water. Trifluoroacetic acid (TFA) (0.1% in DI, 10 μL) was added as an ionization enhancer for spectral collection in the positive ion mode. A Thermo Scientific LTQ XL ESI MS instrument was used for this study. Ion spray voltage was kept at 4.5 kV and the capillary temperature was set at 250 °C. XPS analysis was done to confirm the reduction of Au^{3+} to Au^0. A powdered sample was spotted on the XPS plate. An Omicron ESCA probe spectrometer was used for XPS analysis. Polychromatic Mg Kα ($h\nu = 1236.6$ eV) was used as the ionization source. Curves were smoothed and fitted using the CasaXPS software. Luminescence measurement was carried out in a Jobin Yvon NanoLog fluorescence spectrometer with a band pass of 3 nm for both emission and excitation spectra. UV/Vis spectra were collected using a PerkinElmer Lambda 25 spectrometer in the range of 200–1100 nm. Scanning Electron Microscopic (SEM) and Energy Dispersive Analysis of X-rays (EDAX) images were collected using an FEI QUANTA-200 SEM instrument. High Resolution Transmission Electron microscopic (HRTEM) images were taken using a JEOL 3010 instrument. Picosecond-resolved fluorescence decay transients were measured using a commercially available spectrophotometer (Life Spec-ps, Edinburgh Instruments, UK) with 60 ps instrument response function (IRF). The observed luminescence transients were fitted with a nonlinear least square fitting procedure to a function $(X(t)) = \int_0^t E(t')R((t-t')\mathrm{d}t')$ comprising convolution of the IRF ($E(t)$) with a sum of exponential $\left(R(t) = A + \sum_{i=1}^{N} B_i e^{-t/\tau_i}\right)$ with pre-exponential factors (B_i), characteristic lifetimes (τ_i) and a background (A). Relative concentration in a multi-exponential decay was finally expressed as: $c_n = \frac{B_n}{\sum_{i=1}^{N} B_i} \times 100$. The quality of the curve fitting was evaluated by reduced chi-square. It has to be noted that with our time resolved instrument, we can resolve at least one fourth of the instrument response time constants after de-convolution of the IRF. The Circular Dichroism (CD) spectra were measured in a Jasco 815 spectropolarimeter with a Peltier setup for the temperature-dependent measurements. CD studies were done with a 10 mm path length cell.

2.3 α-Helix calculation

Alpha helix content was calculated from the obtained CD spectra by the formula proposed by Chen *et al.*[39] (α-helix

(%) = $-(\theta + 3000)/39\,000$, where $\theta = \text{MRW} \times \theta_{222}/10lc$, where MRW is mean residual weight (110.9 g per residue for Lyz), θ_{222} is the angle at the wavelength 222 nm, l is path length of the cell (1 cm) and c is the concentration of the sample used for the measurement (10^{-7} g mL^{-1})).

2.4 Synthesis

The synthetic approach for creating luminescent gold clusters was similar to the previously employed methods.[21] Briefly, it involves incubating Lyz with Au^{3+} at a molar ratio of 1 : 4 for 12 hours. The final concentration was 150 μM and 0.625 mM for Lyz and Au^{3+}, respectively. The pH was adjusted to 12 using 1 N NaOH, after adding Au^{3+}. Appearance of red luminescence after 4 hours indicated the formation of clusters in solution. Time and concentration-dependent experiments were conducted for better understanding of the cluster growth mechanism. Most of these were carried out in the solution phase using the as-prepared clusters directly. Several protein-to-gold ratios (1 : 2.5, 1 : 4, 1 : 5, and 1 : 8) were used.

3 Results and discussion

3.1 Formation of Au_{QC}@Lyz and its characterization

Parent Lyz shows its well-defined molecular feature at m/z 14 300 in the linear positive ion MALDI MS spectrum. It is also characterized by the presence of different molecular aggregates at m/z 28 800, 42 900, 57 200 corresponding to dimer, trimer and tetramer, respectively, with a gradual decrease in intensity (blue trace, Fig. 1). Such aggregation can happen in the solution phase as well due to salt bridges formed between the proteins.[40] In the lower mass region ($<m/z$ 8000), the spectra are dominated by multiply charged species and a few fragments. In Fig. 1 (red trace) the spectrum corresponds to the reaction product of 1 : 4 molar ratio of Lyz : Au at pH 12. A unique feature due to the metal cluster appears at m/z 16 270, shifted by m/z 1970 from the parent Lyz, due to 10 Au atoms. This peak is attributed to a quantum cluster of Au_{10} core formed within the protein, referred to as Au_{QC}@Lyz. The di-, tri-, tetra- and even pentamer of Au_{QC}@Lyz showed similar patterns of bound Au atoms. The total number of Au atoms bound, divided by the number of protein molecules in the aggregate confirmed the distribution of 10 Au atoms per protein in each case. This suggests that each protein entity contains a strongly bound, ten-atom gold nanostructure. Further, it signifies that the observed di-, tri-, tetra-, and pentamers are likely to be aggregates of individual protein molecules, each containing a ten-atom cluster of gold within, rather than aggregates of protein molecules bound to a multi-atom gold species. In the latter case, the number of Au atoms cannot increase systematically in multiples of 10 with the aggregation number. Interestingly, it was the cluster feature which was more prominent in the entire mass range and beyond the trimer region; free protein features were nearly absent. The monomer region expanded in the inset of Fig. 1 shows distinct binding of Au to the parent protein. The mass spectrum of Au_{QC}@Lyz exhibits an increased width after the attachment of gold (inset of Fig. 1). This is evident in the monomer region of the parent protein which also shows distinct features spaced by m/z = 197 due to Au ion uptake. The cluster features were stable although minor changes in the nuclearity of the cluster core is evident with time in the monomer region (Fig. S1†). However, the trimer, tetramer and

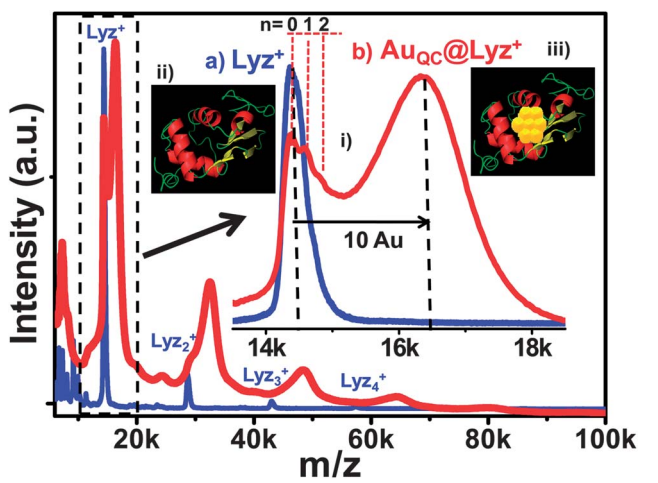

Fig. 1 Positive ion MALDI MS of Lyz at pH 12 in linear mode (a) and Au_{QC}@Lyz after 24 hours of incubation (b). All the spectra were measured in the linear positive mode over the m/z range of 2000–100 000. Both Lyz and Au_{QC}@Lyz showed aggregate formation. The expanded monomer region in inset (i) clearly shows a separation of 10 Au atoms from the parent protein. In the dimer, trimer, tetramer and pentamer regions, the separations are of 20, 30, 40 and 50 Au atoms, respectively. In insets (ii) and (iii), schematic representations of Lyz and Au_{QC}@Lyz, respectively, are shown.

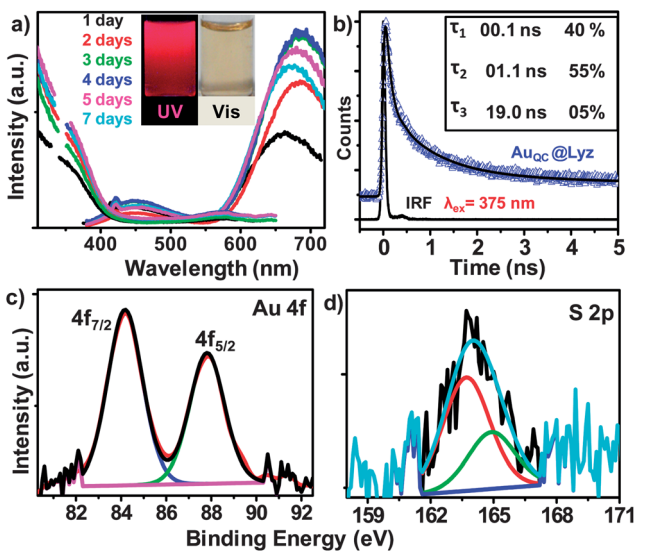

Fig. 2 (a) Time dependent luminescence spectra of the as-synthesized Au_{QC}@Lyz at 365 nm excitation showing an emission maximum around 680 nm. The inset photographs show the color of the cluster solution under ultraviolet and visible radiations, respectively. (b) Luminescence decay of Au_{QC}@Lyz with instrument response function (IRF) ~80 ps. Lifetime values are shown in the inset. Standard error of time components is ~10%. X-ray photoelectron spectra of the as-synthesized Au_{QC}@Lyz showing the presence of (c) Au^0 in Au 4f and (d) thiolate BE in S 2p.

other oligomers did not show significant change over the period investigated. This change in nuclearity is also reflected in the luminescence profile which shows a shift of nearly 25 nm in this time window (Fig. 2a). Two emission maxima, one at 450 nm (which is likely to be from the protein alone, and it has been observed in several instances involving metal ion reduction by aromatic amino acids[26,27,41,42] and also upon the oxidation of protein's intrinsic fluorophores[43]) and the other at 686 nm were observed and the latter was blueshifted to 661 nm after 5 days (excitation wavelength was 365 nm) while the former remained the same. As there is a slight change in the core size, the luminescence is also blueshifted (see the MS data (Fig. S1†)). The decrease in mass spectral intensity of the cluster is evident in the luminescence spectrum as well. Up to a certain period of time, the intensity goes on increasing and after that it again starts decreasing along with a slight blueshift in the peak position. This shift may be due to the loss of one Au atom from the core which is evident from the mass spectral analysis. As luminescence in protein encapsulated noble metal clusters has been studied earlier[21–36] we presented only the essential aspects of relevance here.

The calculated quantum yield (QY) of the cluster is nearly 15.6% taking Rhodamine 6G as the standard (QY = 95% at 488 nm excitation in water).[23] The luminescence decay of the Au_{QC}@Lyz in water was measured by a picosecond-resolved time-correlated single-photon counting (TCSPC) technique. Fig. 2b demonstrates the decay transients of the Au_{QC}@Lyz. Lifetime values of the clusters were obtained by numerical fitting of the luminescence at 650 nm. Lifetimes of Au_{QC}@Lyz were 0.1 ns (40%), 1.1 ns (55%) and 19.0 ns (5%) (see Fig. 2b). Similarity of the lifetime components with the reported other protein protected clusters reveals that the 650 nm emission is coming predominantly from the Au QCs. The obtained lifetime values, in comparison with the previous reports of Au_{25}@proteins,[22,26] suggest this species to be smaller than Au_{25} and the reduction in lifetime is distinct in the short and long components, which in turn is supported by the MS data.

Fluorescence in ligand-protected Au_{QCs} is largely influenced by the nature of the ligands and is not fully understood yet. Murray and co-workers[44] showed that in the case of Au_{38} and Au_{140}, the near infrared luminescence intensity increased linearly with the proportion of polar thiolate ligands. Although there were insignificant changes in the absorption spectra of various ligand exchanged Au_{25} clusters, noticeable changes were seen in their luminescence spectra.[45] Jin and Wu[46] also have recently shown that ligands and their length play a vital role in the luminescence of Au_{25}. Recently, in thiolate protected AuAg alloy clusters, an increase in fluorescence lifetime was observed as a function of ligand length.[47] These observations propose that in bulky ligands as in proteins, there are several contributing effects which enhance the luminescence intensity. Factors such as multiple interaction sites facilitating electron and energy transfer between the amino acids, isolation of the metal core from the medium as seen in Au_{15}@cylcodextrin[48] and distinct Förster resonance energy transfer (FRET) are expected to play crucial roles in the observed high luminescence. We note, however, that the electronic structure of protein encapsulated clusters is entirely different from their monolayer protected analogues as manifested in the differences in their absorption spectra.

Existence of a nearly metallic (Au^0) cluster core is further supported by the photoemission data. Au $4f_{7/2}$ appears at 84.2 eV close to the Au^0 binding energy (BE) (Fig. 2c). The BE is slightly higher than the same for Au^0 due to the core size effect and the bonding environment. $4f_{7/2}$ binding energy values for Au^{3+}, Au^{1+} and Au^0 are 87.3, 85.4 and 84.0 eV, respectively.[25,27] S 2p BE confirms the presence of Au–S bonding (Fig. 2d). The S $2p_{3/2}$ occurs at 163.0 eV which supports the thiolate binding on the Au core. The Au : S atomic ratio found was 12 : 7, which is close to the value corresponding to 10 Au and 8 S, per cluster. Also, it reveals the absence of excess sulphur, unlike that observed in clusters formed with larger proteins like BSA or Lf.[25,26] The spectral width is slightly higher than that observed for Au thin films, suggesting the possibility of multiple oxidation states present in the clusters. No other component such as sulphate, or sulphonate was observed. This may be attributed to the absence of X-ray-induced damage in the sample which supports the complete protection of the cluster core. From the survey spectrum (shown in Fig. S2†) we confirm the existence of all the possible elements: carbon, nitrogen, oxygen, sodium, chlorine, gold and sulphur. All the BE values are corrected with respect to the C 1s binding energy of 285.0 eV. Energy dispersive analysis of X-rays (EDAX) also confirmed the presence of all the elements (Fig. S3†).

A HRTEM study revealed that these clusters have a core size of 1.1 ± 0.1 nm, which is in good agreement with the size of protein protected noble metal clusters (inset of Fig. S4†). Although it is not a confirmative tool to know the size of protein-protected clusters, the observation conclusively establishes the absence of bigger nanoparticles in solution. The common spectroscopic tool, UV/Vis, is inadequate to identify the nature of the core in protein protected gold nanoclusters, since they do not exhibit well defined features of the core unlike the monolayer protected analogues which have well-defined spectroscopic features and are sensitive even in a minor change in the core size. The UV/Vis spectra show two peaks: one near 290 nm which is a characteristic of aromatic amino acids in proteins and the other (hump) around 353 nm, possibly due to oxidized aromatic amino acid residues[42] (Fig. S4†). No plasmon resonance peak was observed which again confirms the absence of bigger nanoparticles in solution.

3.2 Difference in alkali metal binding and Au binding

Binding of metal ions to proteins is expected. However, binding with noble metals is distinctly different in comparison to common ions such as alkali metals. To see this difference, we have performed electrospray ionization mass spectrometry (ESI MS) studies. In the control experiment, 0.1 mM alkali metal chlorides were added to Lyz and ESI MS was recorded (Fig. 3a). The spectra are expanded in the +8 charge state region, in the inset. As the size of the metal ion increases from Na to Cs, the number of attachments decreases. For Na and K, addition of up to 5 metal ions is seen at that concentration; but for Rb it is up

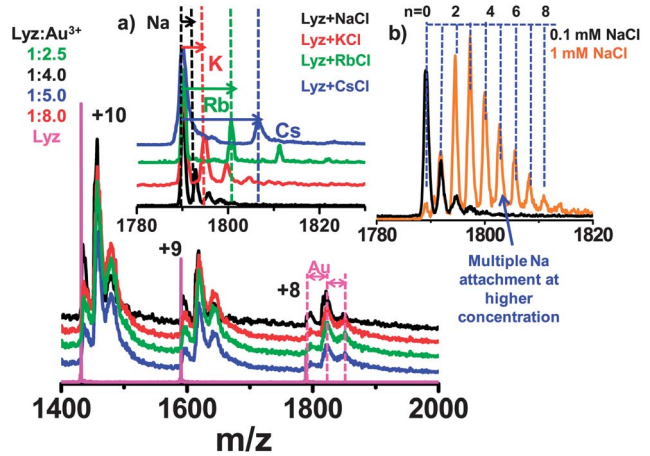

Fig. 3 ESI MS of the Lyz and Au^{3+} mixture without the addition of base showing a fixed number of Au atom attachments to Lyz irrespective of the concentration used. A maximum of three Au atoms are attached to Lyz at the experimental condition. Inset (a) shows different metal ion uptakes at a very low concentration of metal chlorides. Separations from the main protein peak are due to different metal ion uptakes. While Na and K ions show multiple uptakes due to a smaller size, Rb and Cs ions show a limited number of uptakes at the same condition. In inset (b), multiple Na atom attachments are seen at a higher concentration of NaCl, revealing that binding sites for alkali metal atoms are different from that for Au atoms.

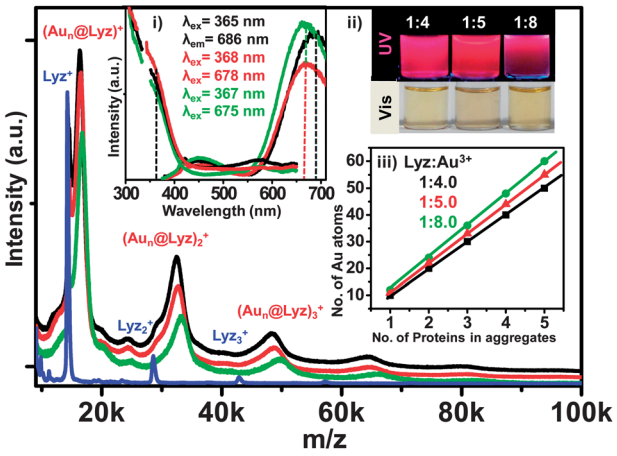

Fig. 4 Concentration dependent MALDI MS at various Lyz to Au^{3+} molar ratios: 1 : 2.5, 1 : 4, 1 : 5 and 1 : 8. Numbers of Au atoms in the cores are 10, 11 and 12 for Lyz to Au^{3+} ratios of 1 : 4, 1 : 5 and 1 : 8, respectively. Inset (i) shows comparative luminescence spectra of different concentrations of Au^{3+}. The excitation wavelengths do not change significantly for different Lyz to Au^{3+} ratios. Emission peak positions vary from 675 to 686 nm (for time dependent luminescence spectra see Fig. 2 and S8–S10†). Inset (ii) shows photographs of different cluster solutions under ultra-violet and visible light. In inset (iii) a comparative plot of the number of gold ions uptaken by various oligomers at different protein to Au^{3+} concentrations after 7 days is shown. Au uptake by different oligomers shows a linear dependence.

to 3 and for Cs it is only up to 2. The same experiment was carried out using a high concentration (1 mM) of Na^+. In this condition, nearly 10 Na ions were bound to the protein (Fig. 3b). So it can be concluded that the number of Na ion uptake increases with increasing concentration. Various mixtures of Lyz : Au^{3+} ratios were taken; namely, 1 : 2.5, 1 : 4, 1 : 5 and 1 : 8. In the ESI MS for all cases (Fig. 3), the same number of Au atom attachments was seen. Au atoms are likely to bind to the cysteine residues of the protein. In Lyz, there are 8 cysteine units to bind with Au, although we see only a few attachments. This may be due to the high charge state of the protein which cannot stabilize large number of Au atoms and overlapping of one charge state region with the next one does not allow us to resolve the exact number of Au atom attachments. On the other hand, there are several carboxyl and hydroxyl groups in the protein for the uptake of alkali metal ions. If we keep on increasing alkali metal ion concentration, proteins will show uptake until all the sites are occupied. But there are also a limited number of free carboxyl and hydroxyl groups; hence alkali metal ion attachment cannot go beyond this. From this study, it is evident that binding of Au is totally different from binding in alkali metal ions. While Au binding is strongly influenced by cysteine residues, alkali metals prefer to bind with the carboxyl and hydroxyl groups of different amino acid residues.

3.3 Dependence of Au^{3+} concentration: clusters and cluster dimers, trimers, mixed dimers

While cluster binding to the protein is evident in Fig. 1 and 4, it is not conclusive whether the cluster is encapsulated within it or not. One of the definite proofs for the existence of the cluster core within is the systematic shift observed in the mass of the protein aggregates. We explored this in two different cases, high and low exposures of gold. The higher concentration regime is discussed first. The amount of Au ion uptake is weakly sensitive to the quantity of Au exposed. Average cluster size ranges from 10–12 in protein to metal ratios of 1 : 4, 1 : 5 and 1 : 8 (Fig. 4). Such cores are designated as Au_{10-12} in the text below. Uptake in the dimer and oligomer regions is directly proportional to the uptake shown by the monomer. At no region of the mass spectrum is seen a trimer or tetramer with the same core as seen in the monomer (Fig. S5 and S6†). The absence of $Au_{10-12}@(Lyz)_{2,3,...}$ species suggests the absence of entities where a single Au_{10-12} core is surrounded by several protein molecules in solution. This is also supported by the metal ion uptake by the parent protein, which shows a series of Au uptake peaks. In the dimer region, a feature appears where the separation between the parent dimer and the new feature is double that of the corresponding peaks in the monomer region. This would imply that the formation of aggregates is either a solution phase effect and are not formed in the gas phase due to the association reactions between vapor phase species. In association reactions, there are multiple possibilities which are not observed. This kind of shift is seen in higher aggregates such as thrice in trimer, quadruple in tetramer, *etc.* This systematic change is depicted in Fig. 4iii. In the lowest concentrations alone, some non-uniformity is seen as mentioned above which appears to be due to the presence of excess protein in which most of the binding sites for gold are free. Although these aggregates exist in the solution, the photophysical properties of the clusters do not show their presence. This appears to be due to large inter-cluster distance as each cluster core is surrounded

by a protein shell. Taking the overall size of Lyz to be nearly 4 nm, the inter-cluster distance is 8 nm which is much larger than that which would facilitate electronic interaction between the cores. This is manifested in the luminescence spectra where only very minor shifts are seen (Fig. 4i). No observable effect is seen in the photographs (Fig. 4ii).

3.4 Cluster growth mechanism: multiple cluster growth through the regeneration of free protein

This change is even more dramatic in the time dependent case presented in Fig. 5 at low concentration, upon exposure of Au over a long time. It is the lowest protein to Au^{3+} conc. ratio that was examined. At a shorter incubation time, of the order of a day, a shoulder comes at a separation of 10 gold atoms in the monomer region while the shift was neither 10 nor 20 in the dimer region. It is a broad hump in-between 10 and 20 Au atoms. With time (for time dependent study see Fig. S7†), the peak in the monomer region starts shifting to a higher mass of 12 Au atoms separation and interestingly the dimer region gets divided into two peaks; one due to 12 Au atoms and another due to ~20 Au atoms. The same thing happens to the trimer region also where peaks are separated by ~12 and ~22 Au atoms. For the tetramer, the separations are 12 and 26 Au atoms. Because of the broad hump, it was not possible to identify other species in the trimer and tetramer regions. After the tetramer region, it is hard to resolve the peak separation due to reduced intensity. As explained earlier, there is a gradual emergence of free protein with time in the cluster system. These free proteins enable the formation of Au_{10-12}@Lyz–Lyz along with $(Au_{10-12}$–$Lyz)_2$ and the possibility of the former increases with time as free Lyz concentration increases. As a result, the dimer region exhibits both these features (Au_{10-12}@Lyz–Lyz and $(Au_{10-12}$–$Lyz)_2$) with a characteristic mass shift. As the free Lyz concentration keeps increasing with time, the dimer region shows only Lyz_2 and Au_{10-12}@Lyz–Lyz features. Corresponding changes are seen in the larger aggregates as well. It is important to note that if one cluster is surrounded by multiple proteins, we would have observed Au_{10-12}–Lyz_n features prominently for dimer, trimer, *etc.* and these are not seen. Instead $(Au_{10-12}$@$Lyz)_n$ features are dominant.

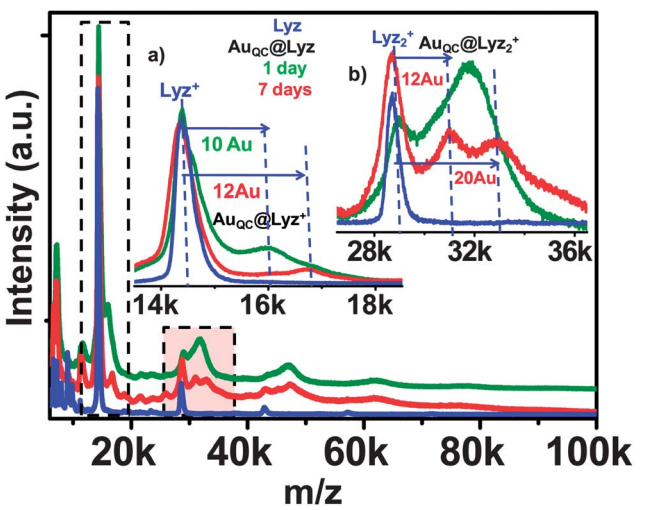

Fig. 5 MALDI MS of a Au_{QC}@Lyz, where the lowest Lyz to Au^{3+} molar ratio (1 : 2.5) was used. There is a clear change in the spectra as the storage time changes from one day (green trace) to 7 days (orange trace). Insets: (a) expanded view of the monomer region and the (b) dimer region. The trimer also has two different separations at 12 and 22 Au atoms. For higher oligomers, the separation was not resolvable.

3.5 Change in the protein secondary structure

Formation of the cluster affects the secondary structure of the protein. Large changes were seen in the fraction of α helices after cluster formation, as a loss of 28% (total helix content decreased from 49% to 21%) was observed in the circular dichroism (CD) spectra. This may be correlated to the structure of lysozyme where cysteine residues are present (at 6, 30, 64, 80, 115 and 127 amino acid positions)[49] and four of which are located in the vicinity of α helices.[41] As the disulphides were broken and used to stabilize the cluster core, drastic changes in the total helix content was observed. Computational studies showed that the disulphide bond can break upon the addition of Au^{3+} to Lyz, as one disulphide bond breaks to give two sulphur ends and two electrons are donated to form the cluster core upon the addition of Au^{3+} alone.[50] A net loss of α-helix structure and increase in β-sheets and random coils is evident from the FTIR spectra, as follows, corroborating the CD observations.

Distinct changes in the amide region were observed. Amide bands I, II and III are characteristic of the protein's secondary structure.[26,51] The band near 1650 cm^{-1} arises mainly from the C=O stretching vibration with a minor contribution from the out of plane C–N stretching. This is attributed as the amide I signature. Another band near 1550 cm^{-1} is due to the out of phase combination of NH in plane bending with a smaller contribution from C=O in plane bending as well as C–C, and C–N stretching. The region 1400–1200 cm^{-1} is due to amide III vibrational modes. A significantly broad band arises near 3300–3000 cm^{-1} due to N–H and O–H stretching vibrations. This region is ascribed as a mixture of amide A and amide B.[26,51] From the IR data (Fig. S11†), it is clear that there are changes in

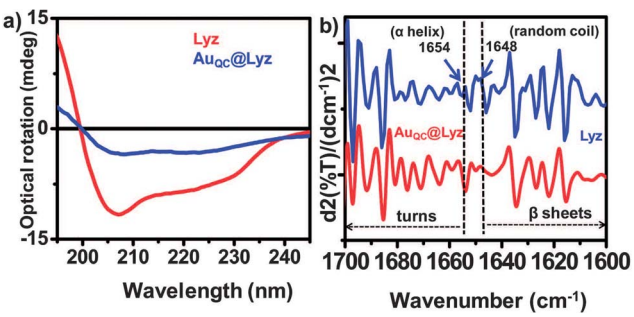

Fig. 6 (a) CD spectra of Lyz and as prepared Au_{QC}@Lyz showing a clear change in ellipticity of the spectra, which indicates a huge change in the alpha helical structure. (b) Double derivative of the infrared (IR) spectra shows the disappearance of the peak at 1654 cm^{-1} in the case of Au_{QC}@Lyz.

the amide region. A band near 700 cm^{-1} can be attributed to $-NH_2$ and NH wagging. Bands at values >2950 cm^{-1} are due to C–H stretching in $-CH_3$, $-CH_2$, and –CH groups. The O–H stretching frequency is also observable as a broad peak around 3500 cm^{-1}. Second derivative IR (in the region 1600–1700 cm^{-1}), which is more sensitive, revealed the changes in the amide region due to cluster formation. Among α-helix (1651–1658 cm^{-1}), β-sheets (1618–1642 cm^{-1}), random coils (1640–1650 cm^{-1}) and turns (1666–1688 cm^{-1}), the α-helix region showed large changes. A clear change can be seen in the α-helix feature at 1654 cm^{-1} which is completely absent in the case of the cluster, because of the huge perturbation of the α-helical regions, which may be due to breakage of disulphide bonds for cluster formation as mentioned above (Fig. 6).

4 Summary and conclusion

A mass spectrometric investigation to understand the nature of gold cluster formation by small proteins, represented by the model protein, lysozyme has been performed. The red emitting cluster formed is of ~10 Au atoms, which is smaller than the reported cluster size in bigger proteins such as BSA or Lf. An interesting phenomenon of protein aggregates formed by cluster containing proteins was observed. Furthermore, the emergence of free protein during the synthesis suggested interprotein metal transfer. In conclusion, we suggest that small protein molecules, such as Lyz, can wrap and stabilize very small cluster cores consisting of 10, 11 and 12 Au atoms. The growth mechanism is highly dependent on the disulphide bond breakage where cysteine residues can form Au–S bonds and the core is stabilized by thiolate linkages. From a comparative study with alkali metal ions, we demonstrated the difference between the binding of Au and Na ions with the protein. Whereas Na^+ binds to carboxyl and hydroxyl groups, Au^+ prefers the sulphurs of cysteines for binding. An extensive MALDI MS study in the entire mass range of the protein and its aggregates suggests that the cluster is held within the protein molecule. In a nutshell, we have demonstrated a confirmative mass spectrometric analysis to prove endoprotein cluster growth using a small protein, Lyz, as a model. This is one of the first steps in understanding of the system and more steps are ahead to elucidate the exact mechanism of this kind of cluster growth. We believe that this study would rationally establish the relationship between the protein (ligand) size and the cluster formed. A detailed understanding of the protein conformational change and, probably, computer simulation of cluster growth would lead to new directions in this area.

Acknowledgements

We thank Department of Science and Technology for funding our research program on nanomaterials. A.B. and N.G. thank Council of Scientific and Industrial Research (CSIR) for a research fellowship. A.B. thanks Amitava Srimany, M. S. Bhootaraju and Jyoti Sarita Mohanty for useful discussions.

References

1 P. L. Xavier, K. Chaudhari, A. Baksi and T. Pradeep, *Nano Rev.*, 2012, **3**, 14767, and the references cited therein.
2 J. Zheng, P. R. Nicovich and R. M. Dickson, *Annu. Rev. Phys. Chem.*, 2007, **58**, 407–431.
3 J. Zheng, C. W. Zhang and R. M. Dickson, *Phys. Rev. Lett.*, 2004, **93**, 077402/1–4.
4 R. Jin, *Nanoscale*, 2010, **2**, 343–362.
5 T. U. B. Rao, B. Nataraju and T. Pradeep, *J. Am. Chem. Soc.*, 2010, **132**, 16304–16307.
6 M. Zhu, E. Lanni, N. Garg, M. E. Bier and R. Jin, *J. Am. Chem. Soc.*, 2008, **130**, 1138–1139.
7 Y. Negishi, K. Nobusada and T. Tsukuda, *J. Am. Chem. Soc.*, 2005, **127**, 5261–5270.
8 Y. Shichibu, Y. Negishi, T. Tsukuda and T. Teranishi, *J. Am. Chem. Soc.*, 2005, **127**, 13464–13465.
9 C. Kumara and A. Dass, *Nanoscale*, 2011, **3**, 3064–3067.
10 C. Kumara and A. Dass, *Nanoscale*, 2012, **4**, 4084–4086.
11 K. Kimura, N. Sugimoto, S. Sato, H. Yao, Y. Negishi and T. Tsukuda, *J. Phys. Chem. C*, 2009, **113**, 14076–14082.
12 M. W. Heaven, A. Dass, P. S. White, K. M. Holt and R. W. Murray, *J. Am. Chem. Soc.*, 2008, **130**, 3754–3755.
13 M. W. Heaven, A. Dass, P. S. White, K. M. Holt and R. W. Murray, *J. Am. Chem. Soc.*, 2008, **130**, 3754–3755.
14 M. Zhu, C. M. Aikens, F. J. Hollander, G. C. Schatz and R. Jin, *J. Am. Chem. Soc.*, 2008, **130**, 5883–5885.
15 H. Qian, W. T. Eckenhoff, Y. Zhu, T. Pintauer and R. Jin, *J. Am. Chem. Soc.*, 2010, **132**, 8280–8281.
16 P. D. Jadzinsky, G. Calero, C. J. Ackerson, D. A. Bushnell and R. D. Kornberg, *Science*, 2007, **318**, 430–433.
17 C. Zeng, H. Qian, T. Li, G. Li, N. L. Rosi, B. Yoon, R. N. Barnett, R. L. Whetten, U. Landman and R. Jin, *Angew. Chem., Int. Ed.*, 2012, **51**, 13114–13118.
18 J. T. Petty, J. Zheng, N. V. Hud and R. M. Dickson, *J. Am. Chem. Soc.*, 2004, **126**, 5207–5212.
19 X. Sun, X. Jiang, S. Dong and E. Wang, *Macromol. Rapid Commun.*, 2003, **24**, 1024–1028.
20 D. Thompson, J. P. Hermes, A. J. Quinn and M. Mayor, *ACS Nano*, 2012, **6**, 3007–3017.
21 J. Xie, Y. Zheng and J. Y. Ying, *J. Am. Chem. Soc.*, 2009, **131**, 888–889.
22 M. A. H. Muhammed, P. K. Verma, S. K. Pal, A. Retnakumari, M. Koyakutty, S. Nair and T. Pradeep, *Chem.–Eur. J.*, 2010, **16**, 10103–10112.
23 X. Le Guével, B. Hötzer, G. Jung, K. Hollemeyer, V. Trouillet and M. Schneider, *J. Phys. Chem. C*, 2011, **115**, 10955–10963.
24 A. Mathew, P. R. Sajanlal and T. Pradeep, *J. Mater. Chem.*, 2011, **21**, 11205–11212.
25 J. S. Mohanty, P. L. Xavier, K. Chaudhari, M. S. Bootharaju, N. Goswami, S. K. Pal and T. Pradeep, *Nanoscale*, 2012, **4**, 4255–4262.
26 P. L. Xavier, K. Chaudhari, P. K. Verma, S. K. Pal and T. Pradeep, *Nanoscale*, 2010, **2**, 2769–2776.
27 K. Chaudhari, P. L. Xavier and T. Pradeep, *ACS Nano*, 2011, **5**, 8816–8827.

28 H. Wei, Z. Wang, L. Yang, S. Tian, C. Hou and Y. Lu, *Analyst*, 2010, **135**, 1406–1410.
29 Y.-H. Lin and W.-L. Tseng, *Anal. Chem.*, 2010, **82**, 9194–9200.
30 W.-Y. Chen, J.-Y. Lin, W.-J. Chen, L. Luo, E. W.-G. Diau and Y.-C. Chen, *Nanomedicine*, 2010, **5**, 755–764.
31 H. Wei, Z. Wang, J. Zhang, S. House, Y.-G. Gao, L. Yang, H. Robinson, L. H. Tan, H. Xing, C. Hou, I. M. Robertson, J.-M. Zuo and Y. Lu, *Nat. Nanotechnol.*, 2011, **6**, 93–97.
32 T.-H. Chen and W.-L. Tseng, *Small*, 2012, **8**, 1912–1919.
33 C.-L. Liu, H.-T. Wu, Y.-H. Hsiao, C.-W. Lai, C.-W. Shih, Y.-K. Peng, K.-C. Tang, H.-W. Chang, Y.-C. Chien, J.-K. Hsiao, J.-T. Cheng and P.-T. Chou, *Angew. Chem., Int. Ed.*, 2011, **50**, 7056.
34 H. Kawasaki, K. Hamaguchi, I. Osaka and R. Arakawa, *Adv. Funct. Mater.*, 2011, **21**, 3508–3515.
35 F. Wen, Y. Dong, L. Feng, S. Wang, S. Zhang and X. Zhang, *Anal. Chem.*, 2011, **83**, 1193–1196.
36 M. A. H. Muhammed, P. K. Verma, S. K. Pal, R. C. A. Kumar, S. Paul, R. V. Omkumar and T. Pradeep, *Chem.–Eur. J.*, 2009, **15**, 10110–10120.
37 C.-A. J. Lin, T.-Y. Yang, C.-H. Lee, S. H. Huang, R. A. Sperling, M. Zanella, J. K. Li, J.-L. Shen, H.-H. Wang, H.-I. Yeh, W. J. Parak and W. H. Chang, *ACS Nano*, 2009, **3**, 395–401.
38 J. Z. Sexton and C. J. Ackerson, *J. Phys. Chem. C*, 2010, **114**, 16037–16042.
39 Y. H. Chen, J. T. Yang and K. H. Chau, *Biochemistry*, 1974, **13**, 3350–3359.
40 B. A. Persson, M. Lund, J. Forsman, D. E. W. Chatterton and T. Ãkesson, *Biophys. Chem.*, 2010, **151**, 187–189.
41 O. L. Muskens, M. W. England, L. Danos, M. Li and S. Mann, *Adv. Funct. Mater.*, 2013, **23**, 281–290.
42 S. Si and T. K. Mandal, *Chem.–Eur. J.*, 2007, **13**, 3160–3168.
43 N. Goswami, A. Makhal and S. K. Pal, *J. Phys. Chem. B*, 2010, **52**, 15236–15243.
44 G. Wang, R. Guo, G. Kalyuzhny, J.-P. Choi and R. W. Murray, *J. Phys. Chem. B*, 2006, **110**, 20282–20289.
45 E. S. Shibu, M. A. Habeeb Muhammed, T. Tsukuda and T. Pradeep, *J. Phys. Chem. C*, 2008, **112**, 12168–12176.
46 Z. Wu and R. Jin, *Nano Lett.*, **10**, 2568–2573.
47 T. Udayabhaskararao, Y. Sun, N. Goswami, S. K. Pal, K. Balasubramanian and T. Pradeep, *Angew. Chem., Int. Ed.*, 2012, **51**, 2155–2159.
48 E. S. Shibu and T. Pradeep, *Chem. Mater.*, 2011, **23**, 989–999.
49 R. Diamond, D. C. Phillips, C. C. F. Blake and A. C. T. North, *J. Mol. Biol.*, 1974, **82**, 371–391.
50 A. Baksi, T. Pradeep, B. Yoon, C. Yannouleas and U. Landman, submitted.
51 N. Goswami, A. Giri, S. Kar, M. S. Bootharaju, R. John, P. L. Xavier, T. Pradeep and S. K. Pal, *Small*, 2012, **8**, 3175–3184.

Electronic supplementary information (ESI) for Nanoscale
This journal is © The Royal Society of Chemistry 2012

Protein-encapsulated gold cluster aggregates: The case of lysozyme†

Ananya Baksi,[a] Paulrajpillai Lourdu Xavier,[a] Kamalesh Chaudhary,[a,b] N. Goswami,[c] S. K. Pal[c] and T. Pradeep[a*]

[a]DST Unit of Nanoscience, Department of Chemistry, Indian Institute of Technology Madras, Chennai-600036, India. *E-mail: pradeep@iitm.ac.in

[b]Department of Biotechnology, Indian Institute of Technology Madras, Chennai-600036, India

[c]Unit of Nanoscience and Technology, Department of Chemical, Biological and Macromolecular Sciences, Satyendra Nath Bose National Centre for Basic Sciences, Block JD, Sector III, Salt Lake, Kolkata 700 098, India

Electronic Supplementary Information 1

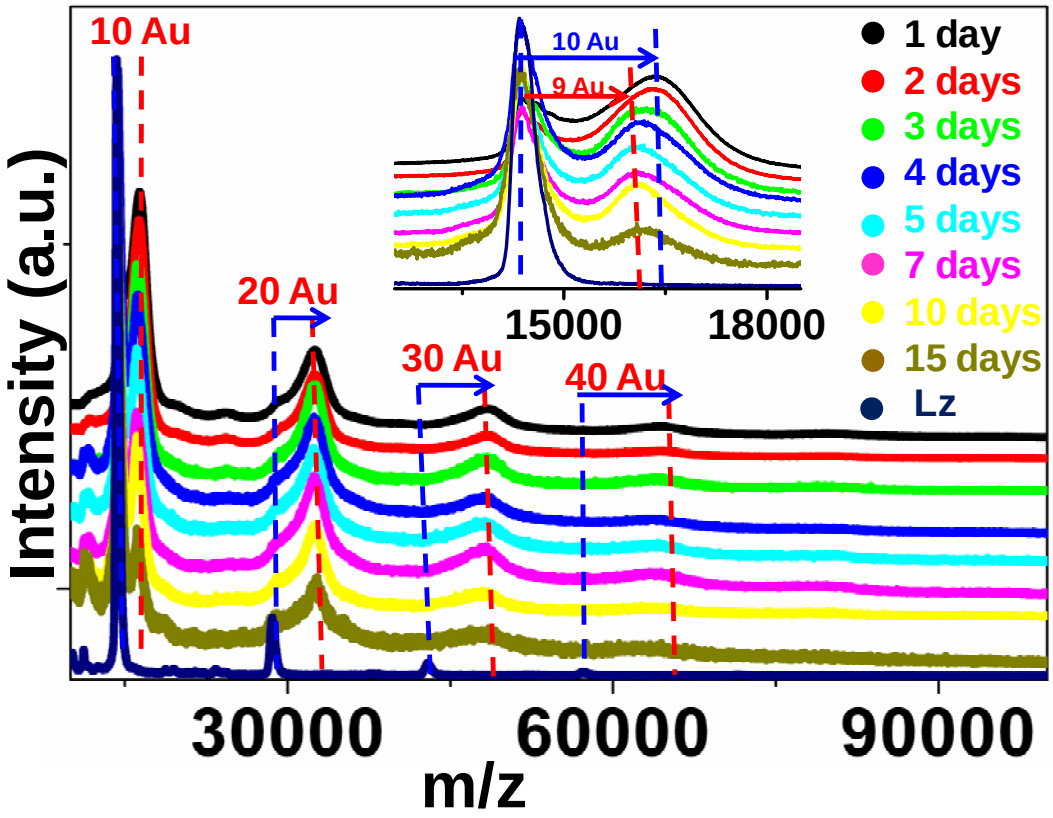

Fig. S1† Time dependent MALDI MS of Lyz: Au^{3+} (molar ratio of 1:4) over 15 days time window. A linear dependence of Au ion uptake is seen for the oligomerized Lyz. While monocation of Au_{QC}@single protein shows a separation of 10 Au atoms from the parent protein peak, oligomerized Lyz show separation of n×10 (where n=2, 3, 4,…) from their parent oligomerized Lyz where n is the aggregation number. Inset shows the monomer region.

Electronic Supplementary Information 2

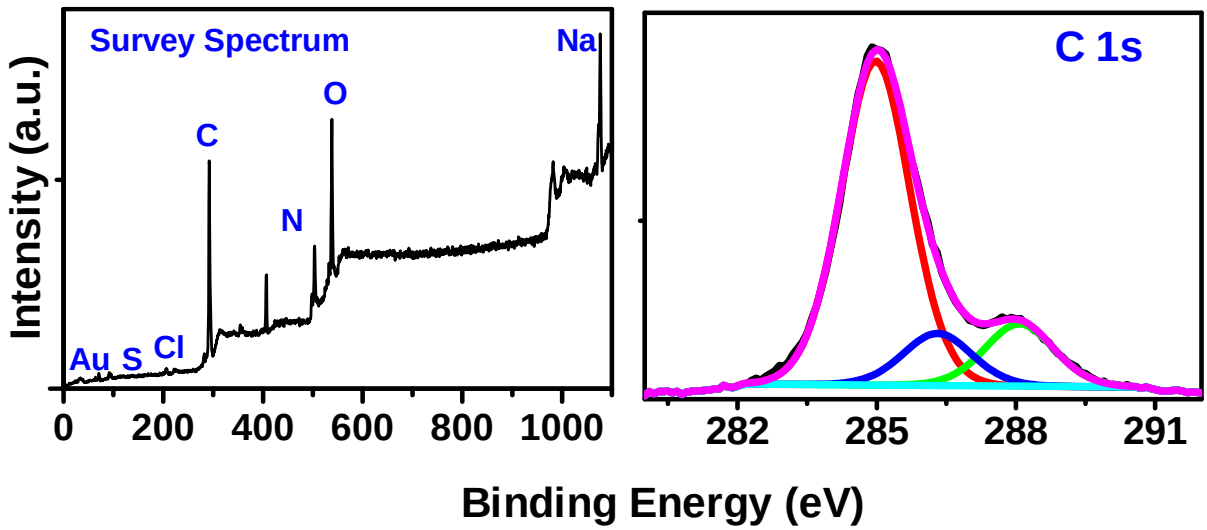

Fig. S2† The survey spectrum is characterized by peaks due to carbon, oxygen, nitrogen, sodium, chlorine, gold and sulphur. Carbon 1s binding energy for the main peak is taken to be 285 eV and other binding energy values have been determined.

Electronic Supplementary Information 3

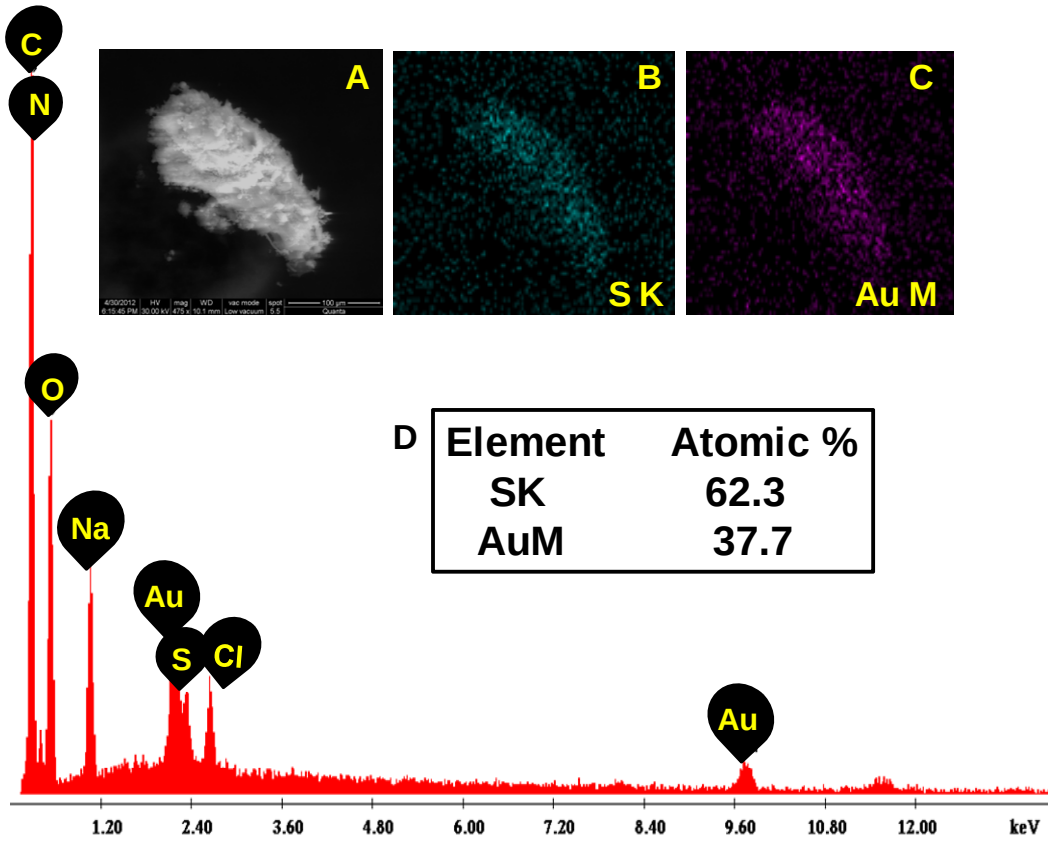

Fig. S3† SEM EDAX spectra of Au_{QC}@Lyz using Lyz: Au^{3+} ratio 1:4. Inset A, is the SEM image of the sample. B and C are EDAX mapping of SK and AuM corresponding to A. D is the quantification of S and Au in the sample.

Electronic Supplementary Information 4

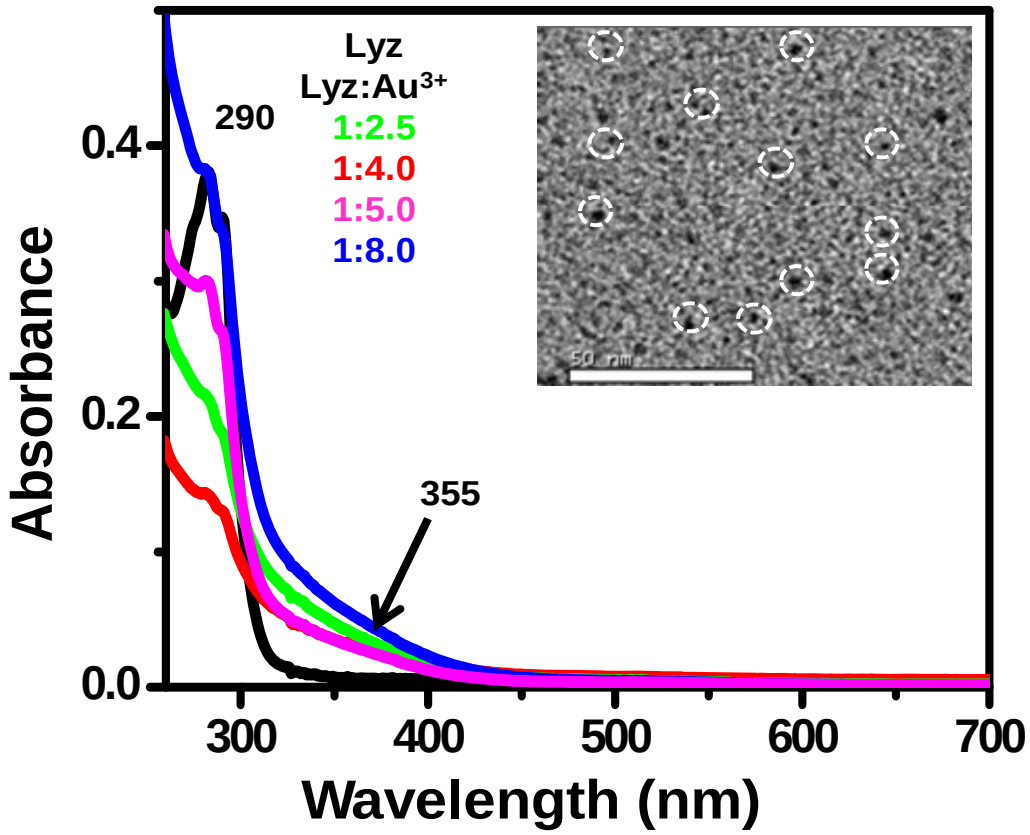

Fig. S4† Concentration dependent UV-Vis spectra of as-synthesized Au_{QC}@Lyz. The peak at 290 nm is assigned to the protein. A characteristic hump near 355 nm is also seen. There is no specific feature of cluster core in these spectra. In the inset, HRTEM image is shown, clusters are sized between 1.1±0.1 nm. There is no feature corresponding to the formation of bigger plasmonic nanoparticles.

Electronic Supplementary Information 5

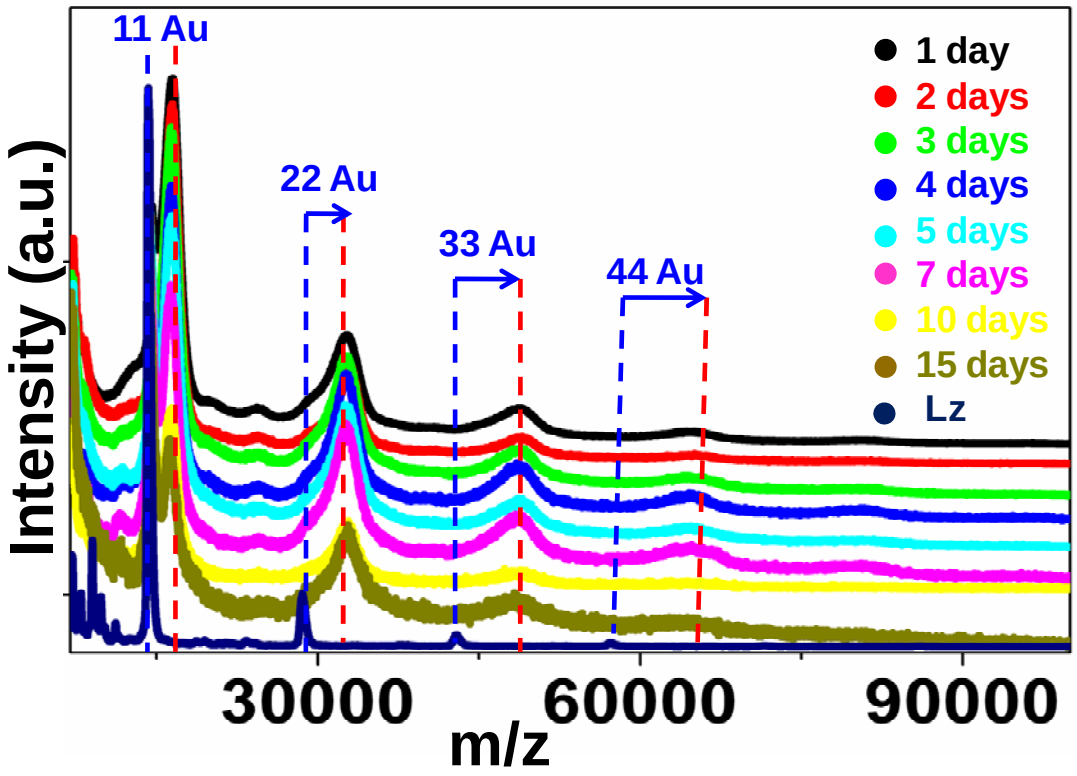

Fig. S5† Time dependent MALDI MS of Lyz: Au^{3+} (molar ratio 1:5) over 15 days time window. A linear dependence of Au uptake is seen for the oligomers. While monomer shows a separation of 11 Au atoms from the parent protein peak, oligomers show separation of n×11 (where n = 2, 3, 4…).

Electronic Supplementary Information 6

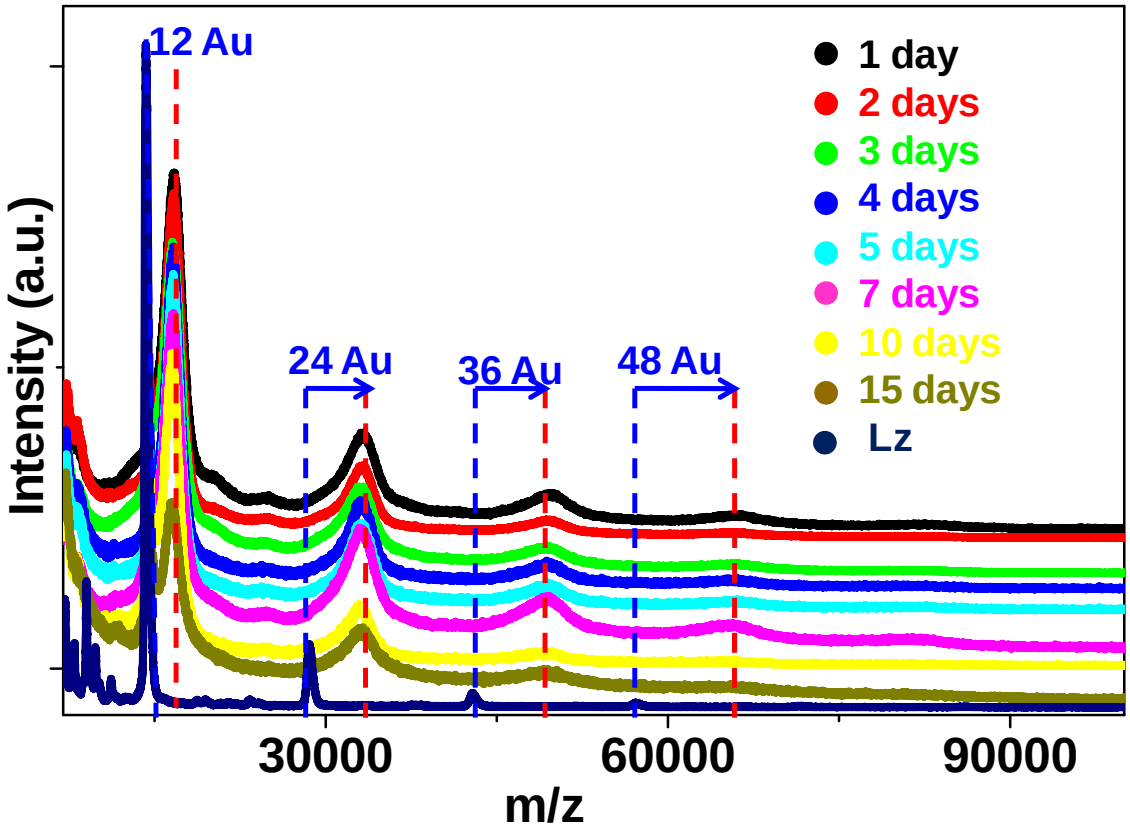

Fig. S6† Time dependent MALDI MS of Lyz: Au^{3+} (1:8 molar ratio) over 15 days time window. A linear dependence of Au uptake is seen for the oligomers. While monomer shows a separation of 12 Au atoms from the parent protein peak, oligomers show separation of n×12 (where n=2, 3, 4,…).

Electronic Supplementary Information 7

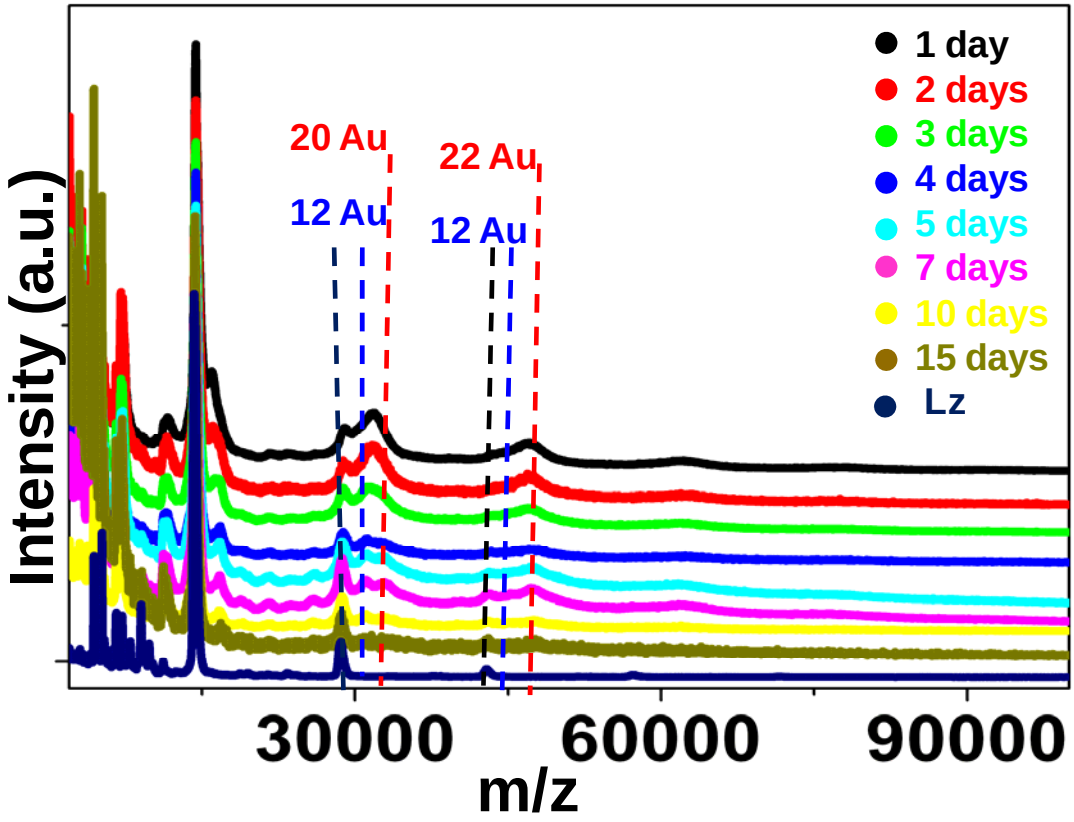

Fig. S7† Time dependent MALDI MS of Lyz: Au^{3+} (1:2.5molar ratio) over 15 days time window. A linear dependence of Au uptake is seen for the oligomers. While monomer shows a separation of 10 Au atoms, after 5 days the peak shifts to 12 Au atoms. In the dimer and trimer regions two distinct peaks appear. For dimer, peaks are separated by 12 and 20 Au atoms while in trimer, peaks are separated by 12 and 22 Au atoms.

Electronic Supplementary Information 8

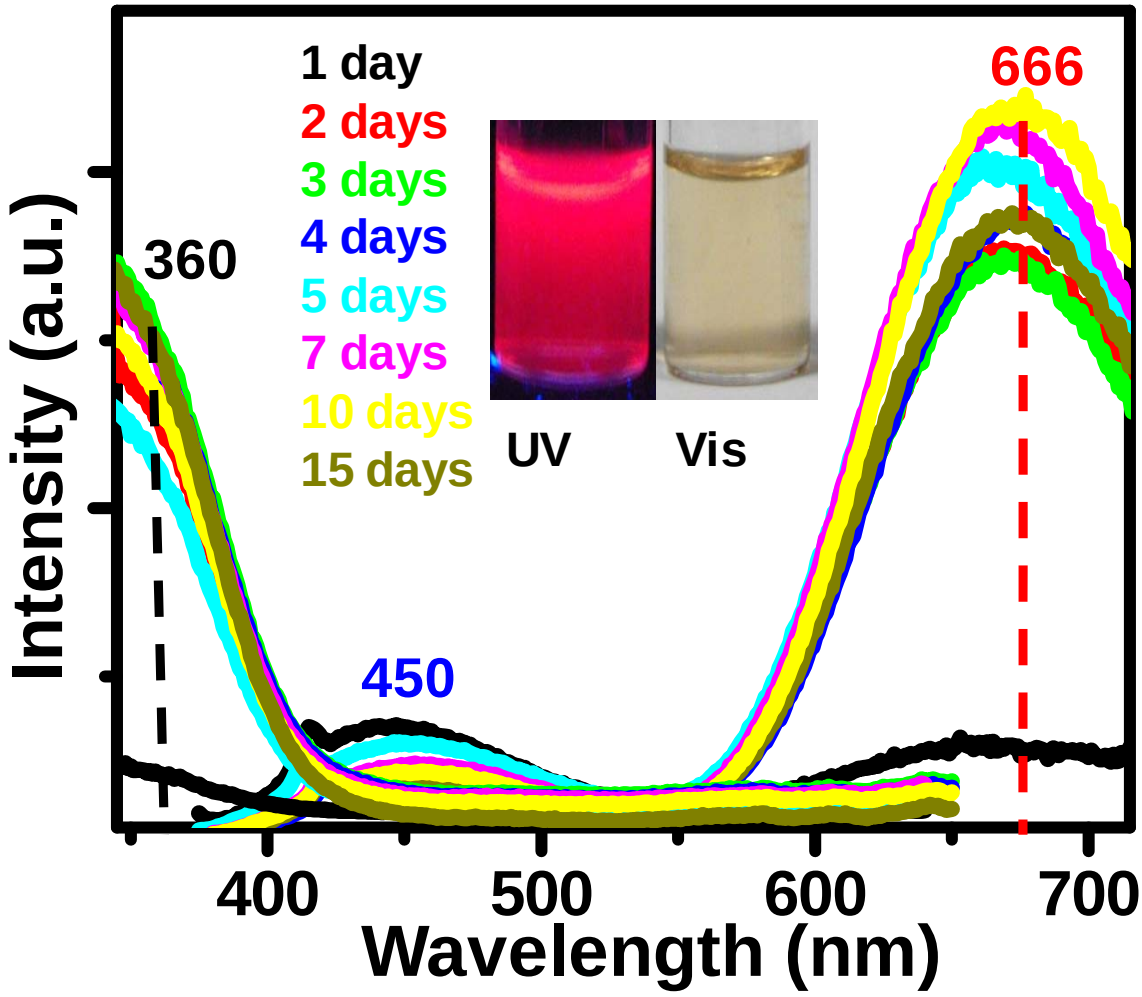

Fig. S8† Time dependent luminescence spectra of Lyz: Au^{3+} (1:5molar ratio) over 15 days time window. Upon exciting at 360 nm, the cluster emits at 666 nm. Insets show the photographs of the sample under ultra-violet and visible light.

Electronic Supplementary Information 9

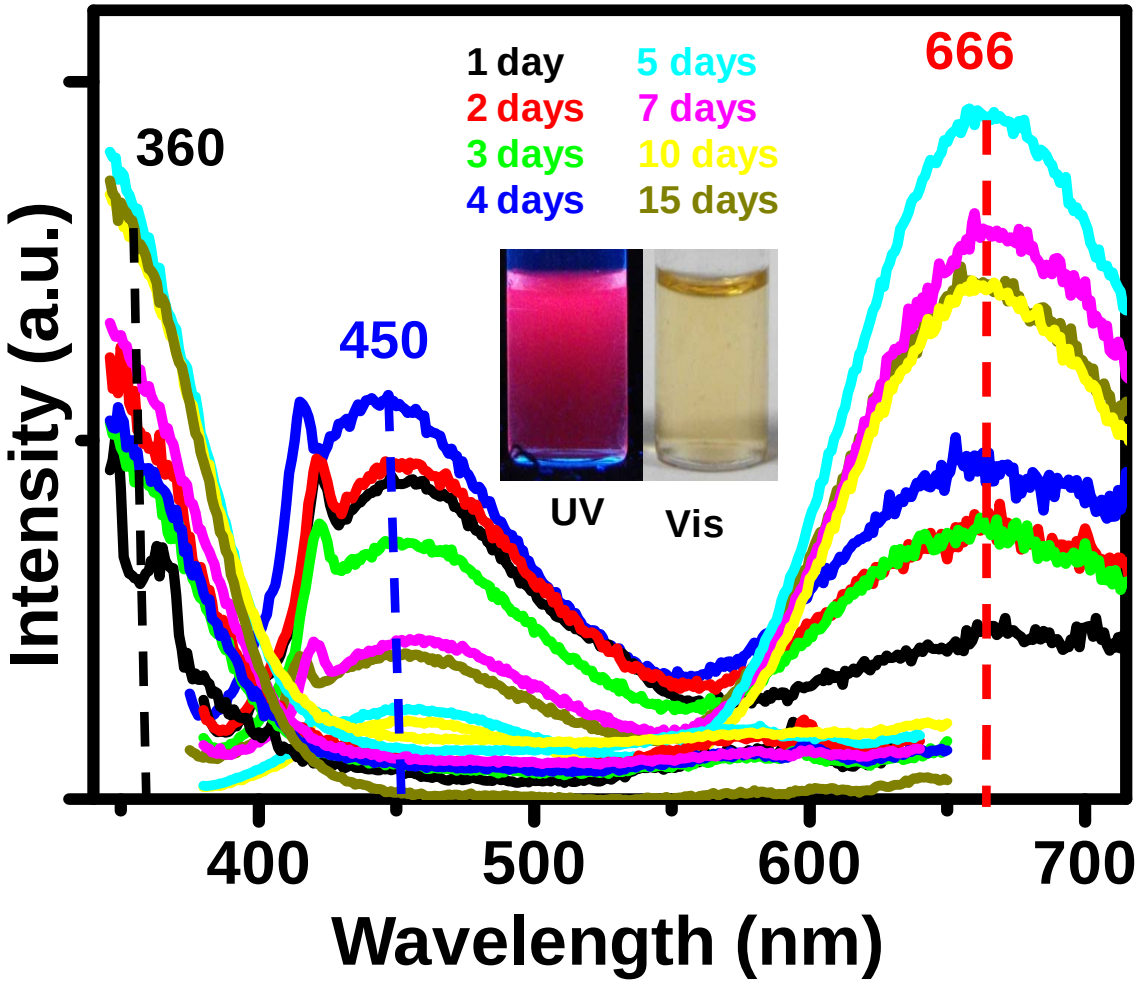

Fig. S9† Time dependent luminescence spectra of Lyz: Au^{3+} (1:8molar ratio) over 15 days time window. Upon exciting at 360 nm the cluster emits at 666 nm. Insets show the photographs of the sample under ultra-violet and visible light.

Electronic Supplementary Information 10

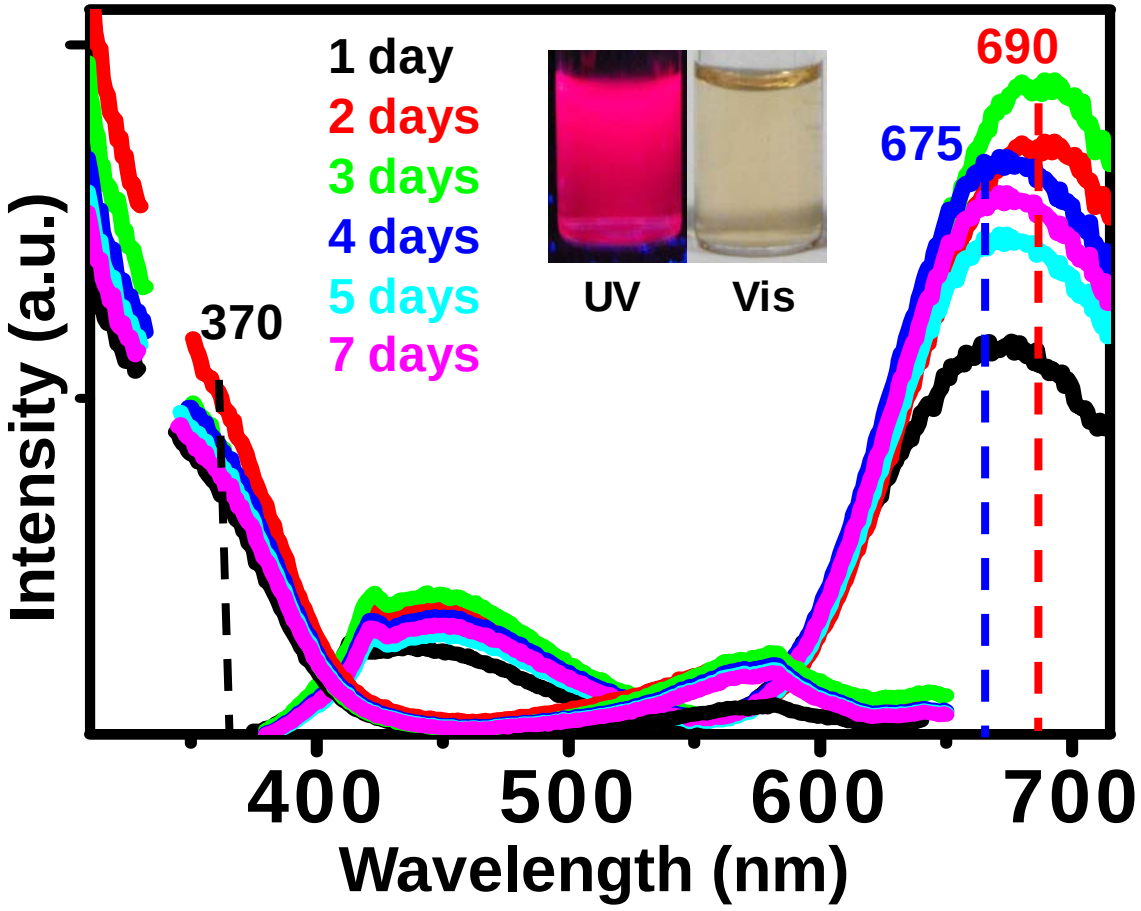

Fig. S10† Time dependent luminescence spectra of Lyz: Au^{3+} (1:2.5 molar ratio) over 7 days time window. Upon exciting at 370 nm the cluster emits at 690 nm which again blue shifts to 675 nm upon longer time. Insets show the photographs of the sample under ultra-violet and visible light. Calculated quantum yield is 15.2%.

Electronic Supplementary Information 11

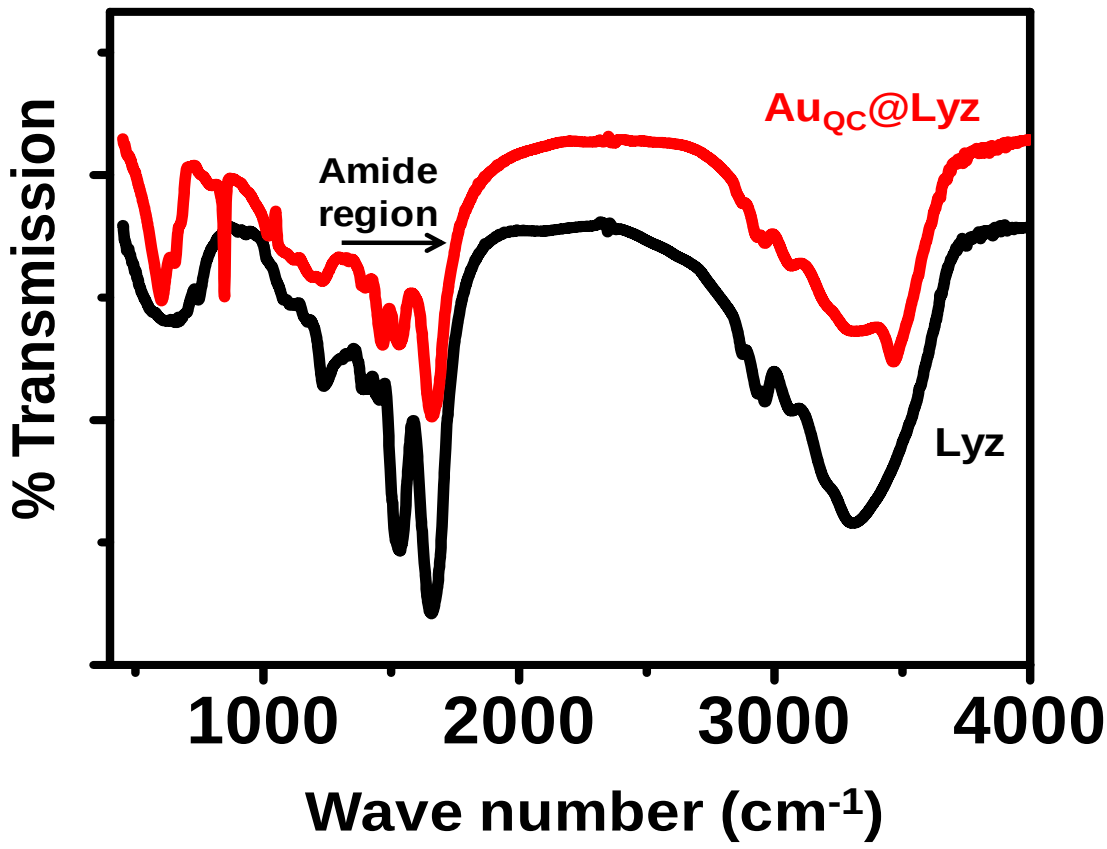

Fig. S11† Infrared (IR) spectra of Lyz and Au_{QC}@Lyz showing significant change in the amide region.

Probing Molecular Solids with Low-Energy Ions

Soumabha Bag, Radha Gobinda Bhuin, Ganapati Natarajan, and T. Pradeep

DST Unit of Nanoscience, Department of Chemistry, Indian Institute of Technology Madras, Chennai 600036, India; email: pradeep@iitm.ac.in

Annu. Rev. Anal. Chem. 2013. 6:97–118

First published online as a Review in Advance on March 14, 2013

The *Annual Review of Analytical Chemistry* is online at anchem.annualreviews.org

This article's doi: 10.1146/annurev-anchem-062012-092547

Keywords

ice, mass spectrometry, soft landing, ion scattering, self-assembled monolayers, phase transition

Abstract

Ion/surface collisions in the ultralow- to low-energy (1–100-eV) window represent an excellent technique for investigation of the properties of condensed molecular solids at low temperatures. For example, this technique has revealed the unique physical and chemical processes that occur on the surface of ice, versus the liquid and vapor phases of water. Such instrument-dependent research, which is usually performed with spectroscopy and mass spectrometry, has led to new directions in studies of molecular materials. In this review, we discuss some interesting results and highlight recent developments in the area. We hope that access to the study of molecular solids with extreme surface specificity, as described here, will encourage investigators to explore new areas of research, some of which are outlined in this review.

1. INTRODUCTION

Chemical phenomena in molecular solids have implications for physics, materials science, biology, and industry. These diverse processes range from adsorption, catalysis, wetting, and diffusion to molecular recognition and self-organization—all of which are central to chemical and biological functionality. Elementary steps involved in these molecular events can lead to complex overall phenomena and require detailed studies of well-characterized surfaces under precise conditions. Mass-selected ions of known kinetic energy impinging on ultrathin films of molecules represent an excellent system in which various chemical phenomena can be modeled. This review outlines some of the most fascinating recent advances in this developing and instrumentation-intensive area.

Molecular solids are composed of periodically arranged molecules that form a lattice. This periodicity may be short or long range, as in amorphous or crystalline solids, respectively. Such solids are not common in the natural environment, where extended solids, such as silica, dominate. The most common molecular solid is water ice; phenomena that occur on the surface of this solid play pivotal roles in atmospheric chemistry, as in the case of ozone layer depletion (1–3). Although elementary chemical reactions such as chlorine radical formation and reactions have been studied, issues such as molecular diffusion, cage formation, and reactivity are important for molecular solids under different pressure and temperature conditions, as in the case of gas hydrates. Thus, molecular chemistry spans a wide range of thermodynamic conditions, from ice particles in interstellar space at 10^{-15} bar to gas-hydrate formation at 10^{5} bar; this review is limited to low-pressure conditions. At low pressure, the molecular flux is correspondingly small, so investigations can be performed only in ultrasensitive environments.

Figure 1 depicts hexagonal crystalline ice (Ih) grown on a Ru(0001) substrate; specifically, three layers of ruthenium atoms in a hexagonal arrangement are shown. During epitaxial growth on the ruthenium surface, the first layer of water molecules is adsorbed onto the surface. A second layer then develops; it is connected by hydrogen bonds to the first layer of water molecules to form a hexagonal cage-like arrangement. In this geometry, each alternative molecule is situated equidistantly above or below a central plane to form a tetrahedral environment. Together, these two layers are known as a bilayer (4). The second layer of water molecules is considered half of the bilayer (hence the term half-bilayer) (**Figure 1**). The bilayer reproduces itself with an interlayer distance of 2.75 Å (5) to produce an Ih network. In **Figure 1**, the atoms are projected toward the reader, away from the text; therefore, the nearest atoms appear largest. Because of this effect, the first and second bilayers appear to have different thicknesses. Because water molecules orient epitaxially on the ruthenium surface, Ru(0001) is an ideal substrate for ice film growth. However, the orientation of water molecules at the ruthenium–ice interface is uncertain.

Typically, all such experiments are performed in ultrahigh-vacuum (UHV) conditions at around 10^{-10} torr. Water vapor is usually condensed on a cold metal surface, typically single crystals whose solid-state structure is similar to that of crystalline ice (CW), to generate thin ice films. The growth of an ice film and its structure are sensitive to the metal surface. Density functional theory calculations suggest that the metal–water interaction is very strong in the case of Ru(0001) surfaces (6). On a Ru(0001) surface, ice growth begins with a small cluster (7). Three-dimensional film growth then occurs through the reproduction of bilayers (7), as described above. In practice, amorphous ice (ASW) is prepared through the deposition of water vapor below 120 K (8). Thereafter, annealing at a temperature above 140 K generates CW. High-density ASW or compact ASW, which has very low porosity, can be prepared by growth of the ice film at ~125 K (9). However, the temperature depends on parameters such as the nature of the surface, the rate of deposition, the annealing rate, and time (5).

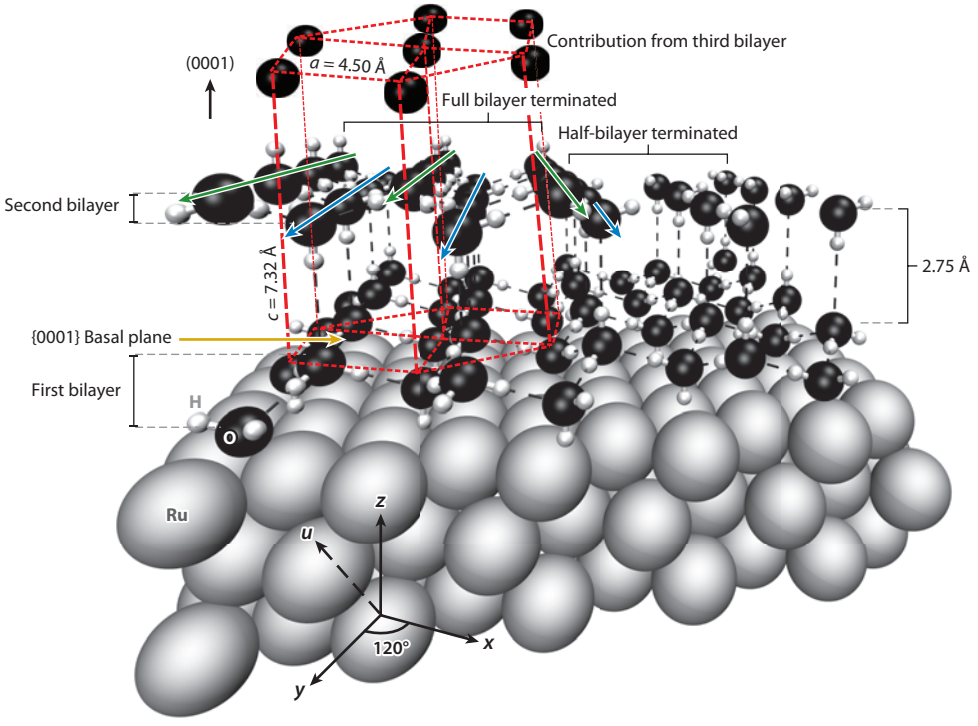

Figure 1

Hexagonal ice growth on a Ru(0001) substrate. The gray balls represent ruthenium atoms, the black balls represent oxygen atoms, and the white balls represent hydrogen atoms. Hydrogen bonds in the ice structure are indicated by the black dashed line between the water molecules. The epitaxial growth of the ice is also depicted. After the ice layer is extended to another bilayer, a unit cell of hexagonal ice can grow. For clarity, the central plane, composed of the second bilayer, is not shown. The circles on the top {0001} plane of the unit cell represent the oxygen atoms forming the third bilayer. The basal {0001} plane is marked by a yellow arrow. Red dashed lines show the unit cell of ice. In the unit cell, *a* and *c* stand for lattice constants of hexagonal ice; *a* is 4.50 Å, and *c* is 7.32 Å. The water molecules forming two half-bilayers (making the full bilayer) are indicated by blue and green arrows. The water molecules arranged along the blue arrow, if extended to the right, form a half-bilayer. This figure is based on several inputs from the literature.

Several techniques have been used to investigate the crystal structure of adsorbed ice films. Of these, helium diffraction and low-energy electron diffraction (LEED) are discussed here. Use of these techniques showed that an ice(0001) film grown on Ru(0001), Pt(111), or Pd(111) terminates as a full bilayer rather than as a half-bilayer (5, 10–12). However, LEED *I–V* (intensity–voltage) experiments (10) and total energy calculations (13) revealed that the topmost layer of the film is modified significantly (5). Also, the upper monolayers undergo large-amplitude vibrational motions, such that the oxygen atoms become invisible to LEED (5, 12). The small (2 × 2) peak in helium diffraction experiments suggests that the topmost layer undergoes reconstruction (12). X-ray absorption studies of the intermolecular distance between ice layers indicated that the interlayer distance at the surface is greater than that in bulk (5).

In addition to the aforementioned techniques, a common analytical method used to study adsorbed molecules is temperature-programmed desorption (TPD) (14–17). Desorption of molecules from ice surfaces can be accompanied by processes in the surface that include diffusion

(18–21), molecular volcano (19), crystallization (22, 23), and polymerization events, all of which have been the subjects of detailed studies. We can better understand the molecular details of processes taking place in such solids by using vibrational spectroscopy, which in conjunction with TPD is often an indispensable tool (24–45). Also, surface-sensitive tools, such as X-ray photoelectron spectroscopy (XPS), have been employed with TPD to study ice films (26, 46). Ions whose energy ranges between 1 and 100 eV (47–71)—which is known as the hyperthermal energy regime and, especially with energies below 10 eV (9, 72, 73), constitutes the ultralow-energy regime—are novel probes for studies of new phenomena. Their novelty arises from the extremely short interaction time between the ions and the surface. For example, Cs^+ ions impinging on a surface with 50-eV translational energy are present only for a few tens of femtoseconds in the vicinity of 10 to 20 monolayers (measured typically in terms of exposure in Langmuirs; 1 Langmuir $= 1 \times 10^{-6}$ torr s of exposure) of condensed molecular solids. The term vicinity refers to an area of radius 4 Å in which chemical interactions can occur (74). First, this extremely short interaction time allows the ions to "observe" the dynamic events of the surface at ultrashort timescales. Second, assuming 10–15% translational-vibrational energy transfer efficiency (74) in collisional events, the surface is sufficiently excited to undergo change in itself or to cause modifications to the colliding ions. This phenomenon causes either reactions or accommodation of the products of collision that preserves the chemical nature of the partners and is known as soft landing (75). Third, given that the collision event is precisely controlled, chemical modifications can be made systematically. Fourth, because the ion beam can be controlled in time, as in the case of an ion pulse, the dynamics of the events can be sampled. Fifth, because the ions possess mass, energy, and direction, all these parameters can be individually or jointly used to capture information on events occurring at the surface. Although many of these low-energy ion phenomena have not yet been investigated adequately, future explorations will undoubtedly be rewarding.

The microscopic processes that occur in these interactions strongly depend on the nature of the projectile, its collision partner on the surface, its geometry and orientation, and the energy of impact. Depending on all these parameters, various techniques (**Table 1**) have been employed to study ion scattering processes. Certain factors, such as (*a*) the ability to create surfaces of interest and manipulate ions with distinct energy, (*b*) the capacity to perform reactions with species derived from mass-selected ions, and (*c*) the ability to carry out reactions in controlled conditions, have contributed to the development of these techniques. All of these processes can broadly be referred to as low-energy ion scattering (LEIS). Therefore, we use this acronym to describe the diverse phenomena that occur in this energy window.

Below, we briefly discuss the instrumentation used to study low-energy ion impact phenomena in molecular solids. We then provide an account of fascinating recent results and describe highlights from the current literature. Finally, we conclude with future directions.

2. INSTRUMENTATION

As mentioned above, this area of research depends greatly on appropriate instrumentation. In this section, we discuss several important techniques.

The essential purpose of instrumentation is evident from the title of this review. Instruments enable production of low-energy ions, impact of ions at molecular surfaces, and analysis of the products and their properties. Depending on the details of the investigation being performed, additional components may be added. The primary instrument may be coupled with other techniques to probe surfaces and ions in more detail. In their simplest configuration, the instrumentation should be capable of ion production and product ion analysis.

Table 1 Various low-energy ion scattering processes

Technique	Abbreviation	Energy range	Use	References
Reactive ion scattering	RIS	10–25 eV	Detection of ionic and neutral species from the surface following ion collisions	76–78
Low-energy sputtering	LES	30–100 eV	Detection of preexisting surface ions at the topmost layer by ion impact	76–78
Reactive landing	RL	10–20 eV	Surface reaction and pattering of molecules on active surfaces by ion impact	79–81
Soft landing	SL	10–20 eV	Deposition of polyatomic ions without damage at the surface by ion collisions	75, 82
Surface-induced dissociation	SID	20–200 eV	Fragmentation of projectile ions and associated chemical reactions	65, 74
Ion/surface reactions	I/S reactions	20–100 eV	Chemical reactions between impinging ions at molecular solids or monolayers	65, 83–85
Chemical sputtering	CS	30–350 eV	Ejection of surface species as ions after charge transfer from the projectile	5, 74, 86

The simplest instruments have two stages. In the first stage, an ion of interest, produced by an ion source, is energy-selected by an analyzer and subsequently collided with a molecular solid surface. In the second stage, the scattered or product ions arising from the surfaces are analyzed by a mass and/or energy analyzer. In addition to mass spectrometry, other techniques that can probe molecular solids are reflection absorption IR spectroscopy (RAIRS), TPD, and XPS. **Figure 2** depicts a typical LEIS instrument coupled with associated components. We briefly describe some of these components below.

2.1. Vacuum System

All ion scattering/collision experiments are carried out under UHV conditions (pressure $<10^{-10}$ mbar) to obtain clean surfaces and to avoid loss of ions due to interactions with gas-phase molecules. Vacuum chambers are made of stainless steel and are connected with a vacuum system to achieve optimum pressure. A vacuum system generally contains turbo molecular pumps (TMPs) backed by additional TMPs and connected to displacement pumps, such as rotary vane or diaphragm pumps. Diaphragm pumps, although more expensive than rotary vane pumps, do not release hydrocarbons. Entrapment pumps, such as titanium sublimation pumps or cryopumps, can be used to create a high vacuum.

2.2. Ion Source

In ion scattering experiments, it is necessary to produce projectile ions prior to collision. Ionization methods depend mainly on two factors, namely the ion of interest and the design of the instrument.

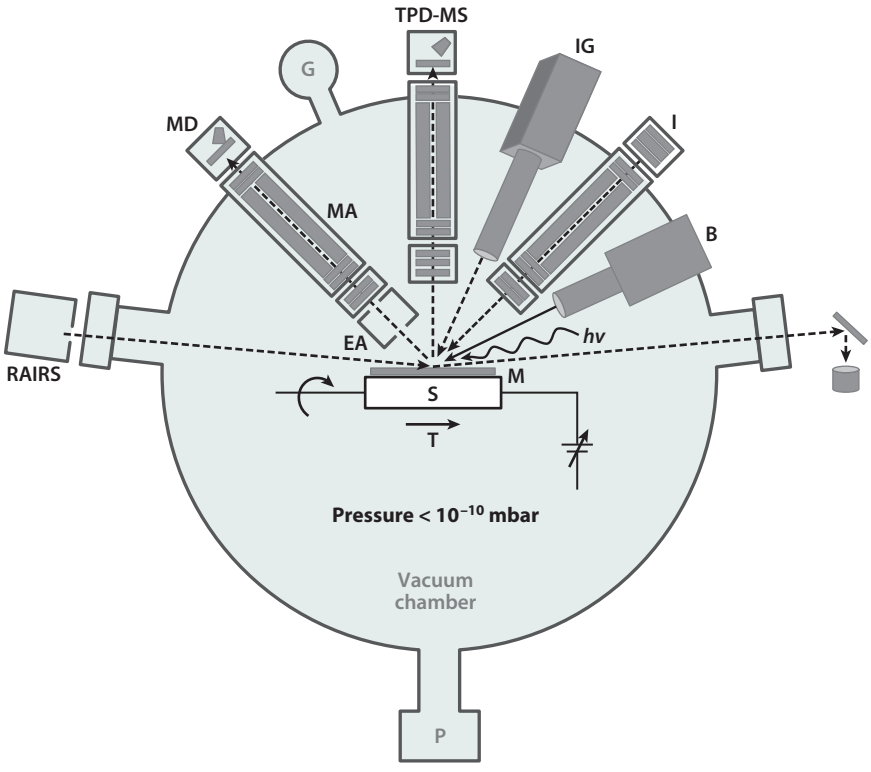

Figure 2

Typical low-energy ion scattering instrument. The circle represents the vacuum chamber connected to the vacuum pump and the pressure gauge. A rotatable substrate is placed at the center of the vacuum chamber, onto which several molecular solids can be deposited. The temperature of the substrate can be regulated by the combined use of a cryostat and a heater. The substrate is connected to a potentiometer, through which voltage to the substrate can be applied. Also shown is a molecular beam deposition module (B), which generates a molecular solid film at slow deposition rates to allow epitaxial growth of the molecules at low temperatures. Abbreviations: EA, energy analyzer; G, pressure gauge; *hv*, light source; I, ion source; IG, ion gun; M, molecular solid; MA, mass analyzer; MD, mass detector; P, vacuum pump; RAIRS, reflection absorption IR spectrometer; S, substrate; TPD-MS, temperature-programmed desorption–mass spectrometer.

The most common ionization methods used in ion/surface collision are electron impact ionization, chemical ionization, and laser-induced ionization. Among these techniques, electron impact ionization is the most common because of the stability of the ion current and the small spread of the ions' kinetic energy. Recently, electrospray ionization and laser desorption/ionization methods were used to produce more complex ions that cannot be created with conventional methods. Several other ion sources (for instance, thermal ionization that produces Cs^+ and Li^+ ions) are also available.

2.3. Mass Spectrometers

The ions are mass-selected and collided on the surface, and the scattered ions are then analyzed with mass spectrometric techniques. Various mass analyzers, such as time-of-flight (TOF), magnetic

sector, quadrupole, linear quadrupole ion trap (56), quadrupole ion trap, Fourier transform–ion cyclotron resonance (FT-ICR), and orbitrap analyzers, may be used for this purpose; we describe the main types in this section.

In a TOF analyzer, ions with different mass-to-charge ratios are dispersed in time after flight through a field-free drift path of known length. The advantages of TOF include the ability to detect high mass ions and efficient analysis of product ions. Magnetic sector analyzers are momentum analyzers; the charged particles are separated by momentum-to-charge ratio in a magnetic field due to the Lorentz force. Quadrupoles are widely used mass analyzers that provide excellent ion transmission and mass resolution. At least three instruments, located at the Indian Institute of Technology (IIT) Madras (52, 53), the Israel Institute of Technology (87), and the University of Arizona (88), use a quadrupole as the mass analyzer in both ion selection and analysis chambers. The instrumental designs used at IIT Madras and Arizona are very similar: Two quadrupoles are positioned at 90°, and at the intersection of the ion optics is a surface whose collision angle is 45° with respect to the surface normal.

FT-ICR mass spectrometers offer very high resolving power and the highest available mass accuracy. One can study the energy of the scattered ions ejected from the surface after projectile ion collision prior to mass analysis by placing an energy analyzer immediately before the mass analyzer. Such analyses can also be performed by stopping potential measurements in quadrupole instruments.

2.4. Temperature-Programmed Desorption

TPD is a widely used spectroscopic technique in which gaseous molecules or atoms adsorbed onto a surface are analyzed by desorption during heating. Heating is carried out by linear temperature ramps. In TPD, the desorbed particles are analyzed either by a pressure gauge or by a mass spectrometer. TPD provides information about, for example, the heat of adsorption, adsorbate coverage, dissociative and nondissociative adsorption processes, the kinetics of desorption, the type of adsorption sites, surface reactions, and the entropy of desorption.

2.5. Reflection Absorption IR Spectroscopy

RAIRS is a well-known surface-sensitive spectroscopic method. In this technique, the incident IR beam (polarized or otherwise) is measured in absorption mode with an external detector following reflection from the surface under study (**Figure 2**). Through measurements of specific vibrational features, RAIRS provides information about the nature of the surface species that arise from surface reactions. It is a powerful tool for surface structure determination due to the dependence of absorption on the polarization of light. RAIRS is an important tool for determination of the binding site of adsorbates such as CO and NO, and it supplies information about the surface reaction pathways for catalytic processes.

3. RESULTS

3.1. Studies Using Self-Assembled Monolayers

One of the most-studied types of molecular solids consists of self-assembled monolayers (SAMs), which are highly ordered molecular films grown on a well-defined surface, usually Au(111). To provide a glimpse into the diverse phenomena that can be observed through LEIS, we present the surprising finding of multiple fluorine abstraction by a single W^+ ion collision event on a

fluorinated SAM. W^+ ions with a laboratory collision energy of 30 eV, produced from the impact of $W(CO)_6$ molecules on a CF_3-terminated SAM (F-SAM) grown on Au(111), to provide a set of peaks corresponding to WF_n^+ ions ($n = 1, 2, \ldots 5$) with a unique intensity pattern (89). Such transition-metal chemistry was subsequently extended to many ions and surfaces in an effort to better understand the chemical nature of surfaces with extreme surface sensitivity. The projectile ions used in these so-called pickup reactions can be considered as chemical probes and used to understand the surface. However, this process also can cause surface transformations that can be used to pattern surfaces with reaction products formed by fluorine removal at selected impact sites. A fascinating aspect of these collisions is the relative interaction between such F-SAM surfaces and certain ions. Miller et al. (82) exploited this property to develop nonreactive patterning based on ion soft landing. Developments in this area have been described in detail elsewhere (81, 90).

Another widely studied molecular solid is water ice. The properties, surface structure, and reactions of ice have been studied in significant detail because of their importance to several chemical and physical processes that occur at low temperatures (90, 91), as well as their catalytic role in polar stratospheric clouds in the depletion of the ozone layer (1–3, 92) and their relevance in chemistry in the interstellar medium (25, 93–95). Ice surfaces prepared at low temperatures offer a unique environment in which to investigate various chemical and physical processes, such as diffusion (21), cluster formation (40, 41), phase transition (96, 97), chemical reaction, hydrogen/deuterium exchange (98–106), interactions with small molecules (46), and adsorption (26, 30). All these phenomena can be promoted and/or identified with hyperthermal energy (1–100-eV) ion collisions. They can also be followed with other well-known detection techniques. Several reviews on this topic are available (48, 74, 81, 86, 107–109). Below, we describe some of these studies to illustrate recent developments.

3.2. Molecular Diffusion/Intermixing

Hyperthermal energy ion collision is an effective technique for the study of ice surfaces and diffusion processes within an ice structure. At low temperatures, ice surfaces provide a reaction environment that is unique in comparison with that of the liquid state. Diffusional mixing of H_2O and D_2O has been investigated with LEIS (110). In this study, the authors deposited amorphous H_2O onto a ruthenium substrate and performed fractional deposition of D_2O onto the H_2O surfaces in the temperature range between 100 and 140 K, followed by time-dependent reactive ion scattering. The time required for interlayer mixing was approximately 1 h at 100 K, but at 140 K, it was several seconds. At higher temperatures, diffusional mixing is easier to perform due to molecular motion and self-diffusion. The activation energy of diffusion measured at the surface was $E_a^{surface} = 14 \pm 2$ kJ mol^{-1}, whereas in the bulk it was $E_a^{bulk} = 71 \pm 4$ kJ mol^{-1} (110, 111). Thus, diffusion at the surface is more significant than in bulk at 100–140 K. This finding indicates higher mobility on the surfaces and demonstrates that reaction preferentially occurs on ice surfaces, rather than in the bulk, at low temperatures.

The transport of protons or hydroxyl ions through ice is a fundamental phenomenon in physical chemistry. Both protons and hydroxyl ions are likely to stay at the surfaces (112, 113). One proton transport experiment involved the deposition of H_2O onto a D_2O layer; the excess protons were generated from HCl ionization at the interfaces. At low temperatures (<120 K), molecular motion was frozen, and proton or hydroxyl ion transport occurred by a proton hopping (Grötthuss) mechanism; molecular reorientation required relatively higher temperatures (100). The same research group also carried out a similar experiment with hydroxyl ions generated by sodium hydrolysis (113). The surface affinity of protons or hydroxyl ions can be used to study catalytic

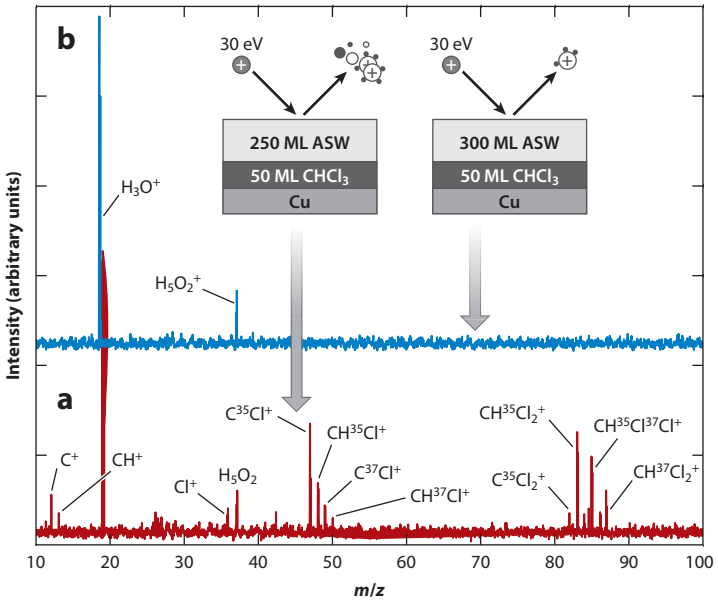

Figure 3

Spectra showing the difference in diffusive mixing between $CHCl_3$ molecules at two different coverages of amorphous ice (ASW): (*a*) 250 and (*b*) 300 monolayers (ML). At 300 ML, the diffusive mixing of $CHCl_3$ molecules stops; the spectrum contains only H_3O^+ and $(H_2O)H_3O^+$ peaks. At 250 ML, all the peaks arising from the $CHCl_3$ molecules are present. Reproduced with permission from Reference 53. Copyright 2007, American Chemical Society.

reactions on ice surfaces. A more recent study revealed the asymmetric transport of hydronium and hydroxyl ions through an ASW surface at low temperatures (<100 K) (78).

Hyperthermal energy Ar^+ ion scattering and sputtering are other important tools to explore the chemistry that occurs at the very top surface of molecular solids. Diffusion of small molecules such as chloromethanes and their interaction with ice have been investigated with hyperthermal energy Ar^+ ion sputtering (53). In this study, different chloromethane molecules were deposited on a polycrystalline copper substrate, followed by water ice deposition; the Ar^+ ion sputtering experiment was then performed in the temperature range between 110 and 150 K. The results showed that various chloromethane molecules diffuse at different rates through ASW. In the case of CCl_4 molecules, diffusive mixing was almost completely precluded, whereas other chloromethane molecules diffused easily through ASW. **Figure 3** shows the diffusive mixing of $CHCl_3$ molecules. When 250 monolayers [one monolayer comprises $\sim 10^{15}$ molecules cm^{-2} (114)] of ASW were deposited on 50 monolayers of $CHCl_3$ molecules, the sputtering spectra showed $CHCl_3$ peaks, along with H_3O^+ peaks. However, for 300 monolayers of ASW, only H_3O^+ and $H_5O_2^+$ peaks were present, implying that $CHCl_3$ molecules can diffuse through 250 monolayers of ASW, whereas CCl_4 molecules can diffuse through only 4 monolayers. The interaction energies between the chloromethanes and ASW are, in order, $CH_3Cl > CH_2Cl_2 > CHCl_3 > CCl_4$—the reverse of what occurs in the liquid-phase interaction.

The interaction between *n*-butanol (NBA) and ice has also been studied. NBA diffused through 1,000 monolayers of ASW, but water did not diffuse through 5 monolayers of NBA (47). Another study of the interaction between carboxylic acids—specifically, formic acid, acetic acid, and propionic acid—and water ice demonstrated structural reorientation and a strong interaction between

acetic acid and formic acid and water ice, which led to the formation of oligomers. Propionic acid did not strongly interact with the water ice (52).

3.3. Molecular Reaction/Interaction

Hyperthermal energy ions are useful for the study of reactions on surfaces and for the production of surface modifications. A recent investigation of ultralow-energy (1-eV) proton collisions on ice surfaces revealed that H_2^+ ions formed from the surfaces (9). **Figure 4** shows the formation of H_2^+ ions from H_2O after collision of 2-eV H^+ ions, as well as the results from 1-eV collisions. H_2^+ ion formation was more efficient in the case of ASW than with CW (9) because of the presence of greater numbers of dangling –OH bonds on ASW. This reaction has implications for interstellar chemistry and plasma-etching processes. A molecular dynamics study of proton collision on CW revealed proton reflection and collision-induced water desorption at low incident energies (0.05–4 eV) (72).

The reaction of small molecules such as CO (34), CO_2 (115), SO_2 (77), and NO_2 (116); hydrolysis of sodium (117); and ionization of HCl molecules (18) have been studied on ice surfaces. The reaction between small molecules on ice surfaces is important in the context of atmospheric and environmental science. Hydrolysis of sodium produces Na^+ and OH^- ions on ice surfaces; the latter tend to reside on the ice surfaces, whereas the former migrate into the bulk (117).

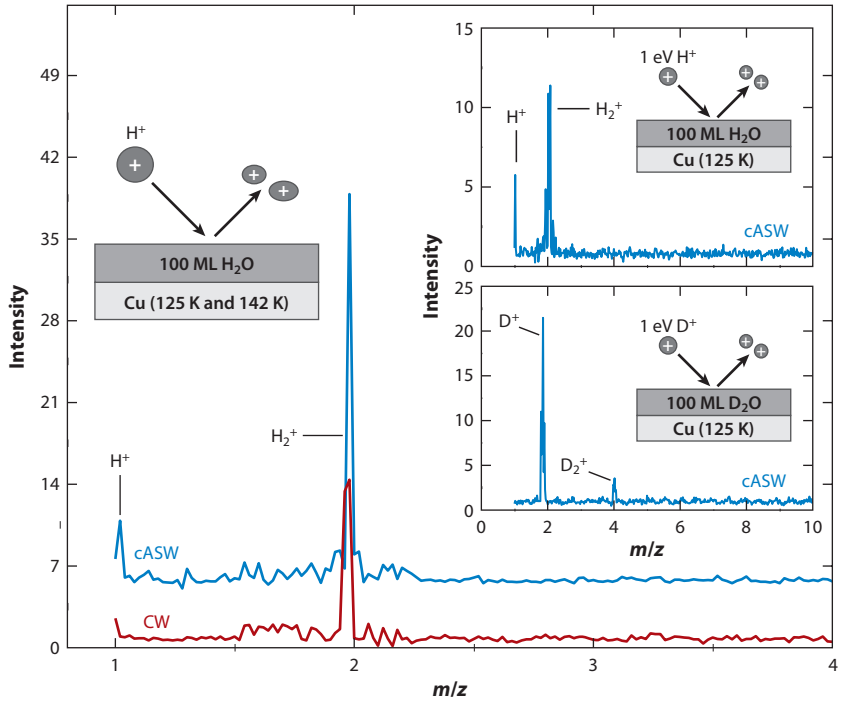

Figure 4

Mass spectrum generated after bombardment of 2-eV H^+ ions on compact amorphous ice (cASW) and crystalline ice (CW). The spectrum from cASW is shifted vertically for clarity. (*Top inset*) The result of collision of 1-eV H^+ ions on cASW and D^+ ions on condensed D_2O, respectively, at 125 K. (*Bottom inset*) A simplification of the experiment shown in the top inset. Abbreviation: ML, monolayers. Reproduced with permission from Reference 9. Copyright 2011, American Chemical Society.

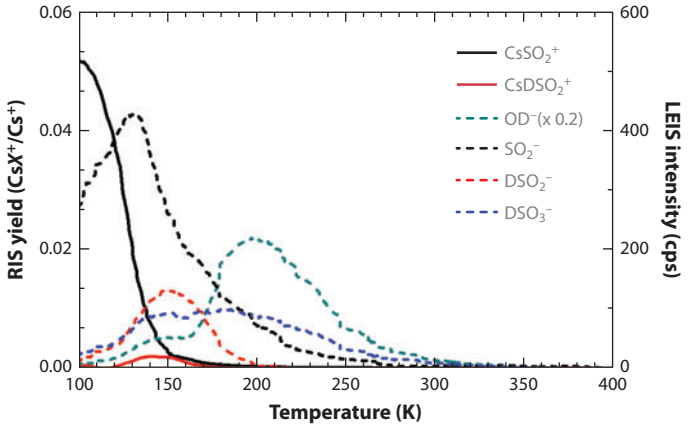

Figure 5

Temperature-programmed low-energy ion scattering (LEIS) measurements for signals of interest detected on the surface of a D_2O–ice film exposed to 0.3 Langmuir of SO_2 at 80 K. The reactive ion scattering (RIS) yield on the left ordinate is the ratio of the LEIS product to the Cs^+ signal intensity (CsX^+/Cs^+, where X is a neutral molecule on the surface). The appearance of $CsSO_2^+$ and $CsDSO_2^+$ signals in LEIS indicates the presence of SO_2 and DSO_2 species, respectively, on the surface. Other LEIS signals observed on the surface include OD^-, SO_2^-, DSO_2^-, and DSO_3^-. The temperature ramping rate was 1 K s^{-1}. Reproduced with permission from Reference 77. Copyright 2009, American Chemical Society.

CO_2 interaction on ice films in both neutral and basic conditions did not yield any CO_2–water complexes or hydrolysis products in the temperature range between 80 and 180 K. Sufficient hydrogen bonding between OH^- ions and the ice surface suppressed the ions' reactivity toward CO_2 (115). NO_2 adsorbs molecularly on ice surfaces at 90 K and readily converts to HONO following heating at 140 K (116). This finding implies that the heterogeneous hydrolysis of NO_2 is an important source of HONO formation. Efficient hydrolysis of NO_2 at ice surfaces suggests that the corresponding atmospheric reaction will be facile at the surfaces of water films, aerosols, and icy particles.

A combination of hyperthermal ion collision and TPD has been used to investigate the interaction of SO_2 and water ice at temperatures above 80 K. **Figure 5** shows the evolution of different chemical species, measured from a D_2O film adsorbed with SO_2 through temperature-programmed LEIS (5). The authors of this study identified three types of intermediate chemical species, including a solvated SO_2 species with a partial negative charge, a partially charged DSO_2 species, and a strongly ionic DSO_3-like species (77). Efficient formation of these species at low temperatures indicates that the reaction involves a low energy barrier.

H_2SO_4 formation has also been observed through the deposition of H_2O and SO_3 in different proportions (77). Interactions between molecules such as Cl_2 (118), Cl_2O (118), and $ClONO_2$ (2, 119), which are relevant to polar stratospheric clouds, have been studied on ice surfaces with static secondary ion mass spectrometry (SIMS) (119). The interaction between Cl_2 and ice was minimal at 90 K. The Cl_2 molecules and water reacted following heating to 130 K, which produced a mixed film of water, HClO, and solvated HCl (118). Unlike Cl_2, Cl_2O did not react with water ice at 90 K; it showed only a hydrogen bond–like interaction at 130 K (118). $ClONO_2$ deposited on pure water ice began to desorb at 120 K without any reaction, but in the presence of HCl it reacted promptly above 120 K and formed NO_3^- ions, providing evidence for the formation of HNO_3 adsorbate (119).

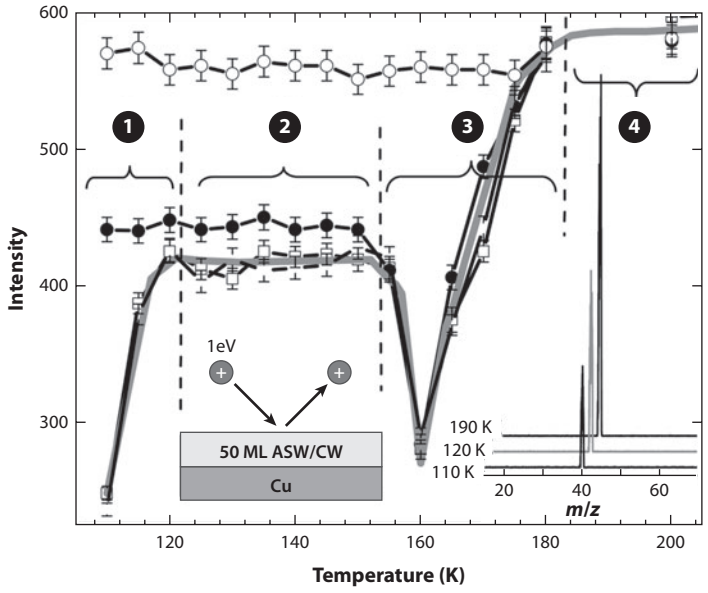

Figure 6

Plot of Ar^+ ion scattering intensity versus temperature variation on various ice surfaces. The ion scattering intensity on a bare copper (Cu) surface is indicated by open circles, on 50 monolayers (ML) of amorphous ice (ASW; H_2O) by open squares, on 50 ML of ASW (D_2O) by filled squares, and on 50 ML of crystalline ice (CW; H_2O) by filled circles. Comparing the ion scattering intensities of these four surfaces shows that the phase transition can be probed with the ultralow-energy ion/surface collision technique. (*Inset*) Typical 1-eV Ar^+ ion scattering mass spectra of 50 ML of ASW for three different temperatures, averaged for 50 scans. Reproduced with permission from Reference 120. Copyright 2008, American Chemical Society.

3.4. The Phase Transition

The phase transition of thin ice films can be studied with different spectroscopic or spectrometric techniques. Two techniques are discussed here.

At IIT Madras (53), ultralow-energy ion scattering was used to probe a phase transition that occurs at approximately 120 K. ASW and CW films were formed on a copper surface, and an ultralow-energy ion scattering experiment was performed as a function of temperature. The result (**Figure 6**) compares the 1-eV Ar^+ ion scattering intensity variation on ASW, with respect to CW. The transformation from ASW to CW is evident at 120 K but was irreversible because the ion scattering intensity did not change when the temperature was lowered from 150 K to 110 K. When the kinetic energy of the impinging ions was increased to 8 eV, the ions were unable to "identify" the structural change on the ice film. Therefore, ultralow-energy ions in the range between 1 and 3 eV should be used for such experiments because, in the ultralow-energy regime, collision of ions with surfaces depends on two factors: the translational energy of the projectile and its potential energy. At 110 K, ice surfaces have a porous structure that disappears at 120 K due to surface reorganization. Thus, trapping and the possibility of neutralization decrease, and the ion scattering intensity in this window increases (**Figure 6**). Moreover, the surface work function varies among different surfaces. CW has a 0.3 eV–higher work function than that of ASW (2.45 eV) (120). The structural transformation from ASW to CW reduces −OH dangling bonds and increases the work function. This change affects the scattering intensity of noble-gas ions, and structural transformations on the surfaces can be identified. In region 2 (120–155 K)

the intensity remains constant because no further change occurs, and in region 3 (155–180 K), desorption causes neutralization of the incoming ions through interaction with desorbing water molecules. Thereafter, the bare copper surface is presented to the incoming ions. This behavior can be verified with appropriate surfaces.

Other investigators used another important technique, temperature-programmed TOF-SIMS, to study phase transition in a series of molecular solids. They studied glass transition (T_g) and film morphology changes in various molecular solids, such as water, methanol, ethanol, and 3-methyl pentane, on different metallic and nonmetallic surfaces. The T_g of vapor-deposited water ice occurred at 136 K, at which temperature water is transformed into a glassy solid (121). However, other reports indicate that the T_g of water is 165 K (122). This study revealed that intermixing of isotopically labeled water ice occurs at 136 K and that a film morphology change takes place at 165 K (122).

Apart from that of water ice, the T_g of methanol has been investigated in detail. The results showed that the T_g of vapor-deposited methanol films begins at 80 K, which is 23 K lower than its calorimetric T_g (22). In addition to water and alcohol, *n*-alkanes with no apparent T_g have also been studied. *n*-Pentane shows translational diffusion before crystallization (123). The translational diffusion in the film indicates that a liquid-like phase may appear immediately before crystallization. Another interesting aspect of such films is that they form droplets after crystallization, and their dewetting temperature depends on their initial thickness (86).

The presence of the liquid-like phase in water ice films has also been investigated. The liquid-like phase (or supercooled water) is important because it can be an extension of liquid water. Its presence in an ice film can be demonstrated in various ways (124), including by observation of the interaction between alkyl halide salts (e.g., LiCl, LiI, and NaCl) and ASW. A drastic increase in the solubility of these salts is expected to occur in supercooled water versus CW because the dissolution of salts into CW is suppressed (125–128). This solubility difference revealed that, above 136 K and below crystallization temperature, there is a phase similar to liquid water, known as the supercooled water phase, wherein molecules have long-range translational diffusion. In this phase, alkali halide salts dissolve. The existence of this phase is limited to the temperature range between 160 and 165 K (127). A further study confirmed that ASW is likely to transform into low-density liquid (LDL) above 136 K, and then to high-density liquid (HDL or supercooled liquid), prior to crystallization. This finding implies that glassy water shows polymorphism, that is, the presence of two distinct phases (129). Interestingly, the LDL is considered ultraviscous because of the lower solubility of alkali halide salts. The transition from LDL to HDL takes place at 160 K (130). Similar to water, molecular solids such as ethanol also showed polymorphism when vapor-deposited. An investigation involving the solubility of LiI in ethanol ice revealed the appearance of the liquid-like phase at 97 K and the crystalline phase at 130 K (131). Another molecular solid, toluene, shows self-diffusion and dewetting at 105 K and 117 K, respectively (132).

The effect of substrate on T_g values has also been explored. The T_g values of thin films are expected to be lower than bulk T_g values because of the nanoconfinement effect, which is similar to the lowering of melting point of such confined crystallites (86, 133, 134). To observe the substrate and the free-surface effect on the T_g value of ASW, investigators vapor-deposited water at 120 K on graphite and other ionic liquids (131). Self-diffusion and film morphology changes were observed in the deposited ice film; these effects arise from instability at the graphite interface. Dewetting of up to 20 monolayers of water was observed on the hydrophobic graphite surface. A similar effect on Ni(111) was not observed because of the presence of a so-called dead layer at the interface between the metal surface and the ice (135).

3.5. Soft Landing and Its Applications in Organometallics

In soft landing, polyatomic ions whose energy is between 10 and 20 eV are deposited intact onto a target surface (82). The ions are not neutralized in this process. Without breaking the covalent bond, the polyatomic ions dissipate the kinetic energy during impact, and the dissipated energy changes the vibrational and electronic energy of the surface and the polyatomic ions. Soft-landing experiments play an important role in the fields of materials science, engineering, catalysis, nanotechnology, and biology (86). In 1977, the Cooks group became the first to conduct a soft-landing experiment (75). In another early study, positively charged organic ions prepared from desorption/ionization were landed on a target surface (136). In subsequent soft-landing experiments, $(CH_3)_2SiNCS^+$ ions, *N*,*N*-dimethyl-*p*-toluidine ions, and *m*-trifluoromethylbenzoyl ions were collided separately on a fluorinated SAM or a long-chain alkyl SAM (H-SAM) (82, 137, 138). The release of projectiles from the SAMs following chemical sputtering illustrates the nondestructive nature of this process.

Soft landing has been used in organometallics; here, metal complex molecules are produced in the gas phase, then gently landed onto the desired surface without any change or rupture of the chemical bond. Complex molecules that are difficult to synthesize in solution chemistry are often used in such cases. Metal–benzene and metal–salen [salen refers to *N*,*N*′-ethylenebis(salicylideneaminato)] are common organometallic compounds used in soft-landing experiments (139, 140). Nakajima and colleagues (139) produced V(benzene)$^+$ and V_n(benzene)$_{n+1}$ ions (known as multidecker sandwich cluster ions) by laser evaporation, followed by soft landing onto an argon matrix prepared on polycrystalline gold surfaces at 18 K. Subsequent IR surface analysis revealed the nondissociative deposition of the desired ions on the surface.

In other studies, ions of transition metals such as titanium, scandium, and chromium were deposited at room temperature onto different SAMs (141, 142). The collision energy ranged between 10 and 20 eV. The soft-landed molecules on the SAMs were stable because the desorption energy calculated from the TPD experiments was high (143). These experiments were performed with V_2(benzene)$_3^+$ multidecker complex ions, which were landed onto a 1-octadecanethiol SAM at a kinetic energy of approximately 20 eV (143, 144). A TPD experiment on the soft-landed surface showed the presence of V(benzene)$_2$ and the V_2(benzene)$_2$ molecules on the surface. These molecules may have arisen from dissociation during landing on the SAM and may subsequently have become immobilized in the SAM layer (**Figure 7**) (86).

The trapping of soft-landed ions depends on the density of the SAMs. SAMs prepared on gold are well ordered and more densely populated than those on silicon. Therefore, the desorption energy of V(benzene)-complex ions from a C_{16}-SAM prepared on Si(111) is much lower than that of a C_{16}-SAM prepared on Au(111) (142). The orientation of the molecules following landing depends on the nature of the SAM. The molecular axis of V(benzene)$_2$ molecules in the H-SAM substrate remains at 70–80° with respect to the surface normal (141). The molecular orientation of other complexes [*M*(benzene)$_2$; M = Ti or Cr] shows a similar trend, although chromium-complex molecules have a lower-than-70° angle with respect to the surface normal (144). However, in the case of F-SAM surfaces, the angles differ because of the repulsion between the π-electron cloud of the benzene ring of the complex and the closest outermost $-CF_3$ and $-CF_2$ groups on the side chain of the fluorocarbon axes of the F-SAM (86).

The reactivity of the complex cations landed on the SAM was subsequently investigated in detail. VO(salen)$^+$ and [Ni(salen)+H]$^+$ ions were produced by electrospray ionization and, after mass selection, were allowed to soft-land onto an F-SAM on gold (145). The TOF-SIMS analysis, performed over 4 days following deposition, caused the reduction of $V^{V}O(salen)^+$ to $V^{III}(salen)^+$. This result indicates that the reduction was interfacial, not beam induced. However, the yield of

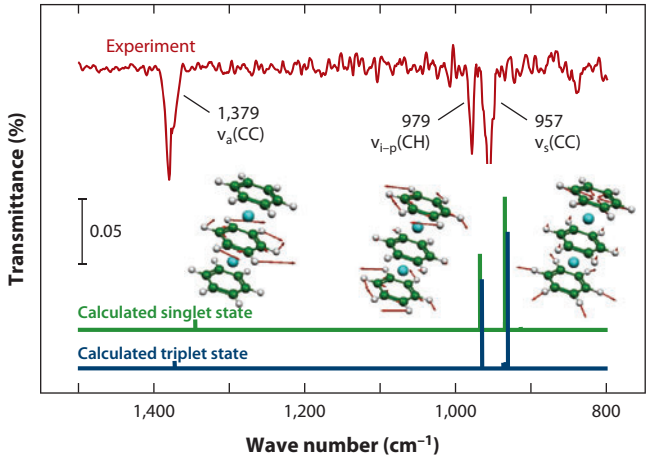

Figure 7

The IR spectrum in the range between 800 and 1,500 cm^{-1} recorded after the soft landing of approximately one monolayer of V_2(benzene)$_3$ ions (2×10^{14} positive ions cm^{-2}) at 200 K onto a 1-octadecanethiol monolayer, along with the computed IR spectra of the singlet and triplet states of V_2(benzene)$_3$ ions. The labels ν_s(CC), ν_{i-p}(CH), and ν_a(CC) stand for the symmetric breathing mode of two terminal benzene rings, the in-plane bending mode of these benzene rings, and the asymmetric C–C stretching mode of the central ring, respectively. Reproduced with permission from Reference 86. Copyright 2012, American Chemical Society.

V^{III}(salen)$^+$ ions depended on the nature of the proton donor molecule needed for the reaction and its residence time on the surface (145). In the reverse reaction, V^{III}(salen)$^+$ was easily converted to $V^{V}O$(salen)$^+$. This catalytic cycle of reduction and oxidation by a soft-landed vanadium complex depended on two factors: the initial number of the proton source molecules and the rate of release of the protons from the proton donor molecules (86).

4. SUMMARY AND FUTURE DIRECTIONS

The selected examples presented in this review, although they offer merely glimpses into an exciting area, establish that many exciting areas of research have yet to be explored. Ultrahigh surface sensitivity that can cause molecular transformations, extract chemical information, preserve ionic species, and accommodate functional moieties—all in a spatially controlled fashion—is the most fascinating aspect of such research. Completely new phenomena are expected to be discovered on solids that have not yet been investigated.

One as-yet-unexplored research avenue involves catalysis at molecular solids. Another pertains to the dynamics of events, which would probably be best explored with pulsed ion beams. All such investigations can generate complete information only in conjunction with computational studies, which can probe ultrafast dynamics. The development of techniques in this area would enrich experimental efforts. From the experimental point of view, all these new approaches would require new instrumentation with high transmission at low energies and high detector sensitivity. Experiments on many molecular solids require temperatures lower than what can be attained with liquid nitrogen. Given these diverse requirements, LEIS as an analytical tool will become more instrumentation intensive during the coming years. Experimental curiosity and possible new phenomena are likely to propel research in this area.

DISCLOSURE STATEMENT

The authors are not aware of any affiliations, memberships, funding, or financial holdings that might be perceived as affecting the objectivity of this review.

ACKNOWLEDGMENTS

T.P. acknowledges the Department of Science and Technology, Government of India, for funding. S.B. and R.G.B. acknowledge the Council of Scientific and Industrial Research for research fellowships.

LITERATURE CITED

1. Molina MJ, Rowland FS. 1974. Stratospheric sink for chlorofluoromethanes: chlorine atom–catalysed destruction of ozone. *Nature* 249:810–12
2. Molina MJ, Tso T-L, Molina LT, Wang FCY. 1987. Antarctic stratospheric chemistry of chlorine nitrate, hydrogen chloride, and ice: release of active chlorine. *Science* 238:1253–57
3. Salcedo D, Molina LT, Molina MJ. 2001. Homogeneous freezing of concentrated aqueous nitric acid solutions at polar stratospheric temperatures. *J. Phys. Chem. A* 105:1433–39
4. Thiel PA, Madey TF. 1987. The interaction of water with solid surfaces: fundamental aspects. *Surf. Sci. Rep.* 7:211–385
5. Park S-C, Moon E-S, Kang H. 2010. Some fundamental properties and reactions of ice surfaces at low temperatures. *Phys. Chem. Chem. Phys.* 12:12000–11
6. Haq S, Clay C, Darling GR, Zimbitas G, Hodgson A. 2006. Growth of intact water ice on Ru(0001) between 140 and 160 K: experiment and density-functional theory calculations. *Phys. Rev. B* 73:115414
7. Hodgson A, Haq S. 2009. Water adsorption and the wetting of metal surfaces. *Surf. Sci. Rep.* 64:381–451
8. Kimmel GA, Petrik NG, Dohnalek Z, Kay BD. 2007. Crystalline ice growth on Pt(111) and Pd(111): nonwetting growth on a hydrophobic water monolayer. *J. Chem. Phys.* 126:114702
9. Bag S, McCoustra MRS, Pradeep T. 2011. Formation of H_2^+ by ultra-low-energy collisions of protons with water ice surfaces. *J. Phys. Chem. C* 115:13813–19
10. Materer N, Starke U, Barbieri A, Van Hove MA, Somorjai GA, et al. 1997. Molecular surface structure of ice(0001): dynamical low-energy electron diffraction, total-energy calculations and molecular dynamics simulations. *Surf. Sci.* 381:190–210
11. Braun J, Glebov A, Graham AP, Menzel A, Toennies JP. 1998. Structure and phonons of the ice surface. *Phys. Rev. Lett.* 80:2638–41
12. Glebov A, Graham AP, Menzel A, Toennies JP, Senet P. 2000. A helium atom scattering study of the structure and phonon dynamics of the ice surface. *J. Chem. Phys.* 112:11011–22
13. Materer N, Starke U, Barbieri A, Van Hove MA, Somorjai GA, et al. 1995. Molecular surface structure of a low-temperature ice Ih(0001) crystal. *J. Phys. Chem.* 99:6267–69
14. Biesecker JP, Ellison GB, Wang H, Iedema MJ, Tsekouras AA, Cowin JP. 1998. Ion beam source for soft-landing deposition. *Rev. Sci. Instrum.* 69:485–95
15. Tsekouras AA, Iedema MJ, Cowin JP. 1999. Soft-landed ion diffusion studies on vapor-deposited hydrocarbon films. *J. Chem. Phys.* 111:2222–34
16. Bolina AS, Wolff AJ, Brown WA. 2005. Reflection absorption infrared spectroscopy and temperature-programmed desorption studies of the adsorption and desorption of amorphous and crystalline water on a graphite surface. *J. Phys. Chem. B* 109:16836–45
17. Engquist I, Lundström I, Liedberg B. 1995. Temperature-programmed desorption and infrared studies of D_2O ice on self-assembled alkanethiolate monolayers: influence of substrate wettability. *J. Phys. Chem.* 99:12257–67
18. Park S-C, Kang H. 2005. Adsorption, ionization, and migration of hydrogen chloride on ice films at temperatures between 100 and 140 K. *J. Phys. Chem. B* 109:5124–32

19. Smith RS, Huang C, Wong EKL, Kay BD. 1997. The molecular volcano: abrupt CCl_4 desorption driven by the crystallization of amorphous solid water. *Phys. Rev. Lett.* 79:909–12
20. Sadtchenko V, Knutsen K, Giese CF, Gentry WR. 2000. Interactions of CCl_4 with thin D_2O amorphous ice films. Part I. A nanoscale probe of ice morphology. *J. Phys. Chem. B* 104:2511–21
21. McClure SM, Barlow ET, Akin MC, Safarik DJ, Truskett TM, Mullins CB. 2006. Transport in amorphous solid water films: implications for self-diffusivity. *J. Phys. Chem. B* 110:17987–97
22. Souda R. 2004. Glass transition and intermixing of amorphous water and methanol. *Phys. Rev. Lett.* 93:235502
23. Kondo T, Kato HS, Bonn M, Kawai M. 2007. Deposition and crystallization studies of thin amorphous solid water films on Ru(0001) and on CO-precovered Ru(0001). *J. Chem. Phys.* 127:094703
24. Borget F, Chiavassa T, Allouche A, Marinelli F, Aycard JP. 2001. Cyanoacetylene adsorption on amorphous and crystalline water ice films: investigation through matrix isolation and quantum study. *J. Am. Chem. Soc.* 123:10668–75
25. Burke DJ, Wolff AJ, Edridge JL, Brown WA. 2008. Thermally induced mixing of water dominated interstellar ices. *Phys. Chem. Chem. Phys.* 10:4956–67
26. Faradzhev NS, Perry CC, Kusmierek DO, Fairbrother DH, Madey TE. 2004. Kinetics of electron-induced decomposition of CF_2Cl_2 coadsorbed with water (ice): a comparison with CCl_4. *J. Chem. Phys.* 121:8547–61
27. Graham JD, Roberts JT. 1995. Interaction of HCl with crystalline and amorphous ice: implications for the mechanisms of ice-catalyzed reactions. *Geophys. Res. Lett.* 22:251–54
28. Schaff JE, Roberts JT. 1994. Structure sensitivity in the surface chemistry of ice: acetone adsorption on amorphous and crystalline ice films. *J. Phys. Chem.* 98:6900–2
29. Schaff JE, Roberts JT. 1996. Toward an understanding of the surface chemical properties of ice: differences between the amorphous and crystalline surfaces. *J. Phys. Chem.* 100:14151–60
30. Schaff JE, Roberts JT. 1998. The adsorption of acetone on thin films of amorphous and crystalline ice. *Langmuir* 14:1478–86
31. Callen BW, Griffiths K, Norton PR. 1992. Observation of free hydroxyl groups on the surface of ultra thin ice layers on nickel(110). *Surf. Sci.* 261:L44–L48
32. Henderson MA. 2002. The interaction of water with solid surfaces: fundamental aspects revisited. *Surf. Sci. Rep.* 46:1–308
33. Hu Y, Griffiths K. 2007. NO–methanol interaction on the surface of Pt(332). *Surf. Sci.* 601:2467–72
34. Hu Y, Norton PR, Griffiths K. 2007. CO–D_2O coadlayers on Pt(111). Vibrational studies at low coverages. *J. Vac. Sci. Technol. A* 25:645–50
35. Maté B, Medialdea A, Moreno MA, Escribano R, Herrero VJ. 2003. Experimental studies of amorphous and polycrystalline ice films using FT-RAIRS. *J. Phys. Chem. B* 107:11098–108
36. Maté B, Rodriguez-Lazcano Y, Herrero VJ. 2012. Morphology and crystallization kinetics of compact (HGW) and porous (ASW) amorphous water ice. *Phys. Chem. Chem. Phys.* 14:10595–602
37. Mitlin S, Leung KT. 2002. Film growth of ice by vapor deposition at 128–185 K studied by Fourier transform infrared reflection–absorption spectroscopy: evolution of the OH stretch and the dangling bond with film thickness. *J. Phys. Chem. B* 106:6234–47
38. Buch V, Devlin JP. 1991. Spectra of dangling OH bonds in amorphous ice: assignment to 2- and 3-coordinated surface molecules. *J. Chem. Phys.* 94:4091–92
39. Buch V, Milet A, Vacha R, Jungwirth P, Devlin JP. 2007. Water surface is acidic. *Proc. Natl. Acad. Sci. USA* 104:7342–47
40. Delzeit L, Rowland B, Devlin JP. 1993. Infrared spectra of hydrogen chloride complexed/ionized in amorphous hydrates and at ice surfaces in the 15–90 K range. *J. Phys. Chem.* 97:10312–18
41. Devlin JP, Joyce C, Buch V. 2000. Infrared spectra and structures of large water clusters. *J. Phys. Chem. A* 104:1974–77
42. Devlin JP, Uras N, Sadlej J, Buch V. 2002. Discrete stages in the solvation and ionization of hydrogen chloride adsorbed on ice particles. *Nature* 417:269–71
43. Rowland B, Fisher M, Devlin JP. 1991. Probing icy surfaces with the dangling-OH-mode absorption: large ice clusters and microporous amorphous ice. *J. Chem. Phys.* 95:1378–84

44. Rowland B, Kadagathur NS, Devlin JP, Buch V, Feldman T, Wojcik MJ. 1995. Infrared spectra of ice surfaces and assignment of surface-localized modes from simulated spectra of cubic ice. *J. Chem. Phys.* 102:8328–41
45. Graham JD, Roberts JT. 1994. Interaction of hydrogen chloride with an ultrathin ice film: observation of adsorbed and absorbed states. *J. Phys. Chem.* 98:5974–83
46. Blanchard JL, Roberts JT. 1994. Interaction of CCl_4 with the surface of amorphous ice. *Langmuir* 10:3303–10
47. Kumar GN, Cyriac J, Bag S, Pradeep T. 2009. Low energy ion scattering investigations of *n*-butanol-ice system in the temperature range of 110–150 K. *J. Phys. Chem. C* 113:14258–63
48. Cooks RG, Ast T, Pradeep T, Wysocki V. 1994. Reactions of ions with organic surfaces. *Acc. Chem. Res.* 27:316–23
49. Kang H. 2011. Reactive ion scattering of low energy Cs^+ from surfaces. A technique for surface molecular analysis. *Bull. Korean Chem. Soc.* 32:389–98
50. Ullah S, Dogar AH, Qayyum A. 2011. Surface-induced dissociation of low energy H_2^+ impact on a carbon surface: a Monte Carlo simulation. *Commun. Theor. Phys.* 55:315–20
51. Feketeova L, Zabka J, Zappa F, Grill V, Scheier P, et al. 2009. Surface-induced dissociation and chemical reactions of $C_2D_4^+$ on stainless steel, carbon (HOPG), and two different diamond surfaces. *J. Am. Soc. Mass Spectrom.* 20:927–38
52. Cyriac J, Pradeep T. 2008. Interaction of carboxylic acids and water ice probed by argon ion induced chemical sputtering. *J. Phys. Chem. C* 112:1604–11
53. Cyriac J, Pradeep T. 2007. Probing difference in diffusivity of chloromethanes through water ice in the temperature range of 110–150 K. *J. Phys. Chem. C* 111:8557–65
54. Rezayat T, Shukla A. 2007. Dissociative scattering of hyperthermal energy CF_3^+ ions from modified surfaces. *J. Chem. Phys.* 126:084701
55. Kim JH, Lahaye RJWE, Kang H. 2007. Evidence for Eley–Rideal abstraction mechanism in reactive ion scattering of Cs^+ from Pt(111) adsorbed with CO and CO_2. *Surf. Sci.* 601:434–40
56. Levandier DJ, Chiu Y-H, Dressler RA, Sun L, Schatz GC. 2004. Hyperthermal reactions of $O^+(^4S_{3/2})$ with CD_4 and CH_4: theory and experiment. *J. Phys. Chem. A* 108:9794–804
57. Levandier DJ, Chiu Y-H, Dressler RA. 2004. Reactions of O^+ with C_nH_{2n+2}, $n = 2$–4: a guided ion beam study. *J. Chem. Phys.* 120:6999–7007
58. Wade N, Jo S-C, Gologan B, Cooks RG. 2003. Differentiation of isomeric oxygenated adsorbates using low-energy ion/surface collisions. *Int. J. Mass Spectrom.* 230:151–59
59. Laskin J, Futrell JH. 2003. Energy transfer in collisions of peptide ions with surfaces. *J. Chem. Phys.* 119:3413–20
60. Han SJ, Lee CW, Lahaye RJWE, Kang H. 2003. Hyperthermal scattering of Cs^+ from Pt(111): the effect of image charge on the ion-surface energy transfer. *Surf. Sci.* 538:184–90
61. Lahaye RJWE, Kang H. 2003. Mechanism for the efficient abstraction of an adsorbate by Cs^+ scattering at hyperthermal energies. *Phys. Rev. B* 67:033401
62. Shukla AK, Futrell JH. 2003. Dynamics of hyperthermal energy ion-surface collisions: dissociative and non-dissociative scattering of ethanol cations from a self-assembled monolayer surface of fluorinated alkyl thiol on Au(111). *Int. J. Mass Spectrom.* 223/224:783–801
63. Hahn JR, Lee CW, Han SJ, Lahaye RJWE, Kang H. 2002. Low-energy Cs^+ scattering from water on Pt(111): a kinetic energy analysis of the Cs^+–water clusters. *J. Phys. Chem. A* 106:9827–31
64. Park S-C, Maeng K-W, Pradeep T, Kang H. 2001. Reactive ion scattering from pure and mixed HCl, NH_3 and D_2O surfaces. *Nucl. Instrum. Methods B* 182:193–99
65. Grill V, Shen J, Evans C, Cooks RG. 2001. Collisions of ions with surfaces at chemically relevant energies: instrumentation and phenomena. *Rev. Sci. Instrum.* 72:3149–79
66. Gu C, Wysocki VH, Harada A, Takaya H, Kumadaki I. 1999. Dissociative and reactive hyperthermal ion-surface collisions with Langmuir–Blodgett films terminated by $CF_3(CH_2)_n^-$, *n*-perfluoroalkyl, or *n*-alkyl groups. *J. Am. Chem. Soc.* 121:10554–62
67. Wade N, Pradeep T, Shen J, Cooks RG. 1999. Covalent chemical modification of self-assembled fluorocarbon monolayers by low-energy $CH_2Br_2^{+\cdot}$ ions: a combined ion/surface scattering and X-ray photoelectron spectroscopic investigation. *Rapid Commun. Mass Spectrom.* 13:986–93

68. Ada ET, Kornienko O, Hanley L. 1998. Chemical modification of polystyrene surfaces by low-energy polyatomic ion beams. *J. Phys. Chem. B* 102:3959–66
69. Hanley L, Lim H, Schultz DG, Wainhaus SB, de Sainte Claire P, Hase WL. 1997. Surface energy transfer by low energy polyatomic ion collisions. *Nucl. Instrum. Methods B* 125:218–22
70. Kang H, Kim KD, Kim KY. 1997. Molecular identification of surface adsorbates. Reactive scattering of hyperthermal Cs^+ from a Ni(100) surface adsorbed with CO, C_6H_6, and H_2O. *J. Am. Chem. Soc.* 119:12002–3
71. Kang H, Yang MC, Kim KD, Kim KY. 1998. Reactive scattering of Cs^+ from chemisorbed molecules on a Ni(100) surface. Secondary neutral mass spectrometry with a hyperthermal ion beam. *Int. J. Mass Spectrom. Ion Process.* 174:143–54
72. Sanfelix PC, Al-Halabi A, Darling GR, Holloway S, Kroes G-J. 2005. Protons colliding with crystalline ice: proton reflection and collision induced water desorption at low incidence energies. *J. Am. Chem. Soc.* 127:3944–51
73. Al-Halabi A, Sanfelix PC, Holloway S, Kroes G-J, Darling GR. 2006. Protons colliding with ice: bouncing, sticking, splashing. *Surf. Sci.* 600:4247–50
74. Cooks RG, Ast T, Mabud MA. 1990. Collisions of polyatomic ions with surfaces. *Int. J. Mass Spectrom. Ion Process.* 100:209–65
75. Franchetti V, Solka BH, Baitinger WE, Amy JW, Cooks RG. 1977. Soft landing of ions as a means of surface modification. *Int. J. Mass Spectrom. Ion Phys.* 23:29–35
76. Kang H. 2005. Chemistry of ice surfaces. Elementary reaction steps on ice studied by reactive ion scattering. *Acc. Chem. Res.* 38:893–900
77. Kim YK, Kim SK, Kim JH, Kang H. 2009. Kinetic isolation of reaction intermediates on ice surfaces. Precursor states of SO_2 hydrolysis. *J. Phys. Chem. C* 113:16863–65
78. Moon E-S, Kim YK, Shin S, Kang H. 2012. Asymmetric transport efficiencies of positive and negative ion defects in amorphous ice. *Phys. Rev. Lett.* 108:226103
79. Volný M, Elam WT, Ratner BD, Turecek F. 2005. Preparative soft and reactive landing of gas-phase ions on plasma-treated metal surfaces. *Anal. Chem.* 77:4846–53
80. Wang P, Hadjar O, Gassman PL, Laskin J. 2008. Reactive landing of peptide ions on self-assembled monolayer surfaces: an alternative approach for covalent immobilization of peptides on surfaces. *Phys. Chem. Chem. Phys.* 10:1512–22
81. Johnson GE, Hu Q, Laskin J. 2011. Soft landing of complex molecules on surfaces. *Annu. Rev. Anal. Chem.* 4:83–104
82. Miller SA, Luo H, Pachuta SJ, Cooks RG. 1997. Soft-landing of polyatomic ions at fluorinated self-assembled monolayer surfaces. *Science* 275:1447–50
83. Ast T, Mabud MA, Cooks RG. 1988. Reactive collisions of polyatomic ions at solid surfaces. *Int. J. Mass Spectrom. Ion Process.* 82:131–50
84. Cristoni S, Rubini S, Bernardi LR. 2007. Development and applications of surface-activated chemical ionization. *Mass Spectrom. Rev.* 26:645–56
85. Sleno L, Volmer DA. 2004. Ion activation methods for tandem mass spectrometry. *J. Mass Spectrom.* 39:1091–112
86. Cyriac J, Pradeep T, Kang H, Souda R, Cooks RG. 2012. Low-energy ionic collisions at molecular solids. *Chem. Rev.* 112:5356–411
87. Kaplan A, Manor Y, Bekkerman A, Tsipinyuk B, Kolodney E. 2003. Implanting atomic ions into surface adsorbed fullerenes: the single collision formation and emission of $Cs@C_{60}^+$ and $Cs@C_{70}^+$. *Int. J. Mass Spectrom.* 228:1055–65
88. Fernandez FM, Smith LL, Kuppannan K, Yang X, Wysocki VH. 2003. Peptide sequencing using a patchwork approach and surface-induced dissociation in sector-TOF and dual quadrupole mass spectrometers. *J. Am. Soc. Mass Spectrom.* 14:1387–401
89. Pradeep T, Riederer DE Jr, Hoke SH II, Ast T, Cooks RG, Linford MR. 1994. Reactions of metal ions at fluorinated SAM (self-assembled monolayer) surfaces: formation of MF_n^+ (M = Ti, Cr, Fe, Mo, and W; n = 1–5). *J. Am. Chem. Soc.* 116:8658–65
90. Maeno N, Ebinuma T. 1983. Pressure sintering of ice and its implication to the densification of snow at polar glaciers and ice sheets. *J. Phys. Chem.* 87:4103–10

91. Pritchard HD, Ligtenberg SRM, Fricker HA, Vaughan DG, van den Broeke MR, Padman L. 2012. Antarctic ice-sheet loss driven by basal melting of ice shelves. *Nature* 484:502–5
92. Prenni AJ, Tolbert MA. 2001. Studies of polar stratospheric cloud formation. *Acc. Chem. Res.* 34:545–53
93. Snow TP, Bierbaum VM. 2008. Ion chemistry in the interstellar medium. *Annu. Rev. Anal. Chem.* 1:229–59
94. Bouwman J, Paardekooper DM, Cuppen HM, Linnartz H, Allamandola LJ. 2009. Real-time optical spectroscopy of vacuum ultraviolet irradiated pyrene: H_2O interstellar ice. *Astrophys. J.* 700:56–62
95. Gibb EL, Whittet DCB, Boogert ACA, Tielens AGGM. 2004. Interstellar ice. The infrared space observatory legacy. *Astrophys. J. Suppl.* 151:35–73
96. Pedersen C, Mihranyan A, Strømme M. 2011. Surface transition on ice induced by the formation of a grain boundary. *PLoS ONE* 6:e24373
97. Koop T, Kapilashrami A, Molina LT, Molina MJ. 2000. Phase transitions of sea-salt/water mixtures at low temperatures: implications for ozone chemistry in the polar marine boundary layer. *J. Geophys. Res.* 105:26393–402
98. Blomquist J, Andersson MP, Uvdal P. 2011. Inducing H/D exchange in ultrathin ice films by proton deficiency. *Phys. Rev. Lett.* 107:216101
99. Gálvez O, Maté B, Herrero VJ, Escribano R. 2011. HDO infrared detection sensitivity and D/H isotopic exchange in amorphous and crystalline ice. *Astrophys. J.* 738:133
100. Lee C-W, Lee P-R, Kim YK, Kang H. 2007. Mechanistic study of proton transfer and H/D exchange in ice films at low temperatures (100–140 K). *J. Chem. Phys.* 127:084701
101. Lu H, McCartney SA, Sadtchenko V. 2009. H/D exchange kinetics in pure and HCl doped polycrystalline ice at temperatures near its melting point: structure, chemical transport, and phase transitions at grain boundaries. *J. Chem. Phys.* 130:054501
102. Moon E-S, Yoon J, Kang H. 2010. Energy barrier of proton transfer at ice surfaces. *J. Chem. Phys.* 133:044709
103. Pan M, Pozun ZD, Yu W-Y, Henkelman G, Mullins CB. 2012. Structure revealing H/D exchange with co-adsorbed hydrogen and water on gold. *J. Phys. Chem. Lett.* 3:1894–99
104. Park S-C, Jung K-H, Kang H. 2004. H/D isotopic exchange between water molecules at ice surfaces. *J. Chem. Phys.* 121:2765–74
105. Souda R. 2005. TOF-SIMS analysis of ion-water interactions. *Nucl. Instrum. Methods B* 232:125–33
106. Weber AS, Hodyss R, Johnson PV, Willacy K, Kanik I. 2009. Hydrogen-deuterium exchange in photolyzed methane-water ices. *Astrophys. J.* 703:1030–33
107. Pachuta SJ, Cooks RG. 1987. Mechanisms in molecular SIMS. *Chem. Rev.* 87:647–69
108. Jacobs DC. 2002. Reactive collisions of hyperthermal energy molecular ions with solid surfaces. *Annu. Rev. Phys. Chem.* 53:379–407
109. Gologan B, Green JR, Alvarez J, Laskin J, Graham CR. 2005. Ion/surface reactions and ion soft landing. *Phys. Chem. Chem. Phys.* 7:1490–500
110. Jung K-H, Park S-C, Kim JH, Kang H. 2004. Vertical diffusion of water molecules near the surface of ice. *J. Chem. Phys.* 121:2758–64
111. Livingston FE, Whipple GC, George SM. 1997. Diffusion of HDO into single-crystal $H_2{}^{16}O$ ice multilayers: comparison with $H_2{}^{18}O$. *J. Phys. Chem. B* 101:6127–31
112. Lee C-W, Lee P-R, Kang H. 2006. Protons at ice surfaces. *Angew. Chem. Int. Ed.* 45:5529–33
113. Kim S, Park E, Kang H. 2011. Segregation of hydroxide ions to an ice surface. *J. Chem. Phys.* 135:074703
114. Moon E-S, Kang H, Oba Y, Watanabe N, Kouchi A. 2010. Direct evidence for ammonium ion formation in ice through ultraviolet-induced acid-base reaction of NH_3 with H_3O^+. *Astrophys. J.* 713:906–11
115. Kim YK, Park S-C, Kim JH, Lee C-W, Kang H. 2008. Interaction of carbon dioxide and hydroxide ion at the surface of ice films. *J. Phys. Chem. C* 112:18104–9
116. Kim SK, Kang H. 2010. Efficient conversion of nitrogen dioxide into nitrous acid on ice surfaces. *J. Phys. Chem. Lett.* 1:3085–89
117. Kim JH, Kim YK, Kang H. 2008. Hydrolysis of sodium atoms on water–ice films: characterization of reaction products and interfacial distribution of sodium and hydroxide ions. *J. Phys. Chem. C* 113:321–27

118. Donsig HA, Herridge D, Vickerman JC. 1998. Static SIMS studies of reactions on mimics of polar stratospheric clouds. II. Low-temperature, low-pressure interactions of Cl_2 and Cl_2O with solid ice films. *J. Phys. Chem. A* 102:2302–8
119. Donsig HA, Herridge D, Vickerman JC. 1999. Static SIMS studies of reactions on mimics of polar stratospheric clouds. III. Mechanism of chlorine nitrate decomposition and reaction. *J. Phys. Chem. A* 103:9211–20
120. Cyriac J, Pradeep T. 2008. Structural reorganization on amorphous ice films below 120 K revealed by near-thermal (~1 eV) ion scattering. *J. Phys. Chem. C* 112:5129–35
121. Johari GP, Hallbrucker A, Mayer E. 1987. The glass-liquid transition of hyperquenched water. *Nature* 330:552–53
122. Yue Y, Angell CA. 2004. Clarifying the glass-transition behavior of water by comparison with hyperquenched inorganic glasses. *Nature* 427:717–20
123. Souda R. 2009. Liquid-like nature of crystalline *n*-butane and *n*-pentane films studied by time-of-flight secondary ion mass spectrometry. *J. Phys. Chem. B* 113:15831–35
124. Jenniskens P, Banham SF, Blake DF, McCoustra MRS. 1997. Liquid water in the domain of cubic crystalline ice I_c. *J. Chem. Phys.* 107:1232–41
125. Souda R. 2006. Time-of-flight secondary ion mass spectroscopy analysis of Na adatoms interacting with water–ice film. *J. Chem. Phys.* 125:044706
126. Souda R. 2006. Evidence of deeply supercooled liquid water in interaction with LiCl. *J. Phys. Chem. B* 110:14787–91
127. Souda R. 2007. Two liquid phases of water in the deeply supercooled region and their roles in crystallization and formation of LiCl solution. *J. Phys. Chem. B* 111:5628–34
128. Souda R. 2007. Hydration of NaCl on glassy, supercooled-liquid, and crystalline water. *J. Phys. Chem. B* 111:11209–13
129. Mishima O, Stanley HE. 1998. The relationship between liquid, supercooled and glassy water. *Nature* 396:329–35
130. Souda R. 2006. Liquid-liquid transition in supercooled water investigated by interaction with LiCl and Xe. *J. Chem. Phys.* 125:181103
131. Souda R. 2008. Roles of deeply supercooled ethanol in crystallization and solvation of LiI. *J. Phys. Chem. B* 112:2649–54
132. Souda R. 2010. Roles of individual and cooperative motions of molecules in glass–liquid transition and crystallization of toluene. *J. Phys. Chem. B* 114:10734–39
133. Kawana S, Jones RAL. 2001. Character of the glass transition in thin supported polymer films. *Phys. Rev. E* 63:021501
134. Souda R. 2012. Nanoconfinement effects on the glass–liquid transition of vapor-deposited 1-pentene. *J. Phys. Chem. C* 116:7735–40
135. Souda R. 2006. Substrate and surfactant effects on the glass-liquid transition of thin water films. *J. Phys. Chem. B* 110:17524–30
136. LaPack MA, Pachuta SJ, Busch KL, Cooks RG. 1983. Surface modification by soft landing of reagent beams. *Int. J. Mass Spectrom. Ion Phys.* 53:323–26
137. Shen J, Yim YH, Feng B, Grill V, Evans C, Cooks RG. 1999. Soft landing of ions onto self-assembled hydrocarbon and fluorocarbon monolayer surfaces. *Int. J. Mass Spectrom.* 182/183:423–35
138. Denault JW, Evans C, Koch KJ, Cooks RG. 2000. Surface modification using a commercial triple quadrupole mass spectrometer. *Anal. Chem.* 72:5798–803
139. Judai K, Sera K, Amatsutsumi Si, Yagi K, Yasuike T, et al. 2001. A soft-landing experiment on organometallic cluster ions: infrared spectroscopy of $V(benzene)_2$ in Ar matrix. *Chem. Phys. Lett.* 334:277–84
140. Peng W-P, Goodwin MP, Chen H, Cooks RG, Wilker J. 2008. Thermal formation of mixed-metal inorganic complexes at atmospheric pressure. *Rapid Commun. Mass Spectrom.* 22:3540–48
141. Nagaoka S, Matsumoto T, Okada E, Mitsui M, Nakajima A. 2006. Room-temperature isolation of $V(benzene)_2$ sandwich clusters via soft-landing into *n*-alkanethiol self-assembled monolayers. *J. Phys. Chem. B* 110:16008–17

142. Matsumoto T, Nagaoka S, Ikemoto K, Mitsui M, Ara M, et al. 2009. Characterization of alkyl monolayer covalently bonded to Si(111) and soft-landing of vanadium-benzene sandwich clusters onto the alkyl monolayer substrate. *Eur. Phys. J. D* 52:99–102
143. Nagaoka S, Matsumoto T, Ikemoto K, Mitsui M, Nakajima A. 2007. Soft-landing isolation of multidecker $V_2(benzene)_3$ complexes in an organic monolayer matrix: an infrared spectroscopy and thermal desorption study. *J. Am. Chem. Soc.* 129:1528–29
144. Nagaoka S, Ikemoto K, Matsumoto T, Mitsui M, Nakajima A. 2008. Thermal and hyperthermal collision-energy depositions of transition metal-benzene sandwich complexes onto a self-assembled *n*-octadecanethiol monolayer. *J. Phys. Chem. C* 112:6891–99
145. Peng W-P, Johnson GE, Fortmeyer IC, Wang P, Hadjar O, et al. 2011. Redox chemistry in thin layers of organometallic complexes prepared using ion soft landing. *Phys. Chem. Chem. Phys.* 13:267–75

Annual Review of
Analytical Chemistry

Volume 6, 2013

Contents

Indexes

Errata

An online log of corrections to *Annual Review of Analytical Chemistry* articles may be found at http://arjournals.annualreviews.org/errata/anchem

ChemPubSoc Europe

DOI: 10.1002/cphc.201200927

Bare Clusters Derived from Protein Templates: Au_{25}^{+}, Au_{38}^{+} and Au_{102}^{+}

Ananya Baksi,[a] Thalappil Pradeep,*[a] Bokwon Yoon,[b] Constantine Yannouleas,[b] and Uzi Landman*[b]

A discrete sequence of bare gold clusters of well-defined nuclearity, namely Au_{25}^{+}, Au_{38}^{+} and Au_{102}^{+}, formed in a process that starts from gold-bound adducts of the protein lysozyme, were detected in the gas phase. It is proposed that subsequent to laser desorption ionization, gold clusters form in the gas phase, with the protein serving as a confining growth environment that provides an effective reservoir for dissipation of the cluster aggregation and stabilization energy. First-principles calculations reveal that the growing gold clusters can be electronically stabilized in the protein environment, achieving electronic closed-shell structures as a result of bonding interactions with the protein. Calculations for a cluster with 38 gold atoms reveal that gold interaction with the protein results in breaking of the disulfide bonds of the cystine units, and that the binding of the cysteine residues to the cluster depletes the number of delocalized electrons in the cluster, resulting in opening of a super-atom electronic gap. This shell-closure stabilization mechanism confers enhanced stability to the gold clusters. Once formed as stable magic number aggregates in the protein growth medium, the gold clusters become detached from the protein template and are observed as bare Au_n^{+} ($n = 25$, 38, and 102) clusters.

1. Introduction

Clusters of noble metals, particularly gold, with precise nuclearity (number of atoms) and overall molecular composition continue to be a topic of intense experimental and theoretical research endeavors. These efforts aim at understanding the basic factors, such as electronic structure, atomic packing, and adsorbed layers that underlie the appearance of certain structural motifs and control the size evolution, which bridges the cluster-size domain with the bulk condensed phase. These studies are also motivated by certain properties exhibited by clusters, such as high chemical reactivity, catalytic activity and intense luminescence, which may be exploited in future technologies.[1] While the structures of bare, as well as protected (passivated), gold clusters have been studied for close to two decades,[2] research activities on ligated analogues have intensified significantly in recent years[3–5] and crystal structures of four of them, namely, $Au_{25}(SR)_{18}$,[3e,f] $Au_{36}(SR)_{24}$,[3k] $Au_{38}(SR)_{24}$,[4e] and $Au_{102}(SR)_{44}$[5a] (SR, alkyl thiolate ligand derived from RSH) have been solved using X-ray crystallography total structure determination, meaning determination of the atomic positions of both the core and surface atoms.

Clusters protected with proteins[6] have been a rather recent addition to this family of materials, with the clusters exhibiting stable luminescence and the proteins retaining their biological activity[6e] and biocompatibility. Certain clusters, for example, Au_{13}, Au_{25}, Au_{38} and some others, have been proposed to exist within protein templates. Mass spectrometry is an indispensible tool for investigations of clusters, particularly since precise measurement of molecular composition is possible with soft ionization methodologies such as laser desorption. However, laser desorption and ionization often result in fragmentation of the S–C bond on the cluster core, resulting in Au_nS_m aggregates. To date, formation of bare gas-phase Au_n clusters, especially those with structural and electronic stability, has not been observed in studies of metal cluster complexes with proteins.

Cluster aggregation and growth from precursors via the assembly of atoms or molecules, is accompanied by energy release and efficient removal of the aggregation and stabilization energy, which is often achieved through collisional cooling and is a prerequisite for stable cluster growth. Typically laser desorption is followed by equilibration of the plasma in an inert gas leading to the formation of clusters. This has been eminently demonstrated in the case of fullerenes.[7] We considered the possibility of forming stable clusters of gold using protein templates as an energy relaxation medium—a heat-bath reservoir—during cluster growth.

In this paper, we show experimentally, through mass spectrometry, and theoretically, using first-principles quantum calculations, that formation of stable gas-phase clusters with spe-

[a] A. Baksi, Prof. Dr. T. Pradeep
DST Unit of Nanoscience (DST UNS)
Department of Chemistry
Indian Institute of Technology Madras
Chennai 600036 (India)
E-mail: pradeep@iitm.ac.in

[b] Dr. B. Yoon, Dr. C. Yannouleas, Prof. Dr. U. Landman
School of Physics
Georgia Institute of Technology
Atlanta, GA 30332-0430 (USA)
E-mail: uzi.landman@physics.gatech.edu

Supporting information for this article is available on the WWW under http://dx.doi.org/10.1002/cphc.201200927.

cific nuclearities (that is, a discrete sequence of cluster sizes characterized by enhanced stability compared to other sizes) can be achieved through the use of biomolecules, in particular, proteins. Here, the proteins act as selective cluster nucleation templates offering spatially confining protective growth volumes and electronic stabilization of the aggregating metal clusters. In addition, the proteins serve as effective reservoirs for the removal of cluster formation and stabilization energy. The results shown herein constitute the first observation of protein-template-derived stable gas-phase clusters of formulae Au_{18}, Au_{25}, Au_{38} and Au_{102}, although their ligand protected analogues have been known for some time. Most of our studies used lysozyme, from chicken egg white (Lyz) as a model protein because of its relatively light mass, which allows the acquisition of high-quality mass spectra in the monomer and oligomer regions. Associated studies have also been conducted with bovine serum albumin (BSA) and native lactoferrin (NLf).

The paper is organized as follows. In the Experimental Section (at the end of the manuscript) we describe the experimental and theoretical methodologies. In Section 2 we present and discuss our experimental (2.1–2.4) and theoretical (2.5) results. We summarize our results in Section 3, and put them in perspective in the light of current and future investigations.

2. Results and Discussion

2.1. Observation of Size-Selected Bare Gold Clusters

A discrete sequence of bare gold clusters of well-defined nuclearities, Au_{25}^+, Au_{38}^+ and Au_{102}^+ were created in a process of laser desorption, which starts from gold-bound precursor adducts (Lyz–Au) of the protein, Lyz. The adducts were made by incubating $HAuCl_4{\cdot}3H_2O$ with Lyz at room temperature (30 °C) at various concentrations (see the Experimental Section). In the Lyz–Au adducts, gold exist in the +1 form as seen from X-ray photoelectron spectroscopy (XPS) in the Au 4f region[6g] and the reduction (Au^{3+} to Au^{1+}) is proposed to occur by amino acids and/or by the oxidation of the cystine disulfide bonds in the protein[11] (Section 2.5). Luminescent gold clusters in protein templates are formed from these adducts upon exposing the system to an alkaline medium.[6g] The Lyz–Au adducts observed by us here, however, are not luminescent in the visible spectral window. Several macromolecules such as DNA are known to produce noble metal clusters although reduction typically uses external reducing agents.[8a] Protein-protected clusters generally invoke the mechanism of tryptophan-induced reduction.[8b] For this study, we prepared the Au^{1+} state in the solution phase and conducted laser desorption on this material in the solid state.

The protein used in this study, lysozyme, has 129 amino acids, including eight cysteine residues, $-SCH_2CH(NH_2)CO_2H$. These cysteine residues form four disulfide bonds, thus making four cystines, located between positions 6–127, 30–115, 64–80 and 76–94. As we show below, our theoretical simulations predicted, and experiments confirm[6i] that interaction with gold results in splitting of the cystine disulfide bonds. For the parent protein, matrix-assisted laser desorption ionization mass spectrometric (MALDI-MS) analysis shows a series of peaks in the positive ion spectrum corresponding to Lyz^+ (*m/z* 14,363) and its oligomers such as Lyz_2^+ (*m/z* ~28810), Lyz_3^+ (*m/z* ~43300), and so forth, along with Lyz^{2+} (*m/z* 7180), with uncertainty increasing with an increase in the mass number. Except for the Lyz^{2+} feature, the mass spectrum of the parent Lyz does not show any signal in the *m/z* range of 3000–9000 (Figure 2, bottom-most trace). However, spectra of the Lyz–Au adduct present a completely different picture where distinctly different peaks are seen. These features keep increasing in intensity as a function of the Au^{3+} concentration used to make the adduct. An examination of the mass spectrum shows that the new peaks are mostly spaced at *m/z* 197, due to Au. The maxima of the peaks correspond to $Au_{18}S_4^+$, Au_{25}^+ and Au_{38}^+ with a separation due to Au on either side of the maxima (Figure 1, note the regions marked a, b and c). While the ions in the Au_{25} region are composed solely of gold, the Au_{18} region shows ions with some sulfur additions, in the form of $Au_{18+n}S_{4+m}^+$. We conjecture here that these sulfur additions are the result of interaction of Au with the protein medium in which the metal cluster ions are formed. This is supported by the predictions of our first-principles calculations (see below) and experimental measurements[6i] (see also Figure S5, Supporting Information). In the Au_{18}^+ region, sulfur attachment is

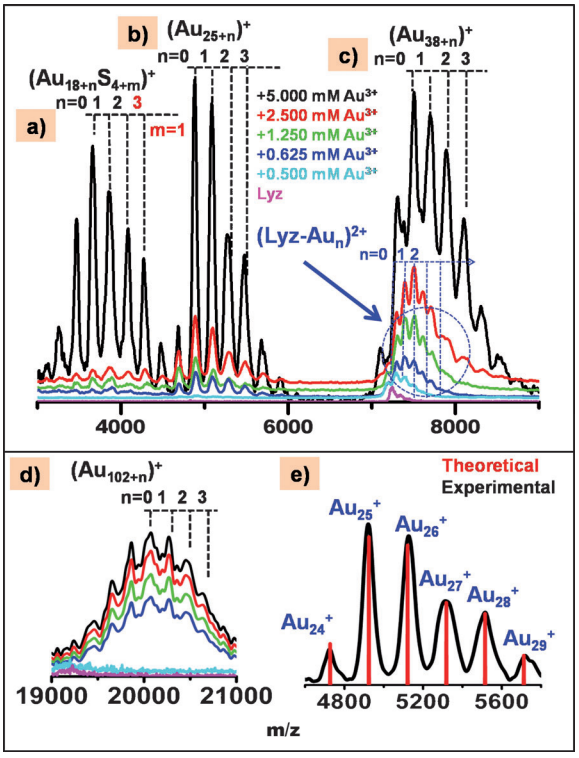

Figure 1. MALDI-MS of Lyz–Au adduct in the linear positive mode showing distinct features of Au clusters. The spectrum of parent Lyz is also shown. The bare cluster series seen are separately shown: a) $Au_{18}S_4$, b) Au_{25} and c) Au_{38} and d) Au_{102}. The peaks show a separation of *m/z* 197. The circled region of (c) shows a Au uptake of Lyz^{2+} with a separation due to the Au^{2+} series. In (e) the experimental spectrum in the Au_{25} region is compared with the calculated peak positions (in red). Colors of the traces correspond to the Au^{3+} concentration used, which are indicated.

again evidenced by additional mass increase in the Au_{20}^+ mass, where the peak corresponds to $Au_{20}S_5^+$. The series of bare clusters are labeled such that the highest-intensity peak is marked as $n=0$. Peaks above and below $n=0$ imply that clusters of relatively poor stability are also formed. It is noteworthy that while different ions are seen in the spectrum around the Au_{18}^+ and Au_{25}^+ regions, the $Au_{18}S_4^+$ and Au_{25}^+ species themselves are highest in intensity.

The Au_{38}^+ region overlaps with Lyz^{2+} and its Au pick-up peaks (see below), but the latter are much weaker in intensity at the highest Au^{3+} concentration used. At this concentration, the mass spectrum is spaced at $m/z=197$, due to gold, while for $(Lyz–Au_n)^{2+}$, the peaks are separated by 99. The nearly 100 Da mass difference (between Au^{2+} and Au^{1+}) is easy to be resolved at this mass range by the instrument.

Upon further examination of the mass spectrum, other ions such as Au_{102}^+ are also observable. In this mass region (Figure 1d), the clusters appear in the spectrum above a gold concentration of 0.625 mM and there was no ion signal of significance below this concentration regime. In this range, adjacent cores are nearly equally stable as intensity difference is not too high between the peaks. The mass assignments are accurate as a comparison of the experimental and theoretical mass numbers in the Au_{25}^+ region would indicate (Figure 1e). For the other regions, experimental and theoretical peak positions are compared in Figure S1.

Lysozyme is a rather small protein and in solution it is unlikely to accommodate gold clusters of 25, 38 or 102 atoms in a single molecule. Indeed as we discuss in section 2.2, a Lyz molecule is found to attach only up to ~10 Au atoms. Consequently, we propose that reactions in the plasma generated after laser ionization/desorption to underlie the formation of the detected gold clusters. Upon laser irradiation, a gaseous plasma is created, composed of ions and neutrals of gold atoms and aggregates, protein molecules, and Lyz–Au adducts, as well as electrons. We also note here that gaseous Lyz–Au adducts are likely to be conformationally modified compared to the solution phase. These plasma constituents interact to form larger aggregates (as known in the case of plasma desorption). Such reactions may include the following reaction schemes (and cascades thereof) [Eqs. (1)–(3)]:

$$Au_n + Au_m^+ \rightarrow Au_{n+m}^+, \quad Au_n + Au_m \rightarrow Au_{n+m} \quad n,m = 1,2,3,\ldots, \tag{1}$$

$$[Lyz - Au_m]^+ + Au_n \rightarrow [Lyz - Au_{m+n}]^+ \quad m = 0,1,2,\ldots; n = 1,2,3\ldots, \tag{2}$$

$$[Lyz - Au_n]^+ + Lyz - Au_m \rightarrow [Lyz - Au_{n+k}]^+ + Lyz - Au_{m-k} \quad n,m = 1,2,3,.; k\ (\leq m) = 1,2,\ldots, \tag{3}$$

where Equation (3) describes metals transfer between two Lyz–Au adducts. As discussed by us below (Section 2.5), in the Lyz–Au_n adduct, the gold cluster is anchored to the protein through binding to the cysteine residues resulting from barrierless cleavage by gold of the cystine disulfide bond with four cystine groups per lysozyme molecule. The disulfide bond cleavage is accompanied by changes in the protein molecular conformation (Sections 2.5 and S5). We note here that Au_n^+ (with $n=1, 2, 3,\ldots$) species are seen in the laser desorption mass spectrum of Au salts. These occur due to photoreduction and reactions of the type described in Equation (1). Larger aggregates by the extension of the same process occur here because of the delayed extraction (used in MALDI-MS) of the ions. In our experiments, the ions (and neutrals) formed are extracted only after a finite delay time of 1200 ns to allow the desorbed species in the gaseous plasma to interact (see description of the MALDI-MS method in the Experimental Section). The plasma reactions between low-energy ions and neutrals have a number of precedents. For example, we note here observation of $C_{(60+n)}^+$ in secondary ion mass spectrometry (SIMS)[9] of C_{60} films (due to gas-phase reactions between C_{60}^+ and C_2 species, derived by fragmentation of C_{60}). In our case, the above reactions are further facilitated by the abundance of protein molecules (and their gold-cluster adducts) in the (plasma) reaction zone, since their relatively large mass slows down their movement and separation from the plasma cloud. Relaxation of the metal cluster aggregation energy (binding and excess vibrational energies) is facilitated by coupling of the growing metal cluster to the large number of degrees of freedom of the host protein molecule. As gold clusters evolve following the above growth processes, certain cluster nuclearities, that is selected cluster sizes (number of gold atoms) of enhanced stability are formed (for the electronic stabilization mechanism of "magic number" cluster sizes, see Section 2.5), and they eventually detach from the lysozyme template, and get detected as bare gold cluster cations.

2.2. Au Uptake by Lyz—Observations in the Solid State

The bare clusters are formed from Au–protein adducts, which are seen in the integral form in the MALDI MS spectra. As mentioned before, the positive ion spectrum of Lyz displays features due to Lyz^+ and its oligomers along with Lyz^{2+} (Figure 2, bottom-most trace). For Au^{1+}–Lyz, these peaks are shifted to higher masses. For the Lyz^+ peak, the maximum intense feature showed a mass shift of about 600 Da from the parent Lyz, due to Au pick-up. Upon closer examination, multiple peaks are seen, starting from parent lysozyme peaks and each one of the peaks is separated by m/z 197 due to Au. A maximum of nine Au additions were seen for Lyz^+, with reduced intensity (this region is expanded in inset a). Gold uptake is also exhibited by Lyz_2^+ giving $(Lyz_2–Au_n)^+$ (inset b). The larger Lyz aggregates (Lyz_3^+, Lyz_4^+,…) also take up gold, as shown in Figure 2, but the resolution is not adequate to see individual Au uptakes clearly at Lyz_3^+ and beyond. The number of Au uptake peaks increases with increase in Au^{3+} concentration (spectra at varying Au^{3+} concentrations are shown in Figure 2) and the intensity of free protein without any Au attachment decreases simultaneously. Thus we conclude that up to ~10 Au attachments are possible in Lyz–Au_n adducts. In any case, at the concentrations used (maximum molar ratios of 1:3 for Lyz:Au), it is unlikely that in solution (and thus in a solid made from that solution) a protein molecule would pick up a much larger

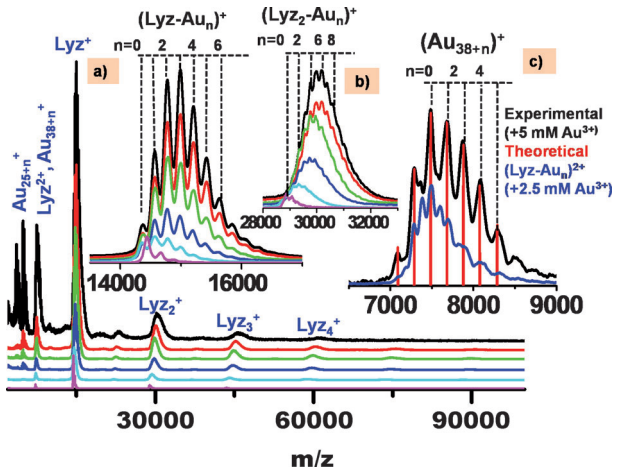

Figure 2. MALDI-MS spectrum of as-synthesized Lyz–Au adduct in the linear positive ion mode at various concentrations of Au^{3+} used for incubation. The spectrum shows Au attachment, seen at the various peaks derived from Lyz such as the monomer (Lyz), dimer (Lyz$_2$), trimer (Lyz$_3$), and so forth. Expanded views show multiple Au attachment to a) Lyz and b) Lyz$_2^+$. In (c) theoretical (red) and experimental (black) values for Au_{38}^+ region along with Au uptake by Lyz^{2+} are compared. In these traces (c), two Au^{3+} concentrations are used: 5 mM (black) and 2.5 mM (blue) because of their good intensity. All the colors used are the same as those mentioned in Figure 1.

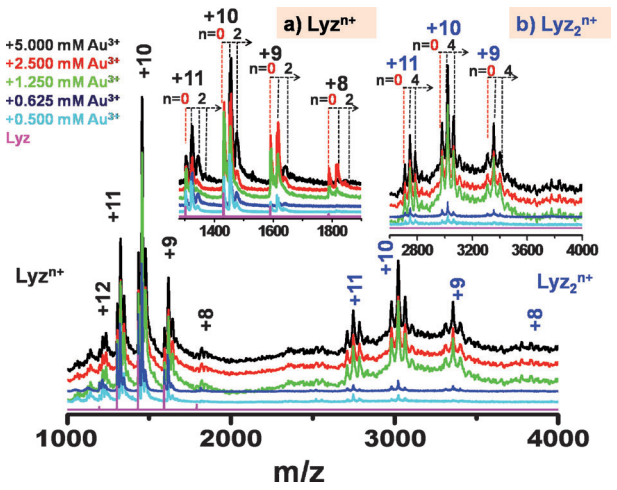

Figure 3. ESI-MS spectrum of Lyz–Au adduct in the positive-ion mode, in the region of *m/z* 500–4000. The peaks observed are due to Au uptake by Lyz at different charge states. Peak separation is corresponding to the Au uptake by that specific charge state. Insets: a) peaks of the Lyz^{n+} series and b) the same for the Lyz_2^{n+} series.

number of gold atoms (e.g. 25, 38 or 102), although aggregates of protein–gold adducts may have such numbers of gold atoms.

The attachment of gold to the lysozyme molecule is likely due to the cystine residues, which act as protecting thiolates and upon reaction with Au^{3+}, the latter is converted to Au^+.[10] The lower mass region of the spectrum shows the bare clusters, shown in Figure 1. As the $(Lyz–Au_n)^{2+}$ peaks overlap with the Au_{38+n}^+ region, we have confirmed the authenticity of the assignments by comparing the spectrum with the calculated masses of Au_{38+n}^+ (Figure 2, inset c) where we can see that some of the peaks due to $(Lyz–Au_n)^{2+}$ are distinctly different.

2.3. Study of the Solution State

To explore whether the gold clusters form in the solution, we undertook an electrospray ionization mass spectrometry (ESI-MS) study of the Lyz–Au adducts. Lysozyme gives well-defined mass spectra and good charge distribution. The +10 charge is the most stable in the case of both the monomer and the dimer in the spectral range studied. From the ESI-MS studies (Figure 3), it is evident that Au is picked up by the protein at all the concentrations studied. Here, larger relative intensities are found for the Au-added peaks with an increase in the Au^{3+} concentration. The separation due to multiple Au atom pick-ups can be also seen at high concentration of Au^{3+}, especially in the dimer region (these are marked in the inset). Both the Lyz monomer and dimer show maximum intensities corresponding to the +10 charge state, implying that this state is the most stable, as in the protein mass spectrum. The separation between the main protein peak and the gold uptake peaks changes with the charge state: the separation is 19.7 for +10 charge while it is 21.9 for +9 and 24.6 for +8. In these spectra, a limited number of Au uptakes is seen, unlike in the MALDI-MS data where up to nine Au additions are seen. This is probably due to the increased Columbic repulsion of multiply charged states as in 10+ and consequent loss of the metal ion to increase the stability. From the ESI-MS data, we conclude that the bare gold clusters observed in the MALDI mass spectrum (Figure 1 and 2) do not form in the solution phase.

2.4. Dependence on Other Factors

Several control experiments were performed and the important ones are presented below:

1) To prove that the chemistry seen is independent of the photon flux, a laser-intensity-dependent study was performed. MALDI-MS did not show significant laser intensity dependence, although the Au_n^+ peaks were enhanced with increasing intensity (Figure S2). No new features were seen at higher intensity. In the Au_{18}^+ region one continues to observe the aforementioned $Au_{18+n}S_{4+m}^+$ features (Figure 1a) even at higher laser intensities, indicating the absence of Au–S bond breakage. These results are important as typically at increased laser intensity, fragmentation occurs, especially when the linkages are weaker as in the case of ligand protection of a metal core.
2) Several proteins known to make luminescent clusters in solution[6] were probed to make bare clusters. The data (Figure S3) suggest that while lysozyme is most efficient in cluster formation, others such as bovine serum albumin (BSA) and NLf also make clusters. The parent proteins do not show any peaks in this mass range.
3) While clusters form in both the positive- and negative-ion modes, cluster formation was more efficient in the former (Figure 4), as typically negative ions are 500 times weaker than the corresponding positive ion signals. No new fea-

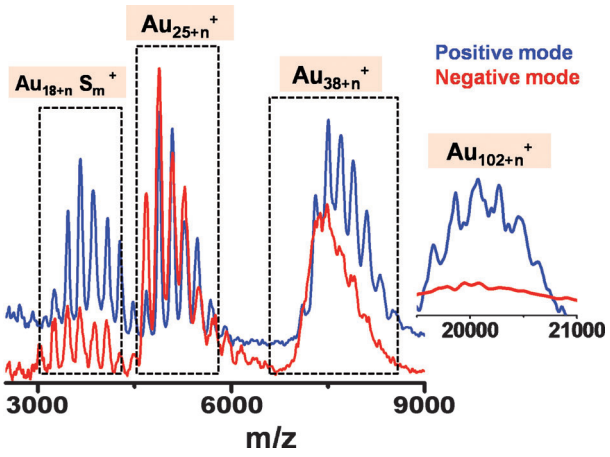

Figure 4. Positive (blue) and negative (red) MALDI-MS spectra of the Lyz–Au adduct in the linear mode at a concentration of 5 mM Au^{3+} as all the peaks are coming with good intensity at this concentration. In the negative mode the intensity is 500 times less than in the positive mode and therefore the spectra above have been scaled suitably.

tures were seen in the negative mode. In the negative mode the Au_{38}^+ and Au_{102}^+ regions are not well-resolved. From this study, it is confirmed that the as-prepared bare clusters are more stable in the cationic form. Therefore, all other studies were carried out in the linear positive mode.

4) The precursor solution was investigated over time to see any time dependent changes occur in MALDI-MS (Figure S4). There was no change in the peak positions in the Au_{18}^+ and Au_{25}^+ region, only the intensity was increased. The enhanced intensity may be due to the availability of more Au^+ ions with time as more Au^{3+} is expected to be consumed to become Au^+. In the Au_{38}^+ region, the spectra show a somewhat more pronounced dependence on the solution incubation time than for the other sizes (Au_{18}^+, Au_{25}^+ and Au_{102}^+ regions). Just after mixing Au^{3+} with the lysozyme, the peaks do not appear properly. However, $(Lyz–Au_n)^{2+}$ peaks that overlap with the Au_{38}^+ came up. After two hours from mixing, the peaks began to appear, but not with sufficient intensity. After four hours of reaction, peaks in the Au_{38}^+ region started to become prominent. But after six hours, the intensity increased significantly and kept getting higher, and by twelve hours, became comparable to the intensity of the Au_{25}^+ region. It is pertinent to note here that it has been reported that in the solution phase, upon passage of time, Au_{25} becomes the only prominent cluster among a mixture of clusters.[3j] The larger mass-spectrometrically-measured abundance of Au_n^+ ($n \leq 38$) bare clusters indicates that it is harder to accommodate and sustain the growth of larger clusters (e.g. $n = 102$) in the lysozyme template. This is most likely because the protein's relatively small size restricts (conformationally) the size of the forming gold cluster. The above-noted somewhat larger sensitivity of the Au_{38}^+ cluster to the solution incubation time, may arise because of specific structural characteristics of certain solution Lyz–gold adducts (with up to about ten gold atoms per lysozyme molecule) that (kinetically) require more time to form, and that subsequent to laser ionization and desorption (Section 2.1) react favorably to form this size cluster. Overall, we conclude that the above observations further supports our conclusions about the role of the protein molecules in the cluster formation process, acting as a gold storage medium, enabling the nucleation, growth and stabilization (see below) of gold clusters.

2.5. Theoretical Studies

Since the mechanisms and dynamics of the cluster growth processes are not amenable for investigation with mass spectrometry, these aspects are outside the scope of this paper. Instead we focus on experimental identification and characterization of the products of the interaction between gold and protein molecules, and on theoretical exploration of certain size-dependent stabilization mechanisms mediated by the interaction of the formed gold clusters with the protein growth medium. In particular, in our theoretical discussion, we focus on binding of the gold clusters to the cysteine residues that result from dissociative interaction of the clusters with the dimeric amino acid, cystine, of the lysozyme molecule.

As aforementioned, cluster formation must be accompanied by efficient dissipation of the heat of aggregation by the growth medium. Macromolecules, in general, and proteins in particular, are characterized by a vast number of degrees of freedom, covering a broad energy (frequency) range. Consequently, it is likely that vibrational motions and (local) conformational changes of the host protein molecules would facilitate efficient removal of the heat generated in the process of gold cluster nucleation and growth. We postulate that the observed growth of metal clusters in the protein environment involves formation of protein-bound metal cluster nuclei whose growth is facilitated by dissipation, annealing and equilibration processes. Furthermore, in this picture, the specific chemistry of the protein template and its interaction with the gold clusters play an important role in (electronic) stabilization of certain self-selecting "magic" sizes. The rest of this section is devoted to investigations of the electronic factors governing such cluster stabilization processes.

Of particular interest is the mass spectrometric measurement pertaining to the formation of a discrete, limited-in-number, series of metal clusters that punctuates the sequence of integers—specifically, gold cation clusters with 25, 38 and 102 atoms (Figure 1). This size-sequence of bare gold clusters is particularly interesting since it is the same as that found earlier for thiolate-protected gold clusters. However, in the latter case, the clusters are protected by a large number of ligands, that is, $Au_{25}(SR)_{18}$,[3e,f] $Au_{38}(SR)_{24}$,[4e] and $Au_{102}(SR)_{44}$[5a] (see also earlier findings in refs. [2b,c]), while in the present case the number of accessible thiols is limited by the number of cystines in the lysozyme molecule. We tacitly assume that because of steric effects (crowding), a given gold aggregate may simultaneously interact (i.e. form an adduct complex) with just a small number of lysozyme molecules, through formation of

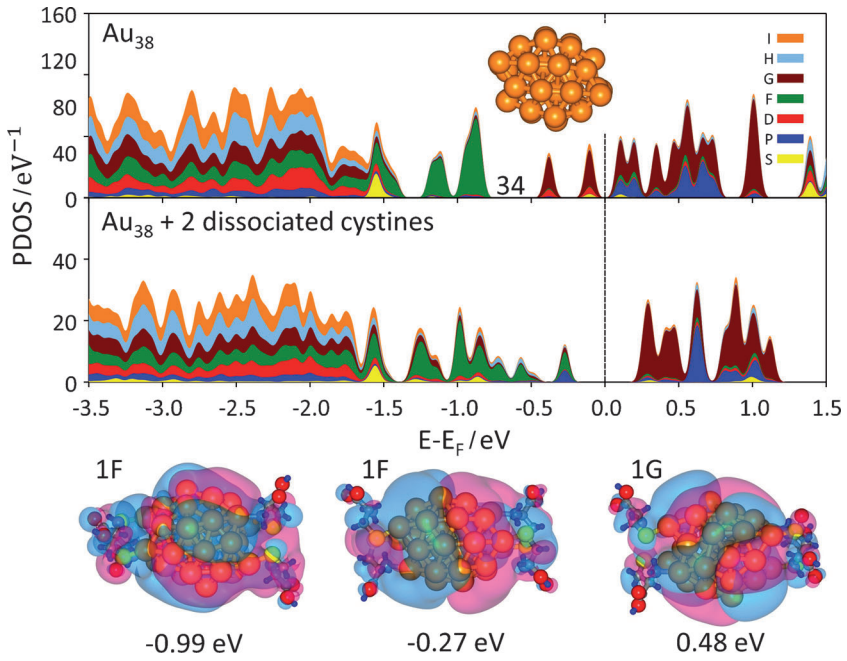

Figure 5. PDOS calculated for an optimized neutral bare Au_{38} cluster (upper panel), with an optimized deformed truncated octahedral, d-TO, structure, shown as an inset, whose energy is lower by 1.07 eV than that of the ideal TO isomer. Also shown is the PDOS for an optimized Au_{38}(cyteine)$_4$ cluster (bottom panel, with the optimized structure shown in Figure 6). The four adsorbed cysteine residues resulted from dissociation of the disulfide bonds in two adsorbed cystine molecules. Also shown for the cluster in the bottom panel are KS orbital images of two of the 1F orbitals near the top of the occupied spectrum (the one with $E-E_F=-0.27$ being the HOMO orbital), and of one of the unoccupied 1G orbitals. The weights of the angular momentum components of the displayed KS orbitals are given in S6. Dashed vertical line at $E-E_F=0$ denotes the location of the midpoint between the HOMO and the LUMO levels. In the orbital isosurface images, positive and negative orbital values are colored light blue and pink, and the orbital energies and symmetries (with the color key given on the right in the upper PDOS panel) are marked. The stabilization (shell closure gap) in the PDOS shown in the bottom panel is 0.54 eV.

gold–sulfur bonds. Indeed we observed gold attachment mainly to Lyz^+ and Lyz_n^+ ($n=2$–4) (see MALDI mass spectra in Figure 2, and related text).

As noted above, our discussion pertaining to the stabilization mechanism of the observed bare clusters (with $n=25$, 38, and 102 gold atoms), focuses on the interaction of the clusters with the thiol groups of the cysteine residues, which form as a result of the dissociative binding of cystine units of lysozyme to the forming clusters. In Figure 5 we display the calculated projected density of states (PDOS) (see the Methods Section), for an optimized (minimum energy) bare Au_{38} cluster (upper panel) and for the optimized structure of Au_{38}(cysteine)$_4$ (lower panel). While cystine is part of the lysozyme protein, we have considered here for simplicity its dissociative adsorption to the metal cluster as a free molecule. An optimal (minimum energy) atomic configuration of the four cysteine residues adsorbed on the Au_{38} cluster is shown in Figure 6. In Figure 5, as well as in the following ones, a vertical dashed line at $E-E_F=0$ denotes the location of the midpoint between the Kohn–Sham (KS) eigen-energies of the highest occupied molecular orbital (HOMO) and the lowest unoccupied one (LUMO).

In the following, we make use of the early proposal[2 g] where a "partial jellium" (PJ) model (used often in recent theoretical work on passivated metal clusters to explain "magic number" stability)[11] was first introduced for the analysis of the electronic structure of gold clusters. In agreement with the PJ model we find that while for a wide range of energies (located at the middle of the energy spectrum) the electronic wavefunctions (KS orbitals) exhibit localized character (associated with the atomic 5d electrons), the orbitals of states with energies near the top or bottom of the spectra are of delocalized (super-atom, jellium-like) character, derived from the atomic 6s electrons (see representative orbital images in Figures 5, 7 and 8). These delocalized states can be assigned particular symmetries [determined with the use of an expansion of the calculated wavefunction in spherical harmonics (see the Methods Section and Figure S5)], following the electronic cluster–shell model (CSM), with a (superatom) aufbau rule : $1S^2\,|\,1P^6\,|\,1D^{10}\,|\,2S^2\,|\,1F^{14}\,|\,2P^6 1G^{18}\,|\,2D^{10}3S^2 1H^{22}\,|\,2F^1$….where S, P, D, F, G, H, and I, correspond, respectively, to angular momenta, $l=0$, 1, 2, 3, 4, 5, and 6. We note here certain possible alterations in level ordering, for example, exchanging the locations of the $1D^{10}$ and $2S^2$ and of $3S^2$ and $1H^{22}$ levels, caused mainly by deviations of the cluster shape from spherical symmetry. In the above CSM scheme, the vertical lines denote shell-closures, with each

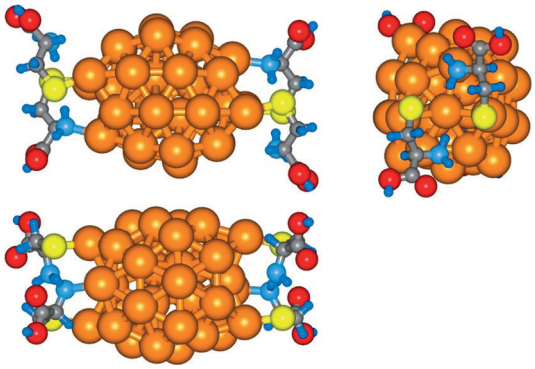

Figure 6. Three views of the structure of Au_{38} (cyteine)$_4$ (gold atoms represented by orange spheres) with four adsorbed cysteine [$HO_2CCH(NH_2)CH_2S$–] residues, resulting from two dissociated cystine units. Sulfur atoms are represented by yellow spheres, oxygen atoms by red spheres, carbons by gray spheres, nitrogen by larger light blue spheres, and hydrogen atoms by small dark blue spheres. The S–S distances, between two neighboring adsorbed cysteine residues, are d(S–S) = 4.50 Å and 4.42 Å, and the average S–Au bond length is 2.36 Å. For an undissociatively adsorbed cystine molecule d(S–S) = 2.21 Å and d(Au–S) = 2.545 Å and 2.495 Å.

closure accompanied by the opening of a stabilizing energy gap. Consequently, closed-shell clusters (that is, where the HOMO state of the cluster closes a shell) possess enhanced stability, and are termed "magic number" (MN) clusters. Such (spherical-like) clusters are comprised of $n^*=2$, 8, 18 (20), 34 (40), 58, 92, … delocalized electrons. In certain cases gaps may also occur at the magic numbers given in parenthesis (depending on the degree of deviation of the cluster structure from spherical symmetry, see for example, Figure 8(B) below).

We observe that for the neutral bare Au_{38} cluster (Figure 5 upper panel), $E-E_F=0$ falls within a dense band of states, that is, with no opening of a stabilization gap. We also note that a gap of 0.48 eV (denoted by the number 34 at the top panel of Figure 5) separates the peaks corresponding to the occupied 1F orbitals (colored green) from the two peaks (occupied by 4e) corresponding to 1G orbitals (colored brown, at the top of the spectrum in Figure 5, upper panel). This 34-electron superatom gap is the result of a $1S^2|1P^6|1D^{10}|2S^2|1F^{14}$ shell closure associated with the population of 17 delocalized orbitals (corresponding to double occupancy by 34 electrons). By itself, the Au_{38} cluster is not a "magic cluster", having an excess of four delocalized electrons (occupying the aforementioned two 1G states) and exhibiting merely a gap $\Delta_{HL}=0.21$ eV between the highest occupied (HOMO) and the lowest unoccupied (LUMO) molecular orbitals. However, we conjecture that the interaction of gold clusters with cystine units of the lysozyme template (four cystines in a lysozyme molecule derived from chicken egg white used in our experiment) may confer enhanced stability of the cluster by transforming it to a magic one. This conjecture is strongly supported by the results shown in Figure 5.

To assess the energetics of the above stabilization mechanism involving interaction of the gold clusters with the protein, we explored the binding of the Au_{38} cluster to the cystine molecules, $(SCH_2CH(NH_2)CO_2H)_2$. As before, for simplicity we consider free cystine molecules, while as part of the lysozyme they are bonded to the protein. A cystine molecule binds to the d-TO 38 atom gold cluster with an energy of 0.58 eV. This adsorption does not have a noticeable effect on the atomic arrangement, electronic structure and stability of the cluster. However, upon dissociation of the cystine molecule on the cluster (a process that entails a very small energy barrier), the two cysteine units (thiolate parts of the dimeric aminoacid, cystine) adsorb strongly to the cluster with a binding energy of 1.97 eV per cystine. Thus, when dissociatively adsorbing two cystine molecules (Figure 6) we get $E[Au_{38}(\text{d-TO})]+2E[\text{cystine})]-E[Au_{38}\ (\text{cysteine})_4]=3.94$ eV, where $E[X]$ denotes the total energy of the species X. The dissociative binding of two cystine molecules to the Au_{38} cluster (see Figure 6) is found to have a profound effect on the electronic structure of the cluster, with the sulfur–gold bonds engaging the four 1G electrons (corresponding to the two occupied peaks, colored brown, near $E-E_F=0$ in the upper panel of Figure 5), and, most importantly, opening a shell-closure stabilization gap $\Delta_{HL}=0.48$ eV (see lower panel, Figure 5). The KS orbital images of two of the 1F delocalized orbitals near the top of the occupied spectrum (the one with $E-E_F=-0.27$ eV being the HOMO orbital), and an image of the unoccupied 1G orbital (see bottom of Figure 5) confirm the above 34-electron superatom electronic shell structure. The above validates our conjecture pertaining to the shell-closure stabilization caused by the interaction of certain gold clusters (particularly Au_n with n close to a magic number, n^*) with the protein template.

The above first-principles calculations predict that the interaction of gold clusters with cystine residues of the lysozyme molecule would result in cleavage of the S–S bonds. This in turn may lead to change in the secondary structure of the protein. Such change is indeed seen in circular dichroism (CD) studies of protein-protected luminescent gold clusters in solution as well as in the IR spectrum of the same material in the solid state.[6i] Cleavage of S–S bonds has been found to lead to changes in the protein secondary structure (see Figure S5). We have shown that 28% of the α-helix structure is lost due to gold-cluster formation. Here we note that most of the cystine residues are in the α-helix region. Therefore S–S bond breakage directly affects the helical structure of the protein. Corresponding changes are also seen in an infrared spectroscopic study. Certain changes are observable also in the amide region (Figure S5). The variations in the α-helix region are better observable in the second derivative of the spectra (Figure S5). Such studies were performed as well on lactoferrin-protected luminescent gold clusters.[6f]

Further evidence for the interaction of the gold clusters with the sulfur-containing residues (cystines) in the lysozyme molecule can be obtained from measurements of XPS spectra. The Au–Cys interaction has a covalent component. Indeed, distinct features are observed in XPS measurements of protein–gold adducts, in the S (2p) and Au (4f) regions, supporting the covalent attachment of Au to the cysteines. The measured S (2p) signal is thiolate-like,[6g–i] supporting the disulfide bond cleavage. However, no corresponding change is seen in the N(1s) region upon the addition of gold to the lysozyme, indicating that formation of lysozyme–gold adducts does not involve bonding of gold to the amide region in the protein.

In Figures 7 and 8 we display the calculated PDOS for Au_{102}^+ (Figure 7) and for Au_{38}^+ and Au_{25}^+ (Figure 8). Such results were obtained for several structural isomers (with optimal cluster structures shown as an inset in Figures 7 and 8). We observe that as in the case of the neutral bare Au_{38} cluster (Figure 5 upper panel) for all the clusters considered here, $E-E_F=0$ falls within a dense band of states, that is, with no opening of a stabilization gap. The key observation is that while Au_n^+, with $n=102$, 38 and 25, are not magic-number clusters, the number of (delocalized) 6s electrons in each of these clusters is rather close to a magic number, that is $n^*=92$, 34, and 20, respectively. Consequently, these clusters may achieve magic-number stabilization even when the depletion in the number of delocalized electrons in the cluster is relatively small (through electronic interaction of the cluster with the protein). Specifically, for the clusters considered by us here (i.e. with $n=102$, 38 and 25), such stabilization through depletion of the number of delocalized electrons entails a rather small number of electrons, that is $n-n^*=10$, 4, and 5 electrons, respectively. As demonstrated by us above for the case of the

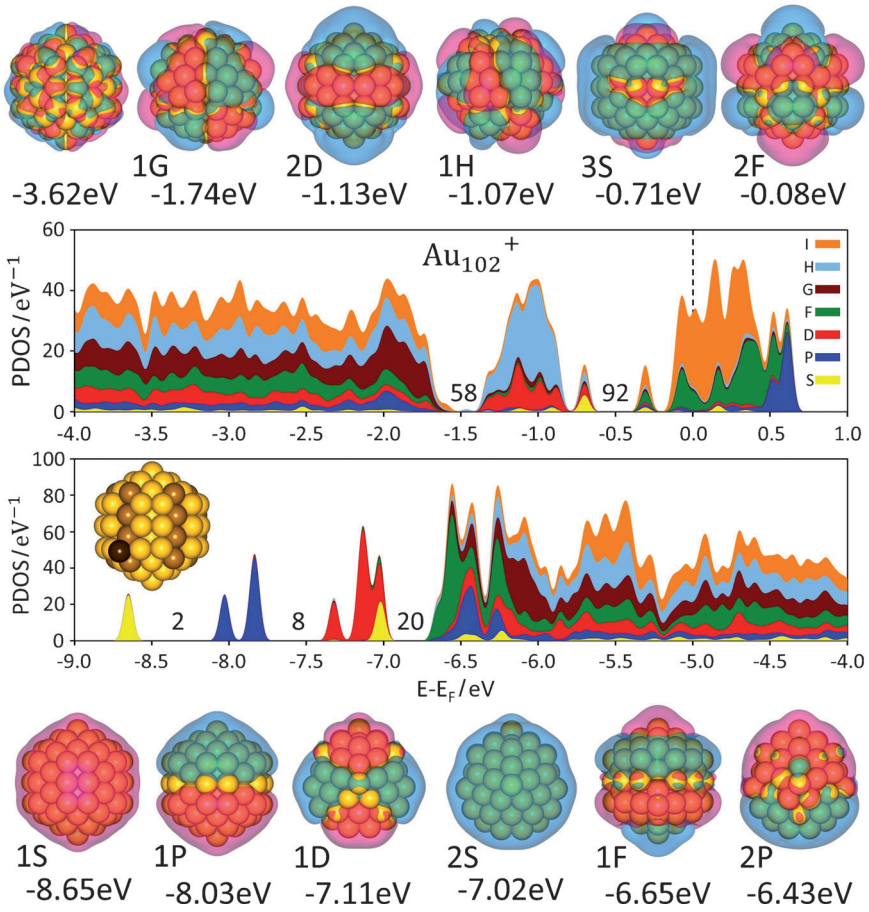

Figure 7. PDOS and KS orbital images calculated for an optimized Marks-decahedral (m-Dh) structure (left inset in bottom panel of the PDOS, with the gold atoms in the m-Dh "grooves" colored brown) of a Au_{102}^{+} cluster; the ideal m-Dh structure is comprised of 101 atoms, the extra atom in the Au_{102}^{+} cluster is positioned in the groove (see the extra atom, colored in darker brown, at the bottom left of the cluster structure shown in the inset). In the orbital isosurface images, positive and negative orbital values are colored light blue and pink, and the orbital energies and symmetries (with the color key given on the right in the upper PDOS panel) are marked. All orbitals shown are of delocalized character except the one at −3.62 eV (left in the upper panel) which corresponds to a localized orbital with atomic d character. The weights of the angular momentum components of the displayed KS orbitals are given in Figure S5. The number of electrons in delocalized orbitals (2, 8, 20, 58, and 92) corresponding to closed shells are marked in the shell-closure gaps. Note in particular the shell closure at $n^{*}=92$ obtained by depletion (10 electrons) of the number of delocalized electrons resulting from the interaction of the cluster with the protein environment and subsequent single ionization. The cluster is characterized by a spin projection $s_z=1/2$.

Au_{38} cluster, such stabilization can occur in the lysozyme template through interactions of the aggregated gold cluster with cystine units of the protein, resulting in breaking of the disulfide bonds and strong binding of the cysteine residues to the cluster (while maintaining their peptide bond linkage to the protein). Once formed as stable magic-number clusters (anchored to the protein), release of the clusters from the protein template and ionization (in the gas phase) brings them to a cationic state Au_n^{+}, $n=102$, 38, and 25. We remark here that the cluster geometries that we describe here differ from those found in the case of the aforementioned thiol-passivated gold clusters,[3–5] since the latter clusters are protected by a large number of strongly interacting adsorbed molecules, whereas in the present case, during the formation process, the interaction between the clusters and the growth environment is of limited nature (only four disulfide groups in a Lyz molecule).

It is proposed that during laser desorption ionization of a protein–Au salt adduct, gold clusters form, with the protein serving as a confining cluster growth environment, providing an effective reservoir for dissipation of the aggregation and stabilization energy of the clusters. Furthemore, the first-principles calculations suggest that electronic interaction between the aggregating metal clusters and the lysozyme molecule (via the sulfur-containing cystine residues) stabilizes specific cluster sizes, at, or in the neighborhood of, electronic magic numbers. Clusters with these magic number sizes form a discrete size sequence with enhanced stability. Specifically, we demonstrate, with the use of results obtained from extensive first-principles calculations, that two cystine units dissociate upon interaction with Au_{38} (see Figure 6). The resulting four cysteine residues engage some of the delocalized electrons of the gold cluster (originating from the $6s^1$ electrons of the gold atoms), thus

Moreover, ultimately, as observed in the mass spectrum, the gold clusters appear bare (i.e. without the stabilizing ligands). We recall here that for the smallest observed gold cluster ions (around $n=18$), some sulfur addition, in the form of $Au_{18+n}S_{4+m}^{+}$ clusters, have been detected (see Figure 1), providing further evidence for the interaction between the gold clusters and the cystine units of the lysozyme prior to release of the clusters to the gas phase. Why the smaller clusters (containing a number of atoms centered on 18) are found to carry some small number of residual sulfur atoms, while the larger clusters (Au_n^{+}, $n=25$, 38, 102) appear bare, remains a topic for future research.

3. Conclusions

We reported here the results of a joint experimental (MALDI and electrospray ionization mass spectrometry) and theoretical (large-scale first-principles DFT electronic structure calculations) investigations pertaining to the formation of a discrete sequence of bare gold clusters of well-defined nuclearity, that is, Au_{25}^{+}, Au_{38}^{+} and Au_{102}^{+}, in the gas phase, by a novel process involving gold-bound complexes of the protein lysozyme.

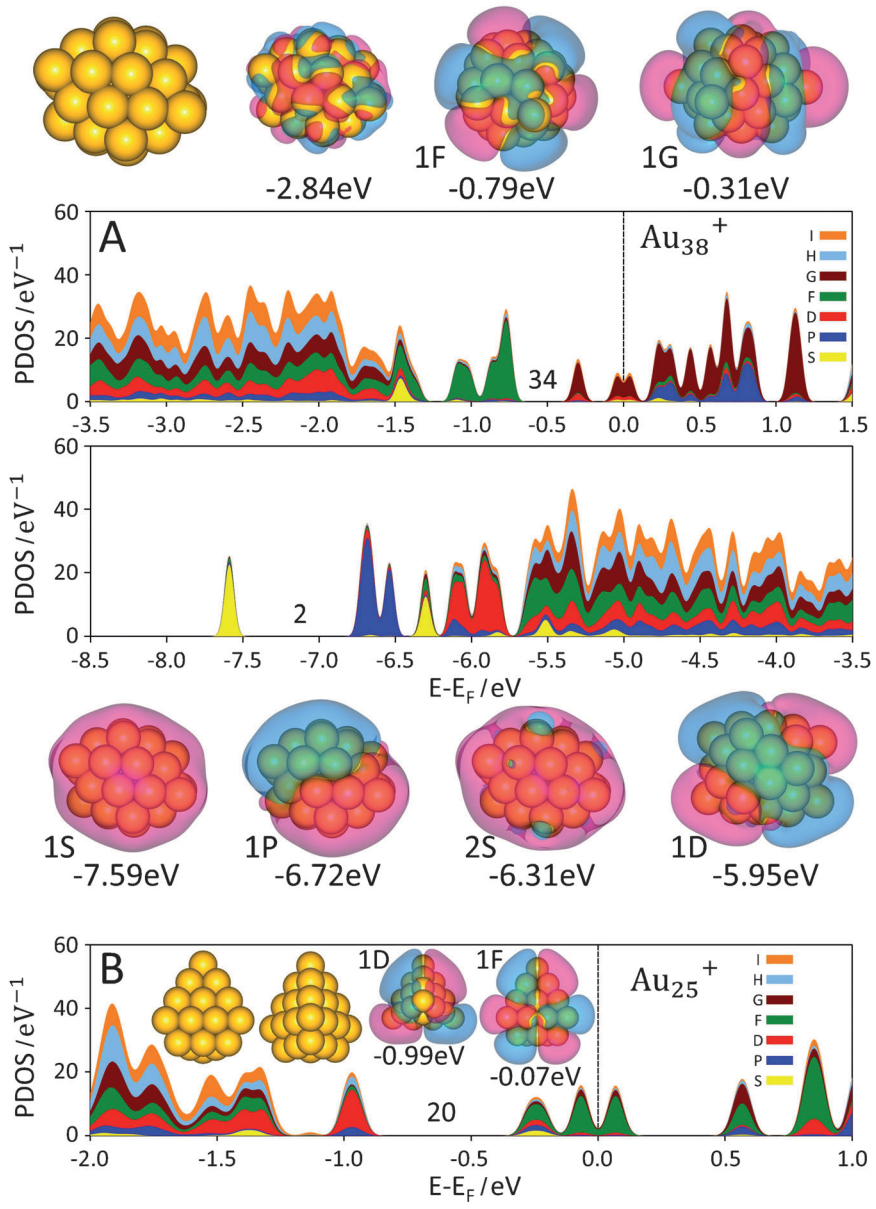

Figure 8. PDOS and KS orbital images calculated for: A) an optimized truncated octahedral (TO) structure (left image in the upper row) of a Au_{38}^+ cluster, and B) an optimized tetrahedral-like structure (atomic structure images of the cluster, viewed from the front and back sides, are given on the left in the bottom panel of the PDOS) of a Au_{25}^+ cluster. In (A) all orbitals shown have delocalized character except that at −3.86 eV which corresponds to a localized one with atomic d character. Note the shell closure at $n^*=34$, obtained by partial depletion (four electrons) of the number of delocalized electrons, and subsequent single-electron ionization. The cluster is characterized by a spin projection $s_z=3/2$. In (B) we limit ourselves to the top part of the electronic spectrum, and display only two delocalized orbitals, one of 1D character (at −0.99 eV, corresponding to shell closure and opening of the 20-electrons shell-closure gap) and the other of 1F character (at −0.07 eV corresponding to the HOMO−1 energy level near $E-E_F=0$). Orbitals in the energy range $-6.0\ \text{eV} < E\text{-}E_F < -1.5\ \text{eV}$ are of localized atomic d character. The delocalized electrons near −6.19 eV occupy a 1P orbital, and those with energy about −6.95 eV occupy a 1S orbital (not shown). The shell closure at $n^*=20$, is obtained by a five-electron depletion of the number of delocalized electrons by interaction with the protein, and subsequent single-electron ionization. The cluster is characterized by a spin projection $s_z=1$. The weights of the angular momentum components of the displayed KS orbitals are given in S6. For other details see caption of Figure 7.

transforming it to a 34-electron closed-shell superatom structure, characterized by a relatively large (HOMO–LUMO) stabilization gap of close to 0.5 eV (see Figure 5). The same mechanism is operative for the other gold cluster sizes found in the experiments.

Our theoretical discussion presents a novel stabilization mechanism operative in the protein environment that explains the emergence of the particular size sequence of clusters observed in our experiments. The mechanism that we propose differs from the one known to apply for the case of protected gold clusters in solution, involving a large number of protective thiolates (SR) covering the surface of the core gold cluster, for example $Au_{25}(SR)_{18}$, $Au_{38}(SR)_{24}$ and $Au_{102}(SR)_{44}$. In contrast to the latter ones, in our present case only a few cystines (between two and five) are required to bind to the gold cluster to achieve magic number stability—this is consistent with the limited number of cystines in a lysozyme molecule (four cystines per lysozyme). While our studies explain the products formed, the dynamics of cluster formation remains a subject for future experimental and theoretical explorations.

In light of the continuing surge in research activity pertaining to the size-specific properties of gold (as well as other noble metal) clusters in nanotechnology, nanocatalysis, biology and nanomedicine (see, e.g. refs. [1,6,12]), we expect our findings to add to the knowledge base that is imperative for future development, design, and implementation of nanoscale instruments and devices. In particular, recent assessment of research directed at using noble metal (particularly gold) nanoparticles to probe biomolecules and biological processes, as well as for diagnostics and/or regulation and modification of cellular functions, has pointed to a need for detailed knowledge concerning the nature and consequences of interaction between metal nanoparticles and biomolecules, proteins in particular.[13]

Experimental and Theoretical Methods

Materials

Tetrachloroauric acid trihydrate ($HAuCl_4 \cdot 3H_2O$) was prepared in our laboratory starting from pure gold. Lysozyme, extracted from chicken egg white and which had >90% purity, was purchased from Sigma Aldrich. Sinapic acid was also purchased from Sigma Aldrich. All the chemicals were used without further purification. Deionized water was used throughout the experiment.

Synthesis of the Lyz–Au Adduct

Lyz–Au adduct was prepared by the same method as described by Chaudhari et al.[6g] Briefly different concentrations of $HAuCl_4 \cdot 3H_2O$ (1 mM-10 mM) were prepared. To 1 mL 1.5 mM of Lyz, 1 mL of $HAuCl_4 \cdot 3H_2O$ solutions of different concentrations were added and the resultant mixtures were stirred with a magnetic stirrer for 5 min and incubated further for 2 h. The samples were taken out and spotted for MALDI-MS analysis. These were also analyzed by ESI-MS.

Spectrometric Analysis and Instrumentation

MALDI-MS Analysis: Sinapic acid was used as the matrix for MALDI-MS analysis. The matrix solution was prepared using 1:3 acetonitrile:0.1% trifluoroacetic acid in deionized (DI) water. Each time while sampling, 5 μL of the sample was mixed with 100 μL of freshly prepared matrix and sonicated gently for 10 s and then 2.5 μL of the mixture was spotted to yield a dried droplet. An Applied Biosystems Voyager DE Pro MALDI MS instrument was used for the measurements. A pulsed nitrogen laser of 337 nm was used for ionizing the sample. Spectra were collected in the linear positive mode and an average of 250 shots were taken for each spectrum. Measurements were also done in the negative mode, where indicated. In time-of-flight mass spectrometry it is assumed that ions are generated instantaneously upon laser irradiation. The time width for N_2 laser pulse is of the order of a few nanoseconds. When the laser intensity is high enough to exceed the ion generation threshold, ions may continue to be generated even after the completion of laser irradiation. To avoid ion loss, and also to improve resolution, a long delay time of few hundred nanoseconds is typically applied between ion generation and ion extraction. In our study we have used a delay time of 1200 ns to allow the desorbed species to interact in the gas phase.

ESI-MS Analysis: 10 μL of the sample was taken and diluted to 2 mL with DI water. To it 10 μL of trifluoroacetic acid (TFA) (0.1% in DI) was added as ionization enhancer for spectral collection in the positive ion mode. A Thermo Scientific LTQ XL ESI MS instrument was used for this study. Ion spray voltage was kept 4.5 kV and the capillary temperature was set at 250 °C.

Computational Methods

The theoretical results described in this paper have been obtained from calculations using spin density functional theory (SDFT)[14] in conjunction with non-local norm-conserving scalar-relativistic soft pseudopotentials[15] with the valence $5d^{10}$ and $6s^1$ electronic states of the gold atoms (as well as the valence electrons of the atoms of the interacting cysteine molecules: sulfur, oxygen, nitrogen and hydrogen) expanded in a plane-wave basis with a 62 Ry kinetic energy cutoff, and employing the Perdew–Burke–Ernzerhof (PBE) functional in the generalized-gradient approximation (GGA) to the exchange–correlation corrections.[16]

The theoretical explorations of the atomic arrangements and electronic structures of the gold clusters and their interactions with the cystine units of the protein employed the SDFT, using the Born–Oppenheimer (BO) molecular dynamics (MD) method, BO–SDF–MD.[14] This method is particularly suitable for investigations of charged systems since it does not employ a supercell (i.e. no periodic replication of the ionic system is used). Structural optimizations were performed using a conjugate-gradient-like method. For the clusters shown in Figures 7 and 8, we find the following spin projection (s_z) values: Au_{102}^+: $s_z=1/2$; Au_{38}^+: $s_z=3/2$; Au_{25}^+: $s_z=1$. The "partial jellium" picture was first introduced in ref. [2g] and used in the analysis of the electronic structures of bare gold anions. In that paper the expansion in spherical harmonics (see below) was done for each gold atom of the cluster taken as a center. Here we choose to perform the analysis with respect to the center of mass of the cluster.

The projected density of states, $w_{i,l}(R_0)$ were calculated[2g] from the KS orbitals $\psi_i(r+R_{cm})$ corresponding to the KS energy eigenvalue ε_i, where R_{cm} is the center of mass of the cluster (taken from here on as the origin, $R_{cm}=0$), using Equation (4):

$$w_{i,l}(R_0) = \sum_{m=-l}^{l} \int_0^{R0} r^2 dr |\phi_{i,lm}(r)|^2 \quad (4a)$$

$$\phi_{i,lm}(r) = \int d\Omega Y_{lm}(\Omega)\psi_i(r) \quad (4b)$$

Here, Y_{lm} is the spherical harmonic function with angular momentum number l and magnetic quantum number m, and angular momenta up to $l=6$ (l symmetry) are considered. The integration is taken in a sphere of radius R_0, chosen as follows for the three cluster sizes: Au_{102}^+: $R_0=11.6$ Å; Au_{38}^+: $R_0=9.3$ Å; Au_{25}^+: $R_0=8.9$ Å. In plotting the PDOS each $w_{i,l}$ is broadened by a Gaussian of width 0.07 eV.

Acknowledgements

A.B and T.P. thank the Department of Science and Technology, Government of India for continuous support our of research program on nanomaterials. A.B. thanks the Council of Scientific and Industrial Research (CSIR) for a fellowship. The work of B.Y., C.Y. and U.L. was supported by the Office of Basic Energy Sciences of the US Department of Energy under Contract No. FG05-86ER45234 and in part by a grant from the Air Force Office of Scientific Research. Computations were made at the GATECH Center for Computational Materials Science.

Keywords: density functional calculations · electronic states · gold clusters · mass spectrometry · protein–gold adducts

[1] a) *Nanocatalysis* (Eds: U. Heiz, U. Landman), Springer, Berlin **2006**; b) G. C. Bond, C. Louis, D. T. Thompson, *Catalysis by Gold*, Imperial College Press, London, **2006**; c) P. L. Xavier, K. Chaudhari, A. Baksi, T. Pradeep, *Nano Rev.* **2012**, *3*, 14767.

[2] a) C. L. Cleveland, U. Landman, *J. Chem. Phys.* **1991**, *94*, 7376–7396. where some of the nomenclature used in this field was introduced and elaborated on; b) R. L. Whetten, J. T. Khoury, M. M. Alvarez, S. Murthy, I. Vezmar, Z. L. Wang, P. W. Stephens, C. L. Cleveland, W. D. Luedtke, U. Landman, *Adv. Mater.* **1996**, *8*, 428–433; c) C. L. Cleveland, U. Landman, T. G. Schaaff, M. N. Shafigullin, P. W. Stephens, R. L. Whetten, *Phys. Rev. Lett.* **1997**, *79*, 1873–1876; d) H. Häkkinen, R. N. Barnett, U. Landman, *Phys. Rev. Lett.* **1999**, *82*, 3264–3267; e) W. D. Luedtke, U. Landman, *J. Phys. Chem.* **1996**, *100*, 13323–13329; f) X. Xing, B. Yoon, U. Landman, J. H. Parks, *Phys. Rev. B* **2006**, *74*, 165423; g) B. Yoon, P. Koskinen, B.

Huber, O. Kostko, B. von Issendorff, H. Häkkinen, M. Moseler, U. Landman, *ChemPhysChem* **2007**, *8*, 157 – 161.

[3] a) Y. Negishi, K. Nobusada, T. Tsukuda, *J. Am. Chem. Soc.* **2005**, *127*, 5261 – 5270; b) Y. Shichibu, Y. Negishi, T. Tsukuda, T. Teranishi, *J. Am. Chem. Soc.* **2005**, *127*, 13464 – 13465; c) E. S. Shibu, M. A. H. Muhammed, T. Tsukuda, T. Pradeep, *J. Phys. Chem. C* **2008**, *112*, 12168 – 12176; d) M. Zhu, E. Lanni, N. Garg, M. E. Bier, R. Jin, *J. Am. Chem. Soc.* **2008**, *130*, 1138 – 1139; e) M. W. Heaven, A. Dass, P. S. White, K. M. Holt, R. W. Murray, *J. Am. Chem. Soc.* **2008**, *130*, 3754 – 3755; f) M. Zhu, C. M. Aikens, F. J. Hollander, G. C. Schatz, R. Jin, *J. Am. Chem. Soc.* **2008**, *130*, 5883 – 5885; g) Z. Wu, J. Suhan, R. Jin, *J. Mater. Chem.* **2009**, *19*, 622 – 626; h) L. A. Angel, L. T. Majors, A. C. Dharmaratne, A. Dass, *ACS Nano* **2010**, *4*, 4691 – 4700; i) J. Akola, K. A. Kacprzak, O. Lopez-Acevedo, M. Walter, H. Grönbeck, H. Häkkinen, *J. Phys. Chem. C* **2010**, *114*, 15986 – 15987; j) A. C. Dharmaratne, T. Krick, A. Dass, *J. Am. Chem. Soc.* **2009**, *131*, 13604 – 13605; k) C. Zeng, H. Qian, T. Li, G. Li, N. L. Rosi, B. Yoon, R. N. Barnett, R. L. Whetten, U. Landman, R. Jin, *Angew. Chem. Int. Ed.* **2012**, *51*, 13114 – 13118.

[4] a) R. L. Donkers, D. Lee, R. W. Murray, *Langmuir* **2004**, *20*, 1945 – 1952; b) V. L. Jimenez, D. G. Georganopoulou, R. J. White, A. S. Harper, A. J. Mills, D. Lee, R. W. Murray, *Langmuir* **2004**, *20*, 6864 – 6870; c) J. Kim, K. Lema, M. Ukaigwe, D. Lee, *Langmuir* **2007**, *23*, 7853 – 7858; d) Y. Pei, Y. Gao, X. C. Zeng, *J. Am. Chem. Soc.* **2008**, *130*, 7830 – 7832; e) O. Toikkanen, V. Ruiz, G. Rönnholm, N. Kalkkinen, P. Liljeroth, B. M. Quinn, *J. Am. Chem. Soc.* **2008**, *130*, 11049 – 11055; f) H. Qian, M. Zhu, U. N. Andersen, R. Jin, *J. Phys. Chem. A* **2009**, *113*, 4281 – 4284; g) O. Lopez-Acevedo, H. Tsunoyama, T. Tsukuda, H. Häkkinen, C. M. Aikens, *J. Am. Chem. Soc.* **2010**, *132*, 8210 – 8218; h) H. Qian, W. T. Eckenhoff, Y. Zhu, T. Pintauer, R. Jin, *J. Am. Chem. Soc.* **2010**, *132*, 8280 – 8281.

[5] a) P. D. Jadzinsky, G. Calero, C. J. Ackerson, D. A. Bushnell, R. D. Kornberg, *Science* **2007**, *318*, 430 – 433; b) Y.-K. Han, H. Kim, J. Jung, Y. C. Choi, *J. Phys. Chem. C* **2010**, *114*, 7548 – 7552.

[6] a) J. Xie, Y. Zheng, J. Y. Ying, *J. Am. Chem. Soc.* **2009**, *131*, 888 – 889; b) M. A. H. Muhammed, P. K. Verma, S. K. Pal, A. Retnakumari, M. Koyakutty, S. Nair, T. Pradeep, *Chem. Eur. J.* **2010**, *16*, 10103 – 10112; c) A. Mathew, P. R. Sajanlal, T. Pradeep, *J. Mater. Chem.* **2011**, *21*, 11205 – 11212; d) H. Wei, Z. Wang, L. Yang, S. Tian, C. Hou, Y. Lu, *Analyst* **2010**, *135*, 1406 – 1410; e) C.-L. Liu, H.-T. Wu, Y.-H. Hsiao, C.-W. Lai, C.-W. Shih, Y.-K. Peng, K.-C. Tang, H.-W. Chang, Y.-C. Chien, J.-K. Hsiao, J.-T. Cheng, P.-T. Chou, *Angew. Chem.* **2011**, *123*, 7194 – 7198; *Angew. Chem. Int. Ed.* **2011**, *50*, 7056 – 7060; f) P. L. Xavier, K. Chaudhari, P. K. Verma, S. K. Pal, T. Pradeep, *Nanoscale* **2010**, *2*, 2769 – 2776; g) K. Chaudhari, P. L. Xavier, T. Pradeep, *ACS Nano* **2011**, *5*, 8816 – 8827; h) J. S. Mohanty, P. L. Xavier, K. Chaudhari, M. S. Bootharaju, N. Goswami, S. K. Pal, T. Pradeep, *Nanoscale* **2012**, *4*, 4255 – 4262; i) A. Baksi, P. L. Xavier, K. Chaudhari, N. Goswami, S. K. Pal, T. Pradeep, *Nanoscale* **2013**, *5*, 2009 – 2016.

[7] H. W. Kroto, J. R. Heath, S. C. O'Brien, R. F. Curl, R. E. Smalley, *Nature* **1985**, *318*, 162 – 163.

[8] a) J. T. Petty, J. Zheng, N. V. Hud, R. M. Dickson, *J. Am. Chem. Soc.* **2004**, *126*, 5207 – 5212; b) J. Zheng, P. R. Nicovich, R. M. Dickson, *Annu. Rev. Phys. Chem.* **2007**, *58*, 409 – 431.

[9] T. Pradeep, R. G. Cooks, *Int. J. Mass Spectrom. Ion Processes* **1994**, *135*, 243 – 247.

[10] C. F. Shaw in *Gold: Progress in Chemistry, Biochemistry & Technology* (Ed.: H. Schmidbaur), Wiley, New York, **1999**, Chap. 10, pp. 260 – 308.

[11] a) H. Häkkinen, *Chem. Soc. Rev.* **2008**, *37*, 1847 – 1859; b) M. Walter, J. Akola, O. Lopez-Acevedo, P. D. Jadzinsky, G. Calero, C. J. Ackerson, R. L. Whetten, H. Grönbeck, H. Häkkinen, *Proc. Natl. Acad. Sci. USA* **2008**, *105*, 9157 – 9162.

[12] a) M. C. Daniel, D. Astruc, *Chem. Rev.* **2004**, *104*, 293 – 346; b) A. Sanchez, S. Abbet, U. Heiz, W.-D. Schneider, H. Hakkinen, R. N. Barnett, U. Landman, *J. Phys. Chem. A* **1999**, *103*, 9573 – 9578; c) C. Harding, V. Habibpour, S. Kunz, A. N.-S. Farnbacher, U. Heiz, B. Yoon, U. Landman, *J. Am. Chem. Soc.* **2009**, *131*, 538 – 548; d) E. C. Dreaden, A. M. Alkikany, X. Huang, C. J. Murphy, M. A. El-Sayed, *Chem. Soc. Rev.* **2012**, *41*, 2740 – 2779; e) R. R. Arvizo, S. Bhattacharyya, R. A. Kudgus, K. Giri, R. Bhattacharya, P. Mukherjee, *Chem. Soc. Rev.* **2012**, *41*, 2943 – 2970; f) T. L. Doane, C. Burda, *Chem. Soc. Rev.* **2012**, *41*, 2885 – 2911.

[13] a) S. Laera, G. Ceccone, F. Rossi, D. Gilliland, R. Hussain, G. Siligardi, L. Calzolai, *Nano Lett.* **2011**, *11*, 4480 – 4484; b) A. A. Shemetovm, I. Nabiev, A. Sukanova, *ACS Nano* **2012**, *6*, 4585 – 4602; c) S. H. De Paoli Lacerda, J. J. Park, C. Meuse, D. Pristinski, M. L. Becker, A. Karim, J. F. Douglas, *ACS Nano* **2010**, *4*, 365 – 379; d) H. Wei, Z. Wang, J. Zhang, S. House, Y.-G. Gao, L. Yang, H. Robinson, L. H. Tan, H. Xing, C. Hou, I. M. Robertson, J.-M. Zuo, Y. Lu, *Nat. Nanotechnol.* **2011**, *6*, 93 – 97; e) T.-H. Chen, W.-L. Tseng, *Small* **2012**, *8*, 1912 – 1919.

[14] R. N. Barnett, U. Landman, *Phys. Rev. B* **1993**, *48*, 2081 – 2097.

[15] N. Troullier, J. L. Martins, *Phys. Rev. B* **1991**, *43*, 1993 – 2006.

[16] J. P. Perdew, K. Burke, M. Ernzerhof, *Phys. Rev. Lett.* **1996**, *77*, 3865 – 3868.

Received: November 9, 2012
Revised: February 15, 2013
Published online on March 18, 2013

CHEMPHYSCHEM

Supporting Information

Bare Clusters Derived from Protein Templates: Au_{25}^{+}, Au_{38}^{+} and Au_{102}^{+}

Ananya Baksi,[a] Thalappil Pradeep,*[a] Bokwon Yoon,[b] Constantine Yannouleas,[b] and Uzi Landman*[b]

cphc_201200927_sm_miscellaneous_information.pdf

S1. Supporting Information 1

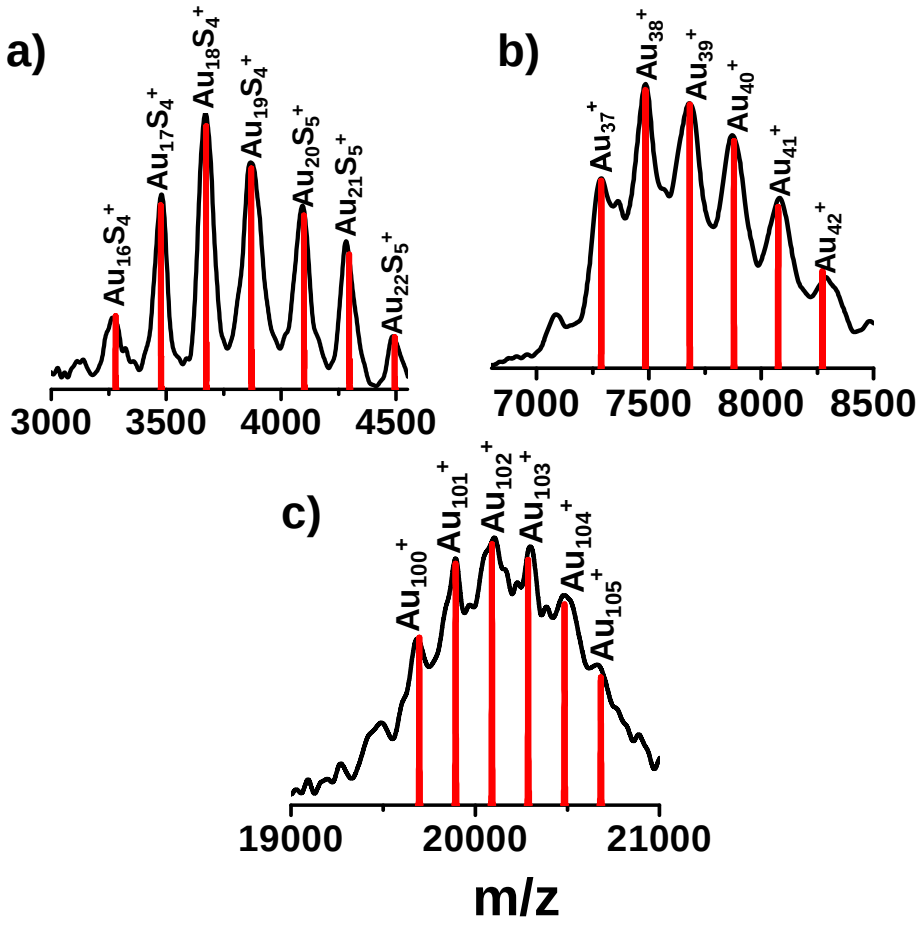

Figure S1. Comparative plot of the theoretical and experimental m/z values of a) $Au_{18}S_{4+m}^+$, b) Au_{38}^+ and c) Au_{102}^+.

S2. Supporting information2

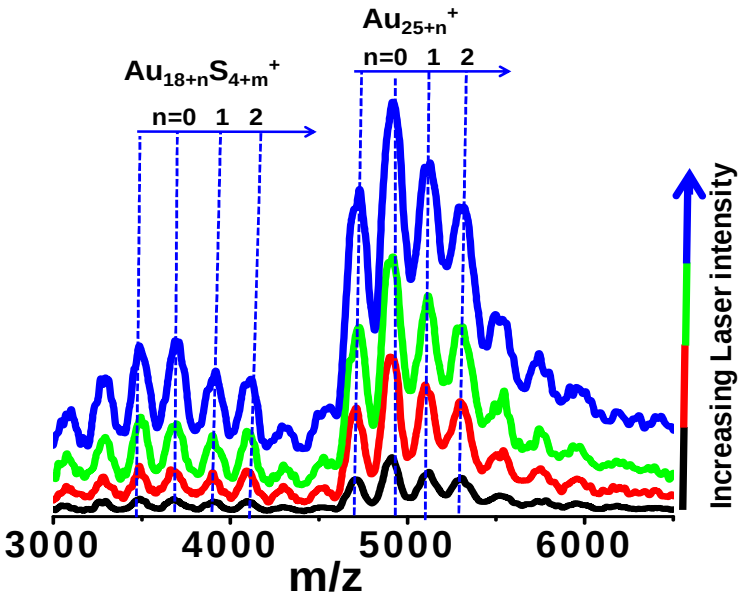

Figure S2. Laser intensity dependence study in MALDI MS with increasing laser intensity in linear positive mode. There is no change in the peak positions with enhanced laser intensity. The spectra were collected for the 1.5 mM Lyz and 5 mM $HAuCl_4.3H_2O$ system in linear positive mode and the laser intensity was varied from 1500 to 1800 (instrumental unit) with an increase of 100 in intensity at each step, plotted in black, red, green and blue, respectively.

S3. Supporting information 3

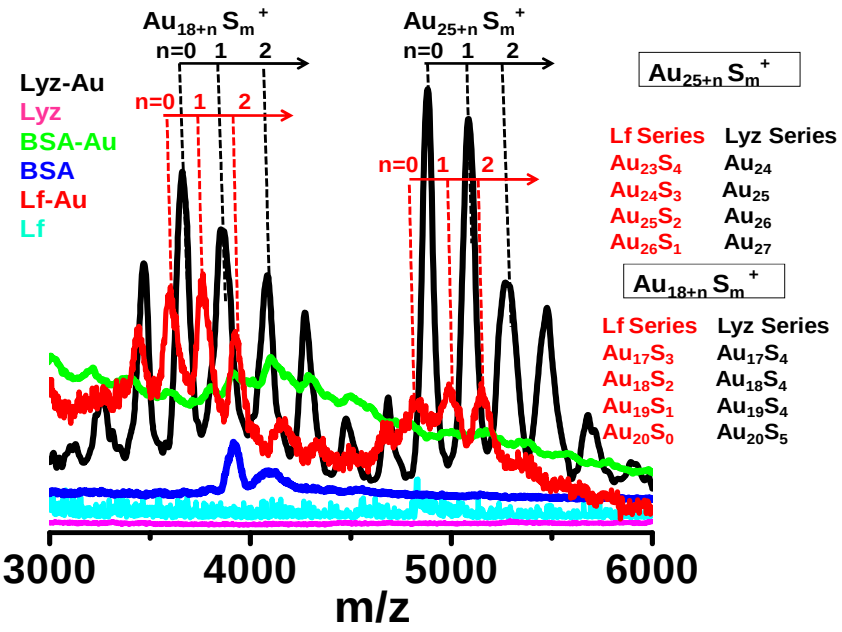

Figure S3. A comparative study of the efficiency of BSA, Lf and Lyz templates for gas phase cluster formation. Spectra show that Lyz is efficient to act as a template for such synthesis.

S4. Supporting Information 4

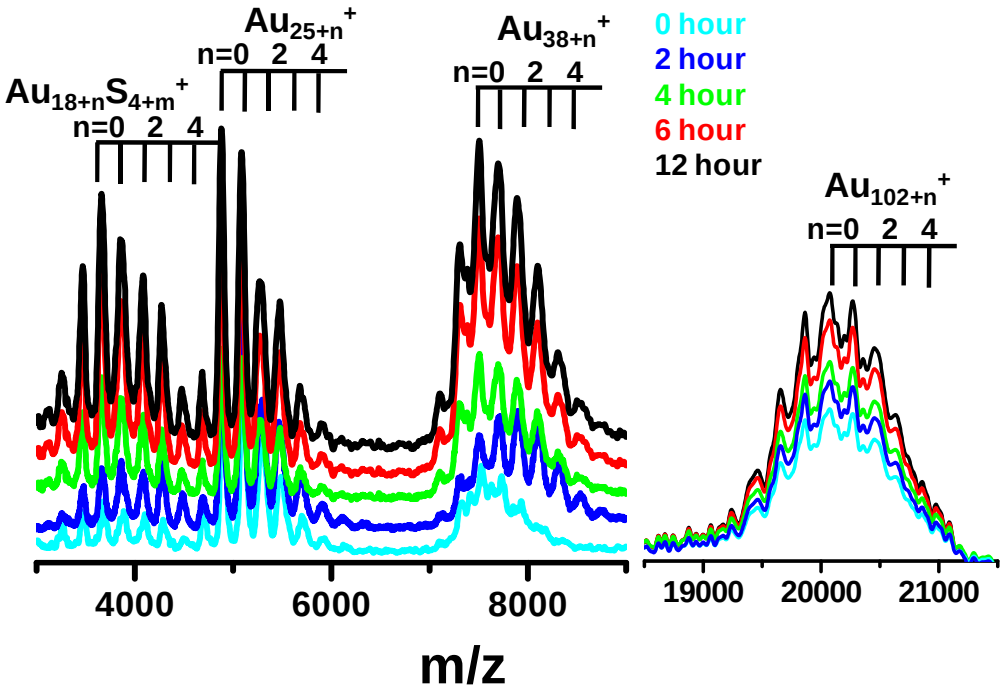

Figure S4. Time dependent MALDI MS study of the as prepared precursor. There is a significant change in the Au_{38} region. At starting, the peaks were appearing along with $(Lyz\text{-}Au_n)^{2+}$ but upon longer time, only cluster related peaks get enhanced.

S5. Supporting Information 5

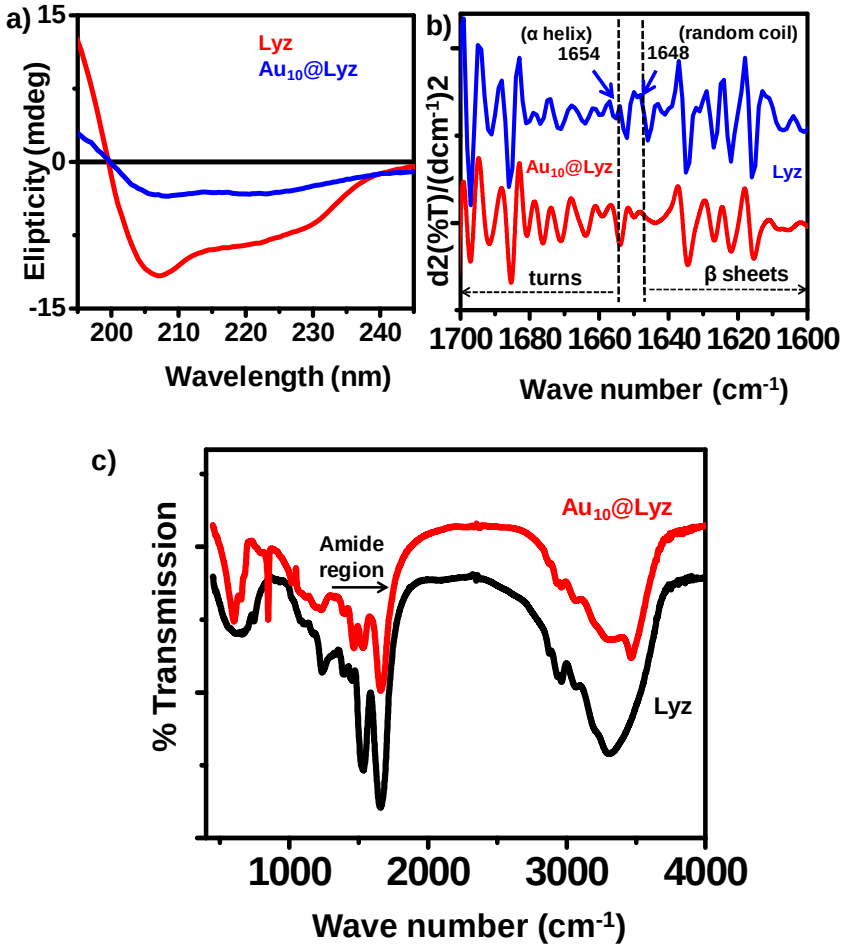

Figure S5: a) CD spectra of Lyz and as prepared Au_{10}@Lyz showing a clear change in ellipticity of the spectra, which indicates a huge change in the alpha helical structure. (b) Double derivative of the infrared (IR) spectra shows the disappearance of the peak at 1654 cm^{-1} in the case of Au_{QC}@Lyz. c) Infrared (IR) spectra of Lyz and Au_{QC}@Lyz showing significant change in the amide region (from the published work of the authors, ref. 6i).

S6. Supporting information 6

In this section we give the weights of the angular momentum components (S, P, S, …..,,I) for the wave functions whose iso-surface images are shown in Figures 5, 7 and 8. In each case, we give the energy ($E-E_F$) of the state and the weights.

Table of weights for Figure 5: Au_{38} (cysteine)$_4$

$E-E_F$ (eV)	S	P	D	F	G	H	I
0.48	0.000	0.015	0.018	0.010	0.577	0.008	0.022
-0.27	0.001	0.144	0.011	0.213	0.058	0.020	0.017
-0.99	0.004	0.004	0.019	0.344	0.027	0.020	0.023

Tables of weights for figures 7 and 8 in the manuscript, corresponding to Au_{102}+, Au_{38}^+, and Au_{25}^+

Au_{102}^+ (Figure 7)

$E-E_F$ (eV)	S	P	D	F	G	H	I
-8.65	0.949	0.008	0.013	0.001	0.003	0.006	0.003
-8.03	0.000	0.946	0.001	0.012	0.001	0.003	0.002
-7.11	0.001	0.006	0.843	0.031	0.014	0.004	0.007
-7.02	0.820	0.004	0.039	0.004	0.017	0.014	0.007
-6.65	0.000	0.054	0.002	0.601	0.004	0.090	0.033
-6.43	0.016	0.444	0.028	0.084	0.073	0.035	0.040
-1.74	0.000	0.001	0.003	0.017	0.151	0.014	0.019
-1.13	0.041	0.002	0.262	0.007	0.027	0.073	0.070

-1.07	0.000	0.000	0.030	0.012	0.015	0.403	0.014
-0.71	0.210	0.006	0.126	0.011	0.030	0.114	0.088
-0.08	0.001	0.021	0.002	0.399	0.004	0.028	0.133

Au_{38}^{+} (Figure 8)

$E-E_F$ (eV)	S	P	D	F	G	H	I
-0.31	0.002	0.014	0.084	0.014	0.387	0.007	0.041
-0.79	0.006	0.002	0.010	0.539	0.021	0.026	0.027
-2.84	0.004	0.010	0.021	0.017	0.047	0.066	0.043
-5.95	0.002	0.060	0.541	0.044	0.052	0.027	0.021
-6.31	0.479	0.019	0.061	0.143	0.051	0.013	0.033
-6.72	0.000	0.762	0.096	0.022	0.009	0.015	0.006
-7.59	0.864	0.020	0.011	0.050	0.015	0.003	0.006

Au_{25}^{+} (Figure 8)

$E-E_F$ (eV)	S	P	D	F	G	H	I
-0.07	0.000	0.009	0.031	0.436	0.073	0.020	0.031
-0.99	0.000	0.065	0.279	0.031	0.012	0.061	0.031

J Nanopart Res (2013) 15:1522
DOI 10.1007/s11051-013-1522-8

BRIEF COMMUNICATION

A copper cluster protected with phenylethanethiol

Anindya Ganguly · Indranath Chakraborty · Thumu Udayabhaskararao · Thalappil Pradeep

Received: 10 December 2012 / Accepted: 15 February 2013

Abstract A copper cluster protected with 2-phenylethanethiol (PET) exhibiting distinct optical features in UV/Vis spectroscopy is reported. Matrix-assisted laser desorption ionisation mass spectrometry of the cluster shows a well-defined molecular ion peak at *m*/*z* 5,800, assigned to $\sim Cu_{38}(PET)_{25}$. Fragmented ions from the cluster show the expected isotope patterns in electrospray ionisation mass spectrometry. The as-synthesized cluster was well-characterised using other tools as well. Clusters undergo decomposition in about 2 h after synthesis as a metallic few-atom core of copper is highly unstable. The products of decomposition were also characterised.

Keywords Atomically precise · Cu cluster · 2-Phenylethanethiol · MALDI MS · ESI MS

Introduction

Noble metal quantum clusters (Lu and Chen 2012; Yuan et al. 2011) belong to an area of intense activity in the recent past. They are remarkable because of their unique absorption (Chaki et al. 2008; Zhu et al. 2008; Habeeb and Pradeep 2011; Mathew et al. 2011) and emission (Xavier et al. 2012; Rao and Pradeep 2010) features as well as due to novel applications (Retnakumari et al. 2010; Muhammed et al. 2009; Goswami et al. 2011; Mathew et al. 2012; Haruta 2005; Xie et al. 2012). Au_{25} (Chaki et al. 2008; Zhu et al. 2008; Shichibu et al. 2005; Shibu et al. 2008), Au_{38} (Pei et al. 2008) and Au_{102} (Jadzinsky et al. 2007) clusters have been investigated in detail due to their enhanced stability. Several silver clusters, e.g., Ag_7 (Rao and Pradeep 2010; Udayabhaskararao et al. 2012), Ag_8 (Rao and Pradeep 2010), Ag_9 (Rao et al. 2010), Ag_{32} (Guo et al. 2012), Ag_{75} (Chakraborty et al. 2012b) and Ag_{152} (Chakraborty et al. 2012a), have also been reported recently. However, efforts on the preparation of monolayer-protected Cu clusters are limited (Vilar-Vidal et al. 2010; Salorinne et al. 2012; Jia et al. 2012; Saumya and Rao 2012; Wei et al. 2011) while there are several reports on copper nanoparticles (Bakshi et al. 2007; Nishida et al. 2011; Prucek et al. 2009; Wei et al. 2010). In terms of applications, copper is more appealing for its availability, lower cost, catalytic activity and electrical conductivity. In this communication, we report a facile one-pot synthesis of a new 2-phenylethanethiol (PET)-protected copper cluster. It has been characterised using UV/Vis absorption spectroscopy, mass spectrometry, high-resolution transmission electron microscopy (HRTEM), X-ray photoelectron spectroscopy and photoluminescence spectroscopy.

Electronic supplementary material The online version of this article (doi:10.1007/s11051-013-1522-8) contains supplementary material, which is available to authorized users.

A. Ganguly · I. Chakraborty · T. Udayabhaskararao · T. Pradeep (✉)
DST Unit of Nanoscience (DST UNS), Department of Chemistry, Indian Institute of Technology Madras, Chennai 600 036, India
e-mail: pradeep@iitm.ac.in

Published online: 12 March 2013

Experimental section

Materials

All the chemicals were commercially available and used without further purification. The used chemicals and solvents are: copper sulphate pentahydrate ($CuSO_4 \cdot 5H_2O$), cupric acetate, cupric chloride, 2-phenylethanethiol, sodium borohydride ($NaBH_4$), ethanol, acetonitrile, tetrahydrofuran (THF) and toluene.

Synthesis of $\sim Cu_{38}(PET)_{25}$

A solid-state route (Rao et al. 2010) was followed for the synthesis of copper clusters protected with PET. Initially, 47 mg of copper sulphate pentahydrate and 150 μL of PET were taken in an agate mortar and ground well for 10 min, then 80 mg of $NaBH_4$ was added and further ground for two more minutes followed by extraction of clusters in ethanol. All the operations were done in laboratory atmosphere (30–35 °C, 80 % relative humidity). The crucial aspect of this procedure is the limited supply of water needed for the reduction, which becomes available from the laboratory atmosphere as well as from the ethanol used for subsequent washing. A solution of the as-synthesized clusters in ethanol was light pink in colour (Fig. 1b). Sequential photographs of the synthesis are given in Supplementary Fig. S1. Blue colour of the copper salt changed to yellow after grinding with PET because of the formation of Cu–thiolates. Reduction of copper thiolate with $NaBH_4$ led to a black paste, which changed to pink when extracted in ethanol.

Characterisation of $\sim Cu_{38}(PET)_{25}$

Perkin Elmer Lambda 25 instrument was used for measuring UV/Vis spectra in the range of 200–1,100 nm. X-ray photoelectron spectroscopy (XPS) measurements were carried out using an Omicron ESCA Probe spectrometer with polychromatic MgKα X-rays ($h\upsilon = 1{,}253.6$ eV). The samples were spotted as drop-cast films on a sample stub. Constant analyzer energy of 20 eV was used for the measurements. The samples were prepared as fast as possible and were inserted into high vacuum within 5 min of synthesis to avoid aerial oxidation. Luminescence measurements were measured with a Jobin Vyon NanoLog instrument. The band passes for excitation and emission were set as

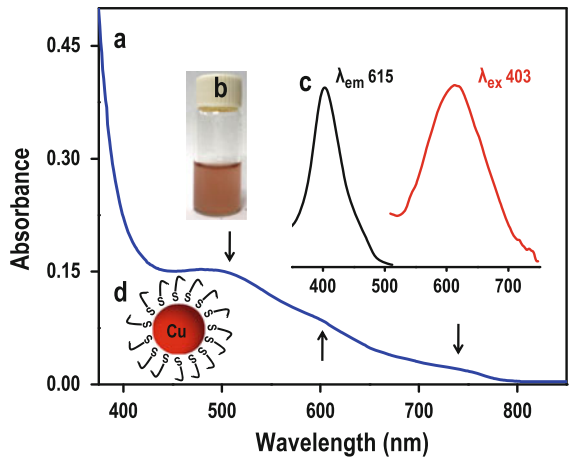

Fig. 1 UV/Vis absorption spectrum of the as-synthesized Cu@PET cluster (*a*) which shows three features at 500, 600 and 750 nm indicated by *arrows*. *Insets* (*b*) Photograph of the cluster solution showing *light pink colour*. (*c*) Luminescence excitation and emission spectra of Cu@PET cluster which emits at 615 nm upon excitation at 403 nm. (*d*) A cartoon representation of the cluster. (Color figure online)

2 nm. Matrix-assisted desorption ionisation mass spectrometry (MALDI MS) analysis were conducted using a Voyager-DE PRO Bio-spectrometry Workstation from Applied Bio-systems. A pulsed nitrogen laser of 337 nm was used for the MALDI MS analysis. Mass spectra were collected in negative ion mode and were averaged for 100 shots. Mass studies were conducted using an electrospray mass spectrometry (ESI MS) system, LTQ XL (Thermo scientific). Sample was taken in ethanol which was electrosprayed for analysis. High-resolution transmission electron microscopy of clusters was carried out with a JEOL 3010 instrument. The samples were drop casted on carbon-coated copper grids and allowed to dry in vacuum desiccators. Scanning electron microscopic (SEM) and energy-dispersive X-ray (EDAX) analyses were done in a FEI QUANTA-200 SEM. For measurements, samples were drop casted on an indium tin oxide-coated conducting glass and dried in vacuum. Powder XRD analysis of the decomposed sample was carried out using PANalytical X'pertPro diffractometer. X-ray diffractogram was collected in the 2θ range of 5–100°.

Results and discussion

The clusters show distinct step-like features at 500, 600 and 750 nm in the UV/Vis spectrum (Fig. 1a).

Interestingly, the clusters emit at room temperature. They show an excitation maximum at 403 nm and an emission maximum at 615 nm (Fig. 1c). From the view point of stability, clusters are short lived: after about 40 min of preparation, they show signs of decomposition which was monitored by optical absorption spectroscopy. The data showed (Supplementary Fig. S2) gradual merging of two humps (at 500 and 600 nm) into one. All the humps disappeared completely after 2 h, indicating the decomposition of the clusters.

Mass spectrometry is an ideal and most useful tool to find the composition of the clusters (Rao and Pradeep 2010; Dass 2009). Matrix-assisted laser desorption ionisation mass spectrometry (MALDI MS) and electrospray ionisation mass spectrometry (ESI MS) studies were conducted on the clusters. It is known that trans-2-[3-(4-tert-butylphenyl)-2-methyl-2-propenylidene]malononitrile (DCTB) gives well-defined mass spectrum for PET-protected clusters (Knoppe et al. 2010). We too used DCTB as the matrix. MALDI MS showed a single peak at *m/z* 5,800 at lowest laser intensity, assigned to $\sim Cu_{38}(PET)_{25}$ (Fig. 2a). No other peak was seen in the mass spectrum indicating the existence of only one type of cluster. The peak showed systematic shift to lower mass numbers upon increasing the laser intensity. This is characteristic of such clusters (Chakraborty et al. 2012b) which show fragmentation upon increasing laser intensity as the metal core–ligand interaction is weak.

ESI MS was performed in the negative ion mode for understanding the composition and the fragmentation pattern (Fig. 2b) of the as-synthesized clusters (Fig. 2c). As in several instances reported in the literature, we could not observe the molecular ion feature in ESI MS. However, we observed peaks corresponding to some of the fragmented ions (Rao and Pradeep 2010) in the case of silver clusters. The isotope patterns matched exactly with the calculated patterns. For instance, the peaks of $[Cu_4(PET)_5]^-$, having an intensity maximum at *m/z* 941 and $[Cu_5(PET)_6]^-$, having an intensity maximum at *m/z* 1,141 (Fig. 2a, b) matched with their calculated patterns. Other identified fragments are $[Cu_{34}(PET)_{23}]^{2-}$, $[Cu_{30}(PET)_{22}]^{2-}$, $[Cu_{29}(PET)_{21}]^{2-}$, $[Cu_{28}(PET)_{18}]^{2-}$ and $[Cu_{28}(PET)_{17}]^{2-}$ with corresponding *m/z* values of 2,655, 2,459, 2,359, 2,124 and 2,056, noted with arrows in Fig. 2c (from right to left). The presence of specific fragments support the existence of a PET-protected cluster in solution.

Because of its low standard reduction potential (0.34 V), copper is prone to aerial oxidation. Therefore, XPS was used to study the oxidation state of copper in the cluster. In view of the aerial oxidation of the cluster, the sample was immediately inserted into the vacuum chamber and analyzed as fast as possible.

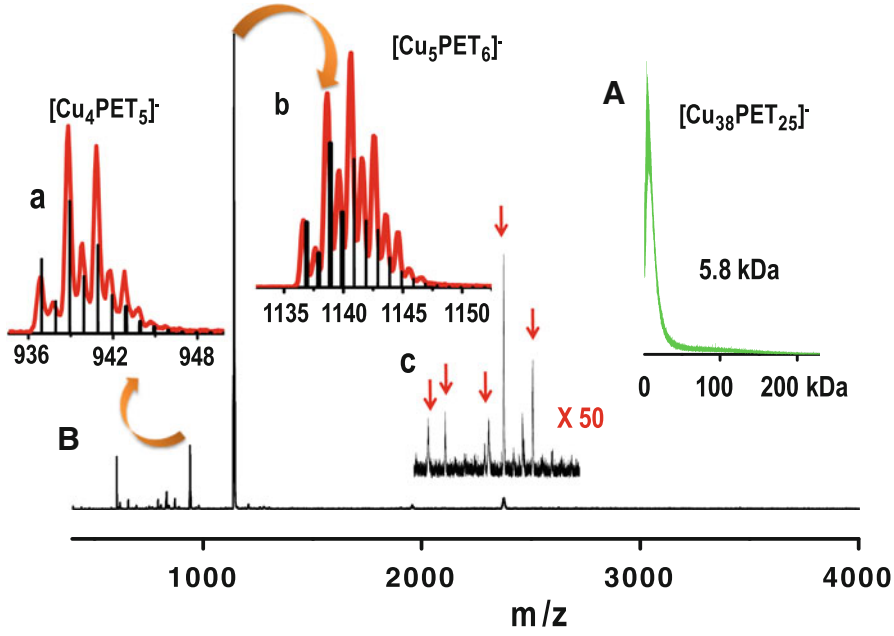

Fig. 2 (*A*) Linear negative ion MALDI mass spectrum of the Cu cluster. A molecular ion peak at *m/z* of 5,800 is clearly observed. The spectrum is shown from the minimum mass region measurable. (*B*) ESI MS data of Cu@PET cluster in the negative mode. *Insets* (*a*) and (*b*): Comparison of the observed isotope patterns (*red*) with the calculated patterns (*black*) of (*a*) $[Cu_4(PET)_5]^-$, *m/z* = 941, and (*b*) $[Cu_5(PET)_6]^-$, *m/z* = 1,141. (*c*) A *y*-axis expanded view of a selected region between *m/z* 2,000 and 3,000. Identified fragments are labelled with *red arrows*. (Color figure online)

No decomposition was seen within the time of sample transfer. The spectrum in the Cu 2*p* region shows two peaks: at 931.6 and 951.5 eV (Fig. 3), which have been assigned to $2p_{3/2}$ and $2p_{1/2}$ features of Cu (0). Binding energy (BE) of $2p_{3/2}$ in Cu^{+} of Cu_2O is 932.1 eV (Ai et al. 2009; Ghodselahi et al. 2008). So, Cu^{+} is unlikely to be present in the cluster. The most important observation is the absence of the satellite peaks. It is known that any species having d^9 (Cu^{2+}) configuration, such as CuO, would show satellite peaks which arise because of the configuration interaction of the $2p^5 3d^9 L$ (L = ligand, RS in the present case) final state (Ghijsen et al. 1988). Hence, the presence of Cu^{2+} is ruled out as well. The BE values are within the range of Cu(0) and Cu(I). Oxidation is very much facile in this size scale and this is likely to be the reason for the observed in-between values. This is the situation seen in Au and Ag clusters as well (Bootharaju and Pradeep 2011). XPS features of all other expected elements have been assigned in the survey spectrum and their expanded versions fitted exactly with that of the expected elements (Supplementary Fig. S3). The S 2*p* region shows a $2p_{3/2}$ feature at 162.9 eV, characteristic of thiolate. The C 1*s* binding energy seen is at 285.0 eV, characteristic of the ligand chain.

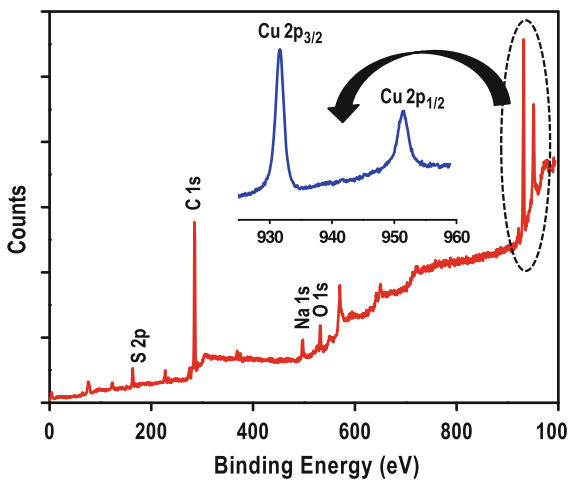

Fig. 3 XPS survey spectrum of Cu@PET cluster (*red*). It identifies the presence of copper, sulphur, carbon, sodium (a trace of Na, probably derived from $NaBH_4$) and oxygen. *Inset* Expanded XPS spectrum in the Cu 2*p* region of Cu@PET cluster (*blue*). Sharp peaks with narrow width are observed. The binding energy suggests the oxidation state of Cu to be close to zero and that of S 2*p* region is characteristic of thiolates. (Color figure online)

Various control experiments were carried out to optimize the conditions for synthesizing the cluster. First, molar ratio of PET with copper sulphate was varied (Supplementary Fig. S4). Five different molar ratios of copper sulphate to PET (1:1, 1:3, 1:5, 1:7 and 1:9) were tried. Among these, only the mixture with 1:5 ratio produced a light pink-coloured solution that showed distinct features in the optical absorption spectrum (Fig. 1a), while others did not have any characteristic features. Second, molar ratio of $NaBH_4$ was varied with respect to copper sulphate for the 1:5 sample. Five different molar ratios of copper sulphate and $NaBH_4$ (1:3, 1:7, 1:10, 1:13 and 1:15) were considered. Among these, the preparation with 1:10 ratio had distinct optical absorption features similar to that shown in Fig. 1a, while others had no characteristic optical absorption (Supplementary Fig. S5). Third, three different salts namely, cupric sulphate, cupric chloride and cupric acetate were used to find whether anion is playing any role for cluster formation/extraction. All of them produced samples of light pink colour; among which, the solution prepared from copper sulphate was most intense. In addition, sample from copper acetate showed the characteristic optical absorption features of $Cu_{38}(PET)_{25}$ which were significantly weaker than the same from cupric sulphate (Supplementary Fig. S6). Sample from cupric chloride did not show the desired optical absorption features. MALDI MS analyses were done for Cu@PET prepared from other two salts as well. The molecular ion peak at *m*/*z* 5,800 was observed for the sample prepared from cupric acetate indicating the presence of $\sim Cu_{38}(PET)_{25}$ in it (Supplementary Fig. S7). Fourth, different solvents (ethanol, acetonitrile, THF and toluene) were tried as extraction media. Among these, ethanol and acetonitrile were effective as solvents. The acetonitrile extract, however, showed weak absorption. Instead of showing three distinct features, it showed a single hump around 500 nm. On the other hand, THF and toluene were not able to extract the cluster as inferred by the absence of pink colour and characteristic absorption features (Supplementary Fig. S8).

Cluster formation was confirmed from the HRTEM images where the clusters appeared as tiny dots (Supplementary Fig. S9). The average diameter of the cluster is 1.4 nm, comparable to that of Au_{38} (Stellwagen et al. 2012). Upon longer electron beam irradiation, the dots grow gradually to form an aggregate, quite similar to that observed in the case of silver clusters

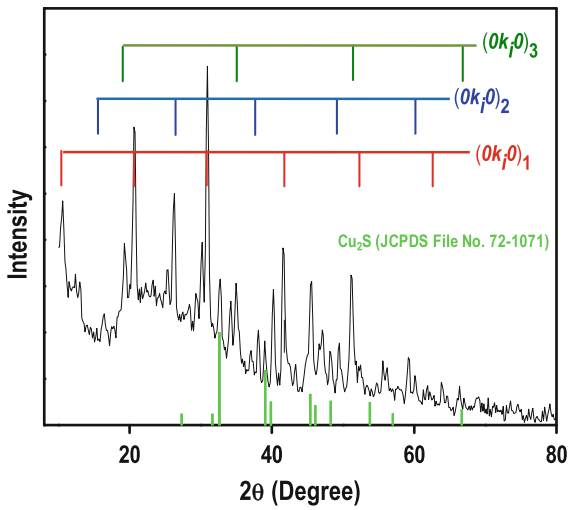

Fig. 4 Powder XRD pattern of the decomposed material consisting of a mixture of Cu_2S and copper thiolates. A few series of intense reflections, indexed as $(0k_i0)$, were observed because of polycrystalline copper thiolates. Successive diffraction peaks are because of differently structured [$(0k_i0)_1$, $(0k_i0)_2$ and $(0k_i0)_3$] multiple layers of copper thiolates. Three series are marked. The JCPDS pattern of Cu_2S is shown in *green*. (Color figure online)

(Rao and Pradeep 2010; Dhanalakshmi et al. 2012). From TEM/EDAX analysis, the Cu:S ratio was found to be 1:0.67, consistent with the proposed composition (1:0.65).

Scanning electron microscopy (SEM) is used to find out the presence of the expected elements in the cluster. It showed the desired elements (Supplementary Fig. S10). The Cu:S ratio was slightly different from the expected value, possibly due to excess thiol in that preparation. Excess thiol is found in the crystals of clusters.

The decomposed material (2 h after the synthesis) was converted to a powder by evaporating the solvent using a rotary evaporator and analyzed by powder X-ray diffraction (PXRD) which showed the presence of copper thiolates along with Cu_2S (Fig. 4) (JCPDS File No-72-1071). The PXRD pattern of longer chain thiolates consist of differently structured and stacked layers of Cu and S atoms (Sandhyarani and Pradeep 2001), oriented in three dimension which produce multiple series of peaks as shown in Fig. 4. Intense periodic diffraction patterns with large d spacing provided evidence for the presence of those layers. Interlayer spacing, d was almost equal to twice the length of alkyl chains because each CuS layer is separated by two alkyl chains. Those periodic reflections have been indexed as $(0k_i0)$ (Espinet et al. 1999; Parikh et al. 1999). Cu_2S reflections match with the standard.

Conclusion

In summary, we have prepared a PET-protected copper cluster for the first time. From the MALDI MS data, a molecular ion peak at m/z 5,800 has been identified and it is assigned to $\sim Cu_{38}(PET)_{25}$. However, the cluster decomposes in about 2 h at room temperature forming a mixture of copper thiolates and cuprous sulphide as characterised by PXRD. It is important to improve the atmospheric stability to find new applications for these systems.

Acknowledgments We thank the Department of Science and Technology, Government of India for financial support. Thanks are due to SAIF, IIT Madras for the PXRD data.

References

Ai Z, Zhang L, Lee S, Ho W (2009) Interfacial hydrothermal synthesis of Cu@Cu_2O core-shell microspheres with enhanced visible-light-driven photocatalytic activity. J Phys Chem C 113(49):20896. doi:10.1021/jp9083647

Bakshi MS, Possmayer F, Petersen NO (2007) Simultaneous synthesis of Au and Cu nanoparticles in pseudo-core-shell type arrangement facilitated by DMPG and 12-6-12 capping agents. Chem Mater 19(6):1257. doi:10.1021/cm062771t

Bootharaju MS, Pradeep T (2011) Investigation into the reactivity of unsupported and supported Ag_7 and Ag_8 clusters with toxic metal ions. Langmuir 27(13):8134. doi:10.1021/la200947c

Chaki NK, Negishi Y, Tsunoyama H, Shichibu Y, Tsukuda T (2008) Ubiquitous 8 and 29 kDa gold:alkanethiolate cluster compounds: mass-spectrometric determination of molecular formulas and structural implications. J Am Chem Soc 130(27):8608. doi:10.1021/ja8005379

Chakraborty I, Govindarajan A, Erusappan J, Ghosh A, Pradeep T, Yoon B, Whetten RL, Landman U (2012a) The superstable 25 kDa monolayer protected silver nanoparticle: measurements and interpretation as an icosahedral $Ag_{152}(SCH2CH2Ph)_{60}$ cluster. Nano Lett 12(11):5861–5866. doi:10.1021/nl303220x

Chakraborty I, Udayabhaskararao T, Pradeep T (2012b) High temperature nucleation and growth of glutathione protected $\sim Ag_{75}$ clusters. Chem Commun 48(54):6788

Dass A (2009) Mass spectrometric identification of $Au_{68}(SR)_{34}$ molecular gold nanoclusters with 34-electron shell closing. J Am Chem Soc 131(33):11666. doi:10.1021/ja904713f

Dhanalakshmi L, Udayabhaskararao T, Pradeep T (2012) Conversion of double layer charge-stabilized Ag@citrate colloids to thiol passivated luminescent quantum clusters. Chem Commun 48(6):859. doi:10.1039/c1cc15604g

Espinet P, Lequerica MC, Martin-Alvarez JM (1982) Synthesis, structural characterization and mesogenic behavior of copper(I) *n*-alkylthiolates. Chem Eur J 5(7):1982–1986. doi:10.1002/(sici)1521-3765(19990702)5:7

Ghijsen J, Tjeng LH, Van EJ, Eskes H, Westerink J, Sawatzky GA, Czyzyk MT (1988) Electronic structure of cuprous and cupric oxides. Phys Rev B 38(16-A):11322

Ghodselahi T, Vesaghi MA, Shafiekhani A, Baghizadeh A, Lameii M (2008) XPS study of the Cu@Cu_2O core-shell nanoparticles. Appl Surf Sci 255(5):2730. doi:10.1016/j.apsusc.2008.08.110

Goswami N, Giri A, Bootharaju MS, Xavier PL, Pradeep T, Pal SK (2011) Copper quantum clusters in protein matrix: potential sensor of Pb^{2+} ion. Anal Chem 83(24):9676. doi:10.1021/ac202610e

Guo J, Kumar S, Bolan M, Desireddy A, Bigioni TP, Griffith WP (2012) Mass spectrometric identification of silver nanoparticles: the case of $Ag_{32}(SG)_{19}$. Anal Chem 84(12):5304. doi:10.1021/ac300536j

Habeeb MMA, Pradeep T (2011) Au_{25}@SiO2: quantum clusters of gold embedded in silica. Small 7(2):204

Haruta M (2005) Catalysis: gold rush. Nature 437(7062):1098. doi:10.1038/4371098a

Jadzinsky PD, Calero G, Ackerson CJ, Bushnell DA, Kornberg RD (2007) Structure of a thiol monolayer-protected gold nanoparticle at 1.1 a resolution. Science 318(5849):430

Jia X, Li J, Han L, Ren J, Yang X, Wang E (2012) DNA-hosted copper nanoclusters for fluorescent identification of single nucleotide polymorphisms. ACS Nano 6(4):3311. doi:10.1021/nn3002455

Knoppe S, Dharmaratne AC, Schreiner E, Dass A, Burgi T (2010) Ligand exchange reactions on Au_{38} and Au_{40} clusters: a combined circular dichroism and mass spectrometry study. J Am Chem Soc 132(47):16783. doi:10.1021/ja104641x

Lu Y, Chen W (2012) Sub-nanometer sized metal clusters: from synthetic challenges to the unique property discoveries. Chem Soc Rev 41(9):3594. doi:10.1039/c2cs15325d

Mathew A, Sajanlal PR, Pradeep T (2011) A fifteen atom silver cluster confined in bovine serum albumin. J Mater Chem 21(30):11205. doi:10.1039/c1jm11452b

Mathew A, Sajanlal PR, Pradeep T (2012) Selective visual detection of TNT at the sub-zeptomole level. Angew Chem Int Ed 51(38):9596–9600. doi:10.1002/anie.201203810

Muhammed MAH, Verma PK, Pal SK, Kumar RCA, Paul S, Omkumar RV, Pradeep T (2009) Bright, NIR-emitting Au_{23} from Au_{25}: characterization and applications including biolabeling. Chem Eur J 15(39):10110. doi:10.1002/chem.200901425

Nishida N, Miyashita A, Hashimoto N, Murayama H, Tanaka H (2011) Regenerative synthesis of copper nanoparticles by photoirradiation. Eur Phys J D 63(2):307. doi:10.1140/epjd/e2011-10515-8

Parikh AN, Gillmor SD, Beers JD, Beardmore KM, Cutts RW, Swanson BI (1999) Characterization of chain molecular assemblies in long-chain, layered silver thiolates: a joint infrared spectroscopy and X-ray diffraction study. J Phys Chem B 103(15):2850. doi:10.1021/jp983938b

Pei Y, Gao Y, Zeng XC (2008) Structural prediction of thiolate-protected Au_{38}: a face-fused bi-icosahedral Au core. J Am Chem Soc 130(25):7830. doi:10.1021/ja802975b

Prucek R, Kvitek L, Panacek A, Vancurova L, Soukupova J, Jancik D, Zboril R (2009) Polyacrylate-assisted synthesis of stable copper nanoparticles and copper(I) oxide nanocubes with high catalytic efficiency. J Mater Chem 19(44):8463. doi:10.1039/b913561h

Rao TUB, Pradeep T (2010) Luminescent Ag_7 and Ag_8 clusters by interfacial synthesis. Angew Chem Int Ed 49(23):3925. doi:10.1002/anie.200907120

Rao TUB, Nataraju B, Pradeep T (2010) Ag_9 quantum cluster through a solid-state route. J Am Chem Soc 132(46):16304. doi:10.1021/ja105495n

Retnakumari A, Setua S, Menon D, Ravindran P, Muhammed H, Pradeep T, Nair S, Koyakutty M (2010) Molecular-receptor-specific, non-toxic, near-infrared-emitting Au cluster-protein nanoconjugates for targeted cancer imaging. Nanotechnology 21(5):055103

Salorinne K, Chen X, Troff RW, Nissinen M, Haekkinen H (2012) One-pot synthesis and characterization of sub-nanometre-size benzotriazolate protected copper clusters. Nanoscale 4(14):4095. doi:10.1039/c2nr30444a

Sandhyarani N, Pradeep T (2001) An investigation of the structure and properties of layered copper thiolates. J Mater Chem 11(4):1294. doi:10.1039/b009837j

Saumya V, Rao TP (2012) Copper quantum cluster–polypyrrole composite film based zero current chronopotentiometric sensor for glutathione. Anal Methods 4(7):1976

Shibu ES, Muhammed MAH, Tsukuda T, Pradeep T (2008) Ligand exchange of $Au_{25}SG_{18}$ leading to functionalized gold clusters: spectroscopy, kinetics, and luminescence. J Phys Chem C 112(32):12168. doi:10.1021/jp800508d

Shichibu Y, Negishi Y, Tsukuda T, Teranishi T (2005) Large-scale synthesis of thiolated Au_{25} clusters via ligand exchange reactions of phosphine-stabilized Au_{11} clusters. J Am Chem Soc 127(39):13464. doi:10.1021/ja053915s

Stellwagen D, Weber A, Bovenkamp GL, Jin R, Bitter JH, Kumar CSSR (2012) Ligand control in thiol stabilized Au_{38} clusters. RSC Adv 2(6):2276. doi:10.1039/c2ra00747a

Udayabhaskararao T, Sun Y, Goswami N, Pal SK, Balasubramanian K, Pradeep T (2012) Ag_7Au_6: a 13-atom alloy quantum cluster. Angew Chem Int Ed 51(9):2155–2159. doi:10.1002/anie.201107696

Vilar-Vidal N, Blanco MC, Lo̓pez-Quintela MA, Rivas J, Serra C (2010) Electrochemical synthesis of very stable photoluminescent copper clusters. J Phys Chem C 114(38):15924. doi:10.1021/jp911380s

Wei Y, Chen S, Kowalczyk B, Huda S, Gray TP, Grzybowski BA (2010) Synthesis of stable, low-dispersity copper nanoparticles and nanorods and their antifungal and catalytic properties. J Phys Chem C 114(37):15612. doi:10.1021/jp1055683

Wei W, Lu Y, Chen W, Chen S (2011) One-pot synthesis, photoluminescence, and electrocatalytic properties of subnanometer-sized copper clusters. J Am Chem Soc 133(7):2060. doi:10.1021/ja109303z

Xavier PL, Chaudhari K, Baksi A, Pradeep T (2012) Protein-protected luminescent noble metal quantum clusters: an emerging trend in atomic cluster nanoscience. Nano Rev 3:14767. doi:10.3402/nano.v3i0.14767

Xie S, Tsunoyama H, Kurashige W, Negishi Y, Tsukuda T (2012) Enhancement in aerobic alcohol oxidation catalysis

of Au_{25} clusters by single Pd atom doping. ACS Catal 2(7):1519. doi:10.1021/cs300252g

Yuan X, Luo Z, Zhang Q, Zhang X, Zheng Y, Lee JY, Xie J (2011) Synthesis of highly fluorescent metal (Ag, Au, Pt, and Cu) nanoclusters by electrostatically induced reversible phase transfer. ACS Nano 5(11):8800–8808. doi:10.1021/nn202860s

Zhu M, Lanni E, Garg N, Bier ME, Jin R (2008) Kinetically controlled, high-yield synthesis of Au_{25} clusters. J Am Chem Soc 130(4):1138. doi:10.1021/ja0782448

Supporting Information

A copper cluster protected with phenylethanethiol

Anindya Ganguly, Indranath Chakraborty, Thumu Udayabhaskararao and Thalappil Pradeep*

**DST Unit of Nanoscience (DST UNS), Department of Chemistry, Indian Institute of Technology Madras, Chennai 600 036, India; Fax: 91-44-2257 0545;*

E-mail: pradeep@iitm.ac.in

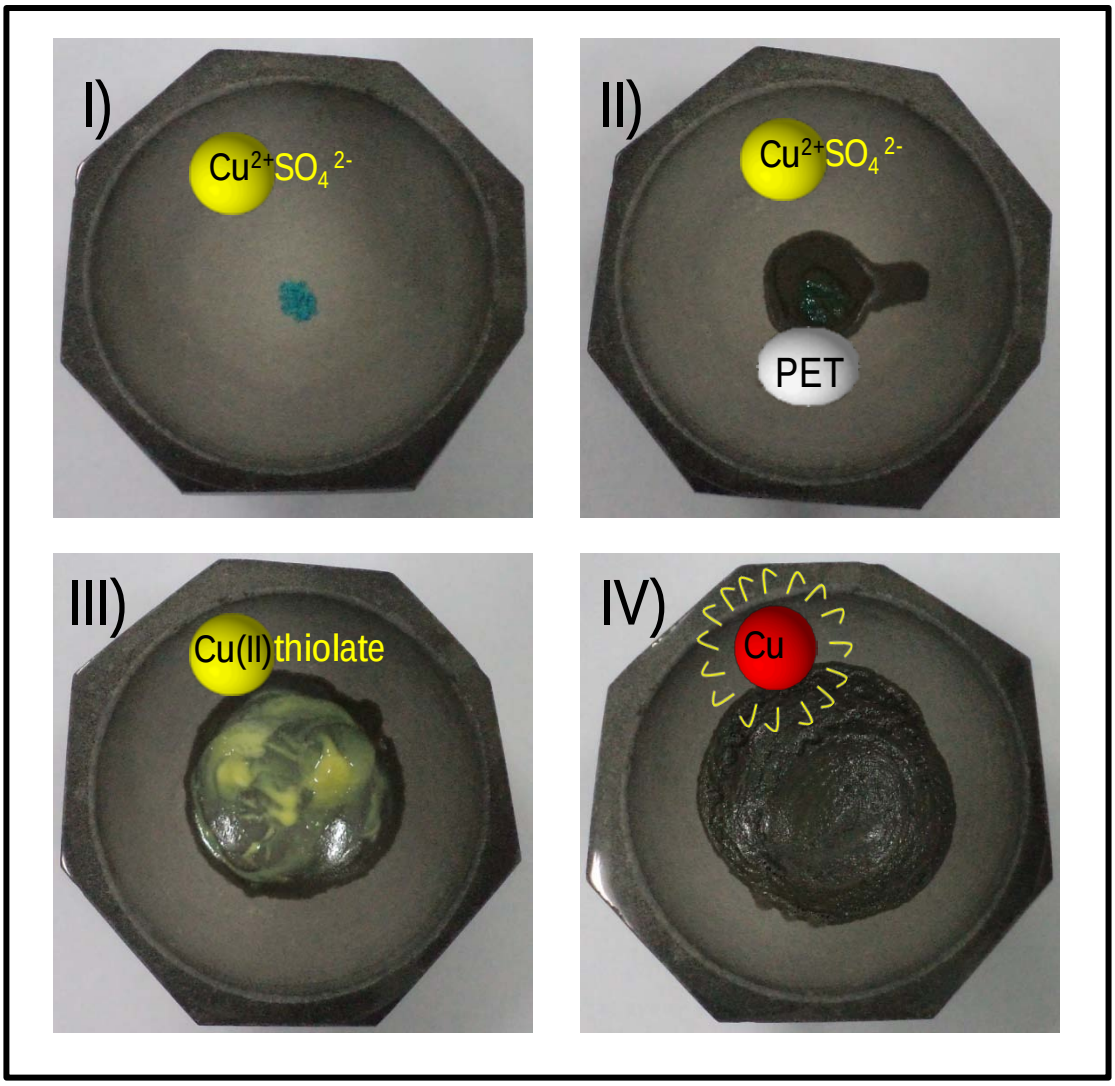

Fig. S1. Top view of different stages during synthesis of the copper cluster. I) $CuSO_4.5H_2O$ in the mortar. II) Immediately after the addition of 2-Phenylethanethiol to copper sulphate. III) Cu-thiolate formed after grinding the copper sulphate - PET mixture for ten minutes. IV) Black paste formed after grinding copper thiolate with $NaBH_4$ for about 3 minutes.

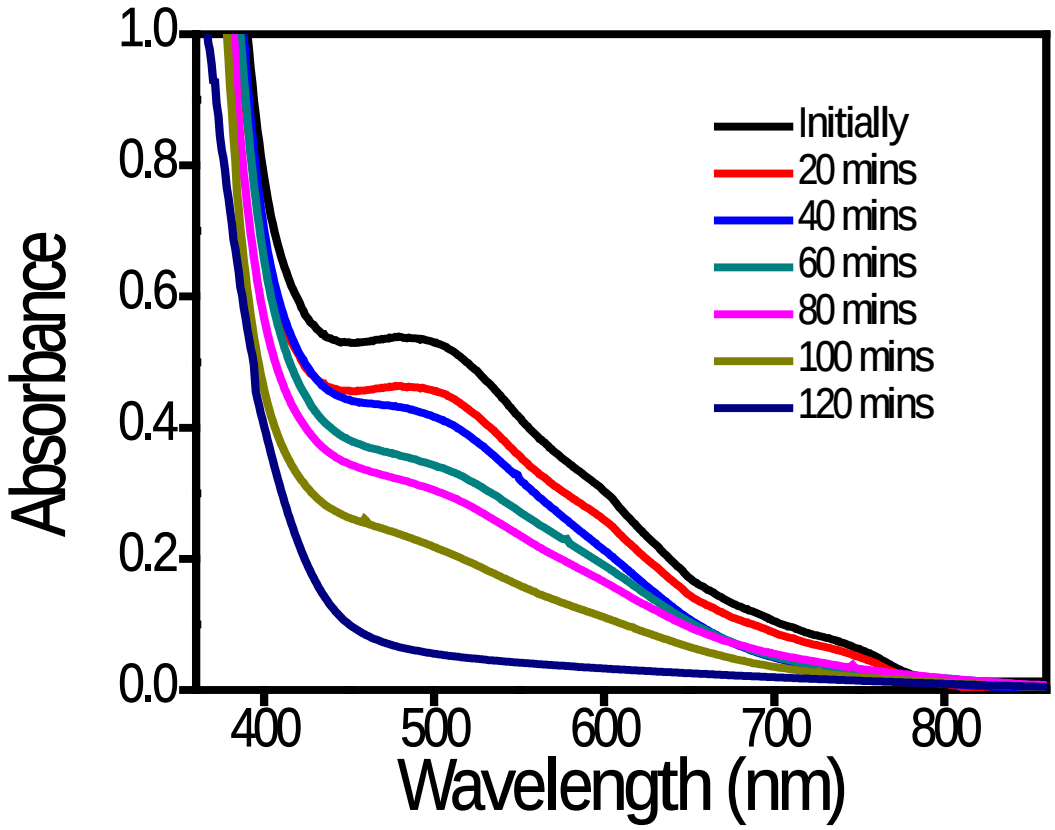

Fig. S2. Time dependent UV/Vis spectra of as-synthesized Cu@PET cluster. Initially, three features at 500, 600 and 750 nm are seen. By about 40 minutes, the humps at 600 and 750 nm have nearly disappeared. Also, from the beginning, the intensity of the hump at 500 nm keeps decreasing, finally merging with the baseline in about 120 minutes.

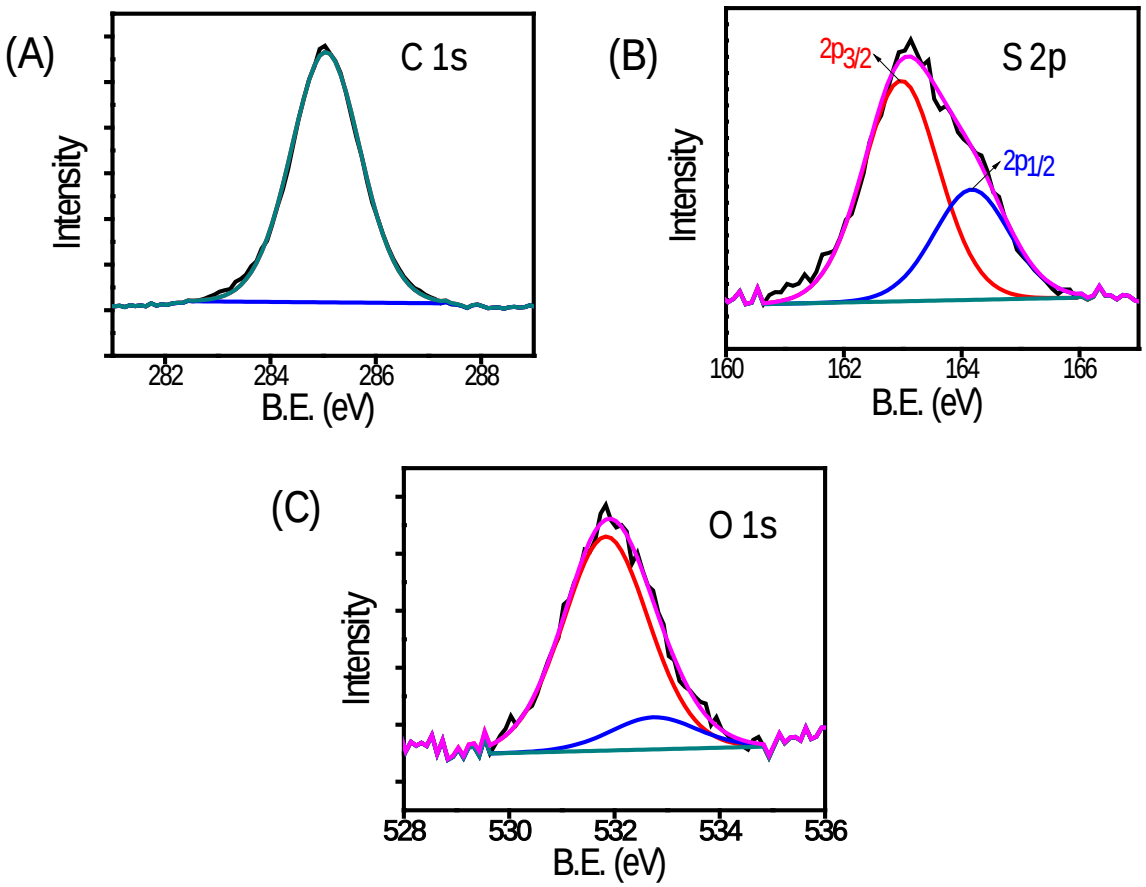

Fig. S3. A, B, and C are the expanded regions in the XPS for C 1s, S 2p, and O 1s, respectively. All the spectral features are fitted to the chemical species expected.

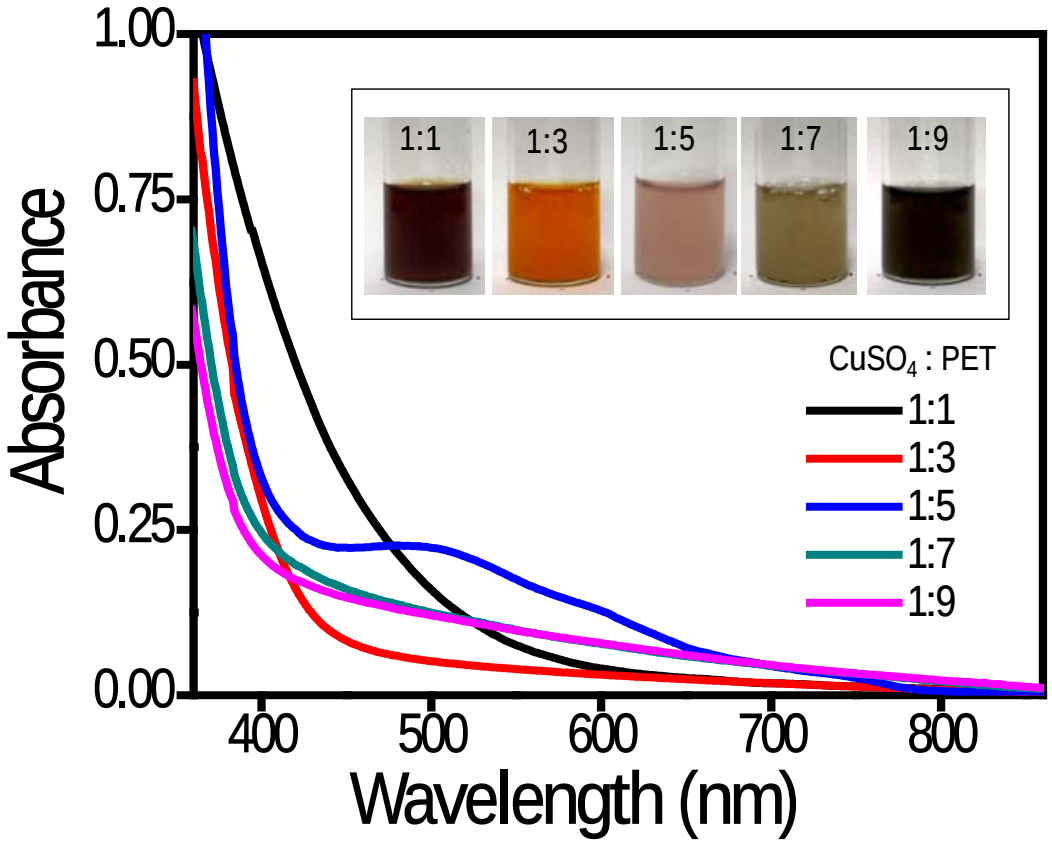

Fig. S4. UV/Vis absorption spectra for preparations with different copper sulphate to PET ratios. Among the five, only the 1:5 sample produced the cluster with features at 500, 600, and 750 nm. Inset shows the photographs after extraction in ethanol.

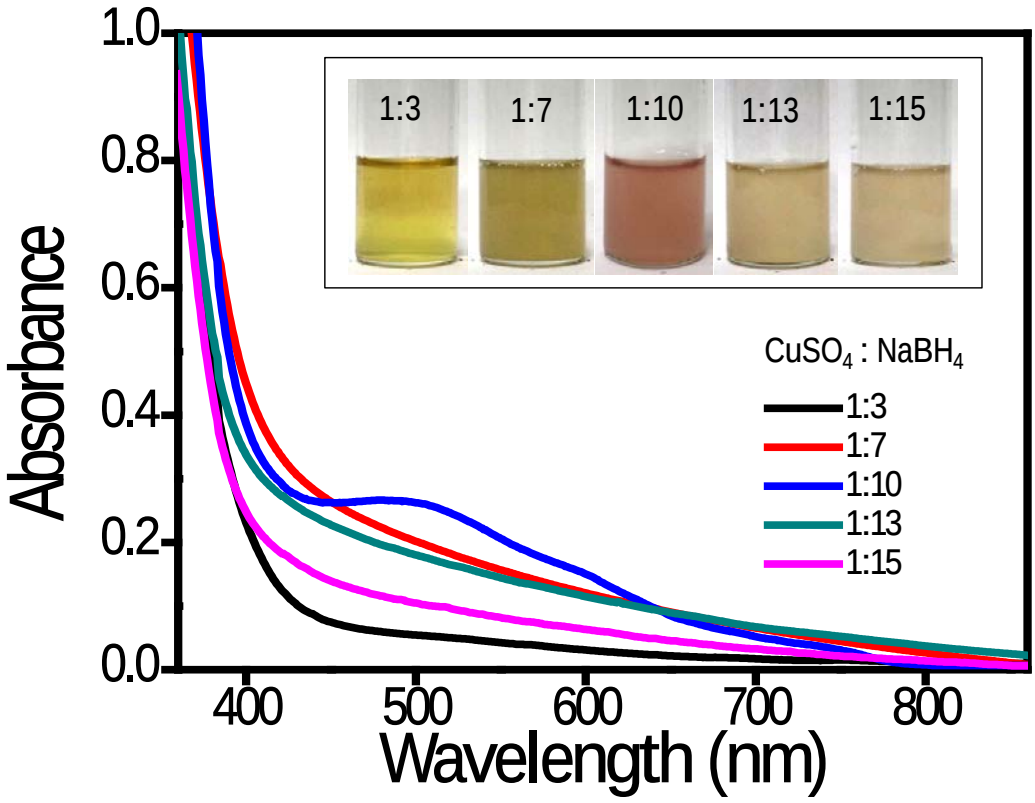

Fig. S5. UV/Vis absorption spectra for the preparations with different copper sulphate to $NaBH_4$ ratios. Among the five, only that with a ratio of 1:10 produced the cluster, $Cu_{38}(PET)_{25}$ with features mentioned earlier. Inset shows photographs of the preparations after extraction in ethanol.

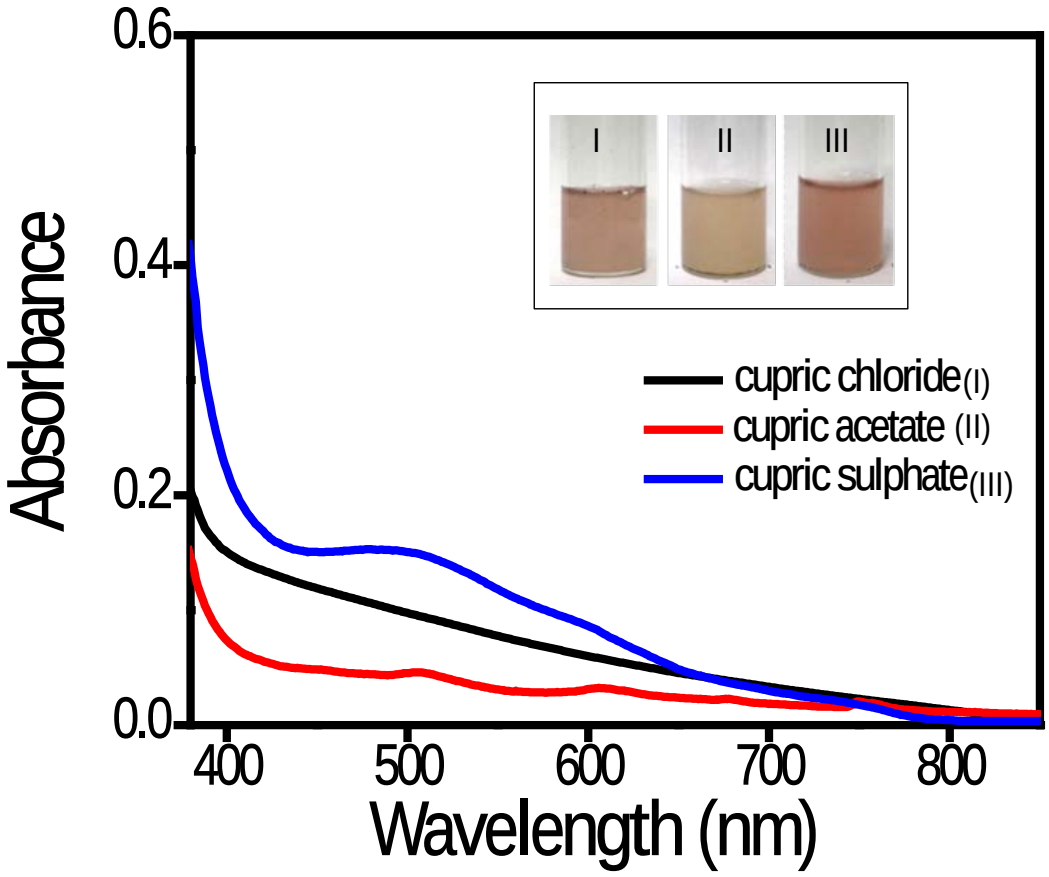

Fig. S6. UV/Vis absorption spectra for preparations with different salt precursors. Sample prepared from copper acetate shows features of $Cu_{38}(PET)_{25}$ though it is weak with respect to the preparation from copper sulphate. On the other hand, sample from $CuCl_2$ does not have the desired features of $Cu_{38}(PET)_{25}$. However, all ethanolic extracts are pink in color (Inset).

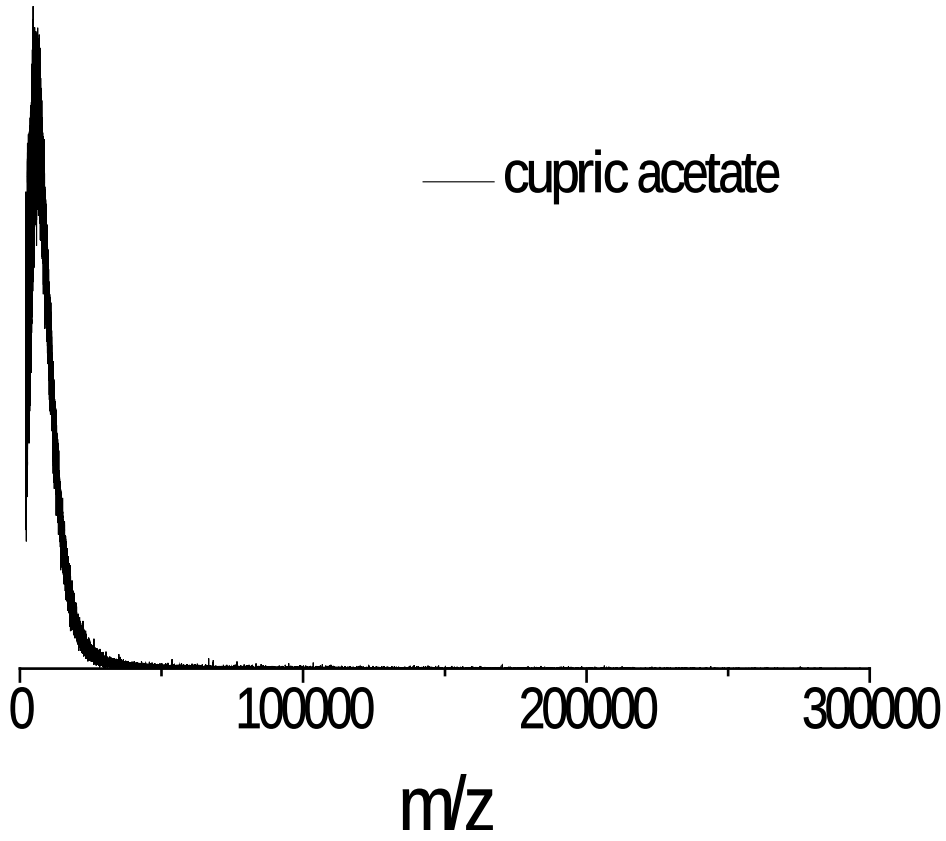

Fig. S7. MALDI mass spectrum of Cu@PET clusters, prepared from copper acetate as the precursor. This shows a molecular ion peak in the negative mode at m/z 5800.

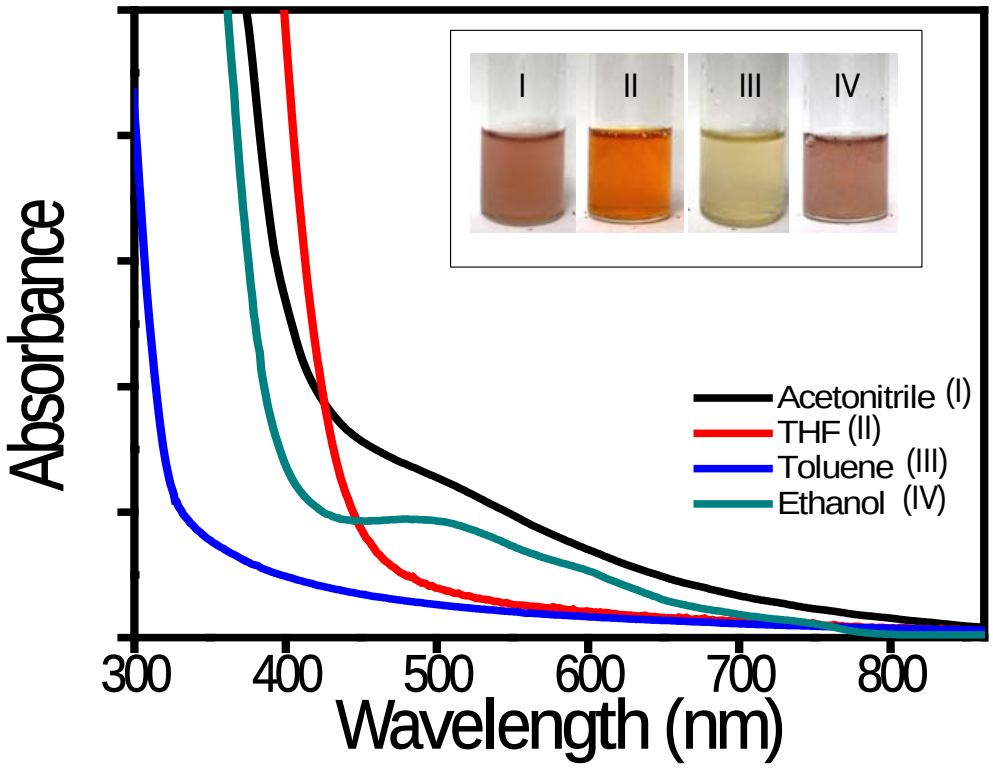

Fig. S8. UV/Vis absorption spectra for different solvents as the extraction media. Ethanol extract showed distinct features of $Cu_{38}(PET)_{25}$ while acetonitrile extract had a single hump at 500 nm. On the other hand, toluene and THF were not able to extract the cluster.

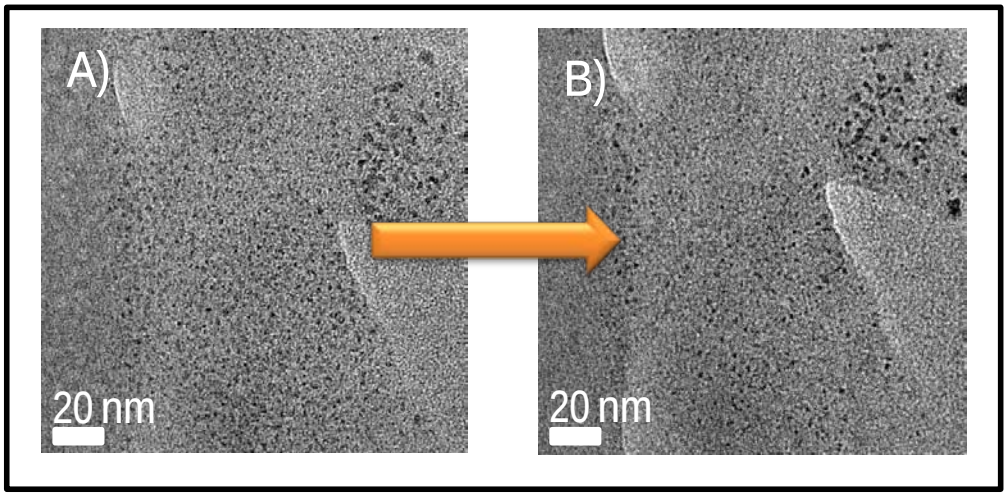

Cu:S = 1:0.67

C)

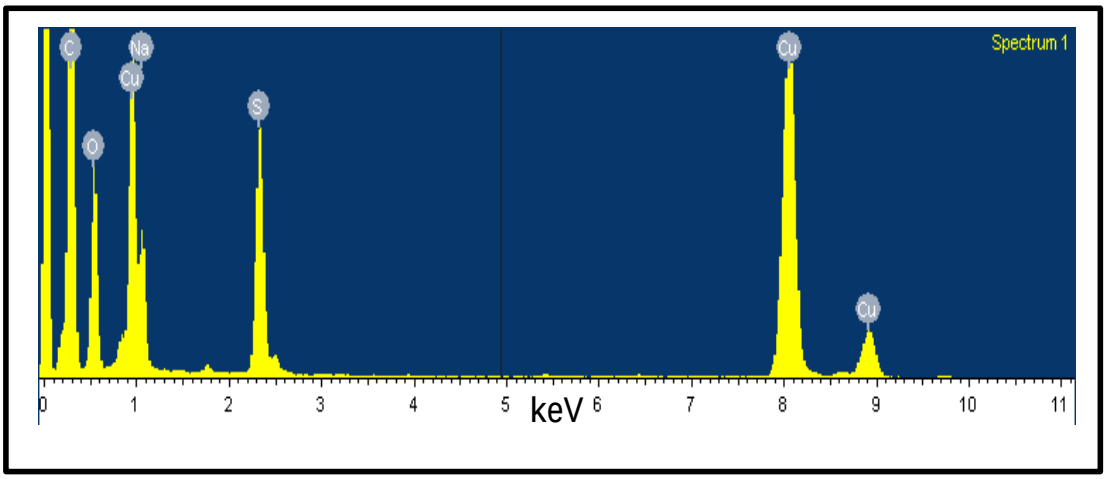

Fig. S9. HRTEM images of (A) as-synthesized $Cu_{38}(PET)_{25}$ cluster which appears as quantum dots, (B) after continued irradiation with electron beam, showing aggregates. (C) EDAX spectrum of the sample showing the elements: Cu, S, C, O, Na. Estimated Cu to S ratio from the spectrum is 1:0.67, consistent with theoretical ratio (1:0.65).

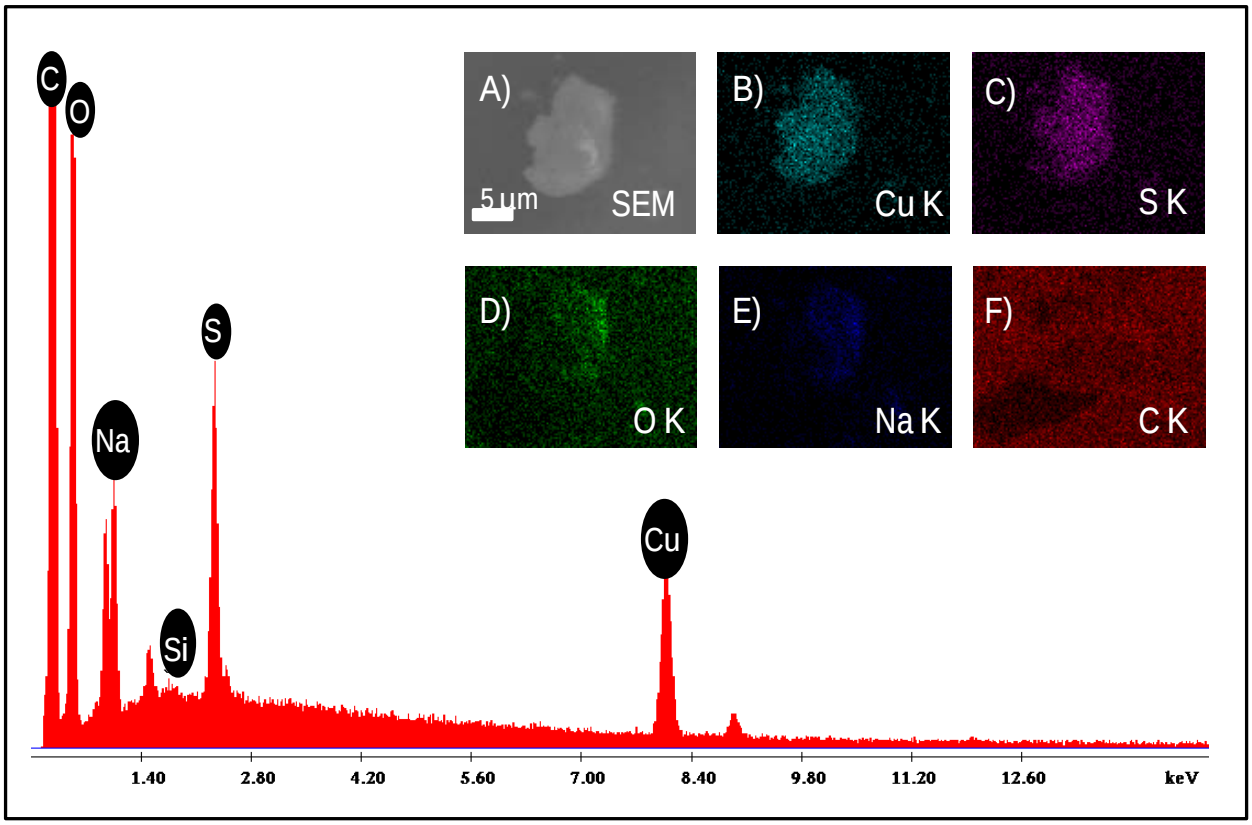

Fig. S10. EDAX spectrum of $Cu_{38}(PET)_{25}$ and Insets show the elemental mapping of a selected region. (A) SEM with (B) copper, (C) sulphur, (D) oxygen, (E) sodium and (F) carbon.

Nanoscale

RSC Publishing

PAPER

View Article Online
View Journal

Unprecedented inhibition of tubulin polymerization directed by gold nanoparticles inducing cell cycle arrest and apoptosis†

Cite this: DOI: 10.1039/c3nr33891f

Diptiman Choudhury,‡§[a] Paulrajpillai Lourdu Xavier,§[c] Kamalesh Chaudhari,[d] Robin John,[c] Anjan Kumar Dasgupta,[b] Thalappil Pradeep*[c] and Gopal Chakrabarti*[a]

The effect of gold nanoparticles (AuNPs) on the polymerization of tubulin has not been examined till now. We report that interaction of weakly protected AuNPs with microtubules (MTs) could cause inhibition of polymerization and aggregation in the cell free system. We estimate that single citrate capped AuNPs could cause aggregation of $\sim 10^5$ tubulin heterodimers. Investigation of the nature of inhibition of polymerization and aggregation by Raman and Fourier transform-infrared (FTIR) spectroscopies indicated partial conformational changes of tubulin and microtubules, thus revealing that AuNP-induced conformational change is the driving force behind the observed phenomenon. Cell culture experiments were carried out to check whether this can happen inside a cell. Dark field microscopy (DFM) combined with hyperspectral imaging (HSI) along with flow cytometric (FC) and confocal laser scanning microscopic (CLSM) analyses suggested that AuNPs entered the cell, caused aggregation of the MTs of A549 cells, leading to cell cycle arrest at the G_0/G_1 phase and concomitant apoptosis. Further, Western blot analysis indicated the upregulation of mitochondrial apoptosis proteins such as Bax and p53, down regulation of Bcl-2 and cleavage of poly(ADP-ribose) polymerase (PARP) confirming mitochondrial apoptosis. Western blot run after cold-depolymerization revealed an increase in the aggregated insoluble intracellular tubulin while the control and actin did not aggregate, suggesting microtubule damage induced cell cycle arrest and apoptosis. The observed polymerization inhibition and cytotoxic effects were dependent on the size and concentration of the AuNPs used and also on the incubation time. As microtubules are important cellular structures and target for anti-cancer drugs, this first observation of nanoparticles-induced protein's conformational change-based aggregation of the tubulin–MT system is of high importance, and would be useful in the understanding of cancer therapeutics and safety of nanomaterials.

Received 30th November 2012
Accepted 11th March 2013

DOI: 10.1039/c3nr33891f

www.rsc.org/nanoscale

1 Introduction

Inadequate understanding of how nanoparticles (NPs) interact with live cellular structures and concomitant effects of such interactions has been one of the major impediments in realizing the promises of nanotechnology to revolutionize biology and medicine.[1–18] Because of the high surface area, inherent energy, chemical potential and different surface chemistry of particles as well as protecting ligands, NPs tend to interact with surrounding species to reduce their energy. Often these interactions lead to distinct changes in the interacting system. If proteins happen to be the surrounding species, interaction with NPs leads to altered conformation, aggregation and loss of functionality in a few cases.[1,3–5] Nevertheless, NPs are also affected by certain consequences due to the interaction of proteins on their surface, such as aggregation, etching and dissolution which would influence their stability and functionality.[1] Various studies focusing on nano–bio interactions have shown that NPs induce undesirable protein conformational changes, including increasing the rate of protein fibrillation in the case of amyloid fibrils and loss of protein function.[5–9] Here, one may note that protein misfolding has been the leading reason in certain neuronal diseases such as

[a]Department of Biotechnology and Dr B. C. Guha Centre for Genetic Engineering and Biotechnology, University of Calcutta, 35 Ballygunge Circular Road, Kolkata, West Bengal, India 700019. E-mail: gcbcg@caluniv.ac.in

[b]Department of Biochemistry, University of Calcutta, 35 Ballygunge Circular Road, Kolkata, West Bengal, India 700019

[c]DST Unit of Nanoscience and Thematic Unit of Excellence, Department of Chemistry, Indian Institute of Technology Madras, Chennai, Tamil Nadu, India 600036. E-mail: pradeep@iitm.ac.in

[d]Department of Biotechnology, Indian Institute of Technology Madras, Chennai, Tamil Nadu, India 600036

† Electronic supplementary information (ESI) available: TEM images, UV-Vis spectra of AuNPs, IC_{50} plot, cell-viability, FT-IR, HSI spectra and spectral images and confocal images of AuNP-treated MCF-7 cells. See DOI: 10.1039/c3nr33891f

‡ Current address: Department of Medicine, Division of Uro-Oncology, Cedars Sinai Medical Centre, 8700-Bevarly Blvd, Los Angeles, California 90048, USA.

§ These authors contributed equally to this work.

Alzheimer's, Parkinson's and bovine spongiform encephalopathy (BSE), a prionic disease.[7,8] Formation of sub-nanometer sized particles in protein templates also leads to conformational change.[10] Halas *et al.* have shown that weakly protected AuNPs caused protein based aggregation of lysozyme at physiological pH.[9] Like NP–protein interaction, knowing how NPs interact with live cells and cellular organelles has been of paramount importance and is indeed a natural extension of the problem mentioned earlier.[12–19] Various NP–cell interactions have exhibited undesirable outcomes, sometimes resulting in disruption of organelles and cell death.[12,15] Au based nanostructures have been one of the promising nanosystems as far as the bio-medical field is concerned.[18–26] Recently, various studies of AuNPs interaction with cells have shown that AuNPs, once believed to be biocompatible, showed unexpected toxicity to human cells under certain conditions.[27–31] Hussain and coworkers studied the surface charge dependent toxicity of AuNPs.[28] We have earlier reported that citrate capped gold nanoparticles without any functionalization can be selectively toxic to lung carcinoma (A549) cells while baby hamster kidney (BHK21) and human hepatocellular liver carcinoma (HepG2) cells remained unaffected; however the molecular mechanism of the toxicity remains unknown.[27] While most studies have addressed the NP–extracellular protein interaction, very few studies have focused on the interaction of AuNPs with intracellular proteins, especially with the cytoskeletal proteins.[4,14,43–46]

Among the numerous intracellular proteins, tubulin is an important cytoskeletal, heterodimeric globular-protein containing α and β subunits, with nearly 20 free thiols. It is involved in microtubule (MT) formation, shows dynamic instability, is responsible for intracellular transport of cargos and several signalling mechanisms, and has been the most desired target to treat cancer.[32] Various drugs have been used to target the tubulin–MT equilibrium.[33,34] Tubulin–MT equilibrium targeting drugs alter the dynamics in two different ways, either by stabilizing the polymer structure of MT as in the case of taxol[35] or by inhibiting the tubulin polymerization into MT as in the case of vinblastine and vitamin K3.[36,37] Several of the tubulin–MT targeting agents show cell cycle arrest at the G_2/M phase of the cell cycle.[38] Among them taxol and colchicine are well-known anti-MT agents. Some of the compounds also show cell cycle arrest at the G_0/G_1 phase. These compounds mainly disrupt the interphase MT network of the cells. For instance, a low concentration of colcemid does not cause disruption of spindle MT or show cell cycle arrest at the G_2/M phase, instead it disrupts inter-phase MT and shows cell cycle arrest at the G_0/G_1 phase.[39–42] Very few studies have been done specifically on tubulin–NP interaction. The studies we came across are: alteration of the position of tryptophan residues in MT by TiO_2 NPs,[43] fabrication of AuNPs in MT filaments polymerized by taxol[44] and remodelling of MT (through acetylation) by reactive oxygen species produced by Fe_2O_3 NPs[45] and recently, a docking study of fullerene interaction with MT.[46] The so-far unaddressed interaction between AuNPs and tubulin and the elusive toxicity mechanism of citrate capped non-functionalized AuNPs in A549 cells[27] have prompted us to carry out this study. We hypothesized that interaction with tubulin could likely result in the toxicity observed, as it has 20 free thiols (since thiols have strong affinity for gold). Hence, we carried out a two phase study investigating the influence of AuNPs on (i) the microtubule assembly *in vitro*, (ii) the microtubule system and the cell cycle in A549 cells.

As experimental outcomes, in this study, to the best of our knowledge till date, for the first time, we report AuNPs-induced conformational change-based inhibition of polymerization and aggregation of tubulin–MT in the cell free system. This is distinctly a new observation as far as the interaction of AuNPs with the tubulin–MT system is concerned. We have also observed AuNPs-induced MT damage-mediated cell cycle arrest at the G_0/G_1 phase and cellular apoptosis in A549 cells *in vitro*. In this study we have carried out experiments using TEM, dark-field microscopy and FTIR, Raman, UV-Visible, fluorescence spectroscopic and molecular biological techniques to know how AuNPs change the tubulin–MT protein equilibrium in a cell free system and in a cancer cell. This study, we believe, would provide a new insight into the intracellular protein–AuNPs interaction and associated toxicity, and also be useful in understanding the safety of nanomaterials.

2 Experimental section

2.1 Materials

Hydrogen tetrachloroaurate ($HAuCl_4 \cdot 3H_2O$), sodium citrate, DAPI, DTNB, mice monoclonal anti-human α tubulin antibody without conjugation, goat monoclonal anti-mouse IgG antibody with rhodamine conjugation, GTP, PIPES, EGTA, RNase A, PI (propidium iodide) and KBr were purchased from Sigma, USA. Nutrient Ham's F12 (supplemented with 1 mM L-glutamine), bovine fetal serum, penicillin–streptomycin mixture and 100 mM fungizone were purchased from HyClone, USA. Trypsin–Versene was purchased from Cambrex Bioscience, USA. Bradford Protein estimation kits were purchased from GeNei, India. Annexin V-FITC apoptosis detection kit was obtained from BD Biosciences, San Diego, CA, USA. The Folin–Ciocalteu reagent and other chemicals of analytical grade were purchased from Sisco Research Laboratories, India.

2.2 Instrumentation

All scattering and absorbance measurements were performed using a UV-Visible spectrophotometer (JASCO V-630) equipped with a variable temperature water bath. The plasmonic shift of NPs was studied using a Perkin Elmer Lambda 25 spectrometer equipped with a variable temperature water bath. All fluorescence measurements were performed using a Photon Technology International Fluorescence spectrophotometer (USA) equipped with a variable temperature Peltier system, and data were analyzed using FeliX32 software. Electron microscopy analysis was done using a JEOL 3010 HRTEM. CD spectroscopic measurements were done using a JASCO CD spectrophotometer J-815. The confocal Raman microscope used was a CRM Alpha 300S (manufactured by WITec, GmbH, Germany) with a 532 nm laser. The excitation laser was focused using a 100× objective,

and the signal was collected in a back scattering geometry and sent to the spectrometer through a multimode fiber. Cell cycle experiments were performed using a Becton Dickinson FACS Calibur, and the data were analyzed using CellQuest program from Becton Dickinson. Bright field images were taken of cells by an Olympus inverted microscope model CKX41. Confocal images were taken with a Zeiss LSM 510 Meta Confocal Laser Scanning Microscope and images were processed with LSM software. Dark field microscopy experiments were done using a Cytoviva microscope, attached to a hyperspectral imaging system. The system captures the VNIR (400–1000 nm) spectrum within each pixel of the scanned field of view and spectral image analysis was done using ENVI software.

2.3 Preparation of AuNPs and purification of mammalian tubulin

AuNPs were prepared by the citrate reduction method. Auric chloride ($HAuCl_4 \cdot XH_2O$) 250 μM was reduced with various concentrations (depending upon size requirements) of tri-sodium citrate.[47] The excess citrate was removed by centrifugation and removing the supernatant and resuspending in water. This procedure was repeated thrice. The particle concentration in molarity (M_{NP}) of AuNPs was determined using the following formula (1). Detailed calculations are given in the ESI,† 1A.

$$M_{NP} = \frac{(\text{molarity of } Au^{3+} \text{ in the solution}) \times (\text{volume of one gold atom})}{(\text{volume of one nanoparticle})} \quad (1)$$

Goat brain tubulin was purified by a temperature-dependent polymerization and depolymerization method.[61,62] Finally, the protein was dissolved in PEM (containing 50 mM PIPES, 1 mM EGTA, and 1 mM $MgSO_4$) buffer at pH 6.9. The protein concentration was estimated using the Bradford Reagent[48] using bovine serum albumin as the standard and further confirmed by the DTNB titration method.[49] The protein was stored at −85 °C for further experiments.

2.4 Polymerization inhibition and aggregation studies

Tubulin (12 μM) was incubated at room temperature in the presence of $AuNP_{40}$ and the extinction spectra were monitored. Purified mammalian tubulin (12 μM) was mixed with 15 pM AuNPs ($AuNP_{20}$, $AuNP_{40}$ and $AuNP_{60}$) and polymerized in PEM–glycerol buffer (50 mM PIPES, 1 mM EGTA, 1 mM $MgSO_4$ and 33% glycerol) at 37 °C just after adding 1 mM GTP in the assembly mixture. The rate and extent of the polymerization reaction were monitored by light scattering at 350 nm.[50–52] Tri-sodium citrate in the corresponding buffer was used as the vector for the control sample. To see the effect of various concentrations of $AuNP_{40}$ on tubulin polymerization, purified tubulin (12 μM) was polymerized in the presence of different concentrations (0, 5, 12.5 and 25.0 pM) of $AuNP_{40}$ and the extent of polymerization was monitored in the same way as before.[51,52] To study the change of the intrinsic fluorescence of tryptophan residues, 1 μM tubulin was incubated with 15 pM of AuNPs at 25 °C. Fluorescence data were corrected for the inner filter effect according to the equation of Lakowicz,[53] $F = F_{obs}\,\text{antilog}(A_{Ex} + A_{Em})/2$ where A_{Ex} stands for the absorbance at the excitation wavelength (295 nm) and A_{Em} stands for the absorbance at the emission wavelength (335 nm). For HRTEM analysis 12 μM tubulin was polymerized in PEM–glycerol buffer in the absence and presence of 25.0 pM $AuNP_{40}$. Samples were then fixed with 0.25% (v/v) glutaraldehyde. Each sample (10 μL) was then loaded on 300 mesh carbon coated copper grids. The samples were allowed to stand for 5 min, and after washing, grids were negatively stained with 2% uranyl acetate. Copper grids were dried under vacuum, and the samples were viewed using TEM.[40] Samples used for TEM were also used for hyper-spectral imaging (dark field microscopy). Samples were spotted on glass coverslips and then air dried for 30 minutes. Pictures were taken using a Cytoviva microscope at 100× magnification.

2.5 Study on the effect of AuNPs on polymerized tubulins (MT)

Tubulin heterodimers were allowed to polymerize in the presence of excess GTP (2 mM) at 37 °C. The system was allowed to polymerize till saturation (25 min) and was monitored by scattering at 350 nm. Then different concentrations of 15 μL of $AuNP_{40}$ (5, 12.5 and 25 pM, respectively) and the buffer (AuNP free buffer after centrifugation at 10 000*g* for 20 minutes) was added to the solution and mixed slowly and scattering at 350 nm was monitored for another 25 minutes. Since AuNPs have a strong extinction at 350 nm, nano-particles were also incubated in protein free buffer (PEM–glycerol–GTP) and used for background correction.

2.6 Studies on conformational change

For CD spectroscopic analysis, tubulin (1 μM) was incubated with different concentrations 0, 10, 25 and 50 pM of $AuNP_{40}$ separately in 20 mM sodium phosphate buffer (pH 6.90) for 60 min at 37 °C. Then CD spectra were taken in the range of 200–260 nm wavelength regions. Phosphate buffer was used for CD as PIPES had high absorbance at 220 nm. Thiol estimation was done using the DTNB titration method. Tubulin (1 μM) was incubated with 25.0 pM of $AuNP_{40}$ for 60 min at 37 °C, and then the sample was titrated with 400 μM DTNB (excess) for 15 min separately, and compared with the control. In the first set 12 μM tubulin was polymerized for 30 min at 37 °C in the presence and absence of 25.0 μM $AuNP_{40}$ and in the second set, 12 μM tubulin was incubated for 3 h at 37 °C (in an unpolymerizing condition) in 25.0 pM $AuNP_{40}$ and FTIR spectra were measured for all sets using a Perkin Elmer Spectrum One instrument. KBr crystals were used to prepare the matrix for the samples. The second derivative of the FTIR spectrum was taken using "Spectrum One" software provided by Perkin Elmer. For each set, at least 5 independent experiments were done. 100 μL of each sample used for FTIR analysis was taken and dried (under vacuum) on an inert glass surface for Raman studies. Raman spectra of all samples were taken using 532 nm laser excitation. For each set, at least 5 independent experiments were done. Western blot experiment was carried out as reported elsewhere. 200 μg of the whole cell extract was used as samples for cell free and

intracellular tubulin systems, respectively. Samples were given cold shock before running the gel. Control and treated A549 cellular protein were collected after cold induced depolymerization for 6 h at 4 °C. Western blot was done after running 6% non-reducing SDS PAGE, using mouse monoclonal anti-α-tubulin antibody as the primary and HRP conjugated goat monoclonal anti-mouse IgG as the secondary antibody. Protein bands were detected in X-ray films using the chemiluminescence technique. Anti-actin and anti-GADPH antibodies were used for the detection in the experiment.

2.7 *In vitro* cell line experiments

Human lung carcinoma A549 and human breast cancer MCF-7 cells were maintained in Ham's F12 supplemented with 1 mM L-glutamine, 10% fetal bovine serum, 0.2% $NaHCO_3$, 1 mM penicillin, 1 mM streptomycin and 1 mM fungizone pH 7.4. Cells were cultured at 37 °C in a humidified atmosphere containing 5% CO_2. Fresh media as well as fresh AuNPs were added every 24 h of the treatment. For each dose, approximately 1×10^6 cells were taken in a 35 mm tissue culture plate and each experiment was repeated at least 5 times.[40,51,52] To analyse the cytotoxic effects of AuNPs, 25 pM of $AuNP_{20}$, $AuNP_{40}$ and $AuNP_{60}$ were incubated for 72 h and the cell viability assay was performed by a trypan blue viable cell count method.[40] For each set, at least 5000 cell counts were taken. To analyse the effect of $AuNP_{40}$ on cell cycle progression, cultured A549 cells were treated with different concentrations of $AuNP_{40}$ (12.5 and 25.0 pM) along with the control for 72 h. After the treatment, cells were fixed with methanol and treated with RNase A and then stained with propidium iodide and cell cycle analysis was carried out in a flow cytometer. To study the apoptotic effect, $AuNP_{40}$ (12.5 and 25.0 pM) treated cells were processed with fluorescence isothiocyanate (FITC)-conjugated Annexin V for 15 minutes at room temperature in a calcium enriched buffer. Propidium iodide (PI) was used as the counter stain for flow cytometric analysis. To study the effect of $AuNP_{40}$ on cellular morphology, A549 cells were grown on coverslips at a concentration around 1×10^5 cm^{-2} and treated with $AuNP_{40}$ as previously mentioned and bright field images were taken. MTs of A549 cells were stained using mouse monoclonal anti-α-tubulin antibody (Sigma) at 1 : 100 dilution and rhodamine conjugated goat monoclonal anti-mouse IgG secondary antibody (Santa Cruz Biotechnology) at 1 : 150 dilution. After staining, confocal images were taken. The cells were treated for a period of 12 h, and 24 h with 25 pM of $AuNP_{40}$ on glass slides in an animal cell culture plate. Images were taken after repeated 1× PBS wash at 37 °C using a halogen lamp (400–1000 nm) as the light source at 100× magnification.

3 Results and discussion

3.1 Structural changes due to tubulin AuNP interactions in a cell free system

Citrate capped spherical AuNPs with sizes of 20 nm ($AuNP_{20}$), 40 nm ($AuNP_{40}$) and 60 nm ($AuNP_{60}$) were prepared by a standard method.[47] AuNP sizes were calculated from the observed extinction coefficients in UV-Vis spectroscopic studies and were further confirmed by electron microscopic studies (Fig. S1†). The polymerization reaction mixture containing 12 μM of tubulin was incubated with 15 pM AuNPs and the surface plasmon resonance (SPR) was monitored by UV-Vis spectroscopy (Fig. 1).

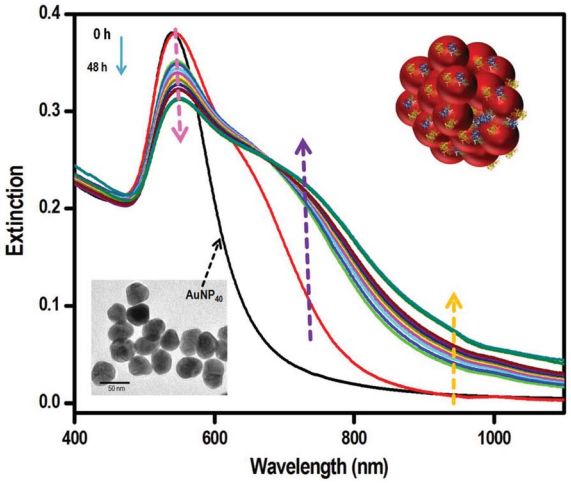

Fig. 1 Structural changes of $AuNP_{40}$ due to interaction with tubulin: shift of SPR of $AuNP_{40}$ (black solid line) from 532 nm to 540 nm (red solid line) due to the initial association of tubulin and change of the dielectric constant of the environment. As a function of incubation time with tubulin, while the SPR intensity at 540 nm decreases, a new plasmon peak, possibly due to closely spaced NPs appears in the near infrared at 750 nm (purple dotted arrow). The increase in the background signal near 1000 nm (yellow dotted arrow) indicates aggregation. Inset (down, left): TEM image showing parent $AuNP_{40}$ (scale bar is 50 nm). Inset (up, right): schematic representation of the closely spaced nanoparticles in association with the protein molecules.

We observed a slight 8 nm red shift, immediately upon the addition of $AuNP_{40}$ to the tubulin mixture which is likely to be due to the change in the dielectric constant of the nanoparticle's environment, induced by the surrounding proteins. As a function of time, while we observed a decrease in the SPR of $AuNP_{40}$ at 540 nm, there was an increase in the absorbance in the NIR region with a single isosbestic point at 683 nm and a new plasmonic peak developed around 750 nm. Increase in the background signal near 1000 nm was also observed which can be attributed to close spacing of AuNPs or aggregation[9,54] (Fig. 1). The presence of a single isosbestic point suggests the involvement of a single intermediate state between the two forms of particles (single particles and protein induced aggregated ones).

To know the fate of the protein's functionality due to the interaction, we monitored the scattering[50] at 350 nm for 30 minutes which corresponds to polymerization of tubulin into MT. Results suggested that AuNPs inhibited the polymerization process significantly. Among the three different sized NPs used for the experiment, $AuNP_{40}$ showed maximum inhibition of polymerization to the extent of 46.13 ± 3.1% while $AuNP_{20}$ and $AuNP_{60}$ showed 12.87 ± 3.2% and 23.91 ± 4.1%, respectively (Fig. 2A) (Table 1). Since $AuNP_{40}$ showed high polymerization inhibition, we chose this system for further microscopic and

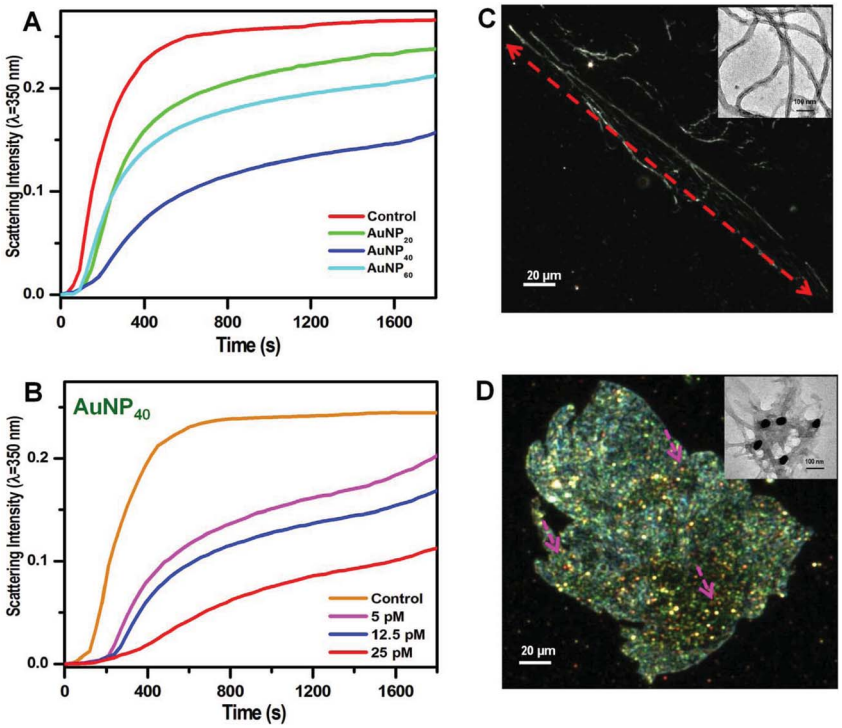

Fig. 2 Effect of AuNPs on the polymerization of purified mammalian tubulin: (A) plots showing the inhibition of polymerization by three differently sized AuNPs. $AuNP_{40}$ (blue solid line) shows maximum initial delay and inhibition of polymerization. (B) $AuNP_{40}$ shows concentration-dependent inhibition of polymerization. (C) Dark field microscopic image (scale bar 20 μm) of polymerized tubulin (MT) in the absence of $AuNP_{40}$ (the red-dotted double sided arrow indicates the formation of long MT). The inset is a transmission electron microscopic (TEM) image (scale bar 100 nm) showing polymerized MT stained with uranyl acetate in the absence of $AuNP_{40}$. (D) In the presence of 25 pM $AuNP_{40}$, MT was not formed, instead extended amorphous aggregates were formed. The dark field microscopic image (scale bar 20 μm) shows one such large aggregate; bright yellow, red and blue spots are $AuNP_{40}$ particles (magenta dotted arrows point at AuNPs) and the inset TEM image (scale bar 100 nm) shows the nanoparticle-induced protein aggregation. Note that very few NPs cause aggregation of a huge number of protein molecules.

spectroscopic studies to probe the reason behind the inhibition of polymerization.

We further studied the concentration dependent inhibition of polymerization by $AuNP_{40}$ at 5.0, 12.5 and 25.0 pM concentrations which exhibited respectively, $28.6 \pm 2.7\%$, $40.32 \pm 1.7\%$ and $60.47 \pm 3.5\%$ inhibition (Fig. 2B) (Table 2). From these observations, we calculated the concentration required for 50% inhibition of polymerization.

The calculated IC_{50} was 18.6 ± 0.9 pM (Fig. S2†) and the molar ratio between $AuNP_{40}$ and tubulin was $1 : 3.16 \times 10^5$ (see the ESI† for the calculation). This implies that a single AuNP is enough to create an avalanche of aggregation when coming in contact with tubulin inside a cell. In order to observe the aggregates, we carried out hyper-spectral imaging using dark field microscopy and TEM studies of tubulin–reaction mixtures with and without $AuNP_{40}$, incubated for the formation of MT. Reaction mixtures without $AuNP_{40}$ formed long fiber-like structures of MT (Fig. 2C) (the inset shows a TEM image), while the reaction mixture with 25 pM $AuNP_{40}$ formed random tubulin aggregates. The association of the nanoparticles with protein aggregates is clear from the figures. In the hyper-spectral image, the red and yellow spots show that they are nanoparticles (Fig. 2D). The inset of the figure shows a TEM image of a portion of such an aggregate. Since we observed that a single nanoparticle could cause 10^5 tubulin molecules to aggregate (Fig. S2†) and all protein molecules could not have interacted with the available AuNPs, there must be a conformational-change-based protein aggregation mechanism, as observed in some neuronal diseases and previous studies.[7,8] To test whether the inhibition of polymerization and aggregate formation (Fig. 2) are due to conformational changes caused by AuNPs, we probed the conformational changes of the protein by a set of standard analytical techniques. Direct microscopic and UV-Vis spectroscopic studies revealed that $AuNP_{40}$ interacted with purified mammalian tubulin and caused aggregation. But surprisingly, circular dichroism (CD) studies showed very little changes in the conformation of MT (Fig. S3†). Hence, to probe the change, Raman spectroscopic investigation was carried out (Fig. 3). Raman spectroscopy can provide insights into the structural modifications in protein upon its interaction with AuNPs.[9] The amide bonds which link amino acids are amide-I, amide-II and

Table 1 Percentage of inhibition of polymerization of tubulin by three differently sized AuNPs

AuNPs (15 pM)	Absorption maximum (nm)	Size of AuNPs (nm)	Inhibition of polymerization (%)
$AuNP_{20}$	525	20	12.87 ± 3.2
$AuNP_{40}$	532	40	46.13 ± 3.1
$AuNP_{60}$	537	60	23.91 ± 4.1

Table 2 Concentration dependent inhibition of polymerization of tubulin by $AuNP_{40}$

Concentration of $AuNP_{40}$ (pM)	Inhibition of polymerization (%)
5.0	28.6 ± 2.7
12.5	40.3 ± 1.7
25.0	60.5 ± 3.5

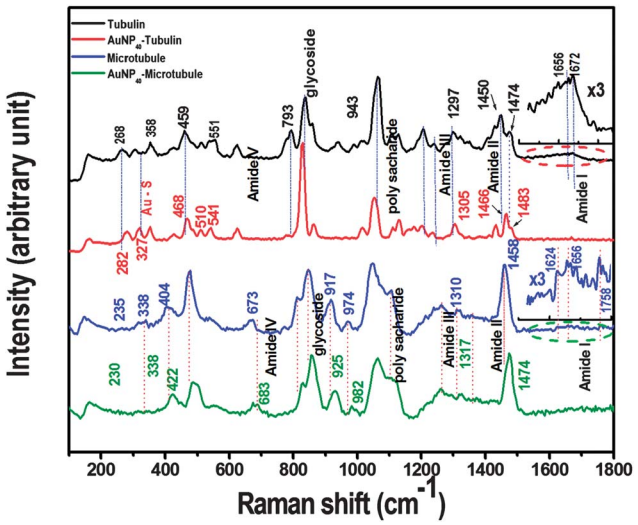

Fig. 3 Raman spectral features for MT and tubulin upon $AuNP_{40}$ treatment: various curves are labelled with the corresponding colors. Important regions (amide-I, amide-II, amide-III, amide-IV, amide-V and glycoside linkage) have been marked by the name of the prominent bond in the region and are discussed in the text and in Table 3. Specific regions are multiplied by 3 to show the features clearly.

amide-III, which give specific vibrational bands in the range of 1600–1690, 1480–1575, 1229–1301 cm^{-1}, respectively.

Other amide vibrational bands come in the range of 625–767 cm^{-1} (OCN bending), 640–800 cm^{-1} (out of plane NH bending), 537–606 cm^{-1} (out of plane C═O bending), and 200–300 cm^{-1} (skeletal torsions) which are assigned as amide-IV, amide-V, amide-VI and amide-VII, respectively.

The amide-I vibrational structure is the most sensitive among all and any alteration of it is a signature for protein secondary structure modification. $AuNP_{40}$ induced some changes in the secondary structures of both the forms (MT and tubulin heterodimer) of the protein. In both the cases, $AuNP_{40}$ altered the protein β sheet regions. In addition to that, alteration at the α-helix region of MT was also observed. Though all the Raman features are not fully understood, alterations in structural features show partial conformational changes. In both sets of our experiment, we observed changes in the protein features (Fig. 3). Each measurement was repeated up to 5 times and in the presence of AuNPs, enhancement in the Raman spectral intensity was observed due to SERS. The Raman feature at 1655 cm^{-1} is due to amide-I (C═O stretching in combination with the contributions from C–N stretching) of the protein's random coiled structure. In the case of tubulin, the shoulder at 1656 cm^{-1} got shifted to a very weak feature at 1668 cm^{-1}, while the other feature at 1672 cm^{-1} disappeared completely upon treatment with AuNPs indicating a possible modification of the secondary structure. In the case of MT, the weak feature at 1656 cm^{-1} disappeared upon interaction with AuNPs. The feature at 1624 cm^{-1} due to the β sheet of MT got shifted to 1628 cm^{-1} upon interaction with AuNPs. The amide II (N–H deformation and contribution from C–N stretching) feature for tubulin β sheets at 1474 cm^{-1} got shifted to 1483 cm^{-1} and the similar feature for MT at 1458 cm^{-1} got shifted to 1474 cm^{-1} during the interaction. The amide II feature for the tubulin α helix at 1450 cm^{-1} was shifted to 1468 cm^{-1}. There was no corresponding feature in the case of MT.[55] Au–S stretching at ~327 cm^{-1} was observed in the $AuNP_{40}$–tubulin sample[56] but was not observed in the AuNP–MT sample; this may suggest that the interaction leading to aggregation requires a specific site or chemical moiety of the tubulin monomer. Since tubulin does not have any disulphide bond, no stretching at 504 or 524 cm^{-1} was observed.[9] Structural modifications upon interaction with AuNPs were observed in various regions like amide III, IV and V and C–O–C bending region (symmetric and asymmetric) as evident from Table 3.

We have also compared FTIR and second derivative FTIR spectra of tubulin and MT before and after interaction with AuNPs. The second derivative of FTIR is sensitive and typically used to analyse the conformational changes in the amide I region of the protein where the changes are difficult to be observed in the primary spectra.[10] Direct comparison of FTIR spectra has not revealed anything significant (Fig. S4†). The amide I (1600–1690 cm^{-1}) band observed is due to characteristic stretching and bending vibrations of the amide bonds, most sensitive to protein secondary structures. Hence we have studied and compared the second derivative of the FTIR spectra in this window (Fig. 4). The band appearing at 1654 cm^{-1} is assigned to the α helix and the bands appearing at 1648 and 1640 cm^{-1} are attributed to disordered α-helices (random coil). The prominent band for β-sheets is observed at 1685 cm^{-1}; it also shows signatures at 1634 and 1627 cm^{-1}. The bands between 1664 and 1682 cm^{-1} are assigned to β-turns.[10] The comparison between spectra of tubulin before and after interaction with AuNPs has shown that there is substantial decrease in the intensity of bands for secondary structures after interaction and is an evidence for the structural changes; such changes could have led to aggregation. However, in the case of MT (polymerized tubulin), no significant changes were observed in the spectra after interaction with $AuNP_{40}$.

In a recent study, Ratnikova *et al.* reported that hydrogen bonding between a tubulin heterodimer and a fullerene derivative can induce conformational change and inhibit polymerization.[46] Hence, not only thiol–Au mediated conformational change, but also interaction of other chemical groups of the protein with AuNPs could contribute to partial conformational change. The exact mechanisms and the chemical moieties involved in these processes would be investigated in detail in a subsequent computational and experimental study.

Each tubulin heterodimer has 12 tryptophan residues which are distributed heterogeneously in α and β-subunits. Direct interaction of a ligand with tubulin may quench the intrinsic

Table 3 Observed Raman shifts (in cm^{-1}) of $AuNP_{40}$-treated MT and tubulin[9,55,56]

MT	$AuNP_{40}$–MT	Possible bond	Tubulin	$AuNP_{40}$–tubulin	Possible bond
235	235	C–C	268	282	C–C
338	338	C–O–C of glycoside		327	Au–S
404	420	—	352	352	—
478	486		427	427	—
528	542	C═O	459	468	
669	673	C═S	551	510	C═O
771	789	O–C–N bending	623	623	C═S
811	824	N–H bending out of plane	793	776	O–C–N bending
847	860	C–O–C	838	829	N–H bending out of plane
917	925	C–O–C	—	864	C–O–C
974	982	Polysaccharide back bones	943	—	C–O–C
1047	1060	Polysaccharide back bones	987	—	Polysaccharide back bones
1107	1102	C–O–C asymmetric	1012	1016	Polysaccharide back bones
1213	1217	Amide III (α helix)	1064	1051	Polysaccharide back bones
1264	1259	Amide III (β sheets)	1107	1111	C–O–C asymmetric
1310	1317	Amide III (random coils)	1128	1128	C═S
1355	1371	C–H bend	1187	1175	—
1458	1474	Amide II (β sheets)	1204	1201	C–C–O stretching
1624	1628	Amide I (β sheets)	1242	1234	Amide III (α helix)
1656	—	Amide I (random coils)	1297	1305	Amide III (β sheets)
—	1700		1322	1326	Amide III (random coils)
1758	—	C═O of alkyl ester	1351	1347	C–H bend
			1450	1468	Amide II (α helix)
			1474	1483	Amide II (β sheets)
			1656	1668	Amide I (random coils)

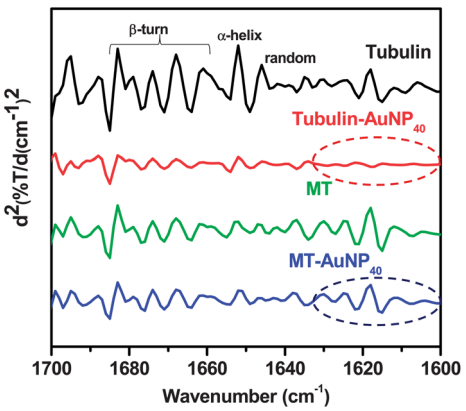

Fig. 4 The second derivative FTIR spectra of the amide I region of tubulin and MT upon interaction with $AuNP_{40}$. Comparisons between specific regions are shown with dotted oval shapes.

tryptophan fluorescence of tubulin. The tryptophan quenching assay (Fig. S5†) also suggested the possibility of the conformational change of the protein upon nanoparticle interaction. Quenching can be due to alteration of the structure or association of AuNPs with the protein (as AuNPs are known to quench fluorescence). Further, as the tubulin heterodimer contains 20 cysteine residues, to monitor the modification of thiol, we did thiol estimation of AuNPs treated tubulin which revealed a loss of 0.6–1 cysteine residues, a loss of 3–5% of the total cysteine content per heterodimer. Even in the case of 25.0 pM $AuNP_{40}$ treatment, we observed only 3–5% loss of the total cysteine content (Fig. S6†). These results indicated that not all thiols are modified and most of them remain free, which further supports the suggestion that conformational change is partial and is reinforced by the Raman spectroscopic observations. To check whether the polymerized tubulins (MT) get depolymerized by the AuNPs (akin to the effect caused by certain MT depolymerising drugs), we monitored the scattering at 350 nm by adding different concentrations of $AuNP_{40}$ to polymerization saturated MT. No significant depolymerization was observed even in the presence of 25 pM of $AuNP_{40}$ (Fig. S7†). These observations further corroborate the results obtained in Raman and FT-IR investigation that polymerized tubulin may undergo lesser conformational changes than free tubulin.

From all the observations made in the cell free system, we have demonstrated that weakly protected AuNPs induce partial conformational changes in tubulin which in turn inhibit polymerization and cause aggregation. One should note that not all proteins undergo such conformational change-based extended aggregation, for example BSA does not get aggregated due to interaction with citrate capped AuNPs;[9,57] thus the observed tubulin aggregation becomes crucial from the point of view of nanotoxicity since it is involved in cellular transport, cell cycle and cell shape stability. Halas *et al.* have also shown that upon protecting the AuNPs with bulky groups such as polyethylene glycol, such extended protein mediated aggregations do not take place.[9] Hence understanding the interaction of bare AuNPs with tubulin becomes crucial. If such an aggregation process happens inside the cell, it is likely to cause cell cycle arrest and apoptosis, and we hypothesized this could be one of the reasons for the selective toxicity observed in the A549 cell line which is a well-known model for microtubule-based studies.

3.2 *In vitro* cell line experiments

To test the above mentioned hypothesis, we incubated the AuNPs of three different sizes (Table 1) for cell viability assay, with the lung cancer cell line (A549), which has a prominent MT network, a widely used cell line in MT targeted drug studies. The cell viability assay results obtained for a 72 h incubation period indicated that $AuNP_{40}$ had the maximum cytotoxicity effect among the three different NPs tested, leaving only 49.86 ± 3.68% of the cells viable while $AuNP_{20}$ and $AuNP_{60}$ left 80.57 ± 4.72% and 59.34 ± 2.75% of cells viable, respectively (Fig. 5A upper panel and Table 4). Cell viability was high for other time intervals, 12, 24 and 48 h, for all three sizes of AuNPs and for different incubation concentrations (Fig. S11†). It has been observed that 40 to 50 nm sized nanoparticles are uptaken more.[58,59] Wei *et al.* observed that 45 nm AuNPs were uptaken more and present in the cytoplasm of lung cancer and HeLa cells using dark field optical sectioning microscopy.[60] This may be the reason for the observed effect: more the uptake, higher the probability of membrane disruption and hence more the probability of toxicity.[61] Since $AuNP_{40}$ caused the maximum cytotoxic effect, we further examined $AuNP_{40}$ treated cells for cell viability, cell cycle arrest, MT damage and apoptosis as a function of its concentration. It indicated that at 12.5 and 25.0 pM of the NPs, 26.0 ± 1.3% and 41.2 ± 2.5% of the cells were in the sub G_0/G_1 phase (hypoploidy) respectively, while only 4.3 ± 0.3% of the control population was in the sub-G_0/G_1 phase (Fig. 5B and C). The calculated IC_{50} value for A549 cells was 29.5 ± 1.7 pM (Fig. S8†). Among a live cell population, the control set had 59.9 ± 1.4% of cells in the G_0/G_1 phase while 12.5 and 25.0 pM $AuNP_{40}$ treated cells had 65.6 ± 1.8% and 71.9 ± 1.1% of the cell population in the G_0/G_1 phase (Fig. 5C and Table 4). These results indicate that AuNPs induce cell cycle arrest at the G_0/G_1 phase (Table 4). To check whether there are onco-cellular apoptosis and cell death pattern, we conducted flow cytometric Annexin V/PI assay. The assay revealed that 72 h incubation of cells with 12.5 and 25.0 pM $AuNP_{40}$ resulted in 22 ± 1% (early = 16.07 ± 0.26% and late = 5.72 ± 0.57%) and 47 ± 1.5% (early = 30.85 ± 0.7 and late = 17.68 ± 0.91%) apoptotic populations, respectively, while the control had only 3 ± 0.5% (early = 2.39 ± 0.23% and late = 0.7 ± 0.14%) apoptotic population (Fig. 5D). Further, investigation of cell

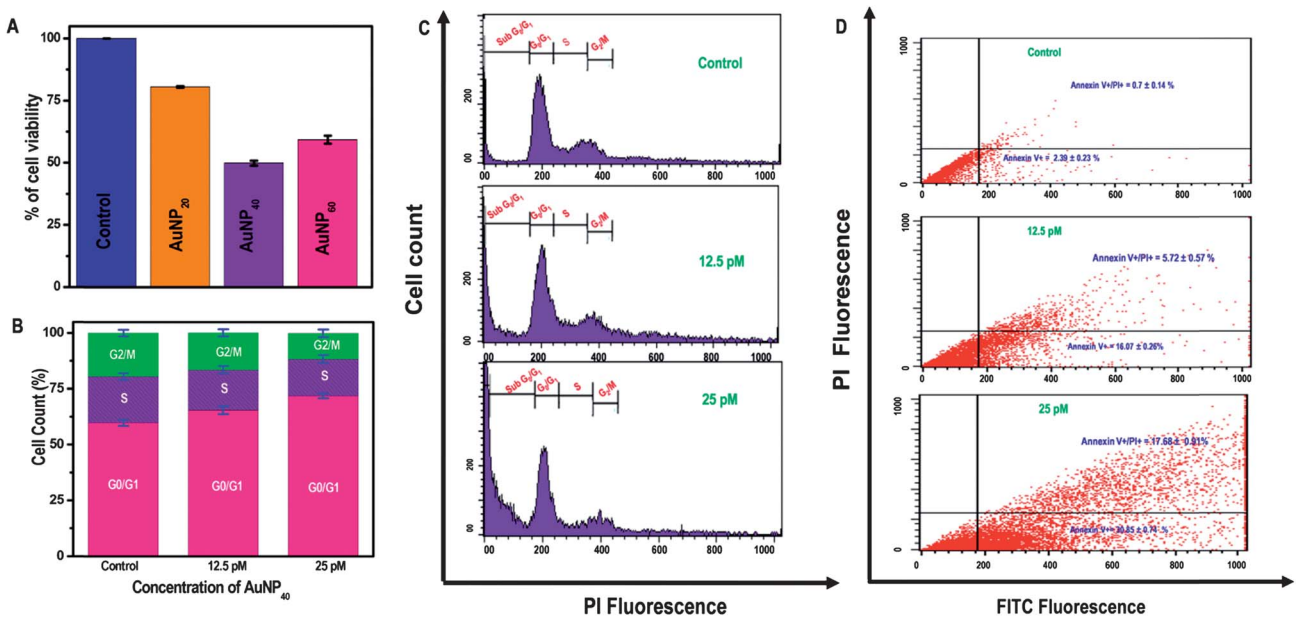

Fig. 5 Effect of AuNPs on cell viability and cell cycle distribution pattern: (A) percentage of cell viability upon incubation with 12.5 pM AuNPs of different sizes for 72 h. (B) Histogram showing cell cycle phase distribution of residual live cells after 72 h of $AuNP_{40}$ treatment (C). FACS data revealing G_0/G_1 cell cycle arrest and induction of A549 cell death after incubation with different concentrations (0, 12.5 and 25.0 pM) of $AuNP_{40}$ for 72 h. (D) Annexin V/PI assay revealing the $AuNP_{40}$ induced apoptosis in lung cancer cells in a concentration dependent manner.

Table 4 Results of flow cytometric cell cycle and Annexin V assays with A549 cells incubated with $AuNP_{40}$ at different concentrations for 72 h. Live cell population alone was considered for cell cycle calculations

			Apoptotic cells %		
Concentration of $AuNP_{40}$	Sub G_0/G_1 %	G_0/G_1 %	Early	Late	Total
Control (0 pM)	4.3 ± 0.3	59.9 ± 1.4	2.39 ± 0.23	0.7 ± 0.14	3 ± 0.5
12.5 pM	26.0 ± 1.3	65.6 ± 1.8	16.07 ± 0.26	5.72 ± 0.57	22 ± 1
25.0 pM	41.2 ± 2.5	71.9 ± 1.1	17.68 ± 0.91	30.85 ± 0.74	47 ± 1

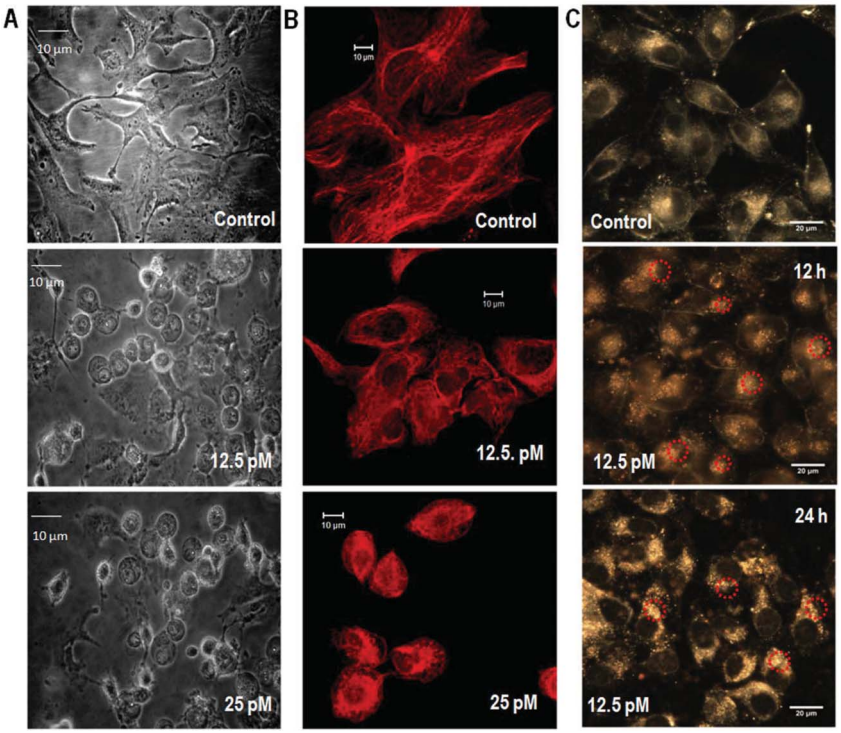

Fig. 6 (A) Phase contrast and (B) confocal images of control and $AuNP_{40}$ treated samples. $AuNP_{40}$ treated samples show MT damage while the control cells show a normal MT network after 72 h. (C) DFM images of the control and treated cells. The right top image is the control and the middle one is 25 pM $AuNP_{40}$ treated cells (incubation time 12 h) which show shrinkage when compared to the control. The right bottom is 12.5 pM $AuNP_{40}$-treated cells (for 24 h) showing more shrinkage than 12 h treated cells. In both 12 h treated and 24 h treated samples, scattering is seen which is distinctly different from that of scattering produced by vesicles in the normal, untreated cells (Fig. S9†). Some of the nanoparticles are labelled with dotted circles in the middle and bottom-most images of C.

morphology by phase contrast microscopy upon $AuNP_{40}$ treatment showed disruption of cell morphology and shrinkage of cellular periphery in a dose dependent manner (Fig. 6A). In phase contrast images, the observed MT network pattern in control samples was well distributed and extended, exhibiting a normal cytoskeletal structure while the $AuNP_{40}$ treated cells showed a damaged and shrunken MT network (Fig. 6B). 12.5 pM and 25.0 pM $AuNP_{40}$ treated cells were immunofluorescent stained with monoclonal anti-α-tubulin antibody and TRITC conjugated anti-mouse IgG secondary antibody. CLSM images were obtained to analyse the morphology. In 12.5 pM treated cells, peripheral MT were damaged and shrunken moderately while in 25.0 pM treated cells, the MT network was damaged extensively (Fig. 6B).

Recently, dark field microscopy (DFM) has been employed to probe the nanoparticle–cell interaction and to study the metabolic processes of cells, particularly in the presence of plasmonic nanoparticle-based smart-constructions to decipher the secrets of cells in real time.[62–64] The uptake of AuNPs by the cells was confirmed by DFM investigation using a hyperspectral imaging system. Hyperspectral imaging of the cells with NPs revealed that the particles were observed in the cytosol of the cell and not in the nucleus, though they were seen around the perinuclear membrane area (Fig. 6C and D). However, during the later period of incubation, nuclear morphology changes were observed, though no nanoparticles entered the nucleus. This can be attributed to the microtubule damage effect, as it is observed that microtubule-damaging drugs induce changes of nuclear morphology. Untreated cells also exhibited some scattering due to vesicles, but the cells with nanoparticles had higher plasmonic scattering which was distinctly different from that of scattering caused by vesicles (Fig. S9†). Shrinkage of the cytosolic portion of the cell was also observed with time (Fig. 6C, 12 h and 24 h). The positive control for MT damage was carried out with vinblastine, as it is known to destabilize MT and it was used for comparison (Fig. S10†).

To check whether actin also was damaged as a function of time, we stained both actin and tubulin with their respective antibodies and analysed in CLSM. In Fig. 7A it can be seen that after 12 and 24 h of incubation, MT (red) is more damaged and disrupted than actin (green) which leads to cell morphology change. To check whether $AuNP_{40}$ could cause aggregation of the tubulin–MT system intracellularly as well and whether the observed apoptosis is due to microtubule damage mediation, we carried out western blot. The experiment was carried out after giving cold shock to the formed microtubules (to the cell extract) which is necessary for depolymerization. A normal microtubule would depolymerize and give rise to tubulin monomers, but the aggregated tubulin–MT system would not become monomers. We compared the control cellular extract of treated and untreated cells by western blot after running in a 6% non-reducing SDS PAGE. We did not observe any aggregation of tubulin in the cellular extract collected from untreated cells (Fig. 7B, lane 1), while western blot of $AuNP_{40}$ treated cells

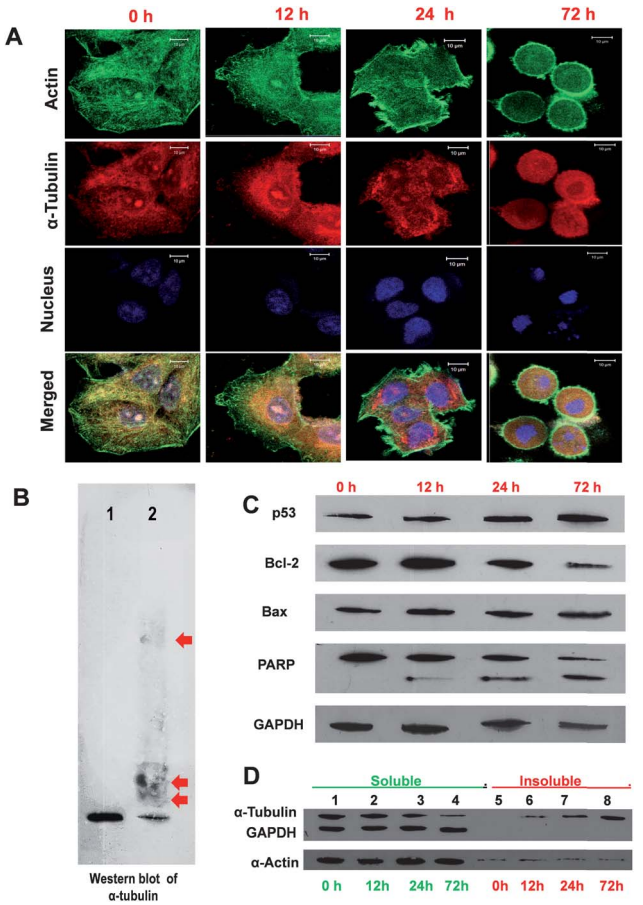

Fig. 7 (A) Confocal fluorescence images of A549 cells treated with $AuNP_{40}$ showing intracellular damage of microtubules as a function of time. Actin and tubulin microtubule are stained with their respective antibodies (actin-green and tubulin-red) and the nucleus is stained with DAPI. I, II, III and IV columns represent incubation times (with $AuNP_{40}$) of 0 h, 12 h, 24 h and 72 h, respectively. The scale bar is 10 μm. The positive control with vinblastine is provided in the ESI, Fig. S10.† (B) Western blot data showing non-aggregated tubulin in control cells (lane 1) and aggregated tubulin in AuNP treated cells (lane 2). (C) Western blot shows upregulation of apoptotic proteins p53 Bax/Bcl-2 and PARP cleavage (GADPH is the loading control). (D) Western blot done after cold depolymerization showing an increase in the aggregated insoluble tubulin while actin does not increase. The loading control GADPH does not aggregate suggesting that the microtubule was damaged and aggregated which induced concomitant cell cycle arrest and apoptosis.

showed tubulin aggregation (Fig. 7B, lane 2). In all cases protein aggregation sizes varied, suggesting that big tubulin aggregates are less likely to be stable and they easily disassociate when treated with SDS (Fig. 7B, lane 2). This signifies less involvement of covalent linkages (S–S, S–Au bonds), which is supported by the observation that less cysteine residues are modified due to AuNPs interaction (Fig. S7†). Hence, the aggregates may not be very stable in nature and easily get disrupted when treated by SDS. This indicates that the protein aggregates are not only formed due to covalent interactions with AuNPs but also due to weak interactions which have to be investigated in future to find the exact mechanism. Supporting the above view of weak interactions, in a study Zhou *et al.* have fabricated AuNPs in taxol polymerized MT, unlike the present study where direct AuNPs–tubulin interaction is monitored. They have reported that aromatic, imidazole group amino acids of tubulin and carboxylates can interact with AuNPs other than the thiol group of amino acids.[46] Results from *in vitro* intracellular experiments suggest that AuNPs interaction with the tubulin–MT system caused cell cycle arrest and apoptosis. Upregulation of proapoptotic proteins like p53 and Bax and down regulation of anti-apoptotic protein Bcl-2 were found (Fig. 7C). Cleavage of poly(ADP-ribose) polymerase (PARP), which is an indicator that the cell is undergoing apoptosis, was also observed (Fig. 7C). PARP is cleaved by caspases which are produced during mitochondrial apoptosis activation indicating that this is a mitochondrial apoptosis. It is known that microtubule damage induces caspase activation which leads to PARP cleavage as in the case of anti-MT drugs.[65] In Fig. 7A, after 24 h no differentiation between MT and actin damage can be made. Hence to check whether actin or other cellular protein also got aggregated (here we used the loading control), western blot was run after separating soluble and insoluble portions of the cell extract after cold depolymerization. WB results showed increase in tubulin aggregation in the insoluble part while actin and the loading control were not found in the insoluble part of the extract which also suggests that the microtubule is intracellularly damaged and aggregated (Fig. 7D). Another observation is that while the cells were highly viable for almost till 48 h (Fig. S11†) and only at 72 h the viability decreases largely and apoptosis is found; in confocal images at 24 h the initiation of damage of microtubules is clearly seen, which also reveals that the MT damage occurred before apoptosis and the observed apoptosis could be a MT-damage mediated one. It may also explain why we see an increasing ratio in PARP cleavage and other apoptotic signatures as a function of time along with increasing tubulin aggregates (Fig. 7C, D). Acetylation, a post translational modification, which can be one of the reasons for resistance to cold depolymerisation and increased half life of MT also could be ruled out. Upon acetylation, one would expect to see more stable, larger MT bundles (mostly near the cell membrane) without affecting the cell viability, but here instead we see disruption of MT leading to cell cycle arrest and apoptosis, further reinforcing the proposed hypothesis.[66,67] Culha and co-workers attempted to study AuNP-induced damage with the mitochondria of A549 cells; however they found no such damage, and reported that even incubating AuNPs with isolated mitochondria did not cause damage. They also suggested that AuNPs could have escaped the endosome and entered the cytosol in the A549 cell.[68] In a recent study, Dawson and co-workers found intracellular tubulin to be bound among many other bound proteins on the surface of silica and polymeric NPs incubated in the cytosolic fluid.[6] In the same study, they introduced the nanoparticles to human plasma (extracellular fluid) first and collected the particles. Then they subsequently introduced the particles to the cytosolic fluid and observed the binding of cytosolic proteins through re-equilibration of extracellular fluid proteins, revealing the dynamic nature and evolution of the protein corona while transferring from one biological fluid to another. This suggests that AuNPs could behave similarly, though they would interact with

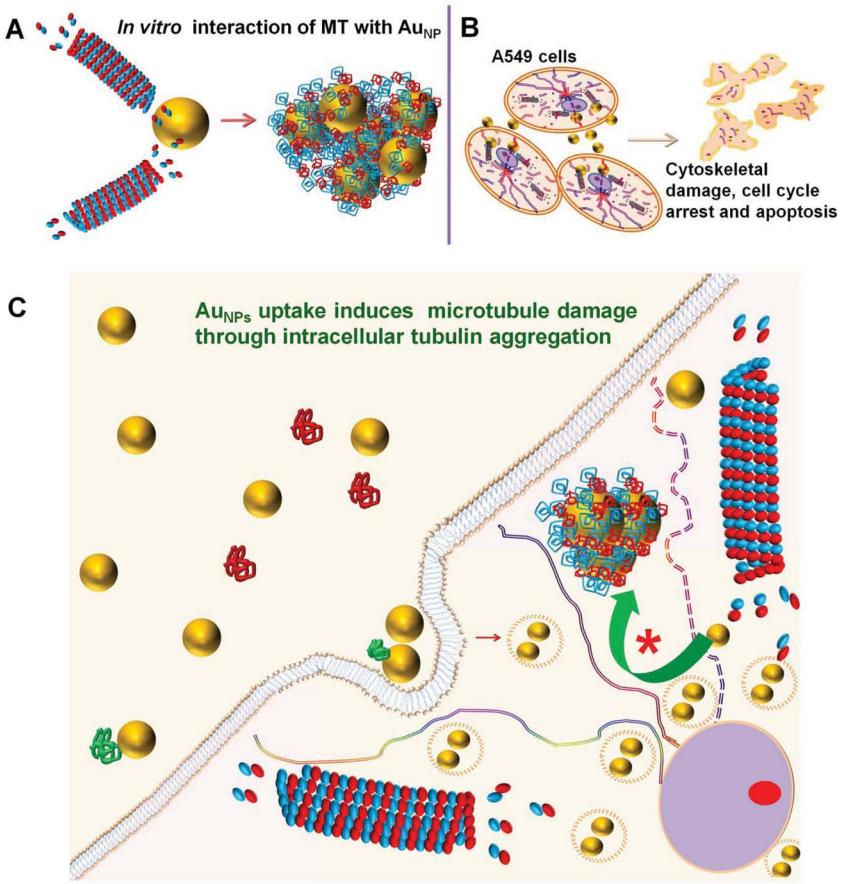

Scheme 1 (A) Representation of AuNPs-induced aggregation of the tubulin–MT system during the polymerization reaction. (B) AuNPs-induced apoptosis *in vitro* in the lung cancer cell line, A549. (C) Schematic of the uptake of AuNPs by A549 cells and insoluble aggregates of tubulin found inside the cell (* (red color) indicates that the intracellular aggregation mechanism is yet to be fully understood), while intracellular tubulin aggregation is clearly evident upon AuNP uptake (see Fig. 7D). The scheme is for illustration purpose only and not to scale.

proteins present in the media. Upon entry into the cell from the cell media or biological fluid, AuNPs could bind to intracellular proteins too through reassociation according to the relative affinities of the interacting proteins with the AuNP surface.[6] In neuronal progenitor cells, it has been observed that polymer coated AuNPs induced cytoskeletal damage.[69] Hence, in the light of the literature and from the observed results such as G_0/G_1 cell cycle arrest and aggregation of intracellular tubulin along with non-aggregation of intracellular actin or GADPH (a house keeping enzyme), it may be concluded that AuNPs interacted with tubulin inside the A549 cells and caused MT damage and subsequent cell cycle arrest and apoptosis. Although we have not studied how exactly AuNPs interact with MT inside the cell, MT damage and aggregation is evident from our observations (Fig. 7D). We also assume that the MT damage is likely to have initiated around the perinuclear region where crowding of AuNPs is seen (Fig. 6C) and where the MTs are nucleated and are densely organized. There are several reports indicating different routes of uptake (including non-specific and unknown routes) of AuNPs,[68,70] however, endocytosis facilitates the nanoparticle uptake prominently.[15] Endosomal escape of nanoparticles is an active area of research which is very important for delivery of drugs and genes. Here the observed effect could take place only if AuNPs escaped from the endosomes or through other unknown routes in which AuNPs were uptaken and have the probability to be present in the cytosol. Recently, Volk and co-workers have shown that gold nanoparticles could escape under low laser intensity (which is too low to cause a photothermal effect) without any photothermal effect from the endosomes and suggested that radical generation could facilitate such an escape.[71] During the late phases, upon maturation of endosomes, we assume that nanoparticles could likely escape.[72] Braeckamns and co-workers suggested that during the late phases the cytoskeleton may be damaged due to the crowding effect of growing nanoparticle containing endosomes.[69] The growth of endosomes upon crowding, ageing, non-thermal membrane disruption and steric effect could have likely resulted in the escape of particles.[61,71,72] However, detailed studies are required to answer these questions which are a subject of future investigation. Apoptosis itself could be caused by several pathways; however, here our observation of the presence of insoluble intracellular aggregation even after cold depolymerisation and the increasing quantity of insoluble aggregates as a function of time suggests a strong contribution of MT damage effect directed by AuNPs and it could be the predominant pathway in this case or one of the

several apotoptic pathways, since multiple toxic effects are seen when gold nanoparticles are uptaken.[69] Nevertheless, the involvement of MT damage in the toxicity effect is clear in the case of A549 cells. The key observations of the present study are illustrated in Scheme 1.

Further, how the presence of AuNPs affects the extracellular matrix and cellular adhesion during the incubation time, their concomitant signalling cascades and how they would in turn remodel or affect the MT would also give much clearer picture of what is happening inside the cell and it is an area of future investigation. We have observed similar effects in the case of the MCF-7 cell line also upon interaction with citrate capped AuNPs (Fig. S12 and S13† for cell viability and microtubule disruption, respectively), although these studies have been limited.

4 Summary and conclusions

In this paper, we have probed the nature of microtubule gold nanoparticle interaction, which has remained unaddressed till date and looked at the toxicity mechanism from the point of view of microtubule damage. Interaction of weakly protected AuNPs with tubulin in the cell free system was investigated in the first part of the study and we found that AuNPs can induce conformational-change-based aggregation in the tubulin–MT system, thus affecting the dynamic equilibrium. Extended aggregates of tubulin with AuNPs were seen by DFM and TEM. Second derivative IR and Raman spectroscopy revealed that partial conformational changes are responsible for the aggregation. Thus we have demonstrated, to the best of our knowledge till date, for the first time that conformational changes induced by the AuNP surface could lead to tubulin–MT aggregation. As the second part of the study, we have checked whether bare AuNPs could do the same inside the A549 cell. The observed experimental results such as G_0/G_1 cell cycle arrest and western blot showing intracellular aggregation of tubulin (while actin and GADPH do not show aggregation) hint that bare gold nanoparticles could cause MT damage-mediated cell cycle arrest and apoptosis in the lung cancer cell line A549, thus providing a plausible explanation for the elusive selective toxicity mechanism of AuNPs in the lung cancer cell line. NMR and computational studies to find the specific sites of tubulin interaction with AuNPs would be carried out in future. Similar studies may be done with engineered tubulin with green fluorescent protein (GFP) to know the *in situ* interaction in live cells. Although there are several reports indicating different uptake pathways of AuNPs, endocytosis plays a prominent role. The endosomal escape of AuNPs is important to cause the observed effects, hence cell biological and synthetic vesicles based studies investigating the bio-physicochemical parameters in which AuNPs' escape is facilitated would be a future study coupled with tubulin polymerization and non-endocytotic delivery experiments, which would help establish the intracellular tubulin aggregation mechanism. Removal of exocytosed AuNPs and quantification of endocytosed particles would also play a significant role in explaining the observed effect in future along with cell-cycle and cell-recovery based studies. We believe that this study offers a new insight into AuNP toxicity and would be useful in cancer therapeutics (where independent activity of AuNPs or the potential of AuNPs in synergy with MT cancer drugs could be harnessed to treat drug resistant lung and other cancer cells susceptible to AuNPs, since intracellular MT damaging property of AuNPs may not be resisted by drug resistant cancer cells) and understanding the safety of nanomaterials.

Acknowledgements

The work was supported by grants from DST, Govt of India (no. SR/SO/BB-14/2008) and the Nanoscience and Nanotechnology Program, University of Calcutta (sanction no. conv/042/NanoPr/2009) awarded to GC. Confocal microscope and FACS facilities were developed by the grant from the National Common Minimum Program, Govt of India. DC is supported by a fellowship from CSIR, Govt of India. DC thanks Dr Hirak Kumar Patra, Dept of Biochemistry, University of Calcutta for discussions. TP thanks the Department of Science and Technology, Government of India for constantly supporting his research program on nanomaterials.

References

1 A. E. Nel, L. Madler, D. Velegol, T. Xia, E. M. V. Hoek, P. Somasundaran, F. Klaessig, V. Castranova and M. Thompson, *Nat. Mater.*, 2009, **8**, 543–557.
2 G. Zuo, Q. Huang, G. Wei, R. Zhou and H. Fang, *ACS Nano*, 2010, **12**, 7508–7514.
3 Z. J. Deng, M. Liang, M. Monteiro, I. Toth and R. F. Minchin, *Nat. Nanotechnol.*, 2011, **6**, 39–44.
4 L. Calzolai, F. Franchini, D. Gilliland and F. Rossi, *Nano Lett.*, 2010, **10**, 3101–3105.
5 T. Cedervall, I. Lynch, S. Lindman, T. Berggård, E. Thulin, H. Nilsson, K. A. Dawson and S. Linse, *Proc. Natl. Acad. Sci. U. S. A.*, 2007, **104**, 2050–2055.
6 M. Lundqvist, J. Stigler, T. Cedervall, T. Berggard, M. B. Flanagan, I. Lynch, G. Eliaz and K. Dawson, *ACS Nano*, 2011, **5**, 7503–7509.
7 V. L. Colvin and K. M. Kulinowski, *Proc. Natl. Acad. Sci. U. S. A.*, 2007, **104**, 8679–8680.
8 L. Fei and S. Perrett, *Int. J. Mol. Sci.*, 2009, **10**, 646–655.
9 D. Zhang, O. Neumann, H. Wang, V. M. Yuwono, A. Barhoumi, M. Perham, J. D. Hartgerink, P. Wittung-Stafshede and N. J. Halas, *Nano Lett.*, 2009, **2**, 666–671.
10 P. L. Xavier, K. Chaudhari, P. K. Verma, S. K. Pal and T. Pradeep, *Nanoscale*, 2010, **2**, 2769–2776.
11 W. Shang, J. H. Nuffer, V. A. Muñiz-Papandrea, W. Colón, R. W. Siegel and J. S. Dordick, *Small*, 2009, **5**, 470–476.
12 S. J. Soenen, P. Rivera-Gil, J. M. Montenegro, W. J. Parak, S. C. D. Smedt and K. Braeckmans, *Nano Today*, 2011, **6**, 446–465.
13 H. D. Summers, P. Rees, M. D. Holton, M. R. Brown, S. C. Chappell, P. J. Smith and R. J. Errington, *Nat. Nanotechnol.*, 2011, **6**, 170–174.
14 T. G. Iversen, T. Skotland and K. Sandvig, *Nano Today*, 2011, **6**, 176–185.

15 R. Lévy, U. Shaheen, Y. Cesbron and V. Sée, *Nano Rev.*, 2010, **1**, 4889.
16 E. C. Dreaden, A. M. Alkilany, X. Huang, C. J. Murphy and M. A. El-Sayed, *Chem. Soc. Rev.*, 2012, **41**, 2740–2779.
17 P. Ghosh, G. Han, M. De, C. K. Kim and V. M. Rotello, *Adv. Drug Delivery Rev.*, 2008, **60**, 1307–1315.
18 B. Kang, M. A. Mackey and M. A. El-Sayed, *J. Am. Chem. Soc.*, 2010, **132**, 1517–1519.
19 S. Mallidi, T. Larson, J. Tam, P. P. Joshi, A. Karpiouk, K. Sokolov and S. Emelianov, *Nano Lett.*, 2009, **9**, 2825–2831.
20 S. Dhar, V. Mali, S. Bodhankar, A. Shiras, B. L. V. Prasad and V. Pokharkar, *J. Appl. Toxicol.*, 2011, **5**, 411–420.
21 J. Nam, N. Won, H. Jin, H. Chung and S. Kim, *J. Am. Chem. Soc.*, 2009, **131**, 13639–13645.
22 W. Lu, S. R. Arumugam, D. Senapati, A. K. Singh, T. Arbneshi, S. A. Khan, H. Yu and P. C. Ray, *ACS Nano*, 2010, **4**, 1739–1749.
23 X. Huang, P. K. Jain, I. H. El-Sayed and M. A. El-Sayed, *Lasers Med. Sci.*, 2008, **23**, 217–228.
24 C. A. Simpson, B. J. Huffman, A. E. Gerdon and D. E. Cliffel, *Chem. Res. Toxicol.*, 2010, **23**, 1608–1616.
25 Y. Zhao, X. Gu, H. Ma, X. He, M. Liu and Y. Ding, *J. Phys. Chem. C*, 2011, **115**, 12797–12802.
26 N. M. Schaeublin, L. K. Braydich-Stolle, A. M. Schrand, J. M. Miller, J. Hutchison, J. J. Schlager and S. M. Hussain, *Nanoscale*, 2011, **3**, 410–420.
27 H. K. Patra, S. Banerjee, U. Chaudhuri, P. Lahiri and A. K. Dasgupta, *Nanomedicine*, 2007, **3**, 111–119.
28 C. Grabinski, N. Schaeublin, A. Wijaya, H. D'Couto, S. H. Baxamusa, K. H. Schifferli and S. M. Hussain, *ACS Nano*, 2011, **5**, 2870–2879.
29 T. S. Hauck, A. A. Ghazani and W. C. Chan, *Small*, 2008, **4**, 153–159.
30 S. Wang, W. Lu, O. Tovmachenko, U. S. Rai, H. Yu and P. C. Ray, *Chem. Phys. Lett.*, 2008, **463**, 145–149.
31 J. A. Khan, B. Pillai, T. K. Das, Y. Singh and S. Maiti, *ChemBioChem*, 2007, **8**, 1237–1240.
32 K. H. Downing and E. Nogales, *Curr. Opin. Cell Biol.*, 1998, **10**, 16–22.
33 M. A. Jordan and L. Wilson, *Nat. Rev. Cancer*, 2004, **4**, 253–265.
34 K. H. Downing, *Annu. Rev. Cell Dev. Biol.*, 2000, **16**, 89–111.
35 N. Kumar, *J. Biol. Chem.*, 1981, **256**, 10435–10441.
36 S. S. Rai and J. Wolff, *J. Biol. Chem.*, 1996, **271**, 14707–14711.
37 B. R. Acharya, D. Choudhury, A. Das and G. Chakrabarti, *Biochemistry*, 2009, **48**, 6963–6974.
38 P. B. Mullan, J. E. Quinn, P. M. Gilmore, S. McWilliams, H. Andrews, C. Gervin, N. McCabe, S. McKenna, P. White, Y. H. Song, S. Maheswaran, E. Liu, D. A. Haber, P. G. Johnston and D. P. Harkin, *Oncogene*, 2001, **20**, 6123–6131.
39 M. Hari, F. Loganzo, T. Annable, X. Tan, S. Musto, D. B. Morilla, J. H. Nettles, J. P. Snyder and L. M. Greenberger, *Mol. Cancer Ther.*, 2006, **5**, 270–278.
40 D. Choudhury, A. Das, A. Bhattacharya and G. Chakrabarti, *Food Chem. Toxicol.*, 2010, **48**, 2872–2880.
41 A. A. Sablina, L. S. Agapova, M. P. Chumakov and B. P. Kopnin, *Cell Biol. Int.*, 1999, **23**, 323–334.
42 S. H. Khan and G. M. Wahl, *Cancer Res.*, 1998, **58**, 396–401.
43 Z. N. Gheshlaghi, G. H. Riazi, S. Ahmadian, M. Ghafari and R. Mahinpour, *Acta Biochim. Biophys. Sin.*, 2008, **40**, 777–782.
44 J. C. Zhou, X. Wang, M. Xue, Z. Xu, T. Hamasaki, Y. Yang, K. Wang and B. Dunn, *Mater. Sci. Eng., C*, 2010, **30**, 20–26.
45 P. L. Apopa, Y. Qian, R. Shao, N. L. Guo, D. Schwegler-Berry, M. Pacurari, D. Porter, X. Shi, V. Vallyathan, V. Castranova, *et al.*, *Part. Fibre Toxicol.*, 2009, **6**, 1–14.
46 T. A. Ratnikova, P. N. Govindan, E. Salonen and P. C. Ke, *ACS Nano*, 2011, **5**, 6306–6314.
47 J. Kimling, M. Maier, M. B. Okenve, V. Kotaidis, H. Ballot and A. Plech, *J. Phys. Chem. B*, 2006, **110**, 15700–15707.
48 M. M. Bradford, *Anal. Biochem.*, 1976, **72**, 248–254.
49 M. Roychowdhury, N. Sarkar, T. Manna, S. Bhattacharyya, T. Sarkar, P. Basusarkar, S. Roy and B. Bhattacharyya, *Eur. J. Biochem.*, 2000, **267**, 3469–3476.
50 D. Hall and A. P. Minton, *Anal. Biochem.*, 2005, **345**, 198–213.
51 S. Mukherjee, B. R. Acharya, B. Bhattacharyya and G. Chakrabarti, *Biochemistry*, 2010, **49**, 1702–1712.
52 T. Deb, D. Choudhury, P. S. Guin, M. B. Saha, G. Chakrabarti and S. A. Das, *Chem.–Biol. Interact.*, 2011, **189**, 206–214.
53 J. R. Lakowicz, *Principles of Fluorescence Spectroscopy*, Kluwer Academic/Plenum Publishers, New York, 2nd edn, 1999.
54 S. K. Ghosh and T. Pal, *Chem. Rev.*, 2007, **107**, 4797–4862.
55 C. F. B. Séné, M. C. McCann, R. H. Wilson and R. Crinter, *Plant Physiol.*, 1994, **106**, 1623–1631.
56 T. G. Spiro and F. J. Farrell, *Inorg. Chem.*, 1971, **10**, 1606–1610.
57 S. H. Brewer, W. R. Glomm, M. C. Johnson, M. K. Knag and S. Franzen, *Langmuir*, 2005, **21**, 9303–9307.
58 A. Albanese, P. S. Tang and W. C. W. Chan, *Annu. Rev. Biomed. Eng.*, 2012, **12**, 1–16.
59 B. D. Chithrani, A. A. Ghazani and W. C. W. Chan, *Nano Lett.*, 2006, **6**, 662–668.
60 S. H. Wang, C. W. Lee, A. Chiou and P. K. Wei, *J. Nanobiotechnol.*, 2010, **8**, 33.
61 M. R. R. D. Planque, S. Aghdaei, T. Roose and H. Morgan, *ACS Nano*, 2011, **5**, 3599–3606.
62 Y. Jun, S. Sheikholeslamia, D. R. Hostetter, C. Tajon, C. S. Craik and A. P. Alivisatos, *Proc. Natl. Acad. Sci. U. S. A.*, 2009, **106**, 17735–17740.
63 N. Liu, M. Hentschel, T. Weiss, A. P. Alivisatos and H. Giessen, *Science*, 2011, **332**, 1407–1410.
64 L. Zhang, Y. Li, D. W. Li, C. Jing, X. Chen, M. Lv, Q. Huang, Y. T. Long and I. Willner, *Angew. Chem., Int. Ed.*, 2011, **50**, 6789–679.
65 R. K. Srivastava, A. R. Srivastava, S. J. Korsmeyer, M. Nesterova, Y. S. Cho-Chung and D. L. Longo, *Mol. Cell. Biol.*, 1998, **18**, 3509–3517.
66 Y. Zilberman, C. Ballestrem, L. Carramusa, R. Mazitschek, S. Khochbin and A. Bershadsky, *J. Cell Sci.*, 2009, **122**, 3531–3541.

67 S. Kapoor and D. Panda, *Biochem. Pharmacol.*, 2012, **83**, 1495–506.
68 Ö. F. Karataş, E. Sezgin, Ö. Aydın and M. Çulha, *Colloids Surf., B*, 2009, **71**, 315–318.
69 S. J. Soenen, B. Manshian, J. M. Montenegro, F. Amin, B. Meermann, T. Thiron, M. Cornelissen, F. Vanhaecke, S. Doak, W. J. Parak, S. D. Smedt and K. Braeckmans, *ACS Nano*, 2012, **6**, 5767–5783.
70 A. França, P. Aggarwal, E. V. Barsov, S. V. Kozlov, M. A. Dobrovolskai and Á. G. Fernández, *Nanomedicine*, 2011, **6**, 1175–88.
71 Z. Krpetic, P. Nativo, V. See, I. A. Prior, M. Brust and M. Volk, *Nano Lett.*, 2010, **10**, 4549–4554.
72 T. Mironava, M. Hadjiargyrou, M. Simon, V. Jurukovski and M. H. Rafailovichi, *Nanotoxicology*, 2010, **4**, 120–137.

Electronic supplementary information (ESI) for Nanoscale
This journal is © The Royal Society of Chemistry 2013

Unprecedented inhibition of tubulin polymerization directed by gold nanoparticles inducing cell cycle arrest and apoptosis†

Diptiman Choudhury,[a,e,§] Paulrajpillai Lourdu Xavier,[c,§] Kamalesh Chaudhari,[d] Robin John,[c] Anjan Kumar Dasgupta,[b] Thalappil Pradeep[c*] and Gopal Chakrabarti[a*]

[a]*Department of Biotechnology and Dr. B. C. Guha Centre for Genetic Engineering and Biotechnology, University of Calcutta, 35 Ballygunge Circular Road, Kolkata, West Bengal, India 700019. *Email: gcbcg@caluniv.in*
[b]*Department of Biochemistry, University of Calcutta, 35 Ballygunge Circular Road, Kolkata, West Bengal, India 700019.*
[c]*Department of Chemistry and DST Unit of Nanoscience, Indian Institute of Technology Madras, Chennai, Tamil Nadu, India 600036. *Email: pradeep@iitm.ac.in*
[d]*Department of Biotechnology, Indian Institute of Technology Madras, Chennai, Tamil Nadu, India 600036.*

[e]*Currently at Department of Medicine, Division of Uro-Oncology, Cedars Sinai Medical Centre, 8700-Bevarly Blvd, Los Angeles, California 90048, USA.*

[§]*these authors contributed equally to this work*

Electronic Supplementary Information 1

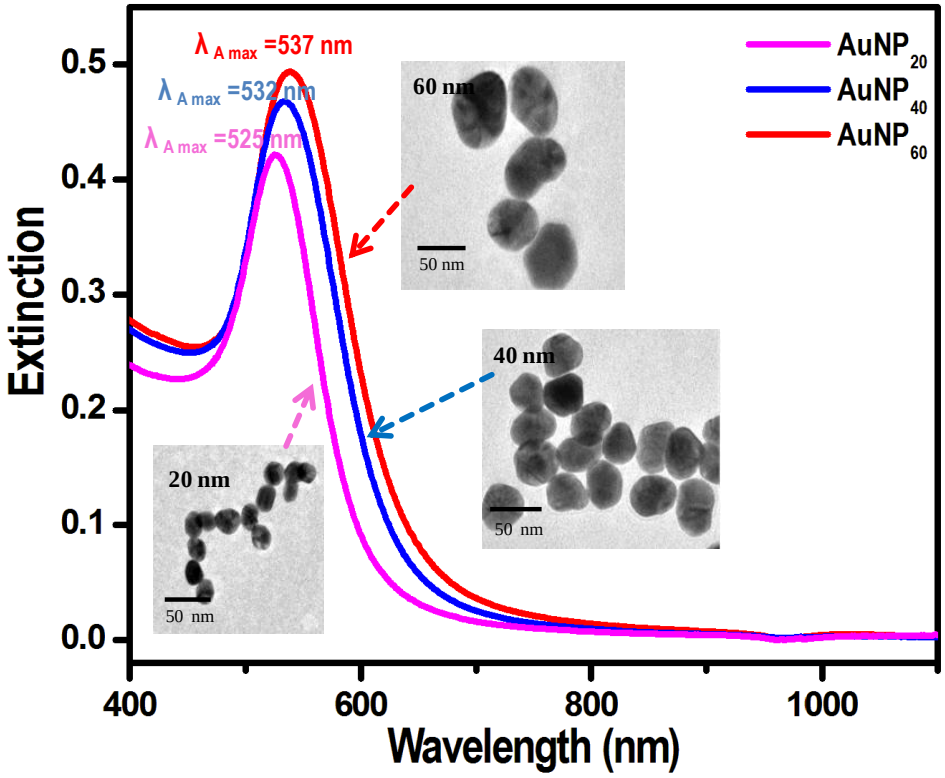

Fig. S1 Extinction spectra of three different sized (20 nm, 40 nm and 60 nm) citrate capped AuNPs with corresponding TEM images, namely $AuNP_{20}$, $AuNP_{40}$ and $AuNP_{60}$. Scale bar for all TEM images is 50 nm.

Electronic Supplementary Information 1A: Calculation of molarity of AuNP

Molarity of AuNPs in solution was calculated using the following formula,

$$M_{NP} = \frac{(Molarity\ of\ Au^{3+}\ in\ the\ solution) \times (Volume\ of\ one\ gold\ atom)}{(Volume\ of\ one\ nanoparticle)}$$

$$M_{NP} = \frac{6MA_r}{\pi D^3 \rho N_A}$$

= (6 * 250 * 197 * 7) / (22 * (40 * 10^{-7})^3 * 19.3 * 6.023 * 10^{23})

= 2068500 / (22 * 64000 * 10^{-21} * 19.3 * 6.023 * 10^{23})

= 2068500 / (22 * 64 * 19.3 * 6.023 * 10^5)

= 2068500 / (163671.4112 * 10^5)

= 12.64 *10^{-5} µM = 126.4 pM which gives molarity of $AuNP_{40}$ in the stock solution as 126.4 pM.

Where,

M = Molarity of Au^{3+} stock in µM

A_r = Atomic weight of Au in g

D = Diameter of nanoparticle in cm

ρ = Density of gold in g/cm^3

N_A = Avogadro number

For $AuNP_{40}$ molarity of stock solution was found to be, 126.4 pM.

Electronic Supplementary Information 2

The extents of polymerization inhibition were around 28.6 ± 2.7%, 40.32 ± 1.7% and 60.47 ± 3.5% in presence of $AuNP_{40}$ at 5, 12.5 and 25 pM, respectively (for 30 minutes). Hence the calculated IC_{50} value (i.e. 50% inhibitory concentration) for $AuNP_{40}$ was 18.6 ± 0.9 pM.

.

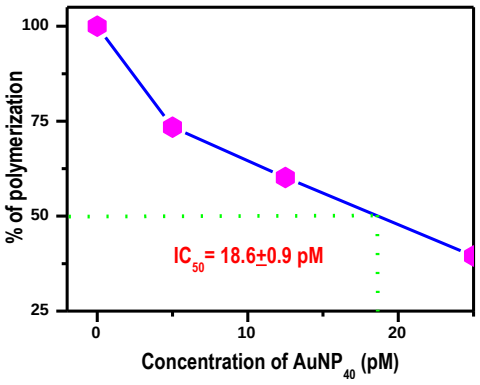

Fig. S2 Plot showing the calculation of IC_{50} concentration of $AuNP_{40}$ for purified mammalian tubulin polymerization. Error in the determination of % polymerization is given in supporting information 1. From the above plot (**Fig. S2**) we can infer that at the IC_{50} dose of $AuNP_{40}$ for polymerization inhibition of tubulin (12 µM) is ~18.6 pM and the molar ratio of $AuNP_{40}$: tubulin is around 1 : 3.16 X 10^5.

Electronic Supplementary Information 3

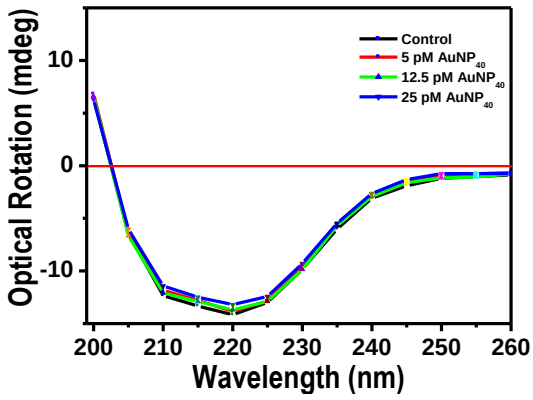

Fig. S3 Circular dichroism spectroscopic measurements revealing no significant change in the secondary structure of tubulin upon interacting with $AuNP_{40}$.

Electronic Supplementary Information 4

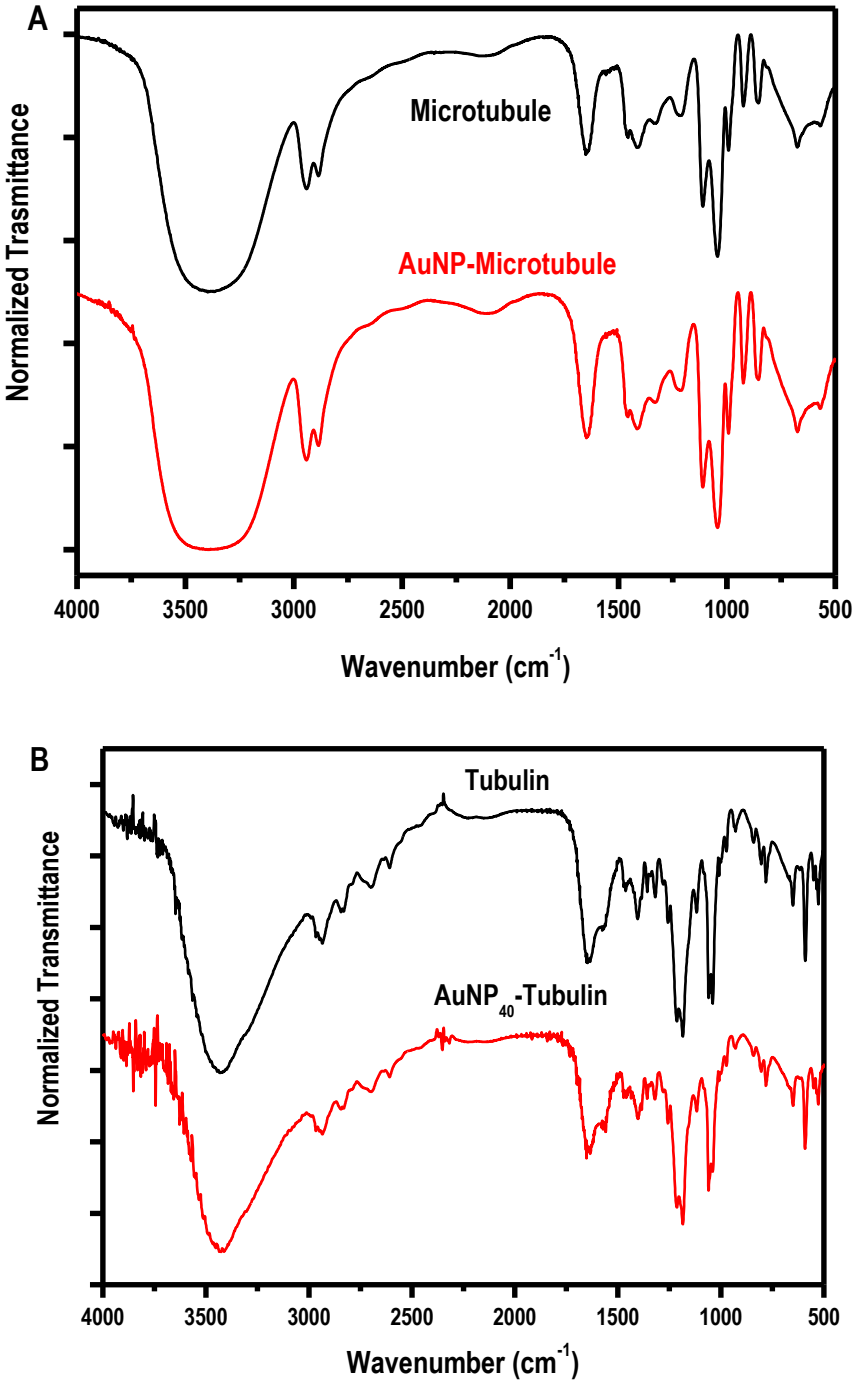

Fig. S4 FTIR spectra of microtubule and tubulin (solid black line in A and B) and $AuNP_{40}$ treated tubulin and microtubule (red solid line in A and B).

Electronic Supplementary Information 5

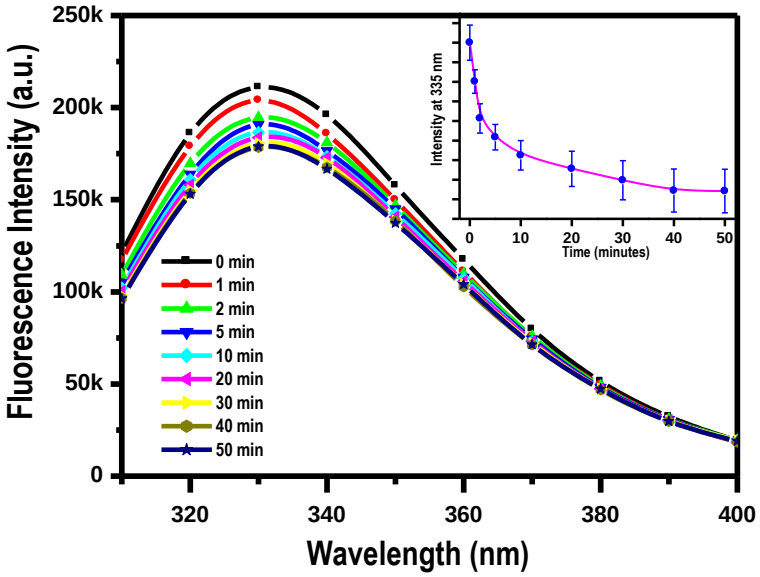

Fig. S5 PL spectra showing the quenching of intrinsic fluorescence of tryptophan upon interaction with $AuNP_{40.}$

Electronic Supplementary Information 6

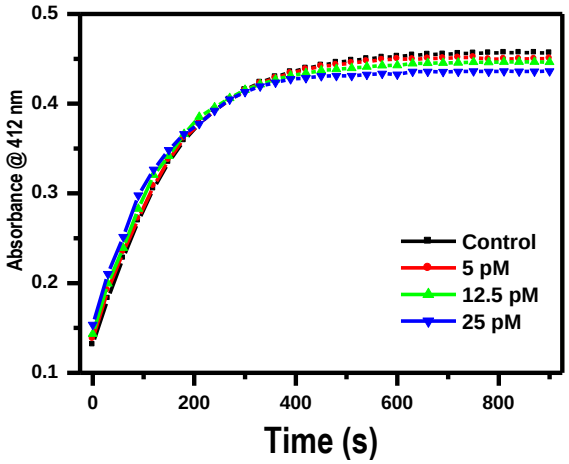

Fig. S7 Thiol estimation with control and tubulin incubated with $AuNP_{40}$ at different concentrations. Results indicated 3-5% loss of cysteine content per heterodimer.

Electronic Supplementary Information 7

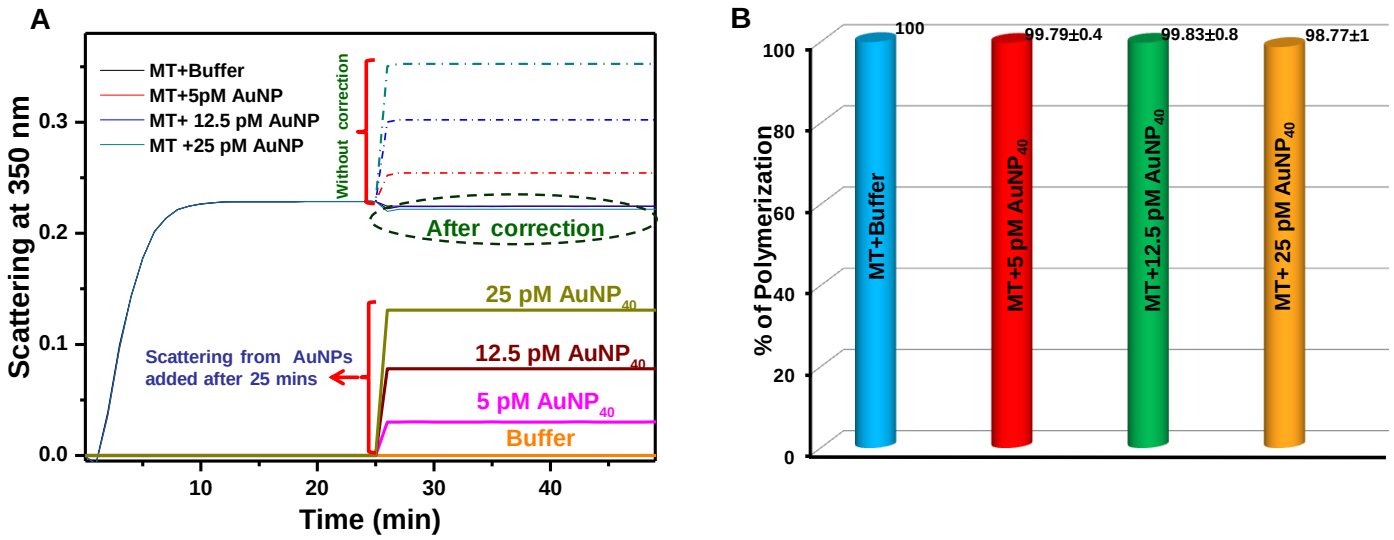

Fig. S7 A) UV-vis spectroscopic study of effect of Au_{NPs} on the polymerized tubulin. After 25 minutes of polymerization, upon addition Au_{NPs} did not depolymerise the polymerized microtubules *in vitro*, as observed from the spectra (highlighted spectral region with dotted ellipse; the original spectra were subtracted with the corresponding scattering spectra of Au_{NPs} for clarity). B) Bar-diagram showing the percentage of retention of polymerized tubulins with various concentrations of Au_{NP}.

Electronic Supplementary Information 8

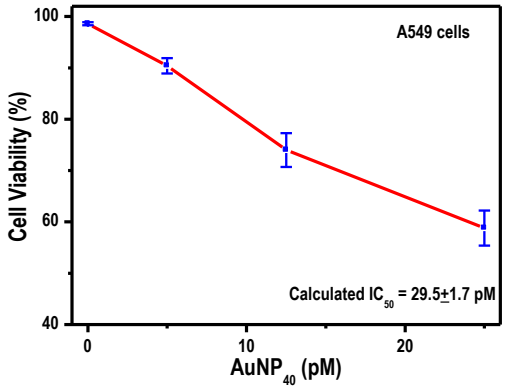

Fig. S8. Cell viability assay results of A549 cells upon 72 h $AuNP_{40}$ treatment. The calculated IC_{50} value was 29.5±1.7 pM.

Electronic Supplementary Information 9A

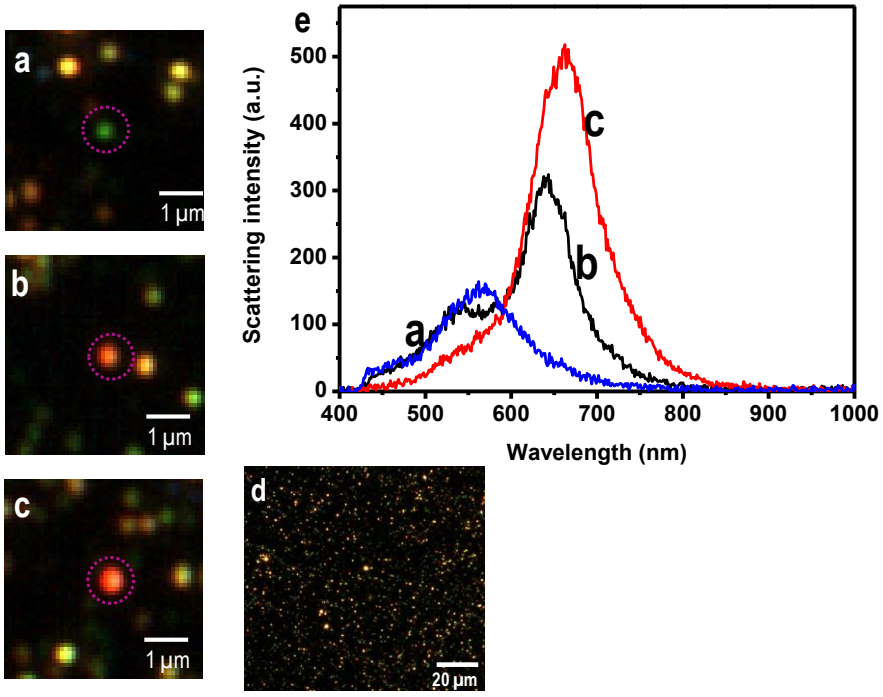

Fig. S9A. Dark field microscopic (DFM) images of $AuNP_{40}$. Left side: images a, b and c are DFM images of $AuNP_{40}$ and d is the large area image from which a, b and c were selected. Right side (e): the corresponding Plasmon Resonance Raleigh Scattering (PRRS) spectra of nanoparticles: a (blue solid line representing AuNP in the image a), b (black solid line representing AuNP in the image b), and c (red solid line representing AuNP in the image c). These particles are labelled in images a, b and c.

Electronic Supplementary Information 9B

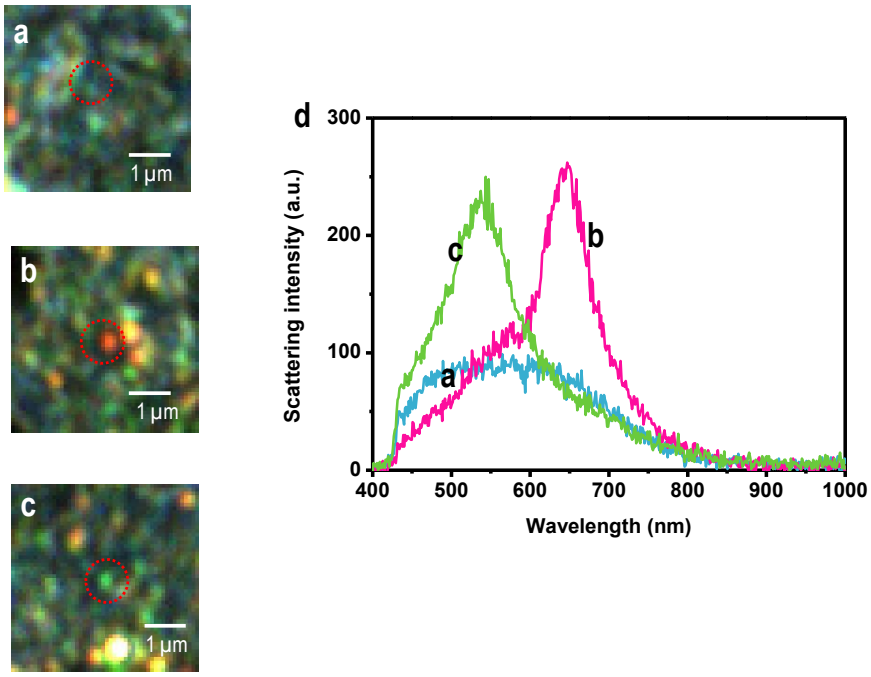

Fig. S9B. AuNPs in the aggregated tubulin matrix. Left: images a, b and c are selected area from Figure 2D. a is part of tubulin aggregate without nanoparticle, b and c are nanoparticles in the aggregated protein matrix. Right (d): the corresponding scattering spectra of a, b and c. a (solid cyan line) is the scattering spectra of protein aggregate in the image a and is broad and low in intensity. b (solid magenta line) and c (green solid line) are scattering spectra (sharp and high in intensity) of nanoparticles in the aggregated protein matrix in the image b and c, respectively. The difference between b and c in the scattering peak position may be due to the surrounding environment. The particles from which spectra are collected are labelled.

Electronic Supplementary Information 9C

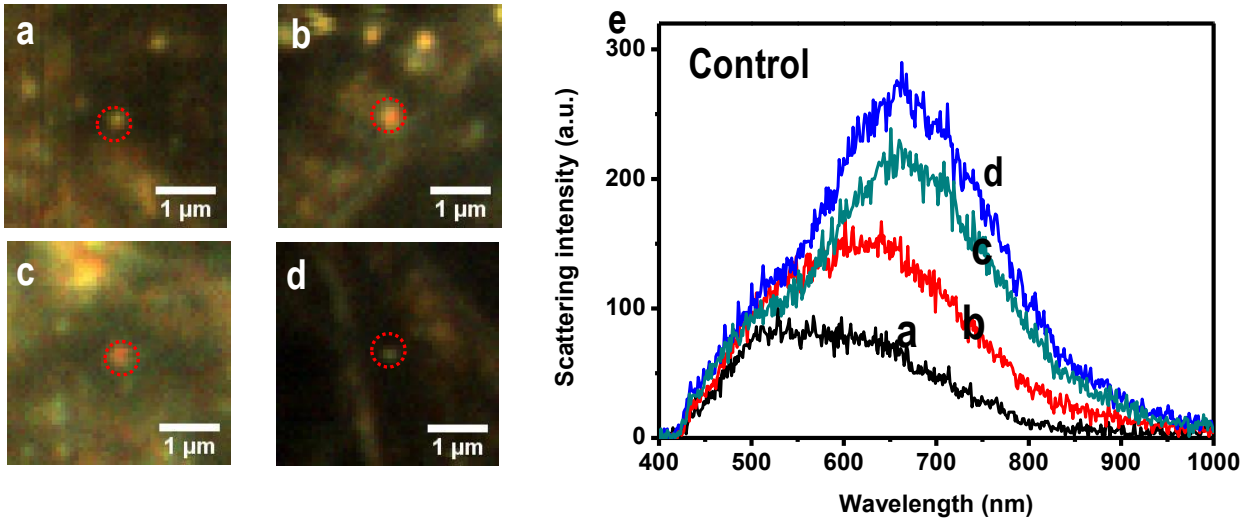

Fig. S8C Scattering from vesicles were observed in the control untreated cells. Left: Images a, b, c and d are four selected area images from the topmost image of Figure 6C. Right (e): Corresponding scattering spectra of vesicles in a, b, c and d. Here the spectra are broad and lesser in intensity unlike those of plasmonic nanoparticles which is a key factor to distinguish nanoparticles from vesicles. The vesicles from which spectra are collected are marked.

Electronic Supplementary Information 9D

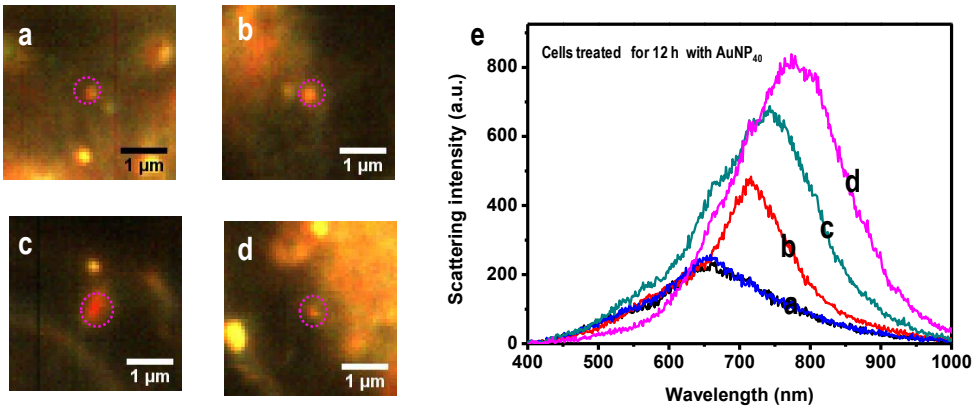

Fig. S9D. Scattering images and spectra of particles uptaken by $AuNP_{40}$ treated cells. Left Side: Images a, b, c and d are selected area images from the middle image of Figure 6C, showing the presence of scattering from AuNPs. Right (e): Corresponding scattering spectra of AuNPs in the right side images a (solid blue line representing AuNPs in image a), b (solid red line representing AuNPs in image b), c (solid green line representing AuNPs in image c) and d (solid magenta line representing AuNPs in image d), respectively. The particles from which spectra are collected are marked.

Electronic Supplementary Information 10

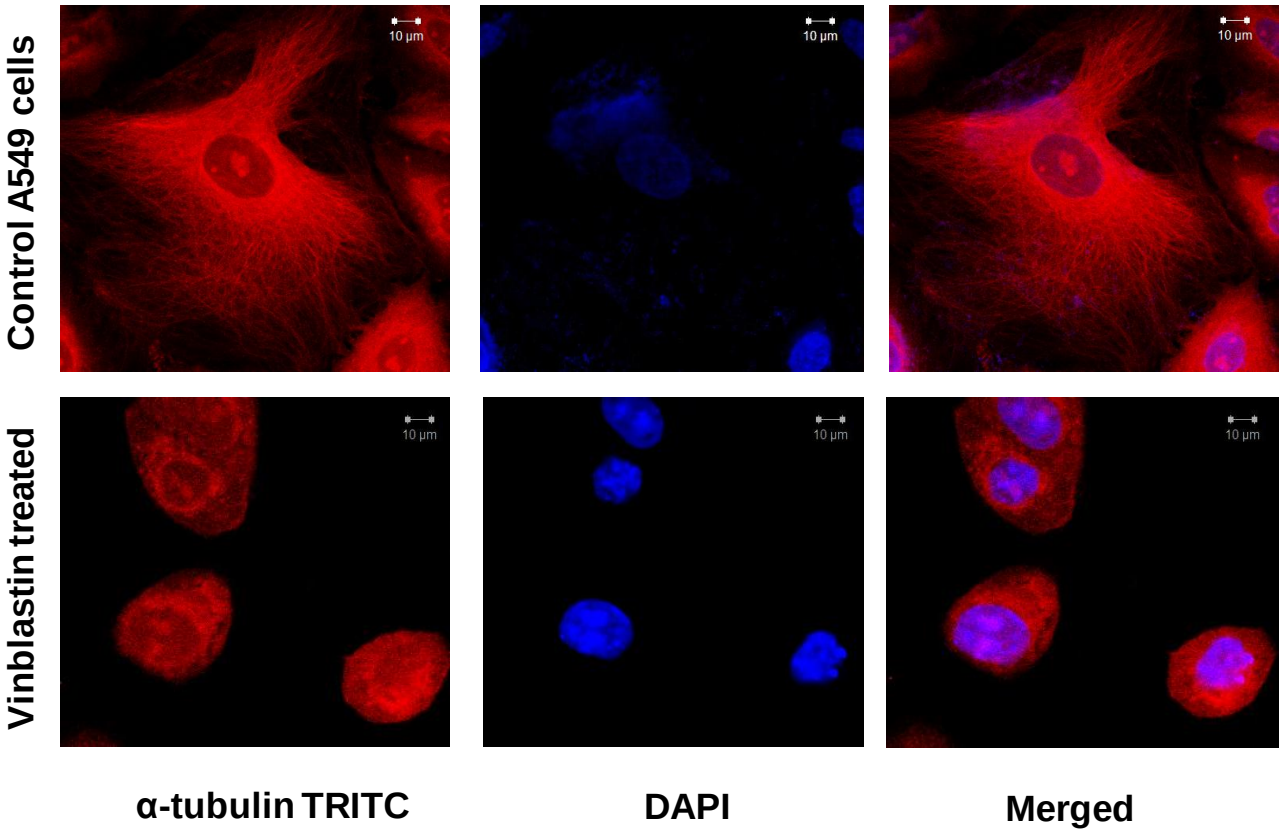

Fig. S10 Positive control: Vinblastin (500 nM) treated A549 cells for 24 hours showing microtubule damage. Upper panel images show control cells (non-treated). Lower panel images show vinblastin treated cells. Nucleus is stained with DAPI (blue) and microtubule is stained with anti-tubulin antibody conjugated with TRITC (red). Scale bar is 10 µm.

Electronic Supplementary Information 11

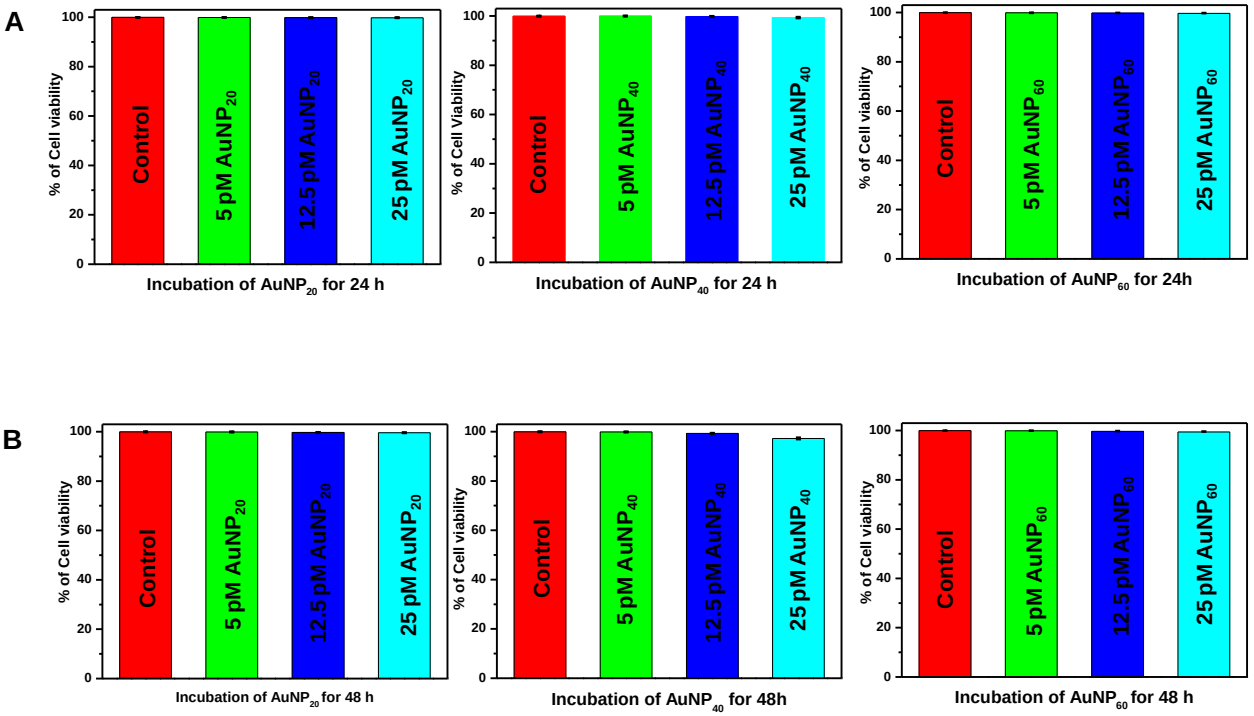

Fig. S11 A) Bar diagram showing % of cell viability for the three different sized AuNPs at different concentrations at 24 h. B) Bar diagram showing % of cell viability for the three different sized AuNPs at different concentrations at 48 h

Electronic Supplementary Information 12

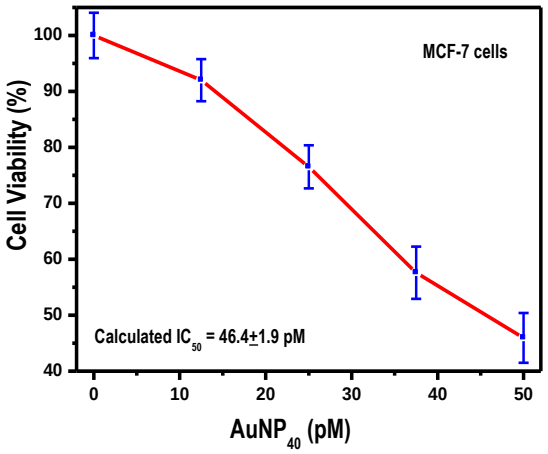

Fig. S12 Cell viability assay of MCF-7 after 72 h treatment with $AuNP_{40}$. The calculated IC_{50} value was 46.4±1.9 pM.

Electronic Supplementary Information 13

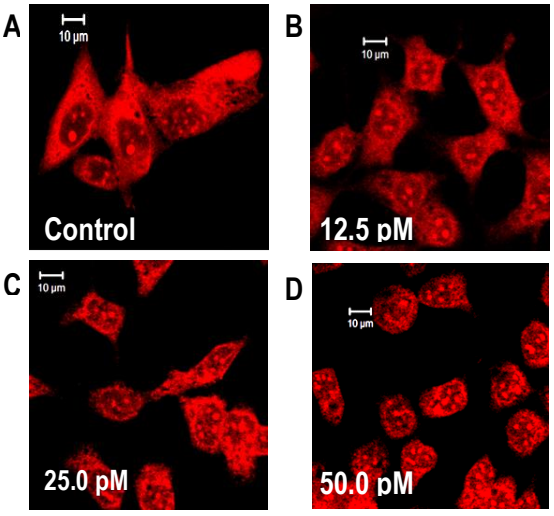

Fig. S13 Observation of a similar effect of AuNPs interacting with MCF-7 cells. The cells were stained with TRITC against anti-α-tubulin antibody. (A) Control MF7 cells, not treated with AuNPs. (B) Treated with 12.5 pM $AuNP_{40}$, (C) treated with 25.0 pM $AuNP_{40}$ and (D) treated with 50.0 pM $AuNP_{40}$. Cellular microtubule structure was monitored after 72 h of incubation.

JACS
JOURNAL OF THE AMERICAN CHEMICAL SOCIETY
Communication
pubs.acs.org/JACS

Separation of Precise Compositions of Noble Metal Clusters Protected with Mixed Ligands

Yoshiki Niihori,[†] Miku Matsuzaki,[†] Thalappil Pradeep,*[,‡] and Yuichi Negishi*[,†]

[†]Department of Applied Chemistry, Faculty of Science, Tokyo University of Science, 1-3 Kagurazaka, Shinjuku-ku, Tokyo 162-8601, Japan

[‡]DST Unit of Nanoscience and Thematic Unit of Excellence, Department of Chemistry, Indian Institute of Technology Madras, Chennai 600 036, India

Supporting Information

ABSTRACT: This report describes the precise and systematic synthesis of $PdAu_{24}$ clusters protected with two types of thiolate ligands (-SR1 and -SR2). It involved high-resolution separation of metal clusters containing a distribution of chemical compositions, $PdAu_{24}(SR1)_{18-n}(SR2)_n$ (n = 0, 1, 2, ..., 18), to individual clusters of specific n using high-performance liquid chromatography. Similar high-resolution separation was achieved for a few ligand combinations as well as clusters with other metal cores, such as Au_{25} and Au_{38}. These results demonstrate the ability to precisely control the chemical composition of two types of ligands in thiolate-protected mono- and bimetallic metal clusters. It is expected that greater functional control of thiolate-protected metal clusters, their regular arrays, and systematic variation of their properties can now be achieved.

Small metal clusters (≤2 nm core diameter) are attracting attention as new functional materials because they have size-specific physical/chemical properties that are not present in their corresponding bulk metals. Among these metal clusters, thiolate-protected metal clusters ($M_n(SR)_m$) have the potential to be useful materials because they are stable chemical substances. Since the first report of thiolate-protected gold clusters ($Au_n(SR)_m$) in 1994,[1] research on $M_n(SR)_m$ has been pursued across a wide range of fields. Through those studies, synthetic methodology for the production of metal clusters, especially $Au_n(SR)_m$, has developed rapidly. Multiple high-resolution size separation methods and techniques for evaluating chemical composition have been established, and it is now possible to treat $Au_n(SR)_m$ as a compound with a well-defined chemical composition.[2−5] Stable clusters (magic clusters) such as $Au_{25}(SR)_{18}$, $Au_{38}(SR)_{24}$, and $Au_{144}(SR)_{60}$ have been reported,[2−5] and methods for size-selective and bulk-scale synthesis have been established.[6−9] Successes in single-crystal X-ray structure analysis[10−13] have clarified the geometrical structure of $Au_n(SR)_m$, and these experimental results, along with theoretical studies,[14] have shown that some types of $Au_n(SR)_m$ have optical isomers. Methods have been established to separate the optical isomers of $Au_{38}(SR)_{24}$.[15] The structural rules for stabilizing $Au_n(SR)_m$ have also been elucidated,[16−19] and design guidelines for producing new stable clusters are emerging. In addition, a number of reports describing precise syntheses of silver clusters[20−22] and alloy clusters[23−27] have been published. Thus, the science of precise and efficient synthesis of metal clusters is becoming more established.

Controlling the chemical composition of the ligands surrounding the metal core of $M_n(SR)_m$ is an effective method for the functionalization of clusters. Changing the physical/chemical properties of $M_n(SR)_m$ can be accomplished by replacing some of its ligands with other thiolates.[9,28−30] In addition, conferring or changing functional properties (e.g., molecular recognition ability, catalytic activity, or fluorescence resonance energy transfer)[31−33] and forming regular arrangements[34] become possible by the introduction of functional thiolates. However, in cluster synthesis, where multiple types of thiolates are used as ligands, a distribution of ligands with varying chemical compositions is formed,[35] with a few limited exceptions.[36] Thus, to achieve precise control of the function and specific arrangement of $M_n(SR)_m$, development of a new methodology for precisely separating clusters, which also controls the chemical composition of the ligands, is needed.[37−41]

This report describes the precise and systematic creation of $PdAu_{24}$ clusters[23,42] with two types of thiolate ligands, -SR1 and -SR2. This was achieved through the separation of metal clusters with ligands having a distribution of chemical compositions using high-performance liquid chromatography (HPLC). This method is applicable to clusters incorporating various ligand combinations, as well as to clusters with other metal cores; therefore, it has broad application potential.

$PdAu_{24}$ clusters[23,42] protected by two types of thiolate ligands were synthesized as described in Supporting Information I. Briefly, $PdAu_{24}(SC_{12}H_{25})_{18}$ with dodecanethiolate ligands was placed in a solution with other thiols (4-*tert*-butylbenzylmercaptan (BBSH), $C_6H_{13}SH$, $C_{10}H_{21}SH$, $C_{16}H_{33}SH$, and PhC_2H_4SH) and made to undergo ligand-exchange reaction.[9,43−47] For $PdAu_{24}$ clusters synthesized in this way, the chemical composition of the ligands had a wide distribution (Figure 1a).[47] For these clusters, the polarities are expected to be different, depending on the chemical composition of the ligands. HPLC with a reverse-phase column is an effective method for separating metal clusters with different polar-

Received: January 28, 2013
Published: March 15, 2013

   dx.doi.org/10.1021/ja4009369 | *J. Am. Chem. Soc.* 2013, 135, 4946−4949

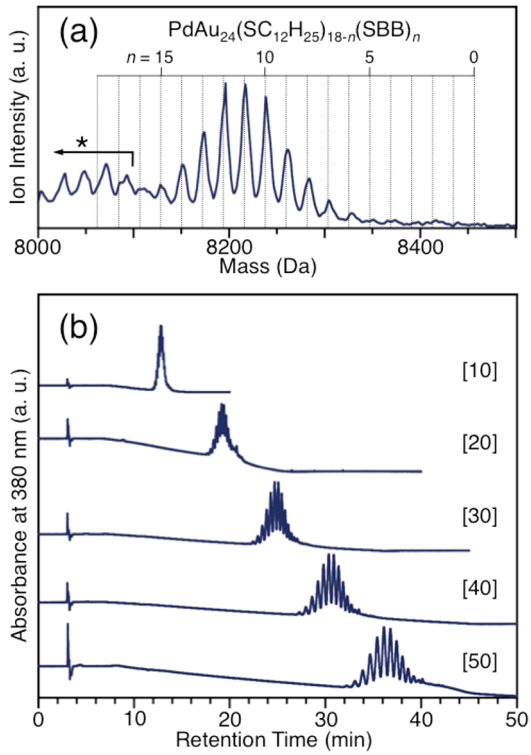

Figure 1. (a) Negative-ion MALDI mass spectrum of $PdAu_{24}(SC_{12}H_{25})_{18-n}(SBB)_n$ (n = 6−16). The asterisk indicates laser-induced fragments.[35] (b) Chromatograms of $PdAu_{24}(SC_{12}H_{25})_{18-n}(SBB)_n$ (n = 6−16) at each gradient program (see the text). The peak observed at 3.0 min was confirmed to be due to the solvent, THF.

ities.[48−50] We separated $PdAu_{24}$ clusters having mixed ligands using various HPLC-based methods.

The high-resolution separation of $PdAu_{24}(SC_{12}H_{25})_{18-n}$-$(SBB)_n$ (n = 6−16) is described below, with the distribution shown in Figure 1a. The separation was accomplished in two steps (Figure S2). First, all clusters were adsorbed onto the stationary phase (the column). Methanol, a solvent in which the clusters were insoluble, was specifically chosen as the mobile phase. Upon injection of a suspension of the clusters, they were adsorbed onto the stationary phase. Next, the adsorbed clusters were eluted slowly from the stationary phase. To accomplish this, the mobile phase was gradually adjusted from pure methanol to tetrahydrofuran (THF) using a linear gradient program (Figure S3). Since $PdAu_{24}(SC_{12}H_{25})_{18-n}$-$(SBB)_n$ dissolves in THF, as the concentration ratio of [THF]/[CH_3OH] was increased, $PdAu_{24}(SC_{12}H_{25})_{18-n}(SBB)_n$ gradually eluted into the mobile phase. Because -SBB (which incorporates a benzene ring) possesses greater polarity than the alkyl chain -$SC_{12}H_{25}$, the $PdAu_{24}(SC_{12}H_{25})_{18-n}(SBB)_n$ containing a greater amount of -SBB eluted into the mobile phase faster (i.e., had a shorter retention time). The two steps described above were the key points to achieving high-resolution separation of $PdAu_{24}(SC_{12}H_{25})_{18-n}(SBB)_n$ (Figure S4).

Figure 1b shows the dependence of $PdAu_{24}(SC_{12}H_{25})_{18-n}$-$(SBB)_n$ chromatograms on the time required to fully replace the mobile phase with THF; the label (e.g., [10]) in the figure indicates that time (in minutes) (also see Figure S3). When the replacement time was 10 min, a set of peaks was observed around a retention time of 11.5 min. In this experiment, only a small gap exists between each peak in a set of peaks, with each peak displaying a large overlap. Taking a longer time to replace the mobile phase resulted in slower elution of the clusters into the mobile phase (i.e., retention time increased). Therefore, greater peak-to-peak separation was obtained, and peak overlap gradually diminished (Figure S5). When the replacement time was set at 40 min or longer, the peaks separated more completely, and peak distribution looked similar to that of the corresponding matrix-assisted laser desorption/ionization (MALDI) mass spectrum (Figures 1a and S6). The fractionation of each peak followed by mass spectrometry analysis revealed that each peak contained clusters with only one chemical composition (Figure S7). Thus, using this method, $PdAu_{24}(SC_{12}H_{25})_{18-n}(SBB)_n$ clusters with ligands of different chemical compositions were separated with high resolution (Figure S8). Similar separation/fractionation experiments were conducted on $PdAu_{24}(SC_{12}H_{25})_{18-n}(SBB)_n$ with various ligand distributions (Figure S9a). Results demonstrated that each distribution was separated into clusters with individual compositions with high resolution (Figure S9b), and all ligand combinations of $PdAu_{24}(SC_{12}H_{25})_{18-n}(SBB)_n$ (n = 0−18) were isolated with high purity (Figure 2); the purity of

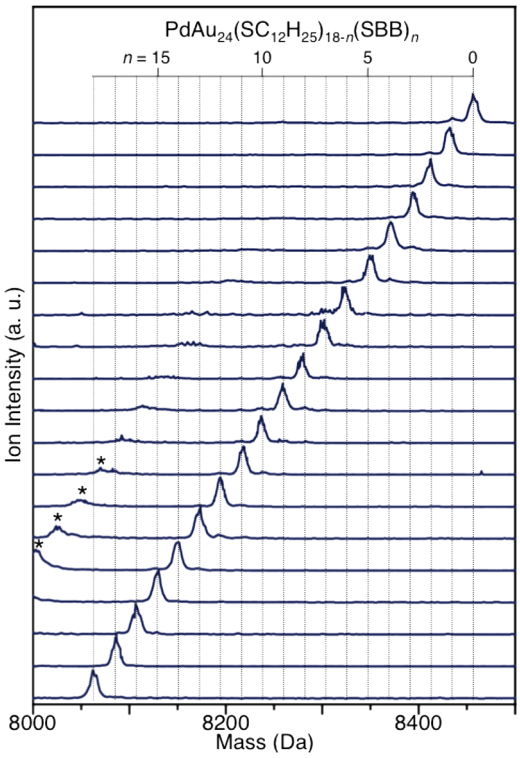

Figure 2. Negative-ion MALDI mass spectra of each cluster of composition $PdAu_{24}(SC_{12}H_{25})_{18-n}(SBB)_n$ (n = 0−18), isolated in this work. The asterisks indicate laser-induced fragments.

each separated cluster, estimated from the mass spectrum (Figure 2), was >95%. In this way, the precise and systematic synthesis and separation of $PdAu_{24}(SC_{12}H_{25})_{18-n}(SBB)_n$ (n = 0, 1, 2, ..., 18) protected by two types of thiolate ligands was achieved for the first time (Figure S10).

To investigate the versatility of this separation method, similar experiments were conducted using $PdAu_{24}$ clusters with combinations of other ligands. $PdAu_{24}(SC_{12}H_{25})_{18-n}$-$(SC_2H_4Ph)_n$ (Figures 3a,b and S11) and $PdAu_{24}(SC_{12}H_{25})_{18-n}$-$(SC_6H_{13})_n$ (Figure S12) underwent similar high-resolution

dx.doi.org/10.1021/ja4009369 | J. Am. Chem. Soc. 2013, 135, 4946−4949

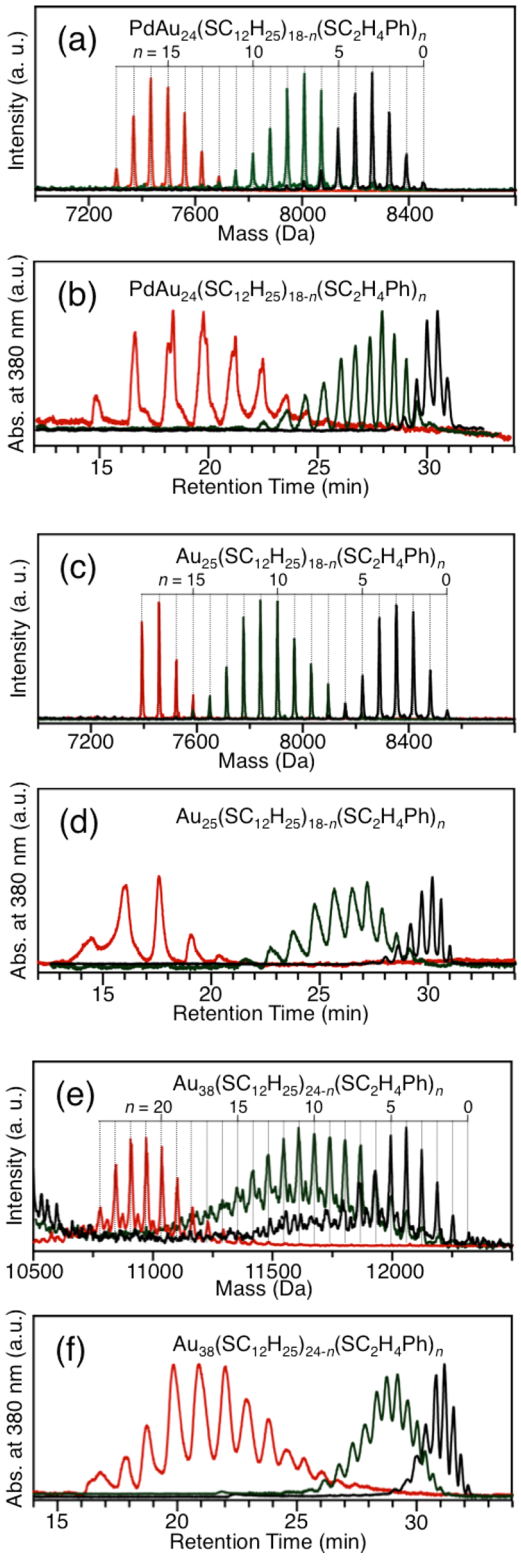

Figure 3. Comparison between the MALDI mass spectrum and chromatogram for (a,b) $PdAu_{24}(SC_{12}H_{25})_{18-n}(SC_2H_4Ph)_n$, (c,d) $Au_{25}(SC_{12}H_{25})_{18-n}(SC_2H_4Ph)_n$, and (e,f) $Au_{38}(SC_{12}H_{25})_{24-n}(SC_2H_4Ph)_n$. MALDI mass spectra (a), (c), and (e) were observed in negative, negative, and positive ion modes, respectively. In (a,b), (c,d), and (e,f), the same color indicates the same sample. The fine structures appearing in the chromatograms (especially (b)) are presumed to be due to the coordination isomers.[51] In (e), peaks which are not assigned to $Au_{38}(SC_{12}H_{25})_{24-n}(SC_2H_4Ph)_n$ are due to laser-induced fragments.

separations.[51] This indicates that the procedure used in the present study is applicable to systems with other ligand combinations also. By using $-SC_{12}H_{25}$ with $-SC_2H_4Ph$ and $-SC_{12}H_{25}$ with $-SC_6H_{13}$, which possess significant differences in relative polarity between them, we ensured that the composition of the ligands affected the solubility of the cluster in the solvent of choice (i.e., mobile phase). Because of this effect, high-resolution separation of $PdAu_{24}$ clusters with combinations of these ligands occurred under the conditions examined in this study. In contrast, for clusters with ligand combinations having smaller polarity differences, $PdAu_{24}(SC_{12}H_{25})_{18-n}(SC_{10}H_{21})_n$ and $PdAu_{24}(SC_{12}H_{25})_{18-n}(SC_{16}H_{33})_n$, the chromatograms did not show clear separation (Figures S13 and S14). This suggests that the precise separation of metal clusters protected by two types of thiolates requires a moderate polarity difference between the two ligand types.

When appropriate ligands were combined, similar high-resolution separation also was achieved for Au_{25} clusters as well as Au_{38} clusters (Figures 3c–f, S15, and S16; samples were prepared as given in Supporting Information I). Thus, the procedure described in this report is effective regardless of the size or composition of the metal core, indicating its broad applicability. The peak resolution and separation of $Au_{25}(SC_{12}H_{25})_{18-n}(SC_2H_4Ph)_n$ were not as sharp as for $PdAu_{24}(SC_{12}H_{25})_{18-n}(SC_2H_4Ph)_n$. $Au_{25}(SR)_{18}$ was synthesized in its negative-ion form $[Au_{25}(SR)_{18}]^-$, but reports have indicated that $[Au_{25}(SR)_{18}]^-$ is oxidized when left in solution, becoming the neutral species $[Au_{25}(SR)_{18}]^0$.[52] For $Au_{25}(SC_{12}H_{25})_{18-n}(SC_2H_4Ph)_n$, this type of distribution of charge states occurs, so an unclear separation of peaks is predicted. In addition, a slight difference in structure exists between $Au_{25}(SR)_{18}$ and $PdAu_{24}(SR)_{18}$; the latter is slightly skewed compared to the former.[23] It is possible that this difference in structure is also associated with the difference in the number of coordination isomers.[51] This could be the reason for the broadness and unclear separation of peaks of $Au_{25}(SC_{12}H_{25})_{18-n}(SC_2H_4Ph)_n$. For $Au_{38}(SC_{12}H_{25})_{24-n}(SC_2H_4Ph)_n$, the broadness and unclear separation are likely to be due to the difference in the number of the coordination isomers in addition to the existence of optical isomers.[15,41]

Finally, although a linear gradient program (Figure S3) was chosen for the experiments described here, the gradient need not necessarily be linear for conducting this type of high-resolution separation. A program that allows each cluster to elute at equivalent intervals will produce a chromatogram that has a shape very similar to the mass spectrum (Figure S17), thus confirming separation of the clusters and making an investigation of the conditions required for separation easier.

In conclusion, the precise and systematic synthesis of metal clusters with two types of thiolate ligands was achieved for the first time. This method has broad applicability and shows potential for use as a basic technology for the study of metal clusters. This study demonstrated the ability to precisely control the chemical compositions of metal clusters with two types of ligands. The results imply that control of the physical/chemical properties of thiolate-protected metal clusters could be achieved at a higher level than previously possible. In addition, information about ligand-exchange effects on the electronic structure of a cluster could be obtained (Figure S10), leading to a deeper understanding of the interactions between the metal core and the ligands[53] and those between the ligands themselves. The results presented imply that structural isomers

dx.doi.org/10.1021/ja4009369 | J. Am. Chem. Soc. 2013, 135, 4946–4949

of clusters with mixed ligands are possible, and investigations of their structure and properties pose challenges for the future.

■ ASSOCIATED CONTENT

Supporting Information

Details of experimental procedures and characterization of the products. This material is available free of charge via the Internet at http://pubs.acs.org.

■ AUTHOR INFORMATION

Corresponding Author

negishi@rs.kagu.tus.ac.jp; pradeep@iitm.ac.in

Notes

The authors declare no competing financial interest.

■ ACKNOWLEDGMENTS

We thank Mr. Wataru Kurashige for technical assistance and valuable comments. Yoshiki Niihori was an exchange student at IIT Madras during the initial stages of this work. This work was financially supported by a research grant from The Mazda Foundation. Research at IIT Madras was supported by the Department of Science and Technology, Government of India.

■ REFERENCES

(1) Brust, M.; Walker, M.; Bethell, D.; Schiffrin, D. J.; Whyman, R. *J. Chem. Soc., Chem. Commun.* **1994**, 801.

(2) Whetten, R. L.; Khoury, J. T.; Alvarez, M. M.; Murthy, S.; Vezmar, I.; Wang, Z. L.; Stephens, P. W.; Cleveland, C. L.; Luedtke, W. D.; Landman, U. *Adv. Mater.* **1996**, *8*, 428.

(3) Parker, J. F.; Fields-Zinna, C. A.; Murray, R. W. *Acc. Chem. Res.* **2010**, *43*, 1289.

(4) Negishi, Y.; Nobusada, K.; Tsukuda, T. *J. Am. Chem. Soc.* **2005**, *127*, 5261.

(5) Tsukuda, T. *Bull. Chem. Soc. Jpn.* **2012**, *85*, 151.

(6) Qian, H.; Zhu, M.; Wu, Z.; Jin, R. *Acc. Chem. Res.* **2012**, *45*, 1470.

(7) Dharmaratne, A. C.; Krick, T.; Dass, A. *J. Am. Chem. Soc.* **2009**, *131*, 13604.

(8) Yu, Y.; Luo, Z.; Yu, Y.; Lee, J. Y.; Xie, J. *ACS Nano* **2012**, *6*, 7920.

(9) Shibu, E. S.; Muhammed, M. A. H.; Tsukuda, T.; Pradeep, T. *J. Phys. Chem. C* **2008**, *112*, 12168.

(10) Jadzinsky, P. D.; Calero, G.; Ackerson, C. J.; Bushnell, D. A.; Kornberg, R. D. *Science* **2007**, *318*, 430.

(11) Heaven, M. W.; Dass, A.; White, P. S.; Holt, K. M.; Murray, R. W. *J. Am. Chem. Soc.* **2008**, *130*, 3754.

(12) Zhu, M.; Aikens, C. M.; Hollander, F. J.; Schatz, G. C.; Jin, R. *J. Am. Chem. Soc.* **2008**, *130*, 5883.

(13) Qian, H.; Eckenhoff, W. T.; Zhu, Y.; Pintauer, T.; Jin, R. *J. Am. Chem. Soc.* **2010**, *132*, 8280.

(14) Lopez-Acevedo, O.; Tsunoyama, H.; Tsukuda, T.; Häkkinen, H.; Aikens, C. M. *J. Am. Chem. Soc.* **2010**, *132*, 8210.

(15) Dolamic, I.; Knoppe, S.; Dass, A.; Bürgi, T. *Nat. Commun.* **2012**, *3*, 798.

(16) Chaki, N. K.; Negishi, Y.; Tsunoyama, H.; Shichibu, Y.; Tsukuda, T. *J. Am. Chem. Soc.* **2008**, *130*, 8608.

(17) Walter, M.; Akola, J.; Lopez-Acevedo, O.; Jadzinsky, P. D.; Calero, G.; Ackerson, C. J.; Whetten, R. L.; Grönbeck, H.; Häkkinen, H. *Proc. Natl. Acad. Sci. U.S.A.* **2008**, *105*, 9157.

(18) Jiang, D.-e. *Chem.—Eur. J.* **2011**, *17*, 12289.

(19) Pei, Y.; Zeng, X. C. *Nanoscale* **2012**, *4*, 4054.

(20) Wu, Z.; Lanni, E.; Chen, W.; Bier, M. E.; Ly, D.; Jin, R. *J. Am. Chem. Soc.* **2009**, *131*, 16672.

(21) Rao, T. U. B.; Nataraju, B.; Pradeep, T. *J. Am. Chem. Soc.* **2010**, *132*, 16304.

(22) Harkness, K. M.; Tang, Y.; Dass, A.; Pan, J.; Kothalawala, N.; Reddy, V. J.; Cliffel, D. E.; Demeler, B.; Stellacci, F.; Bakr, O. M.; McLean, J. A. *Nanoscale* **2012**, *4*, 4269.

(23) Negishi, Y.; Kurashige, W.; Niihori, Y.; Iwasa, T.; Nobusada, K. *Phys. Chem. Chem. Phys.* **2010**, *12*, 6219.

(24) Negishi, Y.; Igarashi, K.; Munakata, K.; Ohgake, W.; Nobusada, K. *Chem. Commun.* **2012**, *48*, 660.

(25) Qian, H.; Jiang, D.-e.; Li, G.; Gayathri, C.; Das, A.; Gil, R. R.; Jin, R. *J. Am. Chem. Soc.* **2012**, *134*, 16159.

(26) Udayabhaskararao, T.; Sun, Y.; Goswami, N.; Pal, S. K.; Balasubramanian, K.; Pradeep, T. *Angew. Chem., Int. Ed.* **2012**, *51*, 2155.

(27) Biltek, S. R.; Mandal, S.; Sen, A.; Reber, A. C.; Pedicini, A. F.; Khanna, S. N. *J. Am. Chem. Soc.* **2013**, *135*, 26.

(28) Lee, D.; Donkers, R. L.; Wang, G.; Harper, A. S.; Murray, R. W. *J. Am. Chem. Soc.* **2004**, *126*, 6193.

(29) Wu, Z.; Jin, R. *Nano Lett.* **2010**, *10*, 2568.

(30) Aikens, C. M. *J. Phys. Chem. Lett.* **2010**, *1*, 2594.

(31) Kim, Y.; Johnson, R. C.; Hupp, J. T. *Nano Lett.* **2001**, *1*, 165.

(32) Zhu, M.-Q.; Wang, L.-Q.; Exarhos, G. J.; Li, A. D. Q. *J. Am. Chem. Soc.* **2004**, *126*, 2656.

(33) Muhammed, M. A. H.; Shaw, A. K.; Pal, S. K.; Pradeep, T. *J. Phys. Chem. C* **2008**, *112*, 14324.

(34) Negishi, Y.; Tsunoyama, H.; Yanagimoto, Y.; Tsukuda, T. *Chem. Lett.* **2005**, *34*, 1638.

(35) Dass, A.; Stevenson, A.; Dubay, G. R.; Tracy, J. B.; Murray, R. W. *J. Am. Chem. Soc.* **2008**, *130*, 5940.

(36) Tang, Z.; Robinson, D. A.; Bokossa, N.; Xu, B.; Wang, S.; Wang, G. *J. Am. Chem. Soc.* **2011**, *133*, 16037.

(37) Zanchet, D.; Micheel, C. M.; Parak, W. J.; Gerion, D.; Alivisatos, A. P. *Nano Lett.* **2001**, *1*, 32.

(38) Ackerson, C. J.; Jadzinsky, P. D.; Jensen, G. J.; Kornberg, R. D. *J. Am. Chem. Soc.* **2006**, *128*, 2635.

(39) Worden, J. G.; Dai, Q.; Shaffer, A. W.; Huo, Q. *Chem. Mater.* **2004**, *16*, 3746.

(40) Park, S.; Hamad-Schifferli, K. *J. Phys. Chem. C* **2008**, *112*, 7611.

(41) Knoppe, S.; Azoulay, R.; Dass, A.; Bürgi, T. *J. Am. Chem. Soc.* **2012**, *134*, 20302.

(42) Fields-Zinna, C. A.; Crowe, M. C.; Dass, A.; Weaver, J. E. F.; Murray, R. W. *Langmuir* **2009**, *25*, 7704.

(43) Guo, R.; Song, Y.; Wang, G.; Murray, R. W. *J. Am. Chem. Soc.* **2005**, *127*, 2752.

(44) Jupally, V. R.; Kota, R.; Dornshuld, E. V.; Mattern, D. L.; Tschumper, G. S.; Jiang, D.-e.; Dass, A. *J. Am. Chem. Soc.* **2011**, *133*, 20258.

(45) Devadas, M. S.; Kwak, K.; Park, J.-W.; Choi, J.-H.; Jun, C.-H.; Sinn, E.; Ramakrishna, G.; Lee, D. *J. Phys. Chem. Lett.* **2010**, *1*, 1497.

(46) Heinecke, C. L.; Ni, T. W.; Malola, S.; Mäkinen, V.; Wong, O. A.; Häkkinen, H.; Ackerson, C. J. *J. Am. Chem. Soc.* **2012**, *134*, 13316.

(47) Niihori, Y.; Kurashige, W.; Matsuzaki, M.; Negishi, Y. *Nanoscale* **2013**, *5*, 508.

(48) Wolfe, R. L.; Murray, R. W. *Anal. Chem.* **2006**, *78*, 1167.

(49) Xie, S.; Paau, M. C.; Zhang, Y.; Shuang, S.; Chan, W.; Choi, M. M. F. *Nanoscale* **2012**, *4*, 5325.

(50) Negishi, Y.; Sakamoto, C.; Ohyama, T.; Tsukuda, T. *J. Phys. Chem. Lett.* **2012**, *3*, 1624.

(51) Even when the chemical composition of metal clusters with two types of thiolate protective ligands is the same, there may be coordination isomers with ligands having different configurational arrangements. The configurational differences between these isomers are expected to affect the polarity slightly on the cluster surfaces. Therefore, in principle, these coordination isomers should be separable using the method described here. Thus, we predict that the detailed peak structure observed in the chromatogram of $PdAu_{24}(SC_{12}H_{25})_{18-n}(SC_2H_4Ph)_n$ (Figure 3b) could be due to coordination isomers. When the peaks of $PdAu_{24}(SC_{12}H_{25})_2(SC_2H_4Ph)_{16}$ were actually fractionated and a mass-spectral analysis was conducted, the mass spectrum of each fraction showed only peaks attributable to $PdAu_{24}(SC_{12}H_{25})_2(SC_2H_4Ph)_{16}$. This strongly supports the above interpretation.

(52) Zhu, M.; Eckenhoff, W. T.; Pintauer, T.; Jin, R. *J. Phys. Chem. C* **2008**, *112*, 14221.

(53) Häkkinen, H. *Nat. Chem.* **2012**, *4*, 443.

SUPPORTING INFORMATION

Separation of Precise Compositions of Noble Metal Clusters Protected with Mixed Ligands

Yoshiki Niihori,[a] Miku Matsuzaki,[a] Thalappil Pradeep,*[b] and Yuichi Negishi,*[a]

[a] *Department of Applied Chemistry, Faculty of Science, Tokyo University of Science, 1-3 Kagurazaka, Shinjuku-ku, Tokyo 162-8601, Japan.* [b] *DST Unit of Nanoscience (DST UNS) and Thematic Unit of Excellence, Indian Institute of Technology Madras, Chennai 600 036, India.*

Supporting Information I

Experimental Methods

A. Chemicals

All chemicals were obtained commercially and used without further purification. Hydrogen tetrachloroaurate tetrahydrate ($HAuCl_4 \cdot 4H_2O$) was obtained from Tanaka Kikinzoku. Palladium sodium chloride trihydride ($Na_2PdCl_4 \cdot 3H_2O$), tetraoctylammonium bromide ($(C_8H_{17})_4NBr$), sodium tetrahydroborate ($NaBH_4$), hexanethiol ($C_6H_{13}SH$), decanethiol ($C_{10}H_{21}SH$), dodecanethiol ($C_{12}H_{25}SH$), hexadecanethiol ($C_{16}H_{33}SH$), methanol (CH_3OH), acetone, toluene, dichloromethane (CH_2Cl_2), and tetrahydrofuran (THF) were obtained from Wako Pure Chemical Industries. 2-Phenylethanethiol (PhC_2H_4SH) was purchased from Tokyo Kasei. The 4-(*tert*-butyl)benzyl mercaptan (BBSH, Scheme S1) were purchased from Aldrich. The matrix, *trans*-2-[3-(4-*tert*-butylphenyl)-2-methyl-2-propenylidene] malononitrile (DCTB) was purchased from Fluka. Deionized water with a resistivity > 18.2 MΩ cm was used.

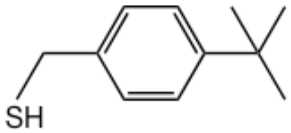

Scheme S1 Molecular structure of 4-(*tert*-butyl)benzyl mercaptan (BBSH)

B. Synthesis of $PdAu_{24}(SC_{12}H_{25})_{18}$, $Au_{25}(SC_{12}H_{25})_{18}$, and $Au_{38}(SC_{12}H_{25})_{24}$

$PdAu_{24}(SC_{12}H_{25})_{18}$ (Fig. S1(a)), $Au_{25}(SC_{12}H_{25})_{18}$ (Fig. S1(b)) and $Au_{38}(SC_{12}H_{25})_{24}$ (Fig. S1(c)) were synthesized by methods reported previously.[1–3]

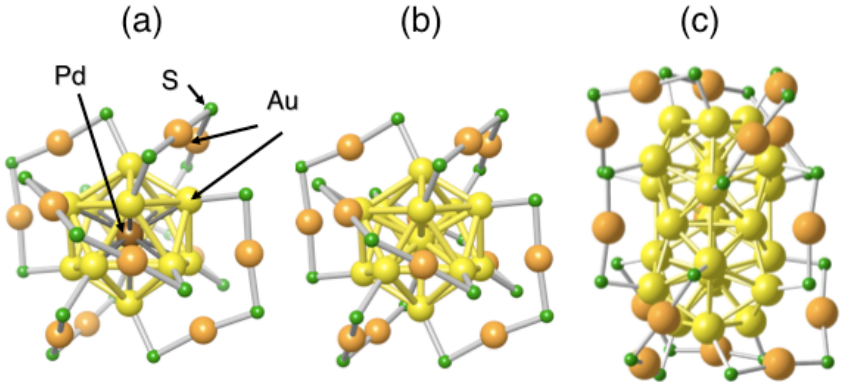

Figure S1. Structural representation of thiolate-protected metal clusters; (a) $PdAu_{24}(SR)_{18}$ (Ref. 1); (b) $Au_{25}(SR)_{18}$ (Refs. 4 and 5); and (c) $Au_{38}(SR)_{24}$ (Ref. 6) (The R moieties are omitted for clarity.)

C. Ligand exchange reactions

An amount of 0.14 μmol of $PdAu_{24}(SC_{12}H_{25})_{18}$, $Au_{25}(SC_{12}H_{25})_{18}$, or $Au_{38}(SC_{12}H_{25})_{24}$ was dissolved in 500 μL of dichloromethane. To this solution, 140 μmol of BBSH, $C_nH_{2n+1}SH$ (n = 6, 10, or 16), or PhC_2H_4SH was added and the solution was stirred at room temperature. The reaction was stopped at specific time duration. The solution was washed with a mixture of methanol and water to remove excess thiols, and the product was characterized by matrix-assisted laser desorption-ionization (MALDI) mass spectrometry. The $PdAu_{24}$, Au_{25}, or Au_{38} clusters with various chemical compositions were synthesized by changing the reaction time.[7]

D. HPLC experiments using a reverse-phase column

HPLC experiments were conducted on a Shimadzu instrument consisting of a CBM-20A controller, DGU-20AR on-line degasser, LC-20AD pump, SIL-20A auto-sampler, CTO-20A column oven, and SPD-M20A photodiode array (PDA) detector at IIT Madras or a Waters instrument consisting of a 600E controller, 486 tunable absorption detector, and 625 pump at Tokyo University of Science. The stainless steel column (250 × 4.6 mm i.d.) packed with 5-μm C18 bonded silica with 300-Å pore size (Theromo Scientific) was used as the reverse-phase column. This column is suitable for the separation of molecules with different polarity and is different from that used by Bürgi *et al*. for the separation of enantiomers of $Au_{38}(SC_2H_4Ph)_{24}$ (Refs. 8-10). Column temperature was 25 °C. The absorbance chromatogram was monitored by the PDA at 380 nm. The absorption spectra of the eluted peaks were collected over 190–800 nm by the PDA. Each sample was first diluted in THF (0.1 mg/5 μL) and then suspended in solution by adding 45 μL of CH_3OH. Then, 40 μL of the sample suspension was injected into the instrument with a mobile phase of methanol (CH_3OH) at a flow rate of 1 mL/min. After sample injection, the amount of THF in the mobile phase was continuously increased using a gradient program that increased the [THF]/[CH_3OH] ratio of the mobile phase from 0% to 100% (Figure S3). After analysis, the chromatogram was corrected by subtracting the background measured without a sample. Similar experiments were performed with the following two columns; a stainless steel column (250 × 4.6 mm i.d.) packed with 5-μm C8 bonded silica with 130-Å pore size (Theromo Scientific), and a stainless steel column (150 × 4.6 mm i.d.) packed with 5-μm phenyl bonded silica with 130-Å pore size (Theromo Scientific). However, the separations of the peaks were poorer under these conditions.

D. Characterization of chemical composition

MALDI mass spectra were collected using a linear time-of-flight mass spectrometer (Applied Biosystems, Voyager Linear RD VDA 500) with a nitrogen laser (wavelength: 337 nm). Measurements were also done with a reflectron time-of-flight mass spectrometer (Applied Biosystems, Voyager DE PRO) at IIT Madras. DCTB was used as the matrix.[8] The cluster-to-matrix ratio was set to be 1:1000.

Supporting Information II

Results

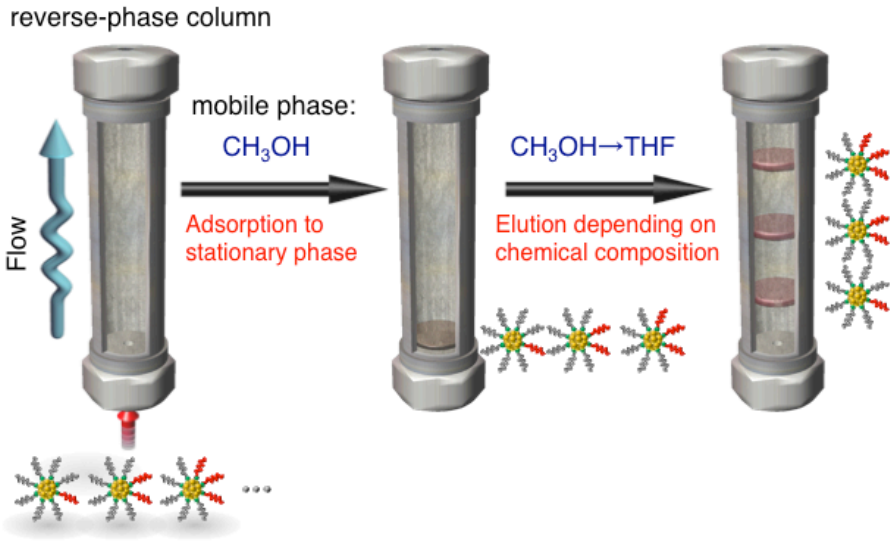

Figure S2. Schematic view of the concept for the high-resolution separation of metal clusters containing two types of thiolates by HPLC involving a reverse-phase column and mobile phase gradient.

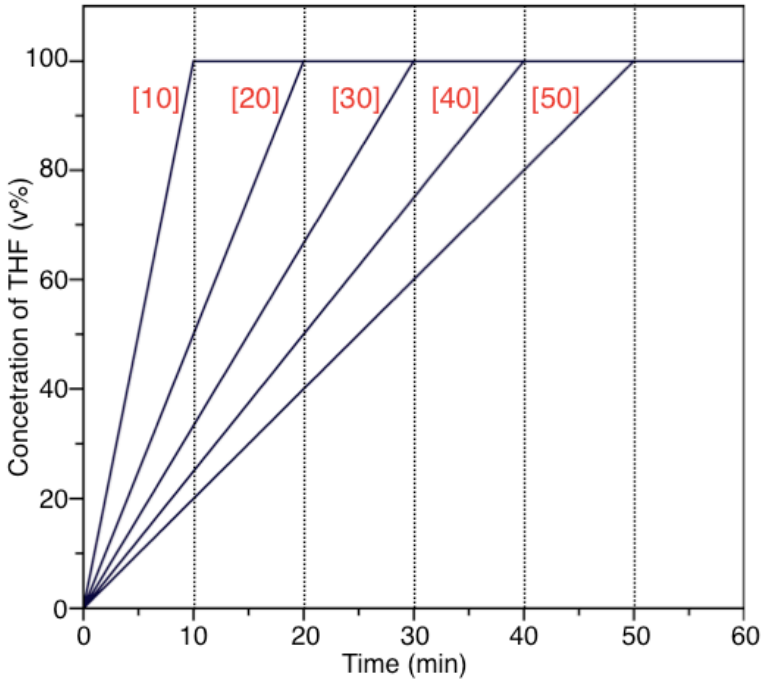

Figure S3. Linear gradient programs used for the high-resolution separation of $PdAu_{24}(SC_{12}H_{25})_{18-n}(SBB)_n$ (n = 6-16) (Figure 1(b)). The label (*e.g.*, [10]) in the figure indicates the time (in minutes) taken to fully replace the mobile phase with THF. The program [40] was used as the gradient program for the high-resolution separation for all of the clusters.

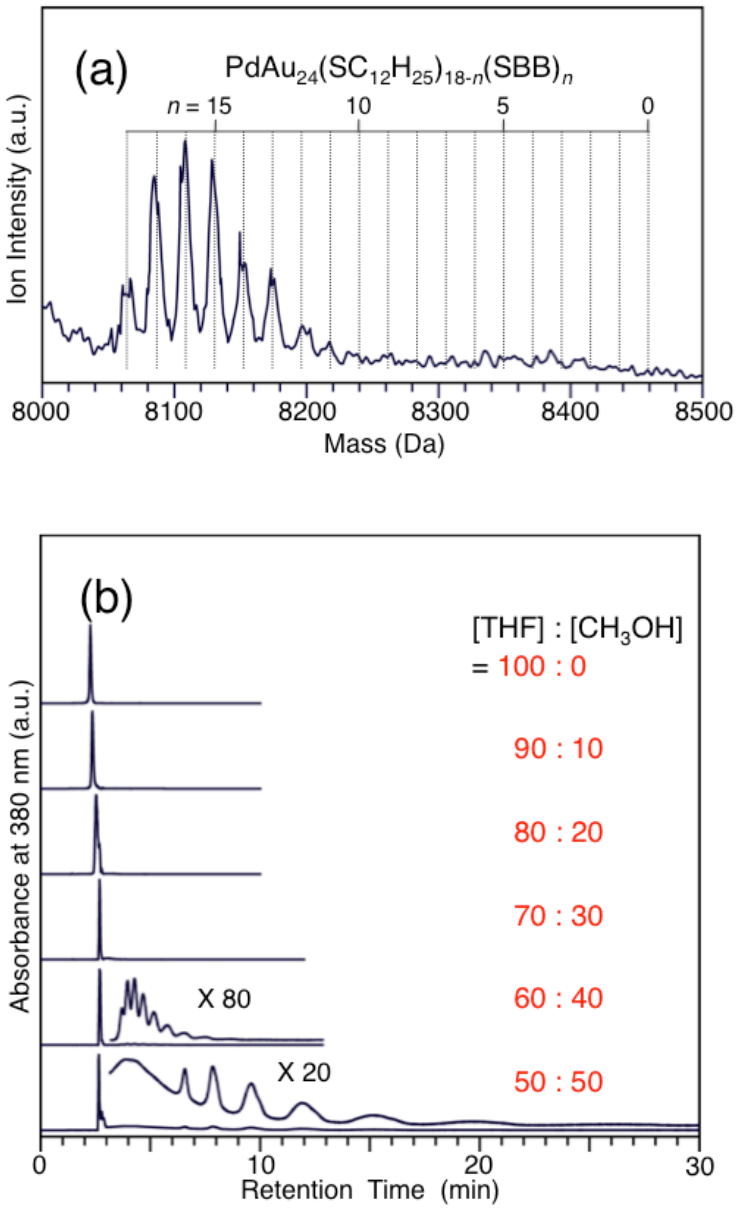

Figure S4. HPLC experiments conducted in an isocratic mode. In these experiments, the mobile phase was fixed to [THF]:[CH_3OH] = 100:0, 90:10, 80:20, 70:30, 60:40, or 50:50. (a) Negative ion MALDI mass spectrum of $PdAu_{24}(SC_{12}H_{25})_{18-n}(SBB)_n$ (n = 11–18) used in these experiments. (b) Chromatograms of $PdAu_{24}(SC_{12}H_{25})_{18-n}(SBB)_n$ (n = 11–18) at each mobile phase. The peaks appearing at 2.3–2.7 min were confirmed to include $PdAu_{24}(SC_{12}H_{25})_{18-n}(SBB)_n$ (n = 11–18). An increase in the concentration of CH_3OH promoted the interaction between $PdAu_{24}(SC_{12}H_{25})_{18-n}(SBB)_n$ and the stationary phase (column). Therefore, peak separations were observed when the concentration of CH_3OH was increased to 40 and 50 v/v% (enlarged spectra). However, even under those conditions, most of $PdAu_{24}(SC_{12}H_{25})_{18-n}(SBB)_n$ was not fixed to the stationary phase (column) and was eluted at 2.3–2.7 min. A further increase in concentration of CH_3OH (> 50 v/v%) resulted in the disappearance of the separated peaks. These results indicate that separating all of the clusters is difficult in isocratic mode. Thus, all the clusters must have to be once fixed on the stationary phase for the separation of all the clusters.

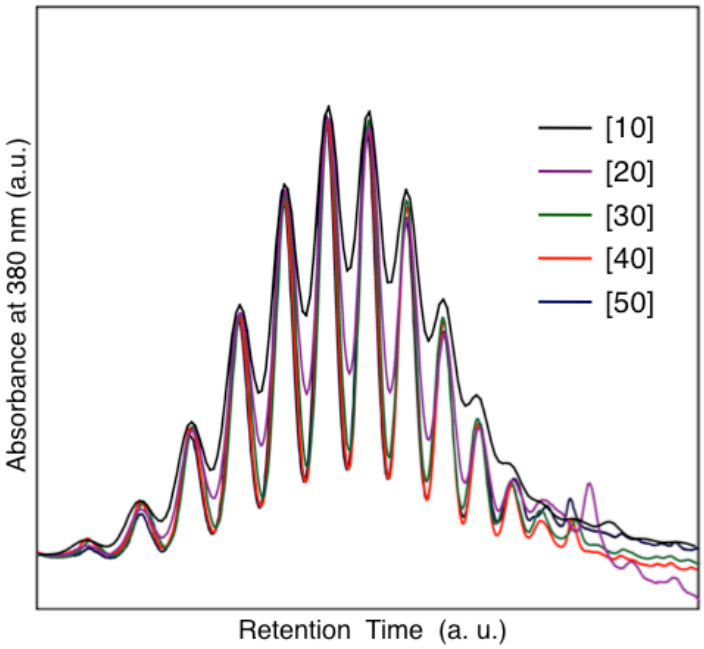

Figure S5. Enlarged chromatograms at each gradient condition. In this figure, the chromatograms are normalized in vertical axis and therefore, the horizontal axis is in arbitrary units. An increase in retention time (Figure 1(b)) resulted in better peak separation under the experimental conditions between [10] and [40]. However, the improvement in resolution was no longer observed at longer retention times (> [40]).

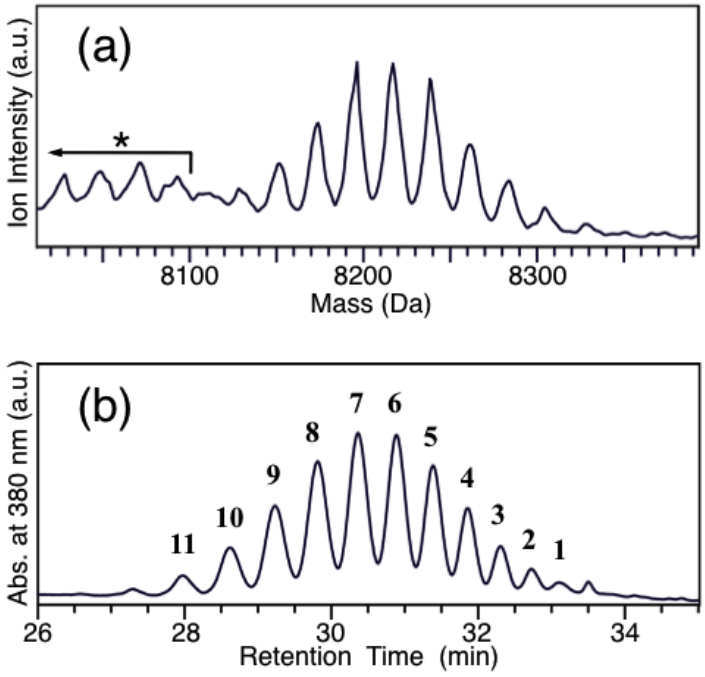

Figure S6. Comparison between the (a) Negative ion MALDI mass spectrum and (b) chromatogram of $PdAu_{24}(SC_{12}H_{25})_{18-n}(SBB)_n$ (n = 6–16) (Figure 1(a)). The chromatogram was obtained using a gradient program, [40]. In the mass spectrum, the asterisk indicates the laser fragments.[11] The shape of the chromatogram is similar to that of the mass spectrum. Each peak in the chromatogram was fractionated (fractions **1**–**11**) and characterized by MALDI mass spectrometry (see Figure S7).

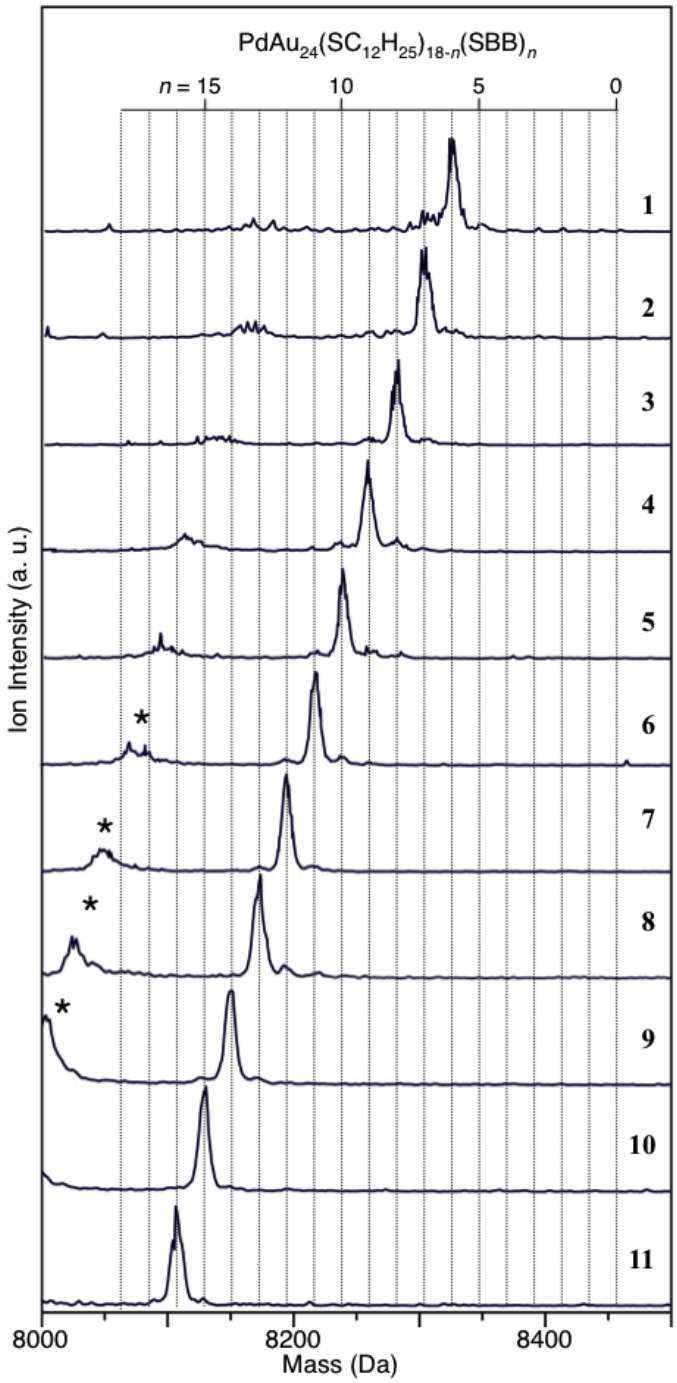

Figure S7. Negative ion MALDI mass spectra of **1**–**11** (Figure S6(a)). The asterisk indicates the laser fragments. These results indicate that peaks **1**–**11** contained only a single $PdAu_{24}(SC_{12}H_{25})_{18-n}(SBB)_n$ and that $PdAu_{24}(SC_{12}H_{25})_{18-n}(SBB)_n$ could be separated at high resolution depending on the chemical composition.

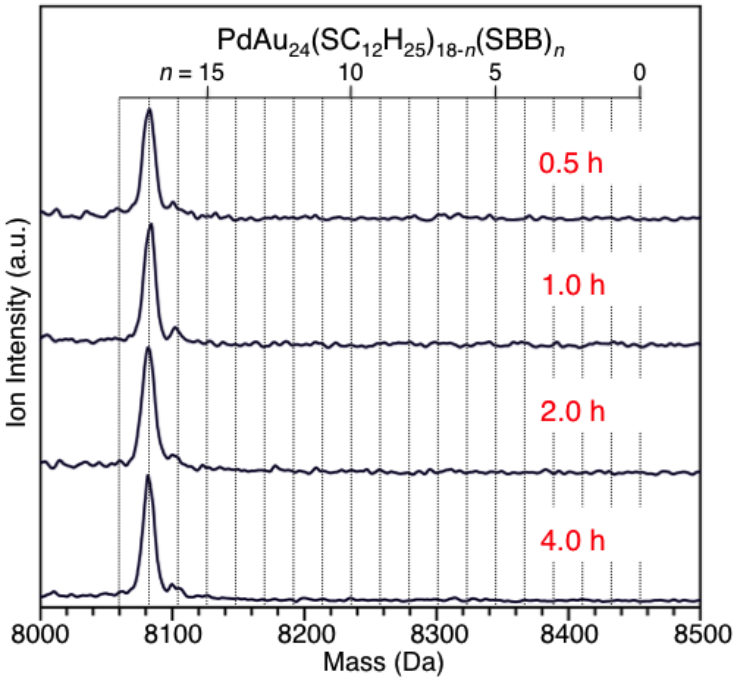

Figure S8. Stability of the isolated $PdAu_{24}(SC_{12}H_{25})(SBB)_{17}$ in CH_2Cl_2 followed by MALDI mass spectrometry. In this experiment, 0.28 mM of $PdAu_{24}(SC_{12}H_{25})(SBB)_{17}$ was diluted in 125 μL of CH_2Cl_2 and left at room temperature. At each time point, a small quantity of the solution was taken and characterized by MALDI mass spectrometry. Results indicated that the isolated $PdAu_{24}(SC_{12}H_{25})(SBB)_{17}$ maintains a chemical composition for at least 4 hours.[7]

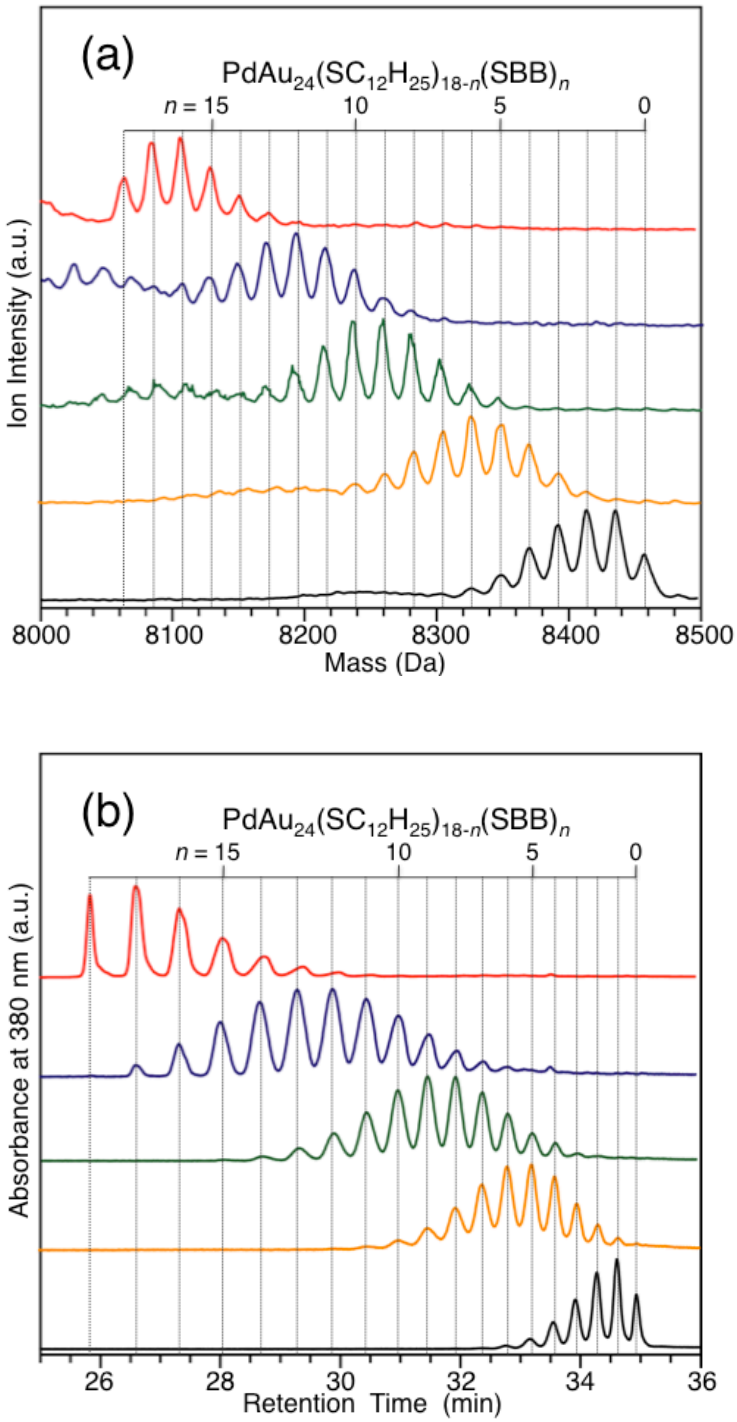

Figure S9. Comparison between (a) Negative ion MALDI mass spectra and (b) chromatograms for $PdAu_{24}(SC_{12}H_{25})_{18-n}(SBB)_n$. The same color indicates the same sample in (a) and (b). A linear gradient program, [40] (Figure S3), was used for these HPLC experiments. In (a), the laser fragment peaks[11] also are included (Figures 1(a) and S6(b)). In (b), each peak is labeled with the chemical compositions that were assigned by the mass analysis of each fraction (Figure 2).

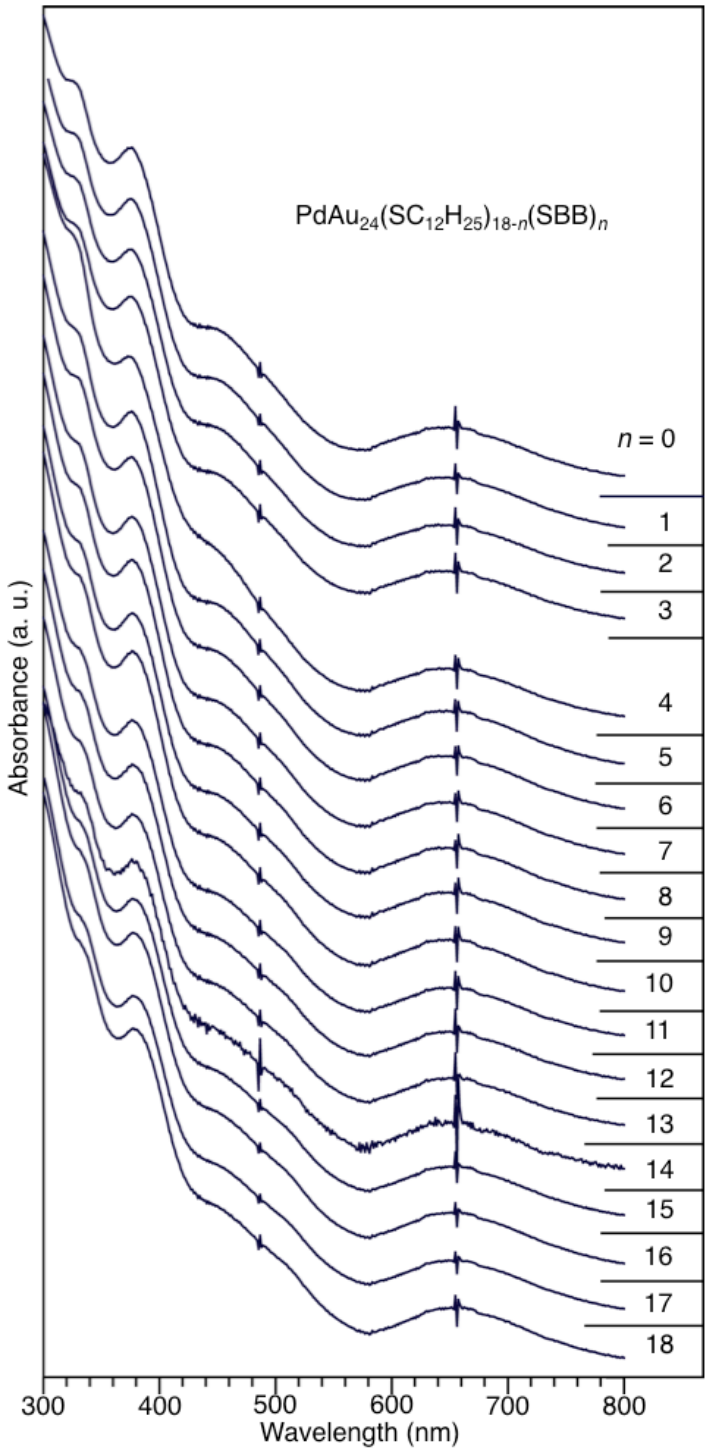

Figure S10. Optical absorption spectra of the isolated $PdAu_{24}(SC_{12}H_{25})_{18-n}(SBB)_n$ (n = 0–18) obtained by the PDA detector. All the spectra were normalized at 670 nm. All of the spectra are nearly similar. However, close comparison indicated that the spectral features are slightly different depending on the chemical composition.

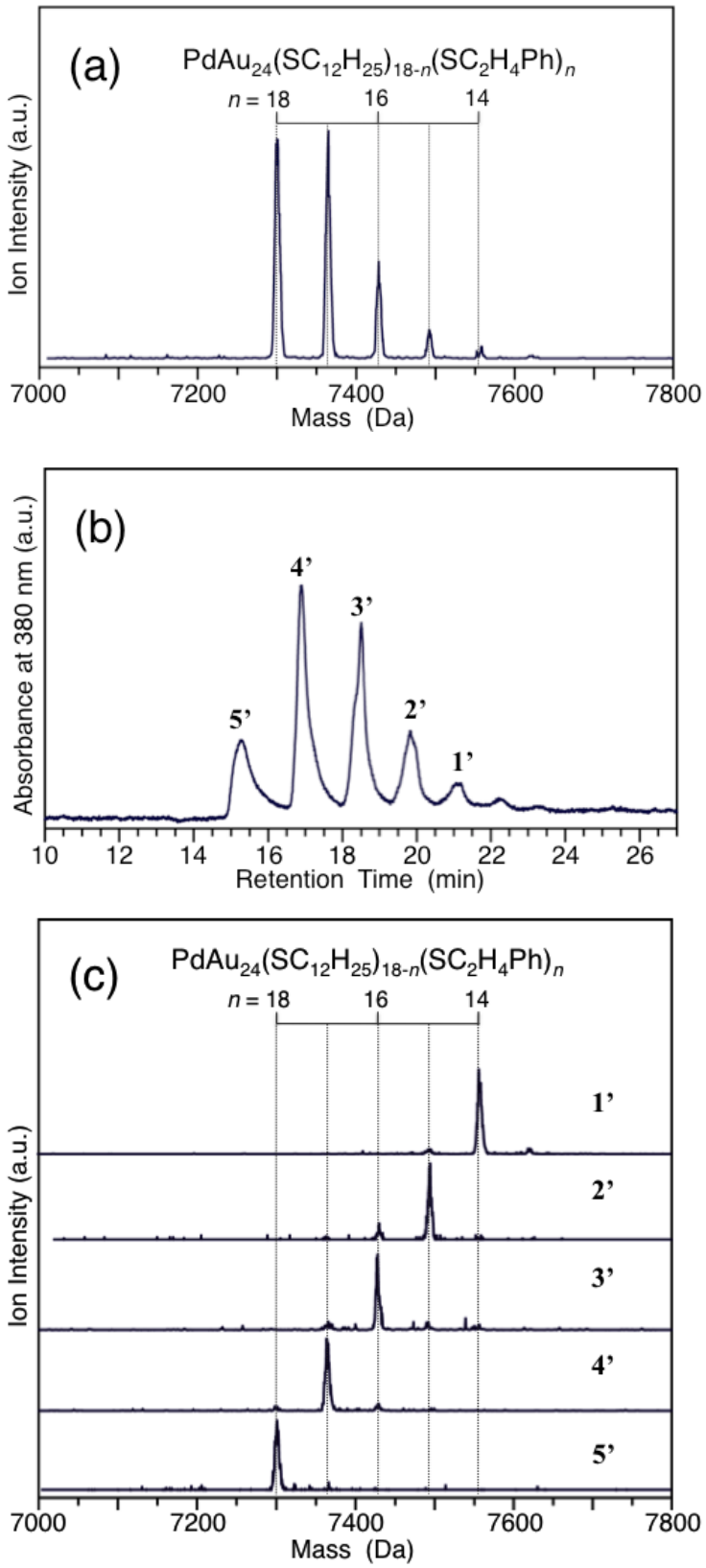

Figure S11. (a) Negative ion MALDI mass spectrum of $PdAu_{24}(SC_{12}H_{25})_{18-n}(SC_2H_4Ph)_n$ (n = 14–18). (b) Chromatograms of these clusters. (c) Negative ion MALDI mass spectra of the fractions of each peak appearing in the chromatogram, **1'–5'**. These results indicate that each peak, **1'–5'**, contains a single $PdAu_{24}(SC_{12}H_{25})_{18-n}(SC_2H_4Ph)_n$ in high purity and that $PdAu_{24}(SC_{12}H_{25})_{18-n}(SC_2H_4Ph)_n$ clusters were separated at high resolution depending on the chemical composition.

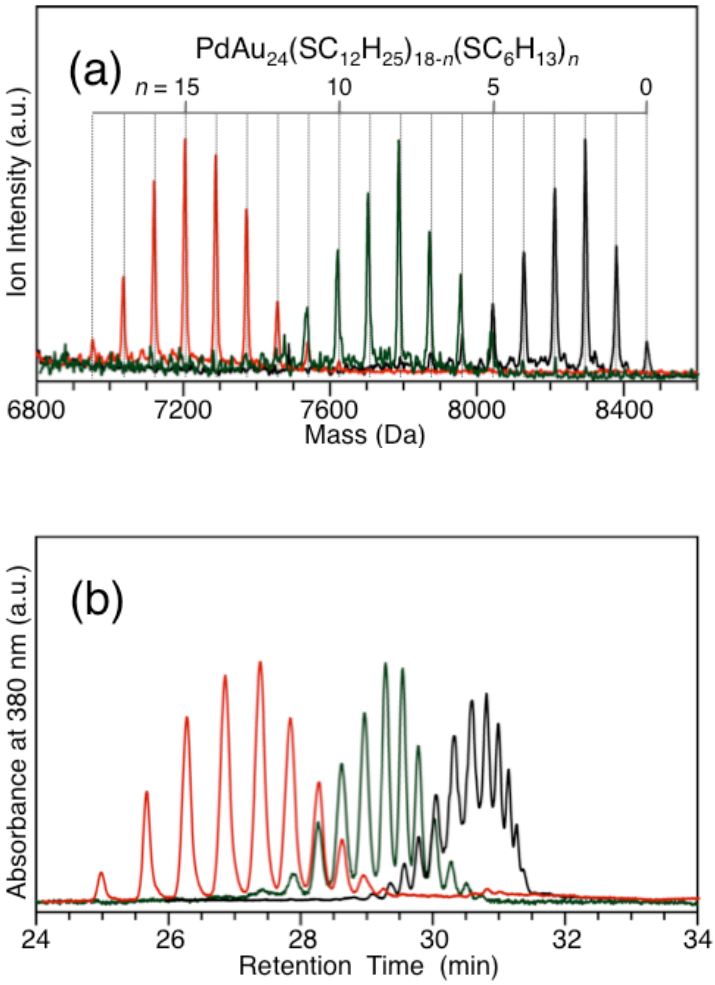

Figure S12. Comparison between the (a) Negative ion MALDI mass spectrum and (b) chromatogram of $PdAu_{24}(SC_{12}H_{25})_{18-n}(SC_6H_{13})_n$. In (a) and (b), the same color indicates the same sample. A linear gradient program, [40] (Figure S3), was used for these HPLC experiments.

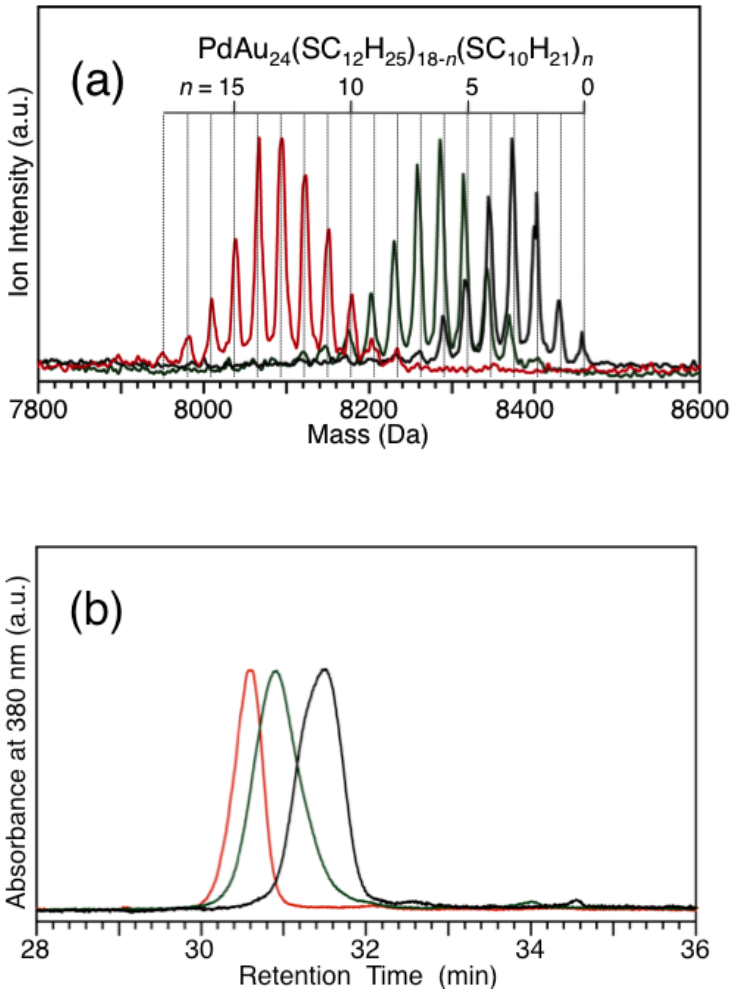

Figure S13. Comparison between the (a) Negative ion MALDI mass spectrum and (b) chromatogram for $PdAu_{24}(SC_{12}H_{25})_{18-n}(SC_{10}H_{21})_n$. In (a) and (b), the same color indicates the same sample. A linear gradient program, [40] (Figure S3), was used for these HPLC experiments.

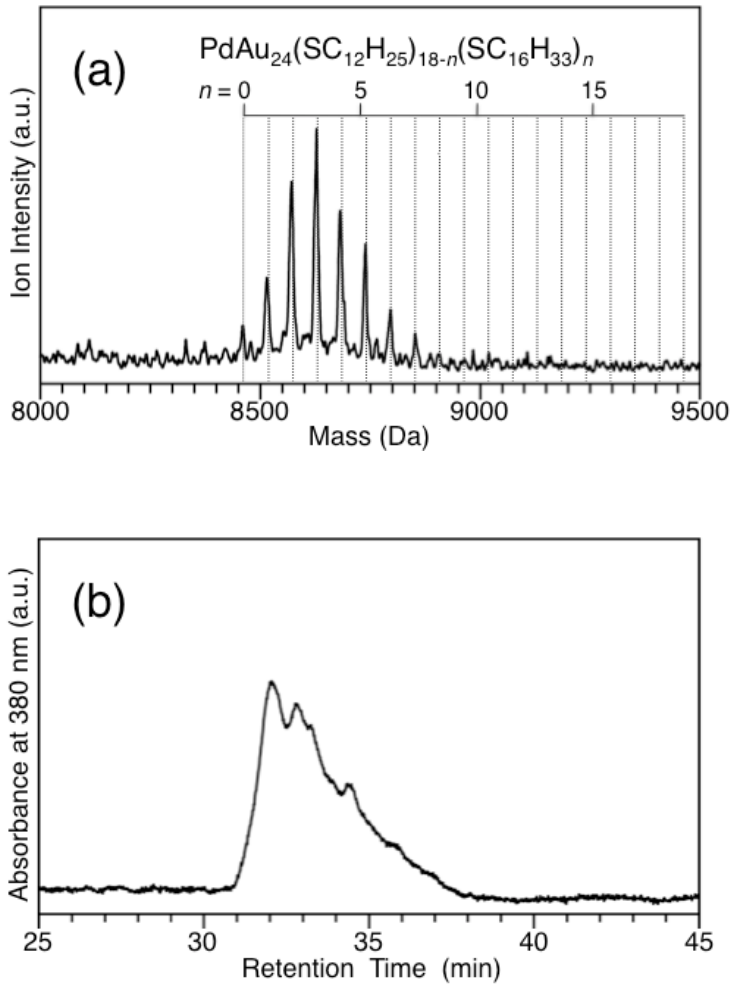

Figure S14. Comparison between the (a) Negative ion MALDI mass spectrum and (b) chromatogram for $PdAu_{24}(SC_{12}H_{25})_{18-n}(SC_{16}H_{33})_n$. A linear gradient program, [40] (Figure S3), was used in this HPLC experiment.

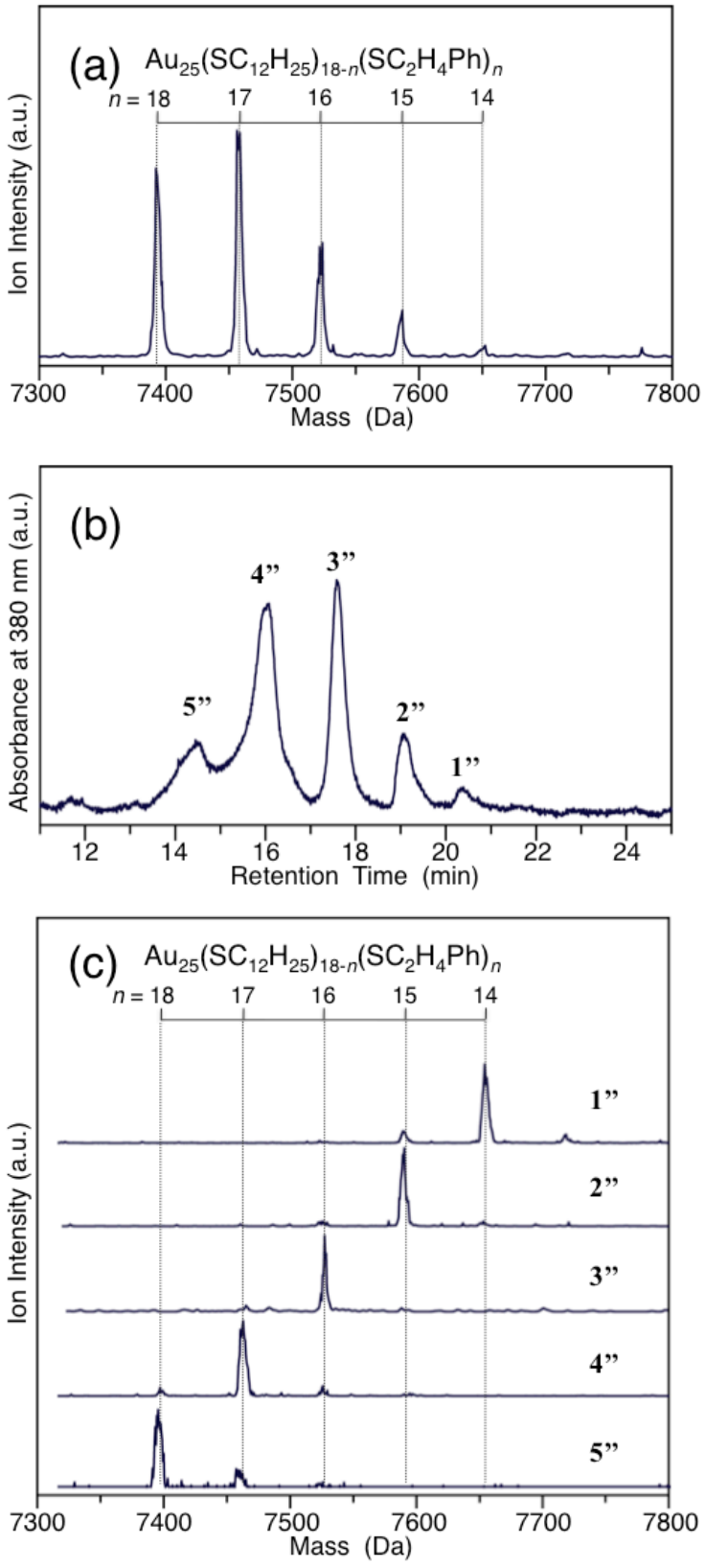

Figure S15. (a) Negative ion MALDI mass spectrum of $Au_{25}(SC_{12}H_{25})_{18-n}(SC_2H_4Ph)_n$ (n = 14–18). (b) chromatogram of these clusters. (c) Negative ion MALDI mass spectra of the fractions of each peak section appeared in the chromatogram, **1’’–5’’**. These results indicate that each peak section, **1’’–5’’**, contains a single $Au_{25}(SC_{12}H_{25})_{18-n}(SC_2H_4Ph)_n$ in high purity and that $Au_{25}(SC_{12}H_{25})_{18-n}(SC_2H_4Ph)_n$ clusters were separated at high resolution depending on the chemical composition.

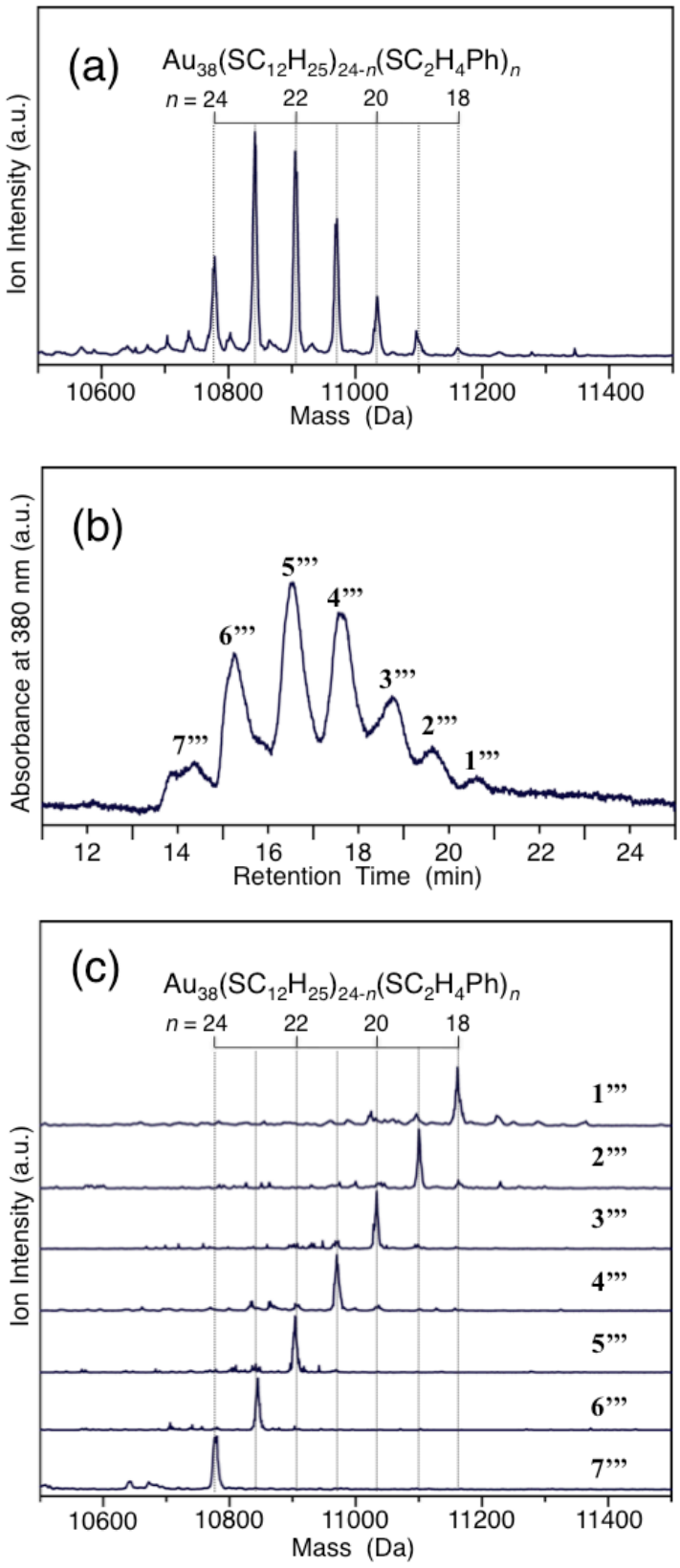

Figure S16. (a) Positive ion MALDI mass spectrum of $Au_{38}(SC_{12}H_{25})_{24-n}(SC_2H_4Ph)_n$ (n = 18–24). (b) Chromatograms of these clusters. (c) Positive ion MALDI mass spectra of the fractions of each peak appearing in the chromatogram, **1'''–7'''**. These results indicate that each peak, **1'''–7'''**, contains a single $Au_{38}(SC_{12}H_{25})_{24-n}(SC_2H_4Ph)_n$ at high purity and that $Au_{38}(SC_{12}H_{25})_{24-n}(SC_2H_4Ph)_n$ clusters were separated at high resolution depending on the chemical composition.

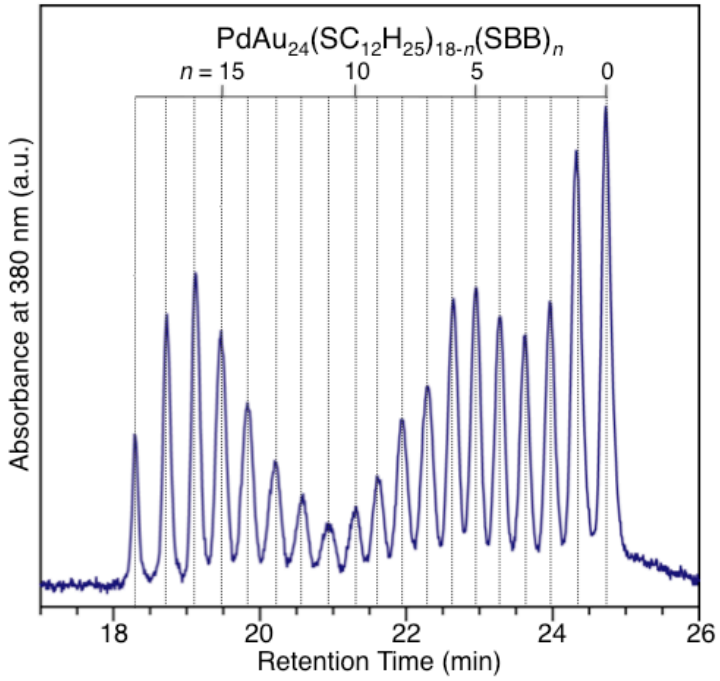

Figure S17. Chromatogram of a mixture of $PdAu_{24}(SC_{12}H_{25})_{18-n}(SBB)_n$ (n = 0–18) observed with a mobile phase gradient program different from that used in this work. This gradient program was composed of a combination of a linear line and a curved line. $PdAu_{24}(SC_{12}H_{25})_{18-n}(SBB)_n$ with a broad distribution (n = 0–18) was prepared by mixing several $PdAu_{24}(SC_{12}H_{25})_{18-n}(SBB)_n$ clusters with different distributions. In this chromatogram, each peak progresses at nearly regular intervals. This peak pattern is consistent with that observed in the mass spectrum. This makes conformation of the separation of each cluster easy and allows an estimate of the abundance ratio of each cluster.

References

1. Negishi, Y.; Kurashige, W.; Niihori, Y.; Iwasa, T.; Nobusada, K. *Phys. Chem. Chem. Phys.* **2010**, *12*, 6219–6255.
2. Negishi, Y.; Chaki, N. K.; Shichibu, Y.; Whetten, R. L.; Tsukuda, T. *J. Am. Chem. Soc.* **2007**, *129*, 11322–11323.
3. Chaki, N. K.; Negishi, Y.; Tsunoyama, H.; Shichibu, Y.; Tsukuda, T. *J. Am. Chem. Soc.* **2008**, *130*, 8608–8610.
4. Heaven, M. W.; Dass, A.; White, P. S.; Holt, K. M.; Murray, R. W. *J. Am. Chem. Soc.* **2008**, *130*, 3754.
5. Zhu, M.; Aikens, C. M.; Hollander, F. J.; Schatz, G. C.; Jin, R. *J. Am. Chem. Soc.* **2008**, *130*, 5883.
6. Qian, H.; Eckenhoff, W. T.; Zhu, Y.; Pintauer, T.; Jin, R. *J. Am. Chem. Soc.* **2010**, *132*, 8280–8281.
7. Niihori, Y.; Kurashige, W.; Matsuzaki, M.; Negishi, Y. *Nanoscale* **2013**, *5*, 508–512.
8. Dolamic, I.; Knoppe, S.; Dass, A.; Bürgi, T. *Nat. Commun.* **2012**, *3*, 798–803.
9. Knoppe, S.; Azoulay, R.; Dass, A.; Bürgi, T. *J. Am. Chem. Soc.* **2012**, *134*, 20302–20305.
10. Knoppe, S.; Dolamic, I.; Dass, A.; Bürgi, T. *Angew. Chem. Int. Ed.* **2012**, *51*, 7589–7591.
11. Dass, A.; Stevenson, A.; Dubay, G. R.; Tracy, J. B.; Murray, R. W. *J. Am. Chem. Soc.* **2008**, *130*, 5940–5946.

Biopolymer-reinforced synthetic granular nanocomposites for affordable point-of-use water purification

Mohan Udhaya Sankar[1], Sahaja Aigal[1], Shihabudheen M. Maliyekkal[1], Amrita Chaudhary, Anshup, Avula Anil Kumar, Kamalesh Chaudhari, and Thalappil Pradeep[2]

Unit of Nanoscience and Thematic Unit of Excellence, Department of Chemistry, Indian Institute of Technology Madras, Chennai 600 036, India

Edited by Eric Hoek, University of California, Los Angeles, CA and accepted by the Editorial Board April 4, 2013 (received for review November 21, 2012)

Creation of affordable materials for constant release of silver ions in water is one of the most promising ways to provide microbially safe drinking water for all. Combining the capacity of diverse nanocomposites to scavenge toxic species such as arsenic, lead, and other contaminants along with the above capability can result in affordable, all-inclusive drinking water purifiers that can function without electricity. The critical problem in achieving this is the synthesis of stable materials that can release silver ions continuously in the presence of complex species usually present in drinking water that deposit and cause scaling on nanomaterial surfaces. Here we show that such constant release materials can be synthesized in a simple and effective fashion in water itself without the use of electrical power. The nanocomposite exhibits river sand-like properties, such as higher shear strength in loose and wet forms. These materials have been used to develop an affordable water purifier to deliver clean drinking water at US $2.5/y per family. The ability to prepare nanostructured compositions at near ambient temperature has wide relevance for adsorption-based water purification.

hybrid | green | appropriate technology | frugal science | developing world

Safe drinking water is a significant, but simple indicator of development. Its availability at point of use can save over 2 million human lives (1) (of the 3.575 million deaths caused by water, sanitation, and hygiene issues, 42.6% are due to diarrhea alone: 3.575 million × 0.426 = 1.523 million lives), can avoid over 2 billion diarrheal infections (2), and can contribute over $4 billion to the global gross domestic product (3) (formula used: Σ (number of deaths attributed to diarrhea in each country × corresponding country's per capita gross domestic product). Considering the challenges associated with traditional disinfectants (4), solutions based on state-of-the-art science and technology hold the key for safe drinking water (5) and novel approaches are being looked at (6, 7). It has been long known that silver, especially in nanoparticle form, is an effective disinfectant and works for a wide spectrum of bacteria and viruses (8, 9). Numerous approaches are available for the synthesis of biocidal silver nanoparticles or colloids, including the use of matrices (10–12). The biocidal property of silver nanoparticles, usually in the size range of 10–20 nm, is attributed to the release of trace quantities of silver ions in water (13–16), which, although being sufficient for microorganism killing, does not exhibit toxicity to humans (17, 18). [Toxicity due to silver nanoparticles themselves is also known (16)]. Although a number of silver-based biocidal compositions have been synthesized, those have not been able to reach the masses in large volumes (e.g., silver nanoparticle-loaded ceramic candles) (19). Massive deployment has been hampered due to the following reasons: (*a*) Drinking water contains many species (e.g., inorganic ions and organics) that anchor on the surface of the nanoparticles, making sustained silver ion release difficult (15); (*b*) suitable anchoring substrates that limit the scaling of nanoparticle surfaces while simultaneously preventing their release into water are not available; and (*c*) continued retention of the nanoparticles in the matrix is difficult.

In this work, we demonstrate a unique family of nanocrystalline metal oxyhydroxide-chitosan granular composite materials prepared at near room temperature through an aqueous route. The origin of crystallinity in the composition is attributed to abundant -O- and -OH functional groups on chitosan, which help in the crystallization of metal oxyhydroxide and also ensure strong covalent binding of the nanoparticle surface to the matrix. X-ray photoelectron spectroscopy (XPS) confirms that the composition is rich with surface hydroxyl groups. Using hyperspectral imaging, the absence of nanoparticle leaching in the water was confirmed. Further, a unique scheme to reactivate the silver nanoparticle surface is used for continual antimicrobial activity in drinking waters. Several other composites have been developed that can scavenge other contaminants in water. We demonstrate an affordable water purification device based on such composites developed over several years and undergoing field trials in India, as a potential solution for widespread eradication of the waterborne disease burden.

Results and Discussion

The antimicrobial composition consists of an aluminum oxyhydroxide–chitosan composite (referred to as BM) with silver particles of 10–20 nm diameter embedded in it (Fig. 1*A* and *SI Appendix*, Fig. S1) and is capable of sustained release of silver ions [40 ± 10 parts per billion (ppb)] in natural drinking water over an extended volume of water passing through it, to achieve effective removal of microorganisms (*SI Appendix*, Fig. S2; see Fig. 3*C*). The antimicrobial composite (referred to as Ag-BM) is unique as it is made in water at near room temperature, using a biopolymer, and dried in ambient conditions to obtain water-insoluble granules, yielding Na_2SO_4 as the major by-product (>90%), thereby making it a green synthesis. The concentration of silver ion leached into drinking water from the prepared composite at relevant temperatures (5–35 °C) (*SI Appendix*, Fig. S3) is significantly less than the maximum permissible limit of 100 ppb (secondary standard, US Environmental Protection Agency), thereby requiring no secondary filtration to remove excess silver ions. This controlled release at temperatures of relevance to drinking-water applications over extended periods is an important advantage of the composite. X-ray diffraction patterns of BM and Ag-BM show the presence of

Author contributions: M.U.S., A.C., A., and T.P. designed research; M.U.S., S.A., S.M.M., A.C., A., A.A.K., and K.C. performed research; M.U.S., S.A., A., and T.P. analyzed data; and M.U.S., S.A., A.C., A., and T.P. wrote the paper.

The authors declare no conflict of interest.

This article is a PNAS Direct Submission. E.H. is a guest editor invited by the Editorial Board.

[1]M.U.S., S.A., and S.M.M. contributed equally to this work.

[2]To whom correspondence should be addressed. E-mail: pradeep@iitm.ac.in.

This article contains supporting information online at www.pnas.org/lookup/suppl/doi:10.1073/pnas.1220222110/-/DCSupplemental.

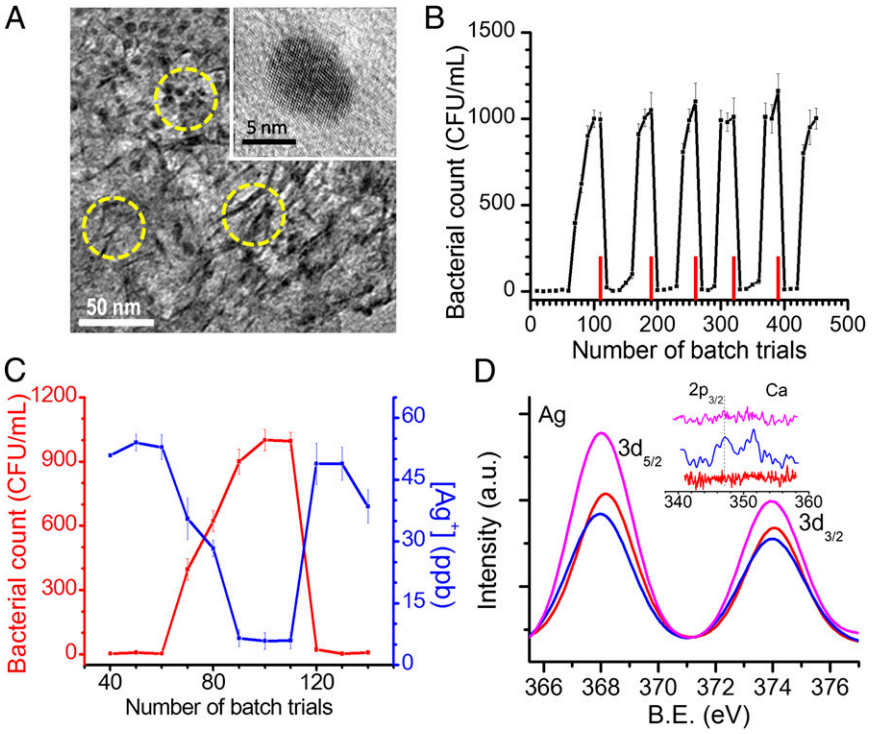

Fig. 1. Characterization of composite and exhibits of its unique antimicrobial activity. (*A*) Transmission electron micrograph of Ag-BM. The composite matrix appears as nanosheets of 3- to 4-nm thickness and the embedded nanoparticles are seen as dots. Some sheets and particles are indicated by circles. The matrix made of the boehmite–chitosan acts like a cage in which the nanoparticles are trapped. The particle sizes are much smaller than those of a typical aqueous phase synthesis. *Inset* shows an expanded view of one particle. (*B*) Bacterial load measured in water as a function of batch upon spiking 10^5 CFU/mL of *E. coli*. Red bars indicate the point of reactivation. (*C*) Silver ion concentration measured by ICP-MS (blue trace) and corresponding bacterial count in CFU/mL for one of the cycles (number of trials: 40th–140th) (red trace) from batch measurements. (*D*) X-ray photoemission spectra of initial (red trace), saturated (blue trace), and reactivated (pink trace) composites in the Ag 3d region and the Ca 2p region (*Inset*). The intensity of Ca 2p (*Inset*) is weak as the coating is thin. The reactivated composite shows an increased Ag 3d intensity due to removal of scale-forming species and better exposure of the nanoparticle surface.

nanocrystalline AlOOH of mean crystallite size of 3.5 nm calculated from the Scherrer formula (*SI Appendix*, Fig. S4).

High-resolution electron micrographs show that the silver nanoparticles are trapped within the AlOOH–chitosan cages, which allow them to be preserved with reduced contact with scale-forming chemical species, yet allowing sufficient interaction with water, due to which sustained release of Ag^+ is possible (Fig. 1*A* and *SI Appendix*, Figs. S1 and S5). The inorganic cages formed by AlOOH are seen as dark lines of 3–4 nm thickness in the transmission electron microscopy (TEM) image and are held together by the chitosan matrix (see below for a discussion of the materials). The nanoparticles are small enough to release Ag^+ and are single crystalline (Fig. 1*A*, *Inset*). This uniformity and reduced particle size are difficult to achieve for silver in a fast, aqueous-phase synthesis.

The composite was tested for antibacterial activity in batch mode (*Materials and Methods*) for more than 400 trials continuously and it exhibited a cyclic pattern of antibacterial action in natural drinking water (Fig. 1*B*). A typical cycle (number of trials: 10th–140th) represents antibacterial performance of Ag-BM at its peak, followed by a drop in performance due to a gradual decrease in Ag^+ release, resulting in an increase in bacterial count in the output water, and finally after reactivation (regaining the ability to leach silver ions) an immediate recovery of performance where Ag^+ release is back to normal (40 ± 10 ppb, Fig. 1*C*).

The concept of reactivation is an important reason behind Ag-BM's long-lasting antimicrobial performance. As seen in Fig. 1*B*, the performance of Ag-BM drops after a certain number of trials (60 trials) due to its continuous exposure to scalants present in water, even though the silver content within the BM matrix is still significant. This drop in performance is explained by studying the XPS of the spent Ag-BM, where the Ag $3d_{5/2}$ peak is at a reduced intensity in comparison with the initial composite (Fig. 1*D*). Factors such as deposition of sparingly soluble species, principally in the form of $CaCO_3$ and silicate precursors, are responsible for the partial filling of the composite with a thin layer of scalants, reducing silver release. The existence of Ca 2p and Si 2p peaks in the XPS spectra of spent Ag-BM proves this (Fig. 1*D*, *Inset* and *SI Appendix*, Fig. S6). SEM-EDAX elemental imaging and spectra also support the presence of deposits containing Ca and Si (*SI Appendix*, Fig. S7). Surface imaging by atomic force microscopy (AFM) shows increased inhomogeneity in the saturated Ag-BM (*SI Appendix*, Fig. S8). The proof of scaling is further substantiated by trials done in natural drinking water and ultrapure water (resistivity: 18 MΩ.cm). In natural drinking water, Ag-BM is subjected to deposition of sparingly soluble species, which limits its efficacy after a period; whereas, due to the nonexistence of these species in ultrapure water, the life of the composite is prolonged and is almost indefinite (*SI Appendix*, Fig. S9). Additionally, the antibacterial efficacy of Ag-BM was tested under prevalent water quality parameters of total dissolved solids (TDS), pH, and total organic carbon (TOC) and performance of the composite was acceptable (*SI Appendix*, Fig. S10). Of the several methods tested, the simplest, most effective, and field implementable one for regaining Ag^+ release is incubating the inactive Ag-BM in water [deionized water or natural drinking water (*SI Appendix*, Fig. S11)] at 70–100 °C for 3–4 h. In a batch experiment, when a finite bacterial colony count (10–50 CFU/mL) was observed in the output, the trials were continued a few more times to ensure the drop in performance and thereafter, the composite was reactivated. The number of trials that can be done after every reactivation slowly reduces with increasing trials. Acid-digested initial Ag-BM showed 0.432% silver by weight, and after 450 trials, it reduced to 0.306%, which corresponds to 71% of Ag still left in the BM matrix. Theoretically, leaching of 29% silver amounts to an average concentration of 50 ppb over 500 batch trials, using 2 g composite. The tests were stopped after 450 trials and Ag-BM was not reactivated further, although the same method may be continued. Innovative reactivation methods may also be used, not limited to the heat treatment method alone (*SI Appendix*, Fig. S12). By using diluted lemon juice, readily available in every home, further reactivation can be done, possibly until the composite gets exhausted completely, i.e., when requisite silver ions cannot be released from the matrix any further.

The composite was tested for antiviral activity in batch mode (*Materials and Methods*) for more than 200 trials continuously in

natural drinking water. The antiviral performance is similar to the antibacterial performance. When the performance deteriorates, the activity is regained after reactivation (*SI Appendix*, Fig. S13).

When a nanocomposite-based approach is used for drinking-water purification, the possibility of nanoparticle release in drinking water exists. To confirm the effective trapping of nanoparticles in the matrix and absence of any observable nanoparticle release in water, dark-field microscopy was done on the bacteria. Microscopic images (Fig. 2 and *SI Appendix*, Figs. S14 and S15) show that although nanoparticles are seen within the bacterial contour of citrate-protected Ag nanoparticle-treated bacterial cells, no nanoparticle is seen in bacterial cells treated with Ag-BM. However, lysis is observed in both cases as observed in the discontinuity of the cell membrane (Fig. 2 *B* and *C* and 2 *D* and *E*, *Insets*). The hyperspectral images of bacterial cells treated with citrate-protected Ag nanoparticles show distinct size-dependent surface plasmon features of the nanoparticles (Fig. 2*D*) that are absent in the case of Ag-BM–treated bacterial cells (Fig. 2*E*). The data conclusively established that silver ions released from Ag-BM are responsible for the antibacterial activity and there is no observable nanoparticle release in water. It is also confirmed that during the interaction of water with the composition, AlOOH–chitosan does not undergo dissolution; aluminum release in water is less than 6 ppb (aluminum secondary standard: 50–200 ppb, US Environmental Protection Agency) and total organic carbon is nearly 0.1 ppm (*SI Appendix*, Fig. S16). Independent spectroscopic measurements of Ag-BM–treated water samples and the cyclic nature of antibacterial performance also support this. The antibacterial activity of Ag-BM was also shown by fluorescence microscopy study of treated bacteria where a mixture of nucleic acid-binding fluorescent dyes [green fluorescent SYTO9 dye and red fluorescent propidium iodide (PI) dye] were used (*SI Appendix*, Fig. S17).

A water purification device (Fig. 3 *A* and *B*) containing 50 g of Ag-BM in cartridge form was assessed for performance under standard test conditions. This filter ran up to 1,500 L with a bacterial input load of 10^5 CFU/mL without the need for reactivation (Fig. 3*C* and *SI Appendix*, Fig. S2). Therefore, by using 120 g composite, safe drinking water can be provided for a family of five for 1 y (assuming daily drinking water consumption of 10 L). This translates to an annual expense of $2 per family. (Cost of media, sediment prefilter, plastic assembly, and cartridge packing are included in the cost calculation.) By reactivating this composite, the life of the cartridge can be enhanced further, thereby reducing the cost. The water purification device has a second-stage axial filtration based on an activated carbon block (Fig. 3*A*) with a nominal pore size of <4 μm, which enables it to remove cysts through physical filtration, and the cyst removal capacity is higher than 5 log (input count, 10^6 particles per liter; output count, <3 particles per liter), in accord with the National Science Foundation (NSF) protocol P231 (*SI Appendix*, Fig. S18). The carbon block has an additional function of removing any organic and bacterial biomass as well, besides removing traces of silver ions or silver bound with microbial debris. However, residual silver ion content may be advantageous in some cases to prevent microbial contamination in water upon storage as well as to prevent bio-fouling of the composite during periods of nonuse.

Considering the fact that some parts of the world have severe chemical contamination in ground water (20), causing life-threatening diseases, suitable unique composites may be packed into the carbon filter to remove harmful chemical contaminants such as arsenic, pesticides, mercury, lead, iron, etc., so that chemically and microbiologically pure water is obtained, depending on the region of use. Composite preparation at room temperature is crucial for addressing health-related contaminants as the method preserves active adsorption sites (for example, surface hydroxyl groups undergo dehydration on exposure to higher temperature).

For example, to remove iron, 100 g iron oxyhydroxide–chitosan composite (*Materials and Methods*) was taken. Feed water containing freshly prepared 5 ± 1 ppm of Fe^{2+} was passed through the composite at a flow rate of 50 mL/min. The output water was tested for both Fe^{3+} and Fe^{2+} by spectrophotometric methods. The column was run for 1,500 L and the output concentration was consistently below 0.3 ppm, thereby adhering to the World Health

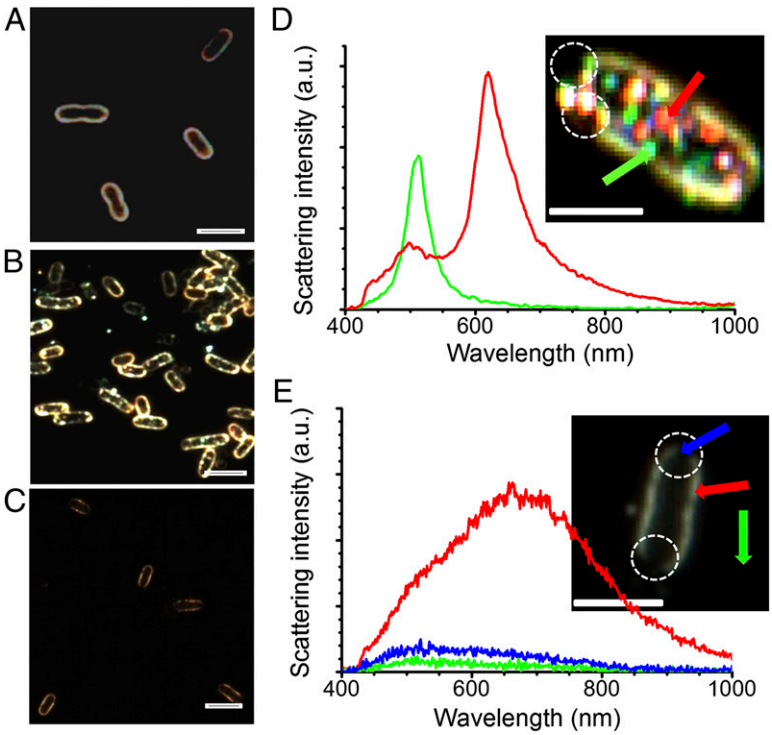

Fig. 2. Microscopic examination of bacterial lysis through dark-field and hyperspectral imaging. (*A*–*C*) Dark-field microscopy images of bacteria in water, bacteria treated with citrate-protected Ag nanoparticles, and bacteria treated with Ag-BM, respectively. (*A*) Continuous bacterial contour. (*B*) Nanoparticles within and outside the bacterial contour, which are seen as bright dots. (*C*) Discontinuous bacterial contour with the absence of nanoparticles from Ag-BM. (*D*) Scattering spectra of single nanoparticles embedded in the bacterial contour. (*Inset*) Hyperspectral image from which the spectra are taken. The spectral traces and the arrows correspond to the same particles. (*E*) Scattering spectra of lysed bacterial border after treating with Ag-BM. *Inset* shows the hyperspectral image of a bacterium treated with Ag-BM. The color of the traces and the points from which spectra are collected (shown by arrows) are the same. Blue and green traces in *E* are nearly the same, indicating that the lysed regions appear like background. Lysis is shown by white circles in the images in *D* and *E*. (Scale bars in all images: 2 μm.) Scattering from nanoparticles is approximately an order of magnitude larger compared with the bacterial contour.

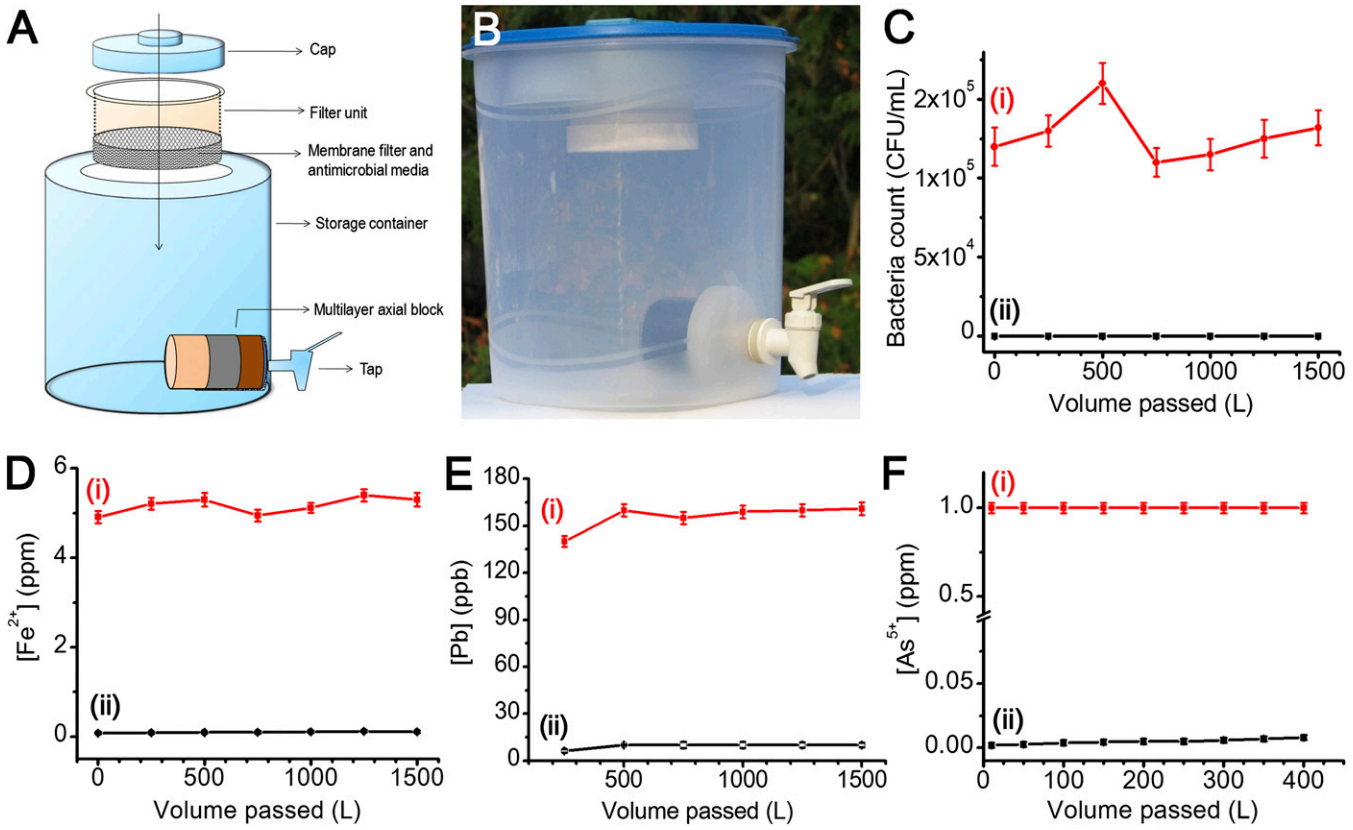

Fig. 3. Water purification device undergoing field trials in India and its performance evaluation. (*A*) Schematic diagram of the device. (*B*) Actual photograph of the device. Construction and assembly of the device are simple and can be done locally. The antimicrobial composition is used as granules and kept in the membrane filter. Carbon block is positioned just before the tap. Carbon block may also be used as a multilayer axial block, comprising adsorbents for specific regional contaminants such as arsenic, iron, and lead. (*C–F*) Column data for the removal of (*C*) *E. coli*, (*D*) Fe^{2+}, (*E*) Pb^{2+}, and (*F*) As^{5+}. Input (*i*) and output (*ii*) concentrations are indicated in *C–F*.

Organization (WHO) norms (Fig. 3*D*). Similarly, to remove lead, 50 g of nano-MnO_2–loaded BM composite was packed in a column and fed with 1,500 L of water spiked with 150 ± 10 ppb of Pb^{2+}. The total concentration of lead in the output water (Pb exists in ionized as well as hydrolyzed form at the pH of drinking water), measured by inductively coupled plasma mass spectrometry (ICP-MS), was consistently below 10 ± 1 ppb, adhering to the WHO norms (Fig. 3*E*). Additionally, arsenic mitigation from drinking water was effectively carried out using iron oxyhydroxide–chitosan composite. Twenty grams of granular composite was packed in a column and fed with 400 L of water spiked with 1 ppm of arsenic (As^{5+}) at a flow rate of 50 mL/min. Total arsenic concentration in the output water, measured by ICP-MS, was less than 10 ppb, below the permissible limit (Fig. 3*F*). Similar performance was seen with an input As^{3+} concentration of 1 ppm. Please note that the input concentrations were the maximum concentrations usually encountered in the field. The carbon block shown in Fig. 3 *A* and *B* may also be used as a multilayer axial block, comprising the above adsorbents for specific regional contaminants such as arsenic, iron, and lead.

To use the composition in a water purification cartridge, it is important that it has satisfactory wet strength to stay intact as a granular composition. Compositions that are obtained as powders offer poor hydraulic conductivity, leading to excessive pressure drop in the water purification cartridge operated with gravity pressure. To find the shear strength of the granular media, a direct shear test was conducted at different normal stresses. The maximum horizontal shear stress exhibited by the iron oxyhydroxide–chitosan composite under each normal stress is shown in *SI Appendix*, Fig. S19 *A* and *B*. These data are plotted in *SI Appendix*, Fig. S20 *A* and *B*. Straight-line approximation of the Mohr–Coulomb failure pattern gave the angle of internal friction (Φ) to be 41.76° and 44.07° for dry and wet media, respectively, showing that the prepared granular media's shear strength is equivalent to that of the Indian standard sand (~35–40°). The compressive strength of the iron oxyhydroxide–chitosan composite was found to be 25 MPa, comparable to that of concrete.

The essence of the approach to prepare the composition is described graphically in Fig. 4. Al^{3+}-complexed chitosan solution (pH 0.8) was treated with an alkali (Fig. 4 *A*, *ii*). Alkali treatment initiates aluminum ion hydrolysis (leading to the formation of aluminum hydroxide nanoparticles) followed by chitosan precipitation (random coiled water-insoluble chitosan network) (Fig. 4 *A*, *iii*). Fig. 4*B* shows photographs of aluminum hydroxide in the dispersed form at a solution pH 4–6 and settled residue of aluminum hydroxide–chitosan at pH 7 and above. Generally, Al^{3+} upon alkaline hydrolysis converts to an aluminum hydroxide gel and prolonged heating of the gel to temperatures above 80 °C leads to redissolution of aluminum hydroxide and subsequent crystallization to aluminum oxyhydroxide. Abundant -O- and -OH groups of chitosan act as nucleation centers for the formation of boehmite nanocrystals and this crystallization is promoted even at room temperature. There are crucial advantages associated with boehmite crystallization at room temperature: (*i*) Surface hydroxyl concentration stays highest whereas exposure to elevated temperature causes their destruction, thereby giving reduced adsorption capacity, and (*ii*) reduced production cost as heating can be avoided completely.

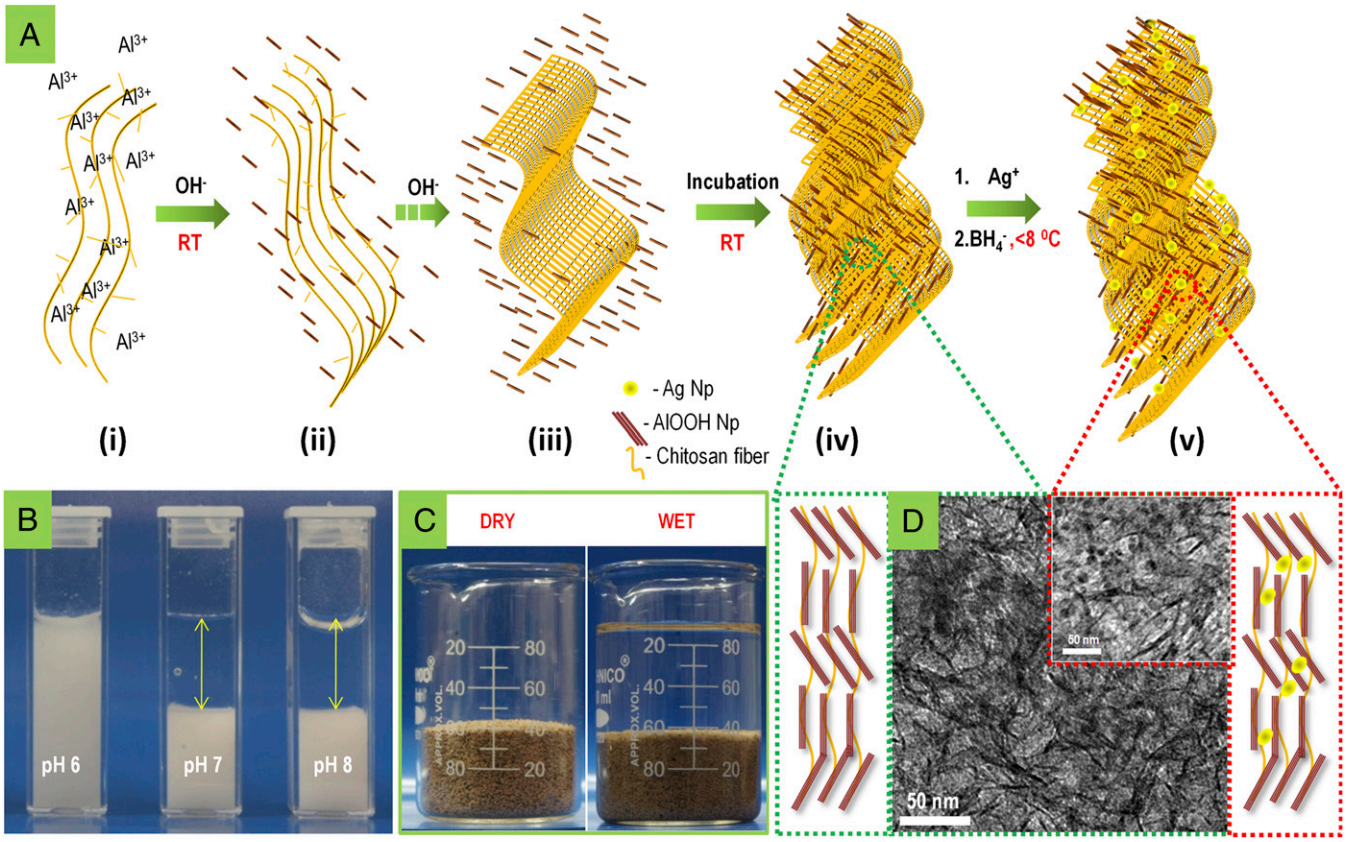

Fig. 4. Mechanism for the preparation of composite and origin of its physical strength in water due to network structure. (*A*) Mechanistic scheme for the formation of Ag-BM composite, as learned through various experiments. (*i–v*) (*i*) Al^{3+} complexes with chitosan solution; (*ii* and *iii*) alkali treatment leads to formation of aluminum hydroxide nanoparticles and random coiled chitosan network; (*iv*) aluminum hydroxide nanoparticles bind to chitosan network, possibly through covalent sharing of oxygen, leading to the formation of aluminum oxyhydroxide; and (*v*) silver nanoparticles form on the aluminum oxyhydroxide–chitosan network. (*B*) Photographs of the system during synthesis. Presence of aluminum hydroxide in the supernatant is clearly visible below pH 6 whereas bound aluminum hydroxide settles at pH 7 and pH 8, leading to a clear supernatant. (*C*) Photographs of the composite granules and of the same in water to illustrate that the material is stable in water. (*D*) Graphical representation and corresponding TEM images showing the aluminum oxyhydroxide-chitosan network without (green box) and with (red box) embedded silver nanoparticles.

We have observed that chitosan has the ability to bind colloidal nanoparticles in a proportion higher than 500 wt/wt% (Fig. 4 *A*, *iv*). Note that the role of chitosan is not merely as a flocculating agent for the precipitation of colloidal nanoparticles. In flocculation, colloidal particles undergo charge neutralization while binding with the flocculating agent. As a consequence, there is a reduction in the capacity to remove charge-bearing contaminants (such as arsenic or fluoride). However, the heavy metal ion-binding capability of aluminum oxyhydroxide–chitosan vis-à-vis equivalent chitosan is similar (Zn^{2+} binding ability: 53 mg/g and 56 mg/g, respectively, at an equilibrium concentration of 50 ppm). This means that functional groups for metal ion binding are largely available, even after hydrolysis of aluminum. A covalent interaction between chitosan and AlOOH ensures that charged sites on AlOOH are available for ion adsorption. Please note that typical sites on an oxide surface are MOH, MOH_2^+, and MO^-, with respective fractions determined by the pH.

Chitosan and AlOOH synergistically participate in the structural integrity of the composite. Chitosan undergoes swelling in water, due to destruction of hydrogen bonding. This behavior is similar to that observed in cellulose. Similarly, AlOOH disintegrates into finer particles upon exposure to water. However, the nanoscale AlOOH–chitosan composite, having a molecular-scale interaction of the individual components, does not exhibit any sign of disintegration in water. We propose that chitosan reinforces the AlOOH structure and vice versa, which imparts exceptional stability and strength to the composite in water (Fig. 4*C*). This molecularly assembled AlOOH–chitosan composite, exhibiting a cage-like structure, plays a critical role in stabilizing the silver nanoparticles (schematically illustrated in Fig. 4*D*). Upon addition of silver ions to AlOOH–chitosan, chitosan binds with silver due to its heavy metal ion-binding capacity. Upon addition of $NaBH_4$, silver ions reduce to zero valent nanoparticles, which are trapped in the AlOOH–chitosan cages (Fig. 4*A*, *v*). The presence of silver nanoparticles in the cage ensures their stabilization, while decreasing their exposure to scalants simultaneously, allowing release of silver ions in natural drinking water.

Conclusions

In their entirety, the proposed device and materials present a compelling solution for achieving the United Nations millennium development goal of sustainable access to safe drinking water. We believe that frugal science (21) based on nanotechnology can make a lasting impact on society. There are over 200 million households in India. Dissemination of this technology in various forms such as cartridges, sachets, etc., can generate large employment opportunities in the villages. The production of composites and water filter devices and their deployment and servicing can contribute to the local economy. Various modifications of the composite with different compositions have been developed with comparable performances.

Materials and Methods

The granular composites, composed of metal oxyhydroxide–chitosan nanostructures, were synthesized by a green synthetic route, which in general comprises hydrolysis of a metal precursor–chitosan complex using an alkaline medium followed by washing and drying at ambient conditions. Metal ion precursors that may be used for the preparation of composites are Al^{3+}, Fe^{3+}, Fe^{2+}, Mn^{2+}, Cu^{2+}, Zn^{2+}, Ti^{4+}, and Ce^{4+}. All syntheses were carried out in water.

Synthesis of the Composite for Bacteria and Virus Removal. An aluminum oxyhydroxide–chitosan nanostructure embedded with silver nanoparticles was synthesized by a two-step process: (*i*) Synthesis of the aluminum oxyhydroxide–chitosan nanostructure (referred to as BM): 1.5 g chitosan was dissolved in 0.5% nitric acid solution and to this mixture, 100 mL of 0.5 M aluminum sulfate was added dropwise. After 3 h incubation, 140 mL of 2 M sodium hydroxide was added dropwise to precipitate aluminum and chitosan. The resultant precipitate was further stirred for 1 h and subsequently washed with copious amounts of water. This precipitate is called BM. (*ii*) Synthesis of silver nanoparticle in BM: After redispersing the precipitate in water, 100 mL of 5 mM silver nitrate was added and incubated for 1 h. Afterwards, 100 mL of 10 mM sodium borohydride was added dropwise at <10 °C and the mixture was stirred continuously. The final precipitate was subsequently washed with copious amounts of water, dried at room temperature (28–30 °C), crushed, and used for further studies. The resulting composite was insoluble in water and appears as light yellow granules, referred to as Ag-BM. The method of composite preparation is water positive by two to three orders of magnitude; i.e., it produces 500 L of clean water for every 1 L of water consumed for material production.

Synthesis of Composite for Heavy Metal Removal. An aluminum oxyhydroxide–chitosan nanostructure embedded with nano-MnO_2 particles was synthesized through a two-step process: (*i*) synthesis of BM and (*ii*) MnO_2 nanoparticles incorporation in BM. Briefly, after redispersing the BM precipitate in water, a freshly prepared MnO_2 nanoparticles suspension was added dropwise and the mixture was stirred continuously. The final precipitate was subsequently washed with copious amounts of water, dried at room temperature, crushed, and used for further studies. The resulting composite was insoluble in water and appeared as black granules.

Synthesis of Composite for Arsenic and Iron Removal. The iron oxyhydroxide–chitosan nanostructure was prepared by the route described in *Synthesis of Composite for Bacteria and Virus Removal* for the preparation of BM. Ferric sulfate was used as the metal ion precursor for iron. The final precipitate was dried at room temperature, crushed, and used for further studies. The resulting composite was insoluble in water and appeared as brown granules.

Synthesis of Silver Nanoparticles for Hyperspectral Imaging. Silver nanoparticles used for hyperspectral imaging (HSI) are prepared through $NaBH_4$ reduction method. $AgNO_3$ (1 mM) was mixed with 1 mM trisodium citrate solution in equal volumes. An equal volume of 10 mM ice-cooled solution of $NaBH_4$ was then added dropwise to the above solution with stirring. The solution turns golden yellow and exhibits an absorption maximum at 390 nm, corresponding to an average particle diameter of 5–10 nm.

Testing protocol for antibacterial and antiviral efficacy. Two grams of Ag-BM was shaken with 100 mL of natural drinking water (see *SI Appendix*, Table S1 for water quality parameters). Antibacterial activity of Ag-BM was measured by spiking the natural drinking water with *Escherichia coli* (*E. coli* ATCC 25922) at a concentration of $\sim 1 \times 10^5$ CFU/mL, whereas antiviral activity was measured by spiking the water with bacteriophage MS2 at a concentration of $\sim 1 \times 10^3$ PFU/mL. Thereafter, the water was left standing for 1 h and subsequently the surviving microorganism count was measured by conventional pour plate (*E. coli*) and plaque assay (bacteriophage MS2) techniques. Colony counts were performed after incubation at 37 °C for 48 h (*E. coli*) and 16 h (bacteriophage MS2). It should be noted that the input bacteria and virus concentration may vary slightly in studies extending for weeks as the cultures are prepared on a daily basis.

Testing protocol for the water purification device. For the water purification device studies, 50 g of the composite was packed in a water purification cartridge (diameter, 70 mm; height, 2 mm) and assembled as a gravity-fed water purifier. The feed water was passed at a flow rate of 1,000 mL/min. The input tap water was periodically subjected to a bacterial load of $\sim 1 \times 10^5$ CFU/mL and the output water was plated in accordance with the protocol to understand the biocidal performance activity. Cyst removal studies were conducted following the NSF protocol P231 and NSF/American National Standards Institute standard 53. Polystyrene beads with a nominal size of 4–6 μm were used as a surrogate for cysts. An input concentration of $\sim 1 \times 10^6$ particles per liter was passed through the carbon block. Input and output concentrations were directly examined by a scanning electron microscope. Output water was concentrated ×1,000 before examination.

Details of the fluorescence microscopy protocol, mechanical testing of composite, and material characterization techniques used in this study are described in *SI Appendix, Methods* and *SI Appendix, Material Characterization*.

ACKNOWLEDGMENTS. We thank M. S. Bootharaju, S. Banupriya, P. R. Sajanlal, Robin John, and Rakhil Akkali for their technical support in conducting X-ray photoelectron spectroscopy, transmission electron microscopy, field emission scanning electron microscopy, atomic force microscopy, and fluorescence microscopy measurements, respectively. We thank Dr. R. G. Robinson and Dr. Manu Santhanam (Department of Civil Engineering) for their technical support in direct shear test and compressive strength analyses. We thank the Department of Science and Technology (Government of India) for constantly supporting our research program on nanomaterials.

1. Prüss-Ustün A, Bos R, Gore F, Bartram J (2008) *Safer Water, Better Health* (WHO, Geneva).
2. Clasen TF, Haller L (2008) *Water quality interventions to prevent diarrhoea: Cost and cost-effectiveness* (WHO, Geneva).
3. (2004) *The World Factbook 2004* (Central Intelligence Agency, Washington, DC).
4. Sedlak DL, von Gunten U (2011) Chemistry. The chlorine dilemma. *Science* 331(6013): 42–43.
5. Shannon MA, et al. (2008) Science and technology for water purification in the coming decades. *Nature* 452(7185):301–310.
6. (2009) *Nanotechnology Applications for Clean Water*, eds Savage N, et al. (William Andrew Publication, Norwich, NY).
7. Kim SJ, Ko SH, Kang KH, Han J (2010) Direct seawater desalination by ion concentration polarization. *Nat Nanotechnol* 5(4):297–301.
8. Pradeep T, Anshup (2009) Noble metal nanoparticles for water purification: A critical review. *Thin Solid Films* 517(24):6441–6478.
9. De Gusseme B, et al. (2010) Biogenic silver for disinfection of water contaminated with viruses. *Appl Environ Microbiol* 76(4):1082–1087.
10. Kumar A, Vemula PK, Ajayan PM, John G (2008) Silver-nanoparticle-embedded antimicrobial paints based on vegetable oil. *Nat Mater* 7(3):236–241.
11. Dai J, Bruening ML (2002) Catalytic nanoparticles formed by reduction of metal ions in multilayered polyelectrolyte films. *Nano Lett* 2(5):497–501.
12. Jain P, Pradeep T (2005) Potential of silver nanoparticle-coated polyurethane foam as an antibacterial water filter. *Biotechnol Bioeng* 90(1):59–63.
13. Liu J, Hurt RH (2010) Ion release kinetics and particle persistence in aqueous nanosilver colloids. *Environ Sci Technol* 44(6):2169–2175.
14. Kittler S, Greulich C, Diendorf J, Köller M, Epple M (2010) Toxicity of silver nanoparticles increases during storage because of slow dissolution under release of silver ions. *Chem Mater* 22(16):4548–4554.
15. Jin X, et al. (2010) High-throughput screening of silver nanoparticle stability and bacterial inactivation in aquatic media: Influence of specific ions. *Environ Sci Technol* 44(19):7321–7328.
16. Marambio-Jones C, Hoek EMV (2010) A review of the antibacterial effects of silver nanomaterials and potential implications for human health and the environment. *J Nanopart Res* 12(5):1531–1551.
17. Nowack B (2010) Chemistry. Nanosilver revisited downstream. *Science* 330(6007): 1054–1055.
18. Berger TJ, Spadaro JA, Chapin SE, Becker RO (1976) Electrically generated silver ions: Quantitative effects on bacterial and mammalian cells. *Antimicrob Agents Chemother* 9(2):357–358.
19. Franz AM (2004) A *performance* study of ceramic candle filters in Kenya including tests for coliphage removal (Massachusetts Institute of Technology, Cambridge, MA). Available at http://dspace.mit.edu/bitstream/handle/1721.1/31120/61162474.pdf.
20. Qiu J (2011) Environmental science. China to spend billions cleaning up groundwater. *Science* 334(6057):745.
21. Whitesides G (2011) The frugal way: The promise of cost-conscious science. *The World in 2012*, ed, Franklin D, The Economist, pp 154.

Supporting Information for

Biopolymer-reinforced synthetic granular nanocomposites for affordable point-of-use water purification

Mohan Udhaya Sankar[a,1], Sahaja Aigal[a,1], Shihabudheen M. Maliyekkal[a,1], Amrita Chaudhary[a], Anshup[a], Avula Anil Kumar[a], Kamalesh Chaudhari[a] and Thalappil Pradeep[a,2]

[a]DST Unit of Nanoscience (DST UNS) and Thematic Unit of Excellence,
Department of Chemistry, Indian Institute of Technology Madras,
Chennai 600 036, India.

[2]Correspondence and requests for composites should be addressed to T.P. (pradeep@iitm.ac.in)

SI Methods

Fluorescence microscopy protocol: 1L of 10^6 CFU/mL *E. coli* containing water was contacted with Ag-BM for an hour and it was repeatedly centrifuged at 20,000 rpm to obtain a bacterial pellet. This pellet was resuspended in 1 mL of 0.85% saline to obtain a final bacterial concentration of 10^9 CFU/mL. Staining was done according to Invitrogen Molecular Probes protocol. Briefly, 3 µL of a fluorescent probe mixture containing 3.34 µM green fluorescent nucleic acid stain SYTO 9 and 15 µM red fluorescent nucleic acid stain PI was combined with 1 mL of bacterial suspension. The mixture was incubated in dark for 15 min at room temperature and a 5 µL aliquot was placed on a glass slide, which was then covered by a cover slip, sealed and examined under Fluorescence microscope. Excitation was done for SYTO 9 at 465-495 nm and at 530-560 nm for PI. Emission was collected using a band pass filter for SYTO 9 at 515-555 nm and a long pass filter for PI at 590 nm.

Mechanical testing of composite: The shear strength of the media was measured at dry and wet conditions, separately. Around ~140 g of granular media was packed in a 6 cm x 6 cm x 6 cm (LxBxH) sample holder and horizontal shear stress was measured under normal stress of 50, 100 and 200 kPa.

SI Material characterization

The identification of the phase(s) of the as-prepared sample was carried out by X-ray powder diffraction (Bruker AXS, D8 Discover, USA) using Cu-Kα radiation at λ = 1.5418 Å. Surface morphology, elemental analysis and elemental mapping studies were carried out using a Scanning Electron Microscope (SEM) equipped with Energy Dispersive Analysis of X-rays (EDAX) (FEI Quanta 200). Field Emission SEM measurements were done with FEI Nova NanoSEM 600 instrument. High Resolution Transmission Electron Microscopy (HRTEM) images of the sample were obtained with JEM 3010 (JEOL, Japan) operating at 300 keV. Elemental mapping was done with a TEM EDAX. X-ray Photoelectron Spectroscopy (XPS) measurements were done using

ESCA Probe TPD of Omicron Nanotechnology. Polychomatic Mg Kα was used as the X-ray source (hv = 1253.6 eV). Binding energy was calibrated with respect to C 1s at 284.5 eV. Total silver, arsenic and lead concentrations in water were estimated using inductively coupled plasma mass spectrometry (ICP-MS) (Agilent Technologies, 7700x ICP-MS and PerkinElmer NexION 300 ICP-MS). Atomic Force Microscopy (AFM) measurements were done using a Witec GmbH confocal Raman microscope (CRM-Alpha300 S). Bacteria treated with silver nanoparticles and those treated with Ag-BM, were viewed under the Cytoviva microscope, attached to a Hyperspectral imaging (HSI) system. The system captures the VNIR (400-1000 nm) spectrum within each pixel of the scanned field of view. The bacteria were treated for a period of 2 h, and 2 µL of the same were spotted on glass slides. The spotted samples were allowed to dry for over 4 h before imaging. Imaging was done at 100x magnification, using a halogen lamp (400-1000 nm) as the light source. Nikon ECLIPSE 80i fluorescence microscope was used to image stained bacteria.

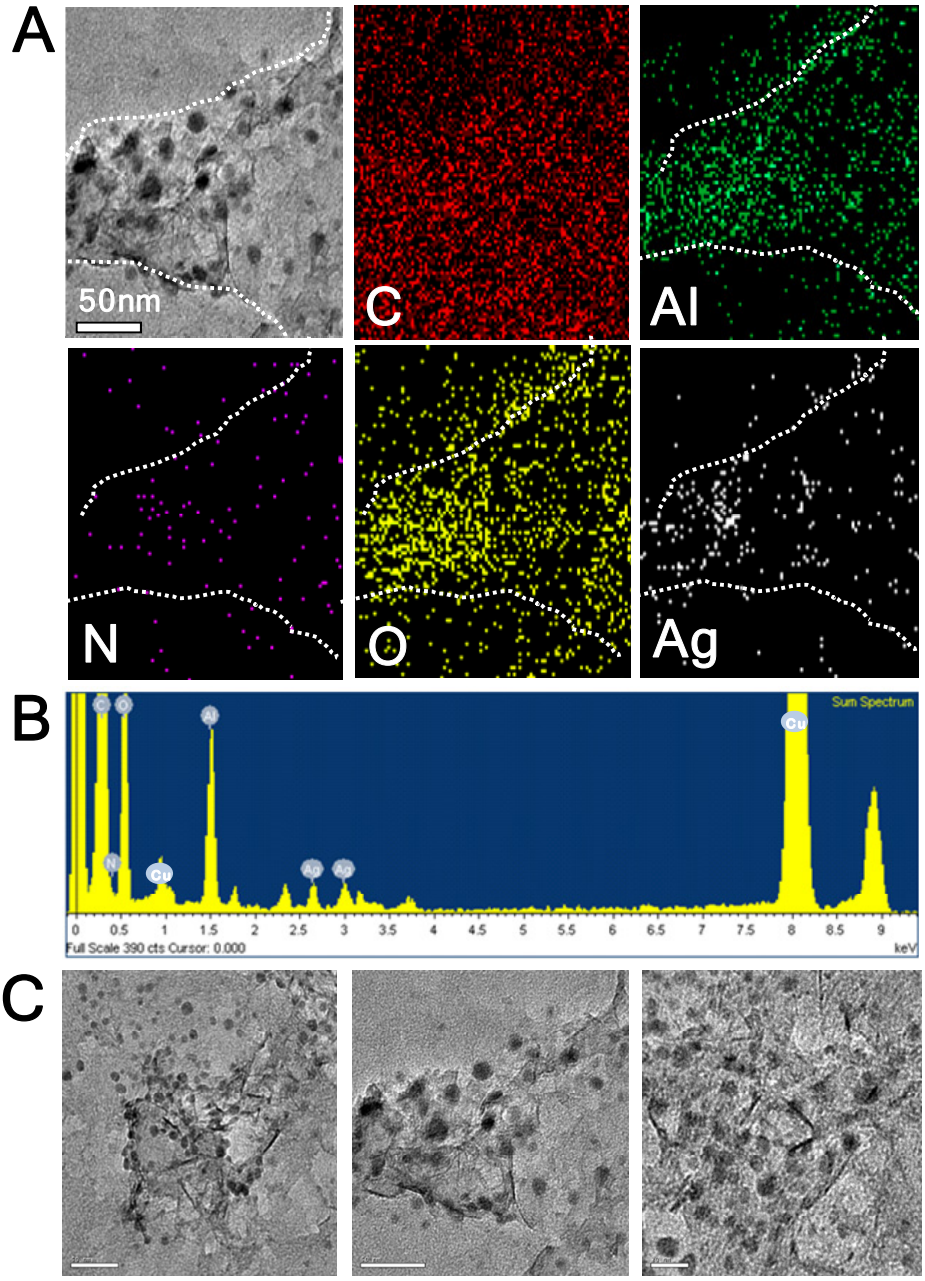

Fig. S1. Transmission electron micrograph and EDAX elemental mapping of Ag-BM. **(*A*)** EDAX elemental imaging of Ag-BM**.** Top extreme left is the TEM image and others are elemental maps from the region. **(*B*)** EDAX spectrum of **(*A*)** confirming the presence Ag. **(*C*)** HRTEM micrographs of Ag-BM (Scale bar is 50 nm). The uniform carbon image is due to the grid and the material. Al and O are present uniformly due to AlOOH and their pattern resembles the pattern of the sample (marked). Ag is also present in this region. The spatial resolution of EDAX resolution is good enough to see isolated particles. The Cu lines are due to the grid used.

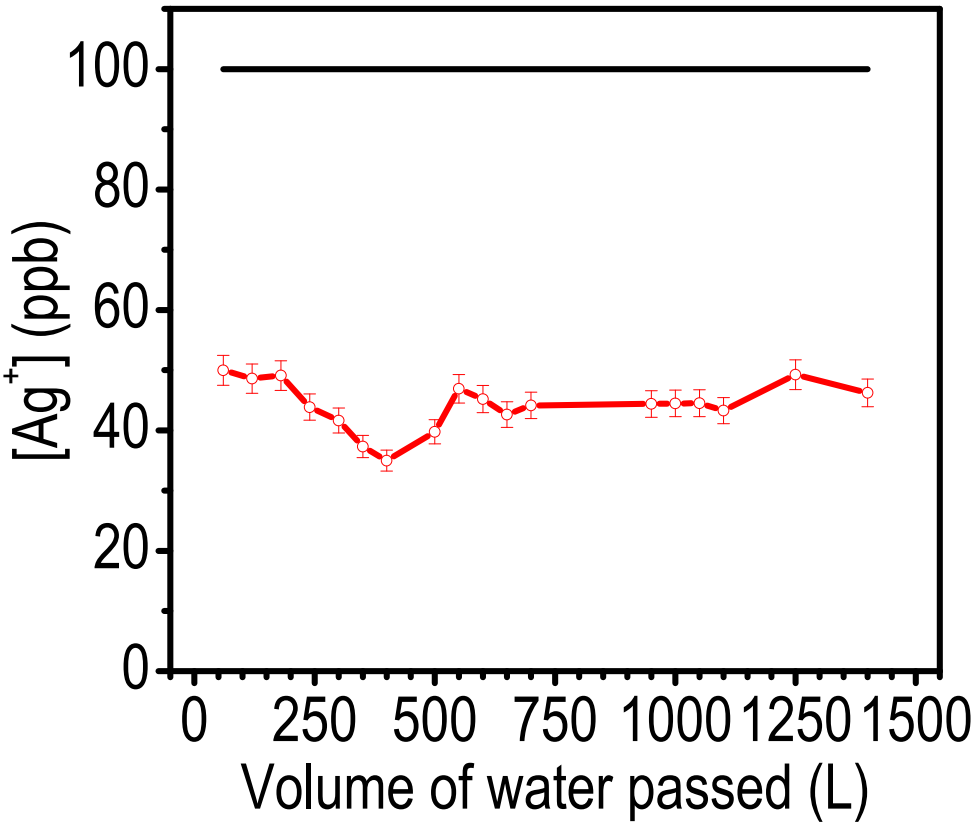

Fig. S2. Performance trials for gravity-fed water purifier device containing Ag-BM as the water purification composite. Analysis of silver ion concentration in output water measured by ICP-MS (red) in cartridge study (refer: *Materials and Methods*). The permissible limit for silver ion concentration in drinking water is shown as black line. Cartridge was run for 1500 L without any reactivation.

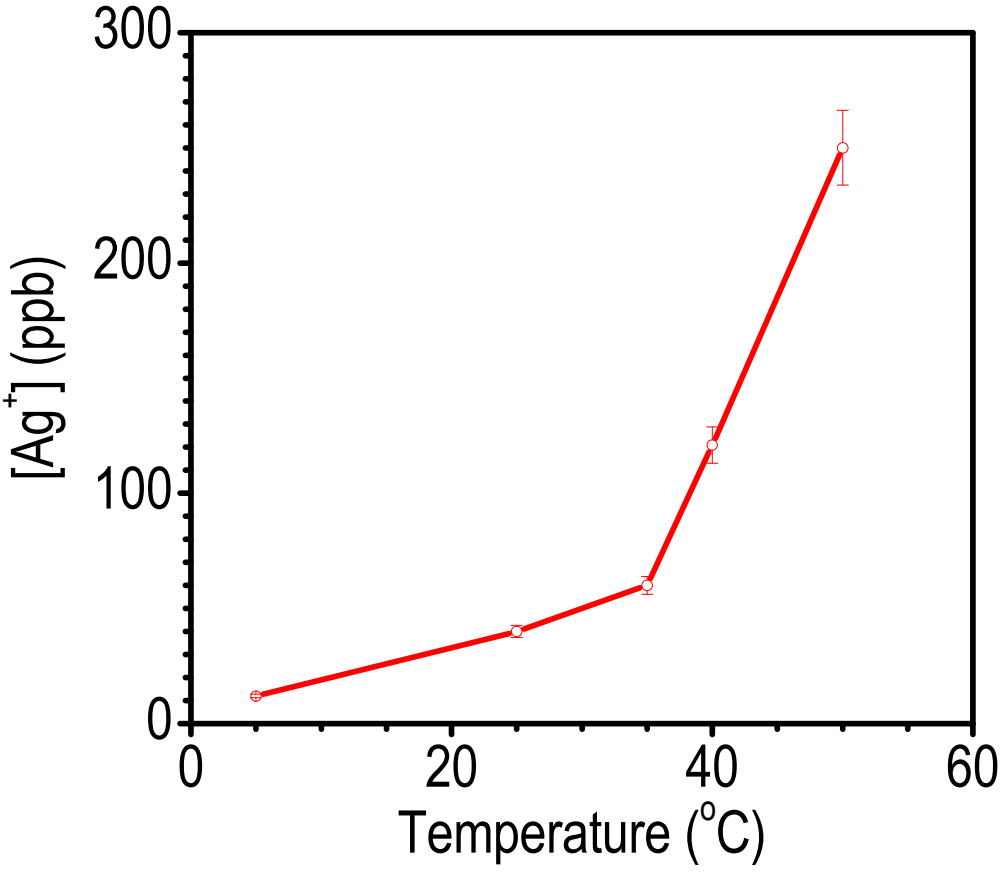

Fig. S3. Silver ion leaching as a function of temperature. Silver ion leaching from Ag-BM in water at temperatures of 5, 25, 35, 40 and 50 ^{0}C (measured using ICP-MS). The amount of silver ions leached in water at RT (25-35 ^{0}C) is 40 ± 10 ppb, when trials were done in batch.

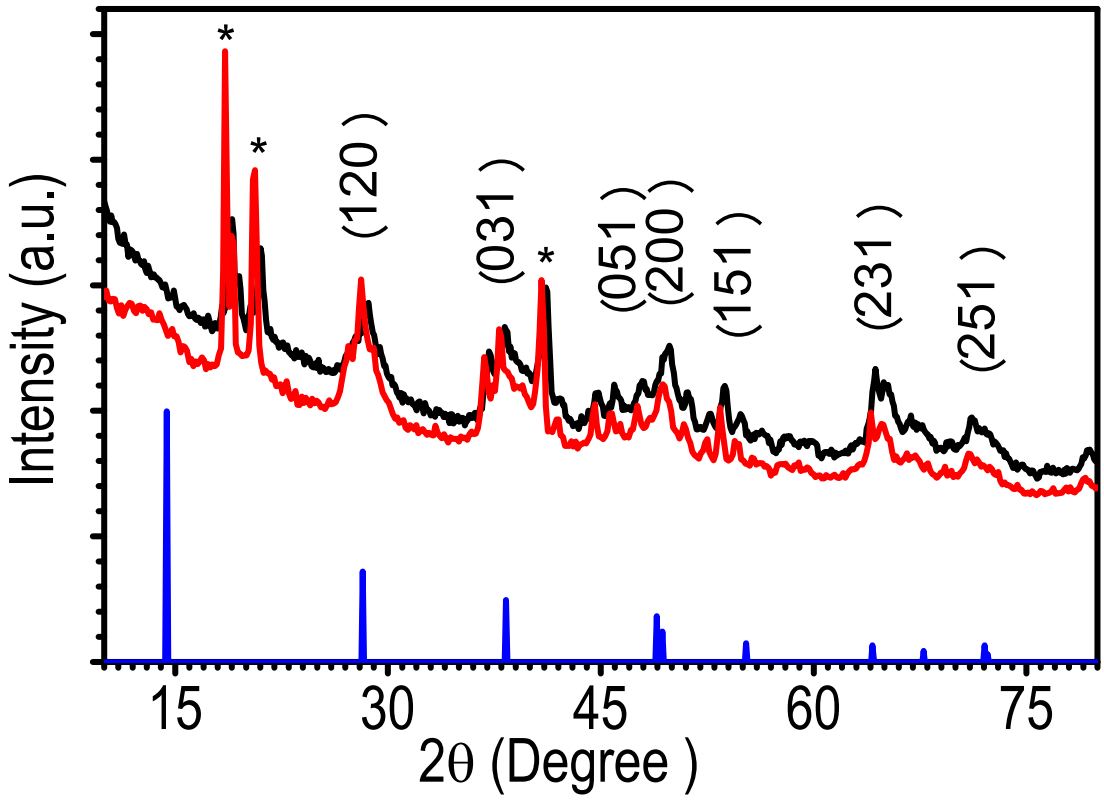

Fig. S4. X-ray diffraction patterns of BM and Ag-BM. XRD patterns of BM (black) and Ag-BM (red). BM showed peaks corresponding to (120), (013), (051), (151), (200), (231) and (251) planes. All these peaks can be indexed to orthorhombic-AlOOH shown in blue colour (JCPDS # 83-2384). The broadened XRD peaks imply that the crystallite size of BM particles is very small. The mean crystallite size calculated from the Scherrer formula shows that AlOOH nanocrystals are of an average size of 3.5 nm. The presence of organic template (chitosan) is also clear from the XRD data. The peaks marked by * corresponding to 2θ (in degrees) = 18.7°, 20.6° and 41.2° are attributed to the presence of the organic template. There is a definite difference in the full-width at half maxima (FWHM) for the peaks corresponding to AlOOH and organic template. Addition of Ag to BM doesn't lead to new diffraction features, presumably due to low concentration of Ag.

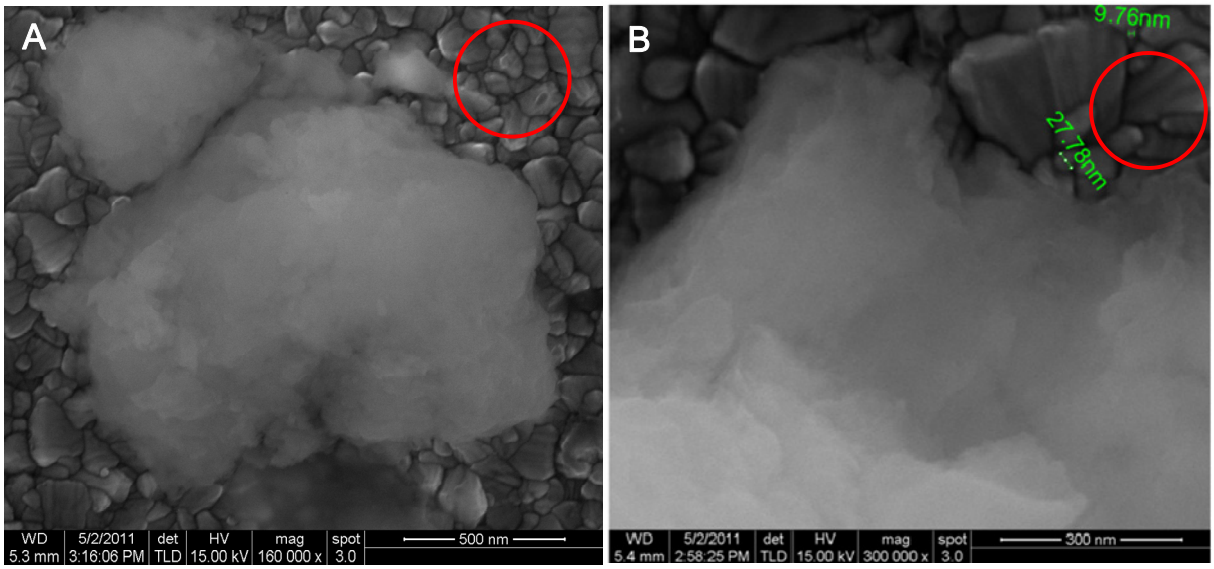

Fig. S5. Field emission scanning electron microscopic image of Ag-BM. FESEM images of an Ag-BM grain at two magnifications. Silver nanoparticles are not seen on the surface of the BM composite, although the substrate particles (ITO, indium tin oxide) in similar size range (10-30 nm) are clearly visible. A part of the ITO coated glass substrate is highlighted by the red circle to illustrate this point. This indicates that silver nanoparticles are embedded and well protected in the BM matrix.

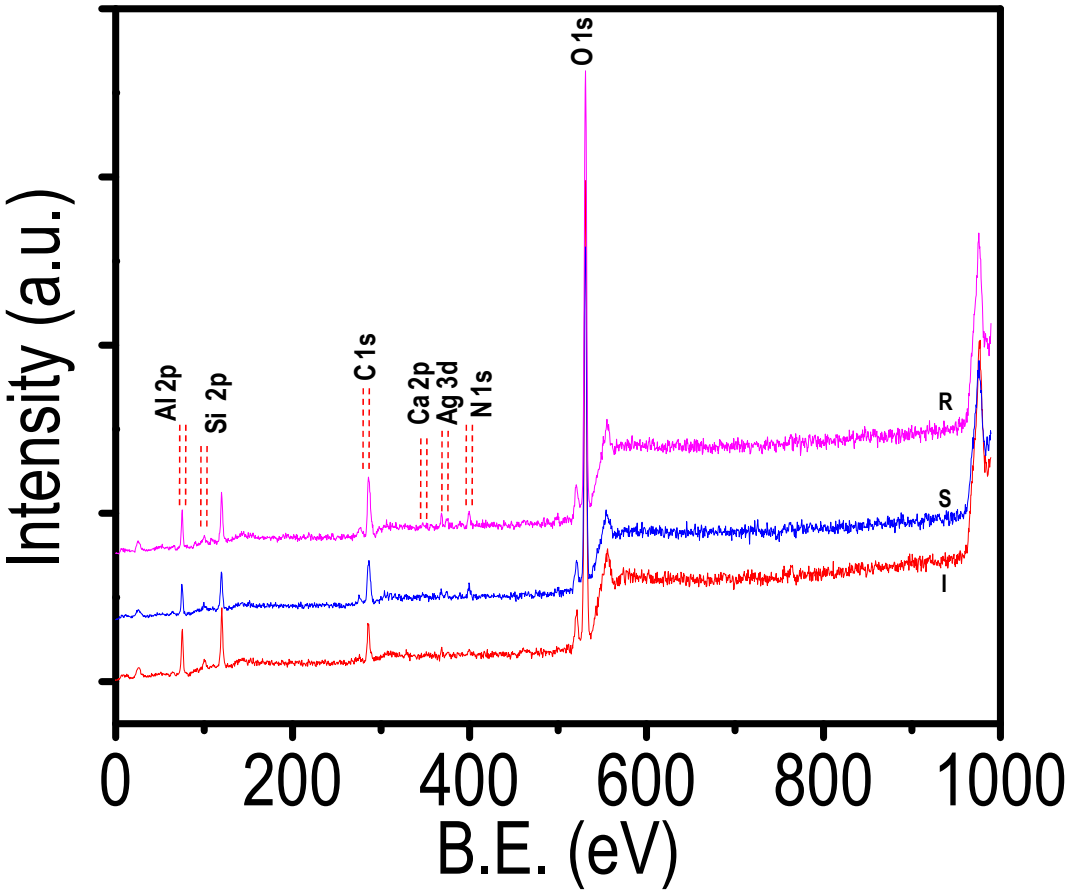

Fig. S6. XPS survey spectra of Ag-BM. XPS survey spectra of Ag-BM samples (I) Prior to use, (S) upon saturation of anti-bacterial activity and (R) upon reactivation in distilled water at 70 °C. The spectra are essentially the same except in Ca 2p and Si 2p regions, which are marked. N 1s is also present in I, although with reduced intensity.

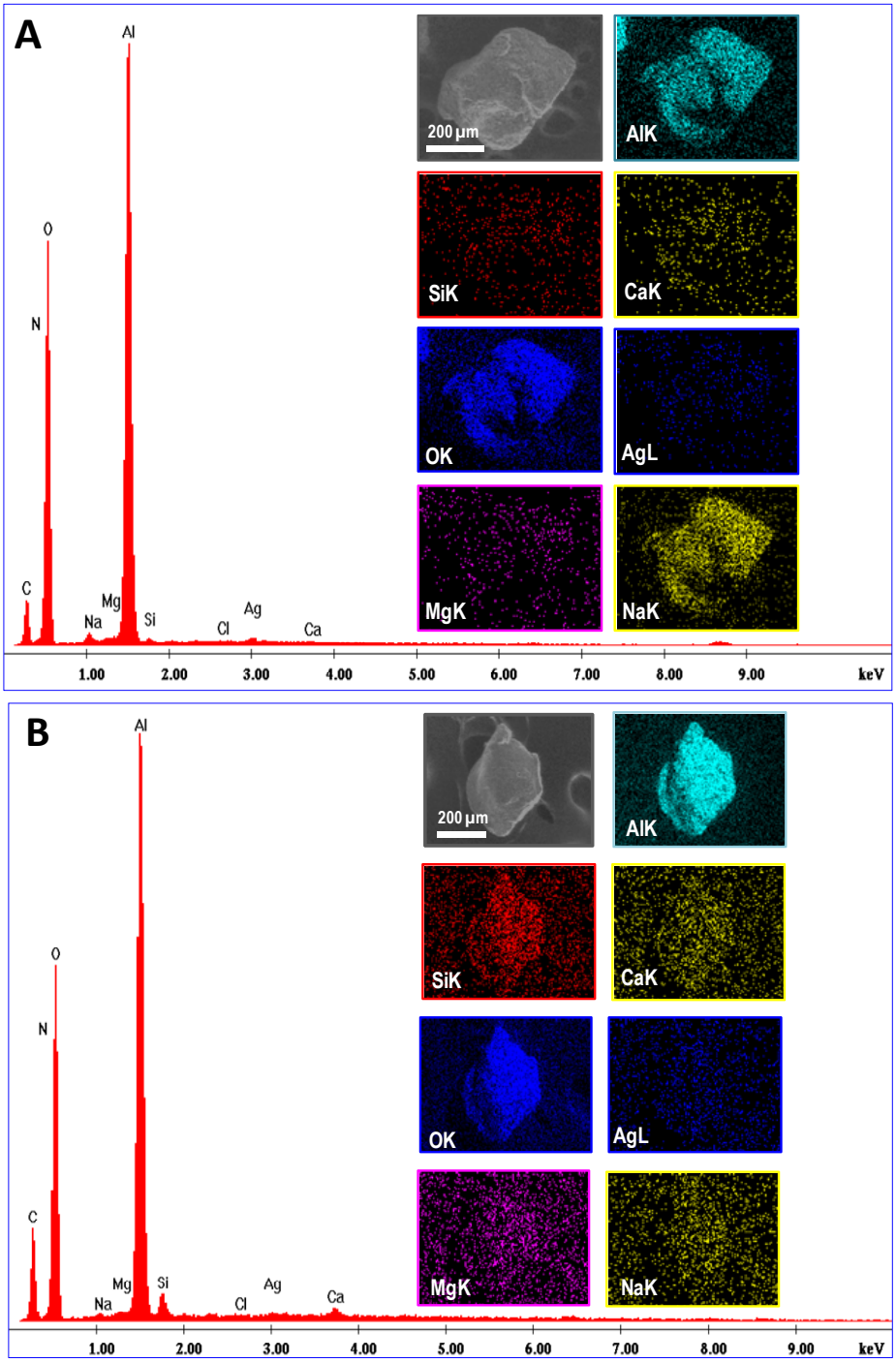

Fig. S7. SEM-EDAX elemental spectrum and elemental imaging. SEM-EDAX of **(*A*)** freshly prepared Ag-BM and **(*B*)** saturated Ag-BM. Natural drinking water (without treatment so that there is a residual bacterial count in it) was used for testing. Presence of deposits containing Ca and Si is seen on the saturated Ag-BM material.

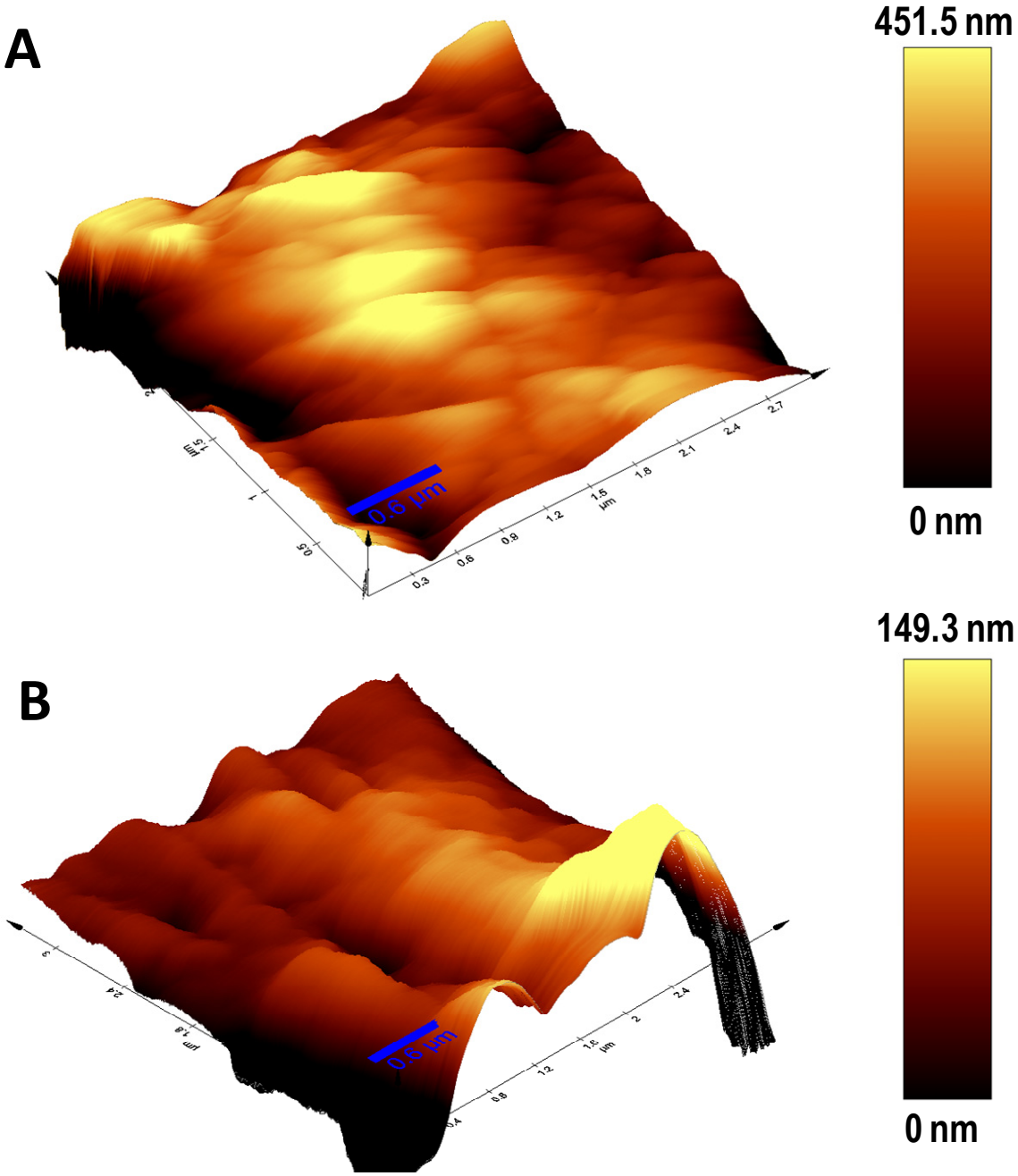

Fig. S8. AFM images of surface roughness of Ag-BM. 3D AFM images of surface roughness of **(*A*)** initial Ag-BM and **(*B*)** saturated Ag-BM. The high profile is also shown. Increased inhomogeneity, possibly due to deposits is seen in *B*.

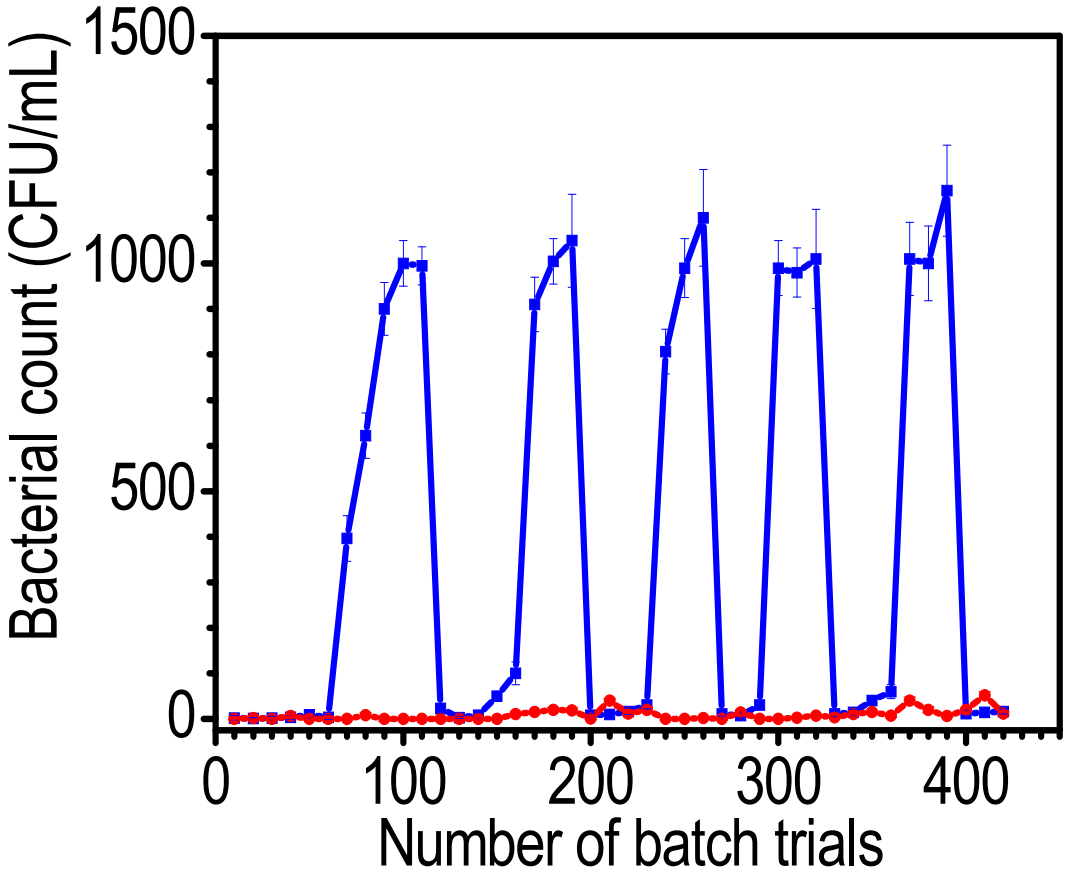

Fig. S9. Effect of water quality on performance of Ag-BM. Performance comparison for Ag-BM shaken in tap water (blue trace) and ultrapure water (red trace). The antibacterial efficacy of the composite in ultrapure water is due to the absence of interfering species typically found in tap water. As in other batch experiments, 2g of the composite was shaken in 100 mL of ultrapure water spiked with 0.85% NaCl (to avoid osmotic rupture) and bacterial input load of 10^5 CFU/mL and the solution was plated after 1 h. The composite works indefinitely without the need for reactivation.

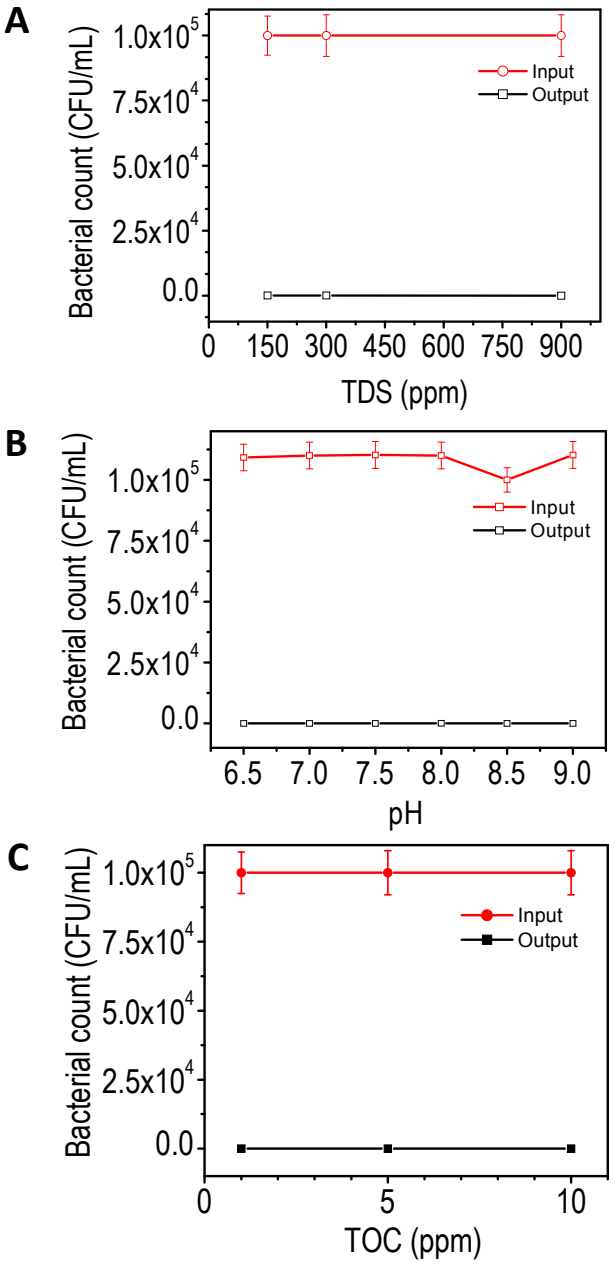

Fig. S10. Effect of variations in input water quality on antibacterial performance of Ag-BM. Performance of Ag-BM against *E. coli* was tested in batch, by varying **(*A*)** the ionic strength of synthetic challenge water (pH held constant at 7.0±0.2), **(*B*)** pH of the synthetic challenge water (TDS held constant at 300 ppm) and **(*C*)** the organic (humic acid) content of the synthetic challenge water (pH and TDS held constant at 7.0±0.2 and TDS 300 ppm, respectively). The average input concentration was $1X10^5$ CFU/mL. Activity of the composite does not diminish with variation in TDS, pH as well as TOC of synthetic challenge water.

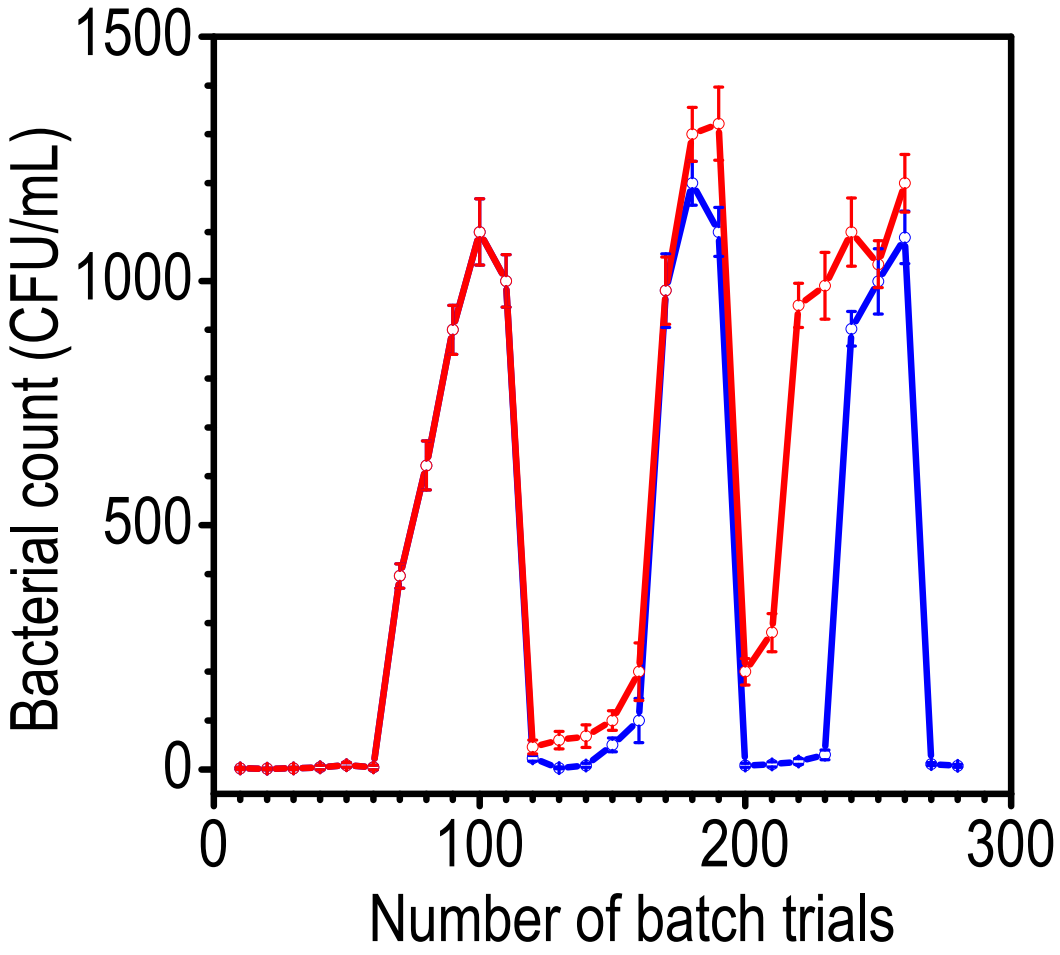

Fig. S11. Effect of water quality used for reactivation of Ag-BM. Performance comparison for Ag-BM reactivated with distilled water (blue trace) and tap water (red trace) at 70 °C. Unlike reactivation of composite in tap water, reactivation in distilled water leads to nearly complete recovery of anti-bacterial performance (output count came to zero). The composite exhibits only 2 cycles of reactivation before getting exhausted in tap water. On the contrary, the composite can be reactivated for at least 5 cycles, if reactivation is conducted in distilled or quality drinking water.

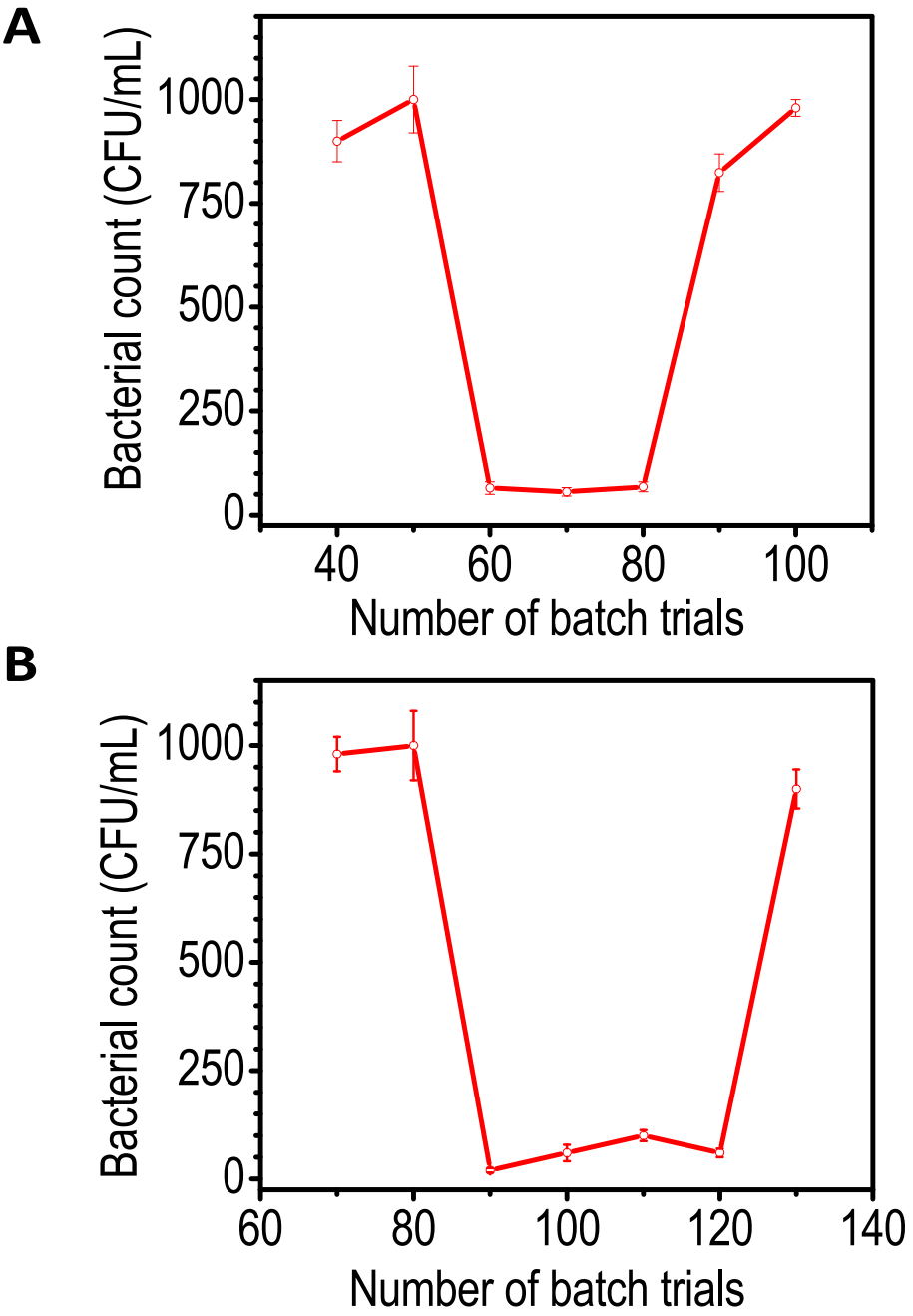

Fig. S12. Antibacterial performance for Ag-BM reactivation by alternate methods. Reactivation using **(*A*)** citric acid (10 mM) (alternatively, 4 drops of fresh lemon juice is used, pH 5.5±0.5) and **(*B*)** hydrogen peroxide (100 ppm). It is evident that chemical methods of reactivation are equally efficient in recovering the performance of the composite.

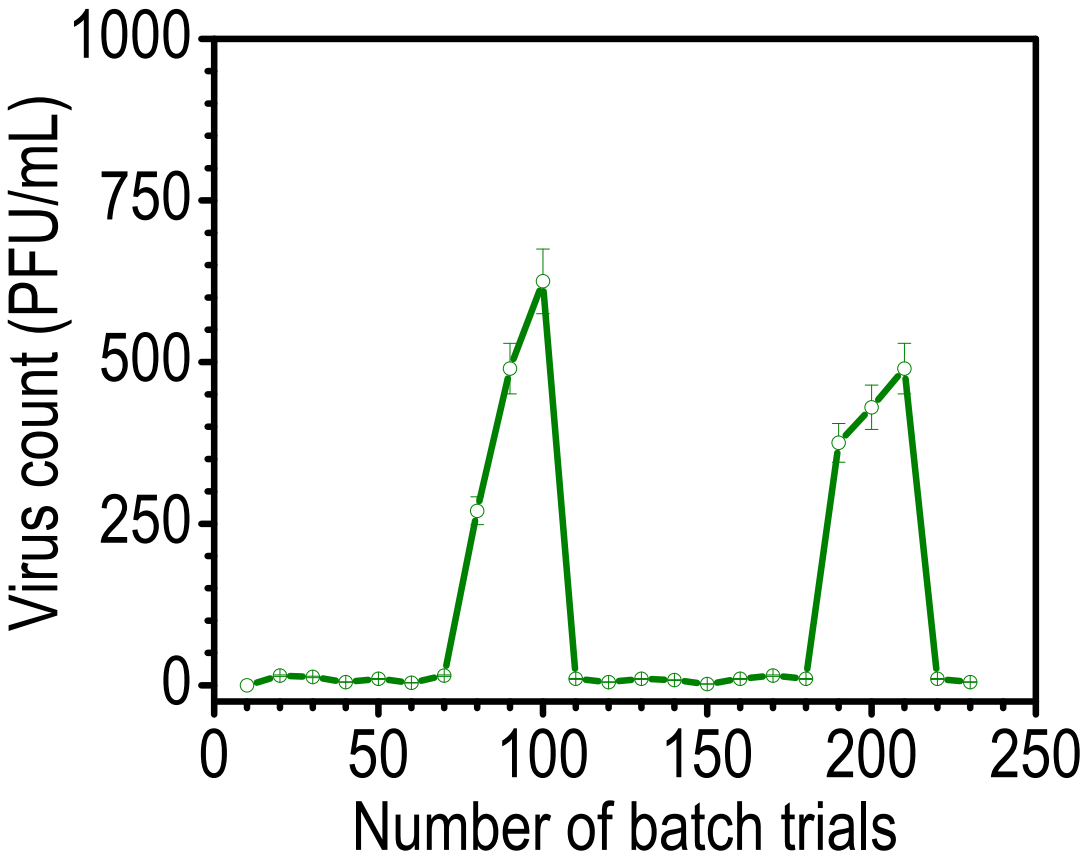

Fig. S13. Antiviral performance trials of Ag-BM in batch. Performance of Ag-BM against MS2 bacteriophage was tested in batch. The average input concentration was 1000 PFU/mL. The composite was reactivated after the 3 consecutive saturation points (trial numbers 80-100 and 190-210) were obtained. The antiviral performance is comparable to antibacterial performance as the composite regains its property after reactivation.

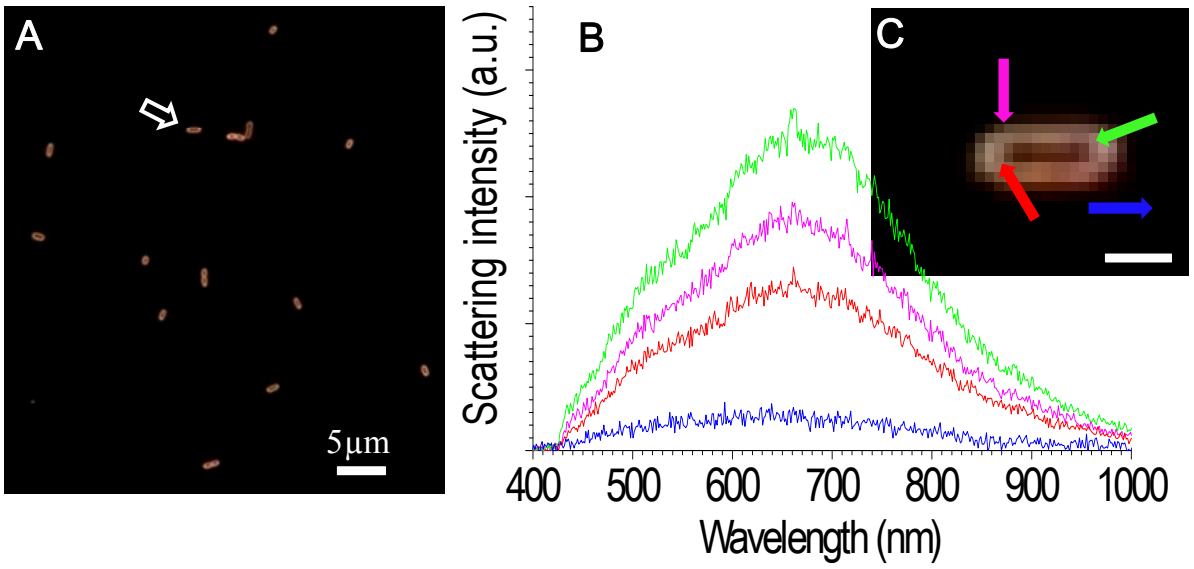

Fig. S14. Hyperspectral imaging of *E. coli*. (*A*) Hyperspectral image of *E. coli*, **(*B*)** spectra collected at various borders of *E. coli* and **(*C*)** expanded hyperspectral image of *E. coli* used for collection of spectra. The scale bar is 1 µm. The spectrum essentially resembles the lamp spectrum as there are no absorbing species in a bacterium.

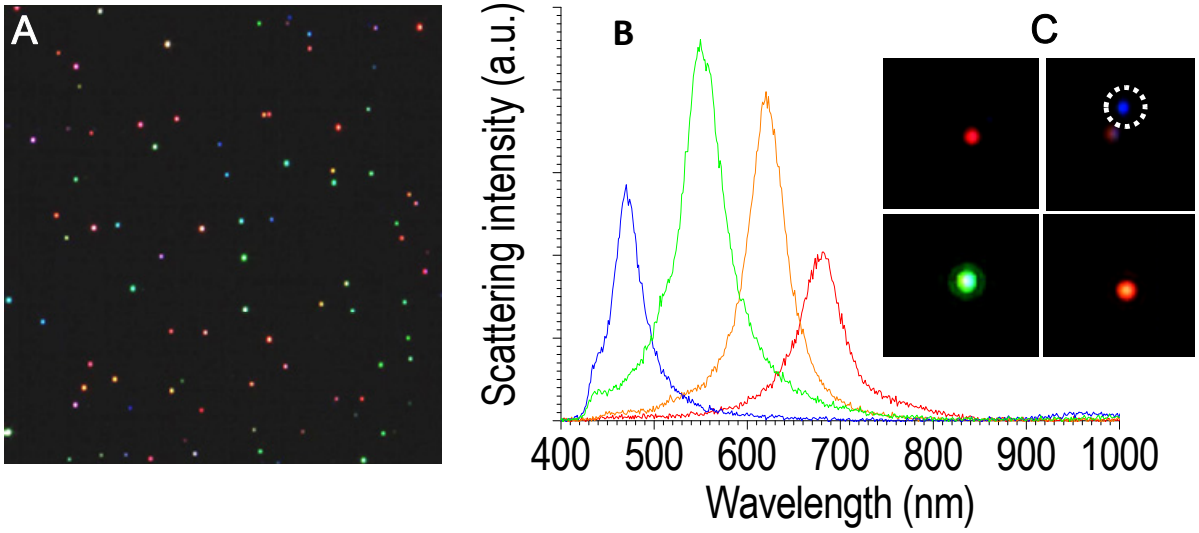

Fig. S15. Hyperspectral imaging (HSI) of silver nanoparticles. HSI images of **(*A*)** nanoparticles in water, **(*B*)** spectra collected for single nanoparticles showing different colors due to differences in absorption maxima and **(*C*)** zoomed images of the corresponding nanoparticles.

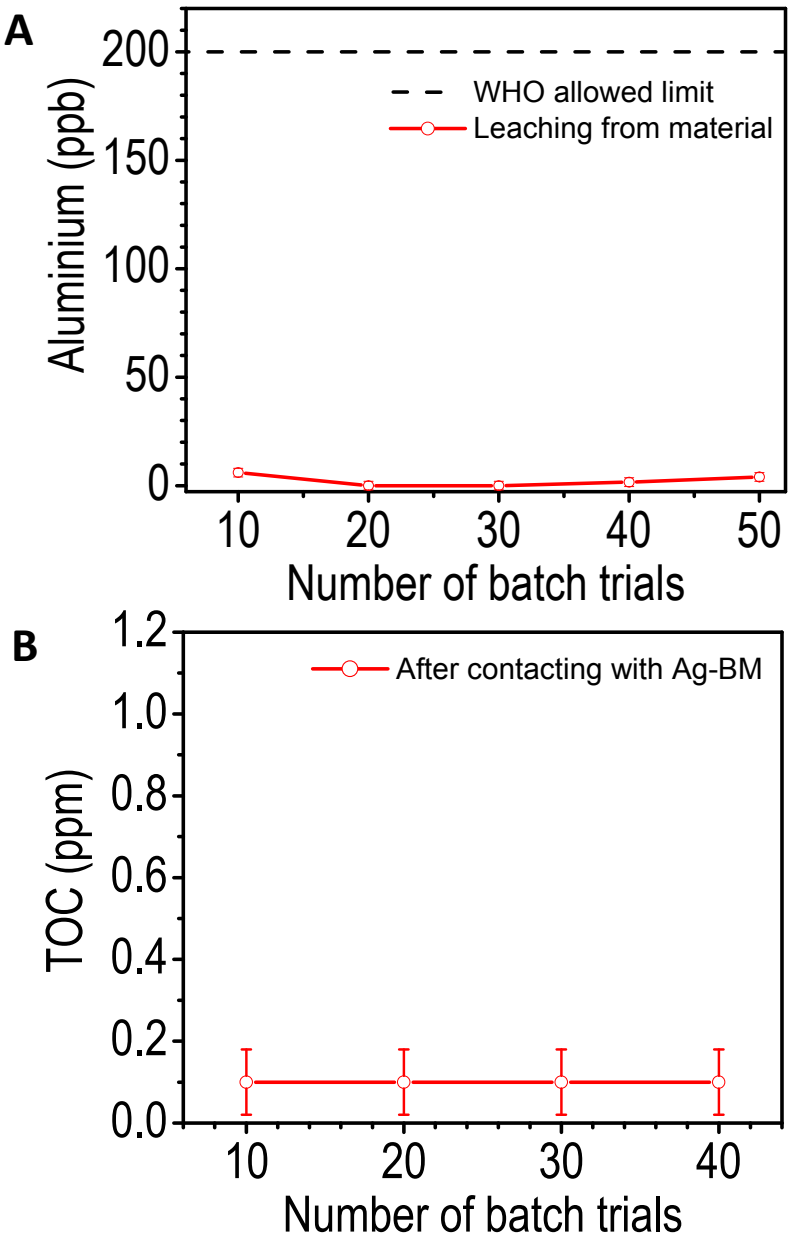

Fig. S16. Analysis of aluminium and TOC leaching. (*A*) Analysis of aluminum concentration in output water measured by ICP-MS (red) in batch trials. The maximum permissible limit for aluminum ion concentration in drinking water is shown as red line. **(*B*)** Analysis of leached total organic carbon (TOC) in output water. The limit of detection of TOC measurement was estimated to be 80 ppb.

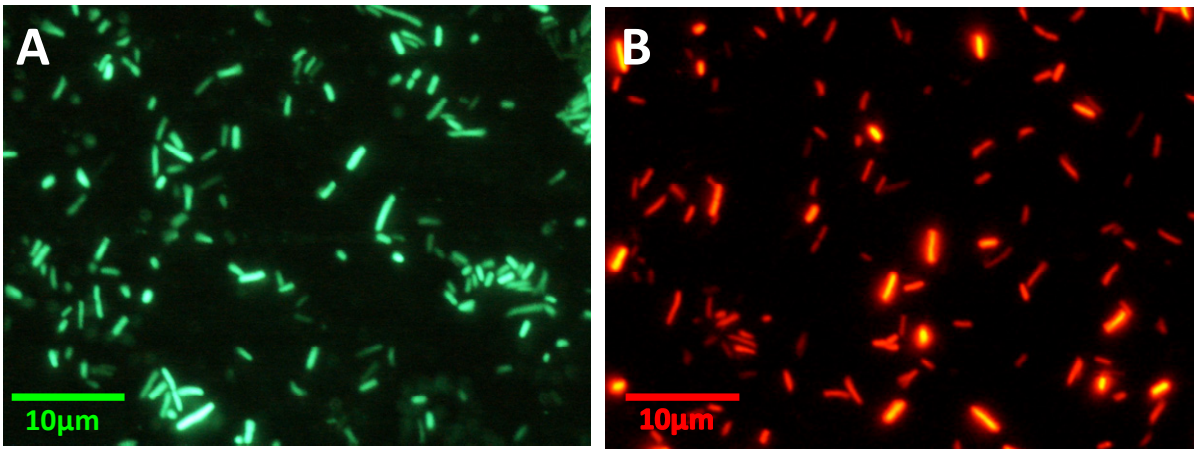

Fig. S17. Fluorescence microscopy study of treated bacteria. Fluorescence microscopy images of bacteria (*E. coli*) after staining with SYTO 9 (green) and PI (red). **(*A*)** Untreated and **(*B*)** treated with Ag-BM composite for 1h. Each image is a result of superposition of an image taken for the green fluorescent dye and red fluorescent dye using the appropriate filters. The scale bar is 10 µm. Fluorescence microscopy study supports that bacteria are killed within 1h after treating with Ag-BM.

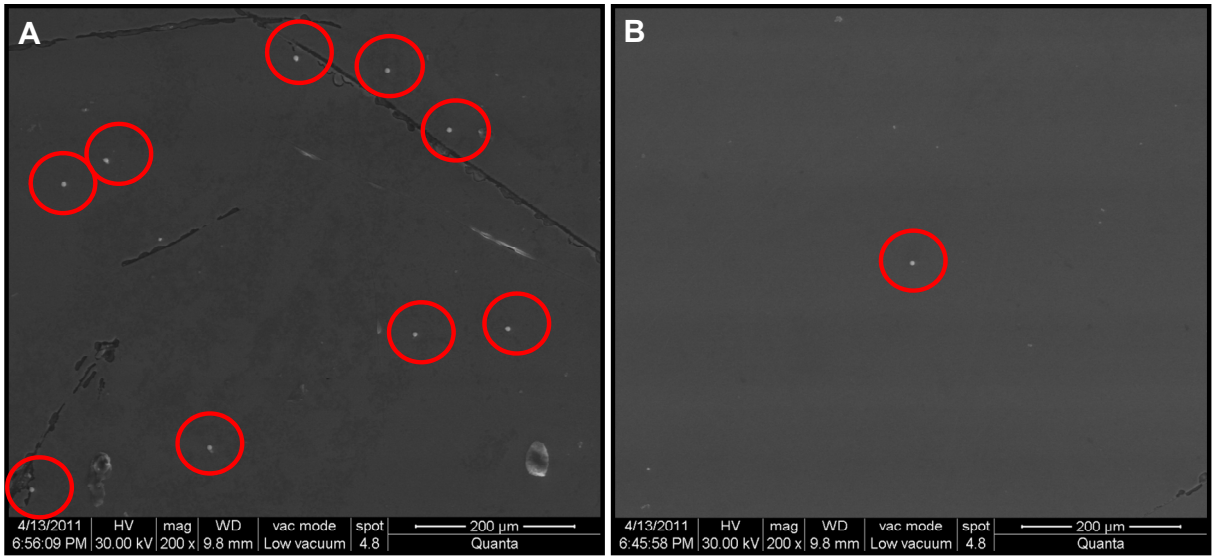

Fig. S18. Cyst removal performance tested with 4-6 micron polystyrene spheres. SEM images of 4-6 micron polystyrene spheres. **(*A*)** Input count: 10^6 particles/L and **(*B*)** output count: 1 particle is seen in the 1000 times concentrated sample (<3 particles/L). The input water containing polystyrene spheres was passed through the porous carbon block as per NSF P231 protocol (polystyrene spheres are used as representative for cyst, in terms of size) and removal capacity is higher than 5 log. The porous carbon block removes cysts through physical filtration.

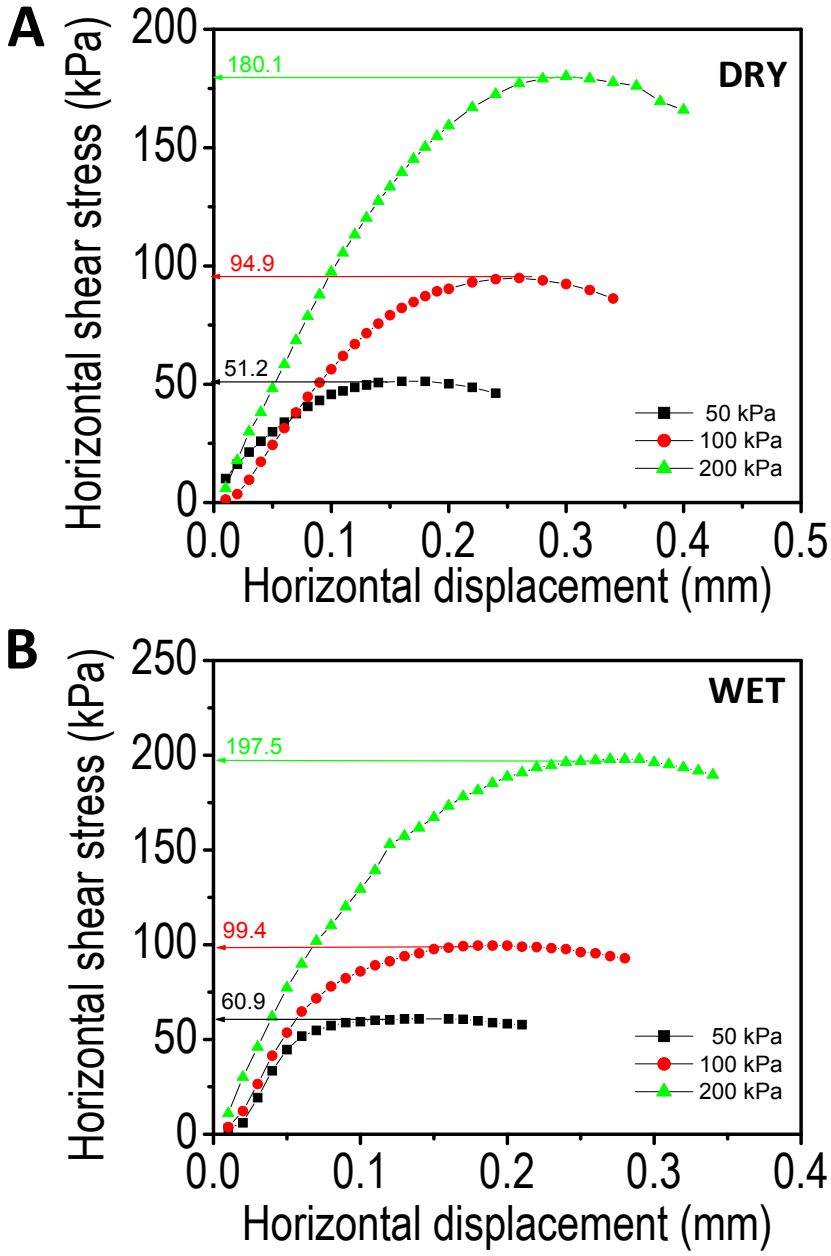

Fig. S19. Direct shear test (Horizontal shear stress vs. Horizontal displacement). Plot of horizontal shear stress vs. horizontal displacement of loosely packed media obtained from direct shear tests: **(*A*)** measured at dry condition and **(*B*)** measured at wet condition.

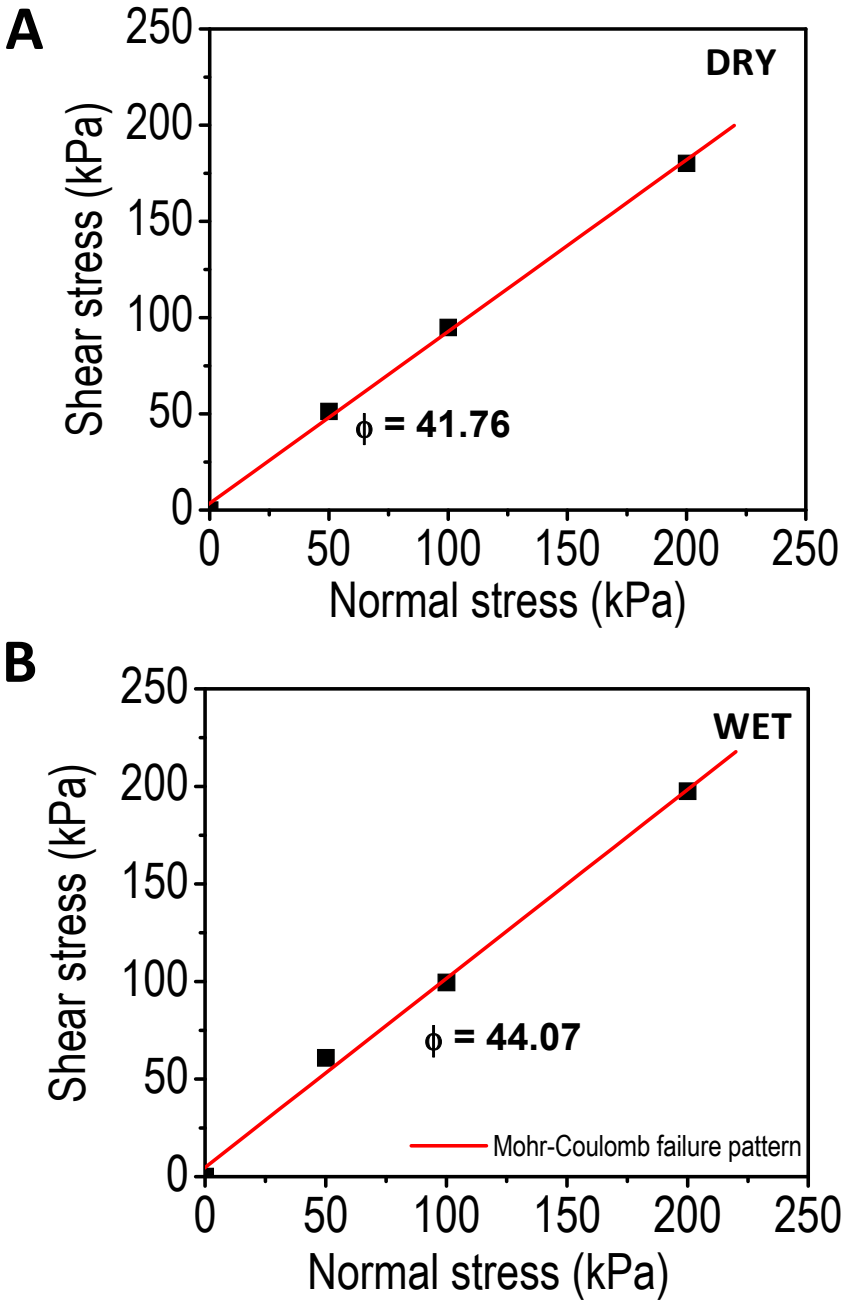

Fig. S20. Mohr-Coulomb failure pattern (Shear stress vs. Normal stress). Plot of shear stress vs. normal stress of loosely packed media showing the straight-line approximation of the Mohr-Coulomb failure pattern: **(*A*)** measured at dry condition and **(*B*)** measured at wet condition.

SUPPORTING TABLE

Table S1. Physicochemical characteristics of influent natural drinking water

(Note: All parameters are expressed in mg L^{-1}, except for pH and conductivity)

Parameters	Value
Total coliforms (CFU/mL)	1-2 x 10^3
p H @25°C	7.8
Conductivity (µS/cm)	640.000
Fluoride	0.573
Chloride	86.340
Nitrate	1.837
Sulphate	32.410
Silicate	15.870
Lithium	ND
Sodium	53.740
Ammonium	ND
Potassium	2.330
Magnesium	14.340
Calcium	28.720

ND-not detected

Natural drinking water (without treatment so that there is a residual bacterial count in it) was used for testing to ensure that that the material functions in the field.

THE JOURNAL OF PHYSICAL CHEMISTRY Letters

Perspective

pubs.acs.org/JPCL

New Protocols for the Synthesis of Stable Ag and Au Nanocluster Molecules

T. Udayabhaskararao and T. Pradeep*

DST Unit of Nanoscience (DST UNS), Thematic Unit of Excellence (TUE), Department of Chemistry, Indian Institute of Technology Madras, Chennai 600 036, India

ABSTRACT: "Catching" metals in the nonmetallic form in solution, as they grow to bulk, is one of the most exciting areas of contemporary materials research. A new kind of stabilization to catch the nonmetallic form of noble metals with small thiols has evolved as an exciting area of synthesis during the past decade. Gold clusters stay in the frontline of this research, yielding new "molecules" composed of a few to several hundreds of atoms. By taking guidelines from gold cluster research, various new protocols for silver nanoclusters were developed. In this Perspective, we highlight the recent advances on the synthesis of atomically precise silver, gold, and their alloy clusters with a special emphasis on silver. As a result of intense efforts of the recent past, clusters such as $Ag_{7,8}(SR)_{7,8}$, $Ag_7(-S-R-S-)_4$, $Ag_9(SR)_7$, $Ag_{32}(SR)_{19}$, $Ag_{44}(SR)_{30}$, $Ag_{140}(SR)_{53}$, $Ag_{280}(SR)_{140}$, and $Ag_{152}(SR)_{60}$ (SR and S−R−S refer to thiolate and dithiolate ligands, respectively) were added to the literature. Moreover, "silver-covered" and "gold-covered" alloy clusters have also been synthesized. Early reports of the crystallization of such clusters are available. Several of these clusters are shown to act as sensors, catalysts, and pesticide degradation agents, which suggests that these materials may find applications in daily life in the foreseeable future.

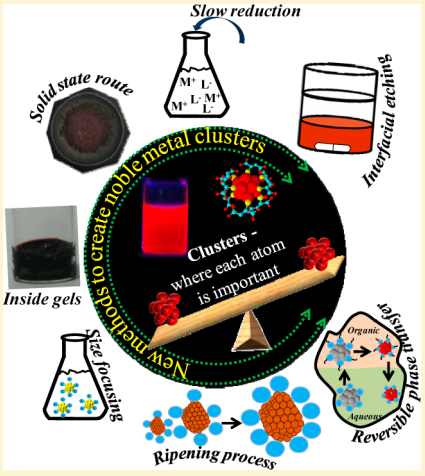

Creation of new materials has always been fascinating to researchers as it provides immense opportunities to study the emergence of novel physical and chemical properties. Often, newly identified materials open up ways to discover novel phenomena. One such example, which changed the directions of noble metal research, is the colloidal gold synthesized by Faraday.[1] Although several methods for the synthesis of colloidal gold were known even earlier, as reviewed previously, the method of Faraday was the first example in which unusual properties of this form of matter were attributed to the divided state of the metal. This has been the seed material for understanding several phenomena experimentally[2] and theoretically.[3] Since then, decades disappeared without significant growth in experimental research in this area. However, theoretical[3] and technological[4] developments have taken place. The synthesis method[5] pioneered by Turkevich et al. showed a convenient method for obtaining gold nanoparticles, 15−30 nm in diameter, formed by the chemical reduction of Au^{3+} using sodium citrate. Here, citrate acts as a capping agent too, and the system is referred to as Au@citrate. A similar method is used to make silver nanoparticles (Ag@citrate) using silver nitrate and sodium citrate.[5] Followed by this, a variety of alkyl chains possessing O, P, N, and S linkers in their head group have been used as protective agents for Ag and Au nanoparticles.[2] Surface plasmon resonance is one of the essential features of these particles of size >2−100 nm.[2] Among several capped nanoparticles, thiolate-protected ones are of greater attention in view of their higher stability[6] and applicability in biology. However, decades spent on thiolate-protected plasmonic systems have now culminated in the discovery of a new form of matter composed of a few atoms, which exhibit molecular behavior.[7] Such particles are called quantum clusters (QCs) or subnanoclusters. They are also referred to as clusters, monolayer-protected clusters, nanocluster molecules, as well as super atoms. They are composed of a few tens to a few hundreds of atoms, having a core with size in the nanometer regime, possessing a discontinuous density of states.[7] Because of their discrete electronic energy levels, they show molecule-like optical transitions in their optical absorption and emission spectra. Although they are composed of a metal core and a ligand shell, the optical properties are dominated by the core-derived states, composed of the metal atoms and the metal−ligand binding shell.[8−10] They are often considered to bridge the gap between atomic/molecular (exhibiting distinct optical properties) and nanoparticle (exhibiting plasmons) behaviors. In this Perspective, clusters and nanoparticles are treated as two distinct regimes of matter.

Unlike the plasmonic systems, TEM investigations have not been hugely successful for these clusters. Mainly two drawbacks, namely, (1) size of these clusters being too small to be observed in standard TEM[11] and (2) electron-beam-induced growth of clusters during microscopic examination, have thwarted TEM investigations. Clusters in the size regime of 1 nm undergo electron-beam-induced coalescence, leading to bigger particles.[12] The tendency of cluster collapse upon irradiation is prominent for Ag clusters. The experimental techniques, used

Received: February 14, 2013
Accepted: April 11, 2013

   dx.doi.org/10.1021/jz400332g | J. Phys. Chem. Lett. 2013, 4, 1553−1564

Creating metal systems in "nonmetallic" form has been a subject of intense research for several decades. Efforts in this area lead to the development of gas-phase and template-assisted clusters of various kinds. Many silver clusters were observed in templates due to the facile photoreduction of silver ions.

especially for characterizing organic and inorganic molecules, such as elemental analysis, UV/vis, mass spectrometry (ESI and MALDI MS), IR, H^1 NMR, and so forth, can be used eminently for characterizing these clusters. In recent years, crystallographic data of $Au_{102}SR_{44}$,[13] $Au_{25}SR_{18}$,[14] $Au_{38}SR_{24}$,[15] $Au_{36}SR_{24}$,[16] and $[Au_{24}(PPh_3)_{10}(SR)_5Cl_2]^+$ (SR = thiolate)[17] have helped in acquiring more knowledge about these systems. Irrespective of whether they are crystalline or not, ESI and MALDI MS studies reveal precise compositions of these clusters.[18,19] In the following, we briefly discuss how research on gold and silver clusters has progressed, principally focusing on the synthesis aspects.

Evolution of Synthetic Efforts. (a) Using Charged Particles and Photons. Both silver and gold in the cluster form have been investigated since the 1980s.[20] In the early period, sputtered M (M = Ag or Au) atoms were obtained from a target of M by impinging inert gas ions or pulsed lasers, which subsequently underwent nucleation to form clusters upon gas-phase coalescence. Inert gases were used for cooling clusters by gas-phase collisions, leading to deactivation and removal of excess internal energy as kinetic energy. During the same time, Ag_n clusters were synthesized in templates such as zeolites.[21] Later, inorganic glasses were also used as solid matrixes to stabilize these clusters. In a general synthesis process, Ag^+-doped zeolites/glasses were prepared initially by well-known techniques.[21] Irradiation of suitable light then makes Ag_n clusters inside of the cavities of these templates. Formation of silver clusters in zeolites was achieved by taking advantage of the photoreducibility of silver ions.[21] Au_n clusters in zeolites appeared only lately, starting with the report of Boudart and Meitzner in the 1980s as quoted in ref 22. Only a few investigations of Au_n clusters in zeolites were available, unlike for Ag_n. Au_n clusters, in comparison to Ag_n, were unstable due to the migration of Au_n clusters to the outer surface of the inorganic templates. The affinity of zeolites toward silver, as opposed to that against gold, is due to the fact that Ag^+ is the only noble monopositive cation that forms a mononuclear species with appreciable stability in water. Among the noble metals, only Ag^+ forms aqueous solutions, which can easily be exchanged in zeolites. Also in contrast to Ag^+, Au^{3+} does not have photoinduced reducibility in the typical photon energies used.[22] Generally, Au^{3+} requires chemical reduction. However, recently, Zhang et al. have achieved red-luminescent Au and Cu clusters through a photoreduction process.[23]

(b) Using Templates. During the same time, another attractive way of creating Ag_n in polymer templates was demonstrated.[24] It is known that bare, small silver clusters are generally short-lived and undergo aggregation, being transformed into plasmonic systems in aqueous solutions, at ambient temperatures.[24] Henglein succeeded in stabilizing such intermediate clusters using sodium polyacrylate. Here, the synthesis involves radiolytic reduction of Ag^+ ions in the presence of sodium polyacrylate. The very first product in the reduction of Ag^+ by the hydrated electron is the silver atom. Atomic Ag, formed rapidly, reacts with Ag^+ to produce a diatomic cluster, Ag^{2+}, which then grows into a stable polyatomic cluster on the polymer chains. The Coulombic repulsion between the chains prevents the clusters from coming closer. A similar scenario to obtain gold clusters is not favorable due to the fact that Au^{3+} is not photoreduced, unlike Ag^+. After the synthesis of red-luminescent silver clusters by Kumecheva and co-workers[25] in the interior cavities of microgels by UV irradiation, several fluorescent silver clusters were synthesized.[26] Ras and co-workers have synthesized PMAA−AgQCs [PMAA = poly(methacrylic acid)] through reduction of Ag^+, which was initiated by visible light. For the first time, they demonstrated strong solvatochromic and solvatofluorochromic properties along with the novel electroluminescence property of these clusters.[26] New methods such as sonochemical[27] and microwave-assisted[28] approaches were used to synthesize polymer-templated AgQCs. Most of the synthetic reports are limited to clusters in water. However, there are reports where clusters, first obtained in water, were subsequently transferred to other solvents. Recently, Diez et al. have succeeded in direct synthesis of blue-, green-, and red-emissive silver clusters in polar and nonpolar solvents (toluene, dichloroethane, THF, DMF, etc).[29] Nevertheless, there have been many polymer-templated, highly luminescent AuQCs but not to the extent of AgQCs.[30] Dendrimer encapsulation is also one of the efficient ways to control the size of the clusters.[31] In recent years, dendrimers are engineered in such a way that they can hold a specific number of atoms.[32]

DNA-hosted luminescent silver clusters have been one of the hot areas of research since the oligonucleotide-encapsulated AgQCs synthesized by Dickson and co-workers.[33] Synthesis and applications of such luminescent silver[34] and gold[30] clusters were thoroughly reviewed. AgQCs of different sizes with blue/green-, yellow-, red-, and NIR-emitting properties were synthesized. Several studies were also carried out to know the importance of bases and base sequences on the formation of oligonucleotide-stabilized lumenescent AgQCs. However, in the case of DNA-template gold clusters, there are not many synthetic and optical tunability reports in the literature. Recently, DNA-templated, blue-[35] and red-[36] emitting gold nanoclusters were synthesized using mild reducing agents. Also, DNA-hosted, sequence-dependent formation of gold clusters was also reported.[37]

Protein-encapsulated Ag or Au clusters are a subject of current research. This subject is extensively reviewed by Xavier et al.[38] The research activity of BSA-protected Ag_n clusters (BSA = bovine serum albumin) intensified following the report of Au_{25}@BSA by Xie et al.[39] MALDI MS is the most important tool to characterize these clusters. Although ESI MS is successfully used to characterize proteins and protein−metal ion complexes, it is not very useful in characterizing their clusters. The number of metal atoms in a given protein-encapsulated cluster can be found from the difference between the mass values of free protein and protein-encapsulated clusters observed in MALDI MS. Au_{25}@BSA is the first system that was observed by MALDI MS. Subsequently, MALDI MS provided the composition of several silver and gold clusters in protein templates. It is worth noting that through mass spectral studies, it was possible to understand the growth of metal

dx.doi.org/10.1021/jz400332g | J. Phys. Chem. Lett. 2013, 4, 1553−1564

clusters in a given protein.[40] Intense research activities are currently undertaken on both Au[41] and Ag[42] @protein systems.

(c) Thiolate-Protected Clusters. Since the Brust−Schiffrin two-phase method for gold nanoparticles reported in 1994, studies of thiolate-protected gold clusters have became a fascinating area of research.[43] Molecular clusters of gold, distinctly different from nanoparticles, were noticed in 1997.[44] Evolution of research on thiol-protected gold clusters has contributed to newer excitement in cluster research.[45,46] Correlation between theoretical and experimental results contributed to understanding these systems in detail. Different aspects of these clusters have been extensively reviewed by Jin,[11] Lu and Chen,[47] and our group.[38] Theoretical studies of these clusters were reviewed by Hakkinen.[48] In the following, we discuss recent developments in terms of synthetic protocols and also our own contributions to the development of new clusters.

Several types of synthetic routes exist that can produce clusters with desired characteristics in the final product. Besides the studies of the effect of thiol and of solvent on the nature of the products, not much information is available on other aspects, for example, on the effect of reducing agents. New protocols showed that the reduction potential of the reducing agent has a tremendous effect on the clusters.[49−51] Ghosh et al. reported[49] a one-step route for the synthesis of an atomically precise cluster, $Au_{18}SG_{14}$ (SG, thiolate of glutathione). It is known that the reduction of Au^{3+} with a strong reducing agent, $NaBH_4$, in the presence of GSH resulted in a mixture of "magic" clusters $(Au_{10}(SG)_{10}$, $Au_{15}(SG)_{13}$, $Au_{18}(SG)_{14}$, $Au_{22}(SG)_{16}$, $Au_{22}(SG)_{17}$, $Au_{25}(SG)_{18}$, $Au_{29}(SG)_{20}$, $Au_{33}(SG)_{22}$, and $Au_{39}(SG)_{24})$,[18] whereas using a slow reducing agent, $NaBH_3CN$, produces one cluster alone, namely, $Au_{18}SG_{14}$. Figure 1a shows the distinct absorption bands of $Au_{18}(SG)_{14}$ clusters, ane centered at 590 nm (2.1 eV), a broad band at 515 nm, (2.4 eV) and another in the UV region at 290 nm (4.2 eV). It exhibits red luminescence at room temperature upon illumination with UV light. The quantum yield is ∼5%, nearly 25-fold higher than that of $Au_{25}SG_{18}$. ESI MS shows a series of multiply charged peaks due to $Au_{18}SG_{14}$ (Figure 1b).

The success of the synthesis of $Au_{18}(SG)_{14}$ is attributed to the use of a mild reducing agent. This demonstrates that as in the case of organic synthesis, here too, controlled reactions are indeed possible. For example, in organic synthesis, sodium cyanoborohydride ($NaBH_3CN$) is used as a mild and selective reducing agent, which gives selective products, whereas the typical strong reducing reagent, $NaBH_4$, is less selective. A mild and selective reducing agent can help in slowing down the nucleation and retard the growth of the nuclei, which may result in the direct formation of smaller Au−SG QCs. A report[50] by Jin et al. presented the synthesis of $Au_{19}(SPh)_{13}$ (PET = phenylethane thiolate) QCs by the combination of both kinetic and thermodynamic control of the reaction. In this case, clusters of different sizes were formed initially, which then underwent size convergence into a monodisperse product by means of a prolonged aging process. For slow reduction, a weaker reducing agent, borane-*tert*-butylamine complex, was used. We note that upon using $NaBH_4$ as the reducing agent, another cluster, $Au_{25}SR_{18}$, is produced.[52] In addition to these reports, a simple method to produce various gold clusters is to use CO as the reducing agent.[51] These results demonstrate that variation in reactions could make single-step methods feasible for $Au_n(SG)_m$ (n = 10, 15, 18, 19, 25, 29, 33) clusters.

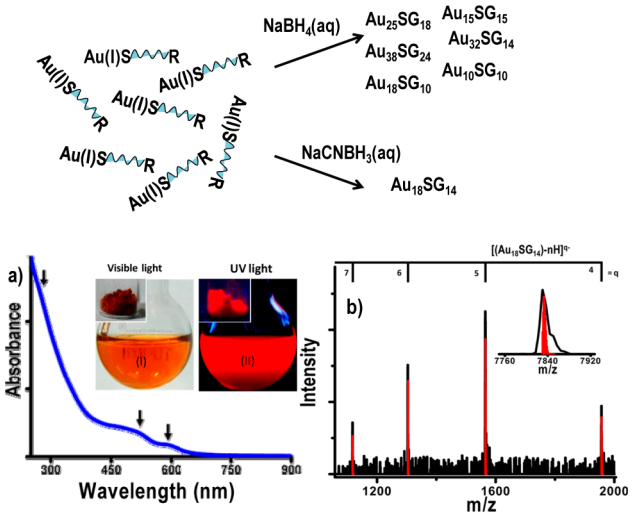

Figure 1. Schematic representation of two reduction processes, one using $NaBH_4$ and the other using $NaCNBH_3$. (a) UV/vis absorption profile of $Au_{18}SG_{14}$ clusters in water. Insets show the photographs of clusters in water upon illuminating with visible and UV light. (b) ESI MS spectrum of $Au_{18}SG_{14}$ in the negative mode, in the region of m/z 1000−2000. The peaks observed are due to $Au_{18}SG_{14}$. Red lines represent the calculated values for the charge states. The inset shows a deconvoluted spectrum based on the multiply charged species observed. Besides the molecular ion feature at m/z 7830, it shows higher mass number shoulders due to sodium addition. Here, the red spectrum gives the expected isotope distribution. Reprinted with permission from ref 49.

The similarity of organic reactions and cluster syntheses is demonstrated by these experiments.

From now onward, we shall describe recent developments of thiolate-protected silver clusters. Application of several traditional routes has resulted in the formation of plasmonic Ag systems and silver thiolates. Synthesis of silver clusters has learned significantly from the gold literature.

Variation in reduction methods produces clusters of different sizes. One such change is varying the strength of the reducing agent in a given reaction. This variation resulted in atomically precise $Au_{18}SG_{14}$ and $Au_{19}SPh_{13}$ nanoclusters.

Silver Clusters. Among a vast amount of research on thiolate-protected noble metal clusters, a major portion has been on gold, and very little has been on silver. This is due to the lack of suitable synthetic methods to produce the latter and also due to their reduced stability. The main difficulty in synthesizing silver clusters is the higher susceptibility of silver to oxidation. It makes conversion of the Ag_n core to Ag_nO_x, resulting the loss of characteristic optical features.[53] More focused research is needed to produce atomically precise Ag analogues of AuQCs. Detailed spectroscopic characterization is another challenge. Obviously, theoretical analyses are also needed.

dx.doi.org/10.1021/jz400332g | J. Phys. Chem. Lett. 2013, 4, 1553−1564

After the successful synthesis of thiolated AuQCs,[7] immediate attention was drawn to produce the Ag analogues. Most of the thiols, which stabilize effectively Au clusters, do not do so for Ag. For the latter, instead of stabilizing at the molecular level, they undergo further growth, forming plasmonic silver nanoparticles. Excellent studies in various areas, especially understanding the electronic band structure in comparison to metals, have appeared on these plasmonic systems.[54] Continuous improvement in this area produced new kinds of thiolated AgQCs, which possess discrete energy levels due to strong quantum confinement. Murray et al. had demonstrated quantized one-electron double-layer charging (QDL) for the first time in silver clusters.[53] Kimura et al. have synthesized mixtures of silver clusters protected with various hydrophilic thiolates and separated them by gel electrophoresis.[55] Molecular behavior is seen in their optical properties. Lack of stability, which thwarts analysis by mass spectrometry, also restricted the initial efforts to characterize their photophysical and chiroptical properties.

(a) Synthetic Diversity. Some successful methods to achieve a handful of silver clusters are interfacial,[56] solid-state,[57] gel-mediated,[58] and reversible phase transfer;[59] ripening,[60] core etching,[61] and high-temperature[62] routes were added to the literature in the recent past. In addition, some traditional routes with minor changes[63−66] were also used for their synthesis. Recently, interfacial synthesis is gaining attention as one of the promising methods for the synthesis of nanomaterials and their assemblies. Various metal nanocrystals and semiconducting materials have been synthesized using the interfacial route.[67] Interfacial properties, such as surface tension and interfacial potential, offer new synthetic variables to make nanomaterials. The interfacial etching route was initially used to synthesize 7 kDa silver QCs.[68] It was reported that clusters were formed only at the interphase. Later, using the same method, gram-scale syntheses of two luminescent silver clusters protected by mercaptosuccinic acid (H_2MSA), having well-defined molecular formulas ($Ag_8(H_2MSA)_8$ and $Ag_7(H_2MSA)_7$), were performed. Here, nanoparticles of different sizes, taken as starting materials, ultimately converged to a mixture of the above two clusters. This reaction was performed in an aqueous−organic biphasic system. During the reaction, the optical absorption spectra of the aqueous phase showed gradual disappearance of the surface plasmon resonance of metallic silver nanoparticles at 400 nm, indicating that nanoparticles were being converted to smaller cluster molecules. The mixture of two clusters, namely, Ag_7 and Ag_8, was separated using gel electrophoresis. Ag_8 exhibits a peak at 520 nm in its optical absorption spectrum (Figure 2) and an emission in the red region. It shows strong temperature-dependent emission. A layer of toluene on top of the aqueous phase might have minimized the direct contact of silver with air during the etching process. Bigger nanoparticles (i.e., initially taken unetched nanoparticles) form a 2-D assembly at the water−toluene interphase in the course of this reaction.

The solid-state method is an interesting and novel route to make diverse silver clusters. Here, the time required to produce the desired cluster is substantially less. High yield of clusters and easy handling of reaction make this route novel. It is expected that this protocol opens up a new way to make a variety of cluster materials. It is in contrast to the general solid-state synthetic routes to make ceramics where most of the reactions take place at high temperatures in order to allow diffusion and nucleation between two or more reagents.

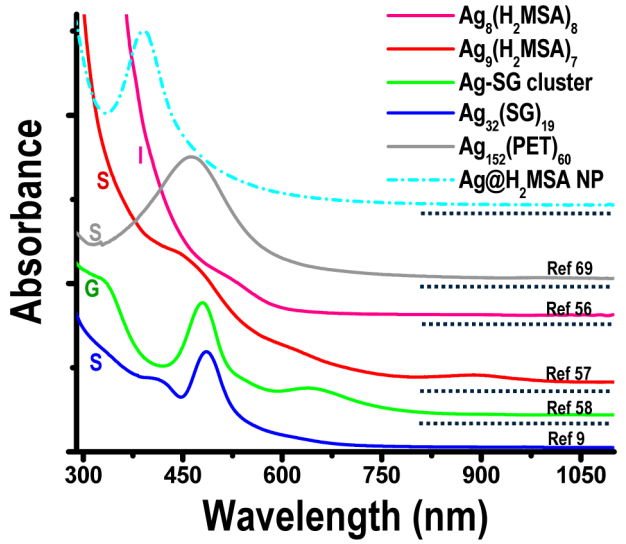

Figure 2. Optical absorption profiles of clusters obtained by different methods. Labels I, S, and G on the traces indicate interfacial, solid-state, and gel-mediated routes, respectively. The dashed trace at the top corresponds to Ag@H_2MSA nanoparticles of 5−10 nm prepared by the traditional method.

Clusters were obtained by grinding metal precursor(s) and ligand (solid or liquid) followed by reduction with solid $NaBH_4$. In this process, initially, silver thiolate is formed due to the reaction between the silver salt such as $AgNO_3$ and thiol (RSH = H_2MSA, GSH, phenylethanethiol (PETH), etc.). High affinity of sulfur toward noble metal ions is the reason for thiolate formation. Upon addition of $NaBH_4$ in the solid form, the ground mixture turns to a brownish-black powder that shows high affinity to water. This situation is different from the synthesis in the solution phase. The essential steps of cluster formation, such as nucleation and growth, are controlled due to the lack of protic solvent as they are mixed in the solid state. Three main contributions have been made using the solid-state route;[9,57,69] these are 9-, 32-, and 152-atom silver clusters protected by thiolates of H_2MSA, GSH, and PETH, respectively. Some more clusters are yet to be characterized fully.[70] $Ag_9(H_2MSA)_7$ was obtained by grinding a mixture of $AgNO_3$ and H_2MSA in a 1:5 molar ratio with $NaBH_4$. Here, all of the precursors are taken in the solid form. The cluster shows a step-like feature in its UV/vis absorption spectrum, similar to the Au_{25} clusters. $Ag_{32}(SG)_{19}$ was also synthesized through the solid-state route, where $AgNO_3$, GSH, and $NaBH_4$ were taken as precursors. Optical absorption spectra of this cluster possess a sharp peak at 480 nm and shoulder peaks at 420 and 610 nm (Figure 2).[9]

Recently, the synthesized Ag_{152} cluster opened the way to fundamental studies and potential applications in this area.[69] It was obtained by a solid-state route in which solid $AgNO_3$ was ground with PETH (oily liquid) in a 1:5.3 molar ratio in a mortar and pestle. Adding 25 mg of $NaBH_4$ (solid) with continued grinding completes the reaction. Immediate extraction of excess thiol in the reaction mixture using ethanol and subsequent dissolution of the residue in either toluene or tetrahydrofuran (THF) gives a solution of the cluster. The crucial aspect of this procedure is the limited supply of water needed for the reduction, which becomes available from the laboratory atmosphere as well as from ethanol used for subsequent washings. The clusters were monodisperse, as confirmed by

dx.doi.org/10.1021/jz400332g | J. Phys. Chem. Lett. 2013, 4, 1553−1564

the HPLC studies. The composition of the cluster Ag_{152} was detected by MALDI MS analyses (Figure 3). The spectra

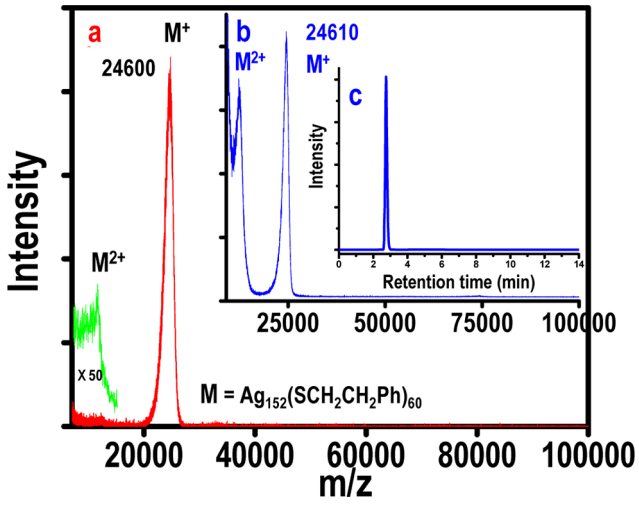

Figure 3. (a) MALDI MS spectrum of an as-synthesized 25 kDa cluster collected in the positive mode. It gives a sharp (fwhm, 1.5 k) molecular peak centered at m/z 24 600 ± 100. A minor peak, at m/z 12 300 ± 30, is seen, which corresponds to the doubly charged species. For clarity, this is expanded 50 times in the vertical axis. (b) Same as (a) but for the HPLC-purified sample, extracted in THF. It shows a narrower peak (fwhm of 1.3 k) at m/z 24 610 ± 80 and a pronounced dication peak at m/z 12 320 ± 30. (c) Chromatogram of the Ag_{152} cluster extracted in THF. Reprinted with permission from ref 69.

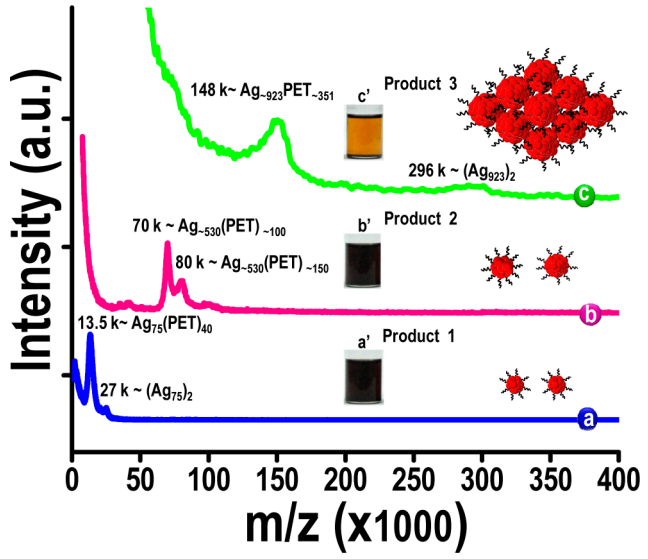

Figure 4. MALDI mass spectra showing the systematic size evolution of a cluster, labeled as product **1**, to particle crystals. A sharp peak centered at m/z 13 k (a) obtained by operating at the threshold laser fluence is assigned as $\sim Ag_{75}(PET)_{40}$ (product **1**), with a hump at m/z of 27 k probably due to the dimer. Product **1** converts to product **2** (b), exhibiting plasmonic absorption, with a mass of 70 k and a weaker feature at 80 k tentatively assigned as $Ag_{\sim 530}(PET)_{\sim 100}$ and $Ag_{\sim 561}(PET)_{\sim 150}$, respectively). Gradual heating allows assembly of plasmonic product **2** to self-organized nanoparticles with definite periodicity (c) composed of ~923 Ag atoms ($Ag_{\sim 923}(PET)_{\sim 351}$). Its dimer at 296 k has also been observed (c). Insets of mass spectra show the corresponding photographs and cartoon representations of the size evolution. In photograph (c′), a black precipitate can be seen at the bottom of the sample vial, corresponding to the SL. Reprinted with permission from ref 70, copyright 2013, Wiley-VCH.

shown in Figure 3 are at the lowest laser power needed to observe ion signals. Mass spectra for the purified and unpurified samples show the same features with a single peak centered at m/z 24 600 [full width at half-maximum (fwhm) of 1.5 k] and the doubly charged cluster at m/z 12 300 ± 30. However, HPLC-subjected samples show sharper peaks compared to the as-synthesized samples. Recent results from our lab have also shown the formation of gold and copper clusters by this route. This synthetic approach may make the synthesis of clusters of other elements feasible, as evidenced by the synthesis of iridium nanoparticles.[90] It is important to point out that because all products are in the solid/pasty state during synthesis, it is possible to collect samples at intermediate steps of reaction in order to get information about the progress of the reaction.

(b) Clusters to Superlattices (SLs). Another interesting report form Sugi et al.[70] described the systematic size evolution of organic-soluble, atomically precise Ag clusters monitored by various techniques. The same protocol as that above was used in this experiment to make clusters. In MALDI MS investigations, the initial product during the synthesis was a 13 kDa cluster (Figure 4a). These clusters transform gradually to more stable plasmonic nanoparticles with moleculear masses of 70 and 80 kDa (Figure 4b). Again, a suspension of these nanoparticles upon constant heating at 100 °C leads to the formation of self-organized nanoparticles of higher molecular mass (148 kDa) (Figure 4c). These clusters of 13, 70, 80, and 148 kDa are tentatively assigned as $Ag_{\sim 75}(PET)_{\sim 40}$, $Ag_{\sim 530}(PET)_{\sim 100}$, $Ag_{\sim 561}(PET)_{\sim 150}$, and $Ag_{\sim 923}(PET)_{\sim 351}$, respectively (as the mass peaks are broad, the atomic composition is approximated). Accompanying this gradual mass evolution, systematic changes in optical absorption spectra are also observed. Those results show the possibility of synthesis of nanomaterials with tunable properties in a one-pot method. Tunability arises as nanoparticle sizes can be controlled as they are formed starting from atomically precise clusters.

(c) Use of Gels. An important issue of concern of synthesis of any desired cluster is related to mass transfer, leading to controlled nucleation. Gels are composed of molecular cages that may be used to control mass transfer and to nucleate the preferred clusters. Cage dimensions and kinetic parameters may be controlled to yield desired results. Molecular cages of polyacrylamide gel were used for the direct synthesis of monodisperse silver−SG clusters in a single step and within 30 min. These clusters show prominent features at 350, 470, and 650 nm in their UV/vis absorption spectrum (sample G of Figure 2). The method involves reductive decomposition of Ag(I)SG thiolates in polyacrylamide gel cavities of submicrometer size. In this method, an acrylamide/bisacrylamide solution containing Ag(I)SG thiolates was allowed to polymerize in a beaker to form a gel. On top of this gel, aqueous $NaBH_4$ was added. The color of the gel changed from light yellow to dark brown within 0.5 h, indicating the formation of clusters inside of the cavities. Free clusters were extracted into water and precipitated using excess ethanol. Dry powder was obtained after the removal of solvent using a rotary evaporator. These clusters can selectively detect Hg(II) ions down to the ppb level.[58] Kitaev et al. also reported on the synthesis of similar clusters by two routes, (1) creating new kinds of reaction environments (cyclic reduction under oxidative conditions, where

dx.doi.org/10.1021/jz400332g | J. Phys. Chem. Lett. 2013, 4, 1553−1564

$NaBH_4$ was used for reduction and H_2O_2 was used for oxidation) for Ag(I)SR, leading to the formation of AgQCs,[65] and (2) a direct process that involves the reduction of Ag(I)SG thiolates using $NaBH_4$ in H_2O/MeOH mixtures at basic conditions.[63]

Addition of new protocols (interfacial, solid-state, and gel-mediated) and the resulting clusters expose enormous opportunities to study silver at the cluster level.

(d) Other Strategies. Bigioni et al.[81] have synthesized crude Ag_mSG_m clusters by the reduction of Ag(I)SG thiolates with $NaBH_4$ in water. A series of clusters were isolated using gel electrophoresis, and their optical properties were studied. Compositions of these clusters were explored using electrophoresis by comparing their relative mobilities with the known gold QCs. Later, Guo et al.[82] studied the composition of one of the clusters isolated from the sixth band of the gel. The optical properties of the cluster are given in Table 1. Figure 5a shows the ESI MS of the cluster at optimized conditions, a series of multiply charged peaks corresponding to $[Ag_{32}(SG)_{19}]^{q-}$ are labeled on the spectrum, where q = 4, 5, 6, 7, and 8. This assignment was further confirmed by the agreement between the experimental and calculated isotope distributions of $[Ag_{32}(SG)_{19}\text{-}4H]^{4-}$ (inset of Figure 5a).

Silver clusters of size ∼2.1 nm were synthesized by incubating as-synthesized polydisperse Ag@SBB (SBB = thiolate of 4-*tert*-butylbenzyl mercaptan (BBSH)) clusters in the presence of clean BBSH at 60 °C.[60] Multiple characterization studies revealed that their chemical composition is $Ag_{280}(SBB)_{120}$. An interesting method reported by Yuan et al. is also added to this list for synthesizing fluorescent metal nanoclusters (Au, Ag, Pt, Cu).[59] It involves the phase transfer of water-soluble nonfluorescent metal nanoclusters (which were synthesized by a common chemical reduction method) to the organic medium by a phase-transfer agent. This method is mainly applicable to the clusters whose surfaces are passivated by ligands that are readily phase-transferable with cetyltrimethylammonium bromide (CTAB). As-synthesized clusters in the aqueous phase are nonfluorescent. In the toluene phase, after phase transfer, mild etching takes place, and the resulting nanoclusters exhibit strong fluorescence. Moreover, the fluorescent clusters can be easily transferred back to the aqueous phase upon adding a salt to remove the hydrophobic cation, CTA^+.

Chemical reduction with minor changes in conditions such as solvent, pH, the ligand, and so forth are able to make molecular silver clusters. Among the well-characterized systems are $Ag_7(DMSA)_4$, $Ag_{44}(4FTP)_{30}$, $Ag_{32}(SG)_{19}$, and $Ag_{280}(SSB)_{120}$. More are waiting to be characterized fully.

Dhanalakshmi et al. showed the synthesis of red-luminescent silver clusters protected by H_2MSA, in milligram quantities by the direct core reduction of Ag@citrate.[61] This route provides nearly pure clusters. On the basis of TG and elemental analysis, the composition of the cluster was tentatively assigned to $Ag_{38}SG_{24}$. An interesting protocol was reported[62] by Indranath et al. for the synthesis of highly stable red-luminescent $\sim Ag_{75}$ clusters. It involves formic-acid-mediated reduction of silver glutathionates in an aqueous medium at higher temperatures (70 °C). Absorption peaks evolved with time at constant temperature of 70 °C (Figure 5b). Here, Ag^+ to reduction was initiated by electrons, which were produced by the decomposition of formic acid. A well-defined spectrum with prominent peaks appeared at the third hour of the reaction. Note that at these temperatures, AgQCs usually undergo decomposition, resulting in the formation of Ag_2S nanoparticles.[84] The optical properties of these clusters remain the same for several months at both room and higher temperatures. So far, this is the first example of the successful synthesis of Ag clusters in solution at higher temperatures.

Silver clusters, namely, intensely and broadly absorbing nanoparticles (IBANs), with high molar extinction coefficients were reported by Bakr et al.[64] The synthetic method belongs to the category of traditional routes but with major alterations. Briefly, IBANs were prepared through the reduction of a silver salt solution in the presence of the capping ligand 4-fluorothiophenol (4FTP) in the usual, one-phase nanoparticle synthesis (4FTP/Ag = 2:1). Initially, 4FTP was stirred with a silver salt in *N*,*N*-dimethylformamide (DMF) for 15 min, followed by the addition of 4 molar excess of $NaBH_4$ in DMF. This resulted in a darkened nanoparticle solution with a UV/vis absorption peak at 450 nm. Transparent yellow solution was formed upon further stirring (4 h), indicating the disassociation of nanoparticles to silver ions or silver thiolates. Remnant $NaBH_4$ in the resultant solution was activated upon the addition of a small amount of water. Again, the solution turned dark and showed a broad peak centered at around 490 nm in its UV/vis spectra. By leaving the reaction at freezer temperatures (−4 °C) over several days (∼less than 1 week), it transferred to IBANs. These IBANs show eight distinct absorption bands with huge extinction cross sections of 2.59×10^5 L mol^{-1} cm^{-1} (Figure 5c). Another report presented the ESI mass spectrum of 4-FTP-protected IBANs with high isotopic separation.[80] It revealed that the compositions of these IBANs are $[Ag_{44}(4FTP)_{30}]^{4-}$ (Figure 5d). These clusters tend to be magic clusters because of their closed electronic shell ($44e^- - 30e^- + 4e^- = 18e^-$).

Interestingly, a few clusters, protected by dithiols, were synthesized with slight changes in the common chemical reduction method. Dimercaptosuccinic acid (DMSA),[71] lipoic acid (LA),[88] and polyethylene glycol (PEG)-appended LA[89] are some of the dithiols that can effectively passivate Ag clusters. Among these, $Ag_7(DMSA)_4$ has been studied in some detail in the literature. Electrochemical,[72] theoretical,[73] and mass spectral[74] studies have been done on this system. LA and related dithiol-protected clusters are highly red-luminescent. The quantum yield can be increased to ∼12%.[89] Compositions of LA-protected clusters are yet to be explored.

Among the Ag clusters described in the previous paragraphs, some, such as Ag_7,[71] Ag_8,[56] and Ag_9,[57] could be categorized as small clusters, and others, such as Ag_{32},[82] Ag_{44},[80] $\sim Ag_{140}$,[53] Ag_{152},[69] and Ag_{280},[60] can be categorized as bigger clusters. Several of them have optimized protocols for their synthesis. Optical absorption profiles of each of the above-mentioned

dx.doi.org/10.1021/jz400332g | J. Phys. Chem. Lett. 2013, 4, 1553−1564

Table 1. List of Silver Clusters Synthesized and Their Essential Properties[a]

formula	synthetic method	cluster analysis	absorption peaks (in nm)	luminescence λ_{ex}	luminescence λ_{em}	other studies
$Ag_{140}(SBB)_{53}$[53]	modified Brust protocol	MALDI MS/EA	475(b)			electrochemistry
$Ag_{280}(SBB)_{120}$[60]	ripening process	ESI MS/TG	700(w) and 800(w)			
$Ag_7(DMSA)_4$[71]	reduction of Ag(I)DMSA in EtOH	ESI MS/MS	500(s), 415(w) and 625(w)			electrochemical,[72] theoretical,[73] and mass spectral[74] studies
$Ag_8(H_2MSA)_8$[56]	interfacial etching	ESI, MALDI MS/EA	550(w)	550	650	catalysis,[75] investigations on Hg(II) ion interaction,[76] theoretical studies,[77] and electron-transfer properties[78]
$Ag_9(H_2MSA)_7$[57]	through solid grinding of $AgNO_3$, H_2MSA, and $NaBH_4$	ESI MS/EA	886(w), 625(w), 450(w), 479(w), and 315(w)	620	720	pesticide degradation[79]
$Ag_{44}(FTP)_{30}$[80]	controlled reductive conditions	ESI MS	multi bands	independent	1345	
$Ag_{32}(SG)_{19}$[9,81,82]	isolated from crude Ag clusters[81,82]	ESI MS	486(s), 415(w) and 330(w)			
	through solid grinding[9] of $AgNO_3$, SG, and $NaBH_4$		486(s), 415(w), and 330(w)	420, 500	680	
$Ag_{152}(PET)_{60}$[69]	grinding of $AgNO_3$, PET, and $NaBH_4$	MALDI MS/ theoretical studies	460(s, broad)	375	800	
7 kDa cluster[68]	interfacial etching	PAGE	550(w)	550	700	Hg(II) sensor
ref 65	cyclic oxidation and reduction of Ag(I)SR		490(s), 660(w), and 335(w)	430, 450	625	chiroptical studies[65]
ref 63	reduction of Ag(I)SR at basic conditions		490(s), 660(w), and 335(w)	495	595	chiroptical studies[63]
ref 58	reduction of Ag(I)SG inside gels		480(s), 640(w), and 330(w)	480	630	Hg(II) sensor,[58] graphene-based composite,[83] and thermal studies[84]
ref 66 Ag@PET	chemical reduction route	TG	469(s)			chiroptical studies
Ag@FTP			395(w) and 462(s)			
Ag@SG			478(s)			
ref 59/$Ag_{29}(SG)_{22}$	cyclic phase transfer	TG/EA				cysteine detection[85]
ref 86	reduction of Ag(I)SG using $N_2H_4{\cdot}2H_2O$ at basic conditions		490(b)	508	620	Hg(II) sensor[86]
ref 87	similar to ref 86		500(b)		660	Pb(II) sensor[87]
refs 88 and 89	reduction of Ag(I)LA in H_2O		435(s), 335(w), and 500(w)	325, 500	650	Hg(II) sensor[88]
Ag_{75} cluster[62]	high-temperature synthesis	MALDI MS	480(s), 420(s), and 320(w)	360, 400, 430	670	
ref 61 (~Ag_{38})	core etching reaction	EA	520(w)			

[a]Abbreviations: EA = elemental analysis; TG = thermogravimetric analysis; b = broad; w = weak; s = strong.

dx.doi.org/10.1021/jz400332g | J. Phys. Chem. Lett. 2013, 4, 1553−1564

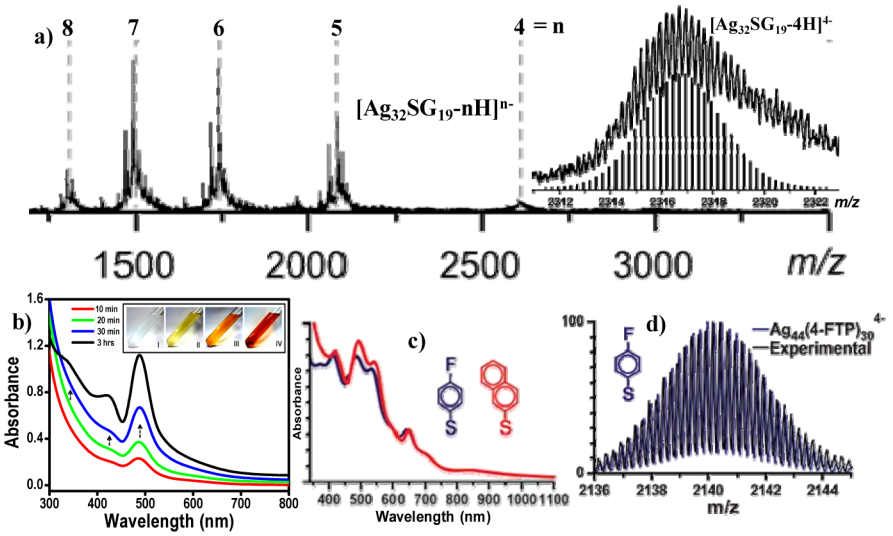

Figure 5. (a) ESI MS of $Ag_{32}(SG)_{19}$. Multiply charged peaks are marked on the spectrum. The inset shows the comparison of the experimental (black trace) and simulated (bars) isotopic distributions for $[Ag_{32}(SG)_{19}\text{-}4H]^{4-}$. (b) UV/vis absorption spectra of the growth of Ag_{75} clusters with time. (Insets) Photographs of the reaction mixture during synthesis at 0 (I), 10 (II), and 20 min (III) and 3 h (IV). (c) UV/vis absorption of $Ag_{44}(4FTP)_{30}^{4-}$ and $Ag_{44}(2NPT)_{30}^{4-}$. (d) ESI MS of $Ag_{44}(4FTP)_{30}^{4-}$. The mass spectrum matches well with the calculated spectrum (blue and black, respectively). (a) Reprinted with permission from ref 82; (b) reprinted with permission from ref 62, copyright 2012, RSC; (c,d) Reprinted with permission from ref 80, copyright 2012, RSC.

clusters is different. The origin of optical transitions in silver nanoclusters is yet to be understood. Some of these clusters were used for applications in several fields. For example, alumina-loaded $Ag_{7,8}$ shows enhanced catalytic activity,[75] and $Ag_{7,8}$ shows sensing of Hg^{2+}.[76] A report by Bootharaju et al.[79] showed that Ag_9 could be used for the removal of pesticides for water purification. Silver clusters protected with −SG with unknown compositions were obtained through hydrazine ($N_2H_4{\cdot}2H_2O$) reduction. They were used for selective sensing of metal ions such as Hg(II)[86] and Pb(II).[87] Protein-protected Ag_{15} clusters, in combination with mesoporous gold nanostars, could be used in the visible detection of TNT down to zeptomolar concentrations.[91] It indicates that application possibilities of these systems are bright. List of various silver clusters reported and their essential properties are listed in Table 1.

Obtaining a desired AgQC depends on a synthetic protocol. Once these are synthesized, they show huge applications in the areas of sensors, catalysts, water purification, and so forth.

Stability of Silver Clusters. From the developments in gold cluster research, it is evident that the effectiveness of the staple motif, super atom electronic count, core stability against dissociation, and a large HOMO−LUMO gap are the factors that decide the stability of these systems.[92] However, chemical interactions too play their part in determining the above factors. Stronger strength of metal−metal and metal−ligand bonds helps to build a stable atomic structure and an effective protection of the core by the staple motif. The connection between bond strength and stability was demonstrated experimentally and theoretically.[93,94] Clusters in the category of super atom (systems satisfying the jellium model) also exhibit higher stability than others. In the case of silver clusters, the Ag−Ag and Ag−S interactions are weaker in comparison to Au−Au and Au−S interactions (Au−Au > Ag−Ag; Au−S > Ag−S). In addition, gold systems possess aurophilic attractions, and the corresponding interactions are less in the case of Ag. These advantages of Au in comparison to Ag help to span the gold cluster research to a broad range of systems.

Practical difficulties to stabilize the silver clusters were overcome by encapsulating them in polymer templates.[63] The degradation rates can be minimized by storing the cluster samples in suitable solvent mixtures[57] and at an optimized pH[57] and, more importantly, keeping the cluster solution at lower temperatures.[64,71] Powder samples are more stable in comparison to their solutions. Some of these clusters are highly stable even at ambient conditions ($Ag_{32}(SG)_{19}$). The stability of the clusters can be easily understood by monitoring the UV/vis of cluster solutions. Characteristic optical properties of a given AgQC are very sensitive to pH, temperature, and solvents.[56,82] In the case of less stable clusters, optical absorption spectra undergo changes with time. We speculate that this happens either by a change in the net charge of the cluster or by the interconversion of isomers or due to the transformation of cluster cores. Some absorption peaks in a particular sample are sensitive, and they disappear rapidly. For example, we have observed the disappearance of the 650 and 350 nm peaks with time in sample G of Figure 2, leaving only an intense peak at 480 nm. It has to be noted that all of the peaks are arising from the same sample, confirmed from gel electrophoresis. In the first case, AgQCs may carry excess negative charge (evident in the case of $[Ag_{44}(4FTP)_{30}]^{4-}$). It is possible to observe a variety of absorption profiles for the same cluster by varying the charge (4^-, 3^-, 2^-, 1^-, 0, 1^+). It is known that minor changes were seen in the case of $[Au_{25}(SG_{18})]^0$ to $[Au_{25}(SG_{18})]^-$. However, crystallographic studies on these clusters are waiting for a better understanding. Recently, there has been some progress in this area due to the single-crystal analysis of AgQCs protected by thiolate and phosphine ligands.[95,96] These studies reveal the different atomic structure of thiolated AgQCs in comparison to

dx.doi.org/10.1021/jz400332g | J. Phys. Chem. Lett. 2013, 4, 1553−1564

AuQCs, suggesting that new structural models may be needed to understand AgQCs.

Alloy Quantum Clusters. Alloy nanoparticles (3−100 nm) made up of Ag and Au were well-studied materials in the recent past.[97] However, efforts to obtain quantum alloy clusters of these elements are very few. Reports include phosphine-protected $Au_{18}Ag_{20}$[98] and $Au_{13}Ag_{12}$[99] clusters. Another kind of material emerging in this area are the Au_nSR_m analogues. There are several successful reports for the synthesis of monodisperse clusters of the type, $Ag_nAu_{25-n}(SR)_{18}$,[100] $(AuAg)_{140}(SR)_{60}$,[101] and $Au_{38-n}Ag_n(SR)_{24}$.[102] These were obtained by the simultaneous reduction of appreciable concentrations of silver and gold salts in suitable conditions. Motivated by these reports, theoreticians have predicted their structural details based on DFT calculations.[103] An important outcome from such calculations is the preferential occupancy of silver on the surface of a gold core. Both experiments and calculations have shown that an increase in the number of silver atoms in $Au_{140}(SR)_{60}$ slightly decreases the optical band gap[104,105] and alters the electronic shell structure, which results in changes in the optical transitions present in the high-energy region (interband transitions). In the case of protein template AgAu alloy clusters, only a few reports are available.[106,107] Among the alloy clusters, $Au_{38-x}Ag_x$@BSA was well-characterized using MALDI MS.[107] Synthesis and studies of alloy clusters in protein templates are awaited.

Another way to produce alloy clusters is to use the advantage of the galvanic exchange process at the atomic level. By the addition of Au(I)SR to silver clusters at suitable conditions, one can produce alloy clusters. Direct addition of Au^{3+} may collapse the clusters. Murray et al. had reported the creation of luminescent alloy clusters through this process.[108] As compared to the parent silver clusters, noticeable changes were observed in the optical properties of alloy clusters. The same methodology was applied on still smaller silver clusters, $Ag_{7,8}(H_2MSA)_8$, which eventually resulted in the formation of a 13-atom alloy cluster.[109] Its chemical composition, $Ag_7Au_6(H_2MSA)_{10}$, was found from ESI MS along with elemental analysis. A galvanic reaction between Au(I) thiolate and crude silver clusters ($Ag_{7,8}(H_2MSA)_{7,8}$) made this alloy cluster. Optical absorption (350 and 692 nm) and luminescence (λ_{ex} 390 and λ_{em} 650 nm) were changed drastically as compared to the parent clusters. Theoretical results suggested that the cluster possessed a distorted icosahedral core. The simulated absorption spectrum of this structure is in agreement with the experimentally obtained spectrum. It is proposed that the clusters obtained in the galvanic exchange process may carry gold on the surface with silver in the core. It is in contrast to the clusters obtained in earlier cases (simultaneous reduction of both metal salts). If this is proven by future theoretical and experimental studies, there is a possibility to have both "silver-covered" and "gold-covered" alloy clusters with tunable electronic, optical, and catalytic properties.

MS/MS Analysis. Most of the compositions of clusters were determined by mass spectrometry. While soft ionization mass spectrometry is an invaluable tool in determining the molecular formulas of clusters, profound structural insights are derived from MS/MS analysis (tandem mass spectrometry). As expected, these kinds of studies were done initially on the well-known cluster $Au_{25}SR_{18}$.[110] MS/MS studies on other magic gold clusters are awaited. Recently, tandem mass spectrometry of $Au_{18}SG_{14}$ by Ghosh et al. showed the possibility of monolayer-protected "super atoms" in the gas phase. Note that so far, we know only about naked (unligated) gas-phase super atoms. Mass spectral peaks of $[Au_{18}(SG)_{14}\text{-}nH]^{q-}$ at m/z 1956.2, 1565.2, 1304.3, and 1117.4 for q = 4, 5, 6, and 7 were subjected to MS/MS analyses. Upon subjecting these peaks to MS/MS, we got several fragments, which were all $8e^-$ entities, that is, $m - n + q = 8$, where m is the number of gold atoms, n is the number of thiolate ligands, and q is the charge on the ligand. For example, $[Au_{18}SG_{14}]^{5-}$ underwent various types of dissociations and produced peaks of 4^- charge during MS/MS at various collision energies. MS/MS for other charged anions also ended with cluster ions carrying 4^- charge. All of them satisfy the condition, $m - n + q = 8$. Here, the electron count includes the charges on the ligands as well. At all collision energies, super atom formation was observed.

Signatures of two kinds of alloy materials, namely, "Au-centered/silver-covered" and "Ag-centered/gold-covered", are seen.

MS/MS studies on $Ag_7(DMSA)_4$ show $Ag_nS_4^-$ ($1 \le n \le 7$) species at various collision energies.[74] The ions $Ag_7S_4^-$, $Ag_6S_4^-$, $Ag_5S_4^-$, $Ag_4S_4^-$, $Ag_3S_4^-$, $Ag_2S_4^-$, and AgS_4^- were formed sequentially from $[Ag_7(DMSA)_4]^{2-}$ with an increase in collision energy (25, 40, 50, 70, 80, 90, and 100 eV, respectively). A DFT-based global-minimum search further confirms that the formed species are stable.

Perspectives. The science of quantum-confined cluster cores of silver with ligand protection possessing well-defined molecular formulas has attracted intense interest in the recent past. Although a uniform synthetic strategy is not available to make clusters of all kinds, available methods can produce a number of cluster cores with several ligands. The most important property of these clusters is their luminescence in the visible region and the sensitivity of this luminescence to various analytes. The composition of clusters can be varied by making alloys, and a few of these are now available. The chemistry of the cluster systems is beginning to evolve, and their specific reactivity is a subject of attention. Noble metal clusters are now made in the confinement of proteins, and applications of these systems are evolving fast. The most immediate need in the chemistry of such systems is crystallization and understanding the properties in a size-dependent fashion. Early signs of expansion of the science of silver clusters are evident from the recent reports. Utilization of their properties in areas such as sensing, environmental remediation, water purification, imaging, and diagnostics will be important areas of exploration.

AUTHOR INFORMATION

Corresponding Author

*E-mail: pradeep@iitm.ac.in. Webpage: http://www.dstuns.iitm.ac.in/.

Notes

The authors declare no competing financial interest.

Biographies

T. Udayabhaskararao received a M.Sc. in Physical chemistry from Andhra University, Visakhapatnam. He is pursuing his Ph.D. at the Indian Institute of Technology Madras under the guidance of Prof. T. Pradeep. He is working on the synthesis and characterization of thiol-protected noble metal nanoclusters.

T. Pradeep is a professor of Chemistry at the Indian Institute of Technology Madras, Chennai, India. His research interests are in molecular and nanoscale materials, and he develops instrumentation for those studies. He is currently involved in establishing a "Thematic Unit of Excellence" on water purification using nanotechnology. He is a Fellow of the Indian Academy of Sciences. Besides textbooks and monographs, he has authored a few popular science books in Malayalam. For more information, see http://www.dstuns.iitm.ac.in/pradeep-research-group.php.

■ ACKNOWLEDGMENTS

We thank the Department of Science and Technology, Government of India for constantly supporting our research program on nanomaterials.

■ REFERENCES

(1) Faraday, M. *Philos. Trans. R. Soc., London* **1857**, *147*, 145−181.
(2) Daniel, M.-C.; Astruc, D. Gold Nanoparticles: Assembly, Supramolecular Chemistry, Quantum-Size-Related Properties, and Applications toward Biology, Catalysis, and Nanotechnology. *Chem. Rev.* **2003**, *104*, 293−346.
(3) Mie, G. *Ann. Phys.* **1908**, *25*, 377.
(4) Knoll, M. K.; Subjective Light, J. Pattern Spectroscopy in the Electroencephalic Range. *Nature (London)* **1959**, *184*, 1823−1824.
(5) Turkevich, J.; Stevenson, P. C.; Hillier, J. A Study of the Nucleation and Growth Processes in the Synthesis of Colloidal Gold. *Discuss. Faraday Soc.* **1951**, *11*, 55−75.
(6) Link, S.; El-Sayed, M. A. *Int. Rev. Phys. Chem.* **2000**, *19*, 409−453.
(7) Templeton, A. C.; Wuelfing, W. P.; Murray, R. W. Monolayer-Protected Cluster Molecules. *Acc. Chem. Res.* **1999**, *33*, 27−36.
(8) Zhu, M.; Aikens, C. M.; Hollander, F. J.; Schatz, G. C.; Jin, R. Correlating the Crystal Structure of A Thiol-Protected Au_{25} Cluster and Optical Properties. *J. Am. Chem. Soc.* **2008**, *130*, 5883−5885.
(9) Udayabhaskararao, T.; Bootharaju, M. S.; Pradeep, T. Thiolate-Protected Ag_{32} Clusters: Mass Spectral Studies of Composition and Insights into the Thiolate Structure from NMR. *Nanoscale* **2013**, submitted.
(10) Walter, M.; Akola, J.; Lopez-Acevedo, O.; Jadzinsky, P. D.; Calero, G.; Ackerson, C. J.; Whetten, R. L.; Grönbeck, H.; Häkkinen, H. A Unified View of Ligand-Protected Gold Clusters As Superatom Complexes. *Proc. Natl. Acad. Sci. U.S.A.* **2008**, *105*, 9157−9162.
(11) Jin, R. Quantum Sized, Thiolate-Protected Gold Nanoclusters. *Nanoscale* **2010**, *2*, 343−362.
(12) Ramasamy, P.; Guha, S.; Shibu, E. S.; Sreeprasad, T. S.; Bag, S.; Banerjee, A.; Pradeep, T. Size Tuning of Au Nanoparticles Formed by Electron Beam Irradiation of Au_{25} Quantum Clusters Anchored within and Outside of Dipeptide Nanotubes. *J. Mater. Chem.* **2009**, *19*, 8456−8462.
(13) Jadzinsky, P. D.; Calero, G.; Ackerson, C. J.; Bushnell, D. A.; Kornberg, R. D. Structure of a Thiol Monolayer-Protected Gold Nanoparticle at 1.1 Å Resolution. *Science* **2007**, *318*, 430−433.
(14) Heaven, M. W.; Dass, A.; White, P. S.; Holt, K. M.; Murray, R. W. Crystal Structure of the Gold Nanoparticle $[N(C_8H_{17})_4][Au_{25}(SCH_2CH_2Ph)_{18}]$. *J. Am. Chem. Soc.* **2008**, *130*, 3754−3755.
(15) Qian, H.; Eckenhoff, W. T.; Zhu, Y.; Pintauer, T.; Jin, R. Total Structure Determination of Thiolate-Protected Au_{38} Nanoparticles. *J. Am. Chem. Soc.* **2010**, *132*, 8280−8281.
(16) Zeng, C.; Qian, H.; Li, T.; Li, G.; Rosi, N. L.; Yoon, B.; Barnett, R. N.; Whetten, R. L.; Landman, U.; Jin, R. Total Structure and Electronic Properties of the Gold Nanocrystal $Au_{36}(SR)_{24}$. *Angew. Chem., Int. Ed.* **2012**, *51*, 13114−13118.
(17) Das, A.; Li, T.; Nobusada, K.; Zeng, Q.; Rosi, N. L.; Jin, R. Total Structure and Optical Properties of a Phosphine/Thiolate-Protected Au_{24} Nanocluster. *J. Am. Chem. Soc.* **2012**, *134*, 20286−20289.
(18) Negishi, Y.; Nobusada, K.; Tsukuda, T. Glutathione-Protected Gold Clusters Revisited: Bridging the Gap between Gold(I)−Thiolate Complexes and Thiolate-Protected Gold Nanocrystals. *J. Am. Chem. Soc.* **2005**, *127*, 5261−5270.
(19) Harkness, K. M.; Cliffel, D. E.; McLean, J. A. Characterization of Thiolate-Protected Gold Nanoparticles by Mass Spectrometry. *Analyst* **2010**, *135*, 868−874.
(20) Wurth, W M. M. Atomic Clusters: From Gas Phase to Deposited. In Woodruff, D. P., Ed.; *The Chemical Physics of Solid Surfaces*; Elsevier; Oxford, U.K., 2007.
(21) Sun, T.; Seff, K. Silver Clusters and Chemistry in Zeolites. *Chem. Rev.* **1994**, *94*, 857−870.
(22) Meitzner, M. B. a. G. *EXAFS Near Edge Structure 3*; Springer Proceedings in Physics, 1984; Vol. *2*.
(23) Zhang, H.; Huang, X.; Li, L.; Zhang, G.; Hussain, I.; Li, Z.; Tan, B. Photoreductive Synthesis of Water-Soluble Fluorescent Metal Nanoclusters. *Chem. Commun.* **2012**, *48*, 567−569.
(24) Henglein, A. Small-Particle Research: Physicochemical Properties of Extremely Small Colloidal Metal and Semiconductor Particles. *Chem. Rev.* **1989**, *89*, 1861−1873.
(25) Zhang, J.; Xu, S.; Kumacheva, E. Photogeneration of Fluorescent Silver Nanoclusters in Polymer Microgels. *Adv. Mater.* **2005**, *17*, 2336−2340.
(26) Diez, I.; Ras, R. H. A. Fluorescent silver nanoclusters. *Nanoscale* **2011**, *3*, 1963−1970.
(27) Xu, H.; Suslick, K. S. Sonochemical Synthesis of Highly Fluorescent Ag Nanoclusters. *ACS Nano* **2010**, *4*, 3209−3214.
(28) Liu, S.; Lu, F.; Zhu, J.-J. Highly Fluorescent Ag Nanoclusters: Microwave-Assisted Green Synthesis and Cr^{3+} Sensing. *Chem. Commun.* **2011**, *47*, 2661−2663.
(29) Diez, I.; Kanyuk, M. I.; Demchenko, A. P.; Walther, A.; Jiang, H.; Ikkala, O.; Ras, R. H. A. Blue, Green and Red Emissive Silver Nanoclusters Formed in Organic Solvents. *Nanoscale* **2012**, *4*, 4434−4437.
(30) Lin, C.-A. J.; Lee, C.-H.; Hsieh, J.-T.; Wang, H.-H.; Li, J. K.; Shen, J.-L.; Chan, W.-H.; Yeh, H.-I.; Chang, W. H. Synthesis of Fluorescent Metallic Nanoclusters toward Biomedical Application: Recent Progress and Present Challenges. *J. Med. Biol. Eng.* **2009**, *29*, 276−283.
(31) Kim, Y.-G.; Oh, S.-K.; Crooks, R. M. Preparation and Characterization of 1−2 nm Dendrimer-Encapsulated Gold Nanoparticles Having Very Narrow Size Distributions. *Chem. Mater.* **2003**, *16*, 167−172.
(32) Kitazawa, H.; Albrecht, K.; Yamamoto, K. Synthesis of a Dendrimer Reactor for Clusters with a Magic Number. *Chem. Lett.* **2012**, *41*, 828−830.
(33) Petty, J. T.; Zheng, J.; Hud, N. V.; Dickson, R. M. DNA-Templated Ag Nanocluster Formation. *J. Am. Chem. Soc.* **2004**, *126*, 5207−5212.
(34) Choi, S.; Dickson, R. M.; Yu, J. Developing Luminescent Silver Nanodots for Biological Applications. *Chem. Soc. Rev.* **2012**, *41*, 1867−1891.
(35) Kennedy, T. A. C.; MacLean, J. L.; Liu, J. Blue Emitting Gold Nanoclusters Templated by Poly-cytosine DNA at Low pH and Poly-adenine DNA at Neutral pH. *Chem. Commun.* **2012**, *48*, 6845−6847.
(36) Liu, G.; Shao, Y.; Ma, K.; Cui, Q.; Wu, F.; Xu, S. Synthesis of DNA-Templated Fluorescent Gold Nanoclusters. *Gold Bull.* **2012**, *45*, 69−74.
(37) Guiying, L.; Yong, S.; Fei, W.; Shujuan, X.; Jian, P.; Lingling, L. DNA-Hosted Fluorescent Gold Nanoclusters: Sequence-Dependent Formation. *Nanotechnology* **2013**, *24*, 015503.
(38) Lourdu Xavier, P.; Chaudhari, K.; Baksi, A.; Pradeep, T. Protein-Protected Luminescent Noble Metal Quantum Clusters: An Emerging Trend in Atomic Cluster Nanoscience. *Nano Rev.* **2012**, *3*, 14767.
(39) Xie, J.; Zheng, Y.; Ying, J. Y. Protein-Directed Synthesis of Highly Fluorescent Gold Nanoclusters. *J. Am. Chem. Soc.* **2009**, *131*, 888−889.
(40) Chaudhari, K.; Xavier, P. L.; Pradeep, T. Understanding the Evolution of Luminescent Gold Quantum Clusters in Protein Templates. *ACS Nano* **2011**, *5*, 8816−8827.

(41) Baksi, A.; Xavier, P. L.; Chaudhari, K.; Goswami, N.; Pal, S. K.; Pradeep, T. Protein-Encapsulated Gold Cluster Aggregates: The Case of Lysozyme. *Nanoscale* **2013**, *5*, 2009−2016.
(42) Anand, U.; Ghosh, S.; Mukherjee, S. Toggling Between Blue- and Red-Emitting Fluorescent Silver Nanoclusters. *J. Phys. Chem. Lett.* **2012**, *3*, 3605−3609.
(43) Brust, M.; Walker, M.; Bethell, D.; Schiffrin, D. J.; Whyman, R. Synthesis of Thiol-Derivatised Gold Nanoparticles in a Two-Phase Liquid−Liquid System. *J. Chem. Soc., Chem. Commun.* **1994**, 801−802.
(44) Alvarez, M. M.; Khoury, J. T.; Schaaff, T. G.; Shafigullin, M. N.; Vezmar, I.; Whetten, R. L. Optical Absorption Spectra of Nanocrystal Gold Molecules. *J. Phys. Chem. B* **1997**, *101*, 3706−3712.
(45) Dolamic, I.; Knoppe, S.; Dass, A.; Bürgi, T. First Enantioseparation and Circular Dichroism Spectra of Au_{38} Clusters Protected by Achiral Ligands. *Nat. Commun.* **2012**, *3*, 798.
(46) Philip, R.; Chantharasupawong, P.; Qian, H.; Jin, R.; Thomas, J. Evolution of Nonlinear Optical Properties: From Gold Atomic Clusters to Plasmonic Nanocrystals. *Nano Lett.* **2012**, *12*, 4661−4667.
(47) Lu, Y.; Chen, W. Sub-Nanometre Sized Metal Clusters: From Synthetic Challenges to the Unique Property Discoveries. *Chem. Soc. Rev.* **2012**, *41*, 3594−3623.
(48) Hakkinen, H. The Gold−Sulfur Interface at the Nanoscale. *Nat. Chem.* **2012**, *4*, 443−455.
(49) Ghosh, A.; Udayabhaskararao, T.; Pradeep, T. One-Step Route to Luminescent $Au_{18}SG_{14}$ in the Condensed Phase and Its Closed Shell Molecular Ions in the Gas Phase. *J. Phys. Chem. Lett.* **2012**, *3*, 1997−2002.
(50) Wu, Z.; MacDonald, M. A.; Chen, J.; Zhang, P.; Jin, R. Kinetic Control and Thermodynamic Selection in the Synthesis of Atomically Precise Gold Nanoclusters. *J. Am. Chem. Soc.* **2011**, *133*, 9670−9673.
(51) Yu, Y.; Luo, Z.; Yu, Y.; Lee, J. Y.; Xie, J. Observation of Cluster Size Growth in CO-Directed Synthesis of $Au_{25}(SR)_{18}$ Nanoclusters. *ACS Nano* **2012**, *6*, 7920−7927.
(52) Zhu, M.; Lanni, E.; Garg, N.; Bier, M. E.; Jin, R. Kinetically Controlled, High-Yield Synthesis of Au_{25} Clusters. *J. Am. Chem. Soc.* **2008**, *130*, 1138−1139.
(53) Branham, M. R.; Douglas, A. D.; Mills, A. J.; Tracy, J. B.; White, P. S.; Murray, R. W. Arylthiolate-Protected Silver Quantum Dots. *Langmuir* **2006**, *22*, 11376−11383.
(54) Collier, C. P.; Saykally, R. J.; Shiang, J. J.; Henrichs, S. E.; Heath, J. R. Reversible Tuning of Silver Quantum Dot Monolayers Through the Metal−Insulator Transition. *Science* **1997**, *277*, 1978−1981.
(55) Nishida, N.; Yao, H.; Ueda, T.; Sasaki, A.; Kimura, K. Synthesis and Chiroptical Study of D/L-Penicillamine-Capped Silver Nanoclusters. *Chem. Mater.* **2007**, *19*, 2831−2841.
(56) Udayabhaskararao, T.; Pradeep, T. Luminescent Ag_7 and Ag_8 Clusters by Interfacial Synthesis. *Angew. Chem., Int. Ed.* **2010**, *49*, 3925−3929.
(57) Udayabhaskararao, T.; Nataraju, B.; Pradeep, T. Ag_9 Quantum Cluster through a Solid-State Route. *J. Am. Chem. Soc.* **2010**, *132*, 16304−16307.
(58) Chakraborty, I.; Udayabhaskararao, T.; Pradeep, T. Luminescent Sub-Nanometer Clusters for Metal Ion Sensing: A New Direction in Nanosensors. *J. Hazard. Mater.* **2012**, *211−212*, 396−403.
(59) Yuan, X.; Luo, Z.; Zhang, Q.; Zhang, X.; Zheng, Y.; Lee, J. Y.; Xie, J. Synthesis of Highly Fluorescent Metal (Ag, Au, Pt, and Cu) Nanoclusters by Electrostatically Induced Reversible Phase Transfer. *ACS Nano* **2011**, *5*, 8800−8808.
(60) Negishi, Y.; Arai, R.; Niihori, Y.; Tsukuda, T. Isolation and Structural Characterization of Magic Silver Clusters Protected by 4-(tert-Butyl)benzyl Mercaptan. *Chem. Commun.* **2011**, *47*, 5693−5695.
(61) Dhanalakshmi, L.; Udayabhaskararao, T.; Pradeep, T. Conversion of Double Layer Charge-Stabilized Ag@Citrate Colloids to Thiol Passivated Luminescent Quantum Clusters. *Chem. Commun.* **2012**, *48*, 859−861.
(62) Chakraborty, I.; Udayabhaskararao, T.; Pradeep, T. High Temperature Nucleation and Growth of Glutathione Protected Ag_{75} Clusters. *Chem. Commun.* **2012**, *48*, 6788−6790.
(63) Cathcart, N.; Kitaev, V. Silver Nanoclusters: Single-Stage Scaleable Synthesis of Monodisperse Species and Their Chirooptical Properties. *J. Phys. Chem. C* **2010**, *114*, 16010−16017.
(64) Bakr, O. M.; Amendola, V.; Aikens, C. M.; Wenseleers, W.; Li, R.; Dal Negro, L.; Schatz, G. C.; Stellacci, F. Silver Nanoparticles with Broad Multiband Linear Optical Absorption. *Angew. Chem., Int. Ed.* **2009**, *48*, 5921−5926.
(65) Cathcart, N.; Mistry, P.; Makra, C.; Pietrobon, B.; Coombs, N.; Jelokhani-Niaraki, M.; Kitaev, V. Chiral Thiol-Stabilized Silver Nanoclusters with Well-Resolved Optical Transitions Synthesized by a Facile Etching Procedure in Aqueous Solutions. *Langmuir* **2009**, *25*, 5840−5846.
(66) Farrag, M.; Thämer, M.; Tschurl, M.; Bürgi, T.; Heiz, U. Preparation and Spectroscopic Properties of Monolayer-Protected Silver Nanoclusters. *J. Phys. Chem. C* **2012**, *116*, 8034−8043.
(67) Rao, C. N. R.; Kalyanikutty, K. P. The Liquid−Liquid Interface as a Medium to Generate Nanocrystalline Films of Inorganic Materials. *Acc. Chem. Res.* **2008**, *41*, 489−499.
(68) Mrudula, K. V.; Udayabhaskararao, T.; Pradeep, T. Interfacial Synthesis of Luminescent 7 kDa Silver Clusters. *J. Mater. Chem.* **2009**, *19*, 4335−4342.
(69) Chakraborty, I.; Govindarajan, A.; Erusappan, J.; Ghosh, A.; Pradeep, T.; Yoon, B.; Whetten, R. L.; Landman, U. The Superstable 25 kDa Monolayer Protected Silver Nanoparticle: Measurements and Interpretation as an Icosahedral $Ag_{152}(SCH_2CH_2Ph)_{60}$ Cluster. *Nano Lett.* **2012**, *12*, 5861−5866.
(70) Sugi, K. S.; Chakraborty, I.; Udayabhaskararao, T.; Jyoti Sarita, M.; Pradeep, T. Evolution of Atomically Precise Silver Clusters to Superlattice Crystals. *Part. Part. Syst. Charact.* **2013**, *30*, 241−243.
(71) Wu, Z.; Lanni, E.; Chen, W.; Bier, M. E.; Ly, D.; Jin, R. High Yield, Large Scale Synthesis of Thiolate-Protected Ag_7 Clusters. *J. Am. Chem. Soc.* **2009**, *131*, 16672−16674.
(72) Lu, Y.; Chen, W. Size Effect of Silver Nanoclusters on Their Catalytic Activity for Oxygen Electro-reduction. *J. Power Sources* **2012**, *197*, 107−110.
(73) Xiang, H.; Wei, S.-H.; Gong, X. Structures of $[Ag_7(SR)_4]^-$ and $[Ag_7(DMSA)_4]^-$. *J. Am. Chem. Soc.* **2010**, *132*, 7355−7360.
(74) Wu, Z.; Jiang, D.-e.; Lanni, E.; Bier, M. E.; Jin, R. Sequential Observation of $Ag_nS_4^-$ $(1 \le n \le 7)$ Gas Phase Clusters in MS/MS and Prediction of Their Structures. *J. Phys. Chem. Lett.* **2010**, *1*, 1423−1427.
(75) Leelavathi, A.; Udayabhaskararao, T.; Pradeep, T. Supported Quantum Clusters of Silver As Enhanced Catalysts for Reduction. *Nanoscale Res. Lett.* **2011**, *6*, 123.
(76) Bootharaju, M. S.; Pradeep, T. Investigation into the Reactivity of Unsupported and Supported Ag_7 and Ag_8 Clusters with Toxic Metal Ions. *Langmuir* **2011**, *27*, 8134−8143.
(77) Sun, Y.; Balasubramanian, K.; Udayabhaskararao, T.; Pradeep, T. First Principles Studies of Two Luminescent Molecular Quantum Clusters of Silver, $Ag_7(H_2MSA)_7$ and $Ag_8(H_2MSA)_8$, Based on Experimental Fluorescence Spectra. *J. Phys. Chem. C* **2011**, *115*, 20380−20387.
(78) Chen, W.-T.; Hsu, Y.-J.; Kamat, P. V. Realizing Visible Photoactivity of Metal Nanoparticles: Excited-State Behavior and Electron-Transfer Properties of Silver (Ag_8) Clusters. *J. Phys. Chem. Lett.* **2012**, *3*, 2493−2499.
(79) Bootharaju, M. S.; Deepesh, G. K.; Udayabhaskararao, T.; Pradeep, T. Atomically Precise Silver Clusters for Efficient Chlorocarbon Degradation. *J. Mater. Chem. A* **2013**, *1*, 611−620.
(80) Harkness, K. M.; Tang, Y.; Dass, A.; Pan, J.; Kothalawala, N.; Reddy, V. J.; Cliffel, D. E.; Demeler, B.; Stellacci, F.; Bakr, O. M.; McLean, J. A. $Ag_{44}(SR)_{30}^{4-}$: A Silver−Thiolate Superatom Complex. *Nanoscale* **2012**, *4*, 4269−4274.
(81) Kumar, S.; Bolan, M. D.; Bigioni, T. P. Glutathione-Stabilized Magic-Number Silver Cluster Compounds. *J. Am. Chem. Soc.* **2010**, *132*, 13141−13143.
(82) Guo, J.; Kumar, S.; Bolan, M.; Desireddy, A.; Bigioni, T. P.; Griffith, W. P. Mass Spectrometric Identification of Silver Nanoparticles: The Case of $Ag_{32}(SG)_{19}$. *Anal. Chem.* **2012**, *84*, 5304−5308.

(83) Chandrasekar, A.; Pradeep, T. Luminescent Silver Clusters with Covalent Functionalization of Graphene. *J. Phys. Chem. C* **2012**, *116*, 14057−14061.
(84) Remya, K. P.; Udayabhaskararao, T.; Pradeep, T. Low-Temperature Thermal Dissociation of Ag Quantum Clusters in Solution and Formation of Monodisperse Ag_2S Nanoparticles. *J. Phys. Chem. C* **2012**, *116*, 26019−26026.
(85) Yuan, X.; Tay, Y.; Dou, X.; Luo, Z.; Leong, D. T.; Xie, J. Glutathione-Protected Silver Nanoclusters as Cysteine-Selective Fluorometric and Colorimetric Probe. *Anal. Chem.* **2013**, *85*, 1913−1919.
(86) Wang, C.; Xu, L.; Wang, Y.; Zhang, D.; Shi, X.; Dong, F.; Yu, K.; Lin, Q.; Yang, B. Fluorescent Silver Nanoclusters as Effective Probes for Highly Selective Detection of Mercury(II) at Parts-per-Billion Levels. *Chem.—Asian J.* **2012**, *7*, 1652−1656.
(87) Singh, A. K.; Kanchanapally, R.; Fan, Z.; Senapati, D.; Ray, P. C. Synthesis of Highly Fluorescent Water-Soluble Silver Nanoparticles for Selective Detection of Pb(II) at the Parts per Quadrillion (PPQ) Level. *Chem. Commun.* **2012**, *48*, 9047−9049.
(88) Adhikari, B.; Banerjee, A. Facile Synthesis of Water-Soluble Fluorescent Silver Nanoclusters and Hg(II) Sensing. *Chem. Mater.* **2010**, *22*, 4364−4371.
(89) Muhammed, M. A. H.; Aldeek, F.; Palui, G.; Trapiella-Alfonso, L.; Mattoussi, H. Growth of In Situ Functionalized Luminescent Silver Nanoclusters by Direct Reduction and Size Focusing. *ACS Nano* **2012**, *6*, 8950−8961.
(90) Redón, R.; Ramírez-Crescencio, F.; Fernández-Osorio, A. L. Solventless Synthesis of Iridium(0) Nanoparticles. *J. Nanopart. Res.* **2011**, *13*, 5959−5965.
(91) Mathew, A.; Sajanlal, P. R.; Pradeep, T. Selective Visual Detection of TNT at the Sub-Zeptomole Level. *Angew. Chem., Int. Ed.* **2012**, *51*, 9596−9600.
(92) Pei, Y.; Zeng, X. C. Investigating the Structural Evolution of Thiolate Protected Gold Clusters from First-Principles. *Nanoscale* **2012**, *4*, 4054−4072.
(93) Kurashige, W.; Yamaguchi, M.; Nobusada, K.; Negishi, Y. Ligand-Induced Stability of Gold Nanoclusters: Thiolate versus Selenolate. *J. Phys. Chem. Lett.* **2012**, *3*, 2649−2652.
(94) Negishi, Y.; Igarashi, K.; Munakata, K.; Ohgake, W.; Nobusada, K. Palladium Doping of Magic Gold Cluster $Au_{38}(SC_2H_4Ph)_{24}$: Formation of $Pd_2Au_{36}(SC_2H_4Ph)_{24}$ with Higher Stability than $Au_{38}(SC_2H_4Ph)_{24}$. *Chem. Commun.* **2012**, *48*, 660−662.
(95) Yang, H.; Lei, J.; Wu, B.; Wang, Y.; Zhou, M.; Xia, A.; Zheng, L.; Zheng, N. Crystal Structure of a Luminescent Thiolated Ag Nanocluster with an Octahedral Ag_6^{4+} Core. *Chem. Commun.* **2013**, *49*, 300−302.
(96) Yang, H.; Wang, Y.; Zheng, N. Stabilizing Subnanometer Ag(0) Nanoclusters by Thiolate and Diphosphine Ligands and Their Crystal Structures. *Nanoscale* **2013**, *5*, 2674−2677.
(97) Ferrando, R.; Jellinek, J.; Johnston, R. L. Nanoalloys: From Theory to Applications of Alloy Clusters and Nanoparticles. *Chem. Rev.* **2008**, *108*, 845−910.
(98) Teo, B. K.; Keating, K.; Kao, Y. H. Observation of Plasmon Frequency in the Optical Spectrum of $Au_{18}Ag_{20}$ Cluster: The Beginning of the Collective Phenomenon Characteristics of the Bulk? *J. Am. Chem. Soc.* **1987**, *109*, 3494−3495.
(99) Teo, B. K.; Shi, X.; Zhang, H. Cluster of Clusters. Structure of a Novel Gold−Silver Cluster $[(Ph_3P)_{10}Au_{13}Ag_{12}Br_8](SbF_6)$ Containing an Exact Staggered-Eclipsed-Staggered Metal Configuration. Evidence of Icosahedral Units As Building Blocks. *J. Am. Chem. Soc.* **1991**, *113*, 4329−4331.
(100) Negishi, Y.; Iwai, T.; Ide, M. Continuous Modulation of Electronic Structure of Stable Thiolate-Protected Au_{25} Cluster by Ag Doping. *Chem. Commun.* **2010**, *46*, 4713−4715.
(101) Kumara, C.; Dass, A. $(AuAg)_{144}(SR)_{60}$ Alloy Nanomolecules. *Nanoscale* **2011**, *3*, 3064−3067.
(102) Kumara, C.; Dass, A. AuAg Alloy Nanomolecules with 38 Metal Atoms. *Nanoscale* **2012**, *4*, 4084−4086.
(103) Malola, S.; Häkkinen, H. Electronic Structure and Bonding of Icosahedral Core−Shell Gold−Silver Nanoalloy Clusters $Au_{144-x}Ag_x(SR)_{60}$. *J. Phys. Chem. Lett.* **2011**, *2*, 2316−2321.
(104) Koivisto, J.; Malola, S.; Kumara, C.; Dass, A.; Häkkinen, H.; Pettersson, M. Experimental and Theoretical Determination of the Optical Gap of the $Au_{144}(SC_2H_4Ph)_{60}$ Cluster and the $(Au/Ag)_{144}(SC_2H_4Ph)_{60}$ Nanoalloys. *J. Phys. Chem. Lett.* **2012**, *3*, 3076−3080.
(105) Guidez, E. B.; Mäkinen, V.; Häkkinen, H.; Aikens, C. M. Effects of Silver Doping on the Geometric and Electronic Structure and Optical Absorption Spectra of the $Au_{25-n}Ag_n(SH)_{18}^-$ (n = 1, 2, 4, 6, 8, 10, 12) Bimetallic Nanoclusters. *J. Phys. Chem. C* **2012**, *116*, 20617−20624.
(106) Liu, H.; Zhang, X.; Wu, X.; Jiang, L.; Burda, C.; Zhu, J.-J. Rapid Sonochemical Synthesis of Highly Luminescent Non-toxic AuNCs and Au@AgNCs and Cu (II) Sensing. *Chem. Commun.* **2011**, *47*, 4237−4239.
(107) Mohanty, J. S.; Xavier, P. L.; Chaudhari, K.; Bootharaju, M. S.; Goswami, N.; Pal, S. K.; Pradeep, T. Luminescent, Bimetallic AuAg Alloy Quantum Clusters in Protein Templates. *Nanoscale* **2012**, *4*, 4255−4262.
(108) Huang, T.; Murray, R. W. Luminescence of Tiopronin Monolayer-Protected Silver Clusters Changes to That of Gold Clusters upon Galvanic Core Metal Exchange. *J. Phys. Chem. B* **2003**, *107*, 7434−7440.
(109) Udayabhaskararao, T.; Sun, Y.; Goswami, N.; Pal, S. K.; Balasubramanian, K.; Pradeep, T. Ag_7Au_6: A 13-Atom Alloy Quantum Cluster. *Angew. Chem., Int. Ed.* **2012**, *51*, 2155−2159.
(110) Fields-Zinna, C. A.; Sampson, J. S.; Crowe, M. C.; Tracy, J. B.; Parker, J. F.; deNey, A. M.; Muddiman, D. C.; Murray, R. W. Tandem Mass Spectrometry of Thiolate-Protected Au Nanoparticles $Na_xAu_{25}(SC_2H_4Ph)_{18-y}(S(C_2H_4O)_5CH_3)_y$. *J. Am. Chem. Soc.* **2009**, *131*, 13844−13851.

THE JOURNAL OF PHYSICAL CHEMISTRY C

Article

pubs.acs.org/JPCC

Distinguishing Amorphous and Crystalline Ice by Ultralow Energy Collisions of Reactive Ions

Soumabha Bag, Radha Gobinda Bhuin, and T. Pradeep*

DST Unit of Nanoscience (DST UNS), Department of Chemistry, Indian Institute of Technology Madras, Chennai-600036, India

Supporting Information

ABSTRACT: Ion scattering using ultralow energy projectiles is considered to be a unique method to probe the nature of molecular surfaces because of its capacity to probe the very top, atomically thin layers. Here, we examine one of the most studied molecular solids, water-ice, using this technique. When ice surface undergoes the amorphous to crystalline transition, an ultralow energy reactive projectile identifies the change through the reaction product formed. It is shown that ultralow energy (2, 3, 4, 5, 6, and 7 eV) CH_2^+ (or CD_2^+) collision on amorphous D_2O (or H_2O) ice makes CHD^+, while crystalline ice does not. The projectile undergoes H/D exchange with the dangling −OD (−OH) bond present on amorphous ice surfaces. It is also shown that H/D exchange product disappears when amorphous ice is annealed to the crystalline phase. The H/D exchange reaction is shown to be sensitive only to the surface layers of ice as it disappears when the surface is covered with long chain alcohols like 1-pentanol as the ice surfaces become inaccessible for the incoming projectile. This article shows that ultralow energy reactive ion collision is a novel method to distinguish phase transitions in molecular solids.

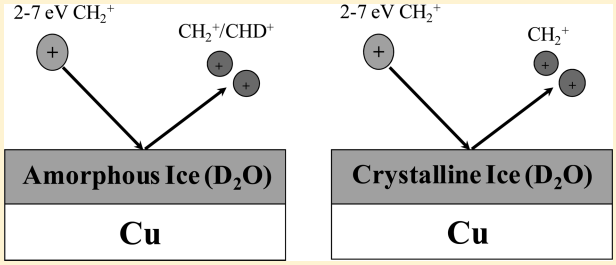

INTRODUCTION

Deposition of water vapor on cold surfaces creates two distinctly different forms of ice, amorphous and crystalline analogues where the former has more than one variety.[1,2] Distinction of these forms is important to conduct model studies as both the amorphous and the crystalline forms have unique chemical and physical properties. Since its first report in 1935, there have been numerous studies on the amorphous form of water.[3−5] While distinction of amorphous solid water (ASW) and crystalline water (CW) is possible by X-ray diffraction,[3] the most common tool for differentiation is infrared spectroscopy.[5−18] Structural differentiation is possible by other methods such as TPD,[13,19] LEED,[20] electron diffraction,[21] and TEM.[11] However, this differentiation must be made at the very top layer as it is the one that accommodates gaseous species of atmospheric relevance. Various ion scattering processes are used to understand molecular solids, in general,[22] and water ice, in particular, and these methods are summarized elsewhere.[23,24]

Low energy ion scattering is a unique tool for surface characterization, especially for molecular surfaces. Reactive collisions can distinguish adsorption geometry as well as the molecular nature of the collision partner. Ions at extremely low energy, of the order of few tens of electronvolt or less, are sensitive to the very top of molecular films,[25] especially the first chemical bond at the vacuum−surface interface. The ion scattering yield varies with the nature of the surfaces, and surface structure differentiation is possible from scattering yield measurements.[26] Such changes are due to the difference in the extent of neutralization, trapping, and accommodation. However, reactive collision in which the scattered ion undergoes chemical transformation by abstraction,[27] exchange,[28] or dissociation[29−33] can also be characteristic of the structure of the surface. When the ion energy is low, of the order of a few electronvolt, this collision event is extremely surface sensitive to the very first chemical bond of the air/vacuum−surface interface and therefore can distinguish structure, specific to the top layers.[25] Ion/surface collisions in the low energy regime need not always be reactive, and such processes have been used to characterize molecular diffusion,[34] nature of surface species,[35] and surface transformations.[36] For example, we have found a new surface transformation at ∼110 K for ASW, and this transformation is noticeable in a film of six or more monolayers of ice. While scattering events have been shown to be sensitive to the nature of the surface (amorphous/crystalline), there has been no report of distinguishing them by reactions.

In this work, we show that exchange reactions of specific ions can distinguish amorphous and crystalline ice. Such reactions occurring under 10 eV are specific to the first chemical bond, and therefore the information derived is unique in comparison to other techniques described earlier. Variation of reactive ions, easily achievable in mass spectrometry, can be used for such structural distinction for other ice. As ion doses are low in this static experiment, the properties of the surfaces can be retained even after prolonged periods of irradiation.[37−40]

Received: February 15, 2013
Revised: May 11, 2013
Published: May 20, 2013

   dx.doi.org/10.1021/jp4016432 | J. Phys. Chem. C 2013, 117, 12146−12152

EXPERIMENTAL SECTION

The instrumental setup and an outline of the experimental procedures are given elsewhere.[34,35] The low energy collision experiments and the precautions used were described earlier.[36] Briefly, the experiments described here were conducted in a double-chamber ultrahigh vacuum (UHV) system with a base pressure of $<5.0 \times 10^{-10}$ mbar. Each region of the system is pumped by a Pfeiffer Vacuum (TMU 261) 210 L/s turbomolecular drag pump. These two pumps are backed by another Pfeiffer Vacuum (TMU 071P) 60 L/s turbomolecular pump, which is further backed by a Pfeiffer Vacuum (MVP 055) 3.3 m^3/h dry pump. The electron impact (EI) source from ABB Extrel was used to generate positive ions. These ions are extracted from the source and transferred into a quadrupole mass filter (Q1) through a set of einzel lenses. Ion kinetic energy was controlled by varying the ion source conditions and tuning the rest of the optics. The scattered ions are detected by another quadrupole (Q3). All of the quadrupoles and control electronics are from Extrel Core Mass Spectrometry.

A high-precision UHV specimen translator with *xyz* axis movement and tilt was used. Polycrystalline copper was used as in previous experiments as the substrate for preparing amorphous and crystalline ice films.[27,41] Substrate plays a crucial role in determining the quality of the grown film. Yet, in the present case, the substrate effect is negligible due to higher coverages used. It may be noted that the dewetting temperature is much higher (~160 K) for 50 monolayer (ML) ice films.[42] The ice film grown at 120 K in ultrahigh vacuum is known to be amorphous in nature and of low porosity, while deposition above 140 K results in crystalline ice (CW).[43] The ice surface is prepared by exposing the cold substrate to water vapor at a specific pressure as described below.

The copper surface was grounded in all of the experiments. By varying the potential of the ion source block and tuning the rest of the ion optics, it was possible to produce a beam current of 1−2 nA for the mass selected ions. Various ions collide with the surface at an angle of 45° with reference to the surface normal, and the scattered ions were analyzed by a second quadrupole. The ions in the entire scattering region feel the same potential, and the einzel lenses on either side of the target surface are nearly at the same potential. Thus, the ions are subjected to a field free condition around the scattering center. Scattering geometry is such that ions do not make a glancing impact. The ion kinetic energy spread is largest at 1 eV, but reduces significantly at higher energies.

Required projectiles were generated by ionizing CH_4 (or CD_4 to produce CD_3^+ and CD_2^+) by electron impact and subsequently selecting the desired ions through quadrupole mass analyzer. CD_4 was purchased from Aldrich. The liquids used in our study (H_2O, deionized water after triple distillation, D_2O, and 1-pentanol) were purified by many freeze−pump−thaw cycles, before use. D_2O (99.96% D isotopic purity) and 1-pentanol were purchased from Aldrich. Molecular surfaces were prepared by depositing the corresponding vapors and were delivered very close to the substrate through a tube. The exposure was controlled by a leak valve. The gas-line was pumped thoroughly by a rotary pump to avoid impurities and contamination. The distance between the gas delivery tube and polycrystalline copper substrate was adjusted to obtain uniform sample growth on the substrate. This was confirmed by our previous experiments. When *n*-butanol (A) was deposited on water ice (B), water molecules could not diffuse through *n*-butanol layers at 120 and 140 K and get detected.[44] This observation confirms that the entire area under investigation had uniform growth of A over B. Nonuniform coverages would have made B to get detected. Delivery of molecules near the substrate ensured that the vapors were not deposited in unwanted areas. The deposition flux of the vapors was adjusted to ~0.1 ML/s. The thickness of the overlayers was estimated assuming that 1.33×10^{-6} mbar/s = 1 ML. The 1 ML ice layers have been estimated to contain $\sim 1.1 \times 10^{15}$ water molecules/cm^2.[45] In all of our experiments with ASW, the deposition temperature was kept at 120 K, which is known to grow ASW films.[46] The pressure(s) of the gas(es) inside the scattering chamber during deposition was 1×10^{-7} mbar. The films were prepared on polycrystalline Cu substrate to make Cu@A (the symbolism implies the creation of a layer of A over Cu). The film thickness was large so that the underlying Cu did not have any effect on the ice layer formed. The spectra presented here were averaged for 75 scans, and the data acquisition time was approximately 0.5 s per scan. The present instrumental setup does not allow temperature programmed desorption (TPD) measurements.

RESULTS

To check the distribution of ion kinetic energy (K.E.) of the input beam, stopping potential measurement was performed at Q1. In this measurement, Q1 was kept in the RF (radio frequency)-only mode where it transmits all ions formed in the source, and Q3 was set to transmit the desired mass. Thereafter, a range of DC voltages are applied across the quadrupoles to stop the desired ions. When the ions are stopped at Q1, for example, the intensity of the ions falls to zero. Figure 1 shows the results of stopping potential

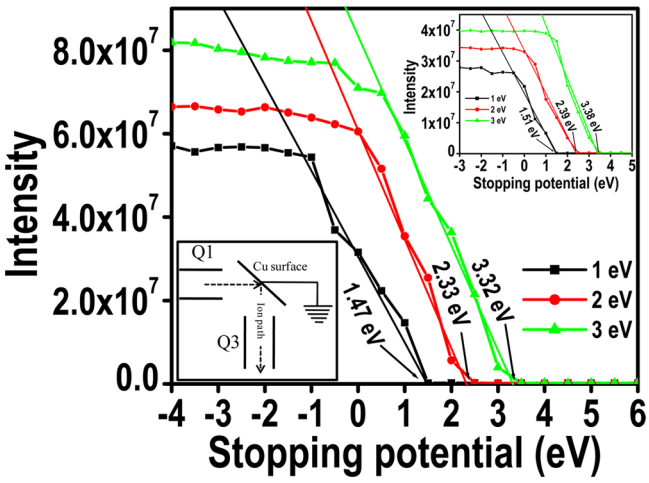

Figure 1. Plot of CH_2^+ stopping potential data at quadrupole 1 (Q1). Results of a similar kind of stopping potential measurement performed with quadrupole 3 (Q3) are shown in the inset. The experimental scheme is shown at the bottom left.

measurements of 1, 2, and 3 eV CH_2^+ ions. It is evident from the figure that for 1 eV ion, the energy spread is 47%, which reduces substantially (10%) in the case of 3 eV ions. With further increase in the input ion kinetic energy up to 8 eV, the spread decreases to 2% (data not shown). It is important to note that this kind of ion energy spread is the best that has been achieved so far in such instrumentation.[23] Increased spread at extremely low energy (1 eV) has been noted before.[36] Stopping

dx.doi.org/10.1021/jp4016432 | J. Phys. Chem. C 2013, 117, 12146−12152

potential measurement in Q3 using CH_2^+ (Q1 was set to select the desired ion and Q3 was kept as RF-only mode) showed little increase in energy spread in comparison to the stopping potential data of Q1. Similar stopping potential experiment using CH_3^+ and CH_4^+ revealed that other ions also followed a similar trend (Supporting Information, item numbers 1 and 2). The exchange experiment can be done with other ions too, but with CH_3^+ being a closed shell ion, exchange is not facile. In the case of CH^+, primary ion beam intensity was too low for low energy ion scattering experiments.

Having established the ion kinetic energy distribution, we performed ion scattering experiments to distinguish the nature of the surfaces. In Figure 2a, 2 eV CH_2^+ ion scattering spectrum

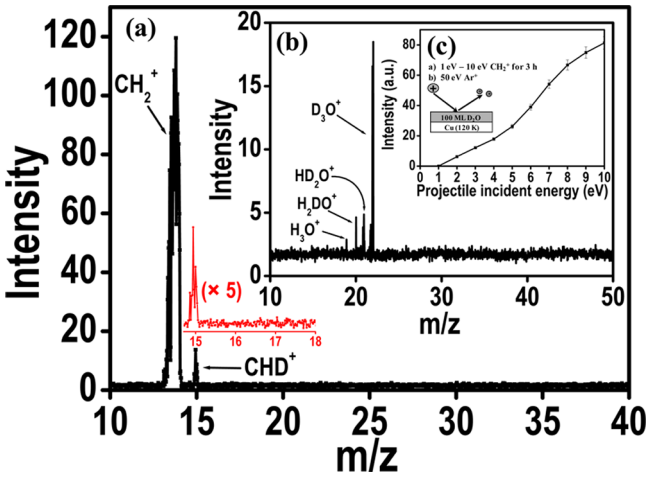

Figure 2. (a) Ion scattering mass spectrum of 2 eV CH_2^+ collision on amorphous D_2O at 120 K. The CHD^+ signal at m/z 15 is also shown separately in red with 5 times intensity enhancement. (b) Chemical sputtering spectra upon 50 eV Ar^+ impact on D_2O surfaces, irradiated with 1−10 eV CH_2^+ for 3 h. (c) The CHD^+ signal intensity with respect to increasing incident energy of CH_2^+. The experimental scheme is shown as an inset.

of D_2O prepared at 120 K is shown where m/z 14 is due to CH_2^+, the incident projectile, while the new peak at m/z 15 is assigned to CHD^+, the H/D exchange product. We have ensured that it is not due to CH_3^+ by conducting CD_2^+ collisions on H_2O (to be discussed later). Scattering experiments using other energy projectiles were also performed. After these experiments, chemical sputtering[47−49] experiments were performed using 50 eV Ar^+. The result is shown in Figure 2b. Peaks at m/z 19, 20, 21, and 22 are assigned to H_3O^+, H_2DO^+, HD_2O^+, and D_3O^+, respectively. This spectrum indicates that all of the H/D exchange products remain present on the surfaces. It may be noted that no such exchange products were seen on the parent D_2O ice surfaces. It also explains that H/D exchange has taken place due to the collision of CH_2^+ with amorphous ice (D_2O). Additionally, Figure 2c presents the normalized intensity plot of CHD^+ signal with respect to increasing CH_2^+ incident energy. This spectrum shows the formation of more CHD^+ as the kinetic energy of CH_2^+ increases.

In the next set of experiments, CH_2^+ was subjected to collisions on crystalline ice (D_2O), generated at 140 K (this temperature was chosen because it is known to give crystalline ice[46,50]). The results of those experiments are shown in Figure 3. It is evident from the figure that CHD^+ signals are absent. However, in this case, also H/D exchange takes place when

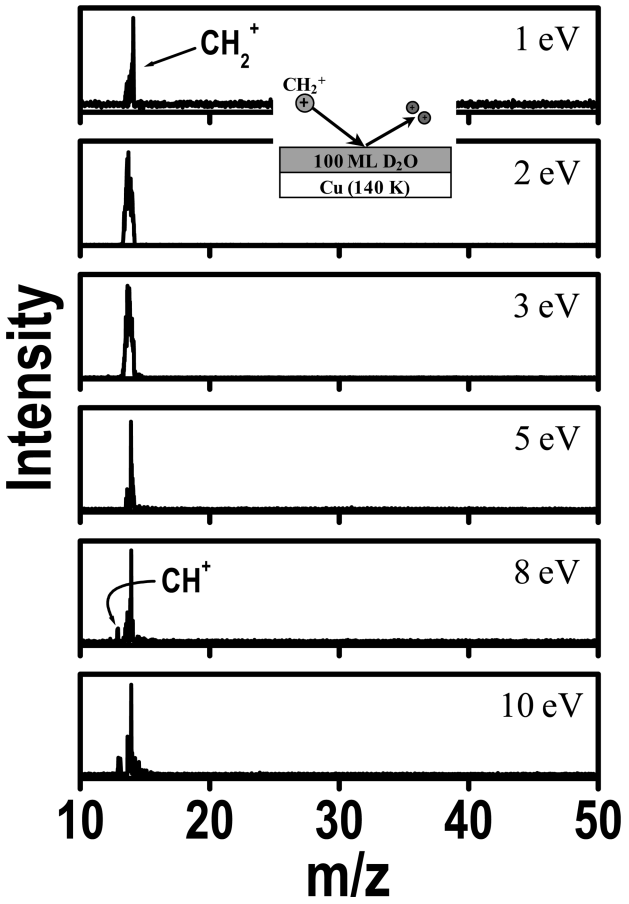

Figure 3. Mass spectra observed upon collisions of varying energy CH_2^+ on 100 ML crystalline ice (D_2O), generated at 140 K.

CH_2^+ ion energy is raised to ∼8 eV. At this energy, fragmentation of CH_2^+ occurs, and fragments, such as CH^+, are believed to react at the surfaces. For further understanding, the CH_2^+ projectiles were replaced with CD_2^+ and were subjected to collide on amorphous ice (generated upon condensing H_2O vapor at 120 K). The exchange product, CHD^+, was observed here also. Subsequently, chemical sputtering experiments were performed on the reacted surfaces. The results are shown in Figure 4. All of the possible H/D exchange products appeared in the sputtering spectrum. When the CHD^+ signal intensity was plotted with increasing CD_2^+ kinetic energy (inset of Figure 4), it showed a shape similar to that of CHD^+ (upon CH_2^+ collision with increasing kinetic energy, Figure 2c). These results confirm that H/D exchange occurs on amorphous ice by ultralow energy reactive projectiles like CH_2^+/CD_2^+ (on D_2O/H_2O).

To understand the difference in reactivity of CH_2^+ on amorphous and crystalline ice, a control experiment was performed at a lower projectile ion flux than the previous experiments (so as to avoid ion-induced surface damage, although insignificant at this energy range). At first, ultralow energy CH_2^+ was subjected to collide on amorphous ice (D_2O), and then the ice layer was annealed at 140 K to make it crystalline. Figure 5 shows the results of an ultralow energy ion scattering experiment performed on amorphous ice. As is evident in the spectra, the H/D exchange is observable by the appearance of CHD^+ signal at 2 eV. At higher energy (8 eV and above) surface-induced dissociation of the projectile led to the generation of various other signals. This experiment was carried

dx.doi.org/10.1021/jp4016432 | J. Phys. Chem. C 2013, 117, 12146−12152

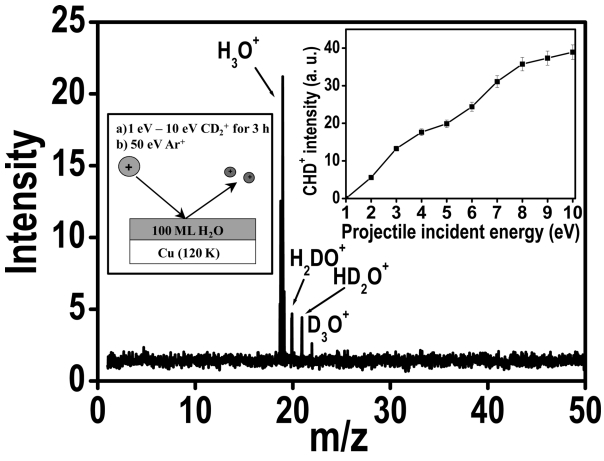

Figure 4. Chemical sputtering spectra observed with 50 eV Ar^+ on reacted amorphous ice (H_2O) formed after impact of 1−10 eV CD_2^+ for 3 h. CHD^+ signal intensity with increasing energy CD_2^+ is shown in one inset. Schematic presentation of the experiments is shown in another inset.

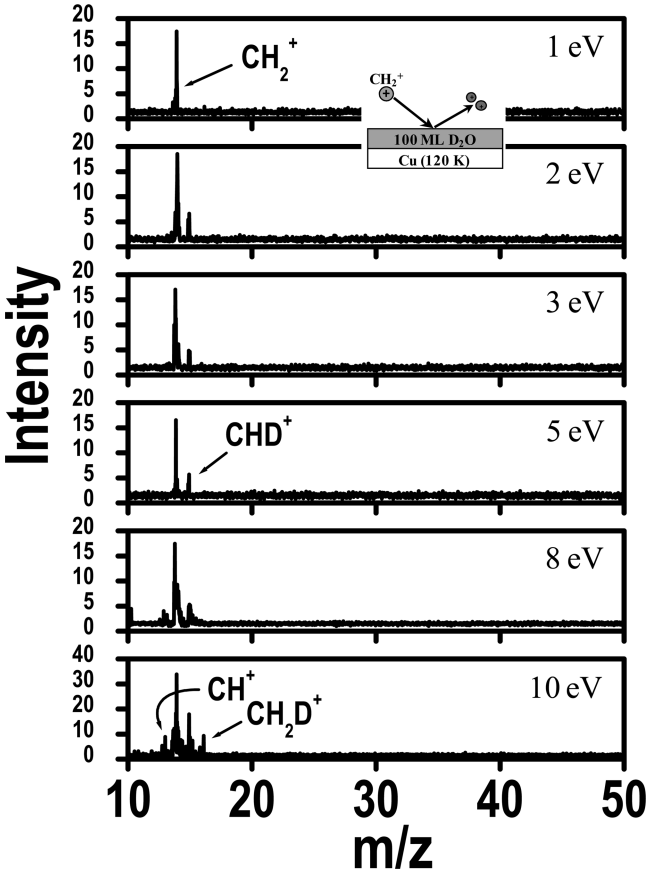

Figure 5. Ion scattering spectra observed upon collision of 1, 2, 3, 5, 8, and 10 eV CH_2^+ on amorphous ice (D_2O). Schematic presentation of the experiment is shown in the inset.

out again by annealing the underlying ASW to CW. After that, when the same experiment was carried out at the same energy window on CW, no H/D exchange was found below 8 eV energy (see Supporting Information, item number 4). The reason is believed to be the chemical reactivity difference between amorphous and crystalline ice surfaces with the incoming projectile. The presence of free hydroxyl bonds on ASW makes the H/D exchange possible with CH_2^+, and, consequently, the product CHD^+ appears. However, there may be other effects also that contribute to the chemical reactivity of the two surfaces (see below). No observable H/D exchange take place upon collision of CH_2^+ on crystalline ice surfaces. However, at a collision energy 8 eV and above, the reactive projectile starts breaking down on the surface of ice, and it generates fragmented products, which can make additional reactions. So, reactive collision at this energy region is not suitable to distinguish ASW and CW. To confirm the process of formation of CHD^+, 50 ML amorphous ice (D_2O) surface was covered with 200 ML 1-pentanol. After that, ultralow energy CH_2^+ was collided on it. Supporting Information item number 5 shows the scattered ion mass spectra observed upon collision of 1, 2, 3, 5, 8, 10 eV CH_2^+ on the condensed 1-pentanol overlayer. It is evident from the spectra that the H/D exchange product CHD^+ is absent. After the ultralow energy collision of CH_2^+, chemical sputtering experiment was performed using 50 eV Ar^+. The inset of Supporting Information item number 5 shows the resultant mass spectrum. The spectra resemble normal chemical sputtering spectra of 1-pentanol. The observation can be explained based on the following results. On 200 ML 1-pentanol covered amorphous ice, reactive collisions of ultralow energy CH_2^+ did not yield any H/D exchange, and no CHD^+ signal appeared during the ultralow energy ion scattering experiment. Additionally, CH_2^+ did not trigger any H/D exchange on 1-pentanol ice itself. Therefore, it may be concluded that the amorphous ice surfaces (D_2O) are responsible for H/D exchange in the projectile; when amorphous ice becomes inaccessible for the projectile (CH_2^+) due to the 1-pentanol overlayer, H/D exchange product does not appear.

DISCUSSION

The study of stopping potential measurement revealed that CH_2^+, CH_3^+, and CH_4^+ follow a similar trend (Figure 1, Supporting Information, item numbers 1 and 2). The stopping potential experiments at Q3 showed that the ion kinetic energy decreases slightly after colliding with the substrate (see Figure 1, inset). The reason for choosing low energy CH_2^+ over CH_3^+ and CH_4^+ is the following. CH_3^+ could not be used as it is a closed shell ion, and hence its reactivity is very low toward water molecules. CH_2^+ (or CD_2^+) and CH_4^+ (or CD_4^+) are suitable ions for the purpose of this reaction as these are open shell ions. CH_4^+ was discarded as it did not produce CH_3D^+ at low energy; instead, it started breaking down on the ice surfaces beyond 5 eV (Supporting Information, item number 3). All of the aforementioned ions undergo thermoneutral reactions with water ice surfaces. When CH_2^+ was allowed to impinge on D_2O, the H/D exchange product CHD^+ was seen. On the other hand, this product is not observed during collision on crystalline ice surfaces.

Results indicate that there are differences in chemical reactivity between amorphous and crystalline ice surfaces as mentioned before. There may be several effects that can affect the change in reactivity of the surfaces in microscopic detail, which include the difference in population of free hydroxyl groups on the two ice surfaces, dewetting,[20,51−56] film morphology change due to collapse of pores,[57] etc. Crystallization-induced dewetting is unlikely to be playing any role in this case as ice films are thick.[36,58] Dewetting of ice films grown on Cu(111) occurs around 160 K for a 50 ML film,[36] and dewetting temperature increases with film thickness.[56]

dx.doi.org/10.1021/jp4016432 | J. Phys. Chem. C 2013, 117, 12146−12152

Note that our experiment is on 100 ML films conducted at 140 K. Morphology change due to the collapse of pores will not contribute at 140 K as the pores collapse near ∼118 K.[59] In view of these facts, it is likely that free hydroxyl groups present on the ice surfaces are responsible for the reactivity change. Shen and colleagues reported coverage of dangling hydroxyl groups on the liquid water−air interface to be one-quarter of the available OH bonds.[19,60] Amorphous ice surfaces have a large number of dangling hydroxyl groups exposed to vacuum.[57,61,62] This population on the surfaces reduces when the amorphous ice is annealed to the crystalline form due to massive reconstruction that takes place during phase transition.[61] It may be noted that the absorbances of dangling hydroxyl bands decrease to near zero values around 140 K.[57] Thus, due to the large population of free hydroxyl groups on the amorphous ice surfaces, a larger extent of H/D exchange reactions occur here. On crystalline ice, the reaction does not occur to the same extent, and CHD^+ is not detected. However, the formation of CHD^+ is not ruled out as crystalline ice surfaces also possess free hydroxyl groups on its surfaces. Probably, the signal intensity is below the limit of detection in the case of CW. The reaction is proposed to proceed as $CH_2^+ + D_2O \rightarrow CHD^+ + HOD$, where CH_2^+ and CHD^+ are the gas-phase species and are detected by the mass spectrometer. Exchange reaction is a thermoneutral process. With increase in CH_2^+ kinetic energy, the H/D exchange product intensity increases (Figure 2c). Two factors are mainly responsible for this. First, scattering intensity increases with the increase in incident ion kinetic energy. Second, above 8 eV kinetic energy, the projectiles were fragmented on ice surfaces, and the products opened another path for more H/D exchange. This also contributed to the enhancement of the intensity of the CHD^+ ion. To establish this reason, ASW layers were prepared, onto which ultralow energy CH_2^+ were subjected to collide. This collision results in normal H/D exchange due to the presence of a large number of dangling −OD bonds on the surfaces (Figure 5) as mentioned above. After that, when the ASW was transformed to CW by annealing at 140 K, the same ultralow energy projectile did not cause detectable H/D exchange (Supporting Information, item number 4) product. The role of ASW in the reactive collision was confirmed by another investigation. First, 50 ML ASW (D_2O) layer was developed on Cu followed by 200 ML 1-pentanol layer. 200 ML thick 1-pentanol ensured that no D_2O molecules diffuse through the 1-pentanol layers and appear on the surface. On this sandwich surface, when the ultralow energy CH_2^+ was impinged, no CHD^+ signal was found. It is concluded that due to the presence of solid 1-pentanol cover, reactive CH_2^+ could not interact with the dangling −OD of the ASW (D_2O). Hence, no H/D exchange product appeared. This was again confirmed by 50 eV Ar^+ sputtering spectra (inset of Supporting Information, item number 5). The mass spectra consist of peaks, which originate from the sputtering of 1-pentanol. These control experiments confirm that the H/D exchange originated from the interaction of ASW (D_2O) surfaces with ultralow energy projectile (CH_2^+). Whenever the ASW surface was modified or covered, low energy H/D exchange did not take place. It can be further confirmed that this kind of ultralow energy reactive scattering is extremely surface sensitive particularly in the projectile kinetic energy range of 2−7 eV.

SUMMARY

This work shows that reactive projectiles of low energy react differently with structurally different surfaces. CH_2^+ with energy in the range 2−7 eV are suitable in differentiating the nature of ice surfaces. ASW (D_2O) surfaces have dangling −OD groups with which CH_2^+ reacts and undergoes H/D exchange to yield CHD^+. Dangling −OD groups population on the surfaces exposed to vacuum are very low on CW (D_2O); therefore, CH_2^+ collisions with this kind of surfaces do not produce any observable H/D exchange. Different experiments discussed in this Article describe a suitable method to distinguish ASW from CW with ultrahigh surface specificity.

ASSOCIATED CONTENT

Supporting Information

(1) Stopping potential experiment of CH_3^+ performed at Q1, (2) stopping potential experiment of CH_4^+ performed at Q1, (3) mass spectra observed upon collision with varying energy of CH_4^+ on 100 ML ASW (D_2O) generated at 120 K, (4) mass spectra observed after collision of varying energy CH_2^+ projectile on crystalline ice (D_2O), which was made after annealing the amorphous ice layer, and (5) mass spectra recorded upon collision of CH_2^+ impinging at 1, 2, 3, 5, 8, and 10 eV kinetic energy. Inset shows sputtering spectra appeared upon the collision of 50 eV Ar^+ on the substrate. This material is available free of charge via the Internet at http://pubs.acs.org.

AUTHOR INFORMATION

Corresponding Author

*Fax: + 91-44 2257-0545. E-mail: pradeep@iitm.ac.in.

Notes

The authors declare no competing financial interest.

ACKNOWLEDGMENTS

T.P. acknowledges the Department of Science and Technology, Government of India, for funding through a Swarnajayanti fellowship. He also thanks the DST for continued support. S.B. and R.G.B. acknowledge the Council of Scientific and Industrial Research (CSIR), Government of India, for their research fellowships.

REFERENCES

(1) Tribello, G. A.; Slater, B.; Salzmann, C. G. A Blind Structure Prediction of Ice XIV. *J. Am. Chem. Soc.* **2006**, *128*, 12594−12595.
(2) Lobban, C.; Finney, J. L.; Kuhs, W. F. The Structure of a New Phase of Ice. *Nature* **1998**, *391*, 268−270.
(3) Burton, E. F.; Oliver, W. F. X-ray Diffraction Patterns of Ice. *Nature* **1935**, *135*, 505−506.
(4) Angell, C. A. Amorphous Water. *Annu. Rev. Phys. Chem.* **2004**, *55*, 559−583.
(5) Olander, D. S.; Rice, S. A. Preparation of Amorphous Solid Water. *Proc. Natl. Acad. Sci. U.S.A.* **1972**, *69*, 98−100.
(6) Callen, B. W.; Griffiths, K.; Norton, P. R. Observation of Free Hydroxyl Groups on the Surface of Ultra Thin Ice Layers on Ni(110). *Surf. Sci.* **1992**, *261*, L44−L48.
(7) Devlin, J. P.; Buch, V. Vibrational Spectroscopy and Modeling of the Surface and Subsurface of Ice and of Ice-Adsorbate Interactions. *J. Phys. Chem. B* **1997**, *101*, 6095−6098.
(8) Delzeit, L.; Powell, K.; Uras, N.; Devlin, J. P. Ice Surface Reactions with Acids and Bases. *J. Phys. Chem. B* **1997**, *101*, 2327−2332.
(9) Devlin, J. P.; Joyce, C.; Buch, V. Infrared Spectra and Structures of Large Water Clusters. *J. Phys. Chem. A* **2000**, *104*, 1974−1977.

(10) Rowland, B.; Kadagathur, N. S.; Devlin, J. P.; Buch, V.; Feldman, T.; Wojcik, M. J. Infrared Spectra of Ice Surfaces and Assignment of Surface-Localized Modes from Simulated Spectra of Cubic Ice. *J. Chem. Phys.* **1995**, *102*, 8328−8341.
(11) Jenniskens, P.; Banham, S. F.; Blake, D. F.; McCoustra, M. R. S. Liquid Water in the Domain of Cubic Crystalline Ice I_c. *J. Chem. Phys.* **1997**, *107*, 1232−1241.
(12) Buontempo, U. Infrared Spectra of Amorphous Ice. *Phys. Lett. A* **1972**, *42*, 17−18.
(13) Bolina, A. S.; Wolff, A. J.; Brown, W. A. Reflection Absorption Infrared Spectroscopy and Temperature-Programmed Desorption Studies of the Adsorption and Desorption of Amorphous and Crystalline Water on a Graphite Surface. *J. Phys. Chem. B* **2005**, *109*, 16836−16845.
(14) Buch, V.; Milet, A.; Vacha, R.; Jungwirth, P.; Devlin, J. P. Water Surface Is Acidic. *Proc. Natl. Acad. Sci. U.S.A.* **2007**, *104*, 7342−7347.
(15) Mate, B.; Medialdea, A.; Moreno, M. A.; Escribano, R.; Herrero, V. J. Experimental Studies of Amorphous and Polycrystalline Ice Films Using FT-RAIRS. *J. Phys. Chem. B* **2003**, *107*, 11098−11108.
(16) Zondlo, M. A.; Onasch, T. B.; Warshawsky, M. S.; Tolbert, M. A.; Mallick, G.; Arentz, P.; Robinson, M. S. Experimental Studies of Vapor-Deposited Water-Ice Films Using Grazing-Angle FTIR-Reflection Absorption Spectroscopy. *J. Phys. Chem. B* **1997**, *101*, 10887−10895.
(17) Rudakova, A. V.; Poretskiy, M. S.; Marinov, I. L.; Tsyganenko, A. A. IR Spectroscopic Study of Surface Properties of Amorphous Water Ice. *Opt. Spectrosc.* **2011**, *109*, 708−718.
(18) Mitlin, S.; Leung, K. T. Surface Chemistry of OH Dangling Bonds in Vapour-Deposited Ice Films at 128−185 K. Hydrogen-Bonding Interactions with Acetone. *Surf. Sci.* **2002**, *505*, L227−L236.
(19) Schaff, J. E.; Roberts, J. T. Toward an Understanding of the Surface Chemical Properties of Ice: Differences Between the Amorphous and Crystalline Surfaces. *J. Phys. Chem.* **1996**, *100*, 14151−14160.
(20) Zimbitas, G.; Haq, S.; Hodgson, A. The Structure and Crystallization of Thin Water Films on Pt(111). *J. Chem. Phys.* **2005**, *123*, 174701/1−174701/9.
(21) Jenniskens, P.; Blake, D. F. Structural transitions in amorphous water ice and astrophysical implications. *Science (Washington, D.C.)* **1994**, *265*, 753−6.
(22) Jacobs, D. C. Reactive Collisions of Hyperthermal Energy Molecular Ions with Solid Surfaces. *Annu. Rev. Phys. Chem.* **2002**, *53*, 379−407.
(23) Cyriac, J.; Pradeep, T.; Kang, H.; Souda, R.; Cooks, R. G. Low-Energy Ionic Collisions at Molecular Solids. *Chem. Rev.* **2012**, *112*, 5356−5411.
(24) Bag, S.; Bhuin, R. G.; Natarajan, G.; Pradeep, T. Probing Molecular Solids with Low-Energy Ions. *Annu. Rev. Anal. Chem.* **2013**, *6*, 97−118.
(25) Cooks, R. G.; Ast, T.; Pradeep, T.; Wysocki, V. Reactions of Ions with Organic Surfaces. *Acc. Chem. Res.* **1994**, *27*, 316−323.
(26) Düerr, H.; Poker, D. B.; Zehner, D. M.; Barrett, J. H. Determination of the Reconstruction of Cu(110)-(2 × 3)-N with High-Energy Ion Scattering. *Phys. Rev. B: Condens. Matter* **1994**, *49*, 16789−16792.
(27) Bag, S.; McCoustra, M. R. S.; Pradeep, T. Formation of H_2^+ by Ultra-Low-Energy Collisions of Protons with Water Ice Surfaces. *J. Phys. Chem. C* **2011**, *115*, 13813−13819.
(28) Kolling, T.; Sun, S.; Weitzel, K.-M. Reactive Scattering of NH_3^+ (v, J) Ions at Film Covered Indium Tin Oxide (ITO) Surfaces. *Int. J. Mass Spectrom.* **2008**, *277*, 245−250.
(29) de, C. H. L.; Sen, A. D.; Shukla, A. K.; Futrell, J. H. Inelastic Ion-Surface Collisions: Scattering and Dissociation of Low Energy Benzene Molecular Cations. *Int. J. Mass Spectrom.* **2001**, *212*, 491−504.
(30) Herman, Z.; Mark, T. D. Collisions of Hydrocarbon Ions of Energies 10−50 eV with Carbon Surfaces: Ion Survival, Dissociation, Chemical Reactions, Scattering. *At. Plasma-Mater. Interact. Data Fusion* **2008**, *14*, 34−43.
(31) Qian, K.; Shukla, A.; Futrell, J. Electronic Excitation in Low-Energy Collisions: A Study of the Collision-Induced Dissociation of Nitromethane Ion by Crossed-Beam Tandem Mass Spectrometry. *J. Am. Chem. Soc.* **1991**, *113*, 7121−7129.
(32) Grill, V.; Shen, J.; Evans, C.; Cooks, R. G. Collisions of Ions With Surfaces at Chemically Relevant Energies: Instrumentation and Phenomena. *Rev. Sci. Instrum.* **2001**, *72*, 3149−3179.
(33) Shukla, A. K.; Futrell, J. H. Tandem Mass Spectrometry: Dissociation of Ions by Collisional Activation. *J. Mass Spectrom.* **2000**, *35*, 1069−1090.
(34) Cyriac, J.; Pradeep, T. Probing Difference in Diffusivity of Chloromethanes through Water Ice in the Temperature Range of 110−150 K. *J. Phys. Chem. C* **2007**, *111*, 8557−8565.
(35) Cyriac, J.; Pradeep, T. Interaction of Carboxylic Acids and Water Ice Probed by Argon Ion Induced Chemical Sputtering. *J. Phys. Chem. C* **2008**, *112*, 1604−1611.
(36) Cyriac, J.; Pradeep, T. Structural Reorganization on Amorphous Ice Films below 120 K Revealed by Near-Thermal (∼1 eV) Ion Scattering. *J. Phys. Chem. C* **2008**, *112*, 5129−5135.
(37) Benninghoven, A.; Sichtermann, W. K. Detection, Identification, and Structural Investigation of Biologically Important Compounds by Secondary Ion Mass Spectrometry. *Anal. Chem.* **1978**, *50*, 1180−1184.
(38) Benninghoven, A. Analysis of Monomolecular Surface Layers of Solids by Secondary Ion Emission. *Z. Phys.* **1970**, *230*, 403−417.
(39) Benninghoven, A.; Hagenhoff, B.; Niehuis, E. Surface MS: Probing Real-World samples. *Anal. Chem.* **1993**, *65*, 630A−640A.
(40) Leute, A.; Rading, D.; Benninghoven, A.; Schroeder, K.; Klee, D. Static SIMS Investigation of Immobilized Molecules on Polymer Surfaces. *Adv. Mater.* **1994**, *6*, 775−780.
(41) Trakhtenberg, S.; Naaman, R.; Cohen, S. R.; Benjamin, I. Effect of the Substrate Morphology on the Structure of Adsorbed Ice. *J. Phys. Chem. B* **1997**, *101*, 5172−5176.
(42) Chen, H.; Aleksandrov, A.; Chen, Y.; Zha, S.; Liu, M.; Orlando, T. M. Probing Water Interactions and Vacancy Production on Gadolinia-Doped Ceria Surfaces Using Electron Stimulated Desorption. *J. Phys. Chem. B* **2005**, *109*, 11257−11262.
(43) Herring, J.; Aleksandrov, A.; Orlando, T. M. Stimulated Desorption of Cations from Pristine and Acidic Low-Temperature Water Ice Surfaces. *Phys. Rev. Lett.* **2004**, *92*, 187602/1−187602/4.
(44) Kumar, G. N.; Cyriac, J.; Bag, S.; Pradeep, T. Low Energy Ion Scattering Investigations of n-Butanol-Ice System in the Temperature Range of 110−150 K. *J. Phys. Chem. C* **2009**, *113*, 14258−14263.
(45) Moon, E.-S.; Kang, H.; Oba, Y.; Watanabe, N.; Kouchi, A. Direct Evidence for Ammonium Ion Formation in Ice Through Ultraviolet-Induced Acid-Base Reaction of NH_3 with H_3O^+. *Astrophys. J.* **2010**, *713*, 906−911.
(46) Moon, E.-S.; Kang, H. Metastable Hydronium Ions in UV-Irradiated Ice. *J. Chem. Phys.* **2012**, *137*, 204704/1−204704/8.
(47) Kasi, S. R.; Kang, H.; Sass, C. S.; Rabalais, J. W. Inelastic Processes in Low-Energy Ion-Surface Collisions. *Surf. Sci. Rep.* **1989**, *10*, 1−104.
(48) Winters, H. F. Chemical Sputtering, a Discussion of Mechanisms. *Radiat. Eff.* **1982**, *64*, 79−79.
(49) Cooks, R. G.; Ast, T.; Mabud, M. A. Collisions of Polyatomic Ions with Surfaces. *Int. J. Mass Spectrom. Ion Processes* **1990**, *100*, 209−265.
(50) Materer, N.; Starke, U.; Barbieri, A.; Van, H. M. A.; Somorjai, G. A.; Kroes, G. J.; Minot, C. Molecular Surface Structure of Ice(0001): Dynamical Low-Energy Electron Diffraction, Total-Energy Calculations and Molecular Dynamics Simulations. *Surf. Sci.* **1997**, *381*, 190−210.
(51) May, R. A.; Smith, R. S.; Kay, B. D. Probing the Interaction of Amorphous Solid Water on A Hydrophobic Surface: Dewetting and Crystallization Kinetics of ASW on Carbon Tetrachloride. *Phys. Chem. Chem. Phys.* **2011**, *13*, 19848−19855.
(52) Beniya, A.; Koitaya, T.; Mukai, K.; Yoshimoto, S.; Yoshinobu, J. Dewetting Growth of Crystalline Water Ice on a Hydrogen Saturated Rh(111) Surface at 135 K. *J. Chem. Phys.* **2011**, *135*, 054702/1−054702/5.

(53) Beniya, A.; Sakaguchi, Y.; Narushima, T.; Mukai, K.; Yamashita, Y.; Yoshimoto, S.; Yoshinobu, J. The Growth Process of First Water Layer and Crystalline Ice on the Rh(111) Surface. *J. Chem. Phys.* **2009**, *130*, 034706/1−034706/10.
(54) Souda, R. Dewetting of Thin Amorphous Solid Water Films and Liquid-Cubic Ice Coexistence in Droplets Studied Using Infrared-Absorption and Secondary-Ion-Mass Spectroscopy. *J. Phys. Chem. B* **2008**, *112*, 11976−11980.
(55) Souda, R. Effects of Methanol on Crystallization of Water in the Deeply Supercooled Region. *Phys. Rev. B: Condens. Matter Mater. Phys.* **2007**, *75*, 184116/1−184116/7.
(56) Kimmel, G. A.; Petrik, N. G.; Dohnalek, Z.; Kay, B. D. Crystalline Ice Growth on Pt(111) and Pd(111): Nonwetting Nrowth on a Hydrophobic Water Monolayer. *J. Chem. Phys.* **2007**, *126*, 114702/1−114702/10.
(57) Smith, R. S.; Zubkov, T.; Dohnalek, Z.; Kay, B. D. The Effect of the Incident Collision Energy on the Porosity of Vapor-Deposited Amorphous Solid Water Films. *J. Phys. Chem. B* **2009**, *113*, 4000−4007.
(58) Stähler, J.; Mehlhorn, M.; Bovensiepen, U.; Meyer, M.; Kusmierek, D. O.; Morgenstern, K.; Wolf, M. Impact of Ice Structure on Ultrafast Electron Dynamics in D_2O Clusters on Cu(111). *Phys. Rev. Lett.* **2007**, *98*, 206105/1−206105/4.
(59) Mehlhorn, M.; Morgenstern, K. Faceting during the Transformation of Amorphous to Crystalline Ice. *Phys. Rev. Lett.* **2007**, *99*, 246101/1−246101/4.
(60) Du, Q.; Freysz, E.; Shen, Y. R. Surface Vibrational Spectroscopic Studies of Hydrogen Bonding and Hydrophobicity. *Science* **1994**, *264*, 826−828.
(61) Witek, H.; Buch, V. Structure of Ice Multilayers on Metals. *J. Chem. Phys.* **1999**, *110*, 3168−3175.
(62) Verdaguer, A.; Sacha, G. M.; Bluhm, H.; Salmeron, M. Molecular Structure of Water at Interfaces: Wetting at the Nanometer Scale. *Chem. Rev.* **2006**, *106*, 1478−1510.

Supporting information

Distinguishing Amorphous and Crystalline Ice by Ultralow Energy Collisions of Reactive Ions

Soumabha Bag, Radha Gobinda Bhuin, and T. Pradeep[*]

DST Unit of Nanoscience (DST UNS), Department of Chemistry, Indian Institute of Technology Madras, Chennai- 600036, India.

*Corresponding author: Fax: + 91-44 2257-0545

E-mail: pradeep@iitm.ac.in

Supporting information 1

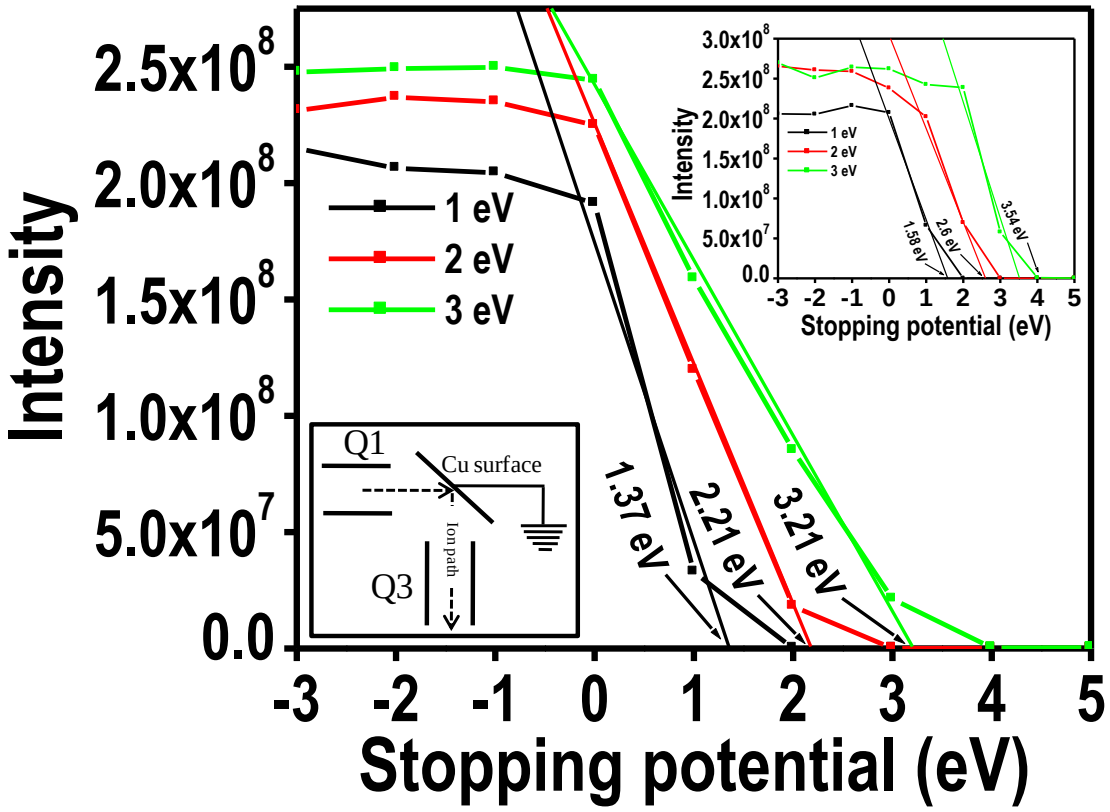

Figure S1. Stopping potential experiment of CH_3^+ performed at Q1. Inset shows the results of the same experiment performed at Q3. A schematic of the experiment is shown in another inset.

Supporting information 2

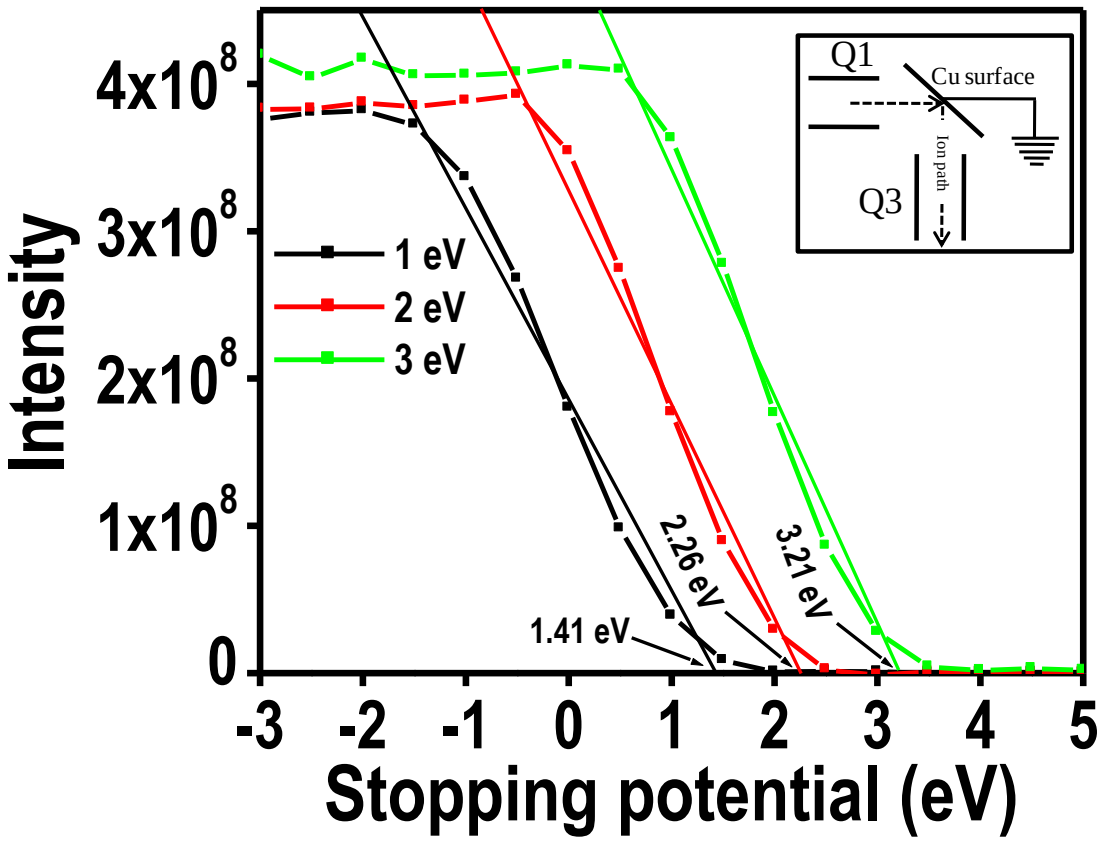

Figure S2. Stopping potential experiment of CH_4^+ performed at Q1. Inset shows the scheme of the experiment.

Supporting information 3

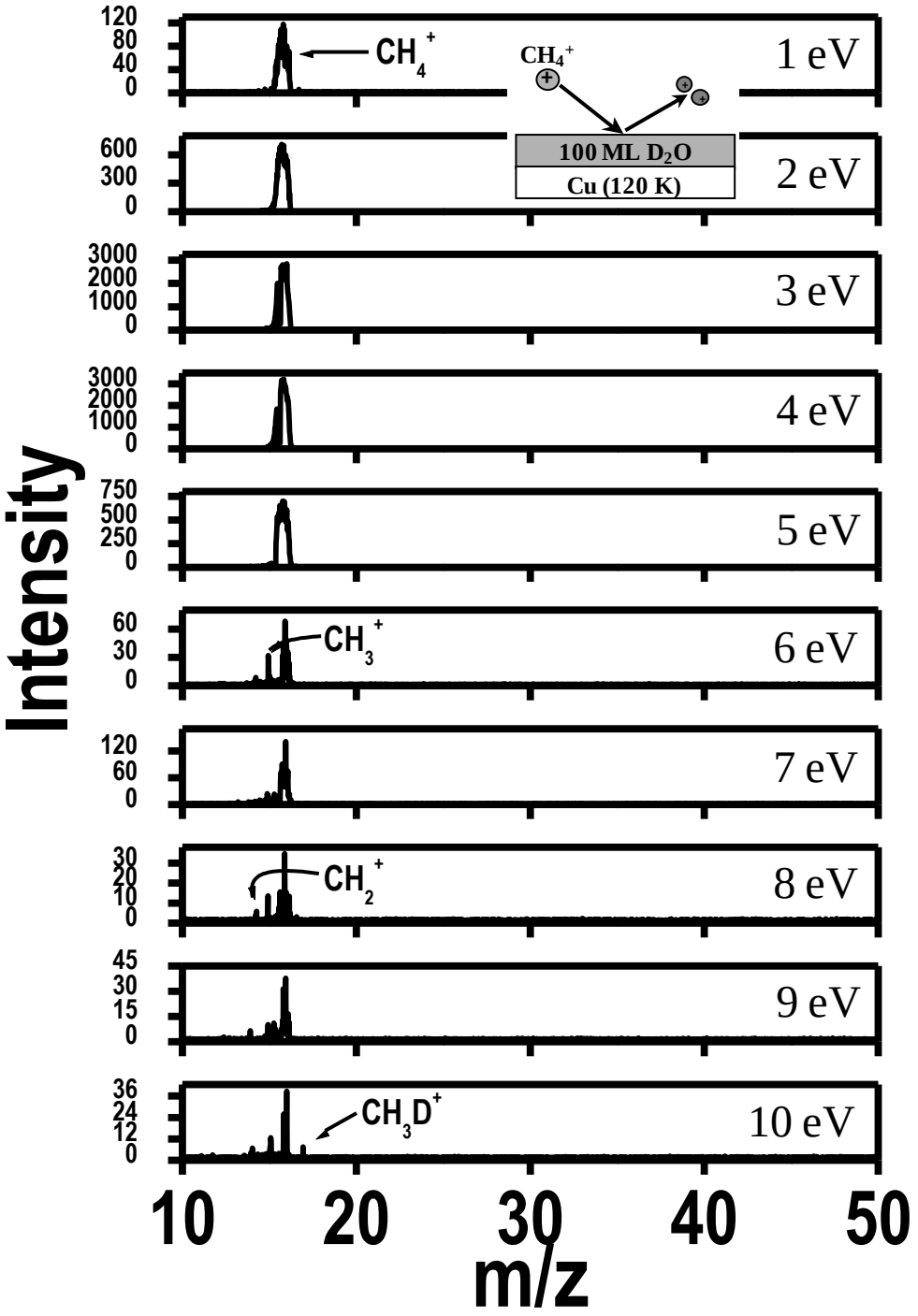

Figure S3. Mass spectra observed upon the collision varying energy of CH_4^+ on 100 ML ASW (D_2O) generated at 120 K.

Supporting information 4

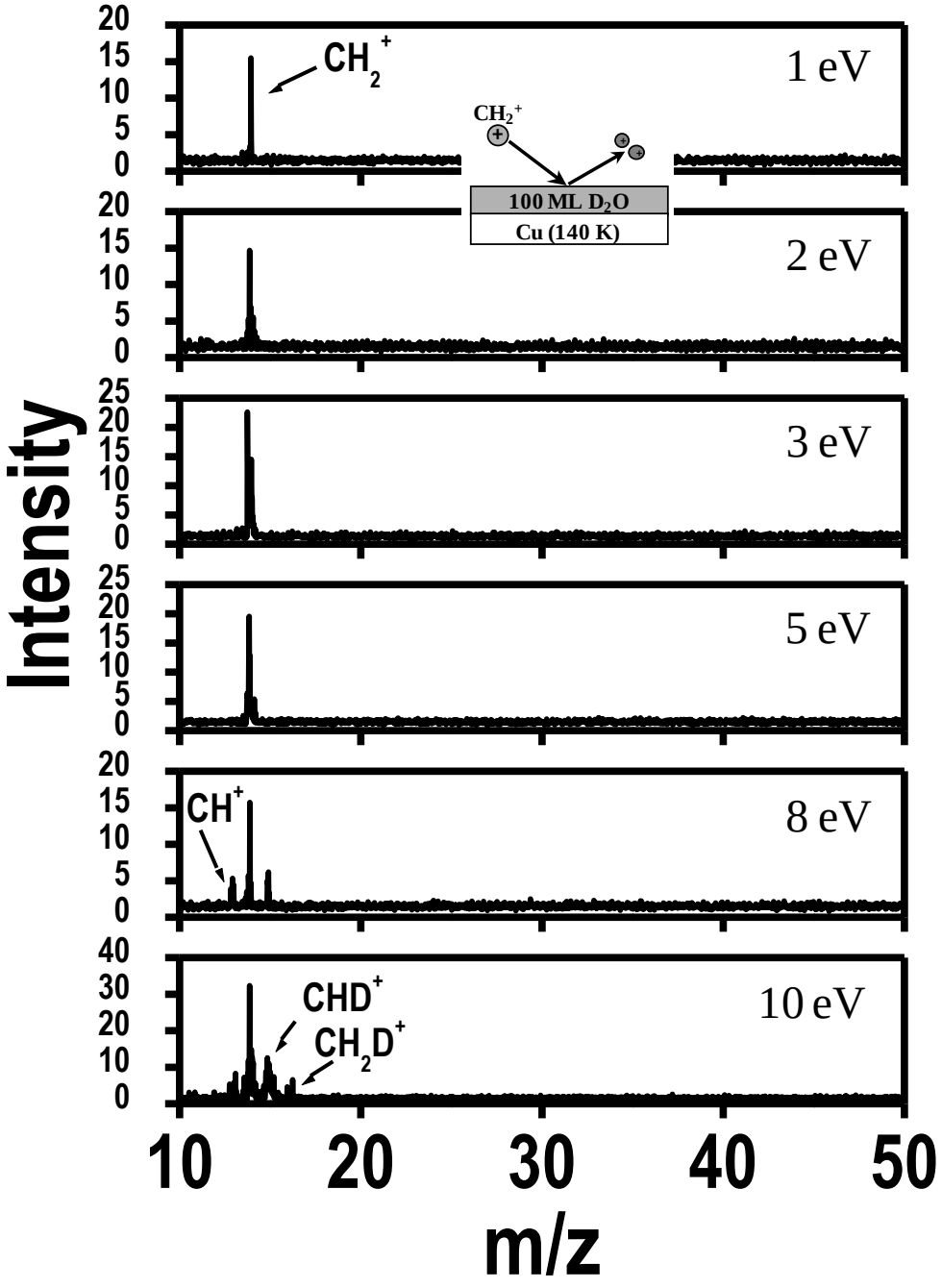

Figure S4: Mass spectra observed after collision of varying energy CH_2^+ projectile on crystalline ice (D_2O) made after annealing of the amorphous ice layer.

Supporting information 5

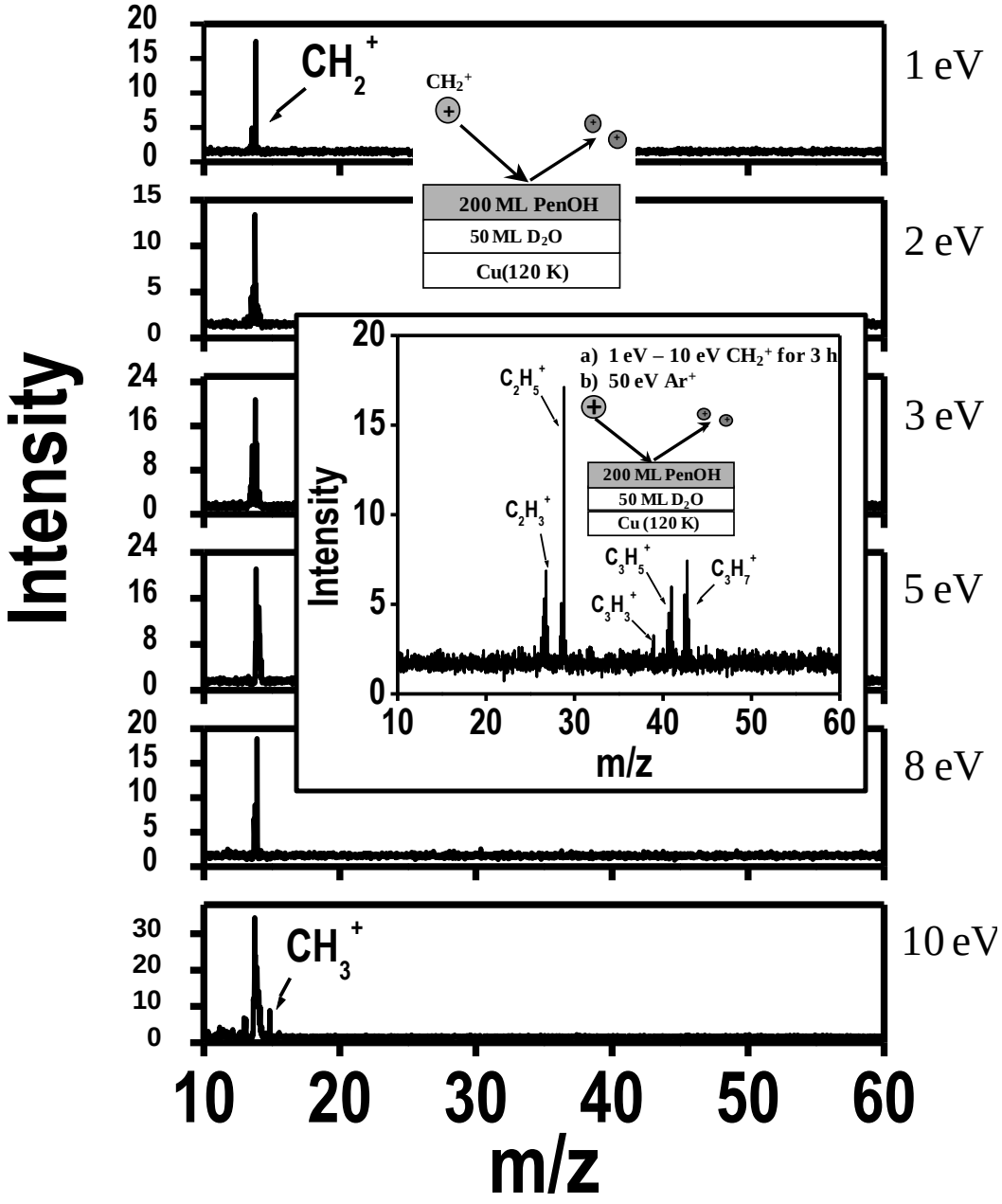

Figure S5: Mass spectra recorded upon collision of ultralow energy (1-10 eV) CH_2^+ ion on condensed 1-pentanol grown on amorphous ice (D_2O). CH_2^+ ion colliding with 1, 2, 3, 5, 8, 10 eV kinetic energy is shown here. Inset shows the sputtering spectra upon the collision of 50 eV Ar^+ ion on the substrate.

Particle
& Particle Systems Characterization
www.particle-journal.com
www.MaterialsViews.com

Single-Cell Investigations of Silver Nanoparticle–Bacteria Interactions

*Sudarsan Vishnupriya, Kamalesh Chaudhari, Ramya Jagannathan, and Thalappil Pradeep**

Interaction of bacteria with citrate-reduced silver nanoparticles (AgNPs) of size 25 nm ± 8.5 nm is studied using Raman spectroscopy in conjunction with plasmon resonance imaging of single bacterial cells. Distribution of isolated nanoparticles (NPs) inside *Escherichia coli* (ATCC 25922; *E. coli*) is observed by hyperspectral imaging (HSI) as a function of incubation time. Time-dependent degradation of bacterial DNA upon incubation of AgNPs with *E. coli* is proven by Raman spectroscopic studies. While attachment of NPs is evident in HSI, molecular changes are evident from the surface-enhanced Raman spectra of adsorbed DNA and its fragments. Distinct enhancement of DNA features is observed upon interaction of AgNPs and the number of such distinct features increases with incubation time, reaches a maximum, and decreases afterwards. This systematic interaction of DNA with the NPs system and its gradual chemical evolution is proven by investigating isolated plasmid DNA. A comparative Raman study with silver ions has shown that DNA features are observable only when bacteria are incubated with AgNPs. Energetics of interaction examined with microcalorimetry suggests the exothermicity of -1.547×10^{10} cal mol^{-1} for the NP–bacteria system. Specific interaction of AgNPs with exocyclic nitrogen present in the bases, adenine, guanine, and cytosine, leads to the changes in DNA.

1. Introduction

One of the rapidly evolving areas of the applications of noble metal nanoparticles (NPs) is water purification.[1,2] Various nanomaterial-based strategies have been developed for the remediation of diverse environmental contaminants, including microbes, in the recent past.[3–5] Silver nanoparticles (AgNPs)-based disinfection is one of the simplest remediation strategies for microbial contamination and has been used from ancient times.[6,7] Recent advancement in the understanding of the chemistry of noble metal NPs has contributed to their intense use in antibacterial applications and this is one of the major reasons for AgNPs to be the most economically significant nanomaterial in use today. Utility of such materials has been demonstrated in recent past with the development of an affordable water purifier using AgNP–biopolymer composites.[8] It is important to point out that noble metal NPs are important in oxidation, dehalogenation, and CH-bond activation and several of these properties have been used in environmental applications.[1,9–11] In the context of microbial disinfection, the mechanism behind the action of AgNPs is still an issue of debate. We shall briefly discuss below the status of the current understanding of the area.

Major events upon exposure of AgNPs to microorganisms are reported to be: i) generation of free radicals reactive oxygen species (ROS),[12,13] ii) subsequent incorporation of AgNPs in the membrane, as well as free radical induced structural changes in it,[14,15] iii) increase in cell permeability to Ag^+ ions and AgNPs[14,16] due to (ii), iv) loss of DNA replicability and protein activity, resulting in the inhibition of cell growth,[17,18] v) accumulation of protein precursors, destabilization of the outer membrane, collapse of the plasma membrane potential and depletion of intracellular adenosine triphosphate (ATP) levels, especially at short exposures,[19] and vi) inhibition of respiratory chain dehydrogenases.[15] There are also conflicting reports on all of these with some studies favoring specific pathways.[13,17,20] Model studies have been performed to understand the interaction of NPs with cellular ingredients such as proteins,[21] lipids,[22] and DNA bases.[23] Recently, Alvarez and co-workers[24] observed that silver ions leaching from AgNPs are the major reason for the antibacterial property of AgNPs. Despite all of these, our knowledge about the microscopic details of disinfection is still inadequate. Absence of the closer view of the interaction of AgNPs at single-cell level prompted us to investigate it at this scale, aided by techniques such as confocal Raman microscopy (CRM) along with the scattering-based hyperspectral imaging (HSI), which enable visual,

S. Vishnupriya, Prof. T. Pradeep
DST Unit on Nanoscience (DST UNS) and
Thematic Unit of Excellence
Department of Chemistry
Indian Institute of Technology Madras
Chennai 600036, India
E-mail: pradeep@iitm.ac.in
K. Chaudhari
DST Unit on Nanoscience (DST UNS)
Department of Chemistry
Department of Biotechnology
Indian Institute of Technology Madras
Chennai, 600036, India
Dr. R. Jagannathan
Chemical Lab
CSIR-Central Leather Research Institute
Chennai 600020, India

DOI: 10.1002/ppsc.201300165

spectral, and chemical observation. Apart from imaging, we have performed isothermal calorimetric studies to understand the thermodynamic aspects of a single AgNP–bacterium interaction with the model organism, *Escherichia coli (E. coli)*.

2. Results and Discussion

2.1. Hyperspectral Analysis

As citrate-reduced AgNPs are well known, their properties are not discussed in detail. Transmission electron microscopy (TEM) images of AgNPs show the particles to be in the range of 25 ± 8.5 nm (Figure S1, Supporting Information) and its polydisperse nature is clearly observed in the HSI image (Figure S2, Supporting Information) where distinctly different particles are seen. The phenomenon of accumulation of AgNPs on bacteria was proved by HSI (**Figure 1**). AgNPs are efficient scatterers and provide good contrast as compared with the cellular components, which enable us to image even a single AgNP and localize it inside or on the periphery of a bacterium. But low resolution and poor scattering limit the HSI of bacteria for in situ observations of the interaction of NPs with cellular components or biomolecules. Figure 1A shows large-area image of *E. coli* treated with AgNPs. Scattering spectra collected from different spots are also shown in Figure 1B and the inset shows the magnified HSI image of a single bacterium, treated with AgNPs. Hyperspectral image of the control bacteria (untreated) is shown in Figure S3 (Supporting Information). AgNPs show a sharp localized surface plasmon resonance peak with large scattering intensity while spectrum of the bare cell membrane of the bacteria shows a broad scattering spectrum with maximum in the blue–green region (400–550 nm). The scattering intensity from the bacterial cell membrane is an order of magnitude weaker than from the NPs. Images of AgNPs-treated bacteria clearly show that AgNPs attach on them (see the circled regions in Figure 1). Time-dependent HSI observations of AgNPs-treated bacteria were made to see the uptake of NPs by bacteria. We see that the number of AgNPs attached to the bacterium has increased with incubation time. Lysis of the bacteria was observed when the treatment time of AgNPs increased for more than an hour (Figure S4, Supporting Information).

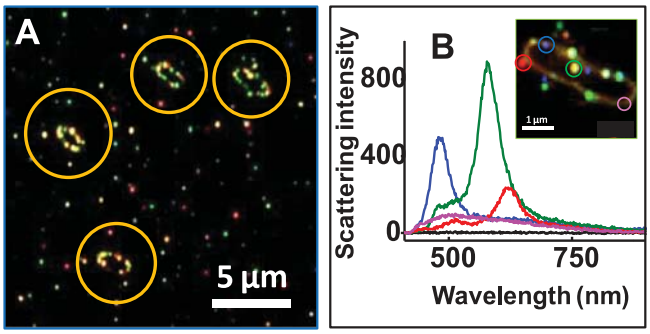

Figure 1. A) Hyperspectral image of *E. coli* after treatment with AgNPs. B) The inset shows an enlarged image of a single bacterium treated with NPs and scattering spectra corresponding to the encircled particles on the bacterium. Colors of the traces correspond to the circles in which a specific particle is selected. The black trace corresponds to the background. The bacterial cell membrane shows a weak scattering spectrum and the scattering spectrum of the NPs shows distinct peak maxima.

2.2. Raman Spectroscopic Analysis

2.2.1. SERS of AgNPs

It may be noted that previous Raman spectroscopic studies of AgNPs and bacteria were principally to detect isolated bacterium[25] and to distinguish different species of bacteria,[26,27] utilizing the surface-enhanced Raman scattering (SERS). The present work we believe is the first report using Raman spectroscopy to know the in situ interaction of AgNPs with single bacteria. Internalization of AgNPs was observed by Raman spectroscopy. Due to the SERS property of AgNPs, the penetration of AgNPs inside the bacterium was reflected as 10- to 100-fold intensity enhancement of the Raman signals of the molecules within a bacterium (**Figure 2**), when spectra are compared without and with AgNPs (Figure 2A,C). This is evident in the Raman images of single bacterial cells also (Figure 2B,D). The accumulation of AgNPs on bacteria is initiated due to good affinity of silver for sulfur-[28] and amine-[29]containing molecules such as proteins present on the outer membrane. It is also supported by isothermal calorimetry (ITC) studies, discussed later.

2.2.2. Time-Dependent Raman Measurements of Bacteria Treated with AgNPs

Temporal Raman spectroscopic observations were performed on the bacteria incubated with AgNPs for 5, 10, 20, 30, and 60 min (Figure S5, Supporting Information). As spectra from single bacterium change significantly from cell to cell, multiple bacteria at each time of incubation were examined. However,

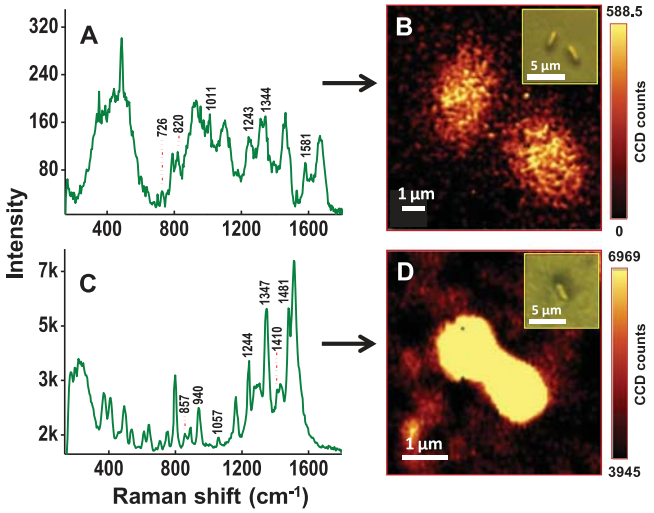

Figure 2. Raman spectra and Raman images of a single bacterium without (A,B) and with treatment (C,D) of AgNPs for 10 min. Intensity scales clearly indicate the large enhancement in the Raman scattering intensity of AgNPs-treated *E. coli* as compared with untreated *E. coli*.

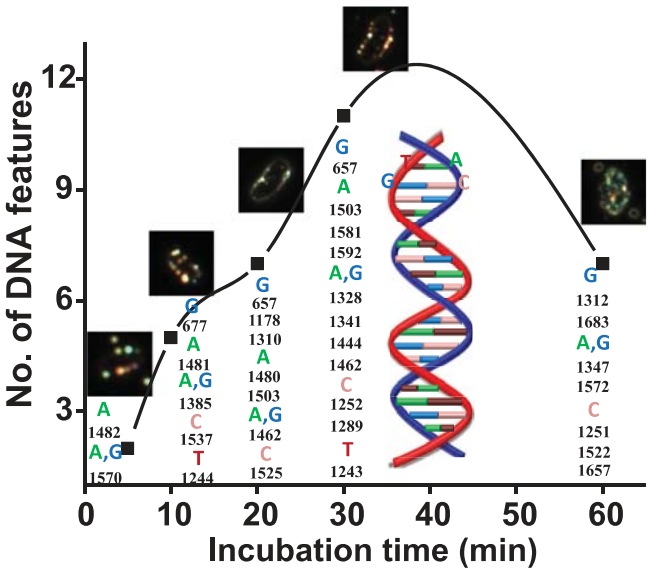

Figure 3. Comparison of the observed number of DNA peaks arising from bacteria treated with AgNPs for various incubation times (5, 10, 20, 30, and 60 min). Corresponding dark-field optical images of a typical bacterium are shown. This comparison clearly shows increase in the number of DNA peaks with the increase in incubation time following a decrease of DNA peaks when the incubation time 1 h. The assignments are based on various reports.[30–38]

spectra were reproducible for both treated and untreated bacteria, in terms of the occurrence of the same spectral features, but not the peak shape. This kind of variation is seen in SERS of molecular mixtures as in this case.[25–27] The occurrence of the same features suggests that with time, molecular-specific interaction of AgNPs with the inner structures of the bacteria occurred as compared with the outer structure. To verify the reproducibility of this data, spectra from five separate bacteria were measured and compared (Figure S5, Supporting Information). Time-dependent data have shown Raman features corresponding to proteins, lipids, carbohydrates, RNA, and DNA. Enhanced intensities of these features indicate the presence of AgNPs on the outer membrane as well as inside the bacteria. Peaks in the Raman spectra of AgNPs-treated and untreated bacteria were assigned using previous reports of Raman spectroscopy of bacteria (Table S6, Supporting Information).[30–38] It is known that AgNPs enhance the membrane permeability, which leads to the entry of particles inside the bacteria[13] and supposedly affect the growth of bacteria by interacting with the DNA.[17] From the experimental data, we observed that the number of distinct Raman peaks arising from the DNA of *E. coli* increases with incubation time of AgNPs; however, after 60 min, this number is reduced (**Figure 3**). It is important to recall that the interaction of AgNPs with mammalian cells leads to DNA degradation.[39,40] The degradation of DNA may be due to the disruption of the electron transfer pathway in mitochondrial respiratory chain by AgNPs, which leads to the production of ROS and interruption of ATP synthesis.[40] Therefore, it is reasonable to conclude that the DNA features we observed in Figure 3 are due to their degradation products. From the Raman study, it is observed that the Raman scattering intensity of the nucleotide bases of DNA such as adenine (A), guanine (G), and cytosine (C) peaks were enhanced, whereas thymine (T) showed only limited enhancement. It has been shown that there can be strong interaction between amines and AgNPs.[29] The interaction of AgNPs with A, G, and C is strong, possibly due to the interaction of AgNPs with the exocyclic nitrogen present in these bases, and this is responsible for the enhancement in the peak intensities of the Raman spectra of these bases. On the other hand, T, devoid of this exocyclic amine group, interacts weakly with AgNPs.[23] Independent studies were done to calculate the SERS enhancement factors for bases treated with AgNPs as explained by Pavan Kumar et al.[41] The enhancement factors determined were in the order, C (9×10^4) > G (7×10^4) > A (5×10^4) > T (2×10^4). From these observations, we concluded that apart from the major effect of AgNPs on membrane damage,[15] they are highly specific towards bacterial DNA. We also observed the lysis of bacteria treated with AgNPs for a period more than an hour. It is supported by the time-dependent HSI images and bright field optical images of the bacteria treated with AgNPs (Figures S4 and S7, Supporting Information). The damage of bacterial membrane was observed in the bacteria treated with AgNPs for more than an hour. However, when the incubation time was less than an hour, observable morphological changes were not seen.

2.2.3. Comparison of Plasmid DNA and E. coli Cells, Both Treated with AgNPs

To confirm that specific peaks in the Raman spectra of *E. coli* cells treated with AgNPs are indeed from DNA, plasmid DNA was isolated from the *E. coli* cells and it was incubated with AgNPs for 20 min and Raman measurements were carried out. The DNA peaks from the treated (20 min) *E. coli* cells were found to be similar to the peaks of plasmid DNA treated with AgNPs (**Figure 4**). The interaction of plasmid DNA with AgNPs also exhibits an enhancement in the peak intensity of the bases

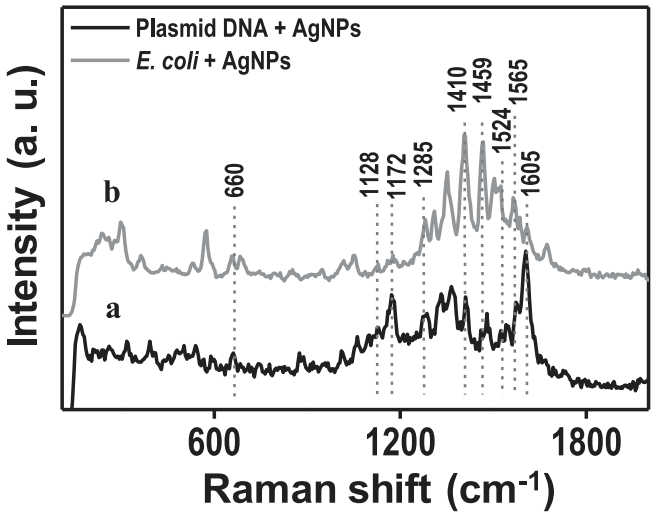

Figure 4. Comparison of the Raman spectra of *E. coli* plasmid DNA and whole *E. coli* cell, both treated with AgNPs. a) Raman spectrum of plasmid DNA treated with AgNPs for 20 min and b) Raman spectrum of *E. coli* cell treated with AgNPs for 20 min. Similar peaks seen are noted.

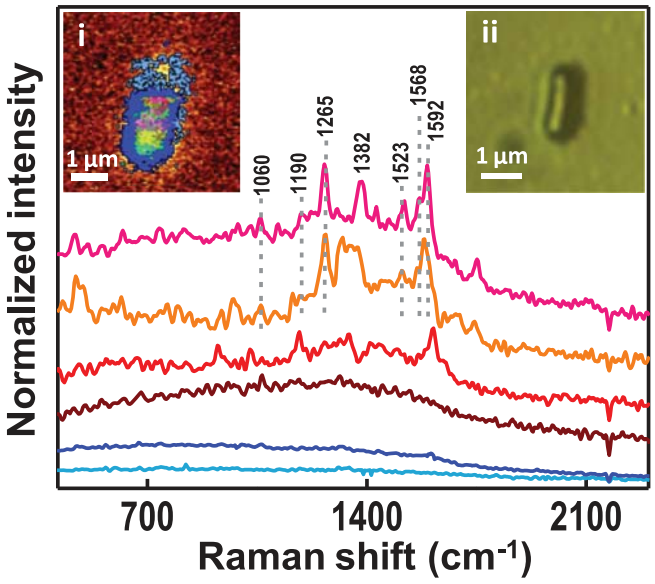

Figure 5. Raman image spectra obtained by the cluster analysis of the Raman image of a single bacterium. Inset i) shows the cluster analysis of the Raman image, which is merged with the original Raman image of a bacterium and inset ii) shows the corresponding optical image of the bacterium imaged. Each specific region in the bacterium has its corresponding Raman spectrum and it is represented in different colors. These spectra are observed from different regions of a single bacterium. There are additional component spectra, which are weaker and are not shown.

such as A, G, and C. The peak intensity of T was weak even in this case also. This observation confirms that there is a strong and specific interaction between AgNPs and A, G, and C bases, while T is weak in its interaction. The assignments of Raman peaks of *E. coli* plasmid DNA treated with AgNPs are shown in Table S8 (Supporting Information).[31,35,37,42–44]

2.3. Cluster Analysis

It was important to see if specific peaks are localized in distinct regions of the bacterium. For this, cluster analysis of the Raman spectra was carried out. Using cluster analysis, thousands of spectra in the Raman spectral image can be classified according to similarities of their features and the image can be mapped to spatially localize the point of interest.[45] **Figure 5** shows the cluster analysis of the Raman image of nanoparticle-treated *E. coli* cell. Different Raman spectra are represented in different colors after the analysis. The peaks corresponding to DNA (1592, 1568, 1523, 1382), proteins (1265,[31] 1190), and lipids (1060) are shown in Figure 5 and these peak assignments are represented in Table S6 (Supporting Information). All the features of each of the components of the cell are not seen, possibly due to the reduced aquisition time used for image collection. The central portions of the image marked with different colors are due to regions with specific Raman spectra, rich in DNA and protein features. Since Raman spectra obtained from cluster analysis are averages of spectra in that particular region, they contain multiple features. But spectra shown in Figure 4 are single-spot spectra obtained by manual monitoring; hence, they show features only from the location where AgNP–DNA interaction happens. This result supports the entry of AgNPs into the bacteria and their interaction with silver-binding proteins and DNA.[28] Most of the intensity in the outer region corresponds to the background and unresolved structures. Upon comparison with the optical image, it is clear that the DNA and protein features are localized within the bacterial contour. The plasmid DNA features (1524, 1565 cm^{-1}) of Figure 4 are clearly manifested in the spectra after cluster analysis.

2.4. Raman Measurements of Bacteria Treated with Ag^+ Ions

Previous studies have proposed that leaching of silver ions from AgNPs affected the DNA of a bacterium leading to its death.[16] To further probe the role of Ag^+ ions, bacteria were incubated with Ag^+ ions at 0.6×10^{-6} M for various time intervals (5, 10, 20, 30, and 60 min) and Raman spectroscopic measurements were done as in the case of AgNPs (Figure S9, Supporting Information). No enhancement in the peaks of Raman spectra was observed at any time interval, unlike in the case of *E. coli* treated with AgNPs. Compared with untreated *E. coli*, which gives 120 counts in the Raman spectrum for a major peak (Figure 2), the Raman spectra of *E. coli* treated with Ag^+ were weaker (Figure S9, Supporting Information). Consequently, several features were poorly reproducible. From the assignment of certain reproducible features, it is observed that DNA features are not enhanced unlike in the case of AgNPs but Raman features for proteins, carbohydrates, and lipids were observed (Table S10, Supporting Information). Ag^+ ions have good antibacterial property and several mechanisms have been proposed in this context.[46–48] Hyperspectral analysis of *E. coli* treated with Ag^+ ions has shown lysis of the cell membrane. Lysis begins after 30 min and can be seen clearly after 1 h of incubation (Figure S11, Supporting Information). AgNPs may leach silver ions within the bacteria and they may be responsible for part of the bactericidal action. The interaction of NPs with specific bacterial components like DNA, proteins, carbohydrates, and lipids was observable only in the case of AgNPs, while the interaction of Ag^+ ions with bacteria was not observable with Raman spectroscopy at the single-cell level as there is no enhancement in the Raman features.

2.5. Isothermal Calorimetry Study

We performed ITC studies to understand the strength of interaction between AgNPs and *E. coli*. ITC responses recorded during the titration of AgNPs against *E. coli* (**Figure 6**A) and the integrated calorimetric response plotted against the molar ratio of *E. coli*/AgNPs (Figure 6B) suggests strong interaction between the two. The exothermic and sigmoidal response for the binding with *E. coli* substrates suggests that as the titration progresses, AgNPs try to occupy all the possible sites of *E. coli* present in the ITC cell and after a few injections, no more AgNPs are left in the cell to occupy the sites, which leads to saturation. We have fitted the integrated calorimetric response with a model of single set of N identical sites on a substrate. However, multiple interactions do take place when bacteria are

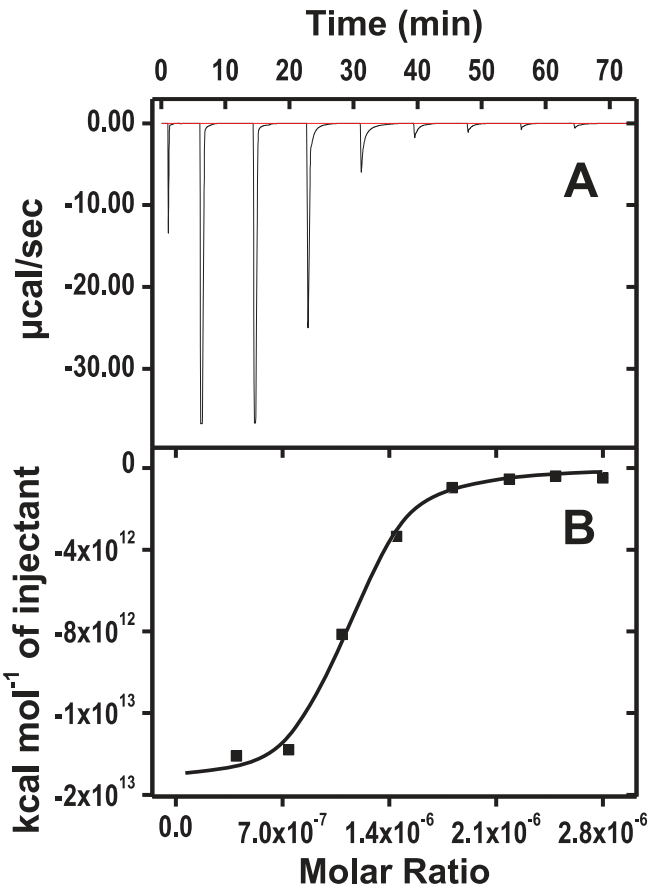

Figure 6. A) ITC responses for the titration of *E. coli* with the AgNPs. B) Integrated calorimetric response plotted against the molar ratio of *E. coli*/AgNPs (concentrations: 1.62×10^{-14} M/1.2×10^{-9} M). Concentration calculations are explained in the Experimental Section.

injected into a pool of AgNPs. The major interaction is believed to be the attachment of AgNPs on bacterial surface and as time progresses, there is possible diffusion of AgNPs through the cell wall of the bacteria and subsequent intracellular interactions with proteins and DNA, as observed in Raman spectroscopy. Also citrate-stabilized AgNPs tend to aggregate with time, especially when they are in reactive environment, like in contact with the bacteria. Part of the interparticle interaction energy released during aggregation is also added to the measured exothermicity. As compared with other macromolecules commonly studied using the ITC technique, *E. coli* substrates have large number of binding sites for AgNPs due to the presence of multiple functionalities and very large surface area (compared to NPs). Hence, this system is far more complex than typical ITC studies for a single ligand–substrate pair. Although the data can be fitted with a model of single set of N identical sites on a substrate, we could not extract the realistic number of binding sites or binding energy per particle due to the additional processes outlined above. Collectively, all the above interactions give an initial exothermicity of -1.547×10^{10} cal mol^{-1} of bacteria, which proves the high strength of interaction. This value of exothermicity is very high as compared with those that are observed for simpler interactions between biomolecules[49,50] but while considering the complexity of the system involving multiple interactions taking place at the same time, these values can be rationalized. Reproducibility of this data was ascertained (Figure S12, Supporting Information).

3. Conclusions

Raman and HSI were performed to understand the interaction of AgNPs with single bacterial cells. HSI supports the accumulation of AgNPs on the bacteria. Raman spectra and corresponding Raman images confirm the distribution of AgNPs within the bacteria. The time-dependent Raman study shows that when the incubation time exceeds an hour, degradation of DNA occurs, causing decrease in specific Raman signals of nucleotides. The interaction of AgNPs occurs mainly with proteins and DNA and their distribution inside the bacteria was shown by the cluster analysis of the Raman image of AgNPs-treated bacterium. While the interaction of AgNPs with bacteria was observable at the single-cell level due to SERS, Ag^+ ion interaction was not observable. Initial exothermicity of -1.547×10^{10} cal mol^{-1} was observed in ITC experiment, which proves the high strength of AgNP–*E. coli* interaction. While the present results confirm chemical degradation of DNA at NPs, additional systematic studies with fluorescence-activated cell sorting (FACS), inductively coupled plasma mass spectrometry (ICP-MS), and scanning transmission electron microscopy (STEM) are necessary to understand the fate of the living system. The accumulation of the Raman spectra from the particle from which plasmon spectrum is collected simultaneously will enable tracking of chemical processes at NPs in real time. This would provide dynamics of such events and we are in the process of developing such measurements.

4. Experimental Section

Materials: Silver nitrate and trisodium citrate were purchased from Rankem and Qualigens. All chemicals were used without further purification.

Synthesis of AgNPs: AgNPs were synthesized by the Turkevich method.[51] In this method, about 17 mg of silver nitrate was mixed with 100 mL of deionized water (1×10^{-3} M) and kept for heating at 100 °C. To this, 40 mg of trisodium citrate was added and boiled for 10 min, until a pale yellow color indicating the reduction of Ag^+ ions was obtained. The solution was cooled immediately under tap water. The final suspension of AgNPs shows a plasmon absorption peak at 420 nm. These particles are in the size range of 25 ± 8.5 nm as confirmed by TEM.

Incubation of E. coli Cells and Plasmid DNA with AgNPs and Ag^+ Ions: An overnight culture of *E. coli* (ATCC 25922) cells was subcultured in LB broth and grown at 37 °C with shaking for 4 h to obtain a log phase culture. The bacterial count was monitored by the conventional plate count method and by reading the optical density at 600 nm. Bacterial culture was centrifuged at 3000 rpm for 5 min and the resultant pellet was washed twice with triply distilled water and subsequently dispersed to eliminate broth interference in the experiment. About 5×10^5 cells from this were taken and added to 1×10^{-3} M concentration of 1 mL AgNPs (concentrations refer to the metal ion used in the synthesis). Assuming that all Ag^+ ions have been reduced to make AgNPs and assuming that most of the particles are spheres of 25 nm diameter, the molar concentration of AgNPs is 1.2×10^{-9} M. The cells were sampled at different time intervals such as 5, 10, 20, 30, and 60 min and visualized under HSI and confocal Raman microscope. Plasmid DNA was isolated

from untreated *E. coli* (DH5α) cells at the concentration of 100 ng μL^{-1} and incubated with AgNPs for 20 min and Raman measurements were carried out. A solution of Ag^+ ions was prepared by dissolving silver nitrate in double-distilled water at the concentration of 0.6×10^{-6} M. About 5×10^5 cells were incubated with 1 mL solution of Ag^+ ions for various incubation times and the respective samples were spotted for HSI and Raman measurements. For ITC analysis, *E. coli* was titrated against AgNPs. *E. coli* cell solution (1.62×10^{-14} M) of 40 μL was injected into 300 μL AgNPs solution (1.2×10^{-9} M) with the time spacing of 500 s between each injection.

Instrumentation Raman Spectroscopic Analysis: Confocal Raman measurements were obtained using a WiTec GmbH CRM Alpha 300 S instrument. The excitation source was 532 nm Nd:YAG laser and the maximum power output of the laser was 40 mW. The laser power was attenuated to ≈15 mW to the sampling point. Measurements were done using a 100× objective. The signal from the sample after excitation was sent to the spectrometer through a multimode fiber. The instrument has a super notch filter fixed in the path of the signal, which effectively cuts off the excitation radiation. The grating used had 600 grooves per mm, which gives a spectral resolution of 4.9 ± 1 cm^{-1}. The dispersed light intensity of the signal from the grating was measured by a Peltier-cooled charge-coupled device (CCD). The maximum area of laser exposure was 750 nm and the collection was done confocally. For most of the imaging measurements, a diffraction-limited spot size was used (the spatial resolution estimated for the 100× objective was 250 nm). The Raman images were collected with the desired area of 22 500 pixels (150 × 150) and Raman imaging was done with an integration time of 50 ms at each pixel. This imaging area corresponds to 8 × 8 μm. Single-spot spectra were taken with the integration time of 1 s. The spectra were collected in the 100–3500 cm^{-1} window. Cluster analysis of the Raman image was performed to segregate similar Raman spectra from the entire area scanned. For the Raman study, the sample solution was spotted on the cover glass and dried in ambience.

Hyperspectral Imaging Analysis: HSI measurements were performed using Cytoviva HSI system. For sample preparation, at each time point 0.5–1 μL sample was spotted on a 1-mm thick ultrasonically cleaned glass slide (SCHOTT) and it was covered with a 0.145-mm thick Nexterion Clean room cleaned glass coverslip (SCHOTT). Measurements were done using 100× oil (Cargille) immersion objective. Spectra were measured with the Specim V10E spectrometer (400–1000 nm) at the spectral resolution of ±1.5 nm. Spectral image analysis was done using the ENVI software.

Isothermal Calorimetry: ITC measurements were done using MicroCal iTC_{200} system (GE Healthcare Life Sciences). Triple-distilled water was used as the reference. Sample cell contained AgNPs solution (1.2×10^{-9} M) with a maximum volume of 300 μL, while bacterial solution of 40 μL having concentration of 1.62×10^{-14} M was used as titrant with the rotation of 200 rpm. Maolarity of AgNPs and bacteria was calculated using the below formula, respectively.

$$\text{Molarity of AgNPs} = \frac{6MA_r}{\pi D^3 \rho N_A}$$

Where M = molarity of $AgNO_3$; A_r= atomic weight in g mol^{-1}; D = diameter in cm; ρ = density in g cm^{-3}; N_A = Avogadro number.

$$\text{Molarity of bacteria} = \frac{N_{E.coli} \times df}{6.023 \times 10^{23}}$$

where

$N_{E.coli}$ = Number of *E. coli* in solution = $OD_{600} \times 10^9$; df = dilution factor

UV–Vis Spectroscopic Analysis: Ensemble-averaged UV–vis absorption spectra were recorded using a PerkinElmer Lambda 25 spectrophotometer.

Transmission Electron Microscopy Analysis: High-resolution transmission electron microscopy (HRTEM) of the sample was carried out using a JEOL 3010 instrument with an ultra high resolution (UHR) polepiece. TEM specimens were prepared by dropping one or two drops of aqueous solution to carbon-coated copper grids and drying under ambient conditions. Measurements were carried out at 200 kV.

Supporting Information

Supporting Information is available from the Wiley Online Library or from the author.

Acknowledgements

The authors thank the Department of Science and Technology (DST), Government of India for constantly supporting our research program on nanomaterials. The authors thank Dr. Nitish Mahapatra and Bhavani Shankar Sahu for providing plasmid DNA.

Received: April 24, 2013
Revised: May 23, 2013
Published online: July 1, 2013

[1] T. Pradeep, Anshup, *Thin Solid Films* **2009**, *517*, 6441.
[2] *Nanotechnology Applications for Clean Water,* (Eds: N. Savage, M. Diallo, J. Duncan, A. Street, R. Sustich), William Andrew, Norwich **2009**.
[3] M. S. Mauter, M. Elimelech, *Environ. Sci. Technol.* **2008**, *42*, 5843.
[4] D. Turkmen, V. Karakoc, L. Uzun, N. Ozturk, S. Akgol, A. Denizli, *Hacettepe J. Biol. Chem.* **2009**, *37*, 157.
[5] W. Tungittiplakorn, C. Cohen, L. W. Lion, *Environ. Sci. Technol.* **2005**, *39*, 1354.
[6] T. A. Dankovich, D. G. Gray, *Environ. Sci. Technol.* **2011**, *45*, 1992.
[7] A. D. Russell, in *Progress in Medicinal Chemistry* (Eds: G. P. Ellis, D. K. Luscombe), Elsevier Science, Amsterdam **1994**, 351–370.
[8] M. Udhaya Sankar, S. Aigal, S. M. Maliyekkal, A. Chaudhary, Anshup, A. Anil Kumar, K. Chaudhari, T. Pradeep, *Proc. Natl. Acad. Sci. USA* **2013**, *110*, 8459.
[9] M. Haruta, N. Yamada, T. Kobayashi, S. Iijima, *J. Catal.* **1989**, *115*, 301.
[10] A. S. Nair, T. Pradeep, *Curr. Sci.* **2003**, *84*, 1560.
[11] M. Conte, H. Miyamura, S. Kobayashi, V. Chechik, *J. Am. Chem. Soc.* **2009**, *131*, 7189.
[12] J. S. Kim, E. Kuk, K. M. Yu, J. H. Kim, S. J. Park, H. J. Lee, S. H. Kim, Y. K. Park, Y. H. Park, C. Y. Hwang, Y. K. Kim, Y. S. Lee, D. H. Jeong, M. H. Cho, *Nanomed. Nanotechnol. Biol. Med.* **2007**, *3*, 95.
[13] E. Hwang, J. Lee, Y. Chae, Y. Kim, B. Kim, B. Sang, M. Gu, *Small* **2008**, *4*, 746.
[14] I. Sondi, B. Salopek-Sondi, *J. Colloid Interface Sci.* **2004**, *275*, 177.
[15] W. R. Li, X. B. Xie, Q. S. Shi, H. Y. Zeng, Y. S. OU-Yang, Y. B. Chen, *Appl. Microbiol. Biotechnol.* **2010**, *85*, 1115.
[16] A. Smetana, K. Klabunde, G. Marchin, C. Sorensen, *Langmuir* **2008**, *24*, 7457.
[17] W. Yang, C. Shen, Q. Ji, H. An, J. Wang, Q. Liu, Z. Zhang, *Nanotechnology* **2009**, *20*, 085102.
[18] S. Shrivastava, T. Bera, A. Roy, G. Singh, P. Ramachandrarao, D. Dash, *Nanotechnology* **2007**, *18*, 225103.
[19] C. N. Lok, C. M. Ho, R. Chen, Q. Y. He, W. Y. Yu, H. Sun, P. K. Tam, J. F. Chiu, C. M. Chen, *J. Proteome Res.* **2006**, *5*, 916.
[20] S. K. Gogoi, P. Gopinath, A. Paul, A. Ramesh, S. S. Ghosh, A. Chattopadhyay, *Langmuir* **2006**, *22*, 9322.
[21] N. S. Wigginton, A. de Titta, F. Piccapietra, J. Dobias, V. J. Nesatyy, M. J. F. Suter, R. Bernier-Latmani, *Environ. Sci. Technol.* **2010**, *44*, 2163.

[22] R. Chen, P. Choudhary, R. N. Schurr, P. Bhattacharya, J. M. Brown, P. C. Ke, *Appl. Phys. Lett.* **2012**, *100*, 013703.
[23] S. Basu, S. Jana, S. Pande, T. Pal, *J. Colloid Interface Sci.* **2008**, *321*, 288.
[24] Z. M. Xiu, Q. B. Zhang, H. L. Puppala, V. L. Colvin, P. J. J. Alvarez, *Nano Lett.* **2012**, *12*, 4271.
[25] M. Kahraman, M. Muge Yazici, F. SahIn, O. F. Bayrak, E. TopCu, M. Culha, *Int. J. Environ. Anal. Chem.* **2007**, *87*, 763.
[26] S. Efrima, B. V. Bronk, *J. Phys. Chem. B* **1998**, *102*, 5947.
[27] R. M. Jarvis, A. Brooker, R. Goodacre, *Anal. Chem.* **2004**, *76*, 5198.
[28] A. Panacek, L. Kvitek, R. Prucek, M. Kolar, R. Vecerova, N. Pizurova, V. K. Sharma, T. Navecna, R. Zboril, *J. Phys. Chem. B* **2006**, *110*, 16248.
[29] S. Nath, S. K. Ghosh, S. Kundu, S. Praharaj, S. Panigrahi, T. Pal, *J. Nanopart. Res.* **2006**, *8*, 111.
[30] L. J. Goeller, M. R. Riley, *Appl. Spectrosc.* **2007**, *61*, 679.
[31] S. Chadha, R. Manoharan, P. Moenne-Loccoz, W. H. Nelson, W. L. Peticolas, J. F. Sperry, *Appl. Spectrosc.* **1993**, *47*, 38.
[32] Q. Wu, T. Hamilton, W. H. Nelson, S. Elliott, J. F. Sperry, M. Wu, *Anal. Chem.* **2001**, *73*, 3432.
[33] R. M. Jarvis, R. Goodacre, *FEMS Microbiol. Lett.* **2004**, *232*, 127.
[34] W. R. Premasiri, D. T. Moir, M. S. Klempner, N. Krieger, G. Jones II, L. D. Ziegler, *J. Phys. Chem. B* **2005**, *109*, 312.
[35] N. Malvadkar, P. Kao, H. Wang, D. L. Allara, M. C. Demirel, *Nanotechnology* **2008**, *2*, 555.
[36] K. A. Britton, R. A. Dalterio, W. H. Nelson, D. Britt, J. F. Sperry, *Appl. Spectrosc.* **1988**, *42*, 782.
[37] Q. Wu, W. H. Nelson, S. Elliot, J. F. Sperry, M. Feld, R. Dasari, R. Manoharan, *Anal. Chem.* **2000**, *72*, 2981.
[38] J. W. Chan, H. Winhold, M. H. Corzett, J. M. Ulloa, M. Cosman, R. Balhorn, T. Huser, *Cytometry Part A: J. Int. Soc. Anal. Cytol.* **2007**, *71*, 468.
[39] S. Singh, V. D'Britto, A. A. Prabhune, C. V. Ramana, A. Dhawan, B. L. V. Prasad, *New. J. Chem.* **2010**, *34*, 294.
[40] P. V. AshaRani, G. L. Kah Mun, M. Prakash Hande, V. Suresh, *ACS Nano* **2009**, *3*, 279.
[41] G. V. Pavan Kumar, S. Shruthi, B. Vibha, B. Ashok Reddy, T. K. Kundu, C. Narayana, *J. Phys. Chem. C* **2007**, *111*, 4388.
[42] H. Deng, V. A. Bloomfield, J. M. Benevides, G. J. Thomas Jr., *Nucl. Acids Res.* **2000**, *28*, 3379.
[43] H. Deng, V. A. Bloomfield, J. M. Benevides, G. J. Thomas Jr., *Biopolymers* **1999**, *50*, 656.
[44] D. Serban, J. M. Benevides, G. J. Thomas Jr., *Biochemistry* **2002**, *41*, 847.
[45] T. Diening, W. Ibach, in *Software Requirements and Data Analysis in Confocal Raman Microscopy* (Eds: T. Diening, O. Hollricher, J. Toporski), Springer, Berlin **2010**, 61–89.
[46] Q. L. Feng, J. Wu, G. Q. Chen, F. Z. Cui, T. N. Kim, J. O. Kim, *J. Biomed. Mater. Res.* **2000**, *52*, 662.
[47] K. B. Holt, A. J. Bard, *Biochemistry* **2005**, *44*, 13214.
[48] M. Yamanaka, K. Hara, J. Kudo, *Appl. Environ. Microbiol.* **2005**, *71*, 7589.
[49] A. Gourishankar, S. Shukla, K. N. Ganesh, M. Sastry, *J. Am. Chem. Soc.* **2004**, *126*, 13186.
[50] K. Chen, Y. Xu, S. Rana, O. R. Miranda, P. L. Dubin, V. M. Rotello, L. Sun, X. Guo, *Biomacromolecules* **2011**, *12*, 2552.
[51] J. Turkevich, P. C. Stevenson, J. Hillier, *Discuss. Faraday Soc.* **1951**, *11*, 55.

Particle
& Particle Systems Characterization

Supporting Information

for *Part. Part. Syst. Charact.*, DOI: 10.1002/ppsc. 201300165

Single-Cell Investigations of Silver Nanoparticle–Bacteria Interactions

Sudarsan Vishnupriya, Kamalesh Chaudhari, Ramya Jagannathan, and Thalappil Pradeep

Particle & Particle Systems Characterization
Submitted to

Supporting Information

for *Part. Part. Sys. Charact.*, DOI: 10.1002/ppsc.((please add manuscript number))

Single Cell Investigations of Silver Nanoparticle–Bacteria Interactions

*S. Vishnupriya, Kamalesh Chaudhari, Ramya Jagannathan and Thalappil Pradeep**

S1. Supporting information 1

TEM image of silver nanoparticles (AgNPs)

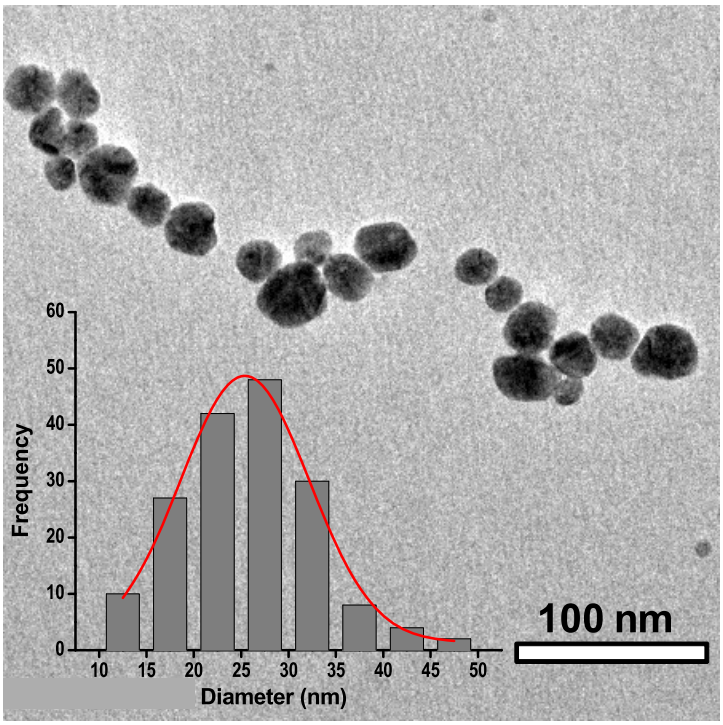

Figure S1. TEM image of silver nanoparticles (AgNPs). Inset: Size distribution of AgNPs plotted from multiple images. Synthesized NPs were of the size 25±8.5 nm. This polydispersity is common in citrate reduced AgNPs.

S2. Supporting information 2

Hyperspectral image of AgNPs and corresponding scattering spectra

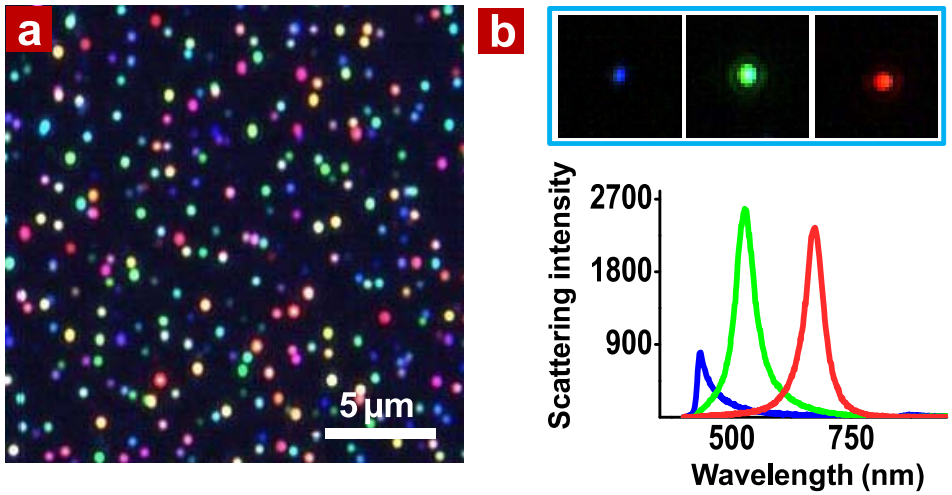

Figure S2. a) Large area hyperspectral image of AgNPs showing the polydisperse nature of the particles, b) enlarged images of single AgNPs of different sizes are shown with their respective scattering spectra.

S3. Supporting information 3

Hyperspectral image and scattering spectrum of untreated bacteria

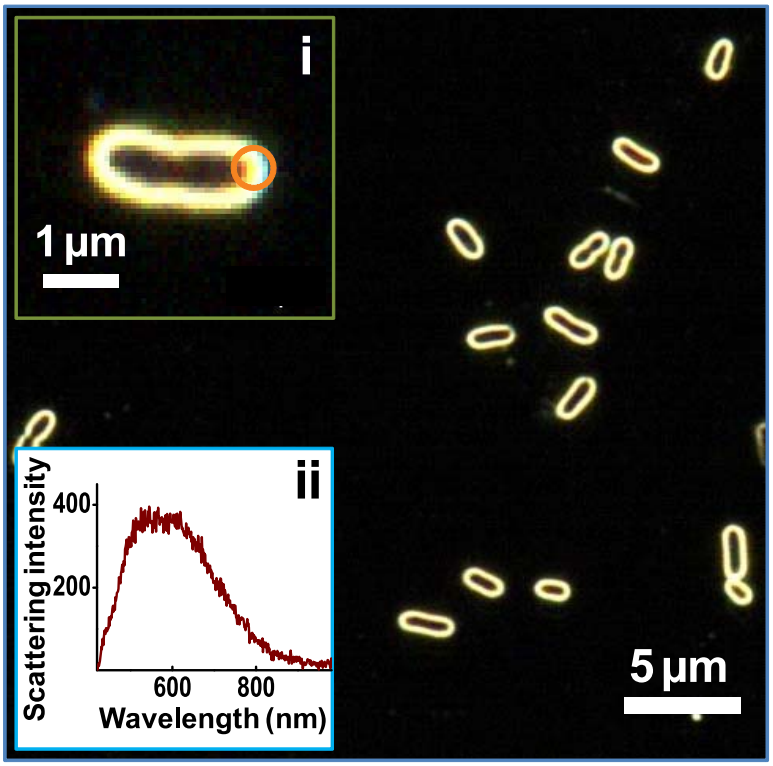

Figure S3. Large area hyperspectral image of untreated bacteria (control). (i) Enlarged image of a single bacterium and (ii) scattering spectrum of same bacterium taken from the encircled region in (i). Note the reduced intensity in comparison to the scattering spectrum from AgNPs (Figure S2). Images have been enhanced digitally.

S4. Supporting information 4

Time dependent study of AgNPs treated bacteria using HSI

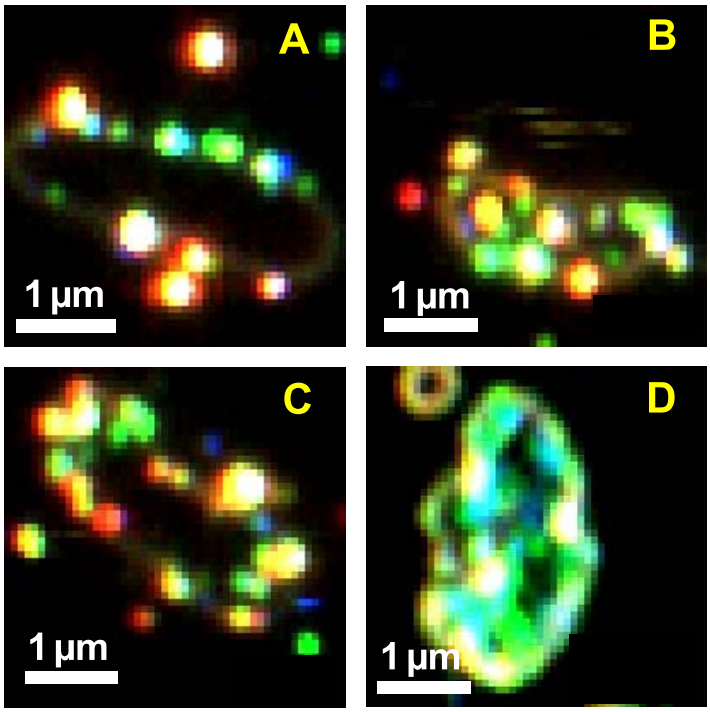

Figure S4. Hyperspectral images of AgNPs treated bacteria for various incubation periods A) 5 min, B) 10 min, C) 30 min and D) 60 min. Increase in the population of NPs attached to the bacterium can be seen with the increase in incubation time. Distortion in the morphology of the bacterium was seen after 60 minutes. The bacterial cell membrane is seen upon closer examination.

S5. Supporting information 5

Time dependent Raman measurements

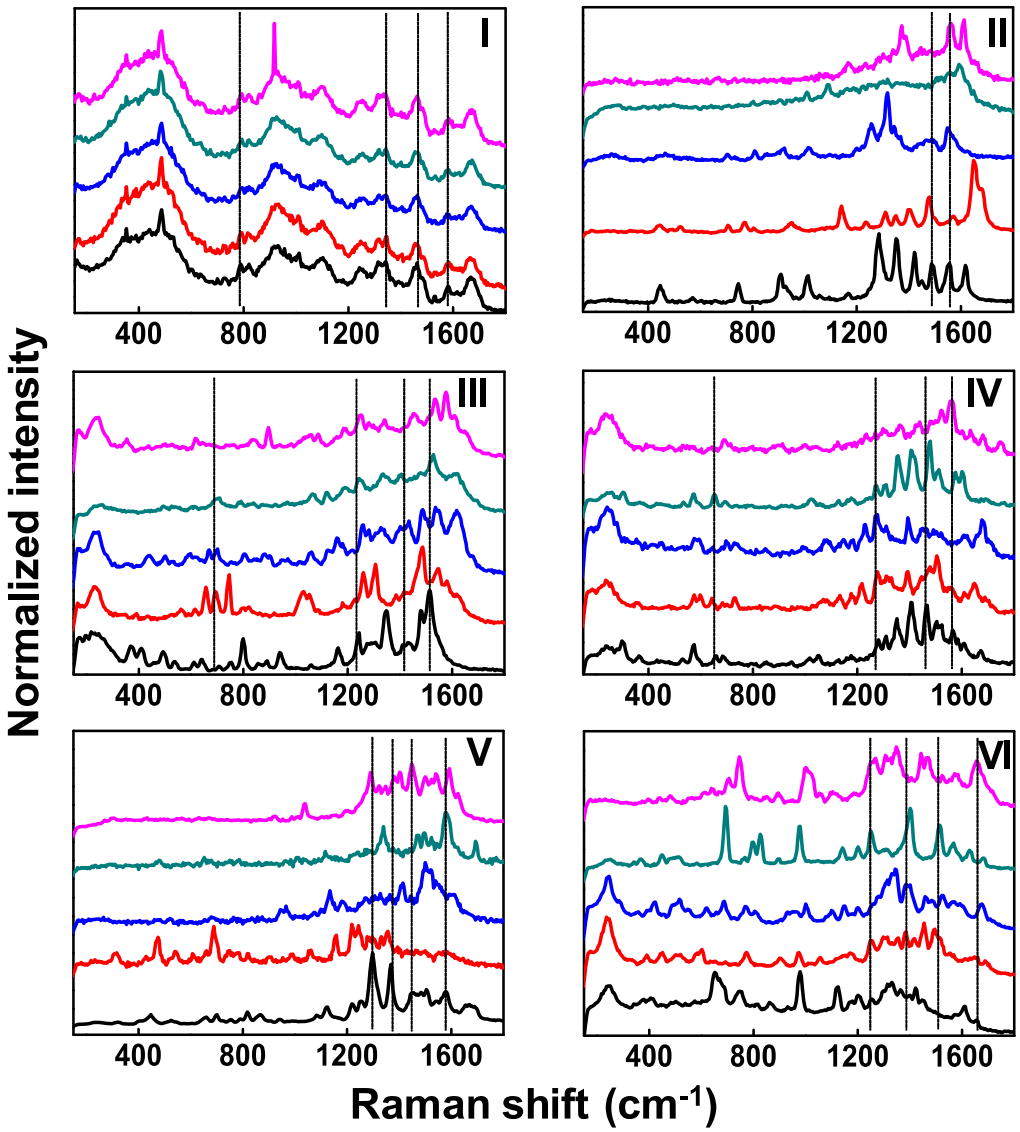

Figure S5. Comparison of the Raman spectra of untreated bacteria (I) and bacteria treated with AgNPs for increasing incubation times: 5, 10, 20, 30 and 60 minutes (II, III, IV, V and VI), respectively. To prove the reproducibility of Raman spectra, spectra from five different bacteria at each time point were measured and compared. These are stacked in each set. Reproducible features of DNA are marked with lines. It may be noted that reproducibility does not imply exact peak shape. Assignments of the peaks were done using previous reports on Raman spectroscopy of bacteria (Table S6). [31-39]

S6. Supporting information 6

Table S6. Assignments of Raman peaks of untreated and AgNPs-treated *E. coli* cells for various time intervals: 5, 10, 20, 30 and 60 minutes. Assignments were done by matching with reported frequencies within ±7 cm^{-1}. Note: bk, dAMP, dGMP, dCMP and dUMP refer to backbone, deoxyadenosine monophosphate, deoxyguanosine monophosphate, deoxycytosine monophosphate and deoxyuridine monophosphate, respectively. The assignments are based on various reports.[31-39]

S. No.	Peaks (cm^{-1})	Assignments	S. No.	Peaks (cm^{-1})	Assignments
1.	657	Guanine, Tyrosine[36]	24.	1341	Adenine, Guanine of DNA/RNA, CH def. of protein[31]
2.	677, 685	dGMP[32]	25.	1342	Tryptophan[32]
3.	726	Adenine[39]	26.	1347	Adenosine and Guanosine[37]
4.	769	Tryptophan[33]	27.	1353	Tryptophan[37]
5.	789	dCMP[32]	28.	1385	Adenine, Guanine[37]
6.	930	DNA bk[39]	29.	1392, 1393, 1396	Uridine[38]
7.	979	Membrane phospholipids[35]	30.	1444	Guanine, Adenine, CH def. of DNA/RNA, CH def. of proteins, lipids, carbohydrates[31]
8.	1002	Phenylalanine[31]	31.	1462, 1463	Guanine, Adenine, CH def. of DNA/RNA, CH def. of proteins, lipids, carbohydrates[31]
9.	1011, 1012	Tryptophan[32]	32.	1471	dUMP[32]
10.	1037	Phenylalanine of protein[31]	33.	1480, 1481, 1482	dAMP[32]
11.	1059	Lipid layer fluidity[35]	34.	1503	Adenosine[38]
12.	1069	C-N str. of proteins, chain C-C str. of lipids[31]	35.	1522, 1525	Cytidine[34]
13.	1090	DNA:O-P-O^- [39]	36.	1529	dCMP[32]
14.	1128, 1132	Protein/lipids/ carbohydrates[31]	37.	1537	Cytidine[37]
15.	1178	Tyrosine[33]	38.	1556	Tryptophan[32]

16.	1185	Tyrosine[32]	39.	1570, 1572	Guanine+Adenine[33]
17.	1230, 1232	Uridine[38]	40.	1581	dAMP[32]
18.	1243, 1244	Thymidine[38]	41.	1592	Adenine ring stretching[36]
19.	1251, 1252	Cytidine[38]	42.	1602	Phenylalanine[32]
20.	1275, 1278	Thymidine[38]	43.	1610	Phenylalanine, Tyrosine[31]
21.	1289	dCMP[32]	44.	1613, 1616	Tryptophan+Tyrosine[33]
22.	1314, 1315	Guanine of DNA/RNA, CH def. of protein[31]	45.	1657	dCMP[32]
23.	1328	Adenine, Guanine, Tyrosine[34]	46.	1683	dGMP[32]

S7. Supporting information 7

Optical images of *E. coli* treated with AgNPs for various time intervals

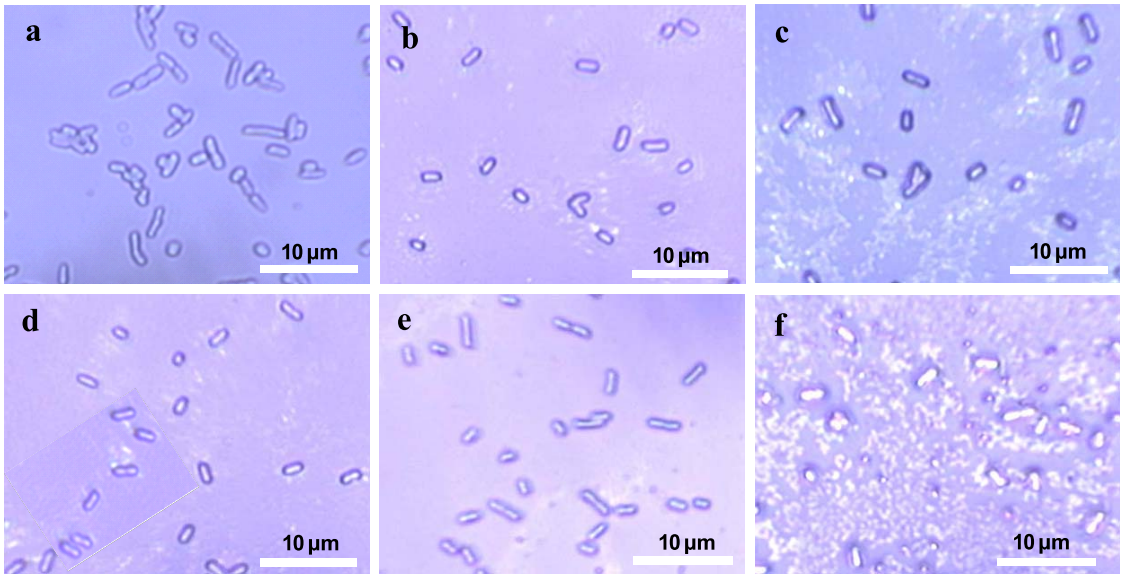

Figure S7. Optical images of untreated bacteria and bacteria treated with AgNPs. Control bacteria (a), and bacteria treated with silver NPs for various incubation times: 5, 10, 20, 30 and 60 minutes (b, c, d, e and f, respectively). Visible change in the bacterial morphology was observed upon longer incubation (f).

S8. Supporting information 8

Table S8. Raman peak assignments of plasmid DNA isolated from control *E. coli* treated with AgNPs. Assignments were done considering an error of ±6 cm^{-1}. Note: **d–**vibration localized in the deoxyribose moiety, **dA, dT, dG, dC–**deoxynucleosides A, T, G, C, **bk-**DNA backbone, **δ–** deformation vibration.[45] The assignments are based on various literature reports.[32,36,38,43-45]

S. No.	Peaks (cm^{-1})	Assignments	S. No.	Peaks (cm^{-1})	Assignments
1.	1670	dT (C=O str.)[43,44]	15.	1331	Guanosine[38]
2.	1605	dC, dG, dA[44]	16.	1315	dG[44]
3.	1591	Adenine ring stretching[36]	17.	1300	Cytidine[38]
4.	1580	Adenosine[44]	18.	1282	Cytosine[32]
5.	1573	Guanosine[38]	19.	1260	dA, dC[45]
6.	1524	dC[44]	20.	1243	dT, dC[44]
7.	1512	dA[44]	21.	1172	dG[44]
8.	1478	Adenosine[38]	22.	1151	dT[44]
9.	1462	d(5'-CH_2δ)[44]	23.	1098	bk (PO_2^- str.)[43,44]
10.	1440	d(CH_2δ)[44]	24.	1085	γ(PO_2^-)[45]
11.	1410	Thymidine[38]	25.	1001	d[44]
12.	1377	dT[43]	26.	976	d[44]
13.	1366	Guanosine[38]	27.	923	d[44]
14.	1339	dA, dG[44]	28.	684	dG[43,44]

S9. Supporting information 9

Time dependent Raman analysis of *E. coli* with Ag^+ ions

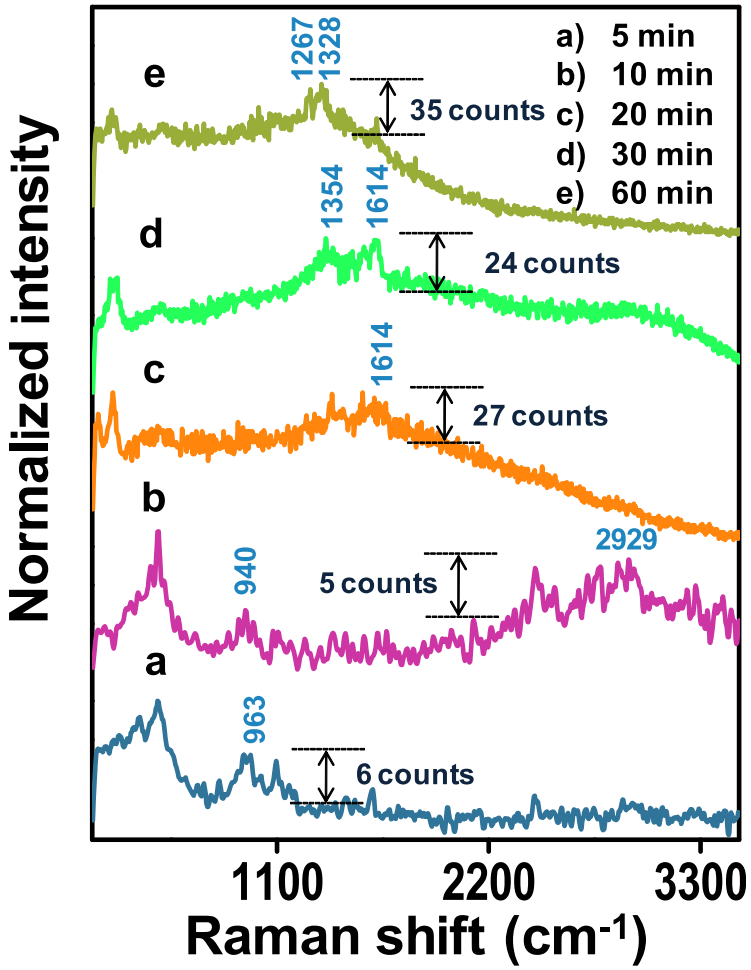

Figure S9. Raman spectra of *E. coli* treated with Ag^+ ions for various time intervals: 5, 10, 20, 30 and 60 minutes. There was no enhancement of peaks in the Raman spectra. Reproducible features are marked on the traces and their assignments are listed in Table S10.[27,31-35,37]

S10. Supporting information 10

Table S10. Assignments of Raman peaks of *E. coli* treated with Ag^{+} ions for various incubation periods (5, 10, 20, 30 and 60 minutes).[27,31-35,37]

S. No	Peaks (cm^{-1})	Assignments
1.	940	α-helix of protein, carbohydrate[31]
2.	963	Membrane phospholipids[35]
3.	1354, 1555, 1614	Tryptophan[37,32,33]
4.	1267	C-O-C modes of pyranose rings[27]
5.	1328	Tyrosine[34]
6.	2929	C-H stretching region[35]

S11. Supporting information 11

Time dependent HSI analysis of *E. coli* treated with Ag^+ ions

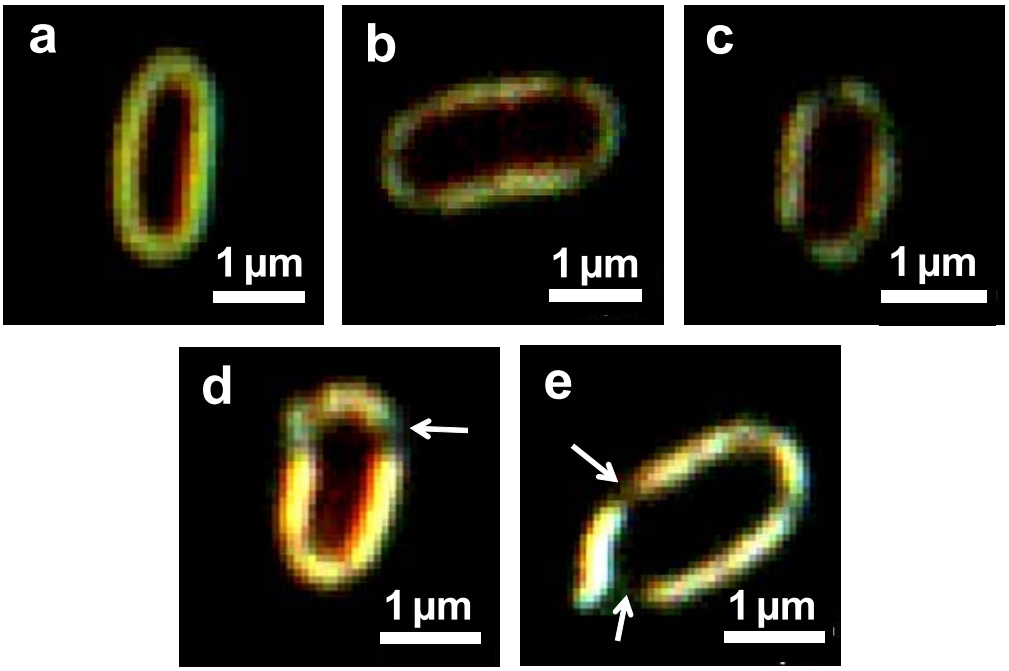

Figure S11. Images obtained from hyperspectral analysis of Ag^+ ion treated *E. coli* for various incubation periods a) 5 min, b) 10 min, c) 20 min, d) 30 min and e) 60 min. For incubation time more than 30 minutes, lysis of the cell membrane of the bacterium was seen as indicated by arrow.

S12. Supporting information 12

ITC measurement of the interaction of AgNPs with bacteria

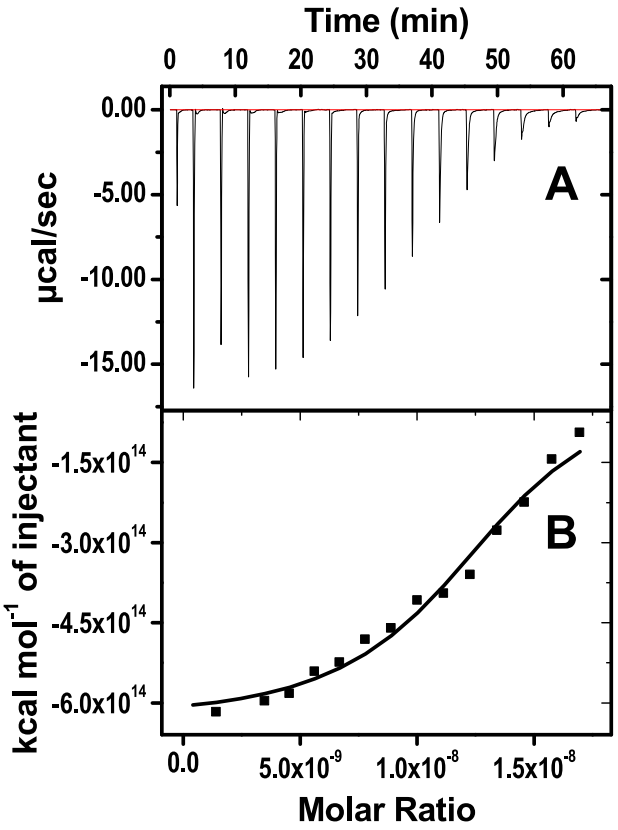

Figure S12. (A) ITC responses for the titration of *E. coli* with the AgNPs. (B) Integrated calorimetric response plotted against the molar ratio of *E. coli*/AgNPs (concentrations – 1.62 x 10^{-14} M/1.2 x 10^{-9} M). Volume of 2.5 µL was injected for every injections with the time gap of 250 seconds.

Langmuir

Article

pubs.acs.org/Langmuir

Facile and Rapid Synthesis of a Dithiol-Protected Ag_7 Quantum Cluster for Selective Adsorption of Cationic Dyes

M. S. Bootharaju and T. Pradeep*

DST Unit of Nanoscience (DST UNS), Department of Chemistry, Indian Institute of Technology Madras, Chennai 600 036, India

Supporting Information

ABSTRACT: We report a facile and rapid (less than 15 min) synthesis of atomically precise, dithiol-protected, silver quantum cluster, $Ag_7(DMSA)_4$ (DMSA: meso-2,3-dimercaptosuccinic acid), through a modified solid state route. The as-synthesized cluster exhibits molecular optical absorption features with a prominent λ_{max} at ~500 nm. Composition of the cluster was confirmed using various spectroscopic and microscopic techniques such as electrospray ionization mass spectrometry (ESI MS), X-ray photoelectron spectroscopy (XPS), X-ray diffraction (XRD), Fourier transform infrared spectroscopy (FTIR), scanning electron microscopy (SEM), transmission electron microscopy (TEM), and energy dispersive analysis of X-rays (EDAX). Clusters supported on neutral alumina have been shown as better adsorbents for selective adsorption of cationic dyes (over anionic dyes) from water. This selectivity for cationic dyes was evaluated by zeta potential (ζ) measurements. The efficiency of clusters for removal of dyes is very high when compared to nanoparticles (NPs) protected with ligands (citrate and mercaptosuccinic acid (MSA)) possessing similar chemical structures as that of DMSA. The higher efficiency of clusters for the removal of dyes is attributed to their smaller size and large surface area compared to the NPs in addition to favorable electrostatic interactions between the clusters and cationic dyes. Adsorption of dyes (cationic and anionic) was enhanced when dye molecules contain hydrogen bond forming functional groups. Supported clusters have been reused up to five cycles without the loss of activity once the adsorbed dye is extracted using suitable solvents.

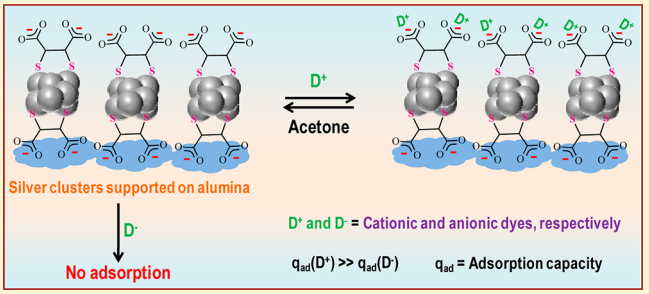

INTRODUCTION

Research on monolayer-protected noble metal (Au, Ag, Cu, Pt, and Pd) quantum clusters is progressively increasing due to their unique and unusual optical, physical, and chemical properties.[1−6] These nanosystems are falling (in length scale) in-between molecules and quantum dots/NPs. The typical cluster size regime is less than 2 nm. Clusters of gold, protected with both water- and organic-soluble ligands, are extensively studied compared to silver analogues. Crystal structures of some of the gold clusters, $Au_{25}(SC_2H_4Ph)_{18}$,[7,8] $Au_{36}(SPh\text{-}tBu)_{24}$,[9] $Au_{38}(SC_2H_4Ph)_{24}$,[10] $Au_{102}(p\text{-}MBA)_{44}$,[11] and $\{[Au_{24}(PPh_3)_{10}(SC_2H_4Ph)_5Cl_2]^+\}$,[12] have been solved. The crystallization of silver clusters is difficult as they are usually less stable compared to the gold ones. However, the crystal structure of $Ag_{14}(SC_6H_3F_2)_{12}(PPh_3)_8$ has been obtained recently.[13] Silver and gold clusters exhibit applications in a variety of fields such as catalysis,[14] sensing,[15,16] biology,[17,18] and electrochemistry.[19] There are numerous methods in the literature for the synthesis of these systems which include interfacial etching,[20] core etching,[21] galvanic exchange,[22] microwave irradiation,[23] sonochemical methods,[24] sunlight-assisted methods[25] and reactions in gel media.[26] Protein-[27] and polymer-coated[23] metal clusters have also been reported. The important and desirable aspects to be considered in the synthesis of clusters are easiness to handle the reaction, short synthesis time and high yield of the product. One of the simple methods to synthesize silver clusters is grinding the precursors of metal and ligand in the solid state, followed by reduction with a reducing agent. Using this method, $Ag_9(MSA)_7$[4] and $Ag_{152}(SC_2H_4Ph)_{60}$[28] clusters have been synthesized. This method is also extended for the synthesis of NPs of C_{60} by grinding C_{60} powder using mortar and pestle.[29]

One of the important aspects of synthesis of clusters is utilizing them for various applications. The luminescence and absorption features of the clusters are very sensitive to metal ions and molecules. This sensitivity is relevant to the environment, particularly water. The luminescence of clusters may be quenched or enhanced depending on the nature of interaction with an analyte.[30−32] Certain clusters exhibit unusual reactivity with ions owing to their small size and large surface area.[33] In this paper, we use this emerging category of materials for an application of relevance to developing societies.

Organic dyes[34] used in textiles, leather, printing, cosmetics, and other industries[34−36] are main water contaminants in industrial areas. Presence of dyes in environment to a degree

Received: March 30, 2013
Revised: May 23, 2013
Published: May 24, 2013

   dx.doi.org/10.1021/la401180r | Langmuir 2013, 29, 8125−8132

greater than the tolerable levels causes undesirable effects not only on the environment but also on human health. The potential toxicity of various azo dyes has been known for a long time. Certain azo dyes are not being used since they are carcinogens.[37] Disazo dyes, based on benzidine, are also found to cause cancer.[38] The presence of these coloring materials in water bodies adversely affects the photosynthetic activity of aquatic life. Also, it reduces the light penetration and increases the chemical oxygen demand (COD).[39] Therefore, it is important to remove them from wastewater. There are two types of dyes, namely, cationic (D^+) and anionic (D^-). Removal of dyes is not a simple task due to the resistance of dyes to aerobic digestion and to biodegradability. Their resistance is due to the presence of stable aromatic rings in their structures. The most commonly used methods to decontaminate wastewater from dyes are coagulation,[40] adsorption,[41,42] oxidation,[43] membrane filtration,[44] photocatalysis,[34,45] biological treatment,[46] etc. Among these, all except adsorption are expensive methods. There are many advantages in adsorption which include simplicity of operation and flexibility in design, high efficiency, recyclability, and insensitivity to toxic substances. Adsorption is prominent when the surface area of the adsorbent is large.

Nanomaterials are important in the purification of water as they exhibit high surface area with a large number of active adsorption sites.[47] In the recent past, several nanomaterials were explored in this context. Importantly, carbon-based materials, such as graphene, graphene−metal/metal oxide composites, carbon nanospheres (CNS), carbon nanotubes (CNT), and activated carbon, show promising adsorption capacities toward dyes.[47,48] Other materials such as polymer-based adsorbents, iron oxide NPs, bimetallic nanosystems, clays, and zeolites are also used for the adsorption of dyes.[36,49] When magnetic NPs are used as adsorbents, the separation of dye-adsorbed NPs from water is achieved simply by using a bar magnet. Noble metal nanoparticles (NPs) are shown to have applications in water purification.[50,51] As clusters are smaller in size compared to NPs, they are expected to exhibit higher surface area and reactivity.

In this paper, we report the facile synthesis and application of atomically precise Ag_7 cluster protected with meso-2,3-dimercaptosuccinic acid (DMSA), having the formula $Ag_7(DMSA_4)$. It is prepared according to the method originally reported for $Ag_9(MSA)_7$,[4] with some modifications in synthesis conditions. Molecular formula of the cluster is obtained by mass spectrometric analysis. The cluster was characterized using various spectroscopic tools. The cluster was synthesized in the solution phase previously by Z. Wu et al.,[52] wherein, synthesis was completed in 12 h. In our method, we achieved it in less than 15 min. As-prepared clusters are supported on neutral alumina and tested for the removal of rhodamine 6G (R6G), methylene blue (MB) and malachite green (MG) [which are cationic] and eriochrome black T (EBT), methyl orange (MO) and methyl red (MR) [which are anionic]. We found that our material shows selectivity toward cationic dyes probably due to favorable electrostatic interactions. The effect of substrate, alumina, was also evaluated. The efficiency of clusters for the removal of dyes is compared with that of Ag NPs protected with (i) trisodium citrate and (ii) mercaptosuccinic acid. Although silver is expensive than carbon and iron-based materials for the removal of dyes, percentage loading of cluster is very less (0.4 wt %). Synthesis of this cluster is easier than other materials in terms of time, easy loading and other factors. The material was found to be recyclable for large number of cycles which makes the present clusters important for this application.

EXPERIMENTAL SECTION

Materials. Silver nitrate ($AgNO_3$; CDH, India), trisodium citrate (TSC, Qualigens), mercaptosuccinic acid (MSA), meso-2,3-dimercaptosuccinic acid (DMSA), sodium borohydride (Sigma Aldrich), and methyl alcohol were received from various laboratories and used as such without further purification. Neutral alumina (60−325 mesh, BSS) was supplied by SRL, India. The BET surface area of alumina was 80.4 m^2/g, and the mean particle size was 0.13 mm. Pore size distribution was 50−60 Å. Dye molecules, rhodamine 6G chloride (R6G), methylene blue (MB), malachite green (MG), eriochrome black T (EBT), methyl orange (MO), and methyl red (MR) were obtained from Sigma Aldrich and used as-received with no further purification.

Synthesis of $Ag_7(DMSA)_4$. The $Ag_7(DMSA)_4$ cluster was synthesized according to the method used for synthesis of $Ag_9(MSA)_7$,[4] with some modifications. Briefly, 23 mg $AgNO_3$ and 25 mg DMSA (1:1 mol ratio) were ground to get a reddish brown thiolate (within 2−3 min.). After that, 25 mg $NaBH_4$ powder was added and grinding was continued for 3−4 min. A quantity of 6 mL ice-cold water was added dropwise to the above mixture along with grinding. The resultant black solution was poured into excess methyl alcohol (nearly 15 mL) which was kept at 0−5 °C. The reddish brown precipitate formed was washed 3−4 times by dispersion and centrifugation using methyl alcohol to remove excess ligand and excess reducing agent. Methyl alcohol was evaporated using a rotary evaporator to get the cluster in powder form.

Preparation of Supported Clusters. A known quantity of cluster in powder form was dissolved in a known volume of water which gives a reddish brown solution. To this, a known amount of neutral alumina was added followed by gentle shaking. This leads to the adsorption of clusters on alumina surface which could be visually observed as the intensity of the brown color of the supernatant decreases while the colorless alumina becomes increasingly colored. At a certain stage of alumina addition, the color of the solution disappeared completely. The absence of cluster in the supernatant was ensured using UV/vis absorption spectroscopy. At the point of surface saturation of alumina, 4 mg of cluster was adsorbed per 1 g of alumina (0.4 wt %).

Synthesis of Ag@citrate and Ag@MSA NPs. Citrate-[53] and MSA-protected[20] Ag NPs were synthesized according to previously reported protocols: (1) To a boiling aqueous solution of $AgNO_3$, trisodium citrate solution was added. Boiling was continued till the solution turned yellow in color. A solution of Ag@citrate was cooled under tap water. (2) The Ag@MSA NPs were synthesized by reducing methyl alcoholic Ag(I)MSA thiolate with aqueous sodium borohydride solution. The resulting black precipitate was washed several times with methyl alcohol to remove excess ligand, and finally methyl alcohol was evaporated to get NPs in powder form. Alumina-supported NPs were prepared as described earlier (at a loading of ∼0.5 wt %). The ligand, DMSA was supported on alumina (500 mg) by stirring a 5 mL solution of DMSA (12 mg/mL, pH 10) at 500 rpm for 15 min. After that, alumina was washed 4 times with distilled water to remove excess DMSA. The presence of DMSA on alumina was confirmed using FTIR spectroscopy.

Adsorption of Dyes onto Supported Clusters/NPs. For this study, 500 mg of supported nanomaterial was separately treated with 3 mL of 5 ppm cationic and anionic dyes. These mixtures were subjected to gentle shaking using a mechanical shaker for the required duration, at room temperature (25 °C). For reuse of the used material, adsorbed dyes were extracted into acetone/ethanol (three times, 4 mL each time). Extraction of dyes was evident by the appearance of color of the dye in the solvent. After extraction of the dye, the adsorbent material was dried in ambience for about 1 min and used for successive adsorption and desorption cycles. The capacity of adsorption (q_e) of dye was calculated using the equation $q_e = (C_0 - C_e)V/m$ mg/g. Here, q_e is the adsorption capacity in mg of dye per gram of cluster excluding

dx.doi.org/10.1021/la401180r | Langmuir 2013, 29, 8125−8132

the mass of alumina, C_0 and C_e are initial and equilibrium concentrations, respectively, in the supernatant of dye solution expressed in mg per liter, V is the volume of solution in mL, and m is the mass of adsorbent in mg.

Instrumentation. UV/vis absorption spectra were recorded using a PerkinElmer Lambda 25 instrument in the spectral range of 200 to 1100 nm. HRTEM of the samples was carried out using a JEOL 3010 instrument with a UHR pole piece. Specimens for TEM analysis were prepared by placing one or two drops of aqueous solution on carbon-coated copper grids and allowing them to dry at room temperature overnight. All measurements were done at 200 kV in order to minimize the damage to the sample by the high energy electron beam. SEM images and EDAX studies were carried out using a FEI QUANTA-200 SEM. For SEM measurements, samples were drop-casted on an indium tin oxide (ITO)-coated conducting glass followed by drying in ambience. The FTIR spectra were recorded using a PerkinElmer Spectrum One instrument. KBr crystals were used as the matrix for preparing the samples. XPS measurements were done using an Omicron ESCA Probe spectrometer with polychromatic Al Kα X-rays ($h\nu$ = 1486.6 eV). The X-ray power applied was 300 W. The pass energy was 50 eV for survey scans and 20 eV for specific regions. The sample solution was spotted on a molybdenum plate and dried in vacuum. Supported cluster powder was pressed as pellets and pasted on the sample plate using conducting carbon tape. The base pressure of the instrument was 5.0 × 10^{-10} mbar. The binding energy was calibrated with respect to the adventitious C 1s feature at 285.0 eV. Most of the spectra were deconvoluted to their component peaks, using the software CASA-XPS. XRD data were obtained with a Shimadzu XD-D1 diffractometer using Cu Kα (λ = 1.54 Å) radiation. The samples were scanned in the 2θ range of 10 to 90°. The ESI mass spectrometric measurements were done in the negative mode using LTQ XL instrument, with m/z = 150−4000. Here, the spray and the extraction are orthogonal to each other. The clusters obtained were dispersed in 1:1 water−methanol solution and used for the measurements. The samples were electrosprayed at a flow rate of 10 μL/min at a temperature of 150 °C. The spectra were averaged for 75 scans. BET surface areas of alumina and supported clusters were measured on the basis of N_2 adsorption−desorption isotherms using MICROMERITICS ASAP 2020 Porosimeter. Zeta potential (ζ) measurements were performed with a HORIBA instrument.

RESULTS AND DISCUSSION

Characterization of As-Prepared Material. As-synthesized material was characterized by various analytical tools. The absorption spectrum of Ag@DMSA in water shows a sharp peak at 500 nm with a shoulder around 620 nm as shown in Figure 1. These features indicate the absence of plasmonic NPs which generally exhibit surface plasmon resonance around 400 nm.[53] The photographs of as-prepared clusters in powder and in solution form (a and b, respectively) are shown as insets of Figure 1. Inset c is a cartoonic representation of the silver cluster protected by DMSA ligand.

As-obtained Ag@DMSA was subjected to electrospray ionization mass spectrometry (ESI MS). Negative mode ESI MS of the cluster in a 1:1 water−methanol mixture, up to m/z = 4000, is shown in Figure 2. It consists of only two major sets of peaks around m/z = 720−800 and 480−540. After careful analysis, these were assigned to doubly and triply charged $Ag_7(DMSA)_4$ ions, respectively, as shown in Figure 2. Expanded view of the spectrum of the doubly charged ion is shown as inset a. On top of graph (a), expected positions for the addition of 0−6 sodium ions are depicted. The MS consists of a series of peaks separated by m/z = 11. This observation confirms the presence of sodium (mass 23) in the doubly charged ions, which substitutes hydrogen, explaining the mass difference (Na−H, 22/2 = 11). Presence of sodium is due to sodium borohydride used in the synthesis. As the DMSA ligand

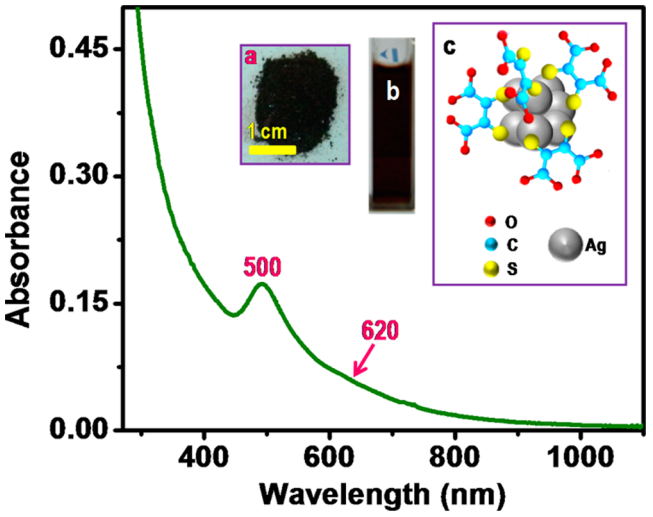

Figure 1. UV/vis absorption spectrum of as-synthesized Ag@DMSA cluster. Insets are photographs of the as-prepared cluster in powder and aqueous solution forms (a and b, respectively). Schematic representation of the cluster is shown in inset c.

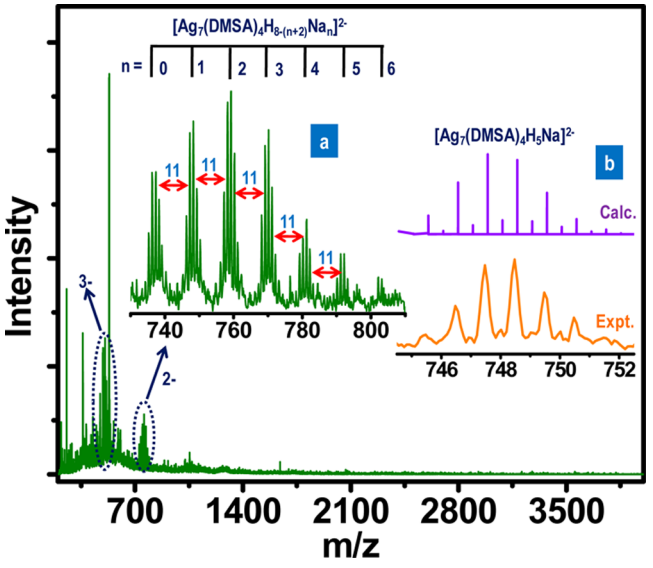

Figure 2. ESI MS of as-synthesized silver clusters (in 1:1 water−methanol volume ratio) in −ve mode. Insets are expanded views of the spectrum of doubly charged species along with sodium adducts. Inset a: Expanded view in m/z = 730−810 range corresponding to the addition of 0−6 Na. Inset b: Expanded view in m/z = 745−752 range corresponding to one sodium addition, $[Ag_7(DMSA)_4H_5Na]^{2-}$. Each peak in the m/z = 730−810 window shows similar isotope distribution.

is a dicarboxylic acid, carboxylic groups can interact with sodium ions. Since there are 8 ligands in the cluster, we can see 6 sodiums added and the remaining two carboxylates are contributing to overall charge. To confirm the chemical formula for this ion, the mass spectrum was calculated for the formula $[Ag_7(DMSA)_4H_5Na]^{2-}$ and compared with the experimental spectrum (inset b). Experimentally observed peaks match well with the calculated peaks confirming the validity of peak assignments.

The spectrum of triply charged ion is expanded and shown in Supporting Information, Figure S1A. The separation of peaks is at a mass of 7.3 which corresponds to the mass of sodium (7.3

dx.doi.org/10.1021/la401180r | Langmuir 2013, 29, 8125−8132

× 3 = 22, substitution of Na in place of H corresponds to the mass difference 22). Similar to the spectrum of the doubly charged ion, there are five peaks corresponding to the five added sodium ions. The remaining three carboxylate groups (out of eight) are contributing to the charge on the ion. For further confirmation, the calculated mass spectrum for the formula $[Ag_7(DMSA)_4H_5]^{3-}$ is compared with the experimental mass spectrum. The peaks match very well (inset of Figure S1B). For additional confirmation, one can go for MS^2 of a particular ion. MS^2 of the species at m/z = 747.4, corresponding to the mono sodium salt of the doubly charged species $[Ag_7(DMSA)_4H_5Na]^{2-}$ is shown in Figure S1B at a nominal collision energy of 15 eV. The major peak is at m/z = 673.4, corresponding to the loss of one DMSA ligand without sulfur [74 = (180−32)/2]. This confirms the assignment. The MS^2 of other species also shows the loss of ligand minus the bonded sulfur, as observed in the previous report.[52] Formation of cluster composition is proved using other spectroscopic tools. Comparison of the FTIR data (Figure S2) of the cluster and the lignad shows the absence of S−H stretching frequency (at 2550 cm^{-1} in parent DMSA) in the cluster, indicating the binding of Ag with the ligand through the S atom. The other characteristic peaks of the ligand are also present, but they are shifted and broadened with respect to that of the parent ligand. This shift and the broadening again confirm the protection of the cluster by the DMSA ligand. SEM-EDAX analysis of the cluster confirms the presence of main elements, Ag, S, and Na, as shown in Figure S3. A large aggregate of clusters was mapped using EDAX. The quantification table of elements suggests the atomic ratio between Ag and S as 0.90 which is close to the composition obtained from MS analysis (0.88). An XPS survey spectrum of the cluster clearly shows the presence of the expected elements, C, S, O, Ag, and Na (Figure 3A). Ag $3d_{5/2}$ is at 368.0 eV (Figure 3B) which is in between that expected for Ag^+ and bulk Ag^0 (367.5 and 368.2 eV, respectively).[22] This shows silver to have more reduced character (Ag^0). Insets of Figure 3A are C 1s and S 2p regions. The C 1s peaks appearing at 285.0, 288.0, and 290.0 eV are assigned to C in C−C, −COO, and possibly, −COONa, respectively. The S $2p_{3/2}$ peak, appearing at 162.0 eV, confirms the presence of S in the thiolate form. Although, MS analysis suggests the presence of a free S−H, we detect in XPS only one type of S. The atomic ratio between Ag and S is found to be 0.91 which is also close to the ratio obtained from MS analysis. TEM (Figure S4A) of cluster confirms the absence of NPs. However, after electron beam irradiation, there was growth of clusters to form aggregates (inset of Figure S4B). This sensitivity to electron beam is common for several silver clusters. XRD also confirms the absence of diffraction peaks corresponding to the NPs or bulk silver (Figure S4B). From all of these observations, formation of clusters in pure form is confirmed.

Application of Clusters in Removal of Dyes. For this study, $Ag_7(DMSA)_4$ clusters were supported on neutral alumina. The advantage of supported clusters is their recyclability. The supported clusters were characterized using SEM-EDAX and XPS techniques. SEM-EDAX analysis shows the presence of the elements in the cluster, Ag and S (Figure S5). The XPS data show the presence of Ag in the zerovalent state as that of parent clusters. Visual inspection of the parent alumina and supported clusters (photographs in Figure 4) support the adsorption of clusters. Nearly 500 mg of supported clusters was treated with 3 mL of 5 ppm R6G for 10 and 15 min. The absorption spectra of residual R6G were recorded and

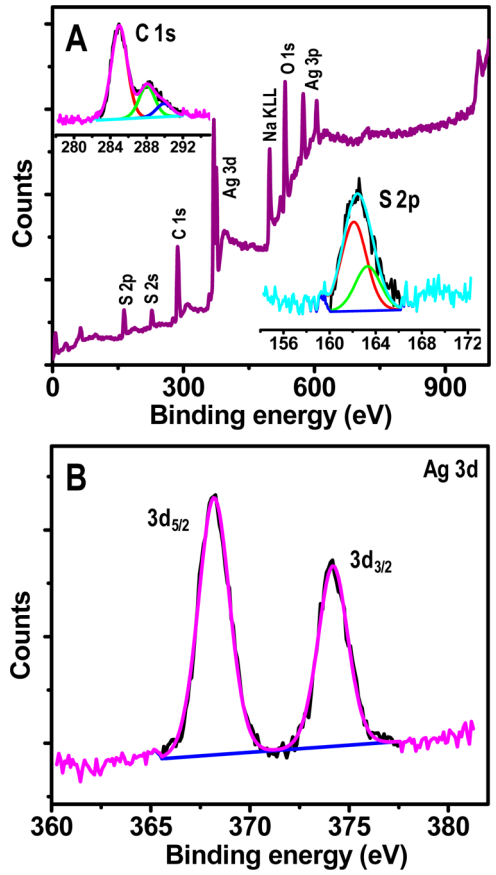

Figure 3. (A) XPS survey spectrum of silver clusters in which the various features are labeled. Insets are C 1s and S 2p regions. (B) Expanded spectrum in the Ag 3d region.

the data are shown in Figure 4F. Effect of bare alumina on adsorption of dye was also checked under the same experimental conditions (Figure 4F). In 10 min, clusters adsorb more than 80%, and in 15 min, it is 99.7%, whereas, bare alumina adsorbs only about 23% in 15 min. This clearly confirms the favorable capacity of supported clusters for R6G removal. The photographs of R6G-adsorbed supported cluster, 5 ppm R6G solution, and R6G solution with supported cluster are shown in Figure 4, panels C, D, and E, respectively. The colors of the materials confirm the adsorption of clusters and R6G. The other confirmation for adsorption of R6G is the observation of luminescence from R6G under UV lamp (inset of Figure 4C).

The zeta potentials (ζ) of as-prepared clusters (unsupported), R6G (1 ppm), and R6G-treated clusters were measured to understand the nature of the interaction between the cluster and R6G at equilibrium at pH (6.3). As $Ag_7(DMSA)_4$ clusters possess carboxylate groups, they exhibit negative zeta potential (−75.7 mV), whereas R6G appears almost neutral (ζ = −0.1 mV). After addition of R6G to the cluster, a decrease in the zeta potential of the cluster (−56.6 mV) was observed at room temperature, indicating charge neutralization due to electrostatic attraction between two oppositely charged ions (inset of Figure 4F). XPS analysis of R6G-treated supported clusters was done to check the change in oxidation state of silver after interaction with the dye (Figure 5). Survey spectra of supported clusters before and after treatment of R6G show the presence of expected elements, Al, C, O, S, and Ag from clusters (Figure 5A). The Ag $3d_{5/2}$ peak

dx.doi.org/10.1021/la401180r | Langmuir 2013, 29, 8125−8132

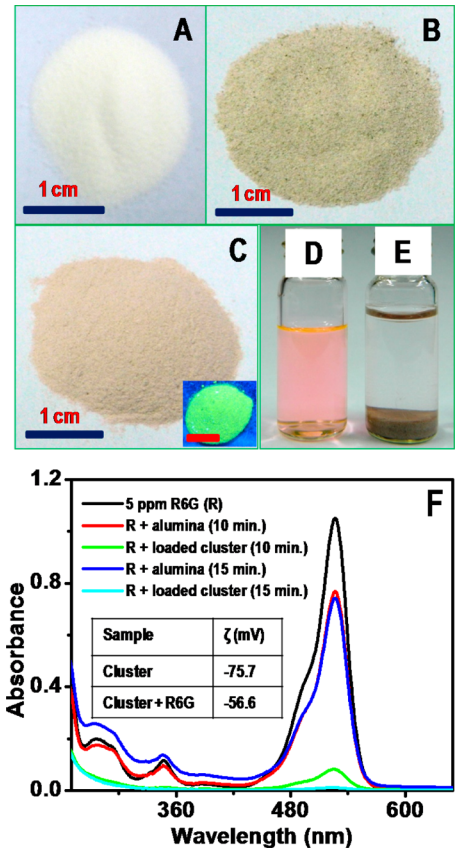

Figure 4. Photographs of bare alumina (A), cluster-loaded alumina (B), 5 ppm R6G adsorbed on supported clusters (C), 3 mL of 5 ppm R6G (D), and D + 500 mg of supported clusters (E). Inset of C is the photograph of material in C under UV lamp. Scale bar is 1 cm. (F) UV/vis absorption spectra of residual R6G solutions treated with 500 mg of various materials for 10 and 15 min. Inset of F is a of table of zeta potentials (ζ) of the unsupported cluster and the cluster treated with R6G at an equilibrium pH of 6.3.

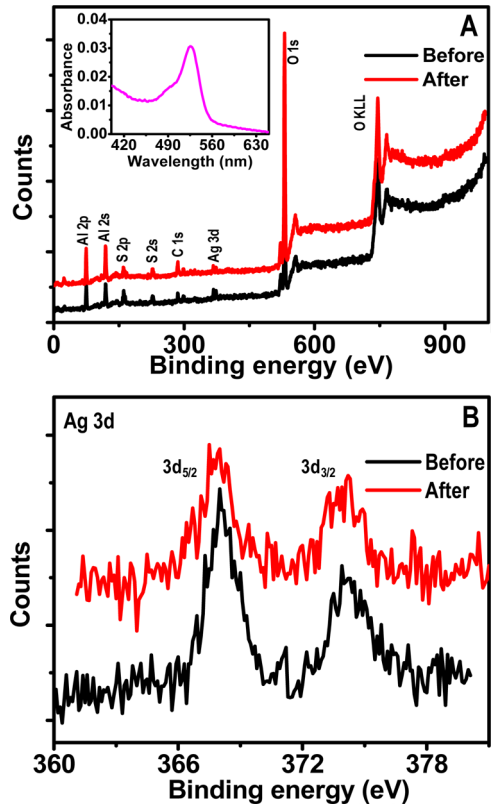

Figure 5. (A) Survey spectra of supported silver clusters before and after R6G adsorption (black and red traces, respectively). (B) Comparison of Ag 3d region. Inset of A is the UV/vis absorption spectrum of extracted R6G from supported clusters. Extraction was done using acetone.

observed at 368.1 eV (assigned to Ag^0 in supported clusters) was not changed after R6G uptake (Figure 5B). This clearly indicates that the uptake of R6G is due to adsorption. Another proof of adsorption is the UV/vis absorption spectrum of adsorbed dye, after extraction with acetone. The spectrum is the same as that of the parent dye (inset of Figure 5A). The spectrum further proves that no cluster is released back into the solution.

Kinetics of Adsorption. For this study, adsorption of 5 mL of 1 ppm R6G on 100 mg of supported cluster was monitored with time in batch. The residual concentrations of R6G in solution after treatment for different time intervals were determined by knowing the absorption intensity at 526.8 nm with reference to a standard calibration curve of R6G. The kinetics of R6G adsorption could be fitted to pseudo first order and pseudo second order equations (Figure S6). For determining the adsorption capacity of clusters for R6G, MB, MR, and MO, 250 mg of loaded cluster was treated with 5 mL of 5 ppm dye solutions for 45 min. The adsorption capacities of R6G, MB, MR, and MO are found to be 17.2, 16.4, 3.2, and 0.2 mg/g of cluster, respectively. The efficiency of supported clusters for R6G adsorption was compared with that of alumina alone, DMSA on alumina, and alumina supported NPs of Ag@citrate and Ag@MSA (sizes of Ag NPs were 30−60 and 15−25 nm, respectively, and loading of these materials on alumina was ~0.5 wt %, comparable to that of clusters) under the same experimental conditions (500 mg material was treated with 3 mL of 5 ppm R6G for 15 min.). Under these conditions, the percent removal of R6G by (i) alumina, (ii) cluster, (iii) Ag@MSA, (iv) Ag@citrate, and (v) DMSA (ii, iii, iv, and v being supported on alumina; presence of DMSA on alumina was confirmed by FTIR analysis) were 22.4, 99.7, 30.0, 29.6, and 29.8%, respectively (Figure S7). These results clearly highlight the importance of clusters for nearly complete adsorption of dye. The reasons for the large adsorption by clusters are their smaller particle size and large surface area which were confirmed by BET surface area measurements. The BET surface areas of alumina and supported clusters were 80.4 and 99.2 m^2/g, respectively. The other reason may be the increased number of functional groups in the cluster (due to small size) compared to nanoparticles for a given quantity of material. The increased reactivity and adsorption capacity of smaller clusters $[Ag_9(MSA)_7]$ compared to nanoparticles are observed in reaction with halocarbons.[54] The higher efficiency of a supported cluster than a supported ligand may be due to the difference in density of functional groups on the alumina surface. For supported clusters, there is possibility for a large number of functional groups per adsorption site due to three-dimensional arrangements of ligands on the cluster (see below in Scheme 1). In the case of ligand alone, there is a maximum of two functional groups per adsorption site.

Recycling of Supported Clusters. About 500 mg of supported cluster (0.4 wt % loading) and 3 mL of 5 ppm R6G were shaken in a conical flask for 15 min using a mechanical

dx.doi.org/10.1021/la401180r | Langmuir 2013, 29, 8125−8132

Scheme 1. Schematic Representation of the Interaction of Cationic and Anionic Dyes with $Ag_7(MDSA)_4$ Clusters Supported on Alumina[a]

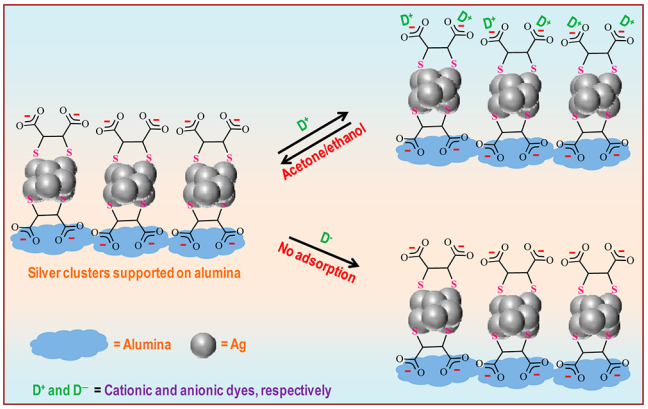

[a]Cationic dyes interact with carboxylate groups of DMSA through electrostatic interaction. Anionic dyes do not show a strong tendency for adsorption. Adsorbed dyes can be extracted using acetone/ethanol, and the supported adsorbent could be used for the next cycle. For clarity, only two ligands per cluster are shown. The sizes of cluster and ligands in the scheme are not to scale.

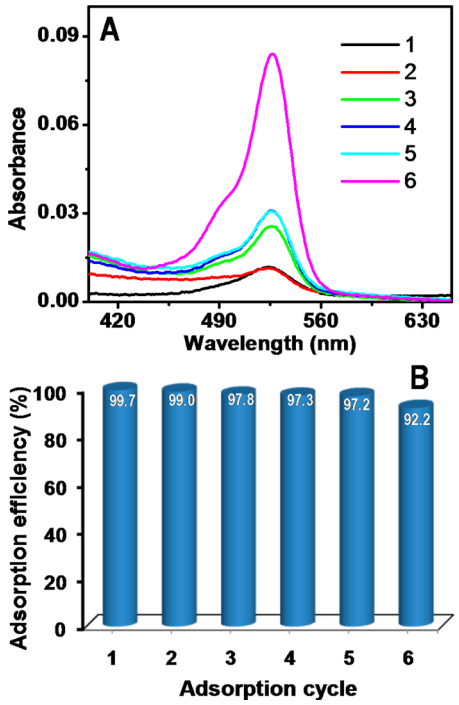

Figure 6. (A) UV/vis absorption spectra of residual R6G left in the supernatant after treating the dye solution with supported clusters at different cycles (1−6). (B) Histogram of percent removal of 5 ppm R6G in different cycles. Error in the evaluation of adsorption efficiency is less than 1%.

shaker. After that, the mixture was centrifuged for 5 min at 5000 rpm. Absorbance of the supernatant was measured, and the concentration of R6G in it was calculated using a calibration curve (Figure S8). After centrifuging, the solid material was rinsed 3 times with 3 mL portions of acetone/ethanol. The progress of extraction of R6G into the solvent could be seen by the color change. After removing all of the solvent, the material was used for next cycle of dye adsorption. All of these steps were followed for 6 cycles. In each cycle, the % of R6G removal was calculated using the absorbance at 526.8 nm (Figure 6A). The removal capacity decreases in successive cycles (Figure 6B). Nevertheless, the removal capacity is 92.2% even in the sixth cycle.

Selectivity of Dye Removal. We found that the clusters are selective toward cationic dyes, whereas they poorly adsorb anionic dyes. For testing the selectivity, we have chosen three cationic (R6G, MB, and MG) and three anionic (EBT, MR, and MO) dyes, the chemical structures of which are shown in Figure 7A. For selectivity studies, we treated 500 mg of loaded cluster with 3 mL of 5 ppm solution of each dye separately. After 15 min, the residual concentration of dye left behind was determined using absorption spectroscopy. A calibration curve was constructed for each dye. Interestingly, only cationic dyes are adsorbed in contrast to anionic dyes. To know the reason for selectivity, zeta potentials were measured. We found that, after the addition of cationic dyes into clusters (unsupported), the negative charge of the cluster gradually decreased, whereas the zeta potential increased slightly on addition of anionic dyes. The decrease of the negative charge on cluster is due to the electrostatic attraction of the positively charged cationic dye with the anionic cluster. In the case of anionic dyes, repulsion between negative charges of carboxylate groups of the cluster and of dyes operates against effective adsorption. The adsorption behavior of the system was also tested in tap water, and the efficiencies were found to be similar (99.7 and 99.3% in distilled water and tap water, respectively, for R6G). Monitoring the adsorption of a mixture of cationic dyes was difficult by absorption spectroscopy as their absorption maxima are similar.

Among the cationic dyes, R6G and MB are prominently adsorbed whereas MG shows ∼50% adsorption (Figure 7B). Data suggest that, besides ionic interactions, functional groups are also important in deciding the extent of adsorption. R6G possesses ester and other oxygen functionalities which can form hydrogen bonding with carboxylate groups of the cluster. In the case of MB, the sulfur atom (Figure 7A) shows affinity toward the Ag cluster. However, in MG, there are no such functionalities except the positive charge. These are possible reasons for the varying adsorption capacities of R6G, MB, and MG. EBT and MR are negatively charged dyes, and they show small but definite adsorption. EBT has two −OH groups and MR has one carboxylate group which would form hydrogen bonding[39] with the cluster functionalities. MO has one sulfonic group which also can form hydrogen bonds but shows poor adsorption. The most probable reason for the poorest adsorption of MO is strong electrostatic repulsion between clusters and MO than in the case of MR. In the case of MO, negative charge can be delocalized on three oxygen atoms, whereas in MR it is on only two oxygens. It is also well-known that the sulfonic group has a higher electronegative center due to its strong electron withdrawing nature than carboxylic groups. These are the probable factors that are responsible for adsorption of the two (EBT and MR) anionic dyes. Above observations are depicted in Scheme 1. Adsorption capacities (q_{ad}) of silver clusters for R6G, MB, MR, and MO are 17.2, 16.4, 3.2, and 0.2 mg/g of cluster, respectively. These values suggest that $q_{ad}(D^+) \gg q_{ad}(D^-)$. Cationic dyes were efficiently adsorbed by anionic clusters, whereas anionic dyes were not. Adsorption of both cationic and anionic dyes was enhanced by the presence of hydrogen bonding functional groups.

dx.doi.org/10.1021/la401180r | Langmuir 2013, 29, 8125−8132

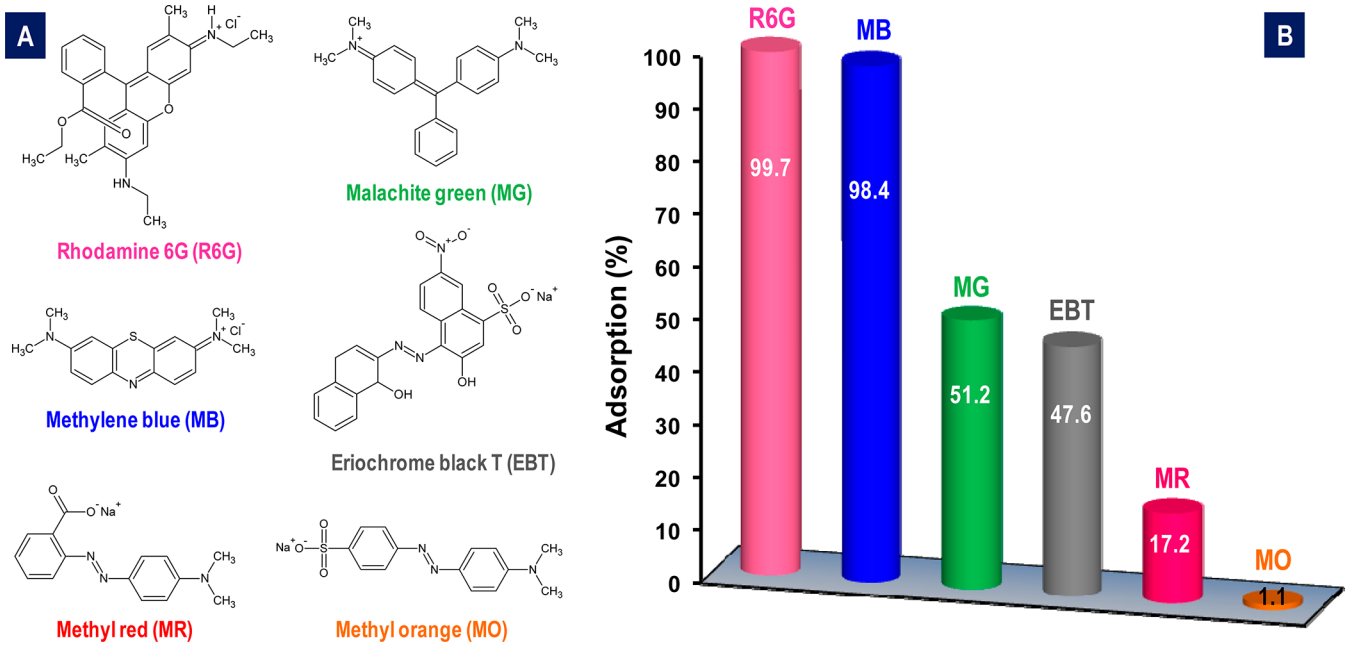

Figure 7. (A) Chemical structures of cationic and anionic dyes (R6G, MG, MB, EBT, MR, and MO) used in the experiment. (B) Histogram representing percent removal of dyes (3 mL of a solution of 5 ppm concentration of each dye was treated with 500 mg quantities of supported clusters for 15 min). Error in the evaluation of adsorption efficiency is less than 1%.

SUMMARY AND CONCLUSIONS

We have synthesized atomically precise silver quantum clusters protected with the dithiol, $Ag_7(DMSA)_4$, using a modified solid state route which takes just about 15 min. The cluster was characterized using several spectroscopic and microscopic analytical tools. The chemical formula of the cluster, $Ag_7(DMSA)_4$ was determined by ESI MS and was confirmed by MS/MS. These clusters, after supporting on alumina, selectively remove cationic dyes. The capacities for the removal of R6G and MB are 17.2 and 16.4 mg/g, respectively. The large capacity of clusters for the removal of dyes, compared to NPs, is attributed to the smaller size and the larger surface area. Possible reason for the preferred adsorption of cationic dyes is electrostatic attraction between the clusters and dyes. Hydrogen bond formation may enhance the adsorption of cationic and anionic dyes when they contain hydrogen bond forming functional groups such as −OH. The supported cluster based adsorbent is reusable after simple extraction of the adsorbed dyes with solvents. Although silver is expensive, the cluster loading is only 0.4 wt %. Small quantities of the material and recyclability make the system useful for water purification applications.

ASSOCIATED CONTENT

Supporting Information

ESI MS, ESI MS/MS, FTIR, TEM, XRD, and SEM-EDAX of unsupported and supported clusters, calibration curve for R6G, comparison of efficiencies of the cluster, and NPs for R6G removal. This material is available free of charge via the Internet at http://pubs.acs.org.

AUTHOR INFORMATION

Corresponding Author

*E-mail: pradeep@iitm.ac.in. Fax: 91-44-2257-0545/0509.

Notes

The authors declare no competing financial interest.

ACKNOWLEDGMENTS

We thank the Department of Science and Technology (DST), Government of India, for constantly supporting our research program on nanomaterials. We thank Mr. A. Narayanan, Department of Chemistry, IIT Madras, for BET surface area measurements. M.S.B. thanks the CSIR for a research fellowship.

REFERENCES

(1) Lu, Y.; Chen, W. Sub-nanometre sized metal clusters: from synthetic challenges to the unique property discoveries. *Chem. Soc. Rev.* **2012**, *41*, 3594.

(2) Jin, R. Quantum sized, thiolate-protected gold nanoclusters. *Nanoscale* **2010**, *2*, 343.

(3) Qian, H.; Zhu, M.; Wu, Z.; Jin, R. Quantum sized gold nanoclusters with atomic precision. *Acc. Chem. Res.* **2012**, *45*, 1470.

(4) Rao, T. U. B.; Nataraju, B.; Pradeep, T. Ag_9 quantum cluster through a solid-state route. *J. Am. Chem. Soc.* **2010**, *132*, 16304.

(5) Kumar, S.; Bolan, M. D.; Bigioni, T. P. Glutathione-stabilized magic-number silver cluster compounds. *J. Am. Chem. Soc.* **2010**, *132*, 13141.

(6) Diez, I.; Ras, R. H. A. Fluorescent silver nanoclusters. *Nanoscale* **2011**, *3*, 1963.

(7) Heaven, M. W.; Dass, A.; White, P. S.; Holt, K. M.; Murray, R. W. Crystal structure of the gold nanoparticle $[N(C_8H_{17})_4][Au_{25}(SCH_2CH_2Ph)_{18}]$. *J. Am. Chem. Soc.* **2008**, *130*, 3754.

(8) Zhu, M.; Aikens, C. M.; Hollander, F. J.; Schatz, G. C.; Jin, R. Correlating the crystal structure of a thiol-protected Au_{25} cluster and optical properties. *J. Am. Chem. Soc.* **2008**, *130*, 5883.

(9) Zeng, C.; Qian, H.; Li, T.; Li, G.; Rosi, N. L.; Yoon, B.; Barnett, R. N.; Whetten, R. L.; Landman, U.; Jin, R. Total structure and electronic properties of the gold nanocrystal $Au_{36}(SR)_{24}$. *Angew. Chem., Int. Ed.* **2012**, *51*, 13114.

(10) Qian, H.; Eckenhoff, W. T.; Zhu, Y.; Pintauer, T.; Jin, R. Total structure determination of thiolate-protected Au_{38} nanoparticles. *J. Am. Chem. Soc.* **2010**, *132*, 8280.

(11) Jadzinsky, P. D.; Calero, G.; Ackerson, C. J.; Bushnell, D. A.; Kornberg, R. D. Structure of a thiol monolayer-protected gold nanoparticle at 1.1 Å resolution. *Science* **2007**, *318*, 430.

(12) Das, A.; Li, T.; Nobusada, K.; Zeng, Q.; Rosi, N. L.; Jin, R. Total structure and optical properties of a phosphine/thiolate-protected Au_{24} nanocluster. *J. Am. Chem. Soc.* **2012**, *134*, 20286.
(13) Yang, H.; Lei, J.; Wu, B.; Wang, Y.; Zhou, M.; Xia, A.; Zheng, L.; Zheng, N. Crystal structure of a luminescent thiolated Ag nanocluster with an octahedral Ag_6^{4+} core. *Chem. Commun.* **2013**, *49*, 300.
(14) Zhu, Y.; Qian, H.; Jin, R. Catalysis opportunities of atomically precise gold nanoclusters. *J. Mater. Chem.* **2011**, *21*, 6793.
(15) Bootharaju, M. S.; Pradeep, T. Investigation into the reactivity of unsupported and supported Ag_7 and Ag_8 clusters with toxic metal ions. *Langmuir* **2011**, *27*, 8134.
(16) Adhikari, B.; Banerjee, A. Facile synthesis of water-soluble fluorescent silver nanoclusters and Hg^{II} sensing. *Chem. Mater.* **2010**, *22*, 4364.
(17) Shang, L.; Dong, S.; Nienhaus, G. U. Ultra-small fluorescent metal nanoclusters: Synthesis and biological applications. *Nano Today* **2011**, *6*, 401.
(18) Zhang, Z.; Xu, L.; Li, H.; Kong, J. Wavelength-tunable luminescent gold nanoparticles generated by cooperation ligand exchange and their potential application in cellular imaging. *RSC Adv.* **2013**, *3*, 59.
(19) Chen, Y.; Shen, Y.; Sun, D.; Zhang, H.; Tian, D.; Zhang, J.; Zhu, J.-J. Fabrication of a dispersible graphene/gold nanoclusters hybrid and its potential application in electrogenerated chemiluminescence. *Chem. Commun.* **2011**, *47*, 11733.
(20) Udaya Bhaskara Rao, T.; Pradeep, T. Luminescent Ag_7 and Ag_8 clusters by interfacial synthesis. *Angew. Chem., Int. Ed.* **2010**, *49*, 3925.
(21) Habeeb Muhammed, M. A.; Verma, P. K.; Pal, S. K.; Retnakumari, A.; Koyakutty, M.; Nair, S.; Pradeep, T. Luminescent quantum clusters of gold in bulk by albumin-induced core etching of nanoparticles: Metal ion sensing, metal-enhanced luminescence, and biolabeling. *Chem.—Eur. J.* **2010**, *16*, 10103.
(22) Udayabhaskararao, T.; Sun, Y.; Goswami, N.; Pal, S. K.; Balasubramanian, K.; Pradeep, T. Ag_7Au_6: A 13-atom alloy quantum cluster. *Angew. Chem., Int. Ed.* **2012**, *51*, 2155.
(23) Liu, S.; Lu, F.; Zhu, J.-J. Highly fluorescent Ag nanoclusters: microwave-assisted green synthesis and Cr^{3+} sensing. *Chem. Commun.* **2011**, *47*, 2661.
(24) Zhou, T.; Rong, M.; Cai, Z.; Yang, C. J.; Chen, X. Sonochemical synthesis of highly fluorescent glutathione-stabilized Ag nanoclusters and S^{2-} sensing. *Nanoscale* **2012**, *4*, 4103.
(25) Adhikari, B.; Banerjee, A. Short-peptide-based hydrogel: A template for the *in situ* synthesis of fluorescent silver nanoclusters by using sunlight. *Chem.—Eur. J.* **2010**, *16*, 13698.
(26) Chakraborty, I.; Udayabhaskararao, T.; Pradeep, T. Luminescent sub-nanometer clusters for metal ion sensing: A new direction in nanosensors. *J. Hazard. Mater.* **2012**, *211−212*, 396.
(27) Xavier, P. L.; Chaudhari, K.; Baksi, A.; Pradeep, T. Protein-protected luminescent noble metal quantum clusters: An emerging trend in atomic cluster nanoscience. *Nano Rev.* **2012**, *3*, 14767.
(28) Chakraborty, I.; Govindarajan, A.; Erusappan, J.; Ghosh, A.; Pradeep, T.; Yoon, B.; Whetten, R. L.; Landman, U. The superstable 25 kDa monolayer protected silver nanoparticle: Measurements and interpretation as an icosahedral $Ag_{152}(SCH_2CH_2Ph)_{60}$ cluster. *Nano Lett.* **2012**, *12*, 5861.
(29) Deguchi, S.; Mukai, S.-a.; Yamazaki, T.; Tsudome, M.; Horikoshi, K. Nanoparticles of fullerene C_{60} from engineering of antiquity. *J. Phys. Chem. C* **2009**, *114*, 849.
(30) Wang, M.; Wu, Z.; Yang, J.; Wang, G.; Wang, H.; Cai, W. $Au_{25}(SG)_{18}$ as a fluorescent iodide sensor. *Nanoscale* **2012**, *4*, 4087.
(31) Yuan, X.; Tay, Y.; Dou, X.; Luo, Z.; Leong, D. T.; Xie, J. Glutathione-protected silver nanoclusters as cysteine-selective fluorometric and colorimetric probe. *Anal. Chem.* **2012**, *85*, 1913.
(32) Guo, Y.; Wang, Z.; Shao, H.; Jiang, X. Stable fluorescent gold nanoparticles for detection of Cu^{2+} with good sensitivity and selectivity. *Analyst* **2012**, *137*, 301.
(33) Zhu, M.; Chan, G.; Qian, H.; Jin, R. Unexpected reactivity of $Au_{25}(SCH_2CH_2Ph)_{18}$ nanoclusters with salts. *Nanoscale* **2011**, *3*, 1703.
(34) Khin, M. M.; Nair, A. S.; Babu, V. J.; Murugan, R.; Ramakrishna, S. A review on nanomaterials for environmental remediation. *Energy Environ. Sci.* **2012**, *5*, 8075.
(35) Ali, H. Biodegradation of synthetic dyes—A review. *Water Air Soil Pollut.* **2010**, *213*, 251.
(36) Zhou, L.; Gao, C.; Xu, W. Magnetic dendritic materials for highly efficient adsorption of dyes and drugs. *ACS Appl. Mater. Interfaces* **2010**, *2*, 1483.
(37) Yahagi, T.; Degawa, M.; Seino, Y.; Matsushima, T.; Nagao, M.; Sugimura, T.; Hashimoto, Y. Mutagenicity of carcinogenic azo dyes and their derivatives. *Cancer Lett.* **1975**, *1*, 91.
(38) Szadowski, J.; Niewiadomski, Z. Synthesis and properties of disazo dyes derived from water-soluble derivatives of benzidine and 4,4′- diaminodiphenylurea. *Dyes Pigm.* **1992**, *19*, 41.
(39) Saha, B.; Das, S.; Saikia, J.; Das, G. Preferential and enhanced adsorption of different dyes on iron oxide nanoparticles: A comparative study. *J. Phys. Chem. C* **2011**, *115*, 8024.
(40) Shi, B.; Li, G.; Wang, D.; Feng, C.; Tang, H. Removal of direct dyes by coagulation: The performance of preformed polymeric aluminum species. *J. Hazard. Mater.* **2007**, *143*, 567.
(41) Gupta, S. S.; Sreeprasad, T. S.; Maliyekkal, S. M.; Das, S. K.; Pradeep, T. Graphene from sugar and its application in water purification. *ACS Appl. Mater. Interfaces* **2012**, *4*, 4156.
(42) Das, S. K.; Khan, M. M. R.; Parandhaman, T.; Laffir, F.; Guha, A. K.; Sekaran, G.; Mandal, A. B. Nano-silica fabricated with silver nanoparticles: antifouling adsorbent for efficient dye removal, effective water disinfection and biofouling control. *Nanoscale* **2013**, DOI: 10.1039/C3NR00856H.
(43) Chen, W.; Lu, W.; Yao, Y.; Xu, M. Highly efficient decomposition of organic dyes by aqueous-fiber phase transfer and *in situ* catalytic oxidation using fiber-supported cobalt phthalocyanine. *Environ. Sci. Technol.* **2007**, *41*, 6240.
(44) Lee, J.-W.; Choi, S.-P.; Thiruvenkatachari, R.; Shim, W.-G.; Moon, H. Submerged microfiltration membrane coupled with alum coagulation/powdered activated carbon adsorption for complete decolorization of reactive dyes. *Water Res.* **2006**, *40*, 435.
(45) Giri, A.; Goswami, N.; Pal, M.; Zar Myint, M. T.; Al-Harthi, S.; Singha, A.; Ghosh, B.; Dutta, J.; Pal, S. K. Rational surface modification of Mn_3O_4 nanoparticles to induce multiple photoluminescence and room temperature ferromagnetism. *J. Mater. Chem. C* **2013**, *1*, 1885.
(46) Allegre, C.; Moulin, P.; Maisseu, M.; Charbit, F. Treatment and reuse of reactive dyeing effluents. *J. Membr. Sci.* **2006**, *269*, 15.
(47) Georgakilas, V.; Otyepka, M.; Bourlinos, A. B.; Chandra, V.; Kim, N.; Kemp, K. C.; Hobza, P.; Zboril, R.; Kim, K. S. Functionalization of graphene: Covalent and non-covalent approaches, derivatives and applications. *Chem. Rev.* **2012**, *112*, 6156.
(48) Ma, J.; Yu, F.; Zhou, L.; Jin, L.; Yang, M.; Luan, J.; Tang, Y.; Fan, H.; Yuan, Z.; Chen, J. Enhanced adsorptive removal of methyl orange and methylene blue from aqueous solution by alkali-activated multiwalled carbon nanotubes. *ACS Appl. Mater. Interfaces* **2012**, *4*, 5749.
(49) Bokare, A. D.; Chikate, R. C.; Rode, C. V.; Paknikar, K. M. Effect of surface chemistry of Fe−Ni nanoparticles on mechanistic pathways of azo dye degradation. *Environ. Sci. Technol.* **2007**, *41*, 7437.
(50) Pradeep, T. Anshup. Noble metal nanoparticles for water purification: A critical review. *Thin Solid Films* **2009**, *517*, 6441.
(51) Bootharaju, M. S.; Pradeep, T. Understanding the degradation pathway of the pesticide, chlorpyrifos by noble metal nanoparticles. *Langmuir* **2012**, *28*, 2671.
(52) Wu, Z.; Lanni, E.; Chen, W.; Bier, M. E.; Ly, D.; Jin, R. High yield, large scale synthesis of thiolate-protected Ag_7 clusters. *J. Am. Chem. Soc.* **2009**, *131*, 16672.
(53) Bootharaju, M. S.; Chaudhari, K.; Pradeep, T. Real time plasmonic spectroscopy of the interaction of Hg^{2+} with single noble metal nanoparticles. *RSC Adv.* **2012**, *2*, 10048.
(54) Bootharaju, M. S.; Deepesh, G. K.; Udayabhaskararao, T.; Pradeep, T. Atomically precise silver clusters for efficient chlorocarbon degradation. *J. Mater. Chem. A* **2013**, *1*, 611.

Supporting information

Facile and rapid synthesis of dithiol-protected Ag_7 quantum cluster for selective adsorption of cationic dyes

M. S. Bootharaju and T. Pradeep*

DST Unit of Nanoscience (DST UNS), Department of Chemistry,

Indian Institute of Technology Madras, Chennai - 600 036, India

***E-mail:** pradeep@iitm.ac.in*

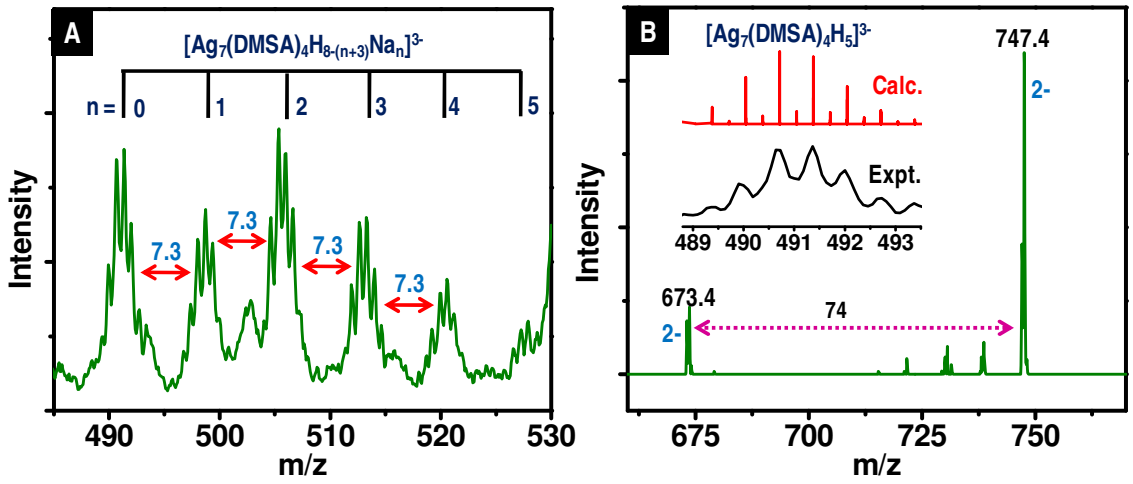

Figure S1. A) ESI MS of as-synthesized silver clusters (in 1:1 water-methanol) in the –ve mode. Peaks corresponding to sodium adducts of triply charged ion are shown above the spectrum. B) MS^2 of m/z 747.4 at a collision energy of 15 eV. Inset of B is a comparison of the calculated and experimental peaks of $[Ag_7(DMSA)_4H_5]^{3-}$.

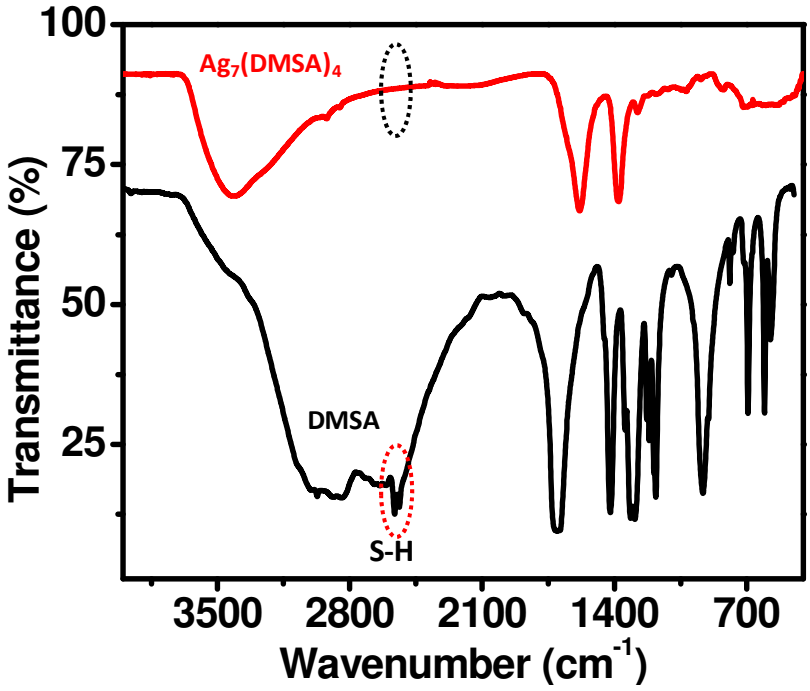

Figure S2. Comparison of FTIR spectra of the ligand, DMSA (black trace) and silver cluster (red trace). Region of S-H stretching frequency (around 2550 cm^{-1}) is marked with dotted ellipses in both the spectra. Absence of S-H stretching frequency in the cluster confirms the binding of both the thiols of DMSA on the Ag cluster.

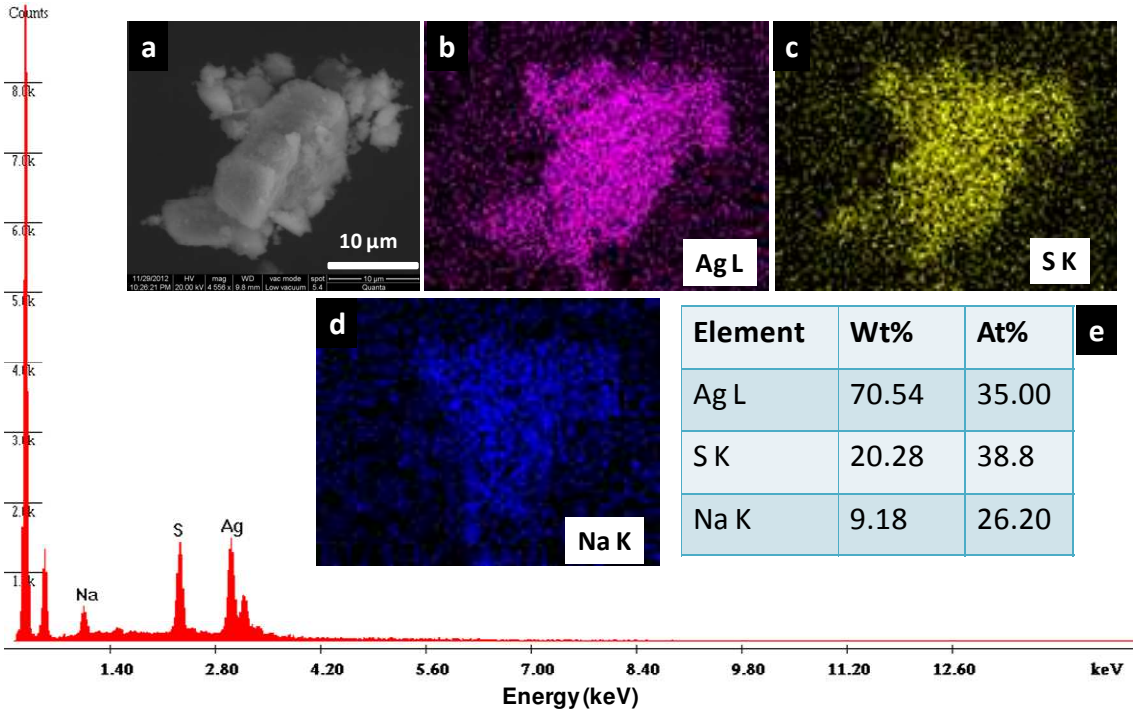

Figure S3. SEM-EDAX spectrum of silver clusters. Insets show the SEM image of an aggregate of clusters and elemental maps of Ag, S and Na (a, b, c and d, respectively). Quantification table of elements is also seen (inset e).

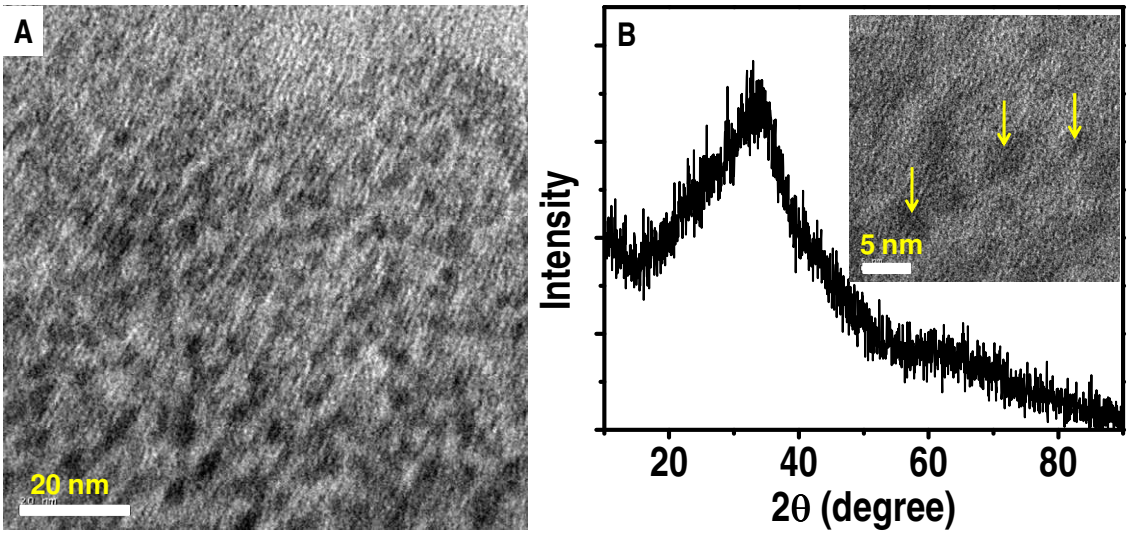

Figure S4. TEM image (A) and XRD pattern (B) of silver clusters. Inset of B is a small area TEM image of clusters after 4 min. of exposure to the electron beam. Arrows indicate regions where the growth of clusters to aggregates, due to irradiation of electron beam, has taken place. Due to electron beam-induced aggregation, TEM is not a good tool to understand such sensitive clusters.

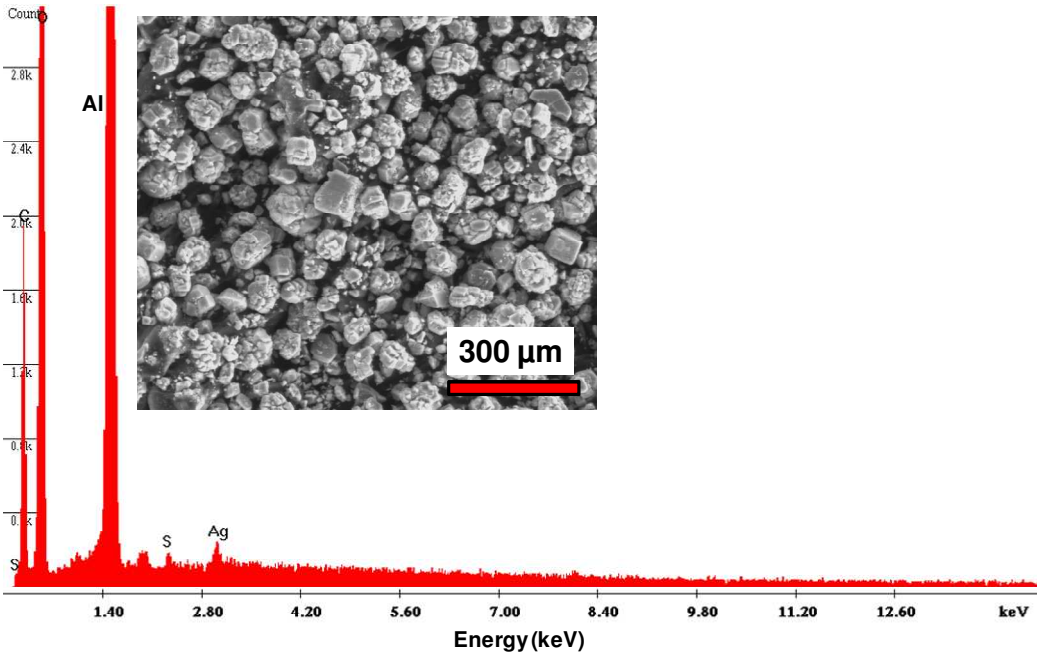

Figure S5. SEM-EDAX spectrum of silver clusters loaded on alumina showing the presence of Ag and S from clusters. Inset is a large area SEM image of the same sample.

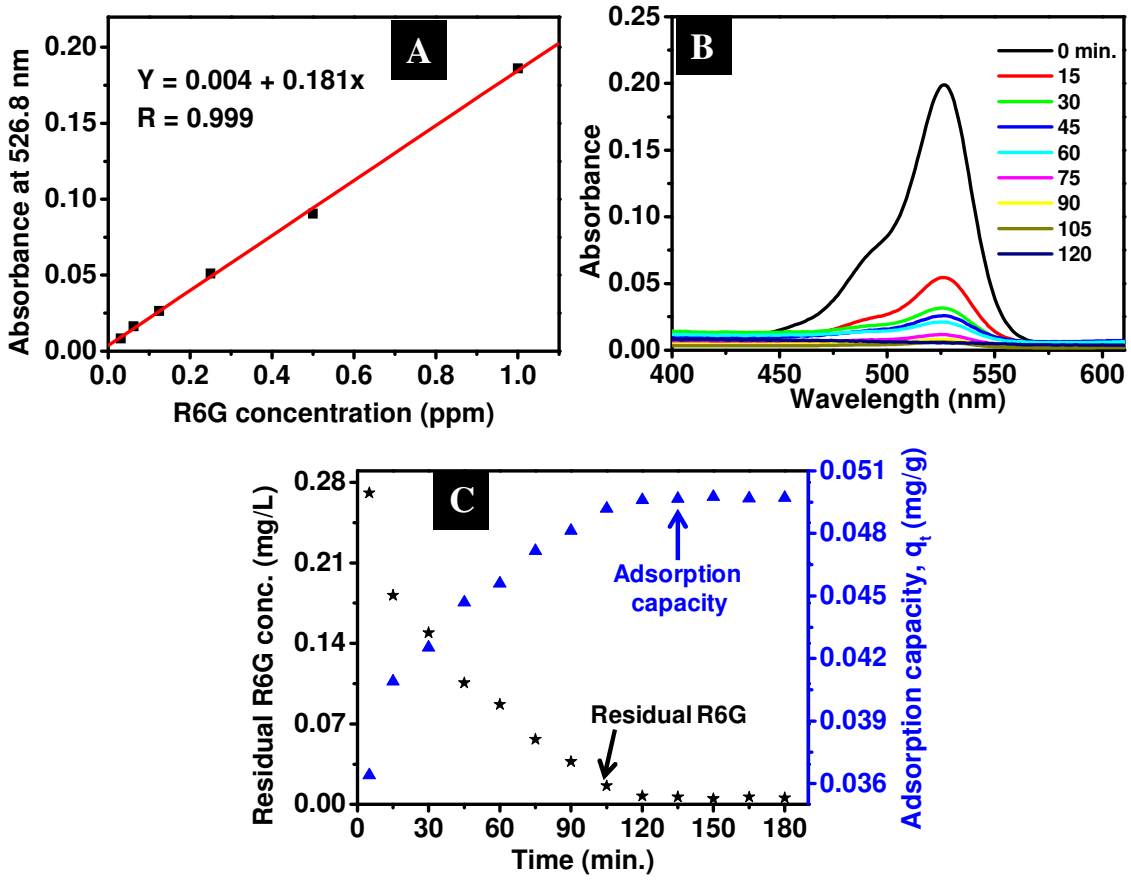

Figure S6. A) Calibration curve for R6G concentration. B) UV/Vis absorption spectra of residual R6G in dye solutions after treating with supported clusters. C) Plots of residual R6G and adsorption capacity (q_t, mg/g) with time. The kinetics followed pseudo first and second orders.

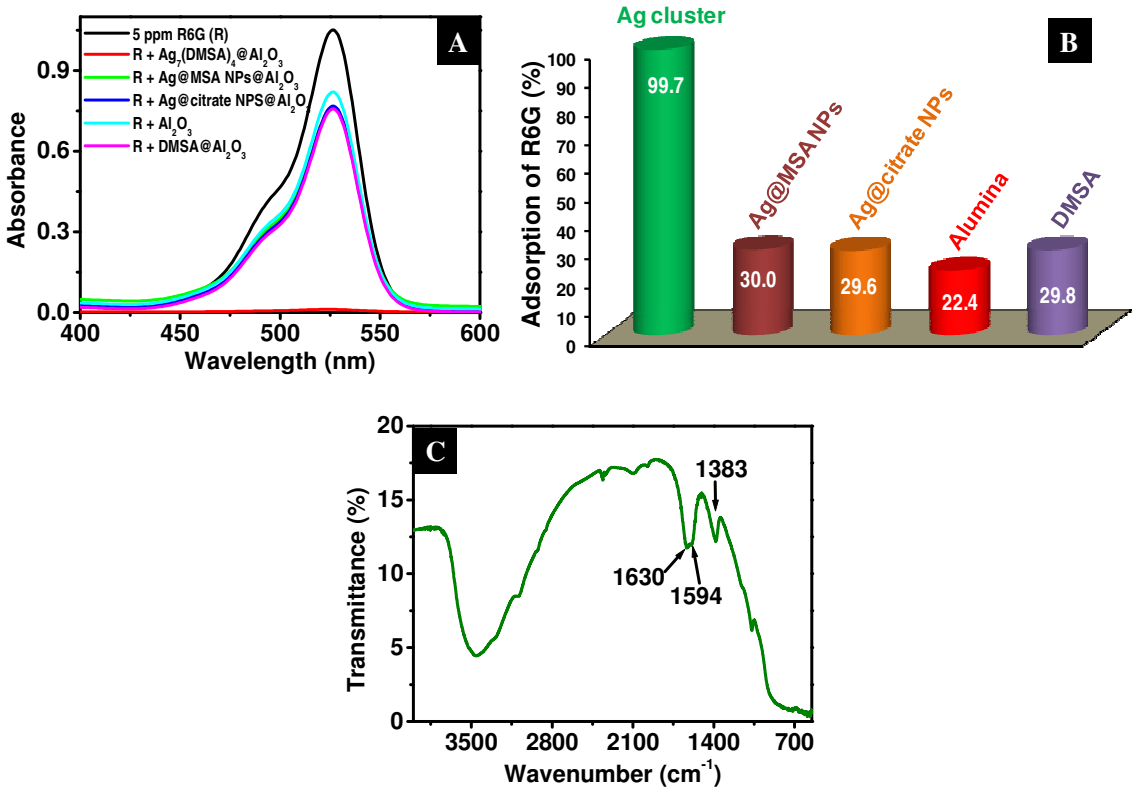

Figure S7. A) UV/Vis absorption spectra of residual R6G after treating with support (alumina), supported clusters, supported ligand, DMSA and supported silver nanoparticles protected with citrate and MSA. B) Histogram of % removal from 3 mL, 5 ppm R6G by supported nanomaterials. C) FTIR spectrum of DMSA supported on alumina.

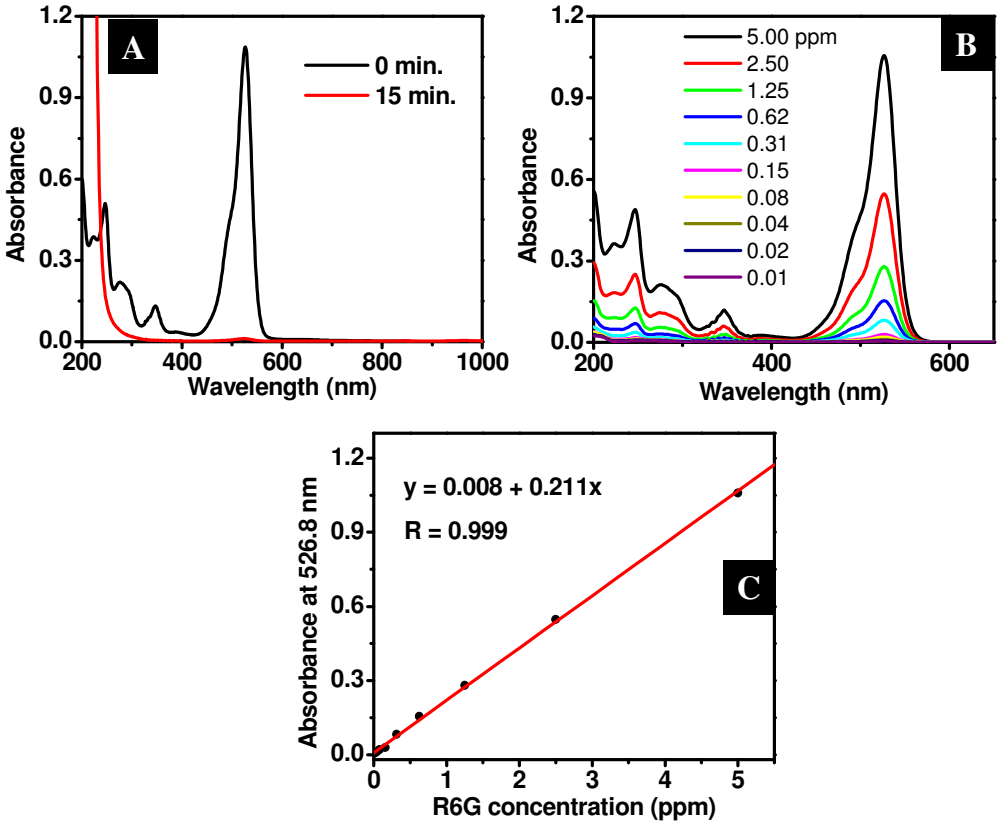

Figure S8. A) UV/Vis absorption spectra of residual R6G in the dye solution after treating with 500 mg of supported silver cluster for 0 and 15 min. B) UV/Vis absorption spectra solutions of R6G with different concentrations. Absorbance values at 526.8 nm are used for constructing calibration graph. C) Calibration plot for R6G.

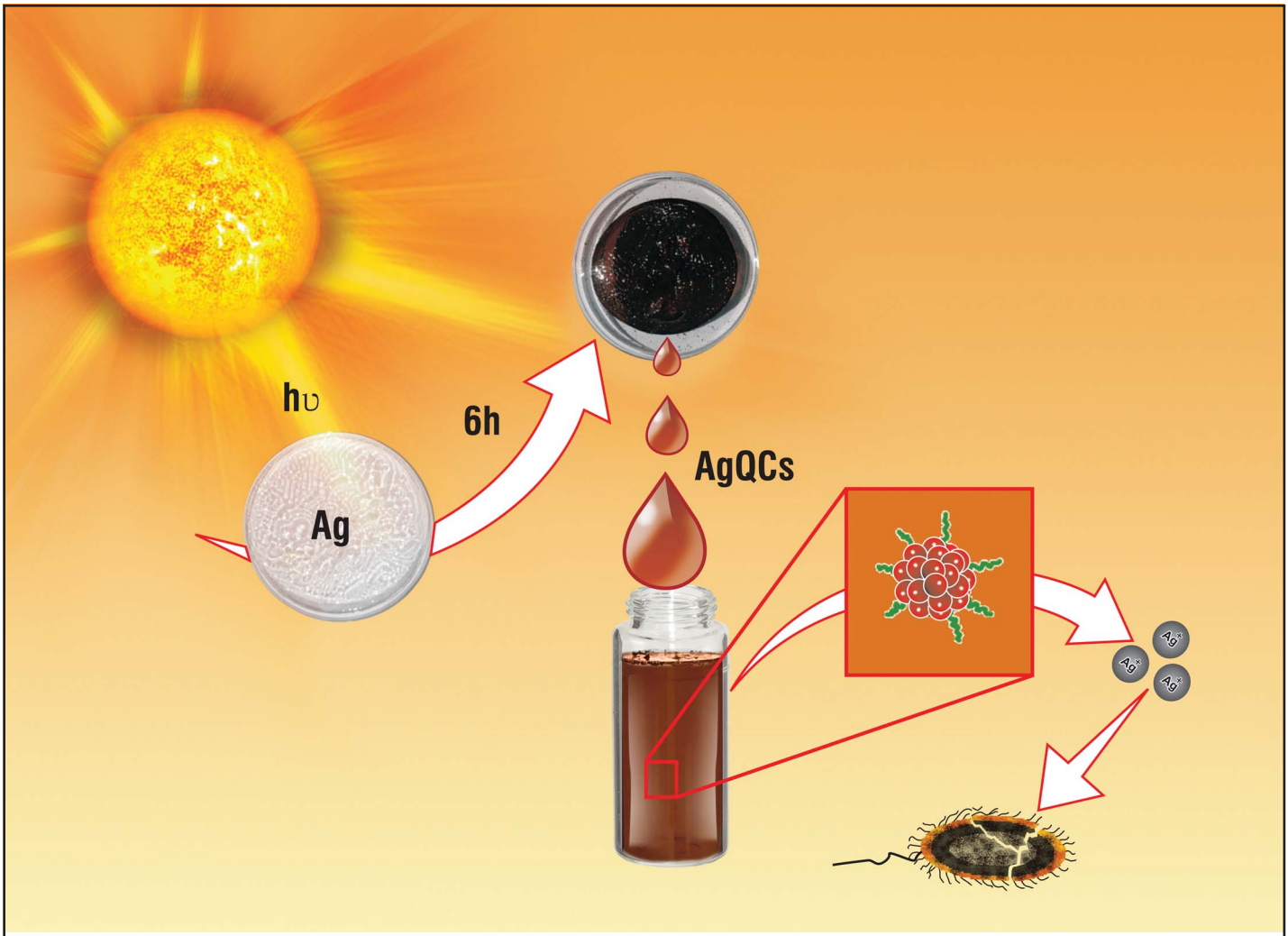

Showcasing research from Prof. T. Pradeep's laboratory at IIT Madras, Chennai, India.

Title: Sunlight mediated synthesis and antibacterial properties of monolayer protected silver clusters

Details of the research undertaken in our laboratory can be found at http://www.dstuns.iitm.ac.in/pradeep-research-group.php. A green route to synthesise glutathione protected atomically precise silver clusters by sunlight irradiation of silver thiolates confined in gel cavities, and the antibacterial properties of the as-synthesized clusters against gram-negative and gram-positive bacteria.

As featured in:

See I. Chakraborty *et al.*,
J. Mater. Chem. B, 2013, **1**, 4059.

RSC Publishing

www.rsc.org/MaterialsB

Registered Charity Number 207890

Journal of Materials Chemistry B

RSC Publishing

PAPER

Sunlight mediated synthesis and antibacterial properties of monolayer protected silver clusters†

Cite this: *J. Mater. Chem. B*, 2013, **1**, 4059

Indranath Chakraborty,‡ T. Udayabhaskararao,‡ G. K. Deepesh and T. Pradeep*

Glutathione protected, silver clusters were synthesized within gel cavities, using sunlight. Compared to the conventional chemical reduction process, this method is cheaper and environmentally friendly as it involves the use of natural resources. The as-synthesized silver quantum clusters in aqueous medium show a distinct step-like behavior in their absorption profile. They have been characterized with various spectroscopic and microscopic techniques such as UV/Vis Spectroscopy, Luminescence Spectroscopy, Fourier Transform Infrared Spectroscopy (FTIR), High Resolution Transmission Electron Microscopy (HRTEM), and X-ray Photoelectron Spectroscopy (XPS). Polyacrylamide gel cavities seemingly control the growth of the particles. The cluster synthesis is scalable by increasing the amount of reagents yielding hundreds of milligrams in a single step. The antibacterial properties of the as-synthesized Ag clusters were studied against a Gram negative and Gram positive organism, *Escherichia coli* and *Staphylococcus aureus*, respectively.

Received 26th April 2013
Accepted 17th June 2013

DOI: 10.1039/c3tb20603c

www.rsc.org/MaterialsB

Introduction

Few-atom noble metal clusters (or quantum clusters, QCs) with discrete electronic structures, exhibiting distinct HOMO–LUMO transitions in optical absorption,[1–4] intrinsic magnetism,[5,6] enhanced photoluminescence,[7–12] and modified redox properties[13–18] are interesting new materials. These properties are fundamentally different from the larger metallic nanoparticles which exhibit surface plasmon resonance arising from the coherent oscillations of free electrons in the conduction band.[19] QCs are good candidates for applications in areas such as catalysis,[20,21] nanoelectronics,[14] sensing,[22,23] *etc.* Several such clusters of noble metals have been synthesized using various templates such as peptides,[24,25] thiols,[26–29] dendrimers,[31] and proteins.[31–34] Among them, the thiol protected ones are more intensely studied with diverse techniques as well-defined compositions can be obtained.[10,16,27–29,31,35–38]

A variety of chemical and physical methods have been developed to produce them and most of the synthetic routes are limited to gold QCs. Although gold and silver belong to the same group, because of differences in their chemical reactivity, the area of silver QCs has not expanded significantly.[39] It is expected that silver may be a better system for sensor applications due to the high extinction coefficient.[40] In our group, we have demonstrated the possibility to synthesize thiol protected silver clusters using interfacial[41] and solid state routes.[29] Glutathione protected clusters may be made through a high temperature nucleation route as well.[24] Jin *et al.* reported dimercaptosuccinic acid protected Ag_7 quantum clusters.[42] Kitaev and Cathcart, reported glutathione (SG) protected silver clusters in a single step.[27] In all of the cases, synthesis involves the use of chemical reducing agents such as $NaBH_4$,[29,43] HCOOH,[24] *etc.* However, it's a challenge to material chemists to synthesize the desired materials using natural resources.[44] To the best of our knowledge, no reports are available on the synthesis of GSH protected silver QCs using sunlight, although several reports are available to make plasmonic nanoparticles using natural sources such as light irradiation[45,46] and by using materials of plant origin.[47] There are also other methods such as microwave irradiation.[48] Some reports are also available for visible light photoactivated clusters.[49–51] Herein we report the synthesis of luminescent ($QY = 5 \times 10^{-3}$) silver QCs protected by glutathione using sunlight, without a chemical reducing agent. The products have been isolated, characterized and applied.

Results and discussion

Initially, the silver thiolate containing polymerized gel appears transparent. Upon exposure to sunlight, there is a gradual color change from colorless to light yellow and finally to brown-black (Fig. 1). At the same time, the softness of the gel decreases and it becomes harder, due to evaporation of water. The conversion to brown-black color indicates the completion of the reaction and formation of clusters, as observed in other methods of cluster synthesis.[22,27] In traditional synthesis, the initially turbid metal thiolates become dark brown or black upon addition of an

DST Unit of Nanoscience (DST UNS), Department of Chemistry, Indian Institute of Technology Madras, Chennai 600 036, India. E-mail: pradeep@iitm.ac.in; Fax: +91-44-2257-0545; +91-44-2257-4208; Tel: +91-44-2257-4208

† Electronic supplementary information (ESI) available: Details of the phase transfer procedure, photographs of large scale synthesis, ESI MS, XPS, FT-IR and PL of AgQCs and other control experiments. See DOI: 10.1039/c3tb20603c

‡ These authors contributed equally.

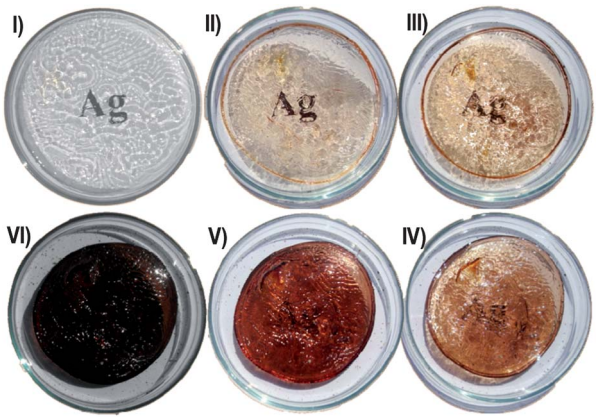

Fig. 1 (I) Photograph of the polymerized form of acrylamide gel along with oligomeric Ag(I)SG, taken in a Petri dish. (II), (III), (IV), (V) and (VI) are photographs corresponding to the exposure to sunlight at different time intervals of 5 min, 30 min, 1 h, 3 h, and 6 h, respectively. The Petri dish was placed on white paper with the label, 'Ag' printed on it. Note the change in transparency from (I) to (VI). The gel shrinks upon irradiation as water evaporates and the dry gel is detached from the Petri dish.

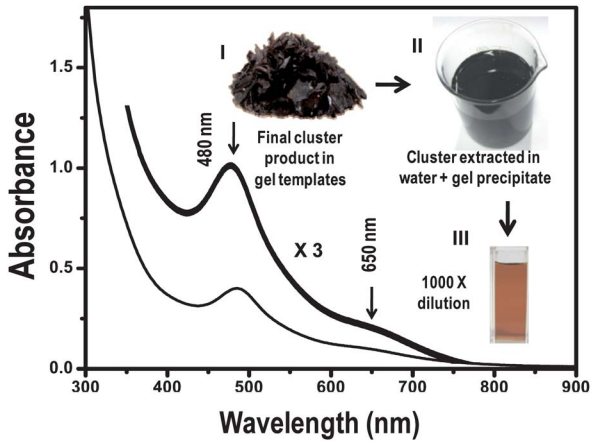

Fig. 2 UV/Vis spectrum of as-synthesized AgQC. Dominant spectral peaks at 480 nm and 650 nm are marked on the enlarged optical spectrum. Insets: (I) photograph of the gel templates containing silver clusters after exposure to sunlight for 6 h. (II) Extracted clusters which are readily soluble in water whereas the gel was insoluble and the solution appears dark brown in color. (III) Upon dilution 1000 times, the solution appears reddish brown and the spectrum is shown as the main figure.

external reducing agent such as sodium borohydride, due to the formation of clusters or nanoparticles. Fig. 1 shows the evolution of cluster formation with the duration of light exposure as manifested by the change in color of the gel. All the images were collected from the same Petri dish. During the progress of the reaction, the transparency of the gel was reduced and finally the gel became opaque due to cluster formation (Fig. 1). In a typical synthesis, we make about 70 mg of the cluster powder following the procedure outlined in the Experimental section.

This method was scalable to make hundreds of milligram quantities of AgQCs in a single step, by increasing the amount of reagents used in the reaction. For larger scale synthesis, 50 mL of the acrylamide gel solution was used and the reagents necessary for polymerization along with Ag(I)SG were taken in a 3 ft $\times$ 2 ft glass tray and the polymerization was started. The tray was irradiated to make the clusters. Photographs of the process are given in Fig. S2.†

When the cluster formation is complete, a flake-like gel appears as shown in Fig. 2 (inset I). For extraction of the clusters, 50 mL of water was added to the final hard gel and the solution was kept at 20 °C for 1 hour (Fig. S3†). Clusters were extracted with water while a colorless gel residue settled at the bottom. A peak at 480 nm (2.58 eV) and a shoulder at 650 nm (1.9 eV) were observed in the UV/Vis spectrum of the cluster (Fig. 2). The cluster in water showed a dominant step-like behavior, typical of this size regime, indicating that the material was composed of a few atoms. Note that the silver cluster synthesized by Kitaev and Cathcart[27] shows similar absorption peaks and they had suggested the possibility of a 25 atom core. The absorption profile also matches that of the cluster (band 6) reported by the Bigioni group.[43] Our group has also reported a silver cluster (GSH protected) with similar absorption features.[22,29] As the plasmon resonance feature around 400 nm is absent in the spectrum, it is clear that larger silver nanoparticles are absent and the spectrum is similar to that of molecules.[29] This is also supported by TEM measurements (see later). The cluster in water is stable for several months without change in its absorption peaks. Clusters in high concentrations appear to have a brown-black color (Fig. 2II) but upon 1000 times dilution, the color becomes reddish brown (Fig. 2III). Time dependent profiles show that the process of reduction is slow and it takes nearly 6 h to get AgQCs. In the initial stages of the reaction, a broad peak at 480 nm appeared (1 h), which became narrow with time and increases in intensity. No observable changes in absorption profiles and peak intensities were seen even after 6 h of irradiation time. The evolution of peaks within 6 h indicates that it is a slow reaction. Time dependent UV/Vis for the evolution of cluster is given in Fig. S4.† Clusters appear as tiny dots in the TEM image (Fig. S5†). Smaller clusters coalesce upon high energy electron beam exposure and nanoparticles of larger dimension are observed. In view of this, a large size distribution (Fig. S5†) from 0.5 to 3 nm was found with an average size distribution of 1.6 nm. This kind of electron-beam induced coalescence was seen earlier.[52] Such coalescence is reduced when the protection is better, for example with a silica coating.[53]

The cluster exhibits luminescence at 710 nm at all (395, 440 and 518 nm) excitation wavelengths (Fig. 3I). The emission and excitation is comparable with the cluster reported by our group.[22] In view of the specific optical absorption and emission features and due to the fact that no nanoparticles are seen in the TEM image, we conclude that monolayer protected silver clusters are formed in the synthesis.

The thiolate form of the glutathione being attached to cluster core is supported by XPS (Fig. 3II). The XPS survey spectrum of the clusters shows all the expected elements (Fig. S6†). Ag $3d_{5/2}$ (BE of 368.1 eV) supports the Ag(0) state (Fig. 3II). Note that there is not much difference in BE between Ag(0) and Ag(I) states. The S $2p_{3/2}$ BE is thiolate-like and a value of 162.0 eV is observed (Fig. S7†). An additional S $2p_{3/2}$ peak at 164.1 eV observed upon peak fitting may be due to other ligand

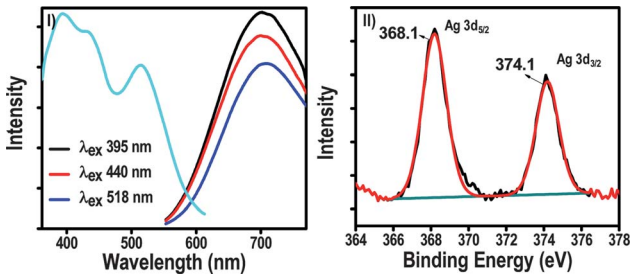

Fig. 3 (I) Luminescence spectra of the as-synthesized cluster, which show three excitation wavelengths and all of these give emission at the same wavelength. (II) X-ray photoelectron spectrum of the cluster in the Ag 3d region. The corresponding peaks are assigned. The peaks are fitted with spin–orbit split components.

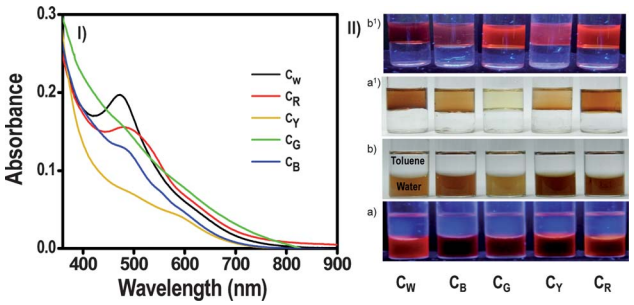

Fig. 4 (I) UV-Vis spectrum of the AgQCs synthesized using various filters: without filter (C_W), blue (C_B), red (C_R), yellow (C_Y) and green (C_G). (II) Photographs of AgQC clusters under visible light (b and a1) and UV light (a and b1), before (a and b) and after (a1 and b1) phase transfer.

binding sites or X-ray induced damage of the monolayer.[54] IR spectrum of the cluster shows that the cluster is connected to glutathione through the thiolate link (Fig. S8†). The S–H stretching at 2552 cm^{-1} of glutathione is absent in the case of the cluster. Electrospray ionization mass spectrometry (ESI MS) analysis (in negative mode) was performed to discover the composition of the cluster but we could see only some fragmented ions with good isotopic distribution (Fig. S9†). The peaks corresponding to *m*/*z* 933 and 1443 were assigned to $Ag_3(SG)_2^+$ and $Ag_4(SG)_3^+$. Upon a closer view, another peak with a difference of *m*/*z* 22 was seen for both the cases which could be attributed to replacement of Na in place of H. Matrix assisted laser desorption ionization mass spectrometry (MALDI MS) did not yield molecular ion signatures, similar to the glutathione protected clusters reported before.[39] Efforts are in progress to find the composition of the cluster. The tiny quantities of the polymeric gel remaining with the cluster seem to prevent it from creating intact ions in the gas phase. ESI MS analysis of silver cluster has been difficult in a number of cases.[39]

We also performed several experiments by exposing the sample to sunlight under different filters. Red, blue, green and yellow filters were used to allow specific light to be exposed to the sample. Depending on the filter used in the synthesis, these clusters are labeled C_W, C_R, C_B, C_G and C_Y (W, R, B, G and Y refer to without filter, with red, blue, green and yellow filters, respectively). The clusters formed were extracted into water. Variation in the absorption profiles were observed by varying the filter as shown in Fig. 4. At the same time, some similarities were also there, like the 480 nm peaks appeared for both the C_W and C_R cluster, but with different width. All these clusters show luminescence in the red region. Their QY is of the order of 10^{-3}. Clusters exhibit significant differences in their excitation and emission profiles. Excitation and emission spectra for C_W, C_R, C_B, C_Y, C_G clusters are given in Fig. S10.† As these clusters are protected with glutathione which is a dicarboxylic acid, it is possible to connect the polar end of the quaternary ammonium salts so that the resultant cluster is soluble in organic solvents. This kind of phase transfer helps in the exploration of properties of the clusters in both organic and aqueous phases.[55] The procedure for phase transfer is given in the ESI.† The absorption profiles of phase transferred clusters are not changed. Luminescence still remained as in the case of the parent clusters indicating that the cluster core is intact even after phase transfer. Photographs of the C_W, C_R, C_B, C_Y and C_G clusters in water and toluene before and after phase transfer in both ambient and UV light are given in Fig. 4II(a, a1, b and b1). These results confirm the fact that the cluster formation is highly dependent on the photon energy.

Several control experiments were done to understand the formation and to improve the yield of the cluster. The same reaction in the absence of sunlight does not produce clusters, showing the importance of light exposure for the synthesis (Fig. S11†). A Petri dish containing polymerized acrylamide gel with Ag(I)SG was kept in sunlight but covered with aluminum foil so that there was no light penetration while there was heat input. After 6 h of exposure, there was no observable color change during the reaction (Fig. S12†). This ruled out the possibility of any thermal effect in cluster synthesis. Upon exposure of aqueous oligomeric Ag(I) SG to sunlight, (Fig. S13†) silver clusters were not formed. It shows featureless UV/Vis spectra which resembled the spectrum of oligomeric Ag(I)SG (figure not shown). In the absence of gel polymerizing agent (APS and TEMED), clusters were formed but optical features were not prominent. The photographs and UV/Vis spectra of cluster, synthesized without gel precursors are given in Fig. 5I.

In another experiment, Ag(I)SG was placed in acetonitrile and exposed to sunlight for 8 h (Fig. S14†). A color change from blackish powder to reddish brown powder occurred indicating the reduction of silver. The final powder was insoluble in

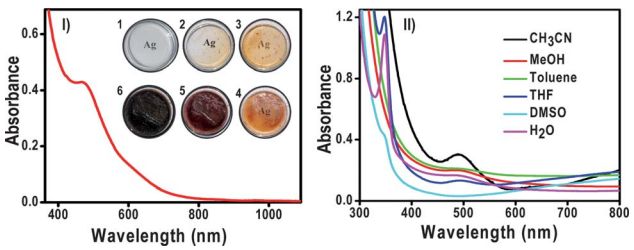

Fig. 5 (I) Inset (1 to 6) are photographs of AgQC synthesized without gel precursors (APS and TEMED) at different time intervals of exposure to sunlight, starting form initial to 6 h. UV/Vis spectrum of AgQC cluster extracted from 4. (II) UV/Vis spectra of AgQC synthesized in different media. Among them, acetonitrile shows enhanced intensity. The presence of gel as impurity in the product leads to increased background in some samples.

acetonitrile but dispersible in water. UV/Vis spectrum of the sample in aqueous medium showed a surface plasmon resonance at 400 nm indicating the formation of silver nanoparticles (Fig. S14†). In the case of acetonitrile, the growth step was not controlled so it produces nanoparticles, whereas in the gel system the growth of clusters was controlled within the gel templates.

A possible mechanism for the formation of the Ag@SG cluster is similar to that reported by Harada and Katagiri[56] where the process involves three main steps, namely photon induced reduction, autocatalytic nucleation and a subsequent growth process (Scheme 1, ESI†). The final growth is controlled by the ligand as well as the gel cavity available. Several other aspects such as temperature and photon energy will also have an influence on the cluster formation. It is known that the quantum efficiency of absorption (number of photons absorbed/total number of photons) is an important factor in the conversion of Ag(I) to Ag(0). This can be improved by choosing a given solvent in the photochemical reaction so that the liquid phase proceeds under the influence of the solvent cage.[57] So, the mechanism of photoreduction by using a solvent as a cage is assumed to be electron transfer from the solvent molecule to the silver ion: $(Ag^{+}, ROH/NH_2/CN)_{cage} + h\nu \rightarrow (Ag, ROH^{+}/NH_2^{+}/CN^{+})_{cage}$.[57] Cluster formation is initiated by the photons of sunlight, through the influence of the solvent cage and then through a autocatalytic nucleation process,[58] further growth happens as described above.

Various solvents such as toluene, acetonitrile, tetrahydrofuran and dimethyl formamide were taken on top of the reaction medium (polymerized gel + Ag(I)SG) and exposed to sunlight (Fig. S15†). This was to check the effect of solvent properties on cluster synthesis. Variations in their absorption profile were observed as the extent of cluster formation was different for each solvent (Fig. 5II). The product obtained in acetonitrile shows better intensity compared to all other solvents. This supports our earlier argument that CH_3CN can facilitate the photochemical reduction of silver. This synthetic method is extendable to get clusters protected with other ligands such as mercaptosuccinic acid (Fig. S16†) and cysteine (Fig. S17†). The possibility of obtaining gold clusters was also checked (Fig. S18†).

The antibacterial activity of monolayer protected AgQCs was evaluated against a Gram negative organism, *Escherichia coli* (Fig. 6) and Gram positive organism, *Staphylococcus aureus* (Fig. S19I†). The result shows that the AgQCs were more active against *E. coli* than towards *S. aureus*. The average diameter of the zone of inhibition for *E. coli* was about 12, 14, 16 and 19 mm, respectively for 10, 20, 30 and 40 μL of synthesized AgQCs. For *S. aureus* (Fig. S19I†), the inhibitory effect was mild when compared to *E. coli*. Here, the diameter of the zone of inhibition was found to be 11, 12, 14 and 16 mm for the 10, 20, 30 and 40 μL of AgQCs, respectively. A solution-based study (Fig. S19II and III†) also shows similar results to those we got for the diffusion method where we could see that AgQCs are much more effective against Gram negative bacteria compared to Gram positive ones. With an increase in cluster concentration, the antibacterial effect also increases, so it is a concentration

Fig. 6 The antibacterial activity of (I) monolayer protected AgQCs compared with (II) glutathione, (III) Ag(I)@SG, (IV) Au_{25}@SG and (V) Ag@SG nanoparticle. In all the cases, Petri dishes of 2.5 cm diameter and *Escherichia coli* bacteria (ATCC 8739) were used.

dependent phenomenon. Experiments using glutathione, Ag(I) SG complex and $Au_{25}(SG)_{18}$ clusters do not show any zone of inhibition which confirms that the antibacterial activity is due to the AgQCs alone. The mechanism of the antibacterial properties can be understood from a recent report of Alvarez *et al.*[59] The fast internalization of silver nanoclusters may be one of the reasons for this activity. The other possibility is the enhanced release of silver ions from the clusters which happens as a result of the following equations.

$$4Ag(0) + O_2 \rightarrow 2Ag_2O \quad (1)$$

$$2Ag_2O + 4H^{+} \rightarrow 4Ag^{+} + 2H_2O \quad (2)$$

The consequent antibacterial action makes the structural changes which result in cell death.[60,61] It is also known that Ag nanoclusters interact with sulfur containing proteins which in turn affects the cell viability.[62] Glutathione protected nanoparticles does not show any antibacterial effect which proves the earlier argument of fast silver ion release from clusters in comparison to nanoparticles.[59]

Conclusion

In summary, we have demonstrated sunlight-induced formation of silver clusters starting from silver thiolate complexes, in suitable gel templates. The as-synthesized AgQCs were extracted into water and made into fine powders using freeze drying. Gel templates were chosen in such a way that they were insoluble in water. AgQCs show step-like features in optical absorption spectrum as well as intense emission in the luminescence spectrum. The cluster formation is sensitive to solvents and ligands. We have demonstrated cluster formation with glutathione as the ligand. A similar method can also be used for gold clusters. These clusters can be phase transferred from aqueous to organic medium. The clusters show enhanced antibacterial action in comparison to plasmonic nanoparticles protected with glutathione.

Experimental section

Chemicals

All the chemicals were commercially available and were used without further purification. Silver nitrate ($AgNO_3$, 99%), glutathione (GSH, 97%), methanol (GR grade), acrylamide (AR grade), *N*,*N*′-methylenebisacrylamide (BIS) (AR grade), ammonium persulfate and *N*,*N*,*N*′,*N*′-tetramethylethylene diamine (TEMED) were purchased from SRL Chemical Co. Ltd., India. Solvents, ethanol (HPLC grade, 99.9%, Aldrich), methanol (HPLC grade, Aldrich), dichloromethane (HPLC grade, 99.9%, Aldrich) were used as received.

Synthesis

A well-known gel, acrylamide:bisacrylamide was used to control the growth of AgQCs. Gel solutions were synthesized similar to the method reported from our group[22] with slight modification in the concentrations of the thiol. In a typical synthesis, 10 g of acrylamide and 0.75 g of bisacrylamide were dissolved in 50 mL of water and sonicated to get a clear solution (which was stored at 10 °C and used as stock solution). 47 mg of silver nitrate and 110 mg of GSH were added to 1 mL of 1 M NaOH; the resultant mixture was sonicated until the solution color changes from turbid to clear pale yellow which is due to the formation of oligomeric silver thiolate. 3 mL of the former solution was poured into a Petri dish which contains 1 mL of silver thiolate and the two were mixed well to form a uniform solution. Then 30 μL of APS (0.1%) and 20 μL TEMED were added to initiate the polymerization. Upon keeping the sample without disturbance, polymerization and formation of the gel was visible after 15–20 min. The sample was kept under sunlight for 6 hours (starting at 9 am, in open air) to yield AgQCs. Chennai, during the period of the experiment (June–December 2011), was sunny for most of the days (average temperature 28 °C). Formation of AgQCs was visible by a change of color from colorless to black-brown. Addition of 10 mL water to the gel results in the extraction of the cluster selectively, leaving gel pieces at the bottom. These were separated from the cluster solution through filtration, followed by centrifugation. The final cluster solution was subjected to freeze drying to yield a powder sample. The cluster was phase transferred to the organic medium to observe its enhanced luminescence properties (ESI, Fig. S1†).

Ag@SG nanoparticles were made with $AgNO_3$ (47 mg) and GSH (110 mg in 50 mL water) followed by rapid addition of $NaBH_4$ (90 mg in 12.5 mL water). It was further purified by ethanol washing and dried in Rotavapor.

Instrumentation

UV/Vis spectra were measured with a Perkin Elmer Lambda 25 instrument in the range of 200–1100 nm. Luminescence measurements were carried out on a Jobin Yvon NanoLog instrument. The band pass for excitation and emission was set as 2 nm. X-ray photoelectron spectroscopy (XPS) measurements were conducted using an Omicron ESCA Probe spectrometer with polychromatic MgKα X-rays ($h\nu = 1253.6$ eV). The samples were spotted as drop-cast films on a sample stub. Constant analyzer energy of 20 eV was used for the measurements. High resolution transmission electron microscopy of clusters was carried out with a JEOL 3010 instrument. The samples were drop cast on carbon-coated copper grids and allowed to dry under ambient conditions. FT-IR spectra were measured with a Perkin Elmer Spectrum One instrument. KBr crystals were used as the matrix for preparing samples.

The bacterial strain, *Escherichia coli* (Gram-negative rod) and *Staphylococcus aureus* (Gram positive) were obtained from the Culture Collection Center (strains used were, ATCC 8739 & MTCC96). The antibacterial activity of the Ag nanoclusters against the organisms were measured using the well-diffusion method. Pure cultures of bacteria were grown in Mueller–Hinton broth (HiMedia, Mumbai, India) at 27 °C on a rotary shaker at 200 rpm. Wells that were 6 mm in diameter were made on the Mueller–Hinton LB plates using a gel puncture. The cultures were swabbed on test media with sterile cotton swabs. About 10, 20, 30 and 40 μL of synthesized Ag nanoclusters were added to the well, and then the plates were incubated in an incubator at 37 °C for 12 h. After incubation, the diameter of the inhibition zone was measured. To compare the antibacterial activity, the experiment was repeated using glutathione, Ag(I)@SG, Au_{25}@SG and Ag@SG nanoparticles instead of AgQCs. Sterile distilled water was put in the control well. For the solution phase antibacterial test, sterile test tubes, each containing 2 mL of nutrient broth medium and the desired amount of Ag nanocluster solutions were inoculated with 10 μL of freshly prepared bacterial suspension. The tubes were incubated at 37 °C in a rotary shaker at 200 rpm. The bacterial growth was evaluated by measuring the increase of the absorbance at 600 nm at regular intervals for 24 hours in a spectrophotometer.

Acknowledgements

We thank the Department of Science and Technology, Government of India for constantly supporting our research program on nanomaterials. I. C. Thanks IITM for a research fellowship.

Notes and references

1 C. M. Aikens, *J. Phys. Chem. C*, 2008, **112**, 19797–19800.
2 Y. Shichibu, Y. Negishi, T. Watanabe, N. K. Chaki, H. Kawaguchi and T. Tsukuda, *J. Phys. Chem. C*, 2007, **111**, 7845–7847.
3 M. Zhu, C. M. Aikens, F. J. Hollander, G. C. Schatz and R. Jin, *J. Am. Chem. Soc.*, 2008, **130**, 5883–5885.
4 K. Nobusada and T. Iwasa, *J. Phys. Chem. C*, 2007, **111**, 14279–14282.
5 Y. Negishi, H. Tsunoyama, M. Suzuki, N. Kawamura, M. M. Matsushita, K. Maruyama, T. Sugawara, T. Yokoyama and T. Tsukuda, *J. Am. Chem. Soc.*, 2006, **128**, 12034–12035.
6 M. Zhu, C. M. Aikens, M. P. Hendrich, R. Gupta, H. Qian, G. C. Schatz and R. Jin, *J. Am. Chem. Soc.*, 2009, **131**, 2490–2492.
7 Y. Bao, C. Zhong, D. M. Vu, J. P. Temirov, R. B. Dyer and J. S. Martinez, *J. Phys. Chem. C*, 2007, **111**, 12194–12198.

8 T. P. Bigioni, R. L. Whetten and Ã. Dag, *J. Phys. Chem. B*, 2000, **104**, 6983–6986.
9 S. Link, A. Beeby, S. FitzGerald, M. A. El-Sayed, T. G. Schaaff and R. L. Whetten, *J. Phys. Chem. B*, 2002, **106**, 3410–3415.
10 E. S. Shibu, B. Radha, P. K. Verma, P. Bhyrappa, G. U. Kulkarni, S. K. Pal and T. Pradeep, *ACS Appl. Mater. Interfaces*, 2009, **1**, 2199–2210.
11 G. Wang, T. Huang, R. W. Murray, L. Menard and R. G. Nuzzo, *J. Am. Chem. Soc.*, 2004, **127**, 812–813.
12 J. Zheng, J. T. Petty and R. M. Dickson, *J. Am. Chem. Soc.*, 2003, **125**, 7780–7781.
13 S. Chen, *J. Phys. Chem. B*, 2000, **104**, 663–667.
14 S. Chen, R. S. Ingram, M. J. Hostetler, J. J. Pietron, R. W. Murray, T. G. Schaaff, J. T. Khoury, M. M. Alvarez and R. L. Whetten, *Science*, 1998, **280**, 2098–2101.
15 D. G. Georganopoulou, M. V. Mirkin and R. W. Murray, *Nano Lett.*, 2004, **4**, 1763–1767.
16 R. S. Ingram, M. J. Hostetler, R. W. Murray, T. G. Schaaff, J. T. Khoury, R. L. Whetten, T. P. Bigioni, D. K. Guthrie and P. N. First, *J. Am. Chem. Soc.*, 1997, **119**, 9279–9280.
17 B. M. Quinn, P. Liljeroth, V. Ruiz, T. Laaksonen and K. s. Kontturi, *J. Am. Chem. Soc.*, 2003, **125**, 6644–6645.
18 Y. Yang and S. Chen, *Nano Lett.*, 2002, **3**, 75–79.
19 C. Burda, X. Chen, R. Narayanan and M. A. El-Sayed, *Chem. Rev.*, 2005, **105**, 1025–1102.
20 H. Tsunoyama, H. Sakurai, N. Ichikuni, Y. Negishi and T. Tsukuda, *Langmuir*, 2004, **20**, 11293–11296.
21 H. Tsunoyama, H. Sakurai, Y. Negishi and T. Tsukuda, *J. Am. Chem. Soc.*, 2005, **127**, 9374–9375.
22 I. Chakraborty, T. Udayabhaskararao and T. Pradeep, *J. Hazard. Mater.*, 2012, **211–212**, 396–403.
23 A. George, E. S. Shibu, S. M. Maliyekkal, M. S. Bootharaju and T. Pradeep, *ACS Appl. Mater. Interfaces*, 2012, **4**, 639–644.
24 I. Chakraborty, T. Udayabhaskararao and T. Pradeep, *Chem. Commun.*, 2012, **48**, 6788–6790.
25 J. M. Slocik and D. W. Wright, *Biomacromolecules*, 2003, **4**, 1135–1141.
26 B. Adhikari and A. Banerjee, *Chem. Mater.*, 2010, **22**, 4364–4371.
27 N. Cathcart and V. Kitaev, *J. Phys. Chem. C*, 2010, **114**, 16010–16017.
28 I. Chakraborty, A. Govindarajan, J. Erusappan, A. Ghosh, T. Pradeep, B. Yoon, R. L. Whetten and U. Landman, *Nano Lett.*, 2012, **12**, 5861–5866.
29 T. U. B. Rao, B. Nataraju and T. Pradeep, *J. Am. Chem. Soc.*, 2010, **132**, 16304–16307.
30 S.-I. Tanaka, J. Miyazaki, D. K. Tiwari, T. Jin and Y. Inouye, *Angew. Chem., Int. Ed.*, 2011, **50**, 431–435.
31 K. Chaudhari, P. L. Xavier and T. Pradeep, *ACS Nano*, 2011, **5**, 8816–8827.
32 C. Shao, B. Yuan, H. Wang, Q. Zhou, Y. Li, Y. Guan and Z. Deng, *J. Mater. Chem.*, 2011, **21**, 2863–2866.
33 P. L. Xavier, K. Chaudhari, P. K. Verma, S. K. Pal and T. Pradeep, *Nanoscale*, 2010, **2**, 2769–2776.
34 J. Xie, Y. Zheng and J. Y. Ying, *J. Am. Chem. Soc.*, 2009, **131**, 888–889.
35 M. A. H. Muhammed, A. K. Shaw, S. K. Pal and T. Pradeep, *J. Phys. Chem. C*, 2008, **112**, 14324–14330.
36 H. Schnöckel, A. Schnepf, R. L. Whetten, C. Schenk and P. Henke, *J. Inorg. Gen. Chem.*, 2011, **637**, 15–23.
37 E. S. Shibu and T. Pradeep, *Chem. Mater.*, 2011, **23**, 989–999.
38 Y. Zhu, H. Qian, B. A. Drake and R. Jin, *Angew. Chem., Int. Ed.*, 2010, **49**, 1295–1298.
39 T. Udayabhaskararao and T. Pradeep, *J. Phys. Chem. Lett.*, 2013, 1553–1564.
40 O. M. Bakr, V. Amendola, C. M. Aikens, W. Wenseleers, R. Li, L. Dal Negro, G. C. Schatz and F. Stellacci, *Angew. Chem., Int. Ed.*, 2009, **48**, 5921–5926.
41 T. Udaya Bhaskara Rao and T. Pradeep, *Angew. Chem., Int. Ed.*, 2010, **49**, 3925–3929.
42 Z. Wu, E. Lanni, W. Chen, M. E. Bier, D. Ly and R. Jin, *J. Am. Chem. Soc.*, 2009, **131**, 16672–16674.
43 S. Kumar, M. D. Bolan and T. P. Bigioni, *J. Am. Chem. Soc.*, 2010, **132**, 13141–13143.
44 Y. Mao, T.-J. Park, F. Zhang, H. Zhou and S. S. Wong, *Small*, 2007, **3**, 1122–1139.
45 J. P. Abid, A. W. Wark, P. F. Brevet and H. H. Girault, *Chem. Commun.*, 2002, 792–793.
46 S. Eustis, G. Krylova, A. Eremenko, N. Smirnova, A. W. Schill and M. El-Sayed, *Photochem. Photobiol. Sci.*, 2005, **4**, 154–159.
47 S. S. Shankar, A. Rai, A. Ahmad and M. Sastry, *J. Colloid Interface Sci.*, 2004, **275**, 496–502.
48 I. Bilecka and M. Niederberger, *Nanoscale*, 2010, **2**, 1358–1374.
49 B. Adhikari and A. Banerjee, *Chem.–Eur. J.*, 2010, **16**, 13698–13705.
50 I. Díez, M. Pusa, S. Kulmala, H. Jiang, A. Walther, A. S. Goldmann, A. H. E. Müller, O. Ikkala and R. H. A. Ras, *Angew. Chem., Int. Ed.*, 2009, **48**, 2122–2125.
51 L. A. Peyser, A. E. Vinson, A. P. Bartko and R. M. Dickson, *Science*, 2001, **291**, 103–106.
52 P. Ramasamy, S. Guha, E. S. Shibu, T. S. Sreeprasad, S. Bag, A. Banerjee and T. Pradeep, *J. Mater. Chem.*, 2009, **19**, 8456–8462.
53 M. A. Habeeb Muhammed and T. Pradeep, *Small*, 2011, **7**, 204–208.
54 M. S. Bootharaju and T. Pradeep, *J. Phys. Chem. C*, 2010, **114**, 8328–8336.
55 M. A. Habeeb Muhammed and T. Pradeep, *J. Cluster Sci.*, 2009, **20**, 365–373.
56 M. Harada and E. Katagiri, *Langmuir*, 2010, **26**, 17896–17905.
57 A. B. Norman, G. R. Smith and H. P. Hopkins, *J. Phys. Chem.*, 1976, **80**, 25–29.
58 K. Mallick, M. J. Witcomb and M. S. Scurrell, *J. Mater. Sci.*, 2004, **39**, 4459–4463.
59 Z.-m. Xiu, Q.-b. Zhang, H. L. Puppala, V. L. Colvin and P. J. J. Alvarez, *Nano Lett.*, 2012, **12**, 4271–4275.
60 S. Kaviya, J. Santhanalakshmi, B. Viswanathan, J. Muthumary and K. Srinivasan, *Spectrochim. Acta, Part A*, 2011, **79**, 594–598.
61 V. Venkatpurwar and V. Pokharkar, *Mater. Lett.*, 2011, **65**, 999–1002.
62 M. Guzman, J. Dille and S. p. Godet, *Nanomedicine*, 2012, **8**, 37–45.

Supplementary information for paper

Sunlight mediated synthesis and antibacterial properties of monolayer protected silver clusters

Indranath Chakraborty[a], T. Udayabhaskararao[b], Deepesh G. K and T. Pradeep*

a and b contributed equally

DST Unit of Nanoscience (DST UNS), Department of Chemistry, Indian Institute of Technology, Madras, Chennai 600 036, India.

**Email: pradeep@iitm.ac.in*

Supporting information 1.

Phase transfer of cluster

The silver cluster is protected with glutathione and is water soluble. This cluster can be transferred from the aqueous to the toluene phase by the phase-transfer reagent, tetraoctylammonium bromide (TOABr). For this, an aqueous solution of cluster (5 mg/mL) was mixed with 5 mM TOABr in toluene and stirred vigorously for 2 min. Silver clusters underwent immediate and complete phase transfer from the aqueous to the toluene layer. The phase transfer can be monitored visually by the color changes in the aqueous and toluene layers. The colorless toluene layer turned reddish brown and the aqueous layer, which was originally reddish brown, turned colorless after stirring. The phase transfer occurred by the electrostatic attraction between the hydrophilic carboxylate anion of the glutathione ligand on the cluster in the aqueous phase and the hydrophobic tetraoctylammonium cation in the toluene phase.

Supporting information 2

Large scale synthesis of Ag@SG clusters

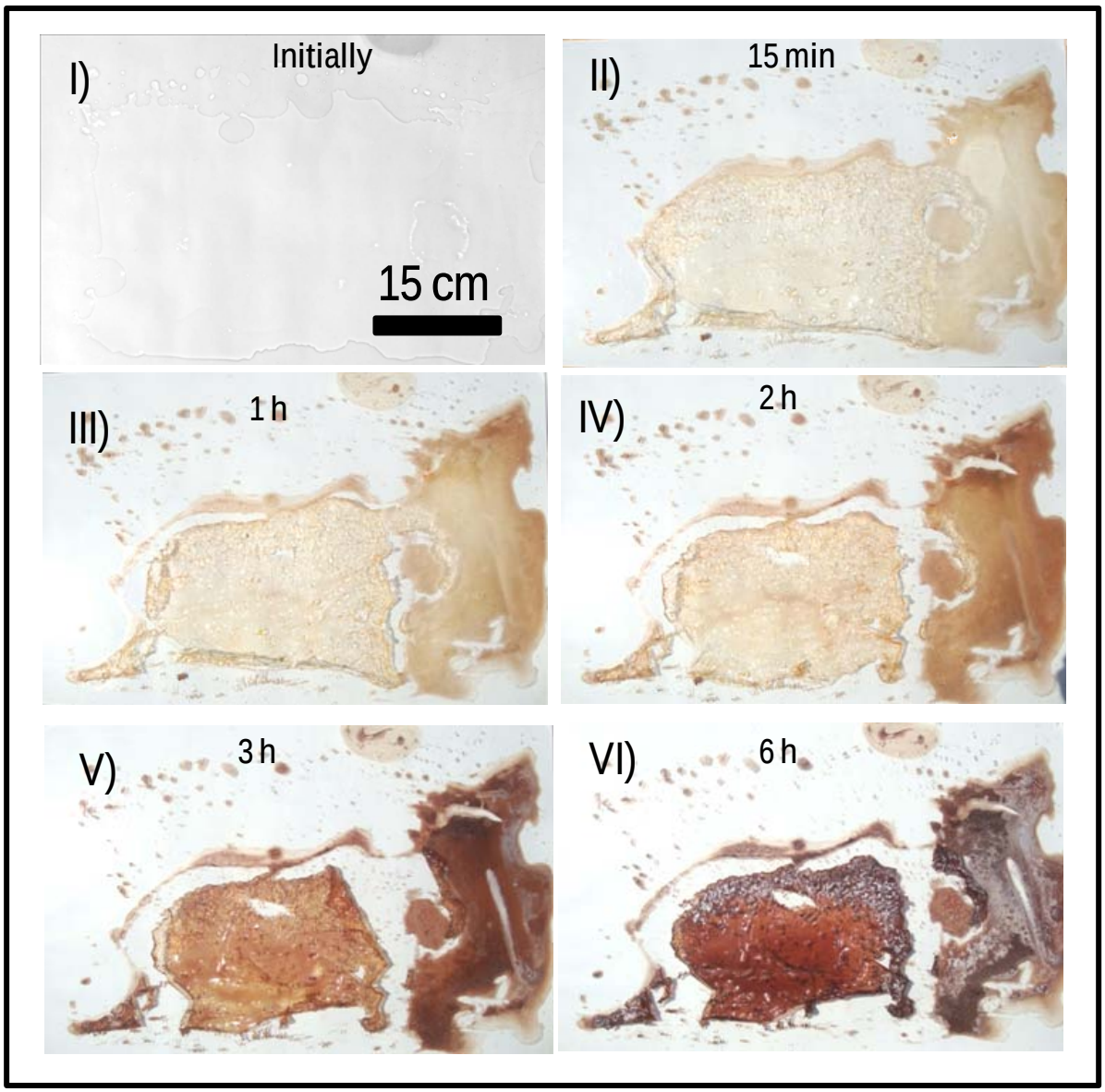

Fig. S2. Polyacrylamide solution along with Ag (I) SG was spread on a glass plate and kept under sunlight for six hours to complete the reaction. I) to VI) show the progress of the reaction with time.

Supporting information 3

Extraction of the cluster

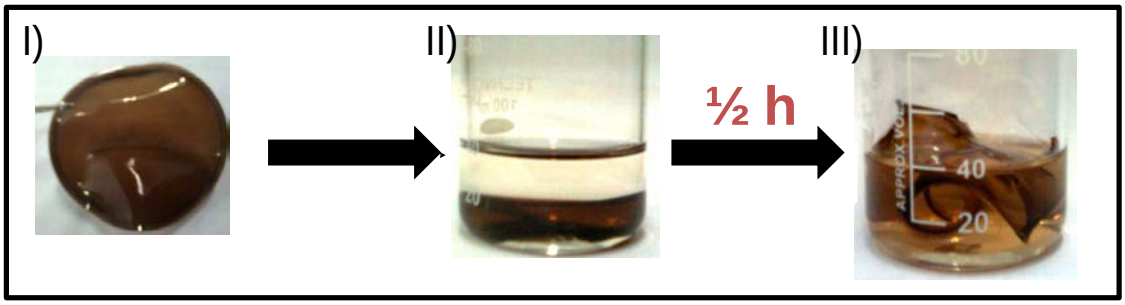

Fig. S3. I) Photograph of the gel template containing Ag@SG clusters. II) These templates were soaked in water for 30 min. III) The clusters were dispersed and the gel remained insoluble.

Supporting information 4

Evaluation of cluster growth monitored by UV

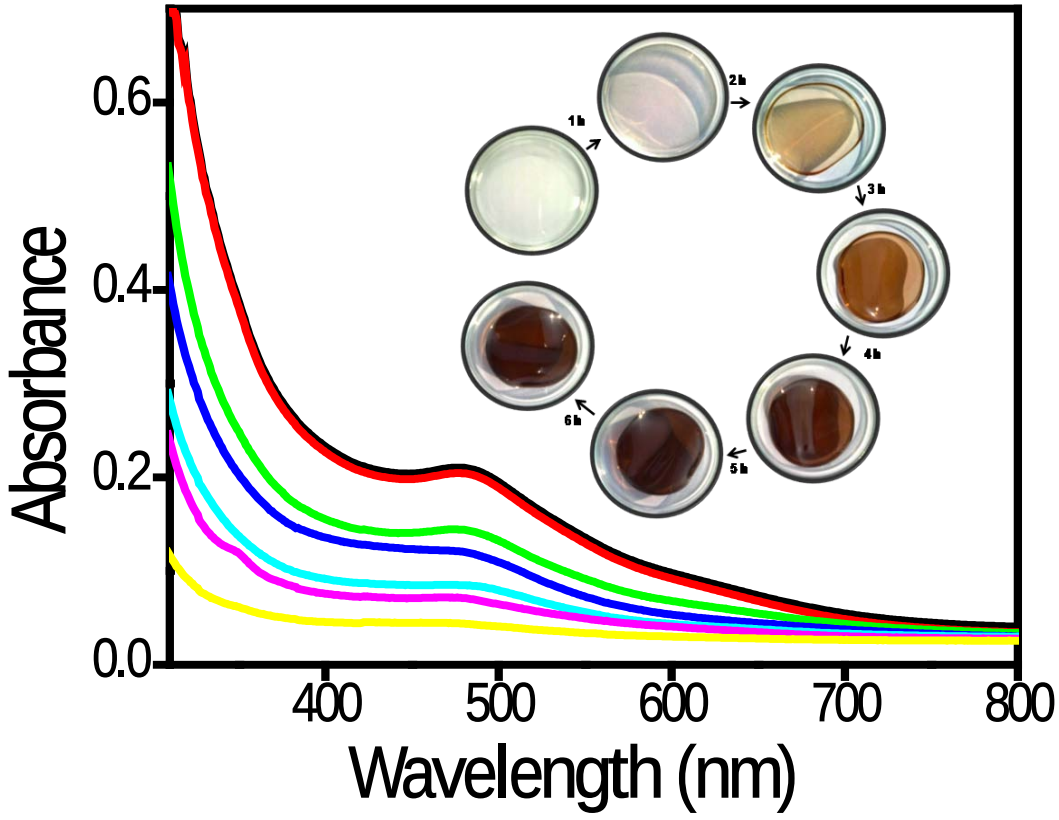

Fig. S4. Time dependent UV/Vis spectra during Ag@SG cluster evaluation. Corresponding photographs are shown in inset.

Supporting information 5

HRTEM images

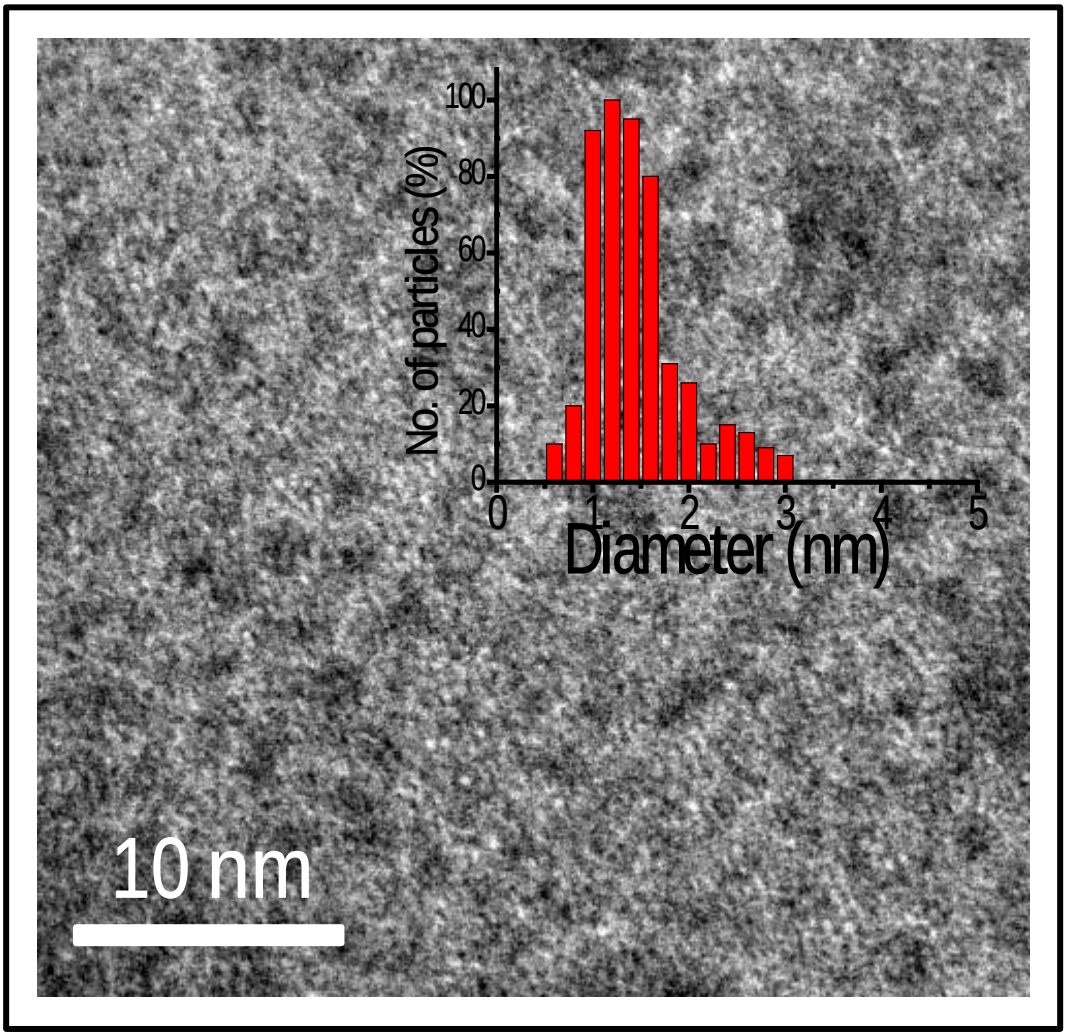

Fig. S5. HTEM image of Ag@SG clusters. Inset shows the size distribution of clusters indicating an average size of 1.6 nm.

Supporting information 6.

XPS survey spectrum

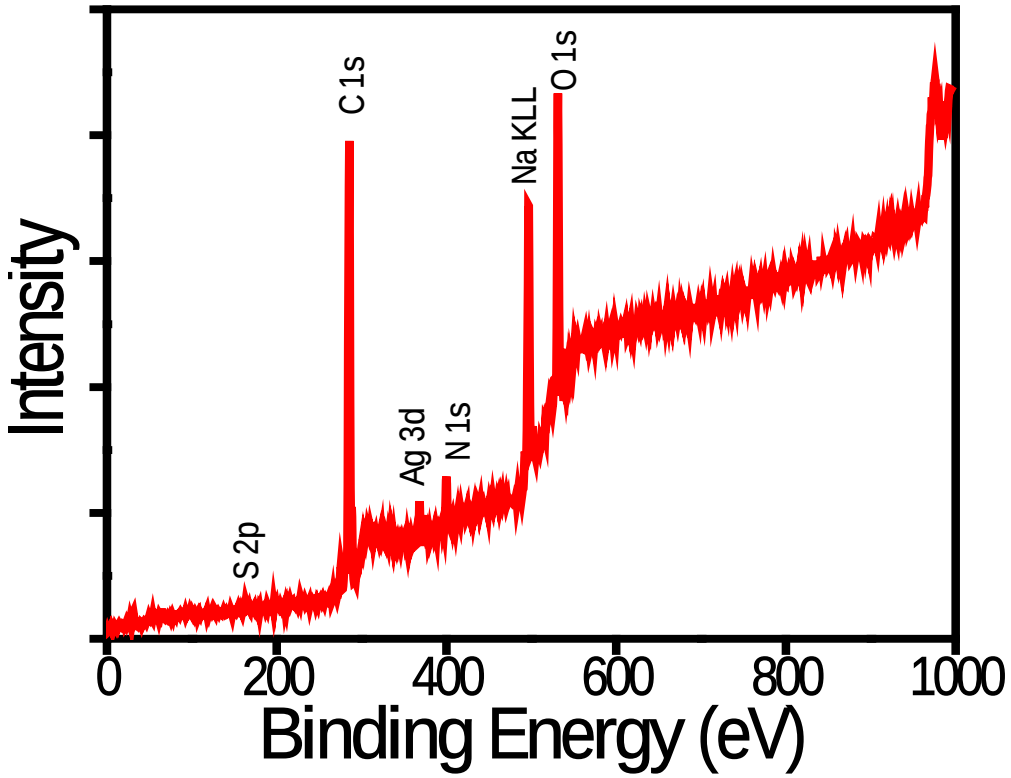

Fig. S6. XPS survey spectrum of the as-synthesized cluster. Individual peaks are labeled.

Supporting information 7.

Elaborated XPS spectra for individual regions

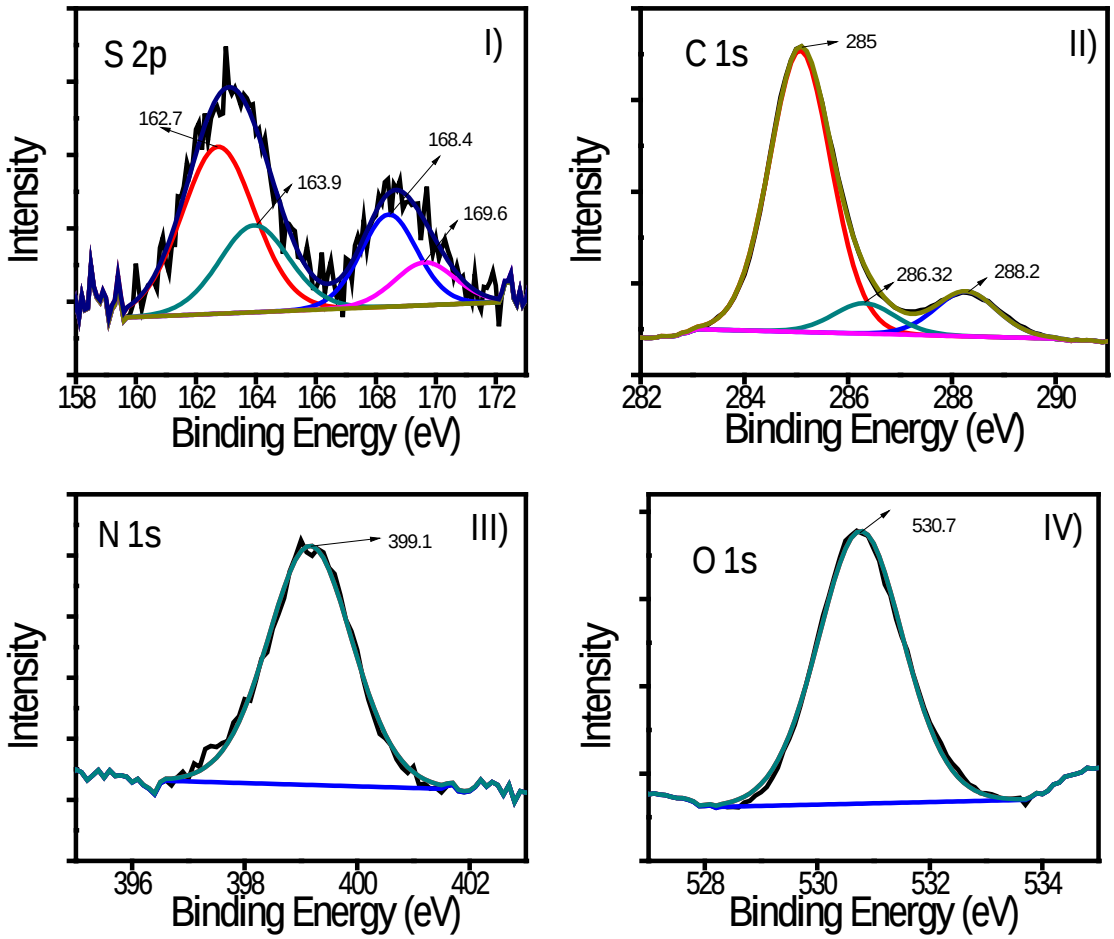

Fig. S7. XPS spectra for individual regions. Spectra were fitted using Casa XPS software.

Supporting information 8

IR spectra of GSH and AgQCs

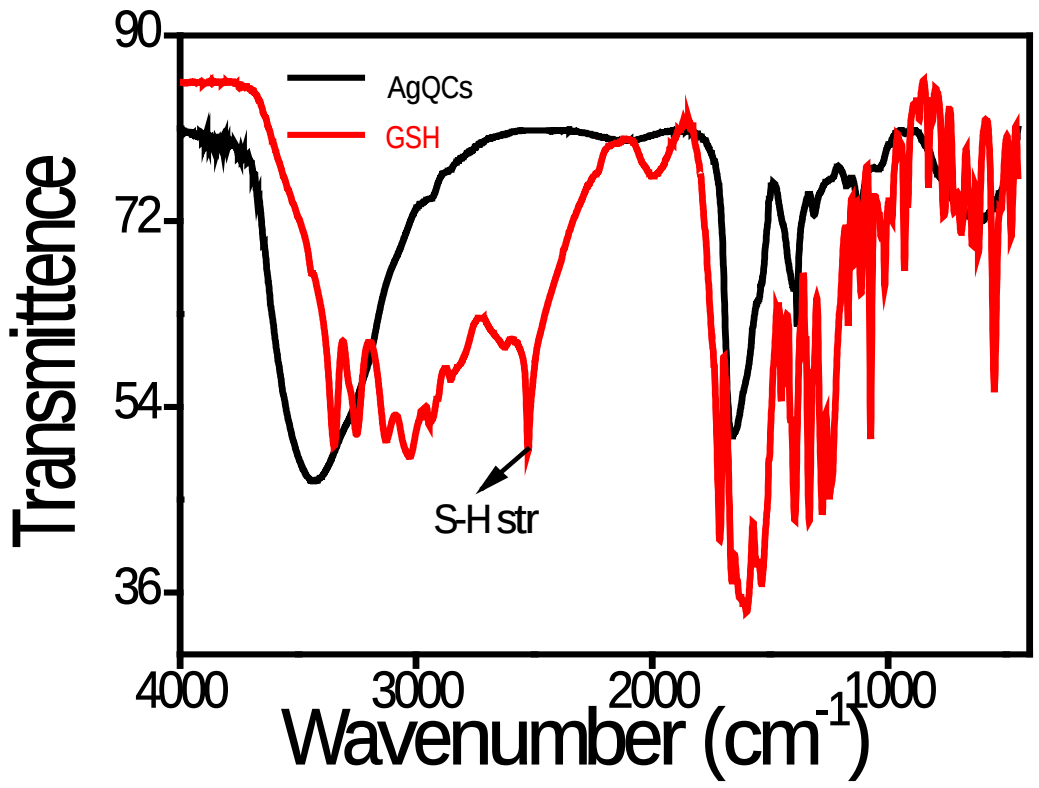

Fig. S8. Comaprative IR spectra of AgQCs and GSH. The absence of band at 2552 cm^{-1} confirms the attachement of glutathione to the cluster core.

Supporting information 9

ESI MS data of Ag@QC

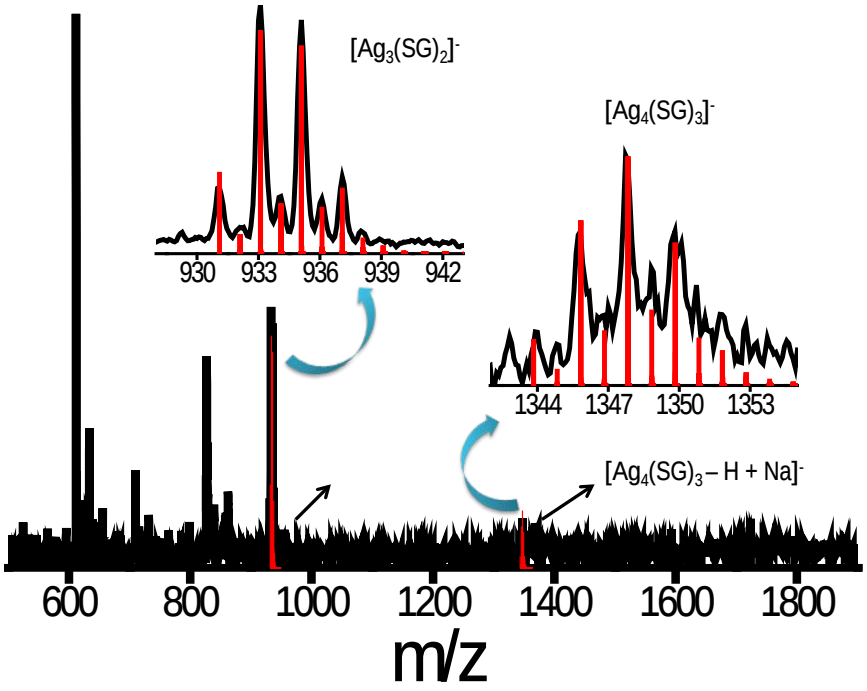

Fig. S9. ESI mass spectrum of as-synthesized cluster in negetive mode. Inset shows some fragments with good isotope distribution.

Supporting information 10

Excitation and emission spectra of the cluster, synthesized using different filters

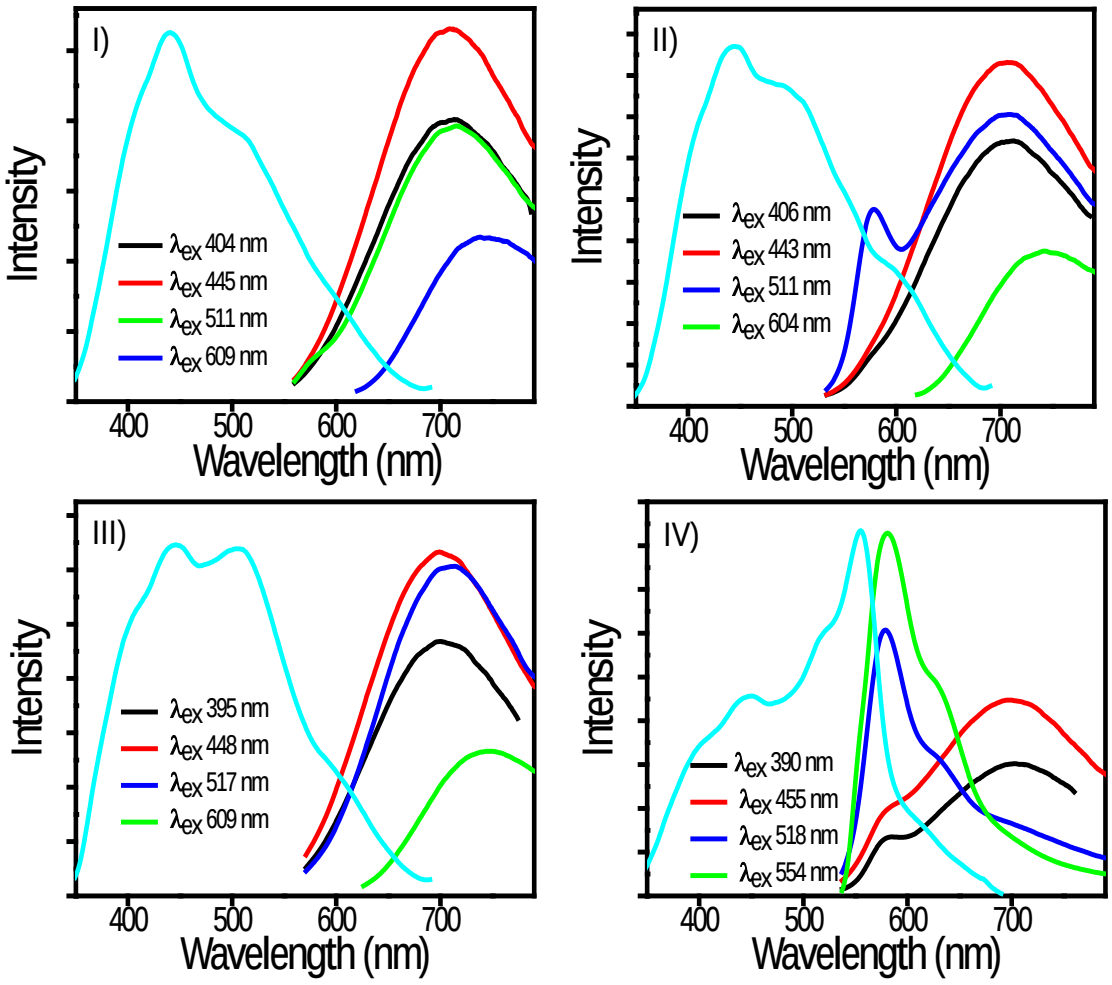

Fig. S10. Exciation and emission spectra of C_R (I), C_Y (II), C_G (III) and C_B (IV).

Supporting information 11

Reaction in dark

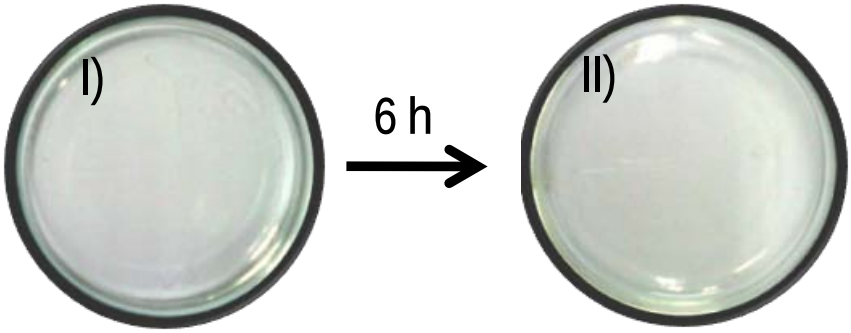

Fig. S11. I) Photograph of the polymeric gel + Ag(I)SG taken in a petri dish kept in dark. Note that gel is transparent. II) After six hours, the same petri dish shows no change in color indicating the absence of reaction under dark conditions.

Supporting information 12

Effect of heat, in the absence of sunlight

Fig. S12. I) Polymerized acrylamide gel along with Ag(I)SG. II) Sample covered with aluminium foil and exposed to sunlight in outdoor air. III) No visible color change after 6 h of exposure to sunlight. The ambience was at 35^{o}C.

Supporting information 13

Oligomeric Ag (I) SG in water and in sunlight

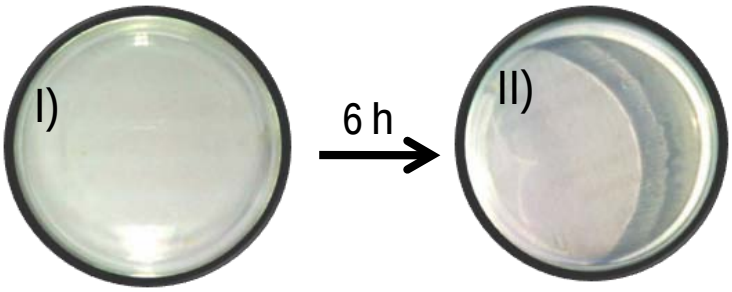

Fig. S13. I) Photograph of the Ag(I)SG in water taken in a petri dish kept under sunlight. II) After six hours the petri dish does not show any change in color indicating that the reaction did not occur.

Supporting information 14

Effect of acetonitrile in the absence of gel

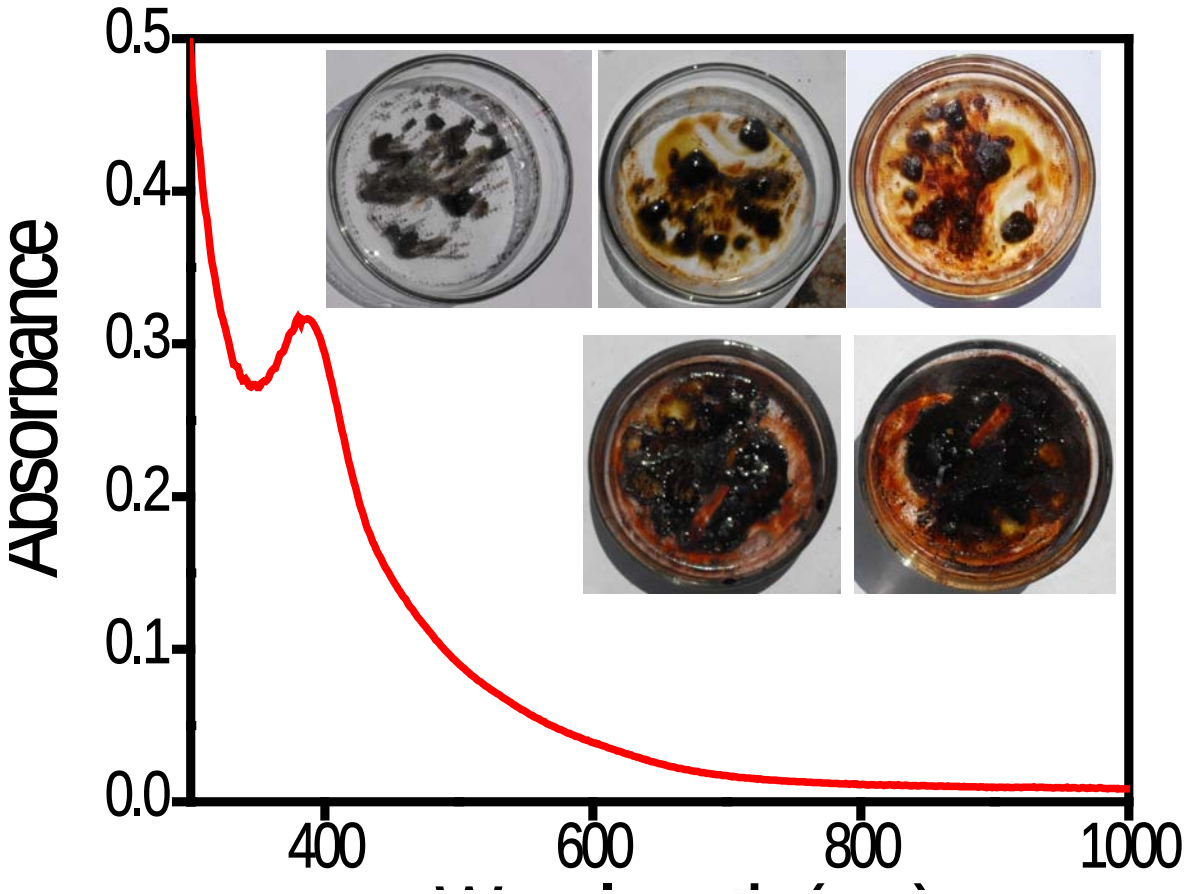

Fig. S14. UV/Vis spectrum of the material formed when acetonitrile was taken in place of gel. Inset shows photographs at different time intervals. This shows the formation of plasmonic nanoparticles.

Supporting information 15

Effect of various solvent during cluster growth

Toluene:

I)

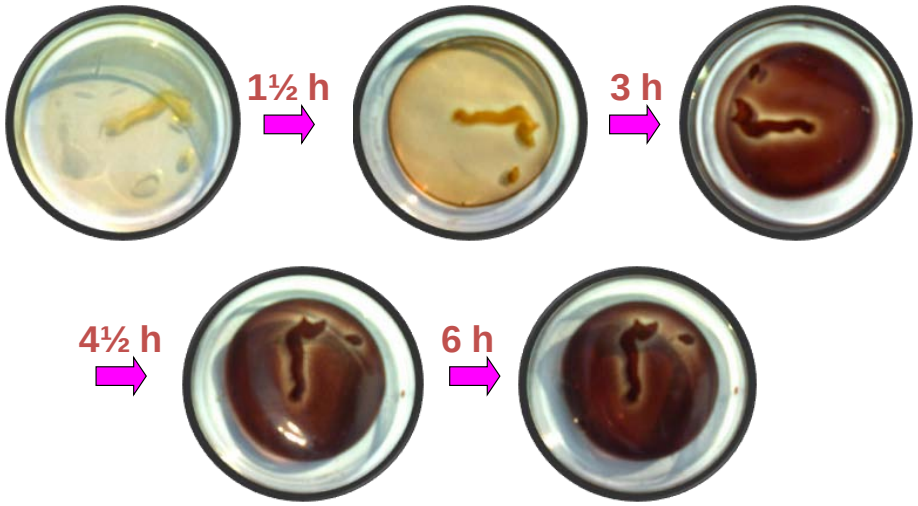

Methanol

II)

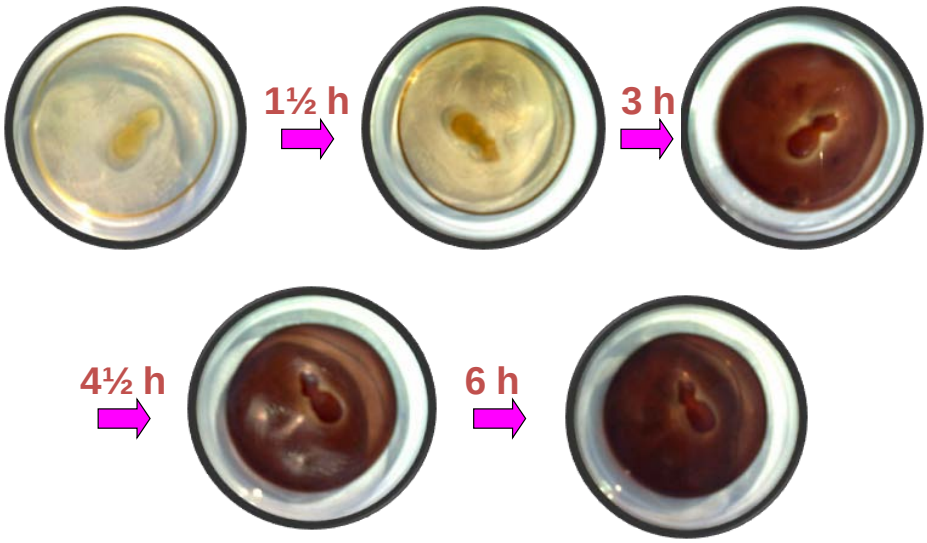

Acetonitrile

III)

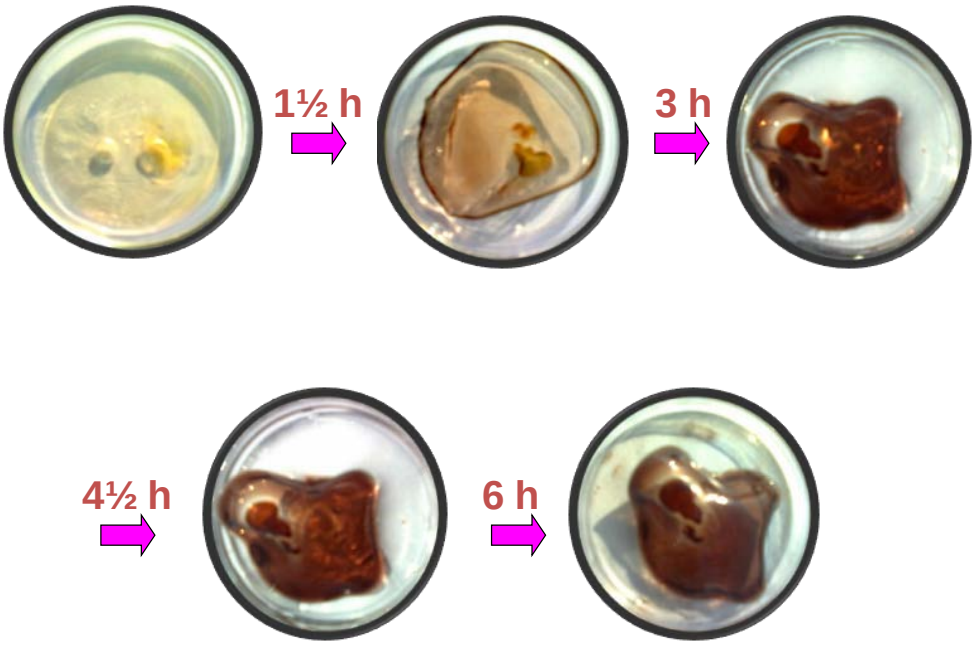

Tetrahydrofuran

IV)

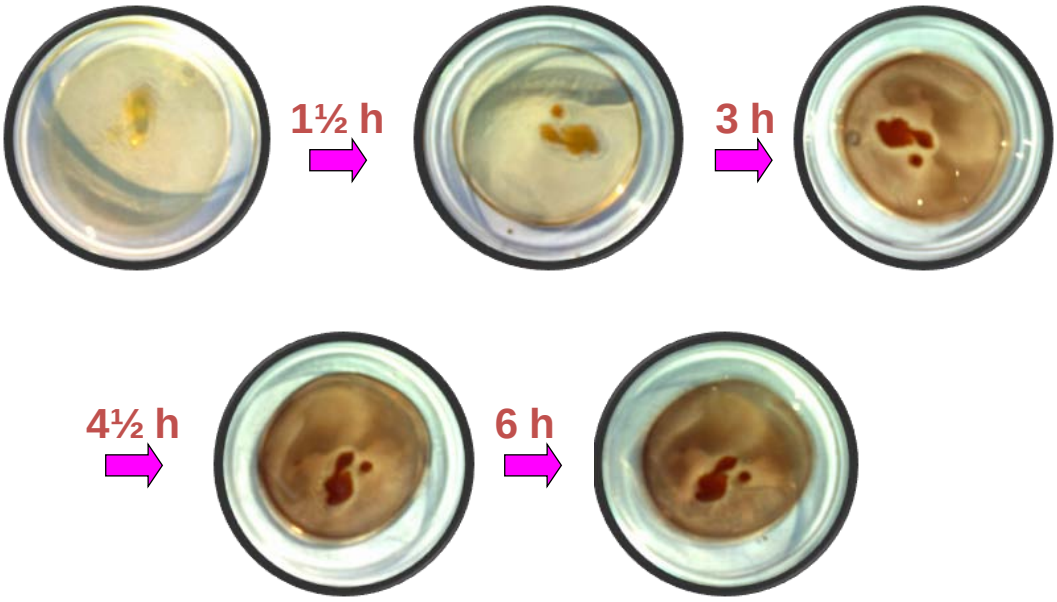

Dimethyl formamide

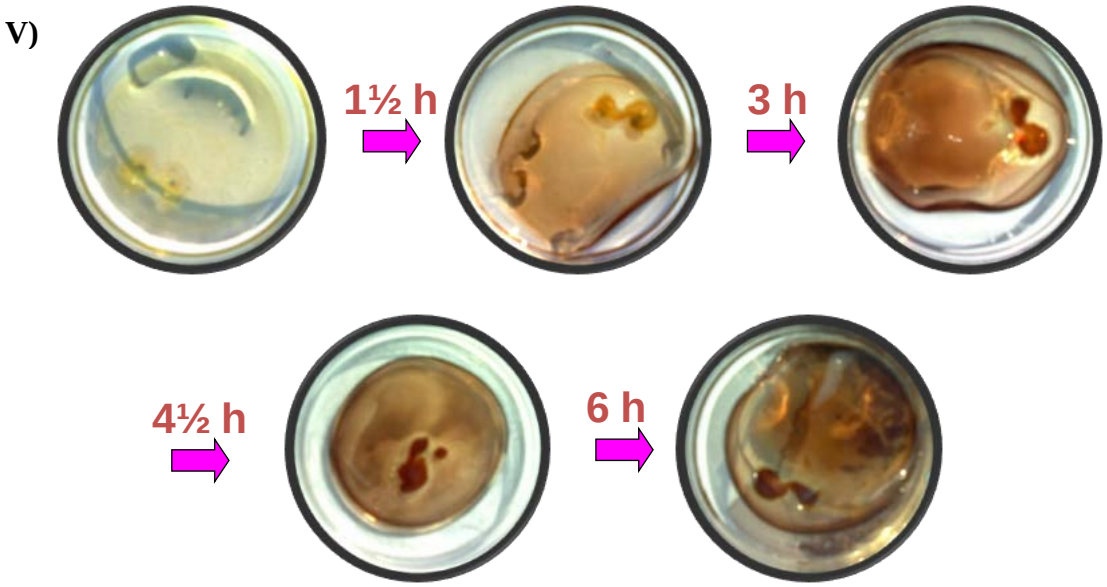

Water

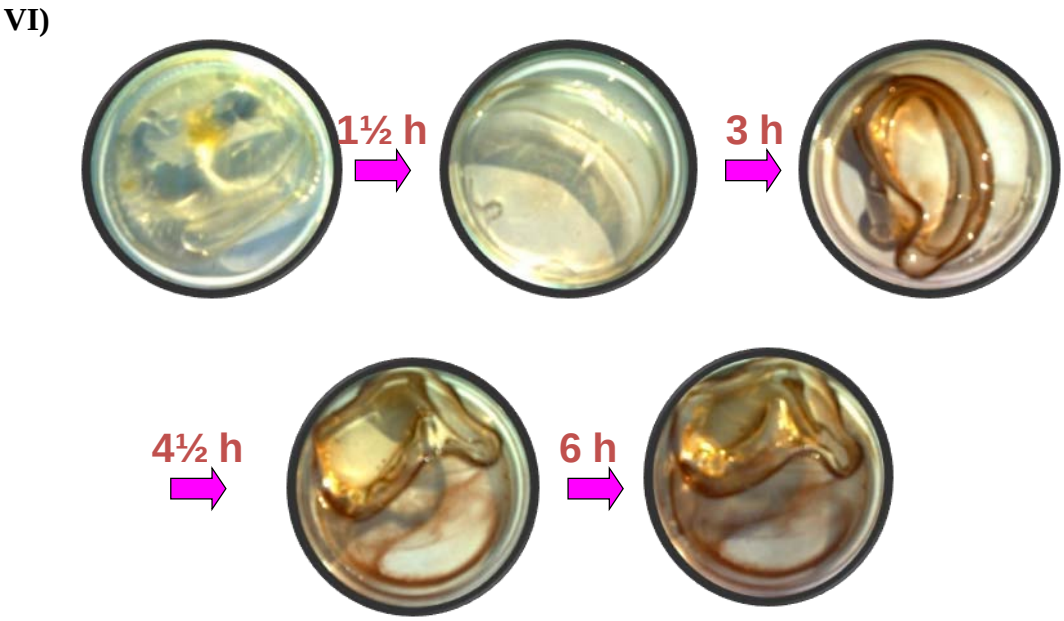

Fig. S15. Effect of various solvents: (I) toluene, II) methanol, III) acetonitrile, IV) tetrahydrofuran, V) dimethyl formamide and VI) water during cluster growth. Solvent volume was kept constant. In water, the clusters were extracted.

Supporting information 16

Evaluation of Ag@MSA cluster growth

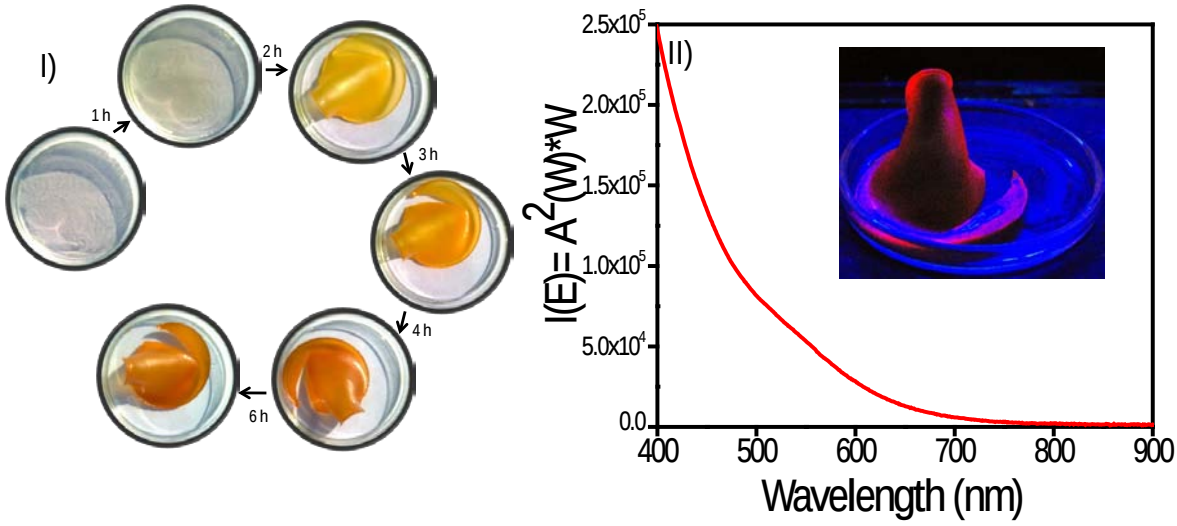

Fig. S16. I) Polymerized acrylamide gel along with Ag (I) MSA. Photographs are of different periods of exposure of sample to sunlight. II) UV/Vis spectrum of Ag@MSA clusters extracted after 6h of exposure. Inset of II) shows a photograph of the sample collected under UV lamp showing red luminescence.

Supporting information 17

Evaluation of Ag@cysteine cluster growth

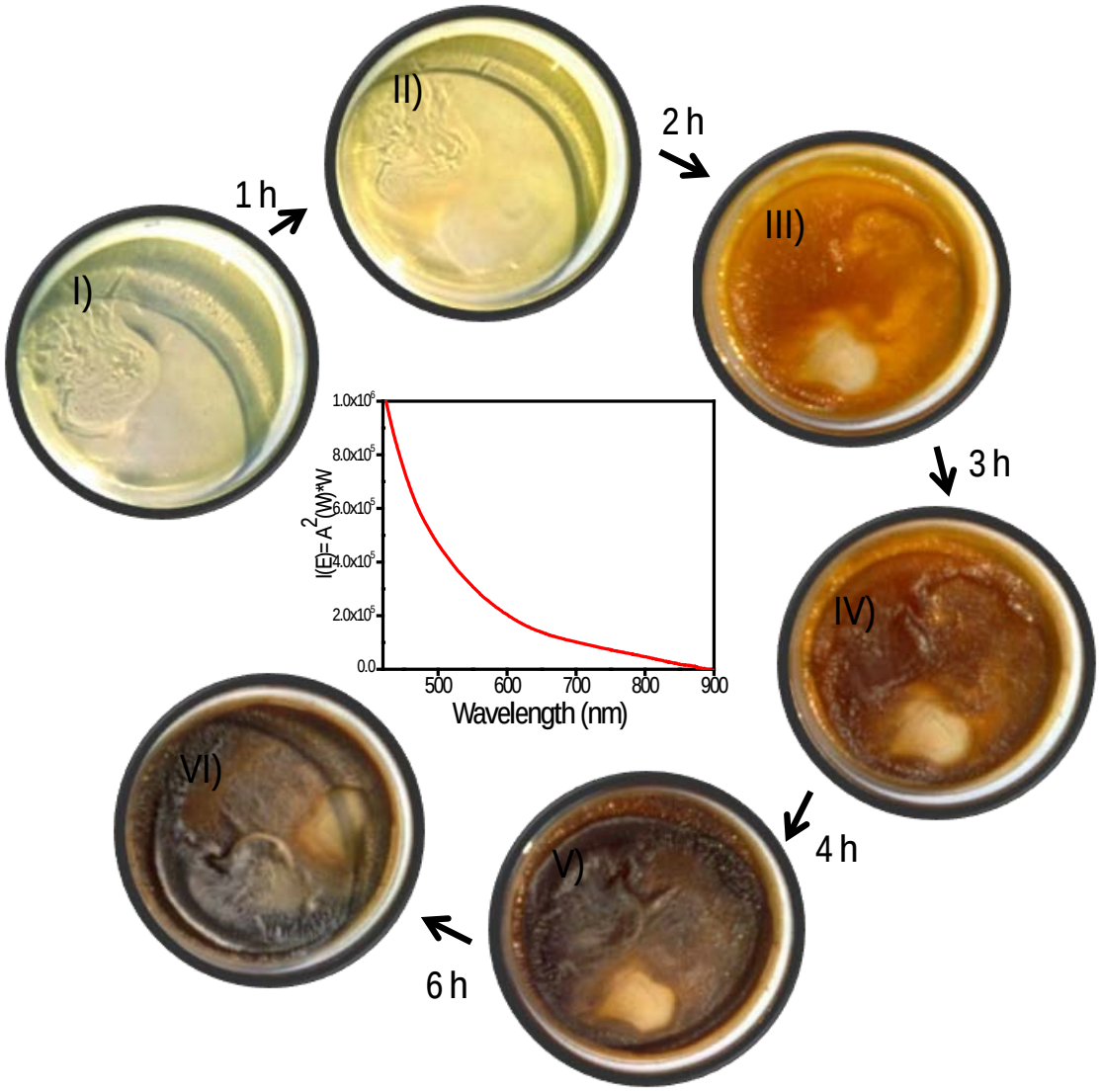

Fig. 17. Polymerized acrylamide gel along with Ag(I)cysteine. I) to VI) are different periods of exposure of sample I) to sunlight. Inset is the UV/Vis spectrum of Ag@cysteine clusters extracted from sample VI).

Supporting information 18.

Gold cluster evolution

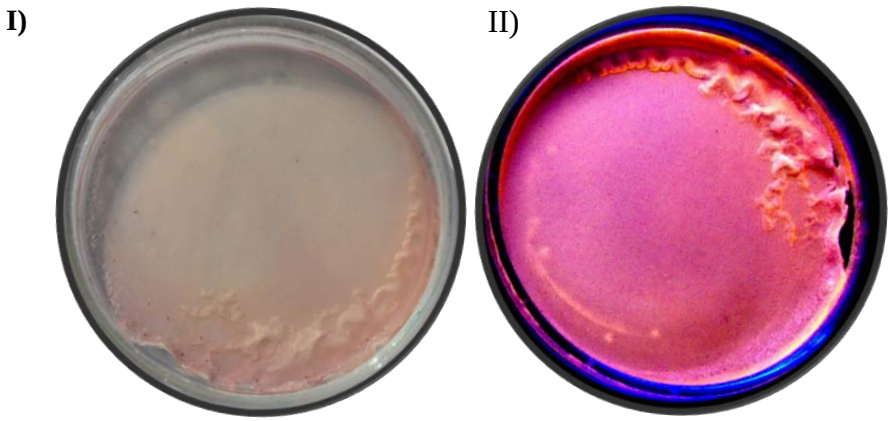

Fig. S18. The photographs of gold cluster made using the same synthetic method. I) Under visible light, and II) under UV light. Intense red fluorescence confirms the formation of clusters.

Supporting information 19.

Antibacterial study with gram positive bacteria

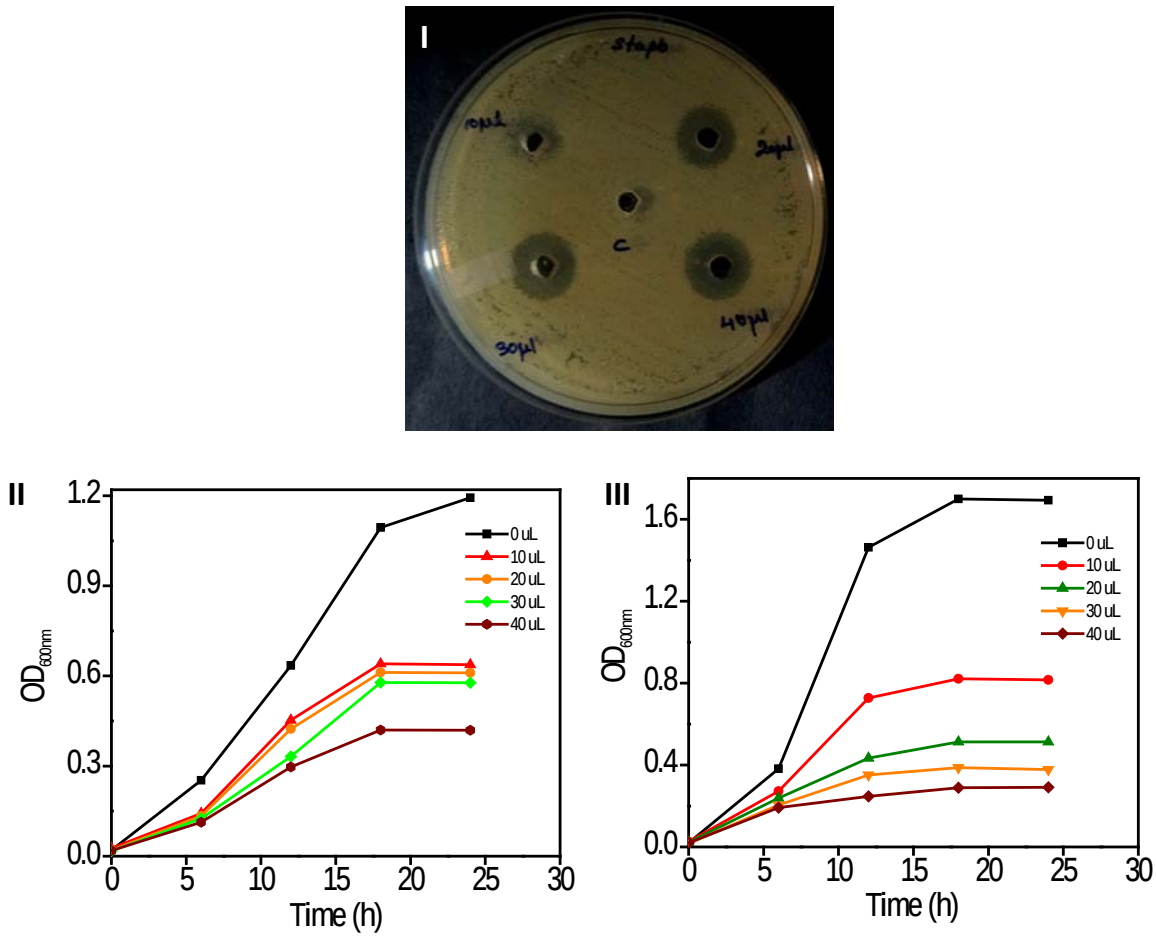

Fig. S19. The antibacterial activity of monolayer protected AgQCs against gram positive bacteria *Staphylococcus aureus* (I). Four different concentrations were used. II and III are the solution based antibacterial study for gram positive and gram negative bacteria, respectively. The spectra show the pronounced effect of AgQCs over gram negative compared to gram positive bacteria.

Scheme 1.

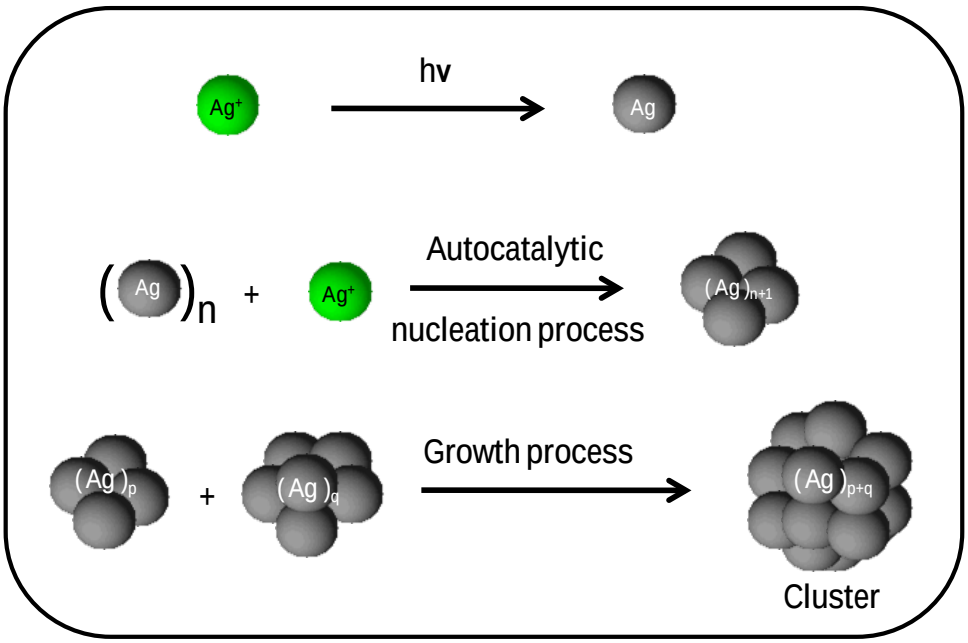

Schematic view of the formation of Ag@SG cluster by photoreduction.

JOURNAL OF AGRICULTURAL AND FOOD CHEMISTRY

Article

pubs.acs.org/JAFC

Understanding the Molecular Signatures in Leaves and Flowers by Desorption Electrospray Ionization Mass Spectrometry (DESI MS) Imaging

R. G. Hemalatha and T. Pradeep*

DST Unit on Nanoscience and Thematic Unit of Excellence, Department of Chemistry, Indian Institute of Technology Madras, Chennai, India

Supporting Information

ABSTRACT: The difference in size, shape, and chemical cues of leaves and flowers display the underlying genetic makeup and their interactions with the environment. The need to understand the molecular signatures of these fragile plant surfaces is illustrated with a model plant, Madagascar periwinkle (*Catharanthus roseus* (L.) G. Don). Flat, thin layer chromatographic imprints of leaves/petals were imaged using desorption electrospray ionization mass spectrometry (DESI MS), and the results were compared with electrospray ionization mass spectrometry (ESI MS) of their extracts. Tandem mass spectrometry with DESI and ESI, in conjunction with database records, confirmed the molecular species. This protocol has been extended to other plants. Implications of this study in identifying varietal differences, toxic metabolite production, changes in metabolites during growth, pest/pathogen attack, and natural stresses are shown with illustrations. The possibility to image subtle features like eye color of petals, leaf vacuole, leaf margin, and veins is demonstrated.

KEYWORDS: *molecular imaging, surface-bound metabolites, electrospray ionization (ESI), desorption electrospray ionization (DESI), mass spectrometry (MS)*

INTRODUCTION

Underlying the incredible beauty of leaves and flowers is their enormous chemical complexity. Various mysteries in plant chemical biology are solved by breakthrough techniques. Different methods of mass spectrometry have contributed significantly to the detection, identification, and quantification of important biomolecules, biomarkers, and other metabolites; even their spatial distribution on surfaces may be visualized with the latest techniques of mass spectrometry imaging (MSI). There are variations in principle, application, and versatility in all the three different mass spectrometric techniques used in MSI, namely secondary ion mass spectrometry (SIMS), matrix-assisted laser desorption ionization mass spectrometry (MALDI MS), and desorption electrospray ionization mass spectrometry (DESI MS).[1] The application of MALDI MSI is high in pharmaceutical research but its major application in plants is for imaging proteins. SIMS imaging in plants has revealed the possibility to get detailed elemental mapping of water and nutrients (major, minor nutrients and other trace elements) in addition to the imaging of molecules like epicuticular waxes, lipids, flavones, and other selected categories of metabolites. DESI MS is distinctly different and often advantageous in biological applications as the process of ionization occurs in ambient conditions and the samples need not be prepared for analysis.[2] More recent studies have demonstrated the need for variations of surfaces, solvents, and methods to suit various plant parts like roots, stems, fruits, bulbs, and rhizomes.[3−9] However, researchers have measured only a limited number of bioactive molecules so far, which have been possible by the chosen techniques, tools, and the technical capacity of particular instrument models available at that time.

Numerous experiments have been performed to understand the response and mechanism of crop plants' survival in various biotic and abiotic stress conditions. It is obvious that the plant surfaces display some changes in color, shape, and stunted growth, etc., when the plants undergo multifaceted stressful conditions. Hence there is specific need to measure the molecular signatures of fragile plant surfaces under healthy conditions and compare their transient changes in conditions of stress. Here we suggest DESI MS based thin layer chromatography (TLC) imprint-imaging as a rapid method for studying metabolites on plant surfaces. The strategy is illustrated with the model plant, Madagascar periwinkle - *Catharanthus roseus* (L.) G. Don. It bears flowers throughout the year, and the whole plant is a rich source of natural alkaloids. Decades of research on *Catharanthus* alkaloids continues even now, because of their high market value and proven potential in the treatment of different types of cancer. It is used as a model for rapid identification of commercially exploited alkaloids that could be engineered to form "differently" from the same indole alkaloid metabolic pathway.[10] Following the recently developed imprint imaging method of DESI MS,[11−13] here, the TLC-imprints of petals and leaves were used to get highly specific, spatially resolved analysis of molecular signatures of *C. roseus*. In addition to DESI MS imaging, tandem mass spectra (MS/MS) were collected from periwinkle leaf/petal extracts and compared with the reports in

Received: March 24, 2013
Revised: July 11, 2013
Accepted: July 12, 2013
Published: July 12, 2013

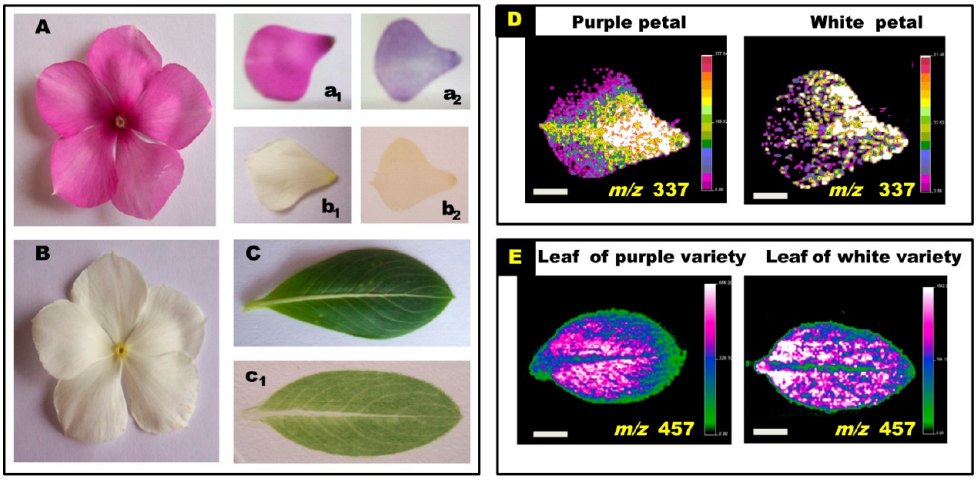

Figure 1. Photographs of flowers, petals, and a leaf of Madagascar periwinkle *C. roseus* and their TLC imprints: Images of (A) pink flower, (a_1) single petal of a pink flower, and (a_2) TLC-imprint of a pink petal. Images B, b_1, and b_2 correspond to the same data for a white flower. Images C and c_1 correspond to a leaf and its imprint. Imprints do not correspond to the same petals or leaf whose photographs are shown. Images D and E correspond to one of the DESI MS images collected from petal and leaf showing the difference in spatial distribution between purple and white varieties of periwinkle, using the ion at m/z 337 and 457, respectively. Scale bars of both the images in D and E are the same (5 mm).

databases. The changes in the spatial distribution of selected metabolites during pest/pathogen attack and under natural stress were imaged. Besides Madagascar periwinkle, different plants like tomato, potato, *Arabidopsis*, tamarind, coriander, amaranthus, neem, patchouli, and wedelia were imaged for their molecular signatures to demonstrate specific applications.

MATERIALS AND METHODS

Materials and Reagents. Leaves and flowers of *C. roseus* and leaves of tomato (*Lycopersicon esculentum* L.), potato (*Solanum tuberosum* L.), tamarind (*Tamarindus indicus* L.), coriander (*Coriandrum sativum* L.) amaranthus (*Amaranthus viridis* L.), neem (*Azadirachta indica* A. Juss.), and wedelia (*Wedelia trilobata* (syn. *Sphagneticola trilobata* L.)) were collected from plants that were growing in the nursery of IIT Madras campus situated in Chennai, Tamilnadu state, India. The plant patchouli (*Pogostemon cablin* (Blanco) Benth.) was a gift from Prof. Vasundhara Mariappa (University of Agricultural Sciences, Bangalore). Tissue cultured plants of *Arabidopsis thaliana* were received as gift from Dr. Baskar (Biotechnology Department, IIT Madras). Methanol and acetonitrile of HPLC grade were purchased from Standard Reagents Pvt. Ltd., Hyderabad, India, and RFCL Limited, New Delhi, India, respectively. TLC plates (Silica gel 60 F_{254} aluminum sheet, 20 × 20 cm) were purchased from Merck KGaA, Darmstadt, Germany. Deionized water was used for making solutions.

Preparation of TLC-Imprints. Fresh plant sample (leaf/petal) with its upper or lower surface facing the silica coating, as per requirement, was placed on the TLC plate of specific dimension. The TLC plate−plant sample pair was covered on either side with tissue paper and manually imprinted using a laboratory hydraulic pellet press by applying a load of 1 ton and 3 tons over an area of 2.5 cm^2 for petals and leaves, respectively, for a period of approximately 5−10 s. The load was optimized individually based on sample physical features (based on the time of collection, surface dryness, and thickness of the leaf/petal). Optimization was necessary as petals required lower load in comparison to leaves. A transparent layer was separated after the release of applied pressure. This layer is due to the waxy coating of the leaf/petal. It was important that the loads were uniform so that the imprints made a true representation of the chemical signatures of the sample (Figure 1 and Figure S1 (Supporting Information)).

Instrumental Setup. Each TLC imprint with the rectangular area occupied by the sample chemical imprint was mapped with optimized spatial resolution (one pixel: 400 μm^2 or 20 × 20 μm) in a lab-built 2D moving stage DESI source, as described earlier.[11−13] Different solvents and mixtures like methanol, methanol−water (3:1 v/v), and acetonitrile were used as spray solvents and delivered at a flow rate of 2 μL/min. Mass spectra were acquired in full scan, positive ion mode, over the mass range from m/z 50 to 1000, using a Thermo LTQ mass spectrometer (San Jose, CA). Auto gain control (AGC) was set to off, and each mass spectrum was collected with optimized scan time. The mass spectra collected as Xcalibur raw data were processed with FireFly data conversion software (http://www.prosolia.com/firefly.php), and images were viewed using BioMap (http://www.maldimsi.org). Tandem mass spectrometric studies were conducted using an ESI attachment of the same Thermo LTQ mass spectrometer, and the data were acquired with Xcalibur software. The plant (leaf and petal) extracts were prepared in ppm concentrations by immersing the leaf/petal in the solvents and solvent mixtures mentioned for an optimized time interval. The centrifuged plant extracts were electrosprayed at a flow rate of 10 μL/min with a spray voltage of 4.5 kV. Mass spectra were acquired for a full scan range of m/z 50−1000, and MS^2 scans were done on all the dominant peaks. To identify the metabolite, the experimental details of MS^2 scans of each peak was submitted to MS/MS spectrum search option of databases,[14−16] with user defined precursor mass and one or more cation/anion adducts. For example, in the METLIN database, the list of adducts given for positive ionization mode are as follows: M + Na, M + NH_4, M + H − $2H_2O$, M + H − H_2O, M + ACN + H, M + 2Na − H, M + 2H, M + 3H, M + H + Na, M + 2H + Na, M + 2Na, M + 2Na + H, M + Li, and M + CH_3OH. For negative ionization, the choices are as follows: M − H, M − H_2O − H, M + Na − 2H, M + Cl, M + K − 2H, M + FA − H, M − 2H, M − 3H, M + CH_3COO, and M + F (The acronyms correspond to ACN = aceonitrile, FA = formic acid). [15]

RESULTS AND DISCUSSION

Direct detection of molecules from plants is known from DESI MS imaging and other recent strategies.[3−9] Yet imaging fragile, short-lived plant surfaces like flower petals and thin leaves like coriander is difficult as they cannot be handled easily on a sample stage. Since ambient imaging with DESI MS requires flat surfaces for a true representation of the molecular concentrations, the plant surfaces were imprinted on TLC plates. Li et al.[12] and Thunig et al.[13] reported that imprints on porous Teflon gave good, stable, and intense signals when compared to direct imaging of plants. Here, besides enhancement in signal, TLC-imprints were ideal for imaging fragile

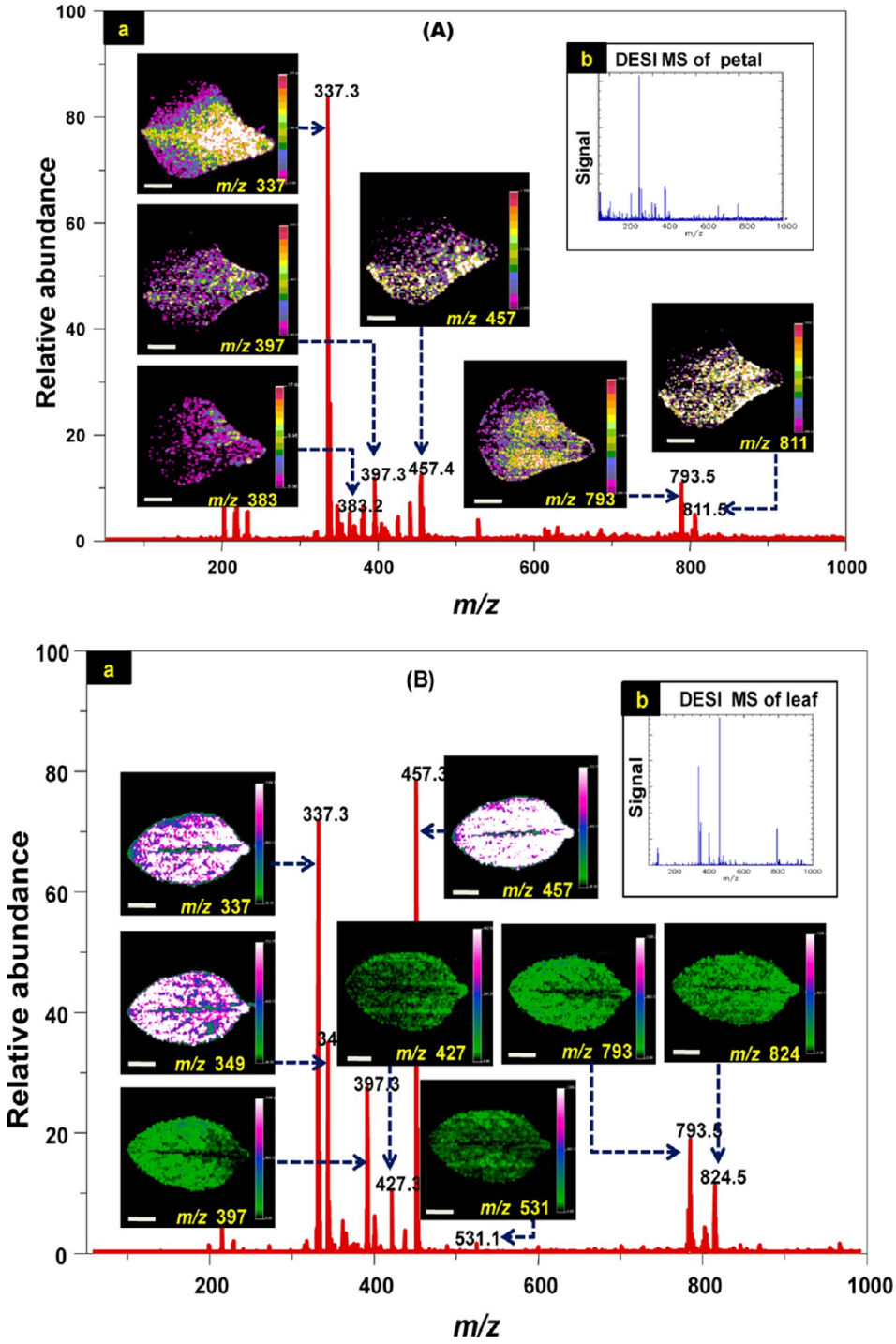

Figure 2. Distribution of metabolites on (A) petal and (B) leaf of *C. roseus*. (A) (a) ESI MS spectrum of petal of *C. roseus*. (b) One of the DESI MS spectra collected from a petal during imaging, corresponding to one pixel (400 μm^2) of the image. Images corresponding to various peaks are shown. Similar data for a leaf is shown in B. The scale is uniform in all the images (5 mm).

plant surfaces, and imprints themselves could be stored for further reference. TLC plates with silica gel coatings are preferable because they provided good quality imprints besides giving good adsorption of different plant-derived molecules and observable chemical changes with time. Figure 1 and Figure S1 of the Supporting Information show that TLC-imprints are truly reflecting the surface. Parts A and B of Figure 1 show the actinomorphic flower (having five identical petals) in pink and white colored varieties of periwinkle. The metabolites on the upper surface of single petal, leaf, and flower could be imprinted (Figure 1a_2, b_2, c_2; no. 2 in Figure S1A) to identify the difference in spatial distribution of specific metabolite between two colored varieties (Figure 1C,D). The undersurface of the petal is transparent (no. 1 in Figure S1A). Applying pressure on the undersurface of petal did not give good imprints (no. 3 in Figure S1A); but in leaves, both surfaces had metabolites (nos. 4, 5 in Figure S1A). Whether petal or leaf, a transparent layer (nos. 6, 7 of Figure S1A) could be separated after imprinting. Likewise, when the plant leaf/petal was kept dipped in solvents for long time, all molecular species got

dx.doi.org/10.1021/jf4011998 | J. Agric. Food Chem. 2013, 61, 7477−7487

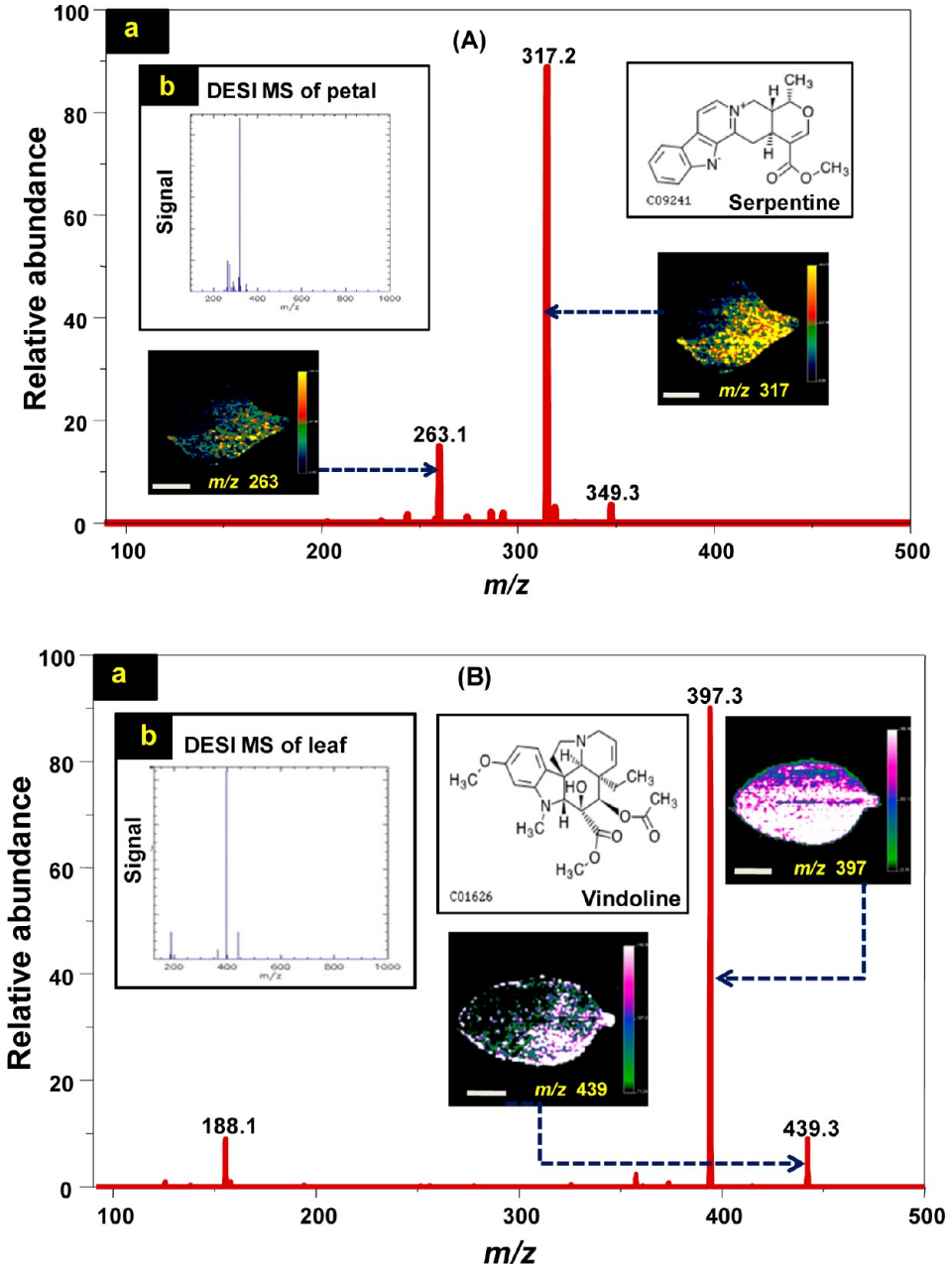

Figure 3. ESI MS tandem mass spectra and DESI MS tandem mass spectral images for (A) serpentine (m/z 349)) on the petal and (B) vindoline (m/z 457) on the leaf of *C. roseus*. The markings on the structures in insets of A and B are from the KEGG database.[21] The main figure corresponds to the spectrum, and the images are based on the intensities of the peaks marked. The spectrum from a pixel of the image is shown in the inset. The scale is uniform in all the images (5 mm).

extracted leaving behind the respective thin membranes. Imaging of TLC-imprints with intact thin membrane did not produce any images though some peaks were detected with low intensity. For easy identification of small molecular metabolites on plant surfaces, typical model plant species like potato, tomato, and *Arabidopsis* with already known bioactive compounds and pathways were chosen. However, the present study is primarily focused on the plant *C. roseus* because the availability of flowers throughout the year helped to do and/or repeat experiments anytime. The suitability of this method to tree species or even weed species is also checked with suitable examples (trees: tamarind, neem; weed: wedelia). Very small flowers like that of neem and *Arabidopsis* could not be imaged. The plant parts like stem, seed, etc. are not suitable for a direct imprinting method described here and need some modified processes which are not discussed here. In all of these selected plants, it is possible to get images for the already reported compounds from plants (indole alkaloids: Madagascar periwinkle; sesquiterpene lactones: wedelia; limonoid terpenes: neem; flavone glycosides: tamarind; polyphenols: coriander; betacyanins: amaranthus; aromatic oils: patchouli) when the same instrumental conditions and solvents were used as per the reports.[17−25] As the DESI MS data are voluminous, only images of the crucial metabolites (in all selected plants) for specific applications are presented (Figures 1−6 and Figures S1−S3 for *C. roseus* and in Figures 4C,D and Figures 6A−P for other plants).

dx.doi.org/10.1021/jf4011998 | *J. Agric. Food Chem.* 2013, 61, 7477−7487

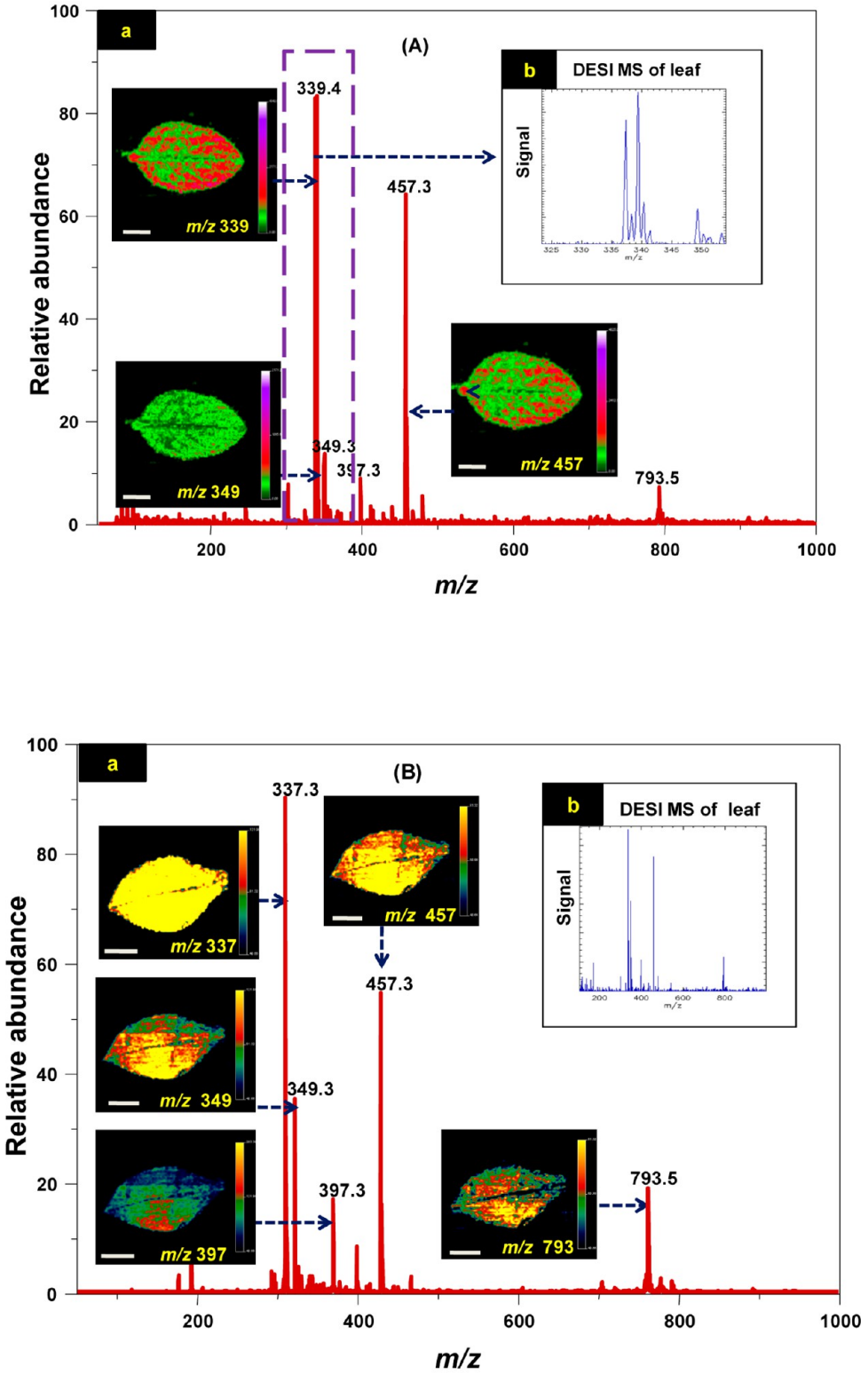

Figure 4. continued

dx.doi.org/10.1021/jf4011998 | J. Agric. Food Chem. 2013, 61, 7477−7487

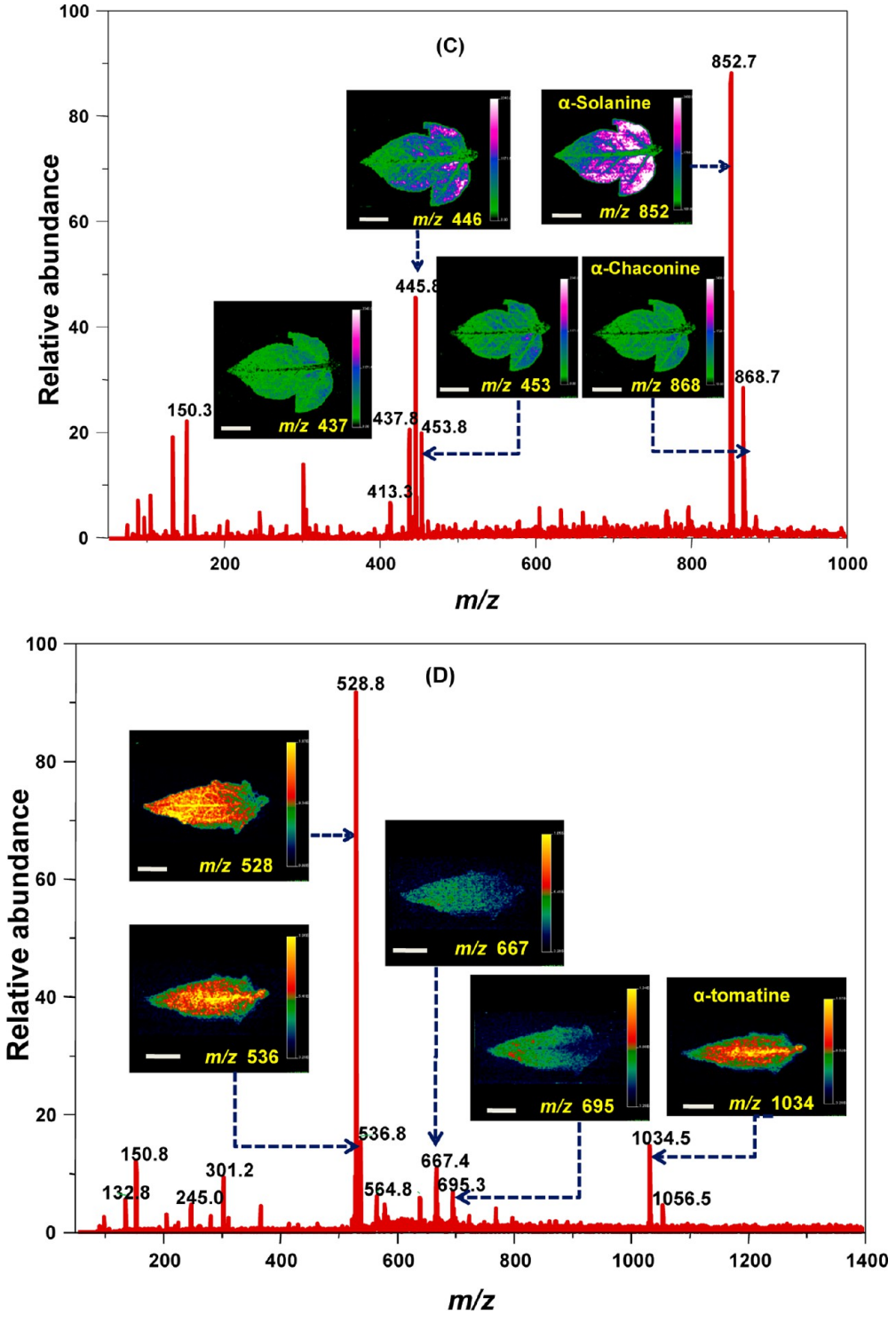

Figure 4. Distribution of selected metabolites on (A) newly emerged leaf and (B) senescent leaf of *C. roseus*. (A) (a) ESI MS spectrum of the leaf of *C. roseus*. Dotted portion is expanded in the inset. (b) One of the DESI MS spectra collected from a leaf during imaging, corresponding to one pixel (400 μm^2) of the image. Similar data for a senescent leaf is shown in B. Distribution of glycoalkaloid in (C) three-leaved stage seedling of potato and (D) mature leaf of tomato. Images corresponding to various peaks are shown. The scale is uniform in all the images (5 mm).

Parts A and B of Figure 2 show the spatial distribution of different metabolite peaks on the petal and leaf of *C. roseus*, detected in positive ionization mode using methanol as the spray solvent. The predominant presence of *m*/*z* 337 on petals (Figure 2A) and *m*/*z* 457 on the leaf (Figure 2B) is revealed. To identify all the eluted peaks, experiments with tandem mass spectral imaging were required. In *C. roseus*, alkaloids were chosen because of their high demand and widespread uses in clinical medicine. Here, the already available indole alkaloid pathway of KEGG (Kyoto Encyclopedia of Genes and Genomes)[21] was used, and the tandem mass spectra of the reported alkaloids were identified. Parts A and B of Figure 3 show the tandem mass spectral images for serpentine and vindoline, which matched with the characteristic ESI MS/MS

dx.doi.org/10.1021/jf4011998 | J. Agric. Food Chem. 2013, 61, 7477−7487

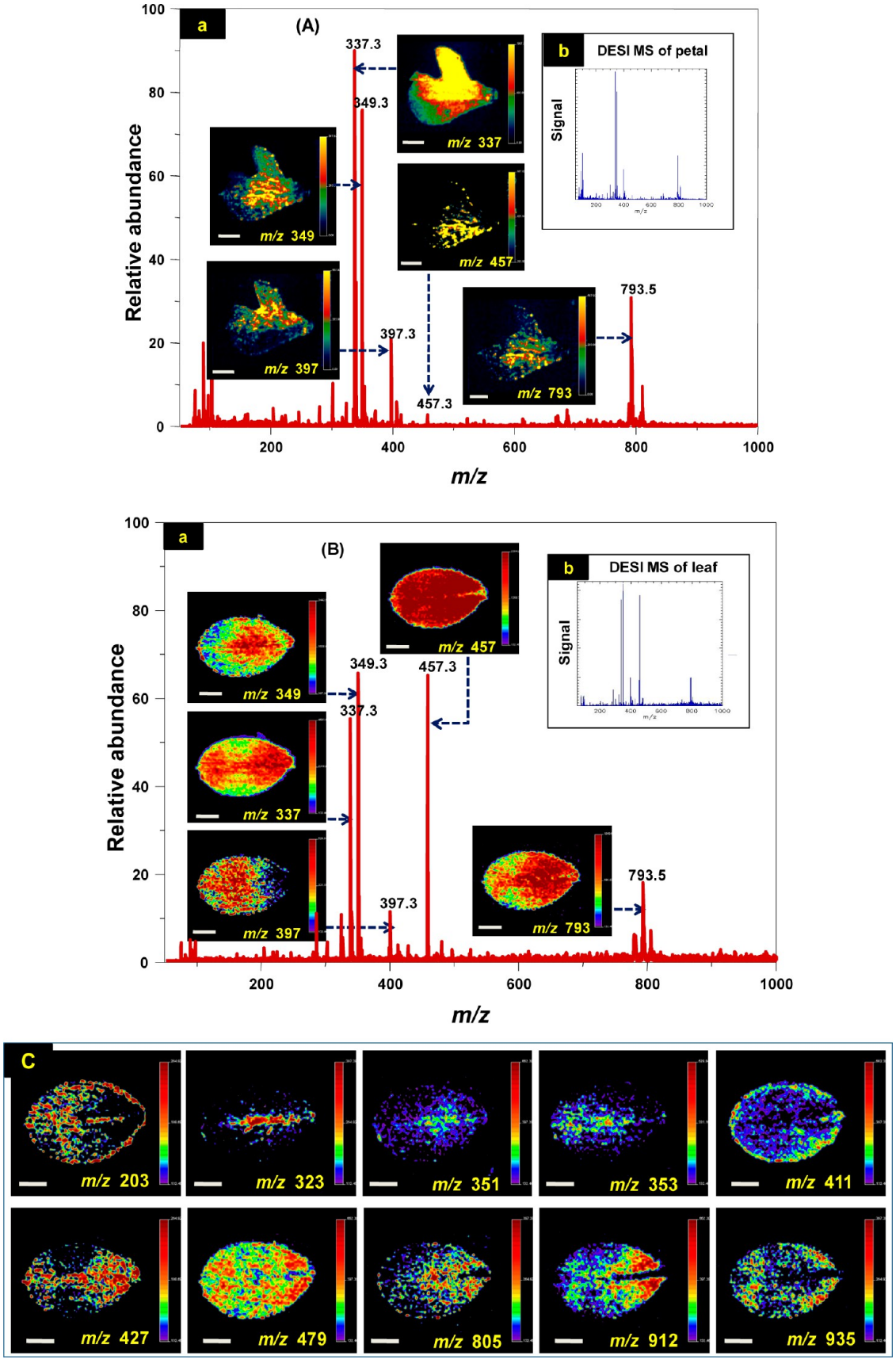

Figure 5. continued

dx.doi.org/10.1021/jf4011998 | J. Agric. Food Chem. 2013, 61, 7477−7487

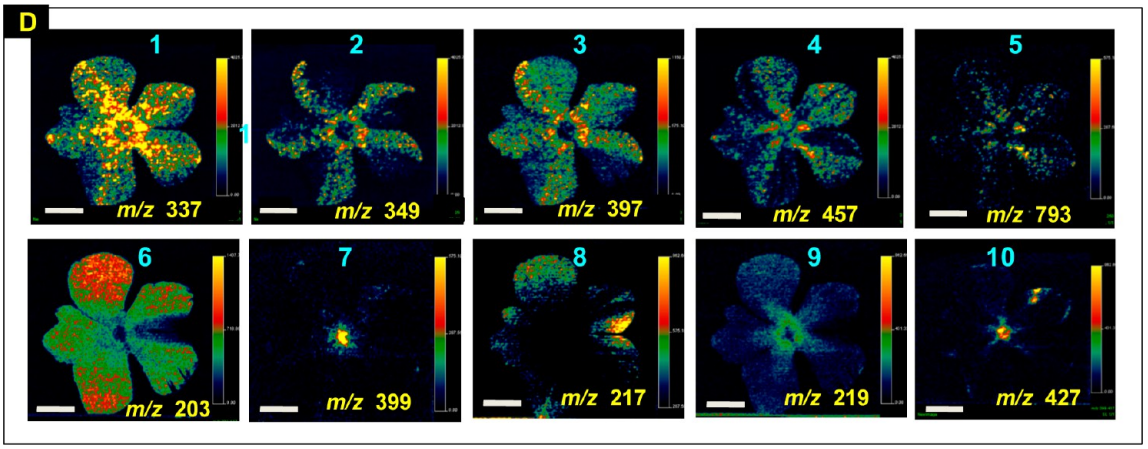

Figure 5. ESI MS spectrum and DESI MS images showing the distribution of selected metabolites during (A) grasshopper attack on petal and (B) wilt disease on leaf of *C. roseus*. (A) (a) ESI MS spectrum of petal. (b) One of the DESI MS spectra collected from the pest attacked petal during imaging corresponding to one pixel (400 μm^2) of the image. Similar data for a diseased leaf is shown in B. (C) DESI MS images of insignificant peaks (relative abundance <10%) in wilt disease. (D) DESI MS images showing distribution of selected metabolite peaks in atrophied flower (no. 1 of Figure S1C) of *C. roseus* during environmental stress. The scale is uniform in all the images (5 mm).

data of plant extracts and the diagnostic fragments available in databases.[18−22] The metabolite peak *m/z* 337 is sharing the tandem mass spectral peak positions of catharanthine and 19-S-vindoline with their characteristic MS/MS data (Figure S2a). As plants may contain complex mixtures under natural conditions, their tandem mass spectral data do not comply fully with the synthetic standards. The metabolites sharing the same *m/z* values (like catharanthine and tabersonine isomers for *m/z* 337, dihydrotabersonine and perivine for *m/z* 339, serpentine and alstonine for *m/z* 349, ajmalicine and hydroxy tabersonine for *m/z* 353, and decaetoxyvindoline and S-adenosyl methionine for *m/z* 399) which may be from the same indole alkaloid or other pathway(s) can also be delineated with their characteristic MS/MS data in databases. The ESI MS/MS of selected peaks are given in Figure S2. The results generated during MS/MS data searches in databases were voluminous when all possible adducts (examples given in the Materials and Methods section) were selected as user inputs; hence only protonated ions are given in this article. The fragmentation patterns of natural compounds are useful in drug discovery,[26] and studies show that modifications of the structure of vindoline lead to a range of antitumor alkaloids (like vinblastine, vincristine, vinorelbine, and vinflunine, etc.)[27] The other peaks that could be assigned using MS/MS spectrum search include akuammicine (*m/z* 323), serpentine (*m/z* 349), ajmalicine (*m/z* 353), methoxy tabersonine (*m/z* 367), lochnerinine (*m/z* 383), echitovenine (*m/z* 397), deacetoxy vindoline (*m/z* 399), vindolidine (*m/z* 427), strictosidine (*m/z* 531), anhydrovinblastine (*m/z* 793), and vinblastine (*m/z* 811). As many of the names of natural products are uncommon in regular analytical chemistry literature, we have summarized in Table S1 of the Supporting Information the essential details of the compounds discussed in this work. Besides alkaloids, the other peaks that eluted (e.g., *m/z* 88, 112, 144, 188, 203, 219, and 233) could be similarly assigned by their MS/MS data by referring to the other metabolic pathways in KEGG database. It may be noted that the mass accuracies mentioned in Table S1 refer to the database and not from the present study. As plethora of information is available for *Catharanthus* in different databases,[18−22] we did not attempt other experiments for separation, characterization, structural identification for molecular variations/relationships, etc. The periwinkle plant(s) collected from different locations were imaged, but the predominant and the coexisting peaks expressed on these surfaces did not change thereby confirming the reproducibility of our results.

To identify the changes in metabolites at various growth stages, the leaves of *C.roseus* at seedling and senescent stages were imaged. Vindoline (*m/z* 457), a predominant metabolite in leaves (Figure 2B), is reported to be confined to aerial parts of plants and is not produced in cultures.[28] Here imaging of healthy, young, and mature leaves of *C. roseus* showed the relative abundance of vindoline (*m/z* 457) but the predominance of *m/z* 339 is seen in newly emerged leaf of young seedlings[19] (Figure 4A). In the senescing leaf (Figure 4B), there was predominance of *m/z* 337 over *m/z* 457.

Imaging changes in metabolites during growth stages has implication in agricultural and food crops. The toxic metabolites that need to be monitored may be produced in plants during early stages of growth (e.g., a natural toxin-glycoalkaloid(s) in Solanaceous crops such as potato, tomato)[29] or during senescence (as in tobacco, the back conversion of nicotine to nornicotine leading to the formation of a carcinogenic precursor N′-nitrosonornicotine).[30] Though the toxicities of glycoalkaloids is well known, their bioactivities,[29] particularly the anticancer activity, are desirable.[31−34] The variation in content of glycoalkaloid[35] is found in plant parts, particularly in leaves where metabolic activity is more; hence testing for glycoalkaloid content is mandatory at different stages. Figure 4C shows that imaging techniques may be a rapid method in identifying the spatial distribution of α-solanine and α-chaconine, the two crucial glycoalkaloids in very young seedlings of potato.[31] When a mature leaf of tomato was imaged, the distribution of typical glycoalkaloid peaks for α-tomatine (*m/z* 1034.7 and 528.9)[33] was evident as shown in Figure 4D.

DESI MS imaging is used in the detection of pathogens;[36] here the possibility to view metabolites particularly at the site of pest attack (*m/z* 337 in Figure 5A: chewing pest, grasshopper attack on petal) and pathogen attack (*m/z* 793 in Figure S3A, Supporting Information: leaf spot disease on leaf) are shown. Figure 5B shows metabolite changes during wilt disease on leaf.

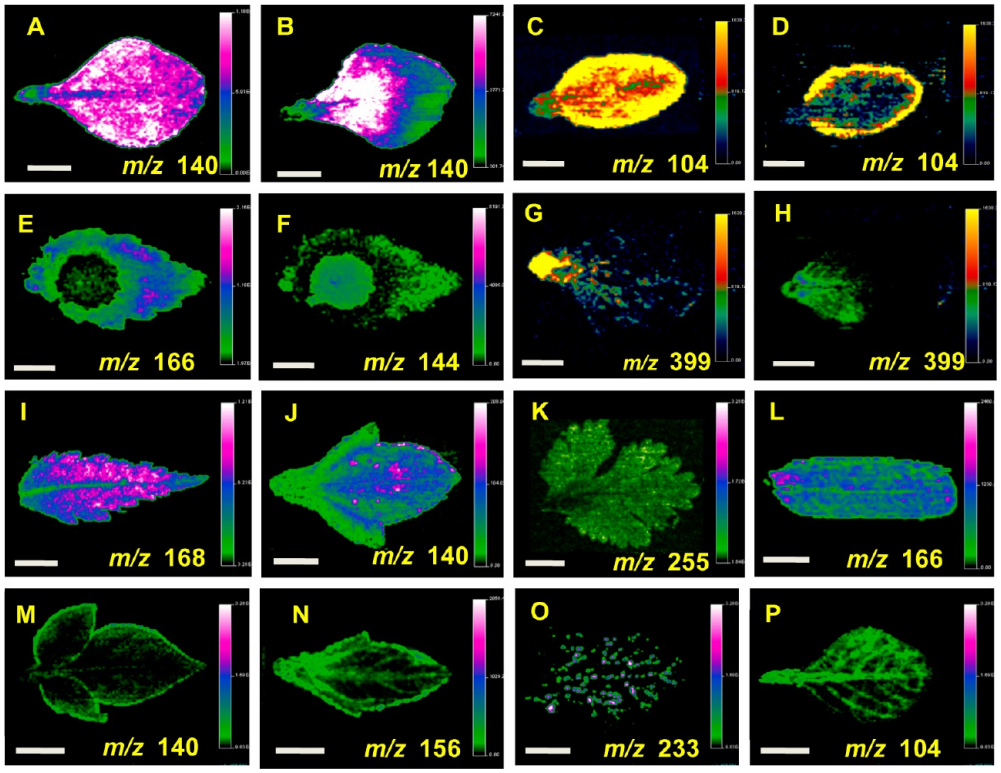

Figure 6. DESI MS images showing (A, B) difference in distribution of m/z 140 on the lower surface of leafy vegetable amaranthus for identification from weed admixtures, (C, D) difference in distribution of m/z 104 on rosette and cauline leaves of tissue cultured *Arabidopsis thaliana*, (E, F) location of secretory gland in leaf of patchouli, (G, H) distribution of eye color imparting metabolite (m/z 399) in petal and leaf of *C. roseus*, (I, J, K, L) typical leaf shape in neem, wedelia, coriander, and tamarind, respectively, and (M, N, O, P) spatial distribution showing metabolites present on the leaf margin and veins on potato, wedelia, coriander, and amaranthus, respectively . The scale is uniform in all the images (5 mm).

Figure S3B in the Supporting Information shows the changes in spatial distribution of m/z 349 during aphid attack on the lower surface of the leaf. It is interesting to note that the changes in the relative abundance of peaks m/z 349, m/z 397, and m/z 793 were observed in all of those cases (Figure 5A,B, and Figure S3A,B) besides changes in intensity of m/z 337 and m/z 457. Although some peaks in ESI spectra were having very low intensity, their surface images were pronounced in DESI MS, implying their stable expression in nature and also their relationship with the prominent compounds (Figure 5C). In order to avoid loss of data, baseline correction or statistical methods were not applied.

Though flower of *C. roseus* is actinomorphic (Figure 1A,B), some atrophied flowers (Figure S1C, with changes in shapes, size, and color of petals) were observed during environmentally stressed conditions in naturally growing plants. As the upper surfaces showed specific changes, the TLC-imprint (no. 6 of Figure S1C) of an atrophied flower is imaged and results are given in Figure 5D. The changes in spatial distribution of alkaloids (m/z 349, m/z 397, and m/z 793) and other metabolites (m/z 203, m/z 219, and m/z 427) can be observed in images 6−10 of Figure 5D. The spatial distribution of commonly known Catharanthus alkaloids in petal or leaf (Figure 2A,B) is indeed new information from this study. Their coexistence with other phenolic compounds and the expression in pest/pathogen attack or abiotic stress will add to the existing knowledge[37−39] that these could be looked at as biomarker metabolites in biotic and abiotic stresses. Hence imaging plant surfaces, immediately after finding changes on their physical features, may serve as a rapid test to identify molecular signatures in stress and to take suitable prophylactic measures for saving crop plants.

The spatial distribution of particular metabolite(s) between different colored varieties of *C. roseus* (Figure 1D,E) shows that imaging can help in comparing different varieties or species. Identification of leafy vegetable amaranthus types remains a challenge due to admixtures with weeds.[40] As in Figure 6A,B, imaging the upper and lower surfaces of leaves show a difference in spatial distribution of metabolites which may be significant in identifying vegetable amaranthus leaf from the weed admixtures.

Parts C and D of Figure 6 show the spatial distribution of metabolite (m/z 104) in two different types of leaves in the same plant (cauline and rosette leaves in tissue cultured *Arabidopsis thaliana*). Here tissue cultured *Arabidopsis* plants are chosen because enhancing the production of bioactive molecules through tissue culture or in vitro manipulations is done in different plant varieties.

Very subtle features on the surface of leaves and petals that are not visible in photographs of TLC-imprints are reflected in DESI MS images. For example, Figure 6E,F shows the presence of vacuole or subsurface secretory gland in the leaf of patchouli,[41] which is invisible in its TLC-imprint (Figure S1B, no.6). The spatial distribution images of the undamaged vacuole/secretory gland in patchouli leaf shows that the pressure is not emptying the contents on TLC-imprints. Likewise, the metabolite (m/z 399) imparting color to visible patterns on the flower eye of *C. roseus* was imaged (as in image 7 of Figure 5D for flower and in Figure 6G for petal); though invisible in the TLC-imprint of leaf, Figure 6H shows that the

dx.doi.org/10.1021/jf4011998 | J. Agric. Food Chem. 2013, 61, 7477−7487

metabolite (m/z 399) is confined to the base of the leaf. As in Figure 6I−L, the typical/conspicuous leaf shapes (serrated margin of neem, trilobed shape of wedelia, parsley leaf like shape of coriander) of plants can be imaged. Parts M−P of Figure 6 show the presence of metabolite peak at leaf veins and margin, which unravels the possibilities to image diseases expressed on leaf veins or margins.[42]

Though TLC-imprints produce flat surfaces, there are possibilities of defects in images arising from imprints due to manual errors as with improper pressing (Figure S4A). Also, the surface changes in TLC-imprints during storage (Figure S4B) produced time-dependent variations in images; the changes were evident in petal imprints within a few days but leaf imprints lasted for months. Also, there may be defects in imaging (Figure S4C) due to the instrumental setting errors.[43] In addition, the interfering peaks sometimes masked the presence of predominant metabolite image(s) (Figure S4D). As plants are complex, no single method can be fully effective to understand plant system biology or plant molecular signatures at a given time. Hence new methods[44] may be employed to better interpret the results obtained from the DESI MS imaging technique. Since all biological samples are highly variable due to changes in edaphic and climatic conditions, the results given here may vary depending on a number of factors including tropical and temperate growth variations. Even the plant metabolite profile database created for the model plant *Arabidopsis* is not complete.[45] Moreover, the TLC-imprinting method needs to be modified suitably for other plant parts like stem, root, seed, etc., and an amenable strategy is needed for imprinting leathery textured leaves and latex containing plants. With suitable manipulations to overcome these limitations, this method would be useful for preserving the molecular information of plant species. As imprints can be transported and stored at ease, this methodology will become useful in herbarium documentation.

■ ASSOCIATED CONTENT

Supporting Information

Additional figures and table as described in the text. This material is available free of charge via the Internet at http://pubs.acs.org.

■ AUTHOR INFORMATION

Corresponding Author

*Tel.: +91-044-2257 4208. Fax: +91-044-2257 0545/0509. E-mail: pradeep@iitm.ac.in.

Funding

Financial support is from the Department of Science and Technology (DST) and the Department of Biotechnology, Government of India.

Notes

The authors declare no competing financial interest.

■ ACKNOWLEDGMENTS

The authors thank Prof. M. Vasundhara of GKVK campus, University of Agricultural Sciences, Bangalore, for providing the patchouli plants, and Dr. R. Baskar of IIT Madras for providing the tissue cultured *Arabidopsis* plants. T.P. thanks the Department of Science and Technology, Government of India, for equipment support through the Nano Mission.

■ REFERENCES

(1) Lee, Y. J.; Perdian, D. C.; Song, Z.; Yeung, E. S.; Nikolau, B. J. Use of mass spectrometry for imaging metabolites in plants. *Plant J.* **2012**, *70*, 81−95.

(2) Takats, Z.; Wiseman, J. M.; Gologan, B.; Cooks, R. G. Mass spectrometry sampling under ambient conditions with desorption electrospray ionization. *Science* **2004**, *306*, 471−473.

(3) Kauppila, T. J.; Talaty, N.; Salo, P. K.; Kotiaho, T.; Kostiainen, R.; Cooks, R. G. New surfaces for desorption electrospray ionization mass spectrometry: porous silicon and ultra-thin layer chromatography plates. *Rapid Commun. Mass Spectrom.* **2006**, *20*, 2143−2150.

(4) Muller, T.; Oradu, S.; Ifa, D. R.; Cooks, R. G.; Krautler, B. Direct plant tissue analysis and imprint imaging by desorption electrospray ionization mass spectrometry. *Anal. Chem.* **2011**, *83*, 5754−5761.

(5) Badu-Tawiah, A.; Bland, C.; Campbell, D. I.; Cooks, R. G. Non-aqueous spray solvents and solubility effects in desorption electrospray ionization. *J. Am. Soc. Mass Spectrom.* **2010**, *21*, 572−579.

(6) Liu, J.; Wang, H.; Cooks, R. G.; Ouyang, Z. Leaf spray: Direct chemical analysis of plant material and living plants by mass spectrometry. *Anal. Chem.* **2011**, *83*, 7608−7613.

(7) Peng, Y.e; Zhang, S.; Wen, F.; Ma, X.; Yang, C.; Zhang, X. In vivo nanoelectrospray for the localization of bioactive molecules in plants by mass spectrometry. *Anal. Chem.* **2012**, *84*, 3058−3062.

(8) Grieving, M. P.; Patti, G. J.; Siuzdak, G. Nanostructure-Initiator mass spectrometry metabolite analysis and imaging. *Anal. Chem.* **2011**, *83*, 2−7.

(9) Joyce, N. I.; Eady, C. C.; Silcock, P.; Perry, N. B.; van Klink, J. W. Fast phenotyping of LFS-silenced (tearless) onions by desorption electrospray ionization mass spectrometry (DESI-MS). *J. Agric. Food Chem.* **2013**, *61*, 1449−1456.

(10) O'Connor, S. E.; Maresh, J. Chemistry and biology of monoterpene indole alkaloid biosynthesis. *J. Nat. Prod. Rep.* **2006**, *23*, 532−547.

(11) Ifa, D. R.; Srimany, A.; Eberlin, L. S.; Naik, H. R.; Bhat, V.; Cooks, R. G.; Pradeep, T. Tissue imprint imaging by desorption electrospray ionization mass spectrometry. *Anal. Methods* **2011**, *3*, 1910−1912.

(12) Li, B.; Bjarnholt, N.; Hansen, S. H.; Janfelt, C. Characterization of barley leaf tissue using direct and indirect desorption electrospray ionization imaging mass spectrometry. *J. Mass Spectrom.* **2011**, *46*, 1241−1246.

(13) Thunig, J.; Hansen, S. H.; Janfelt, C. Analysis of Secondary plant metabolites by indirect desorption electrospray ionization imaging mass spectrometry. *Anal. Chem.* **2011**, *83*, 3256−3259.

(14) http://spectra.psc.riken.jp/menta.cgi/search/fragment.

(15) http://metlin.scripps.edu/spec_search.php.

(16) Horai, H.; Arita, M.; Kanaya, S.; Nihei, Y.; Ikeda, T.; Suwa, K.; Ojima, Y.; Tanaka, K.; Tanaka, S.; Aoshima, K.; Oda, Y.; Kakazu, Y.; Kusano, M.; Tohge, T.; Matsuda, F.; Sawada, Y.; Hirai, M. Y.; Nakanishi, H.; Ikeda, K.; Akimoto, N.; Maoka, T.; Takahashi, H.; Ara, T.; Sakurai, N.; Suzuki, H.; Shibata, D.; Neumann, S.; Iida, T.; Funatsu, K.; Matsuura, F.; Soga, T.; Taguchi, R.; Saito, K.; Nishioka, T. MassBank: a public repository for sharing mass spectral data for life sciences. *J. Mass Spectrom.* **2010**, *45*, 703−714.

(17) Ferreres, F.; Pereira, D. M.; Valentao, P.; Oliveira, J. M.; Faria, J.; Gaspar, L.; Sottomayor, M.; Andrade, P. B. Simple and reproducible HPLC-DAD-ESI-MS/MS analysis of alkaloids in Catharanthus roseus roots. *J. Pharm. Biomed. Anal.* **2010**, *51*, 65−69.

(18) Van Moerkercke, A.; Fabris, M.; Pollier, J.; Baart, G. J.; Rombauts, S.; Hasnain, G.; Rischer, H.; Memelink, J.; Oksman-Caldentey, K. M.; Goossens, A. CathaCyc, a metabolic pathway database built from Catharanthus roseus RNA-Seq data. *Plant Cell Physiol.* **2013**, *54*, 673−685.

(19) http://metnetdb.org/mpmr_public/experiments/?expid=139 (accessed on June 8, 2013).

(20) http://www.biologie.uni-freiburg.de/data/bio2/schroeder/Index_English_Catharanthus.html (accessed on June 8, 2013).

(21) http://www.genome.jp/kegg/pathway/map/map00901.html (accessed on June 8, 2013).

(22) http://www.ncbi.nlm.nih.gov/pccompound (accessed on June 8, 2013).
(23) Sharma, V.; Walia, S.; Kumar, J.; Nair, M. G.; Parmar, B. S. An efficient method for the purification and characterization of nematicidal azadirachtins A, B, and H, using MPLC and ESIMS. *J. Agric. Food Chem.* **2003**, *51*, 3966−3972.
(24) That, Q. T.; Jossang, J.; Jossang, A.; Kim, P. P. N.; Jaureguiberry, G. Wedelolides A and B: Novel sesquiterpene δ-lactones, (9R)-eudesman-9,12-olides, from *Wedelia trilobata*. *J. Org. Chem.* **2007**, *72*, 7102−7105.
(25) Sudjaroen, Y.; Haubner, R.; WÃ1/4rtele, G.; Hull, W. E.; Erben, G.; Spiegelhalder, B.; Changbumrung, S.; Bartsch, H.; Owen, R. W. Isolation and structure elucidation of phenolic antioxidants from tamarind (*Tamarindus indica* L.) seeds and pericarp. *Food Chem. Toxicol.* **2005**, *43*, 1673−1682.
(26) Tozuka, Z.; Kaneko, H.; Shiraga, T.; Mitani, Y.; Beppu, M.; Terashita, S.; Kawamura, A.; Kagayama, A. Strategy for structural elucidation of drugs and drug metabolites using (MS)n fragmentation in an electrospray ion trap. *J. Mass Spectrom.* **2003**, *38*, 793−808.
(27) Keglevich, P.; Hazai, L.; Kalaus, G.; Szantay, C. Modifications on the basic skeletons of vinblastine and vincristine. *Molecules* **2012**, *17*, 5893−5914.
(28) Guirimand, G.; Guihur, A.; Poutrain, P.; Hericourt, F.; Mahroug, S.; St-Pierre, B.; Burlat, V.; Courdavault, V. Spatial organization of the vindoline biosynthetic pathway in *Catharanthus roseus*. *J. Plant Physiol.* **2011**, *168*, 549−557.
(29) Milner, S. E.; Brunton, N. P.; Jones, P. W.; O'Brien, N. M.; Collins, S. G.; Maguire, A. R. Bioactivities of glycoalkaloids and their aglycones from *Solanum* species. *J. Agric. Food Chem.* **2011**, *59*, 3454−3484.
(30) Siminszky, B.; Gavilano, L.; Bowen, S. W.; Dewey, R. E. Conversion of nicotine to nornicotine in *Nicotiana tabacum* is mediated by CYP82E4, a cytochrome P450 monooxygenase. *Proc. Natl. Acad. Sci. U.S.A.* **2005**, *102*, 14919−14924.
(31) Matsuda, F.; Morino, K.; Miyazawa, H.; Miyashita, M.; Miyagawa, H. Determination of potato glycoalkaloids using high-pressure liquid chromatography−electrospray ionisation/mass spectrometry. *Phytochem. Anal.* **2004**, *15*, 121−124.
(32) Reddivari, L.; Vanamala, J.; Safe, S. H.; Miller, J. C., Jr. The bioactive compounds alpha-chaconine and gallic acid in potato extracts decrease survival and induce apoptosis in LNCaP and PC3 prostate cancer cells. *Nutr. Cancer.* **2010**, *62*, 601−610.
(33) Cataldi, T. R.; Lelario, F.; Bufo, S. A. Analysis of tomato glycoalkaloids by liquid chromatography coupled with electrospray ionization tandem mass spectrometry. *Rapid Commun. Mass Spectrom.* **2005**, *19*, 3103−3110.
(34) Choi, S. H.; Lee, S. H.; Kim, H. J.; Lee, I. S.; Kozukue, N.; Levin, C. E.; Friedman, M. Changes in free amino acid, phenolic, chlorophyll, carotenoid, and glycoalkaloid contents in tomatoes during 11 stages of growth and inhibition of cervical and lung human cancer cells by green tomato extracts. *J. Agric. Food Chem.* **2010**, *58*, 7547−7556.
(35) Itkin, M.; Rogachev, I.; Alkan, N.; Rosenberg, T.; Malitsky, S.; Masini, L.; Meir, S.; Iijima, Y.; Aoki, K.; de Vos, R.; Prusky, D.; Burdman, S.; Beekwilder, J.; Aharoni, A. GLYCOALKALOID METABOLISM1 is required for steroidal alkaloid glycosylation and prevention of phytotoxicity in tomato. *Plant Cell* **2011**, *23*, 4507−4525.
(36) Lane, A. L.; Nyadong, L.; Galhena, A. S.; Shearer, T. L.; Stout, E. P.; Parry, R. M.; Kwasnik, M.; Wang, M. D.; Hay, M. E.; Fernandez, F. M.; Kubanek, J. Desorption electrospray ionization mass spectrometry reveals surface-mediated antifungal chemical defense of a tropical seaweed. *Proc. Natl. Acad. Sci. U. S. A.* **2009**, *106*, 7314−7319.
(37) Vazquez-Flota, F.; Carrillo-Pech, M.; Minero-Garcia, Y.; De Lourdes Miranda-Ham, M. Alkaloid metabolism in wounded *Catharanthus roseus* seedlings. *Plant Physiol. Biochem.* **2004**, *42*, 623−628.
(38) Roepke, J.; Salim, V.; Wu, M.; Thamm, A. M.; Murata, J.; Ploss, K.; Boland, W.; De Luca, V. Vinca drug components accumulate exclusively in leaf exudates of Madagascar periwinkle. *Proc. Natl. Acad. Sci. U.S.A.* **2010**, *107*, 15287−15292.
(39) Ferreres, F.; Figueiredo, R.; Bettencourt, S.; Carqueijeiro, I.; Oliveira, J.; Gil-Izquierdo, A.; Pereira, D. M.; Valentao, P.; Andrade, P. B.; Duarte, P.; Barcelo, A. R.; Sottomayor, M. Identification of phenolic compounds in isolated vacuoles of the medicinal plant *Catharanthus roseus* and their interaction with vacuolar class III peroxidase: an H(2)O(2) affair? *J. Exp. Bot.* **2011**, *62*, 2841−2854.
(40) Khan, M.; Musharaf, S.; Ibrar, M.; Hussain, F. Pharmacognostic evaluation of the *Amaranthus viridis* L. *Res. Pharm. Biotechnol.* **2011**, *3*, 11−16.
(41) Maeda, E.; Miyake, H. Leaf anatomy of patchouli with reference to the disposition of mesophyll glands. *Jpn. J. Crop Sci.* **1997**, *66* (2), 307−317.
(42) Cazorla, F. M.; Vázquez, M. A.; Rosales, J.; Arrebola, E.; Navarro, J.; Pérez-García, A.; De Vicente, A. First report of bacterial leaf spot (*Pseudomonas syringae* pv. *coriandricola*) of coriander in Spain. *J. Phytopathol.* **2005**, *153*, 181−184.
(43) Kertesz, V.; Van Berkel, G. J. Scanning and surface alignment considerations in chemical imaging with desorption electrospray mass spectrometry. *Anal. Chem.* **2008**, *80*, 1027−1032.
(44) Campbell, D.; Ferreira, C.; Eberlin, L.; Cooks, R. G. Improved spatial resolution in the imaging of biological tissue using desorption electrospray ionization. *Anal. Bioanal. Chem.* **2012**, *404*, 389−398.
(45) Bais, P.; Moon-Quanbeck, S. M.; Nikolau, B. J.; Dickerson, J. A. Plantmetabolomics.org: mass spectrometry-based *Arabidopsis* metabolomics–database and tools update. *Nucleic Acids Res.* **2012**, *40* (Database issue), D1216−20.

Nanoscale

RSC Publishing

PAPER

View Article Online
View Journal | View Issue

Cite this: *Nanoscale*, 2013, **5**, 9404

Thiolate-protected Ag_{32} clusters: mass spectral studies of composition and insights into the Ag–thiolate structure from NMR†

T. Udayabhaskararao, M. S. Bootharaju and T. Pradeep*

Received 11th April 2013
Accepted 23rd July 2013

DOI: 10.1039/c3nr03463a

www.rsc.org/nanoscale

Clusters composed of a 32 silver atom core, protected with thiolates of glutathione (GSH) and *N*-(2-mercaptopropionyl)glycine (MPGH), were synthesized by a solid-state route in milligram scale. They do not exhibit surface plasmon resonance unlike their larger sized nanoparticle analogues but show molecule-like features in absorption and luminescence spectra, falling in the visible window. The compositions $Ag_{32}SG_{19}$ (SG: thiolate of glutathione) and $Ag_{32}MPG_{19}$ (MPG: thiolate of MPGH) were identified from electrospray ionization mass spectrometry (ESI MS). Matrix-assisted laser desorption/ionization mass spectrometry (MALDI MS) was not successful for –SG protected clusters as reported before, but for $Ag_{32}MPG_{19}$ a peak at 6.1 kDa was seen at a threshold laser intensity. This peak shifted to low mass region with increasing laser intensity due to systematic losses of Ag_2S. Further confirmation of the composition $Ag_{32}SG_{19}$ was made using various studies such as XPS and EDAX. One-dimensional (1D) and two-dimensional (2D) NMR spectroscopic investigations of $Ag_{32}SG_{19}$ provided interesting spectral features which indicated the dominant –[SR–Ag–SR]– structural motif. This structural motif as the predominant entity is found for the first time in silver clusters.

Introduction

Quantum clusters (QCs) of noble metals are molecules composed of a few to a hundred metal atom cores – even more in some cases – protected with ligands, especially thiols, and are fundamentally different from their bulk and plasmonic analogues in terms of their optical, electronic, and structural properties.[1–4] In the initial years of study, a mixture of gold QCs with unknown compositions were synthesized by the reduction of Au^{3+} in the presence of glutathione (GSH, the thiolate form is written as SG).[5] These clusters were isolated using the technique of gel electrophoresis and their spectroscopic properties were examined in detail. Molecular formulae of these clusters were later understood as $Au_{10}SG_{10}$, $Au_{15}SG_{13}$, $Au_{18}SG_{14}$, $Au_{22}SG_{16}$, $Au_{22}SG_{17}$, $Au_{25}SG_{18}$, $Au_{29}SG_{20}$, $Au_{33}SG_{22}$ and $Au_{39}SG_{24}$ using mass spectral studies.[6] Subsequently, several new protocols were developed to synthesize these QCs individually, *i.e.* well-defined monodisperse Au_nSR_m.[7–11] Depending on the synthesis conditions, type of protecting ligand, solvent polarity and strength of reducing agent, various monodisperse clusters such as $Au_{25}SR_{18}$, $Au_{38}SR_{24}$ and $Au_{144}SR_{60}$ were synthesized.[12] Size exclusion chromatography was used to detect some of the less prominent clusters such as $Au_{40}SR_{24}$ and $Au_{55}SR_{30,31}$.[13–15] In addition to them, Au_{19},[16] Au_{18}[10] and Au_{20}[17] were also synthesized by controlling the kinetics of the reaction through a slow reduction process. Availability of clusters with known composition, especially crystallization of some of them ($Au_{25}SR_{18}$,[18,19] $Au_{38}SR_{24}$,[20] $Au_{36}SR_{24}$[21] and $Au_{102}SR_{44}$[22]) helped to understand them in greater detail. But corresponding developments have not happened in silver clusters. Although several QCs of silver with known chemical composition such as water soluble Ag_7,[23] $Ag_{7,8}$,[24] and Ag_9,[25] as well as organic soluble $\sim Ag_{140}$[26] and Ag_{280}[27] have been made, the growth of the area is not comparable to that of gold analogues. Recently, there has been rapid progress in this area due to the single crystal analysis of Ag_{14},[28] Ag_{16}[29] and Ag_{32}[29] protected by the combined use of thiolate and phosphine ligands. Analogous to the thiol-protected clusters, they also possess molecule-like behaviour in their optical properties but systematic changes in these properties were not seen due to size and structural differences in cores (such as Ag_6^{4+}, Ag_8^{6+}, and Ag_{22}^{12+}). For example, while Ag_{14} is yellow emissive, Ag_{16} and Ag_{32} exhibit blue emission. Their structures are interesting and provide new insights into the atomic structure of thiolated–Ag QCs in comparison to Au QCs.

In recent years, a variety of methods have been developed to produce stable thiolate-protected silver QCs. Among them is the synthesis through a solid-state route.[25] The time required to produce the desired cluster is substantially less here. High yield

DST Unit of Nanoscience (DST UNS) and Thematic Unit of Excellence (TUE), Department of Chemistry, Indian Institute of Technology Madras, Chennai-600 036, India. E-mail: Pradeep@iitm.ac.in

† Electronic supplementary information (ESI) available: Details of experimental procedures and characterization using UV-vis, luminescence, TEM, ESI MS, XPS, FTIR, XRD of $Ag_{32}SG_{19}$ clusters. See DOI: 10.1039/c3nr03463a

of clusters and easy handling of the reaction made this route novel. It is expected that this protocol opens up a new way for the synthesis of a variety of cluster materials. For example, by varying precursor ratios, reducing agents, temperature and solvents, numerous cluster materials are produced through this route. Here, we report the preparation of thiolated Ag_{32} clusters with two ligands in aqueous phase through this method and their most essential characterization. Assignment of chemical composition was made based on mass spectrometry (MS) including electrospray ionization (ESI) and matrix-assisted laser desorption ionization (MALDI), coupled with elemental analysis and X-ray photoelectron spectroscopy (XPS). We proposed the Ag–thiolate structure of the cluster based on a detailed nuclear magnetic resonance spectroscopic (NMR) study.

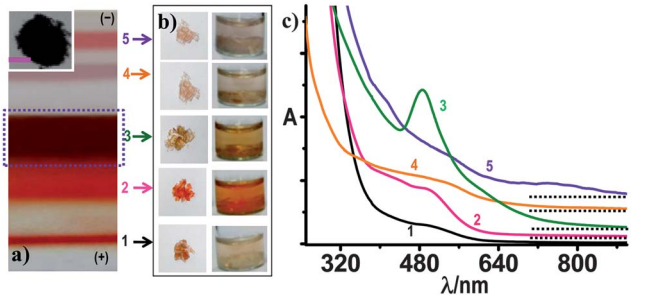

Fig. 1 (a) Distinct bands are seen in the gel, derived from the crude cluster (black powder in inset of a). Scale bar on inset of (a) is 1 cm. (b) Photographs of solidified gel fractions of clusters 1–5 (left) and their water extracts (right). (c) UV-vis absorption spectra of clusters 1–5 extracted from each band after gel electrophoresis of the crude cluster.

Experimental section

Materials and methods

Chemicals. All the chemicals were commercially available and were used without further purification. Silver nitrate ($AgNO_3$, 99%), glutathione (GSH, 97%), *N*-(2-mercaptopropionyl) glycine (MPGH, Aldrich), acrylamide (AR grade), *N*,*N*′-methylenebisacrylamide (BIS) (AR grade), ammonium persulfate and *N*,*N*,*N*′,*N*′-tetramethylethylene diamine (TEMED) were purchased from SRL Chemical Co. Ltd., India. Sodium borohydride ($NaBH_4$, 99.99%, Aldrich), ethanol (HPLC grade, 99.9%, Aldrich) and methanol (HPLC grade) were used as received.

Synthesis of $Ag_{32}SG_{19}$. About 23 mg of $AgNO_3$(s) was added to 200 mg of GSH(s) at room temperature and the mixture was ground well in a mortar to make Ag(I)SG thiolate. About 25 mg $NaBH_4$(s) was added and grinding was continued for 10 more minutes. After that, 10 mL of distilled water was added slowly (in one mL steps) which resulted in the formation of a reddish brown solution. Clusters were precipitated immediately by the addition of excess ethanol. The resulting precipitate was collected and washed repeatedly with ethanol through centrifugal precipitation. Finally, the precipitate was dried and collected as a reddish brown powder (~26 mg). This was termed as crude cluster (CC) in this paper. The dried product was stored in the laboratory atmosphere. Photographs of the synthesis at various stages are shown in ESI, Scheme S1.† The powder was dissolved in water (10 mg mL^{-1}) and kept under ambient conditions overnight. This resulted in a color change from reddish brown to pale pinkish red. This was referred to as aged crude clusters (ACC).

Polyacrylamide gel electrophoresis (PAGE). PAGE was performed using a previously reported procedure.[30] A gel electrophoresis unit with 1 mm thick spacer (Bio-rad, Mini-protein Tetra cell) was used to process the PAGE. The total contents of the acrylamide monomers were 28% (BIS : acrylamide) = (7 : 93) and 3% (BIS : acrylamide) = (7 : 93) for the separation and condensation gels, respectively. The eluting buffer consisted of 192 mM glycine and 25 mM tris(hydroxymethylamine). The crude cluster was dissolved in 5% (v/v) glycerol–water solution (1.0 mL) at a concentration of 10 mg mL^{-1}. The sample solution (1.0 mL) was loaded onto a 1 mm gel and eluted for 4 h at a constant voltage of 150 V to achieve separation as shown in Fig. 1. The gel fractions containing the clusters were cut out, ground, and dipped in ice cold distilled water (2 mL) for 10 min. Subsequently, the solutions were centrifuged at 20 000 rpm for 5 min at −10 °C, followed by filtering with filter paper having 0.22 μm pores to remove the gel lumps suspended in the solution. Separation of cluster 3 was done carefully. For measurements we have cut only the top portion of band 3 (marked in the PAGE photograph) where it is separated far away from the adjacent clusters. Clusters 2 and 3 are merged only at their boundary. Cluster 2 showed as a separate band which indicates that it was not fully mixed with cluster 3. Further PAGE on cluster 3 shows the same UV-vis, luminescence and ESI MS as that of cluster 3.

Synthesis of $Ag_{32}MPG_{19}$. About 23 mg of $AgNO_3$(s) was added to 110 mg of MPGH(s), 1.5 mg of NaOH(s) at room temperature and the mixture was ground well in a mortar to make Ag(I)MPG thiolate. About 25 mg $NaBH_4$(s) was added and grinding was continued for 10 more minutes. After that, 10 mL of distilled water was added slowly (in one mL steps) which resulted in the formation of a reddish brown solution. Clusters were precipitated immediately by the addition of excess ethanol. The resulting precipitate was collected and washed repeatedly with ethanol through centrifugal precipitation. Finally, the precipitate was dried and collected as a reddish brown powder. The powder was dissolved in water (10 mg mL^{-1}) and kept at 10 °C overnight. The resultant solution is called Ag@MPG clusters in the text. Through ESI MS and MALDI MS the composition of the cluster is understood to be $Ag_{32}MPG_{19}$.

Instrumentation. UV-vis spectra were measured with a PerkinElmer Lambda 25 instrument in the range of 200–1100 nm. Luminescence measurements were carried out on a Jobin Yvon NanoLog instrument. The band pass for excitation and emission was set as 2 nm. Circular dichroism studies were measured using a Jasco Model J-810 circular dichroism spectropolarimeter in the range of 200–800 nm. X-ray photoelectron spectroscopy (XPS) measurements were conducted using an Omicron ESCA Probe spectrometer with polychromatic Mg Kα X-rays ($h\nu$ = 1253.6 eV). The samples were spotted as drop-cast films on a sample stub. A constant analyzer energy of 20 eV was used for the measurements. High resolution transmission electron microscopy of clusters was carried out with a JEOL 3010

instrument. The samples were drop-cast on carbon-coated copper grids and allowed to dry under ambient conditions. FTIR spectra were measured with a PerkinElmer Spectrum One instrument. KBr crystals were used as the matrix for preparing samples. ^{1}H NMR were measured with a 500 MHz Bruker Advance III spectrometer operating at 500.13 MHz and equipped with a 5 mm triple-resonance PFG probe. Solutions were made in 99.98% D_2O (Aldrich) and sealed immediately. The signal of the solvent served as the reference for the field-frequency lock. All experiments were performed at a temperature of 25 °C. Standard Bruker pulse programs (Topspin 2.1) were employed throughout. As PAGE purified samples contain tiny quantities of the gel, ^{1}HNMR was performed with the aged crude, which was identical to cluster 3. Mass studies were conducted using an electrospray mass spectrometry (ESI MS) system, LTQ XL (Thermo scientific). Samples of 50 ppm concentration, taken in a 3 : 7 water–methanol mixture, were electrosprayed. Negative ion spectra showed characteristic features in view of the carboxylate species present. Positive ion spectra did not have distinct molecular ion features. Optimized conditions for the negative ion spectra were: capillary temperature: 150 °C, capillary voltage: −34 V, source voltage: −5.7 kV, tubular lens voltage: −110 V and flow rate: 5 μL min^{-1}. Matrix-assisted desorption ionization mass spectrometry (MALDI MS) studies were conducted using a Voyager-DE PRO Biospectrometry Workstation from Applied Biosystems. A pulsed nitrogen laser of 337 nm was used near threshold laser intensity in negative mode. Matrix solution was prepared by dissolving 10 mg of α-cyano-4-hydroxycinnamic acid (CHCA) matrix in a 1 : 1 mixture of acetonitrile (0.5 mL) and trifluoroacetic acid (0.5 mL, 0.1% in DI water). 2 μL of as-synthesized Ag@MPG clusters in water were uniformly mixed with 5 μL of matrix solution. A volume of 2.5 μL of the cluster–matrix mixture was spotted on the target and allowed to dry under ambient conditions. Scanning electron microscopic (SEM) and energy dispersive X-ray (EDAX) analyses were done in a FEI QUANTA-200 SEM. For measurements, samples were drop-cast on an indium tin oxide coated conducting glass and dried in vacuum. Powder XRD patterns of the samples were recorded using a PANalytical X'pertPro diffractometer. The powder samples of parent silver nanoparticles and clusters were taken on a glass plate and the X-ray diffractogram was collected from 5 to 100 degrees in 2 theta using Cu Kα radiation.

Results and discussion

Crude cluster was obtained by grinding the metal precursor and the ligand followed by reduction with $NaBH_4$(s). In this process, initially silver thiolate is formed due to the reaction between $AgNO_3$ and GSH at the interface. High affinity of sulfur to noble metal ions is responsible for thiolate formation which was confirmed from the IR spectrum of the ground mixture, where the S–H_{str} of GSH was absent. Upon addition of sodium borohydride in the solid form, the ground mixture turns to a brownish black powder which shows high affinity to water. At this point, compounds are mixed well, the essential steps of particle formation such as nucleation and growth are controlled due to the lack of protic solvent, which facilitates fast reduction to form metallic particles. This control is important in minimizing the formation of a mixture of clusters compared to solution phase synthesis.

The crude cluster (CC) in water shows an absorption profile different from plasmonic nanoparticles. A peak at 480 nm and shoulders at 550 and 350 nm were observed (Fig. S2a†). Silver clusters protected by glutathione and analogous thiols exhibit distinct features in the region of 300–800 nm.[23–27,30–38] This product, CC, is a mixture of individual silver QCs, as revealed by polyacrylamide gel electrophoresis (PAGE, detailed procedure is in experimental section). Five different bands were separated and are clearly observable on the gel as shown in Fig. 1a. These five bands of different clusters were cut and soaked in ice cold distilled water. Individual clusters were extracted into water, and their distinctive aspects are clearly observable by the appearance of their respective colors. Photographs of the five solid gels and the cluster solutions are given in Fig. 1b. Clusters extracted from these bands are referred to as clusters 1–5, corresponding to the band labels in Fig. 1a. Absorption profiles of all the clusters in water show molecule-like behavior (Fig. 1c). Cluster 5 shows a near-IR absorption peak at 750 nm, along with two other peaks at 540 and 415 nm. Cluster 4 shows a broad peak centered at 550 nm, along with small humps at 350 and 640 nm. Cluster 3 shows a sharp peak 480 nm along with a shoulder peak at 610 nm. Cluster 2 shows distinct peaks at 420, 430 and 490 nm. Cluster 1 shows a broad peak at 490 nm. UV-vis investigations show that the band gaps of these clusters vary with core sizes. A blue shift in the HOMO–LUMO gap with decreasing core size is observed (traces 5 to 1), as seen in gold[6] and silver[31] clusters. The luminescence properties also change in clusters 1–5. Clusters 4 and 5 did not show visible luminescence whereas 2 and 3 exhibit luminescence with maxima at 670 and 680 nm, respectively (Fig. S3†). The shift in luminescence maxima is consistent with the change in cluster size. The yield of CC was ~26 mg, starting from 23 mg of $AgNO_3$. Cluster 3 shows better yield (~15 mg from 23 mg of $AgNO_3$) and stability than the other QCs.

About 10 mg of crude cluster was dissolved in 1.0 mL water and kept under ambient conditions overnight. There was a black precipitate and a clear solution. The precipitate was discarded, which may be due to the decomposition of other metastable clusters. The resultant supernatant is referred to as aged crude cluster (ACC). Aging resulted in a change of color of the solution from reddish brown (CC) to faint pinkish red (ACC) and this change is also reflected in the corresponding powder samples. The powder samples of CC and ACC are black and reddish brown, as shown in insets of Fig. 1a and 2b, respectively.

The absorption spectra of ACC (Fig. S2b†) and cluster 3 (Fig. 1) were similar and therefore, the discarded residue may be due to the decomposition of metastable clusters, 5, 4, 2 and 1. ^{1}HNMR data also support the conversion of a mixture of clusters to a single cluster as there is a reduction in peak width (see later). Features in the circular dichroism (CD) spectrum of ACC matched with its absorption peaks in the 300–700 nm range (Fig. S4†) with strong Cotton signals due to the intrinsic chiral

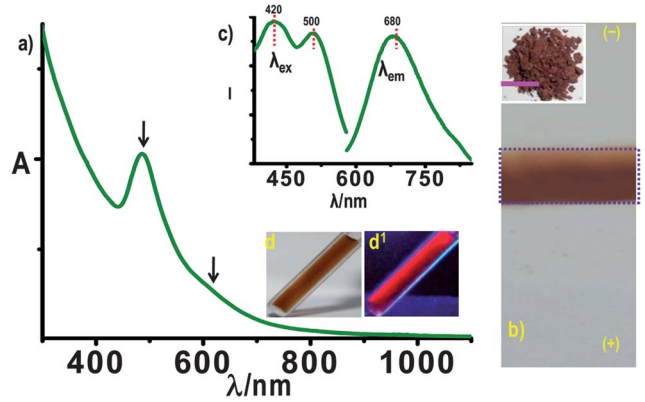

Fig. 2 (a) UV-vis absorption spectrum of the sample in (b). Distinct peaks are marked. (b) Photograph of the PAGE band derived from aged crude. Inset of (b) is the aged crude cluster in powder form. Scale bar on inset of (b) is 1 cm. (c) Excitation and emission spectra of the same. Photographs of this solution in water collected under visible (d) and UV light (d^1).

metal core.[30,33,35,37] It is also noted that the CD signals are in agreement with the glutathione protected silver cluster reported by Kitaev *et al.*[37] The powder obtained after freeze-drying the ACC solution was subjected to PAGE, which showed the presence of a single band (Fig. 2b) whose absorption and luminescence profiles (Fig. 2a† and inset c, respectively) match perfectly with those of cluster 3 (both the bands exhibiting the same mobilities are marked with dotted boxes in Fig. 1a and 2b, respectively). Absorption spectral features of cluster 3 and Ag@SG clusters from the literature[25,31,37] are comparable (Fig. S5†). All of them show similarities in the sharp and shoulder peaks at ~480 and ~610 nm, respectively. The cluster solution exhibits luminescence in the red region, photographs of the solution under visible and UV light are shown in insets d and d^1, respectively, in Fig. 2. Interestingly, the absorption spectrum of recently crystallized Ag_{32} cluster[29] also exhibits a strong peak at 485 nm and a weak peak at 600 nm along with a few additional structures at 450 and 750 nm; the latter two are absent in our present system. Also the crystallized cluster[29] exhibits blue emission but the present system is red emitting. These differences in the optical properties of the systems may be due to the ligand-dependent structural changes. It has to be noted that the ligand 1,2-bis(diphenylphosphino)ethane (DPPE), useful to join tetrahedrally coordinated shell-Ag atoms of the Ag_{22}^{12+} core, is absent in the present system.

The cluster was characterized with various tools as well. As ACC, its PAGE-purified product and cluster 3 gave identical results; the former was used for most of the studies, unless noted otherwise. The cluster responsible was identified as $Ag_{32}SG_{19}$ and the details will be discussed below.

It is worth noting that there are some minor differences in the absorption spectra of ACC and the PAGE-purified product (cluster 3). However, absorption profiles of the PAGE product of ACC (Fig. 2a) and cluster 3 (Fig. 1, trace 3) are the same. An extra peak was observed at 420 nm in ACC (Fig. S2†) and not in the PAGE purified products. Although there is this difference, the excitation and emission spectra for all the clusters are the same (Fig. S3† and 2c). This difference in the absorption spectra is due to the difference in pH of the solutions. Absorption profiles of these clusters show slight changes with pH. The 420 nm peak in ACC at pH 4.2 was absent at pH 6.0. The running gel in electrophoresis is maintained at pH 8.8, and this results in a change in pH after PAGE. Another important aspect to mention is that the 420 nm band of the excitation spectrum of ACC (Fig. 2c) resembles the UV-vis spectrum, indicating that this peak is part of the absorption spectrum and is not due to another cluster. These aspects indicate that they are the same chemically.

Although crystallography is needed for complete characterization, most of the information on the composition of QCs is available from mass spectrometry.[4,6] It is also important to note that –SG protected clusters are difficult to crystallize and crystal structures of none of them have been available till now. The chemical compositions of –SG protected gold clusters were understood solely based on ESI MS.[6] Unlike in the case of gold QCs, obtaining quality ESI MS of silver clusters is difficult due to their poor stability. In most cases, the ESI conditions, especially the capillary and transfer tube temperatures, cause decomposition of the clusters. As a result, only a few Ag QCs with known composition exist up to now. Most of the studies of these clusters are limited to understanding their optical properties,[30,33–37,39] and applications in sensing.[40–42]

Negative ion ESI MS of cluster 3 and aged cluster in a water : methanol mixture yield the same ESI MS data. The spectra are composed of a series of multiply charged anions originating from deprotonation of the carboxyl moieties of the –SG ligands as it is a dicarboxylic acid. It can undergo two ionizations, but in the pH of the cluster solution (~4.2), a monoanion $(SG–H)^-$ is preferred. However, –SG ligand can also

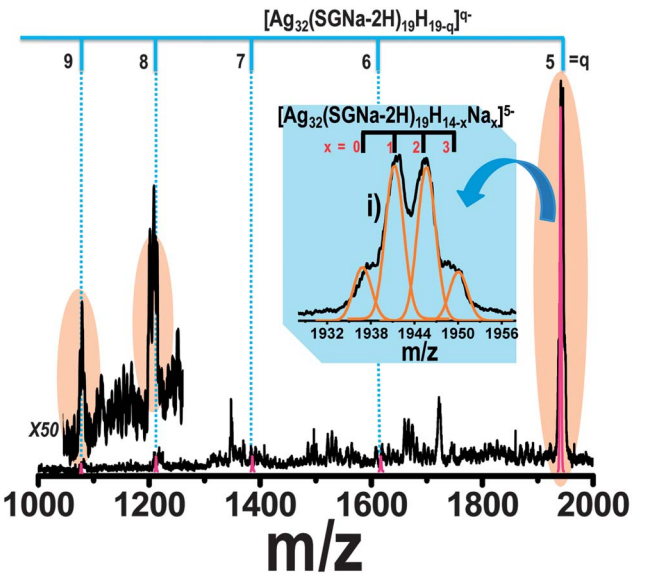

Fig. 3 ESI MS of $Ag_{32}SG_{19}$ in negative mode in the range of m/z 1000–2000. Calculated positions corresponding to the multiply charged species (5^- to 9^-) of $[Ag_{32}(SGNa\text{-}2H)_{19}H_{19-q}]^{q-}$ are shown on the top of the spectrum. Pink colored peaks correspond to the calculated peaks positions of $[Ag_{32}(SGNa\text{-}2H)_{19}H_{19-q}]^{q-}$. Inset (i) is a comparison of the calculated and experimental spectra of $[Ag_{32}(SGNa\text{-}2H)_{19}H_{14-x}Na_x]^{5-}$, where $x = 0$, 1, 2 and 3.

exist as a sodium salt and therefore the monoanion formed may be represented as $(-SGNa\text{-}2H)^-$. As there are multiple SG ligands, there are a number of such species.

Cluster 3 shows a series of peaks in the range of *m/z* 1200–2500 (Fig. 3). However, it is quite difficult to understand the peaks due to the complexity of the spectrum. Recently, Griffith *et al.*[43] reported the mass spectrum of $Ag_{32}SG_{19}$, isolated from gel electrophoresis of crude clusters. The absorption profile of this cluster matches well with our cluster (Fig. S5†). But, the mass spectral series obtained by Griffith *et al.* is different from our study. This discrepancy may be due to the synthesis protocol which adds sodium ions in our case and also due to instrumental variations. The calculated multiply charged peaks for $[Ag_{32}(SGNa\text{-}2H)_{19}H_{19-q}]^{q-}$ are matching well with the ESI MS data [note: $Ag_{32}(SGNa\text{-}2H)_{19}H_{19}$ is the parent neutral molecule]. For example, a highly intense peak centred at *m/z* 1941 corresponds to $[Ag_{32}(SGNa\text{-}2H)_{19}H_{14}]^{5-}$. Upon close observation we find that the peak is composed of four peaks at *m/z* 1936 $[Ag_{32}(SGNa\text{-}2H)_{19}H_{14}]^{5-}$, *m/z* 1941 $[Ag_{32}(SGNa\text{-}2H)_{19}NaH_{13}]^{5-}$, *m/z* 1945 $[Ag_{32}(SGNa\text{-}2H)_{19}Na_2H_{12}]^{5-}$ and *m/z* 1949 $[Ag_{32}(SGNa\text{-}2H)_{19}Na_3H_{11}]^{5-}$ (inset i, Fig. 3). Such sodium additions are common in cluster mass spectrometry.[23,25] Similarly, mass spectral peaks corresponding to $[Ag_{32}(SGNa\text{-}2H)_{19}H_{19-q}]^{q-}$ also appeared at the calculated positions, where *q* is the overall charge of the cluster (6, 7, 8 and 9). For example, the peaks due to $[Ag_{32}(SGNa\text{-}2H)_{19}H_{13}]^{6-}$, $[Ag_{32}(SGNa\text{-}2H)_{19}H_{12}]^{7-}$, $[Ag_{32}(SGNa\text{-}2H)_{19}H_{11}]^{8-}$ and $[Ag_{32}(SGNa\text{-}2H)_{19}H_{10}]^{9-}$ are at *m/z* 1617, 1386, 1212, and 1078, respectively. Although the calculated positions match well, the resolution at these charge states is not adequate to see the isotope pattern of silver. The peaks are quite broad and several other peaks surround the main peak. This complication is due to the presence of sodium adducts. The other complication corresponds to a cleavage of the amide bond between glutamic acid and cysteine, a fragmentation process commonly observed in glutathione, as evidenced by its presence in the tandem mass (mass spectrometry/mass spectrometry, MS/MS) spectrum of glutathione itself (Fig. S6†). This kind of fragmentation is also observed for glutathione protected gold clusters.[10] ESI MS in the range of *m/z* 400–1200 shows low mass region peaks at *m/z* 936, 828, 522 and 414 assigned to $[Ag_3SG_2\text{-}H]^-$, $[Ag_2SG_2\text{-}H]^-$, $[Ag_2SG\text{-}H]^-$ and $[AgSG\text{-}H]^-$, respectively (Fig. S7†). We measured the mass spectrum of the well-known cluster, $Au_{25}SG_{18}$ under these conditions and the expected spectrum was seen (Fig. S8†), which confirms the accuracy of the data.

In view of the poorly resolved peaks in the ESI MS data, we wanted to have additional information on the composition of the cluster using other methods. The best option is to compare the results with another soft ionization technique. MALDI MS of the cluster was not successful for further confirmation of the assignment. Note that so far there is no report of the MALDI MS of intact clusters protected with glutathione. In order to obtain both MALDI MS and ESI MS, we tried to synthesize a cluster having the same core with ligands such as cysteine, mercaptosuccinic acid and *N*-(2-mercaptopropionyl)glycine. Among them, the cluster protected with *N*-(2-mercaptopropionyl) glycine (MPGH; its thiolate is labeled as MPG) was selected for further study as its absorption profiles matched exactly with

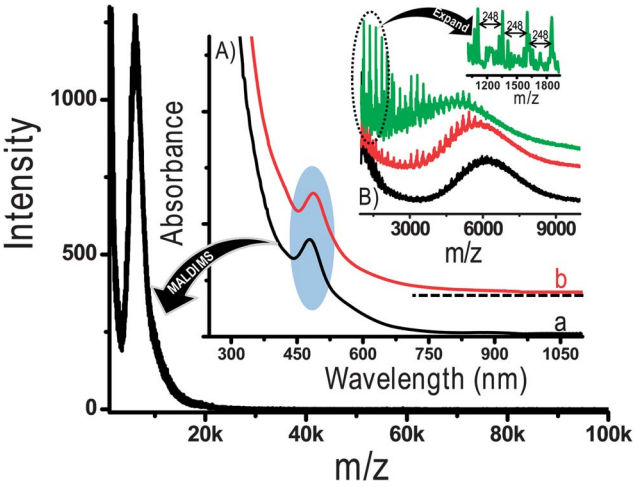

Fig. 4 MALDI MS of Ag@MPG in negative mode. (A) UV-vis absorption spectra of Ag@MPG (a) and $Ag_{32}SG_{19}$ (b) clusters at pH 6.0. (B) Laser dependent MALDI MS spectra of the Ag@MPG cluster at near threshold intensity (black trace, ~1700) and at higher laser intensities (red and green traces). Inset of B show the expanded region of MALDI MS at high laser intensity (~3500).

cluster 3 ($Ag_{32}SG_{19}$). The cluster also gave acceptable MALDI and ESI MS features. We present these data below.

MPG protected Ag QCs (Ag@MPG) were synthesized using the same method used for $Ag_{32}SG_{19}$ (see Experimental section). Precipitate of clusters was taken in 10 mL distilled water and kept for aging at 10 °C. The pH of the resultant solution was 6.0. It showed a sharp peak at ~480 nm and a shoulder around ~600 nm in its absorption profile (inset of Fig. 4). At the same pH, $Ag_{32}SG_{19}$ also shows the same absorption spectrum. The similarity in absorption profiles of these clusters proves that both have the same cluster core. In the case of the luminescence spectrum, there is a slight shift (10–15 nm) in the emission peak position. Unlike in the case of $Ag_{32}SG_{19}$, these clusters do not show visible luminescence under UV light illumination, indicating very low quantum yields compared to glutathione protected ones. It is known that –SG protected Au_{25} shows higher quantum yield compared to other thiols.[44] It is attributed to the electron donating capability (of –SG) due to the presence of electron rich groups (*e.g.*, carboxylic and amino groups). In the case of MPG, the smaller number of electron rich groups made the system have lower quantum yield. Ag@MPG clusters exhibit a single emission at 700 nm when excited at 470 and 540 nm (Fig. S9†). However, there is a slight shift in excitation and emission positions of the clusters ($Ag_{32}SG_{19}$ and Ag@MPG). Note that ligands play an important role in the luminescence profile.[8,44]

This cluster was subjected to MALDI MS using CHCA as the matrix. Negative ion mode MALDI MS (Fig. 4) at threshold laser power (~1700) shows a peak maximum at ~6.1 k. No cluster other than the species giving the 6.1 k maximum was present in the sample. The peak was quite broad compared to the calculated peak and also in comparison to typical MALDI MS data of Au clusters.

Upon closer observation, the 6.1 k peak is composed of peaks spaced at *m/z* 248, especially on the left of the peak, suggesting progressive loss of Ag_2S. Thus, even at threshold laser intensity,

selective fragmentation occurs. The loss of Ag-MPG thiolates is unlikely, which would have given a much larger spacing of *m*/*z* 270. This loss is reflected in the experimentally observed mass spectral position (6.1 k) while the calculated peak position for $Ag_{32}MPG_{19}$ is 6.5 k which was confirmed by ESI MS (see below). We conclude that the alkyl chains are partially dissociated (~3 alkyl groups (~0.13 kDa for each); 6.5–6.1 kDa = 0.4 kDa) from the cluster core during ionization, which also explains the increased peak width. Indeed, loss of alkyl chains by carbon–sulfur (C–S) bond cleavage is common in monolayer protected clusters of gold and silver. The peak at 6.1 k is increasingly shifted towards the low mass region with increasing laser intensity and the spectrum is dominated by a series of peaks separated by *m*/*z* 248 due to Ag_2S loss indicating the loss of a major portion of the alkyl chains (inset of Fig. 4B). By the use of a more optimized matrix, this fragmentation may be avoided. It is important to note that an optimized matrix such as *trans*-2-[3-(4-*tert*-butylphenyl)-2-methyl-2-propenylidene]malononitrile (DCTB) is essential for a high quality mass spectrum of $Au_{25}PET_{18}$.[4]

The Ag@MPG clusters were also subjected to ESI MS. Fig. 5 shows the negative ion (ESI) mass spectrum of Ag@MPG clusters in a water : methanol mixture. MPG is a monocarboxylic acid and its ionization by the loss of H^+ results in $(MPG\text{-}H)^-$. A series of multiply charged species were observed in the mass spectrum of the cluster due to $[Ag_{32}(MPG\text{-}H)_{19}Na_xH_{19-x-q}]^{q-}$, where $q = 3$, 4 and 5. The multiply charged peaks are quite broad due to the addition of sodium ($x = 8$, 9 and 10). Just as in the case of –SG, half the carboxylate functional groups contain sodium. For example, the peak at *m*/*z* 2254 (due to the triply charged species) is due to the merging of peaks corresponding to $[Ag_{32}(MPG\text{-}H)_{19}Na_8H_8]^{3-}$, $[Ag_{32}(MPG\text{-}H)_{19}Na_9H_7]^{3-}$ and $[Ag_{32}(MPG\text{-}H)_{19}Na_{10}H_6]^{3-}$ (inset of Fig. 5). However, there is complexity in the data (extra peaks in the spectrum labeled with *) which may be superimposition of other charged species or other possible fragmentations. In order to understand the system in detail, an improved mass spectrum is required. This is difficult in view of the multiply charged species, although we are continuing our efforts. Peaks of other charges, $[Ag_{32}(MPG\text{-}H)_{19}Na_8H_7]^{4-}$ and $[Ag_{32}(MPG\text{-}H)_{19}Na_8H_6]^{5-}$, were also seen with good intensity. Even at low capillary temperatures, clusters undergo fragmentation resulting in peaks in the low mass region. These fragment peaks appeared with characteristic mass spacing due to silver isotopes, *i.e.* *m*/*z* 2. These peaks at *m*/*z* 1080 and 1188 correspond to $[Ag_4MPG_4\text{-}H]^-$ and $[Ag_5MPG_4\text{-}H]^-$, respectively. These peaks and their sodium adducts are labeled in Fig. 5. The intense peak at *m*/*z* 1902 in the mass spectrum corresponds to the triply charged sodium salt of $Ag_{27}MPG_{16}$, derived from the loss of silver thiolates ($[Ag_5MPG_3\text{-}H]$, which appeared in the low mass region, shown in orange color), from its parent ion, $[Ag_{32}(MPG\text{-}H)_{19}Na_8H_8]^{3-}$. The expanded spectrum of $[Ag_5MPG_3\text{-}H]^-$ is given in Fig. S10.† Based on the agreement between the experimental and calculated peaks, the composition of Ag@MPG clusters is confirmed as $Ag_{32}MPG_{19}$.

The monolayer binding in $Ag_{32}SG_{19}$ through thiolate is supported by XPS (Fig. S11†) and FTIR spectroscopy (Fig. S12†). The XPS survey spectrum shows all the expected elements. The Ag 3d peak is close to an Ag(0) value of 368.0 eV. Note that there is not much difference in the binding energy between Ag(0) and Ag(I) states. The S $2p_{3/2}$ peak is thiolate-like with an observed value of 162.0 eV (Fig. S11c†). This is in agreement with the IR spectrum (Fig. S12†), which suggests the loss of thiolate proton upon cluster formation. From EDAX, the Ag : S atomic ratio measured is 1 : 0.56 ± 0.03 which matches with the expected value of 1 : 0.59 for $Ag_{32}SG_{19}$ (Fig. S13†). A broad peak centered around $2\theta \approx 38°$ in the X-ray diffraction (XRD) pattern is seen, as in the case of Au or Ag QCs,[17,24,25] which shows the absence of metallic nanoparticles (Fig. S14†). The clusters appear as tiny dots in TEM with a size of ~1.0 nm (Fig. S15†).

A recent breakthrough in metal cluster research is the structure determination of $Au_{102}SR_{44}$ followed by those of $Au_{25}SR_{18}$ and $Au_{38}SR_{24}$. Although the "divide and protect" concept (metal core with neutral atoms protected by metal thiolate) was proposed theoretically by Hakkinen *et al.*[45] on $Au_{38}(SR)_{24}$, an understanding of this kind of clusters has taken place only after the above structural data. In $Au_{102}SR_{44}$,[22] the inner core of the cluster contains 79 Au atoms (which are all in neutral state) protected by nineteen $-[RS_C\text{–}Au\text{–}S_CR]-$ and two $-[RS_C\text{–}Au\text{–}S_B(R)\text{–}Au\text{–}S_CR]-$ units, where $(R)S_B$ and RS_C correspond to bridging and core-attached thiolates, respectively. $Au_{38}SR_{24}$[20] contains a face-fused biicosahedral Au_{23} core capped by three $-[RS_C\text{–}Au\text{–}S_CR]-$ and six $-[RS_C\text{–}Au\text{–}S_B(R)\text{–}Au\text{–}S_CR]-$ units. In the case of $Au_{25}SR_{18}$, there are two types of ligands, 6 bridging and 12 core-attached thiolates.[19] The whole entity may be represented as $Au_{13}[RS_C\text{–}Au\text{–}S_B(R)\text{–}Au\text{–}S_CR]_6$. The occupancy of $-[RS_C\text{–}Au\text{–}S_CR]-$ and $-[RS_C\text{–}Au\text{–}S_B(R)\text{–}Au\text{–}S_CR]-$ in Au_{102}, Au_{38}, Au_{25} is 19 : 2, 3 : 6, and 0 : 6. From these observations, as

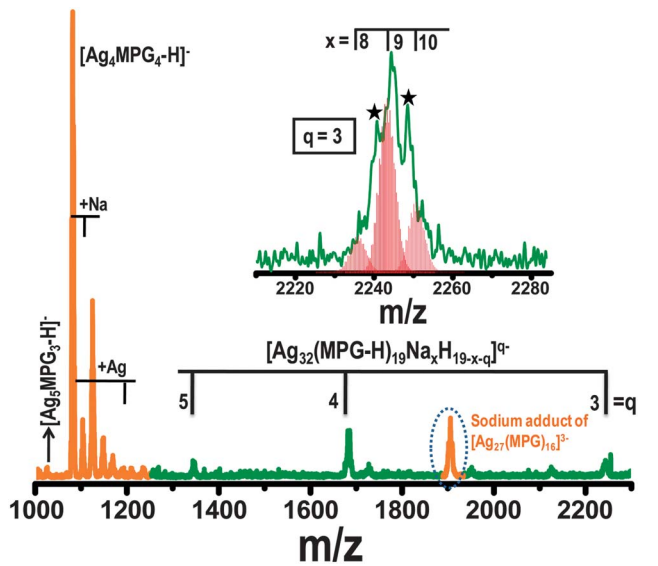

Fig. 5 ESI MS of $Ag_{32}MPG_{19}$ in the negative mode in the range of *m*/*z* 1000–2300. Calculated positions corresponding to the multiply charged species of $[Ag_{32}(MPG\text{-}H)_{19}Na_xH_{19-x-q}]^{q-}$, where $q = 3$, 4 and 5 (shown on the top of the spectrum). Inset shows a comparison of the calculated and experimental spectra of species with $x = 8$, 9, 10 and $q = 3$. These species are $[Ag_{32}(MPG\text{-}H)_{19}Na_8H_8]^{3-}$, $[Ag_{32}(MPG\text{-}H)_{19}Na_9H_7]^{3-}$ and $[Ag_{32}(MPG\text{-}H)_{19}Na_{10}H_6]^{3-}$. The fragments, $[Ag_{27}(MPG\text{-}H)_{16}]^{3-}$ and the Ag thiolates are shown in another color.

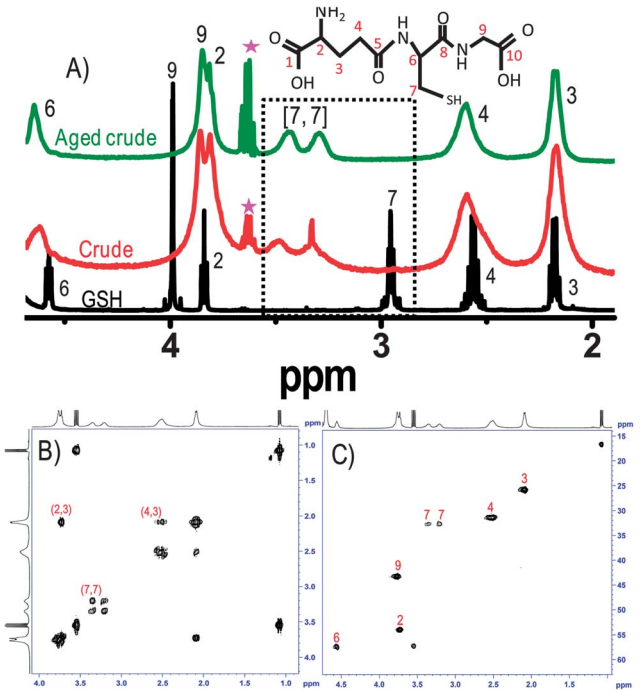

Fig. 6 (A) ^{1}H NMR spectra of GSH, crude cluster and aged crude. The peaks in the dotted box are due to H-7. Peaks at ~3.6 ppm (marked with *) are due to residual EtOH. 2D NMR spectra of $Ag_{32}SG_{19}$ clusters. (B) COSY spectrum. (C) HSQC spectrum. Solvent: D_2O. Note that the CH_3CH_2 signal (^{1}H: 1.1 and 3.6 ppm, ^{13}C: 15.2 and 58.0 ppm) in COSY and HSQC spectra is from residual CH_3CH_2OH. COSY showed the coupling information from the cross peaks. [4,3] and [2,3] protons are coupled together as understood from their cross peaks, marked in (B). H-7 also produces cross peaks without coupling with other sets of protons. In (C), H-7 protons show two signals at 3.2 and 3.5 ppm originating from the same carbon (C-7, 32.0 ppm), due to two hydrogen atoms on C-7.

the size of the core increases to 102, the structure is dominated by –[RS_C–Au–S_CR]–[19,22] while in the smaller clusters, –[RS_C–Au–S_B(R)–Au–S_CR]– units dominate.

Apart from crystal structure studies, NMR can also be used to study the Au-thiolate structure effectively.[8,46,47] For example, independent NMR studies revealed the presence of two kinds of sulfur environments in 2 : 1 ratio (where 2 RS_C : 1 S_BR) in $Au_{25}SR_{18}$.[46,48] Motivated by the recent developments and our own earlier studies,[8] we performed NMR analysis of $Ag_{32}SG_{19}$. It reveals that the structure of the thiolated cluster is quite different from the phosphine analogue.[49] The presence of the inner core and outer shell with metal thiolate is understood from a detailed analysis of NMR.

^{1}H NMR data of the cluster are presented in Fig. 6. Chemical shifts for H-3, H-4, H-2, H-9, and H-6 of glutathionate (–SG) in $Ag_{32}SG_{19}$ are 2.17, 2.60, 3.81, 3.87, and 4.64 ppm, respectively (Fig. 6A, refer to the structure for peak assignments). Protons H-7 (= 3CH–CH_2–S–) signals are significantly shifted downfield in the range of 3.2–3.5 ppm with broadening followed by splitting, noted as [7,7] in Fig. 6A. Downfield shift of H-7 can be understood in terms of its close proximity to the silver core. To know the cause of splitting and nature of the staple motif on the cluster surface in comparison to the structures presented above, homonuclear correlation spectroscopy (COSY) and heteronuclear single quantum correlation (HSQC) were performed (Fig. 6B and C, respectively).

The two-dimensional (2D) NMR data of Ag_{32} clearly rule out complete protection of the core by –[RS_C–Ag–S_B(R)–Ag–S_CR]– units which would have resulted in two pairs of peaks at 2 : 1 ratio for –S_CR and –S_BR, respectively. It is to be noted that the two peaks in a pair correspond to two hydrogen atoms on the 7th position of glutathione. But, we have seen only one pair of peaks, labeled [7,7], which are in 1 : 1 ratio. The presence of the 1 : 1 intensity ratio indicates that all the thiolates are in equivalent environments. Based on the Au–thiolate structure of gold clusters, one can see that the –[S_C–Ag–S_C]– unit alone possesses equivalent thiolates. These results suggest that the Ag–thiolate structure for $Ag_{32}SG_{19}$ is dominated by –[RS_C–Ag–S_CR]–. However, complete protection of –[RS_C–Ag–S_CR]– is also not possible due to the presence of an odd number of ligands (19 SR). It suggests the presence of other Ag–thiolates. But peaks corresponding to them are not detected in NMR, indicating that they are few in number. From the theoretical study of Xiang *et al.*[50] and Balasubramanian *et al.*,[51] we know that –[RS–Ag–RS]– is a stable structural motif for a thiolate-protected Ag QCs. To the best of our knowledge, this is the first experimental evidence for the –[RS–Ag–RS]– structural motif in thiolated Ag QCs. It is in contrast to Au_{25} and Au_{38} clusters, where NMR study reveals that they are dominated by –[RS_C–Au–S_B(R)–Au–S_CR]–.

Summary and conclusions

In summary, we have synthesized –SG protected Ag_{32} clusters. Assignment was made based on ESI MS and MALDI MS experiments. Clusters were characterized with ^{1}H NMR, 2D NMR, XRD, *etc.* A cluster with same core was synthesized with MPG as a protecting ligand. ESI MS and MALDI MS also confirm the $Ag_{32}MPG_{19}$ composition. Based on NMR investigations, we suggest that most likely the Ag–thiolate is composed of –[S–Ag–S]– motifs. We believe that facile synthesis and the structural insights presented here will stimulate further experimental and theoretical studies on this system.

Acknowledgements

We thank the Department of Science and Technology, Government of India for constantly supporting our research program on nanomaterials. M.S.B. thanks the CSIR for a research fellowship.

References

1 U. Kreibig and M. Vollmer, in *Optical Properties of Metal Clusters*, ed. J. P. Toennies, Springer, Berlin, 1995.
2 L. M. Liz-Marzán, *Langmuir*, 2006, **22**, 32–41.
3 J. Zheng, P. R. Nicovich and R. M. Dickson, *Annu. Rev. Phys. Chem.*, 2007, **58**, 409–431.
4 R. Jin, *Nanoscale*, 2010, **2**, 343–362.
5 T. G. Schaaff, G. Knight, M. N. Shafigullin, R. F. Borkman and R. L. Whetten, *J. Phys. Chem. B*, 1998, **102**, 10643–10646.

6 Y. Negishi, K. Nobusada and T. Tsukuda, *J. Am. Chem. Soc.*, 2005, **127**, 5261–5270.
7 M. A. H. Muhammed, P. K. Verma, S. K. Pal, R. C. A. Kumar, S. Paul, R. V. Omkumar and T. Pradeep, *Chem.–Eur. J.*, 2009, **15**, 10110–10120.
8 E. S. Shibu, M. A. H. Muhammed, T. Tsukuda and T. Pradeep, *J. Phys. Chem. C*, 2008, **112**, 12168–12176.
9 E. S. Shibu and T. Pradeep, *Chem. Mater.*, 2011, **23**, 989–999.
10 A. Ghosh, T. Udayabhaskararao and T. Pradeep, *J. Phys. Chem. Lett.*, 2012, **3**, 1997–2002.
11 E. S. Shibu, B. Radha, P. K. Verma, P. Bhyrappa, G. U. Kulkarni, S. K. Pal and T. Pradeep, *ACS Appl. Mater. Interfaces*, 2009, **1**, 2199–2210.
12 R. Jin, H. Qian, Z. Wu, Y. Zhu, M. Zhu, A. Mohanty and N. Garg, *J. Phys. Chem. Lett.*, 2010, **1**, 2903–2910.
13 H. Qian, Y. Zhu and R. Jin, *J. Am. Chem. Soc.*, 2010, **132**, 4583–4585.
14 H. Qian and R. Jin, *Chem. Commun.*, 2011, **47**, 11462–11464.
15 H. Tsunoyama, Y. Negishi and T. Tsukuda, *J. Am. Chem. Soc.*, 2006, **128**, 6036–6037.
16 Z. Wu, M. A. MacDonald, J. Chen, P. Zhang and R. Jin, *J. Am. Chem. Soc.*, 2011, **133**, 9670–9673.
17 M. Zhu, H. Qian and R. Jin, *J. Am. Chem. Soc.*, 2009, **131**, 7220–7221.
18 M. Zhu, C. M. Aikens, F. J. Hollander, G. C. Schatz and R. Jin, *J. Am. Chem. Soc.*, 2008, **130**, 5883.
19 M. W. Heaven, A. Dass, P. S. White, K. M. Holt and R. W. Murray, *J. Am. Chem. Soc.*, 2008, **130**, 3754–3755.
20 H. Qian, W. T. Eckenhoff, Y. Zhu, T. Pintauer and R. Jin, *J. Am. Chem. Soc.*, 2010, **132**, 8280–8281.
21 C. Zeng, H. Qian, T. Li, G. Li, N. L. Rosi, B. Yoon, R. N. Barnett, R. L. Whetten, U. Landman and R. Jin, *Angew. Chem., Int. Ed.*, 2012, **51**, 13114–13118.
22 P. D. Jadzinsky, G. Calero, C. J. Ackerson, D. A. Bushnell and R. D. Kornberg, *Science*, 2007, **318**, 430–433.
23 Z. Wu, E. Lanni, W. Chen, M. E. Bier, D. Ly and R. Jin, *J. Am. Chem. Soc.*, 2009, **131**, 16672–16674.
24 T. Udayabhaskararao and T. Pradeep, *Angew. Chem., Int. Ed.*, 2010, **49**, 3925–3929.
25 T. Udayabhaskararao, B. Nataraju and T. Pradeep, *J. Am. Chem. Soc.*, 2010, **132**, 16304–16307.
26 M. R. Branham, A. D. Douglas, A. J. Mills, J. B. Tracy, P. S. White and R. W. Murray, *Langmuir*, 2006, **22**, 11376–11383.
27 Y. Negishi, R. Arai, Y. Niihori and T. Tsukuda, *Chem. Commun.*, 2011, **47**, 5693–5695.
28 H. Yang, J. Lei, B. Wu, Y. Wang, M. Zhou, A. Xia, L. Zheng and N. Zheng, *Chem. Commun.*, 2013, **49**, 300–302.
29 H. Yang, Y. Wang and N. Zheng, *Nanoscale*, 2013, **5**, 2674–2677.
30 N. Nishida, H. Yao, T. Ueda, A. Sasaki and K. Kimura, *Chem. Mater.*, 2007, **19**, 2831–2841.
31 S. Kumar, M. D. Bolan and T. P. Bigioni, *J. Am. Chem. Soc.*, 2010, **132**, 13141–13143.
32 O. M. Bakr, V. Amendola, C. M. Aikens, W. Wenseleers, R. Li, L. Dal Negro, G. C. Schatz and F. Stellacci, *Angew. Chem., Int. Ed.*, 2009, **48**, 5921–5926.
33 N. Nishida, H. Yao and K. Kimura, *Langmuir*, 2008, **24**, 2759–2766.
34 N. Cathcart, P. Mistry, C. Makra, B. Pietrobon, N. Coombs, M. Jelokhani-Niaraki and V. Kitaev, *Langmuir*, 2009, **25**, 5840–5846.
35 H. Yao, M. Saeki and K. Kimura, *J. Phys. Chem. C*, 2010, **114**, 15909–15915.
36 K. V. Mrudula, T. Udayabhaskararao and T. Pradeep, *J. Mater. Chem.*, 2009, **19**, 4335–4342.
37 N. Cathcart and V. Kitaev, *J. Phys. Chem. C*, 2010, **114**, 16010–16017.
38 I. Diez and R. H. A. Ras, *Nanoscale*, 2011, **3**, 1963–1970.
39 M. Farrag, M. Thämer, M. Tschurl, T. Bürgi and U. Heiz, *J. Phys. Chem. C*, 2012, **116**, 8034–8043.
40 C. Wang, L. Xu, Y. Wang, D. Zhang, X. Shi, F. Dong, K. Yu, Q. Lin and B. Yang, *Chem.–Asian J.*, 2012, **7**, 1652–1656.
41 A. K. Singh, R. Kanchanapally, Z. Fan, D. Senapati and P. C. Ray, *Chem. Commun.*, 2012, **48**, 9047–9049.
42 B. Adhikari and A. Banerjee, *Chem. Mater.*, 2010, **22**, 4364–4371.
43 J. Guo, S. Kumar, M. Bolan, A. Desireddy, T. P. Bigioni and W. P. Griffith, *Anal. Chem.*, 2012, **84**, 5304–5308.
44 Z. Wu and R. Jin, *Nano Lett.*, 2010, **10**, 2568–2573.
45 H. Hakkinen, M. Walter and H. Grönbeck, *J. Phys. Chem. B*, 2006, **110**, 9927–9931.
46 Z. Wu, C. Gayathri, R. R. Gil and R. Jin, *J. Am. Chem. Soc.*, 2009, **131**, 6535–6542.
47 H. Qian, M. Zhu, C. Gayathri, R. R. Gil and R. Jin, *ACS Nano*, 2011, **5**, 8935–8942.
48 Z. Wu and R. Jin, *ACS Nano*, 2009, **3**, 2036–2042.
49 G. Schmid, *Chem. Soc. Rev.*, 2008, **37**, 1909–1930.
50 H. Xiang, S.-H. Wei and X. Gong, *J. Am. Chem. Soc.*, 2010, **132**, 7355–7360.
51 Y. Sun, K. Balasubramanian, T. Udayabhaskararao and T. Pradeep, *J. Phys. Chem. C*, 2011, **115**, 20380–20387.

Electronic Supplementary Information (ESI) for:

Thiolate-protected Ag_{32} clusters: Mass spectral studies of composition and insights into the Ag-thiolate structure from NMR

T. Udayabhaskararao, M. S. Bootharaju, and T. Pradeep*

DST Unit of Nanoscience (DST UNS) and Thematic Unit of Excellence (TUE), Department of Chemistry, Indian Institute of Technology Madras, Chennai-600 036, India

*E-mail: pradeep@iitm.ac.in

Contents

Electronic Supplementary Information 1

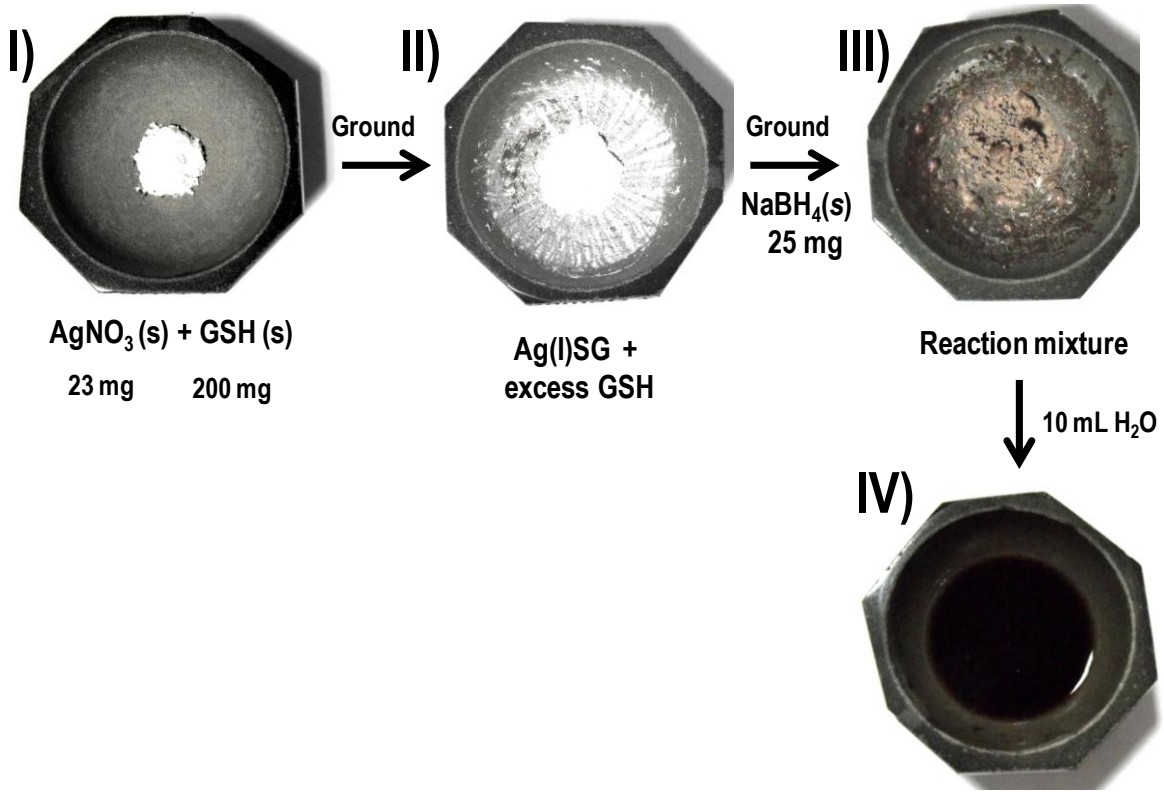

Scheme S1. Photographs representing the changes at various stages during the synthesis of $Ag_{32}SG_{19}$ clusters. Photograph I is the initial mixture of silver nitrate and glutathione (both are colorless solids). Grinding the above for 10 minutes leads to the formation of an Ag(I)SG thiolate (photograph II). This thiolate shows a featureless spectrum in its UV-vis profile (measured in water, data not shown). To this mixture, $NaBH_4$(s) was added and ground (photograph III). A 10 mL of distilled water was added to the above mixture (photograph IV). This solution contains mixture of clusters which shows distinct peaks as shown in Figure 1a.

Electronic Supplementary Information 2

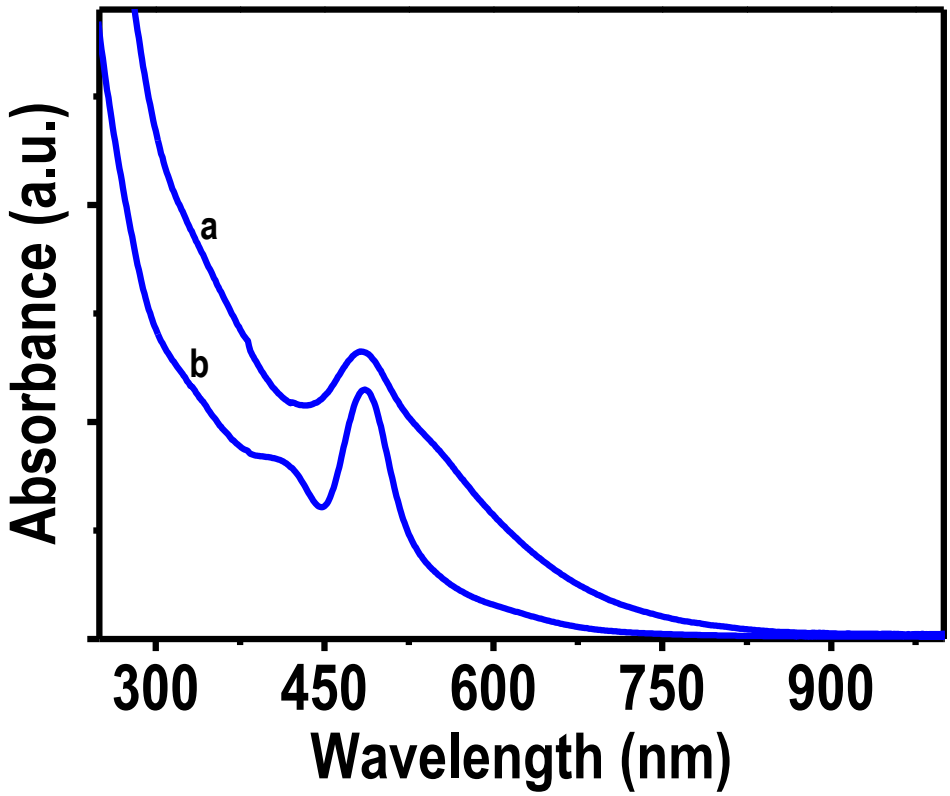

Figure S2. UV-vis absorption spectra of (a) the as-synthesized crude cluster, CC and (b) the solution obtained after keeping the crude cluster overnight at ambient conditions (giving aged crude, ACC). The spectrum of ACC is comparable to cluster 3 (trace 3, shown in Figure 1), except for the feature at 420 nm.

Electronic Supplementary Information 3

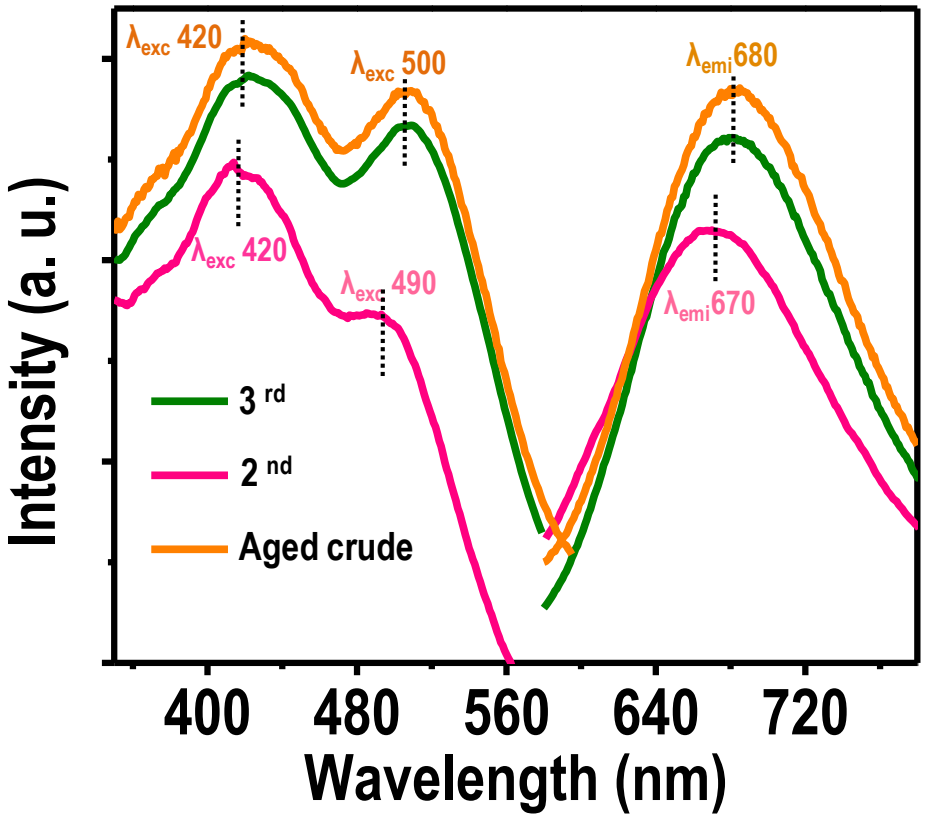

Figure S3. Photoluminescence spectra of clusters extracted from 2nd and 3rd bands of gel electrophoresis of CC. ACC also shows luminescence similar to cluster 3.

Electronic Supplementary Information 4

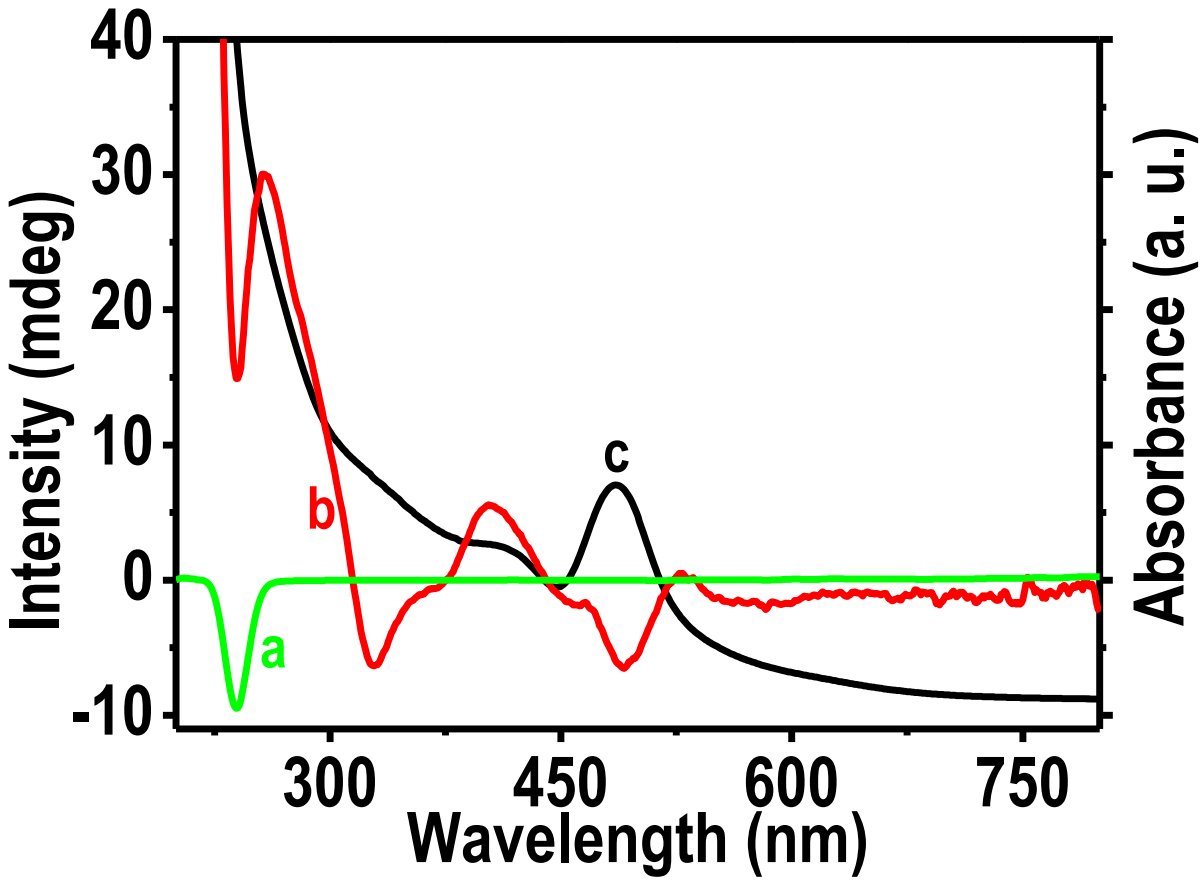

Figure S4. CD spectra of GSH (a) and $Ag_{32}SG_{19}$ (b) compared with the absorption of ACC solution (c).

Electronic Supplementary Information 5

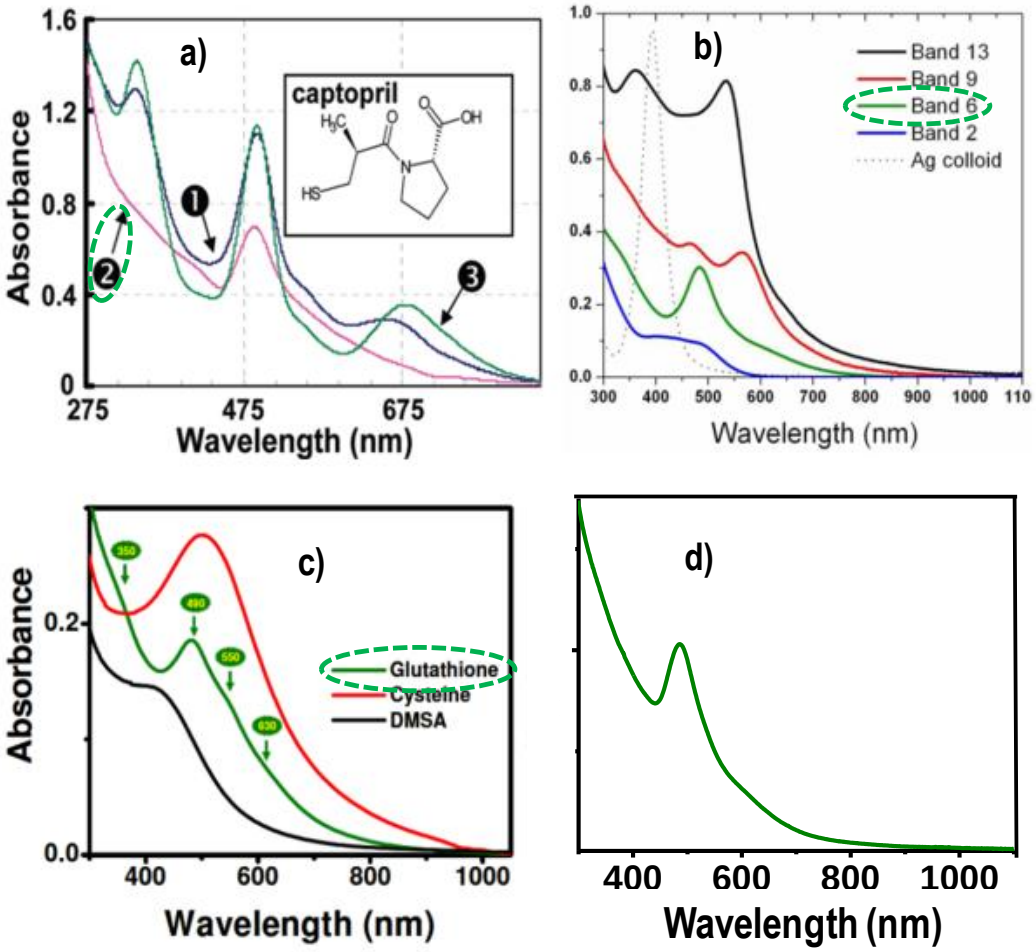

Figure S5. Absorption spectra of -SG protected Ag clusters (marked in green ellipse) from various groups, Kitaev *et al.*[1] (a), Bigoni *et al.*[2] (b) and Pradeep *et al.*[3] (c), compared with the present cluster (d). Spectra a, b and c are reprinted from references 1, 2 and 3, respectively.

Electronic Supplementary Information 6

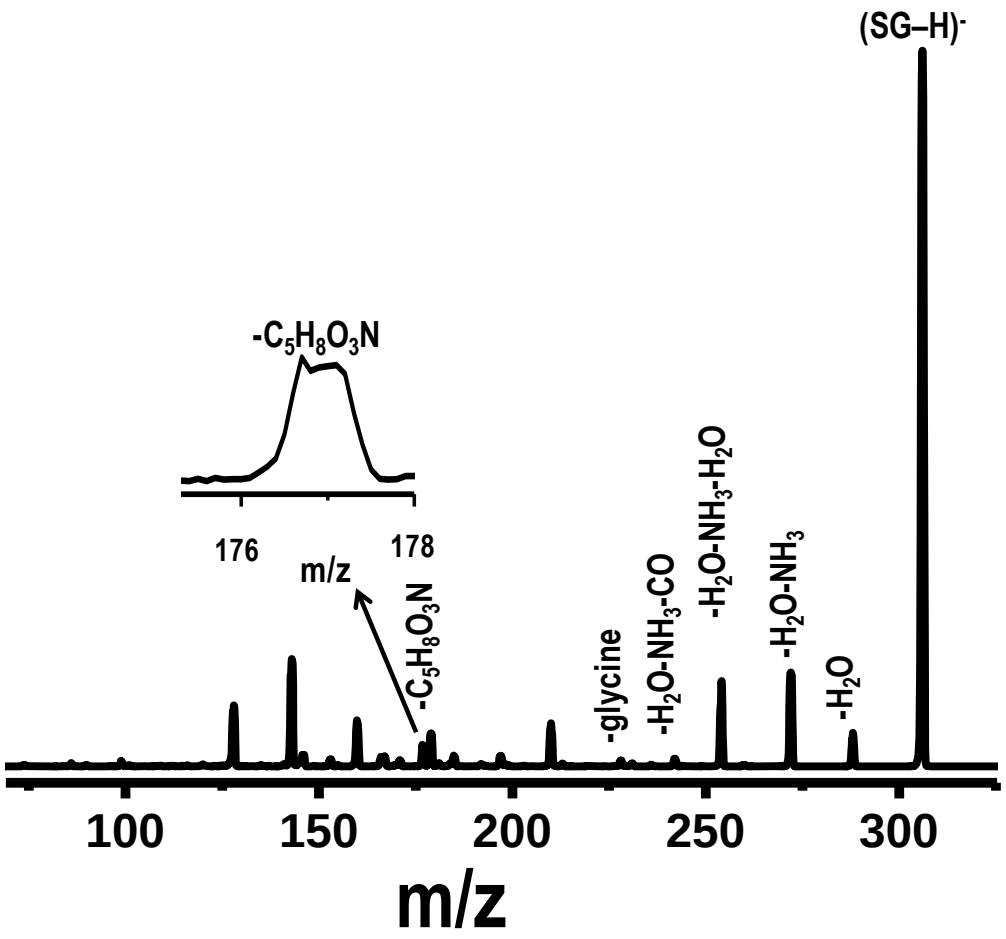

Figure S6. MS/MS spectrum of m/z 306 peak (anoin of glutathione) in the negative mode. Apart from the common H_2O and NH_3 losses, one prominent loss is due to $C_5H_8O_3N$.

Electronic Supplementary Information 7

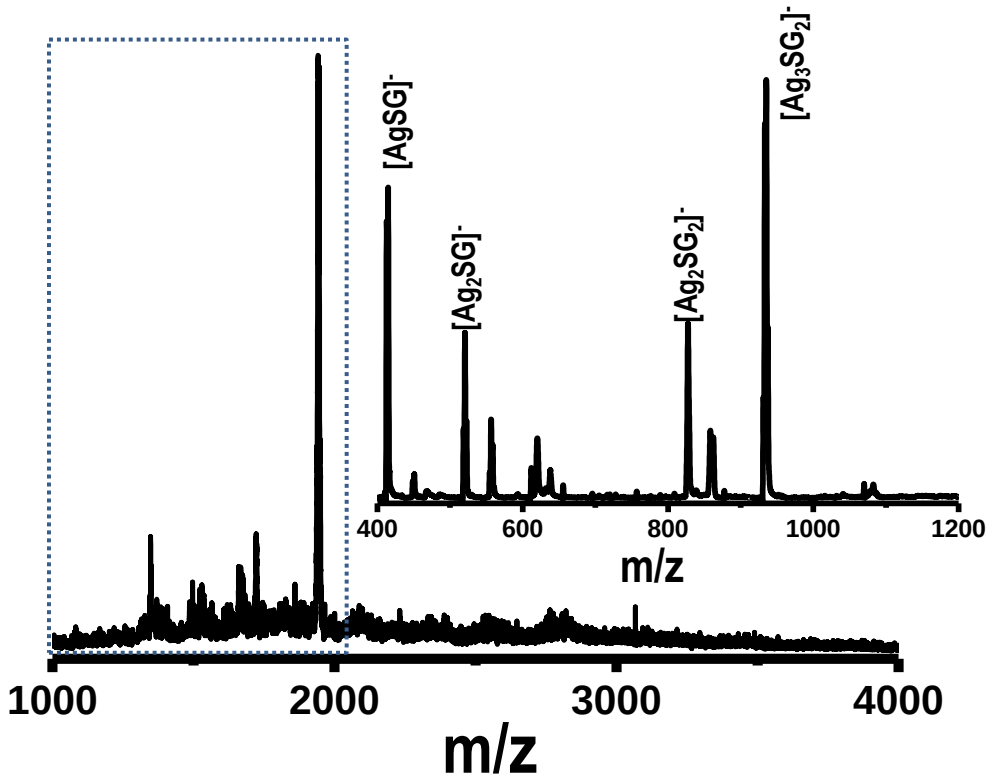

Figure S7. ESI MS of $Ag_{32}SG_{19}$ measured in the negative mode in the range of m/z 500-4000. The peaks of interest given in main text are in the marked region. Inset shows the ESI MS at the low mass region (m/z 400-1200). Peaks at m/z 936, 828, 522 and 414 are assigned to $[Ag_3SG_2\text{-}H]^-$, $[Ag_2SG_2\text{-}H]^-$, $[Ag_2SG\text{-}H]^-$ and $[AgSG\text{-}H]^-$, respectively.

Electronic Supplementary Information 8

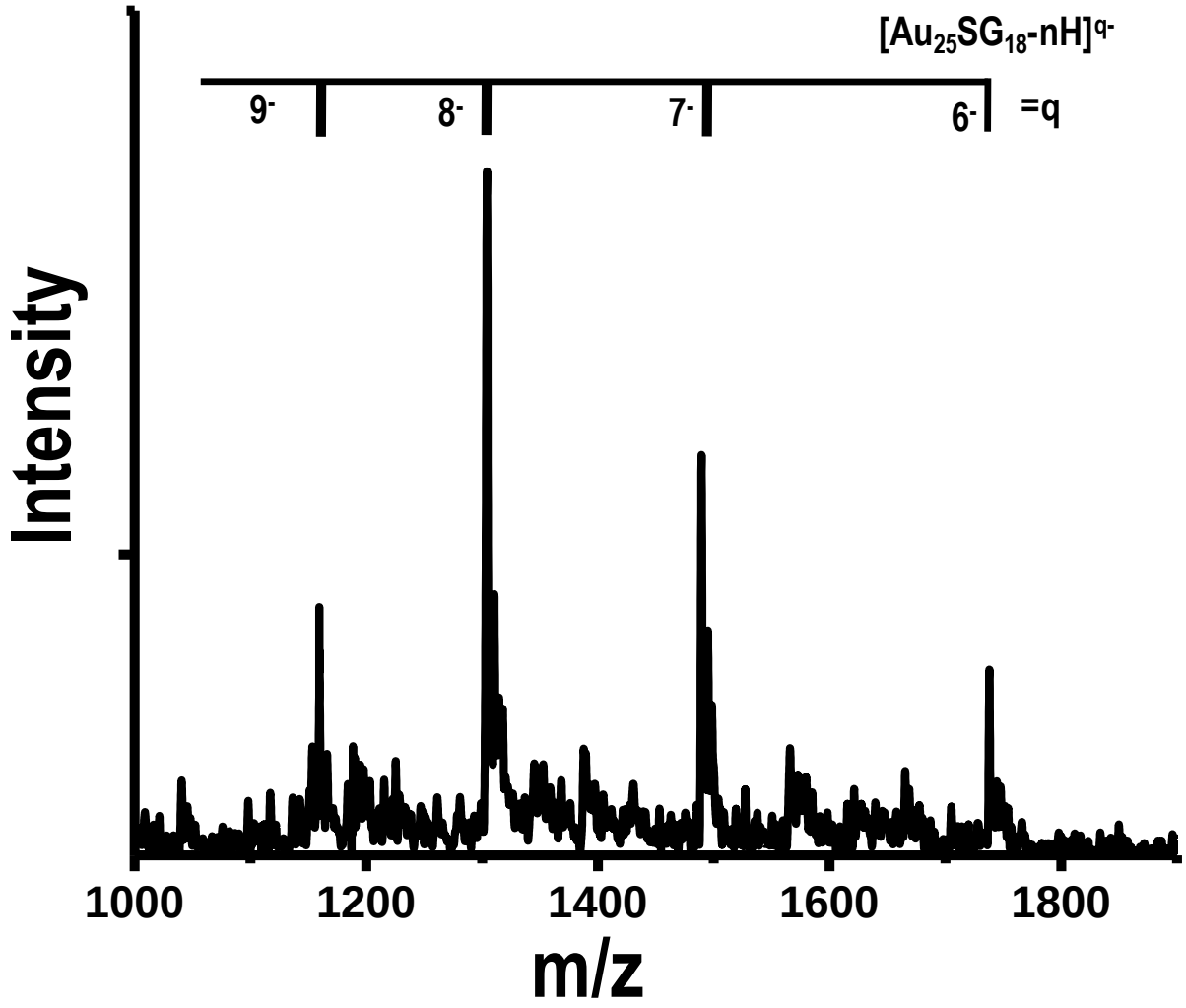

Figure S8. ESI MS of $Au_{25}SG_{18}$, measured under the same conditions as in the case of $Ag_{32}SG_{19}$. Spectrum shows the multiply charged species of $[Au_{25}SG_{18}\text{-}nH]^{q-}$ (where q= 6, 7, 8 and 9), which are labeled. The optimized conditions for this measurement are reported in the instrumentation section.

Electronic Supplementary Information 9

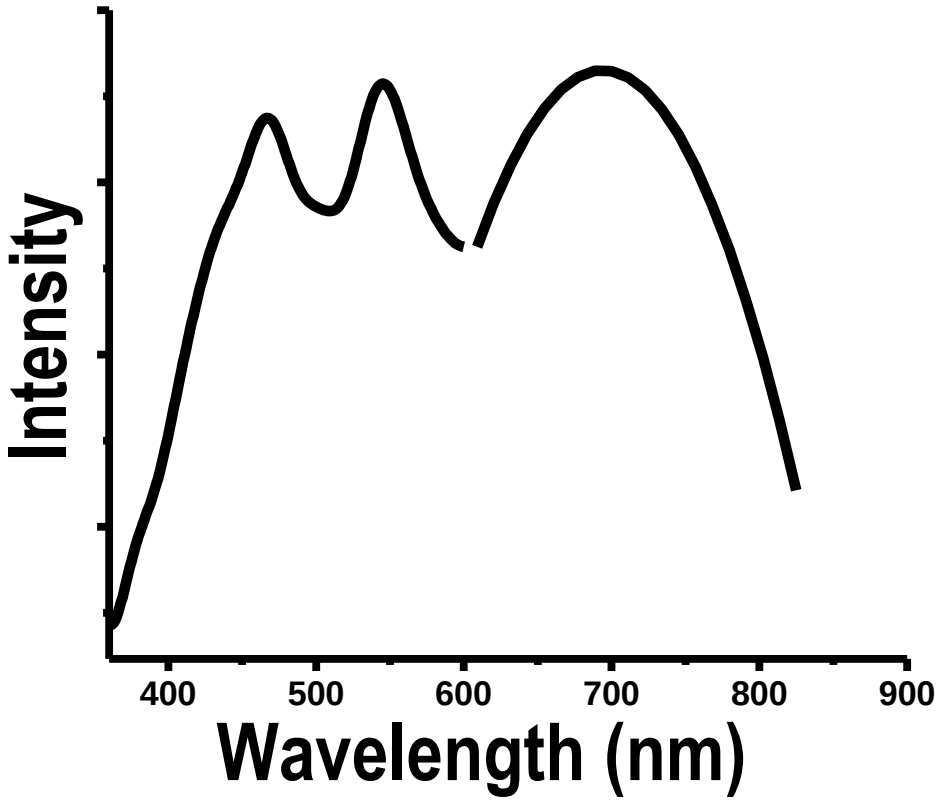

Figure S9. Photoluminescence spectra of Ag@MPG clusters in water at room temperature.

Electronic Supplementary Information 10

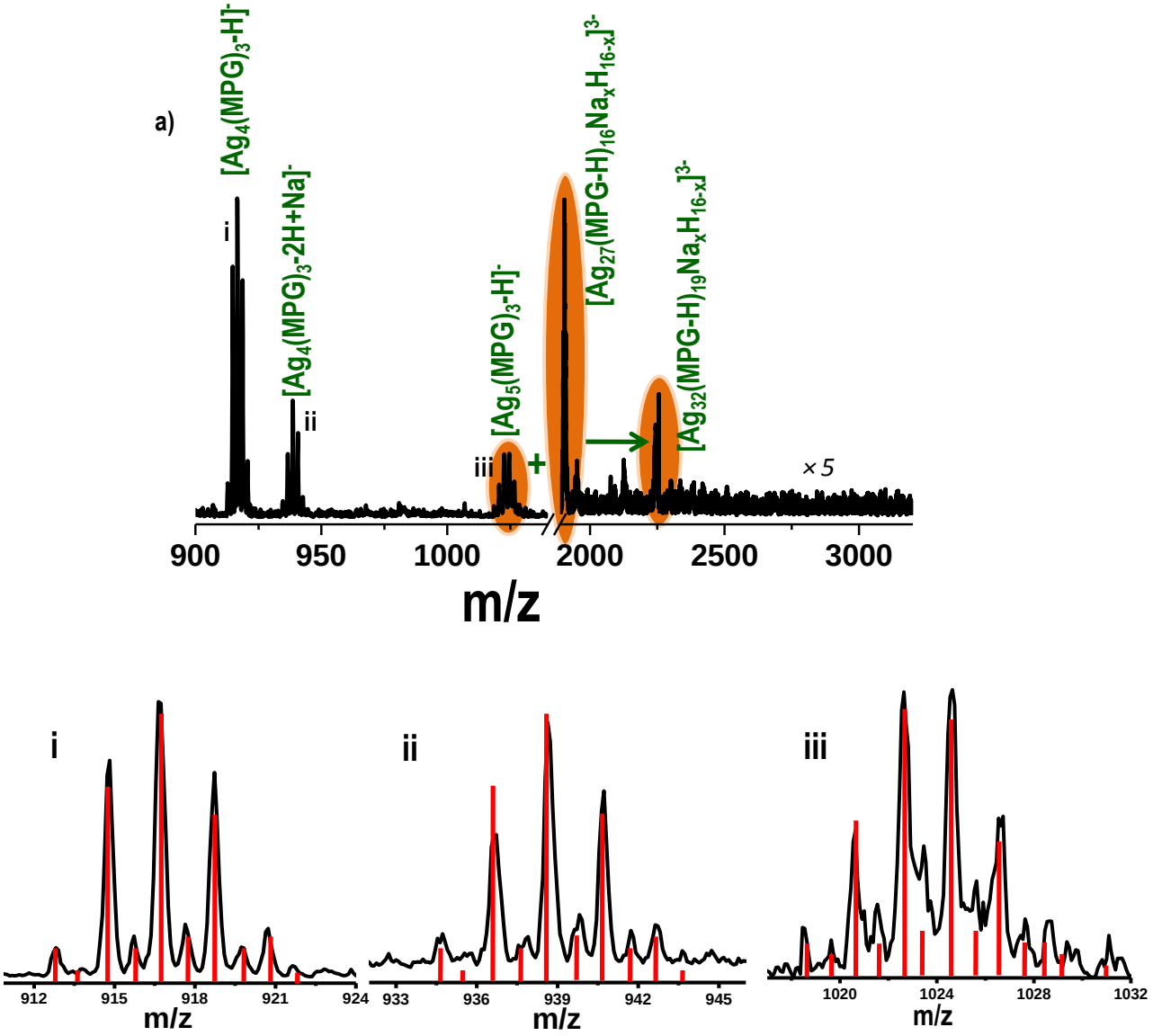

Figure S10. a) ESI MS of $Au_{32}MPG_{19}$, measured in the negative mode in the range of m/z 900-3200. All the peaks are marked with their respective ions. Sodium adduct of $Ag_{27}MPG_{16}$ is obtained due to the loss of Ag_5MPG_3 species (iii) from $[Ag_{32}(MPG\text{-}H)_{19}Na_xH_{16-x}]^{3-}$. Mass spectrum in the range m/z 1000-3200 is enhanced for 5 times in the vertical axis. Labels i, ii and iii are $[Ag_4MPG_3\text{-}H]^-$, $[Ag_4MPG_3\text{-}H+Na]^-$ and $[Ag_5MPG_3\text{-}H]^-$, respectively. Simulated spectra for i, ii and iii, depicted with lines match well with the experiment.

Electronic Supplementary Information 11

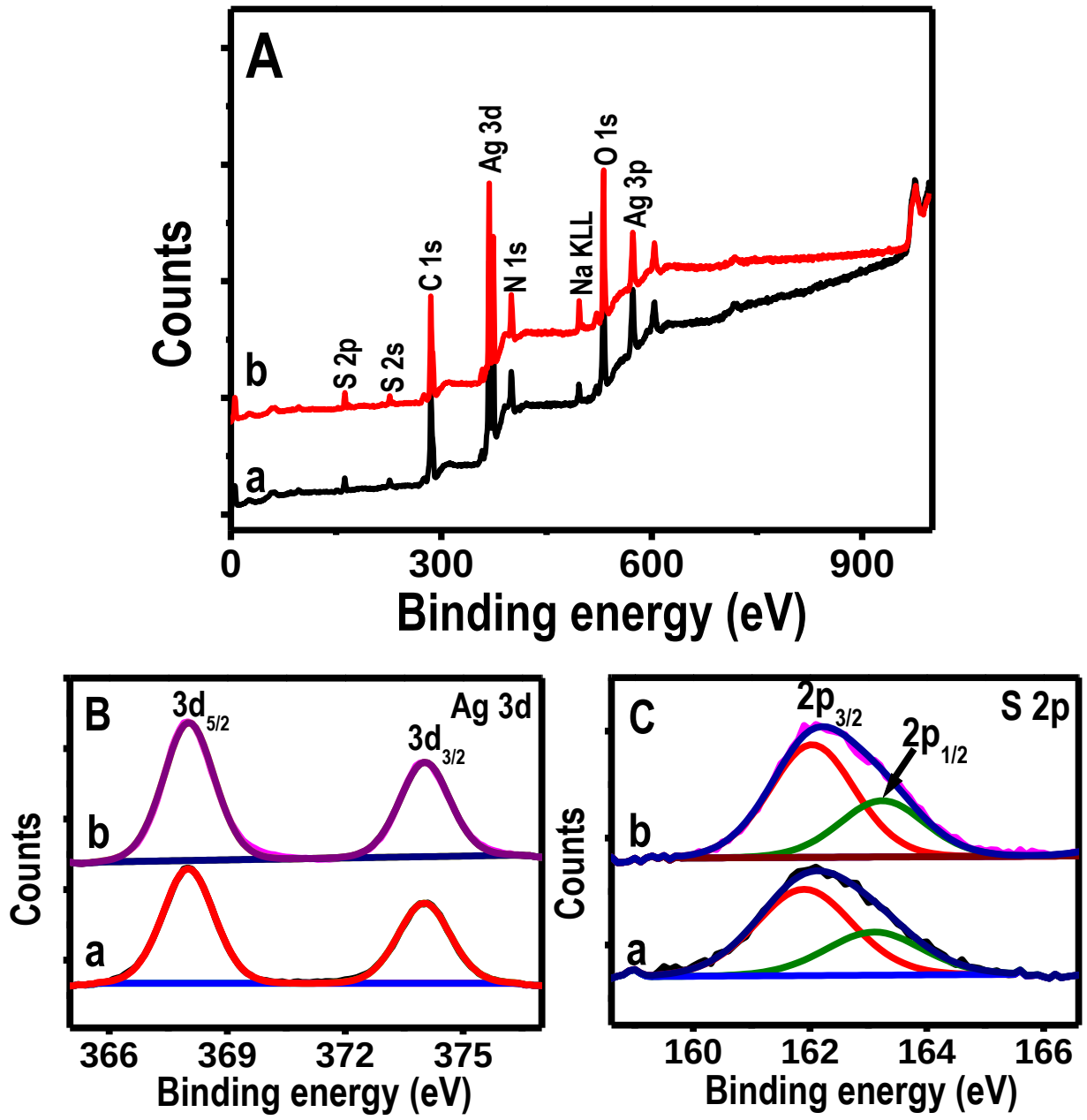

Figure S11. XPS survey spectra, Ag 3d and S 2p regions (A, B and C, respectively) of the crude and $Ag_{32}SG_{19}$ clusters (traces a and b, respectively). The Ag:S atomic ratio is 1:0.57±0.03 for $Ag_{32}SG_{19}$ which matches with the expected value 1:0.59.

Electronic Supplementary Information 12

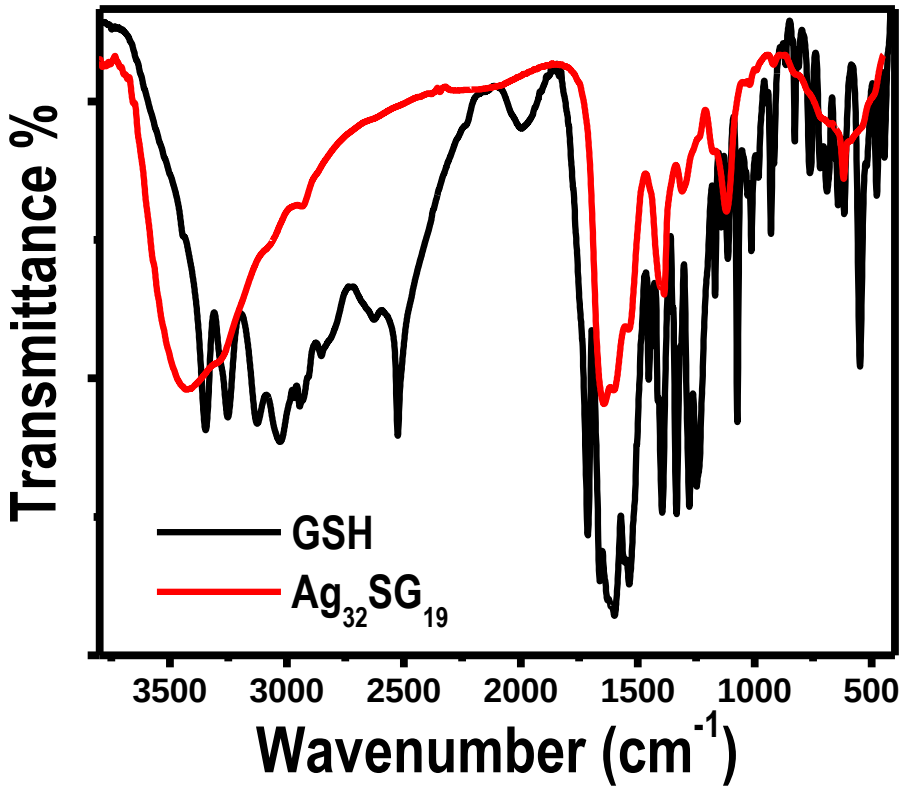

Figure S12. FTIR spectra of GSH and $Ag_{32}SG_{19}$. The S−H stretching feature at 2572 cm^{-1} in GSH is absent in cluster which is in agreement with the XPS data. GSH features in the region 2000-500 cm^{-1} confirm the presence of SG protection of the cluster.

Electronic Supplementary Information 13

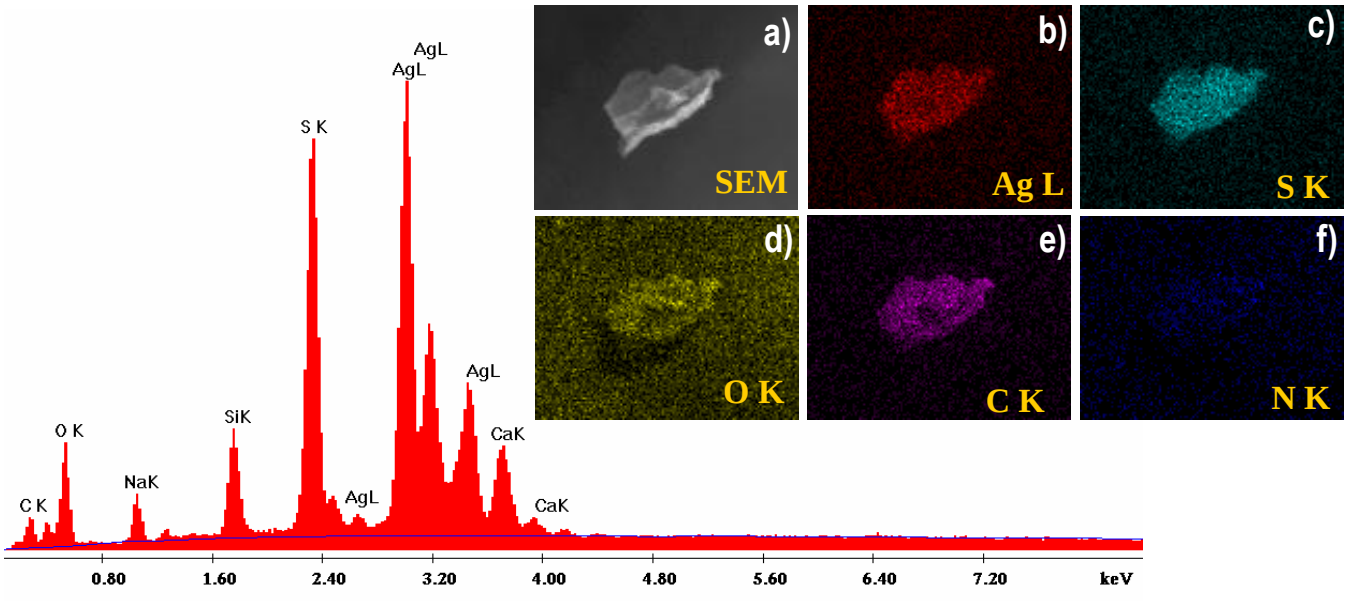

Figure S13. SEM-EDAX spectrum of $Ag_{32}SG_{19}$. (a) SEM image of the $Ag_{32}SG_{19}$ cluster aggregate from which the EDAX spectrum is taken. Elemental maps of (b) Ag L_α, (c) S K_α, (d) O K_α, (e) C K_α and (f) N K_α are shown. Si K_α is due to the substrate used. Ag:S atomic ratio measured is 1:0.56±0.03 which matches with the expected value of 1:0.59 for $Ag_{32}SG_{19}$.

Electronic Supplementary Information 14

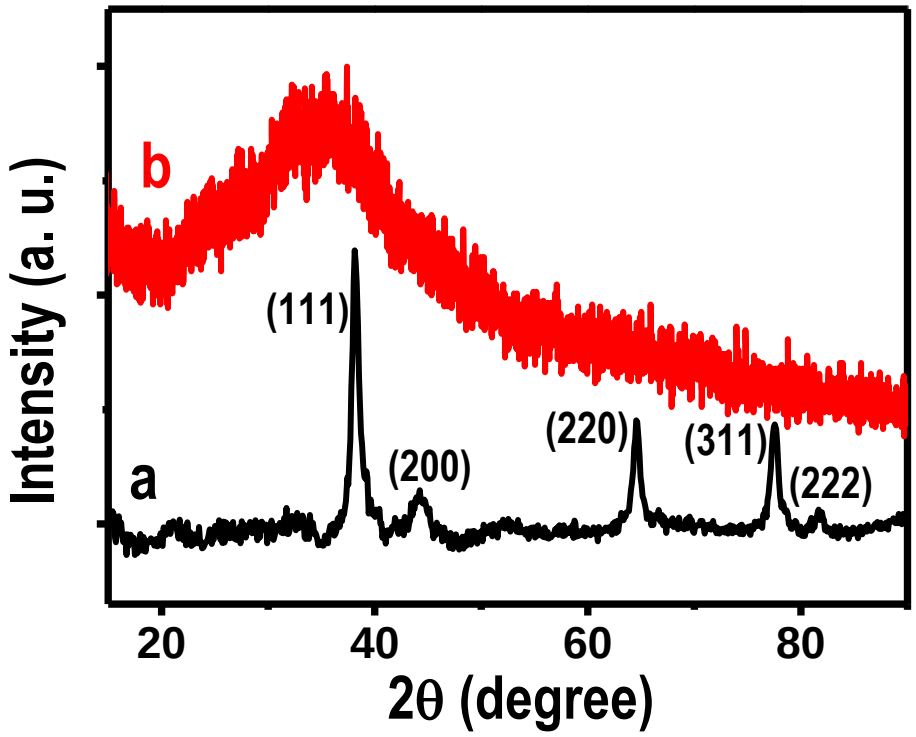

Figure S14. Comparison of the X-ray diffraction patterns of glutathione protected silver nanoparticles (Ag@SG NPs) and $Ag_{32}SG_{19}$ clusters (traces a and b, respectively). Nanoparticles show peaks corresponding to Ag planes (111), (200) (220), (311) and (222) whereas $Ag_{32}SG_{19}$ shows a broad peak around $2\theta \approx 38^{o}$.

Electronic Supplementary Information 15

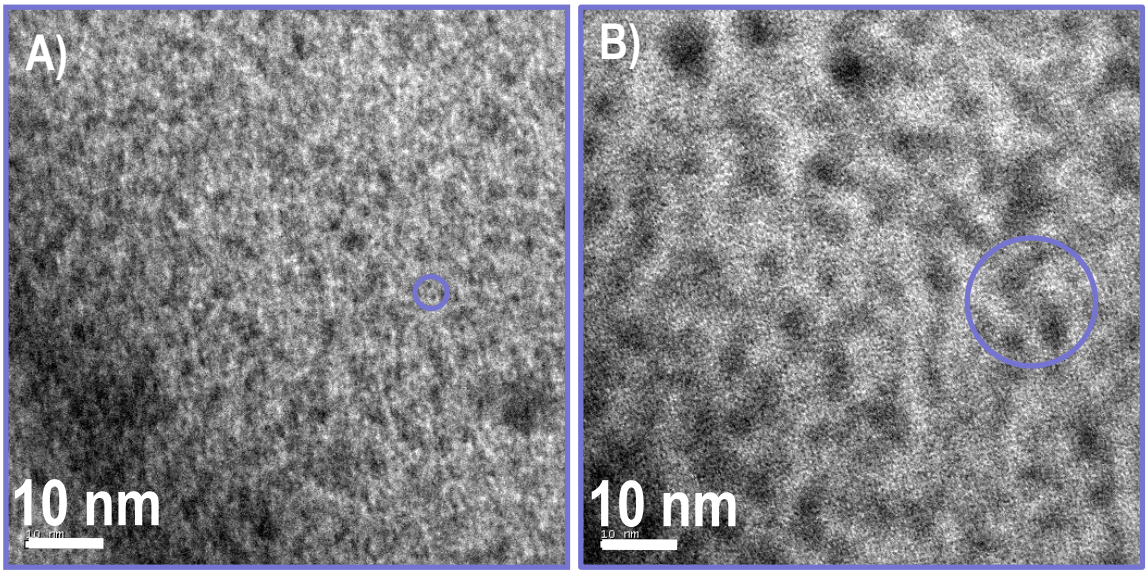

Figure S15. TEM images of the $Ag_{32}SG_{19}$ before (A) and after electron beam irradiation for 5 min (B). Both are from the same regions of the grid. QCs are strongly sensitive to electron beam exposure and they convert gradually to larger aggregates or nanoparticles during TEM examination.

References

(1) N. Cathcart and V. Kitaev, *J. Phys. Chem. C* 2010, **114**, 16010.
(2) S. Kumar, M. D. Bolan and T. P. Bigioni, *J. Am. Chem. Soc.* 2010, **132**, 13141.
(3) T. Udayabhaskararao, B. Nataraju and T. Pradeep, *J. Am. Chem. Soc.* 2010, **132**, 16304.

THE JOURNAL OF PHYSICAL CHEMISTRY Letters

Letter

pubs.acs.org/JPCL

Atomically Precise Silver Clusters as New SERS Substrates

Indranath Chakraborty,[†] Soumabha Bag,[†] Uzi Landman,[‡] and Thalappil Pradeep*[,†]

[†]DST Unit of Nanoscience (DST UNS) and Thematic Unit of Excellence (TUE), Department of Chemistry, Indian Institute of Technology Madras, Chennai 600 036, India

[‡]School of Physics, Georgia Institute of Technology, Atlanta, Georgia 30332, United States

Supporting Information

ABSTRACT: An atomically precise silver cluster, Ag_{152} protected with thiolate ligands, was used as a surface-enhanced Raman scattering (SERS) substrate. The cluster shows intense enhancement of Raman signals of crystal violet with an enhancement factor of 1.58×10^9. Adaptability of the substrate for a wide range of systems starting from dyes to biomolecules is demonstrated. Solid-state drop casting method was used here, and SERS signals were localized on the Ag_{152} crystallites, confirmed from Raman images. Excellent periodicity of clusters, their plasmonic nature, and absence of visible luminescence are the main reasons for this kind of large enhancement. SERS was compared with smaller clusters and larger nanoparticles, and the size regime of Ag_{152} was found to be optimum. Several control experiments were done to understand the SERS activity in detail. The method has wide adaptability as the cluster can be easily drop-casted on any surface like paper, cotton, and so forth to produce effective SERS media. The work suggests that atomically precise clusters, in general, can show SERS activity.

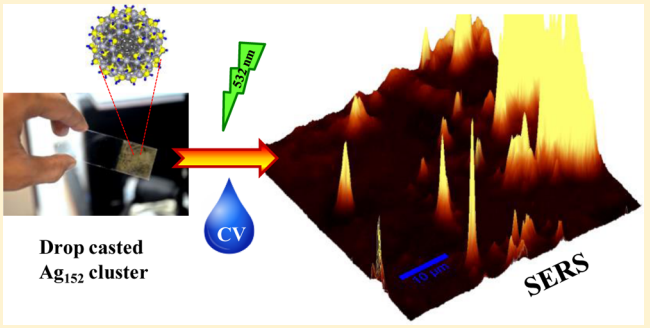

SECTION: Physical Processes in Nanomaterials and Nanostructures

Nanoscale atomic clusters of noble metals, especially gold and silver, are emerging materials with novel properties.[1] While much of the research effort in this area is focused on gold aggregates,[2−8] studies of silver clusters are relatively scarce, though several well-characterized systems have been explored rather recently.[9−13] Characteristic features in optical absorption and visible-to-near-infrared luminescence have made these molecular systems new probes for analytical methodologies using spectroscopy. As the nuclearity (number of atoms in the cluster) increases, light emission shifts to the red and near-infrared regions, and the absorption spectrum resembles that of nanoparticles (NPs), with characteristic plasmon absorption-like features. The emergence of plasmonic properties in atomically precise clusters has been demonstrated with Ag_{152}.[9] This size regime is one at which visible luminescence nearly disappears, and its absence may be advantageous for scattering-based spectroscopies. In the past several years, atomically precise clusters have been used for metal ion sensing,[14] biolabeling,[3,15] cancer targeting,[16] catalysis,[17] and many other applications.[18] The small size, reduced or absent cytotoxicity, diverse functionalization, and incorporation ability in various matrixes are among the specific advantages of such systems. The addition of other properties to the above list, in particular, surface-enhanced Raman scattering (SERS),[19−27] promises to increase efforts aimed at understanding and utilizing these new materials.

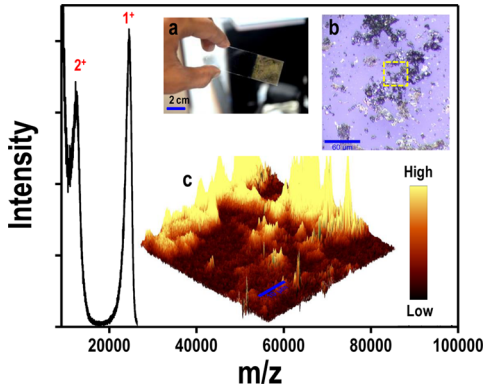

Figure 1. MALDI mass spectrum of a purified Ag_{152} cluster sample in toluene. A DCTB matrix was used. It gives a sharp molecular ion peak at m/z 24 610 ± 50 along with a prominent dication peak at m/z 12 300 ± 30. Inset (a) shows a photograph of a drop-casted film of a Ag_{152} cluster on a glass slide. Multiple drop-castings can be done to increase film thickness. Inset (b) shows the optical image of a drop-casted film with crystal violet (CV) as an analyte. The image shows microcrystallites of the cluster. A selected area of (b) was chosen for Raman imaging, and the corresponding 3D view (with Raman intensities in the narrow window) is given in inset (c).

Received: July 8, 2013
Accepted: July 30, 2013
Published: July 30, 2013

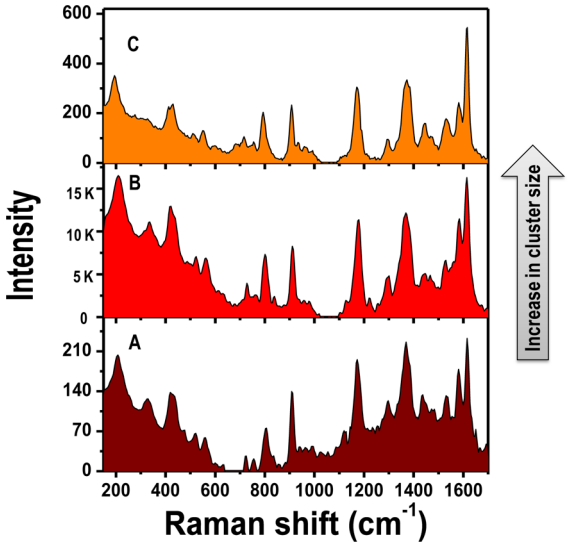

Figure 2. Comparative SERS spectra of CV on a drop-casted film of a Ag_{55} cluster (A), Ag_{152} cluster (B), and 3−4 nm Ag NP (C). Similar experimental conditions and the same laser intensities were used for all of the cases shown. A PET-protected Ag_{55} cluster and NPs were used here. The 50 μM CV was taken as the analyte. The spectra show unprecedented enhancement of the Ag_{152} cluster compared to the Ag_{55} and the silver NP (compare the *y* axes).

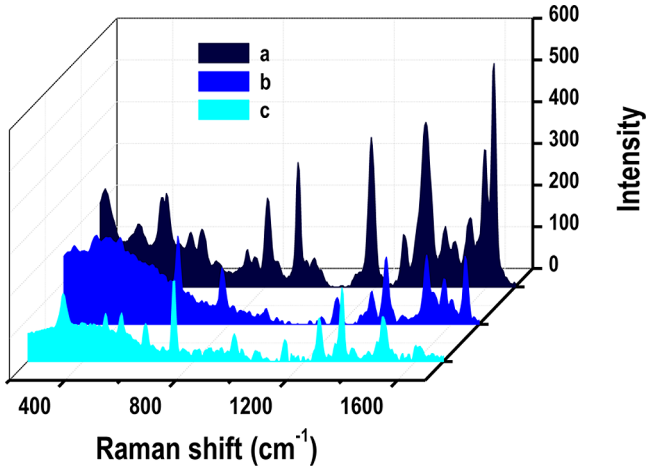

Figure 3. The adaptability with other analytes is shown here; a, b, and c show the SERS spectra of CV, rhodamine 6G (R6G), and adenine, respectively. Characteristic Raman features of each of the analytes are present. The 10^{-7} M CV and R6G and 10^{-6} M adenine were used for the experiments. Instrumental parameters were kept constant.

In this Letter, we show the occurrence of intense SERS in a Ag_{152} cluster. This is the first report of the observation of SERS in monolayer protected silver clusters, and therefore, it extends the scope of applications of atomically precise clusters. The results presented here using several analytes confirm the adaptability of the substrate for diverse systems. Besides solid-state measurements, we demonstrated the use of this material for solution-phase studies as well. The enhancement in the solid state is attributed to the creation of hot spots at specific regions spread over the crystallites. The observation of an enhancement factor (EF) on the order of 1.5×10^9 for Ag_{152} suggests a significant cost savings associated with the use of these materials in comparison to typical silver NP systems composed of ∼10 000 atoms. The results of our study can be understood on the basis of reports where molecular systems have been predicted to exhibit pronounced Raman enhancement.[28]

As the characterization and properties of the Ag_{152} cluster have been reported previously,[9] we present here only the most essential features that are of relevance to this study. The cluster shows a well-defined MALDI mass spectrum (Figure 1A) at *m*/*z* 24 610 with a prominent dication feature at *m*/*z* 12 300 with *trans*-2-[3-(4-*tert*-butylphenyl)-2-methyl-2-propenylidene] malononitrile (DCTB) as the matrix.[10,29] The cluster exhibits faceted crystallites in SEM images (Figure S1, Supporting Information), which also show the expected elements and the intensities (data not shown) in energy-dispersive analysis of X-rays (EDAX). Transmission electron microscopic (TEM) images confirm the high uniformity of the cluster size and shape (Figure S1, Supporting Information) and also suggest excellent periodicity, which might be a reason for generating hot spots on crystallite surfaces for the observed SERS activity.

An optical image of a portion of a drop-casted film is displayed in Figure 1b, showing the microcrystalline nature of the cluster. The Raman spectrum of crystal violet (CV) on a drop-casted film of Ag_{152} is shown in Figure S2a (Supporting Information). The spectrum shows all of the features of bulk CV, and comparison of both is given in Figure S2 (Supporting Information). The observed enhancement factor[30,31] (EF = 1.58×10^9, details are in Supporting Information Table 1) is unprecedented, and it is almost 3−4 orders of magnitude greater than the corresponding silver NP system reported in the literature.[32] The SERS is localized on the crystallites of Ag_{152}, as confirmed from the Raman image shown in Figure 1c. The Raman image was collected based on the intensities in the 1605−1646 cm^{-1} window. An image collected for a wider window (150−1700 cm^{-1}, in which CV has its characteristic signals) also shows (Figure S3, Supporting Information) a similar pattern. The direct correlation between the Raman image and the optical image confirms (Figure S4A and B, Supporting Information) the existence of active sites on the crystallites. The corresponding spectra from dark green and light yellow regions (Figure S4C and D, Supporting Information) reflect the presence and absence of CV characteristics, respectively, which proves that SERS sites are the microcrystals of Ag_{152}.

The SERS EF of the Ag_{152} clusters is compared in Figure 2 with that of the corresponding silver NP system with PET (phenylethanethiol, in the thiolate form) protection. A film of PET-protected plasmonic NPs of 3−4 nm diameter, prepared through the use of a similar procedure to that used for the Ag_{152} cluster, exhibits an EF of 7.5×10^5. Additionally, we find that a similarly prepared Ag_{55} cluster system, also protected with PET, shows a reduced EF of 2.7×10^5. The unusually large SERS enhancement of the Ag_{152} clusters compared to larger NPs and smaller clusters may originate from the periodic arrangement of the nanocrystallites, which brings about the formation of hot spots between the clusters. The absence of emission in the visible region assists the acquisition of the Raman spectrum, which may be an issue for smaller and inherently luminescent clusters.[10,12,33] Another source for the high SERS enhancement of the Ag_{152} clusters is their optical absorption spectrum, which is comparable to the plasmon resonance of the silver NPs, and it overlaps with the excitation line. From the foregoing, we would like to emphasize that the observed EFs are not of the isolated clusters but of their solid-state analogues, which correspond to aggregated structures. However, the nature of

dx.doi.org/10.1021/jz4014097 | J. Phys. Chem. Lett. 2013, 4, 2769−2773

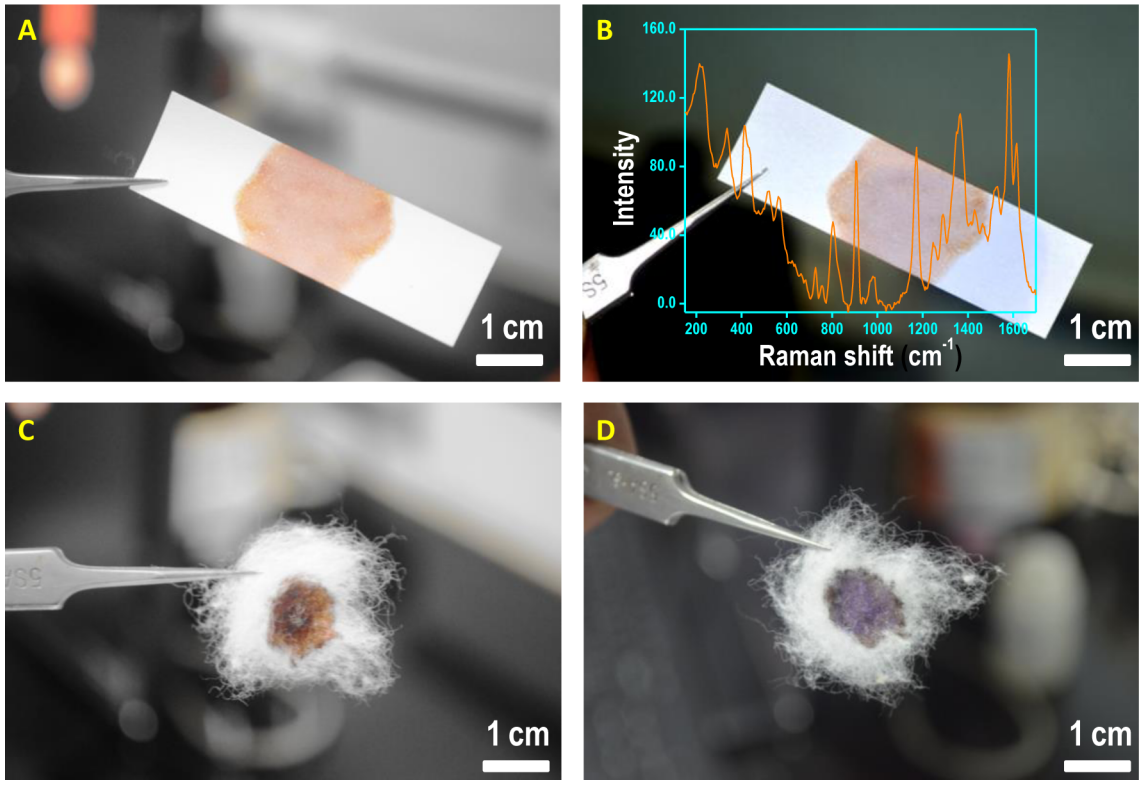

Figure 4. Photographs of Ag_{152} clusters coated on paper (A,B) and cotton (C,D) before (A,C) and after (B,D) CV was drop-casted. The inset of (B) shows the Raman spectrum of CV taken from the cluster-coated paper substrate.

the intercluster regions responsible for enhancement cannot be evaluated from the current experiments as they are under subdiffraction limits and are not probed here.

Several control experiments were done to understand how the nature of the films affects the SERS property of the clusters. A decrease in the concentration of the Ag_{152} clusters by dilution of the solution used for drop-casting (Figure S5, Supporting Information) or an increase in the concentration by performing multiple coatings (Figure S6, Supporting Information) decreases the SERS intensity. Variations in the coverage or concentration suggests that a specific morphology and number of particles are important, which is in accordance with previous observations.[28] Besides the solid-state drop-casting method, we have also studied SERS in the solution phase (data not shown), where the EF (9.5×10^8) is somewhat lower. The concentration dependence of the analyte (Figure S7, Supporting Information) shows the lower detection limit of CV to be 10^{-9} M. The corresponding spectrum has been expanded 10 times to allow clear inspection of the features. The intensity of the 1379 cm^{-1} peak is plotted against the concentration, which shows the limit of detection. As clusters are susceptible to electron- and laser-induced damage, we characterized the film before and after SERS measurements. Although UV/vis does not show any (Figure S8, Supporting Information) significant change, we could see visible damage of the film morphology after each experiment (data not shown). Along with PET-protected silver NPs, the SERS of Ag_{152} clusters was compared also with that of citrate-capped NPs. In the latter case, an expected enhancement (EF = 1.98×10^6), as reported in the literature,[32] was seen. The TEM image and corresponding UV/vis spectra for the citrate- and PET-capped NPs are given in Figure S9 (Supporting Information).

Another advantage of cluster-based materials is that they are soluble in diverse media, and as a result, effective substrates can be prepared easily. The cluster can be coated on paper (Figure 4A), cotton (Figure 4C), silk, as well as other materials, and such active substrates can be dipped in analyte solutions, and SERS measurements can be made. The clusters get coated uniformly over the substrates, and the amount of silver loaded to get complete coverage is much smaller in comparison to that for plasmonic NPs, which contributes to the reduced cost of such subtrates. Luminescence from paper and cotton, which contain cellulose and other organic matter, can pose difficulties for SERS detection. Consequently, glass was chosen as a better substrate. It is important to note that clusters can be used to create patterns, as described in our previous study, on gold clusters,[34] and such patterned surfaces will be useful for diagnostics.

To check whether the SERS is restricted to CV, other analytes were tried. Rhodamine 6G (R6G), which is another often-used analyte for SERS experiments, shows a SERS signal even at 10^{-7} M concentration (Figure 3b). Similar enhancement was found for the biomolecule, adenine (Figure 3c). The corresponding EFs are 1.08×10^8 and 1.30×10^8 for R6G and adenine, respectively. The most intense bands in these cases and their intensities are given in Table 2 (Supporting Information). The Raman spectra consist of all of the characteristic features of R6G and adenine, as reported in the literature.[35,36] These results suggests that the Ag_{152} cluster system can be employed as a universal SERS substrate.

It may be noted that the resonance Raman (RR)[37−39] effect, strongly sensitive to the excitation energy,[40] cannot be avoided for the case of CV as the excitation wavelength is 532 nm. Even for R6G, it can interfere,[39] but adenine, which does not show a RR effect[41−44] for this excitation, also shows similar enhance-

dx.doi.org/10.1021/jz4014097 | J. Phys. Chem. Lett. 2013, 4, 2769−2773

ment, suggesting that the enhancement here is principally due to SERS. To further prove the point, additional measurements were carried out at 633 nm excitation. For R6G, CV, and adenine (all measured at 5 μM concentration, drop-casted), a glass substrate gave spectra comparable to those reported here with EFs of 1.1×10^8, 1.6×10^9, and 1.4×10^8, respectively. Comparative spectra due to 532 and 633 nm excitations are given in Figure S10A (Supporting Information). Hence, the enhancement here is largely due to SERS.

In summary, the results presented in this Letter show that atomically precise clusters are new candidates for SERS measurements. Their plasmon-like optical feature, crystalline nature (of the individual nanoclusters and their assembly), and the absence of visible luminescence are among the main reasons for this enhancement. Unprecedented EFs, broad applicability to a number of analytes, and adaptability to various substrates, including glass, paper, and cotton, suggest the possibility for surface functionalization, which makes this system highly useful along with the large reduction in cost in comparison to plasmonic nanosystems.

EXPERIMENTAL METHODS

Details of the chemicals used are given in the Supporting Information. $Ag_{152}(PET)_{60}$ [PET: phenylethanethiol, in the thiolate form] was synthesized by a solid-state method.[11] Briefly, the method involves grinding of $AgNO_3$ with PET in a molar ratio of 1:5.3 to form silver thiolate. Subsequent addition of 0.675 mmol of $NaBH_4$ in the solid state and continuous grinding created the cluster, which was initially extracted in ethanol to remove the unreacted thiol by centrifugation followed by re-extraction of the residue with toluene (additional details are given in the Supporting Information). Ag_{55} clusters and Ag NPs protected with PET were also prepared. The clusters were characterized by a number of analytical methods (details are in the Supporting Information).

This cluster solution was drop-casted on glass coverslips to create SERS-active substrates. Analyte solutions were drop-casted on them and were left to dry in ambient laboratory conditions. Raman investigations were done with 532 and 633 nm excitation using a WITec confocal Raman microscope (details are given in the Supporting Information). All of the spectra were collected after background correction to exclude fluorescence interference.[40] For comparison, data without background correction is given in Figure S10B (Supporting Information) (for 532 nm excitation).

ASSOCIATED CONTENT

Supporting Information

Details of experimental procedures, EF calculation and characterization of Ag_{152} clusters and other materials, one-to-one correlation of the Raman image with the optical image, control experiments with variation in concentrations and coatings, comparison with data from nanoparticles, images from different substrates, SERS spectra at two excitations, and data without background correction. This material is available free of charge via the Internet at http://pubs.acs.org.

AUTHOR INFORMATION

Corresponding Author

*E-mail: pradeep@iitm.ac.in. Fax: + 91-44 2257-0545.

Notes

The authors declare no competing financial interest.

ACKNOWLEDGMENTS

We thank the Department of Science and Technology, Government of India for constantly supporting our research program on nanomaterials. I.C. thanks IITM and S.B. thanks CSIR, Govt. of India for research fellowships. Work by U.L. was supported by the U.S. Air Force Office of Scientific Research and by the Office of Basic Energy Sciences of the U.S. D.O.E. under Contract No. FG05-86ER45234.

REFERENCES

(1) Jin, R. Quantum Sized, Thiolate-Protected Gold Nanoclusters. *Nanoscale* **2010**, *2*, 343−362.

(2) Jadzinsky, P. D.; Calero, G.; Ackerson, C. J.; Bushnell, D. A.; Kornberg, R. D. Structure of a Thiol Monolayer-Protected Gold Nanoparticle at 1.1 Å Resolution. *Science* **2007**, *318*, 430−433.

(3) Muhammed, M. A. H.; Verma, P. K.; Pal, S. K.; Kumar, R. C. A.; Paul, S.; Omkumar, R. V.; Pradeep, T. Bright, NIR-Emitting Au_{23} from Au_{25}: Characterization and Applications Including Biolabeling. *Chem.—Eur. J.* **2009**, *15*, 10110−10120.

(4) Negishi, Y.; Nobusada, K.; Tsukuda, T. Glutathione-Protected Gold Clusters Revisited: Bridging the Gap between Gold(I)Thiolate Complexes and Thiolate-Protected Gold Nanocrystals. *J. Am. Chem. Soc.* **2005**, *127*, 5261−5270.

(5) Pei, Y.; Gao, Y.; Zeng, X. C. Structural Prediction of Thiolate-Protected Au_{38}: A Face-Fused Bi-Icosahedral Au Core. *J. Am. Chem. Soc.* **2008**, *130*, 7830−7832.

(6) Shibu, E. S.; Pradeep, T. Quantum Clusters in Cavities: Trapped Au_{15} in Cyclodextrins. *Chem. Mater.* **2011**, *23*, 989−999.

(7) Zeng, C.; Qian, H.; Li, T.; Li, G.; Rosi, N. L.; Yoon, B.; Barnett, R. N.; Whetten, R. L.; Landman, U.; Jin, R. Total Structure and Electronic Properties of the Gold Nanocrystal $Au_{36}(SR)_{24}$. *Angew. Chem., Int. Ed.* **2012**, *51*, 13114−13118.

(8) Zhu, M.; Aikens, C. M.; Hollander, F. J.; Schatz, G. C.; Jin, R. Correlating the Crystal Structure of A Thiol-Protected Au_{25} Cluster and Optical Properties. *J. Am. Chem. Soc.* **2008**, *130*, 5883−5885.

(9) Chakraborty, I.; Govindarajan, A.; Erusappan, J.; Ghosh, A.; Pradeep, T.; Yoon, B.; Whetten, R. L.; Landman, U. The Superstable 25 kDa Monolayer Protected Silver Nanoparticle: Measurements and Interpretation as an Icosahedral $Ag_{152}(SCH_2CH_2Ph)_{60}$ Cluster. *Nano Lett.* **2012**, *12*, 5861−5866.

(10) Chakraborty, I.; Udayabhaskararao, T.; Pradeep, T. High Temperature Nucleation and Growth of Glutathione Protected ~Ag_{75} Clusters. *Chem. Commun.* **2012**, *48*, 6788−6790.

(11) Rao, T. U. B.; Nataraju, B.; Pradeep, T. Ag_9 Quantum Cluster through a Solid-State Route. *J. Am. Chem. Soc.* **2010**, *132*, 16304−16307.

(12) Rao, T. U. B.; Pradeep, T. Luminescent Ag_7 and Ag_8 Clusters by Interfacial Synthesis. *Angew. Chem., Int. Ed.* **2010**, *49*, 3925−3929.

(13) Yang, H.; Lei, J.; Wu, B.; Wang, Y.; Zhou, M.; Xia, A.; Zheng, L.; Zheng, N. Crystal Structure of a Luminescent Thiolated Ag Nanocluster with an Octahedral Ag_6^{4+} Core. *Chem. Commun.* **2012**, *49*, 300−302.

(14) Chakraborty, I.; Udayabhaskararao, T.; Pradeep, T. Luminescent Sub-nanometer Clusters for Metal Ion Sensing: A New Direction in Nanosensors. *J. Hazard. Mater.* **2012**, *211*−*212*, 396−403.

(15) Lin, C.-A. J.; Yang, T.-Y.; Lee, C.-H.; Huang, S. H.; Sperling, R. A.; Zanella, M.; Li, J. K.; Shen, J.-L.; Wang, H.-H.; Yeh, H.-I.; Parak, W. J.; Chang, W. H. Synthesis, Characterization, and Bioconjugation of Fluorescent Gold Nanoclusters toward Biological Labeling Applications. *ACS Nano* **2009**, *3*, 395−401.

(16) Kong, Y.; Chen, J.; Gao, F.; Brydson, R.; Johnson, B.; Heath, G.; Zhang, Y.; Wu, L.; Zhou, D. Near-Infrared Fluorescent Ribonuclease-A-Encapsulated Gold Nanoclusters: Preparation, Characterization, Cancer Targeting and Imaging. *Nanoscale* **2013**, *5*, 1009−1017.

(17) Nie, X.; Qian, H.; Ge, Q.; Xu, H.; Jin, R. CO Oxidation Catalyzed by Oxide-Supported $Au_{25}(SR)_{18}$ Nanoclusters and Identification of Perimeter Sites as Active Centers. *ACS Nano* **2012**, *6*, 6014−6022.

(18) Schmid, G.; Baumle, M.; Geerkens, M.; Heim, I.; Osemann, C.; Sawitowski, T. Current and Future Applications of Nanoclusters. *Chem. Soc. Rev.* **1999**, *28*, 179−185.
(19) Anema, J. R.; Li, J.-F.; Yang, Z.-L.; Ren, B.; Tian, Z.-Q. Shell-Isolated Nanoparticle-Enhanced Raman Spectroscopy: Expanding the Versatility of Surface-Enhanced Raman Scattering. *Annu. Rev. Anal. Chem.* **2011**, *4*, 129−150.
(20) Fan, M.; Andrade, G. F. S.; Brolo, A. G. A Review on the Fabrication of Substrates for Surface Enhanced Raman Spectroscopy and Their Applications in Analytical Chemistry. *Anal. Chim. Acta* **2011**, *693*, 7−25.
(21) Kim, K.; Shin, K. S. Surface-Enhanced Raman Scattering: A Powerful Tool for Chemical Identification. *Anal. Sci.* **2011**, *27*, 775−783.
(22) McNay, G.; Eustace, D.; Smith, W. E.; Faulds, K.; Graham, D. Surface-Enhanced Raman Scattering (SERS) and Surface-Enhanced Resonance Raman Scattering (SERRS): A Review of Applications. *Appl. Spectrosc.* **2011**, *65*, 825−837.
(23) Stiles, P. L.; Dieringer, J. A.; Shah, N. C.; Van Duyne, R. P. Surface-Enhanced Raman Spectroscopy. *Annu. Rev. Anal. Chem.* **2008**, *1*, 601−626.
(24) Wang, Y.; Yan, B.; Chen, L. SERS Tags: Novel Optical Nanoprobes for Bioanalysis. *Chem. Rev.* **2013**, *113*, 1391−1428.
(25) Sonntag, M. D.; Klingsporn, J. M.; Garibay, L. K.; Roberts, J. M.; Dieringer, J. A.; Seideman, T.; Scheidt, K. A.; Jensen, L.; Schatz, G. C.; Van Duyne, R. P. Single-Molecule Tip-Enhanced Raman Spectroscopy. *J. Phys. Chem. C* **2011**, *116*, 478−483.
(26) Moore, J. E.; Morton, S. M.; Jensen, L. Importance of Correctly Describing Charge-Transfer Excitations for Understanding the Chemical Effect in SERS. *J. Phys. Chem. Lett.* **2012**, *3*, 2470−2475.
(27) He, J.; Lin, X.-M.; Divan, R.; Jaeger, H. M. In-Situ Partial Sintering of Gold-Nanoparticle Sheets for SERS Applications. *Small* **2011**, *7*, 3487−3492.
(28) Mullin, J.; Schatz, G. C. Combined Linear Response Quantum Mechanics and Classical Electrodynamics (QM/ED) Method for the Calculation of Surface-Enhanced Raman Spectra. *J. Phys. Chem. A* **2012**, *116*, 1931−1938.
(29) Dass, A. Mass Spectrometric Identification of $Au_{68}(SR)_{34}$ Molecular Gold Nanoclusters with 34-Electron Shell Closing. *J. Am. Chem. Soc.* **2009**, *131*, 11666−11667.
(30) Kumar, G. V. P.; Shruthi, S.; Vibha, B.; Reddy, B. A. A.; Kundu, T. K.; Narayana, C. Hot Spots in Ag Core−Au Shell Nanoparticles Potent for Surface-Enhanced Raman Scattering Studies of Biomolecules. *J. Phys. Chem. C* **2007**, *111*, 4388−4392.
(31) Shibu, E. S.; Kimura, K.; Pradeep, T. Gold Nanoparticle Superlattices: Novel Surface Enhanced Raman Scattering Active Substrates. *Chem. Mater.* **2009**, *21*, 3773−3781.
(32) Stamplecoskie, K. G.; Scaiano, J. C.; Tiwari, V. S.; Anis, H. Optimal Size of Silver Nanoparticles for Surface-Enhanced Raman Spectroscopy. *J. Phys. Chem. C* **2011**, *115*, 1403−1409.
(33) Diez, I.; Kanyuk, M. I.; Demchenko, A. P.; Walther, A.; Jiang, H.; Ikkala, O.; Ras, R. H. A. Blue, Green and Red Emissive Silver Nanoclusters Formed in Organic Solvents. *Nanoscale* **2012**, *4*, 4434−4437.
(34) Shibu, E. S.; Radha, B.; Verma, P. K.; Bhyrappa, P.; Kulkarni, G. U.; Pal, S. K.; Pradeep, T. Functionalized Au_{22} Clusters: Synthesis, Characterization, and Patterning. *ACS Appl. Mater. Interfaces* **2009**, *1*, 2199−210.
(35) Dieringer, J. A.; Wustholz, K. L.; Masiello, D. J.; Camden, J. P.; Kleinman, S. L.; Schatz, G. C.; Van Duyne, R. P. Surface-Enhanced Raman Excitation Spectroscopy of a Single Rhodamine 6G Molecule. *J. Am. Chem. Soc.* **2008**, *131*, 849−854.
(36) Majoube, M. Vibrational Spectra of Adenine and Deuterium-Substituted Analogues. *J. Raman Spectrosc.* **1985**, *16*, 98−110.
(37) Johnson, B. B.; Peticolas, W. L. The Resonant Raman Effect. *Annu. Rev. Phys. Chem.* **1976**, *27*, 465−521.
(38) Kleinman, S. L.; Ringe, E.; Valley, N.; Wustholz, K. L.; Phillips, E.; Scheidt, K. A.; Schatz, G. C.; Van Duyne, R. P. Single-Molecule Surface-Enhanced Raman Spectroscopy of Crystal Violet Isotopologues: Theory and Experiment. *J. Am. Chem. Soc.* **2011**, *133*, 4115−4122.
(39) Kneipp, K.; Kneipp, H.; Itzkan, I.; Dasari, R. R.; Feld, M. S. Ultrasensitive Chemical Analysis by Raman Spectroscopy. *Chem. Rev.* **1999**, *99*, 2957−2976.
(40) Kim, H.; Kosuda, K. M.; Van Duyne, R. P.; Stair, P. C. Resonance Raman and Surface- And Tip-Enhanced Raman Spectroscopy Methods to Study Solid Catalysts and Heterogeneous Catalytic Reactions. *Chem. Soc. Rev.* **2010**, *39*, 4820−4844.
(41) Huang, R.; Zhao, L.-B.; Wu, D.-Y.; Tian, Z.-Q. Tautomerization, Solvent Effect and Binding Interaction on Vibrational Spectra of Adenine−Ag^+ Complexes on Silver Surfaces: A DFT Study. *J. Phys. Chem. C* **2011**, *115*, 13739−13750.
(42) Muniz-Miranda, M.; Gellini, C.; Pagliai, M.; Innocenti, M.; Salvi, P. R.; Schettino, V. SERS and Computational Studies on MicroRNA Chains Adsorbed on Silver Surfaces. *J. Phys. Chem. C* **2010**, *114*, 13730−13735.
(43) Papadopoulou, E.; Bell, S. E. J. Structure of Adenine on Metal Nanoparticles: pH Equilibria and Formation of Ag^+ Complexes Detected by Surface-Enhanced Raman Spectroscopy. *J. Phys. Chem. C* **2010**, *114*, 22644−22651.
(44) Papadopoulou, E.; Bell, S. E. J. Surface Enhanced Raman Evidence for Ag^+ Complexes of Adenine, Deoxyadenosine and 5′-dAMP Formed in Silver Colloids. *The Analyst* **2010**, *135*, 3034−3037.

Supporting information for the paper:

Atomically Precise Silver Clusters as New SERS Substrates

Indranath Chakraborty,[1] Soumabha Bag,[1] Uzi Landman[2] and Thalappil Pradeep[1*]

1DST Unit of Nanoscience (DST UNS), Department of Chemistry, Indian Institute of Technology Madras, Chennai 600 036, India; Fax: 91-44-2257 0545;

2School of Physics, Georgia Institute of Technology, Atlanta, GA 30332, USA

* E-mail: pradeep@iitm.ac.in

Materials and methods:

1. Chemicals

Silver nitrate ($AgNO_3$, 99% Aldrich), sodium borohydride (NaBH4, 99.9%, Aldrich); 2-phenylethanethiol (PETH, 98%, Aldrich); crystal violet, R6G (S. D. Fine Chem. Ltd, India), adenine (99%, Aldrich); ethanol (Changshu Yangyuan Chemical, China, AR grade), tetrahydrofuran (THF) (MERCK, HPLC grade) and toluene (Rankem, AR grade) were used in this synthesis. All the chemicals were commercially available and were used without further purification. Locally available cotton and paper were used as a substrate.

2. Synthesis of $Ag_{152}(SCH_2CH_2Ph)_{60}$

The synthesis of Ag_{152} cluster protected by PET (2-phenylethanethiol, in the thiolate form) involves the following steps. Initially, 23 mg of $AgNO_3$ and 100 µL of PET were ground well in a clean agate mortar using a pestle. The color of the mixture changes to pale orange showing the formation of silver thiolate. To this mixture, 25 mg of solid $NaBH_4$ were added and the content was mixed well. 3 mL of ethanol was added to the mixture and mixed well after which 2 mL of ethanol was added for the washing the mixture. The mixture was kept for 15-30 sec till there is a color change from pale orange to deep grey. The contents were then taken into a centrifuge tube and centrifuged at 1600 rpm. The centrifugate was removed and the residue was dissolved in 5 mL toluene/THF. The Ag_{152} clusters were obtained from the toluene extract, which was dark brown in color.

3. Synthesis of $Ag_{55}(SCH_2CH_2Ph)_{31}$

Similar to the above experiment only the silver and thiol ratio was taken as 1:4 and the cluster was again washed with heptanes after ethanol wash followed by the extraction in toluene.

4. Synthesis of Ag@PET nanoparticle

Similar to above experiment; here silver nitrate and thiol ratio is 1:1

5. Drop casting method

5 µL of cluster solution was taken and drop casted on a glass slide to make a thin film and kept under ambient condition for drying. The analyte solutions were then drop casted on the film of the cluster and dried. The dried films were inserted into Raman spectrometer for the SERS measurements. For solution phase experiments, the analyte (in methanol) was mixed with cluster solution and a drop of the mixture was examined by the microRaman set-up.

6. Instrumentation

UV-Vis spectra were measured with a PerkinElmer Lambda 25 instrument in the range of 200-1100 nm. High resolution transmission electron microscopy (TEM) of clusters was carried out with a JEOL 3010 instrument. The TEM samples were drop casted on carbon-coated copper grids and allowed to dry under ambient conditions. Matrix-assisted desorption ionization mass spectrometry (MALDI MS) studies were conducted using a Voyager-DE PRO Biospectrometry Workstation from Applied Biosystems. The matrix used was DCTB (at 1:100 ratio of sample to matrix). A pulsed nitrogen laser of 337 nm was used for the MALDI MS studies. Mass spectra were collected in positive ion mode and were averaged for 200 shots. Scanning electron microscopic (SEM) was performed with a FEI QUANTA-200 SEM. For measurements, samples were drop casted on an indium tin oxide (ITO) coated glass and dried in vacuum. Raman spectra and images were done with a WITec GmbH, Alpha-SNOM alpha300 S confocal Raman microscope having a 532 nm and 633 nm laser as the excitation source. Background correction was done with the help of the software equipped with the Raman instrument. Initially, the spectrum is fitted with a proper polynomial which was subtracted from the original spectrum.

7. EF calculation

The enhancement factor[1] (EF) was calculated using the standard formula

$$EF = I_{SERS} * C_{NR} / I_{NR} * C_{SERS}$$

where I_{SERS} and I_{NR} are the integral intensity obtained by SERS and normal Raman scattering measurements, respectively. C_{SERS} and C_{NR} are the concentration of molecules used for SERS and

normal Raman scattering measurements, respectively. Maximum intense peak was considered for EF calculation.

Table 1. EF calculation

Substrate	**Molecule**	**C_{SERS}**	**I_{SERS}**	**C_{NR}/I_{NR}**	**EF**
Ag_{55} cluster	CV	5×10^{-5} M	210	6.6×10^{-2}	2.70×10^{5}
Ag@PET NP	CV	5×10^{-5} M	570	6.6×10^{-2}	7.52×10^{5}
Ag@Citrate	CV	5×10^{-5} M	1500	6.6×10^{-2}	1.98×10^{6}
Ag_{152} cluster	CV	5×10^{-9} M	120	6.6×10^{-2}	1.58×10^{9}
	R6G	1×10^{-7} M	180	6.0×10^{-2}	1.08×10^{8}
	Adenine	1×10^{-6} M	200	6.5×10^{-1}	1.30×10^{8}

Another way[2] of EF calculation is

$$EF = (I_{SERS}/I_{norm})(N_{bulk}/N_{surf})$$

Where I_{SERS}, I_{norm}, N_{bulk}, and $N_{surface}$ are the measured SERS intensities for a monolayer of probe molecules (CV) on the Ag_{152} film, the measured intensity of non-enhanced or normal Raman scattering from a bulk sample, the number of the probe molecules under laser illumination for the bulk sample, and the number of the probe molecules on Ag_{152} cluster, respectively. N_{bulk} and N_{surf} values were calculated on the basis of the estimated density of the surface species or bulk sample and the corresponding sampling areas. N_{bulk} and N_{surf} can be calculated form the following equation,

$$N_{surf} = 4\pi r^2 CAN$$

$$N_{bulk} = Ah\rho/M$$

where r (1 nm), C ($10^6/\mu M^3$), A (3.14 x $1\mu M^2$), and N (4250/ μM^2) are the average radius of the particles in the Ag_{152} cluster, surface density of the CV monolayer, the area of the laser spot, and the surface coverage of the particles (particles/ μm^2) in the Ag_{152} cluster, respectively. Parameters A, h (10 μM), ρ (0.83 g/cm^3), and M (407.99 g) are the area of the laser spot, the penetration depth, the density of solid CV (~0.83 gcm^{-3}), and the molecular weight of CV, respectively. The EF is calculated to be 1.96×10^9 for Ag_{152} with CV as the analyte.

Table 2. Frequencies and intensities of the most intense bands of Figures 2 & 3.

Figure No.	**Substrate**	**Molecule**	**Frequency (cm^{-1})**	**I_{max}**
2	Ag_{55} cluster	CV	1614	210
	Ag_{152} cluster	CV	1614	16110
	AgNPs	CV	1614	570
3	Ag_{152} cluster	CV	1614	500
		R6G	1360	180
		Adenine	730	200

Supporting information 1

.

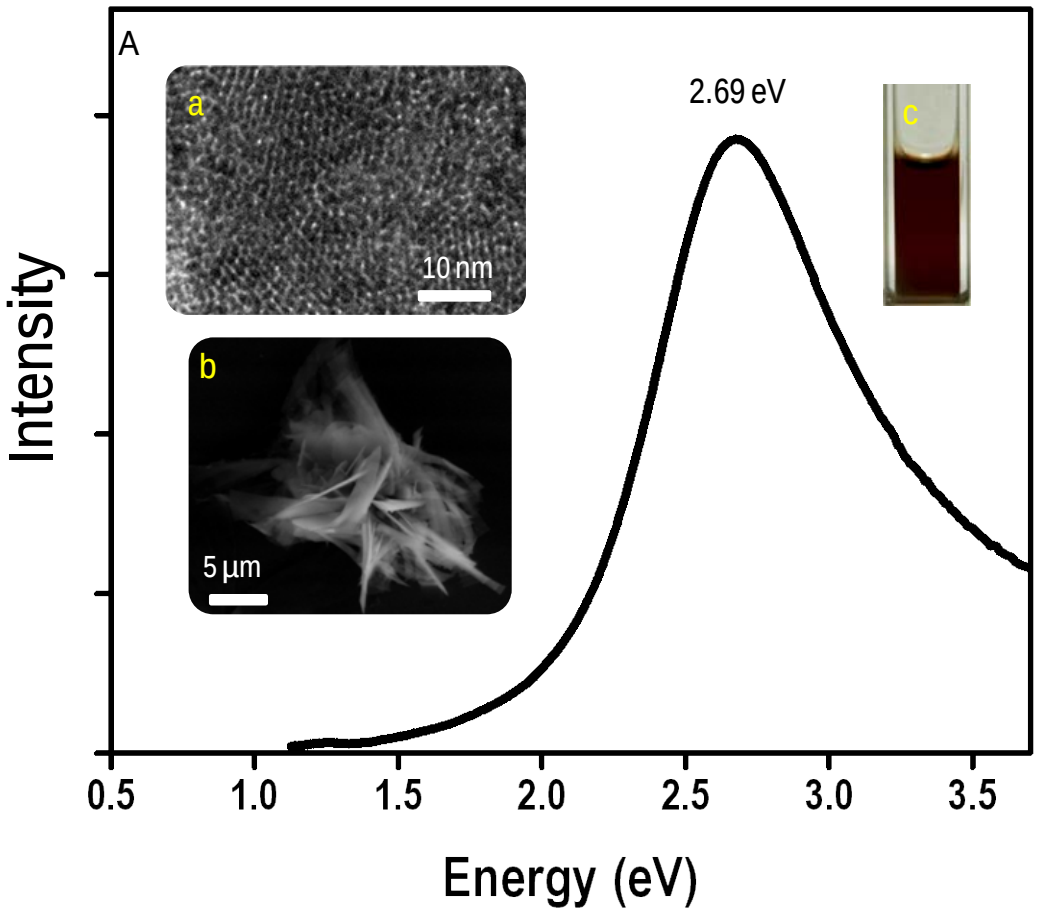

Figure S1. The optical absorption spectra of purified Ag_{152} clusters plotted in terms of energy (A), it shows the plasmonic band at 2.69 eV (460 nm). Inset: a) TEM image of the cluster which shows periodic arrangement of clusters and mono dispersity, b) SEM image of microcrystals of the cluster, and c) photograph of Ag_{152} cluster solution in toluene, taken in a cuvette.

Supporting information 2

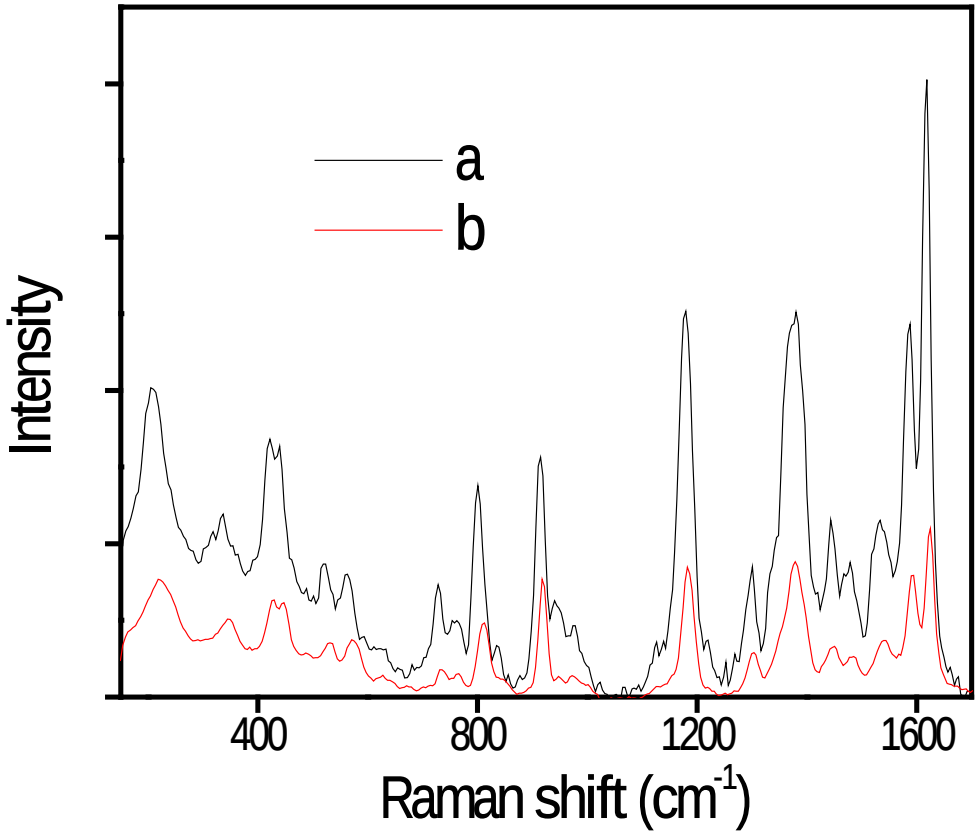

Figure S2. The SERS spectrum of CV (5 μM) taken from (a) drop casted film of Ag_{152} cluster and (b) Raman spectrum of bulk CV.

Supporting information 3

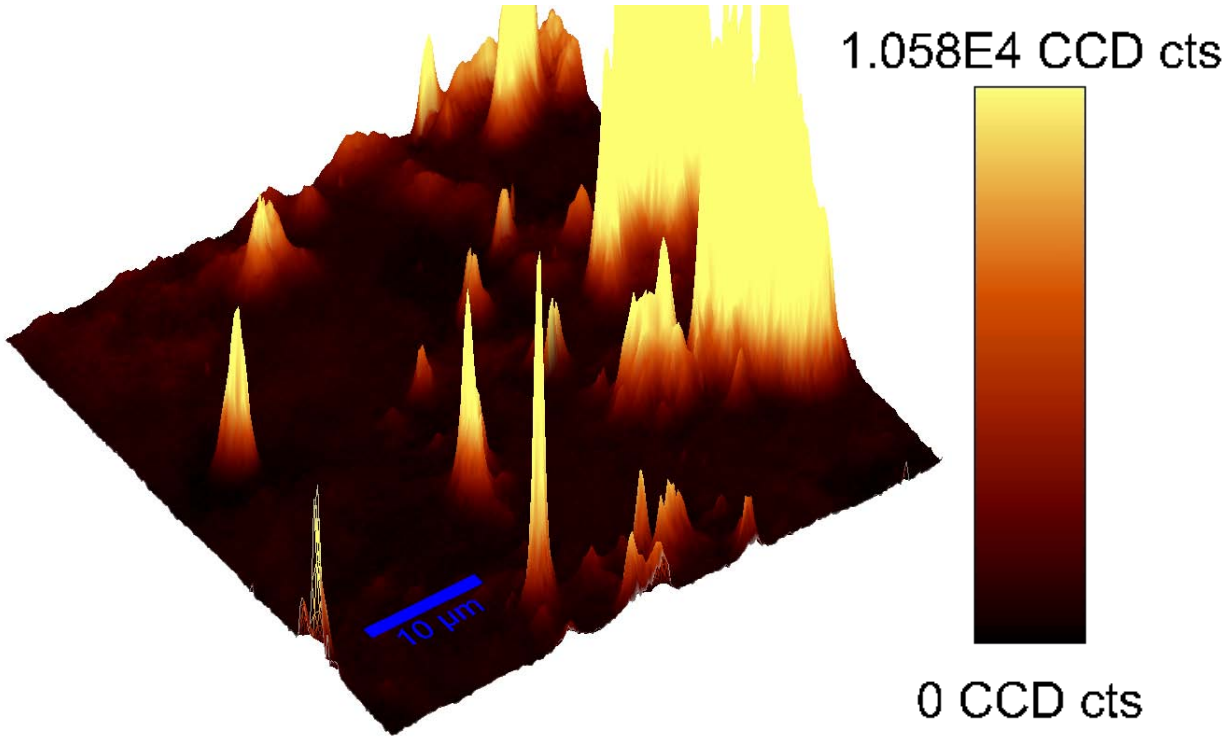

Figure S3. The Raman image of a selected area collected in a wider (150 cm^{-1} to 1700 cm^{-1}) window.

Supporting information 4

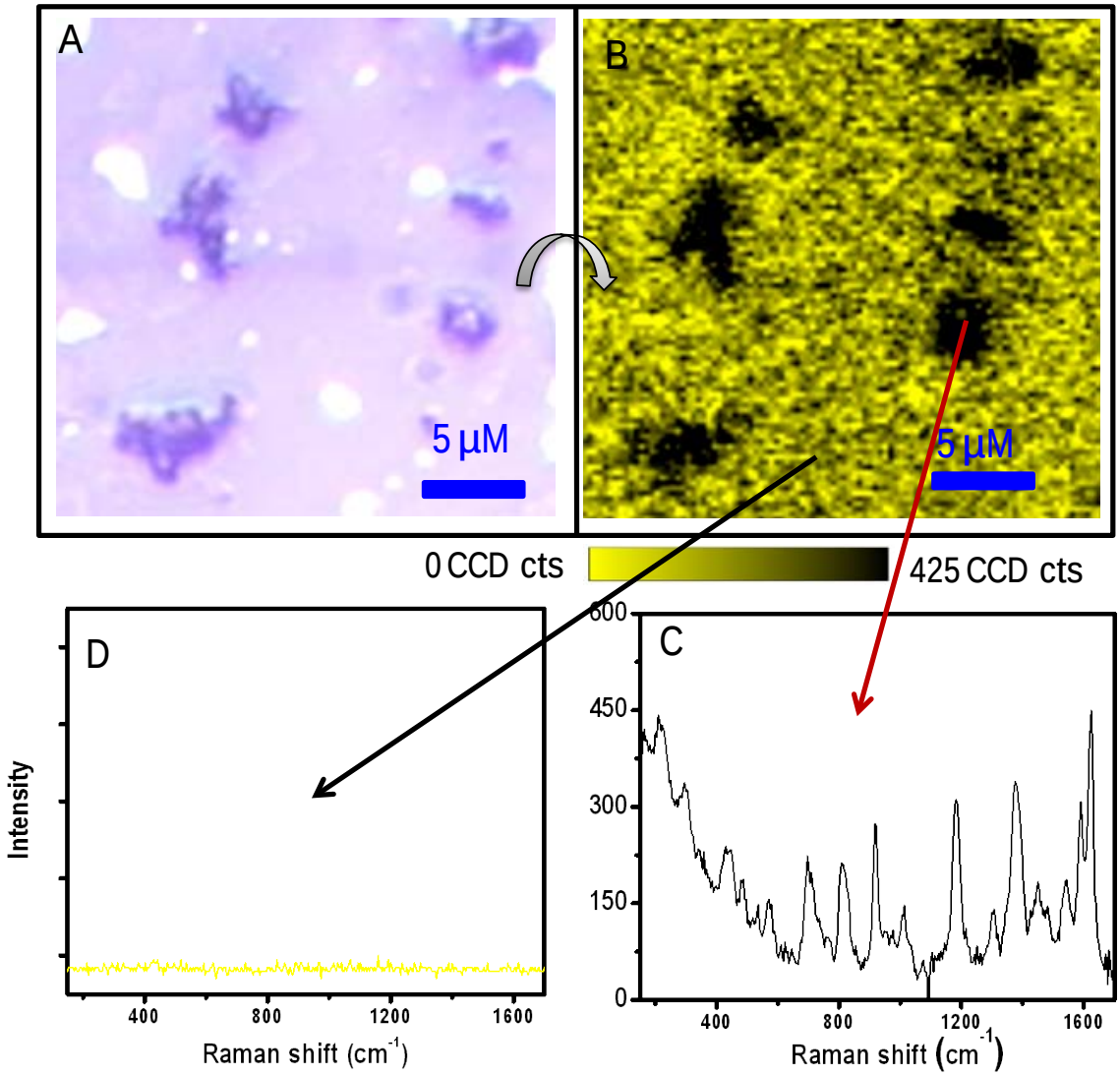

Figure S4. A: the optical image of a selected part of the sample. B: Corresponding Raman image, which shows that the "hot spot" are on the cluster surface and intensity comes spontaneously form all the area of each microcrystal. C and D: SERS spectra from the dark green and light yellow zone, respectively.

Supporting information 5

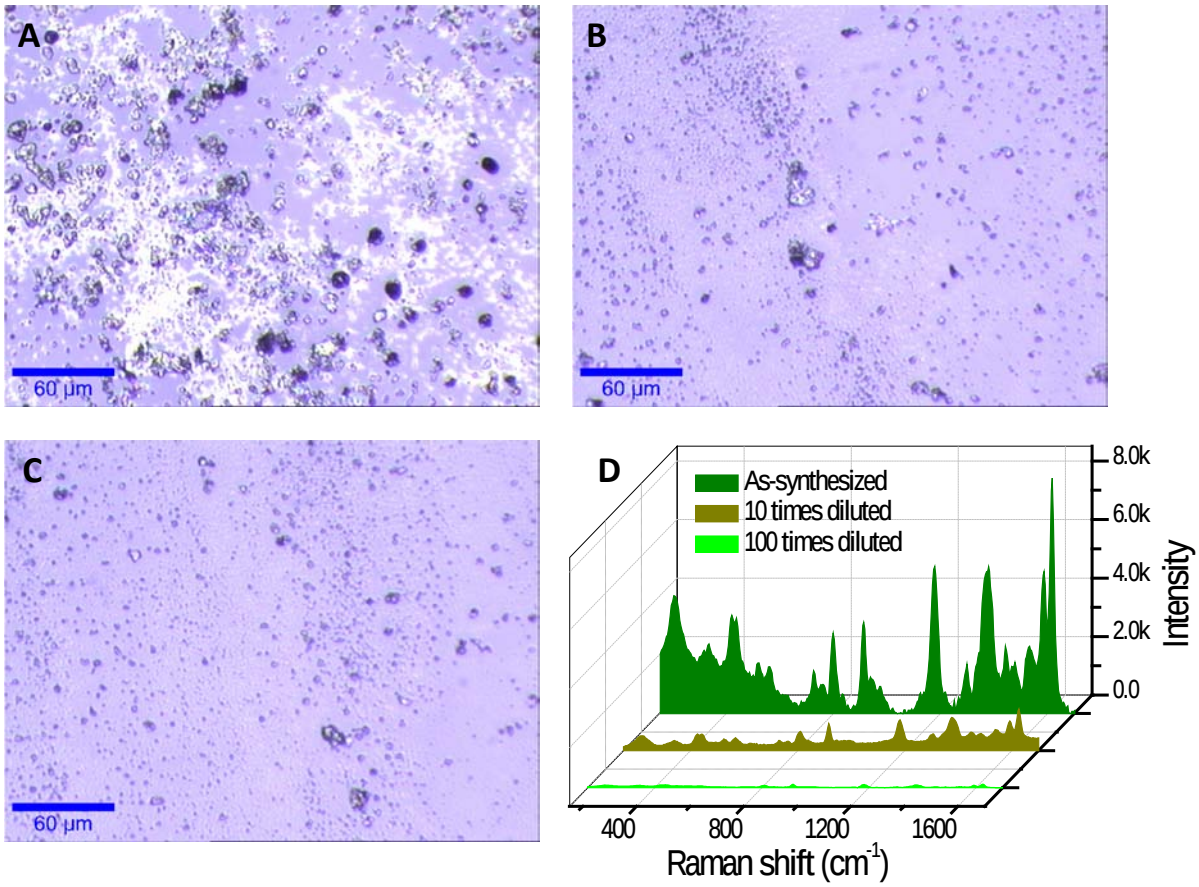

Figure S5. Morphological change on dilution of the cluster solution; A: drop casted as-synthesized clusters, B: 10 times diluted; and C: 100 times diluted. D: SERS spectra for different cluster concentrations among which as-synthesized cluster showing maximum SERS intensity. For all the cases, same concentration (5 µM) of CV was added.

Supporting information 6

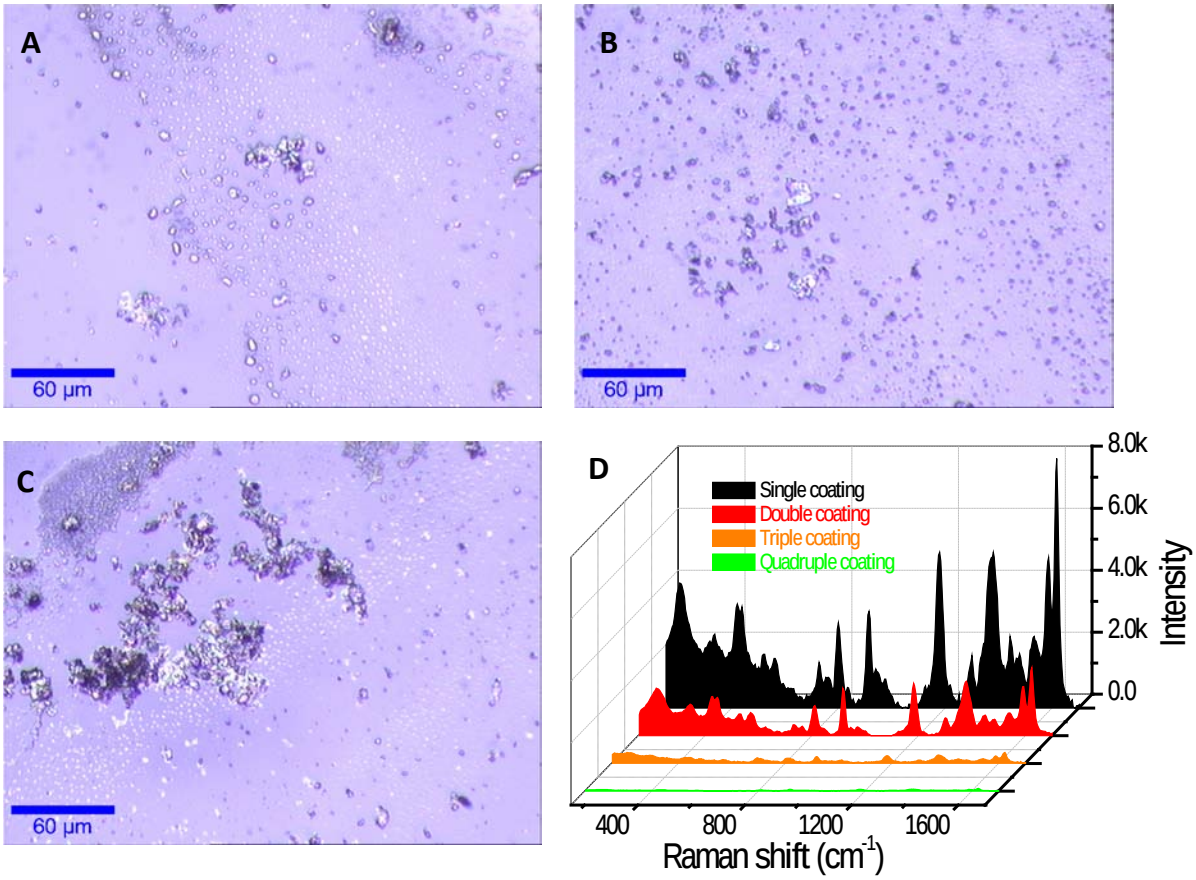

Figure S6. Morphological change in coating variation; A: single coating, B: double coating; C: triple coating. D: SERS spectra for different number of coatings. Single coating shows the maximum intensity. For all the cases, same concentration (5 µM) of CV was used.

Supporting information 7

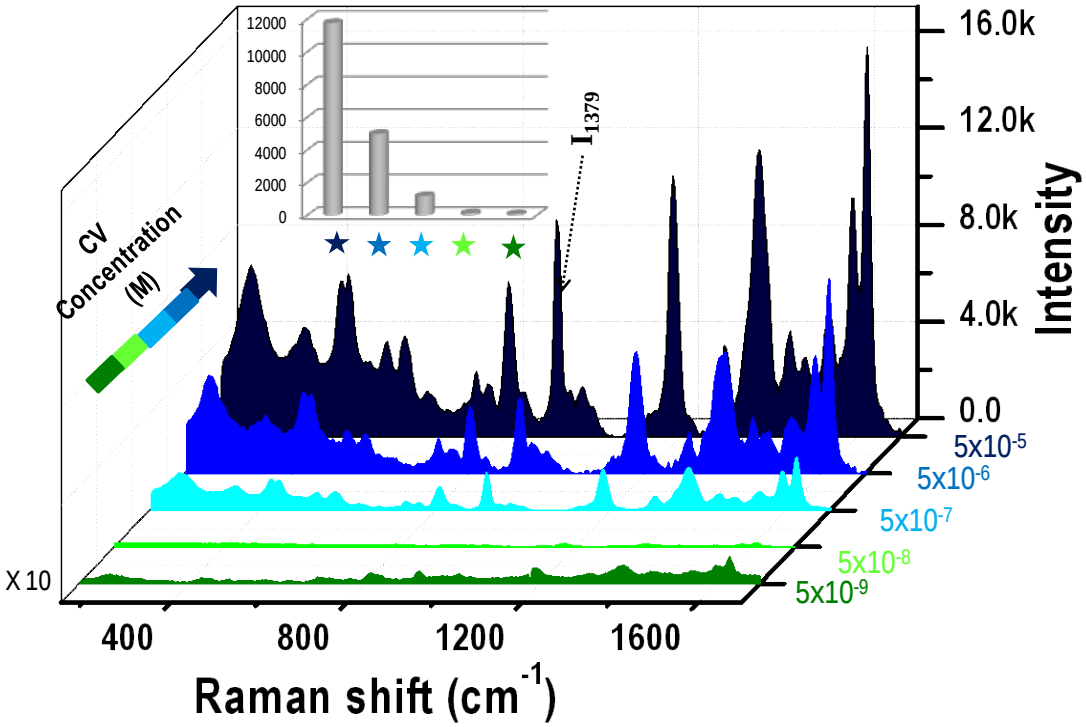

Figure S7. The SERS spectra of crystal violet with different concentrations. The lower detection limit is 5×10^{-9} M. The spectrum is expanded 10 times in the Figure. Inset shows the intensity of the 1379 cm^{-1} peak for all the CV concentrations.

Supporting information 8

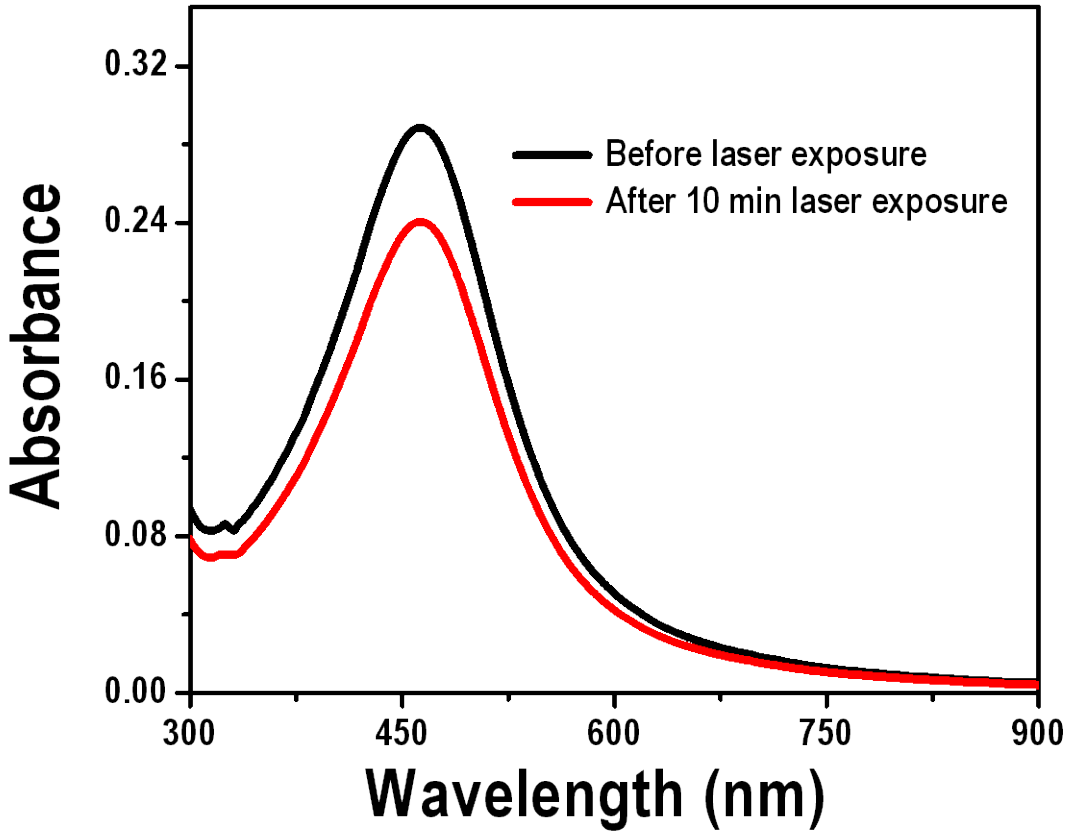

Figure S8. UV/Vis of cluster solution taken before and after the laser exposure. There as some laser induced damage to the cluster. For this experiment, the selected area was exposed for 10 minutes and redispersed in toluene to check the UV/Vis.

Supporting information 9

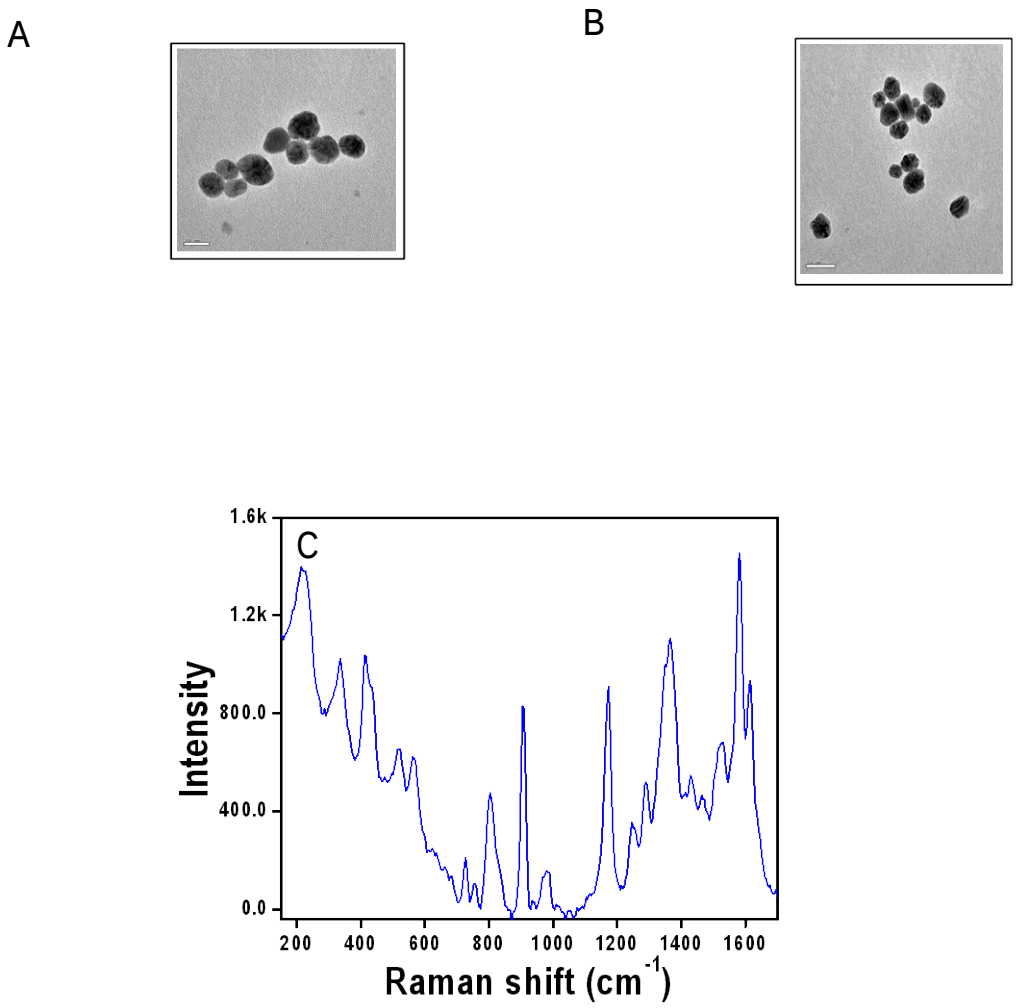

Figure S9. UV/Vis spectra of Ag@citrate (A) and Ag@PET (B) nanoparticles which show the characteristic SPR at 400 nm and 460 nm, respectively. Insets show the corresponding TEM images. C: Raman spectrum of CV taken from a drop casted film of Ag@citrate nanoparticle.

Supporting information 10

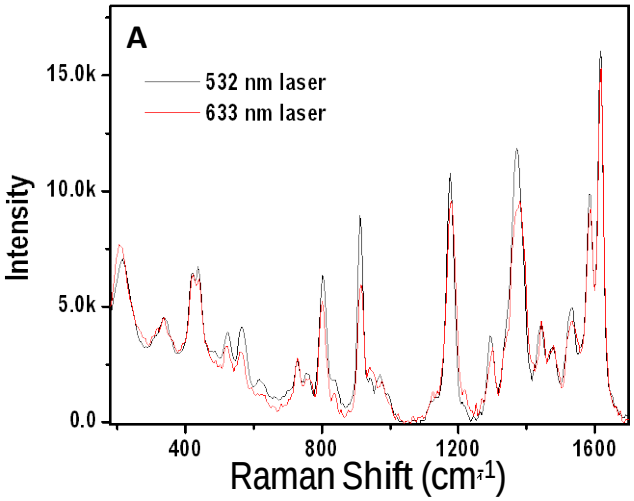

Figure S10. SERS spectra of 50 µM CV with 532 (black trace) and 633 nm (red trace) excitation (A). The corresponding data without background correction is given in Figure B (for 532 nm excitation).

1. Kumar, G. V. P.; Shruthi, S.; Vibha, B.; Reddy, B. A. A.; Kundu, T. K.; Narayana, C. Hot Spots in Ag Core−Au Shell Nanoparticles Potent for Surface-Enhanced Raman Scattering Studies of Biomolecules. *The Journal of Physical Chemistry C* **2007,** *111* (11), 4388-4392.
2. Shibu, E. S.; Kimura, K.; Pradeep, T. Gold Nanoparticle Superlattices: Novel Surface Enhanced Raman Scattering Active Substrates. *Chemistry of Materials* **2009,** *21* (16), 3773-3781.

THE JOURNAL OF PHYSICAL CHEMISTRY Letters

Letter

pubs.acs.org/JPCL

$Ag_{44}(SeR)_{30}$: A Hollow Cage Silver Cluster with Selenolate Protection

Indranath Chakraborty,[†] Wataru Kurashige,[‡] Keita Kanehira,[‡] Lars Gell,[§] Hannu Häkkinen,[§] Yuichi Negishi,*[,‡] and Thalappil Pradeep*[,†]

[†]DST Unit of Nanoscience (DST UNS) and Thematic Unit of Excellence (TUE), Department of Chemistry, Indian Institute of Technology Madras, Chennai 600 036, India

[‡]Department of Applied Chemistry, Faculty of Science, Tokyo University of Science, 1-3 Kagurazaka, Shinjuku-ku, Tokyo 162-8601, Japan

[§]Departments of Chemistry and Physics, Nanoscience Center, University of Jyväskylä, Box 35, FI-40014 Jyväskylä, Finland

Supporting Information

ABSTRACT: Selenolate protected, stable and atomically precise, hollow silver cluster was synthesized using solid state as well as solution state routes. The optical absorption spectrum shows multiple and sharp features similar to the thiolated Ag_{44} cluster, $Ag_{44}(SR)_{30}$ whose experimental structure was reported recently. High-resolution electrospray ionization mass spectrometry (HRESI MS) shows well-defined molecular ion features with two, three, and four ions with isotopic resolution, due to $Ag_{44}(SePh)_{30}$. Additional characterization with diverse tools confirmed the composition. The closed-shell 18 electron superatom electronic structure, analogous to $Ag_{44}(SR)_{30}$ stabilizes the dodecahedral cage with a large HOMO−LUMO gap of 0.71 eV. The time-dependent density functional theory (TDDFT) prediction of the optical absorption spectrum, assuming the $Ag_{44}(SR)_{30}$ structure, matches the experimental data, confirming the structure.

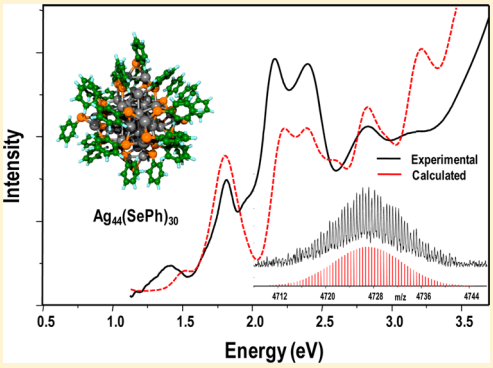

SECTION: Physical Processes in Nanomaterials and Nanostructures

Noble metal nanoparticles[1−4] and their atomically precise analogues,[5−7] called by various names (artificial atoms, nanomolecules, and quantum clusters), due to their diverse and technologically relevant properties have had a profound impact on the science of nanosystems.[8−16] Nearly all of these systems have been prepared with thiols[8,11,15,17−19] as their protecting agents, although phosphines have been the preferred ligands in the early period of this science.[20−24] Accurate structures of some of the thiolated clusters are now available in the literature.[25−30] Most of these pertain to gold and the first crystal structures of silver analogues[31,32] have just appeared. Many other silver clusters have been identified by mass spectrometry.[33−36] The most recent $Ag_{44}(SR)_{30}$ system forms a Keplerate solid of concentric icosahedral and dodecahedral atom shells, which are further protected by six $Ag_2(SR)_5$ units in an octahedral geometry, as revealed from single crystal studies.[37,38] It is the first hollow cage system of a noble metal cluster to have been crystallized with thiolate protection although a cage structure has been predicted for $Au_{144}(SR)_{60}$[39] and more recently for $Ag_{152}(SR)_{60}$.[40]

In this Letter, we report the $Ag_{44}(SePh)_{30}$ (**1**) system, the very first selenolate analogue of a silver cluster with nearly identical properties of the thiolate system. Examples of selenolate protected clusters are very few in the literature; those available are on gold and show higher stability compared to the thiolate analogues.[41−44] However, selenolate protected silver nanoparticles have been reported by Zaluzhna et al.[45] The homologous family of $Ag_{44}(XR)_{30}$ system[37,38,46−48] (X = S, Se) and their unique properties with molecule-like optical absorption, high stability, easy synthesis, and potential to scale up are expected to attract immediate attention of the scientific community. Density functional theory (DFT) calculations reveal that the exceptional stability of the cluster can be traced back to a strong electronic shell closing at 18 electrons similar to the reported case of the $Ag_{44}(SR)_{30}^{4-}$ cluster[38] and time-dependent DFT (TDDFT) calculations of $Ag_{44}(SePh)_{30}^{4-}$ based on the reported structure of the thiolate analog predict an optical absorption spectrum in complete agreement with the experiment.

$Ag_{44}(SePh)_{30}$ (**1**) was made initially via a solid state method originally reported for the $Ag_9(SR)_7$ system, with significant modifications (see the Experimental Methods section for details).[49] Solid state reaction conducted in a mortar and pestle under ambient atmospheric condition results in a series of color changes (photographs are given in Figure S1). In the solid state route, the cluster growth is controlled by the limited supply of water needed for the reduction of silver thiolate by $NaBH_4$ (s), which becomes available from the laboratory atmosphere as well as from the ethanol used for subsequent washing.[40] The cluster appeared deep pink (inset of Figure 1)

Received: September 3, 2013
Accepted: September 20, 2013

   dx.doi.org/10.1021/jz401879c | J. Phys. Chem. Lett. 2013, 4, 3351−3355

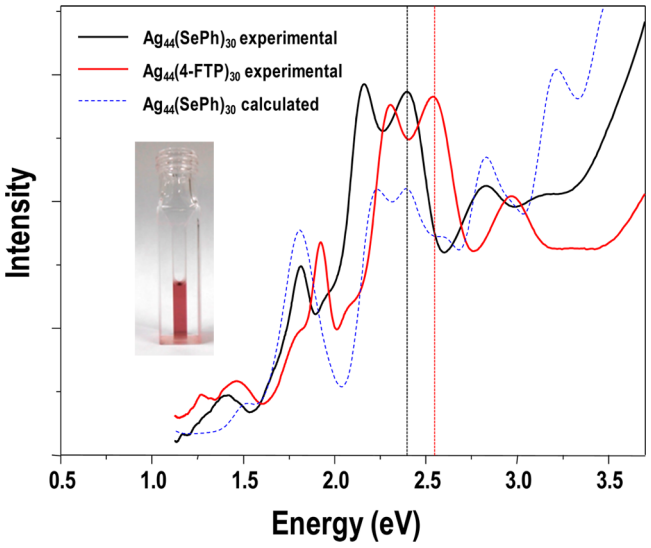

Figure 1. The optical absorption spectra for cluster **1** (black trace) and **2** (red trace), respectively, in acetone and THF solvent, plotted in terms of energy. Dashed blue line shows the corresponding calculated optical absorption spectrum of cluster **1**. The individual optical transitions in the calculated spectrum are broadened by 0.05 eV Gaussians, and the intensity is scaled to match with the experimental spectrum; details are given in the Supporting Information. The spectrum reveals multiple maxima with five prominent bands and three broad bands. The computed spectral features are matching very well with cluster **1**. The red shift in the Se analogue, shown with vertical lines originates from a simple size effect as discussed in the text. Inset shows the photograph of cluster **1** solution in acetone, taken in a cuvette.

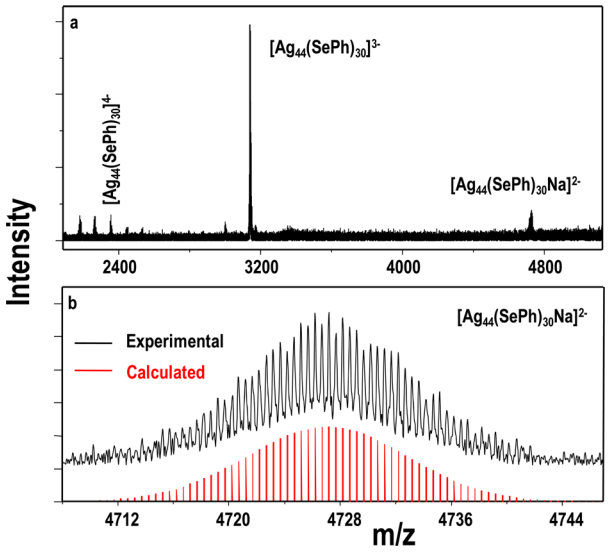

Figure 2. (a) HRESI MS of as-synthesized cluster **1** taken in negative mode. The spectrum shows clear 2-, 3- and 4-ions of the $Ag_{44}(SePh)_{30}$. Clean spectrum suggests the purity of the as-synthesized cluster. Sodium exists as the counterion. (b) Expanded mass spectrum of the 2-ion (black traces). Spectrum is matching exactly with the calculated one (red trace).

in acetone/acetonitrile that was stored at 4 °C in a refrigerator. The yield was 80%. It is important to note that at room temperature (25 °C) and atmospheric conditions, the cluster degrades in 15 days forming yellow Ag-selenolates. However, stability is of the order of months in the solid state in the refrigerator. We have also used a solution phase route to make the clusters, a modified version of the process used to make $Ag_{44}SR_{30}$.[47] The corresponding thiolated cluster, $Ag_{44}(4\text{-FTP})_{30}$ (FTP = 4-Fluorothiophenol) (**2**) was also prepared for comparison.[47,48] Details of experimental procedures and characterization methods including density functional computations are given in the Supporting Information.

The optical absorption spectrum of **1** (black trace in Figure 1 and S2Aa) shows characteristic features in the 300 to 900 nm region. Five intense bands at 1.41(879), 1.82 (681), 2.16 (574), 2.40 (516) and 2.82 (440) eV (nm) along with three broad bands centered around 1.27 (970), 1.95 (635) and 3.14 (395) eV (nm) were seen. Interestingly, the spectral features are matching with the corresponding thiolated Ag_{44} cluster **2** (red trace in Figure 1 and S2Ab) identified by Harkness et al.[48] However, some red shift is seen, attributed to a size effect as discussed later. Here, it may be noted that the ligand does not contain substituents on the phenyl ring, which would modify the electron density. The profound similarity of the spectrum with that of cluster **2** made us explore its properties in greater detail. The cluster synthesized through the solution phase shows similar features in the optical absorption spectra as the cluster made through the solid state. Comparative spectra for both are given in Figure S2B. The time-dependent data for the cluster synthesized through solid (Figure S3A) and solution (Figure S3B) state routes show increased stability of the samples under ambient conditions.

Further confirmation of the composition comes from mass spectrometry. Electrospray ionization mass spectrometry gave sharp and distinct 4-, 3-, and 2- features of $Ag_{44}(SePh)_{30}$ and the spectrum reveals $Ag_{44}(SePh)_{30}$ as an integral species (Figure 2a). The 2- feature shows a series of closely spaced peaks centered at m/z 4727.5 with a width of ±12, due to the characteristic isotope distribution which matches well with the calculated pattern. The experimental and calculated spectra are compared in Figure 2b. It is important to note that Se has six isotopes and in conjunction with the two isotopes of silver with equal abundance, peaks in the 4- and 3- regions are complex. Sodium exists as a countercation with the cluster. Despite these complexities, expanded spectrum in the 3- charge state clearly shows the isotope resolution (Figure S4). The 4- feature is weak and, consequently, the isotope resolution is unclear (Figure S4). The reason behind higher intensity of 3- compared to 4- is unknown, but it is important to note here that the intensity also depends on instrument parameters. We optimized the conditions to achieve the best isotope resolution, irrespective of relative intensity. Although a 4- ion is seen, we note that ESI MS does not confirm the existence of this charge state in solution as additional ionization events can occur during electrospray. Even 5-, 6-, and 7- peaks are also observed for $Ag_{44}(SR)_{30}$.[46]

The mass spectrometric suggestion of the molecular formula was confirmed by various analytical measurements. Thermogravimetric (TG) analysis of **1** shows a single and sharp mass loss (at ~240 °C) of 48.38%, as expected (Figure 3a). Part of the counterion, sodium (as $Ag_{44}(SePh)_{30}$ is a 4- species, see below) may still be attached with the cluster at 550 °C, which leaves some uncertainty in calculating the exact % loss. The weight loss starts from ~200 °C, which is quite a high temperature compared to the most stable $Au_{25}(SeR)_{18}$ cluster,[41] suggesting high stability and rigidity of the cluster. A cluster core of 1.0 ± 0.2 nm was confirmed from TEM (Figure 3b),

dx.doi.org/10.1021/jz401879c | J. Phys. Chem. Lett. 2013, 4, 3351−3355

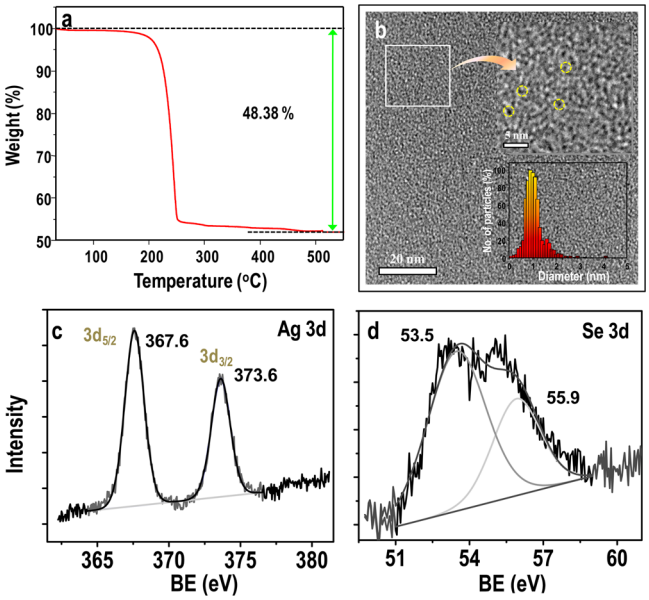

Figure 3. (a) TG analysis of cluster **1**. The spectrum shows a sharp loss at 240 °C. Mass loss started from ∼200 °C onward, suggesting high stability for the cluster. HRTEM image in b shows tiny particles and an expanded portion is given in the inset. Some particles are marked with yellow circles. Inset shows the size distribution. Narrow distribution suggests high uniformity of the cluster. Expanded XPS spectra of Ag 3d (c) and Se 3d (d). Peak positions are marked accordingly. The 55.9 eV feature in d is due to X-ray induced damage of the sample.

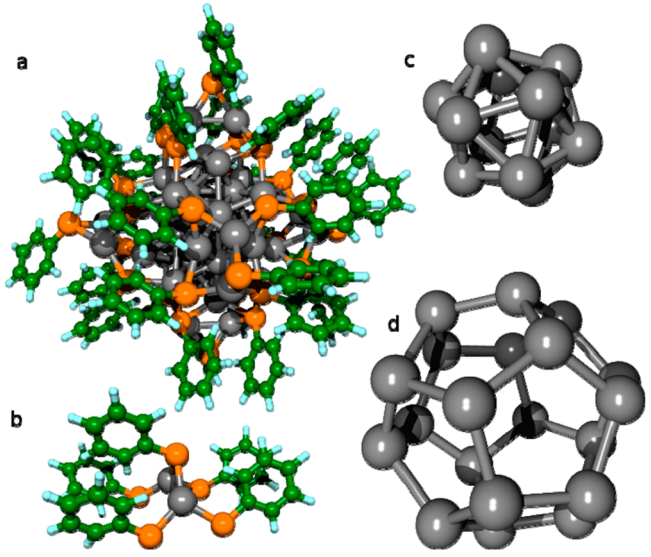

Figure 4. (a) Computationally relaxed structure of the $Ag_{44}(SePh)_{30}^{4-}$ cluster, showing in addition (b) the structure of one $Ag_2(SePh)_5$ surface unit and the (c) icosahedral and (d) dodecahedral shells of the metal core. Ag: gray; Se: orange; C: green; H: cyan.

which is quite similar to that reported for the $Ag_{44}(SR)_{30}$ cluster where the core size was found to be 1.3 nm. Uncertainty of the measurement at such small core sizes prevented us from getting a closer value. The narrow size distribution suggests uniformity of the cluster. Elemental analysis (Figure S5) showed an Ag:Se ratio (1:0.679) similar to that expected (1:0.682). Other expected elements are also seen in the spectrum. The loss of Se−H proton (at 3.5 ppm) was seen in ^{1}HNMR, which confirms the binding of silver with the selenolate species (Figure S6). Because of metal attachment to the ligand, the aromatic protons show downfield shift and they get broadened as expected.

XPS of **1** shows the expected elements in the predictable intensity pattern (Figure S7). Ag 3d appears at 367.6 eV, typical of metallic silver (Figure 3c). It is important to note that the difference between Ag(0) and Ag(I) is small (0.5 eV)[50] and a precise determination of the valence state is not possible with the available instrumental resolution. Se 3d appears at 53.5 eV as expected (Figure 3d) for the selenolate system.[43] However, as there is a possibility of X-ray induced damage, the Se 3d region shows an additional feature at 55.9 eV. This kind of X-ray-induced damage is seen in the thiolate system,[51] possibly due to the sulfate or sulfonate species, arising from X-ray exposure.

Motivated by the similarity of the measured optical spectra of $Ag_{44}(XR)_{30}$ (X = S, Se) clusters, we performed DFT computations of the electronic ground state and TDDFT computations on the optical spectrum (blue trace in Figure 1) of $Ag_{44}(SePh)_{30}^{4-}$ based on the resolved structure[38] of the thiolate analogue, $Ag_{44}(SPhF_2)_{30}^{4-}$ (for computational details, see Supporting Information). Very small but systematic expansion of the selenolate protected cluster as compared to the thiolate-analogue was observed in the DFT-optimized structure of (**1**) shown in Figure 4 (for comparison of important bond lengths, see S8 Table 1). These differences are mainly due to the slightly larger covalent/ionic radius of Se compared to S. The free electron count of the compound in the 4- charge state is 18, applying the simple electron counting rule of ref 52. This corresponds to the $1S^2$ $1P^6$ $1D^{10}$ superatom electron configuration, thus leaving the $2S^2$ and $1F^{14}$ manifolds empty (see Figure S9 showing the electronic density of states for the region of the superatom 1D, 2S, and 1F states). The destabilization of the $2S^2$ superatom state is due to the hollow cage structure of the inner metal core.

The calculated HOMO−LUMO gap is 0.71 eV showing the electronic stability. The HOMO−LUMO optical transition is, however, dipole-forbidden, and the optical gap is therefore slightly larger. The calculated optical absorption spectrum of $Ag_{44}(SeR)_{30}$ for charge state 4- matches with all the observed major features, thus indicating that the known structure of $Ag_{44}(SR)_{30}$ is very likely the structure of $Ag_{44}(SeR)_{30}$ as well. The slight red shift of the excitations as compared to the thiolate cluster can be understood as a size effect from a slightly larger total volume of the selenolate cluster, as most of the transitions involve not only metal core electrons but the pi-systems of the ligand layer as well, in analogy to the corresponding thiolate-stabilized cluster.[38]

In summary, we show the existence of an extremely stable silver cluster system protected with selenolate, $Ag_{44}(SePh)_{30}$. The UV−Vis spectrum of this compound is almost identical to the recently (structurally) solved $Ag_{44}(SR)_{30}$, and TDDFT computations assuming the structure of the thiolate cluster reproduce the experimental UV−Vis data accurately. The stability of the cluster arising from the closed shell 18-electron system and structurally stable Keplerate core is clear from the electronic structure calculations. We believe that similarity of the $Ag_{44}(XR)_{30}$ (X = S, Se) system would lead to the exploration of properties of analogous metal nanosystems.

dx.doi.org/10.1021/jz401879c | J. Phys. Chem. Lett. 2013, 4, 3351−3355

EXPERIMENTAL METHODS

Materials used in the synthesis are listed in the Supporting Information.

1. Solid State Synthesis of Cluster 1. Initially, 23 mg of $AgNO_3$ (s) and 30 μL of benzeneselenol (l) were ground well in a clean agate mortar using a pestle. The color of the mixture changes to yellowish orange showing the formation of silver selenolate. To this mixture, 25 mg of solid $NaBH_4$ were added and the content was ground well until the color became dark yellow. Then, 5 mL of ethanol was added to the mixture and mixed well. Ethanol was added to wash out the extra ligand. The mixture was kept for 15−30 s until there was a color change from dark yellow to deep brown. The contents were then taken in a centrifuge tube and centrifuged at 3600 rpm for 4 min. The centrifugate was removed, and the residue was dissolved in acetone and again centrifuged for 3 min. The cluster, extracted in acetone, was collected and the residue was discarded. Deep pink colored Ag_{44} cluster was obtained in acetone and it was stored in a refrigerator at ∼4 °C. The percentage yield was 80%. Similarly, the Ag_{44} cluster can also be extracted in tetrahydrofuran (THF) and acetonitrile. In THF, it is comparatively less stable (stable up to 15 days) in contrast to acetonitrile and acetone (stable up to 2 months at ambient condition).

2. Solution Phase Synthesis of Cluster 1. This is a modified procedure of Bakr et al.,[40] where a two step synthesis route was followed. First, silver trifluoroacetate (15.78 mg, 0.0714 mmol) was dissolved in 7.2 mL acetonitrile and stirred for 5 min. Benzeneselenol (5 μL, 0.0471 mmol) was added to that solution and was left to stir for another 15 min (Solution A). In another conical flask, 28.6 mL acetonitrile solution of $NaBH_4$ (10.8 mg, 0.286 mmol) was kept for stirring for 30 min (Solution B). Then, Solution B was added to Solution A, and the reaction mixture was left to stir for 3 h at room temperature. The deep pink colored cluster was formed after 3 h and it was stored in refrigerator at ∼4 °C.

Computational methods are presented in the Supporting Information.

ASSOCIATED CONTENT

Supporting Information

Details of experimental procedures, instrumentation, description of the computational methods, photographs during synthesis, ^{1}HNMR, SEM/EDAX, XPS, comparative UV/Vis spectra prepared by solid & solution state routes, time dependent spectra and the analysis of the electronic structure of cluster **1**. This material is available free of charge via the Internet at http://pubs.acs.org.

AUTHOR INFORMATION

Corresponding Authors

*Fax: + 91-44 2257-0545; E-mail: pradeep@iitm.ac.in.

*E-mail: negishi@rs.kagu.tus.ac.jp.

Notes

The authors declare no competing financial interest.

ACKNOWLEDGMENTS

T.P. thanks the Department of Science and Technology (DST), Government of India, for constantly supporting his research program on nanomaterials. I.C. thanks IITM for research fellowships. Y.N. wishes to express his gratitude to the Toden foundation and Tokyo Ohka foundation for partial financial support. T.P. and H.H. acknowledge financial support from the bilateral Academy of Finland−DST India research program.

REFERENCES

(1) Brust, M.; Walker, M.; Bethell, D.; Schiffrin, D. J.; Whyman, R. Synthesis of Thiol-Derivatised Gold Nanoparticles in a Two-Phase Liquid−Liquid System. *J. Chem. Soc. Chem. Commun.* **1994**, *7*, 801−802.

(2) Brust, M.; Kiely, C. J. Some Recent Advances in Nanostructure Preparation from Gold and Silver Particles: A Short Topical Review. *Colloids Surf. A* **2002**, *202* (2−3), 175−186.

(3) Daniel, M.-C.; Astruc, D. Gold Nanoparticles: Assembly, Supramolecular Chemistry, Quantum-Size-Related Properties, and Applications toward Biology, Catalysis, and Nanotechnology. *Chem. Rev.* **2003**, *104* (1), 293−346.

(4) Eustis, S.; El-Sayed, M. A. Why Gold Nanoparticles Are More Precious than Pretty Gold: Noble Metal Surface Plasmon Resonance and Its Enhancement of the Radiative and Nonradiative Properties of Nanocrystals of Different Shapes. *Chem. Soc. Rev.* **2006**, *35* (3), 209−217.

(5) Jin, R. Quantum Sized, Thiolate-Protected Gold Nanoclusters. *Nanoscale* **2010**, *2* (3), 343−362.

(6) Wilcoxon, J. P.; Abrams, B. L. Synthesis, Structure and Properties of Metal Nanoclusters. *Chem. Soc. Rev.* **2006**, *35* (11), 1162−1194.

(7) Diez, I.; Ras, R. H. A. Fluorescent Silver Nanoclusters. *Nanoscale* **2011**, *3* (5), 1963−1970.

(8) Parker, J. F.; Fields-Zinna, C. A.; Murray, R. W. The Story of a Monodisperse Gold Nanoparticle: $Au_{25}L_{18}$. *Acc. Chem. Res.* **2010**, *43* (9), 1289−1296.

(9) Xie, J.; Zheng, Y.; Ying, J. Y. Protein-Directed Synthesis of Highly Fluorescent Gold Nanoclusters. *J. Am. Chem. Soc.* **2009**, *131* (3), 888−889.

(10) Choi, S.; Dickson, R. M.; Yu, J. Developing Luminescent Silver Nanodots for Biological Applications. *Chem. Soc. Rev.* **2012**, *41* (5), 1867−1891.

(11) Muhammed, M. A. H.; Verma, P. K.; Pal, S. K.; Kumar, R. C. A.; Paul, S.; Omkumar, R. V.; Pradeep, T. Bright, NIR-Emitting Au_{23} from Au_{25}: Characterization and Applications Including Biolabeling. *Chem.—Eur. J.* **2009**, *15* (39), 10110−10120.

(12) Chakraborty, I.; Bag, S.; Landman, U.; Pradeep, T. Atomically Precise Silver Clusters as New SERS Substrates. *J. Phys. Chem. Lett.* **2013**, *4* (16), 2769−2773.

(13) Chaudhari, K.; Xavier, P. L.; Pradeep, T. Understanding the Evolution of Luminescent Gold Quantum Clusters in Protein Templates. *ACS Nano* **2011**, *5* (11), 8816−27.

(14) Habeeb Muhammed, M. A.; Verma, P. K.; Pal, S. K.; Retnakumari, A.; Koyakutty, M.; Nair, S.; Pradeep, T. Luminescent Quantum Clusters of Gold in Bulk by Albumin-Induced Core Etching of Nanoparticles: Metal Ion Sensing, Metal-Enhanced Luminescence, and Biolabeling. *Chem.—Eur. J.* **2010**, *16* (33), 10103−10112.

(15) Udaya Bhaskara Rao, T.; Pradeep, T. Luminescent Ag_7 and Ag_8 Clusters by Interfacial Synthesis. *Angew. Chem., Int. Ed.* **2010**, *49* (23), 3925−3929.

(16) Xavier, P. L.; Chaudhari, K.; Baksi, A.; Pradeep, T. Protein-Protected Luminescent Noble Metal Quantum Clusters: An Emerging Trend in Atomic Cluster Nanoscience. *Nano Rev.* **2012**, *3*, 14767.

(17) Kimura, K.; Sugimoto, N.; Sato, S.; Yao, H.; Negishi, Y.; Tsukuda, T. Size Determination of Gold Clusters by Polyacrylamide Gel Electrophoresis in a Large Cluster Region. *J. Phys. Chem. C* **2009**, *113* (32), 14076−14082.

(18) Cathcart, N.; Mistry, P.; Makra, C.; Pietrobon, B.; Coombs, N.; Jelokhani-Niaraki, M.; Kitaev, V. Chiral Thiol-Stabilized Silver Nanoclusters with Well-Resolved Optical Transitions Synthesized by a Facile Etching Procedure in Aqueous Solutions. *Langmuir* **2009**, *25*, 5840−5846.

(19) Udayabhaskararao, T.; Pradeep, T. New Protocols for the Synthesis of Stable Ag and Au Nanocluster Molecules. *J. Phys. Chem. Lett.* **2013**, *4* (9), 1553−1564.

(20) Bellon, P.; Manassero, M.; Sansoni, M. Crystal and Molecular Structure of Tri-iodoheptakis(tri-*p*-fluorophenylphosphine)-undecagold. *J. Chem. Soc., Dalton Trans.* **1972**, *14*, 1481−1487.
(21) Bellon, P. L.; Cariati, F.; Manassero, M.; Naldini, L.; Sansoni, M. Novel Gold Clusters. Preparation, Properties, and X-ray Structure Determination of Salts of Octakis(triarylphosphine)enneagold, $[Au_9L_8]X_3$. *J. Chem. Soc., D: Chem. Commun.* **1971**, *22*, 1423−1424.
(22) Schmid, G.; Pfeil, R.; Boese, R.; Bandermann, F.; Meyer, S.; Calis, G. H. M.; van der Velden, J. W. A. $Au_{55}[P(C_6H_5)_3]_{12}Cl_6$ — Ein Goldcluster Ungewöhnlicher Größe. *Chem. Ber.* **1981**, *114* (11), 3634−3642.
(23) Schmid, G. The Relevance of Shape and Size of Au_{55} Clusters. *Chem. Soc. Rev.* **2008**, *37* (9), 1909−1930.
(24) Bartlett, P. A.; Bauer, B.; Singer, S. J. Synthesis of Water-Soluble Undecagold Cluster Compounds of Potential Importance in Electron Microscopic and Other Studies of Biological Systems. *J. Am. Chem. Soc.* **1978**, *100* (16), 5085−5089.
(25) Heaven, M. W.; Dass, A.; White, P. S.; Holt, K. M.; Murray, R. W. Crystal Structure of the Gold Nanoparticle $[N(C_8H_{17})_4][Au_{25}(SCH_2CH_2Ph)_{18}]$. *J. Am. Chem. Soc.* **2008**, *130* (12), 3754−3755.
(26) Zhu, M.; Aikens, C. M.; Hollander, F. J.; Schatz, G. C.; Jin, R. Correlating the Crystal Structure of a Thiol-Protected Au_{25} Cluster and Optical Properties. *J. Am. Chem. Soc.* **2008**, *130* (18), 5883−5885.
(27) Qian, H.; Eckenhoff, W. T.; Zhu, Y.; Pintauer, T.; Jin, R. Total Structure Determination of Thiolate-Protected Au_{38} Nanoparticles. *J. Am. Chem. Soc.* **2010**, *132* (24), 8280−8281.
(28) Jadzinsky, P. D.; Calero, G.; Ackerson, C. J.; Bushnell, D. A.; Kornberg, R. D. Structure of a Thiol Monolayer-Protected Gold Nanoparticle at 1.1 Å Resolution. *Science* **2007**, *318* (5849), 430−433.
(29) Zeng, C.; Qian, H.; Li, T.; Li, G.; Rosi, N. L.; Yoon, B.; Barnett, R. N.; Whetten, R. L.; Landman, U.; Jin, R. Total Structure and Electronic Properties of the Gold Nanocrystal $Au_{36}(SR)_{24}$. *Angew. Chem., Int. Ed.* **2012**, *51* (52), 13114−13118.
(30) Zeng, C.; Li, T.; Das, A.; Rosi, N. L.; Jin, R. Chiral Structure of Thiolate-Protected 28-Gold-Atom Nanocluster Determined by X-ray Crystallography. *J. Am. Chem. Soc.* **2013**, *135*, 10011−10013.
(31) Yang, H.; Lei, J.; Wu, B.; Wang, Y.; Zhou, M.; Xia, A.; Zheng, L.; Zheng, N. Crystal Structure of a Luminescent Thiolated Ag Nanocluster with an Octahedral Ag_6^{4+} Core. *Chem. Commun.* **2013**, *49* (3), 300−302.
(32) Yang, H.; Wang, Y.; Zheng, N. Stabilizing Subnanometer Ag(0) Nanoclusters by Thiolate and Diphosphine Ligands and Their Crystal Structures. *Nanoscale* **2013**, *5* (7), 2674−2677.
(33) Bertorelle, F.; Hamouda, R.; Rayane, D.; Broyer, M.; Antoine, R.; Dugourd, P.; Gell, L.; Kulesza, A.; Mitric, R.; Bonacic-Koutecky, V. Synthesis, Characterization and Optical Properties of Low Nuclearity Liganded Silver Clusters: $Ag_{31}(SG)_{19}$ and $Ag_{15}(SG)_{11}$. *Nanoscale* **2013**, *5* (12), 5637−43.
(34) Guo, J.; Kumar, S.; Bolan, M.; Desireddy, A.; Bigioni, T. P.; Griffith, W. P. Mass Spectrometric Identification of Silver Nanoparticles: The Case of $Ag_{32}(SG)_{19}$. *Anal. Chem.* **2012**, *84* (12), 5304−8.
(35) Wu, Z.; Lanni, E.; Chen, W.; Bier, M. E.; Ly, D.; Jin, R. High Yield, Large Scale Synthesis of Thiolate-Protected Ag_7 Clusters. *J. Am. Chem. Soc.* **2009**, *131* (46), 16672−16674.
(36) Chakraborty, I.; Udayabhaskararao, T.; Pradeep, T. High Temperature Nucleation and Growth of Glutathione Protected ~ Ag_{75} Clusters. *Chem. Commun.* **2012**, *48* (54), 6788−6790.
(37) Desireddy, A.; Conn, B. E.; Guo, J.; Yoon, B.; Barnett, R. N.; Monahan, B. M.; Kirschbaum, K.; Griffith, W. P.; Whetten, R. L.; Landman, U.; Bigioni, T. P. Ultrastable Silver Nanoparticles. *Nature* **2013**, DOI: 10.1038/nature12523.
(38) Yang, H.; Wang, Y.; Huang, H.; Gell, L.; Lehtovaara, L.; Malola, S.; Häkkinen, H.; Zheng, N. All-Thiol-Stabilized Ag_{44} and $Au_{12}Ag_{32}$ Nanoparticles with Single-Crystal Structures. *Nat. Commun.* **2013**, DOI: 10.1038/ncomms3422.
(39) Lopez-Acevedo, O.; Akola, J.; Whetten, R. L.; Grönbeck, H.; Häkkinen, H. Structure and Bonding in the Ubiquitous Icosahedral Metallic Gold Cluster $Au_{144}(SR)_{60}$. *J. Phys. Chem. C* **2009**, *113* (13), 5035−5038.
(40) Chakraborty, I.; Govindarajan, A.; Erusappan, J.; Ghosh, A.; Pradeep, T.; Yoon, B.; Whetten, R. L.; Landman, U. The Superstable 25 kDa Monolayer Protected Silver Nanoparticle: Measurements and Interpretation as an Icosahedral $Ag_{152}(SCH_2CH_2Ph)_{60}$ Cluster. *Nano Lett.* **2012**, *12* (11), 5861−5866.
(41) Kurashige, W.; Yamaguchi, M.; Nobusada, K.; Negishi, Y. Ligand-Induced Stability of Gold Nanoclusters: Thiolate versus Selenolate. *J. Phys. Chem. Lett.* **2012**, *3* (18), 2649−2652.
(42) Kurashige, W.; Yamazoe, S.; Kanehira, K.; Tsukuda, T.; Negishi, Y. Selenolate-Protected Au_{38} Nanoclusters: Isolation and Structural Characterization. *J. Phys. Chem. Lett.* **2013**, 3181−3185.
(43) Negishi, Y.; Kurashige, W.; Kamimura, U. Isolation and Structural Characterization of an Octaneselenolate-Protected Au_{25} Cluster. *Langmuir* **2011**, *27* (20), 12289−12292.
(44) Xu, Q.; Wang, S.; Liu, Z.; Xu, G.; Meng, X.; Zhu, M. Synthesis of Selenolate-Protected $Au_{18}(SeC_6H_5)_{14}$ Nanoclusters. *Nanoscale* **2013**, *5* (3), 1176−82.
(45) Zaluzhna, O.; Zangmeister, C.; Tong, Y. J. Synthesis of Au and Ag Nanoparticles with Alkylselenocyanates. *RSC Adv.* **2012**, *2* (19), 7396−7399.
(46) AbdulHalim, L. G.; Ashraf, S.; Katsiev, K.; Kirmani, A. R.; Kothalawala, N.; Anjum, D. H.; Abbas, S.; Amassian, A.; Stellacci, F.; Dass, A.; Hussain, I.; Bakr, O. M. A Scalable Synthesis of Highly Stable and Water Dispersible $Ag_{44}(SR)_{30}$ Nanoclusters. *J. Mater. Chem. A* **2013**, *1*, 10148−10154.
(47) Bakr, O. M.; Amendola, V.; Aikens, C. M.; Wenseleers, W.; Li, R.; Dal Negro, L.; Schatz, G. C.; Stellacci, F. Silver Nanoparticles with Broad Multiband Linear Optical Absorption. *Angew. Chem.* **2009**, *121* (32), 6035−6040.
(48) Harkness, K. M.; Tang, Y.; Dass, A.; Pan, J.; Kothalawala, N.; Reddy, V. J.; Cliffel, D. E.; Demeler, B.; Stellacci, F.; Bakr, O. M.; McLean, J. A. $Ag_{44}(SR)_{30}^{4+}$: A Silver-Thiolate Superatom Complex. *Nanoscale* **2012**, *4* (14), 4269−4274.
(49) Rao, T. U. B.; Nataraju, B.; Pradeep, T. Ag_9 Quantum Cluster through a Solid-State Route. *J. Am. Chem. Soc.* **2010**, *132* (46), 16304−16307.
(50) Bootharaju, M. S.; Pradeep, T. Uptake of Toxic Metal Ions from Water by Naked and Monolayer Protected Silver Nanoparticles: An X-ray Photoelectron Spectroscopic Investigation. *J. Phys. Chem. C* **2010**, *114* (18), 8328−8336.
(51) Chakraborty, I.; Udayabhaskararao, T.; Pradeep, T. Luminescent Sub-nanometer Clusters for Metal Ion Sensing: A New Direction in Nanosensors. *J. Hazard. Mater.* **2012**, *211*, 396−403.
(52) Walter, M.; Akola, J.; Lopez-Acevedo, O.; Jadzinsky, P. D.; Calero, G.; Ackerson, C. J.; Whetten, R. L.; Grönbeck, H.; Häkkinen, H. A Unified View of Ligand-Protected Gold Clusters As Superatom Complexes. *Proc. Natl. Acad. Sci. U.S.A.* **2008**, *105* (27), 9157−9162.

Supporting Information

$Ag_{44}(SeR)_{30}$: A Hollow Cage Silver Cluster with Selenolate Protection

Indranath Chakraborty,[1] Wataru Kurashige,[2] Keita Kanehira,[2] Lars Gell,[3] Hannu Häkkinen,[3] Yuichi Negishi,[2] and Thalappil Pradeep[1]**

1 DST Unit of Nanoscience (DST UNS) and Thematic Unit of Excellence (TUE), Department of Chemistry, Indian Institute of Technology Madras, Chennai 600 036, India; Fax: 91-44-2257 0545;

2 Department of Applied Chemistry, Faculty of Science, Tokyo University of Science, 1-3 Kagurazaka, Shinjuku-ku, Tokyo 162-8601, Japan.

3 Departments of Chemistry and Physics, Nanoscience Center, University of Jyväskylä, Box 35, FI-40014 Jyväskylä, Finland.

1. Chemicals

Silver nitrate ($AgNO_3$, 97%), silver trifluoroacetate (97%), sodium borohydride ($NaBH_4$, 97%), bezeneselenol (95%), ethanol (AR grade), acetone (AR grade), tetrahydrofuran (AR grade) and acetonitrile (AR grade) are from Wako Pure Chemical Industries. All the chemicals were commercially available and were used without further purification.

2. Instrumentation

The UV/Vis measurements were carried out using a double-beam spectrometer (Jasco V-630). The absorbance of raw spectral data are corrected [I(E)] using the following equation and plotted in terms of energy [(1239.8/ Wavelength in nm) = Energy in eV].

$$I(E) = \frac{I(w)}{\partial E/\partial w} \propto I(w)w^2$$

Electrospray ionization mass spectrometry (ESI MS) was performed using a Fourier-transform ion cyclotron resonance (ESI-FT-ICR) (Bruker, Solarix). 1 mg/mL solution of Ag_{44} cluster (in acetone) was used for the measurements with a flow rate of 800 μL/h and the spectra were collected in negative mode. ^{1}HNMR spectra were measured using a 500 MHz Bruker Advance III spectrometer operating at 500.13 MHz and equipped with a 5 mm triple-resonance PFG probe. The sample was prepared in $(CD_3)_2CO$. Thermogravimetric analysis (TGA; Bruker, TGA2000SA) was performed using 4.7 mg of Ag_{44} cluster at a heating rate of 10 °C/min in the temperature range of 25–500 °C. Transmission electron microscopy (TEM) images were recorded using an electron microscope (Hitachi, H-7650) operated at 100 kV, typically using a magnification of 100,000. The samples were drop casted on carbon-coated copper grids and allowed to dry under ambient conditions. Scanning electron microscopic (SEM) and energy dispersive X-ray (EDAX) analyses were performed with a FEI QUANTA-200 SEM. For

measurements, samples were drop casted on an indium tin oxide (ITO) coated glass and dried in vacuum. X-ray photoelectron spectroscopy (XPS) measurements were conducted using an Omicron ESCA Probe spectrometer with polychromatic MgKα X-rays (hυ=1253.6 eV). The samples were spotted as drop-cast films on a sample stub. Constant analyzer energy of 20 eV was used for the measurements.

3. Computational methods

We used density functional theory (DFT) as implemented in the real-space code-package GPAW (Grid-based projector-augmented wave method).[2] Structure optimization was performed using full ligands as used in the experiment, the Perdew-Burke-Ernzerhof (PBE) functional,[3] 0.2 Å grid spacing and 0.05 eV/Å convergence criterion for the maximum forces acting on atoms in clusters. The GPAW set-ups for Ag include scalar-relativistic corrections. Superatom electron state symmetries were analyzed by projecting the wave functions to spherical harmonics with respect to the center of mass of the cluster as described in Ref. 4. Optical absorption spectra were calculated for the PBE relaxed structures using linear response time-dependent DFT and Casida method.[5]

Supporting information 1.

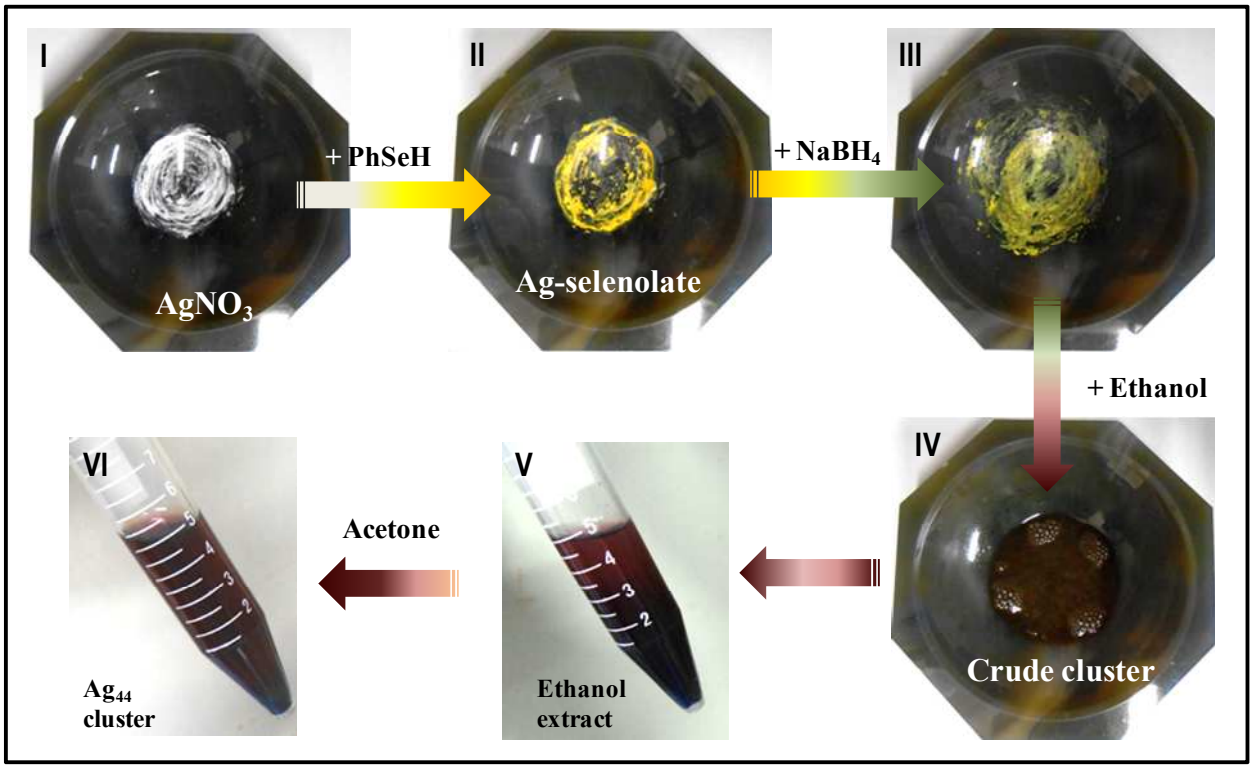

Figure S1. Photographs of various steps during the synthesis. I) ground silver nitrate in a mortar, II) addition of benzeneselenol (PhSeH) to I, III) addition of $NaBH_4$ to II, IV) ethanol addition to III, V) reaction mixture in a centrifuge tube for centrifugation, VI) residue after centrifugation, extracted in acetone. The solution, being concentrated, does not show the pink color clearly. The reduction started when $NaBH_4$ was added and the limited supply of humidity from laboratory atmosphere and moisture from ethanol controlled the growth. Up to step 3, reaction occurs in the solid state. Extraction and washing can also contribute to reduction but the process has started in step 3 itself which gets completed in step 4, after the addition of ethanol. However, upon keeping the system in humid air, reaction can be completed, but will take longer time. The product is also different.

Supporting information 2.

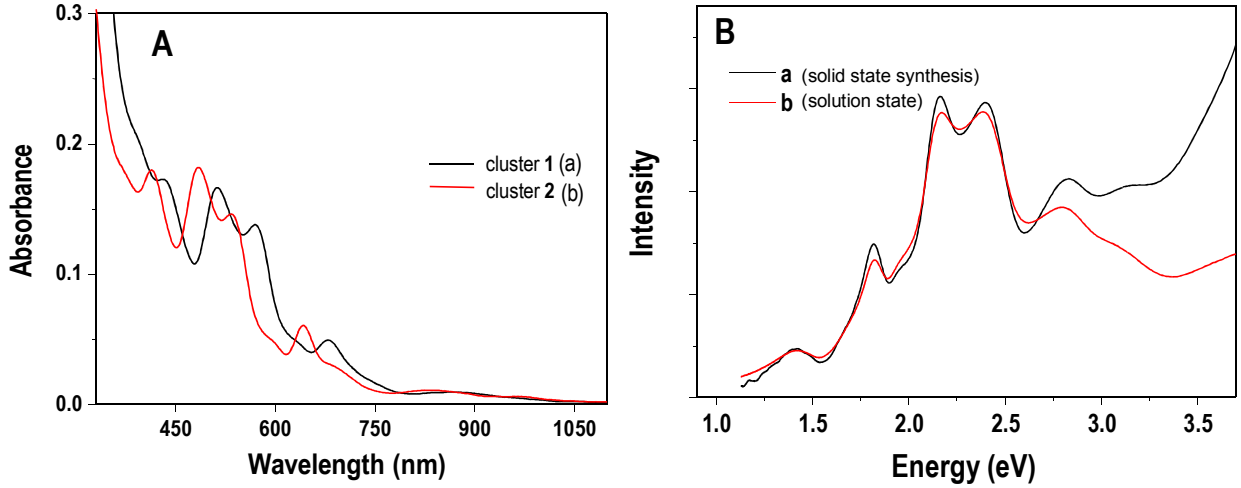

Figure S2. A: The optical absorption spectra for clusters **1** and **2** in acetone and THF, respectively. 'B' shows Comparative UV/Vis spectra of cluster **1** synthesized through solid (a) and solution state (b) routes. Difference, especially in the high energy region is due to the solvents used for measurements (solution phase – acetonitrile and solid state - acetone).

Supporting information 3.

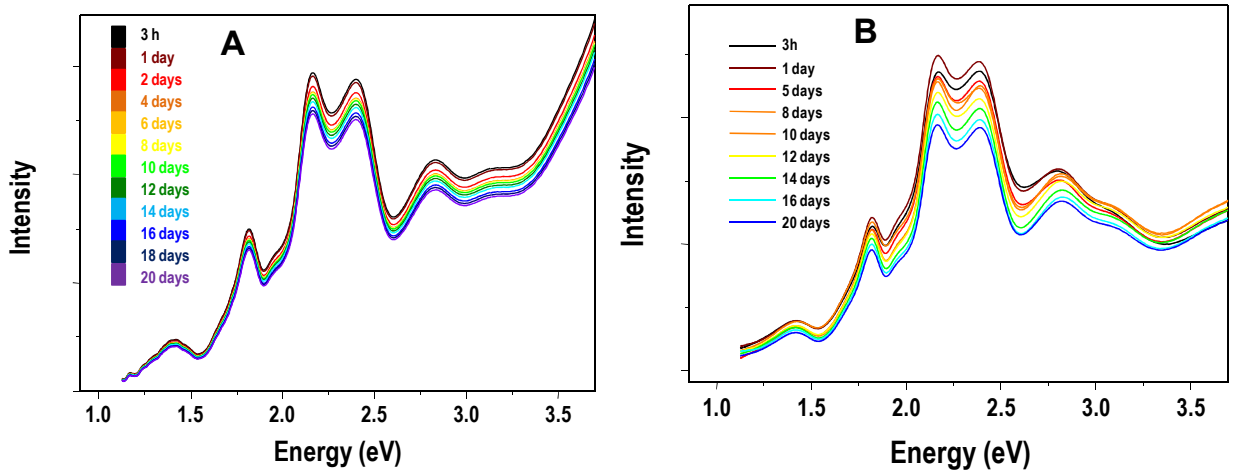

Figure S3. Time dependent UV/Vis spectra of cluster **1** synthesized through the solid and solution state routes (A and B, respectively).

Supporting information 4.

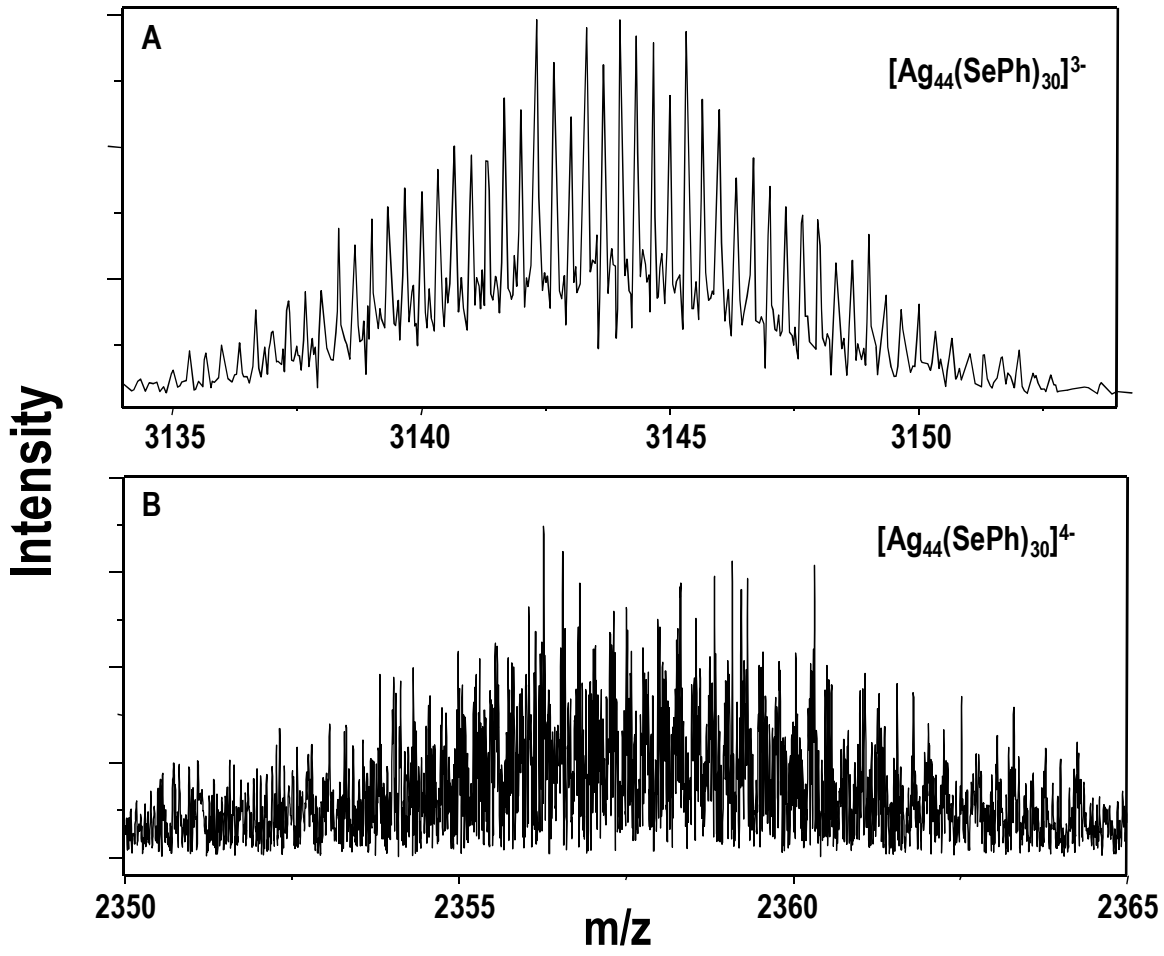

Figure S4. Expanded mass spectra in the 3- and 4- regions of cluster **1**.

Supporting information 5.

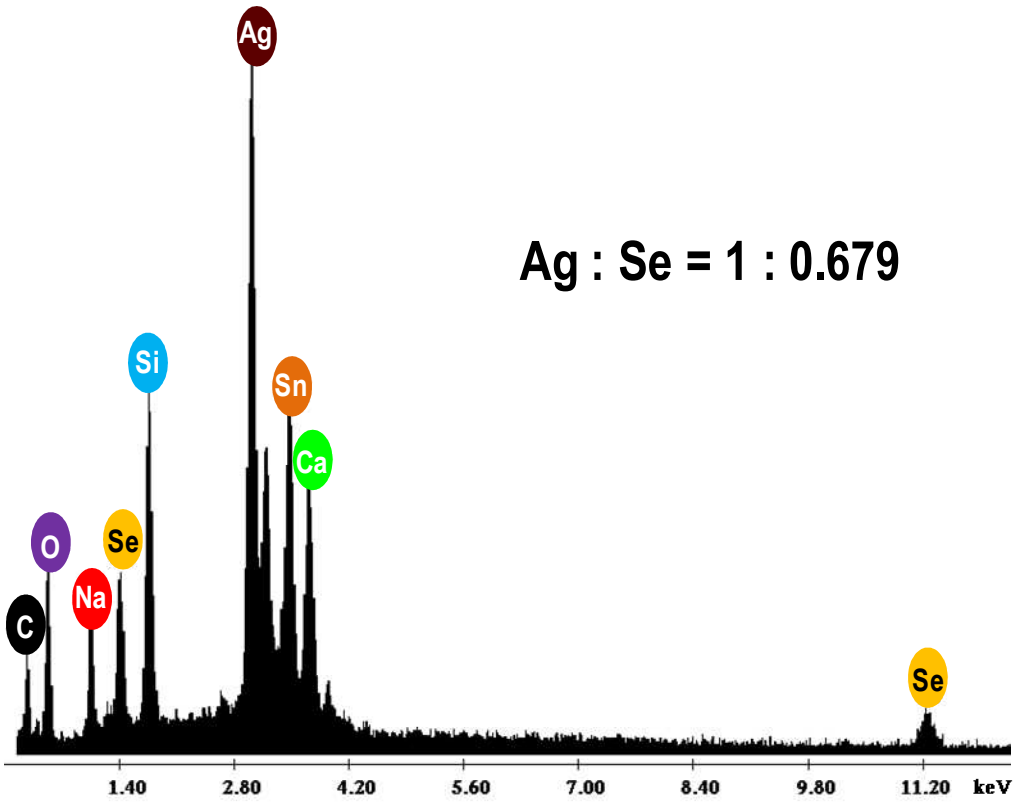

Figure S5. SEM/EDAX spectrum of cluster **1** showing the expected elements. Ca, Sn, and Si are coming from the indium tin oxide plate used as the substrate for drop casting the sample.

Supporting information 6.

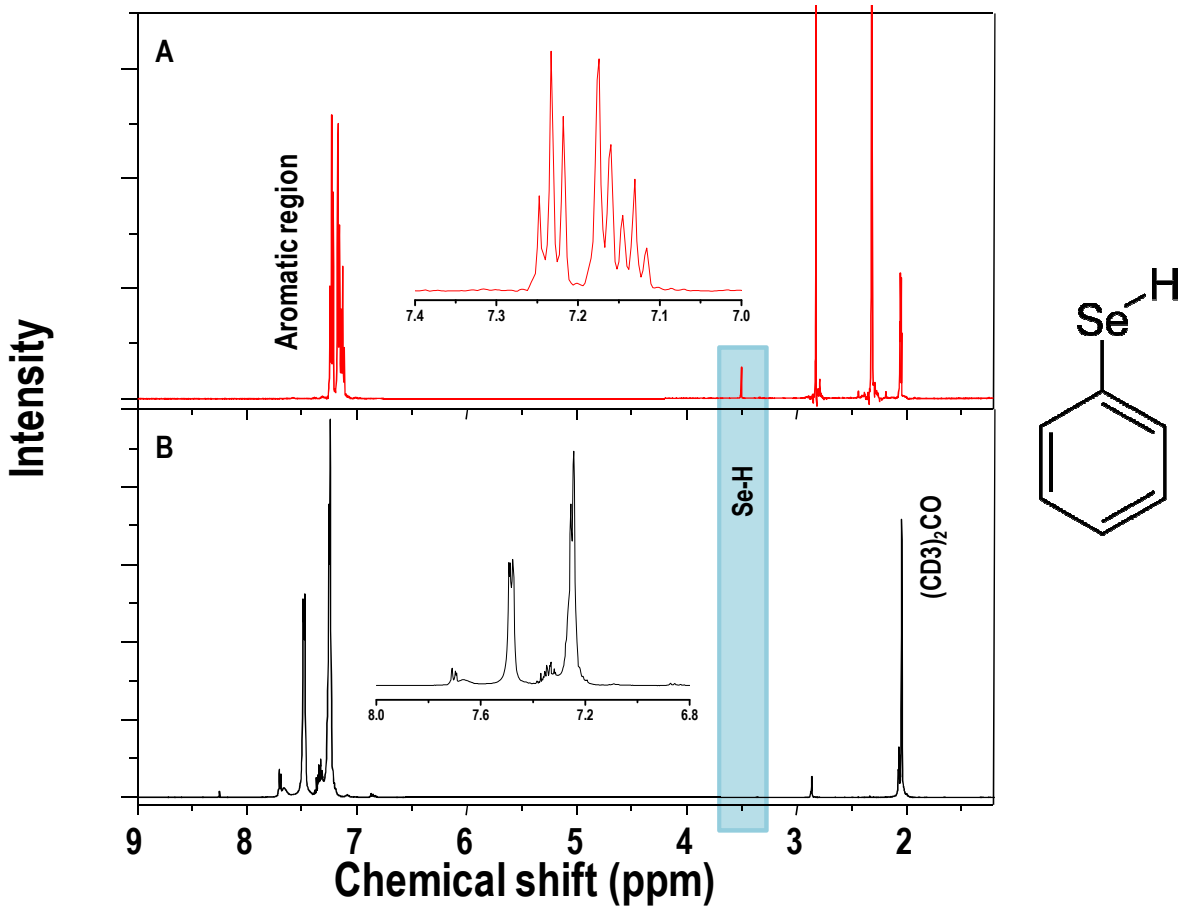

Figure S6. ^{1}HNMR spectra of benzeneselenol (A) and cluster **1** (B). The sample was taken in $(CD_3)_2CO$.

Supporting information 7.

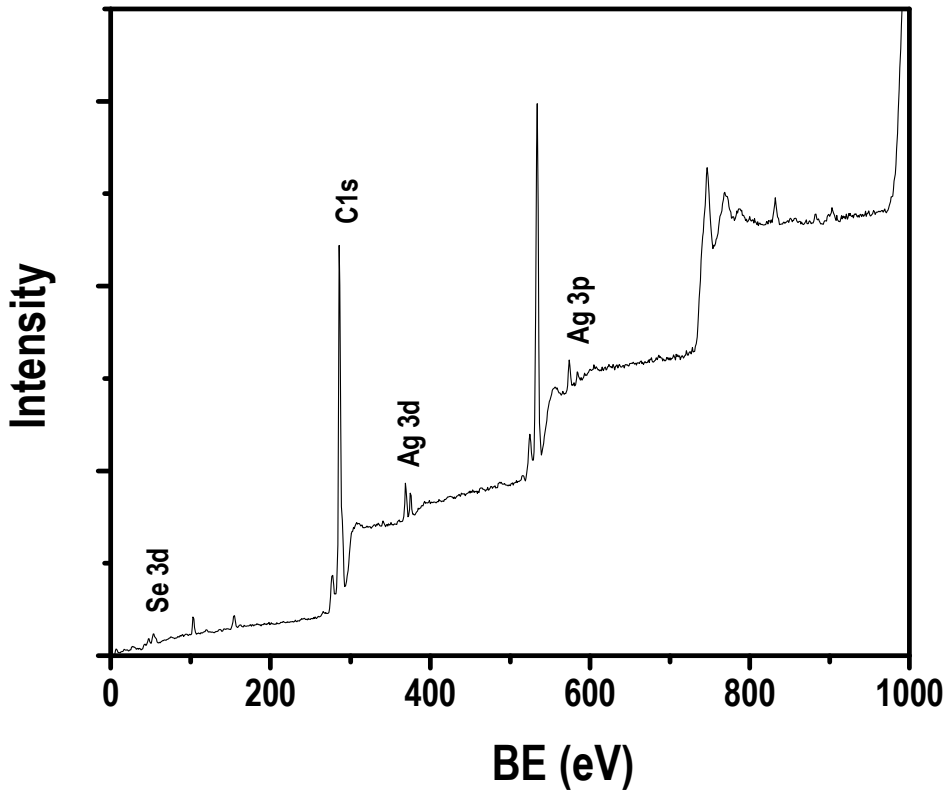

Figure S7. XPS survey spectrum of cluster **1**.

Supporting information 8.

	Ag_{12}	$Ag_{12} \rightarrow Ag_{20}$	Ag_{20}	Ag – X (X = Se, S)
[a]$Ag_{44}(SePh)_{30}^{4-}$	2.908	2.906	3.262	2.713
[b]$Ag_{44}(SPhF_2)_{30}^{4-}$	2.881	2.879	3.231	2.595

Table 1. Selected bond lengths in the clusters (in Å). Ag_{12} denotes bond lengths in the first icosahedral shell, Ag_{12} → Ag_{20} between the first and the second (dodecahedral) shell, and Ag_{20} within the second shell. [a] This work, [b] from ref. 38 in the main text.

Supporting information 9.

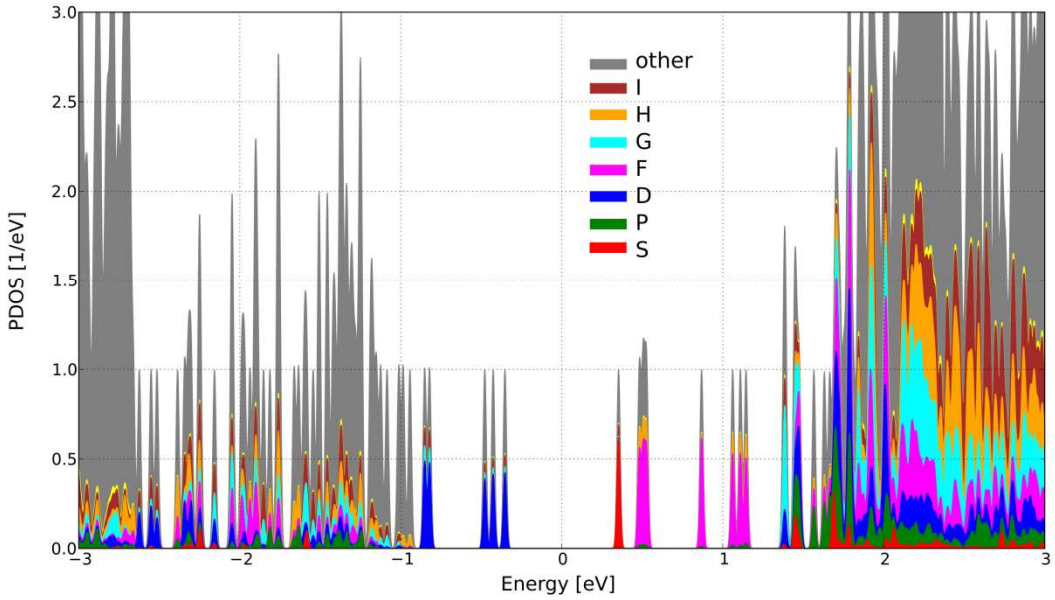

Figure S9. Analysis of the electronic structure of $[Ag_{44}(SePh)_{30}]^{4-}$ as shown by a projected density of electron states (PDOS) vs. state energy in eV. The colors denote weights of projections of individual Kohn-Sham electronic states onto various spherical harmonics centered at the center-of-mass of the cluster. The projection is done up to the angular momentum of L = 6 (I symmetry) as described in detail in ref. 38. (C). The gray area in the peaks shows the weights of angular momenta L > 6. The HOMO-LUMO gap is centered around zero energy. The states around the HOMO- LUMO gap, in the region -1 eV to +1.5 eV, can be described by a single dominant angular momentum character that changes from D-symmetry (blue) to S-symmetry (red) over the HOMO-LUMO gap. Immediately after the S-state, there is a sequence of 7 F – symmetric states. Thus in this energy region, the superatom state sequence $1D^{10}\,2S^2\,2F^{14}$ is seen. The occupied states in the region -2.6 eV to -1 eV are dominantly ligand states, and the silver 4d states span energies < -2.6 eV.

References

(1) Bakr, O. M. et al., *Angew. Chem.* **2009**, *121*, 6035.

(2) Enkovaara, J. et al., *J. Phys. Condens. Matter* **2010**, *22*, 253202.

(3) Perdew, J.P.; Burke. K.; Ernzerhof, M. *Phys. Rev. Lett.* **1996**, *77*, 3865.

(4) Walter, M. et al., *PNAS* **2008**, *105*, 9157.

(5) Walter, M. et al., *J. Chem. Phys.* **2008**, *128*, 244101.

Nanoscale

RSC Publishing

PAPER

Noble metal alloy clusters in the gas phase derived from protein templates: unusual recognition of palladium by gold†

Cite this: *Nanoscale*, 2013, **5**, 12245

Ananya Baksi and T. Pradeep*

Matrix assisted laser desorption ionization of a mixture of gold and palladium adducts of the protein lysozyme (Lyz) produces naked alloy clusters of the type $Au_{24}Pd^+$ in the gas phase. While a lysozyme–Au adduct forms Au_{18}^+, Au_{25}^+, Au_{38}^+ and Au_{102}^+ ions in the gas phase, lysozyme–Pd alone does not form any analogous cluster. Addition of various transition metal ions (Ag^+, Pt^{2+}, Pd^{2+}, Cu^{2+}, Fe^{2+}, Ni^{2+} and Cr^{3+}) in the adducts contributes to drastic changes in the mass spectrum, but only palladium forms alloys in the gas phase. Besides alloy formation, palladium enhances the formation of specific single component clusters such as Au_{38}^+. While other metal ions like Cu^{2+} help forming Au_{25}^+ selectively, Fe^{2+} catalyzes the formation of Au_{25}^+ over all other clusters. Gas phase cluster formation occurs from protein adducts where Au is in the 1+ state while Pd is in the 2+ state. The creation of alloys in the gas phase is not affected whether a physical mixture of Au and Pd adducts or a Au and Pd co-adduct is used as the precursor. The formation of Au cores and AuPd alloy cores of the kind comparable to monolayer protected clusters implies that naked clusters themselves may be nucleated in solution.

Received 12th August 2013
Accepted 24th September 2013

DOI: 10.1039/c3nr04257j

www.rsc.org/nanoscale

1. Introduction

Monolayer protected sub-nanometer clusters of noble metals having precise composition are some of the most fascinating materials of current research.[1–5] Intense luminescence, unusual catalysis, and novel physical properties (such as magnetism) have made these systems subjects of passionate research. Despite the discovery of numerous clusters with diverse composition,[6–26] only four clusters, namely, $Au_{25}(SR)_{18}$,[7,11] $Au_{38}(SR)_{24}$,[23] $Au_{102}(SR)_{40}$,[24] and most recently $Au_{36}(SR)_{24}$ (ref. 26) have been crystallized so far. The possibility of modifying the composition by alloying the core has been explored in several cases. Recently, $Au_{24}Pd(SR)_{18}$ (ref. 27) and $Au_{36}Pd_2(SR)_{24}$ (ref. 28) have been characterized. Along with monolayer protected clusters, analogous systems with macromolecular protection, especially in protein templates, have also been made.[29–48] Bovine serum albumin (BSA),[29–36] lactoferrin (Lf),[37,38] lysozyme (Lyz)[39–44] and some other proteins like insulin[45] are used for these kinds of studies, among which BSA is the most thoroughly studied. Cluster cores composed of Au_{25} and Au_{13} are most stable in larger proteins like BSA[29] and Lf[37,38] whereas the fairly smaller Au_{10} core is being stabilized by Lyz.[43] Analogous clusters of Ag[31] and recently Cu[46] clusters have been investigated, although less commonly. Alloys of Au and Ag[36] with distinct composition have also been prepared in proteins like BSA. Utilization of these clusters using their enhanced luminescence due to Föster resonance energy transfer (FRET) and biocompatibility due to the presence of proteins along with the specific molecular affinity has made them promising for biolabelling applications[30,45] and specific molecular sensing.[40]

While protected clusters have been many, the naked analogues of them, *i.e.* clusters without protection have not been seen in mass spectrometric investigations of gas phase clusters. In other words, while $Au_{25}(SR)_{18}$ is known to be stable, its gas phase analogue, naked Au_{25}, has not been observed. This is true for all the clusters belonging to this category. Creation of clusters with unusual stability in gas phase experiments requires the aggregation and stabilization energy to be removed efficiently. It has been seen recently that this is indeed possible by the use of protein templates in laser desorption and ionization experiments.[44] These investigations show the formation of gas phase clusters of naked metal cores of magic numbers such as Au_{18}^+, Au_{25}^+, Au_{38}^+ and Au_{102}^+, where cluster formation is proposed to occur in the vicinity of protein, in the gas phase.

Such observations suggest the possibility of creating naked alloy cores of specific composition in similar experiments. In this paper, we report the formation of naked alloy cores of specific nuclearity in the gas phase, derived from lysozyme and metal ion-catalyzed enhancement of specific cluster cores. Among a number of metals investigated (Ag, Pt, Pd, Cu, Fe, Ni and Cr), only palladium (Pd) is shown to create alloy cores similar to the ones seen in monolayer protected clusters. A new

DST Unit of Nanoscience (DST UNS) and Thematic Unit of Excellence, Department of Chemistry, Indian Institute of Technology Madras, Chennai 600036, India. E-mail: India.pradeep@iitm.ac.in; Fax: +91-44 2257-0545

† Electronic supplementary information (ESI) available. See DOI: 10.1039/c3nr04257j

cluster core is also observed with Pd. The results reiterate the possibility of creating stable unprotected alloy cluster nuclei using macromolecular templates. The presence of Pd ions in the system catalyzes the formation of Au_{38}^{+} when incubated for 48 hours. Peak positions remain essentially the same in the case of positive and negative ion modes. We have also studied the effect of ionization method on the number of metal ion attachments to protein and found that the observed affinity is different when the ionization method is changed from ESI to MALDI. Similar peaks are observable whether Au and Pd adducts are mixed together to get the precursor or Pd^{2+} salt is directly added to the Au–Lyz adduct. Specific metal ions can enhance formation of Au_{25}^{+}. Here we propose a plasma reaction in the gas phase between ions and molecules in the plasma. The deposition of such clusters on active substrates can create novel catalysts for examining elementary catalytic processes.

2. Experimental

2.1. Materials

Tetrachloroauric acid trihydrate ($HAuCl_4 \cdot 3H_2O$) was prepared in our laboratory starting from pure gold. Lysozyme, extracted from chicken egg white (>90% purity), and sinapic acid used as a MALDI MS matrix were purchased from Sigma Aldrich. Palladium chloride ($PdCl_2$) was purchased from Rankem. All the chemicals were used without further purification. Deionized water was used throughout the experiment.

2.2. Synthesis of metal adducts

When metal ions are added to the protein solution, they are taken up by the amino acids of the protein and form adducts or complexes. In the case of addition of Au^{3+} to protein, it results in the formation of an Au^{+}–protein adduct as seen in X-ray photoelectron spectroscopy.[38] Further reduction of this gold bound protein complex under basic conditions produces solution phase luminescent quantum clusters.[29] Here we have restricted our study up to the complex formation step. Solution phase cluster formation has been studied elsewhere.[43] The metal–protein adducts were prepared in two different ways:

(a) Au–Lyz and Pd–Lyz adducts were prepared by mixing Lyz and the specific metal salts to get a final concentration of 1.5 mM Lyz and 5 mM in terms of metal ions and incubating the mixture for 2 hours. The resulting adducts were mixed together in different concentration ratios (Au : Pd = 1 : 3, 1 : 1 and 3 : 1) and incubated for 4 hours and the resultant product was subjected to MALDI MS analysis. These samples are labeled as Au–Pd mixed adducts. The best result was obtained for the 3 : 1 Au : Pd mixed adduct.

(b) For the other case, first, the Au–Lyz adduct was prepared as above mentioned by mixing Au^{3+} and Lyz followed by incubating the mixture. To this adduct, different volumes of $PdCl_2$ were added directly to get Au–Lyz : $PdCl_2$ ratios of 5 : 1, 5 : 2, 5 : 3, and 5 : 4. The resultant mixture was further incubated for four hours and subjected to MALDI MS study. These samples are labeled as Au–Pd co-adducts.

2.3. Spectrometric analysis and instrumentation

MALDI MS analysis. Experiments were conducted in a matrix assisted laser desorption ionization time-of-flight (MALDI TOF) spectrometer. For this, an Applied Biosystems Voyager-De Pro MALDI TOF instrument was used. The spectra were collected in the m/z range of 2000–100 000 using a N_2 laser at 337 nm. For acquiring each spectrum, a minimum of 100 laser shots were fired and the data were averaged. Laser power was kept at a slightly higher value than the threshold power for this system (threshold laser power for these systems is about 1800 in terms of the instrumental unit, we have kept the power at 2200). The minimum delay time used was 10 ns and the maximum was 1500 ns for a delay time-dependent experiment. For all other experiments, the delay time was kept at 1000 ns. The samples probed were protein–metal conjugates or adducts of specific composition. Laser induced desorption–ionization and associated chemistry produced naked clusters in the gas phase. Instrumental resolution was $\Delta m/z = 2$ Da in the range investigated. All the compositions were compared with their isotope patterns. Sinapic acid was used as a matrix for these experiments. To 10 mg of sinapic acid, 1 mL of 0.1% trifluoroacetic acid (TFA) and an acetonitrile mixture (3 : 1) were added. For spotting, 100 μL of matrix was mixed well with 5 μL of the sample to be analyzed and spotted to get a dry droplet. The same procedure was repeated at least for three different sets for each sample (prepared separately) to check the reproducibility. All the instrument parameters are listed below for linear positive mode and are applicable for the specific instrument used:

Instrument mode: linear, positive
Delay time: 1000 ns (minimum is 10 ns)
Laser intensity: 2200 (instrumental unit)
Mass range (Da): 2000–100 000
Low mass gate (Da): 500
Calibrated for the matrix: Sinapic acid
Voltages:
Accelerating: 2000 V
Grid: 87 (0.0–99.9% is the instrument range)
Grid wire: 0.03 (0.000–0.300% is the range)

ESI MS analysis. For the solution phase study, electrospray ionization mass spectrometry (ESI MS) was carried out. For this experiment, an Applied Biosystems 3200 QTRAP LC/MS/MS was used. Spectra were collected in the m/z range of 500–1700 and data were averaged for 100 scans. Declustering and entrance potentials were optimized at 50 and 10 V, respectively. As prepared Au, Pd and mixed adducts were used for this purpose. All the spectra were collected in positive ion mode. 10 μL of TFA was added to 1 mL of these solutions to enhance ionization. Spectra were deconvoluted using Magtran software to get singly charged species from a series of multiply charged spectra (for Lyz, the parent spectrum contains +9 to +12 charge states in the m/z window investigated).

XPS analysis. XPS analysis was done using an Omicron ESCA probe spectrometer and polychromatic Mg Kα ($h\nu = 1236.6$ eV) was used as the ionization source. Curves were smoothed and fitted using the CasaXPS software. For this analysis, a 3 : 1 Au–Pd mixed adduct of Lyz was used.

SEM/EDAX analysis. Scanning Electron Microscopy (SEM) and Energy Dispersive Analysis of X-ray (EDAX) images were collected using an FEI QUANTA-200 SEM instrument.

3. Results and discussion

3.1. Gas phase gold–palladium alloy formation

For our study, we have used a small protein lysozyme (Lyz, molecular weight 14.3 kDa) as the template for gas phase alloy cluster formation. It contains 129 amino acid residues among which eight are cysteines forming 4 disulphide bonds. The overall size of the protein is around 4 nm and contains 49% helical structure. The structure and position of the cysteines and disulphide bonds are presented in Fig. S1.† This helical structure is greatly affected by the breakage of disulphide bonds and an overall 28% loss in helicity was observed in a previous study upon cluster formation.[43] Unlike other proteins, the Lyz mass spectrum is dominated by its monomer as well as aggregates. For example, Lyz^+ appears at 14.3 kDa, whereas Lyz_2^+, Lyz_3^+, and Lyz_4^+ appear at 28.6, 42.9, and 57.2 kDa, respectively. Once metal ions like Au^{3+} are added to the system, amino acids reduce Au^{3+} to Au^+ and metal–protein adducts form. Adducts form when Pd^{2+} too is added to the system. These transition metals have higher affinity towards sulphur; therefore it is obvious that an M–S bond will be formed. By this process, the disulphide bond has to break to accommodate multiple metal ions inside the protein. For the Au^{3+} addition, we have seen a maximum of 10 Au attachments to protein,[44] which implies that there are other binding sites also present in the system like carboxyl or amine groups. When both Au and Pd adducts are mixed together as described in 2.2, they form a mixed adduct. These adducts are subjected to MALDI MS analysis and the corresponding mass spectra were collected. Fig. 1 compares the positive ion MALDI MS spectra of the Au adduct of Lyz with those of mixed Au and Pd adducts and parent Lyz. In the full mass range, Lyz shows a series of peaks attributed to Lyz^+, Lyz_2^+, Lyz_3^+, *etc.* In the lower mass region (*m*/*z* 2000–11 000), the spectrum is dominated by the +2 charge state, no other charge state or fragments were observed. As before, the Au adduct shows bare cluster cores with a specific number of atoms like Au_{18}^+, Au_{25}^+, Au_{38}^+ and Au_{102}^+.[44] These peaks appear with additional features separated by one gold atom and they may be represented as $Au_{18\pm n}^+$, $Au_{25\pm n}^+$, *etc.* ($n = 0, 1, 2,\ldots$). In all of the clusters, the cores try to achieve electronic stability by accruing electrons from ligands and this is shown in the form of sulfur addition peaks for specific clusters like $Au_{18}S_4^+$.

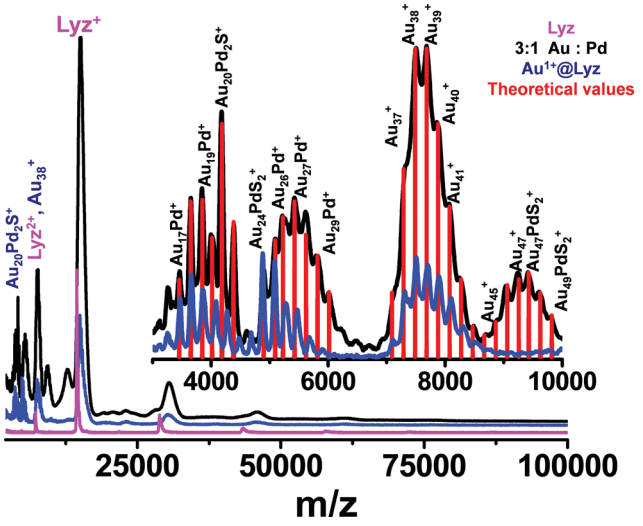

Fig. 1 MALDI MS study of Au and Au–Pd adducts of Lyz in the positive ion mode in the range of 2000–100 000 Da. The 3000–10 000 Da region has been expanded in the inset. Au–Pd adducts show distinctly different features compared to Au-alone adducts, due to the formation of alloys. The assigned peaks match well with the theoretical values.

In the mass spectrum of the Au–Pd adduct, besides the peaks observed for Au, new peaks attributed to alloys are also observed. These are particularly seen in the case of cluster ions of Au_{18} and Au_{25}. While the cluster region of Au_{38} does not show any alloy formation, the peak intensity is greatly enhanced in comparison to the Au adduct. The spectra in the Au_{18} and Au_{25} region show markedly different distributions. While Au_{18}^+ and Au_{25}^+ were the most intense features in the parent adduct, the alloy ions exhibit a completely different intensity pattern possibly due to their different stability. All the assigned peaks match well with their calculated spectra as represented in the inset of Fig. 1. In the Au_{18}^+ region, a series of peaks appear in an envelope starting from $Au_{16}Pd^+$ and continue up to $Au_{19}Pd^+$. The very next peak appears with another Pd attached to it. In this envelope, $Au_{20}Pd_2S^+$ is the most intense peak. After $Au_{22}PdS^+$, this envelope overlaps with the Au_{25}^+ region. Starting from $Au_{23}Pd^+$, the envelope continues with Pd attachment with a few sulfur additions. Unlike in the solution phase, where $Au_{24}Pd(SR)_{18}$ is found to be the most stable,[27] $Au_{27}Pd^+$ shows the highest intensity in the gas phase, although neighboring peaks do not vary much in terms of abundance. This implies nearly equal stability of the alloy cores in that region in the gas phase.

Interestingly, the Au_{38} region does not show any Pd attachment. Although it is possible to get $Au_{36}Pd_2(SR)_{24}$[28] by doping Pd to Au_{38} in the solution phase, using a protein template, it is not easy to get the same core in the gas phase as protein allows Au_{38}^+ to acquire structural and electronic stability as already discussed above. One extra envelope appears after the Au_{38} region which was not present in the case of the Au adduct. Here, $Au_{47}PdS_2^+$ is having the maximum intensity. Other peaks with Pd doping have also been observed, although the intensities do not differ much. It should be noted that Au_{47}^+ is not a magic number core neither by the number of core atoms nor by the electron count and it was not observed with the Au–Lyz adduct. So the presence of Pd helps in the formation of metastable cluster cores in the gas phase through the interaction with protein. The same sample was analyzed in linear negative mode too. Peak positions remain essentially the same in negative ion mode although there is slight change in their intensity distribution. No new peak appears in this case (Fig. S2†).

We have also conducted a laser intensity-dependent study to check whether there is any role of laser intensity in the formation of these clusters. The threshold laser intensity is the

minimum intensity where we can see the appearance of the specific peaks. It is often a practice to keep the experimental laser intensity slightly higher than the threshold intensity to avoid laser induced damage and at the same time get good quality data. In our case, threshold laser intensity was found to be 1800 in terms of the instrumental unit (details of experimental parameters are given in the Experimental section under the MALDI MS analysis sub-section). At the minimum laser intensity (*i.e.*, threshold intensity) also we can see the same peaks as described above for the 3 : 1 Au : Pd mixed adduct. We have slowly increased the intensity to 2600 with an increment of 200 step size (Fig. S3†). Peak positions remain the same as well as the intensity distribution for all the laser intensities studied. The best spectrum was observed with a laser intensity of 2200 and the same was used for all the other studies.

Formation of specific cores can be explained in terms of the enhanced stability of such cores in the gas phase. Au_{25} and Au_{38} systems are known to have magic number stability through a closed shell electronic structure. Magic number configuration (n^*) requires a certain number of delocalized electrons like $n^* =$ 2, 8, 18 (20), 34 (40), 58, 92, *etc.* For example, Au_{38} contains 38 delocalized electrons and hence is not a magic number. To achieve magic number stability, it has to lose 4 electrons which is possible by interacting with the protein. The key observation from a theoretical calculation reported before[44] predicts that these clusters formed in the gas phase namely, Au_{25}^+, Au_{38}^+, *etc.* do not have a magic number to begin with but require the removal of n–$n^* = 5, 4$ electrons, respectively to achieve it.[44] This is possible through the interaction with the cystines (dimeric cysteine). We have calculated the interaction with only the cystine part of the protein, as simulating the whole protein is really difficult. When one cystine (S–S bond) breaks on the cluster surface, two cysteines form and the cluster core loses two electrons by this process. For the Au_{38}^+ system, it requires interaction with two cystines to lose 4 electrons and become a 34 electron system giving magic number stability. By this process, a HOMO–LUMO gap of $\Delta_{HL} = 0.48$ eV opens up (whereas for the neutral Au_{38} cluster, $\Delta_{HL} = 0.0$ eV) and the cluster gets electronic stabilization. This is also reflected in their calculated structures.

From this part of the study, it can be concluded that Pd forms an alloy with gold in the gas phase and it also facilitates the emergence of metastable clusters in the gas phase. It is noted that very small gas phase Au–Pd alloys have been reported.[49,50] Incorporation of a single Pd to Au cluster core enhances its catalytic activity tremendously.[49]

3.2. Unusual recognition of palladium by gold in the gas phase

As discussed in the previous section, Pd is recognized by Au in the gas phase. There are several metals known to form alloys with gold in the bulk as well as in the nanosize regime, like Ag, Cu, Pt, *etc.* In Fig. 2, we present the mass spectra with different metal ions spanning the 3d, 4d and 5d elements which are typically known to form alloys with gold. As we can see, only in the case of Pd, distinct alloy formation is noticed and in this

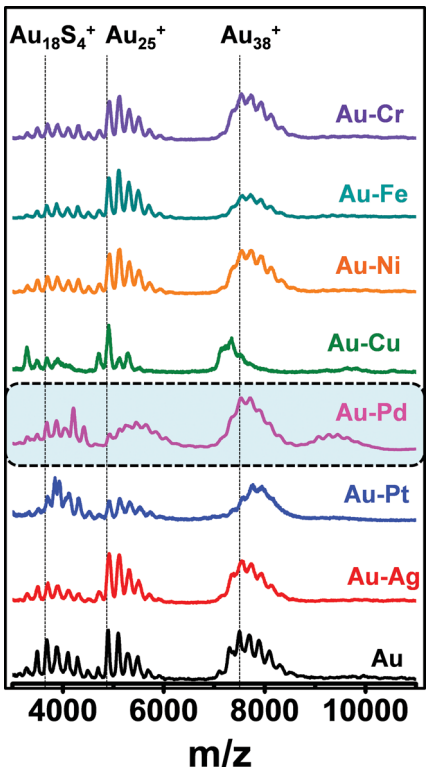

Fig. 2 MALDI MS study of the effect of metal ions on the gas phase alloy formation. 3d, 4d and 5d metal ions, known to form alloys with gold, are chosen for this study. All the concentration ratios of Au and M-adducts are the same. Mixed adducts of gold and individual metal have been used for this study. Only Pd shows distinct alloy formation, which has been highlighted.

spectrum we mark a region with a black rectangle to show the difference. Au–Lyz and M–Lyz (M = Ag, Pt, Pd, Cu, Ni, Cr and Fe) adducts were mixed together in a 3 : 1 ratio and a MALDI MS study was carried out. With the addition of the Pt–Lyz adduct, nearly all the peak positions remain the same but the envelope changes and the $Au_{18}S_4^+$ region becomes more intense than the Au_{25}^+ region. The $Au_{19}S_4^+$ peak splits into two, separated by 100 mass units (Fig. S4†). The peak at m/z 3839 can be assigned as $Au_{19}S_3^+$ and the next peak at m/z 3935 can be attributed to $Au_{19}S_6^+$, considering no alloy formation with Pt. Since atomic weights of Pt and Au are very close, it is difficult to decide whether any alloy formation has happened or not in this case. Ag is well known to form both solution phase Ag_{QC} and AuAg alloy clusters in proteins and also with monolayer protection. But the gas phase reactivity does not match with the expected solution phase interaction as Ag does not form an alloy with Au under similar conditions. Several gas phase Au–Ag alloys have been reported previously.[51–53] Very small cores like Au_mAg_n ($m + n = 3, 5$)[51] as well as bigger cores like Au_mAg_n ($m + n = 19$–45)[53] are also studied in the context of gas phase reactivity like binding activity with O_2 and CO for conversion to CO_2. But in the case of our gas phase cluster synthesis using protein templates, without any reducing agent, no alloy formation was observed. The Au_{25}^+ intensity gets enhanced in the presence of Ag to a greater extent than Au alone but the peak positions remain the same (Fig. S5†). Therefore, we can catalytically

enhance the formation of Au_{25}^{+} in the gas phase from the protein template by incorporating Ag in the system. Copper is also known to form an alloy with gold and recently Negishi's group could dope a maximum of five copper atoms in the $Au_{25}(SR)_{18}$ system.[54] In the gas phase, however, a drastic change was found in the overall spectrum upon Cu addition. As Cu has a high affinity towards sulphur, it occupies Au binding sites in Lyz. This effect is reflected in the main protein peak also where only a few Au attachments are observed. In the inset of Fig. S6,† a monomer of the Au–protein adduct and the Au–Cu adduct of Lyz is compared. It is clear that in the case of the Au–Cu adduct, the number of Au attachments is less (a maximum of 10 Au attachments are seen for the Au adduct, whereas only two Au attachments are seen for the Au–Cu adduct). The same thing is also reflected in the aggregates marked by green dotted circles. Interesting changes occur in the lower mass region where gas phase clusters form. The mass spectrum indicates that exclusively Au_{25}^{+} species form in that range and the shape of the envelope changes (Fig. S6 inset (b)†). So by adding Cu to the gas phase Au precursor, we can selectively get Au_{25}^{+} prior to the mixture of clusters. In the presence of 3d transition metals like Ni, Cr and Fe, the intensity of the Au_{25}^{+} region enhances relative to Au_{18}^{+} and Au_{38}^{+} regions, compared to the Au-alone case (Fig. S7–S9†). Therefore, catalytic enhancement of Au_{25}^{+} is possible by using these metal ions. This effect is maximum in the case of Fe addition where the intensity of $Au_{18}S_4^{+}$ and Au_{38}^{+} regions remains the same but the intensity of the Au_{25}^{+} region increases to a greater extent compared to Ni and Cr. In all the cases, the $Au_{18}S_4^{+}$ intensity decreases. No alloy formation was observed in any of these cases. This study concludes that Pd is the only metal recognized (selected) by Au in gas phase alloy formation. If we consider electrochemical potential for Au, Pd, Pt, Ag and Cu, standard reduction potentials are as follows:

$$Cu^{2+} + e^{-} \rightarrow Cu^{+},\ E^{0} = 0.159\ V$$

$$Cu^{+} + e^{-} \rightarrow Cu,\ E^{0} = 0.520\ V$$

$$Ag^{+} + e^{-} \rightarrow Ag,\ E^{0} = 0.7996\ V$$

$$Pd^{2+} + 2e^{-} \rightarrow Pd,\ E^{0} = 0.915\ V$$

$$Pt^{2+} + 2e^{-} \rightarrow Pt,\ E^{0} = 1.188\ V$$

$$Au^{3+} + 2e^{-} \rightarrow Au^{+},\ E^{0} = 1.36\ V$$

$$Au^{+} + e^{-} \rightarrow Au,\ E^{0} = 1.83\ V$$

From these electrode potentials, it is clear that Au^{3+} can be easily reduced to an intermediate Au^{+}–protein complex. It is this Au^{+}–complex that forms the Au clusters in the gas phase which are in the Au(0) state. Both Pd^{2+} and Pt^{2+} have reduction potentials next to Au^{+} and it is likely that Pd^{2+} and Pt^{2+} can be reduced to Pd^{0} and Pt^{0} in the gas phase. But as Pt and Au mass numbers are almost the same, we cannot exactly tell if there is any alloy formation or not with Pt. But Pd and Au mass difference is nearly 90 amu and it is rather easy to distinguish Pd added alloy cluster peaks from the original Au cluster peaks.

3.3. Difference in metal ion binding

From the previous discussion, it is clear that only Pd is recognized by gold in the gas phase. If we see carefully, the binding tendency of these metal ions is completely different from each other. To verify our argument, we have performed a detailed ESI MS and MALDI MS study for each metal adduct of protein, namely, Au, Ag, Pd, and Pt. The same protein to metal ratio (Lyz 1.5 mM and M ion 5 mM) was used to avoid concentration-dependent issues. As we have shown before, with all the concentration of Au^{3+} used, we can see only upto 3 Au attachments to the protein. As there are only 8 cysteines in the protein and Au binding is strongly dependent on the number of cysteine residues and hence after a certain Au^{3+} concentration binding sites are saturated. When these adducts were examined using MALDI MS, a maximum of 10 Au attachments were observed and bare clusters were formed as already described. This decrease in the number of Au attachments in the solution phase mass spectrum (ESI MS) can be attributed to charge-induced dissociation of the high charge states (+8 to +12 are normally observable for Lyz and Lyz_2 in positive mode ESI MS).[43,44] Binding of Ag ions to protein is completely different from Au (Fig. S10†). For both monomer and dimer regions, a +8 charge state shows the maximum number of Ag attachments (more than 12 Ag attachments are observed). Another interesting observation is that for this specific charge state, two consecutive Ag bound peaks have the same intensity. These 8 Ag attachments can be justified considering 8 cysteines and similar intensity patterns can be due to the breakage of 4 cystine bonds. Once one cystine bond is broken, two Ag can be attached to two different sulphur ends with equal probability and hence the same intensity for two consecutive Ag bound peaks. So, Ag can be attached to cysteines as well as –COOH or NH_2 groups (as more than 8 Ag are attached) but the binding affinity is different. When the same sample is used for MALDI MS analysis, it shows no Ag attachment to it, which implies that Ag is loosely bound to the protein and at the experimental conditions used, it desorbs from the template and we cannot see any attachment. We have not seen any gas phase bare Ag cluster either, unlike in the case of Au (Fig. S11†). For the Pd–Lyz adduct, we see multiple peaks separated by Pd in the ESI MS analysis. A maximum of 8 Pd attachments can be seen clearly in this case (Fig. S12†). As Pd has multiple isotopes, the peaks are broader but due to poor resolution, clear isotope distribution is not seen for that charge state. The same sample shows only a single Pd attachment in MALDI MS analysis (Fig. S13†) but no gas phase Pd clusters were observed. When Pt–Lyz adducts were studied using ESI MS analysis, a maximum of 6 Pt attachments were observed (Fig. S14†). Strangely, odd numbered Pt attached peak intensities are very poor compared to the even numbered Pt attached peaks which again proves indirectly the breakage of S–S bonds in cystines. Unlike in other metal ions, Pt shows nearly the same number of attachments in MALDI MS also where we see a broad peak separated by 8 Pt from the parent protein peak and the free protein peak is not observed in this case. Dimer, trimer, *etc.* comprise a multiple of 8 Pt as observed for Au. The peak position remains the same whether we use

additional NaOH or $NaBH_4$ (Fig. S15†). This confirms strong binding affinity of Pt towards Lyz. From these studies, it is confirmed that metal ion binding affinities are different for each system and the observed spectrum depends strongly on the ionization method used (ESI or MALDI).

3.4. Solution phase studies of Au–Pd mixed adducts

In order to check the possibility of formation of the above mentioned alloy clusters in solution, electrospray ionization spectra of Au, Pd and Au–Pd adducts of Lyz were analyzed. While Au shows a limited number of attachments (up to 3) to Lyz, Pd has multiple attachments to Lyz (up to 8). When these two adducts are mixed together in different ratios like 1 : 3, 1 : 1 and 3 : 1 (with respect to Au and Pd adducts of Lyz, respectively), mixed attachment features appear in the positive ion mode of ESI MS (Fig. 3a). Distinct separations for Au and Pd are observed. As two Pd attachments and one Au attachment fall at nearly the same mass range and also Pd has multiple isotopes, it is hard to differentiate them. From this solution phase study, we conclude that both Au and Pd can be attached simultaneously to Lyz. However, no naked alloy clusters were seen in solution. This concludes that cluster formation occurs in the gas phase. Lyz as well as metal adducts of Lyz show multiple charge states like +12, +11, +10 and +9 in the mass range studied. Each of these spectra can be deconvoluted to get the molecular ion peaks arising from these charge states. The deconvoluted spectrum of Au–Lyz shows two peaks due to one and two Au attachments to it, whereas Pd–Lyz shows two peaks due to three and four Pd attachments. When these two adducts are mixed in a 3 : 1 ratio, the deconvoluted spectrum shows multiple peaks including parent protein besides Pd as well as Au attachment peaks and mixed Au : Pd peaks, as shown in Fig. 3b.

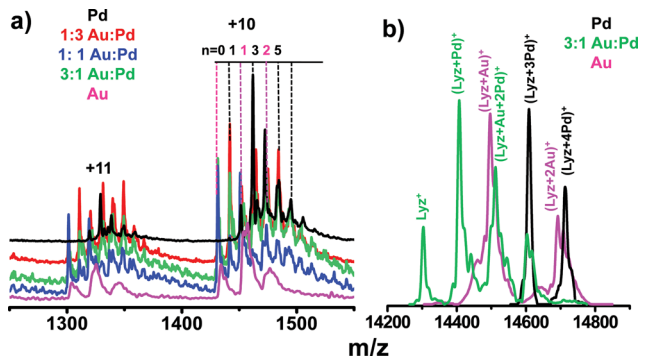

Fig. 3 (a) ESI MS of Au, Pd and Au–Pd mixed adducts of Lyz showing individual peaks due to Au and Pd attachments. In the mixture, Au and Pd attachment peaks are seen. (b) Deconvoluted spectra of Au, Pd and mixed adducts of Lyz. The 3 : 1 Au : Pd adduct shows peaks due to simultaneous attachment of Au and Pd.

3.5. Alloy formation in the solution state

As reported in our previous study, a small Au cluster core (Au_{10-12}) can be stabilized inside a single Lyz molecule.[43] Here red luminescent Au clusters were prepared by reduction of Au^{3+} to Au^0 in the basic medium. The monomer as well as aggregates show the same kind of cores inside a single protein. As per example, in the monomer region, the cluster peak is separated by 10–12 Au atoms depending on the Lyz : Au^{3+} ratio used from the free protein peak and the core is assigned as Au_{10-12}@Lyz. Whereas $(Au_{10-12}@Lyz)_n$ (n = 2, 3, 4, …) are also observable in the whole mass range studied. Addition of an external reducing agent to the basic medium is required to reduce Ag^+ to Ag^0 for forming red luminescent Ag clusters. For our study, we have used a 1 : 4 ratio of Lyz : Ag^+ and the cluster core obtained by this process is assigned as Ag_{13}@Lyz (see Fig. 4 inset). The Au–Lyz adduct and Ag–Lyz adducts were mixed together in 1 : 3 and 3 : 1 ratios and reduced further using $NaBH_4$ to luminescent alloy clusters and the mass spectra were studied for the same. From the mass spectra it is clear that, by varying the Au : Ag adduct ratio, we can control the core composition and this process is also tunable as described earlier from our group for BSA protected Au–Ag alloy clusters.[36] The same procedure was followed for Pd alloy formation also. But only one Pd attachment was observed in this process as shown in the mass spectrum (Fig. S16†). So, from this study it is confirmed that, solution phase alloy formation is completely different from gas phase alloy formation. We have observed that, in the gas phase, the Au–Ag alloy cannot be formed but the same can be formed by using the solution state co-reduction method. Alloy formation with Pd is also distinctly different from the gas phase. This study conclusively proves the specific recognition of Pd over other metals in the gas phase.

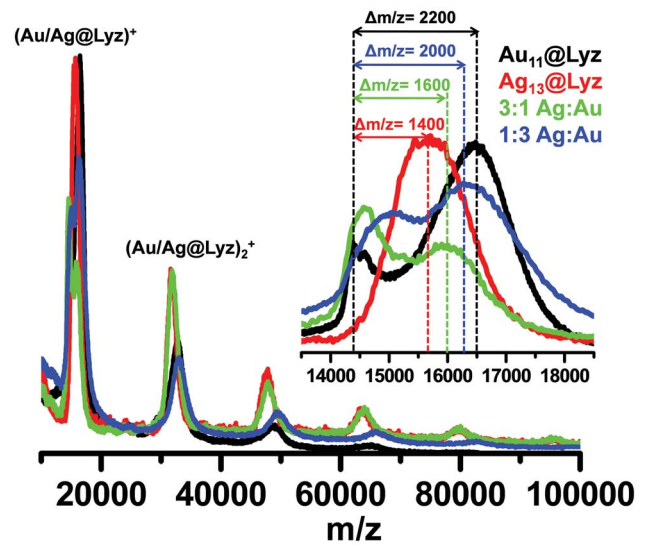

Fig. 4 MALDI MS of Au_{QCs}@Lyz, Ag_{QCs}@Lyz and Au–Ag_{QCs}@Lyz in the linear positive mode showing distinct separation from the parent protein peak due to the specific number of Au and Ag. The monomer region is expanded in the inset showing tunable alloy formation by varying the Au and Ag precursor concentrations.

3.6. Concentration and time dependent studies

Cluster distribution and their intensities are affected by the precursor composition as well as time of incubation. Data presented in Fig. 5 show that while the gross features are unaffected with variation in composition, Au_{38}^+ intensity is greatly enhanced with the Pd content. Various ratios of Au and Pd adducts of Lyz were used (1 : 1, 1 : 3 and 3 : 1 in terms of Au : Pd adducts), but in the case of the 3 : 1 ratio, peaks are well resolved. Suppression of

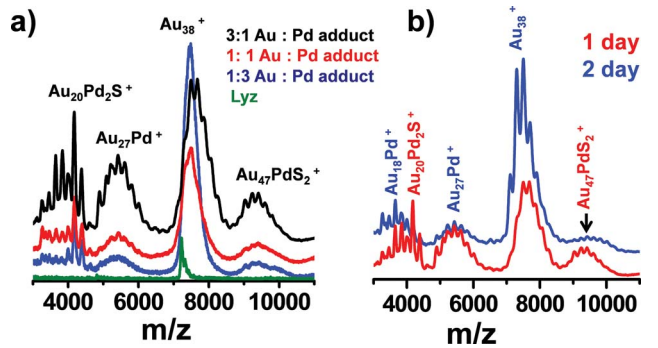

Fig. 5 (a) Concentration dependent study of different Au : Pd adducts of Lyz. The 3 : 1 Au : Pd adduct of Lyz shows good intensity and resolvable peak separation. (b) Time dependent study of the 3 : 1 Au : Pd adduct of Lyz showing catalytic enhancement of Au_{38}^+ over incubation time.

other clusters and enhancement of Au_{38}^+ are also seen upon increasing the time of incubation to 48 hours. A catalytic enhancement of Au_{38}^+ is inferred from the spectra.

3.7. Direct addition of $PdCl_2$

To check whether the preformed M-protein adduct is necessary for alloy formation, we designed our experiment in a slightly different way. To verify the role of the Pd precursor in the alloy formation process, $PdCl_2$ was added directly to the Au–Lyz adduct and the product was examined in MALDI MS. For this study, $PdCl_2$ was directly added to Au–Lyz in various ratios (Au–Lyz : $PdCl_2$ = 5 : 1, 5 : 2, 5 : 3 and 5 : 4). Gas phase alloy formation was observable with minimum $PdCl_2$ addition also in the Au_{18}^+ region (Fig. 6), where starting from $Au_{16}PdS^+$ to $Au_{19}PdS^+$, peaks appear with equal Au spacing. After $Au_{19}PdS^+$, the next peak is separated by Pd and assigned as $Au_{19}Pd_2S^+$. In this case also, we found $Au_{20}Pd_2S^+$ to be the most intense peak in the Au_{18}^+ region as seen in the case of the Au–Pd mixed adduct discussed in 3.1. In the Au_{25}^+ region, we have a single Pd attachment to the core as we have seen for the previous case. A small hump appears just after the Au_{25}^+ peak, separated by *m/z* 106 and attributed to $Au_{25}Pd^+$. It is clear that alloy cores remain the same in terms of their nuclearity for both the cases. Therefore, it can be said that Lyz can uptake Pd simultaneously in the presence of Au also. From the protein template, both the metals come to the gas phase and the alloy was formed. This study again proves gas phase association of Au and Pd to form alloy clusters.

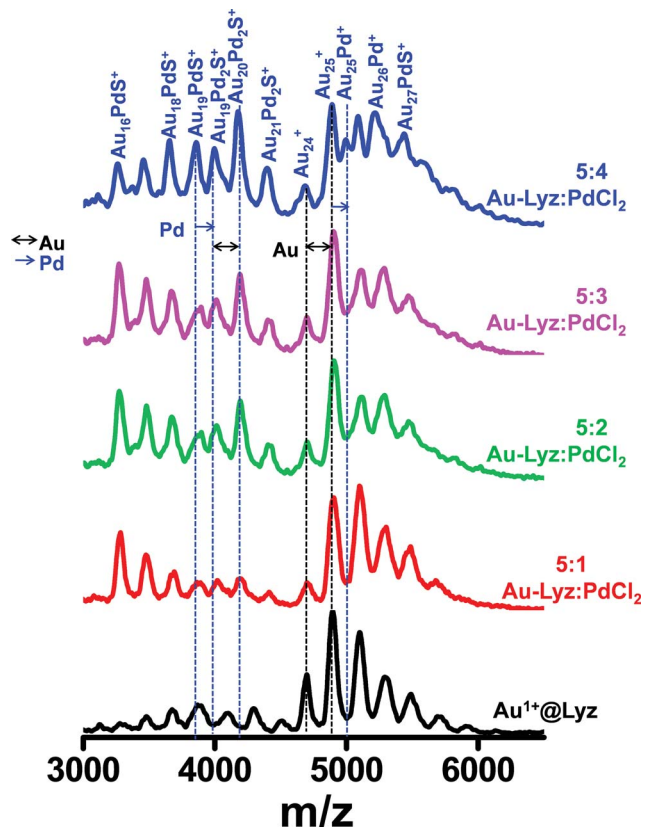

Fig. 6 Effect of direct $PdCl_2$ addition to Au–Lyz adducts probed by MALDI MS with different Au–Lyz : $PdCl_2$ ratios (as mentioned on the traces). With minimum $PdCl_2$ addition, alloy forms as observed in the Au_{18}^+ region but the Au_{25}^+ region remains unchanged. In the case of the highest Au–Lyz : $PdCl_2$ ratio, alloy formation is observed with a few sulfur attachments.

3.8. XPS and EDAX analyses

Once metal salts are added to the protein, amino acid residues reduce metal ions and the protein itself gets oxidized. In the case of Au^{3+} addition to protein, Au^{3+} gets reduced to Au^{1+} by the amino acids under normal conditions as previously reported for Au clusters synthesized in Lf. We have used the Au–Pd mixed adduct for XPS analysis. In our case also we found that the Au $4f_{7/2}$ binding energy appears at 85.0 eV (Fig. 7A) in the protein conjugate confirming that most of the Au^{3+} is reduced to Au^{1+} by the protein. But for Pd, the $3d_{5/2}$ binding energy is at 337.1 eV (Fig. 7B) corresponding to Pd^{2+}. Therefore, amino acids of protein cannot reduce Pd^{2+} to Pd^0 or any intermediate oxidation state in this process. The presence of all possible elements is proved by the survey spectrum as well as by SEM EDAX (Fig. 7). From this study, we determined the atomic ratios of Au : S : Pd to be 1 : 3.6 : 0.6 and the expected ratio is 1 : 2.4 : 1 on the basis of components used. From the EDAX mapping, it is confirmed that, Au and Pd are taken up together by the protein.

3.9. Mechanism of alloy formation and delay time dependence

While the cluster is being formed, there is a need to remove the heat of aggregation from the system. This is often practiced using the macromolecular template. Protein being a large molecule has a high number of degrees of freedom and can act as a heat reservoir to allow cluster growth in the gas phase. Lyz is a very small protein having only 8 Cys residues. So it is unlikely that Au_{38}^+ or $Au_{47}PdS_2^+$ will form inside a single molecule of Lyz. From XPS study, we have confirmed that, Au^0 or Pd^0 does not exist in the solution under normal reaction conditions. Therefore, we propose involvement of plasma in this reaction. Gaseous plasma is produced by heating the sample with laser. This plasma contains ions, molecules, aggregates, protein molecules, Lyz–Au adducts, Lyz–Pd adducts as well as mixed adducts and electrons. Under gaseous plasma conditions, conformation of the adducts will not be the same

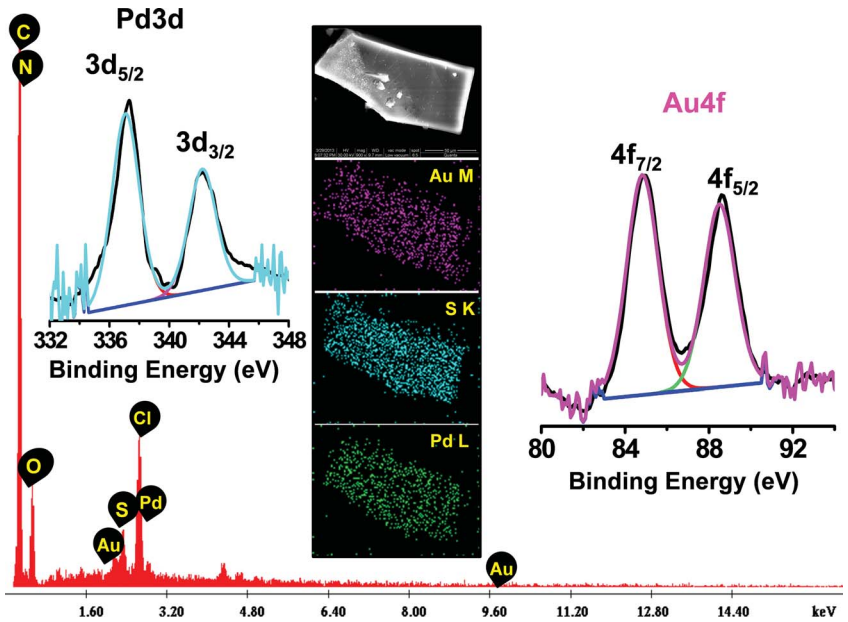

Fig. 7 SEM-EDAX of the 3 : 1 Au : Pd adduct of Lyz, showing the presence of all possible elements. The inset (i) shows the EDAX mapping of the object shown in the SEM image at the top. (A) and (B) are XPS spectra of Au–Lyz and Pd–Lyz adducts showing that Au^{3+} is reduced to Au^{1+} after adduct formation with protein, whereas Pd^{2+} remains in the same oxidation state.

like in the solution phase. Constituents will interact with each other to form larger aggregates. Bare cluster formation and stabilization requires interaction with the protein molecules. This can happen through several unimolecular reactions like:

$$Au_n^+ + Au_m \rightarrow Au_{n+m}^+,\ m = 0, 1, 2, \ldots; n = 1, 2, 3, \ldots \quad (1)$$

$$[Lyz\text{–}Au_m]^+ + Au_n \rightarrow [Lyz\text{–}Au_{m+n}]^+,\ m = 0, 1, 2, \ldots; n = 1, 2, 3, \ldots \quad (2)$$

$$[Lyz\text{–}Au_n]^+ + Lyz\text{–}Au_m \rightarrow [Lyz\text{–}Au_{n+k}]^+ + [Lyz\text{–}Au_{m-k}],\ k(<m) = 1, 2, \ldots; n, m = 1, 2, 3, \ldots \quad (3)$$

Eqn (3) involves intermolecular metal ion transfer. We know that, when the small Au cluster core nucleates, it attracts other Au atoms or ions towards itself through aurophilic interactions and starts growing. For solution phase cluster growth also we see intermolecular metal ion transfer, which is reflected in the regeneration of free protein upon longer incubation time.[38,43]

The same kind of reactions can be written for Pd also. Here we note that, we did not see free Pd clusters in the gas phase in our experimental conditions. Although, Pd_n clusters are known to exist in the gas phase and their reactivity is also studied.[55] Au and Pd ions and adducts are formed simultaneously inside the plasma and can interact with each other to form alloys. Here we note that, we did not see more than two Pd attachments in any case.

$$Au_n^+ + Pd_m \rightarrow Au_nPd_m^+,\ m = 0, 1, 2, \ldots; n = 1, 2, \ldots \quad (4)$$

$$Au_n + Pd_m^+ \rightarrow Au_nPd_m^+,\ m = 0, 1, 2, \ldots; n = 1, 2, \ldots \quad (5)$$

$$[Lyz\text{–}Au_m]^+ + Pd_n \rightarrow [Lyz\text{–}Au_mPd_n]^+,\ m = 0, 1, 2, \ldots; n = 1, 2, \ldots \quad (6)$$

$$[Lyz\text{–}Au_n]^+ + Lyz\text{–}Pd_m \rightarrow [Lyz\text{–}Au_nPd_k]^+ + [Lyz\text{–}Pd_{m-k}],\ k(<m) = 1, 2, \ldots; n, m = 1, 2, \ldots \quad (7)$$

Besides these, there can be several reactions in which anions and electrons can participate. Similar kinds of mechanisms can be extended for negative ions also as the same clusters form in the negative mode. In the case of laser irradiation, it is always seen that the C–S bond breaks and M_nS_m aggregates form. In

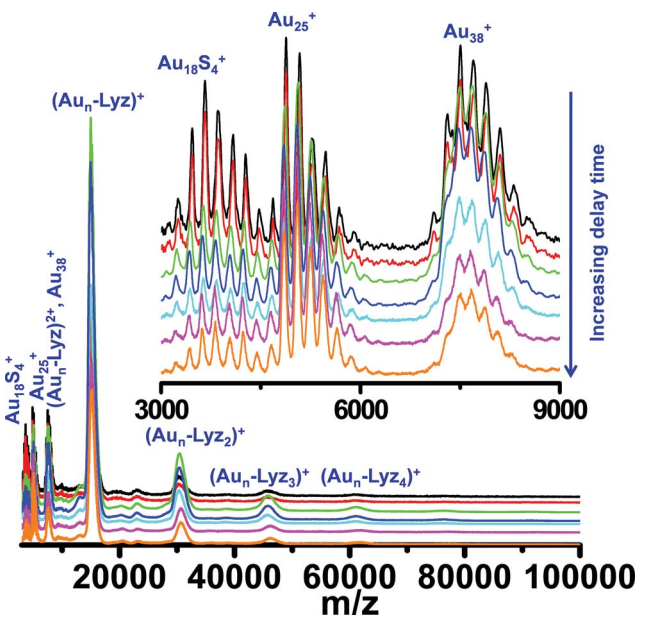

Fig. 8 MALDI MS spectra of delay time dependent bare cluster formation of Au^+@Lyz. There is no signature of any new cluster core formation with varying delay times. The inset shows an expanded view of m/z 3000 to 9000. With changing delay times no new peak appears.

our study, we observed cluster cores with sulfur attachment ($Au_{20}Pd_2S^+$, $Au_{47}PdS_2^+$, *etc.*) which again proves involvement of proteins in cluster formation as there is no other source for sulphur in the system.

This kind of plasma reactions can also happen with large protein aggregates due to the delayed extraction of the ionized species. The finite time lag between laser desorption/ionization and extraction of ions is referred to as the delay time. Normally, for smaller molecules, a shorter delay time is enough to efficiently extract all the ions to the detector but for larger molecules, like proteins, a longer delay time is generally used. To check the delay time dependence on the gas phase cluster formation, we have performed the experiment with the Au–Lyz adduct. If we allow the plasma to react longer, we may get larger cluster cores or a certain cluster core may form in high abundance. However, we saw that there is actually not much delay time dependence as both the cluster cores as well as protein are small. With varying delay time, the peak positions remain essentially the same. In Fig. 8 delay time dependent-MALDI MS spectra are plotted for the Au^+@Lyz adduct and from these spectra, it is evident that no new peaks appear. In the inset, *m*/*z* 3000–9000 has been expanded. In this region alone, the peak intensities change with delay time. Thus we conclude that the delay time used for the reaction is sufficient for inter- and intra-molecular reactions to occur within the plasma.

4. Conclusions

The data presented show the existence of naked clusters of specific composition. Incidentally at least one of the cluster cores found, namely $Au_{24}Pd^+$ is known to exist in the monolayer protected clusters. Besides these alloy clusters, the presence of Pd in the condensed phase enhanced the formation of one component clusters such as Au_{38}^+. The results point to the catalytic stabilization of certain cluster nuclei. It is seen that Pd is the most important metal recognized by the naked Au clusters while other metals do not show alloy formation under such conditions. Although formation of selective clusters like Au_{25}^+ is observed in the case of Cu^{2+} addition, the presence of silver enhances the formation of Au_{25}^+ while Pt^{2+} enhances $Au_{18}S_4^+$. Other metal ions used in this study like Fe^{2+}, Ni^{2+}, and Cr^{3+} catalyze the formation of the $Au_{25\pm n}^+$ envelope. Fe^{2+} is catalyzed most efficiently among the three ions. Clusters are formed from metal adducts in the proteins in which gold is in the 1+ state while Pd in the 2+ state. Unusual recognition of Pd as evidenced by the enhanced formation of Au_{38}^+ and selective formation of Pd containing alloys of the kind $Au_{20}Pd_2S^+$, $Au_{27}Pd^+$, and $Au_{47}PdS_2^+$ suggests the participation of palladium in the growth process. Although Ag is not recognized by Au in the gas phase, it is possible to create luminescent Au–Ag alloy clusters, with tunable composition, in solution. We suggest that naked alloy clusters of this kind derived from macromolecular templates may be deposited on active substrates and used for model catalysis. Microscopy and spectroscopy of such naked clusters formed in the gas phase will be interesting.

Acknowledgements

A.B. and T.P. thank the Department of Science and Technology, Government of India for continuous support of our research program on nanomaterials. A.B. thanks the Council of Scientific and Industrial Research (CSIR) for fellowship. A.B. thanks Mr. M.S. Bootharaju for XPS and Ms Shridevi S. Bhat for SEM-EDAX analysis.

References

1 P. L. Xavier, K. Chaudhari, A. Baksi and T. Pradeep, *Nano Rev.*, 2012, **3**, 14767 and the references cited there in.
2 J. Zheng, C. Zhang and R. M. Dickson, *Phys. Rev. Lett.*, 2004, **93**, 077402.
3 J. Zheng, P. R. Nicovich and R. M. Dickson, *Annu. Rev. Phys. Chem.*, 2007, **58**, 409–431.
4 R. Jin, *Nanoscale*, 2010, **2**, 343–362.
5 *Catalysis by Gold*, ed. G. C. Bond, C. Louis and D. T. Thompson, World Scientific, 2006.
6 M. Zhu, E. Lanni, N. Garg, M. E. Bier and R. Jin, *J. Am. Chem. Soc.*, 2008, **130**, 1138–1139.
7 M. Zhu, C. M. Aikens, F. J. Hollander, G. C. Schatz and R. Jin, *J. Am. Chem. Soc.*, 2008, **130**, 5883–5885.
8 Y. Shichibu, Y. Negishi, T. Tsukuda and T. Teranishi, *J. Am. Chem. Soc.*, 2005, **127**, 13464–13465.
9 E. S. Shibu, M. A. H. Muhammed, T. Tsukuda and T. Pradeep, *J. Phys. Chem. C*, 2008, **112**, 12168–12176.
10 Y. Negishi, K. Nobusada and T. Tsukuda, *J. Am. Chem. Soc.*, 2005, **127**, 5261–5270.
11 M. W. Heaven, A. Dass, P. S. White, K. M. Holt and R. W. Murray, *J. Am. Chem. Soc.*, 2008, **130**, 3754–3755.
12 A. Dass, *J. Am. Chem. Soc.*, 2009, **131**, 11666–11667.
13 Z. Wu, J. Suhan and R. Jin, *J. Mater. Chem.*, 2009, **19**, 622–626.
14 L. A. Angel, L. T. Majors, A. C. Dharmaratne and A. Dass, *ACS Nano*, 2010, **4**, 4691–4700.
15 J. Akola, K. A. Kacprzak, O. Lopez-Acevedo, M. Walter, H. Gronbeck and H. Hakkinen, *J. Phys. Chem. C*, 2010, **114**, 15986–15994.
16 O. Toikkanen, V. Ruiz, G. Ronnholm, N. Kalkkinen, P. Liljeroth and B. M. Quinn, *J. Am. Chem. Soc.*, 2008, **130**, 11049–11055.
17 H. Qian, M. Zhu, U. N. Andersen and R. Jin, *J. Phys. Chem. A*, 2009, **113**, 4281–4284.
18 Y. Pei, Y. Gao and X. C. Zeng, *J. Am. Chem. Soc.*, 2008, **130**, 7830–7832.
19 O. Lopez-Acevedo, H. Tsunoyama, T. Tsukuda, H. Hakkinen and C. M. Aikens, *J. Am. Chem. Soc.*, 2010, **132**, 8210–8218.
20 J. Kim, K. Lema, M. Ukaigwe and D. Lee, *Langmuir*, 2007, **23**, 7853–7858.
21 V. L. Jimenez, D. G. Georganopoulou, R. J. White, A. S. Harper, A. J. Mills, D. Lee and R. W. Murray, *Langmuir*, 2004, **20**, 6864–6870.
22 R. L. Donkers, D. Lee and R. W. Murray, *Langmuir*, 2008, **24**, 5976.
23 H. Qian, W. T. Eckenhoff, Y. Zhu, T. Pintauer and R. Jin, *J. Am. Chem. Soc.*, 2010, **132**, 8280–8281.

24 P. D. Jadzinsky, G. Calero, C. J. Ackerson, D. A. Bushnell and R. D. Kornberg, *Science*, 2007, **318**, 430–433.
25 Y.-K. Han, H. Kim, J. Jung and Y. C. Choi, *J. Phys. Chem. C*, 2010, **114**, 7548–7552.
26 C. Zeng, H. Qian, T. Li, G. Li, N. L. Rosi, B. Yoon, R. N. Barnett, R. L. Whetten, U. Landman and R. Jin, *Angew. Chem., Int. Ed.*, 2012, **51**, 13114–13118.
27 Y. Negishi, W. Kurashige, Y. Niihori, T. Iwasa and K. Nobusada, *Phys. Chem. Chem. Phys.*, 2010, **12**, 6219–6225.
28 Y. Negishi, K. Igarashi, K. Munakata, W. Ohgake and K. Nobusada, *Chem. Commun.*, 2012, **48**, 660–662.
29 J. Xie, Y. Zheng and J. Y. Ying, *J. Am. Chem. Soc.*, 2009, **131**, 888–889.
30 M. M. A. Habeeb, P. K. Verma, S. K. Pal, A. Retnakumari, M. Koyakutty, S. Nair and T. Pradeep, *Chem.–Eur. J.*, 2010, **16**, 10103–10112.
31 A. Mathew, P. R. Sajanlal and T. Pradeep, *J. Mater. Chem.*, 2011, **21**, 11205–11212.
32 C. V. Durgadas, C. P. Sharma and K. Sreenivasan, *Analyst*, 2010, **136**, 933–940.
33 D. Hu, Z. Sheng, P. Gong, P. Zhang and L. Cai, *Analyst*, 2010, **135**, 1411–1416.
34 C. Guo and J. Irudayaraj, *Anal. Chem.*, 2011, **83**, 2883–2889.
35 H.-W. Li, K. Ai and Y. Wu, *Chem. Commun.*, 2011, **47**, 9852–9854.
36 J. S. Mohanty, P. L. Xavier, K. Chaudhari, M. S. Bootharaju, N. Goswami, S. K. Pal and T. Pradeep, *Nanoscale*, 2012, **4**, 4255–4262.
37 P. L. Xavier, K. Chaudhari, P. K. Verma, S. K. Pal and T. Pradeep, *Nanoscale*, 2010, **2**, 2769–2776.
38 K. Chaudhari, P. L. Xavier and T. Predeep, *ACS Nano*, 2011, **5**, 8816–8827.
39 H. Wei, Z. Wang, L. Yang, S. Tian, C. Hou and Y. Lu, *Analyst*, 2010, **135**, 1406–1410.
40 Y.-H. Lin and W.-L. Tseng, *Anal. Chem.*, 2010, **82**, 9194–9200.
41 W.-Y. Chen, J.-Y. Lin, W.-J. Chen, L. Luo, D. E. Wei-Guang and Y.-C. Chen, *Nanomedicine*, 2010, **5**, 755–764.
42 T.-H. Chen and W.-L. Tseng, *Small*, 2012, **8**, 1912–1919.
43 A. Baksi, P. L. Xavier, K. Chaudhari, N. Goswami, S. K. Pal and T. Pradeep, *Nanoscale*, 2013, **5**, 2009–2016.
44 A. Baksi, T. Pradeep, B. Yoon, C. Yannouleas and U. Landman, *ChemPhysChem*, 2013, **14**, 1272–1282 and the references cited there in.
45 C.-L. Liu, H.-T. Wu, Y.-H. Hsiao, C.-W. Lai, C.-W. Shih, Y.-K. Peng, K.-C. Tang, H.-W. Chang, Y.-C. Chien, J.-K. Hsiao, J.-T. Cheng and P.-T. Chou, *Angew. Chem., Int. Ed.*, 2011, **50**, 7056–7060.
46 N. Goswami, A. Giri, M. S. Bootharaju, P. L. Xavier, T. Pradeep and S. K. Pal, *Anal. Chem.*, 2011, **83**, 9676–9680.
47 Y.-C. Shiang, C.-C. Huang, W.-Y. Chen, P.-C. Chen and H.-T. Chang, *J. Mater. Chem.*, 2012, **22**, 12972–12982.
48 S. M. Lystvet, S. Volden, G. Singh, M. Yasuda, O. Halskau and W. R. Glomm, *RSC Adv.*, 2013, **3**, 482–495.
49 S. M. Lang, A. Frank, I. Fleischer and T. M. Bernhardta, *Eur. Phys. J. D*, 2013, **67**, 19.
50 D. W. Yuan, Y. Wang and Z. Zeng, *J. Chem. Phys.*, 2005, **122**, 114310.
51 D. M. Popolan, M. Noessler, R. Mitric, T. M. Bernhardt and V. Bonacic-Koutecky, *Phys. Chem. Chem. Phys.*, 2010, **12**, 7865–7873.
52 T. M. Bernhardt, J. Hagen, S. M. Lang, D. M. Popolan, L. D. Socaciu-Siebert and L. Woste, *J. Phys. Chem. A*, 2009, **113**, 2724–2733.
53 H. J. De, N. Veldeman, P. Claes, E. Janssens, M. Andersson and P. Lievens, *J. Phys. Chem. A*, 2011, **115**, 2103–2109.
54 Y. Negishi, K. Munakata, W. Ohgake and K. Nobusada, *J. Phys. Chem. Lett.*, 2012, **3**, 2209–2214.
55 W. E. Kaden, T. Wu, W. A. Kunkel and S. L. Anderson, *Science*, 2009, **326**, 826–829.

Electronic Supplementary Information

Noble metal alloy formation in the gas phase derived from protein templates: Unusual recognition of palladium by gold

Ananya Baksi and T. Pradeep*

DST Unit of Nanoscience (DST UNS), Department of Chemistry, Indian Institute of Technology Madras, Chennai 600036, India.

Electronic Supplementary Information 1

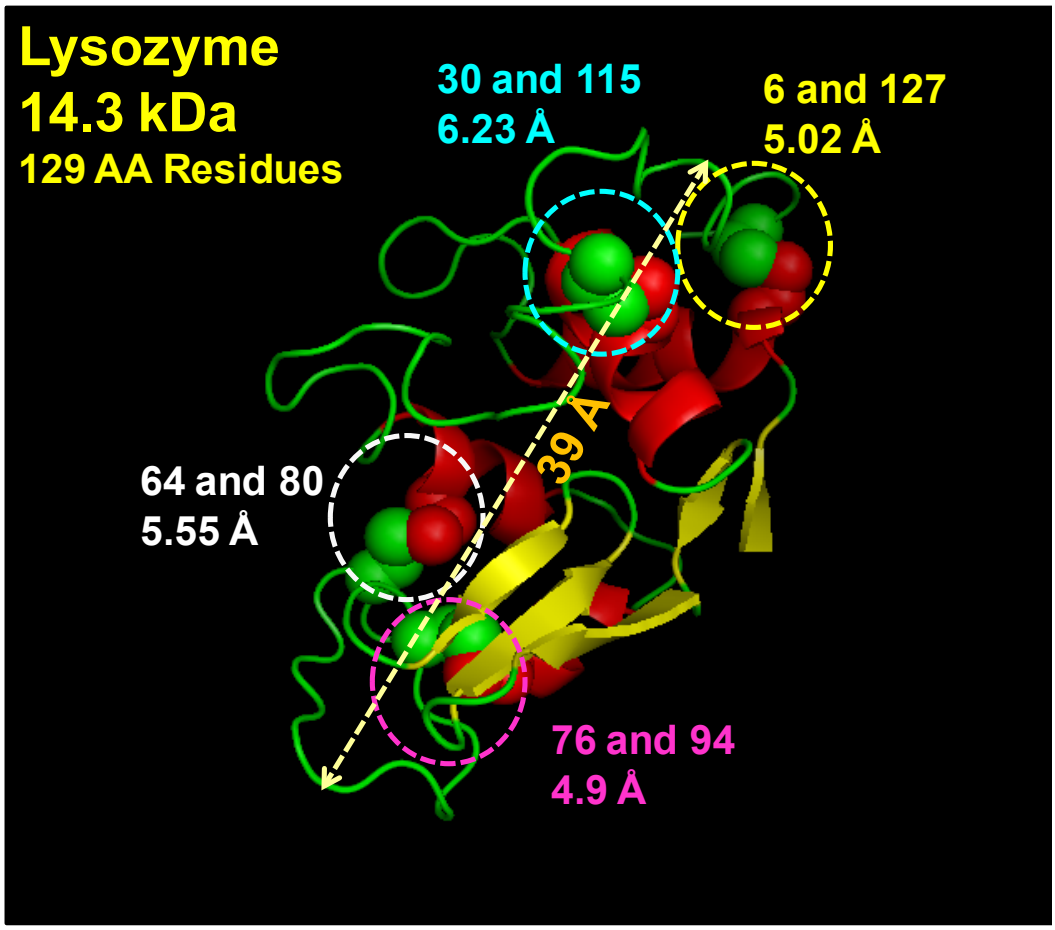

Fig. S1† Structure of the protein, lysozyme having a molecular weight of 14.3 kDa and 129 amino acid residues among which eight are cysteines marked as circles. The typical distance and S-S bond lengths are shown. This figure is reproduced from PDB file 2LYZ (*J.Mol.Bio.* 1974, **82**, 371-391) using PyMOL software.

Electronic Supplementary Information 2

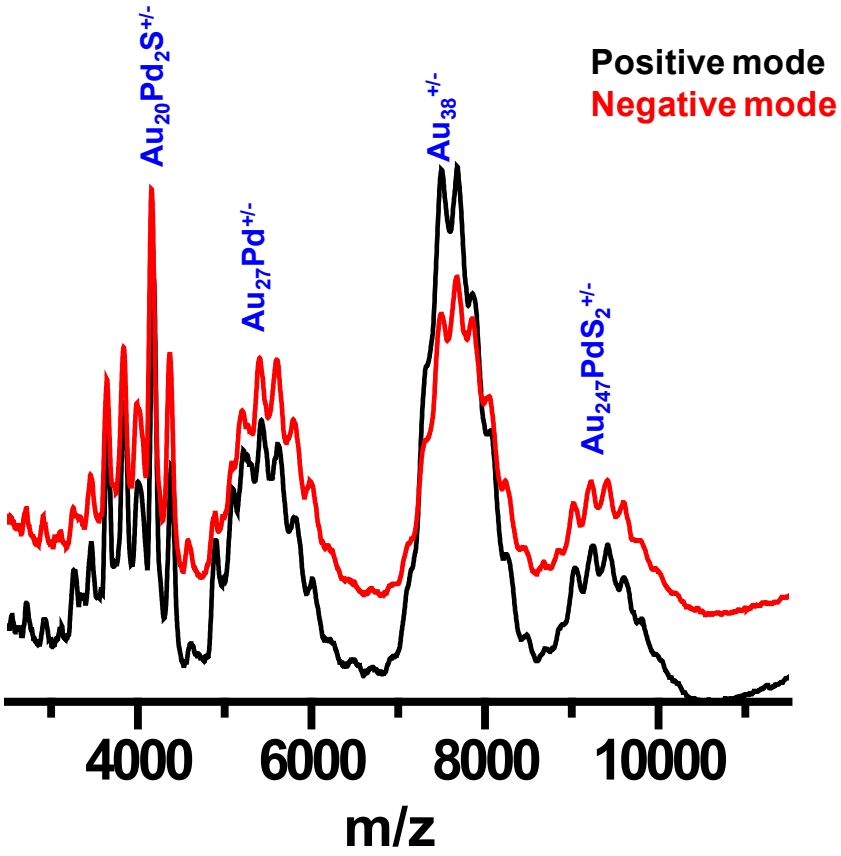

Fig. S2† Comparison between linear positive and negative mode MALDI MS of 3:1 Au:Pd adduct of Lyz, showing the same peaks in both the cases.

Electronic Supplementary Information 3

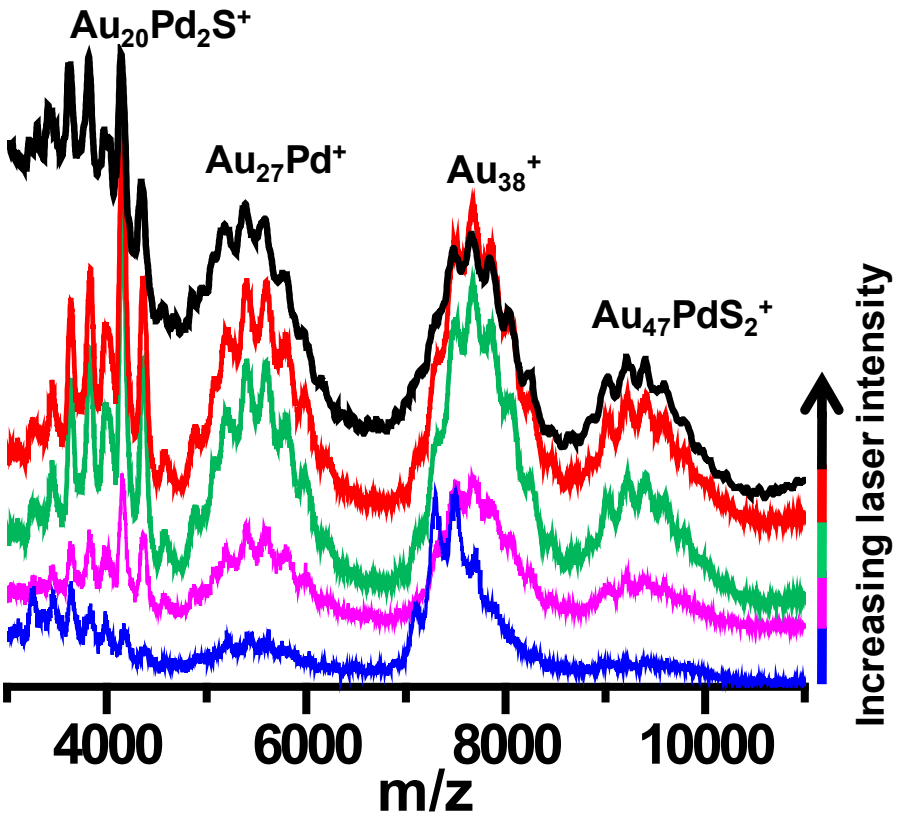

Fig. S3† Laser intensity dependent study of MALDI MS with increasing laser intensity in linear positive mode. There is no change in the peak position with enhanced laser intensity. The spectra were collected for the 3:1 Au:Pd mixed adduct system in linear positive mode and the laser intensity was varied from 1800 to 2600 (instrumental unit) with an increase of 200 in intensity at each step, plotted in blue, magenta, green, red and black, respectively.

Electronic Supplementary Information 4

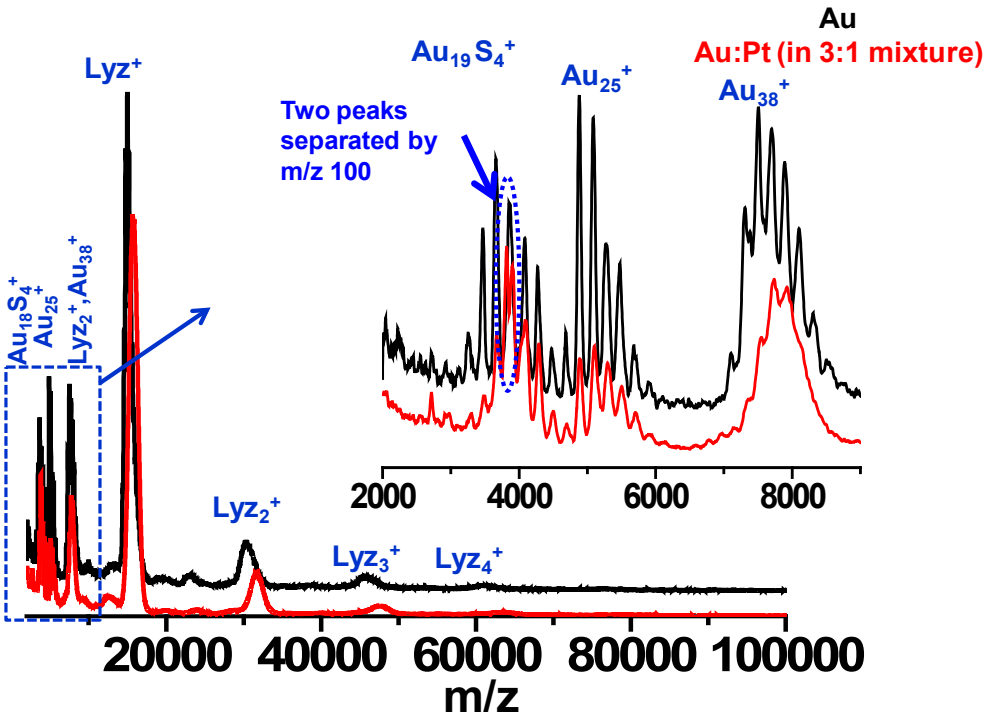

Fig. S4† Comparison between the MALDI MS of 3:1 Au:Pt adduct and Au only adduct of Lyz in linear positive ion mode. $Au_{19}S_4^+$ splits into two peaks separated by m/z 100. Other peak positions remain the same, although intensity of Au_{25}^+ and Au_{38}^+ regions decreases relative to $Au_{18}S_4^+$.

Electronic Supplementary Information 5

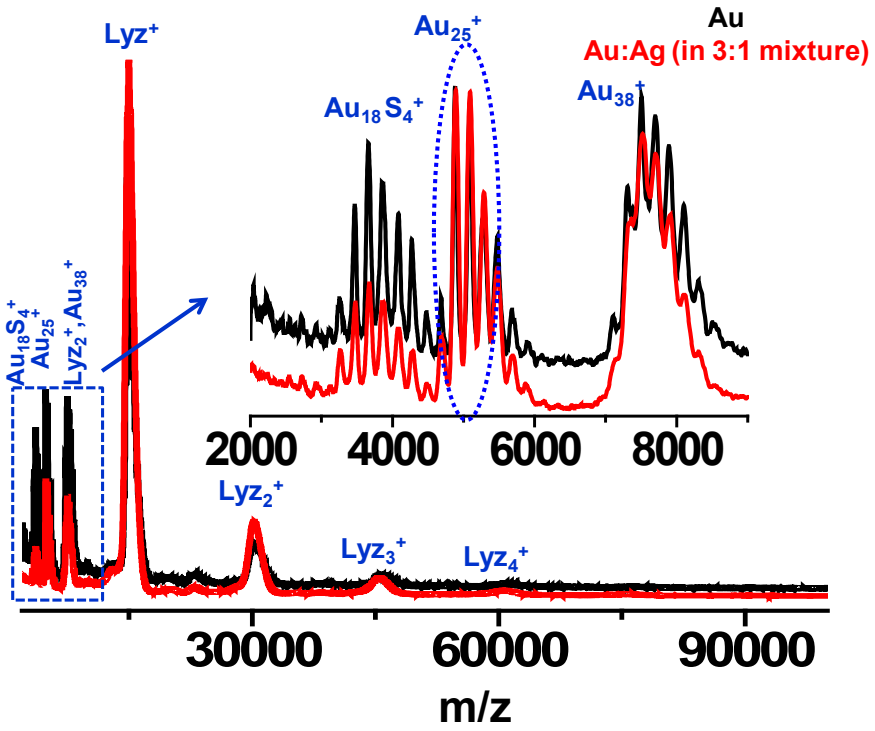

Fig. S5† Comparison between the MALDI MS of 3:1 Au:Ag adduct and Au only adduct of Lyz in linear positive ion mode. No alloy was formed, only Au_{25}^{+} region intensifies.

Electronic Supplementary Information 6

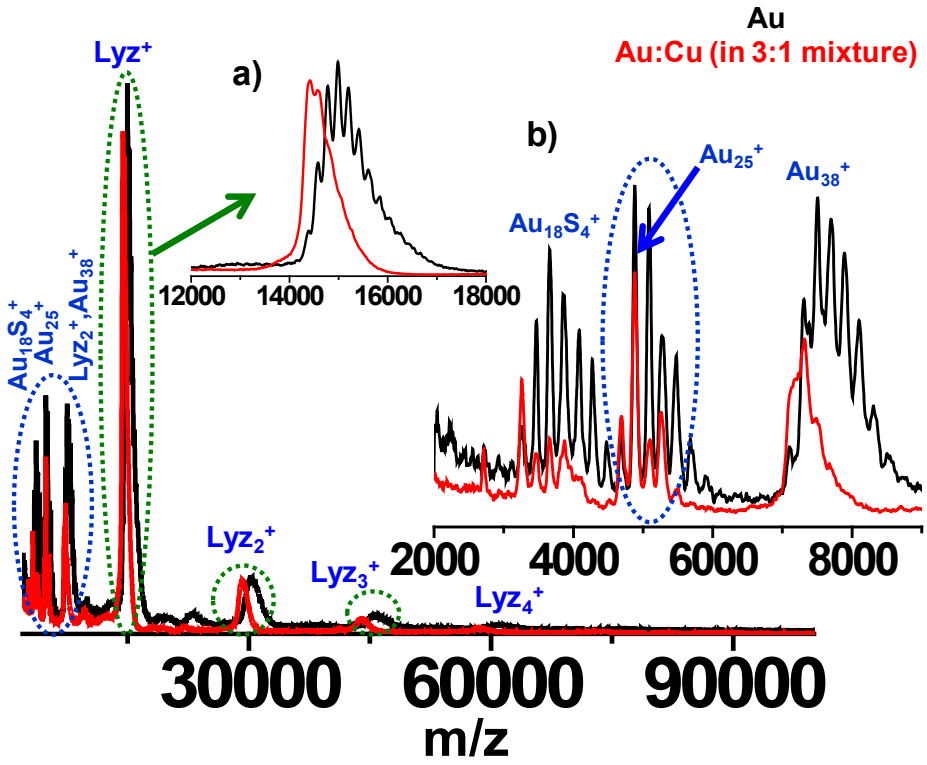

Fig. S6† Comparison between the MALDI MS of 3:1 Au:Cu adduct and Au only adduct of Lyz in linear positive ion mode. Large change in the overall spectrum is observable. Inset a) shows less number of Au attachment to parent Lyz monomer in case of Cu addition compared to Au alone sample. Inset b) is shows that preferentially Au_{25}^{+} is formed when Cu is present in the system.

Electronic Supplementary Information 7

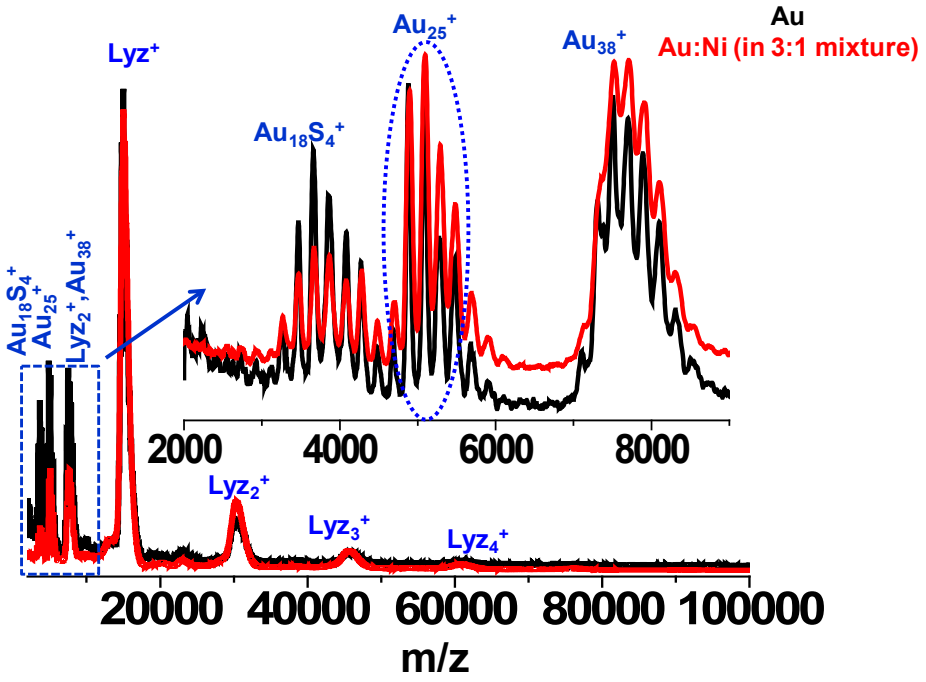

Fig. S7† Comparison between the MALDI MS of 3:1 Au:Ni adduct and Au only adduct of Lyz in linear positive ion mode. No alloy was formed, only Au_{25}^{+} region intensifies.

Electronic Supplementary Information 8

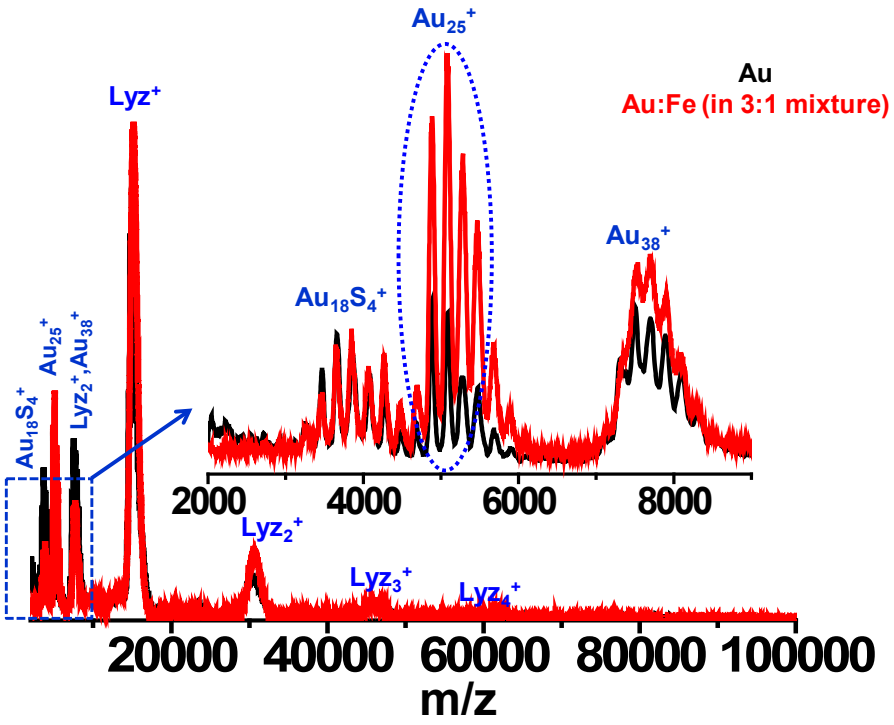

Fig. S8† Comparison between the MALDI MS of 3:1 Au:Fe adduct and Au only adduct of Lyz in linear positive ion mode. No alloy was formed, only Au_{25}^{+} region intensifies.

Electronic Supplementary Information 9

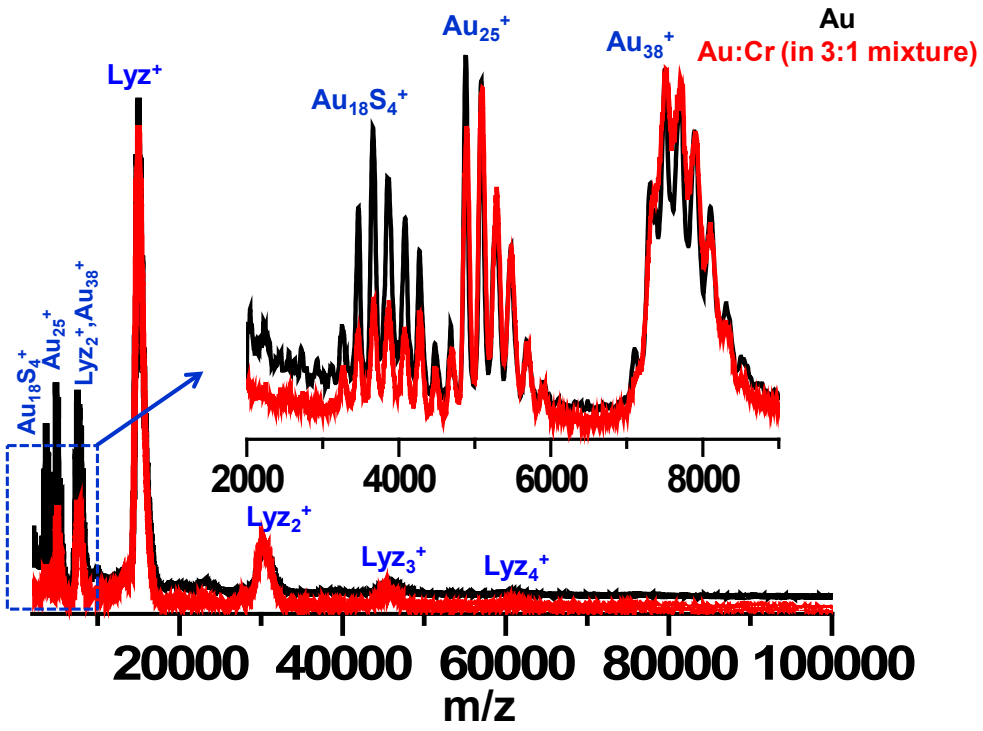

Fig. S9† Comparison between the MALDI MS of 3:1 Au:Cr adduct and Au only adduct of Lyz in linear positive ion mode. No alloy was formed, only Au_{25}^{+} region intensifies.

Electronic Supplementary Information 10

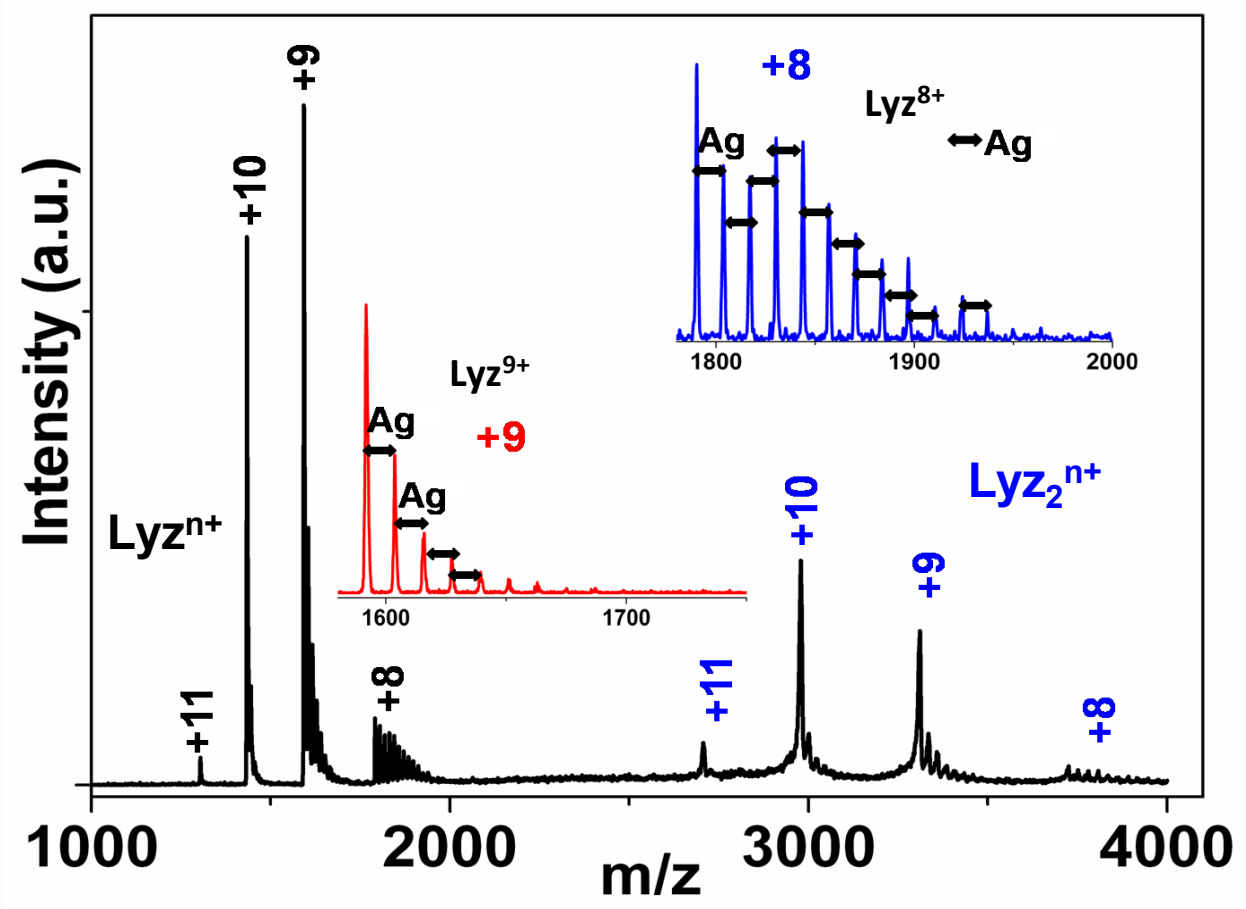

Fig. S10† Positive mode ESI MS of Ag-Lyz adduct showing multiple Ag additions to various charge states for both monomer and dimer of Lyz. In the inset, +8 and +9 charge states of Lyz are expanded. For Lyz^{8+} we can see that two consecutive Ag addition peaks have same intensity which is not seen for the +9 charge state.

Electronic Supplementary Information 11

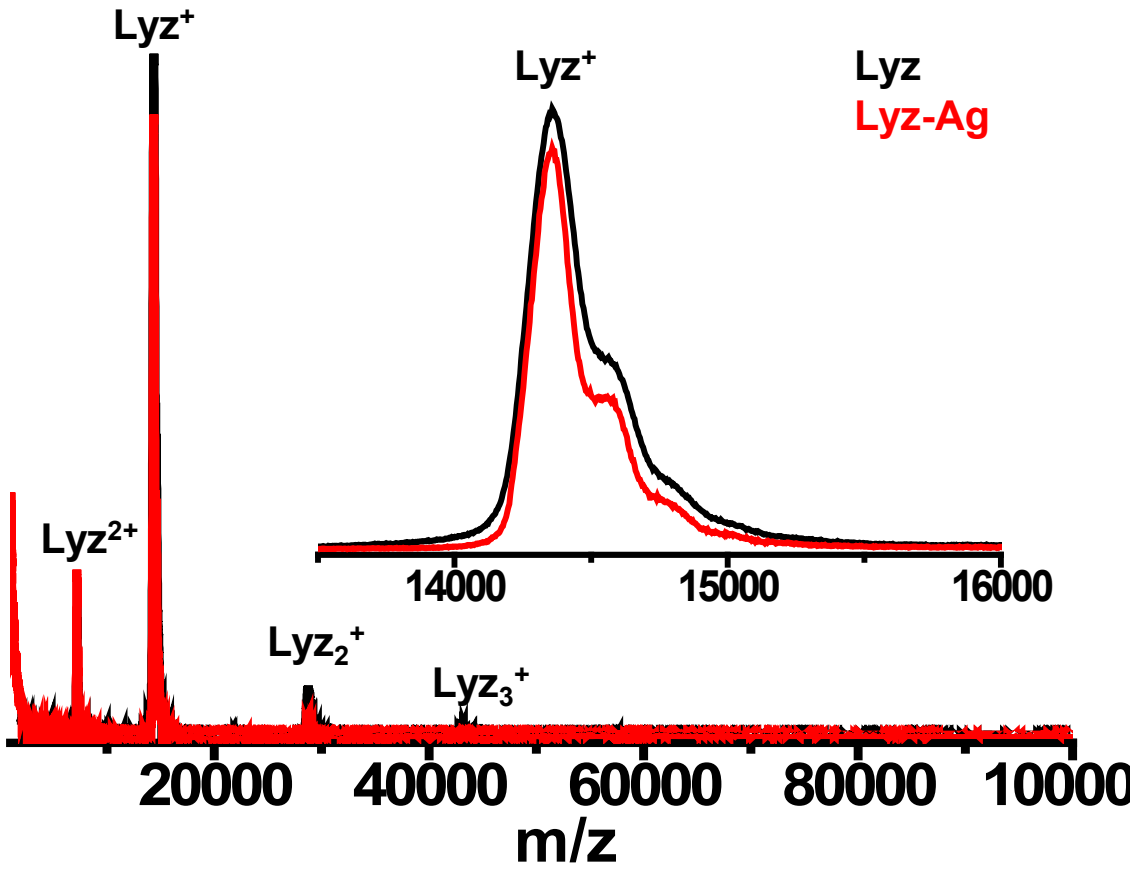

Fig. S11† MALDI MS of Ag-Lyz adduct in the linear positive mode showing no Ag attachment to it which implies that loosely bound Ag atoms have been desorbed during laser ablation.

Electronic Supplementary Information 12

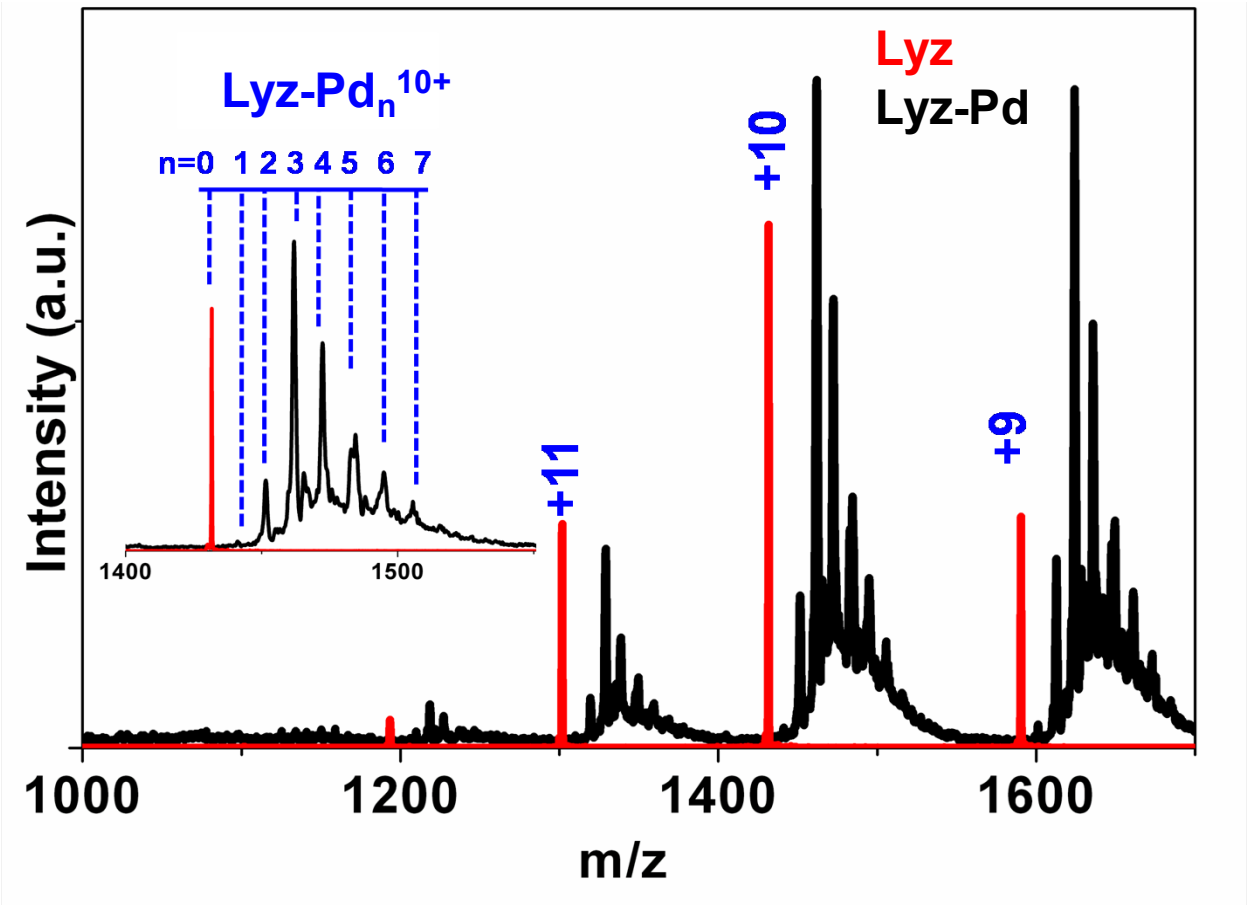

Fig. S12† Comparative ESI MS of Lyz and Pd-Lyz adduct in positive ion mode showing multiple Pd attachment to respective charge states. 10+ charge state has been expanded in the inset and Pd added peaks are marked.

Electronic Supplementary Information 13

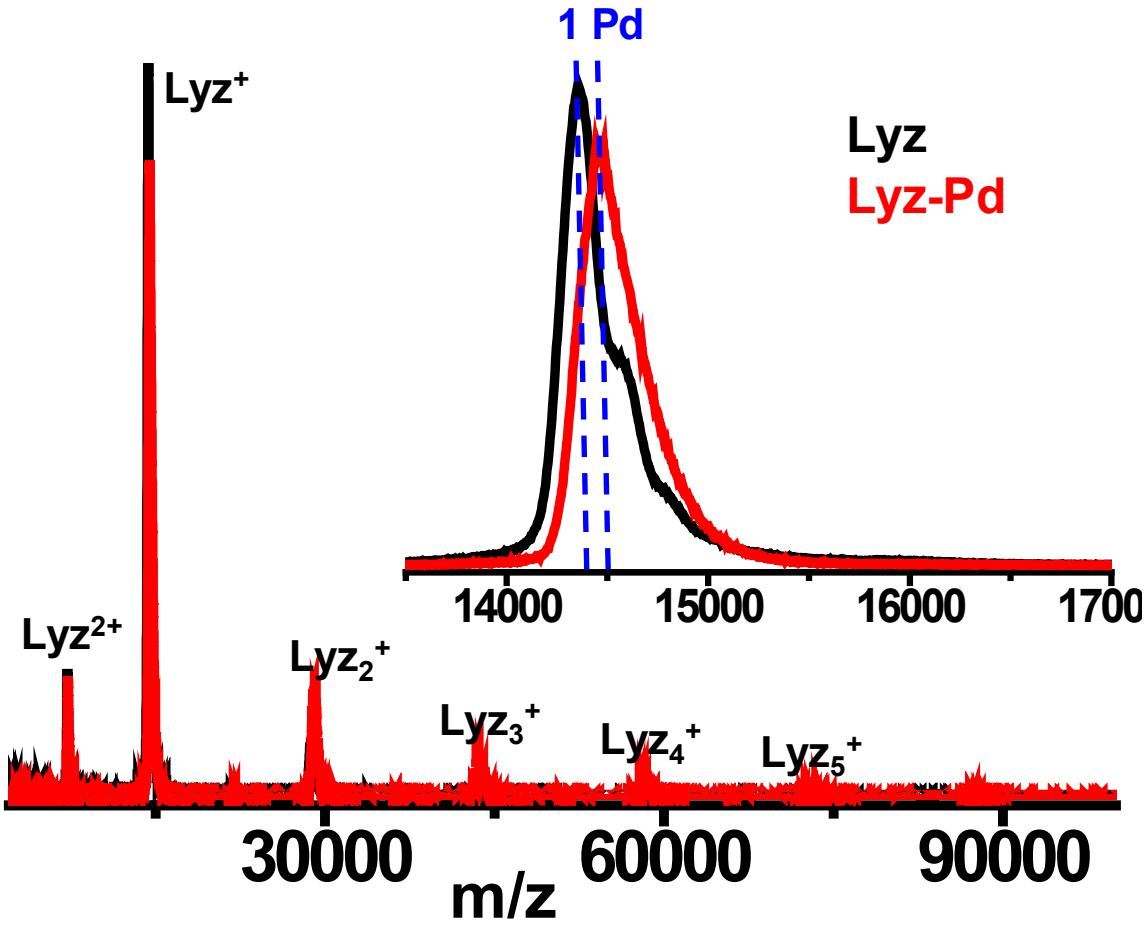

Fig. S13† Comparative MALDI MS of Lyz and Pd-Lyz adduct in linear positive ion mode showing Pd attachment to the respective charge state.

Electronic Supplementary Information 14

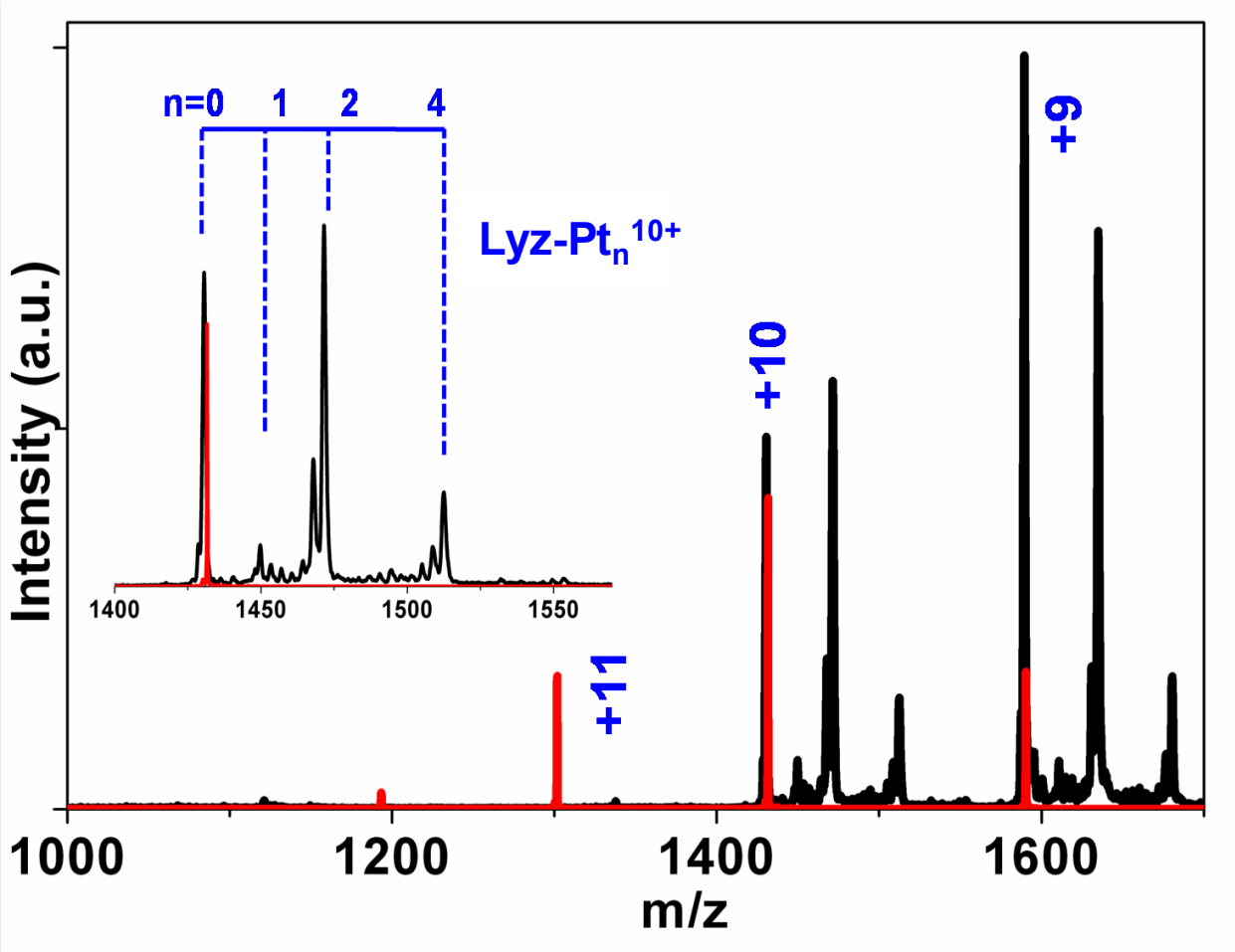

Fig. S14† Comparative ESI MS of Lyz and Pt-Lyz adduct in the positive ion mode showing multiple Pt attachment to the respective charge state. 10+ charge state has been expanded in the inset and Pt added peaks are marked. Odd number Pt attachment peaks are weak.

Electronic Supplementary Information 15

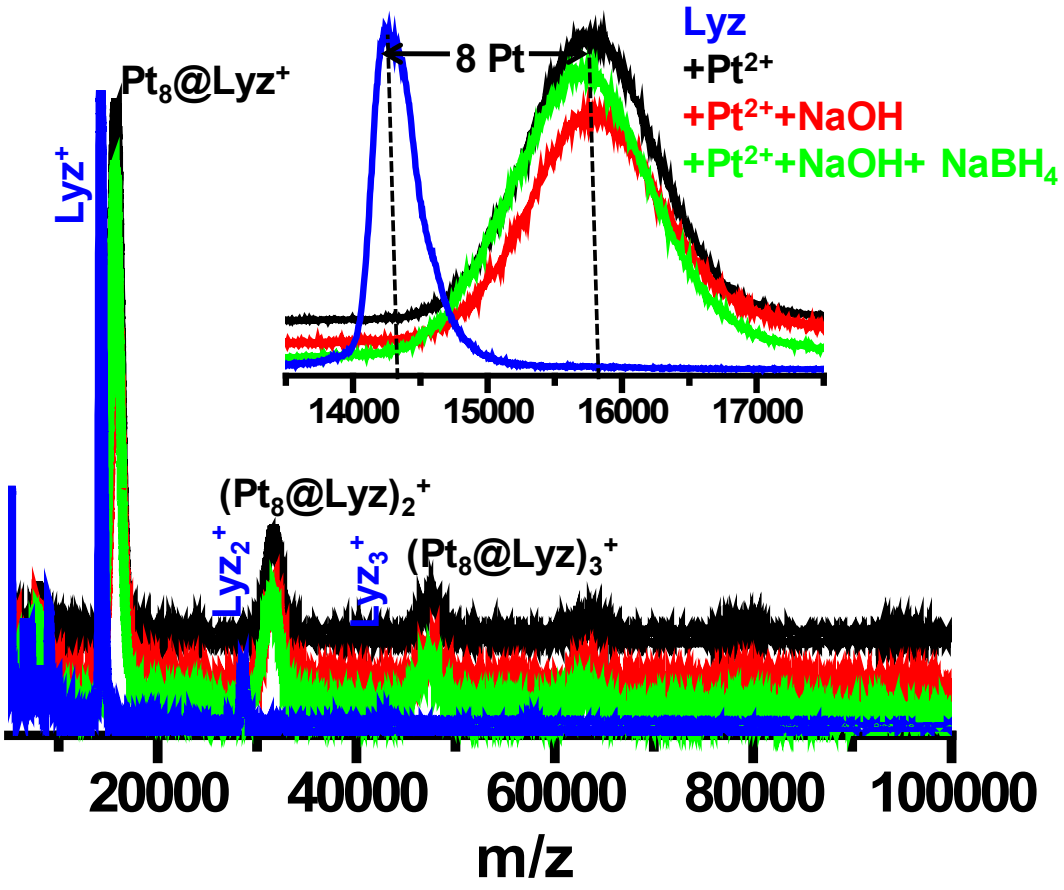

Fig. S15† Comparative MALDI MS of Lyz and Pt-Lyz at various conditions in linear positive mode showing 8 Pt attachments to protein at all conditions. Monomer region is expanded in the inset.

Electronic Supplementary Information 16

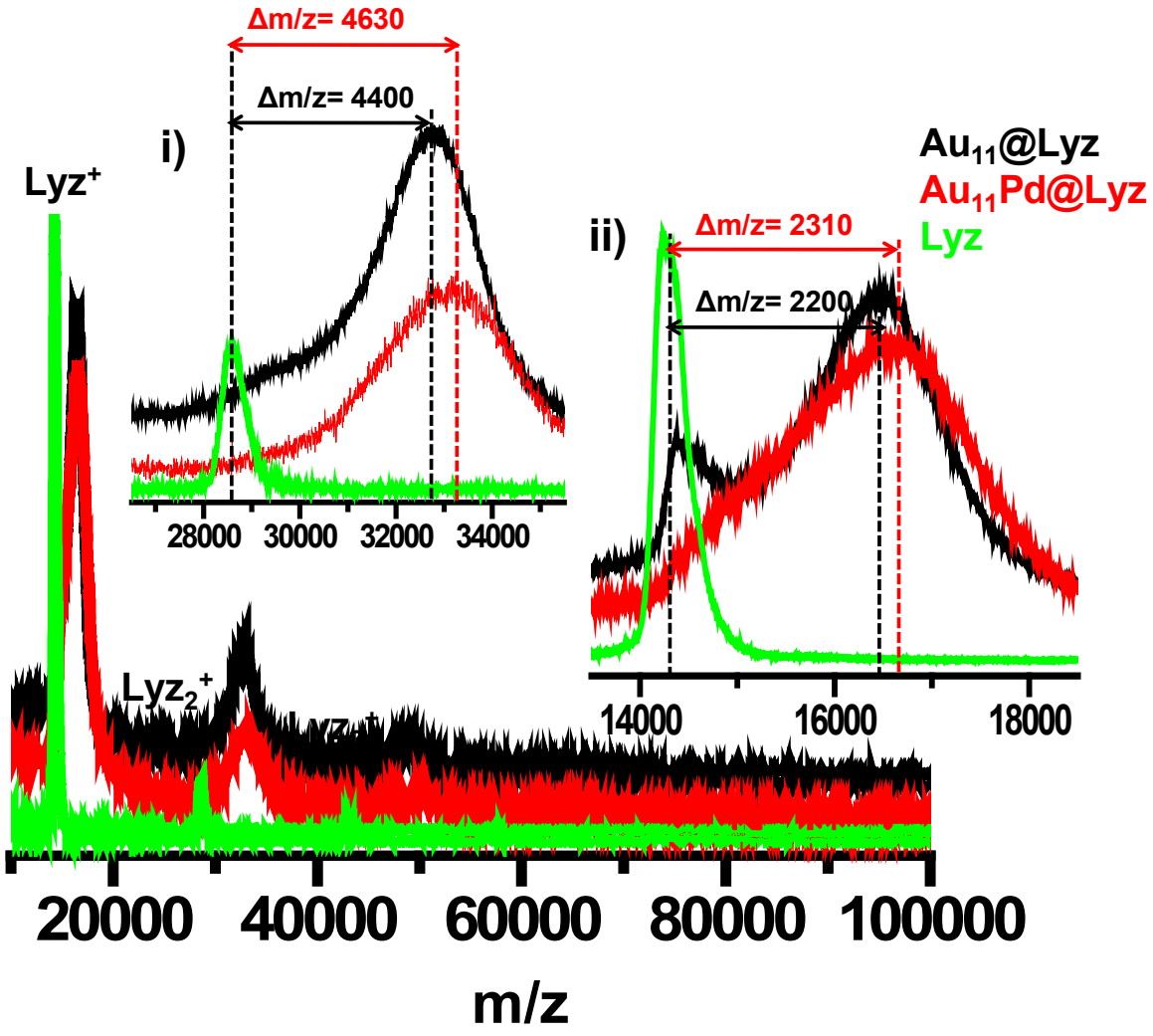

Fig. S16† MALDI MS of Au_{QCs}@Lyz and Au-Pd_{QCs}@Lyz in linear positive mode showing one (likely) Pd attachment to the existing Au_{11} core. The separation is clearly visible for the dimer region expanded in the inset i). Monomer region is expanded in inset ii).

JrnlID 13361_ArtID 786_Proof# 1 - 05/12/2013

J. Am. Soc. Mass Spectrom. (2013)
DOI: 10.1007/s13361-013-0786-7

RESEARCH ARTICLE

Studying Reaction Intermediates Formed at Graphenic Surfaces

Depanjan Sarkar, Soujit Sen Gupta, Rahul Narayanan, T. Pradeep

Thematic Unit of Excellence and DST Unit of Nanoscience (DST UNS), Department of Chemistry, Indian Institute of Technology Madras, Chennai, 600036, India

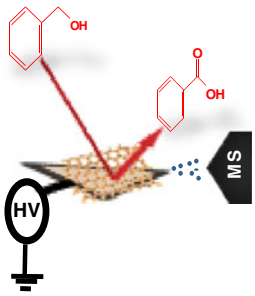

Abstract. We report in-situ production and detection of intermediates at graphenic surfaces, especially during alcohol oxidation. Alcohol oxidation to acid occurs on graphene oxide-coated paper surface, driven by an electrical potential, in a paper spray mass spectrometry experiment. As paper spray ionization is a fast process and the time scale matches with the reaction time scale, we were able to detect the intermediate, acetal. This is the first observation of acetal formed in surface oxidation. The process is not limited to alcohols and the reaction has been extended to aldehydes, amines, phosphenes, sugars, etc., where reaction products were detected instantaneously. By combining surface reactions with ambient ionization and mass spectrometry, we show that new insights into chemical reactions become feasible. We suggest that several other chemical transformations may be studied this way. This work opens up a new pathway for different industrially and energetically important reactions using different metal catalysts and modified substrate.

Key words: Paper spray, Graphene, Oxidation reaction, Intermediates

Received: 9 September 2013/Revised: 10 November 2013/Accepted: 14 November 2013

Introduction

Understanding intermediates in chemical reactions has been one of the most fascinating areas of physical chemistry [1-3]. From solution phase kinetics to femtosecond methods in gas phase using molecular beams, reaction monitoring in real time has evolved continuously [4-6]. As the time scale of monitoring decreases, it becomes possible to sample intermediates at various stages of a chemical event, thereby creating potential energy hyper-surfaces. As many of the complex reactions occur at ambient pressure, sampling of the species involved for spectroscopic studies poses new challenges. Mass spectrometry, one of the important tools in investigating chemical species has undergone a radical change with the realization of new ambient ionization tools like desorption electrospray ionization (DESI) [7-9], paper spray ionization [10-14], leaf spray ionization [15-17], etc. At the same time, several processes of chemical relevance occur at new materials such as graphene. Combining the power of mass spectrometry to precisely identify the species formed at active surfaces and ambient ionization tools to create such species under conditions of relevance to chemical reactions enable new capabilities. Such capabilities of reaction monitoring within desorption-ionization time scale from active surfaces offer new ways of looking at intermediates [18]. This may also be viewed as a methodology to understand catalysis or catalytic processes in real time. Thus, some of the central areas of physical chemistry may have direct relevance to the proposed study.

Graphene and its chemical variants, such as reduced graphene oxide (RGO) and graphene oxide (GO), can participate in redox reactions as shown by the formation of composites [19-21]. Such nanoparticle-embedded graphenes are shown to be useful for contaminant sensing and water purification [22-24] as well as solar energy conversion [25]. Chemistry on graphenic surfaces is of interest for physical chemists [26-29]. Making an active graphenic surface and combining it with DESI allow us to observe reaction products and intermediates formed on them in real time. Immediate sampling of the species formed allows rapid identification of reactions. Reaction kinetics and mechanism can also be studied in specific cases.

Paper spray is a new method of ionization in mass spectrometry. In this method, a triangularly cut paper is used

Electronic supplementary material The online version of this article (doi:10.1007/s13361-013-0786-7) contains supplementary material, which is available to authorized users.

Correspondence to: T. Pradeep; *e-mail:* pradeep@iitm.ac.in

as a substrate on which the sample and the solvent are added together or sample is spotted on the paper, prior to the addition of the spraying solvent and a high potential of the order of a few kV is applied to the paper to form ions, ejected out in the solvent spray. Because paper is a porous material, the solution is dragged through it by capillarity and, because of the high electric field near the tip, the analyte gets ejected. The time scale of paper spray is sufficiently long for the interaction of the sample with the substrate. If the substrate is such that it can react or interact with the sample, the products formed may be studied directly.

In this work, we report a phenomenon of direct oxidation of alcohols and other functional groups on graphenic surfaces. Observation of the products in real time allows the detection and identification of intermediates of this oxidation. This is the first report of online monitoring of such intermediates, like acetal, in a simple oxidation reaction. The reaction, consequently, leads to the reduction of the substrate, GO to RGO, as seen by Raman spectroscopy [30, 31]. We show that such reactions, however, do not occur on graphene in solution. Development of this methodology of observing intermediates at modified surfaces would enable the understanding of several heterogeneous processes.

Experimental and methods

For the paper spray measurements, Whatman 42 filter paper was cut into the shape of an isosceles triangle, 10 mm long and 5 mm wide at the base. GO and RGO samples were prepared as reported in our previous paper [32]. RGO-Ag composites were synthesized as reported in our previous work [23]. The triangularly cut papers were taken in a petri dish and the GO suspension was drop-casted on them. The petri dish containing the papers wetted with GO was kept at room temperature for drying. Dried papers turned brown in color as they were coated with GO. Raman measurements of these papers showed the presence of GO on them. They were used for all paper spray measurements. The experimental procedure is illustrated in Scheme 1.

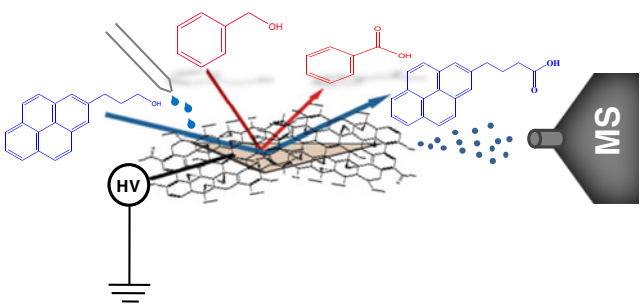

Scheme 1. Paper spray ionization using GO-coated paper. The paper tip to the mass spectrometer distance is much less than it appears. Typical reactants and products are also shown

The GO-coated paper was attached to a metal clip for applying high voltage. Both positive and negative potentials were used. RGO-coated and RGO-Ag composite coated papers were prepared similarly. A certain (5 µL) amount of solution was applied on the paper and high voltage was applied. The spray coming out of the tip of the paper was analyzed by a mass spectrometer. The whole process was carried out under atmospheric pressure and at room temperature, in air. Dilute solutions of sample (10 ppm) gave good results. With concentrated solutions (>100 ppm), peaks of parent ions were very intense, indicating that the fraction of oxidation process is less as the reaction is surface-limited. Benzyl alcohol (RFCL Ltd.); triphenylphosphine (Spectrochem Pvt. Ltd.); diphenylamine, fructose, and sucrose (E. Merck (India) Ltd.) were used as samples for our paper spray experiments. HPLC grade methanol purchased from Sigma-Aldrich and Millipore water were used as solvents.

For all paper spray experiments, an ion trap LTQ XL mass spectrometer of Thermo Scientific, San Jose, CA, USA was used. To do paper spray measurements, an attachment was added to the mass spectrometer (Scheme 1). The triangularly cut paper was set at a distance of approximately 5 mm from the mass spectrometer inlet in all the cases. Mass spectra were acquired both in positive and negative ion modes depending upon the compounds, in the mass range of *m/z* 50 to 1000 under the following conditions: source voltage 2–5 kV, positive and negative, depending upon the analyte, capillary temperature 150 °C, capillary voltage ±40 V, and tube lens voltage ±100 V, for positive and negative modes, respectively. All the paper spray ionization mass spectra presented correspond to an average of 50 scans. Different solvents like water, acetonitrile, methanol, and mixture of methanol:water in different ratios were used as solvents for these experiments. Among all the solvents, methanol water was the best. So, 10 ppm solution of each sample was made in 1:1 methanol:water solvent and used for our paper spray experiments. GO-coated paper was fixed on a coverslip and Raman measurement was done near to the tip area of the paper using a 532 nm laser excitation. A Witec confocal Raman microscope was used for collecting the spectra. The same paper was used continuously for paper spray, 60 cycles of measurements were done with 5 µL of solution each time, and a Raman spectrum was taken from the same area as before. ESI MS of benzyl alcohol treated with GO was taken to confirm that GO in the absence of potential does not do oxidation under the conditions investigated. This sample was electrosprayed at a flow rate of 5 µL/min and mass spectra were taken in negative ion mode in the mass range of *m/z* 50 to 250. Following parameters were used for all the ESI experiments: Source voltage –5 kV, sheath gas (nitrogen) flow rate 8 (manufacturer's unit) and all other parameters are same as paper spray. All ESI mass spectra presented correspond to an average of 100 scans. Tandem mass spectrometric experiments were carried out with collision induced dissociation.

Results and Discussion

Figure 1 shows the negative ion mode mass spectra of benzyl alcohol, collected using Whatman 42 filter paper (normal paper) and GO-coated paper. Figure 1a shows that on normal paper, *m/z* 91 is the most dominant peak in the spectrum, due to $C_7H_7^-$, which is the most stable fragment from benzyl alcohol. However, in the case of GO-coated paper (Figure 1b), two peaks at *m/z* 123 and *m/z* 121 were observed as the most prominent peaks in the mass spectrum. The peak at *m/z* 121 is due to benzoic acid which was formed due to the oxidation of benzyl alcohol and that at *m/z* 123 is due to an intermediate formed during the oxidation process (see below). Other graphenic surfaces like graphite-coated paper (Supplementary Figure S1B) also show oxidation of alcohol to acid but there, the spectrum was not clear; the peaks at *m/z* 121 and 123 were seen along with several other peaks, which may be due to different hydrocarbons. But GO-coated paper produced a comparatively cleaner mass spectrum. More importantly, relative intensities of the peaks at *m/z* 121 and 123 are much higher than graphite-coated paper. RGO-coated paper did not show any oxidation of benzyl alcohol (Supplementary Figure S1A). As GO-coated paper showed the best result among all other graphenic/graphitic surfaces, it was used as the substrate in the subsequent experiments.

The observed oxidation is strictly a surface phenomenon and the applied potential has an important role on it. To understand this, solution phase experiments were carried out. These experiments were done in two different ways; first, in a beaker, GO suspension and 1:1 methanol water solution of benzyl alcohol were taken and stirred for a long time. Supplementary Figure S1D shows the ESI-MS spectrum of the above product after 30 min of stirring. No peak at *m/z* 121 or at 123 was seen, which proves that oxidation did not occur in the absence of potential. Supplementary Figure S1E shows the results of our second solution phase experiment. Here, 1:1 methanol:water solution of benzyl alcohol was taken on an indium tin oxide (ITO)-coated glass plate and the potential was applied for 5 min.

The ESI mass spectrum of the mixture (Supplementary Figure S1E) shows that here also no noticeable peak at *m/z* 121 or 123 was seen. These experiments suggested that neither graphene oxide nor high voltage alone was capable of doing the oxidation; both are needed together for this reaction to occur.

We know that high current of the order of ~0.1–1 μA is involved in the paper spray process [33]. Due to the applied high potential of 2–5 kV, there is a large electric field near the tip of the paper. We propose that the electric field near the tip activates the GO surface and that is high enough to break some of the epoxide bonds in GO. Our solution-phase experiments (Supplementary Figure S1D and E) show that there is no reaction during electrospray. Although there is a large body of literature on reactions during electrospray, no oxidation is occurring in the present case in such experiments. This fact emphasizes the effect of electric field formed at graphene to be an important factor in the observed reaction.

Tandem mass spectrometric studies of the peaks at *m/z* 121 and 123 in negetive mode confirm that they are indeed the oxidation product and intermediate of the oxidation process, respectively. Figure 2a and b shows a negetive mode MS^2 spectrum of *m/z* 121, taken from pure benzoic acid (using Whatman 42 filter paper as substrate) and product of benzyl alcohol oxidation on GO-coated paper, respectively. Both the spectra show *m/z* 91 as the main fragment. From these two spectra, we conclude that the peak at *m/z* 121 is indeed due to benzoic acid and is formed in situ on the GO surface during paper spray (see below for more experiments on this). Figure 2c is a MS^2 spectrum of *m/z* 123 that shows *m/z* 121 as a main fragment of it. Figure 2d is a MS^3 spectrum of *m/z* 123 that shows a peak at *m/z* 91 as the main fragment of *m/z* 121, just as in other cases. This established that the compound corresponding to *m/z* 121 is derived from *m/z* 123; hence *m/z* 123 is indeed an intermediate of this oxidation process. From earlier reports of alcohol oxidation [34], we know that acetal is an intermediate of this process. Acetal is 2 mass units higher than the corresponding acid; hence it is likely that *m/z* 123 is the corresponding acetal intermediate for benzyl alcohol oxidation. Although direct confirmation of acetal intermediate has not been possible, our results in conjunction with Reference [34] suggest the existence of this species.

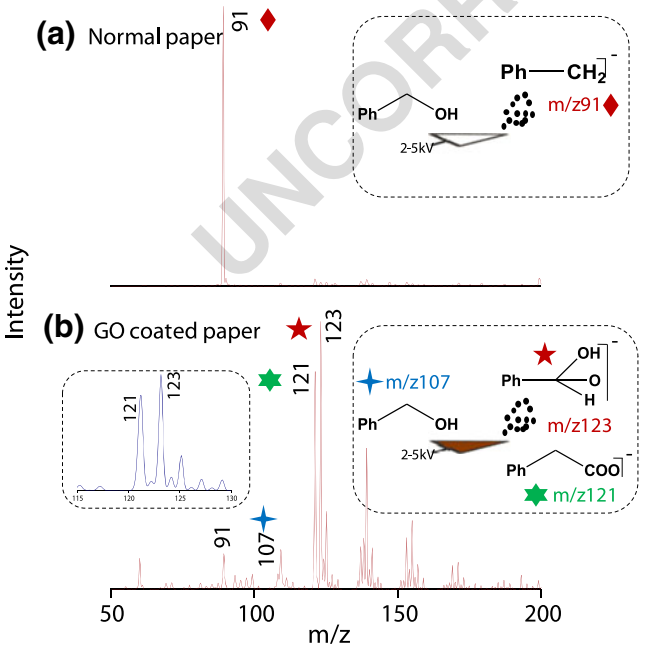

Figure 1. Paper spray ionization mass spectrum (–ve mode) of benzyl alcohol using **(a)** Whatman 42 filter paper; **(b)** GO-coated Whatman 42 filter paper. Insets show schematics of the experimental observations, and zoomed spectrum in **(b)** is from *m/z* 115 to 130

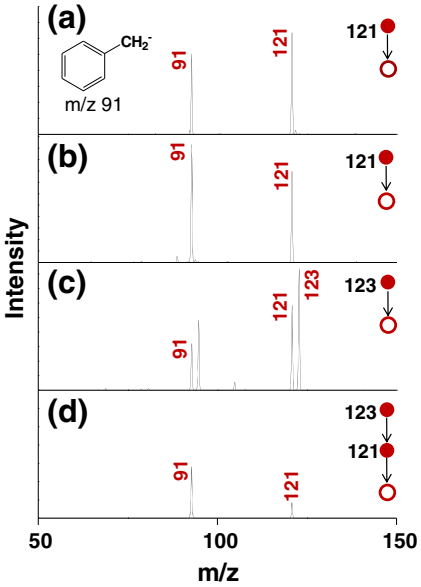

Figure 2. Results of tandem mass spectrometric experiments. **(a)** MS^2 of *m/z* 121 from pure benzoic acid. **(b)** MS^2 of *m/z* 121, **(c)** MS^2 of *m/z* 123, and **(d)** MS^3 of *m/z* 123 from the oxidation reaction of benzyl alcohol by GO-coated paper spray ionization

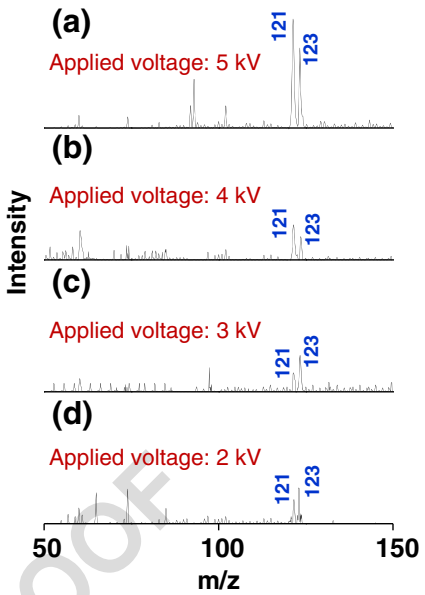

Figure 3. Paper spray mass spectra (–ve ion mode) of benzyl alcohol at different applied voltages. The applied potential varied from 5 to 2 kV from A to D

To further validate the identity of the product, we collected the product of benzyl alcohol oxidation, measured its Raman spectrum, and compared it with that of pure benzoic acid. Supplementary Figure S2A shows the Raman spectrum of the product that was collected on an ITO plate by keeping it in front of the tip area of the paper at a distance of 5 mm. As the ITO plate was grounded, charged species that were sprayed from the tip of the paper were accumulated on the ITO plate and became neutralized upon deposition. The substrate was washed with cold water as benzoic acid is insoluble in cold water. The product was dissolved in MeOH and spotted on a glass cover slip for taking the Raman spectrum, in order to avoid the ITO features in the spectrum. Supplementary Figure S2B shows the Raman spectrum of pure benzoic acid, which is similar to the product spectrum. Thus, oxidation of benzyl alcohol takes place on GO-coated paper.

Figure 3 show that the conversion of alcohol to acid through the intermediate follows different kinetics at different voltages. At lower voltages of 2–3 kV, relative intensity of the peak at *m/z* 123 is higher than the peak at *m/z* 121 and at higher voltages of 4–5 kV, the situation is reversed. From this data, we may suggest that at lower voltages, formation of intermediate is at a higher rate and at higher voltages, second step of the reaction (i.e., formation of acid from intermediate is much faster than the first step. Same reaction was performed multiple times using different alcohols; all of them showed the same result. From these data, we can conclude that a simple organic reaction like oxidation of alcohol can be monitored using this methodology. Although several studies of intermediates have been reported [35-37], a simple species such as acetal has not yet been seen experimentally. In paper spray process, ion formation is very fast; ions come out from the tip of the paper as soon as sample solution (or sample followed by solvent) is applied. So, it is capable of forming intermediate ions along with reactants, and the products formed can be studied simultaneously.

To know the fate of the GO surface, we did Raman measurements of the substrate before and after the oxidation reaction. Raman spectra were taken from the tip area of the triangularly cut paper. We added 5 µL of the sample solution for a single spray process and the same paper was used continuously for 60 spray cycles during 90 min of operation. Figure 4a and b show the total ion chromatogram (TIC) and the average mass spectrum of the above process. The behavior of TIC suggests that the surface activity increases with time and it saturates subsequently. We believe that after a few cycles of paper spray, the paper was saturated with the applied solvent and became more conductive. Therefore, the potential applied was able to activate GO surface to a greater extent and after some time, the conductivity became constant, which may be the reason for the above behavior. The average mass spectrum shows the two most abundant peaks at *m/z* 121 and 123, which establishes that the oxidation of alcohol is continuously occurring throughout the spray process.

Figure 4c shows the Raman spectrum of the same paper before and after the reaction. The D and G bands of graphene are plotted in the spectrum and there is a shift of G band by 13 cm^{-1} towards the lower wave number region after the reaction. This shift indicates that GO on the surface

JrnlID 13361_ArtID 786_Proof# 1 - 05/12/2013

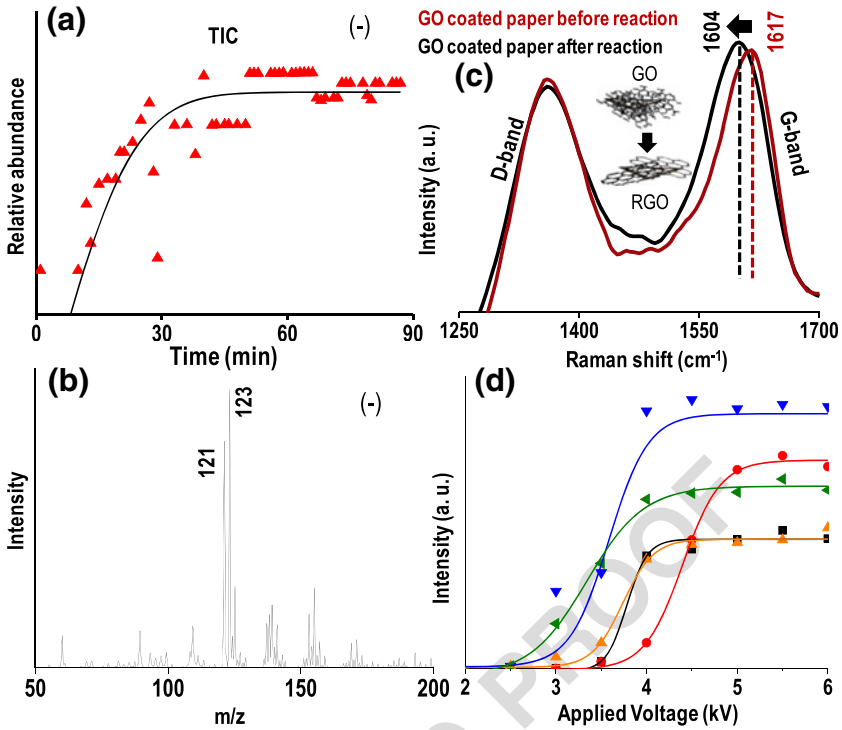

Figure 4. **(a)** TIC during the continuous oxidation of benzyl alcohol. Total ion intensities in the range of m/z 50 to 200 were monitored in each paper spray event. **(b)** Average mass spectrum of the reaction of benzyl alcohol oxidation for 60 cycles. **(c)** Raman spectrum of GO-coated paper before and after the reaction. **(d)** Plot of spray voltage dependence of different alcohols towards oxidation. ■ 1-pentanol, ◀ 1-hexanol, ● 2-phenyl ethanol, ▲ 1-pyrene butane, and ▼ benzyl alcohol

of the paper is converted to RGO after the reaction [38, 39]. Thus, graphene oxide undergoes reduction when alcohol is oxidized to acid. From literature [40], we know that intensity of G band in the Raman spectrum of GO depends on the number of layers in GO. In this case, an intense G band indicates that there are multiple layers of GO on the paper; this is also supported by the fact that a single GO-coated paper can show oxidation for several minutes (>90 min). Raman measurement of the same GO-coated paper before and after reaction was not possible because of laser-induced damage of the paper. Owing to irradiation of laser (532 nm), the spot of irradiation turns black and intensities of D and G band reduce with subsequent irradiations. So, for our Raman measurement, two identically sized papers were cut and coated with equal volume (10 μL) of GO suspension. Then one of them was used as reference (before reaction) and the other as sample (after reaction).

To explore the role of potential in the oxidation process, we did voltage-dependent paper spray of different alcohols on GO-coated paper. Figure 4d shows the voltage dependence of different alcohols towards oxidation. In this graph, intensities of the product acid are plotted with respect to the applied voltage. From the graph, it is clear that for each alcohol, there is a threshold potential above which oxidation process is facile and, after a certain applied potential, the intensity becomes constant. This graph also supports our other observation that alcohols containing aromatic rings are prone to oxidization more easily than other aliphatic alcohols. Threshold potential of oxidation for 1-pentanol and 1-hexanol is much higher than other aromatic alcohols. 1-Pyrene butanol has minimum threshold potential for oxidation as it is a larger π-electron system. As Raman measurements of the paper after reaction shows that GO changes to RGO after the reaction, we propose that the epoxy oxygen present in GO reacts with these molecules and oxidizes them. In this process, potential also has an important role perhaps potential activates the process [41]. We propose that the reaction observed is electro-oxidation during paper spray and involves transient adsorption of the analyte at the surface. This process becomes facile on graphenic surfaces. We tried oxidation of other compounds like triphenylphosphine, dimethylamine, etc. but in these cases we did not get any peak for the intermediate. It may be noted that there is no report of intermediates for these oxidation reactions in the literature. To show that this oxidation reaction is not limited to benzyl alcohol, we performed oxidation of other alcohols as well. Figure 5 shows the GO-coated paper spray mass spectrum of 1-hexanol, 2-phenyl ethanol, and 1-pyrene butanol. In all the cases, we found peaks for corresponding acids and the intermediates. Hence, for multistep reactions, intermediates are detected using this process. Figure 5 also shows the

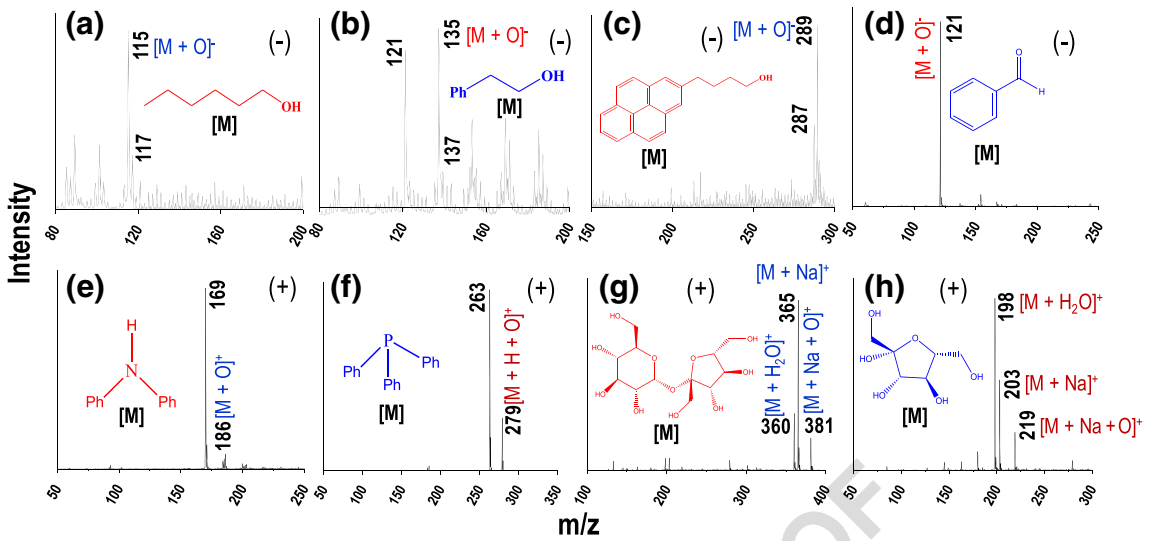

Figure 5. Oxidation of **(a)** hexanol, **(b)** phenyl ethanol, **(c)** pyrene butanol, **(d)** benzyldehyde, **(e)** diphenyl amine, **(f)** triphenylphosphine, **(g)** sucrose, and **(h)** fructose during paper spray ionization using GO-coated paper as the substrate. (+) and (–) denote positive and negative ion mode mass detection, respectively

structure of each compound. From this data, it is clear that intermediates of in-situ oxidation of alcohol to acid can be detected on GO surfaces. If the mass spectrum for 1-hexanol is compared with those of the other two alcohols, it can be noticed that the relative intensity of the peak due to the acid and the intermediate is weak in the former. This may be due to the better interaction of aromatic alcohols with the GO surface, by π-interactions.

To show that this in-situ oxidation process on GO-coated paper spray is not limited to alcohols, we did oxidation of other functional groups. Figure 5 shows the mass spectra of in-situ oxidation of other functional groups. Figure 5d shows in-situ oxidation of benzaldehyde on a GO-coated paper. The –ve ion mode mass spectrum, using paper spray method shown in this figure contains the most intense peak at *m/z* 121, which is due to benzoic acid, the oxidation product of

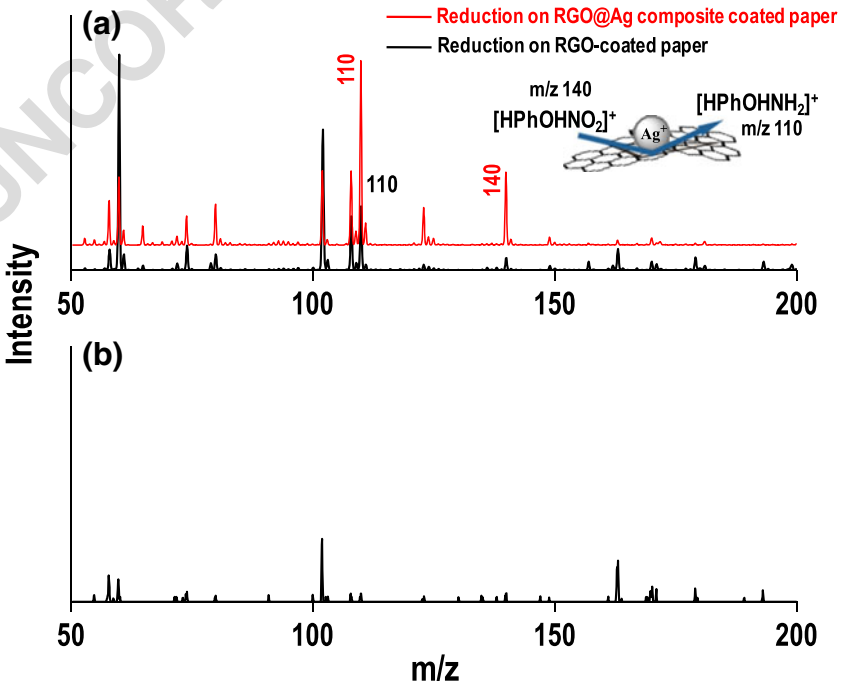

Figure 6. **(a)** Positive mode mass spectra for reduction of 4-nitrophenol on RGO-coated paper (black trace) and RGO-Ag composite coated paper (red trace). **(b)** Positive mode mass spectrum of MeOH on RGO-Ag composite coated paper

benzaldehyde. Figure 5e shows oxidation of diphenylamine. The mass spectrum shown here is in + ve mode using 1:1 methanol water solution of diphenylamine (methanol was used to increase the solubility in water). The most intense peak at *m/z* 169 corresponds to the singly charged parent. There are two other peaks at *m/z* 185 and 186, which are 16 and 17 Da higher than the molecular ion peak. We speculate these peaks to be one O addition and one O + H addition to diphenylamine.

Figure 5f shows oxidation of triphenylphosphine on GO-coated surface. Mass spectrum, taken in + ve ion mode using 1:1 water methanol as solvent, shows an intense peak at *m/z* 263, attributable to $[M + H]^+$ and another peak at *m/z* 279, attributable to $[M + O + H]^+$. Figure 5g and h show + ve mode mass spectra of sucrose and fructose, respectively. In these cases also, we observed peaks corresponding to the oxidation products. Peak at *m/z* 381 for sucrose, $[M + Na + O]^+$ and peak at *m/z* 219 for fructose, $[M + Na + O]^+$ can be seen. Supplementary Figure S3 shows the tandem mass spectrometric study on fructose, diphenyl amine, and triphenylphosphine. From these MS^2 data, identities of the oxidized peak have been confirmed. From these spectra, it is evident that all these compounds having different functional groups undergo in-situ oxidation during paper spray ionization using GO-coated paper.

To understand the chemical properties of graphenic surfaces in more detail, another reaction, namely, reduction of nitro functional group to amine, was studied. Figure 6a shows positive mode paper spray mass spectra of 4-nitrophenol on RGO-coated (black trace) and RGO-Ag composite-coated (red trace) paper. Mass spectra shown in Figure 6a clearly show that both the substrates give the reduction product (i.e., 4-aminophenol (*m/z* 110)] but it is clear that in case of RGO-Ag composite-coated paper, the relative intensity of the product is higher than the other. From these data, we may suggest that reduction is more feasible for the composite.

From the structure of graphene, we know that there is a readily available electron in the third dimension for each carbon atom due to the conjugated π orbital, which makes graphene highly conductive and chemically active. Graphene surface can easily donate that electron to other molecules in order to reduce them, especially when electrically activated. This may be the reason for the reduction of NO_2 functional group to NH_2 on the graphene surface. In the case of RGO-Ag composite, some of these free electrons of graphene were used for the reduction of Ag^+ to Ag^0. As Ag^+ is more stable electronically, it gets oxidized as soon as it interacts with a potential substrate. Although RGO itself is a strongly reducing substrate, Ag^+/Ag^0 redox couple in the composite helps it in the reduction process. Figure 6b shows positive mode mass spectrum of MeOH on RGO-Ag composite coated paper, which shows that certain peaks arise because of the background. Although the present reaction did not yield an intermediate, reduction reaction of this kind is observable directly.

From the data presented, we can suggest that direct measurements of intermediates should be possible at graphenic surfaces. Ag^0/Ag^+ system influences chemical reactions. Therefore, using such modified surfaces and different catalysts such as metal clusters, it may be possible to trigger chemically and industrially important reactions and sample the products and intermediates.

Conclusion

The results discussed here show that chemical reactions occur at active graphene surfaces, and they can be monitored in real time. This monitoring may also lead to the detection of intermediates in favorable cases. Quantitative analysis of the concentration using embedded standards would enable the measurement of kinetic parameters of the reactions. Extension of such methodologies may be useful in developing new forms of sensors. We propose that ambient ionization methods, in conjunction with active surfaces, may be considered as a new platform for chemical analysis in real time. Although the time scale of ionization and analysis pose restrictions on the time resolution, we believe that the method presented here would allow the understanding of typical organic reactions better. Using activated graphenic surfaces, for example with embedded and metal catalysts, industrially relevant processes may be attempted.

Acknowledgments

The authors acknowledge financial support from the Department of Science and Technology (DST), Government of India. D.S. and R.N. thank University Grants Commission (UGC), Government of India for his research fellowship. S.S.G. thanks the SERB, CII and Thermax India Pvt. Ltd. for a research fellowship.

References

1. Bentrup, U.: Combining in situ characterization methods in one set-up: looking with more eyes into the intricate chemistry of the synthesis and working of heterogeneous catalysts. Chem. Soc. Rev. **39**, 4718–4730 (2010)
2. Anna, J.M., Baiz, C.R., Ross, M.R., McCanne, R., Kubarych, K.J.: Ultrafast equilibrium and non-equilibrium chemical reaction dynamics probed with multidimensional infrared spectroscopy. Int. Rev. Phys. Chem. **31**, 367–419 (2012)
3. Badu-Tawiah, A.K., Eberlin, L.S., Ouyang, Z., Cooks, R.G.: Chemical aspects of the extractive methods of ambient ionization mass spectrometry. Annu. Rev. Phys. Chem. **64**, 481–505 (2013)
4. Friscic, T., Halasz, I., Beldon, P.J., Belenguer, A.M., Adams, F., Kimber, S.A.J., Honkimaeki, V., Dinnebier, R.E.: Real-time and in situ monitoring of mechanochemical milling reactions. Nat. Chem. **5**, 145 (2013)
5. Rosspeintner, A., Lang, B., Vauthey, E.: Ultrafast photochemistry in liquids. Annu. Rev. Phys. Chem. **64**, 247–271 (2013)
6. Frontiera, R.R., Mathies, R.A.: Femtosecond stimulated Raman spectroscopy. Laser Photonics Rev. **2011**(5), 102–113 (2011)
7. Takats, Z., Wiseman, J.M., Gologan, B., Cooks, R.G.: Mass spectrometry sampling under ambient conditions with desorption electrospray ionization. Science **306**, 471–473 (2004)

8. Ifa, D.R., Manicke, N.E., Dill, A.L., Cooks, R.G.: Latent fingerprint chemical imaging by mass spectrometry. Science **321**, 805 (2008)
9. Eberlln, L.S., Norton, I., Orringer, D., Dunn, I.F., Liu, X., Ide, J.L., Jarmusch, A.K., Ligon, K.L., Jolesz, F.A., Golby, A.J., Santagata, S., Agar, N.Y.R., Cooks, R.G.: Ambient mass spectrometry for the intraoperative molecular diagnosis of human brain tumors. Proc. Natl. Acad. Sci. U.S.A. **110**, 1611–1616, S1611/1–S1611/7 (2013)
10. Liu, J., Wang, H., Manicke, N.E., Lin, J.-M., Cooks, R.G., Ouyang, Z.: Development, characterization, and application of paper spray ionization. Anal. Chem. **82**, 2463–2471 (2010)
11. Wang, H., Liu, J., Cooks, R.G., Ouyang, Z.: Paper spray for direct analysis of complex mixtures using mass spectrometry. Angew. Chem. Int. Ed. **49**, 877/880, S877/1–S877/7 (2010)
12. Yang, Q., Manicke, N.E., Wang, H., Petucci, C., Cooks, R.G., Ouyang, Z.: Direct and quantitative analysis of underivatized acylcarnitines in serum and whole blood using paper spray mass spectrometry. Anal. Bioanal. Chem. **404**, 1389–1397 (2012)
13. Zhang, Z., Cooks, R.G., Ouyang, Z.: Paper spray: a simple and efficient means of analysis of different contaminants in foodstuffs. Analyst **137**, 2556–2558 (2012)
14. Oradu, S.A., Cooks, R.G.: Multistep mass spectrometry methodology for direct characterization of polar lipids in green microalgae using paper spray ionization. Anal. Chem. **84**, 10576–10585 (2012)
15. Liu, J., Wang, H., Cooks, R.G., Ouyang, Z.: Leaf spray: direct chemical analysis of plant material and living plants by mass spectrometry. Anal. Chem. **83**, 7608–7613 (2011)
16. Tadjimukhamedov, F.K., Huang, G., Ouyang, Z., Cooks, R.G.: Rapid detection of urushiol allergens of Toxicodendron genus using leaf spray mass spectrometry. Analyst **137**, 1082–1084 (2012)
17. Sarkar, D., Srimany, A., Pradeep, T.: Rapid identification of molecular changes in tulsi (Ocimum sanctum Linn) upon ageing using leaf spray ionization mass spectrometry. Analyst **137**, 4559–4563 (2012)
18. Perry, R.H., Splendore, M., Chien, A., Davis, N.K., Zare, R.N.: Detecting reaction intermediates in liquids on the millisecond time scale using desorption electrospray ionization. Angew. Chem. Int. Ed. **50**, 250–254 (2011)
19. Zhang, Q., Peng, W., Wang, Z., Li, X., Xiong, X., Guo, H., Wang, Z., Wu, F.: Li4Ti5O12/reduced graphene oxide composite as a high rate capability material for lithium ion batteries. Solid State Ionics **236**, 30–36 (2013)
20. Qi, X., Pu, K.-Y., Li, H., Zhou, X., Wu, S., Fan, Q.-L., Liu, B., Boey, F., Huang, W., Zhang, H.: Amphiphilic graphene composites. Angew. Chem. Int. Ed. **49**, 9426/9429, S9426/1–S9426/11 (2010)
21. Xiang, Q., Yu, J., Jaroniec, M.: Graphene-based semiconductor photocatalysts. Chem. Soc. Rev. **41**, 782–796 (2012)
22. Sreeprasad, T.S., Sen, G.S., Maliyekkal, S.M., Pradeep, T.: Immobilized graphene-based composite from asphalt: facile synthesis and application in water purification. J. Hazard. Mater. 246/247, 213–220 (2013)
23. Sreeprasad, T.S., Maliyekkal, S.M., Lisha, K.P., Pradeep, T.: Reduced graphene oxide-metal/metal oxide composites: facile synthesis and application in water purification. J Hazard. Mater. **186**, 921–931 (2011)
24. Sreeprasad, T.S., Pradeep, T.: Graphene for environmental and biological applicatios—a review. Int. J. Mod. Phys. B **26**, 1242001/1–1242001/26 (2012)
25. Lightcap, I.V., Kamat, P.V.: Graphitic design: prospects of graphene-based nanocomposites for solar energy conversion, storage, and sensing. Acc. Chem. Res. [ahead of print]
26. Li, Y., Chen, Z.: XH/π (X = C, Si) interactions in graphene and silicene: weak in strength, strong in tuning band structures. J. Phys. Chem. Lett. **4**, 269–275 (2013)
27. Xue, Y., Liu, Y., Lu, F., Qu, J., Chen, H., Dai, L.: Functionalization of graphene oxide with polyhedral oligomeric silsesquioxane (POSS) for multifunctional applications. J. Phys. Chem. Lett. **3**, 1607–1612 (2012)
28. Krishnamurthy, S., Kamat, P.V.: Galvanic exchange on reduced graphene oxide: designing a multifunctional two-dimensional catalyst assembly. J. Phys. Chem. C **117**, 571–577 (2013)
29. Radich, J.G., Kamat, P.V.: Making graphene holey. Gold-nanoparticle-mediated hydroxyl radical attack on reduced graphene oxide. ACS Nano **7**, 5546–5557 (2013)
30. Wan, W.-B., Zhao, Z.-B., Hu, H., Zhou, Q., Fan, Y.-R., Qiu, J.-S.: "Green" reduction of graphene oxide to graphene by sodium citrate. Xinxing Tan Cailiao **26**, 16–20 (2011)
31. Chua, C.K., Pumera, M.: Reduction of graphene oxide with substituted borohydrides. J. Mater. Chem. A **1**, 1892–1898 (2013)
32. Sen, G.S., Manoj, S.V., Krishnan, S., Sreeprasad, T.S., Singh, P.K., Pradeep, T., Das, S.K.: Thermal conductivity enhancement of nanofluids containing graphene nanosheets. J. Appl. Phys. **110**, 084302/1–084302/6 (2011)
33. Espy, R.D., Muliadi, A.R., Ouyang, Z., Cooks, R.G.: Spray mechanism in paper spray ionization. Int. J. Mass Spectrom. 325/327, 167–171 (2012)
34. March, J.: Advanced Organic Chemistry: Reactions, Mechanisms, and Structure, 4th ed., pp. 1495. Wiley, (1992)
35. Roberts, A., Furdui, C., Anderson, K.S.: Observation of a chemically labile, noncovalent enzyme intermediate in the reaction of metal-dependent Aquifex pyrophilus KDO8PS by time-resolved mass spectrometry. rapid commun. mass spectrom. **24**, 1919–1924 (2010)
36. Xu, G.-M., Chen, B., Guo, B., He, D.-X., Yao, S.-Z.: Detection of intermediates for the Eschweiler-Clarke reaction by liquid-phase reactive desorption electrospray ionization mass spectrometry. Analyst **136**, 2385–2390 (2011)
37. Foley, D.A., Doecke, C.W., Buser, J.Y., Merritt, J.M., Murphy, L., Kissane, M., Collins, S.G., Maguire, A.R., Kaerner, A.: ReactNMR and ReactIR as reaction monitoring and mechanistic elucidation tools: the NCS mediated cascade reaction of alpha-thioamides to alpha-Thio-beta-chloroacrylamides. J. Organic Chem. **76**, 9630–9640 (2011)
38. Kudin, K.N., Ozbas, B., Schniepp, H.C., Prud'homme, R.K., Aksay, I.A., Car, R.: Raman spectra of graphite oxide and functionalized graphene sheets. Nano Lett. **8**, 36–41 (2008)
39. Zhu, Y., Murali, S., Cai, W., Li, X., Suk, J., Potts, J.R., Ruoff, R.S.: Graphene and Graphene oxide: synthesis, properties, and applications. Adv. Mater. **22**(46), 5226 (2010)
40. Yang, H., Hu, H., Wang, Y., Yu, T.: Rapid and non-destructive identification of graphene oxide thickness using white light contrast spectroscopy. Carbon **52**, 528–534 (2013)
41. Li, G., Li, X., Ouyang, Z., Cooks, R.G.: Carbon–carbon bond activation in saturated hydrocarbons by field-assisted nitrogen fixation. Angew. Chem. Int. Ed. **52**, 1040–1043 (2013)

EurJIC European Journal of Inorganic Chemistry
ChemPubSoc Europe
FULL PAPER

DOI:10.1002/ejic.201301424

Luminescent AgAu Alloy Clusters Derived from Ag Nanoparticles – Manifestations of Tunable Au^{I}–Cu^{I} Metallophilic Interactions

Kumaranchira R. Krishnadas,[a] Thumu Udayabhaskararao,[a] Susobhan Choudhury,[b] Nirmal Goswami,[b] Samir Kumar Pal,[b] and Thalappil Pradeep*[a]

Keywords: Clusters / Nanoparticles / Luminescence / Closed-shell ions / Metallophilic interactions / Silver / Gold

Luminescent AgAu alloy quantum clusters are synthesized by a simple method that utilizes the galvanic reduction of polydisperse plasmonic silver nanoparticles. The clusters are characterized by ultraviolet–visible (UV/Vis) absorption spectroscopy, photoluminescence (PL) spectroscopy, X-ray photoelectron spectroscopy (XPS), transmission electron microscopy (TEM), and matrix-assisted laser desorption ionization mass spectrometry (MALDI MS). Selective and tunable quenching of cluster luminescence by Cu^{II} ions is observed and depends highly on the solvent as well as the protecting ligands. Metal-ion selectivity is exclusively caused by metallophilic interactions with the cluster core, and the tunability depends on the nature of the protecting ligands as well as solvent effects. Detailed XPS and time-resolved luminescence measurements reveal that the tunability of luminescence quenching is achieved by the systematic variation of the metallophilic interactions between the Au^{I} ions of the alloy cluster and Cu^{I} ions formed by the reduction of Cu^{II} ions by the cluster core. This is the first report of tunable metallophilic interactions between monolayer-protected quantum clusters and a closed-shell metal ion. We hope that these results will draw more attention to the field of quantum cluster–metal ion interactions and provide useful insights into the stability of these clusters, origin of their intense luminescence, mechanisms of metal-ion sensing, and also help in the development of methods for tuning their properties.

Introduction

Inherent molecule-like properties and synergistic effects owing to the presence of heteroatoms make dimetallic quantum clusters fascinating materials in modern cluster science. Doping with other metals has been shown to enhance the chemical stability[1] as well as tune the electronic structure of quantum clusters.[2] The presence of a heteroatom in the core is expected to result in unusual chiroptical and magnetic properties in dimetallic clusters. Despite their promising applications, the synthesis of such dimetallic quantum clusters with atomically precise composition is a big challenge. Among these clusters, Au–Ag[3] and Au–Pd[4] systems are common systems, and Au–Cu,[5] Au–Pt,[6] and Ag–Ni[7] clusters have also been reported. The simultaneous reduction of individual precursors[3–7] and galvanic reduction of presynthesized quantum clusters[10,11] are some of the methods utilized for the synthesis of dimetallic quantum clusters. Although galvanic reduction is extensively utilized for the synthesis of dimetallic nanocrystals with controlled shapes and compositions,[8] it is rarely utilized for the synthesis of atomically precise quantum clusters. Murray et al. have shown that it is possible to make dimetallic clusters from silver clusters[9] by this method, and galvanic reduction has recently been utilized to synthesize atomically precise Ag–Au clusters from presynthesized thiolate-protected[10] and protein-protected silver clusters.[11]

The interaction of metal ions with quantum clusters is an active topic of research. Metal ions induce new chemical and electrochemical reactivities in clusters and modify their absorption and emission features. Muhammed et al.[12a] reported the first metal-ion-induced changes in the optical properties of quantum clusters, and their reactivities with metal ions were investigated.[12b] Quantum confinement in nanoparticles significantly alters their redox potentials[13] and results in unexpected electrochemical reactions that cannot be explained by conventional electrochemistry.[14] Although there are some previous investigations on the size-dependent changes in the reduction potential of metal clusters,[15] the electrochemical reactivities of metal clusters remain largely unexplored. Metal-ion-induced changes in

[a] DST Unit of Nanoscience (DST UNS) and Thematic Unit of Excellence (TUE), Department of Chemistry, Indian Institute of Technology Madras,
Chennai 600036, India
E-mail: pradeep@iitm.ac.in
www.dstuns.iitm.ac.in
[b] Department of Chemical Biological & Macromolecular Sciences, S. N. Bose National Centre for Basic Sciences, Block JD, Sector III,
Salt Lake, Kolkata 700098, India
Supporting information for this article is available on the WWW under http://dx.doi.org/10.1002/ejic.201301424.

cluster luminescence has been extensively exploited for highly selective and sensitive detection of these species.[16] The distinct roles of the inner core and ligand shells of these clusters and photophysical mechanisms behind these interactions have not been investigated in detail. Recently, metallophilic interactions between closed-shell metal ions with quantum dots[17] and protein-protected Au clusters[18] were shown to result in quenching of their luminescence. Metallophilic interactions, weak bonding interactions between two closed-shell metal ions, are a well-known phenomenon in Au^{I} complexes and heterometallic clusters of transition metals.[19] However, this is not a well-recognized phenomenon in monolayer-protected noble-metal quantum clusters. Pyykko et al. presented the first theoretical studies on the interactions between a closed-shell Au_n cluster and closed-shell Au^{I} species.[20] This work raised the possibility of metallophilic interactions between the inner Au_n core and Au^{I} ions in the protecting thiolate staple motifs of the clusters and is of immediate relevance to monolayer-protected quantum clusters. Explorations of such interactions in these systems may provide valuable insights into their stability, the origin of their intense luminescence, mechanisms of metal-ion sensing, and may also offer strategic methods for tuning their properties.

Here, we present the utility of the galvanic reduction reaction as a simple method for the synthesis of luminescent monodisperse AgAu quantum clusters protected by mercaptosuccinic acid (AgAu@MSA) derived from polydisperse plasmonic Ag nanoparticles (AgNPs). These clusters are synthesized at room temperature and no external reducing agent is required. The use of Ag nanoparticles as the precursor, instead of atomically precise Ag quantum clusters, makes the method more facile and scalable because of the inherent instability and difficult synthesis of the latter. The intense red luminescence of these clusters under UV irradiation and their high stability in aqueous solutions may make this material useful for biological applications. The luminescence of this cluster is selectively quenched by Cu^{II} ions. Detailed X-ray photoelectron spectroscopy (XPS) measurements show that Cu^{II} ions are reduced by interactions with the clusters. Even though Murray et al. and Wu et al. have shown that negatively charged as well as neutral Au_{25} clusters can reduce more reactive metal ions such as Ag^{I} and Cu^{II} ions,[14] no such reports exist on the redox reactivities of alloy clusters. Time-resolved as well as steady-state luminescence measurements show that this reactivity leads to metallophilic interactions between the Au^{I} ions of the clusters and Cu^{I} ions formed by the reduction of Cu^{II} ions by the clusters. Also, we report the solvent- and protecting-ligand-dependent tunability of these interactions, which are reflected in the changes in the luminescence of the cluster. Reports on such tunable metal-ion interactions with the clusters are scarce in the literature. This is the first report of tunable metallophilic interactions between monolayer-protected quantum clusters and a closed-shell metal ion. These metallophilic-interaction-induced changes in cluster luminescence are useful for the selective detection of Cu^{II} ions in water below permissible levels.[16h]

Results and Discussion

Synthesis and Characterization of Alloy Clusters

AgAu@MSA clusters were synthesized by galvanic reduction of AgNPs by Au^{I}–MSA thiolates. Figure 1 shows the time-dependent changes in the UV/Vis features during the reaction. The plasmonic feature at 410 nm of AgNPs disappeared immediately after the addition of Au^{I}-MSA solution, and a new feature appeared at around 600 nm, which gradually disappeared and the spectrum became featureless. The solution was stirred for one hour and centrifuged subsequently to remove larger alloy nanoparticles and AgCl. The UV/Vis spectrum of the resuspended precipitate (Figure S1) showed a broad peak at ca. 600 nm, which is between the Au and Ag plasmonic peaks. This may be due to the formation of larger AgAu alloy nanoparticles. We propose that during the galvanic reduction, larger nanoparticles in the polydisperse AgNP sample react with Au^{I}–MSA to form larger AgAu dimetallic nanocrystals, and very small particles undergo galvanic reduction to form AgAu dimetallic quantum clusters (a schematic of the reaction is given in the inset of Figure 1). The TEM images shown in the inset of Figure 1 clearly show the decrease in the particle size from AgNPs to AgAu@MSA clusters. As the larger nanoparticles have lower solubility in methanol, these dimetallic nanoparticles precipitate, and the smaller dimetallic clusters remain in solution. The formation of AgCl was confirmed by XRD analyses of the precipitate (Figure S2).

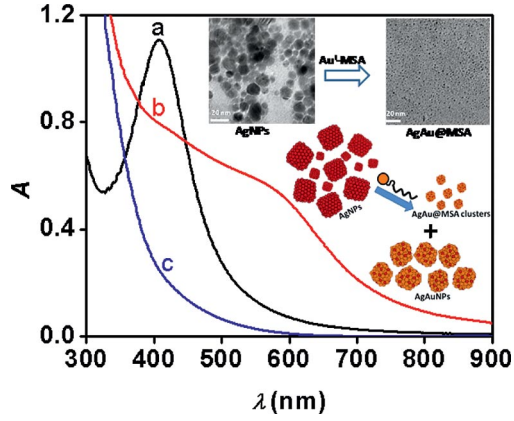

Figure 1. Time-dependent changes in the UV/Vis features during the reaction between AgNPs and Au^{I}–MSA thiolates in methanol. (a) UV/Vis spectra of AgNPs in methanol, (b) immediately after the addition of Au^{I}–MSA, and (c) after one hour of the reaction.

Insets a and a′ in Figure 2 show the photographs of the precursor AgNPs under visible and UV light, respectively. Immediately after the addition of Au^{I}–MSA, this solution showed red emission under UV illumination. The time-dependent evolution of the luminescence features is shown in Figure S3, and typical luminescence features of the cluster are shown in Figure 2. The cluster showed a broad emission peak at 675 nm at 365 nm excitation. Insets b and b′ of Figure 2 show the photographs of the AgAu@MSA cluster under visible and UV light, respectively.

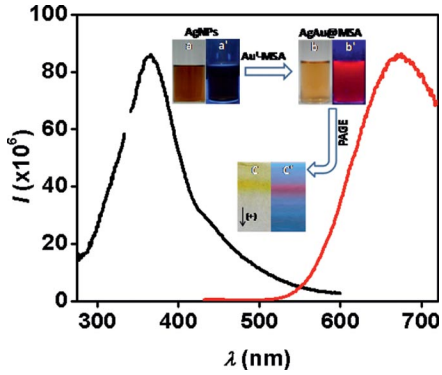

Figure 2. Excitation and emission spectra of AgAu@MSA clusters in methanol. The insets are the photographs of (a and a′) the AgNP solution, (b and b′) the AgAu@MSA solution, and (c and c′) the PAGE-separated clusters under visible and UV light, respectively. The discontinuity in the excitation peak shows the position at which the secondary of the emission maximum appears.

Polyacrylamide gel electrophoresis (PAGE) was performed to check the purity of the as-synthesized clusters (details in the Supporting Information). The inset photographs (c and c′) of Figure 2 show the presence of a single band of the gel after PAGE separation. The band appeared light yellow under visible light and bright red under a UV lamp. This shows that monodisperse dimetallic clusters can be synthesized from polydisperse plasmonic silver nanoparticles by using the galvanic reduction method.

The XPS survey spectrum shown in Figure 3 (a) indicates the presence of all expected elements. The Au $4f_{7/2}$ peak at 84.1 eV shows that the Au atoms are in the zero oxidation state. The Ag $3d_{5/2}$ peak at 368.0 eV[10] indicates the presence of metallic Ag in the cluster. The S $2p_{3/2}$ peak at 162.2 eV suggests that sulfur is attached to the metal core in the form of thiolate.[22] Energy-dispersive X-ray analysis (EDAX) also confirmed the presence of the constituent elements in the cluster (Figure S4).

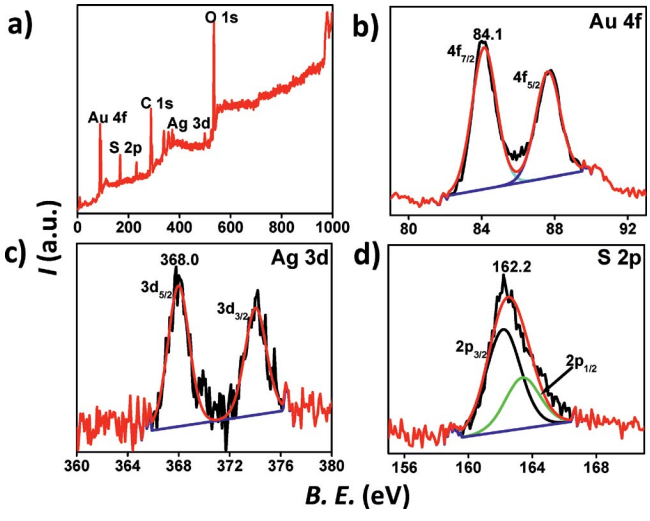

Figure 3. (a) XPS survey spectrum of the AgAu@MSA cluster and expanded regions of it showing the (b) Au 4f, (c) Ag 3d, and (d) S 2p features.

Figure 4 shows the matrix-assisted laser desorption ionization mass spectra (MALDI MS) of the clusters after ligand exchange with hexanethiol. Ligand exchange was attempted because MSA-protected clusters do not give intact ions in MALDI MS. This is also the case with glutathione-protected clusters.[23] The inset of Figure 4 shows the luminescence spectral features of the cluster before (in water) and after (in toluene) ligand exchange. The excitation maximum of the cluster shows a blueshift of ca. 20 nm after ligand exchange, and the emission maximum is blueshifted by ca. 5 nm. These shifts could be caused by the difference in the polarities of water and toluene. The excitation and emission spectral shapes are preserved after ligand exchange, which shows that the composition of the cluster core is unchanged. At the threshold laser fluence, a peak at 17 kDa appears, and the peak shifts to the lower mass region owing to fragmentation of the cluster upon increasing laser fluence.

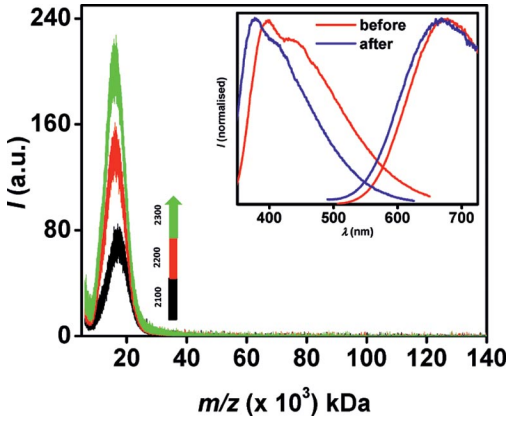

Figure 4. Laser-intensity-dependent MALDI MS spectra of the AgAu clusters, ligand-exchanged with hexanethiol. The numbers by the side of the arrow indicate the laser intensity as given by the instrument. The inset shows the excitation and emission spectra of the cluster before and after ligand exchange.

Tunable Interactions of the Alloy Clusters with Cu^{II} Ions

Interactions of metal ions with the quantum clusters affect their absorption and emission features. Metal-ion-induced luminescence changes of quantum clusters were utilized extensively for the selective detection of trace quantities of metal ions.[16,24] To study the interaction of metal ions with the AgAu@MSA clusters, the luminescence spectra of these clusters were measured in the presence of various metal ions. Aqueous solutions of various metal ions (100 μL, 100 ppm) were added to the cluster solution in methanol. The luminescence of the AgAu@MSA clusters was quenched immediately after the addition of a Cu^{II} solution. Figure 5 (a) shows that quenching is selective to Cu^{II} ions, and there is no significant decrease in luminescence intensity upon the addition of other metal ions. The addition of Cu^{II} ions resulted in gradual precipitation of the clusters from the solution. These observations may invoke the possibility of aggregation-induced luminescence

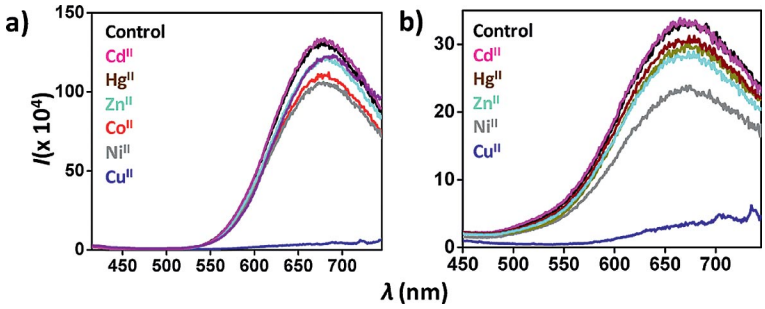

Figure 5. Emission spectra of (a) AgAu@MSA clusters in methanol and (b) AgAu@BBS clusters in THF in the presence of various metal ions.

quenching, resulting from the binding of Cu^{II} ions to the carboxylate groups of the MSA ligands, which was suggested as a metal-ion-induced quenching mechanism in noble-metal clusters.[24] Aggregation-induced quenching occurs by the reabsorption of the emitted radiation from the fluorophore, and for this phenomenon to be feasible, the Stokes shift of the fluorophore should be very small. The large Stokes shift (ca. 310 nm) of the AgAu@MSA cluster also suggests that this phenomenon is not likely. The UV/Vis absorption spectrum of the cluster was featureless, and no new features were observed after treatment with the Cu^{II} salt (Figure S5). Moreover, aggregation induced by the Cu^{II} ions should not affect the cluster core and, hence, the binding energies of the core atoms will not be shifted. XPS measurements (Figure 8) show that the Au binding energy is shifted to higher values. This evidence clearly indicates the absence of aggregation-induced quenching.

To determine whether the observed metal-ion selectivity is due to the specific interaction of Cu^{II} ions with the core or the carboxylate groups of the ligand shell of the AgAu cluster, quenching experiments were performed with clusters that had been ligand-exchanged with *tert*-butylbenzyl mercaptan (BBSH). As the sulfur atom of this ligand is bound to the AgAu core of the cluster and there are no other functional groups such as –COOH, the possibility of ligand–Cu^{II} interactions is eliminated. Interestingly, the luminescence of the ligand-exchanged cluster (AgAu@BBS) was also quenched by Cu^{II} ions (Figure 5, b), that is, the selectivity towards Cu^{II} ions was retained even after ligand exchange. These observations clearly suggest that the origin of metal-ion selectivity is the interaction of Cu^{II} ions with the AgAu core of the cluster.

The addition of oxalic acid (OA) into the Cu^{II}-treated AgAu@MSA solution in methanol (solution 1) resulted in complete recovery of the luminescence (Figure 6, a). This shows that the interaction of Cu^{II} ions with the clusters is almost completely reversible in methanol. As oxalic acid is a very strong chelator for Cu^{II} ions, it forms stable copper oxalate, which results in the recovery of the luminescence. The addition of Cu^{II} ions into a mixture of OA and the clusters did not result in any quenching (Figure S6); this shows that OA effectively prevents cluster–Cu^{II} interactions. Interestingly, the luminescence of a AgAu@BBS–Cu^{II} mixture in tetrahydrofuran (THF; solution 3) was not at all recovered by the addition of OA (Figure 6, c). To check the role of change in solvent from methanol to THF on the observed irreversibility, quenching experiments were performed with AgAu@MSA clusters in THF. Interestingly,

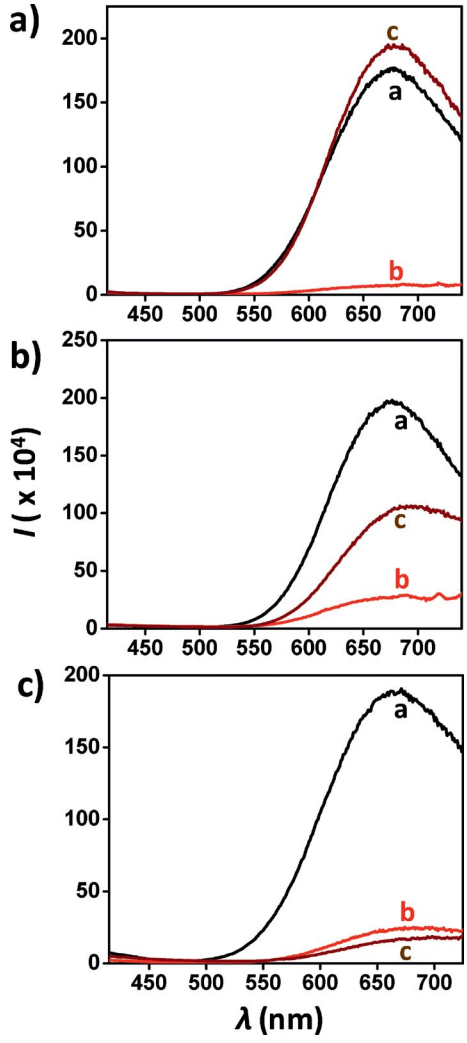

Figure 6. Emission spectra of (a) AgAu@MSA clusters in methanol and (b) THF and (c) AgAu@BBS clusters in THF showing the changes in luminescence upon the addition of Cu^{II} ions and OA. In each panel, traces a–c corresponds to the pure cluster, the cluster with Cu^{II} ions, and the cluster with Cu^{II} ions and OA, respectively.

we observed a partial recovery (Figure 6, b) of the luminescence upon the addition of OA into a AgAu@MSA–Cu^{II} mixture in THF (solution 2). This indicates that in addition to the solvent, the nature of the protecting ligand is also important in the determination of the reversibility of the interaction (see below for possible effects of solvent and protecting ligands). These observations show that the cluster–Cu^{II} interactions that lead to luminescence quenching are tunable with respect to the solvent and the nature of the protecting ligand. However, we observed a redshift of the emission maximum (ca. 5 nm for solution 1 and ca. 10 nm for solutions 2 and 3) upon the addition of Cu^{II} ions, and the shift was retained even after the addition of OA.

XPS measurements of the Cu^{II}-treated clusters (Figure 7) show that the Cu $2p_{3/2}$ peak is shifted to lower binding energies compared to that of metallic Cu (935.5 eV). Cu^{II} shows a well defined peak shape with characteristic satellite structure. The presence of Cu 2p features in all the treated samples indicates that Cu is part of the samples. Note that the XPS sample preparation involves washing the sample. However, complete absence of the satellite structure in these samples suggests reduction of the Cu^{II} ions. For solution 1, the Cu $2p_{3/2}$ peak is at 932.5 eV, whereas for solutions 2 and 3, these peaks are shifted to 932.3 and 932.2 eV, respectively. As the difference in the Cu^{I} and Cu^{0} binding energies is only ca. 0.1–0.2 eV,[25] it is difficult to assign the exact Cu oxidation states in the mixtures. However, the reduction of Cu^{II} to Cu^{I}/Cu^{0} is evident from these measurements. The characteristic ligand-to-metal charge-transfer satellite of Cu^{II} at 946 eV is absent in the treated samples, indicating the complete absence of the Cu^{II} state in the samples.

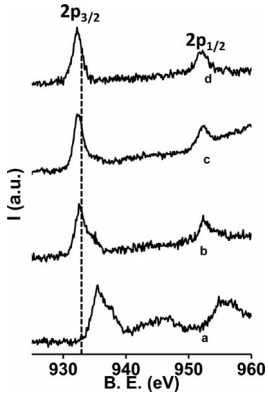

Figure 7. Cu 2p regions in the X-ray photoelectron spectra of pure and Cu^{II}-treated AgAu clusters. Traces a–d correspond to $CuSO_4$ and solutions 1, 2, and 3, respectively.

Figure 8 shows the Au 4f binding energies for the pure and Cu^{II}-treated clusters. The Au $4f_{7/2}$ peak for the pure AgAu@MSA cluster is at 84.1 eV. For solutions 1 and 2, this peak is shifted to 84.6 eV. This peak shifts further to 85.0 eV for solution 3. The binding energies for Ag were almost unchanged for the pure as well as Cu^{II}-treated clusters (Figure S7). This clearly indicates that the Cu^{II} ions interact preferentially with the Au atoms of the alloy cluster. Elemental analysis (Figure S4) shows that the alloy cluster is mostly composed of Au. Galvanic reduction by Au^{I} thiolates is initiated on the surface of the AgNPs, and most of the Ag atoms will be released as Ag^{I} ions and a few Ag atoms will be entrapped by Au atoms. Hence, these Ag atoms are more likely to be in the inner core of the cluster, which make them inaccessible to the Cu^{II} ions. This could be the reason for the preferential interaction of the Cu^{II} ions with the Au atoms of the cluster.

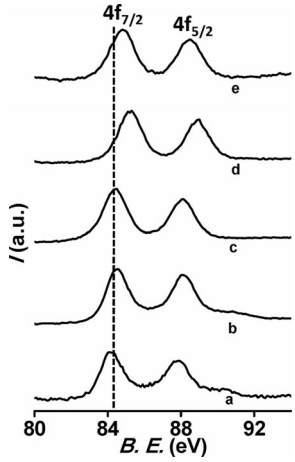

Figure 8. Au 4f region in the X-ray photoelectron spectra of pure and Cu^{II}-treated AgAu clusters. Traces a–e correspond to pure AgAu@MSA and solutions 1–4, respectively.

Notably, the observed trend in reversibility of the luminescence parallels the changes in the Au $4f_{7/2}$ binding energies. The Au $4f_{7/2}$ peak for solutions 1 and 2 (for which the luminescence was completely and partially reversible, respectively) is at 84.6 eV, which is between those for the pure clusters (84.1 eV) and AgAu@BBS (85.0 eV). The shift in the Au $4f_{7/2}$ peak (from 84.1 to 85.0 eV) is maximum for solution 3, for which irreversible quenching of luminescence was observed.

We suggest that the clusters can undergo two kinds of interactions with Cu^{II} ions. XPS measurements clearly indicate that the Cu^{II} ions are reduced as a result of their interactions with the cluster. The decrease in Cu binding energy (to that of Cu^{I}/Cu^{0}) and increase in that of Au in the clusters may be an indication of a redox reaction between the cluster core and Cu^{II} ions (reaction 1). The redshift of the emission maximum of the clusters after treatment with Cu^{II} ions could be an indication of the oxidation of the clusters. The reduction of the Cu^{II} ions by a noble metal such as Au may seem contradictory when considering the conventional electrochemical potentials. It is to be noted that the standard electrochemical potentials in the literature are those of bulk electrodes. In the case of nanoparticles, especially at the quantum cluster regime, electrochemical potentials will be very much determined by quantum confinement effects. A few earlier investigations[15c,15d] on small metal clusters have shown that their reduction potentials were lower than the bulk values. Hence, at the cluster regime, these types of redox processes are feasible. Another possibility for the reduction of the Cu^{II} ions is the replacement of some of the Au^{I} ions of the thiolate staple motifs by Cu^{II} ions, which may lead to the formation of a mixed thiolate shell contain-

ing both Au^{I} and Cu^{I} ions (reaction 2). This leads to the reduction of Cu^{II} to Cu^{I} as in the case of copper thiolates.[26] We could not confirm this interaction by an analysis of the S 2p binding energies of the samples as there were no significant changes in the S 2p binding energies of solutions 1 and 2, compared to that of pure clusters. Notably, the S 2p binding energies of copper and gold thiolates are almost the same (ca. 162 eV).[22,26] However, for solution 3, the S $2p_{3/2}$ binding energy was 162.7 eV (data not shown), which is higher than that of the pure clusters (162.2 eV). XPS of the OA-treated solution 1 (solution 4; sample for which luminescence was completely recovered) indicates that the Au 4f binding energies remain at higher values (84.6 eV). This shows that the clusters undergo an irreversible oxidation as a result of their interactions with the Cu^{II} ions (reaction 1). Reaction 2 is expected to result in complete reversibility of the Au 4f binding energies to those of the pure clusters after treatment with OA, as all of the Cu^{I} ions are completely removed by OA. Once the Cu^{I} ions have been removed by OA, the Au^{I} ions can bind with the ligands (released from Cu^{I}), and this will regenerate the pure clusters and should lead to the reversal of the Au 4f binding energies to that of the pure clusters. However, this reversal of binding energies was not observed. These observations indicate that reaction 1, that is, the galvanic reduction, is the most likely interaction between the clusters and Cu^{II} ions.

To understand the mechanism of the observed fluorescence quenching of AgAu@MSA clusters in presence of Cu^{II} ions, we plotted (Figure 9) the fractional fluorescence according to the Stern–Volmer Equation (1).

$$\frac{F_0}{F} = 1 + K_D[Q] \quad (1)$$

F_0 and F are the fluorescence intensity in the absence and presence of quencher, respectively, [Q] is the concentration of quencher and K_D is the Stern–Volmer quenching constant. From Figure 9, we have found a linear response of fluorescence as a function of Cu^{II} ion concentration. This result indicates that the nature of quenching is dynamic.

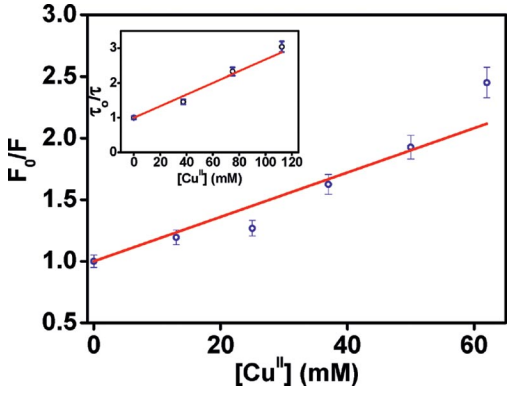

Figure 9. Stern–Volmer plot for the luminescence quenching of AgAu@MSA clusters in methanol upon the addition of Cu^{II} ions. The inset shows the change of τ_0/τ_{av} with Cu^{II} ion concentration.

Picosecond time-resolved luminescence measurement is a useful technique to aid understanding of the photophysical processes behind the observed quenching of the AgAu@MSA clusters. A gradual and significant decrease in the average lifetime (Figure S8 and Table S1) with increasing quencher concentration indicates the occurrence of dynamic quenching. The plot of τ_0/τ_{av} against Cu^{II} concentration (inset of Figure 9) was linear, as expected for a dynamic quenching process. The decay profiles for pure clusters and solution 1 are shown in Figure 10. The decay transients are fitted tri-exponentially, and the fitting parameters are tabulated in Table 1. Similar decay behaviors were also observed for solutions 2 and 3 (Tables S2 and S3, Figure S9 and S10, respectively). The decay profiles indicate the dynamic nature of quenching for all cases.

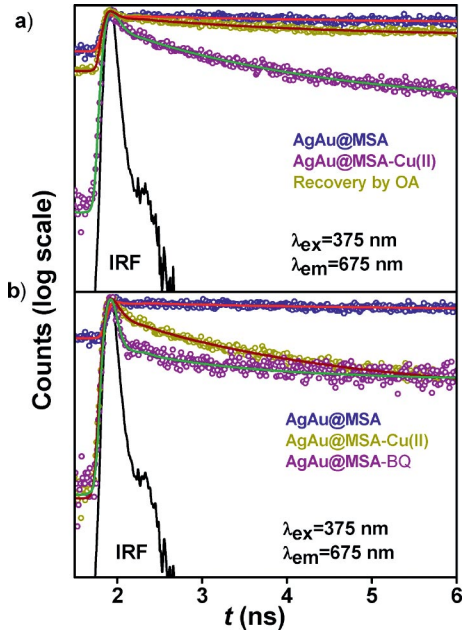

Figure 10. Picosecond time-resolved fluorescence transients of AgAu@MSA clusters in methanol. (a) The quenching of luminescence lifetime upon the addition of Cu^{II} ions and its recovery upon the addition of OA and (b) upon the addition of Cu^{II} ions and benzoquinone.

Table 1. Picosecond time-resolved luminescence transients of AgAu@MSA before and after the treatment with Cu^{II} and recovery by OA in methanol. AgAu@MSA was also treated with BQ.

System	τ_1 [ns] (%)	τ_2 [ns] (%)	τ_3 [ns] (%)	τ_{av} [ns]
Pure AgAu@MSA cluster in methanol	0.16 (38)	1.12 (20)	50 (42)	21.3
Cluster with Cu^{II}	0.10 (65)	1.24 (22)	12 (13)	1.93
Cluster with OA	0.09 (52)	1.64 (20)	50 (28)	14.4
Cluster with BQ	0.07 (71)	1.58 (9)	55 (20)	11.2

Dynamic quenching can occur through various processes such as Förster resonance energy transfer (FRET) and photoinduced electron transfer (PET). However, the absence of any permanent oscillating dipole (owing to the acceptor) rules out the possibility of a FRET process. The absence of an electron transfer processes is further confirmed by con-

trol experiments with benzoquinone (BQ), a well-known electron acceptor. In presence of BQ, an ultrafast time component (70 ps) evolves with very sharp decay with a contribution of 71% (Figure 10, b). No such drastic changes in the ultrafast components are observed for the Cu^{II}-treated samples, which rules out the possibility of an ultrafast PET process from the cluster to the Cu^{II} ions. This is supported by measurements at different Cu^{II} ion concentrations, for which the gradual reduction of the longer time component was observed with minor alteration of the shorter time constant (Figure S8 and Table S1).

Similar lifetime decay patterns were reported for Au_{25}@BSA clusters upon the interaction with Hg^{II} ions.[18a] This was attributed to metallophilic bond-induced quenching of the delayed fluorescence. The observations of the reduction of the Cu^{II} ions along with the similarity in the decay patterns of the AgAu clusters strongly suggest the possibility of metallophilic interactions. We suggest the following mechanism for the observed selective and tunable quenching interactions. The Cu^{II} ions are first reduced to Cu^{I} by a redox reaction with the AgAu core of the cluster (reaction 1). The $3d^{10}$ orbital of the Cu^{I} ions and the $5d^{10}$ orbital of either the Au^{I} ions of the thiolate staple motifs or the Au atoms of the partially oxidized cluster take part in metallophilic interactions. As the staple motifs have a significant role in the electronic structure of monolayer-protected clusters,[27] these interactions can lead to changes in the electronic structure and to quenching. Metallophilic interactions between Au^{I} and Cu^{I} ions are recognized both theoretically and experimentally in diverse systems and have been utilized in applications such as vapochromic sensors.[28] We suggest that galvanic reduction-induced metallophilic interactions are the key factor that determines the selectivity towards metal ions. Among the metal ions tested, only the Cu^{II} and Hg^{II} systems possess positive reduction potentials and, hence, these ions can be reduced most easily by the quantum clusters. The reduction potentials of the other metal ions are negative and, hence, they cannot be reduced by these clusters. In addition to the electrochemical potentials, the requirement of a closed-shell electronic configuration for metallophilic interactions immediately reveals the reason behind the observed metal-ion selectivity. Among Cu^{II} and Hg^{II}, only Cu^{II} can attain a closed-shell configuration (of Cu^{I}) from core-induced reduction, and this might be the reason behind the observed selectivity towards Cu^{II}. Even though Hg^{II} can be reduced to Hg^{I} by the cluster, this reduction will lead to the formation of an ion without a closed-shell configuration. Notably, the addition of Hg^{II} ions to the clusters does not lead to any immediate luminescence quenching. However, quenching owing to the addition of Hg^{II} ions was observable only after about 5 h (data not shown). Earlier studies on the reaction of quantum clusters with Hg^{II} ions show that the Hg^{II} ions were reduced mostly to Hg^{I} and not to Hg^{0}.[12b] This could be due to the high affinity of mercury towards the thiolate ligands of the cluster.

We suggest that solvents as well as protecting ligands play a crucial role in the tunability of the luminescence quenching of these AgAu clusters. Solvents can induce structural changes in the cluster core as well as the thiolate staple motifs. Recent studies on Au–Cu clusters protected by alkynyl ligands[29a] show that solvents can induce structural reorganization of clusters by affecting the strength of metallophilic bonding, and this leads to changes in the luminescence features. Studies on Au^{I} thiolates have shown that solvents can induce Au^{I}–Au^{I} metallophilic interactions caused by aggregation and lead to visible photoluminescence.[29b] These solvent effects will modulate the strength of Au^{I}–Cu^{I} boding in these clusters and lead to tunable quenching interactions. As mentioned earlier, changes in the bonding of thiolate staple motifs alter the electronic structure of clusters, which in turn affects the luminescence features of the cluster.[27]

Metallophilic bonding can originate from different types of interactions between the closed-shell species such as van der Waals, ionic, and charge-transfer forces. Theoretical studies on Au^{I}–Cu^{I} metallophilic bonds[28a] show that this bond is mainly due to ionic forces between the two species. Hence, changes in the solvent polarity are expected to significantly affect the nature of this bond. As the polarity of the solvent decreases, the ionic-interaction-based metallophilic bond becomes less feasible and the bond becomes more covalent in nature and, hence, stronger. Therefore, the Au^{I}–Cu^{I} bond will be weaker (i.e., this bond will be only metallophilic in nature) in a polar solvent such as methanol than in THF. The efficient chelation of Cu^{I} species happens in methanol and in turn results in complete recovery of the luminescence. The complete recovery of luminescence was further confirmed by experiments with the clusters in acetone as another polar solvent (Figure S11). We also observe the recovery in the time-resolved measurements (see Figure 10, a). In THF, the metallophilic contributions to the Au^{I}–Cu^{I} bond will be less, and the covalent nature of the bond increases. This makes the Au^{I}–Cu^{I} bond stronger and, hence, chelation with OA will be less facile. This could be the reason for the partial recovery of luminescence for the AgAu@MSA clusters in THF. Note that the dielectric constants of methanol, acetone, and THF are 33, 21, and 7.5, respectively. However, we could not demonstrate the irreversible quenching for the MSA-protected sample in a solvent less polar than THF because of the insolubility of the clusters and Cu^{II} salts in such solvents. In the case of the ligand-exchanged clusters, the Au^{I}–Cu^{I} bond experiences a much more nonpolar environment (owing to the BBSH or hexanethiol ligand shell) compared to the case with the AgAu@MSA clusters in THF. Therefore, the Au^{I}–Cu^{I} bond will be strongest for the ligand-exchanged cluster in THF. In this case, the chelation of the Cu^{I} ions with OA will be least facile. This could be the reason behind the irreversible quenching of the ligand-exchanged cluster. The selectivity towards Cu^{II} ions and irreversibility of the luminescence quenching are further confirmed with clusters that are ligand-exchanged with hexanethiol.

To check the practical utility of these interactions for Cu^{II} detection, the luminescence intensities of aqueous solutions of AgAu@MSA with different Cu^{II} concentra-

tions (in parts per million) were measured (Figure 11). A good linear response of the materials towards Cu^{II} ions was observed. From this plot, the detection limit is 0.5 ppm, which is well below the permissible limit of Cu^{II} ions in water (1.3 ppm). As the reduction potentials of the clusters depend on their composition, we expect that these interactions can be utilized for ultra-low-level detection with clusters of varied composition, which can be easily synthesized by our method.

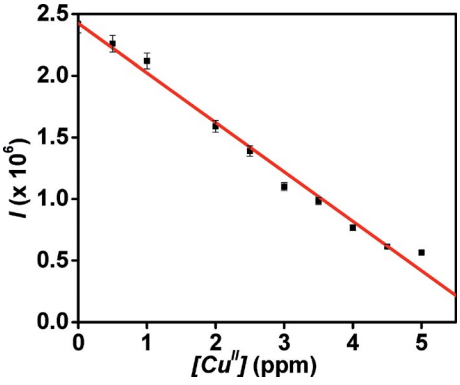

Figure 11. Variation of the luminescence intensity of the AgAu@MSA clusters in water with concentration of Cu^{II} ions, immediately after the addition.

Conclusions

Luminescent AgAu dimetallic quantum clusters were synthesized by a simple method that utilizes the galvanic reduction of polydisperse plasmonic nanoparticles. The clusters were characterized by various spectroscopic and microscopic tools. The luminescence of the clusters is selectively quenched by Cu^{II} ions, and the quenching is highly tunable depending on the solvent and the ligand used. Detailed XPS measurements indicate that the clusters undergo a redox reaction with Cu^{II} ions. Steady-state as well as time-resolved luminescence measurements prove that the tunability is due to the galvanic reduction-induced tunable metallophilic interactions between the Au^{I} ions of the cluster and Cu^{I} ions formed by the reduction of Cu^{II} ions by the cluster. This is the first report of tunable metallophilic interactions between monolayer-protected quantum clusters and a closed-shell metal ion. We hope that our results draw more attention to the chemistry of quantum clusters with metal ions in general and the metallophilic interactions of clusters in particular.

Experimental Section

Materials: Chloroauric acid ($HAuCl_4 \cdot 3H_2O$), mercaptosuccinic acid (MSA), and 4-*tert*-butylbenzyl mercaptan (BBSH) were purchased from Sigma–Aldrich. Silver nitrate and tetrahydrofuran (THF) were purchased from RANKEM. Hexanethiol was purchased from Fluka. Oxalic acid, $CuSO_4 \cdot 5H_2O$, $CdCl_2$, $ZnSO_4$, $HgCl_2$, $NiCl_2$, and $Co(OAc)_2$ were purchased from Merck. All chemicals were used without any further purification.

AgAu@MSA Clusters: MSA-protected AgNPs were synthesized by following a reported procedure.[21] A stock solution was prepared by dissolving purified AgNPs (80 mg) in distilled water (10 mL). Au^{I} MSA thiolate was prepared in distilled water by dissolving MSA powder (8.5 mg) in aqueous $HAuCl_4$ solution (5 mL, 5 mM). All reactions were performed at room temperature. For the synthesis of the AgAu@MSA clusters, the stock AgNP solution (0.5 mL) was diluted with methanol (to 10 mL). Au^{I}–MSA solution (2 mL) was added into the methanolic AgNP solution with stirring. The reaction was monitored by time-dependent UV/Vis absorption and photoluminescence measurements. Larger AgAu alloy nanoparticles and AgCl were removed by ultracentrifugation, and AgAu@MSA clusters were obtained as a clear solution in methanol. This solution was concentrated by rotary evaporation and then freeze-dried to afford a pasty material; excess thiolates prevented the production of clean powders from the system. Ethyl acetate was added to this pasty material to precipitate the pure AgAu@MSA, which was then collected and dried in nitrogen to afford dry powder samples.

Ligand Exchange of AgAu@MSA Clusters: The ligand (BBSH or hexanethiol) was dissolved in methanol (70 μL in 2 mL). This solution was added to AgAu@MSA cluster solution (2 mL) in distilled water, and the mixture was stirred at room temperature for 2 min. Toluene (4 mL) was then added, and the mixture was stirred further for 3 min at room temperature. The aqueous layer became colorless, and the toluene layer became light yellow indicating the completion of the ligand exchange. The toluene layer was separated to afford a clear solution of ligand-exchanged AgAu cluster.

Instrumentation: UV/Vis absorption spectra were recorded with a Perkin–Elmer Lambda 25 instrument in the spectral range 200–1100 nm. Transmission electron microscopy (TEM) of the samples was performed by using a JEOL 3010 instrument with an ultrahigh resolution (UHR) polepiece. TEM specimens were prepared by drop-casting one or two drops of the aqueous solution to carbon-coated copper grids and allowed to dry at room temperature overnight. All measurements were performed at 200 kV to minimize the damage of the sample by the high-energy electron beam. X-ray photoelectron spectroscopy (XPS) measurements were performed with an Omicron ESCA Probe spectrometer with polychromatic Mg-K_α X-rays ($h\nu$ = 1253.6 eV). The X-ray power applied was 300 W. The pass energy was 50 eV for survey scans and 20 eV for specific regions. Sample solutions were spotted on a molybdenum sample plate and dried in vacuo. The base pressure of the instrument was 5.0×10^{-10} mbar. The binding energy was calibrated with respect to the adventitious C 1s feature at 285.0 eV. Deconvolution of the spectra was performed by using the CASAXPS software. Matrix-assisted laser desorption/ionization mass spectrometry (MALDI MS) studies were conducted with a Voyager-DE PRO Biospectrometry Workstation from Applied Biosystems. A pulsed nitrogen laser of 337 nm was used for the MALDI MS studies. The samples were mixed with a *trans*-2-[3-(4-*tert*-butylphenyl)-2-methyl-2-propenylidene]malononitrile (DCTB) matrix in 1:1 ratio, spotted on the target plate, and allowed to dry under ambient conditions. Mass spectra were collected in the negative-ion mode and were averaged for 200 shots. Scanning electron microscopy (SEM) and energy-dispersive X-ray (EDAX) analysis were performed with an FEI QUANTA-200 SEM. For measurements, samples were drop-casted on an indium tin oxide coated conducting glass and dried in ambient conditions. Picosecond-resolved fluorescence decay transients were measured and fitted by using a commercially available spectrophotometer (Life Spec-ps, Edinburgh Instruments, UK) with an 80 ps instrument response function (IRF).

Supporting Information (see footnote on the first page of this article): Procedure for the PAGE experiment, UV/Vis spectra of the product and byproducts, XRD pattern of the AgCl formed as a byproduct, time-dependent evolution of the photoluminescence of the clusters during the reactions, EDAX spectrum and elemental composition of the cluster, UV/Vis spectra of the cluster in methanol with and without Cu^{II} ions, emission spectra of AgAu@MSA in methanol containing oxalic acid and its stability of fluorescence upon the addition of Cu^{II} ions, Ag 3d regions in the X-ray photoelectron spectra of pure and Cu^{II}-treated AgAu@MSA clusters, lifetime measurements of alloy clusters containing different Cu^{II} concentrations, lifetime decay profiles and fitting parameters for solutions 2 and 3, luminescence data showing the complete reversibility of the quenching in acetone.

Acknowledgments

The authors thank the Department of Science and Technology (DST), New Delhi, Government of India, for constantly supporting our research programme on nanomaterials. S. K. P. thanks the DST for financial grants (DST/TM/SERI/2k11/103 and SB/S1/PC-011/2013). Mr. M. S. Bootharaju is thanked for the assistance in XPS measurements. K. R. K. thanks the University Grants Commission (UGC), New Delhi for a research fellowship. N. G. and S. C. thank the Council of Scientific and Industrial Research (CSIR), New Delhi for fellowships.

[1] Y. Negishi, K. Igarashi, K. Munakata, W. Ohgake, K. Nobusada, *Chem. Commun.* **2012**, *48*, 660–662.
[2] Y. Negishi, T. Iwai, *Chem. Commun.* **2010**, *46*, 4713–4715.
[3] C. Kumara, A. Dass, *Nanoscale* **2011**, *3*, 3064–3067.
[4] a) Y. Negishi, W. Kurashige, Y. Niihori, T. Iwasa, K. Nobusada, *Phys. Chem. Chem. Phys.* **2010**, *12*, 6219–6225; b) S. Xie, H. Tsunoyama, W. Kurashige, Y. Negishi, T. Tsukuda, *ACS Catal.* **2012**, *2*, 1519–1523.
[5] Y. Negishi, K. Munakata, W. Ohgake, K. Nobusada, *J. Phys. Chem. Lett.* **2012**, *3*, 2209–2214.
[6] H. Qian, D. Jiang, G. Li, C. Gayathri, A. Das, R. R. Gil, R. Jin, *J. Am. Chem. Soc.* **2012**, *134*, 16159–16162.
[7] S. R. Biltek, S. Mandal, A. Sen, A. C. Reber, A. F. Pedicini, S. N. Khanna, *J. Am. Chem. Soc.* **2013**, *135*, 26–29.
[8] a) S. Xie, M. Jin, J. Tao, Y. Wang, Z. Xie, Y. Zhu, Y. Xia, *Chem. Eur. J.* **2012**, *18*, 14974–14980; b) H. Zhang, M. Jin, J. Wang, W. Li, P. H. C. Camargo, M. J. Kim, D. Yang, Z. Xie, Y. Xia, *J. Am. Chem. Soc.* **2011**, *133*, 6078–6089; c) W. Zhang, J. Yang, X. Lu, *ACS Nano* **2012**, *6*, 7397–7405.
[9] T. Huang, R. W. Murray, *J. Phys. Chem. B* **2003**, *107*, 7434–7440.
[10] T. U. B. Rao, Y. Sun, N. Goswami, S. K. Pal, K. Balasubramanian, T. Pradeep, *Angew. Chem.* **2012**, *124*, 2197; *Angew. Chem. Int. Ed.* **2012**, *51*, 2155–2159.
[11] J. S. Mohanty, P. L. Xavier, K. Chaudhari, M. S. Bootharaju, N. Goswami, S. K. Pal, T. Pradeep, *Nanoscale* **2012**, *4*, 4255–4262.
[12] a) M. A. H. Muhammed, T. Pradeep, *Chem. Phys. Lett.* **2007**, *449*, 186–190; b) M. S. Bootharaju, T. Pradeep, *Langmuir* **2011**, *27*, 8134–8143.
[13] P. Hoyer, H. Weller, *Chem. Phys. Lett.* **1994**, *221*, 379–384.
[14] a) J.-P. Choi, C. A. Fields-Zinna, R. L. Stiles, R. Balasubramanian, A. D. Douglas, M. C. Crowe, R. W. Murray, *J. Phys. Chem. C* **2010**, *114*, 15890–15896; b) Z. Wu, *Angew. Chem.* **2012**, *124*, 2988; *Angew. Chem. Int. Ed.* **2012**, *51*, 2934–2938.
[15] a) A. Henglein, *J. Phys. Chem.* **1993**, *97*, 5457–5471; b) J. Belloni, *Catal. Today* **2006**, *113*, 141–156; c) K. Mallick, Z. L. Wang, T. Pal, *J. Photochem. Photobiol. A: Chem.* **2001**, *140*, 75–80; d) H. Remita, S. Remita, in: *Recent Trends in Radiation Chemistry* (Eds.: J. F. Wishart, B. S. M. Rao), World Scientific Publishing Co. Pte. Ltd., Singapore, **2010**, chapter 13.
[16] a) Y. Guo, Z. Wang, H. Shao, X. Jiang, *Analyst* **2012**, *137*, 301–304; b) M. A. H. Muhammed, P. K. Verma, S. K. Pal, A. Retnakumari, M. Koyakutty, S. Nair, T. Pradeep, *Chem. Eur. J.* **2010**, *16*, 10103–10112; c) I. Chakraborty, T. Udayabhaskararao, T. Pradeep, *J. Hazard. Mater.* **2012**, *211–212*, 396–403; d) G.-Y. Lan, C.-C. Huang, H. T. Chang, *Chem. Commun.* **2010**, *46*, 1257–1259; e) B. Adhikari, A. Banerjee, *Chem. Mater.* **2010**, *22*, 4364–4371; f) H. Liu, X. Zhang, X. Wu, L. Jiang, C. Burda, J. J. Zhu, *Chem. Commun.* **2010**, *47*, 4237–4239; g) A. George, E. S. Shibu, S. M. Maliyekkal, M. S. Bootharaju, T. Pradeep, *ACS Appl. Mater. Interfaces* **2012**, *4*, 639–644; h) Y.-T. Su, G.-Y. Lan, W.-Y. Chen, H.-T. Chang, *Anal. Chem.* **2010**, *82*, 8566–8572; i) N. Goswami, A. Giri, M. S. Bootharaju, P. L. Xavier, T. Pradeep, S. K. Pal, *Anal. Chem.* **2011**, *83*, 9676–9680; j) E. S. Shibu, T. Pradeep, *Chem. Mater.* **2011**, *23*, 989–999.
[17] N. Goswami, A. Giri, S. Kar, M. S. Bootharaju, R. John, P. L. Xavier, T. Pradeep, S. K. Pal, *Small* **2012**, *8*, 3175–3184.
[18] a) P. Yu, X. Wen, Y.-R. Toh, J. Huang, J. Tang, *Part. Part. Syst. Charact.* **2013**, *30*, 467–472; b) J. Xie, Y. Zheng, J. Y. Ying, *Chem. Commun.* **2010**, *46*, 961–963.
[19] a) H. Schmidbaur, S. Cronje, B. Djordjevic, O. Schuster, *Chem. Phys.* **2005**, *311*, 151–161; b) P. Pyykko, *Chem. Rev.* **1988**, *88*, 563–594; c) S. Sculfort, P. Braunstein, *Chem. Soc. Rev.* **2011**, *40*, 2741–2760; d) H. Schmidbaur, A. Schier, *Chem. Soc. Rev.* **2008**, *37*, 1931–1951.
[20] P. Pyykko, X.-G. Xiong, J. Li, *J. Chem. Soc., Faraday Discuss.* **2011**, *152*, 169–178.
[21] T. Udayabhaskararao, T. Pradeep, *Angew. Chem.* **2010**, *122*, 4017; *Angew. Chem. Int. Ed.* **2010**, *49*, 3925–3929.
[22] M. S. Bootharaju, G. K. Deepesh, T. Udayabhaskararao, T. Pradeep, *J. Mater. Chem. A* **2013**, *1*, 611.
[23] E. S. Shibu, B. Radha, P. K. Verma, P. Bhyrappa, G. U. Kulkarni, S. K. Pal, T. Pradeep, *ACS Appl. Mater. Interfaces* **2009**, *1*, 2199–2210.
[24] a) C.-C. Huang, Z. Yang, K. H. Lee, H. T. Chang, *Angew. Chem.* **2007**, *119*, 6948; *Angew. Chem. Int. Ed.* **2007**, *46*, 6824–6828; b) W. Chen, X. Tu, X. Guo, *Chem. Commun.* **2009**, 1736–1738.
[25] Z. Ai, L. Zhang, S. Lee, W. Ho, *J. Phys. Chem. C* **2009**, *113*, 20896–20902.
[26] N. Sandhyarani, T. Pradeep, *J. Mater. Chem.* **2001**, *11*, 1294–1299.
[27] Z. Wu, R. Jin, *Nano Lett.* **2010**, *10*, 2568–2573.
[28] a) M. Rodriguez-Castillo, M. Monge, J. M. Lopez-de-Luzuriaga, M. E. Olmos, A. Laguna, F. Mendizabal, *Comput. Theor. Chem.* **2011**, *965*, 163–167; b) S. Tsukamoto, S. Sakaki, *Dalton Trans.* **2013**, *42*, 4809; c) E. Strasser, V. J. Catalano, *J. Am. Chem. Soc.* **2010**, *132*, 10009–10011.
[29] a) I. O. Koshevoy, Y. C. Chang, A. J. Karttunen, M. Haukka, T. Pakkanen, P.-T. Chou, *J. Am. Chem. Soc.* **2012**, *134*, 6564–6567; b) Z. Luo, X. Yuan, Y. Yu, Q. Zhang, D. T. Leong, J. Y. Lee, *J. Am. Chem. Soc.* **2012**, *134*, 16662–16670.

Received: November 7, 2013
Published Online: ■

Quantum Clusters

Keywords: Clusters / Nanoparticles / Luminescence / Closed-shell ions / Metallophilic interactions / Silver / Gold

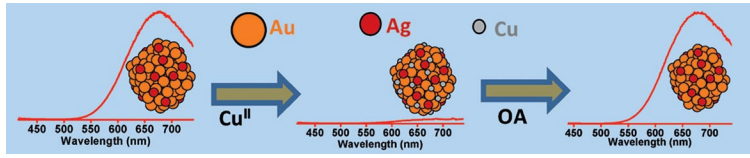

Luminescent AgAu alloy quantum clusters are synthesized by the galvanic reduction of polydisperse plasmonic silver nanoparticles. Selective and tunable luminescence quenching by Cu^{II} ions depends on the solvent and protecting ligands. The tunability is achieved by variation of the metallophilic interactions between the Au^{I} ions of the cluster and Cu^{I} ions formed by reduction by the cluster core.

Eur. J. Inorg. Chem. **2014** · © WILEY-VCH Verlag GmbH & Co. KGaA, 69451 Weinheim, 2014 · ISSN 1099–0682

SUPPORTING INFORMATION

DOI: 10.1002/ejic.201301424
Title: Luminescent AgAu Alloy Clusters Derived from Ag Nanoparticles – Manifestations of Tunable Au^{I}–Cu^{I} Metallophilic Interactions
Author(s): Kumaranchira R. Krishnadas, Thumu Udayabhaskararao, Susobhan Choudhury, Nirmal Goswami, Samir Kumar Pal, Thalappil Pradeep*

Supporting Information 1

Procedure for polyacrylamide gel electrophoresis (PAGE):
A gel electrophoresis unit with 1 mm thick spacer (Bio-rad, Mini-protein Tetra cell) was used to process the PAGE. The total contents of the acrylamide monomers were 30% (bis(acrylamide:acrylamide) = 7:93) and 3% (bis(acrylamide:acrylamide) = 6:94) for the separation and condensation gels, respectively. The eluting buffer consisted of 192 mM glycine and 25 mM tris(hydroxymethylamine). The cluster was dissolved in 5% (v/v) glycerol-water solution (1.0 mL). The sample solution (1.0 mL) was loaded onto a 1 mm gel and eluted for 4 h at a constant voltage of 100 V to achieve separation.

Supporting Information 2

UV-vis spectra of the AgAu@MSA cluster and AgAuNPs formed during galvanic displacement reaction

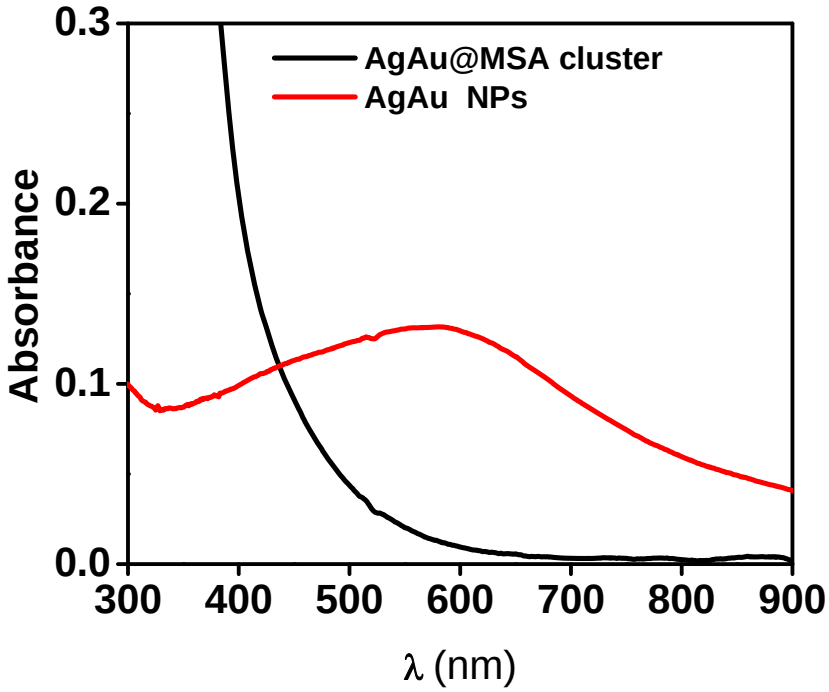

Figure S1. UV-vis spectra of the product (AgAu@MSA) and the byproduct (AgAuNPs) after the reaction between AgNPs and Au^{I}-MSA thiolate.

Supporting Infromation 3

XRD pattern of AgCl formed during galvanic displacement reaction

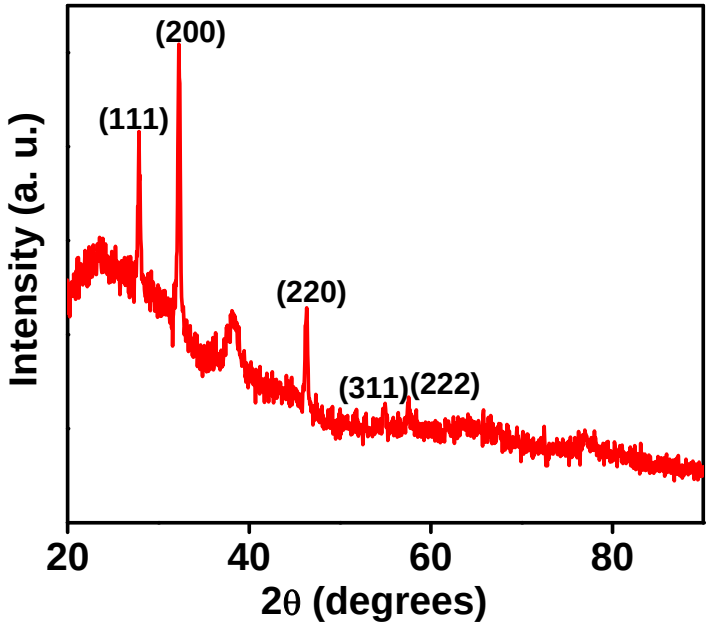

Figure S2. XRD pattern of the precipitate obtained after the reaction between AgNPs and the Au^{I}-MSA thiolate, in methanol. The peaks are due to the AgCl crystals formed during the galvanic displacement reaction. The peak at around 37 may be due to the AgAuNPs formed.

Supporting Information 4

Time-dependent evolution of luminescence during galvanic displacement reaction

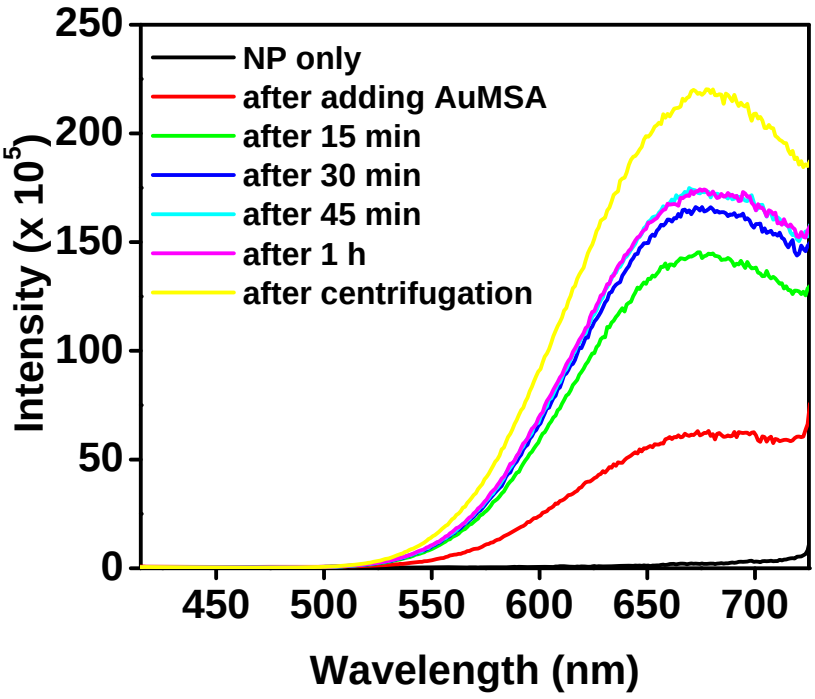

Figure S3. Time-dependent evolution in the photoluminescence showing the formation of AgAu@MSA clusters during the galvanic exchange reaction.

Supporting Information 5

EDAX spectrum and elemental composition of the AgAu@MSA cluster

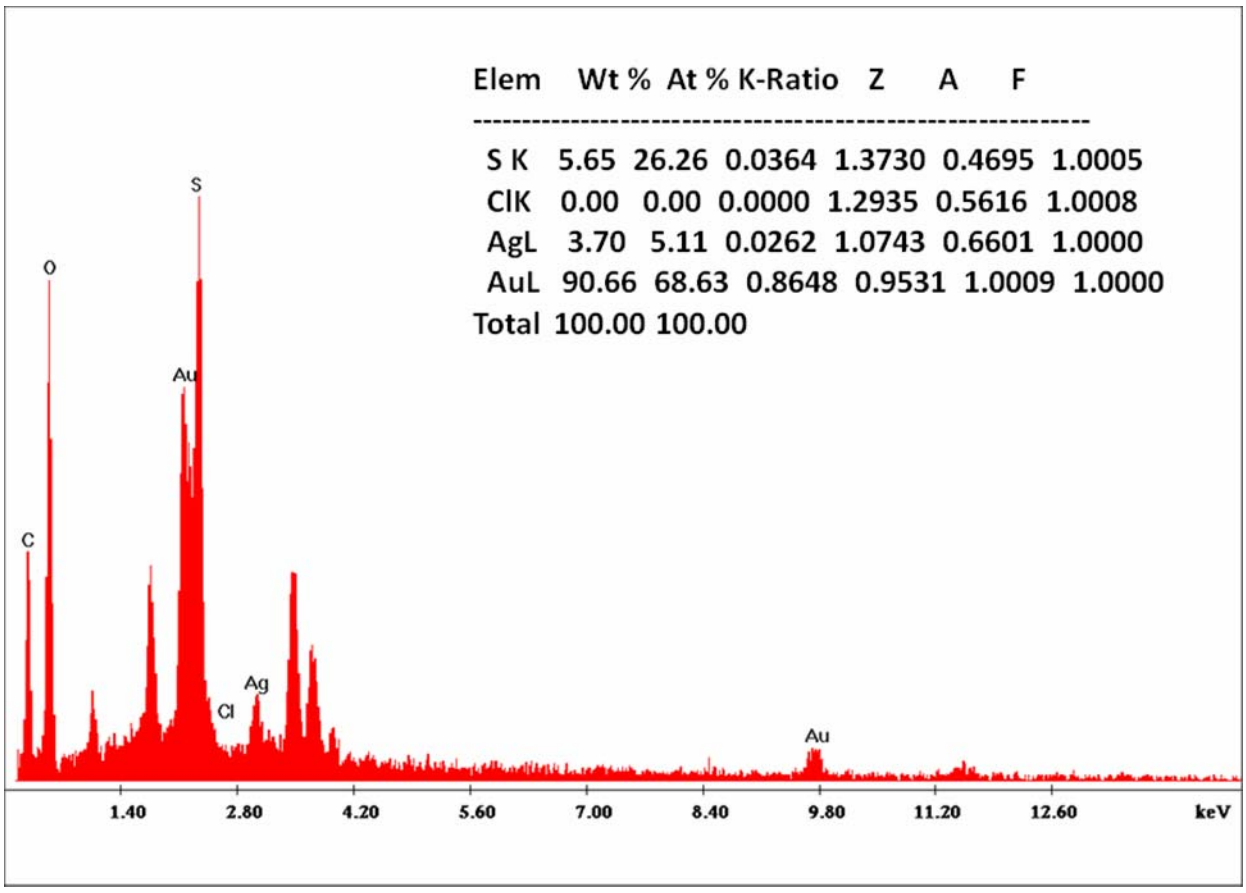

Figure S4. EDAX spectrum and elemental composition of the AgAu@MSA cluster.

Supporting Information 6

UV-vis spectra of the clusters in methanol with and without Cu^{II}

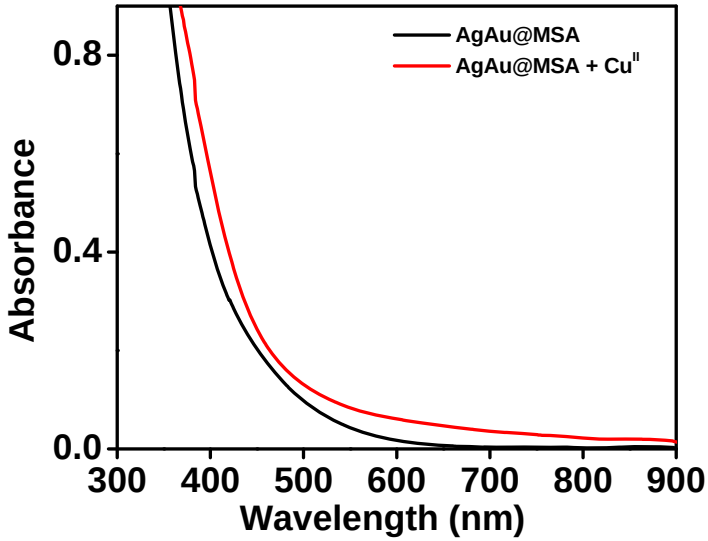

Figure S5. UV-vis absorption spectra of AgAu@MSA clusters in methanol with and without Cu^{II}.

Supporting Information 7

Photoluminescence data showing the ability of OA to prevent metal ion quenching

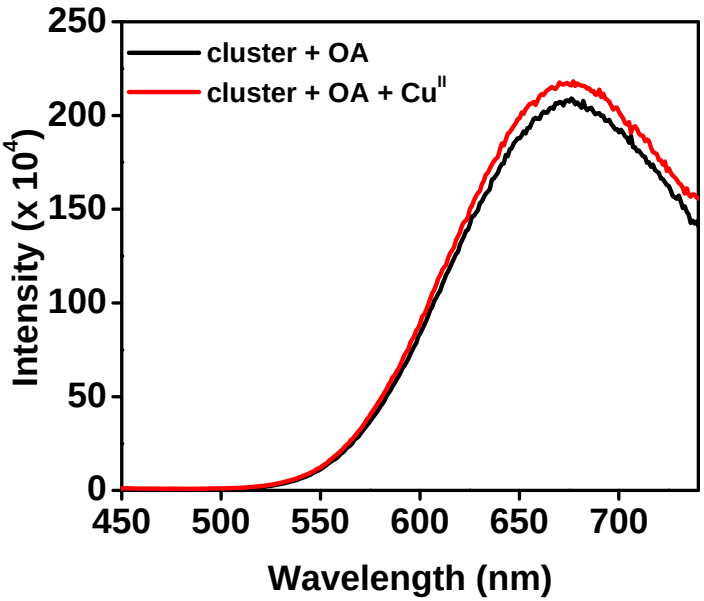

Figure S6. Emission spectra of the AgAu@MSA cluster solution in methanol containing oxalic acid and its stability of fluorescence upon the addition of Cu^{II}.

Supporting Information 8

Ag 3d regions in the XPS spectra of pure and Cu^{II}-treated clusters

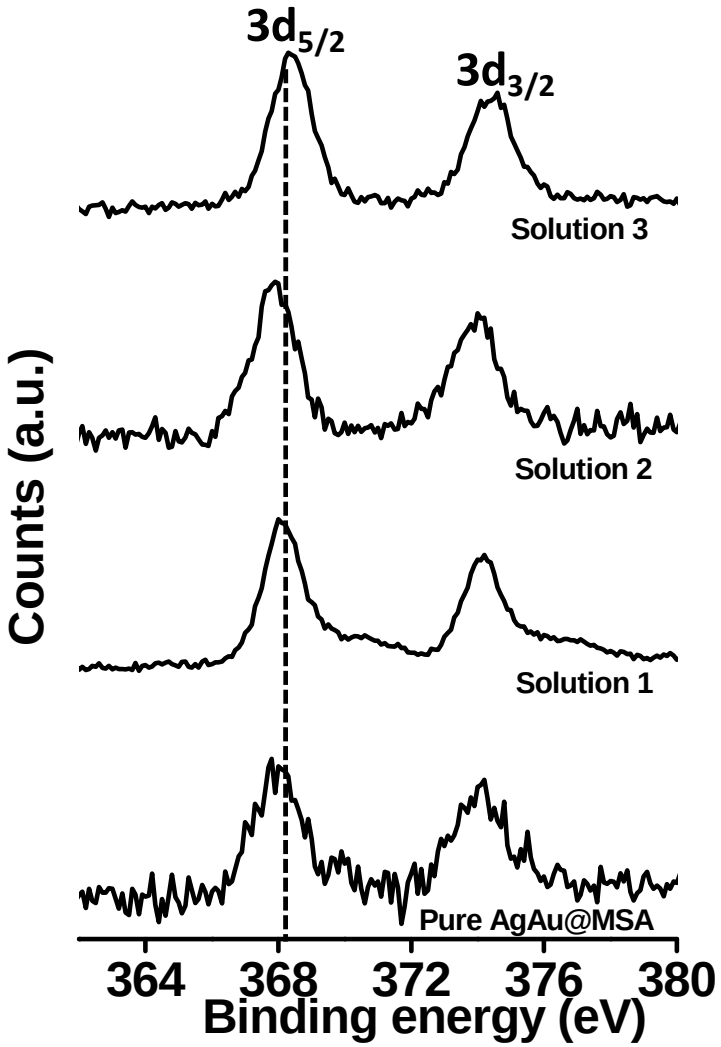

Figure S7. Ag 3d regions in the X-ray photoelectron spectra of pure and Cu^{II}-treated AgAu@MSA clusters.

Supporting Information 9

Lifetime measurements of alloy clusters containing different concentrations of Cu^{II}

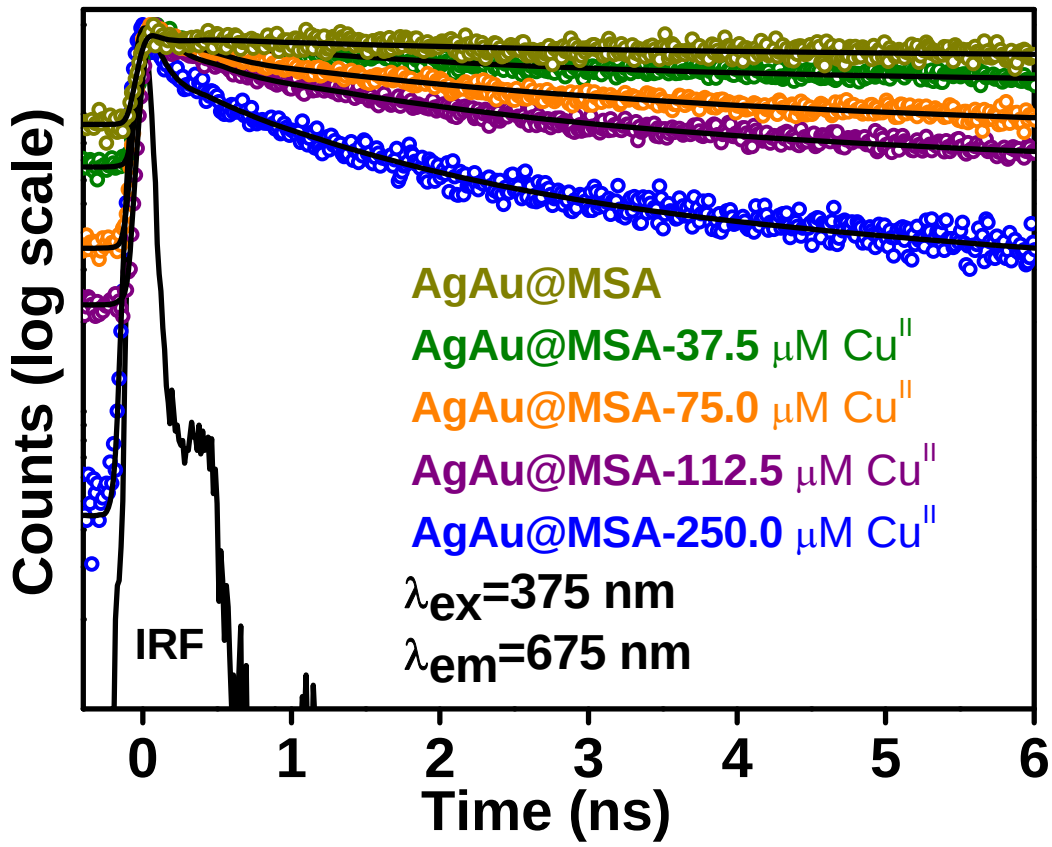

Figure S8. Picosecond time-resolved fluorescence transients of AgAu@MSA clusters containing different concentration of Cu^{II} in methanol.

Table S1. Picosecond time-resolved luminescence transients of AgAu@MSA clusters containing different concentration of Cu^{II} in methanol . The luminescence of these clusters (λ_{max} = 675 nm) is measured using a 375 nm excitation laser.

Concentration of Cu^{II} added to AgAu@MSA cluster in methanol	**τ_1 ns (%)**	**τ_2 ns (%)**	**τ_3 ns (%)**	**τ_{av} (ns)**
0	0.16 (38)	1.12 (20)	50.00(42)	21.28
37.5 μM	0.14 (42)	1.77 (21)	46.77 (37)	17.88
75 μM	0.12 (46)	1.75 (26)	30.45(28)	8.95
112.5μM	0.11(54)	1.60(26)	24.08(20)	5.36
250 μM	0.10 (65)	1.24 (22)	12.00 (13)	1.93

Supporting Information 10

Lifetime decay profiles and fitting parameters of solutions 2 and 3

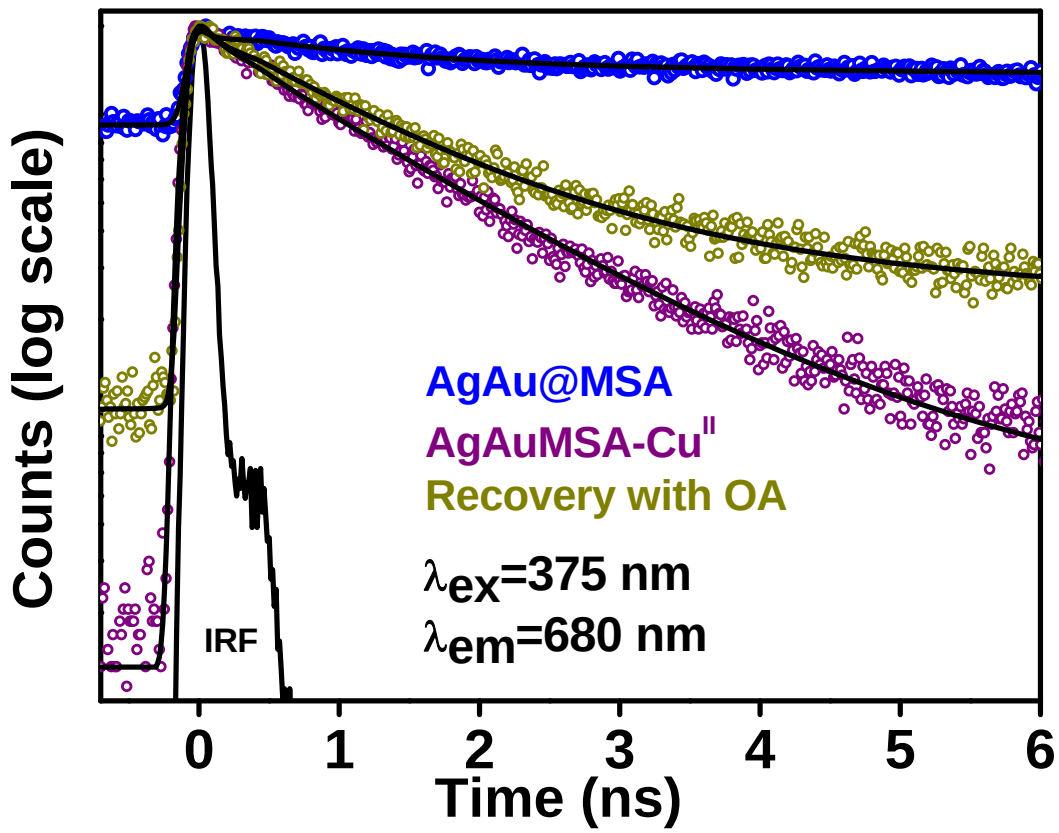

Figure S9. Picosecond time-resolved fluorescence transients of AgAu@MSA clusters in THF showing the quenching of the luminescence lifetime upon the addition of Cu^{II} and its partial recovery upon the addition of OA.

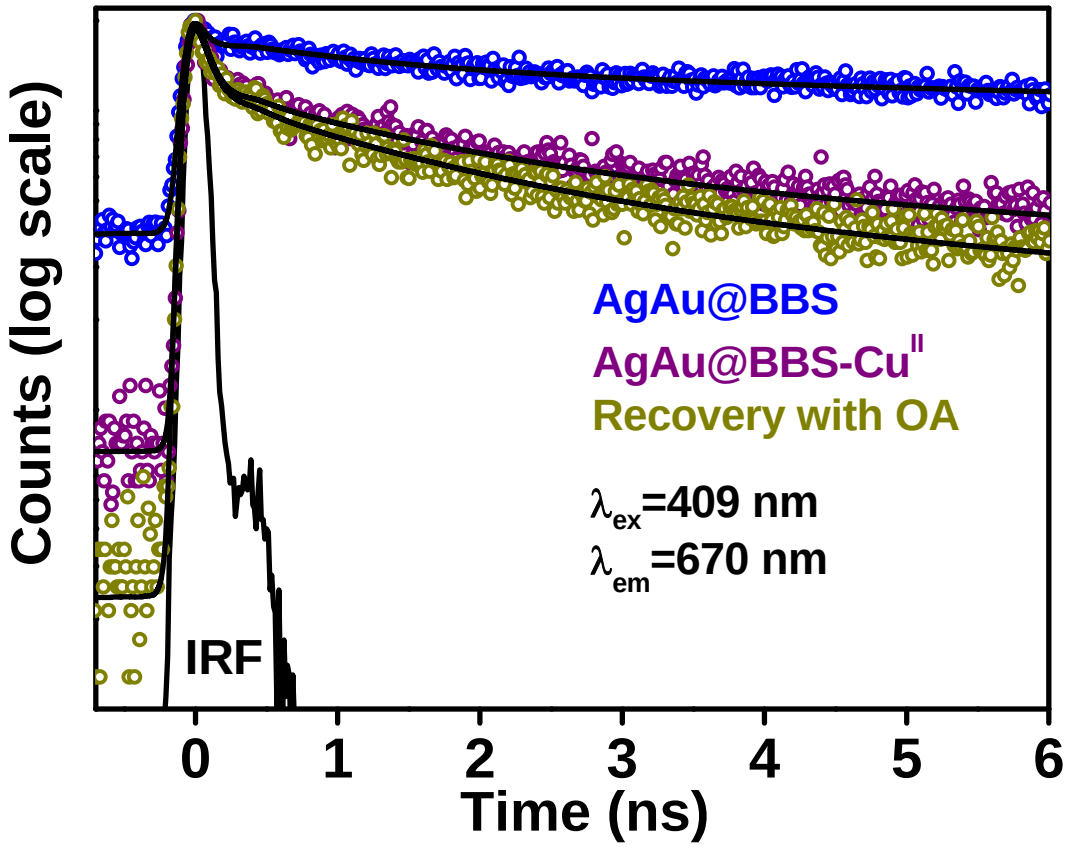

Figure S10. Picosecond time-resolved fluorescence transients of AgAu@BBS clusters in THF showing the quenching of the luminescence lifetime upon the addition of Cu^{II} and its irreversibility upon the addition of OA.

Table S2. Picosecond time-resolved luminescence transients of pure and Cu^{II}-treated AgAu@MSA cluster in THF. The luminescence of these clusters (λ_{max} = 680 nm) is measured using a 375 nm excitation laser.

Cluster system	τ_1 ns (%)	τ_2 ns (%)	$\tau_3$ns (%)	τ_{av} (ns)
Pure AgAu@MSA cluster in THF	0.24(23)	1.24 (35)	48.37 (42)	20.74
Cluster with Cu^{II}	0.18 (27)	1.44 (70)	15.56 (3)	1.39
Cluster with OA	0.21 (25)	1.45 (68)	32.28(7)	3.38

Table S3. Picosecond time-resolved luminescence transients of pure and Cu^{II}-treated AgAu@BBS cluster in THF. The luminescence of these clusters (λ_{max} = 670 nm) is measured using a 409 nm excitation laser.

Cluster system	$\tau_1$ns (%)	τ_2 ns (%)	$\tau_3$ns (%)	τ_{av} (ns)
AgAu@BBSH cluster in THF	0.15 (43)	2.5 (19)	41.12 (38)	21.28

Cluster with Cu^{II}	0.082 (71)	1.81 (17)	18.51 (12)	2.60
Cluster with OA	0.106 (69)	1.84 (19)	15.09 (12)	2.17

Supporting Information 11

Luminescence data showing the complete reversibility of the quenching in acetone as solvent

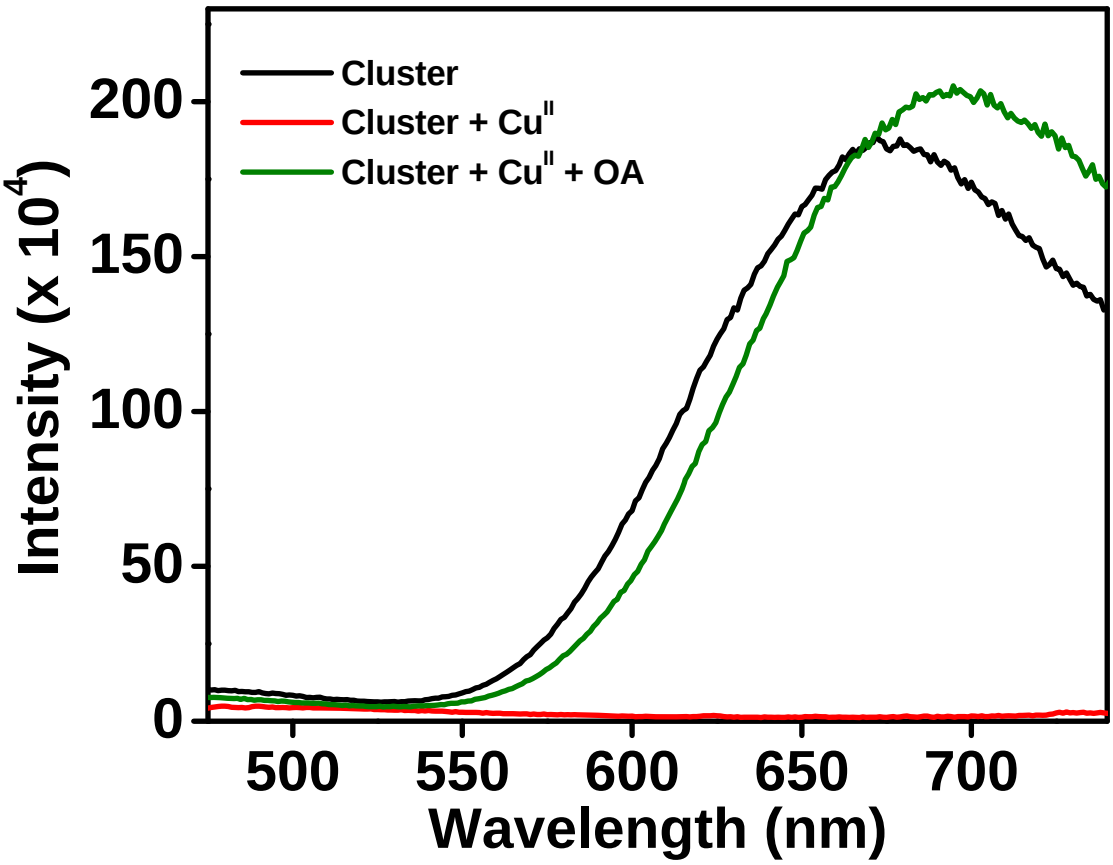

Figure S11. Luminescence data showing the quenching of the luminescence of AgAu@MSA clusters in acetone upon the addition of Cu^{II} and its complete recovery upon the addition of OA.

Nanoscale

PAPER

View Article Online
View Journal

Luminescent iron clusters in solution†

Cite this: DOI: 10.1039/c3nr05784d

Nirmal Goswami,‡[a] Ananya Baksi,‡[b] Anupam Giri,[a] Paulrajpillai Lourdu Xavier,[b] Gautam Basu,[c] Thalappil Pradeep*[b] and Samir Kumar Pal*[a]

Received 30th October 2013
Accepted 26th November 2013

DOI: 10.1039/c3nr05784d

www.rsc.org/nanoscale

Metal clusters, composed of a few atoms at the core, exhibit unique properties and have potential applications. Although atomically precise clusters of noble metals have been synthesized, analogous systems of reactive metals, such as iron, have not been realized in solution due to high reactivity. Here we report the synthesis and characterization of novel iron clusters in the hemoglobin matrix that are highly luminescent (quantum yield 10% at 565 nm). The super-paramagnetic iron clusters, after successful ligand exchange from protein and phase transfer from water to chloroform using tri-octylphosphineoxide (TOPO), were detected as $[Fe_{10}(TOPO)_3(H_2O)_3]^+$, $[Fe_{13}(TOPO)_2(H_2O)]^+$ and $[Fe_8(TOPO)(H_2O)_2]^+$ by mass spectrometry. This study lays the groundwork for exploiting unique properties of soluble iron clusters.

Introduction

Atomically precise metal particles, comprising of only a few atoms with dimensions comparable to the Fermi wavelength of electrons, are called quantum clusters (QCs). The resulting quantum confinement produces unique optical, electronic and chemical properties of QCs that are dramatically different from those of nanoparticles (NPs) which exhibit plasmon absorption. Unusual properties of QCs make them attractive as novel systems of choice for exploring a wide range of phenomena like catalysis, metal ion sensing, and bio-imaging.[1–4] Several monolayer-protected noble metal QCs have been reported to date and a few crystal structures are also known.[5–8] Current research in this area is mostly limited to noble metals, especially Au and Ag, due to their inertness, stability and ease of synthesis. Particularly, QCs of Au (Au_{QCs}) have been well studied because of their unusual stability under ambient conditions and wide spectral tunability, yielding diverse optoelectronic properties.[9–15] Efforts to synthesize atomically precise Ag_{QCs} have been limited due to their higher reactivity.[16,17] Some Ag_{QCs} have also been crystallized.[18] More recently, a growing number of studies have reported Cu_{QCs} and Pt_{QCs}.[19,20] In addition to the nature of the metal, the nature of the ligand can also affect the stability and properties of QCs. Macromolecular templates, where proteins act as ligands, are rather recent entries in the field.[21–23] Several proteins have been used as ligands for such cluster synthesis due to their biocompatibility and high photoluminescence quantum yield of the QCs. The general synthetic route is to first form a metal–protein adduct followed by reduction at elevated pH where the protein acts as the reducing agent or by reduction using an external reducing agent and confining the newly formed cluster core by the protein scaffold simultaneously. These highly luminescent protein-protected clusters are being used as sensors for environmentally hazardous metal ions and other sensitive molecules such as explosives. A number of groups have used protein-protected luminescent QCs in biolabeling.[24,25] It is anticipated that noble metal QCs would be less toxic and more suitable as carriers of biological cargo.[26] However, therapeutic studies have shown that they may not be completely free of side effects.[27] For this field to evolve, it is imperative that novel QCs be explored with characteristics of noble metal QCs but with better biocompatibility and newer properties. Apart from being better biocompatible and cheaper, unique catalytic and magnetic properties of Fe make Fe_{QCs} important candidates among the yet to be explored QCs. Since the first example of metallic Fe NPs (~100 nm),[28] several attempts have been made to characterize them.[29–31] Although recipes to synthesize metallic Fe NPs in the 3–100 nm window exist, new approaches are required for synthesizing Fe_{QCs}. Nanometer sized Fe^0 inherently suffers from instability because of easy surface oxidation upon exposure to air and in the presence of water, making the synthesis of Fe-clusters difficult. Nevertheless, it is important to note that Fe-clusters are known in the gas phase.[32–35] Obviously, suitable chemical procedures and appropriate protection would enable their synthesis in the solution state.

[a]Department of Chemical, Biological & Macromolecular Sciences, Unit for Nanoscience & Technology, S. N. Bose National Centre for Basic Sciences, Block JD, Sector III, Salt Lake, Kolkata 700098, India. E-mail: skpal@bose.res.in

[b]DST Unit of Nanoscience (DST UNS) and Thematic Unit of Excellence (TUE), Department of Chemistry, Indian Institute of Technology Madras, Chennai 600036, India. E-mail: pradeep@iitm.ac.in

[c]Department of Biophysics, Bose Institute P 1/12, C. I. T. Road, Scheme VIIM, Kolkata 700054, West Bengal, India

† Electronic supplementary information (ESI) available. See DOI: 10.1039/c3nr05784d

‡ These authors contributed equally.

Here we describe the first efficient synthesis of highly luminescent and water-soluble Fe_{QCs}, starting from hemoglobin (Hb), a Fe-containing metalloprotein which acts as the iron source as well as the protecting agent. We have employed an efficient ligand exchange strategy with a smaller ligand, trioctyl phosphine oxide (TOPO), and subsequent phase transfer of the cluster from water to chloroform for detailed structural characterization. A number of complementary experimental techniques, including mass spectroscopy, NMR, FT-IR and optical spectroscopy, were used to obtain the precise molecular signature of the clusters in the solution phase. We believe this work will enrich the area further and open a new window to the theoretical as well as the experimental community to understand and evolve this system towards real applications.

Results and discussion

Hemoglobin is a major component of blood that transports oxygen from the respiratory organs (lungs or gills) to the rest of the body. It contains Fe ions, present either as Fe^{2+} or Fe^{3+}, coordinated by four nitrogen atoms of porphyrin present in the protein. In this study, we used Hb as a source of Fe ions as well as the protecting agent to make luminescent Fe_{QCs}. The synthetic approach relies on the extraction of the porphyrin-bound Fe^{2+}/Fe^{3+} in the Hb-matrix using piperidine followed by the reduction of Fe^{2+}/Fe^{3+} with $NaBH_4$ at room temperature (see details in the S1†). After ~12 h of incubation with $NaBH_4$, the solution turned yellowish brown and showed strong yellow luminescence under UV light (Fig. S2†), indicating a change in the oxidation state of the Fe atom in the Hb-matrix. After lyophilization and re-suspension of the product in water, the aqueous solution exhibited the same yellow luminescence under UV light (inset of Fig. 1A). The aqueous phase also showed discrete bands centered at 344 (3.60), 420 (2.95), 507 (2.45) and 639 nm (1.94 eV) (Fig. 1A). Such molecule-like discrete bands are unique to QCs.[36] The absence of any characteristic band corresponding to Fe NPs (at 360 nm) further confirmed that the Fe_{QCs} present in the aqueous phase were nearly pure in the as-synthesized form and were mostly free of large NPs.[31] The Fe_{QCs} showed a luminescence band at 567 nm (2.19 eV) upon photo-excitation at 530 nm (2.34 eV) (Fig. 1A). The quantum yield (QY) of Fe_{QCs} in water (at 565 nm) was determined to be 10%, using Rhodamine 6G (QY = 95% in CH_3CH_2OH) as the reference.

It is well known that the intrinsic fluorescence of proteins, due to aromatic amino acids like tryptophan, can show a tail in the blue region. Furthermore, Hb consists of four porphyrin moieties which are well-known to be red emitting. To rule out potential artifacts, we conducted several control experiments by taking account of all potential products that might have formed after the reaction of $NaBH_4$ and piperidine, in the presence of specific proteins (see Fig. S3–10 and Table S1†). First, we considered apo-myoglobin, as Hb contains four myoglobin units. The observed excitation as well as the emission peaks (Fig. S3†) clearly rule out the possibility of any photoluminescence (PL) due to protein residues peaking at 565 nm. Second, we considered hemato-porphyrin as a prototype of the porphyrin unit present in the protein and performed the same experiment. Upon the treatment of $NaBH_4$ and piperidine, the PL peaks of hemato-porphyrin remained unchanged (Fig. S4†). The observation indicates that the porphyrin moiety is not responsible for the 565 nm PL peak. Finally, hemato-porphyrin was attached to apo-myoglobin as a mimic of Hb (without iron) and treated with $NaBH_4$ and piperidine. Binding of apo-myoglobin with hemato-porphyrin was checked with lifetime measurements (Fig. S9†). The figure indicates that the decay is slower compared to hemato-porphyrin after the treatment. In Fig. S5,† the absence of the 565 nm peak justifies the role of Fe in the yellow luminescence. Our control experiments rule out the possibility of any kind of PL contribution from the protein matrix and support the formation of a new type of material in the protein environment. The occurrence of visible luminescence in a material composed of iron is intriguing. Why should a non-noble metal like Fe show such unique optical properties is still unclear and detailed theoretical studies are needed to establish the precise origin of the optical bands.

Transmission electron microscopic (TEM) images indicated the presence of a large quantity of tiny particles with good uniformity (Fig. 1B). However, conventional HRTEM is not a reliable technique for evaluating the size distribution of QCs due to electron beam-induced coalescence.[37] Although X-ray crystallography is the best method to understand the structure and composition of any material in detail, to date no protein-protected clusters could be crystallized. Mass spectroscopy is a robust technique for characterizing proteins and metal clusters. Matrix-assisted laser desorption ionization mass spectrometry (MALDI MS) and electrospray ionization mass spectrometry (ESI MS) are better suited to study the composition of QCs. MALDI MS of Hb, using DHB as the matrix (details in the ESI†), showed two peaks at m/z 15 230 and 15 990 Da due to the α-globin chain (MW: 15 126.4 Da) and β-globin chain (MW: 15 867.2 Da) of Hb. These peaks were shifted to m/z values 15 760 and 16 500 Da, respectively in the case of Fe_{QCs}@Hb (Fig. 1C) confirming successful cluster formation. This mass difference corresponds to 7–10 Fe atoms and the composition can be roughly assigned to Fe_{7-10}@Hb. However, due to resolution limitations in the higher mass range, the exact number of Fe atoms, determined from the mass difference, may not be correct. This problem was circumvented by a ligand-exchange strategy with a small ligand, tri-octylphosphineoxide (TOPO) (see later in the text). The ligand-exchanged clusters were characterized using ESI MS analysis, a more accurate technique for assigning the composition of molecules containing multiple isotopes.

The oxidation state of Fe was investigated by a number of techniques. X-ray photoelectron spectroscopy (XPS) is the most appropriate method to confirm the oxidation state of the core for atomically precise noble metal clusters. In the present study, although we attempted to obtain the XPS spectrum, due to the inherent poor signal intensity of Fe 2p in XPS as well as the low density of clusters in the protein, we could not establish the oxidation state of Fe in the cluster. Instead, we have performed an indirect method to verify the oxidation state of Fe that we refer to as the "luminal experiment" (details in S1†). Briefly, Hb-bound Fe^{2+}/Fe^{3+} in blood is a catalyst for the

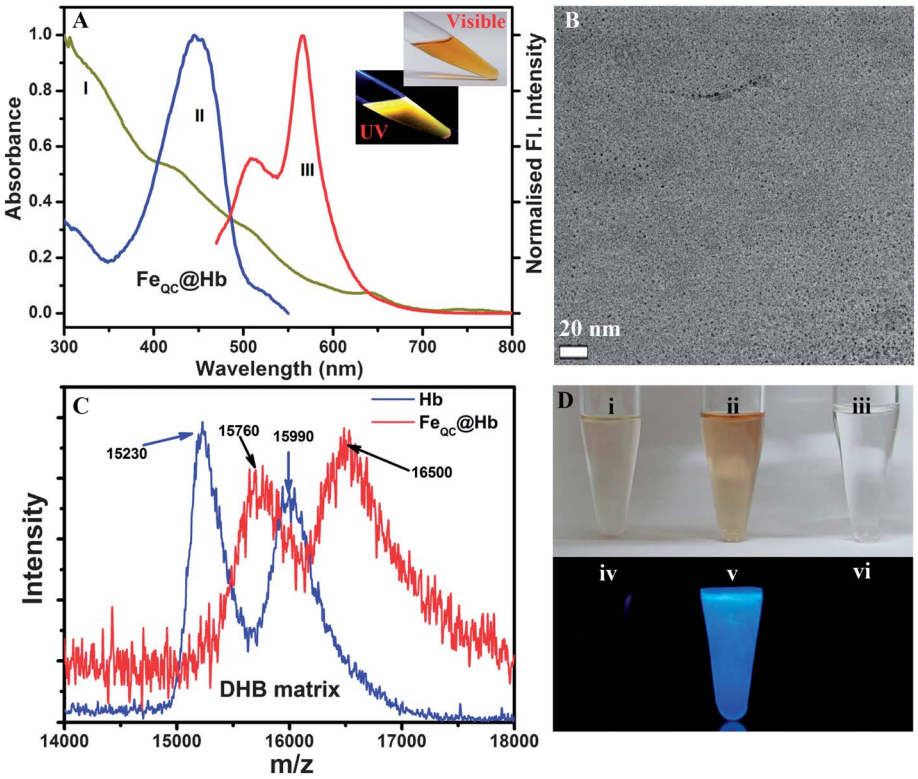

Fig. 1 (A) UV-vis absorption spectrum (yellow) of the water soluble cluster indicates the discrete, molecular like bands. Excitation (blue) and PL (red) spectra of Fe_{QC}@Hb in water where, excitation wavelength = 530 nm and PL wavelength = 565 nm. (B) TEM image of Fe_{QC}@Hb shows a core size of less than 2 nm. Several tiny particles of nearly uniform size are spread over the grid. (C) MALDI-TOF mass spectra of Hb (blue) and Fe_{QC}@Hb (red) in the linear positive mode using the dihydroxybenzoic acid (DHB) matrix. (D) Upper panel: bright field photographs of the luminol–hydrogen peroxide mixture after the addition of (i) Fe_{QC}@Hb (ii) Hb and (iii) water (control). Lower panel: dark field photograph of the luminol–hydrogen peroxide mixture after the addition of (iv) Fe_{QC}@Hb (v) Hb and (vi) water (control). Note that, the chemiluminescence observed for the luminol–hydrogen peroxide mixture (vi) is very poor; however, increases several folds in the presence of Hb (v) because of the presence of Fe^{2+} and Fe^{3+}. In the case of Fe_{QC}@Hb, the solution does not show any chemiluminescence revealing that Fe is in the zero oxidation state.

chemiluminescence reaction that causes luminol to intensely glow blue in the presence of peroxide.[38] During this reaction, Fe^{2+}/Fe^{3+} is reduced with the concomitant oxidation of H_2O_2 to O_2. However, if Fe is already in the 'zero' oxidation state, it cannot catalyze the chemiluminescence reaction. Unlike the case with Hb, Fe_{QC}@Hb could not induce a blue glow in a mixture of luminol and H_2O_2 (Fig. 1D) suggesting that the as-prepared QCs are in the metallic state.

Although water-soluble, protein protected Fe_{QCs} showed evidence of high stability and quantum efficiency, accurate molecular identification by MALDI MS analysis was a major problem. It has been demonstrated that TOPO (tri-octylphosphineoxide) can be used as a stabilizing agent for Fe nanoparticles.[31] Moreover, TOPO can be used for preventing aggregation and slowing down oxidation of the Fe nanoparticles by air.[31] To work in a lower mass range, we chose TOPO, an organic ligand, for ligand exchange as well as for transferring the Fe_{QCs} into chloroform (details in S1†). TOPO-capped Fe_{QCs} (Fe_{QC}@TOPO) in chloroform also exhibited discrete, molecule-like bands at 355 (3.49), 402 (3.09), 516 (2.40), and 570 nm (2.18 eV) (Fig. 2A). The bands were shifted from the corresponding bands of Fe_{QC}@Hb in aqueous medium (Fig. 1A). Note that during ligand exchange, phase transfer was partial which indicated that only a part of the clusters is present in the organic phase. Excitation and photoluminescence (PL) spectra of Fe_{QC}@TOPO in chloroform are shown in Fig. 2B. ^{1}H-NMR experiments showed the chloroform layer, containing TOPO, to be free of Hb or piperidine (Fig. S11†). The presence of tiny Fe_{QCs} in the chloroform layer was verified from TEM images and energy dispersive spectroscopy (Fig. S12†). The clusters aggregated upon long-time electron beam irradiation forming nanoparticles (Fig. S12†), as seen before in the case of Au clusters.[37] Therefore, it is fair to conclude that the 565 nm peak originates solely from Fe_{QC}@TOPO. We note that the PL peak remained constant during phase transfer while the absorption spectra changed. For Au clusters, Negishi *et al.* have shown that when the core size changes from Au_{10} to Au_{18} the lowest energy absorption peak changes from 330 nm to 570 nm, whereas the PL maximum remains constant at 1.5 eV.[13] Akin to the Au clusters, we anticipate that iron clusters with different core sizes present in chloroform could have similar luminescence, however, with different extinction compared to the clusters present in water. The solution of Fe_{QC}@TOPO was brown under visible light but exhibited a bright yellow color when irradiated with UV light (Fig. 2B inset). Using Rhodamine 6G as the reference, the QY of the Fe_{QC}@TOPO was determined to be

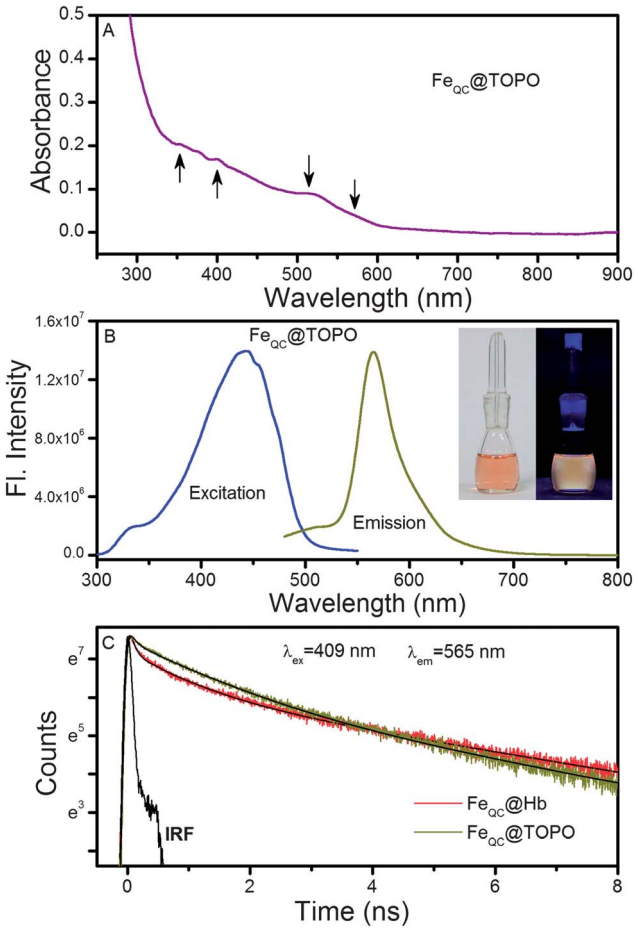

Fig. 2 (A) UV-vis absorption spectrum of Fe$_{QC}$@TOPO in chloroform after solvent correction. Arrows indicate the absorption bands. (B) Excitation and PL spectra of Fe$_{QC}$@TOPO in chloroform solution. Inset shows the photograph of the cluster solution in chloroform under (I) visible and (II) UV light. (C) Photoluminescence decay of Fe$_{QC}$@Hb and Fe$_{QC}$@TOPO with instrument response function (IRF) ~60 ps. Standard error of decay time components is ~10%.

12%. Fig. 2C shows the decay transients of the Fe$_{QCs}$ before and after phase transfer. Luminescence lifetime values of the Fe$_{QCs}$, obtained from luminescence transients observed at 565 nm were 0.08 (64%), 0.91 (22%), and 3.90 (14%) ns in water and 0.11 (43%), 1.14 (38%), and 3.60 (19%) ns in chloroform. The observed differences of the transients are not very significant and probably arise due to reduction of the non-radiative decay in non-polar chloroform.[39] The luminescence transients were found to be almost invariant as a function of excitation wavelengths (375, 409 and 445 nm), which provided strong evidence that the observed clusters have a similar luminescence profile (Fig. S13†).

In order to obtain more definite mass spectral signatures, we performed ESI MS analysis of TOPO capped Fe$_{QCs}$ in 9 : 1 chloroform : acetonitrile in positive ion mode, in the m/z range of 100–4000 Da. TOPO showed an intense peak at m/z 387 due to its molecular ion peak. The TOPO dimer and other fragments were also observable in the lower mass region (m/z < 800). In the region beyond m/z 800, specific peaks due to clusters appear while the lower mass region is dominated by ligand peaks (Fig. 3). In this figure, the expanded cluster region shows the presence of multiple cores namely, $[Fe_8(TOPO)(H_2O)_2]^+$, $[Fe_{10}(TOPO)_3(H_2O)_3]^+$ and $[Fe_{13}(TOPO)_2(H_2O)]^+$. It is to be noted that, unlike several Au clusters,[40] we have not seen any multiply charged species and all the compositions were verified with theoretically calculated isotope patterns. Along with the major peaks observed as discussed above, several small intensity peaks are also visible in the range studied. Most of the peaks are fragments of the above mentioned peaks. One can envisage three different ways of fragmentation, as observed in the present study: (a) direct loss of TOPO, (b) loss of water (one or multiple) molecule, and (c) loss of a TOPO fragment namely, the octyl group. For instance, the peak at m/z 1131 is a TOPO-devoid fragment of $[Fe_{13}(TOPO)_2(H_2O)]^+$. Similarly, the peak at m/z 1386 corresponds to the TOPO-devoid fragment of $[Fe_{10}(TOPO)_3(H_2O)_3]^+$. The m/z 1257 peak is assigned to $[Fe_8(TOPO)_2(H_2O)_2]^+$ and hence, the m/z 870 peak is probably due to $[Fe_8(TOPO)(H_2O)_2]^+$, arising after the loss of one TOPO moiety. These are examples of direct loss of the TOPO moiety from the parent cluster. The fragmentations were ascertained by extensive MS/MS studies (see later). Loss as well as addition of water molecules were also observed in some cases. Two peaks, at m/z 1368 and m/z 1404, accompanying the m/z 1386 peak (assigned to $[Fe_{10}(TOPO)_2(H_2O)_3]^+$), arise due to the loss/gain of one water molecule as $[Fe_{10}(TOPO)_3(H_2O)_2]^+$ and $[Fe_{10}(TOPO)_3(H_2O)_4]^+$ respectively. Water loss was also observed in the case of $[Fe_8(TOPO)_2(H_2O)_2]^+$, where loss of two water molecules and one ligand leads to a bare Fe_8^+ core (see Fig. 4). The peak centered

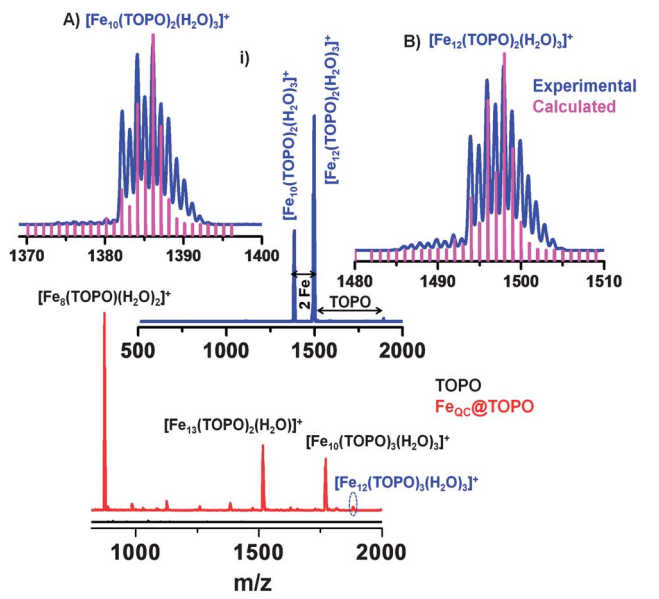

Fig. 3 ESI MS of TOPO and Fe$_{QCs}$@TOPO in the mass range m/z 800–2000 Da showing the presence of $[Fe_8(TOPO)(H_2O)_2]^+$, $[Fe_{10}(TOPO)_3(H_2O)_3]^+$, $[Fe_{12}(TOPO)_3(H_2O)_3]^+$ and $[Fe_{13}(TOPO)_2(H_2O)]^+$. Inset (i) shows MS/MS of $[Fe_{12}(TOPO)_3(H_2O)_3]^+$ where ligand as well as Fe loss is also observable. (A and B) $[Fe_{12}(TOPO)_2(H_2O)_3]^+$ and $[Fe_{10}(TOPO)_2(H_2O)_3]^+$ are compared with the theoretically calculated isotope patterns of these species.

around *m*/*z* 1660 is due to the loss of an octyl group from TOPO from the parent ion $[Fe_{10}(TOPO)_3(H_2O)_3]^+$, which confirms the presence of the third type of fragmentation pattern.

Another kind of fragmentation could be the loss of Fe. This fragmentation pattern is seen for $[Fe_{12}(TOPO)_3(H_2O)_3]^+$. The presence of a Fe_{12} core was confirmed from the MS/MS data, where the parent peak, $[Fe_{12}(TOPO)_3(H_2O)_3]^+$, shows the loss of two Fe atoms yielding $[Fe_{10}(TOPO)_2(H_2O)_3]^+$ along with $[Fe_{12}(TOPO)_2(H_2O)_3]^+$ (Fig. 3i). The same $[Fe_{10}(TOPO)_2(H_2O)_3]^+$ fragment was seen in the MS/MS of $[Fe_{10}(TOPO)_3(H_2O)_3]^+$ (see Fig. 4), where the parent cluster loses one ligand molecule to generate the observed fragment. Fig. 3A and B clearly show that the calculated and the experimentally observed isotope patterns match very well. Although the mass of two Fe atoms and that of one octyl group are nearly identical, the mismatch in the observed isotope pattern in the case of $[Fe_{10}(TOPO)_2(H_2O)_3]^+$ rules out the presence of the octyl group.

Extensive MS/MS studies were performed to understand the cluster compositions. Collision energy dependent MS/MS study of the clusters showed consecutive ligand losses for all the clusters investigated (Fig. S14–S18†). In Fig. 4A, MS/MS data for $[Fe_{10}(TOPO)_3(H_2O)_3]^+$, $[Fe_{12}(TOPO)_3(H_2O)_3]^+$ and $[Fe_{13}(TOPO)_2(H_2O)]^+$ are shown, keeping all experimental parameters and collision energies identical. In all the cases, ligand loss can be seen with good isotope distribution, matching with the calculated spectrum (data for $[Fe_{13}(TOPO)_2(H_2O)]^+$ are shown in Fig. 4B). The presence of Fe was also confirmed by conducting MS/MS on each peak in a given envelope for the isotopes. For example, in the case of $[Fe_{13}(TOPO)_2(H_2O)]^+$, peaks in the range *m*/*z* 1514–1522 Da were chosen with an isotope width of 1 Da and MS/MS was performed (Fig. 4C). Each peak yielded a distribution of peaks that arose principally due to the presence of Fe. For $[Fe_8(TOPO)(H_2O)_2]^+$, ligand as well as water loss could be observed, producing a bare $[Fe_8]^+$ core (Fig. 4D and S17†). The presence of water, bound to the cluster core, was also observed in the MS/MS study for the Fe_{13} core, where, upon higher collision energy, $[Fe_{13}(TOPO)_2(H_2O)]^+$ loses two ligands to yield $[Fe_{13}(H_2O)]^+$ (Fig. S16†). This study proves the presence of attached water to the cluster core, which may act as a ligand. We observed the loss of TOPO in most of the cases, which could be a reason behind the less than expected number of observed ligands attached to the core. It is possible that before we could detect the ion in ESI MS, the cluster might have already lost some ligands which was seen in the case of $[Fe_8(TOPO)_2(H_2O)_2]^+$ (Fig. S18†). Another reason for the discrepancy might be that the steric hindrance due to the presence of three octyl chains

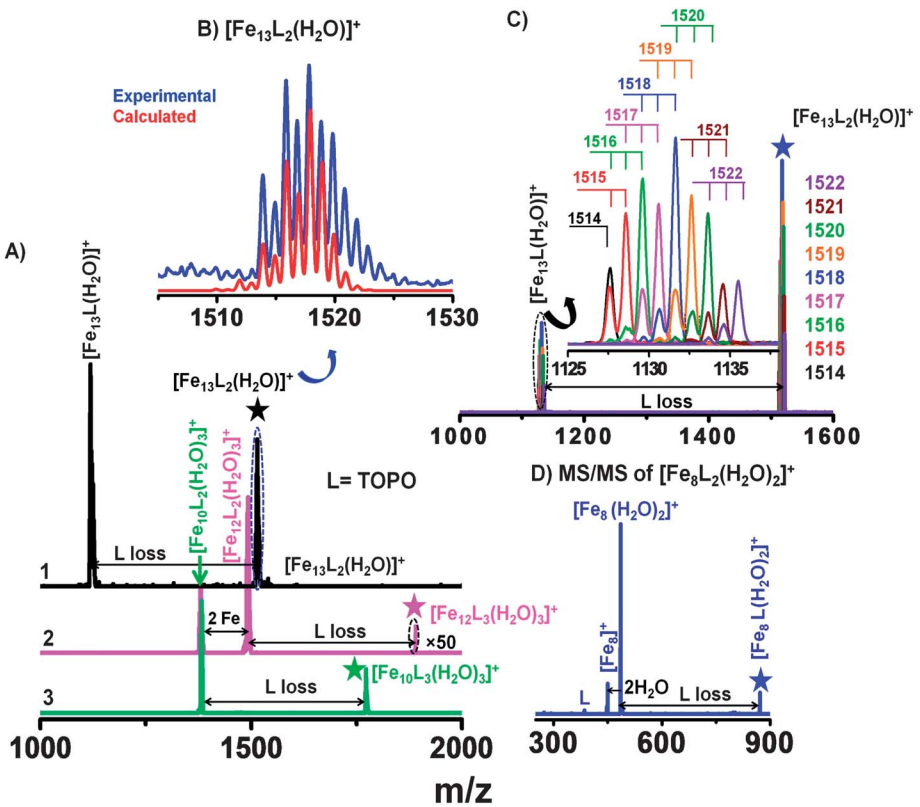

Fig. 4 (A) ESI MS/MS of (1) $[Fe_{13}(TOPO)_2(H_2O)]^+$ (black), (2) $[Fe_{12}(TOPO)_3(H_2O)_3]^+$ (magenta) and (3) $[Fe_{10}(TOPO)_3(H_2O)_3]^+$ (green), showing subsequent ligand losses. For all the cases, parent ions are marked with stars and for fragments, the compositions are indicated. $[Fe_{12}(TOPO)_3(H_2O)_3]^+$ shows two Fe losses also. In this case, the intensity of the parent peak has been multiplied by 50 to make it visible. (B) $[Fe_{13}(TOPO)_2(H_2O)]^+$ spectrum is compared with the calculated spectrum. (C) MS/MS spectra of each peak in the $[Fe_{13}(TOPO)_2(H_2O)]^+$ envelope, with a mass width of 1 Da. Fragment peaks after ligand loss are expanded in the inset, showing isotope distribution, principally due to iron. The parent ion chosen for MS/MS is mentioned above the isotope pattern observed. (D) ESI MS/MS of $[Fe_8(TOPO)_2(H_2O)_2]^+$ showing ligand as well as water losses to give a bare $[Fe_8]^+$ core.

present in a single TOPO molecule acted as a deterrent to attachment of more TOPO ligands. However, only a detailed theoretical study on the position and conformation of the ligands and structure of the cluster core can sort out this puzzle.

Bound water molecules have been reported earlier for dendrimer capped Au_8 nanodots by Dickson *et al.*[41] However, the presence of three water molecules bound to Fe, a metal much more reactive than Au, was totally unexpected. The MS data were complemented by the solid-state FT-IR studies of TOPO and Fe_{QC}@TOPO where it was found that both TOPO and Fe_{QC}@TOPO contain small amounts of water (Fig. S19†). To further probe the nature of water in TOPO and Fe_{QC}@TOPO, ^{1}H NMR studies were performed on TOPO and Fe_{QC}@TOPO in $CDCl_3$. Superimposed ^{1}H-NMR spectra of TOPO and Fe_{QC}@TOPO are shown in Fig. 5. Except for one singlet resonance (2.32 ppm for TOPO and 1.69 ppm for Fe_{QC}@TOPO samples), the two spectra are identical and are in agreement with the previously published spectrum of TOPO.[42] The unique singlet peaks in each spectrum, distinct from pure water signal in chloroform (7.24 ppm), could be attributed to TOPO/Fe_{QC}@TOPO bound water since the peaks disappeared upon addition of D_2O. This is consistent with the presence of bound water molecules associated with Fe_{QC}@TOPO (from ESI MS and FT-IR) and TOPO (from FT-IR). If the water signal in Fe_{QC}@TOPO indeed corresponds to molecules bound to Fe_{QCs}, then the super-paramagnetic Fe_{QC}-center (Fig. S20†) is expected to induce faster relaxation and an upfield chemical shift of the Fe_{QC}-bound water resonance. Compared to that in TOPO, the water signal in Fe_{QC}@TOPO showed an upfield shift (0.63 ppm) and faster relaxation, both in terms of spin-lattice relaxation time $T1$ (2.54 s in TOPO and 1.13 s in Fe_{QC}@TOPO) and line width or $1/T2^*$ (0.019 ppm in TOPO and 0.034 ppm in Fe_{QC}@TOPO). The presence of the upfield shifted and broadened water peak (Fig. 5) in the background of all other proton peaks (due to TOPO) establishes a strong interaction of water molecules on the cluster surface.

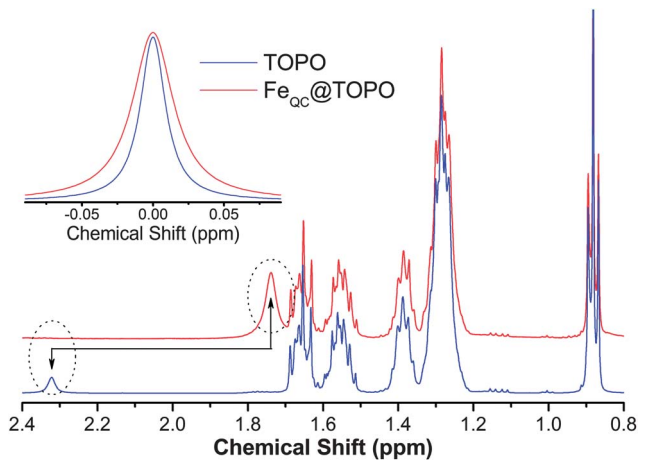

Fig. 5 ^{1}H-NMR spectra of TOPO (blue) and Fe_{QC}@TOPO (red). Bound water resonances for both the samples are marked with dotted circles. Broadening of the Fe_{QC}@TOPO-bound water resonance is shown in the inset.

Conclusion

In summary, we have devised a facile synthetic route for preparing atomically precise and highly luminescent Fe_{QCs}. These clusters synthesized in solution have been detected as $[Fe_8(TOPO)(H_2O)_2]^+$, $[Fe_{10}(TOPO)_3(H_2O)_3]^+$, $[Fe_{12}(TOPO)_2(H_2O)_3]^+$ and $[Fe_{13}(TOPO)_2(H_2O)]^+$, with well-defined and unique isotope distribution in ESI MS. The cluster contains water molecules as revealed by our MS/MS analysis which was corroborated by FT-IR and NMR spectroscopic studies. It is anticipated that a theoretical study will provide further insights into the structure, stability and conformation of the cluster. We believe that this new material holds promise for fundamental applications like catalysis, imaging and sensing.

Acknowledgements

N.G. and A.B thank CSIR, India, for fellowships. A.G. thanks UGC, India, for a fellowship. We thank Mr Barun Majumder for his assistance in NMR experiments. We thank DST for financial grants (DST/TM/SERI/2k11/103 and SB/S1/PC-011/2013). T.P. thanks the Nano Mission of DST, Government of India for constantly supporting his research program.

References

1 N. de Silva, J.-M. Ha, A. Solovyov, M. M. Nigra, I. Ogino, S. W. Yeh, K. A. Durkin and A. Katz, *Nat. Chem.*, 2010, **2**, 1062–1068.
2 Z. Wu, M. Wang, J. Yang, X. Zheng, W. Cai, G. Meng, H. Qian, H. Wang and R. Jin, *Small*, 2012, **8**, 2028–2035.
3 C.-A. J. Lin, T.-Y. Yang, C.-H. Lee, S. H. Huang, R. A. Sperling, M. Zanella, J. K. Li, J.-L. Shen, H.-H. Wang, H.-I. Yeh, W. J. Parak and W. H. Chang, *ACS Nano*, 2009, **3**, 395–401.
4 P. L. Xavier, K. Chaudhari, A. Baksi and T. Pradeep, *Nano Rev.*, 2012, **3**, 14767.
5 M. Zhu, C. M. Aikens, F. J. Hollander, G. C. Schatz and R. Jin, *J. Am. Chem. Soc.*, 2008, **130**, 5883–5885.
6 H. Qian, W. T. Eckenhoff, Y. Zhu, T. Pintauer and R. Jin, *J. Am. Chem. Soc.*, 2010, **132**, 8280–8281.
7 P. D. Jadzinsky, G. Calero, C. J. Ackerson, D. A. Bushnell and R. D. Kornberg, *Science*, 2007, **318**, 430–433.
8 M. W. Heaven, A. Dass, P. S. White, K. M. Holt and R. W. Murray, *J. Am. Chem. Soc.*, 2008, **130**, 3754–3755.
9 A. Dass, *J. Am. Chem. Soc.*, 2009, **131**, 11666–11667.
10 J. Akola, M. Walter, R. L. Whetten, H. Häkkinen and H. Grönbeck, *J. Am. Chem. Soc.*, 2008, **130**, 3756–3757.
11 Z. Y. Li, N. P. Young, M. Di Vece, S. Palomba, R. E. Palmer, A. L. Bleloch, B. C. Curley, R. L. Johnston, J. Jiang and J. Yuan, *Nature*, 2008, **451**, 46–48.
12 I. Dolamic, S. Knoppe, A. Dass and T. Bürgi, *Nat. Commun.*, 2012, **3**, 798.
13 Y. Negishi, K. Nobusada and T. Tsukuda, *J. Am. Chem. Soc.*, 2005, **127**, 5261–5270.
14 R. L. Whetten and R. C. Price, *Science*, 2007, **318**, 407–408.
15 P. R. Nimmala and A. Dass, *J. Am. Chem. Soc.*, 2011, **133**, 9175–9177.

16 H. Xu and K. S. Suslick, *Adv. Mater.*, 2010, **22**, 1078–1082.
17 T. U. B. Rao, B. Nataraju and T. Pradeep, *J. Am. Chem. Soc.*, 2010, **132**, 16304–16307.
18 H. Yang, Y. Wang, H. Huang, L. Gell, L. Lehtovaara, S. Malola, H. Hakkinen and N. Zheng, *Nat. Commun.*, 2013, **4**, 3422–3428.
19 N. Goswami, A. Giri, M. S. Bootharaju, P. L. Xavier, T. Pradeep and S. K. Pal, *Anal. Chem.*, 2011, **83**, 9676–9680.
20 S.-I. Tanaka, J. Miyazaki, D. K. Tiwari, T. Jin and Y. Inouye, *Angew. Chem., Int. Ed.*, 2011, **50**, 431–435.
21 J. Xie, Y. Zheng and J. Y. Ying, *J. Am. Chem. Soc.*, 2009, **131**, 888–889.
22 K. Chaudhari, P. L. Xavier and T. Predeep, *ACS Nano*, 2011, **5**, 8816–8827.
23 A. Baksi, P. L. Xavier, K. Chaudhari, N. Goswami, S. K. Pal and T. Pradeep, *Nanoscale*, 2013, **5**, 2009–2016.
24 C. A. J. Lin, T. Y. Yang, C. H. Lee, S. H. Huang, R. A. Sperling, M. Zanella, J. K. Li, J. L. Shen, H. H. Wang, H. I. Yeh, W. J. Parak and W. H. Chang, *ACS Nano*, 2009, **3**, 395–401.
25 M. A. H. Muhammed, P. K. Verma, S. K. Pal, A. Retnakumari, M. Koyakutty, S. Nair and T. Pradeep, *Chem. – Eur. J.*, 2010, **16**, 10103–10112.
26 Y. Pan, S. Neuss, A. Leifert, M. Fischler, F. Wen, U. Simon, G. Schmid, W. Brandau and W. Jahnen-Dechent, *Small*, 2007, **3**, 1941–1949.
27 R. Bhattacharya and P. Mukherjee, *Adv. Drug Delivery Rev.*, 2008, **60**, 1289–1306.
28 K. S. Suslick, S. B. Choe, A. A. Cichowlas and M. W. Grinstaff, *Nature*, 1991, **353**, 414–416.
29 T. Ling, L. Xie, J. Zhu, H. Yu, H. Ye, R. Yu, Z. Cheng, L. Liu, G. Yang, Z. Cheng, Y. Wang and X. Ma, *Nano Lett.*, 2009, **9**, 1572–1576.
30 L.-M. Lacroix, S. b. Lachaize, A. Falqui, M. Respaud and B. Chaudret, *J. Am. Chem. Soc.*, 2008, **131**, 549–557.
31 L. Guo, Q. Huang, X.-y. Li and S. Yang, *Phys. Chem. Chem. Phys.*, 2001, **3**, 1661–1665.
32 B. H. Weiller, P. S. Bechthold, E. K. Parks, L. G. Pobo and S. J. Riley, *J. Chem. Phys.*, 1989, **91**, 4714–4727.
33 S. C. Richtsmeier, E. K. Parks, K. Liu, L. G. Pobo and S. J. Riley, *J. Chem. Phys.*, 1985, **82**, 3659–3665.
34 A. W. Castleman, Jr. and R. G. Keesee, *Annu. Rev. Phys. Chem.*, 1986, **37**, 525–550.
35 D. B. Jacobson and B. S. Freiser, *J. Am. Chem. Soc.*, 1984, **106**, 4623–4624.
36 H. Qian, M. Zhu, Z. Wu and R. Jin, *Acc. Chem. Res.*, 2012, **45**, 1470–1479.
37 P. Ramasamy, S. Guha, E. S. Shibu, T. S. Sreeprasad, S. Bag, A. Banerjee and T. Pradeep, *J. Mater. Chem.*, 2009, **19**, 8456–8462.
38 A. L. Rose and T. D. Waite, *Anal. Chem.*, 2001, **73**, 5909–5920.
39 T. Udayabhaskararao, Y. Sun, N. Goswami, S. K. Pal, K. Balasubramanian and T. Pradeep, *Angew. Chem., Int. Ed.*, 2012, **51**, 2155–2159.
40 J. B. Tracy, M. C. Crowe, J. F. Parker, O. Hampe, C. A. Fields-Zinna, A. Dass and R. W. Murray, *J. Am. Chem. Soc.*, 2007, **129**, 16209–16215.
41 J. Zheng, J. T. Petty and R. M. Dickson, *J. Am. Chem. Soc.*, 2003, **125**, 7780–7781.
42 J. Kříž, J. i. Dybal, E. Makrlík, J. Budka and P. Vaňura, *J. Phys. Chem. A*, 2009, **113**, 5896–5905.

Supplementary Materials

Luminescent Iron Clusters in Solution

Nirmal Goswami[a,#], Ananya Baksi[b,#], Anupam Giri[a], Paulrajpillai Lourdu Xavier[b], Gautam Basu[c], Thalappil Pradeep[b]* and Samir Kumar Pal[a]*

[a]Department of Chemical, Biological & Macromolecular Sciences, S. N. Bose National Centre for Basic Sciences, Block JD, Sector III, Salt Lake, Kolkata 700 098, India.

[b]DST Unit of Nanoscience (DST UNS), Department of Chemistry, Indian Institute of Technology Madras, Chennai 600036, India.

[c]Department of Biophysics, Bose Institute P 1/12, C. I. T. Road, Scheme VIIM, Kolkata 700054 West Bengal, India.

#These authors contributed equally to this work.

S1. Materials

Hemoglobin (Hb), sodium borohydride, tri-octylphosphine oxide (TOPO), Luminol, Rhodamine and chloroform were purchased from Sigma-Aldrich. Piperidine was purchased from Spectrachem. Milli-Q (From Millipore) water was used throughout the experiments. All the chemicals were used as received without further purification.

Synthesis of the protein-incorporated Fe_{QCs}:

In a typical synthesis, first, 60 mg of Hb was dissolved in 5 mL Milli-Q water. 12 mL of piperidine was then added to the protein solution to extract the iron from the protein. The solution was then stirred for 15 min at room temperature. Second, 36 mg of 3 mL ice cold sodium borohydride was slowly added to the solution under vigorous stirring. The reaction mixture was then stirred for 24 hrs, resulting in the formation of a yellowish brown solution that showed a strong yellow luminescence under UV lamp (Figure S1).

Ligand exchange and phase transfer from water to chloroform:

For phase transfer, 0.01M of TOPO was taken in 3 mL of chloroform on the bottom of 3.0 mL (10 mg/ mL) of aqueous Fe_{QC}@Hb solution. The mixture was gently stirred for 8-12 hrs at 298 K. Exchange can be observed directly by visible color change of the organic phase from colorless to reddish brown.

Evidence of "zero oxidation state" of Fe_{QC} in Hb matrix:

Detection procedure using chemiluminescence: Luminol solution was prepared (1g/mL) and solution was kept in three test tubes (each contains 1 mL of 1g/mL luminol solution). 0.2 mL of each sample [e.g., Fe_{QC}@Hb (2.2 mg/mL), Hb (2.2 mg/mL) and water] was added to that luminol solution. Finally, 1 mL of 3% hydrogen peroxide was added and the photographs were taken immediately.

Quantum yield calculation:

The quantum yield was calculated according to the following equation:

$$Q = Q_R \left(\frac{I}{I_R} \right) \left(\frac{OD_R}{OD} \right) \left(\frac{n^2}{n_R^2} \right) \quad (1)$$

where Q and Q_R are the quantum yield of the sample and reference (Rhodamine in methanol), I and I_R are the integrated fluorescence intensities of the sample and reference, OD and OD_R are the optical densities of the sample and reference at the excitation wavelength, and n and n_R are the refractive indices of the chloroform/protein and reference solutions. The absolute quantum yield of Rhodamine 6G in ethanol, was taken to be 95%.

Methods

UV–vis Absorption Spectroscopy:

Optical absorption spectra of the solutions were measured with a Shimadzu spectrophotometer.

Photoluminescence (PL) spectroscopy:

The PL spectra were recorded on a Jobin Yvon Fluoromax-3 fluorometer.

Time correlated single photon counting:

Picosecond-resolved fluorescence decay transients were measured by using a commercially available spectrophotometer (Life Spec-ps, Edinburgh Instruments, UK) with 60 ps instrument response function (IRF). The observed luminescence transients were fitted by using a nonlinear least square fitting procedure to a function $(X(t) = \int_0^t E(t')R(t-t')dt')$ comprising of convolution of the IRF $(E(t))$ with a sum of exponential $(\mathrm{R(t)} = \mathrm{A} + \sum_{\mathrm{i=1}}^{\mathrm{N}} \mathrm{B_i e^{-t/\tau_i}})$ with pre-exponential factors (B_i), characteristic lifetimes (τ_i) and a back ground (A). Relative concentration in a multi exponential decay was finally expressed as: $c_n = \frac{B_n}{\sum_{i=1}^{N} B_i} \times 100$. The quality of the curve fitting was evaluated by reduced chi-square and residual data. It has to be noted that with our time resolved instrument, we can resolve at least one fourth of the instrument response time constants after the de-convolution of the IRF.

Transmission electron microscopy (TEM):

TEM images were taken using a FEI TecnaiTF-20 field-emission high-resolution transmission electron microscope operating at 200 kV. Samples for TEM imaging were prepared by placing a drop of as-prepared QCs solution on a carbon coated Cu grid and the solvent was evaporated under a bulb.

Matrix-assisted laser desorption mass spectrometry (MALDI-MS):

An Applied Biosystems Voyager DE Pro MALDI TOF MS instrument was used for the mass spectral analysis of Hb and Fe_{QC}@Hb. A pulsed nitrogen laser of 337 nm was used for sample ionization. 2, 5-dihydroxy benzoic acid (DHB) was used as the matrix. Samples were prepared by dissolving 2 μL of the as-synthesised Fe_{QC}@Hb in 40 μL DHB matrix (5 mg/mL of DHB was prepared in 1:1 water methanol mixture) and 2 μL of the resulting mixture was spotted and kept for drying in ambient environment. Spectra were collected in the linear positive mode and an average of 250 shots was taken for each spectrum.

Electrospray ionization mass spectrometry (ESI-MS):

The ESI mass spectrometric measurements of Fe_{QC}@TOPO were done in the positive mode using a Thermo Scientific LTQ XL ESI MS, with a mass range of m/z 100-4000, in which the spray and the extraction are orthogonal to each other. The clusters, obtained after freeze drying were dispersed in 9:1 chloroform and acetonitrile mixture and used for mass

spectrometric measurements. The spectra were averaged for 200 scans. Ion spray voltage was kept at 2.5 kV and capillary temperature was set at 275°C.

Fourier transform infrared spectroscopy (FT-IR Spectroscopy):

FT-IR spectra were measured with a Perkin Elmer Spectrum One instrument. KBr crystals were used as the matrix for sample preparation. Powder samples of TOPO and Fe_{QC}@TOPO (which were collected after lyophilisation) were measured.

Vibrating sample magnetometer (VSM):

Magnetic measurements were performed in a Lake Shore VSM with an electromagnet that can produce field up to 1.6T.

Nuclear magnetic resonance (NMR):

NMR experiments were performed on samples in $CDCl_3$ solution using a Bruker DRX 500 MHz spectrometer.

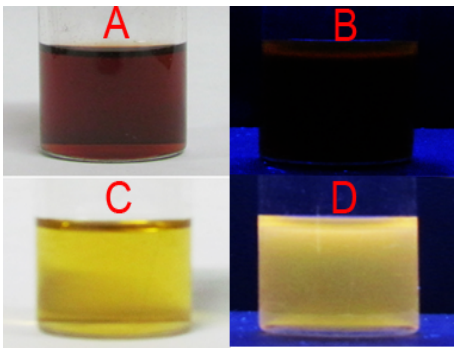

Figure S2. Photographs of (A) Hb (left upper panel) and (C) Fe_{QC}@Hb (left lower panel) in water-piperidine solvent and their corresponding photographs (B) (right upper panel) and (D) (right lower panel) under UV light. Change in colour (A to C i.e., brown to yellow) under visible light indicates the change of Fe oxidation state.

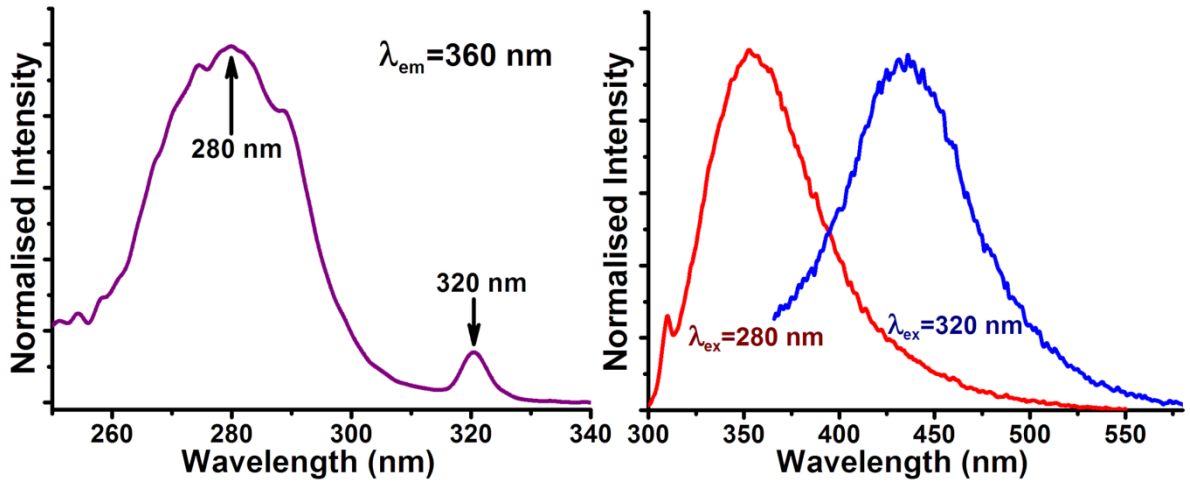

Figure S3. Excitation (left) and PL (right) spectra of Apo-myoglobin after the addition of piperidine and sodium borohydride indicates that 440 nm emission peak (blue) is originate from protein. Arrows indicate the excitation peaks. The peak at 280 nm is attributed to the tryptophan residues in Apo-myoglobin. The other peak at 320 nm is originated from the protein (Apo-myoglobin), which may be attributed to the photoproducts of some aromatic amino acids.

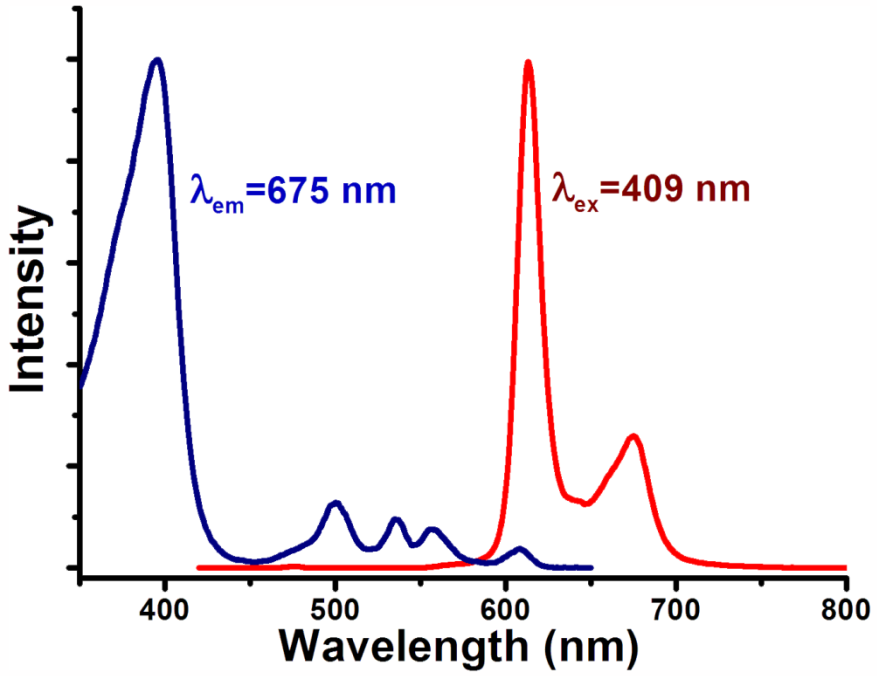

Figure S4. Excitation (blue) and PL (red) spectra of Hemato-porphyrin after the treatment with piperidine and sodium borohydride.

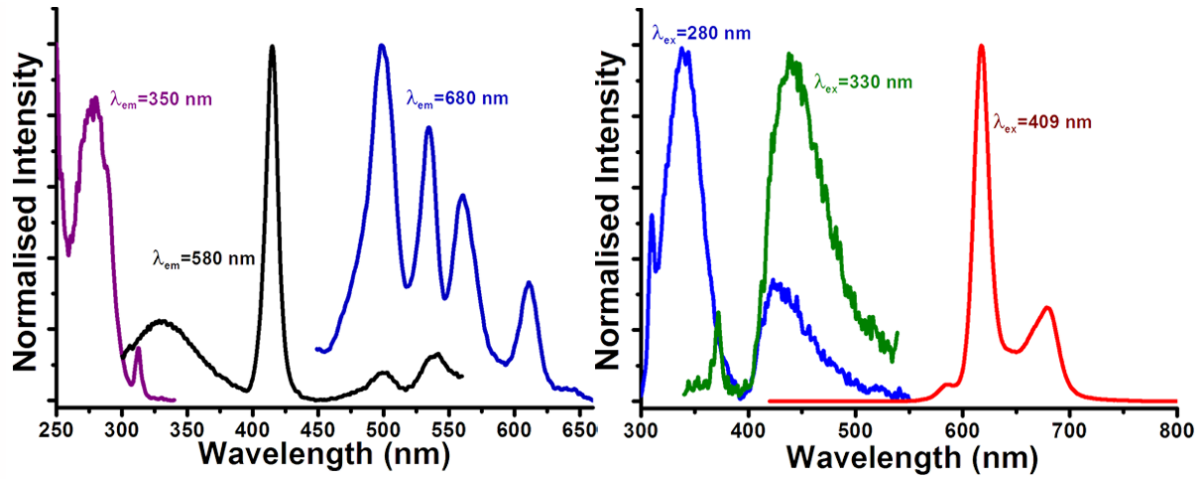

Figure S5. Excitation (left) and PL (right) spectra of Apo-myoglobin-Hemato-porphyrin complex after the addition of piperidine and sodium borohydride. Absence of any yellow luminescence justifies the role of Fe ions for the generation of 565 nm PL peak.

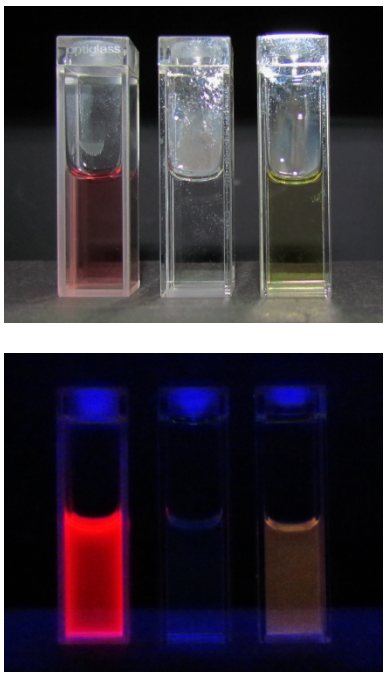

Figure S6. Photographs of Hemato-porphyrin, Apo-myoglobin and Holo-myoglobin (from left to right; after the addition of piperidine and sodium borohydride) under visible (upper panel) and UV light (lower panel). The photographs show the difference of PL under same excitation (365 nm UV light).

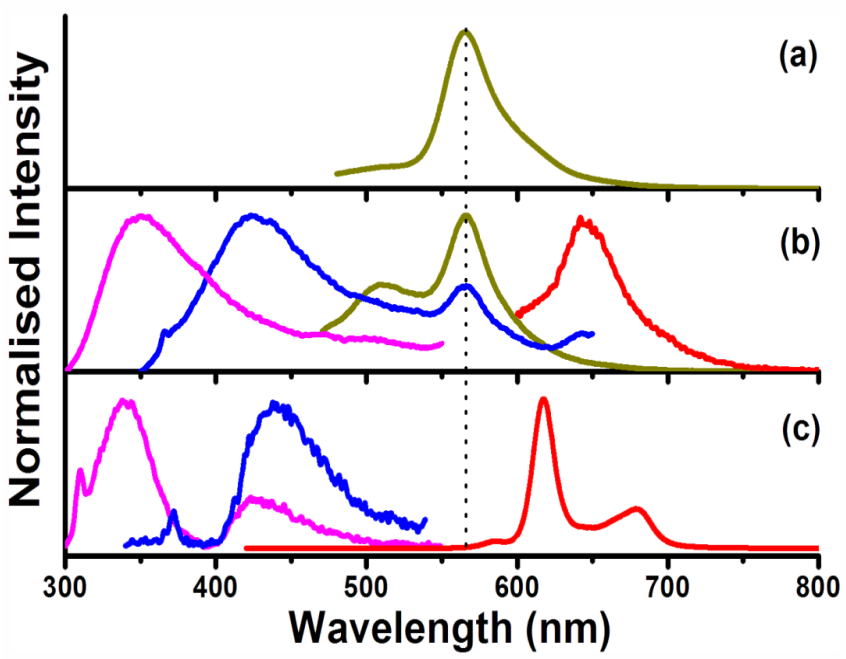

Figure S7. PL spectra of (a) Fe_{QC}@TOPO in chloroform, (b) Fe_{QC}@Hb and (c) Apo-myoglobin-Hemato-porphyrin complex after the addition of piperidine and sodium borohydride. Excitation wavelengths are 280 nm for pink, 330 nm for blue, 450 nm for yellow and 580 nm for red. The spectra clearly notify that 565 nm peak is due to Fe_{QCs}, not from any protein residues.

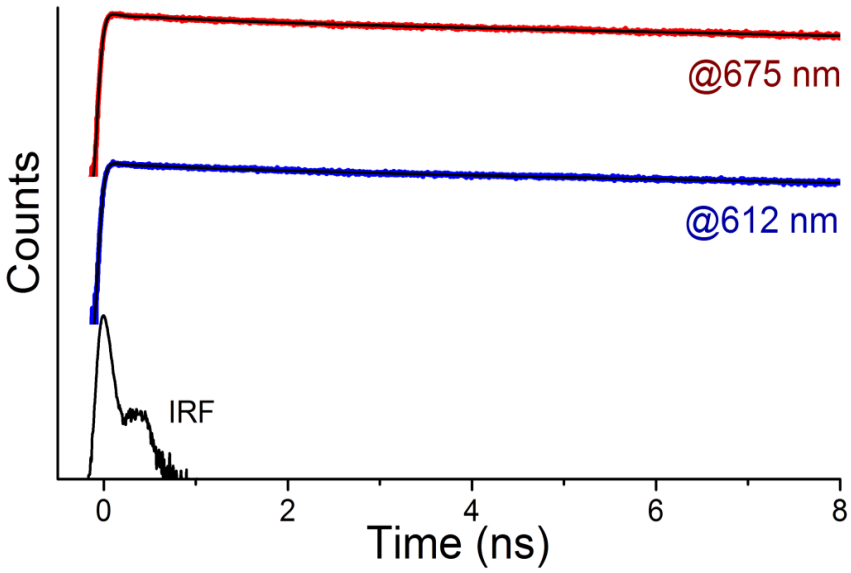

Figure S8. Picosecond-resolved fluorescence transients (Y axis is in ln scale) of Hemato-porphyrin, after the addition of piperidine and sodium borohydride, collected at 612 nm (blue) and 675 nm (red) respectively. Excitation wavelength was 375 nm in both cases. Note that the transients of Fe_{QC}@Hb or Fe_{QC}@TOPO (See Figure 2c in the manuscript) were faster than these PL decays (Table S1) indicating the origin of 565 nm PL from different species in the Fe_{QC} samples apart from porphyrin unit. Base lines are shifted for clarity.

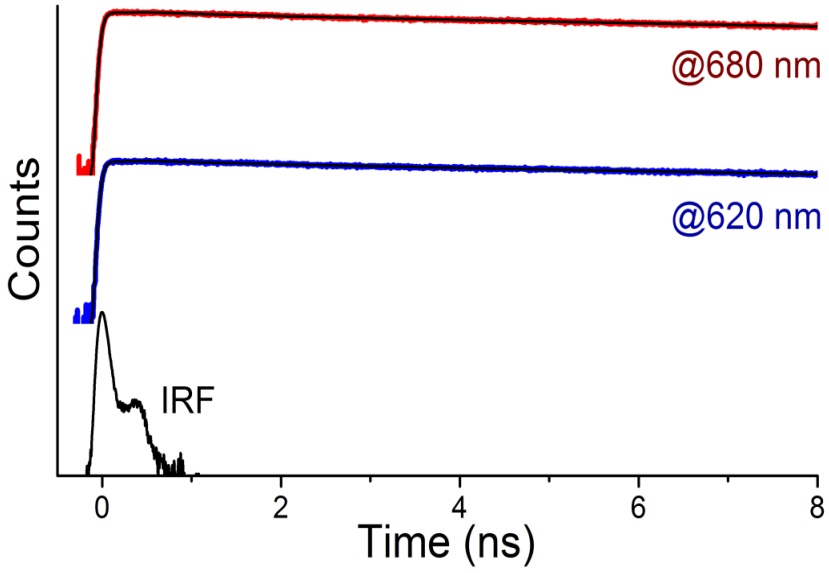

Figure S9. Picosecond-resolved fluorescence transients (Y axis is in ln scale) of Apo-myoglobin-Hemato-porphyrin complex, after the treatment with piperidine and sodium borohydride, collected at 620 nm (red) and 680 nm (blue), respectively. Excitation wavelength was 375 nm. The decay transients are found to be slower after the treatment compared to Hemato-porphyrin suggesting the binding of Hemato-porphyrin to Apo-myoglobin. Base lines are shifted for clarity.

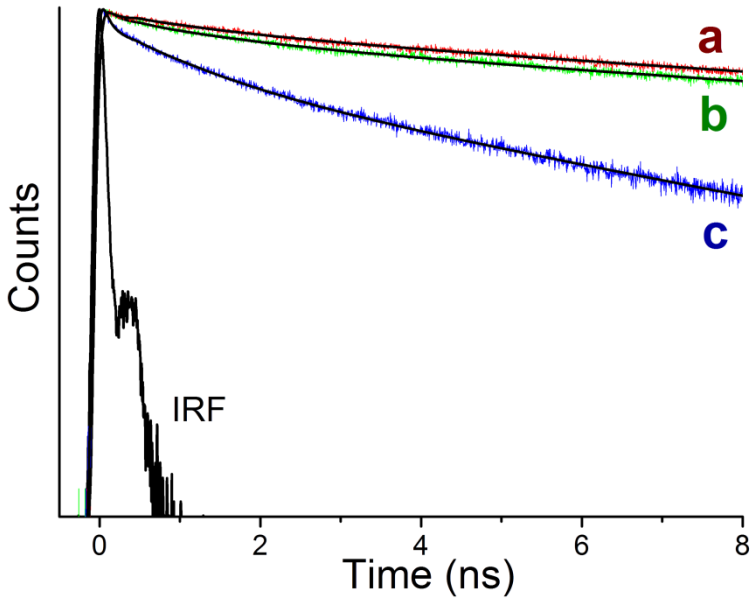

Figure S10. Picosecond-resolved fluorescence transients (Y axis is in ln scale) of (a) Apo-myoglobin-Hemato-porphyrin complex, (b) Hemato-porphyrin and (c) Fe_{QC}@Hb, collected at 650 nm respectively. Excitation wavelength was 375 nm. (All the decays have been taken after the treatment of sodium borohydride in water + piperidine mixture). Decay of Fe_{QC}@Hb is different from treated Hemato-porphyrin and Hemato-porphyrin-Apo myoglobin complex, suggesting that the peak at 647 nm originates from the QC's.

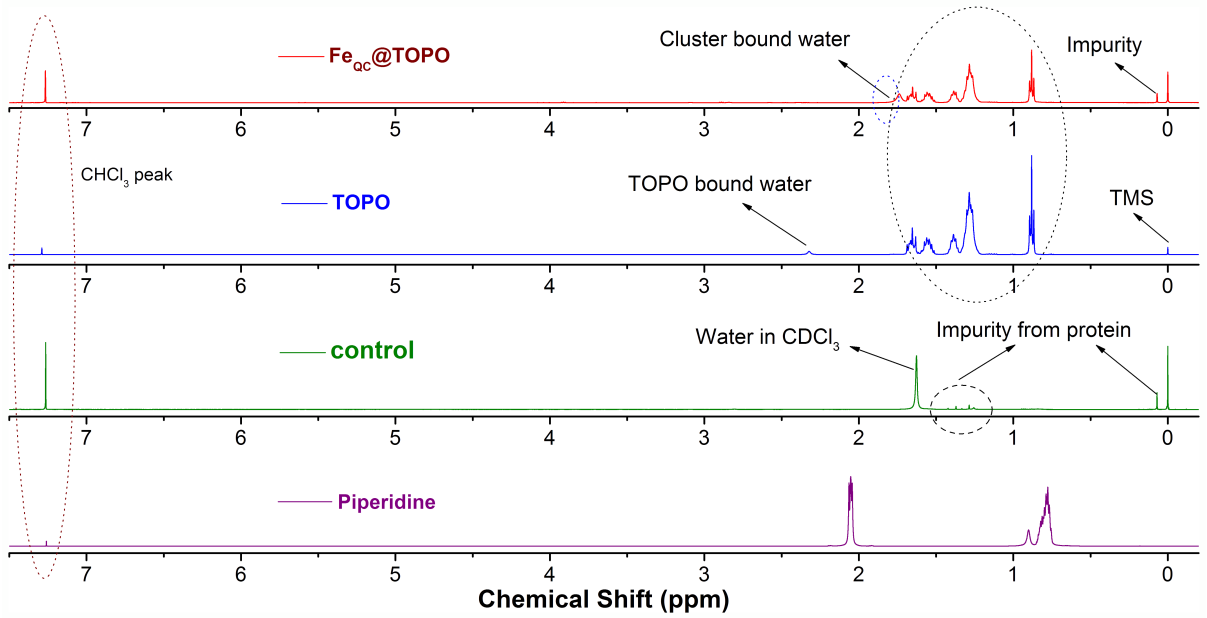

Figure S11. ^{1}H-NMR spectra of piperidine, TOPO, Fe$_{QC}$@TOPO and the control sample in $CDCl_3$ solution. For control, phase transfer has been performed by taking 3 mL of chloroform on the bottom of 3.0 mL (10 mg/ mL) of aqueous Fe$_{QC}$@Hb solution. The mixture was gently stirred for 8-12 hrs at 298 K. Finally, the solution in chloroform was lyophilized and $CDCl_3$ was added to perform the NMR experiment. From the figure it is clear that Fe$_{QC}$@TOPO is free from piperidine and protein residues.

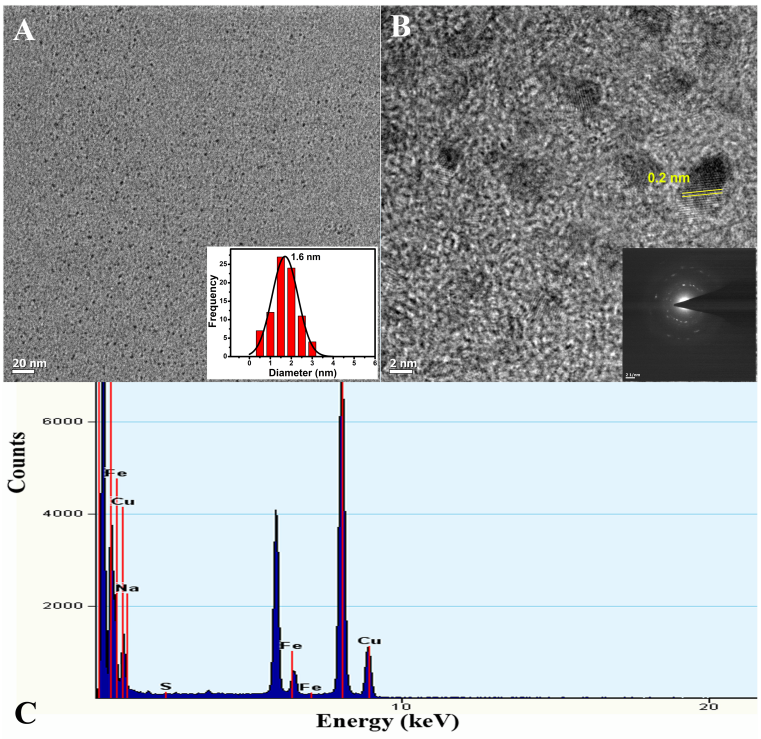

Figure S12. TEM image (A) of Fe$_{QC}$@TOPO shows the presence of tiny QCs. Inset shows the size distribution of the QCs. The scale bar in the TEM image is 20 nm. (B) TEM image of iron cluster aggregates upon 20 min electron beam irradiation. Crystal lattice of the one grown particle is shown by lines. Inset shows the corresponding SAED pattern. (C) EDS spectrum shows the presence of iron.

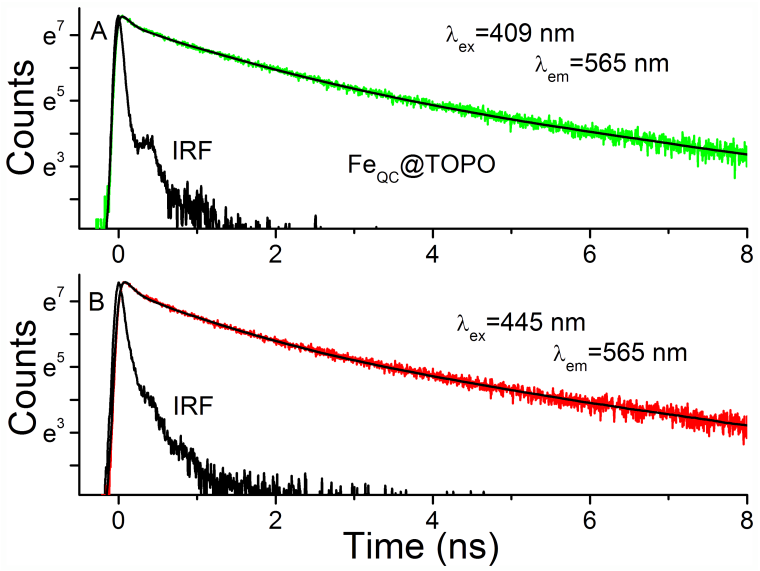

Figure S13. Picosecond-resolved fluorescence transients of Fe_{QC}@TOPO (A) at 409 nm excitation and (B) 445 nm excitation, show the lifetime profiles are independent of the excitation wavelength.

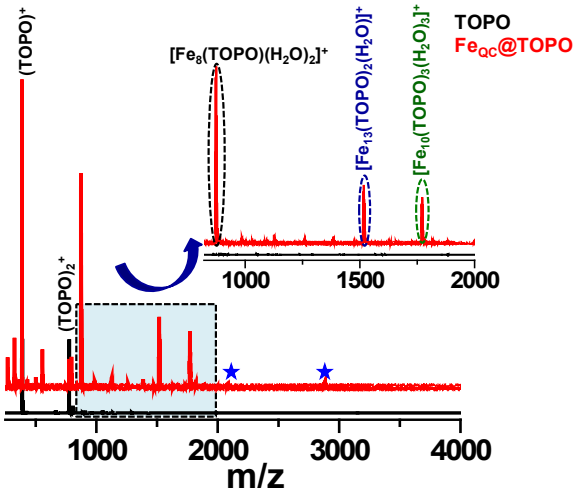

Figure S14. ESI MS spectra of TOPO and Fe_{QC}@TOPO in a larger mass window. The region, m/z 800-2000, marked with dotted rectangle is expanded in the inset. Major peaks are labelled. Other peaks are fragments from these peaks, as confirmed from MS/MS. The peaks labelled * are unidentified ions.

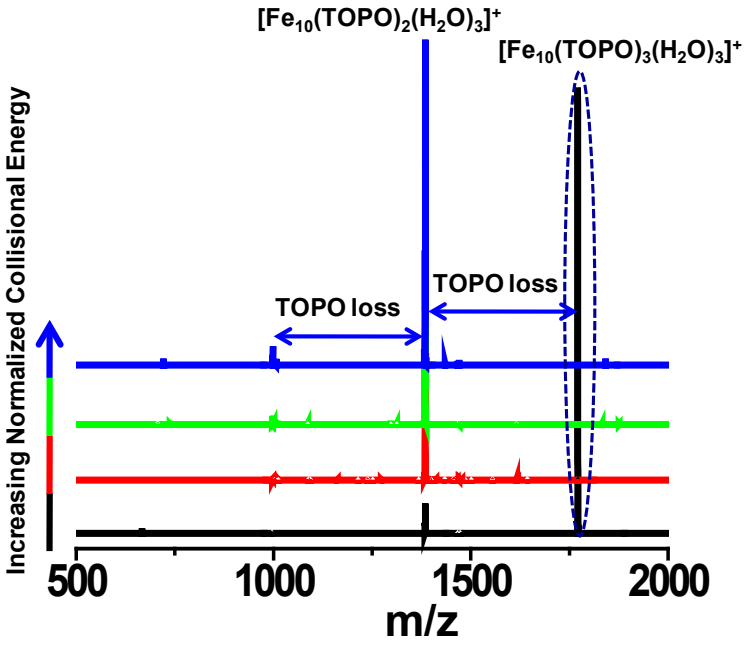

Figure S15. ESI MS/MS of $[Fe_{10}(TOPO)_3(H_2O)_3]^+$ with increasing collisional energy (CE) showing multiple ligand losses.

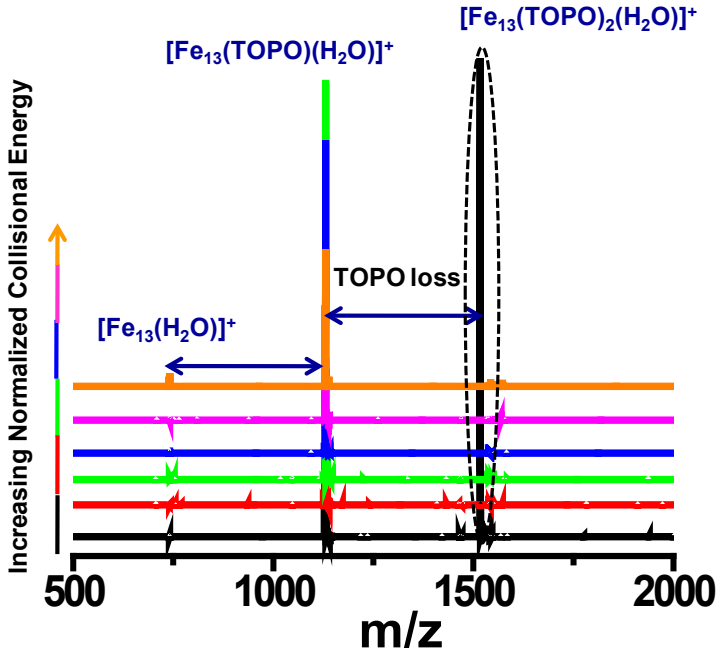

Figure S16. ESI MS/MS of $[Fe_{13}(TOPO)_2(H_2O)]^+$ with increasing collision energy (CE) showing multiple ligand losses.

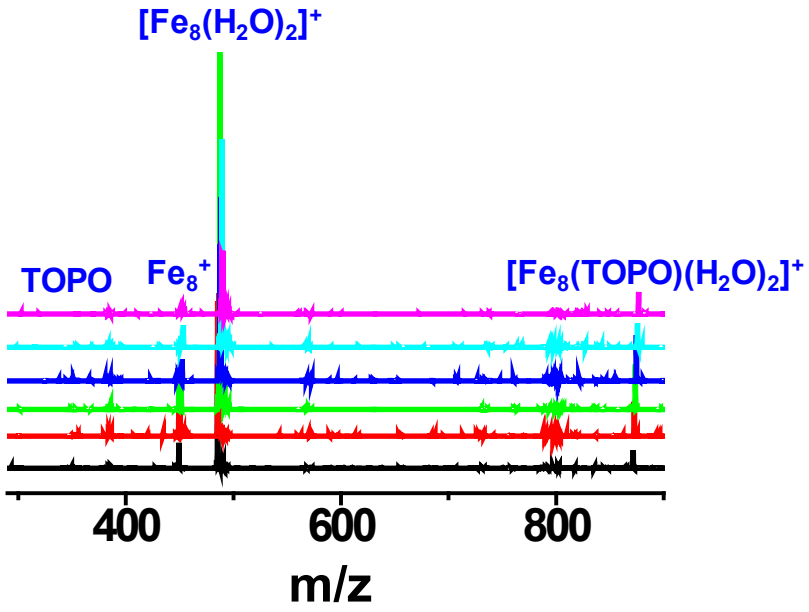

Figure S17. ESI MS/MS of $[Fe_8(TOPO)(H_2O)_2]^+$ with increasing collision energy (CE) showing ligand as well as water losses.

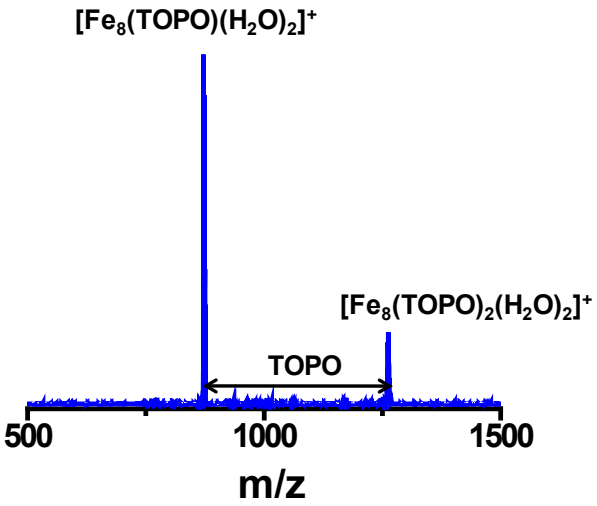

Figure S18. ESI MS/MS of $[Fe_8(TOPO)_2(H_2O)_2]^+$ showing ligand loss.

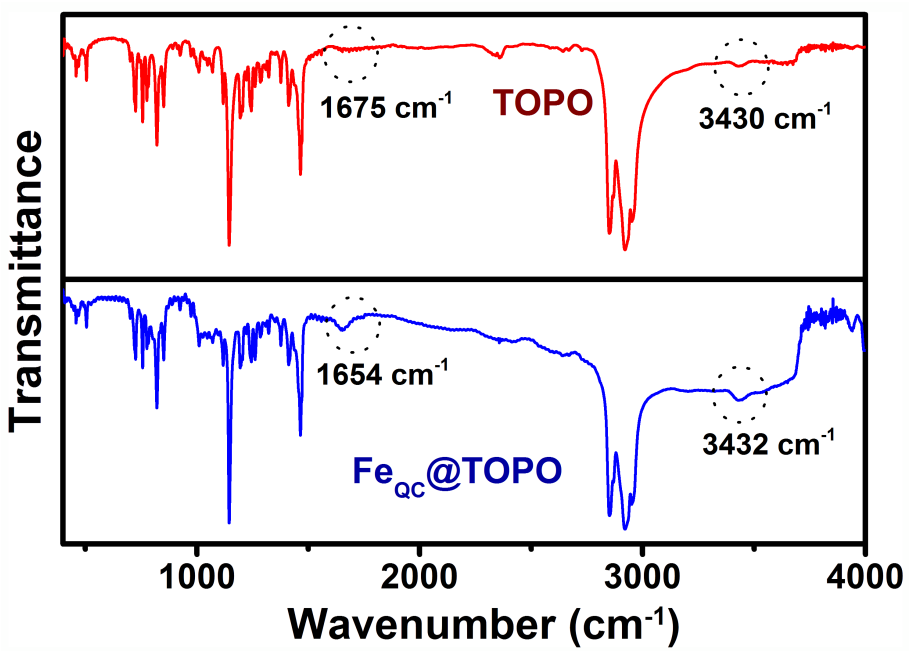

Figure S19. FT-IR spectra of TOPO and Fe_{QC}@TOPO show the presence of water vibration bands marked with dotted circles.

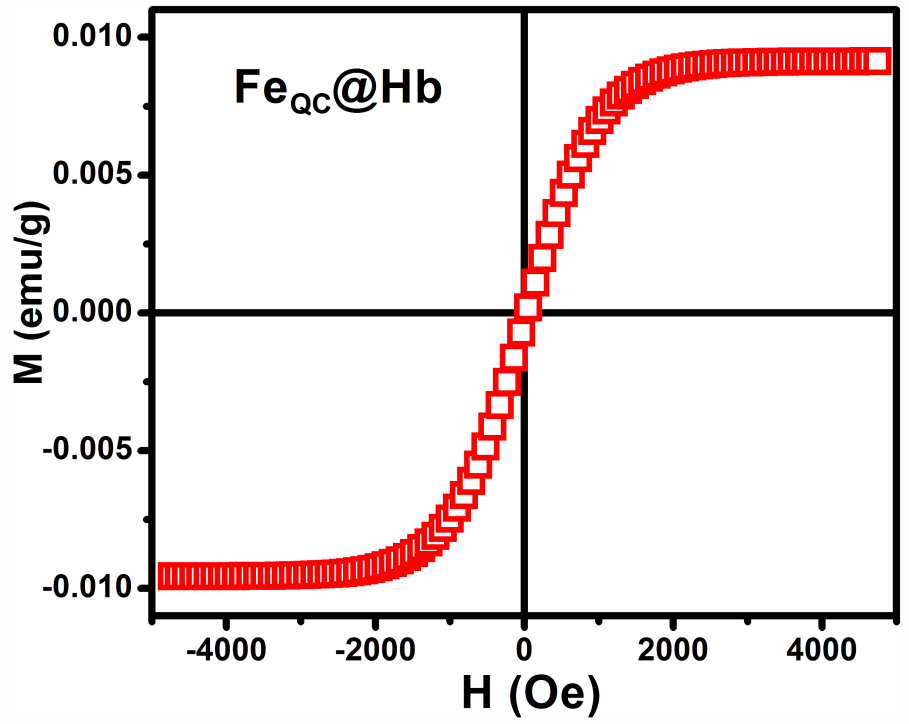

Figure S20. Vibrating sample magnetometer (VSM) data of Fe_{QCs} show the super-paramagnetic behaviour of the QCs (plotted after subtracting the diamagnetic background from the sample holder).

Table S1. Lifetime values (excitation at 375 nm) of the control experiments have provided the evidence of formation of Fe_{QCs} in the protein matrix. Values in parentheses represent the relative weight percentage of the time component with a standard error of ~ 10%.

Name	Wavelength (nm) (λ_{max})	Lifetimes (ns) (Percentage)			Average Lifetime (ns)
Fe_{QC}@Hb	450	0.05 (78%)	0.67 (16%)	3.84 (06%)	0.39
	565	0.08 (64%)	0.91 (22%)	3.90 (14%)	0.80
	650	0.07 (49%)	1.02 (25%)	4.79 (26%)	1.53
Hemato-porphyrin	612	0.14 (20%)	1.24 (13%)	14.78 (67%)	10.15
	650	0.16 (24%)	1.4 (20%)	13.77 (56%)	7.98
	675	0.125 (21%)	1.25 (16%)	14.06 (63%)	9.00
Fe_{QC}@Holo-Myoglobin	450	0.05 (88%)	0.10 (05%)	4.78 (02%)	0.21
	565	0.17 (52%)	0.84 (39%)	3.04 (09%)	0.70
	650	0.14 (37%)	1.16 (34%)	4.08 (29%)	1.63
Apo-Myoglobin & Hemato-porphyrin complex	620	-	1.13 (09%)	15.29 (91%)	14.06
	650	0.15 (19%)	1.40 (17%)	14.07 (64%)	9.30
	680	-	1.03 (13%)	14.78 (87%)	13.03

Sequential Electrochemical Unzipping of Single-Walled Carbon Nanotubes to Graphene Ribbons Revealed by *in Situ* Raman Spectroscopy and Imaging

Robin John,[†,▽] Dhanraj B. Shinde,[‡,▽] Lili Liu,[§] Feng Ding,[§,⊥] Zhiping Xu,[∥] Cherianath Vijayan,[†] Vijayamohanan K. Pillai,[#,*] and Thalappil Pradeep[△,*]

[†]Department of Physics, Indian Institute of Technology Madras, Chennai 600 036, India, [‡]Physical and Materials Chemistry Division, National Chemical Laboratory, Pune 411 008, India, [§]Beijing Computational Science Research Center, Beijing 100084, People's Republic of China, [⊥]Institute of Textiles and Clothing, Hong Kong Polytechnic University, Kowloon, Hong Kong S. A. R., People's Republic of China, [∥]Department of Engineering Mechanics, Tsinghua University, Beijing 100084, People's Republic of China, [#]Central Electrochemical Research Institute, Karaikudi 630 006, India, and [△]DST Unit of Nanoscience and Thematic Unit of Excellence, Department of Chemistry, Indian Institute of Technology Madras, Chennai 600 036, India. [▽]R. John and D. B. Shinde contributed equally.

ABSTRACT We report an *in situ* Raman spectroscopic and microscopic investigation of the electrochemical unzipping of single-walled carbon nanotubes (SWNTs). Observations of the radial breathing modes (RBMs) using Raman spectral mapping reveal that metallic SWNTs are opened up rapidly followed by gradual unzipping of semiconducting SWNTs. Consideration of the resonant Raman scattering theory suggests that two metallic SWNTs with chiralities (10, 4) and (12, 0) get unzipped first at a lower electrode potential (0.36 V) followed by the gradual unzipping of another two metallic tubes, (9, 3) and (10, 1), at a relatively higher potential (1.16 V). The semiconducting SWNTs with chiralities (11, 7) and (12, 5), however, get open up gradually at ±1.66 V. A rapid decrease followed by a subsequent gradual decrease in the metallicity of the SWNT ensemble as revealed from a remarkable variation of the peak width of the G band complies well with the variations of RBM. Cyclic voltammetry also gives direct evidence for unzipping in terms of improved capacitance after oxidation followed by more important removal of oxygen functionalities during the reduction step, as reflected in subtle changes of the morphology confirming the formation of graphene nanoribbons. The density functional-based tight binding calculations show additional dependence of chirality and diameter of nanotubes on the epoxide binding energies, which is in agreement with the Raman spectroscopic results and suggests a possible mechanism of unzipping determined by combined effects of the structural characteristics of SWNTs and applied field.

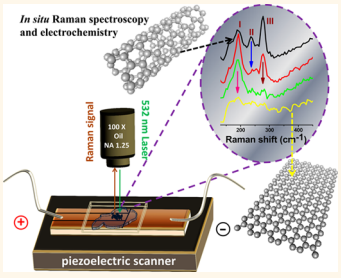

KEYWORDS: graphene · single-walled carbon nanotubes · electrochemistry · Raman spectral mapping · density functional-based tight binding calculations

Carbon has been exciting to scientists for centuries and still continues to fascinate the scientific community in the form of nanometer-sized allotropes such as bucky balls[1] and nanotubes[2] and, more recently, in the form of the ideal atomic layer, graphene.[3] Numerous chemical variants of these have also been explored. Both single-walled carbon nanotubes (SWNTs) and graphene possess unique properties with diverse applications in electronics[4−6] and quantum computing[7] and, above all, possess the ability to unravel many fundamental questions related to ballistic-thermal and -electronic transport.[8−13] SWNTs require high purity and accurate characterization in terms of chiralities and length and diameter distribution for them to be used in most of the specific applications. A similar scenario exists in the case of graphene as well, being vulnerable to drastic changes in the band structure with increasing number of layers,[14] changes in the edge states,[15] *etc.*

It has been understood both theoretically and experimentally that graphene ribbons can have a band gap that could be tuned by varying its width[16,17] and geometry.[18] Nanoribbons are considered important because of the emerging local magnetism with very specific edge states.[19] There are also attempts to use these nanoibbons in electronics by visualizing them as active channel

* Address correspondence to pradeep@iitm.ac.in; vijay@cecri.res.in.

Received for review June 28, 2013 and accepted December 5, 2013.

Published online 10.1021/nn403289g

materials in field effect transistors.[20,21] Hence, it is desirable to have a precise method without any over-oxidation to convert specific SWNTs to graphene nanoribbons and thereby create graphenic materials of desired properties. This concept was also aided by the ability to separate SWNTs according to their metallicity[22] and diameter,[23] which eventually helps in getting graphene ribbons of specific width and edge structure. In this context, recently, Dhanraj *et al.* devised an electrochemical route to convert multiwalled nanotubes into multilayered graphene nanoribbons (GNRs).[24] In brief, nanoribbons of a few layers of graphene have been prepared from carbon nanotubes (CNT) by a two-step electrochemical approach consisting of oxidation of CNTs at controlled potential, followed by reduction to form GNRs having smooth edges and fewer defects, as evidenced by multiple characterization techniques, including Raman spectroscopy, atomic force microscopy, and transmission electron microscopy (TEM). However, neither the role of electric field nor the mechanism of opening and the sequence of events between CNT breaking (oxidative cleavage of the C−C bond) and GNR formation has been probed. Answers to questions such as, is the unzipping fundamentally different for metallic and semiconducting CNTs, where does the curvature break, and what is the reason for selecting a mixture of semiconducting and metallic CNTs, have not been explored, although both single and multiwalled CNTs have been shown to generate GNRs with controlled widths and fewer defects. An *in situ* spectroscopic investigation of various stages of the above sequential processes can possibly reveal the mechanism of unzipping of nanotubes and selective breaking, if any. This will also be important to understand the mechanism of unzipping of SWNTs to GNRs by other methods such as laser cutting and chemical unzipping.[25,26]

RESULTS AND DISCUSSION

We report an *in situ* Raman spectroscopic and microscopic investigation (see Methods and Materials for a detailed description) of the electrochemical unzipping of SWNTs to form graphene ribbons. It was desirable to have a different electrochemical setup that enables this process to be observable in real time. An electrochemical cell was constructed by making a discontinuity on a conducting indium tin oxide (ITO)-coated glass plate to have both electrodes (working and counter) laterally mounted on the same surface in order to suit Raman measurements. The constraint due to the microscopic setup (limited working distance of the objective used) did not allow us to have a cell thicker than 0.24 mm. SWNT dispersion (Methods and Materials) in *N*,*N*-dimethyl formamide (DMF) was deposited on the working electrode, which was kept under the microscope. A particular portion of the

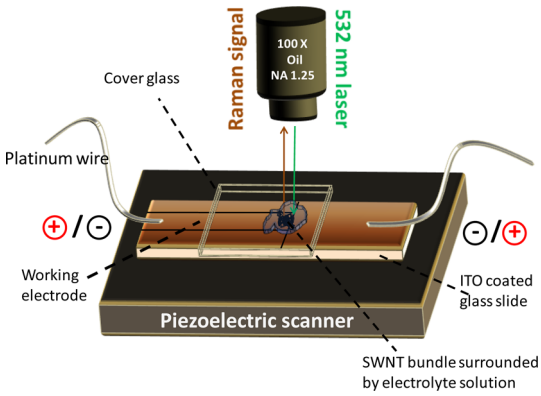

Figure 1. Schematic of the experimental setup used for the *in situ* Raman spectroscopic investigation of the unzipping of SWNTs with orthogonal laser illumination and spectral collection in the backscattering geometry, inside the electrochemical cell. Various parts of the electrochemical cell and essential parts of the Raman spectrometer are labeled. The connections to the electrodes from the dc source are given using a 0.1 mm thick Pt wire.

nanotube sample, say a bundle which contains many SWNTs, was selected and continually imaged using Raman spectral features keeping the same region (20 μm × 20 μm) by varying the potentiostatic conditions. A schematic of the experimental setup used for the study is given in Figure 1 (details are given in the Materials and Methods).

An average micro-Raman spectrum from the drop-casted SWNT on the working electrode shows all the expected features such as the radial breathing modes (RBMs) appearing in the spectral window of 180−280 cm^{-1}, a not so prominent D band (1345 cm^{-1}), a G band (1593 cm^{-1}), and a 2D band (2660 cm^{-1}). A high-resolution RBM spectrum collected for the same sample using a grating of 1800 grooves/mm shows three distinct features at 196 (designated here on as RBM I), 240 (RBM II), and 276 (RBM III) cm^{-1}. RBMs II and III indicate the presence of a number of metallic nanotubes (mSWNT), and RBM I is due to a couple of semiconducting tubes (sSWNT) with different chiralities. By considering the resonance (532 nm laser, 2.33 eV) condition of our measurement, the bundling of SWNTs, the peak positions, and the peak width of ω_{RBM}, a more reasonable assignment of the chiralities can be suggested as follows: 196 cm^{-1} [(11, 7) or (12, 5), interband transition E_{33} = 2.37 or 2.35 eV, diameter d = 1.25 or 1.2 nm, semiconducting], 240 cm^{-1} [(10, 4) or (12, 0), E_{11} = 2.24 or 2.23 eV, d = 0.98 or 0.94 nm, metallic], 276 cm^{-1} [(9, 3) or (10, 1), E_{11} = 2.43 or 2.41 eV, d = 0.85 or 0.83 nm, metallic].[27−29] While the data from one set of SWNT bundles is presented here, data from other bundles are presented in the Supporting Information. Each data set has also been checked for reproducibility.

Spatially resolved Raman spectra (see Materials and Methods) were collected in the spectral window of 0−3900 cm^{-1} for various electrochemical conditions

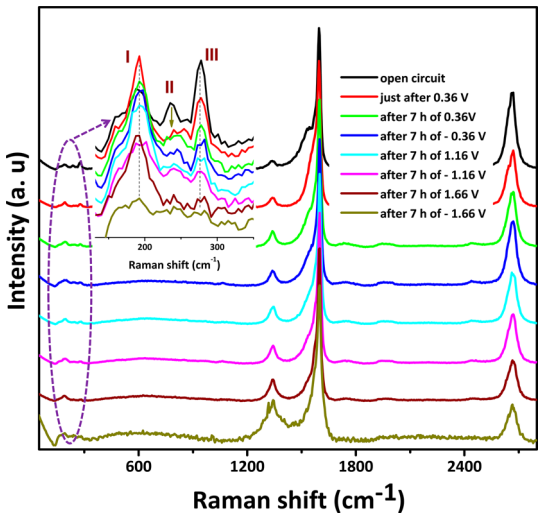

Figure 2. Raman spectra of gradual unzipping of SWNTs. Inset displays the averaged RBM spectra from the sample for various conditions. The black trace is that of the parent material. The red trace (immediately after the application of 0.36 V) shows near-complete disappearance of the second RBM. The third RBM disappears with various conditions, as one can see from the decrease in intensity of the peak around 276 cm^{-1}. Various conditions are labeled by different color. A considerable decrease in the width of the G band is observed, suggesting the reduction in metallicity along with an increase in the D band, which implies increased defects formed during unzipping. The variations in the 2D band at 2660 cm^{-1} band have been discussed elsewhere in the text. Featureless regions of the spectra are used to place the insets.

(labeled in Figure 2). Figure 2 shows the evolution of the average spectral features of the SWNT sample upon various cycles of electrochemical processes. A decrease in peak width of the G band was observed as time evolves and with increased potentials, which is indicative of reduction in the metallicity of the SWNT bundle. There was also an increase in the D band intensity, suggesting increased defects (see Figures 4 and 5 and the subsequent text for detailed discussion). The spectral position of the 2D band remains unchanged with a slight decrease in the peak width, suggesting the single-layer nature of the formed graphene ribbon with uncoupled ribbons. The inset of Figure 2 gives the evolution of the three RBMs of the average spectrum collected from the SWNT bundle, say RBM I (196 cm^{-1}), RBM II (240 cm^{-1}), and RBM III (276 cm^{-1}), which are labeled in the graph as I, II, and III, respectively. It is evident that immediately after the application of 0.36 V (red trace) to the working electrode, the intensity of feature II, corresponding to SWNTs with chiralities (10,4) and (12, 0), gradually disappears along with a considerable decrease in the intensity of feature III.

This remarkable change in RBM II *suggests rapid unzipping at a relatively lower anodic potential.* The subsequent steps show a gradual decrease in the intensity of RBM III, although the intensity of feature I was almost constant. However, after 7 h of application of 1.66 V to the working electrode, the intensity of RBM III (mSWNT) almost disappears (wine red colored trace), while the intensity of RBM I (another type of sSWNT) disappears only after the application of −1.66 V. The electrochemical potentials have been calibrated by carrying out separate experiments under identical conditions of the two-electrode *in situ* electrochemical cells in a three-electrode setup using a mercury/mercurous sulfate reference electrode. The hump still existing at the position of RBM II at the higher potentials is due to the fact that the spectra given in Figure 2 are averages of all the spectra collected throughout the region of the SWNT bundle. Upon examination of smaller areas, we see that there is a complete disappearance of this band immediately after the application of 0.36 V (Figure S1). We believe that there are inhomogeneities in the potential across a large area, and unzipping proceeds only slowly in such regions, explaining this overall spectral behavior.

Images corresponding to different phonon modes in SWNTs were filtered from the spectral map, and they reveal similar morphology, confirming the presence of high-quality SWNTs. A comparison of the images obtained from specific vibrational features for various electrochemical oxidizing conditions further confirms the sequential unzipping of different kinds of SWNTs to form graphene ribbons. Figure 3 compares the morphological features filtered using RBM I (178−206 cm^{-1}), RBM II (228−256 cm^{-1}), and RBM III (264−288 cm^{-1}) for potentials of 0 V (open circuit with no external bias), 0. 36 V (immediately after the application), and 1.16 and 1.66 V, applied to the working electrode for 7 h each. Three columns contain images filtered using RBM features of three pairs of SWNTs. The first column (RBM I) is the image due to sSWNTs (11, 7) or (12, 5), and the second (RBM II) and third (RBM III) columns correspond to mSWNTs (10, 4) or (12, 0) and (9, 3) or (10, 1), respectively. The spectral window for each set of RBMs is given at the top of each column. Each row corresponds to various potentiostatic conditions (as labeled at the left of each column) showing a different extent of oxidation of various types of nanotubes. The corresponding images after intermittent reducing potentials (by the application of −0.36, −1.16, and −1.66 V for 7 h) are shown in Figure S2 (Supporting Information).

The first row (Figure 3a−c) shows the presence of the three RBMs prior to the application of potential (*i.e.*, open circuit with no external bias denoted by 0 V) to the electrodes of the cell. The second row shows the presence of RBM I (d) and RBM III (f) in the imaged structure with a disappearance of the image filtered using RBM II (e) immediately after the application of 0.36 V to the working electrode. This is indicative of the rapid unzipping of two of the mSWNTs, (10, 4) and (12, 0). Figure 3 h and i show the absence of RBMs II

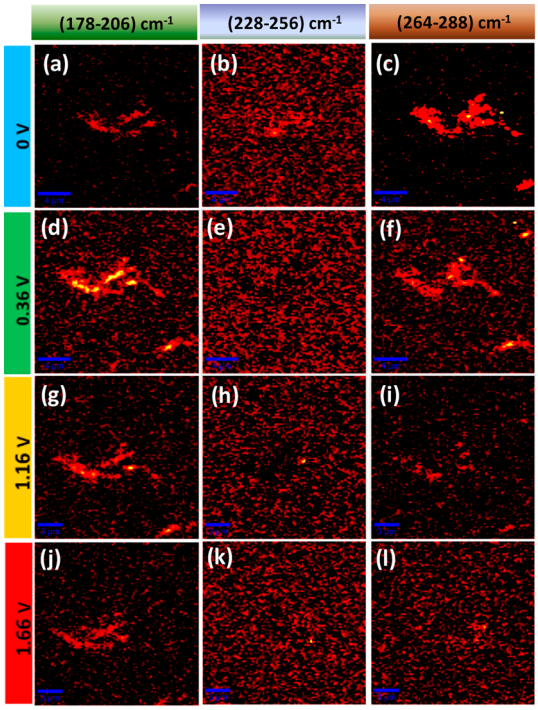

Figure 3. Evolution of the RBM region during electrochemical unzipping. Three columns contain images filtered using the RBMs of three different types of SWNTs. RBM I is due to sSWNTs (filtering windows is 178−206 cm^{-1}), whereas RBMs II and III are from mSWNTs (228−256 and 264−288 cm^{-1}, respectively). Each row corresponds to various stages of unzipping (corresponding to different oxidizing potentials as labeled at the left of each column) for the disappearance of various types of nanotubes. Raman images a−c show the presence of the three types of SWNTs prior to the application of potential (open circuit, *i.e.*, zero applied bias) to the electrodes of the cell. The second row shows the presence of RBM I (d) and RBM III (f) in the imaged structure with a disappearance of the image due to RBM II (e) immediately after the application of 0.36 V to the working electrode; images h and i show the absence of RBM II and III (mSWNTs), respectively, after the application of 1.16 V for a period of 7 h to the working electrode. Image j shows clear reduction in the intensity of RBM I throughout the bundle, along with the absence of RBM II (k) and III (l) after the application of 1.66 V to the working electrode for a period of 7 h. The color scaling varies slightly in each of the figures as the absolute intensities may not be the same in all the images. While the scale bar is 4 μm for images in the first two rows (a−f), it is 3 μm for the last two rows (g−l).

and III, suggesting the unzipping of another two types of mSWNTs, (9, 3) and (10, 1), after the application of 1.16 V for a period of 7 h. Figure S1 (Supporting Information) shows the disappearance of RBM I, suggesting the opening of sSWNTs (11, 7) and (12, 5) with the disappearance of the 196 cm^{-1} peak after the application of −1.66 V for a period of 7 h.

Although specific morphological features due to the three RBMs disappear sequentially with the application of the electric field, other morphological features filtered using D, G, and 2D remain more or less invariant. This is especially significant for unraveling the sequence of events associated with defect generation and lose of curvature. Figure 4 shows the Raman images filtered from 1320 to 1380 cm^{-1} (D band), 1565−1615 cm^{-1} (G), and 2620−2700 cm^{-1} (2D) before (a, b, and c) and after (d, e, and f) electrochemical processing. It is self-evident that the image filtered from G and 2D remains intact, whereas the features due to the D band are enhanced during the process, indicating additional defects formed upon unzipping (shown in Figure 4d). These preserved features arising from the planar sp^2-hybridized hexagonal carbon lattice along with the disappearance of RBMs suggest the unzipping of SWNTs to form GNRs. The images filtered using D, G, and 2D bands for the intermediate steps (immediately after the application of 0.36, 0.36, −0.36, 1.16, −1.16, and 1.66 V applied continuously for 7 h) are shown in Figures S3, S4, and S5. Additional measurements have been conducted on different bundles to confirm this phenomenon (Figures S6, S7, and S8). Formation of graphene ribbons was confirmed by TEM (Figures S9 and 10).

The relative intensity of RBM III with respect to that of RBM I (blue scatter) plotted in Figure 5a clearly shows a reduction at various steps (electrochemical conditions), numbered from 1 to 7 (same order as in Figure 2). We have excluded the eighth step (*i.e.*, −1.66 V applied to the working electrode) as in most cases the RBMs I and III are not present or are negligible to take a ratio. A considerable increase in the intensity of the D (1345 cm^{-1}) band is observed with each step. The I_D/I_G ratio has increased (Figure 2) from 0.039 (for open circuit) to 0.246 (after the application of −1.66 V for 7 h), suggesting the unzipping of SWNTs along with the addition of some undesirable defects. We have tried to analyze the G band and a broad shoulder present at its lower wavenumber region by deconvoluting the region from 1520 to 1610 cm^{-1} with two adjacent Lorentzian peaks (see a representative fit in Figure S11). The peak in the spectral range of 1520 to 1580 cm^{-1} (labeled as G* here on) accounts for the metallicity of the bundle, whose position and width vary with the electrochemical conditions. The peak width of the G (1596 cm^{-1}) band decreased from 23 cm^{-1} for the pristine SWNT to 18 cm^{-1} for the seventh step with a small increase to 19 cm^{-1} for the last step, *i.e.*, application of −1.66 V for 7 h. This variation in the peak width of the G band is also displayed in Figure 5a (wine color scatter), against various steps. The data plotted are the average of the information from four sets of *in situ* Raman spectroscopic data. The standard deviation is given as the error bar. The G* band shows a large decrease in its area and width along with a shift of the center maximum of the Lorentzian peak (details are given in Table S1 and Figure S12). This along with the variation in the RBM intensity ratio (blue scatter) explicitly confirms reduction

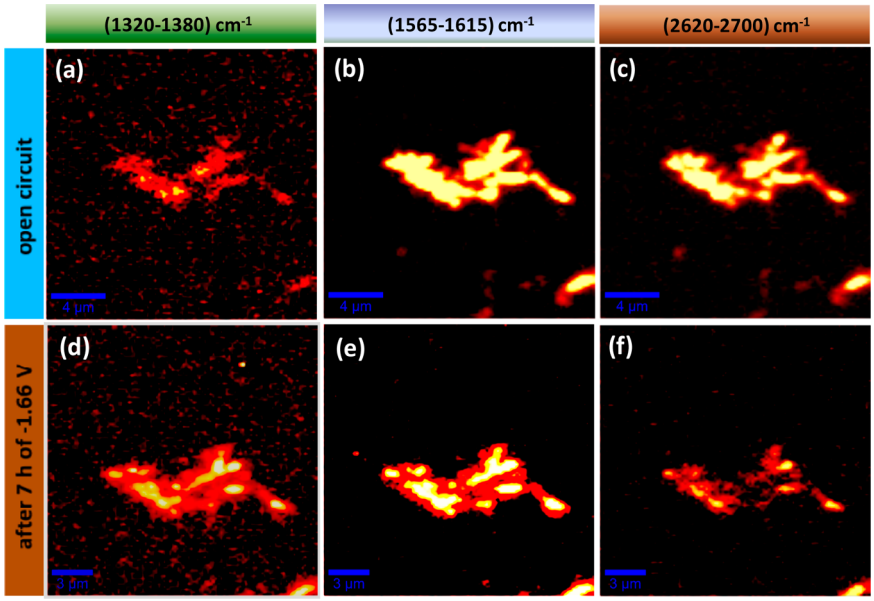

Figure 4. Transformation of SWNTs to graphene ribbons. The first row (a, b, and c) presents the images of the SWNT prior to the electrochemical unzipping, filtered using D (1320−1380 cm^{-1}), G (1565−1615 cm^{-1}), and 2D (2620−2700 cm^{-1}) bands, respectively (scale bar is 4 μm). The second row (e, f, and g) shows the images of the unzipped SWNTs filtered using D, G, and 2D bands. The presence of the G and 2D bands suggests that the sp^2-hybridized carbon structure is intact with an increase in the defect density (scale bar is 3 μm).

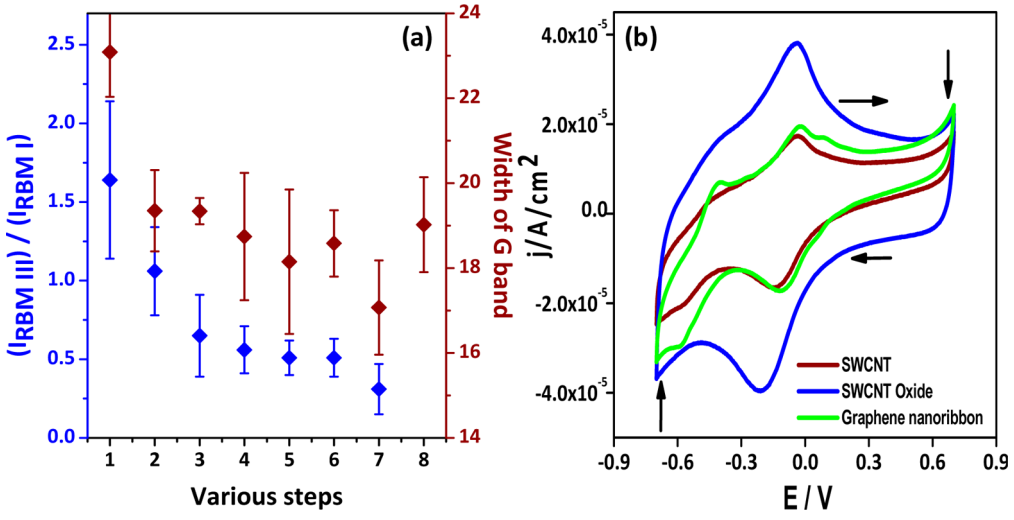

Figure 5. (a) Variation in the intensity ratios of the third RBM to that of the first RBM (blue) and variation of the peak width of the G band (wine color) for various steps (electrochemical conditions labeled in Figure 2 in the same order). Each point is the mean of the ratios from all four sets of *in situ* Raman data considered in the article. Their standard deviation is given as the error bar. (b) Cyclic voltammograms of pristine SWNT mixture, SWNT oxide, and graphene nanoribbons in the potential window from −0.7 to 0.7 V *vs* MMS in 0.5 M H_2SO_4 (same as used for the *in situ* Raman measurements) using a glassy carbon electrode at 100 mV/s scan rate. Arrows in the figure indicate the potential where SWNTs are selectively oxidized or reduced.

in metallicity.[30] We have also fitted the 2D band with a Lorentzian to measure the variation accurately. It is seen that there is a decrease in the intensity of the 2D band as the transformation progresses. We have also found from the spectral deconvolution data that there is a decrease in the width of the 2D band (Figure S13), which is an indication of the decoupling of the layers: the separation of individual tubes from one another upon unzipping in this particular experiment. As the sample under study was a bundle (not isolated SWNTs), it is intuitive that the integrity of the bundle might be affected by the unzipping process, as evident from Figure S10. However, it is difficult to know the details of the modification happening to the bundle using the available observations. The variation of the RBM at negative electrode potentials can happen only after the prior application of a positive potential. This suggests that the oxidation followed by reduction enhances unzipping.

The applied electric field initiates the breaking of sp^2 carbon bonds, perhaps at the middle (longitudinal) region of the side wall of the nanotubes, where a few topological defects can act as the epicenter (Stone–Wales defects). The above argument is supported by molecular dynamic simulations on MWNTs[31] and our TEM measurements (Figure S10 D). This defect generation continues in the longitudinal direction due to the field gradient, as evidenced by the subtle changes in the voltammogram (Figure 5b) similar to the changes seen in *in situ* Raman features. Broken SWNTs along a straight line are stretched farther away by the tension in the curved surface, which could result in the transformation into graphene oxide layers.[32] Cyclic voltammograms for the oxidation of SWNTs within the potential window from −0.7 to 0.7 V (*vs* mercury/mercurous sulfate (MMS) reference electrode) show surface-confined peaks at the beginning with a capacitance value of 50 F/g. However, after 7 h of oxidation at a potential of 0.7 V, there is a large increase in the capacitance (83 F/g), partly due to the change in surface area originating from the morphological changes and the remaining contribution due to the creation of oxygen-containing moieties.

More significantly, the increase in nonfaradaic current with time suggests subtle morphological changes, including that of the area. By keeping the potential at 0.7 V for 7 h, the oxidation of SWNTs generates an enormous number of oxygen functionalities (mainly for semiconducting types). At the end, interestingly the open-circuit potential also increases by 55 mV, clearly revealing the formation of many of these groups, which usually happens because of the creation of functional groups due to oxidation. Oxidative unzipping, which increases the surface area per SWNT, also enhances the capacitance, accounting for the increase in area as well as the formation of functional groups (especially, oxygen-containing functional groups). After selective reduction of SWNT oxide at −0.7 V for 7 h, there is a gradual decrease in the capacitance ascribed to the removal of oxygen functionalities (from X-ray photoelectron spectra in ref 18) from unzipped tubes implying faster kinetics compared to that during the oxidation step.[33] Peaks at −0.57 and −0.38 V correspond to oxygen reduction and hydroxide formation.

In addition to the electric field effects as addressed above, structural characteristics of SWNTs such as chirality and diameter could also lead to specified preferences for the unzipping process, as evidenced by the *in situ* Raman spectroscopic measurements. In order to clarify their influence and to understand further the fundamental role of oxygen in unzipping, we have performed calculations using the spin-polarized density-functional tight-binding (DFTB) method. On the basis of geometrical optimization of three sets of SWNTs with different chiralites and diameters, relative energy changes in forming epoxy groups on the outer walls were studied. We classify carbon nanotubes by their diameter into three sets; the first set includes chiralities (4, 4), (5, 2), and (7, 0), the second set (5, 5), (6, 3), and (9, 0), and the last set (6, 6), (7, 4), and (11, 0). All three sets of SWNTs have lengths between 2 and 3 nm. Both ends of the SWNTs are terminated chemically by hydrogen atoms.

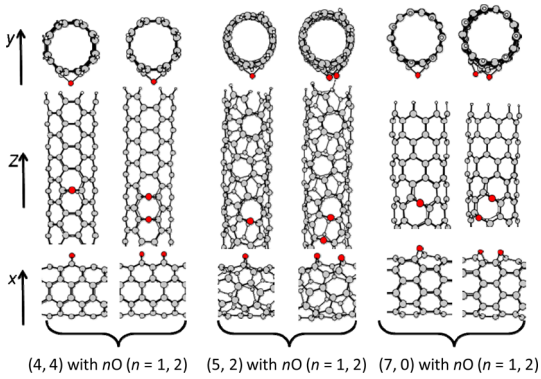

Figure 6. Optimized configurations of (4, 4), (5, 2), and (7, 0) SWNTs with *n*O (*n* = 1, 2) by self-consistent charge formalism (SCC-DFTB-D). These chiralities were chosen so that the *n*O addition is visually identifiable along with clarity in the direction of oxygen addition. A number of various chiralitites were used for the DFTB-D study of the dependence of the *n*O binding energy on the oxygen attachment direction and diameter of the SWNT.

By forming epoxy groups on graphitic carbon structures, the underlying sp^2 carbon–carbon bonds will be elongated; thus SWNTs can be unzipped, or cut, by oxidation into graphene nanoribbons with specific width depending on the structures of SWNTs.[34] It is shown that, by preferential aligning, the total energy of epoxidized SWNTs could be lowered.[35,36] As illustrated in Figure S14, there are several possible pathways for cutting by binding oxygen atoms, as described by their relative orientation to the axis of SWNTs. In the first set of SWNTs for example, there are two cutting directions for armchair (4, 4) nanotubes, with different angles to the axis, 0° and 30°, respectively. For chiral (5, 2) SWNTs, angles are 16.1°, 52.9°, and 76.1°, and for zigzag (7,0) SWNTs, the angles are 30° and 60° for zigzag nanotube (7,0). The other two sets have similar cutting mechanisms with multiple pathways. All the structures have been optimized, and the most stable structures in the first set of SWNTs and their oxidized derivatives are shown in Figure 6. For the armchair and chiral SWNTs, the ground states of the products are closed-shell singlet, while for zigzag ones, quintet states with four unpaired electrons on the nanotube ends are preferred energetically. The energies of epoxidized structures with one and two oxygen atoms are listed in Table S2.

According to the Bell–Evans–Polanyi (BEP) principle, the difference in activation energy between two reactions of the same family is proportional to the

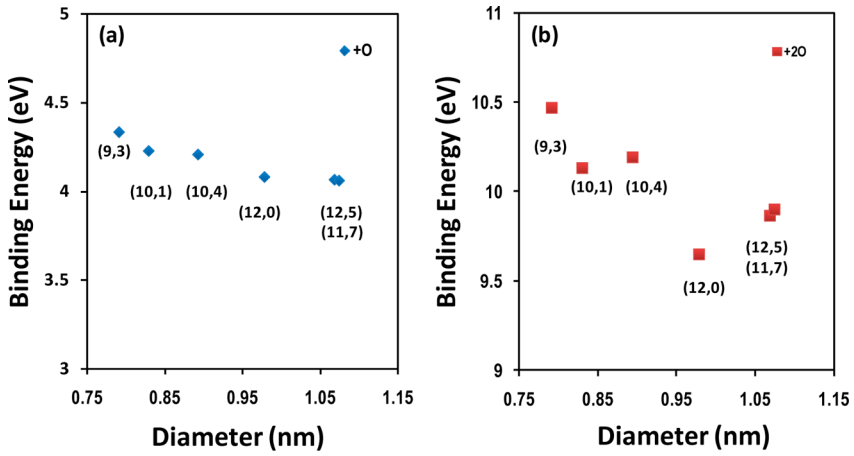

Figure 7. Dependance of oxygen binding on the diameter of SWNT. Variation of the binding energy (E_b) of the SWNTs + O (n = 1, blue data) (a) and (n = 2, maroon) (b) with the diameter of SWNTs.

difference of their enthalpy of reactions. Thus the binding energies calculated here offer explicit evidence to assess the reaction barrier of SWNT oxidation.[37] This is confirmed by direct comparison between calculated binding energies and reaction barriers using the climbing nudged energy band (CNEB) method using the first-principles method (details given in the Supporting Information as text and Figure S15). From the results we can clearly see that, for SWNTs with the same chirality, it turns out that SWNTs with smaller diameters have higher oxygen-binding energies; that is, one oxygen cutting through epoxidation is energetically more favorable for SWNTs with smaller diameters than those with larger diameters. As an example, E_b for (7, 0) is 5.1436 eV, while for (9, 0) and (11, 0), it is 4.3011 and 4.1384 eV, respectively. For all structures under investigation, we find the direction of epoxidation prefers to be aligned to the nanotube axis. There is also a distinct dependence of E_b on the angle of chirality θ (for a nanotube with chiral index (n, m), $\theta = \tan^{-1}[\sqrt{3}m/(m + 2n)]$, *e.g.*, $\theta = 0°$ and 30° for zigzag and armchair CNTs, respectively) of an SWNT, as shown in Figure S16. As the chiral angle of graphene lattice increases, E_b decreases and the binding of oxygen atoms through epoxy groups is less preferred.

In order to correlate the DFT calculations with the *in situ* Raman spectroscopic observations, we have performed similar calculations for SWNTs with the chiralities, the same as in the Raman studies (Table S3 and Figure S17). The calculations matched well with our experimental results for certain SWNTs, as the binding energies of 2O addition for (12, 0), (12, 5), and (11, 7) with relatively large diameters are 9.65, 9.86, and 9.90 eV, whereas for (9, 3), (10, 1), and (10, 4) the binding energies are 10.47, 10.14, and 10.20 eV, respectively (Figure 7). The data indicate that, for the first three SWNTs, oxygen addition is more difficult when compared to the later ones. The energetics of oxygen addition is a direct measure of the ease of unzipping; that is, (9, 3) and (10, 1) can be be unzipped with lesser energy (low electrode potentials), whereas (12, 5) and (11, 7) need relatively higher energy to get unzipped. These structural characteristics, with additional effects of the applied field clarified above (not included in the calculations), and potentially the interaction between substrate and SWNTs[38] determine the preference of oxidation and cutting processes of SWNTs.

CONCLUSIONS

Here we report an *in situ* Raman spectroscopic and microscopic investigation of the electrochemical unzipping of SWNTs. From careful observation of the RBMs and by using inputs from resonant Raman scattering theory, we understand that two types of metallic SWNTs with chiralities (10, 4) and (12, 0) are opened up rapidly at 0.36 V followed by a gradual opening of another two metallic SWNTs with chiralities (9, 3) and (10, 1) at 1.16 V. This is again followed by the slow unzipping of another two kinds of semiconducting nanotubes with chiralities (11, 7) and (12, 5) at a relatively high potential (−1.66 V). It has been observed that smaller size SWNTs are unzipped at relatively low electrode potentials. A gradual decrease in the metallicity of the SWNT ensemble was confirmed from the careful observation of the width of the G band. An increase in the D (defect) band with retention of the 2D band suggests unzipping of nanotubes forming graphene ribbons. A CV study confirms selective oxidation of SWNTs at an applied potential of 0.7 V for 7 h. Oxidative unzipping is evidenced by the improvement in capacitance. In the next reduction step, SWNT-oxide becomes graphene, which is clear from the subtle changes in the voltammograms with a decrease in the capacitance. On the basis of DFTB calculations, we show that there is a dependence of the diameter and chirality of an SWNT on the binding energies of single and double oxygen atoms as in-line epoxy groups. This trend is similar to the *in situ* Raman spectroscopic

observations, suggesting that the mechanism of unzipping is likely to be the formation of epoxides on SWNTs and their successive transformation to graphene ribbons.

METHODS AND MATERIALS

Preparation of the SWNT Sample. The sample of SWNTs from Carbon Nanotechnologies Inc., which is a mixture of semiconducting and metallic nanotubes, was purified according to the following protocol. The mixture was heated for 12 h at 250 °C in a furnace. It was further treated with 15 mL of concentrated HCl, thereby removing the metal catalysts as their chlorides. The acid-treated sample was then filtered using a membrane (0.2 μm pore size) filter to obtain bucky paper, which was neutralized with a 1 M solution of $NaHCO_3$, until the filtrate showed a pH greater than 7.0. The unreacted acid was removed followed by washing with copious amounts of water. The residue collected was dried at 70 °C for 6 h and preserved under vacuum until further use. The dispersion of the purified SWNT was prepared by taking 1 mg of the sample in 10 mL of dimethyl formamide (purchased from Qualigens) and sonicating it for 2 h with control over temperature.

Electrochemical Cell for *in Situ* Raman Measurements. A 50 μL sample of the SWNT dispersion in DMF was drop casted on the working electrode of the electrochemical cell. The cell was designed in such a way that both the electrodes (working and counter) are on the conducting side of the indium-doped tin oxide coating (conductivity of 40 Ω cm^{-1}, purchased from Nikon Sheet Glass Ltd.). We made a discontinuity on the conducting side of the glass slide by removing the conducting layer by scratching to create the electrodes (inset of Figure 1). The cell was covered with a coverglass, through which the process of unzipping can be observed using Raman spectroscopy. Three sides of the cell were sealed with Teflon tape to make it a cavity with one side open in order to allow the insertion of the electrolyte. The electrolyte (0.5 M H_2SO_4) was injected into the cell with the help of a syringe, which was then distributed into the cell by means of capillary action as a cell column thickness of around 0.15 mm was used. A coverglass-corrected (∞/0.17) 100$\times$ oil immersion objective (NA 1.3) whose working distance is 0.23 mm was used for spectral measurements. The potential was applied using a dc source in the range -5.0 to $+5.0$ V.

Confocal Raman Spectroscopy and Imaging. Confocal Raman measurements were done with a WiTec GmbH, CRM αS300 instrument having a 532 nm Nd:YAG laser as the excitation source. The effective scan range of the spectrometer was 0$-$3800 cm^{-1} with a 600 grooves/mm grating, and the dispersed light intensity was measured by a Peltier-cooled charge coupled device (CCD). Raman imaging was done using the same grating, with an integration time of 100 ms. The piezoelectric scanner with maximum scanning area of 100 μm $\times$ 100 μm enabled the movement of the electrochemical cell (which is at the focal plane of the objective) for scanning. Each image contains 200 pixels in 200 lines (40 000 pixels) with each pixel having a Raman spectrum of a particular spatial position. Single-spot spectra were also acquired with larger integration times. For improved resolution and to ascertain peak positions, 1800 grooves/mm grating was used while acquiring single-spot spectra. The intensities of the desired portion of the spectra, collected over all of the pixels, were compared by Scan CTRL Spectroscopy Plus Version 1.32 software, to construct color-coded images. Also, the image corresponding to various features of graphene, namely, RBM I, RBM II, RBM III, D, G, and 2D, was filtered from the image using WiTec Project 3.2.

Transmission Electron Microscopy. TEM imaging was performed using a JEOL 3010 instrument. The accelerating potential used for imaging the graphene ribbons was 200 kV. The sample was drop cast on a copper grid and was dried in ambient conditions prior to the TEM analysis.

Density Functional Theory Calculations. All calculations here are carried out using the DFTB+ program.[39,40] DFTB is an approximate density functional theory method based on the tight-binding approach that utilizes an optimized minimal linear combination of atomic orbital (LCAO) Slater-type all-valence basis set and a two-center approximation for Hamiltonian matrix elements. The Coulombic interaction between partial atomic charges was determined using the self-consistent charge (SCC) formalism. Slater$-$Kirkwood-type dispersion was employed for van der Waals and $\pi-\pi$ stacking interactions. This approach has been shown to give a reasonably good prediction of carbon nanostructures and their functional derivatives.[41,42]

Conflict of Interest: The authors declare no competing financial interest.

Acknowledgment. T.P. thanks DST for financial support through the Nano Mission. R.J. thanks UGC for a fellowship. Mr. C. R. Arunkumar, CSM, POSTECH, South Korea, is thanked for initial discussions on DFT. Prof. Shigeo Maruyamma and Mr. Pei Zhao are thanked for technical advice on indexing the chiralities of SWNTs. Mr. Anirban Som is thanked for TEM measurements. V.K.P. and D.B.S. acknowledge financial support of CSIR through the project NWP0022.

Supporting Information Available: Raman images filtered from RBM I, RBM II, RBM III, D band, G band, and 2D band for all eight electrochemical conditions (steps) are given along with the average Raman spectra obtained from automated cluster analysis (which showed similarity to the manually averaged spectra) by the WiTec Project software. TEM images are also included to show the unzipped SWNTs. Supporting evidence for the Bell$-$Evans$-$Polanyi principle by additional first-principles calculations is provided, which compares binding energies of oxygen atoms and the reaction barriers. This material is available free of charge *via* the Internet at http://pubs.acs.org.

REFERENCES AND NOTES

1. Kroto, H. W.; Heath, J. R.; O'Brien, S. C.; Curl, R. F.; Smalley, R. E. C60: Buckminsterfullerene. *Nature* **1985**, *318*, 162–168.
2. Iijima, S. Helical Microtubules of Graphitic Carbon. *Nature* **1991**, *354*, 56–58.
3. Novoselov, K. S.; Geim, A. K.; Morozov, S. V.; Jiang, D.; Zhang, Y.; Dubonos, S. V.; Grigorieva, I. V.; Firsov, A. A. Electric Field Effect in Atomically Thin Carbon Films. *Science* **2004**, *306*, 666–669.
4. Lin, Y. M.; Dimitrakopoulos, C.; Jenkins, K. A.; Farmer, D. B.; Chiu, H. Y.; Grill, A.; Avouris, Ph. 100-GHz Transistors from Wafer-Scale Epitaxial Graphene. *Science* **2010**, *327*, 662.
5. Kedzierski, J.; Hsu, P. L.; Healey, P.; Wyatt, P. W.; Keast, C. L.; Sprinkle, M.; Berger, C.; de Heer, W. A. Epitaxial Graphene Transistors on SiC Substrates. *IEEE Trans. Electron Devices* **2008**, *55*, 2078–2085.
6. Schwierzl, F. Graphene Transistors. *Nat. Nanotechnol.* **2010**, *89*, 487–496.
7. Candini, A.; Klyatskaya, S.; Ruben, M.; Wernsdorfer, W.; Affronte, M. Graphene Spintronic Devices with Molecular Nanomagnets. *Nano Lett.* **2011**, *11*, 2634–2639.
8. Shiomi, J.; Maruyama, S. Diffusive-Ballistic Heat Conduction of Carbon Nanotubes and Nanographene Ribbons. *Int. J. Thermophys.* **2010**, *31*, 1945–1951.
9. Brar, V. W.; Wickenburg, S.; Panlasigui, M.; Park, C. H.; Wehling, T. O.; Zhang, Y.; Decker, R.; Girit, C.; Balatsky, A. V.; Louie, S. G.; *et al*. Observation of Carrier-Density-Dependent Many-Body Effects in Graphene *via* Tunneling Spectroscopy. *Phys. Rev. Lett.* **2010**, *104*, 036805 (1$-$4).
10. Novoselov, K. S.; Jiang, Z.; Zhang, Y.; Morozov, S. V.; Stormer, H. L.; Zeitler, U.; Maan, J. C.; Boebinger, G. S.; Kim, P.; Geim, A. K. Room-Temperature Quantum Hall Effect in Graphene. *Science* **2007**, *315*, 1379.

11. Levy, N.; Burke, S. A.; Meaker, K. L.; Panlasigui, M.; Zettl, A.; Guinea, F.; Castro Neto, A. H; Crommie, M. F. Strain-Induced Pseudo Magnetic Fields Greater Than 300 T in Graphene Nanobubbles. *Science* **2010**, *329*, 544–547.
12. Shinde, D. B.; Pillai, V. K. Electrochemical Resolution of Multiple Redox Events for Graphene Quantum Dots. *Angew. Chem., Int. Ed.* **2013**, *52*, 2482–2485.
13. Wallace, P. R. The Band Theory of Graphite. *Phys. Rev.* **1947**, *71*, 622–634.
14. Odom, T. W.; Huang, J. L.; Kim, P.; Lieber, C. M. Atomic Structure and Electronic Properties of Single-Walled Carbon Nanotubes. *Nature* **1998**, *391*, 62–64.
15. Nakada, K.; Fujita, M.; Dresselhaus, G.; Dresselhaus, M. S. Edge State in Graphene Ribbons: Nanometer Size Effect and Edge Shape Dependence. *Phys. Rev. B* **1996**, *54*, 17954–17961.
16. Han, M. Y.; Ozyilmas, B.; Zhang, Y.; Kim, P. Energy Band-Gap Engineering of Graphene Nanoribbons. *Phys. Rev. Lett.* **2007**, *98*, 206805(1−4).
17. Son, Y. W.; Cohen, M. L.; Louie, S. G. Energy Gaps in Graphene Nanoribbons. *Phys. Rev. Lett.* **2006**, *97*, 216803 (1−4).
18. Mohanty, N.; Moore, D.; Xu, Z.; Sreeprasad, T. S.; Nagaraja, A.; Rodriguez, A. A.; Berry, V. Nanotomy-Based Production of Transferable and Dispersible Graphene Nanostructures of Controlled Shape and Size. *Nat. Commun.* **2012**, *3*, 844(1−8).
19. Huang, L. F.; Zhang, G. R.; Zheng, X. H.; Gong, P. L.; Cao, T. F.; Zeng, Z. Understanding and Tuning the Quantum-Confinement Effect and Edge Magnetism in Zigzag Graphene Nanoribbon. *J. Phys.: Condens. Matter.* **2013**, *25*, 055304 (1−8).
20. Chen, Z.; Lin, Y. M.; Rooks, M. J.; Avouris, Ph. Graphene Nanoribbon Electronics. *Phys. E (Amsterdam, Neth.)* **2007**, *40*, 228–232.
21. Wang, X.; Ouyang, Y.; Li, X.; Wang, H.; Guo, J.; Dai, H. Room-Temperature All-Semiconducting Sub-10-nm Graphene Nanoribbon Field-Effect Transistors. *Phys. Rev. Lett.* **2008**, *100*, 206803(1−4).
22. Maeda, Y.; Kimura, S.; Kanda, M.; Hirashima, Y.; Hasegawa, T.; Wakahara, T.; Lian, Y.; Nakahodo, T.; Tsuchiya, T.; Akasaka; *et al*. Large-Scale Separation of Metallic and Semiconducting Single-Walled Carbon Nanotubes. *J. Am. Chem. Soc.* **2005**, *127*, 10287–10290.
23. Heller, D. A.; Mayrhofer, R. M.; Baik, S.; Grinkova, Y. V.; Usrey, M. L.; Strano, M. S. Concomitant Length and Diameter Separation of Single-Walled Carbon Nanotubes. *J. Am. Chem. Soc.* **2004**, *126*, 14567–14573.
24. Shinde, D. B.; Debgupta, J.; Kushwaha, A.; Aslam, M.; Pillai, V. K. Electrochemical Unzipping of Multi-walled Carbon Nanotubes for Facile Synthesis of High-Quality Graphene Nanoribbons. *J. Am. Chem. Soc.* **2011**, *133*, 4168–4171.
25. Kosynkin, D. V.; Higginbotham, A. L.; Sinitskii, A.; Lomeda, J. R.; Dimiev, A.; Price, B. K.; Tour, J. M. Longitudinal Unzipping of Carbon Nanotubes to Form Graphene Nanoribbons. *Nature* **2009**, *458*, 872–876.
26. Elias, A. L.; Botello-Mendez, A. R.; Meneses-Rodriguez, D.; Gonzalez, V. J.; Ramirez-Gonzalez, D.; Ci, L.; Munoz-Sandoval, E.; Ajayan, P. M.; Terrones, H.; Terrones, M. Longitudinal Cutting of Pure and Doped Carbon Nanotubes to Form Graphitic Nanoribbons Using Metal Clusters as Nanoscalpels. *Nano Lett.* **2010**, *10*, 366–372.
27. Jorio, A.; Saito, R.; Hafner, J. H.; Lieber, C. M.; Hunter, M.; McClure, T.; Dresselhaus, G.; Dresselhaus, M. S. Structural (*n*,*m*) Determination of Isolated Single-Wall Carbon Nanotubes by Resonant Raman Scattering. *Phys. Rev. Lett.* **2007**, *86*, 1118–1121.
28. Dresselhaus, M. S.; Dresselhaus, G.; Saito, R.; Jorio, A. Exciton Photophysics of Carbon Nanotubes. *Annu. Rev. Phys. Chem.* **2007**, *58*, 719–747.
29. Araujo, P. T.; Doorn, S. K.; Kilina, S.; Tretiak, S.; Einarsson, E.; Maruyama, S.; Chacham, H.; Pimenta, M. A.; Jorio, A. Third and Fourth Optical Transitions in Semiconducting Carbon Nanotubes. *Phys. Rev. Lett.* **2007**, *98*, 067401(1−4).
30. Dresselhaus, M. S.; Jorio, A.; Souza Filha, A. G.; Dresselhaus, G.; Saito, R. Raman Spectroscopy on One Isolated Carbon Nanotubes. *Phys. B (Amsterdam, Neth.)* **2002**, *323*, 15–20.
31. dos Santos, R. P. B.; Perim, E.; Autreto, P. A. S.; Brunetto, G.; Galvao, D. S. On the Unzipping of Multiwalled Carbon Nanotubes. *Nanotechnology* **2012**, *23*, 465702(1−7).
32. Kim, W. S.; Moon, S. Y.; Bang, S. Y.; Choi, B. G.; Ham, H.; Sekino, T.; Shim, K. B. Fabrication of Graphene Layers from Multiwalled Carbon Nanotubes Using High DC Pulse. *Appl. Phys. Lett.* **2009**, *95*, 0831031–0831033.
33. Ramesha, G. K.; Sampath, S. Electrochemical Reduction of Oriented Graphene Oxide Films: An *in-Situ* Raman Spectroelectrochemical Study. *J. Phys.Chem. C* **2009**, *113*, 7985–7989.
34. Jiang, L.; Zhang, L.; Wang, X.; Diankov, G.; Dai, H. Narrow Graphene Nanoribbons from Carbon Nanotubes. *Nature* **2009**, *458*, 877–880.
35. Li, J. L.; Kudin, K. N.; McAllister, M. J.; Prud'homme, R. K.; Aksay, I. A.; Car, R. Oxygen-Driven Unzipping of Graphitic Materials. *Phys. Rev. Lett.* **2006**, *96*, 176101(1−4).
36. Xu, Z.; Xue, K. Engineering Graphene by Oxidation: A First-Principles Study. *Nanotechnology* **2010**, *21*, 045704–045707.
37. Aradi, B.; Hourahine, B.; Frauenheim, T. DFTB+, a Sparse Matrix-Based Implementation of the DFTB Method. *J. Phys. Chem. A* **2007**, *111*, 5678–5684.
38. Evans, M. G.; Polanyi, M. Inertia and Driving Force of Chemical Reactions. *Trans. Faraday Soc.* **1938**, *34*, 11–24.
39. Zhang, C.; Bets, K.; Lee, S. S.; Sun, Z.; Mirri, F.; Colvin, V. L.; Yakobson, B. I.; Tour, J. M.; Hauge, R. H. Closed-Edged Graphene Nanoribbons from Large-Diameter Collapsed Nanotubes. *ACS Nano* **2012**, *6*, 6023–6032.
40. DFTB code can be found at http://www.dftb.org.
41. Zheng, G.; Elstner, S. M.; Morokuma, K. Performance of the DFTB Method in Comparison to DFT and Semiempirical Methods for Geometries and Energies of C20−C86 Fullerene Isomers. *Chem. Phys. Lett.* **2005**, *412*, 210–216.
42. Gao, X. F.; Liu, L. L.; Irle, S.; Nagase, S. Carbon Spiral Helix: A Nanoarchitecture Derived from Monovacancy Defects in Graphene. *Angew. Chem., Int. Ed.* **2010**, *49*, 3200–3202.

Supplementary Information

Sequential Electrochemical Unzipping of Single Walled Carbon Nanotubes to Graphene Ribbons Revealed by *in-situ* Raman Spectroscopy and Imaging

Robin John,[&¥] Dhanraj B. Shinde,[$¥] Lili Liu,[‡] Feng Ding,[‡ □] Zhiping Xu,[#]

Cherianath Vijayan,[&] Vijayamohanan K. Pillai,[£*] and Thalappil Pradeep[€*]

[&]Department of Physics, Indian Institute of Technology Madras, Chennai 600 036, India

[$]Physical and Materials Chemistry Division, National Chemical Laboratory, Pune, India

[‡] Beijing Computational Science Research Center, Beijing 100084, Peoples Republic of China

[□]Institute of Textiles and Clothing, Hong Kong Polytechnic University, Kowloon, Hong Kong S. A. R., China

[#]Department of Engineering Mechanics, Tsinghua University, Beijing 100084, Peoples Republic of China

[£]Central Electrochemical Research Institute, Chennai, Karaikudi 630 006, India

[€]DST Unit of Nanoscience and Thematic Unit of Excellence, Department of Chemistry, Indian Institute of Technology Madras, Chennai 600 036, India

[¥]Equally contributing authors

*Email : pradeep@iitm.ac.in & vk.pillai@ncl.res.in

Complete disappearance of RBM from specific sample regions.

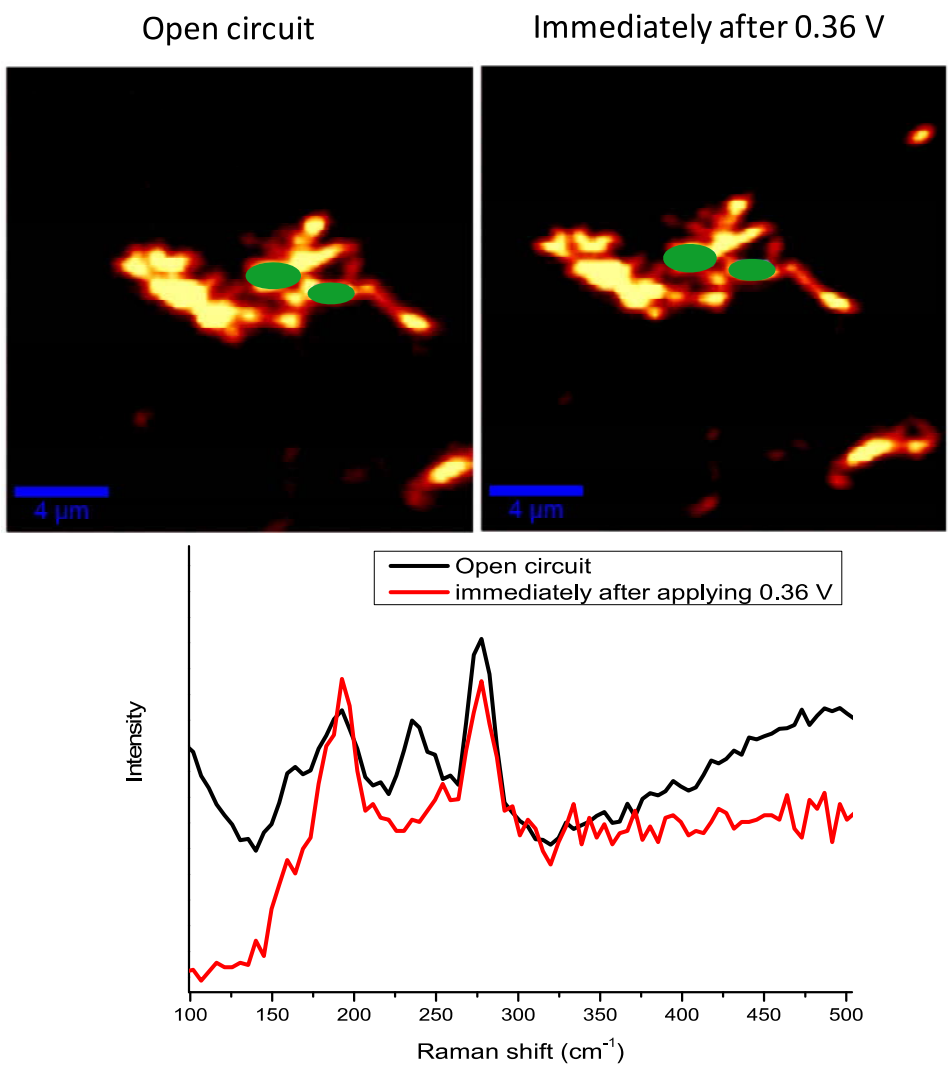

Figure S1. Images showing the bundle at two electrochemical conditions (given at the top of the images) and the RBM spectra corresponding to these conditions from specific sample areas (marked green) show the complete disappearance of RBM II.

Note: It might appear that there is considerable intensity of RBM II for some electrochemical conditions other than open circuit (Figure 2). This is basically due to an averaging effect. Generally, we take spectra from regions where there is an increase in the D band intensity in

order to study the spectral evolution, as presented in Figure 2. It should be noted that the unzipping process need not happen throughout the sample region under study due to the possible inhomogeneity in the local potential. In order to clarify the statement that there is disappearance of RBM II at 0.36 V, we have selected certain specific regions of the sample (marked by green color in the above images) for two electrochemical conditions and averaged spectra from those regions are presented above. It is evident that there is clear disappearance of RBMII.

Variations of the spectral images at the intermittent electrode potentials.

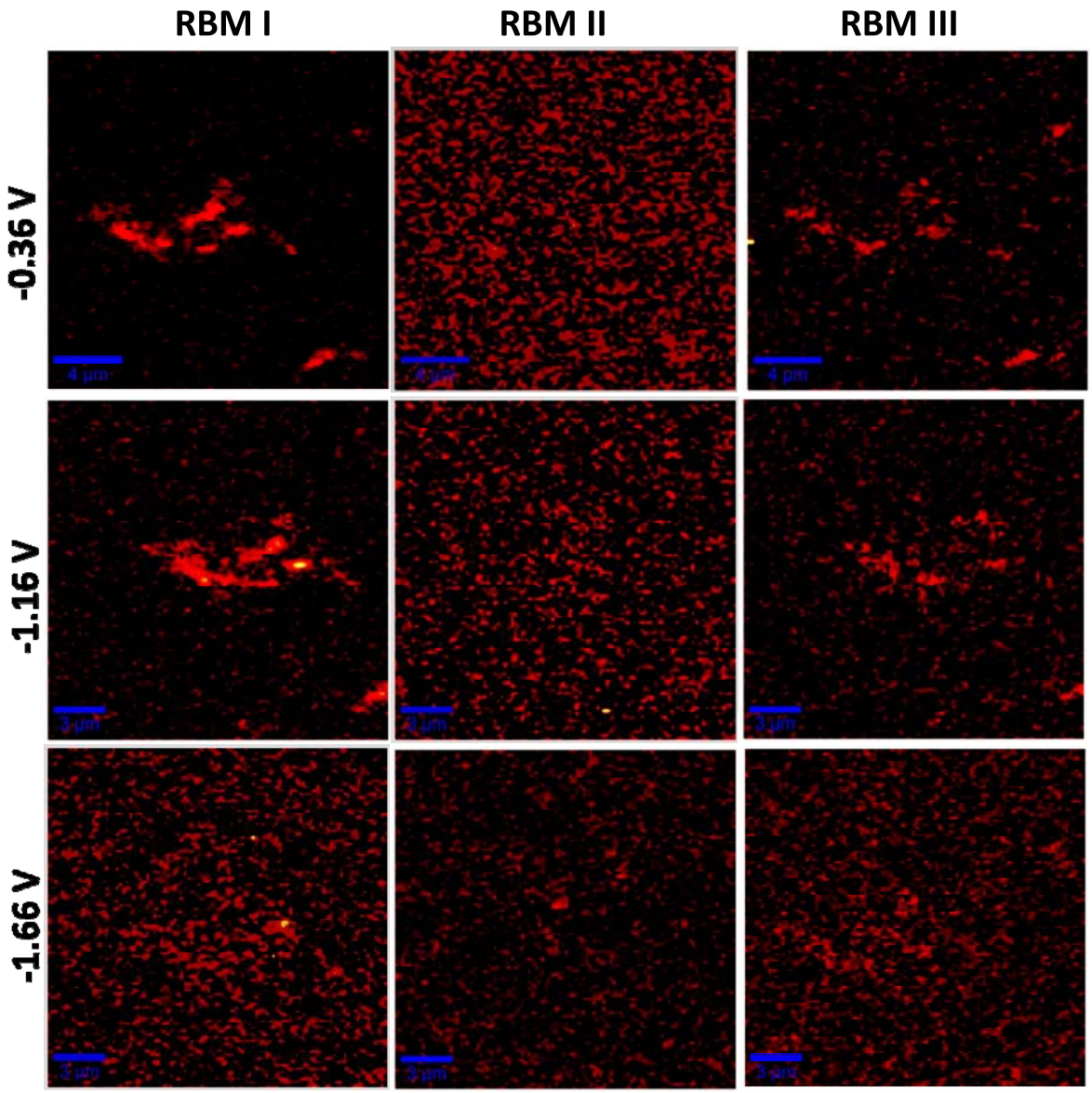

Figure S2. Evolution of RBM for various intermediate reduction steps corresponding to the oxidizing steps given in Figure 2 of the main article. The types of RBMs are being labeled at the top of each column. Each row gives the images of three RBMs at the conditions given at the left of the respective row.

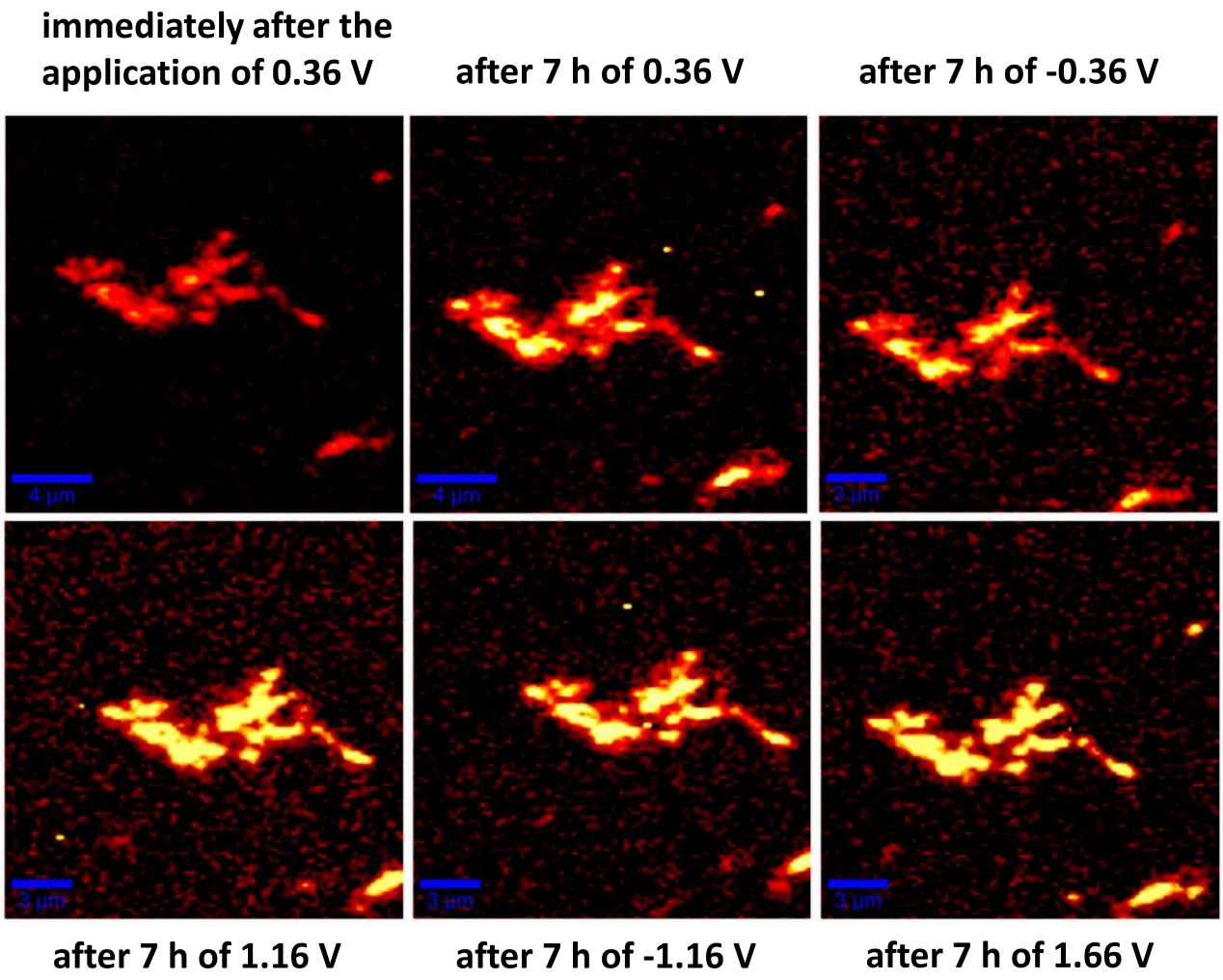

Figure S3. Evolution of the D band for various intermediate potentiostatic conditions such as just after 0.36 V (a), after 7 h of 0.36 V (b), after 7 h of -0.36 V (c), after 7 h of 1.16 V (d), after 7 h of -1.16 V (e), and after 7 h of 1.66 V (f).

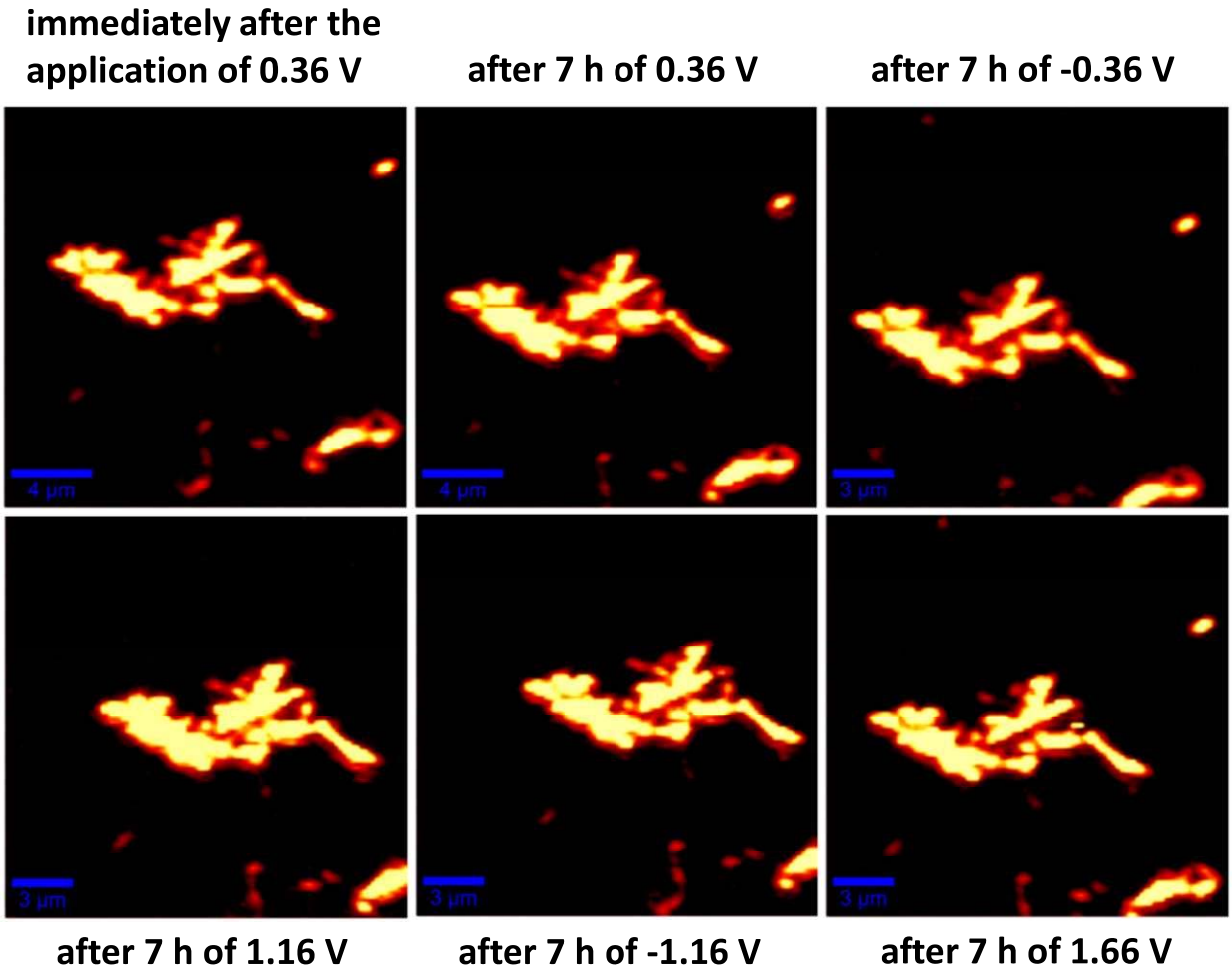

Figure S4. Evolution of the G band for various intermediate potentiostatic conditions such as just after 0.36 V (a), after 7 h of 0.36 V (b), after 7 h of - 0.36 V (c), after 7 h of 1.16 V (d), after 7 h of -1.16 V (e) and after 7 h of 1.66 V (f).

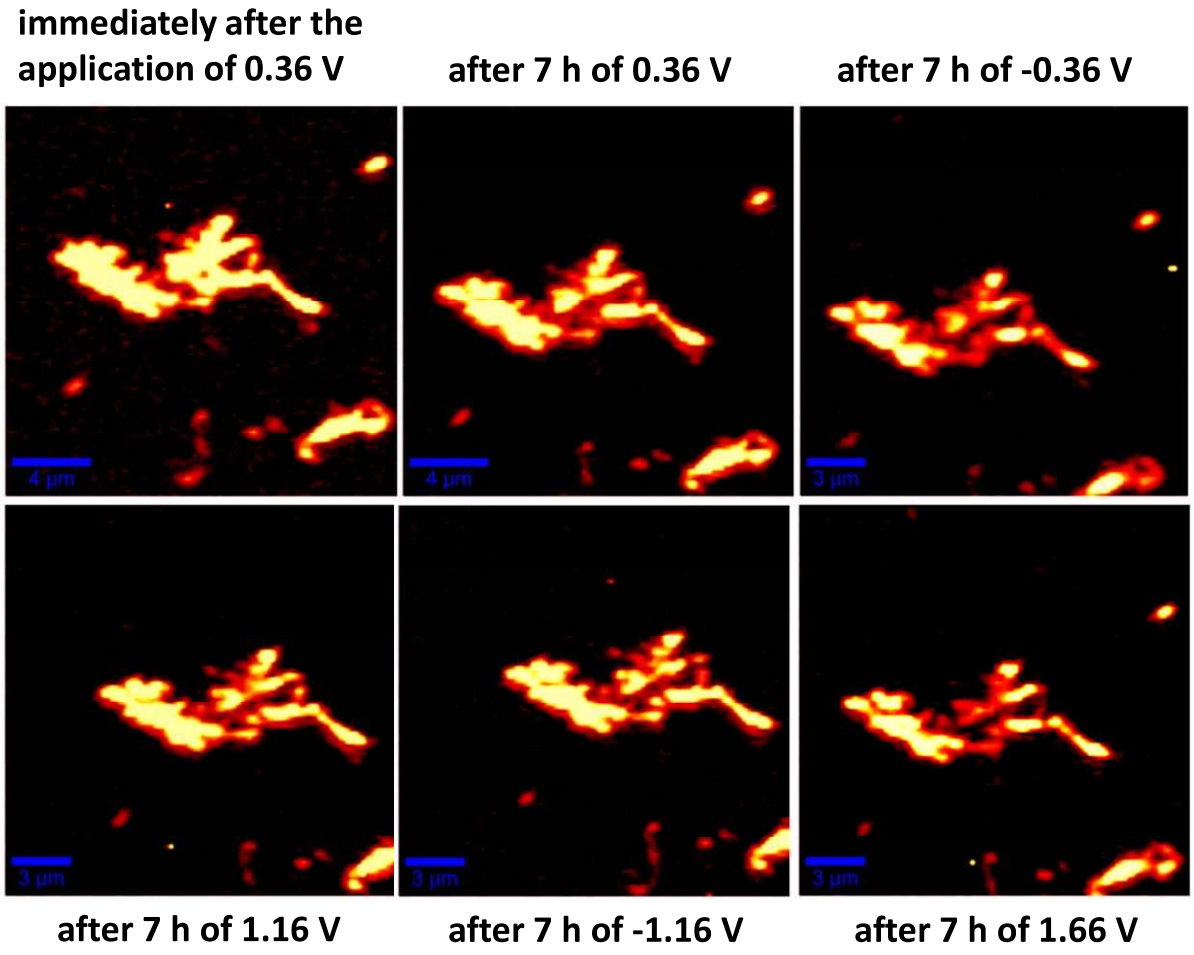

Figure S5. Evolution of the 2D band for various intermediate potentiostatic conditions such as just after 0.36 V (a), after 7 h of 0.36 V (b), after 7 h of - 0.36 V (c), after 7 h of 1.16 V (d), after 7 h of -1.16 V (e) and after 7 h of 1.66 V (f.)

Reproducibility of Raman spectroscopic observations.

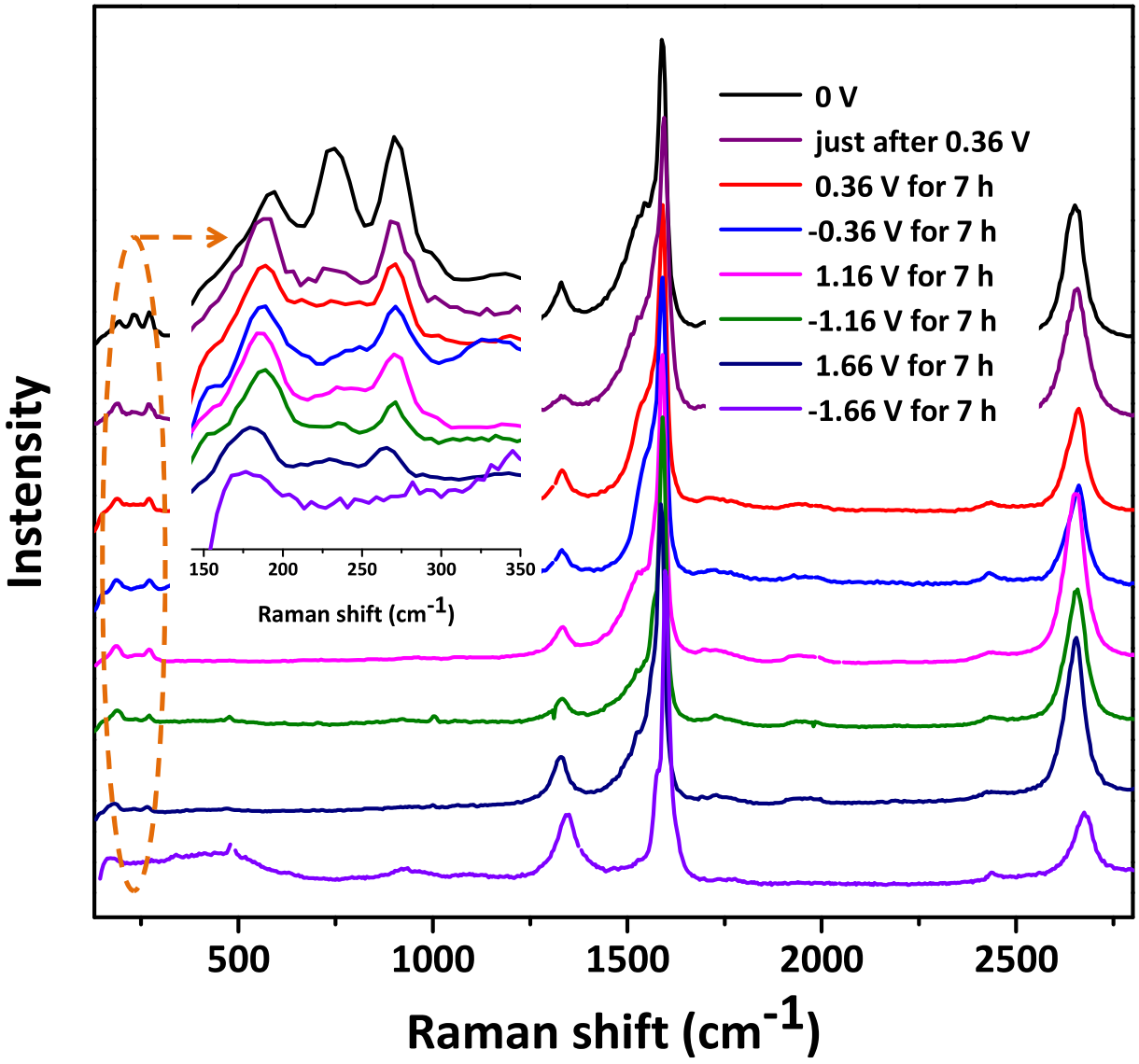

Figure S6. Variation of the different spectral features of a particular SWNT bundle under various electrochemical conditions as labeled in the graph. Inset is showing the variation of the RBM regions showing a response similar to what is described in Figure 2. This set of data also shows a similar kind of response for the variation of the peak structure and width in the G band region. There is also a reduction in the intensity of the 2D band along with a slight decrease in

its width. $I_{RBM\ III}$ / $I_{RBM\ I}$ vary from 1.86 to 0.54 along with an increase in D band intensity. Featureless regions of the spectra are used to place the insets.

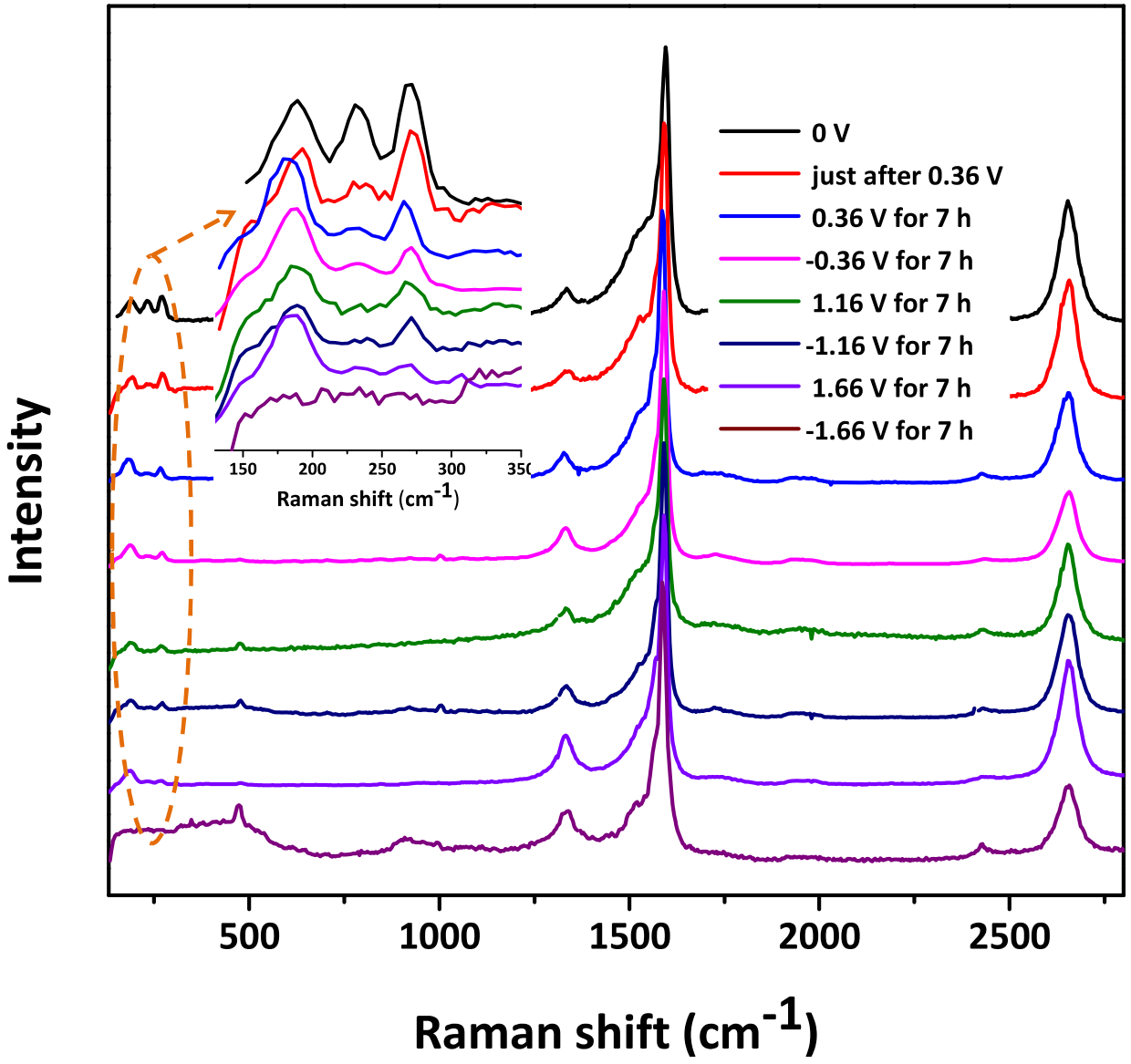

Figure S7. Variation of the different spectral features of another SWNT bundle under various electrochemical conditions as labeled in the graph. Inset is showing the variation of the RBM regions showing a response similar to what is described in Figure 2. A similar kind of response for the variation of the peak structure and width in the G band region was observed in this case

too. $I_{RBM\ III}$ / $I_{RBM\ I}$ vary from 1.26 to 0.25 along with an increase in the D band intensity. Featureless regions of the spectra are used to place the insets.

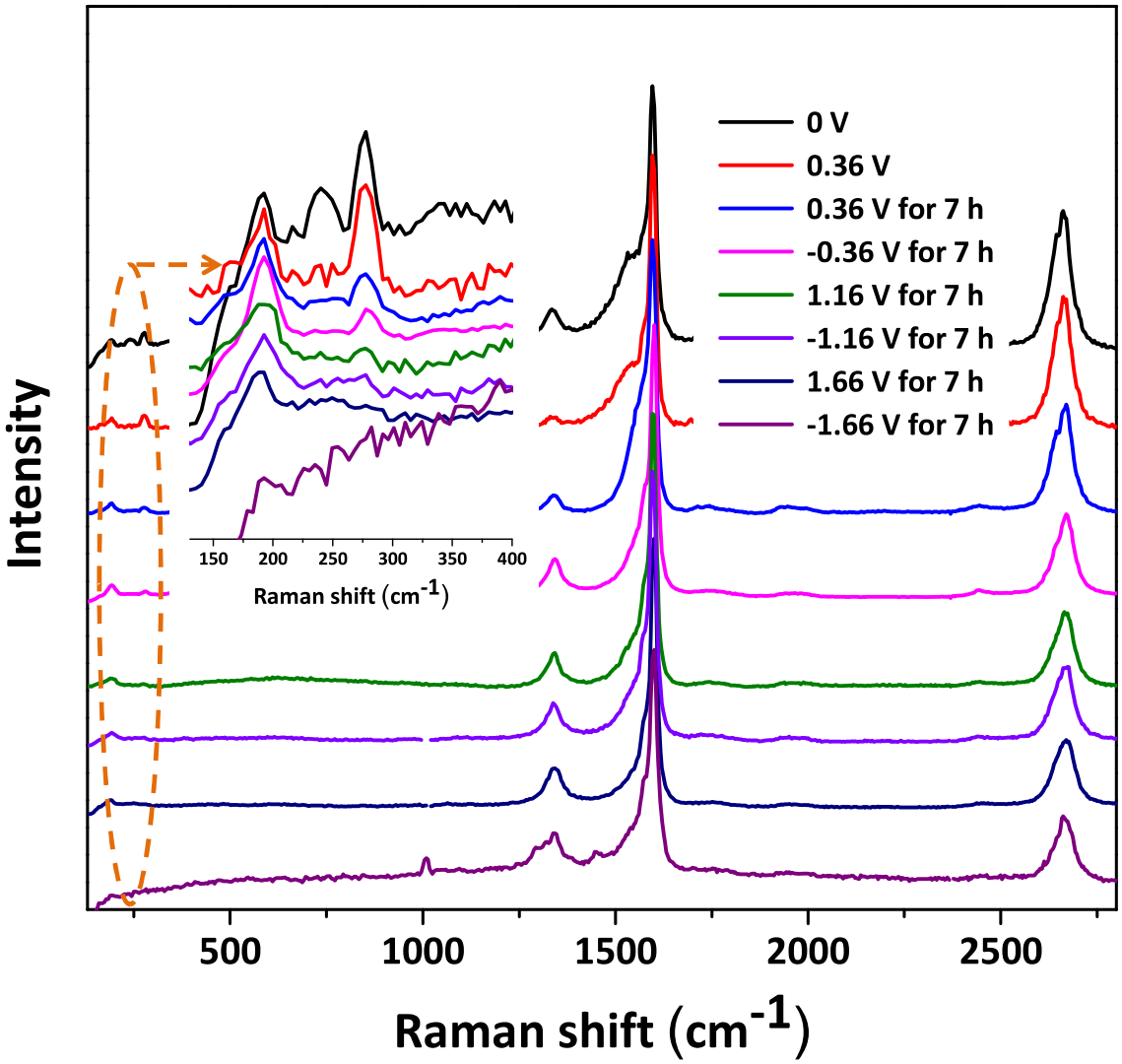

Figure S8. Variation of the different spectral features of another SWNT bundle under various electrochemical conditions as labeled in the graph. Inset is showing the variation of the RBM regions showing a response similar to what is described in Figure 2. This set of data also a similar kind of response for the variation of the peak structure and width in the G band region. $I_{RBM\ III}$ / $I_{RBM\ I}$ vary from 2.5 to 0.19 along with an increase in D band intensity. This along with

Figure S6 and S7 shows the reproducibility of the experimental results presented in the manuscript. Featureless regions of the spectra are used to place the insets.

Transmission electron microscopy to verify the formation of GNRs from SWNTs.

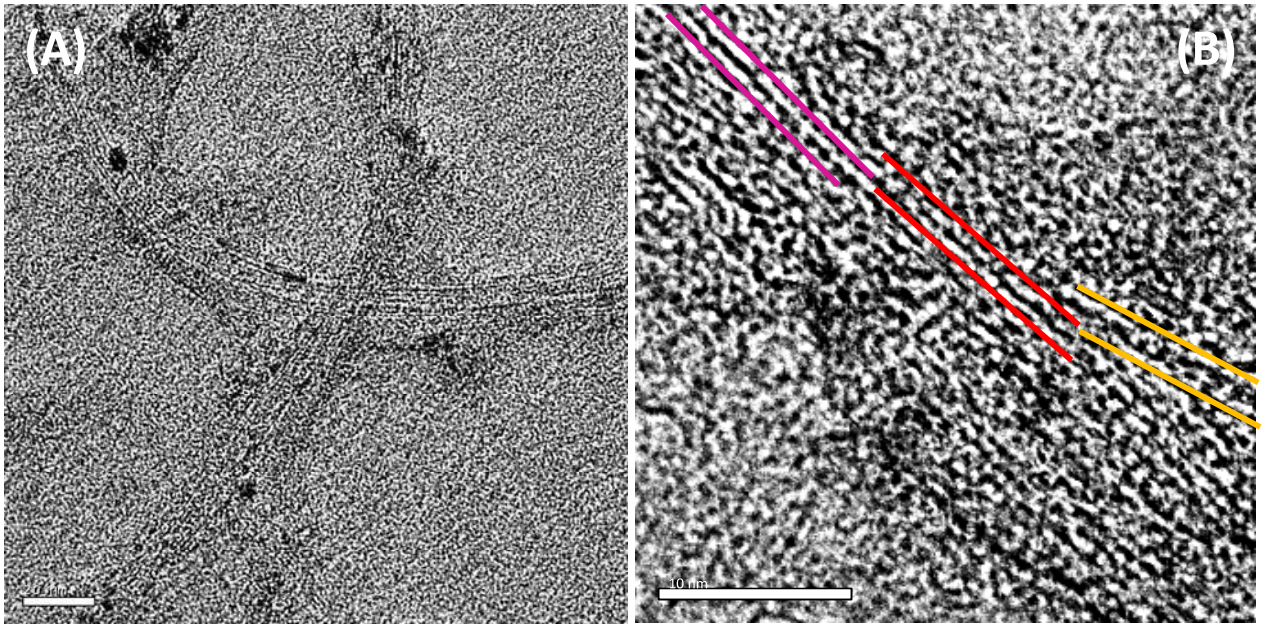

Figure S9. (A) TEM image showing the pristine SWNT bundle (scale bar is 20 nm) and (B) High resolution image of another bundle showing the well defined edges of the SWNTs (scale bar - 10 nm). The guide to eye lines in B with colors magenta, red and dark yellow are placed parallel to the walls of SWNTs with diameters 1.2, 1.0 and 1.6 nm, respectively. The SWNT image of the sample shows the integrity of the bundle.

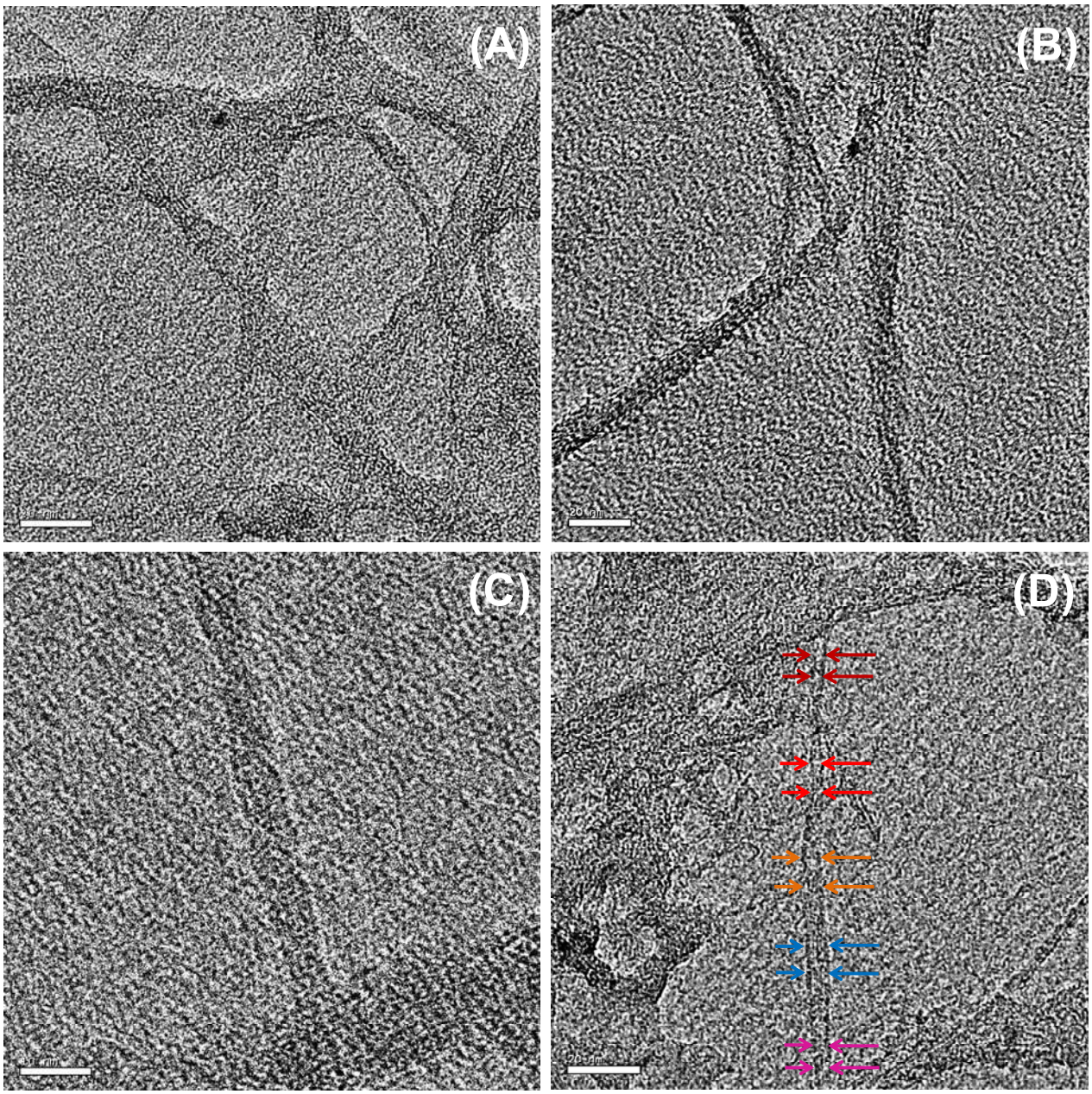

Figure S10. TEM images (A-D) showing unzipped SWNTs as graphene nanoribbons. The scale bar is 20 nm for all figures except for C in which the scale bar is 10 nm. Figure A shows criss-crossed graphene ribbons whereas B shows a twisted ribbon. Both A and B in effect show the separation of the ribbons from the bundle upon unzipping. Figure C shows a single graphene ribbon whose average width is around 6 nm. A closer look at image D reveals that an SWNT (1.4

nm, wine red colored arrows) opens up into a graphene ribbon (5 nm, blue colored arrows). The width is 2.5 nm where the red arrows are present and it is 4 nm where the dark yellow arrows are pointed at. The bottom part of the image shows a narrow ribbon of width 3.5 nm (magenta arrows). Considering the diameters of the SWNTs used, this image represent most likely the partial unzipping of an SWNT and it appears that the unzipping originates at the middle portion (lengthwise) of the side wall rather than at the ends of the nanotubes.

Evolution of the G Band region to show the reduction in metallicity.

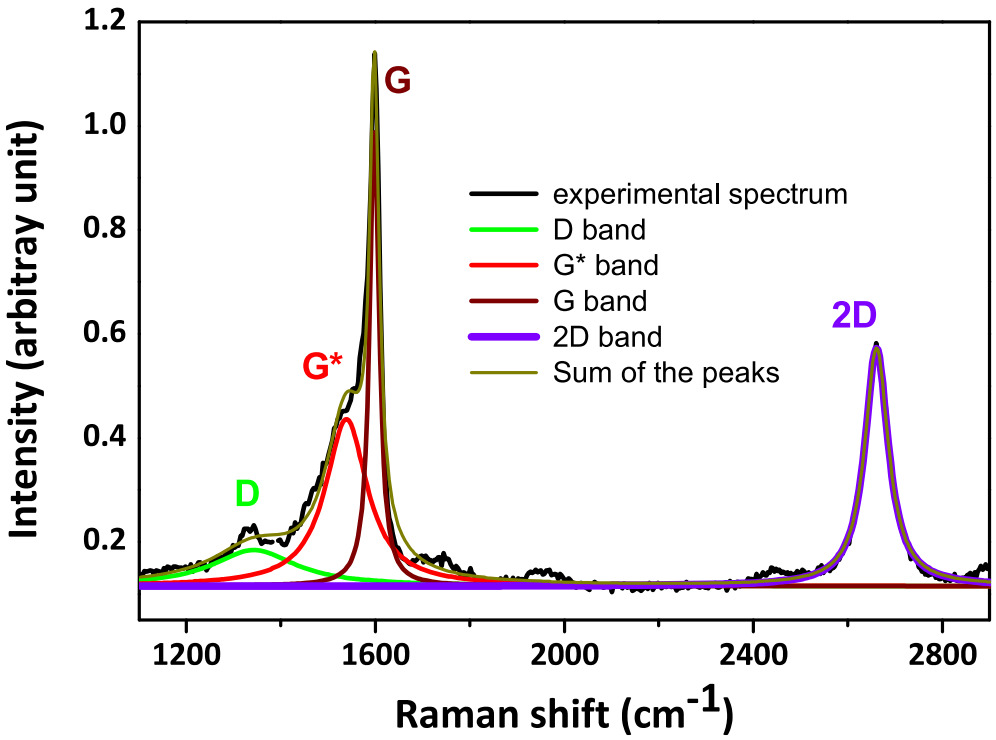

Figure S11. Deconvolution of the Raman spectrum. Raman spectra fitted with 4 Lorentzian peaks, one at D band centered around 1345 cm^{-1}, another 2 peaks at the G band region, out of which the peak at lower Raman shift is denoted G* and the one around 1598 cm^{-1} is the G band itself with the last one being the 2D band. As it was obvious that there will be an increase in the D band intensity, we focused our attention majorly on to the last 3 peaks namely, G*, G and 2D.

Three parameters of each of the component peaks, such as peak position, width and area are evaluated for all 4 sets (Figure 2, S17, S18 and S19) of unzipping data out of which only that of the Raman data in Figure 2 are given below as a table (Table S1). Statistical variations of some of these parameters are given in Figure 5a, S12 and S13.

Table S1. **Deconvolution of the Raman spectra with 3 Lorentzian components.**

Various steps	Electrochemical conditions	Peak position cm^{-1}	Area	Peak width (cm^{-1})	R^2 value	Reduced χ^2 (10^{-4})
1	0 V – open circuit	1551 (G*)	31.8	89.8	0.965	2.54
		1596 (G)	25.5	18.7		
		2659 (2D)	39.1	52.8		
2	Immediately after 0.36 V	1568 (G*)	28.5	50.6	0.970	2.06
		1596 (G)	25.4	18.7		
		2660 (2D)	29.8	53.5		
3	7 h of 0.36 V	1564 (G*)	26.7	67.1	0.962	2.43
		1597 (G)	26.1	18.4		
		2661 (2D)	28.2	49.7		
4	7 h of -0.36 V	1565 (G*)	25.5	68.4	0.968	2.11
		1598 (G)	25.4	18.1		
		2661 (2D)	33.7	50.3		
5	7 h of 1.16 V	1570 (G*)	24.5	63.0	0.959	2.44
		1598 (G)	24.7	17.5		
		2662 (2D)	26.2	49.6		
6	7 h of -1.16 V	1569 (G*)	23.0	61.2	0.959	2.39
		1598 (G)	25.3	17.6		
		2662 (2D)	25.4	49.8		
7	7h of 1.66 V	1576 (G*)	19.4	49.3	0.955	2.44
		1597 (G)	23.4	15.9		
		2663 (2D)	20.7	48.6		
8	7 h of -1.16 V	1578 (G*)	29.9	56.3	0.922	3.82
		1598 (G)	30.2	19.1		
		2662 (2D)	16.2	46.4		

The values of the coefficient of determination (R^2) and the reduced χ^2 are given in the table to assess the quality of the fit. The R^2 values give a better estimate of the quality of the fit as the reduced χ^2 values might get scaled with a scaling of the intensity values (all spectra are

normalized using the G band and translated vertically for clarity). The peak widths given in the table are full width at half maximum (FWHM). The possibility of giving a similar deconvolution data for the RBM region will be improper as the intensity of RBM peaks are generally very less and also because of the lack of proper peak shape owing to the low intensity. Also there can be a confusion arising due to the averaging effect as discussed in Figure S1 and the following text.

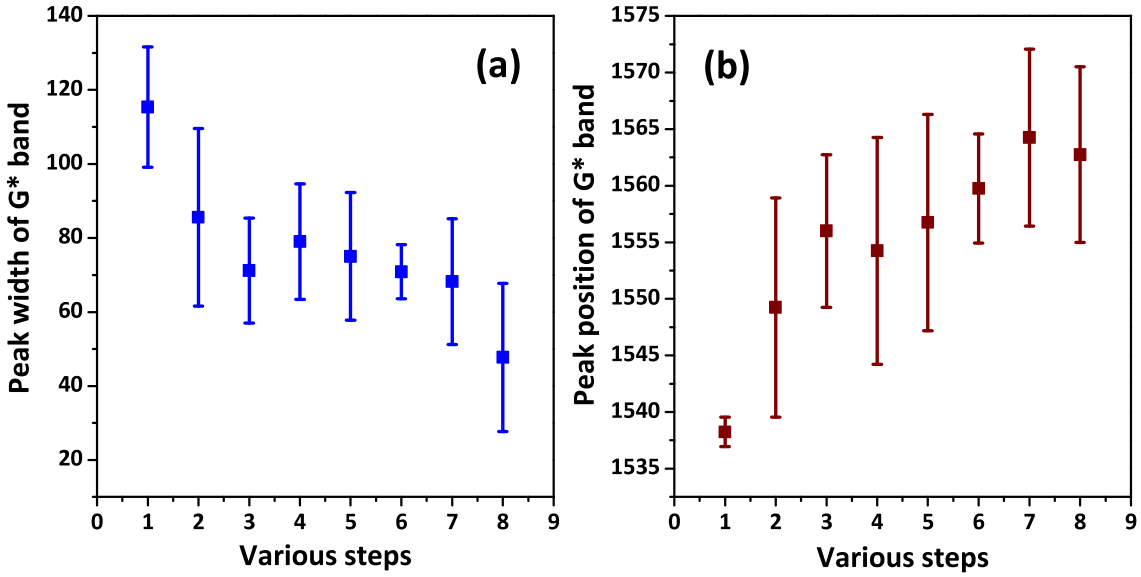

Figure S12. (a) Variation of the average of G* (labeled in Figure S11) band peak width for the successive variations in the electrochemical conditions and (b) Variation of the average position of the G* band. These data were obtained by considering all 4 sets of unzipping data (Figure 2, S6, S7 and S8) and their standard deviation from the mean value is presented as the error bar.

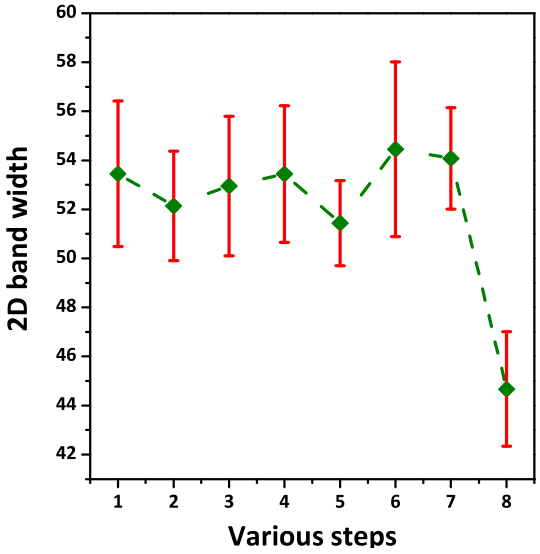

Figure S13. Variation of the width of the Lorentian peak fitted to the 2D band centered at 2660 cm^{-1}. This data was obtained by considering all 4 sets of unzipping data (Figure 2, S6, S7 and S8) and their standard deviation from the mean value is presented as the error bar.

Details of the DFTB calculations.

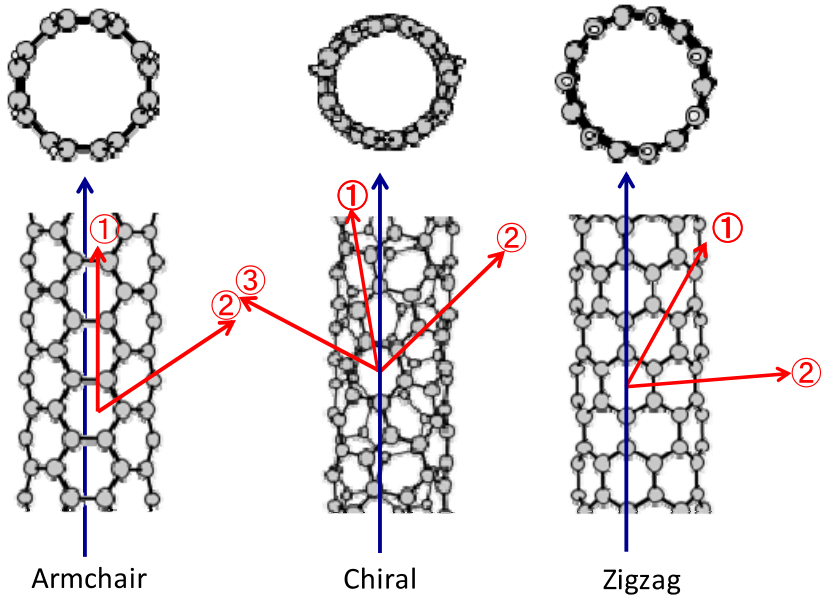

Figure S14. Schematic showing various cutting (oxygen attachment) directions of CNTs with different chiralities. The 1-oxygen and 2-oxygen binding energies were calculated for similar

directions of the SWNTs having chiral indices of interest and presented in the following discussion.

Relation between the oxygen binding energies and reaction barrier of oxidation

In physical chemistry, there is a general rule as the Bell–Evans–Polanyi (BEP) principle,[1-4] which observes that the difference in activation energy between two reactions of the same family is proportional to the difference of their enthalpy of reaction. It indicated that for a series of SWCNTs, the oxidation process happened on the tubes are coincident of the BEP principle. The reaction energy barrier is proportional to the binding energy calculated in this work.

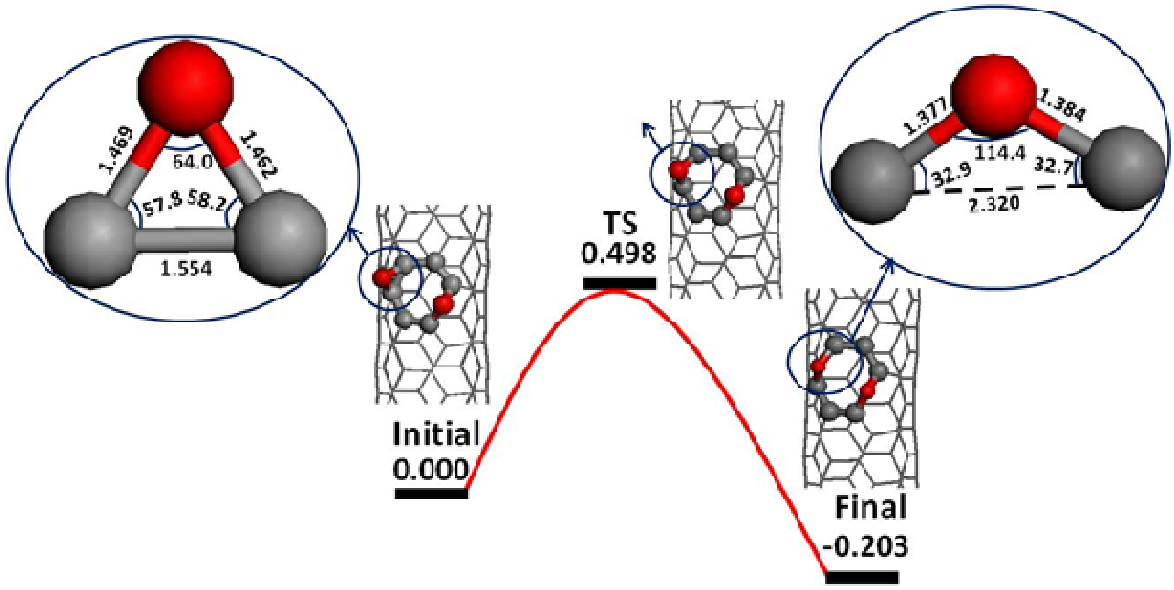

Figure S15. The transition state and barrier (in eV) of the sencond Oxygen adding process in SWCNT (4,4).

To certify the validity of this principle in our system, we performed density functional theory (DFT) based first-principles transition-state calculations for a (4,4) nanotube with oxygen atoms added in different directions. The generalized gradient approximation (GGA) with the Perdew-Burke-Ernzerhof (PBE) functional was used in the calculations.[5] The plane wave basis set with

an energy cutoff of 400 eV was used and the criterion of convergence is set as the force on atom below 0.03 eV/Å. The transition states were searched and their barriers were calculated by the climbing nudged energy band (cNEB) method as implemented in the Vienna Ab initio Software Package (VASP).[6,7] It is found that if the oxygen adding direction (defined by the angle θ along the tube axis) of (4,4) nanotube is 0^o, the transition state does not exist, indicating a spontaneous reaction. However, if $\theta = 60^o$, there is an energy barrier of 0.498 eV (see Figure S15). It turns out that SWNTs with smaller diameters have higher oxygen binding energies and binding oxygen atoms through epoxy groups is preferred. The transition states calculations are consistent with the BEP principle, allowing us to make the abovementioned conclusion with DFTB calculations for the oxygen binding energies.

Table S2. The binding energies and chiralities of the three sets of SWNTs

CNTs(+O)	Singlet (eV)	Quintet (eV)	Binding energy (eV)
(4,4)	-6921.31		
(4,4)-0°-O	-7011.18		5.90
(4,4)-0°-2O	-7101.49		12.23
(4,4)-60°-O	-7009.55		4.27
(4,4)-60°-2O	-7097.03		7.77
(5,2)	-7455.52		
(5,2)-16.1°-O	-7545.43		5.92
(5,2)-16.1°-2O	-7635.81		12.32
(5,2)-52.9°-O	-7543.83		4.33
(5,2)-52.9°-2O	-7632.66		9.18
(5,2)-76.1°-O	-7543.79		4.28
(5,2)-76.1°-2O	-7631.52		8.04
(7,0)		-6710.62	
(7,0)-30°-O		-6799.74	5.14
(7,0)-30°-2O		-6889.64	11.07
(7,0)-90°-O		-6798.84	4.25
((7,0)-90°-2O		-6886.51	7.93
(5,5)	-8667.97		

(5,5)-0°-O	-8757.33		5.38
(5,5)-0°-2O	-8847.40		11.47
(5,5)-60°-O	-8756.01		4.07
(5,5)-60°-2O	-8843.42		7.50
(6,3)	-8078.05		
(6,3)-19.11°-O	-8167.47		5.44
(6,3)-19.11°-2O	-8257.51		11.50
(6,3)-79.11°-O	-8166.00		3.98
(6,3)-79.11°-2O	-8253.46		7.45
(6,3)-139.11°-O	-8166.15		4.12
(6,3)-139.11°-2O	-8253.91		7.90
(9,0)		-8646.05	
(9,0)-30°-O		-8734.33	4.30
(9,0)-30°-2O		-8824.29	10.29
(9,0)-90°-O		-8733.98	3.95
(9,0)-90°-2O		-8821.39	7.39
(6,6)	-10412.23		
(6,6)-0°-O	-10501.24		5.04
(6,6)-0°-2O	-10591.20		11.01
(6,6)-60°-O	-10499.99		3.79
(6,6)-60°-2O	-10577.52		7.36
(7,4)	-11895.93		
(7,4)-21.05°-O	-11985.02		5.11
(7,4)-21.05°-2O	-12074.85		10.96
(7,4)-81.05°-O	-11983.78		3.88
(7,4)-81.05°-2O	-12071.16		7.27
(7,4)-141.05°-O	-11983.91		3.99
(7,4)-141.05°-2O	-12071.52		7.64
(11,0)		-10578.29	
(11,0)-30°-O		-10666.41	4.14
(11,0)-30°-2O		-10756.09	9.84
(11,0)-90°-O		-10666.11	3.84
(11,0)-90-2O		-10753.44	7.19
O	-83.98		

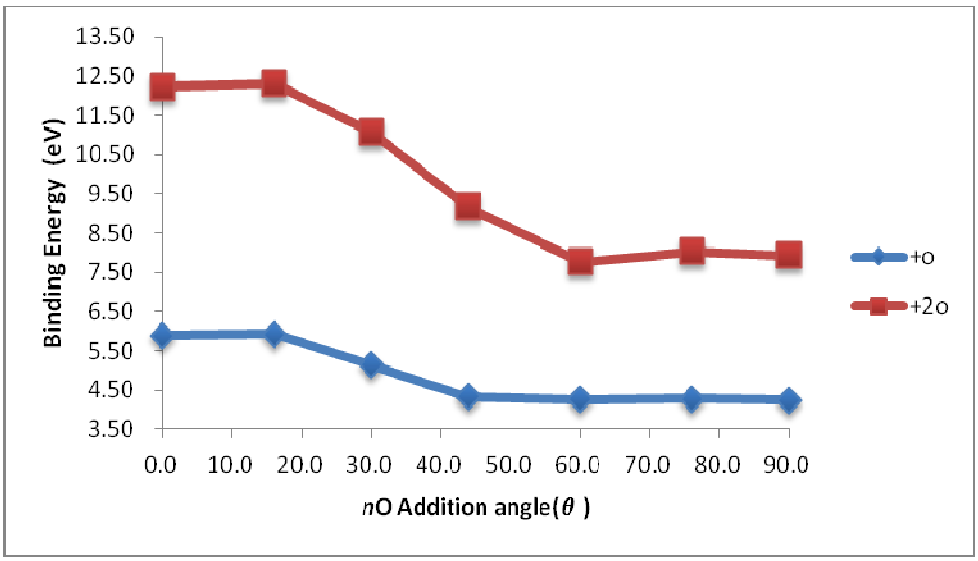

Figure S16. The relationship between the binding energy (E_b) of the CNTs + nO (n = 1, 2) and and the nO addition angle with respect to the tube axis of SWNTs in the first set of calculations. Details are given in Table S2.

Table S3. Details of the DFT calculations for the SWNTs with same chiralities as in the Raman spectroscopic observations.

CNTs	Diameter (nm)	Singlet (eV)	Triplet (eV)	Quintet (eV)	Binding energy (hartree) (eV)	Binding energy (eV)
(9,3)-13.90°-O	0.791		-434.38		-0.16	4.34
(9,3)-46.10°-O			-434.37		-0.15	3.99
(9,3)-73.90°-O			-434.36		-0.14	3.83
(9,3)-13.90°-2O			-437.69		-0.38	10.47
(9,3)-46.10°-2O			-437.59		-0.28	7.73
(9,3)-73.90°-2O			-437.57		-0.26	7.17
(10,1)-4.72°-O	0.829			-416.22	-0.16	4.23
(10,1)-55.28°-O				-416.21	-0.15	4.10
(10,1)-64.72°-O				-416.21	-0.14	3.85

(10,1)-4.72°-2O				-419.52	-0.37	10.14
(10,1)-55.28°-2O				-419.50	-0.35	9.64
(10,1)-64.72°-2O				-419.42	-0.27	7.22
(10,4)-16.10°-O	0.893	-505.36			-0.15	4.21
(10,4)-43.90°-O		-505.35			-0.14	3.91
(10,4)-76.10°-O		-505.35			-0.14	3.77
(10,4)-16.10°-2O		-508.67			-0.37	10.20
(10,4)-43.90°-2O		-508.57			-0.28	7.55
(10,4)-76.10°-2O		-508.56			-0.27	7.08
(12,5)-16.63°-O	1.068	-611.78			-0.15	4.06
(12,5)-43.37°-O		-611.77			-0.14	3.84
(12,5)-76.63°-O		-611.77			-0.14	3.71
(12,5)-16.63°-2O		-615.08			-0.36	9.86
(12,5)-43.37°-2O		-614.99			-0.27	7.42
(12,5)-76.63°-2O		-614.98			-0.26	6.99
(11,7)-22.69°-O	1.074	-692.37			-0.15	4.06
(11,7)-37.31°-O		-692.36			-0.14	3.81
(11,7)-82.69°-O		-692.360			-0.14	3.72
(11,7)-22.69°-2O		-695.67			-0.36	9.90
(11,7)-37.31°-2O		-695.58			-0.27	7.26
(11,7)-82.69°-2O		-695.57			-0.26	7.03

Two sets of results came out of the DFTB calculations as given in the above tables. (i) The *n*O binding energy increses with decrease in SWNT diamater and (ii) as the angle between the cutting direction (*n*O addition) and the tube axis is smaller, the cutting is easier to happen, evidenced by an increase in binding energy.

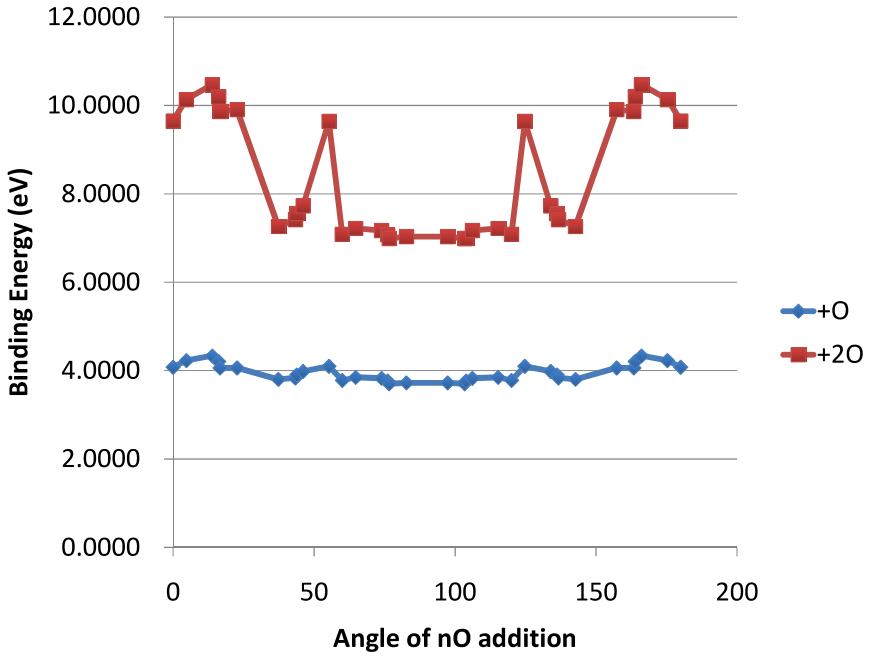

Figure S17. The relationship between the binding energy (Eb) of the CNTs + *n*O (n = 1, 2) and the angle of epoxy addition with respect to the axis of SWNTs used in the Raman experiment.

References

1. Dill, K. A.; Bromberg, S. Molecular Driving Forces, *Garland Science,* New York, **2003**.

2. Bell, R. P. The Theory of Reactions Involving Proton Transfer. *Proc. Roy. Soc. London, Ser. A.* **1936**, *154*, 414-429.

3. Evans, M. G.; Polanyi, M. Some Applications of the Transition State Method to the Calculation of Reaction Velocities, Especially in Solution. *Trans. Faraday Soc.* **1935**, *31*, 875-894.

4. Evans, M. G.; Polanyi, M. Inertia and Driving Force of Chemical Reactions. *Trans. Faraday Soc.* **1938**, *34*, 11-24.

5. Perdew, J. P.; Burke, K.; Ernzerhof, M. Generalized Gradient Approximation Made Simple**.** *Phys. Rev. Lett.* **1996,** *77*, 3865-3868.

6. Kresse, G.; Furthmuller, J. Efficient Iterative Schemes for *ab-initio* Total Energy Calculations Using a Plane-Wave Basis Set. *Phys. Rev. B* **1996**, *54*, 11169-11186.

7. Kresse, G.; Furthmuller, J. Efficiency of *ab-initio* Total Energy Calculations for Metals and Semiconductors Using a Plane-Wave Basis Set. *Comput. Mater. Sci.* **1996**, *6*, 15-50.

Supramolecular Functionalization and Concomitant Enhancement in Properties of Au_{25} Clusters

Ammu Mathew,[†] Ganapati Natarajan,[†] Lauri Lehtovaara,[‡] Hannu Häkkinen,[‡] Ravva Mahesh Kumar,[§] Venkatesan Subramanian,[§] Abdul Jaleel,[⊥] and Thalappil Pradeep[†,*]

[†]DST Unit of Nanoscience (DST UNS) and Thematic Unit of Excellence, Department of Chemistry, Indian Institute of Technology Madras, Chennai 600036, India, [‡]Departments of Chemistry and Physics, Nanoscience Center, University of Jyväskylä, 40014 Jyväskylä, Finland, [§]Chemical Laboratory, CSIR-Central Leather Research Institute, Adyar, Chennai 600020, India, and [⊥]Proteomics Core Facility, Rajiv Gandhi Centre for Biotechnology, Thiruvananthapuram 695014, India

ABSTRACT We present a versatile approach for tuning the surface functionality of an atomically precise 25 atom gold cluster using specific host–guest interactions between β-cyclodextrin (CD) and the ligand anchored on the cluster. The supramolecular interaction between the Au_{25} cluster protected by 4-(*t*-butyl)benzyl mercaptan, labeled $Au_{25}SBB_{18}$, and CD yielding $Au_{25}SBB_{18}\cap CD_n$ (n = 1, 2, 3, and 4) has been probed experimentally using various spectroscopic techniques and was further analyzed by density functional theory calculations and molecular modeling. The viability of our method in modifying the properties of differently functionalized Au_{25} clusters is demonstrated. Besides modifying their optoelectronic properties, the CD moieties present on the cluster surface provide enhanced stability and optical responses which are crucial in view of the potential applications of these systems. Here, the CD molecules act as an umbrella which protects the fragile cluster core from the direct interaction with many destabilizing agents such as metal ions, ligands, and so on. Apart from the inherent biocompatibility of the CD-protected Au clusters, additional capabilities acquired by the supramolecular functionalization make such modified clusters preferred materials for applications, including those in biology.

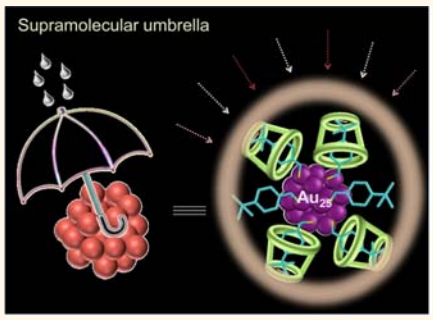

KEYWORDS: supramolecular chemistry · quantum clusters · Au_{25} · cyclodextrin · inclusion complex

Distinct properties of nanomaterials arise from diverse attributes, the most important being size, shape, chemical functionalization, and interparticle organization.[1−3] Interfacing individual nanoparticles with functional supramolecular systems is a fascinating prospect which provides them with new capabilities. In this paper, we introduce a method for such surface modifications in atomically precise gold clusters, which are emerging materials due to their unique optical and catalytic properties.[4−8] They are called by various names such as quantum clusters (QCs), nanomolecules, molecular clusters, superatoms, *etc.* Unique molecule-like absorption (especially that of $Au_{25}SR_{18}$ (SR denotes the surface thiolate ligand)) and photoluminescence properties of QCs are the result of confinement of electronic wavefunctions[4,5,9−11] which can be manipulated by the modification of the ligand environment.[12−15] The physicochemical interactions occurring at the surface of QCs may change the efficiency of radiative recombination, which may ultimately result in the enhancement or quenching of their optical properties. QCs, as tunable nanoscale light sources, have found numerous applications in biology, bioanalytics, and optoelectronics.[16−19] Many of these applications require engineering of their surfaces with functional ligands. Different approaches have been developed to achieve this, such as ligand exchange[7] and subsequent isolation of clusters with precise composition,[20] click chemistry, and so on.[21−25] As a complementary and even more versatile concept, especially for solution-state applications, we introduce the possibility of supramolecular chemistry with QCs, which enables their precise surface functionalization with molecules that can take part in additional events. These surface modifications are important to enable the use of diverse properties of such molecular nanosystems.[26]

Being the most popular supramolecular host molecule, β-cyclodextrin (β-CD), cyclic

* Address correspondence to pradeep@iitm.ac.in.

Received for review May 17, 2013 and accepted December 6, 2013.

Published online 10.1021/nn406219x

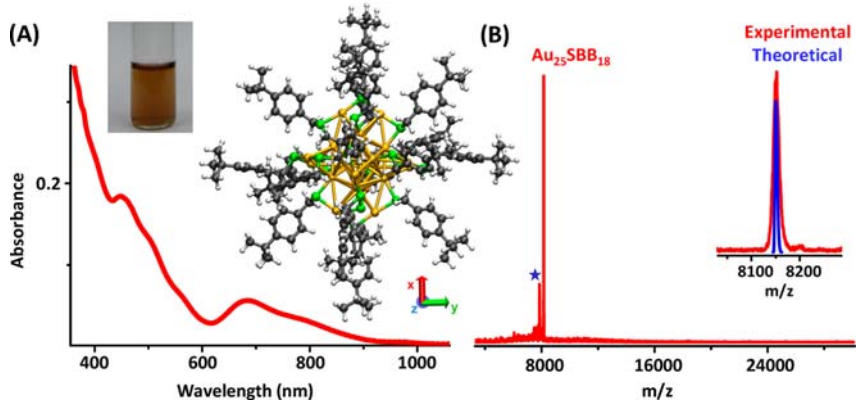

Figure 1. UV−vis absorption spectra (A) and MALDI (L) mass spectra in the positive ion mode (B) of $Au_{25}SBB_{18}$. Inset shows a photograph of the cluster (diluted) in THF. Inset of (A) also shows a visualization of the DFT-optimized structure of $Au_{25}SBB_{18}$. Gold atoms are shown in gold, sulfur atoms in green, carbon atoms in dark gray, and hydrogen atoms in white. The bridging sulfurs lie along Cartesian axis directions. Here, $Au_{25}SBB_{18}$ and its Cartesian axes have been oriented so that the environment around the ligands can be seen clearly. In this particular orientation, the $x-y$ plane is in the plane of the paper as shown by the red and green arrows, and the z-axis is going into the plane of the paper as indicated by the blue arrow. Inset of (B) compares the theoretically calculated and experimentally observed molecular ion peak of the cluster. A fragment of ionization $(Au_{25}SBB_{16}S_2)^+$ is marked by $*$. The peak at m/z 8151 is due to $Au_{25}SBB_{18}$.

oligosaccharide comprising seven α-D-glucopyranose units linked by α(1−4) glycosidic bonds, has molecule-accepting cavities which are specific to hydrophobic guest molecules of suitable size and geometry.[26] In addition to other applications, this feature has been exploited for the design and construction of molecular sensors in which the inclusion of the guest molecule triggers a signal which can be detected.[27,28] Binding of β-CD molecules to various guest-functionalized materials has been utilized for various applications in water purification and biology.[29−31] Owing to the high vulnerability of the 4-(*t*-butyl)benzyl group to form stable host/guest inclusion complexes with β-CD molecules, we synthesized a new 25 atom gold QC protected by 4-(*t*-butyl)benzyl mercaptan (BBSH) and explored its precise surface functionalization with β-CD molecules. The partial inclusion complex formed due to the host−guest interactions between β-CD and SBB ligand anchored on the Au_{25} cluster may be represented as X∩Y, where X and Y are substrate and receptor molecules, respectively, as suggested by Lehn[32] and colleagues.[33] Strong inclusion interactions between the inner cavity of β-CD and ligand molecules on the QC have been probed by various spectroscopic techniques and density functional theory (DFT) calculations. Detailed studies on the stability of the functionalized cluster in the presence of metal ions and ligands have also been performed. As the binding of the substrate to its receptor involves a molecular recognition process, presence of a more competitive guest molecule can effectively tune the host−guest reactivity and alter the supramolecular environment around the cluster, suggesting potential applications in sensing. Beyond enhanced stability and sensing properties, creating such precise CD-functionalized clusters can lead to numerous applications in biology and therapeutics since such materials can be envisaged to develop drug delivery vehicles that can be tracked simultaneously.

RESULTS AND DISCUSSION

There is a strong motivation for making quantum clusters protected with ligands as we wish to use their molecular recognition properties to build supramolecular structures. Here, we synthesized a 25 atom QC of gold with remarkable stability using BBSH as the ligand by following a facile one-pot strategy. BBSH was chosen as the ligand due to its strong tendency to form an inclusion complex with β-CD (binding constant and other data are presented later in the text). The bulkiness of this ligand, while reported to provide higher oxidation resistance to larger Ag clusters (Ag_{140} and $Ag_{\sim 280}$), was also viewed as a challenge for the synthesis of clusters with smaller cores.[34,35] The formation of a well-characterized Au_{25} cluster with BBSH ligand throws light onto the possibility of such smaller core sizes with Ag, too. In view of various reports on the Au_{25} core, protected with other ligands such as GSH and PET,[5,11,36] we present only the relevant characteristics of $Au_{25}SBB_{18}$ in the main text. Most of the other spectroscopic and microscopic data are presented in Supporting Information (SI).

The cluster has well-defined optical and mass spectral features. The optical absorption spectrum (Figure 1A) of the dark brownish solution revealed discrete molecule-like features which are characteristic, and often described, as the fingerprint of Au_{25} QCs.[5,7,37] A key parameter which decides the formation of $Au_{25}SBB_{18}$

is the molar ratio of Au and BBSH, which significantly affects the yield of Au_{25}. While the formation of $Au_{25}SBB_{18}$ required a ratio of 1:6 at an optimized condition, lower thiol ratios resulted in larger clusters which were noticeable from the changes in the optical absorption spectra (see Figure S1 in SI).

The molecular composition of the cluster was confirmed by MALDI (L) MS, where L denotes analysis in the linear mode (Figure 1B). An intact molecular ion peak was observed at *m/z* 8151, which also indicated the purity of the prepared cluster. The experimental spectrum and the theoretical prediction matched perfectly as shown in the inset of Figure 1B. Molecular ion peak was observed in both the positive and the negative ion modes (Figure S2). An additional fragment corresponding to the C−S bond cleavage (marked with an asterisk in Figure 1) was observed. Due to the bulky nature of the ligand, a mass loss of *m/z* 294 corresponding to two BB groups ($-CH_2-C_6H_4-C(CH_3)_3$) from the parent cluster was identified apart from peaks due to the loss of Au_4SBB_4 from the parent ion (see Figure S2), a common phenomenon observed in such Au_{25} clusters.[11,38] A precise control of the threshold laser intensity was crucial to observe the molecular ion peak without fragmentation (Figure S3). A DFT-optimized model of $[Au_{25}SBB_{18}]^-$ is shown in the inset of Figure 1A. While the core and staple motifs are preserved from the $Au_{25}PET_{18}$ case, there are differences in the directions of the SBB ligands when compared to their PET counterparts, and these are attributed to differences in the rotation angles of ligands about their S−C bonds. We note that, in general, the SBB ligands point away from the core, enabling their inclusion into CD. This scenario may be contrasted with that of $Au_{25}PET_{18}$, where the ligands do not point outward from the core,[37] and hence it would be difficult for a CD to form an inclusion complex with it (see later). ESI MS of the cluster (Figure S4) in the negative mode yielded fragments in the low mass region corresponding to $(AuSBB_2)^-$, $(Au_2SBB_3)^-$, $(Au_3SBB_4)^-$, and $(Au_4SBB_5)^-$ due to fragmentation of staples from the cluster surface. The average size of the cluster was <2 nm as confirmed by TEM (Figure S5), and it did not show any electron-beam-induced aggregation, a common phenomenon observed in other Ag and Au clusters. This may be due to the better stability provided by the bulky ligand shell around the cluster. Elemental analysis of the cluster (Figure S6) showed a Au/S ratio of 1:0.73, in agreement with $Au_{25}SBB_{18}$. With the confirmation that the cluster formed is $Au_{25}SBB_{18}$, we move to the construction of the supramolecular adducts.

The 4-(*t*-butyl)benzyl group of the SBB ligand on Au_{25} is an interesting entity as it acts as a recognition site for stable host/guest inclusion complexes with β-CD molecules. Pure and modified CDs have been widely documented to form stable host/guest inclusion complexes with hydrophobic molecules of appropriate size so as to be included in its cavity.[39,40] Such complexes are stable, and the products can be isolated. Several inorganic complexes bearing 4-(*t*-butyl)phenyl groups have been reported to form stable host/guest complexes with β-CD.[41−45] $Au_{25}SBB_{18}\cap CD_n$ (n = 1−4) were made as described in the Experimental Methods section. Initially, the $Au_{25}SBB_{18}$ cluster in THF was mixed with different mole ratios of CD in water and subjected to sonication. Though CD host−guest interactions are known to be most powerful in water, yield of the CD-functionalized cluster analogues (as observed in ESI MS) was poor when the experiment was conducted under conditions of excess water. The tendency of $Au_{25}SBB_{18}$ to aggregate in highly polar medium may prevent the efficient interaction between CD and the guest molecules from forming inclusion complexes in excess water. The CD molecules themselves form tubular assemblies specifically in THF medium,[46] and this formation is facilitated by the presence of small amounts of water.[46,47] This was confirmed from SEM observations (Figure S7). Intermolecular H bonding between the hydroxyl groups on the outer rim of CD molecules, mediated by water, holds them together to form the assembly. Such channel structures of CDs are capable of forming inclusion complexes.[46,47] During the formation of such superstructures, the SBB group present on the cluster may also get entrapped inside the CD cavity. Addition of excess water results in the collapse of CD assemblies releasing the $Au_{25}SBB_{18}\cap CD_n$ adducts.

Cluster-entrapped supramolecular adducts of CD ($Au_{25}SBB_{18}\cap CD_n$, where n = 1−4) can be extracted into the organic layer. Due to the presence of more hydrophobic SBB groups on the cluster surface ($18 - n$, where $n < 4$), the adducts are hydrophobic in nature and allow this preferential extraction into the organic layer. In agreement with this, LDI MS of the aqueous layer showed a broad peak at higher mass range albeit with very low intensity (Figure S8). We noticed that the intensities of MALDI and ESI MS spectra of the CD-incorporated Au_{25} cluster in the crude product (before adding excess water) were weak, whereas a significant enhancement in the adduct intensities was observed in both MALDI and ESI MS after addition of excess water. The purified organic layer, devoid of free CD molecules, was used for subsequent characterization as described in the Experimental Methods section. The hydrophobic interactions between the SBB ligand-protected Au_{25} cluster and β-CD were studied by a combination of absorption, fluorescence, MALDI MS, ESI MS, and NMR spectroscopies.

MALDI MS of the cleaned organic layer was done with linear (MALDI (L)) and reflectron modes (denoted as MALDI (R)) as well as in TOF TOF mode (MALDI TOF TOF). MALDI (L) MS (Figure S9) measurements of the cluster−CD adduct resulted in a broadened mass spectrum. Factors such as ion kinetic energy distribution of the ejected ions as well as their spatial and temporal distributions are strongly influenced by the

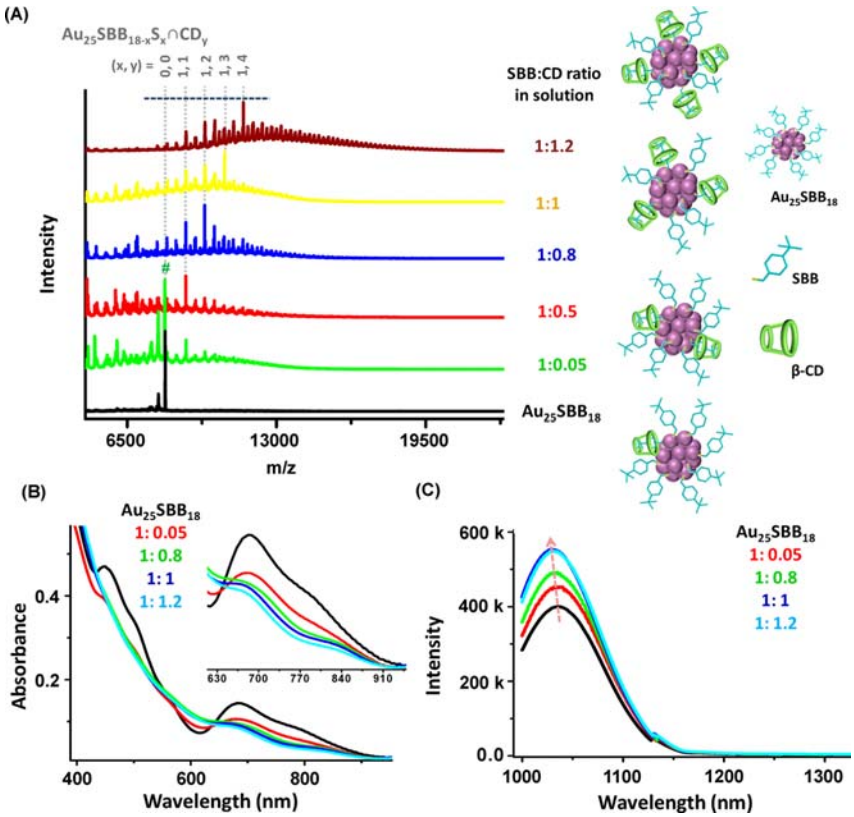

Figure 2. (A) Effect of MALDI TOF TOF mass spectra of $Au_{25}SBB_{18}$ (black trace) with increasing SBB/CD ratio (green to brown trace) in solution. Schematic representations of the cluster with different amounts of CD inclusions are also shown. At 1:0.05, some parent $Au_{25}SBB_{18}$ is also seen, shown with #. UV−vis absorption spectra (B) and luminescence spectra (λ_{ex} 992 nm) (C) of the $Au_{25}SBB_{18}$ cluster with increasing amounts of CD inclusion.

molecular weight, nature of ions, and the matrix,[48,49] which are important in the present case in determining the spectral width. Though the peaks were broad, the peak maximum of samples made with increasing CD concentration in solution shifted toward higher mass numbers, suggesting the complexation of β-CD on the cluster surface. The difference in energy distribution of the ions arising from the desorption ionization event, the possibility of large internal energy distributions of the ejected ions as well as metastable fragmentation due to the presence of flexible supramolecular interactions may be the reason for the significant spread for the ions.[50−53] This spread is evidenced from the fact that the broad distributions in MALDI (L) MS transform to narrow lines over a broad background in the TOF TOF mode with the MALDI (R) MS giving an intermediate distribution. Figure S9 compares the MALDI (L) and MALDI (R) mass spectra.

To confirm this, MALDI TOF TOF mass spectra of mixtures of various SBB/CD ratios were collected wherein better peak resolutions were obtained, as shown in Figure 2A, indicating that improved resolution requires TOF TOF measurements and longer path lengths. The mole ratio of SBB ligand to β-CD in solution for each case is indicated on the figure. Schematic representations of the cluster with various amounts of CD inclusions are also shown in Figure 2. Peak corresponding to the parent $Au_{25}SBB_{18}$ is marked with #. Spectra corresponding to intermediate SBB/CD ratios are shown in Figure S10. Well-defined peaks corresponding to $Au_{25}SBB_{18}\cap CD_n$ (where n = 1−4) were observed under different conditions. The trend observed in CD adduct intensities with an increase in SBB/CD is the same as seen in MALDI MS (Figure S9), confirming that the energy spread of the ions in MALDI MS was the reason for the poor resolution.

As in the case of ligand exchange reactions of clusters,[20,54−56] at each ratio of reactants, one can observe multiple peaks due to the existence of various species in solution. However, formation of certain cluster−adduct combinations is indeed higher than the others depending on the incoming β-CD concentration. While a statistical distribution of species always exists in solution and precise control of the formation of exclusively one adduct is difficult, it is indeed possible to create one particular adduct with a higher proportion than the rest by careful control of the precursor ratios.[57] The relative intensities of individual peaks shown in Figure 2A for each ratio suggest such an effect.

It may be noted that optimum laser fluence (lowest fluence needed to observe ion signals) was used for all

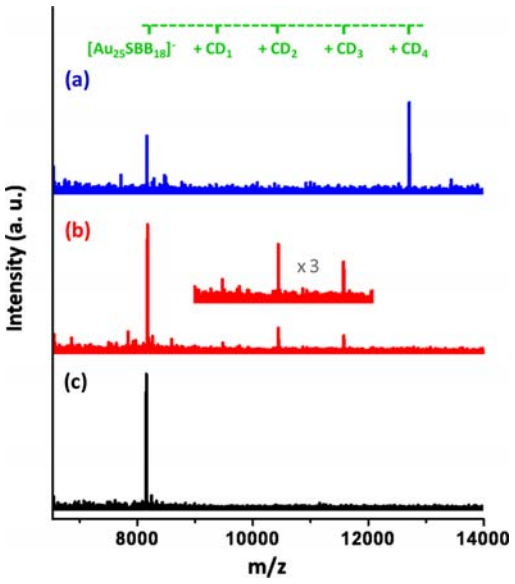

Figure 3. ESI mass spectra in the negative mode for $[Au_{25}SBB_{18}]^-$ and its CD-functionalized analogues collected using a Q TOF (Synapt G2 HDMS, Waters) mass spectrometer (details are in the Instrumentation section). SBB/CD ratios used for the synthesis were 1:1.2, 1:1, and 1:0 for traces a to c, respectively. Part of trace b is expanded to show the features clearly.

the measurements. The dependence of laser fluence on both the MALDI and MALDI TOF TOF mass spectra for $Au_{25}SBB_{18}\cap CD_4$ is shown in Figure S11. It is also important to mention that the MALDI event can cause fragmentation of the adducts and part of the distribution of the lower mass ions may also be due to this. Ion/molecule reactions in the plasma can lead to gas-phase products at higher masses, not originally present in solution. All of these aspects are inherent complications in the spectrum, and therefore, it is important to study the product distribution using other methods.

We conducted extensive ESI MS measurements to understand the existence of various species in solution. Spectrum in the negative mode confirmed the mass assignment mentioned earlier. Figure 3 shows distinct peaks corresponding to various $Au_{25}SBB_{18}\cap CD_n$ (where $n = 2-4$) clusters. Unlike MALDI, matrix interactions and laser-induced fragmentation of the products can be avoided in this case. Although at lower ratios the parent Au_{25} peak was dominant compared to the adducts (for $n = 2$ and 3) and multiple species existed in solution, at a SBB/CD ratio of 1:1.2, greater abundance for $Au_{25}SBB_{18}\cap CD_4$ species was seen. A possible reason could be the geometric stability of the $Au_{25}SBB_{18}\cap CD_4$ cluster adducts in comparison to that of others. From our simulations, the higher stability of these species compared to $Au_{25}SBB_{18}\cap CD_n$ (where $n < 4$) was attributed to the binding of four CDs in tetrahedral locations (explained later) which would minimize inter-CD interactions and thus lower the total energy of the structure. Second, the tight packing of the four CDs on the cluster surface sterically hinders further CD molecules from interacting with its surface, which also enhances its stability. Data presented in Figure 3 suggest the existence of one dominant supramolecular adduct, $Au_{25}SBB_{18}\cap CD_4$ in solution at a SBB/CD ratio of 1:1.2. Further increase in CD concentration in solution did not result in another species, indicating that addition of more CD molecules onto the cluster surface with retention of the Au_{25} core is unlikely. Ligand-induced core etching was seen at larger concentrations of CD as we have reported previously.[58] The bulky nature of the BBS group may sterically hinder an incoming CD group adjacent to it. Careful control over CD concentration was essential to not cause additional effects. Such control is necessary to achieve specific products in the case of clusters, as seen in the case of ligand exchange and core alloying.[20,54−57] UV−vis absorption spectra (Figure 2B) of these samples showed a nominal decrease in intensity of the characteristic absorption features of the cluster, especially the absorption band found at 685 nm. The ~20 nm shift observed in the UV−vis spectra strongly indicates the modification of the molecule.

Au_{25} QCs are known for their luminescence emission in the near-infrared (NIR) region. In order to study the influence of CD encapsulation on the optical property of Au_{25} QC, we analyzed the NIR luminescence of Au_{25} before and after CD functionalization. The bare $Au_{25}SBB_{18}$ cluster showed a luminescence maximum at 1030 nm at room temperature (see Figure S12). Though various excitation wavelengths showed slight changes in the emission maxima, emission at 1030 nm was the most dominant and intense among others. Upon β-CD inclusion, the cluster samples showed a pronounced enhancement in their luminescence intensity (Figure 2C). Enhancement of optical properties in such surface-modified clusters is in accordance with previous reports.[59,60] Upon silica coating of Au_{25}, both absorption and emission intensities are enhanced.[59] In $Au_{23}SG_{18}$, upon phase transfer, due to additional protection of the cluster by the phase transfer agent, the nonradiative decay rate is reduced, enhancing emission.[60] In the present case, this enhanced luminescence remained almost the same even after 2 weeks in ambient conditions, suggesting the enhanced stability of the cluster as a result of complexation with β-CD molecules.

Computational studies were conducted in order to ascertain whether the attachment of cyclodextrin molecules to $Au_{25}SBB_{18}$ is feasible and, if so, their locations and the maximum number of such attachments. Au_{25} consists of a 13 atom icosohedral Au core surrounded by six $-S_{nb}-Au-S_b-Au-S_{nb}-$ staples,[37,61] where S_b denote the six bridging sulfurs and S_{nb} the 12 nonbridging sulfurs. The bridging sulfurs join exterior gold atoms to each other in the staple, while the

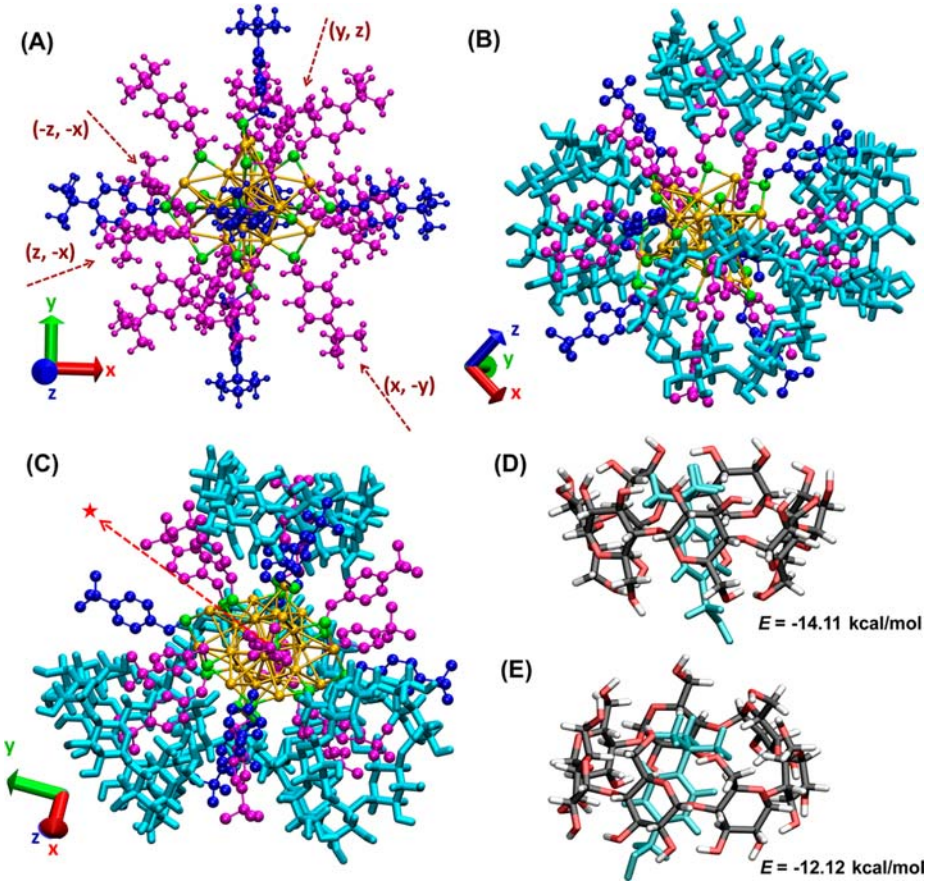

Figure 4. (A) View of DFT-optimized structure of $Au_{25}SBB_{18}$ where the bridging ligands are shown in blue and the nonbridging ligands in magenta. The ligands identified for the attachment of the four CDs are marked by arrows and by the pairs of Cartesian directions marked next to the arrow. The sulfur and gold atoms are colored green and gold, as in Figure 1A inset, and the Cartesian *x*, *y*, and *z* axes are shown by the red, blue, and green arrows. In the front (B) and back (C) views of $Au_{25}SBB_{18}\cap CD_4$, the hydrogen atoms are not shown on the SBB ligands for clarity. The four CD molecules are shown in cyan in the stick molecular representation and are approximately arranged in a tetrahedral shape. The binding energies in kcal/mol for the isolated BBSH∩CD complexes with the *t*-butyl group of BBSH molecule entering (D) the narrow rim and (E) the wider rim of the CD are shown next to the respective configurations. In (D) and (E), for clarity, all the atoms of the BBSH molecule are shown in one color, cyan, while oxygen, carbon, and hydrogen atoms of CD are shown in red, black, and white, respectively.

nonbridging sulfurs connect the core Au atoms to an exterior Au atom. Ligands may be classified as bridging (shown in blue color in Figure 4A) and nonbridging (shown in magenta color in Figure 4A), depending on the type of sulfur they are connected to. While the bridging ligands lie 0.5−0.9 Å farther away from the core, as seen in Figure 4A, and are more easily accessible to CDs in solution, they are fewer than the nonbridging ligands. Due to the six two-fold axes of the icosahedral core,[37,61] we rotated the structure so that the SBB bridging ligands lay along the six Cartesian axes *d*, where *d* stands for $\pm x$, $\pm y$, or $\pm z$. The nonbridging ligands may be associated with a Cartesian plane quadrant or diagonal denoted by the pair (d_1, d_2), where the order of d_1 and d_2 is unimportant and they are perpendicular. This notation may be used to identify ligands uniquely; the bridging ligands are specified by Cartesian directions, while the nonbridging ligands are specified by a pair of perpendicular directions. If one examines the model of $Au_{25}SBB_{18}$, one can see that the bridging ligands appear to be more crowded, as shown in the inset of Figure 1A and Figure 4A, while there is greater space around the nonbridging ligands. We confirmed this by studying the ligand orientations of the 3D model of $Au_{25}SBB_{18}$ (a structure file is provided in XYZ format along with SI). Hence, it would be possible for a CD to make a closer approach and include a greater portion of a nonbridging rather than a bridging ligand. A closer CD position is in better agreement with the NMR data due to the proximity between the aromatic SBB protons and the H^3 and H^5 CD protons.

A model of $Au_{25}SBB_{18}\cap CD_4$ is shown in Figure 4B,C, showing the four CDs in an approximately tetrahedral arrangement attached to nonbridging ligands with their narrow end facing the cluster core. A tetrahedral arrangement would be expected to minimize inter-CD interactions. We also note here that the exclusive use of bridging ligands for CD attachment would impose a perpendicular arrangement rather than tetrahedral.

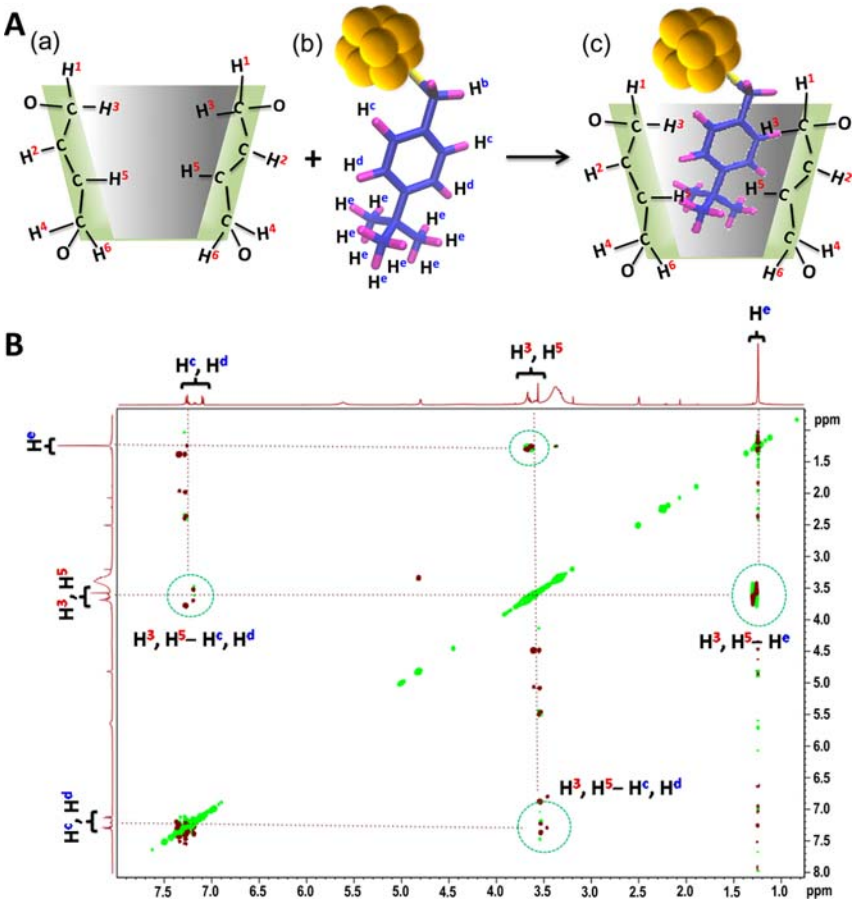

Figure 5. (A) Schematic showing the inclusion complex between SBB ligand on the QC and β-CD (a−c represent CD, $Au_{25}SBB_{18}$, and $Au_{25}SBB_{18}\cap CD_4$, respectively). Different types of protons and their interactions are also marked. (B) Two-dimensional ROESY spectrum showing interaction between the inner cavity protons of CD and SBB ligand, which appear as cross-peaks in the spectrum (marked by circles).

The nonbridging ligands used were denoted by $(-z,-x)$, $(x,-y)$, (y,z), and $(z,-x)$. We remark here that the structure shown in Figure 4B is one possible local minimum and further simulations would be needed to determine the lowest energy structures completely. Structural isomerism is possible as the choice of ligands for CD attachment is non-unique. Full details of the procedure to construct this model may be found in SI 13.

Interestingly, though there are groups of free ligands which are spread over a large space to fit a fifth CD, albeit with tight packing, the specific orientation of free ligands prevents further attachment of another CD. This region of space can be seen in more detail in the back view of the structure shown in Figure 4C (further views are shown in Figure S13). A ligand which appears to have sufficient space around it can be seen at the center of Figure 4C and is marked with a red star. However, it is still too close to the CD at its lower right to enable another CD to be attached to it. This steric hindrance is in striking agreement with the experimental mass spectral results showing four attached CDs as the maximum observed.

Being an efficient tool in CD complexation studies, NMR spectroscopy (especially 2D NMR) can provide information on the details of interaction of β-CD and the SBB ligands of the cluster such as mode of penetration (through narrow rim or through the wide rim of CD) of the guest molecule, extent of guest inclusion in the CD cavity, orientation of the guest molecule inside the cavity, *etc*. Various protons corresponding to the ligands and that of the CD are marked in the schematic shown in Figure 5. Inner protons in β-CD are represented as H^3 and H^5, while the outer protons are marked as H^1, H^2, H^4, and H^6. In the case of the SBB ligand, aromatic protons are named as H^c and H^d, while *t*-butyl protons and the CH_2 protons are represented as H^e and H^b, respectively (see Figure 5A). The ^1H NMR spectrum of the β-CD-encapsulated cluster shows induced chemical shifts for certain protons of β-CD and BBS thiol, which are shown in Figure S14. β-CD protons were shifted further upfield than parent β-CD protons, whereas BBS protons were shifted downfield post-encapsulation. The upfield shift of β-CD cavity protons is attributed to the magnetic anisotropy affects in the β-CD cavity,[62,63] arising due to the inclusion of

a π-electron-rich group (here the aromatic ring of BBS). The formation of the supramolecular complex between β-CD and $Au_{25}SBB_{18}$ cluster was verified by 2D ROESY spectroscopy (Figure 5). This is critical in the study of the interaction between host CDs and guest molecules since protons of both the species are closely located in space after complex formation. The ROESY spectrum of the supramolecular cluster complex shows clear NOE correlations between BBS protons and the protons of β-CD. Aromatic protons of the BBS group (H^c and H^d) show cross-peaks with the inner protons (mainly H^3 and H^5) of β-CD. This confirms the formation of an inclusion complex. Moreover, strong cross-peaks were also observed between the protons of the *t*-butyl group (H^e) with inner cavity protons of β-CD, namely, H^3 and H^5, indicating that they are spatially close to each other. Presence of native as well as complexed *t*-butyl protons was observed in the ^{1}H NMR spectra after complexation (pink and green traces in Figure S14), indicating that all the BBS ligands are not complexed with CD. CH_2 group protons of BBS (H^b) did not show any noticeable cross-peaks with inner H^3 and H^5 protons of CD in the ROESY spectrum. This may be because the penetration of BBS ligand on Au_{25} into the β-CD cavity is not deep enough for the group to interact with inner cavity protons of the latter. The 2D COSY experiments also provide information on the coupling of protons between the two moieties. The cross-peaks corresponding to coupling between H^e, H^c, and H^d protons of the BBS ligand with that of H^3 and H^5 of CD are marked in Figure S15.

The feasibility of encapsulation of BBSH inside the β-CD cavity was further confirmed by the detailed analysis of the inclusion complex prepared by the reaction between β-CD and free BBSH thiol. LDI MS of BBSH∩CD showed the presence of a single sharp peak at *m/z* 1316, which matched well with the theoretical prediction (Figure S16). ESI MS of BBSH∩CD and pure β-CD are compared in Figure S17. Tandem mass spectrometry data with fragmentation products of peaks at *m/z* 1316 and 1338 corresponding to the loss of BBSH (180 Da) from parent BBSH∩CD are also shown in Figure S17. Binding constant for BBSH∩CD was measured using fluorescence spectral titration (Figure S18). ^{1}H NMR and 2D COSY spectrum of BBSH∩CD clearly suggests the complexation between β-CD and BBSH thiol (Figure S19).

In view of getting more insight into the structure of the most stable inclusion complex, DFT calculations were performed on isolated BBSH∩CD supramolecular adducts. These calculations predict the existence of two different possibilities of encapsulation of BBSH ligand in the β-CD cavity in solution, that is, either through the wide rim (Figure 4E) or through its narrow rim (Figure 4D). The inclusion complex resulting from the entry of BBSH through the narrow end was more stable by 1.99 kcal/mol than that through the wide rim. However, from the ^{1}H NMR data (see Figure S19), we could not precisely determine the chemical shift for the inner and outer protons of CD after complexation since they appeared as broad and diffused peaks. This could be due to the existence of different types of SBB ligands on the cluster surface, namely, the included ones and the unincluded ones on a given cluster (see Figure S14). The former being in two forms (narrow and wider rim entry). Thus, though complexation of CD on Au_{25} was confirmed, the direction of the inclusion was not clearly assignable using NMR data. Such difficulties have been reported previously.[64]

In order to study the specificity of β-CD in forming a supramolecular complex with BBSH-protected QC, we extended our study to a different QC system of the same core size (Au_{25}) but having PET as the protecting ligand (see Experimental Methods section for details). $Au_{25}PET_{18}$ was chosen as it is a well-studied and characterized system.[37,61,65,66] Unlike the SBB ligand which readily forms the inclusion complex, $Au_{25}PET_{18}$ did not show such an effect (black trace in Figure 6) upon treatment with similar concentrations of β-CD. The spectrum of a $Au_{25}PET_{18}$ + CD mixture shows only a peak due to free $Au_{25}PET_{18}$ at *m/z* 7391. This matches with the theoretical prediction that formation of an inclusion complex on PET-protected Au_{25} may not be facile due to specific orientation of the ligands as noted earlier. This specificity in complexation of the β-CD cavity for certain ligands was exploited subsequently. A complementary protocol for the incorporation of β-CD on such clusters would be the replacement of "ligand 1" (PET) with "ligand 2" (BBSH∩CD) on $Au_{25}PET_{18}$. This was achieved by following a simple ligand exchange route. For this, initially the BBSH∩CD complex was prepared (treated as ligand 2) which was subsequently allowed to react with the $Au_{25}PET_{18}$ cluster. This resulted in replacement of three PET ligands by BBSH∩CD (existing as Na adducts, denoted as SBB∩CD-Na as CD-Na interaction is strong) on the QC, which was evident from the MALDI MS data (Figure 6). The well-defined peak in the positive ion mode found at *m/z* 10990 corresponds to the ligand-exchanged product, $Au_{25}PET_{15}(SBB∩CD\text{-}Na)_3$. Loss of the $CH_2-CH_2-C_6H_5$ group from the ligand, PET, due to C−S cleavage leading to $Au_{25}PET_{14}S_1(SBB∩CD\text{-}Na)_3$ at *m/z* 10884 was also observed. Also, peaks due to the loss of BB∩CD-Na and $CH_2-CH_2-C_6H_5$ fragments from the cluster leading to $Au_{25}PET_{14}S_2(SBB∩CD\text{-}Na)_2$ and $Au_{25}PET_{13}S_3(SBB∩CD\text{-}Na)_2$ were also identified (marked with red and green stars (*), respectively, in Figure 6). The mass spectrum was in complete agreement with the expected values (see inset of Figure 6). Peaks marked "a" and "b" in the spectrum correspond to the loss of AuL (L = PET) from $Au_{25}PET_{15}(SBB∩CD\text{-}Na)_3$ and $Au_{25}PET_{14}S_2(SBB∩CD\text{-}Na)_2$, respectively. Replacement of PET with a CD-containing ligand did not affect optical absorption spectra of the clusters

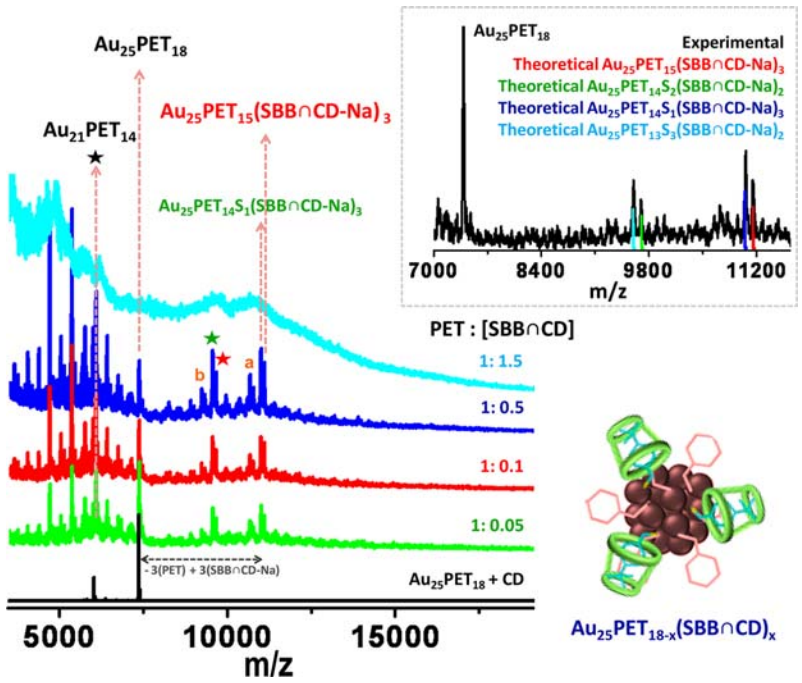

Figure 6. Positive ion MALDI mass spectra showing the effect of addition of β-CD (black trace) and increasing amounts of BBSH∩CD (green to cyan trace) to $Au_{25}PET_{18}$. Inset shows the experimental and theoretical match between the predicted values. Ligand-exchanged products are marked in the spectra, and a schematic of the same is also shown. Fragments from the parent cluster are marked with a star.

significantly (Figure S20) and showed an enhancement of luminescence intensity of the cluster. Note that it is important to exercise careful control over the ratio of PET/SBB∩CD during ligand exchange reactions as evident from the traces, green to cyan in Figure 6. The amount of incoming ligand, SBB∩CD, was deliberately kept low to enable minimal exchange. However, three ligand substitution seems to be the most favored among others.

Surface engineering of QCs by supramolecular chemistry brought many added advantages to the QCs. The instability of QCs, particularly in the presence of certain metal ions, is a major issue in terms of utilizing such materials for commercial applications. Metal-ion-induced quenching of cluster luminescence is a commonly observed phenomenon in most QCs.[36,67−69] While being an efficient metal ion sensor, its application capabilities toward sensing other analytes of interest are limited due to this aspect, especially in complex environments containing multitudes of cations. Interaction with metal ions can also result in irreversible damage to the cluster and also can cause its decomposition.[70,71] Incorporation of CDs on cluster systems has advantages such as increased stability due to lack of accessibility to the core by incoming metal ions and ligands. The stability of $Au_{25}SBB_{18}$∩CD_4 over the parent cluster was monitored by their reactivity toward metal ion (Cu^{2+}) and other ligands. Cu^{2+} ions react readily with noble metal QCs.[69,72] Here, $Au_{25}SBB_{18}$ and its CD-functionalized analogue, $Au_{25}SBB_{18}$∩CD_4, were treated with varying amounts of Cu^{2+} ions (see SI 21 for details), and its effect on cluster luminescence was studied. Though luminescence intensities of both $Au_{25}SBB_{18}$ and its CD-protected analogue were quenched with the addition of Cu^{2+} ions, the extent of quenching observed in $Au_{25}SBB_{18}$∩CD_4 was less than that in bare $Au_{25}SBB_{18}$ upon treatment with identical concentrations of Cu^{2+} ions (Figure S21). This may be due to the reduced accessibility of the metal ions to the Au_{25} core owing to the bulky nature of the CD species on the cluster surface. Exposure of the CD-protected cluster ($Au_{25}SBB_{18}$∩CD_4) to lower amounts of Cu^{2+} ions (0.05 mL, 250 mM) showed only 30% quenching in its luminescence, whereas $Au_{25}SBB_{18}$ showed 70% quenching. However, with higher amounts of Cu^{2+} ions, the difference in % quenching observed in both cases showed an exponential decrease. This could be due to the effective penetration of the metal ions, owing to their small size, through the protective CD shell around the cluster core. Direct interaction of CD with metal ions, though possible, is unlikely in this case as such interaction requires a highly alkaline medium (pH >12).[73]

The stability of β-CD-functionalized QCs toward ligand exchange reactions was studied by treating such species with excess ligand of another thiol (thiol-2). This was thought to be another important way to see the difference in core accessibility. $Au_{25}PET_{18}$ was chosen for this study as it gave better mass spectrum compared to $Au_{25}SBB_{18}$ systems, post-complexation. Both bare $Au_{25}PET_{18}$ and $Au_{25}PET_{15}$-$(SBB∩CD\text{-}Na)_3$ were treated with excess amounts of thiol-2, in this case free BBSH, and the mass spectrum

was recorded (see Figure S22). In the case of $Au_{25}PET_{18}$, the PET ligands were easily replaced by BBS thiols to give ligand-exchanged products with varying amounts of mixed ligand-protected clusters. But for $Au_{25}PET_{15}(SBB\cap CD\text{-}Na)_3$, the mass spectra showed no shift toward the higher mass region, indicating that ligand exchange was not facile in such systems compared to the bare species. Also, though the CD-functionalized entities were unaffected by BBSH, free $Au_{25}PET_{18}$, which was also present in the solution, showed complete ligand exchange to form $Au_{25}SBB_{18}$ *in situ* (marked on the graph).

Yet another interesting aspect of CDs is their capability in sensing molecules. Competitive guests can replace the existing guests from the CD cavity, and therefore, this can be used in sensing such molecules. An example is provided by 1-adamantanethiol (AdT). Inclusion complexes of CD with adamantyl groups are well-known,[31,74,75] and such products are stable. Many such exchanges of CD guests with adamantyl groups have been reported previously. Both $Au_{25}SBB_{18}$ and $Au_{25}SBB_{18}\cap CD_4$ were treated with the same amount of AdT (Figure S23). Quenching of luminescence was observed in both cases, but in $Au_{25}SBB_{18}$, although an initial decrease in luminescence intensity was noted, probably due to dilution effect/slight ligand exchange, further exposure to AdT did not seem to have an effect on the cluster luminescence. Addition of similar amounts of AdT on $Au_{25}SBB_{18}\cap CD_4$ resulted in substantial reduction of its luminescence intensity (red data points in Figure S23). This effect may be attributed to the fact that, as AdT is a better "guest" for CD than BBS, effective removal of CD from the BBS ligand on the Au_{25} leads to the drastic quenching of luminescence (note that formation of $Au_{25}SBB_{18}\cap CD_4$ resulted in enhanced luminescence). UV optical absorption spectra collected from the samples also gave supporting evidence. While no drastic change was observed upon addition of AdT to bare $Au_{25}SBB_{18}$ clusters, AdT addition to $Au_{25}SBB_{18}\cap CD_4$ indicated gradual evolution of spectral features corresponding to the formation of free $Au_{25}SBB_{18}$ in the solution (green trace in Figure S23D). This reappearance of the Au_{25} cluster features in UV spectra could be due to complex formation between the competitive guest AdT and CD, AdT∩CD, thereby the BBS ligand becomes free on Au_{25} QCs.

CONCLUSION

In summary, we demonstrated surface functionalization of the Au_{25} clusters based on specific host–guest interactions between β-CD and (*t*-butyl)benzyl groups of $Au_{25}SBB_{18}$, which imparts new properties to the clusters. A detailed spectroscopic evaluation of the interactions between the QC and β-CD was conducted. More detailed understanding of the formation of an inclusion complex on the QC surface and a possible structure of $Au_{25}SBB_{18}\cap CD_4$ were provided by DFT calculations and molecular modeling. The observed experimental results were in accordance with the theoretical predictions. The viability of this method in modifying the surface characteristics of differently functionalized QCs has also been demonstrated. Unusual stability and optical properties of CD-functionalized QCs over bare clusters were observed. Our study opens up new possibilities of supramolecular surface-engineered QCs which could overcome some of the limitations of native QCs for potential applications.

EXPERIMENTAL METHODS

Materials. Tetrachloroauric(III) acid ($HAuCl_4\cdot 3H_2O$) and methanol were purchased from SRL Chemical Co. Ltd., India. 4-(*t*-Butyl)benzyl mercaptan $(CH_3)_3C-C_6H_4-CH_2SH$ (BBSH), 2-phenylethanethiol $C_6H_5-CH_2-CH_2SH$ (PET), 1-adamantanethiol (AdT), and sodium borohydride ($NaBH_4$) were purchased from Sigma Aldrich. β-CD was purchased from Wako Chemicals, Japan. Tetrahydrofuran was purchased from Rankem, India. All chemicals were of analytical grade and were used without further purification. Glassware was cleaned thoroughly with aqua regia (HCl/HNO_3, 3:1 vol %), rinsed with distilled water, and dried in an oven prior to use. Triply distilled water was used throughout the experiments.

Synthesis of $Au_{25}SBB_{18}$. $Au_{25}SBB_{18}$ was synthesized using a modified procedure of Jin *et al.* used to prepared $Au_{25}PET_{18}$.[76] In a typical synthesis, 10 mL of $HAuCl_4\cdot 3H_2O$ (14.5 mM in THF) was added to 15 mL of BBSH thiol (89.2 mM in THF) while stirring it at 400 rpm at room temperature (29 °C) in a round-bottom flask. The solution becomes colorless after 15 min, indicating the formation of the Au(I) thiolates. An aqueous solution of 2.5 mL of $NaBH_4$ (0.4 M) was added rapidly to the reaction mixture under vigorous stirring (1100 rpm), and the solution turned from colorless to black, indicating the formation of clusters. The reaction was allowed to proceed with constant stirring for 3 h under ambient conditions and then for 3 h at 45 °C. The crude solution thus obtained had a dark brownish color and showed characteristic UV absorption features of Au_{25} clusters even without any purification. The solution was left overnight to yield monodisperse species. Solvent was removed under vacuum, and the cluster was first washed with water and later precipitated with methanol. The precipitate ($Au_{25}SBB_{18}$) was collected after washing repeatedly with methanol and was dried. For the $Au_{25}PET_{18}$ cluster, the same protocol was followed with the addition of 15 mL of PET (114 mM in THF) instead of BBSH, maintaining other parameters the same.

Synthesis and Reactivity of $Au_{25}SBB_{18}\cap$CD Systems. Approximately 3 mg of purified $Au_{25}SBB_{18}$ was dissolved in 3 mL of THF, and 0.1 mL of β-CD solution (in water) of appropriate concentration was added, such that specific SBB/β-CD ratio was maintained in the solution (1:0.5, 1:0.8, 1:1, and 1:1.2 for $Au_{25}SBB_{18}\cap CD_n$, where $n = 1-4$, respectively). The mixture was carefully sonicated for about 10 min at room temperature. The reaction was allowed to proceed under constant stirring (400 rpm) for 30 min at room temperature with intermittent sonication for 1 min at every 10 min intervals. After the reaction, the CD-encapsulated clusters were recovered by the addition of excess water, which resulted in the separation of two layers. The deep brown upper layer (organic) was collected and washed with water to remove unbound CD which dissolves in it. Note that free BBSH in the cluster solution that forms an inclusion complex with CD (denoted as BBSH∩CD) will also be removed in this process as it becomes hydrophilic due to CD encapsulation.

Due to the presence of a greater number of hydrophobic BBS groups (in comparison to the BBSH∩CD moieties), CD-functionalized Au_{25} QCs (denoted as $Au_{25}SBB_{18}$∩CD) remained in the organic layer and were used for further studies. SBB/β-CD mole ratio of 1:1.2, corresponding to $Au_{25}SBB_{18}$∩CD_4, was used for detailed experiments unless otherwise mentioned. For sensing experiments with AdT, 1 mg/mL of both the naked and CD-functionalized $Au_{25}SBB_{18}$ was treated with 0.025 and 0.2 mL of 30 mM AdT in THF.

Instrumentation. Mass spectral studies were carried out using a Voyager DE PRO biospectrometry workstation (Applied Biosystems) matrix-assisted laser desorption ionization (MALDI) time-of-flight (TOF) mass spectrometer both in the linear and reflectron modes (denoted as MALDI (L) and MALDI (R) MS, respectively) as well as using a MALDI TOF TOF (UltrafleXtreme, Bruker Daltonics) mass spectrometer. In the case of MALDI TOF MS, a pulsed nitrogen laser of 337 nm was employed (maximum firing rate, 20 Hz; maximum pulse energy, 300 μJ) for the measurements. The MALDI TOF TOF mass spectrometer utilizes a 1 kHz smartbeam-II laser, FlashDetector system, and a minimum 4 GHz digitizer. Mass spectra were collected in positive and negative ion modes and were averaged for 500−700 shots. DCTB (trans-2-[3-(4-*t*-butylphenyl)-2-methyl-2-propenylidene]malononitrile) was used as the matrix for all MALDI MS measurements. All spectra were measured at threshold laser intensity to keep fragmentation to a minimum unless otherwise mentioned. Concentration of the analyte and the mass spectral conditions (laser intensity and spectrometer tune files) were optimized to get good quality spectra. UV−vis absorption spectra were collected using a Perkin-Elmer Lambda 25 spectrophotometer. The experiments were carried out at room temperature, and the absorption spectra were recorded from 200 to 1100 nm. Luminescence measurements were done on a Jobin Yvon NanoLog instrument. The band pass for excitation and emission was set at 5 nm. Electrospray ionization (ESI) mass spectrometric measurements were done in the negative mode using LTQ XL, with a mass range of *m/z* 150−4000 and using a Synapt G2 HDMS, quadrupole time-of-flight (Q TOF), ion mobility, orthogonal acceleration mass spectrometer with electrospray (ESI) ionization having a mass range up to 32 kDa. The Synapt instrument used for ESI measurements combined exact-mass quadrupole and high-resolution time-of-flight mass spectrometer with Triwave technology, enabling measurements in TOF mode. The purified samples were dispersed in THF and used for both mass spectrometric measurements. The samples were electrosprayed at a flow rate 5 μL/min and at a capillary temperature of 150 °C. The spectra were averaged for 80−100 scans. Scanning electron microscopic (SEM) and energy-dispersive analysis of X-ray (EDAX) images were obtained using a FEI QUANTA-200 SEM. For the SEM and EDAX measurements, samples were spotted on a carbon substrate and dried in ambient temperature. Transmission electron microscopy (TEM) was conducted using a JEOL 3011, 300 kV instrument with an ultra-high-resolution (UHR) polepiece. The samples were prepared by dropping the dispersion on amorphous carbon films supported on a copper grid and dried in laboratory conditions. ^{1}H NMR and 2D rotating frame nuclear Overhauser effect (ROESY) spectra were recorded on a 500 MHz Bruker Avance III spectrometer operating at 500.15 MHz equipped with a 5 mm smart probe. A 1:1 solvent mixture of 99.9% DMSO-d_6 (Aldrich) and 99.9% $CDCl_3$ (SRL) was used to prepare samples and sealed immediately from the laboratory atmosphere. $CDCl_3$ solvent signal served as the reference for the field-frequency lock, and tetramethylsilane was used as the internal reference. All experiments were performed at 25 °C. Standard Bruker pulse programs (Topspin 3.0) were employed throughout. The 1D spectra were acquired with 32K data points. The data for phase-sensitive ROESY experiments were acquired with a spectral width of 4464 Hz in both the dimensions. For each spectrum, 4 transients of 2048 complex points were accumulated for 256 t_1 increments and a relaxation delay of 1.975 s was used. A continuous-wave (CW) spin-lock mixing time of 200 ms was employed. Prior to Fourier transformation, zero filling to 1K*1K complex points was performed and apodized with a weighted function (QSINE) in both dimensions. All the data were processed on a HP workstation, using Topspin 3.0 software.

Theoretical Calculations. Many properties of QCs have been calculated using DFT efficiently by using smaller CH_3 ligands.[77−79] However, here the formation of an inclusion complex requires keeping all the SBB ligands intact, and this increases the CPU resources needed for the calculations significantly. For the computational modeling of $Au_{25}SBB_{18}$, we used density functional theory (DFT) as implemented in the real-space code-package GPAW.[80−82] Structure optimization was performed using full ligands as used in the experiments, Perdew−Burke−Ernzerhof (PBE) functional,[83] 0.2 Å grid spacing, and 0.05 eV/Å criterion for the residual forces for optimization. The GPAW setups for Au include scalar relativistic corrections. The structures of $Au_{25}SBB_{18}$ and $Au_{25}SBB_{18}$∩CD_4 were built up with the help of Ecce builder[84] and Avogadro[85] software packages, and visualizations were created with visual molecular dynamics (VMD)[86] software. We generated the initial structure for the optimization of $Au_{25}SBB_{18}$ using a model of $Au_{25}PET_{18}$ taken from one of its known crystal structures[61] and then replacing the PET ligands with SBB ligands. A preoptimization of only the ligand positions, keeping the core and staples fixed, was then carried out using a UFF force field[87] as implemented in Avogadro. The model of $Au_{25}SBB_{18}$∩CD_4 was constructed by sequentially attaching four β-CDs to the DFT-optimized structure of $Au_{25}SBB_{18}$ using Avogadro. The ligand and β-CD positions of $Au_{25}SBB_{18}$∩CD_4 were optimized by the UFF force field[87] keeping the Au and S atoms fixed. The calculations on BBSH∩CD were carried out with Gaussian 09[88] using the B3LYP and hybrid meta-GGA functionals in order to describe the noncovalent forces more accurately, and the basis set was selected according to the size of the system. Further details of all the calculations can be found in the Supporting Information 13.

Conflict of Interest: The authors declare no competing financial interest.

Acknowledgment. We thank the Department of Science and Technology, Government of India (DST), for constantly supporting our research program on nanomaterials. A.M. thanks CSIR for a research fellowship. T.P., G.N., L.L., and H.H. thank the DST and the Academy of Finland for funding through an Indo-Finland initiative. Mr. T. Karthik, Mr. Mohan, and Mr. Venkadesh are thanked for NMR measurements, and Arun Surendran at Rajiv Gandhi Centre for Biotechnology (RGCB) is thanked for help in mass spectrometric measurements.

Supporting Information Available: Additional data on characterization of $Au_{25}SBB_{18}$, $Au_{25}SBB_{18}$∩CD_4, and BBSH∩CD adducts along with details of theoretical calculations and optimized structures are provided. XYZ files containing structural coordinates of BBSH∩CD (wide and narrow end entry), $Au_{25}SBB_{18}$, and $Au_{25}SBB_{18}$∩CD_4 are also given. Data demonstrating the enhanced stability of the $Au_{25}SBB_{18}$∩CD_4 supramolecular adduct and its sensing properties are also provided. This material is available free of charge *via* the Internet at http://pubs.acs.org.

REFERENCES AND NOTES

1. Daniel, M. C.; Astruc, D. Gold Nanoparticles: Assembly, Supramolecular Chemistry, Quantum-Size-Related Properties, and Applications toward Biology, Catalysis, and Nanotechnology. *Chem. Rev.* **2004**, *104*, 293–346.
2. Burda, C.; Chen, X.; Narayanan, R.; El-Sayed, M. A. Chemistry and Properties of Nanocrystals of Different Shapes. *Chem. Rev.* **2005**, *105*, 1025–1102.
3. Templeton, A. C.; Wuelfing, W. P.; Murray, R. W. Monolayer-Protected Cluster Molecules. *Acc. Chem. Res.* **2000**, *33*, 27–36.
4. Hakkinen, H. The Gold−Sulfur Interface at the Nanoscale. *Nat. Chem.* **2012**, *4*, 443–455.
5. Negishi, Y.; Nobusada, K.; Tsukuda, T. Glutathione-Protected Gold Clusters Revisited: Bridging the Gap between Gold(I)−Thiolate Complexes and Thiolate-Protected Gold Nanocrystals. *J. Am. Chem. Soc.* **2005**, *127*, 5261–5270.

6. Ramakrishna, G.; Varnavski, O.; Kim, J.; Lee, D.; Goodson, T. Quantum-Sized Gold Clusters as Efficient Two-Photon Absorbers. *J. Am. Chem. Soc.* **2008**, *130*, 5032–5033.
7. Shibu, E. S.; Habeeb Muhammed, M. A.; Tsukuda, T.; Pradeep, T. Ligand Exchange of $Au_{25}SG_{18}$ Leading to Functionalized Gold Clusters: Spectroscopy, Kinetics, and Luminescence. *J. Phys. Chem. C* **2008**, *112*, 12168–12176.
8. Udayabhaskararao, T.; Pradeep, T. New Protocols for the Synthesis of Stable Ag and Au Nanocluster Molecules. *J. Phys. Chem. Lett.* **2013**, *4*, 1553–1564.
9. Aikens, C. M. Geometric and Electronic Structure of $Au_{25}(SPhX)_{18}^-$ (X = H, F, Cl, Br, CH_3, and OCH_3). *J. Phys. Chem. Lett.* **2010**, *1*, 2594–2599.
10. Akola, J.; Walter, M.; Whetten, R. L.; Häkkinen, H.; Grönbeck, H. On the Structure of Thiolate-Protected Au_{25}. *J. Am. Chem. Soc.* **2008**, *130*, 3756–3757.
11. Parker, J. F.; Fields-Zinna, C. A.; Murray, R. W. The Story of a Monodisperse Gold Nanoparticle: $Au_{25}L_{18}$. *Acc. Chem. Res.* **2010**, *43*, 1289–1296.
12. Jung, J.; Kang, S.; Han, Y. K. Ligand Effects on the Stability of Thiol-Stabilized Gold Nanoclusters: $Au_{25}(SR)_{18}^-$, $Au_{38}(SR)_{24}$, and $Au_{102}(SR)_{44}$. *Nanoscale* **2012**, *4*, 4206–4210.
13. Kurashige, W.; Yamaguchi, M.; Nobusada, K.; Negishi, Y. Ligand Effects on the Stability of Thiol-Stabilized Gold Nanoclusters: $Au_{25}(SR)_{18}^-$, $Au_{38}(SR)_{24}$, and $Au_{102}(SR)_{44}$ *J. Phys. Chem. Lett.* **2012**, *3*, 2649–2652.
14. Wang, G.; Guo, R.; Kalyuzhny, G.; Choi, J.-P.; Murray, R. W. NIR Luminescence Intensities Increase Linearly with Proportion of Polar Thiolate Ligands in Protecting Monolayers of Au_{38} and Au_{140} Quantum Dots. *J. Phys. Chem. B* **2006**, *110*, 20282–20289.
15. Verma, A.; Stellacci, F. Effect of Surface Properties on Nanoparticle–Cell Interactions. *Small* **2010**, *6*, 12–21.
16. Demchenko, A. P.; Habeeb Muhammed, M. A.; Pradeep, T. Luminescent Quantum Clusters of Gold as Bio-Labels. In *Advanced Fluorescence Reporters in Chemistry and Biology II*; Springer: Berlin, 2010; Vol. 9, pp 333–353.
17. Choi, S.; Dickson, R. M.; Yu, J. Developing Luminescent Silver Nanodots for Biological Applications. *Chem. Soc. Rev.* **2012**, *41*, 1867–1891.
18. Zhou, C.; Long, M.; Qin, Y.; Sun, X.; Zheng, J. Luminescent Gold Nanoparticles with Efficient Renal Clearance. *Angew. Chem., Int. Ed.* **2011**, *50*, 3168–3172.
19. Jin, R. Quantum Sized, Thiolate-Protected Gold Nanoclusters. *Nanoscale* **2010**, *2*, 343–362.
20. Niihori, Y.; Matsuzaki, M.; Pradeep, T.; Negishi, Y. Separation of Precise Compositions of Noble Metal Clusters Protected with Mixed Ligands. *J. Am. Chem. Soc.* **2013**, *135*, 4946–4949.
21. Heinecke, C. L.; Ni, T. W.; Malola, S.; Mäkinen, V.; Wong, O. A.; Häkkinen, H.; Ackerson, C. J. Structural and Theoretical Basis for Ligand Exchange on Thiolate Monolayer Protected Gold Nanoclusters. *J. Am. Chem. Soc.* **2012**, *134*, 13316–13322.
22. Woehrle, G. H.; Brown, L. O.; Hutchison, J. E. Thiol-Functionalized, 1.5-nm Gold Nanoparticles through Ligand Exchange Reactions: Scope and Mechanism of Ligand Exchange. *J. Am. Chem. Soc.* **2005**, *127*, 2172–2183.
23. Zhang, S.; Li, Z.; Samarajeewa, S.; Sun, G.; Yang, C.; Wooley, K. L. Orthogonally Dual-Clickable Janus Nanoparticles *via* a Cyclic Templating Strategy. *J. Am. Chem. Soc.* **2011**, *133*, 11046–11049.
24. Schieber, C.; Bestetti, A.; Lim, J. P.; Ryan, A. D.; Nguyen, T.-L.; Eldridge, R.; White, A. R.; Gleeson, P. A.; Donnelly, P. S.; Williams, S. J.; *et al.* Conjugation of Transferrin to Azide-Modified CdSe/ZnS Core–Shell Quantum Dots Using Cyclooctyne Click Chemistry. *Angew. Chem., Int. Ed.* **2012**, *51*, 10523–10527.
25. Yao, H.; Saeki, M.; Kimura, K. Induced Optical Activity in Boronic-Acid-Protected Silver Nanoclusters by Complexation with Chiral Fructose. *J. Phys. Chem. C* **2010**, *114*, 15909–15915.
26. Rekharsky, M. V.; Inoue, Y. Complexation Thermodynamics of Cyclodextrins. *Chem. Rev.* **1998**, *98*, 1875–1918.
27. Ogoshi, T.; Harada, A. Chemical Sensors Based on Cyclodextrin Derivatives. *Sensors* **2008**, *8*, 4961–4982.
28. Liu, Y.; Chen, Y. Cooperative Binding and Multiple Recognition by Bridged Bis(β-cyclodextrin)s with Functional Linkers. *Acc. Chem. Res.* **2006**, *39*, 681–691.
29. Depalo, N.; Comparelli, R.; Huskens, J.; Ludden, M. J. W.; Perl, A.; Agostiano, A.; Striccoli, M.; Curri, M. L. Phase Transfer of CdS Nanocrystals Mediated by Heptamine β-Cyclodextrin. *Langmuir* **2012**, *28*, 8711–8720.
30. Chalasani, R.; Vasudevan, S. Cyclodextrin-Functionalized Fe_3O_4@TiO_2: Reusable, Magnetic Nanoparticles for Photocatalytic Degradation of Endocrine-Disrupting Chemicals in Water Supplies. *ACS Nano* **2013**, *7*, 4093–4104.
31. Park, J. H.; Hwang, S.; Kwak, J. Nanosieving of Anions and Cavity-Size-Dependent Association of Cyclodextrins on a 1-Adamantanethiol Self-Assembled Monolayer. *ACS Nano* **2010**, *4*, 3949–3958.
32. Lehn, J. M. *Supramolecular Chemistry: Concepts and Perspectives*; Wiley-VCH: New York, 1995.
33. Kauffmann, E.; Dye, J. L.; Lehn, J. M.; Popov, A. I. A Study of the Inclusive and Exclusive Cesium Cryptates in Nonaqueous Solvents by Cesium-133 NMR. *J. Am. Chem. Soc.* **1980**, *102*, 2274–2278.
34. Negishi, Y.; Arai, R.; Niihori, Y.; Tsukuda, T. Isolation and Structural Characterization of Magic Silver Clusters Protected by 4-(*tert*-Butyl)benzyl Mercaptan. *Chem. Commun.* **2011**, *47*, 5693–5695.
35. Branham, M. R.; Douglas, A. D.; Mills, A. J.; Tracy, J. B.; White, P. S.; Murray, R. W. Arylthiolate-Protected Silver Quantum Dots. *Langmuir* **2006**, *22*, 11376–11383.
36. Habeeb Muhammed, M. A.; Pradeep, T. Reactivity of Au_{25} Clusters with Au^{3+}. *Chem. Phys. Lett.* **2007**, *449*, 186–190.
37. Zhu, M.; Aikens, C. M.; Hollander, F. J.; Schatz, G. C.; Jin, R. Correlating the Crystal Structure of a Thiol-Protected Au_{25} Cluster and Optical Properties. *J. Am. Chem. Soc.* **2008**, *130*, 5883–5885.
38. Angel, L. A.; Majors, L. T.; Dharmaratne, A. C.; Dass, A. Ion Mobility Mass Spectrometry of $Au_{25}(SCH_2CH_2Ph)_{18}$ Nanoclusters. *ACS Nano* **2010**, *4*, 4691–4700.
39. Hapiot, F.; Tilloy, S.; Monflier, E. Cyclodextrins as Supramolecular Hosts for Organometallic Complexes. *Chem. Rev.* **2006**, *106*, 767–781.
40. Villalonga, R.; Cao, R.; Fragoso, A. Supramolecular Chemistry of Cyclodextrins in Enzyme Technology. *Chem. Rev.* **2007**, *107*, 3088–3116.
41. May, B. L.; Gerber, J.; Clements, P.; Buntine, M. A.; Brittain, D. R. B.; Lincoln, S. F.; Easton, C. J. Cyclodextrin and Modified Cyclodextrin Complexes of *E*-4-*tert*-Butylphenyl-4′-oxyazobenzene: UV–Visible, ^{1}H NMR and *Ab Initio* Studies. *Org. Biomol. Chem.* **2005**, *3*, 1481–1488.
42. Breslow, R.; Halfon, S. Quantitative Effects of Antihydrophobic Agents on Binding Constants and Solubilities in Water. *Proc. Natl. Acad. Sci. U.S.A.* **1992**, *89*, 6916–6918.
43. Antelo, A.; Jover, A.; Galantini, L.; Meijide, F.; Alcalde, M.; Pavel, N.; Tato, J. Formation of Host–Guest and Sandwich Complexes by a β-Cyclodextrin Derivative. *J. Inclusion Phenom. Macrocyclic Chem.* **2011**, *69*, 245–253.
44. Ruebner, A.; Yang, Z.; Leung, D.; Breslow, R. A Cyclodextrin Dimer with a Photocleavable Linker as a Possible Carrier for the Photosensitizer in Photodynamic Tumor Therapy. *Proc. Natl. Acad. Sci. U.S.A.* **1999**, *96*, 14692–14693.
45. Schmidt, B. V. K. J.; Hetzer, M.; Ritter, H.; Barner-Kowollik, C. Cyclodextrin-Complexed RAFT Agents for the Ambient Temperature Aqueous Living/Controlled Radical Polymerization of Acrylamido Monomers. *Macromolecules* **2011**, *44*, 7220–7232.
46. Chung, J. W.; Kang, T. J.; Kwak, S.-Y. Guest-Free Self-Assembly of α-Cyclodextrins Leading to Channel-Type Nanofibrils as Mesoporous Framework. *Langmuir* **2007**, *23*, 12366–12370.
47. Rusa, C. C.; Bullions, T. A.; Fox, J.; Porbeni, F. E.; Wang, X.; Tonelli, A. E. Inclusion Compound Formation with a New Columnar Cyclodextrin Host. *Langmuir* **2002**, *18*, 10016–10023.

48. Karas, M.; Bahr, U.; Gießmann, U. Matrix-Assisted Laser Desorption Ionization Mass Spectrometry. *Mass Spectrom. Rev.* **1991**, *10*, 335–357.
49. Hillenkamp, F.; Karas, M.; Beavis, R. C.; Chait, B. T. Matrix-Assisted Laser Desorption/Ionization Mass Spectrometry of Biopolymers. *Anal. Chem.* **1991**, *63*, 1193A–1203A.
50. Karas, M.; Bahr, U.; Strupat, K.; Hillenkamp, F.; Tsarbopoulos, A.; Pramanik, B. N. Matrix Dependence of Metastable Fragmentation of Glycoproteins in MALDI TOF Mass Spectrometry. *Anal. Chem.* **1995**, *67*, 675–679.
51. Gross, J.; Leisner, A.; Hillenkamp, F.; Hahner, S.; Karas, M.; Schäfer, J.; Lützenkirchen, F.; Nordhoff, E. Investigations of the Metastable Decay of DNA under Ultraviolet Matrix-Assisted Laser Desorption/Ionization Conditions with Post-Source-Decay Analysis and Hydrogen/Deuterium Exchange. *J. Am. Soc. Mass Spectrom.* **1998**, *9*, 866–878.
52. Zenobi, R.; Knochenmuss, R. Ion Formation in MALDI Mass Spectrometry. *Mass Spectrom. Rev.* **1998**, *17*, 337–366.
53. Whittal, R. M.; Li, L. High-Resolution Matrix-Assisted Laser Desorption/Ionization in a Linear Time-of-Flight Mass Spectrometer. *Anal. Chem.* **1995**, *67*, 1950–1954.
54. Dass, A.; Holt, K.; Parker, J. F.; Feldberg, S. W.; Murray, R. W. Mass Spectrometrically Detected Statistical Aspects of Ligand Populations in Mixed Monolayer $Au_{25}L_{18}$ Nanoparticles. *J. Phys. Chem. C* **2008**, *112*, 20276–20283.
55. Knoppe, S.; Dharmaratne, A. C.; Schreiner, E.; Dass, A.; Bürgi, T. Ligand Exchange Reactions on Au_{38} and Au_{40} Clusters: A Combined Circular Dichroism and Mass Spectrometry Study. *J. Am. Chem. Soc.* **2010**, *132*, 16783–16789.
56. Beqa, L.; Deschamps, D.; Perrio, S. P.; Gaumont, A.-C.; Knoppe, S.; Bürgi, T. Ligand Exchange Reaction on $Au_{38}(SR)_{24}$, Separation of $Au_{38}(SR)_{23}(SR')_1$ Regioisomers, and Migration of Thiolates. *J. Phys. Chem. C* **2013**, *117*, 21619–21625.
57. Kurashige, W.; Munakata, K.; Nobusada, K.; Negishi, Y. Synthesis of Stable Cu_nAu_{25-n} Nanoclusters (n = 1−9) Using Selenolate Ligands. *Chem. Commun.* **2013**, *49*, 5447–5449.
58. Shibu, E. S.; Pradeep, T. Quantum Clusters in Cavities: Trapped Au_{15} in Cyclodextrins. *Chem. Mater.* **2011**, *23*, 989–999.
59. Habeeb Muhammed, M. A.; Pradeep, T. Au_{25}@SiO_2: Quantum Clusters of Gold Embedded in Silica. *Small* **2011**, *7*, 204–208.
60. Habeeb Muhammed, M. A.; Verma, P. K.; Pal, S. K.; Kumar, R. C. A.; Paul, S.; Omkumar, R. V.; Pradeep, T. Bright, NIR-Emitting Au_{23} from Au_{25}: Characterization and Applications Including Biolabeling. *Chem.—Eur. J.* **2009**, *15*, 10110–10120.
61. Heaven, M. W.; Dass, A.; White, P. S.; Holt, K. M.; Murray, R. W. Crystal Structure of the Gold Nanoparticle $[N(C_8H_{17})_4][Au_{25}(SCH_2CH_2Ph)_{18}]$. *J. Am. Chem. Soc.* **2008**, *130*, 3754–3755.
62. Chen, M.; Diao, G.; Zhang, E. Study of Inclusion Complex of β-Cyclodextrin and Nitrobenzene. *Chemosphere* **2006**, *63*, 522–529.
63. Upadhyay, S.; Ali, S. Solution Structure of Loperamide and β-Cyclodextrin Inclusion Complexes Using NMR Spectroscopy. *J. Chem. Sci.* **2009**, *121*, 521–527.
64. Maffeo, D.; Leondiadis, L.; Mavridis, I. M.; Yannakopoulou, K. Positive Effect of Natural and Negatively Charged Cyclodextrins on the Stabilization of Penicillins towards β-Lactamase Degradation Due to Inclusion and External Guest−Host Association. An NMR and MS Study. *Org. Biomol. Chem.* **2006**, *4*, 1297–1304.
65. Dharmaratne, A. C.; Krick, T.; Dass, A. Nanocluster Size Evolution Studied by Mass Spectrometry in Room Temperature $Au_{25}(SR)_{18}$ Synthesis. *J. Am. Chem. Soc.* **2009**, *131*, 13604–13605.
66. Qian, H.; Jiang, D.-E.; Li, G.; Gayathri, C.; Das, A.; Gil, R. R.; Jin, R. Monoplatinum Doping of Gold Nanoclusters and Catalytic Application. *J. Am. Chem. Soc.* **2012**, *134*, 16159–16162.
67. Huang, C. C.; Yang, Z.; Lee, K. H.; Chang, H. T. Synthesis of Highly Fluorescent Gold Nanoparticles for Sensing Mercury(II). *Angew. Chem., Int. Ed.* **2007**, *119*, 6948–6952.
68. Mathew, A.; Sajanlal, P. R.; Pradeep, T. Selective Visual Detection of TNT at the Sub-Zeptomole Level. *Angew. Chem., Int. Ed.* **2012**, *51*, 9596–9600.
69. Habeeb Muhammed, M. A.; Verma, P. K.; Pal, S. K.; Retnakumari, A.; Koyakutty, M.; Nair, S.; Pradeep, T. Luminescent Quantum Clusters of Gold in Bulk by Albumin-Induced Core Etching of Nanoparticles: Metal Ion Sensing, Metal-Enhanced Luminescence, and Biolabeling. *Chem.—Eur. J.* **2010**, *16*, 10103–10112.
70. Xie, J.; Zheng, Y.; Ying, J. Y. Highly Selective and Ultrasensitive Detection of Hg^{2+} Based on Fluorescence Quenching of Au Nanoclusters by Hg^{2+}—Au^{+} Interactions. *Chem. Commun.* **2010**, *46*, 961–963.
71. Huang, C. C.; Yang, Z.; Lee, K. H.; Chang, H. T. Synthesis of Highly Fluorescent Gold Nanoparticles for Sensing Mercury(II). *Angew. Chem., Int. Ed.* **2007**, *46*, 6824–6828.
72. Liu, G.; Feng, D.-Q.; Chen, T.; Li, D.; Zheng, W. DNA-Templated Formation of Silver Nanoclusters as a Novel Light-Scattering Sensor for Label-Free Copper Ions Detection. *J. Mater. Chem.* **2012**, *22*, 20885–20888.
73. Norkus, E. Metal Ion Complexes with Native Cyclodextrins. An Overview. *J. Inclusion Phenom. Macrocyclic Chem.* **2009**, *65*, 237–248.
74. Böhm, I.; Isenbügel, K.; Ritter, H.; Branscheid, R.; Kolb, U. Cyclodextrin and Adamantane Host−Guest Interactions of Modified Hyperbranched Poly(ethylene imine) as Mimetics for Biological Membranes. *Angew. Chem., Int. Ed.* **2011**, *50*, 7896–7899.
75. Harries, D.; Rau, D. C.; Parsegian, V. A. Solutes Probe Hydration in Specific Association of Cyclodextrin and Adamantane. *J. Am. Chem. Soc.* **2005**, *127*, 2184–2190.
76. Wu, Z.; Suhan, J.; Jin, R. One-Pot Synthesis of Atomically Monodisperse, Thiol-Functionalized Au_{25} Nanoclusters. *J. Mater. Chem.* **2009**, *19*, 622–626.
77. Walter, M.; Akola, J.; Lopez-Acevedo, O.; Jadzinsky, P. D.; Calero, G.; Ackerson, C. J.; Whetten, R. L.; Gronbeck, H.; Hakkinen, H. A Unified View of Ligand-Protected Gold Clusters as Superatom Complexes. *Proc. Natl. Acad. Sci. U. S.A.* **2008**, *105*, 9157–9162.
78. Akola, J.; Walter, M.; Whetten, R. L.; Hakkinen, H.; Gronbeck, H. On the Structure of Thiolate-Protected Au_{25}. *J. Am. Chem. Soc.* **2008**, *130*, 3756–3757.
79. Lopez-Acevedo, O.; Akola, J.; Whetten, R. L.; Gronbeck, H.; Hakkinen, H. Structure and Bonding in the Ubiquitous Icosahedral Metallic Gold Cluster $Au_{144}(SR)_{60}$. *J. Phys. Chem. C* **2009**, *113*, 5035–5038.
80. Mortensen, J. J.; Hansen, L. B.; Jacobsen, K. W. Real-Space Grid Implementation of the Projector Augmented Wave Method. *Phys. Rev. B* **2005**, *71*, 035109.
81. Enkovaara, J.; Rostgaard, C.; Mortensen, J. J.; Chen, J.; Dułak, M.; Ferrighi, L.; Gavnholt, J.; Glinsvad, C.; Haikola, V.; Hansen, H. A.; *et al.* Electronic Structure Calculations with GPAW: A Real-Space Implementation of the Projector Augmented-Wave Method. *J. Phys.: Condens. Matter* **2010**, *22*, 253202.
82. Bahn, S. R.; Jacobsen, K. W. An Object-Oriented Scripting Interface to a Legacy Electronic Structure Code. *Comput. Sci. Eng.* **2002**, *4*, 56–66.
83. Perdew, J. P.; Burke, K.; Ernzerhof, M. Generalized Gradient Approximation Made Simple. *Phys. Rev. Lett.* **1996**, *77*, 3865–3868.
84. Black, G. D.; Schuchardt, K. L.; Gracio, D. K.; Palmer, B. In *Computational Science - ICCS 2003, International Conference*, Saint Petersburg, Russian Federation, Melbourne, Australia, Proceedings 2660; Sloot, P. M. A., Abramson, D., Bogdanov, A. V., Dongarra, J., Eds.; Springer-Verlag: Berlin, Germany, 2003; Vol. 81, pp 122−131.
85. Hanwell, M.; Curtis, D.; Lonie, D.; Vandermeersch, T.; Zurek, E.; Hutchison, G. Avogadro: An Advanced Semantic Chemical Editor, Visualization, and Analysis Platform. *J. Cheminf.* **2012**, *4*, 1–17.

86. Humphrey, W.; Dalke, A.; Schulten, K. J. VMD - Visual Molecular Dynamics. *Mol. Graphics* **1996**, *14*, 33–38.
87. Rappe, A. K.; Casewit, C. J.; Colwell, K. S.; Goddard, W. A.; Skiff, W. M. UFF, a Full Periodic Table Force Field for Molecular Mechanics and Molecular Dynamics Simulations. *J. Am. Chem. Soc.* **1992**, *114*, 10024–10035.
88. Frisch, M. J.; Trucks, G. W.; Schlegel, H. B.; Scuseria, G. E.; Robb, M. A.; Cheeseman, J. R.; Scalmani, G.; Barone, V.; Mennucci, B.; Petersson, G.; *et al. Gaussian 09*, revision A.1.; Gaussian, Inc.: Wallingford, CT, 2009.

Supporting information (SI) for the paper:

Supramolecular Functionalization and Concomitant Enhancement in Properties of Au_{25} Clusters

Ammu Mathew, Ganapati Natarajan, Lauri Lehtovaara, Hannu Häkkinen, Ravva Mahesh Kumar[‡], Venkatesan Subramanian[‡], Abdul Jaleel[#] and Thalappil Pradeep[*]

DST Unit of Nanoscience (DST UNS) and Thematic Unit of Excellence (TUE), Department of Chemistry, Indian Institute of Technology Madras, Chennai 600036, India.

Departments of Chemistry and Physics, Nanoscience Center, University of Jyväskylä, Finland.

[‡]*Chemical Laboratory, CSIR-Central Leather Research Institute, Adyar, Chennai 600020, India.*

[#]*Proteomics Core Facility, Rajiv Gandhi Centre for Biotechnology, Thiruvananthapuram 695014, India*

[*]E-mail: pradeep@iitm.ac.in

Table of contents

Supporting information 1

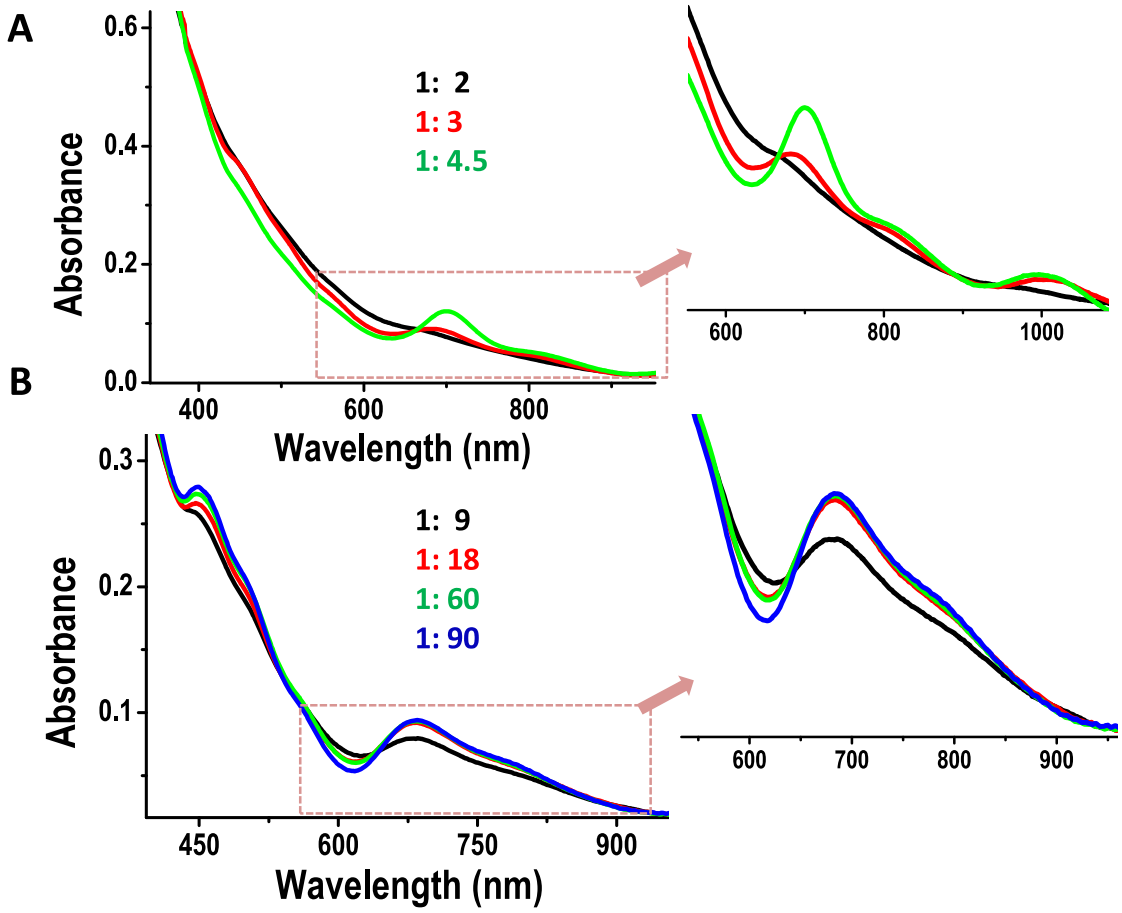

Figure S1. Effect of UV-vis optical absorption spectra for various Au:BBSH ratios used for cluster synthesis. An optimum Au:S ratio of 1:6 was employed for typical synthesis of $Au_{25}SBB_{18}$ (see Figure 1 in paper). While lower thiol ratios (A) showed significant changes in the absorption profile indicating that clusters of higher core sizes are getting formed, even a ten fold increase in thiol (B) compared to the optimised synthesis did not seem to yield still smaller clusters.

Supporting information 2

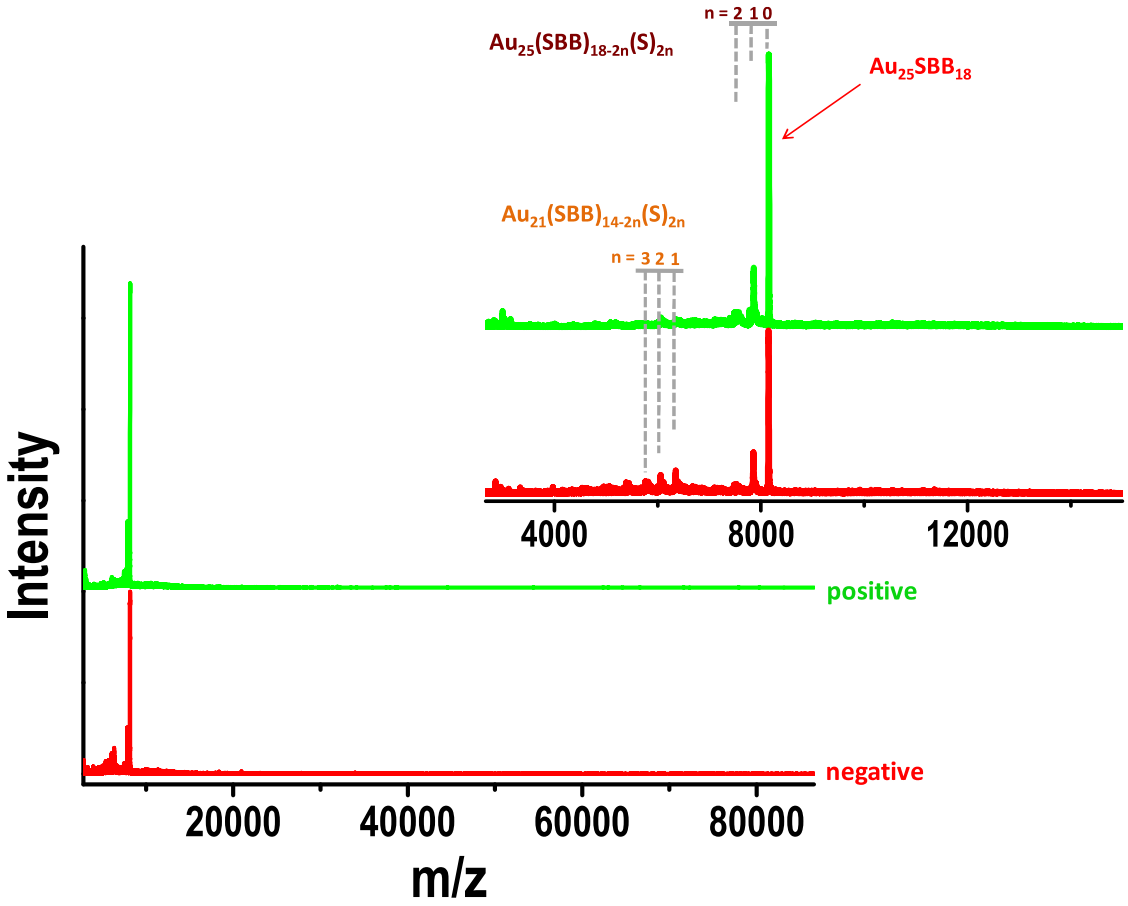

Figure S2. Full range MALDI (L) mass spectra of $Au_{25}SBB_{18}$ cluster in both positive and negative ion modes. Fragmentation due to the C-S cleavage of SBB ligand on the cluster surface can be observed apart from the molecular ion peak (these features are expanded in the inset). Loss of $[Au_4L_4]$ fragment from the parent cluster is a typical phenomenon in Au_{25} clusters. Here, we observed similar fragments corresponding to $[Au_4SBB_4BB_{2n}]$ loss, where n = 1, 2, 3 in the negative ion mode from parent $Au_{25}SBB_{18}$. The additional BB losses observed in the negative mode (red trace in inset) could be due to the facile C-S cleavage as in the case of the molecular ion peak at 8151 Da. DCTB was used as the matrix and threshold laser intensities were employed for all the measurements.

Supporting information 3

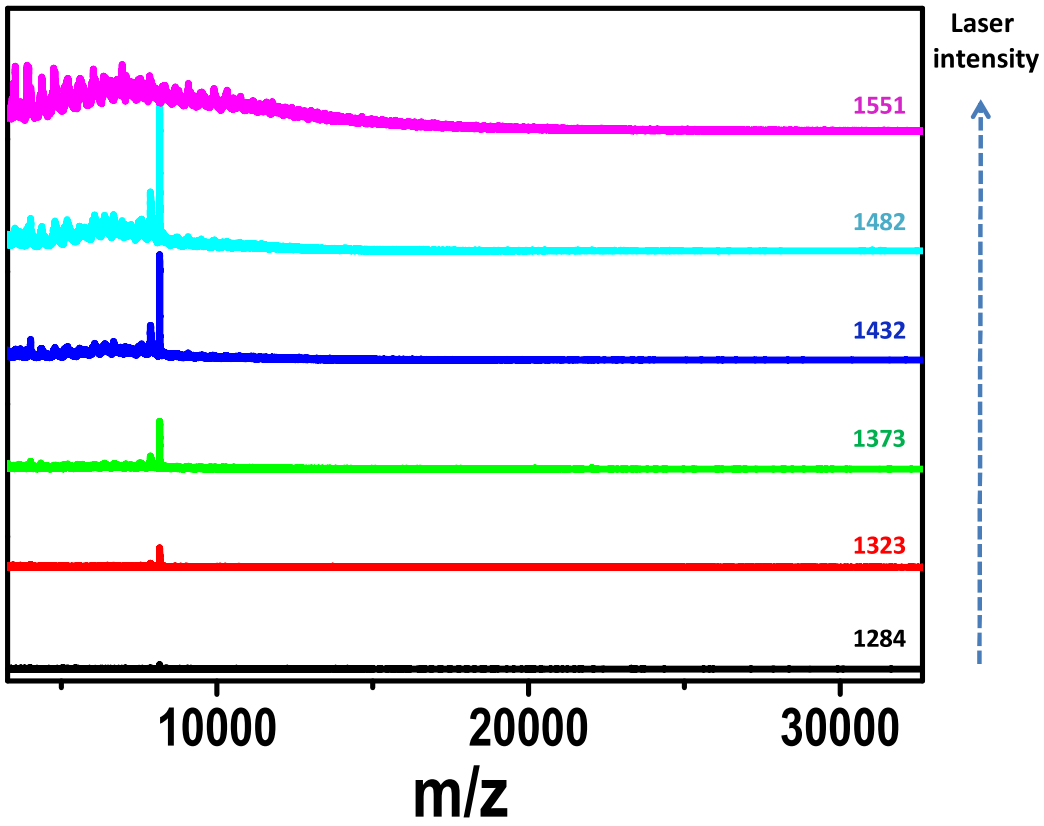

Figure S3. MALDI (L) mass spectra of the purified $Au_{25}SBB_{18}$ cluster at different laser intensities in the positive mode. Control over the laser intensity is vital to observe the molecular ion peak of the cluster without fragmentation. Laser intensity (shown at the right extreme) is as given by the instrument and has not been calibrated to a standard unit.

Supporting information 4

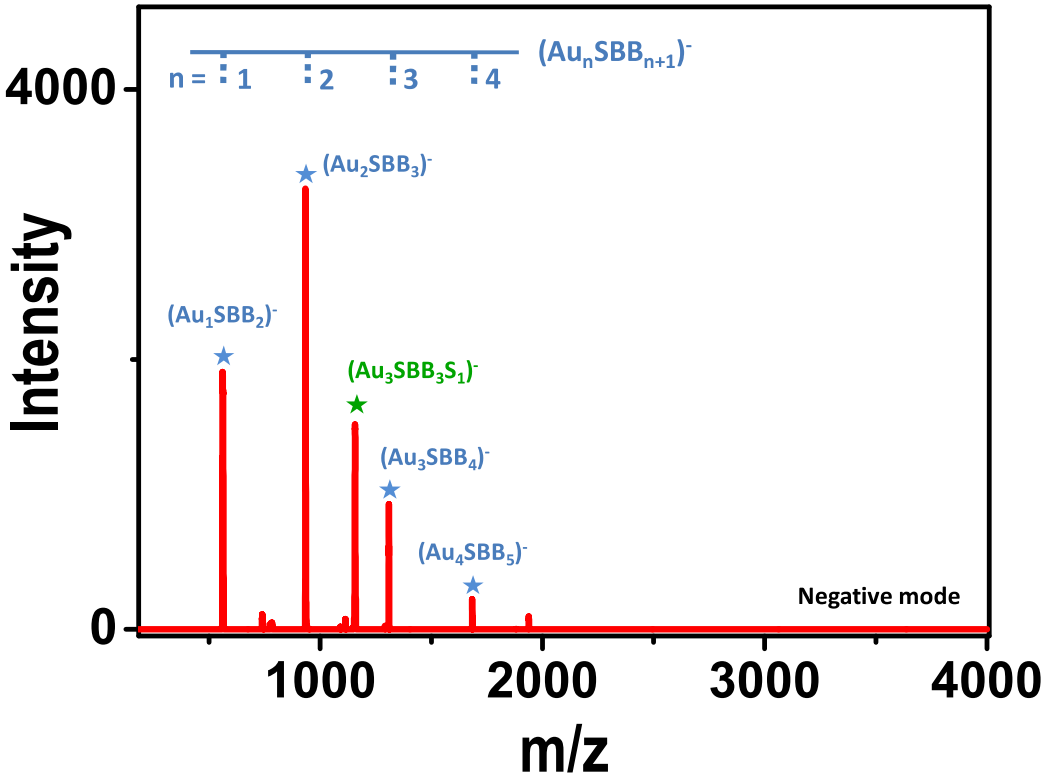

Figure S4. ESI MS of $Au_{25}SBB_{18}$ in negative ion mode showing fragments from the cluster in the low mass region.

Supporting information 5

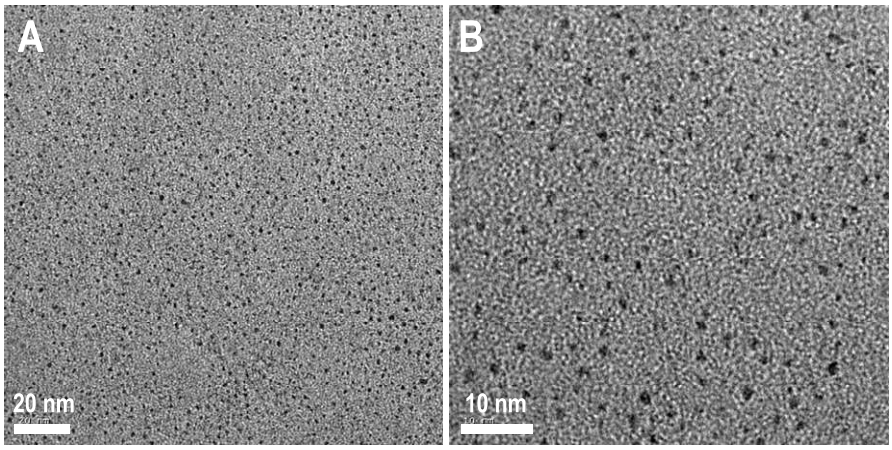

Figure S5. TEM images of $Au_{25}SBB_{18}$. Two magnifications are shown. Unlike in typical thiolated clusters, these samples are resistant to electron beam induced aggregation.

Supporting information 6

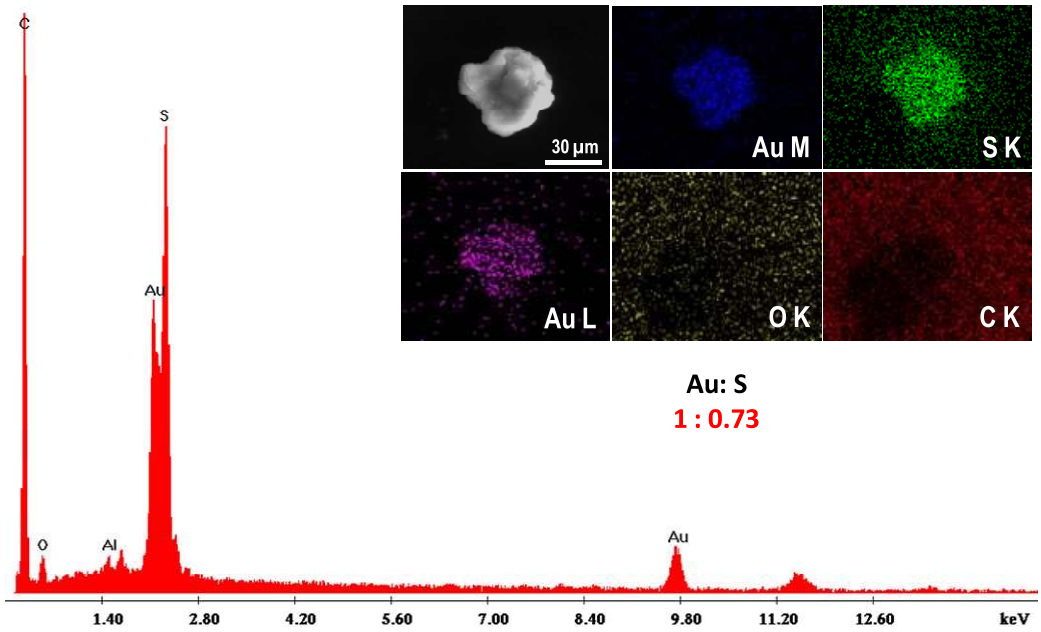

Figure S6. SEM and EDAX characterization of $Au_{25}SBB_{18}$ cluster. Carbon and aluminium are from the substrate used for the measurement. Contrast of carbon is low due to the use of carbon tape as the substrate. The scale is same for all images.

Supporting information 7

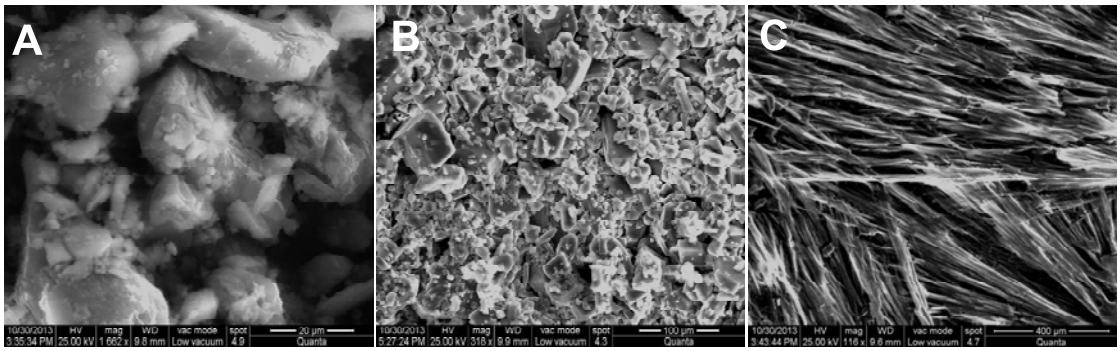

Figure S7. SEM images of (A) native β-CD powder, (B) drop cast β-CD solution in water and (C) drop cast β-CD solution in THF:water (30:1) mixture, after sonication. The formation of needle-like superstructures by self assembly occurred only in the case of reaction in THF:water (30:1) solvent mixture. Presence of minimal amount of water molecules can enhance the possibility of intermolecular hydrogen bonding between the hydroxyl group present on the outer rim of CD molecules. Control experiments in water (B), did not result in formation of superstructures. Thus the dispersion of β-CD molecules by sonication in THF and their subsequent self assembly by re-formation of the strong hydrogen bonding between the CDs with the aid of THF results in these superstructures.

Supporting information 8

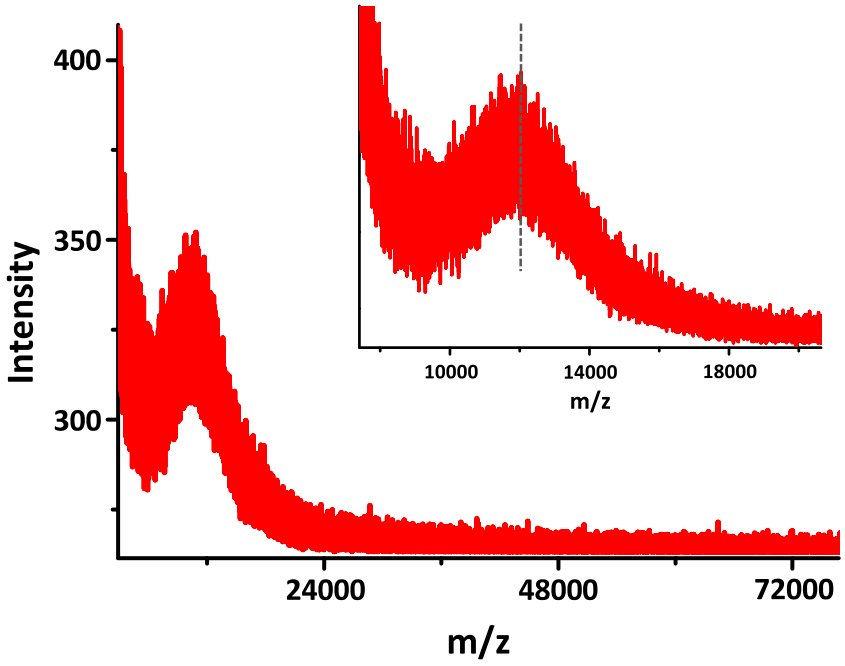

Figure S8. LDI mass spectrum of the aqueous layer, post synthesis of the CD-functionalised $Au_{25}SBB_{18}$ clusters. Addition of excess water to the microtubular arrangement of CD and cluster leads to the formation of $Au_{25}SBB_{18}\cap CD_n$ (where n=1-4). Though we found better mass spectral intensities for the adducts from the organic layer (see Figure 2 in main text), probably due to the existence of more number of hydrophobic SBB groups on the cluster surface (18-n, where n<4), analysis of the aqueous layer showed a broad peak at higher mass range too albeit with reduced intensity. Inset shows an expanded view. Peak maximum corresponding to $Au_{25}SBB_{18}\cap CD_4$ is marked with a line.

Supporting information 9

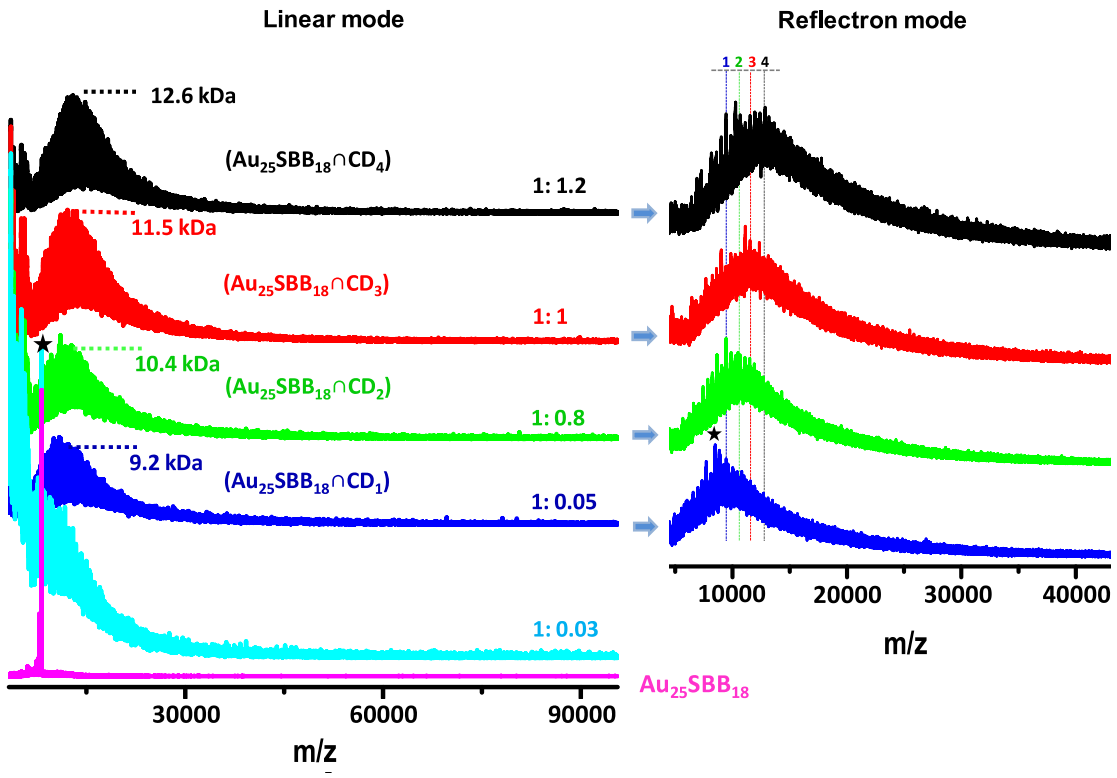

Figure S9. Positive mode MALDI (L) and MALDI (R) mass spectra of $Au_{25}SBB_{18}$ with increasing SBB:CD ratios in solution. The peak maxima shift with increasing BBS:CD ratio. This gradual increase is marked. Peak corresponding to parent $Au_{25}SBB_{18}$ is marked using a *. These peak positions are the same in both the data sets, but in the reflectron mode the peaks are better resolved as the resolution is improved. These peaks resolve even better in the MALDI TOF TOF mode (see S10).

Supporting information 10

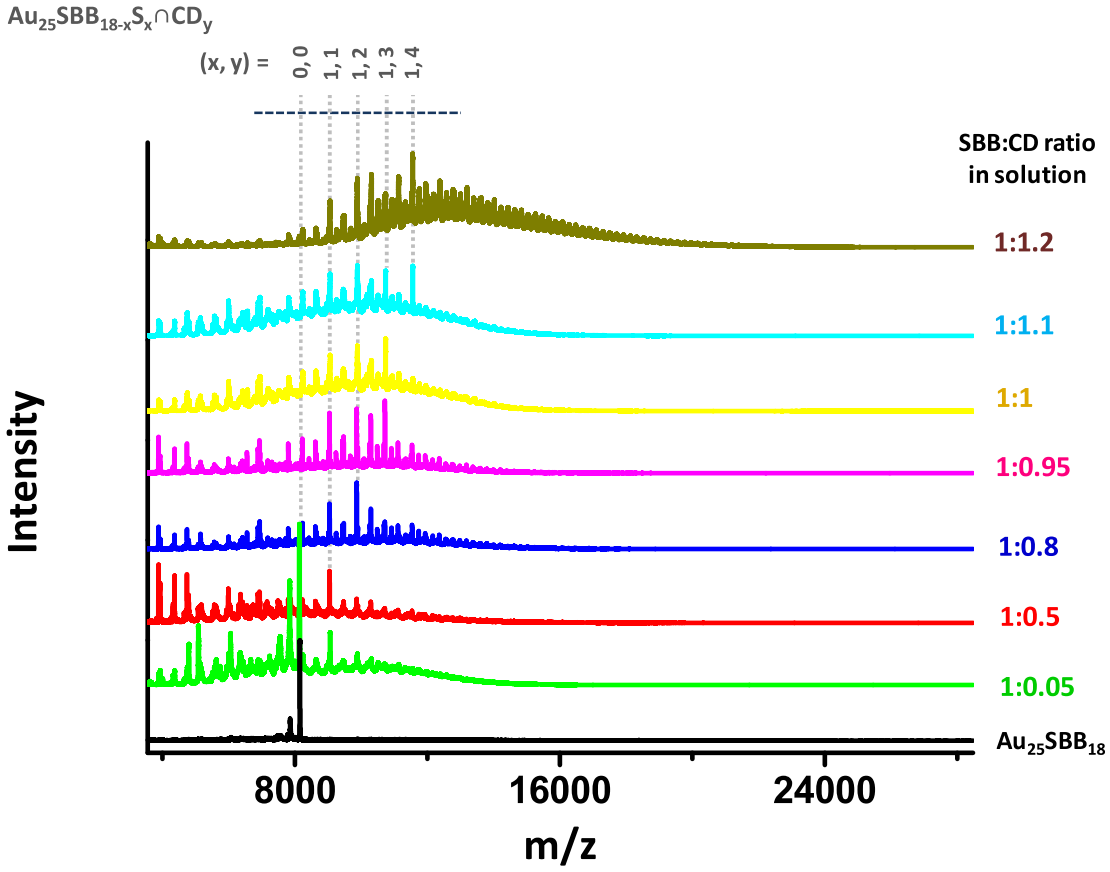

Figure S10. MALDI TOF TOF mass spectra of $Au_{25}SBB_{18}$ with increasing SBB:CD ratios (green to brown) in solution. The peaks are better resolved than in S9.

Supporting information 11

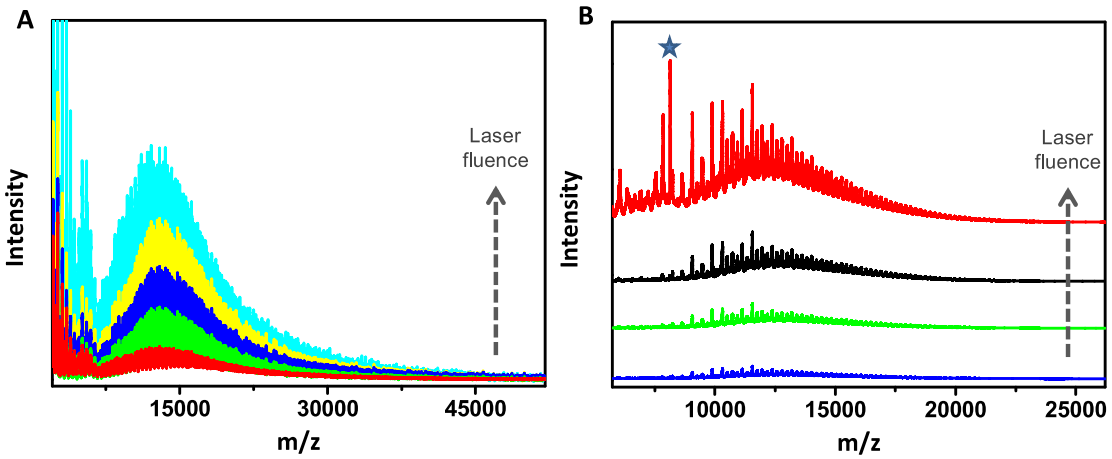

Figure S11. MALDI (L) mass spectra (A) and MALDI TOF TOF mass spectra (B) of $Au_{25}SBB_{18}\cap CD_4$ at different laser intensities in the positive mode. Note that though the background of the spectra increases with more laser fluence, the peak maxima and relative individual peak intensities remain the same except for red trace in (B) wherein peak due to $Au_{25}SBB_{13}S_5$ (marked with a *) gain intensity at higher laser fluence due to cleavage of C-S bond and loss of CDs. There are threshold laser powers above which fragmentations occur.

Supporting information 12

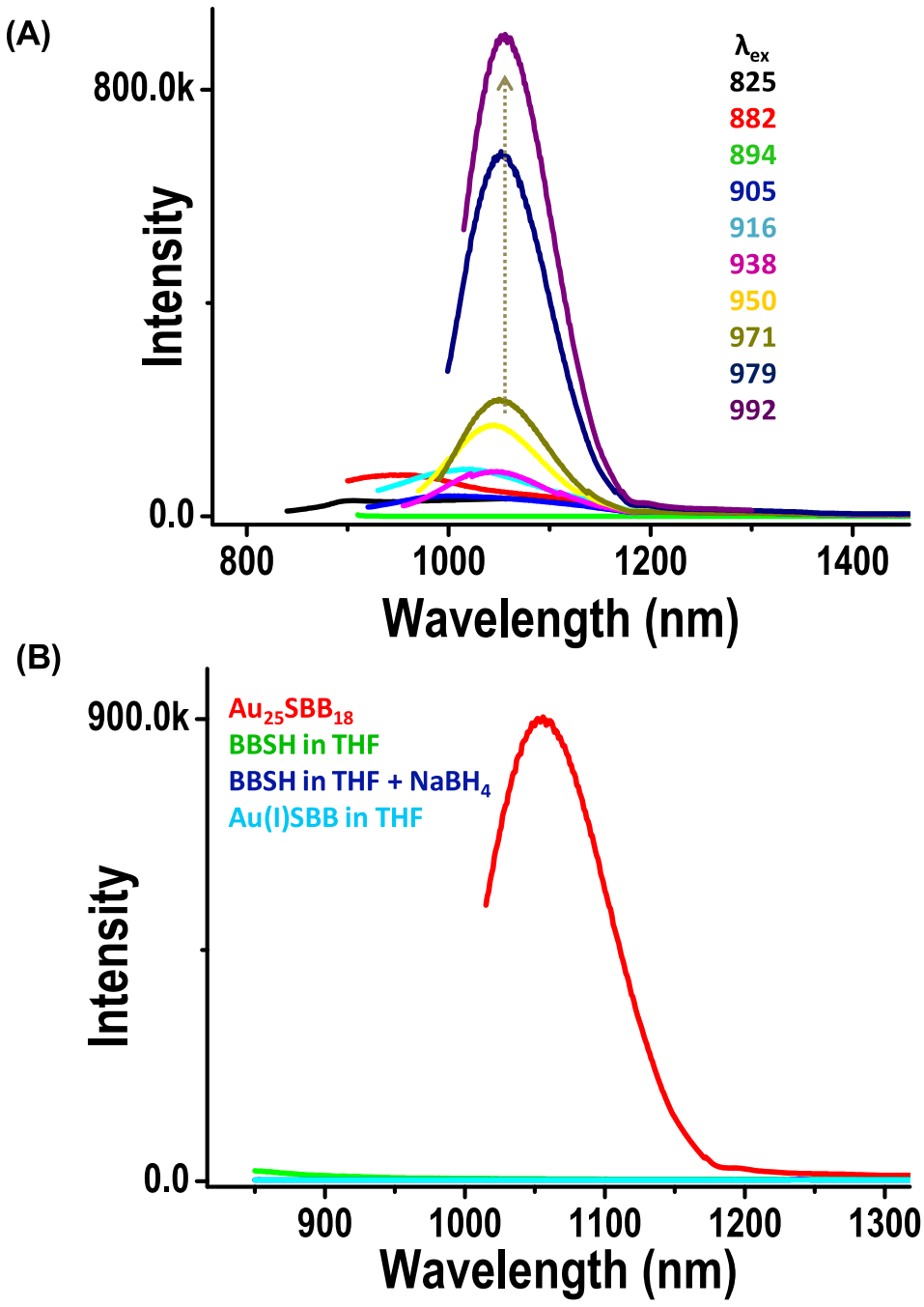

Figure S12. NIR luminescence observed from the bare $Au_{25}SBB_{18}$ cluster at (A) various excitation wavelengths and (B) comparison with the spectra (λ_{ex} 992 nm) of various starting materials.

Supporting Information 13

Structural optimization of $Au_{25}SBB_{18}$

The cluster was rotated so that the *x*-axis lay along the axis of the cluster passing through its center and the bridging sulfur atoms which were spaced the furthest distance apart.

Cluster boundary conditions were used and the size of the simulation box was chosen to be 34 Å, leaving about 9 Å of buffer space around the molecule. A negative charge was added to the molecule.

$Au_{25}SBB_{18}\cap CD_4$

Ligand structure of $Au_{25}SBB_{18}$ and CD attachment

The precise arrangement around any given ligand will affect whether that ligand may be a likely one for CD complexation. It was observed that bridging ligands were generally surrounded by ligands which were quite close to it, while the ligands neighboring a non-bridging ligand were spread further apart. The number of nearest-neighbor ligands to a CD centered on a chosen ligand was four.

The model of $Au_{25}SBB_{18}\cap CD_4$ was constructed by making attachments of CDs to the DFT optimized structure of $Au_{25}SBB_{18}$ using molecular builder software. The narrow side of the CD was attached first as this would reduce steric hindrance and this configuration had a lower binding energy as an isolated complex. The choice of ligands also affects the depth of penetration of the CD onto the ligand, which is lesser in the case of the bridging ligands due to greater steric hindrance from the neighbouring ligands. For non-bridging ligands both the aromatic BBS protons and *t*-butyl group protons would be close to the inner CD protons, which also agrees with the NMR data. For bridging ligands the inner H^3 and H^5 protons of the CD would be closer to the *t*-butyl groups.

The non-bridging ligand denoted by *(y,-z)*, in the notation described in the main paper, was easily accessible due to the widely separated positions of the surrounding ligands and hence was chosen for making the first attachment of the CD. The attachment was made in a stepwise fashion starting by including the *t*-butyl group and then by bringing the narrow end of the CD further over the ligand and then reoptimizing using a UFF force field until its position was in agreement with the NMR data. We also rejected position changes which increased the total energy. During the optimization, the core and staple atoms, *i.e.* the Au and S atoms, were kept fixed in their positions from DFT, while the other atoms were allowed to move. This process was repeated three more times by making CD attachments to the *(-z, -x), (x,-y) and (z,-x)* non-bridging ligands which were easily accessible. The energy of the final structure in the UFF force field was 60,323 kcal/mol.
From our calculations on BBSH∩CD, it is energetically favourable for the included ligand to be at an angle with respect to the CD. Tilting the CD to the angles found in the optimized geometries of BBSH∩CD was found difficult due to the presence of the neighboring ligands. The relative angle of the CD and included ligand varies due to the differing orientations of the included ligand and its neighbors. We remark here that further force-field calculations and molecular dynamics simulations would be necessary to determine more precise attachment

geometries as several different configurations which differ in depth and angle of attachment are consistent with the NMR data.

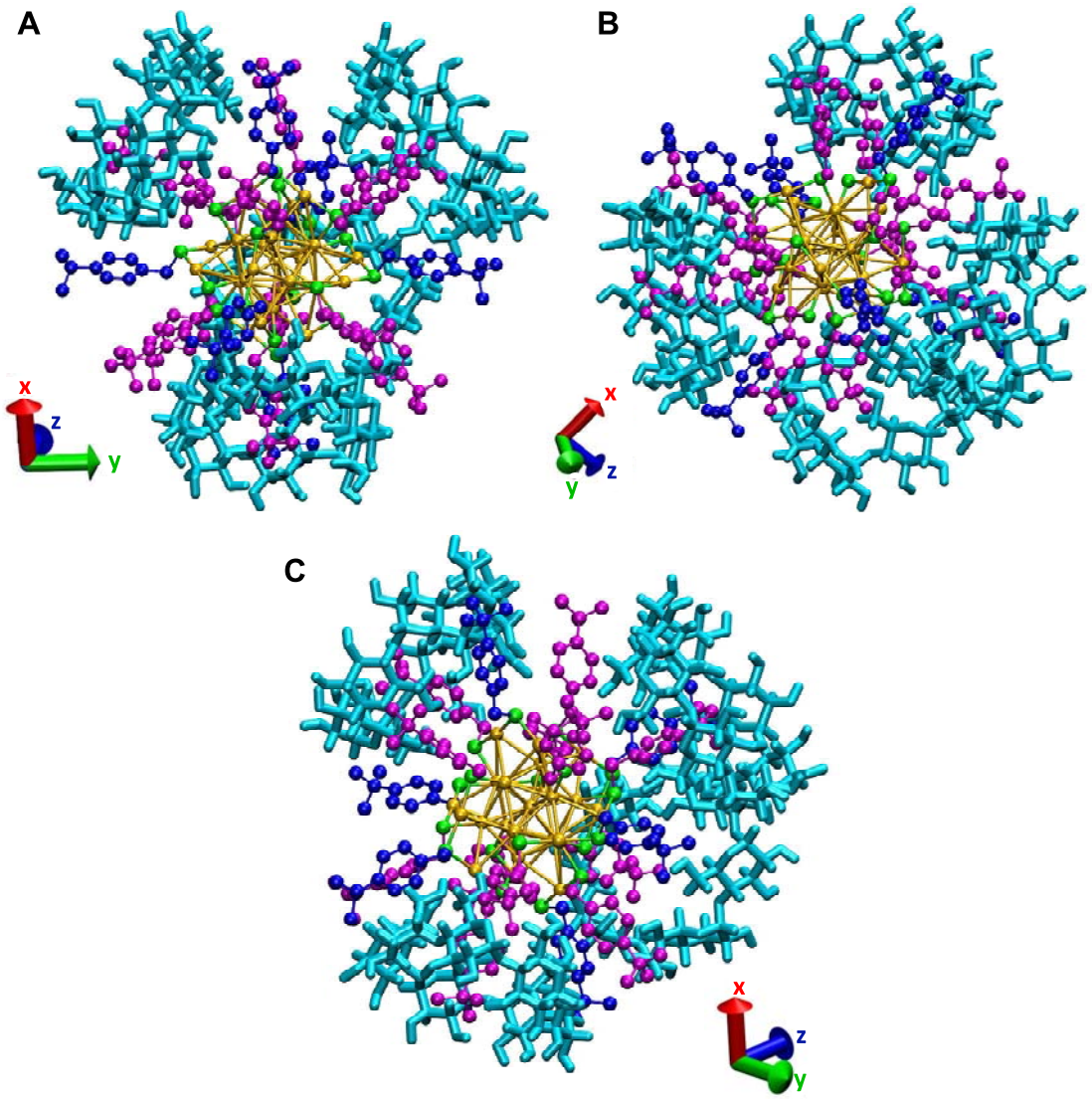

Figure S13. Different views of the $Au_{25}SBB_{18}\cap CD_4$ model. Hydrogen atoms are not shown on the SBB ligands for clarity. Sulfur and gold atoms are shown in green and gold, respectively, while the carbon atoms of the bridging and non-bridging ligands are shown in blue and magenta, respectively. The four attached CDs are shown in cyan in the stick molecular representation. The cartesian *x*, *y*, and *z* axes are shown by the red, green and blue arrows, respectively.

DFT calculations on BBSH∩CD

In this section we give full details of the DFT calculations performed on the BBSH∩CD inclusion complexes and discuss some of the theoretical results presented in the paper in

more detail. All calculations were performed with the Gaussian 09 code.[1] The experimental structure of β-cyclodextrin ($C_{70}H_{42}O_{35}$) was obtained from the Hic-Up Database and was based on the Protein Data Bank file pdb1z0n.ent.[2] As the downloaded structure was without hydrogen atoms these were added to this structure and the hydrogen positions were optimized at B3LYP/6-31G* keeping all the other atoms fixed in the same positions as experiment. The geometry of BBSH molecule ($C_{11}H_{15}SH$) was obtained from the web database ChemSpider.[3] A geometry optimization at the B3LYP/6-311+G** level was carried out. The optimization resulted in small changes in the geometry, as the plane of the benzene ring rotated to be perpendicular to the plane containing the C_1-C_2 bond (carbons are numbered starting from the sulfur end).

The above geometries of CD and BBSH were then used for creating the initial configurations of two BBSH∩CD adducts. The BBSH molecule was inserted into the CD cavity with the *t*-butyl group going in first. The alignment of the BBSH molecule was such that its C_1-C_2 axis was along the axis of the CD passing through the CD centre and perpendicular to the planes of its openings. Two such initial configurations were constructed by insertion into the wide and narrow ends of the CD. The geometry optimizations were carried out using the meta-GGA hybrid functional m052-X, which describes more accurately the non-covalent interactions found in the adducts, in conjunction with 6-31G* and 6-31+G** basis sets. During the optimization, the CD atoms were kept fixed and only the BBSH atoms were allowed to move. This was done not only to speed up the computations but also because β-CD adopts what is known as the anhydrous configuration after a full DFT geometry optimization,[4] which is different from its structure in a solvent.

The optimized geometries of the adducts are shown in Figure 4D (narrow end entry) and 4E (wide end entry), indicating the stability of these adducts due to non-covalent interactions. We did not find a significant change in the geometries with increase in the size of the basis set, and we have presented results using 6-31G* in Figures 4D and 4E. The BBSH molecule adopted a slanted configuration with its C_1-C_2 axis parallel to the side of the CD in both the narrow and wide entry cases. Binding energies of the narrow and wide entry configurations were performed using the Boys counterpoise correction method[5] with the m052-X/6-31+G** level of theory. The binding energy is about 2 kcal/mol less for the narrow case. We might attribute this to stronger π-bonding between the BBSH aromatic ring and the inner CD protons in the narrow case because of the shorter inter-proton distance caused by the narrowing of the profile of the CD.

A careful note of the relative positions of BBSH and CD protons was made in order that agreement with NMR experimental data might be evaluated. Referring to Figure 4D and 4E we see the following. In the narrow case, the H^b group protons are located around the level of the O-H^1 protons, the lower aromatic H^c protons (closest to the sulfur end) are around the level of the H^2 protons of CD, the upper aromatic H^d protons are situated around the level of the H^3 CD protons, while the *t*-butyl group H^e protons are situated between the level of the H^5 and H^6 CD protons. In the wide case, the H^b protons are slightly below the H^6 protons and not inside the CD, the lower aromatic H^c protons are at the H^5 proton level, the upper aromatic H^d protons are the at H^3 proton level, while the *t*-butyl group H^e protons are between the H^5, H^6 and H^7 protons.

NMR data suggests an interaction between both the aromatic and *t*-butyl group protons of BBSH with the H^3 and H^5 inner CD protons, which is also in good general agreement with both the structures. However it is not possible to identify the specific NMR fingerprints of

each of the structures from the experimental data which suggests the possibility of NMR calculations at DFT level. The arrangement of the included ligand and the CD were found to be different for inclusion complexes formed with ligands attached to the cluster rather than isolated ligands. Firstly, the presence of a gold core and -Au-S-Au-S-Au- staples attached to the sulfur of the SBB ligand decreases the penetration depth of the CD. Secondly, the steric hindrance caused by the presence of about four or five ligands around the CD decreases both the CD penetration depth and the angle between the CD and the ligand.

Supporting information 14

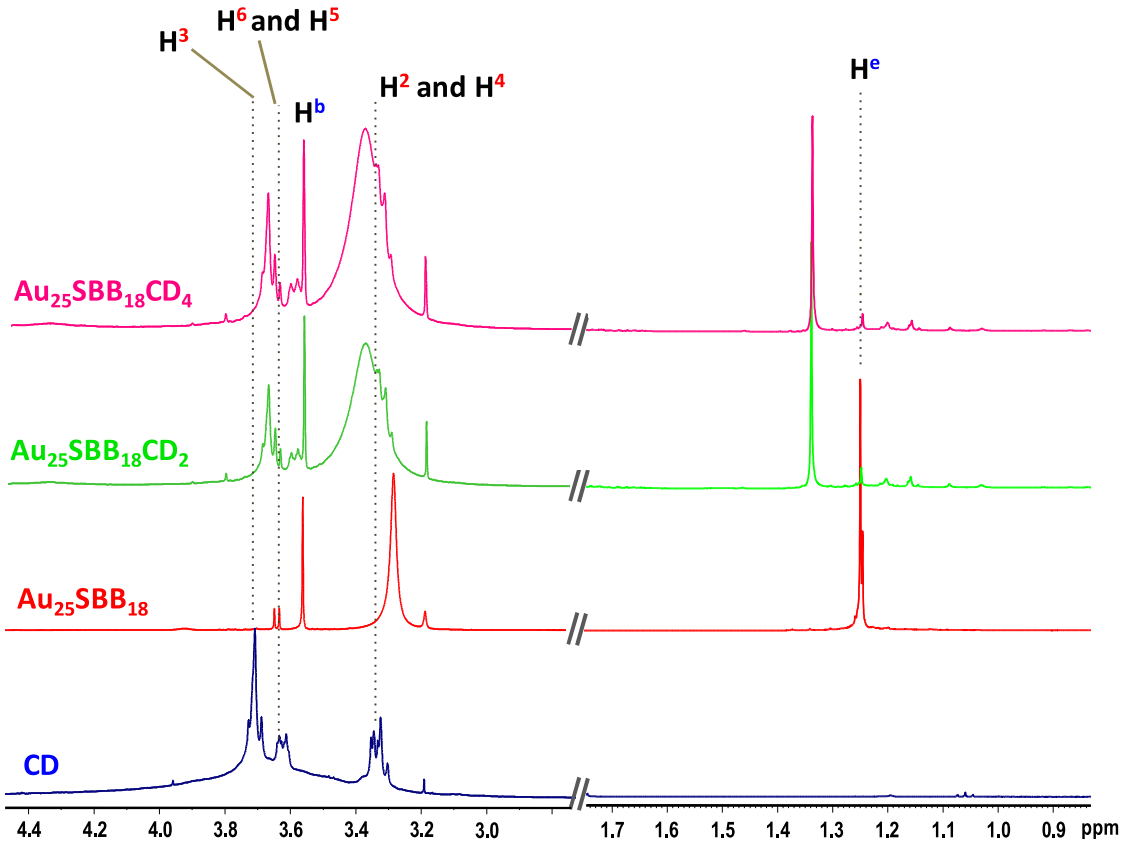

Figure S14. ^{1}H NMR of β-CD, $Au_{25}SBB_{18}$ and $Au_{25}SBB_{18}\cap CD_x$ in 1:1 solvent mixture of DMSO-d6 and $CDCl_3$ at 25 ^{o}C. Here signals due to unreacted H^e protons of BBS can also be observed (green and pink trace) which suggests the existence of free and complexed BBS on the cluster.

Supporting information 15

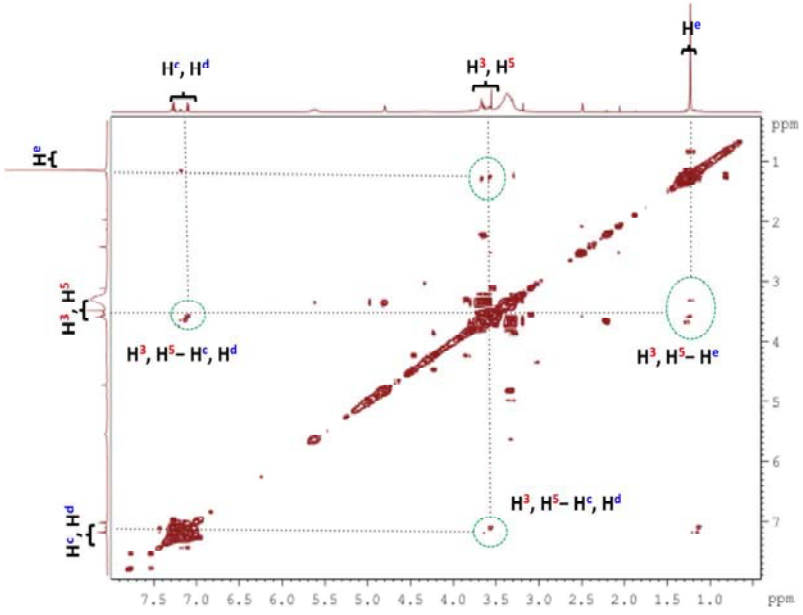

Figure 15. 2D COSY spectrum of $Au_{25}SBB_{18}\cap CD_4$ in 1:1 mixture of DMSO-d6 and $CDCl_3$ at 25 ^{o}C.

Supporting information 16

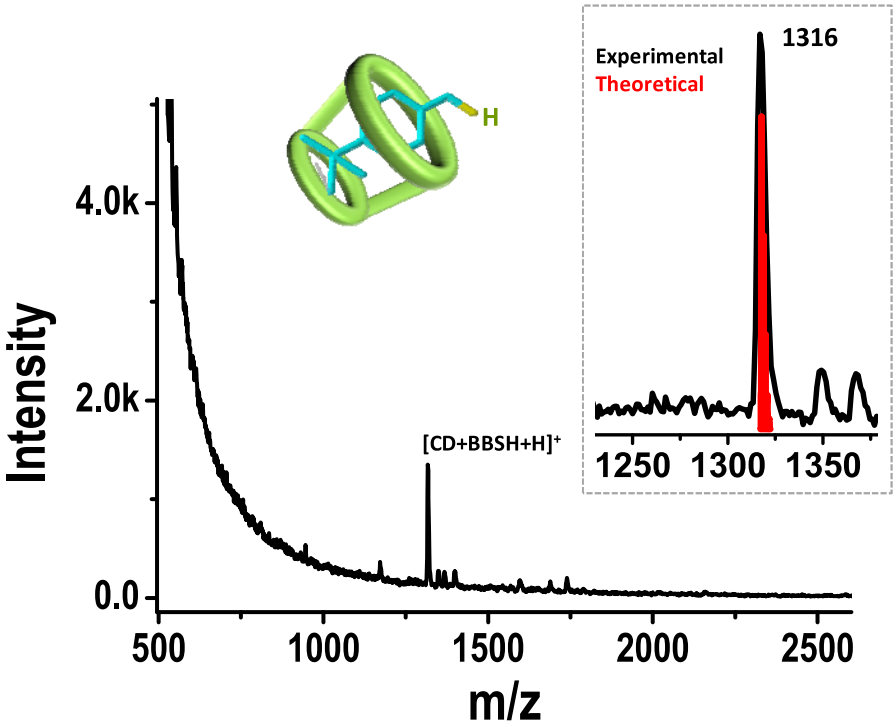

Figure S16. LDI MS of BBSH∩CD in the positive ion mode.

Supporting information 17

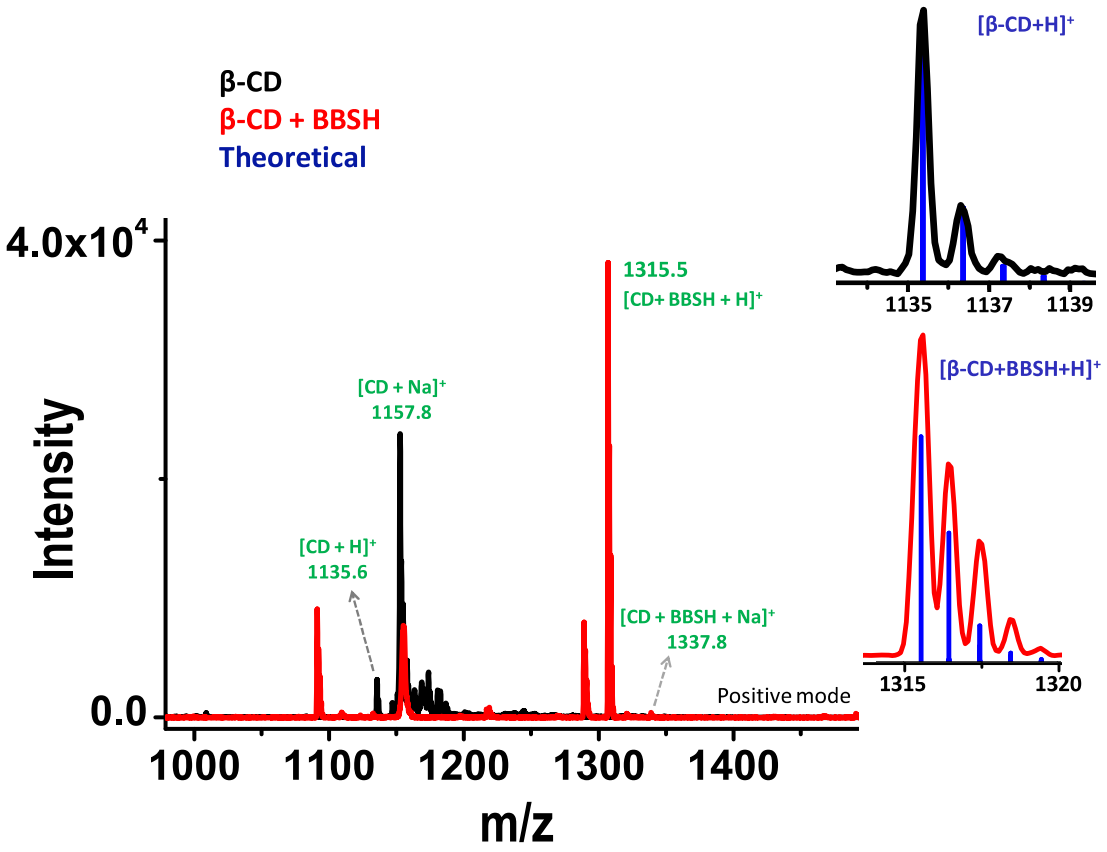

Figure S17a. ESI MS of β-CD and BBSH∩CD inclusion complex in the positive ion mode. Expanded views are given in the inset.

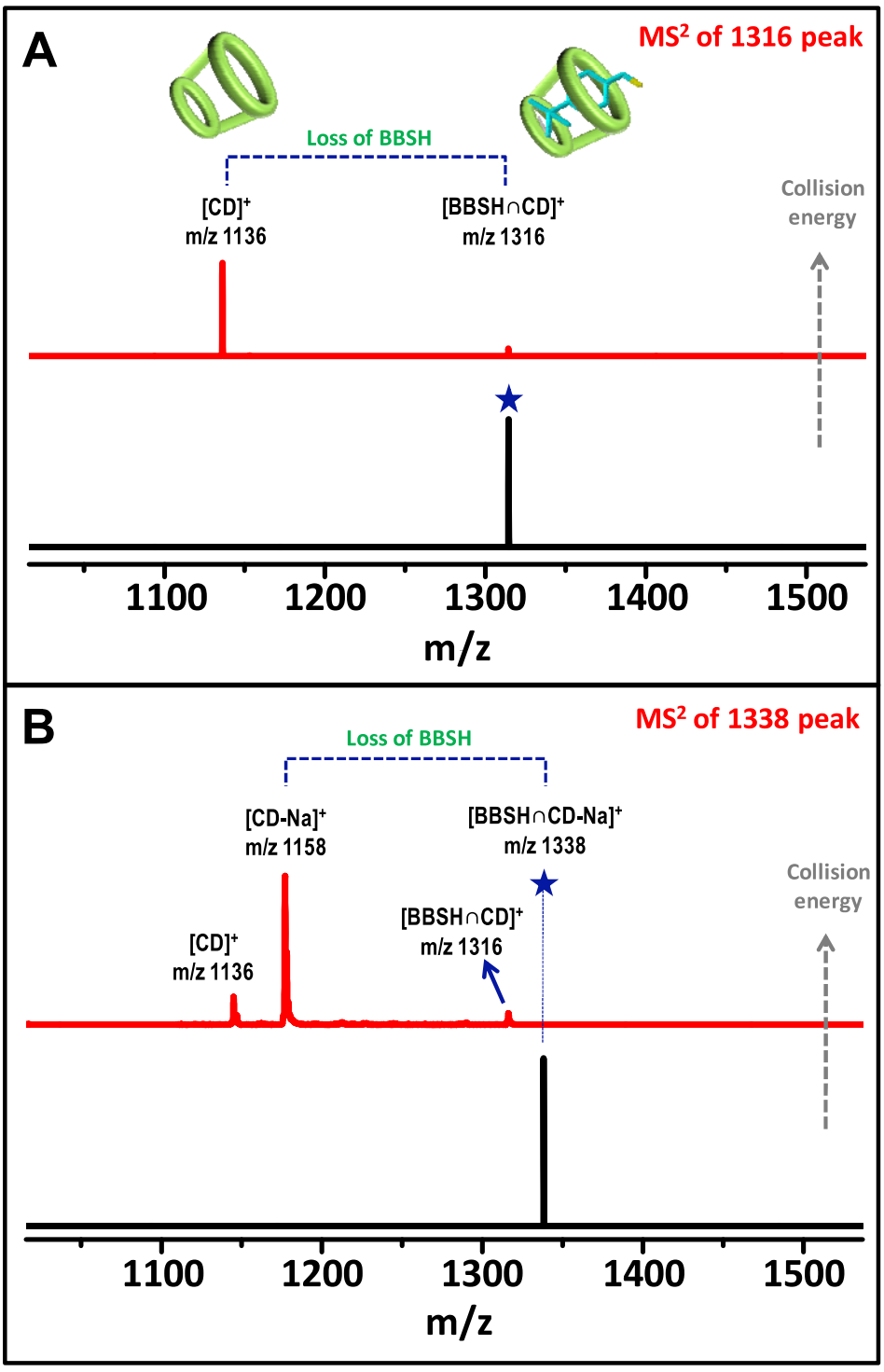

Figure S17b. Tandem mass ESI spectra (positive ion mode) for the peak at m/z 1316 (A) and 1338 (B) with increasing collision energy. Fragment ions are also marked. In the MS^2 spectrum of m/z 1338, the peaks formed at m/z 1158, 1316 and 1136 correspond to the loss of BBSH (180 Da) and Na (23 Da) from the parent ions.

Supporting information 18

The binding constant of a simple host-guest adduct, BBSH∩CD was measured in the same medium used for complexation of clusters using fluorescence spectral titrations.[6, 7] From the modified Benesi-Hildebrand equation, the linear plot of the reciprocal of the change in fluorescence intensity (ΔF) and the reciprocal of the molar concentration of cyclodextrin ($[CD]_0$) indicated a 1:1 stoichiometric complex with a binding constant of ~1776 M^{-1}. However, for $Au_{25}SBB_{18}$ and CD, such measurements using normal complexation titration, NMR, etc. were not attempted as multiple stoichiometries, $Au_{25}SBB_{18}∩CD_n$ (where n=1 to 4), can exist in solution thereby making calculation of binding constants difficult.

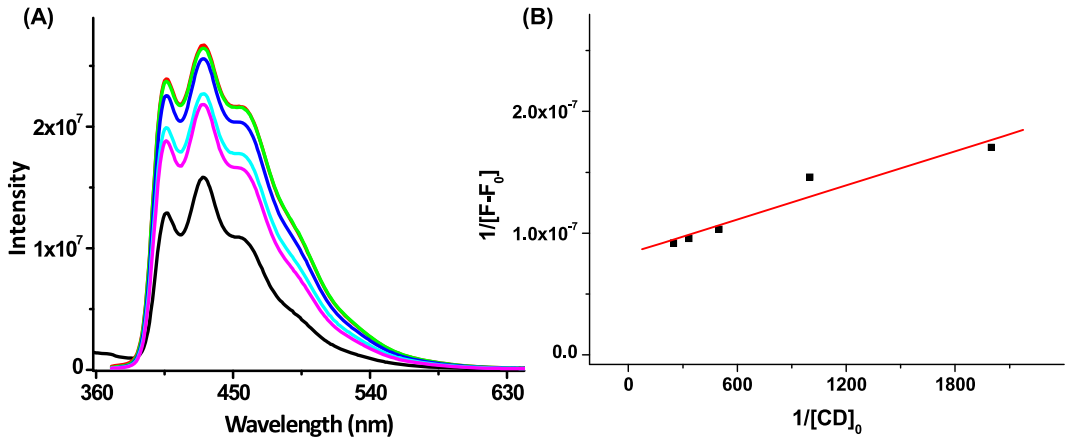

Figure S18. (A) Emission spectra of BBSH solution ($6.9*10^{-5}$ M) in THF/water mixture in the presence and absence of β-CD. From bottom to top: [β-CD] = 0, 0.5×10^{-3}, 1×10^{-3}, 2×10^{-3}, 3×10^{-3} and 4×10^{-3} M. (B) Plot of reciprocal of the change in fluorescence intensity (ΔF) and the reciprocal of the molar concentration of cyclodextrin ($[CD]_0$)

Supporting information 19

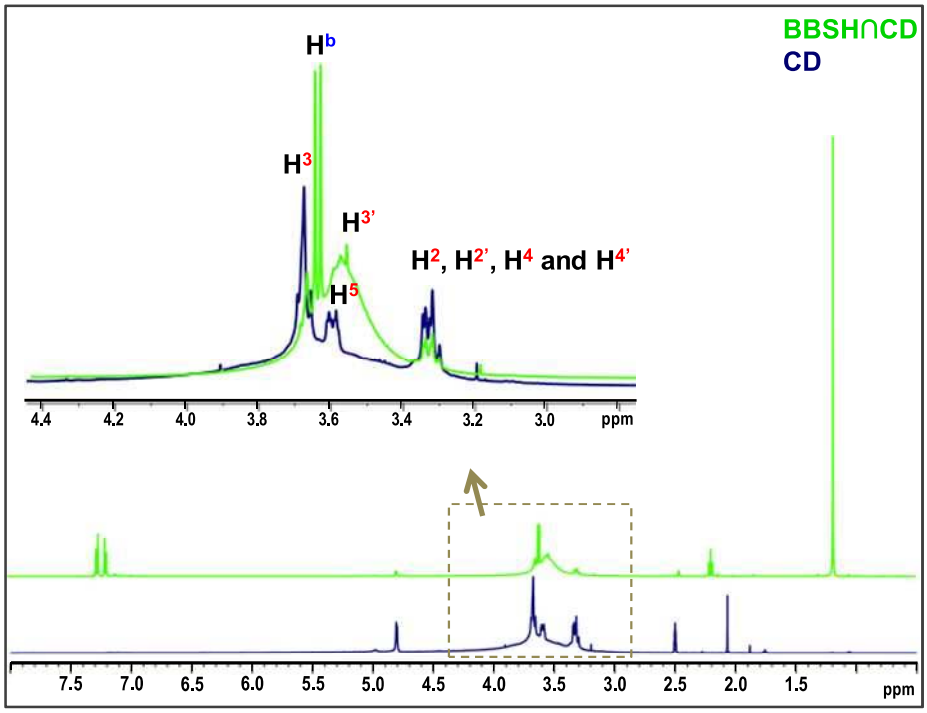

Figure 19a. Comparison of ^{1}H NMR of CD (blue trace) and BBSH∩CD (green trace) inclusion complex in 1:1 mixture of DMSO-d6 and $CDCl_3$ at 25 ^{o}C.

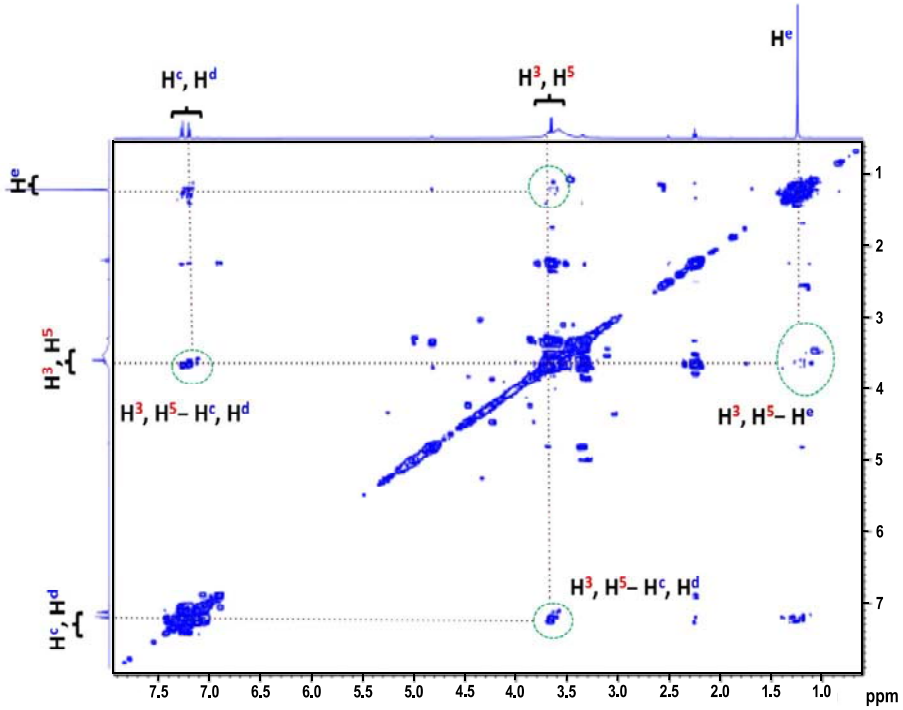

Figure 19b. 2D COSY spectrum of BBSH∩CD in 1:1 mixture of DMSO-d6 and $CDCl_3$ at 25 ^{o}C.

Supporting information 20

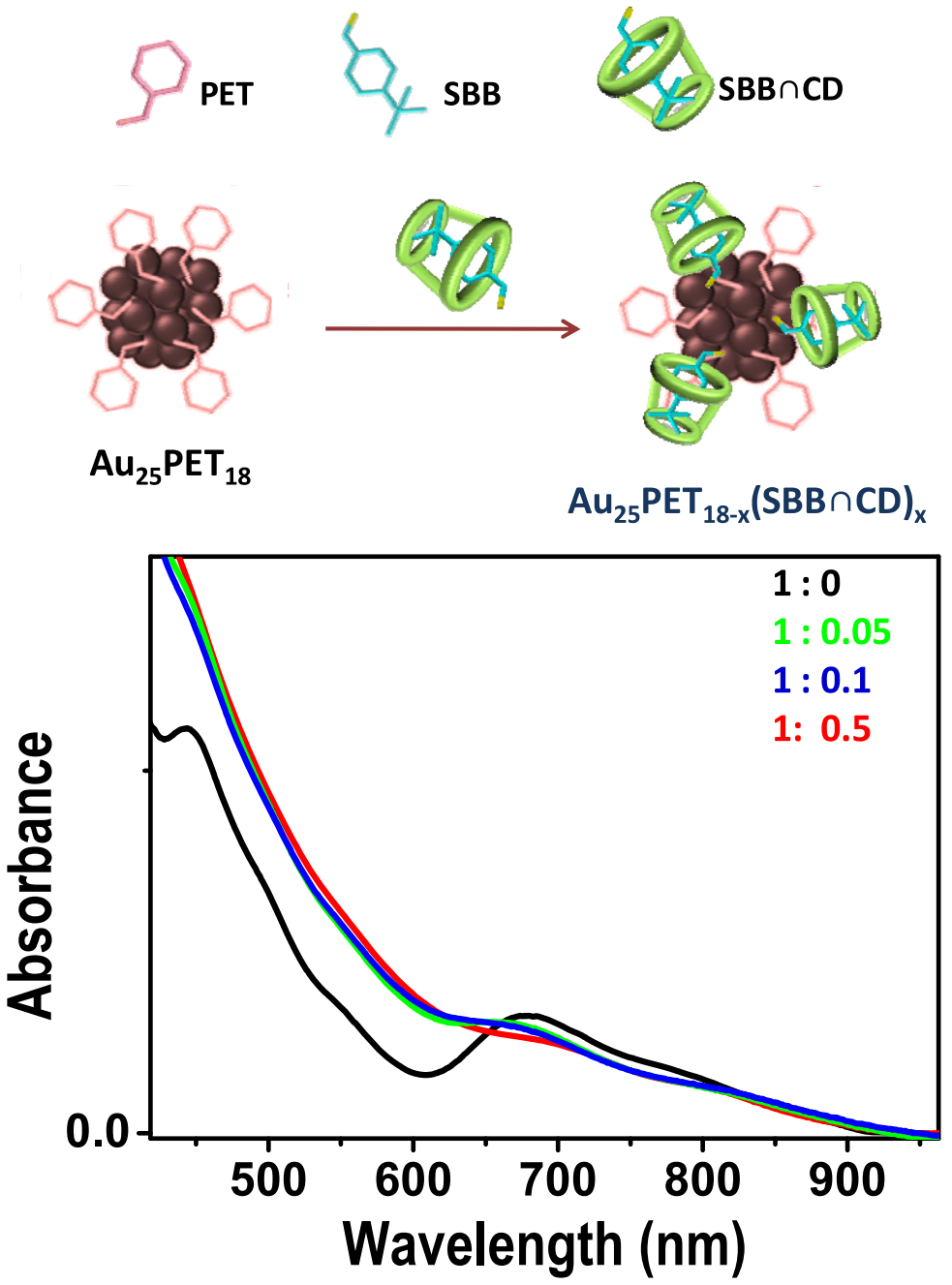

Figure S20. Effect of UV-vis absorption spectra after ligand exchange reaction of $Au_{25}PET_{18}$ with SBB∩CD (as incoming ligand). The PET:SBB∩CD ratios are shown.

Supporting information 21

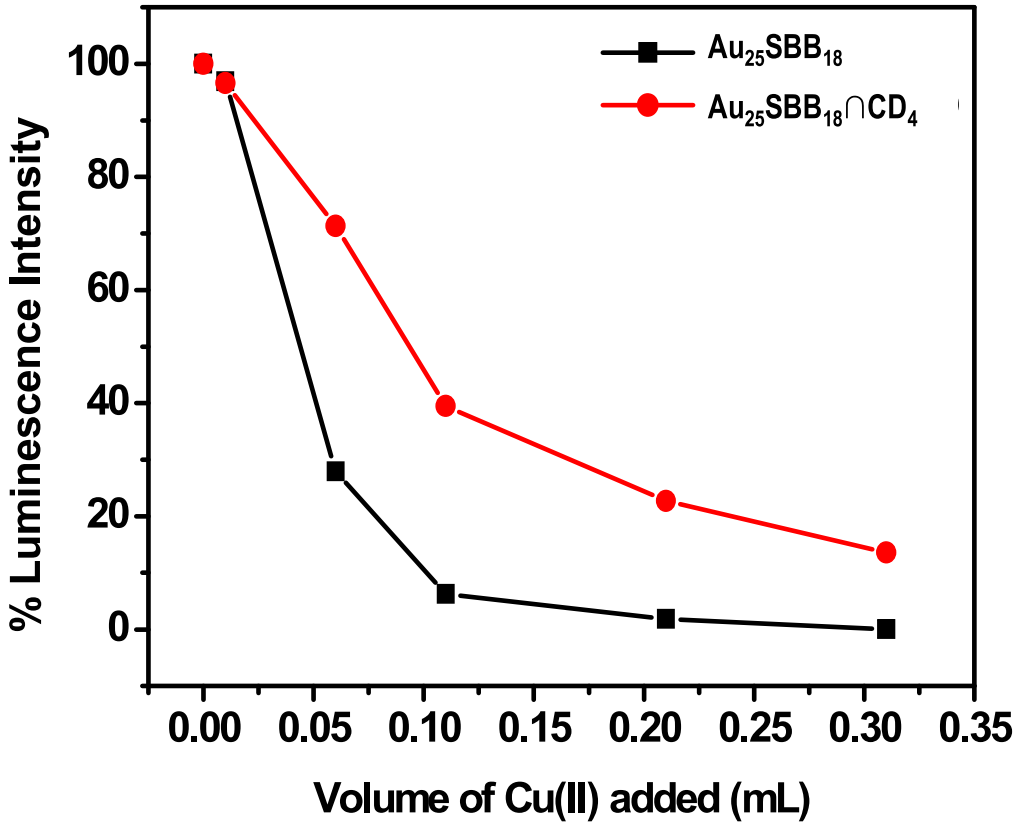

Figure S21. Quenching of (A) bare $Au_{25}SBB_{18}$ and (B) $Au_{25}SBB_{18}\cap CD_4$ upon treatment with an aqueous solution of 250 mM Cu^{2+} solution (note that clusters were taken in THF solvent so as to allow better miscibility). The spectra were measured after 5 minutes of addition.

Supporting information 22

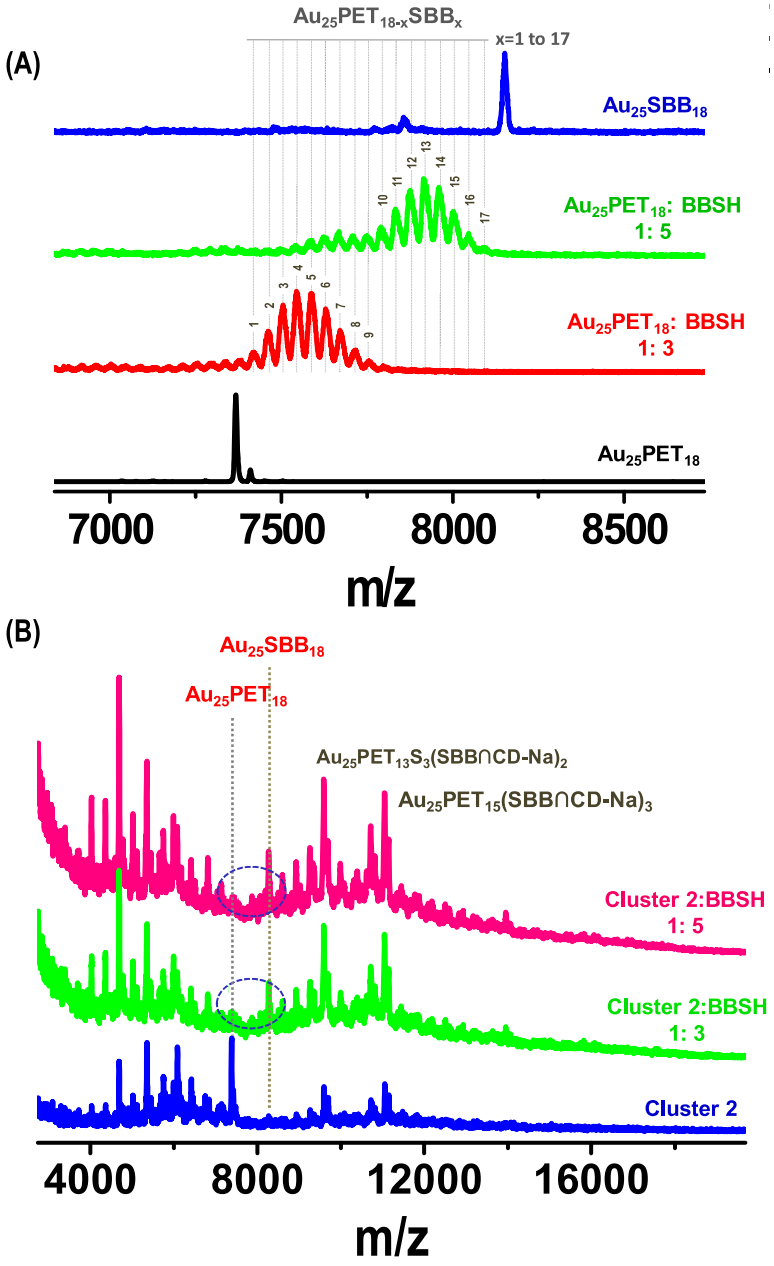

Figure S22. MALDI (L) mass spectra of bare $Au_{25}PET_{18}$ (A) and BBSH∩CD incorporated $Au_{25}PET_{18}$ QCs (denoted as 'Cluster 2' in the figure) (B) with excess BBSH thiol. In the case of $Au_{25}PET_{18}$ with excess BBSH (A), peaks corresponding to various ligand exchanged species, $Au_{25}PET_{18-x}SBB_x$ (where x=0 to 17) separated by m/z 42 due to the exchange of PET (MW 137.2) for BBS (MW 179.3), are seen under various conditions (labelled in figure). Spectrum corresponding to bare $Au_{25}SBB_{18}$ is also shown for comparison (blue trace in A). For (B), various amounts of BBSH was added to 'Cluster 2' which is a mixture of $Au_{25}PET_{18}$ and BBSH∩CD incorporated $Au_{25}PET_{18}$ QCs. While $Au_{25}PET_{18}$ ligand exchanges completely with BBSH to give a peak at m/z 8152 corresponding to $Au_{25}SBB_{18}$ (marked on the graph), peaks due to $Au_{25}PET_{15}(SBB∩CD\text{-}Na)_3$ and $Au_{25}PET_{13}S_3(SBB∩CD\text{-}Na)_2$ do not show any shift and their relative intensities are unaffected indicating the absence of ligand exchange.

Supporting information 23

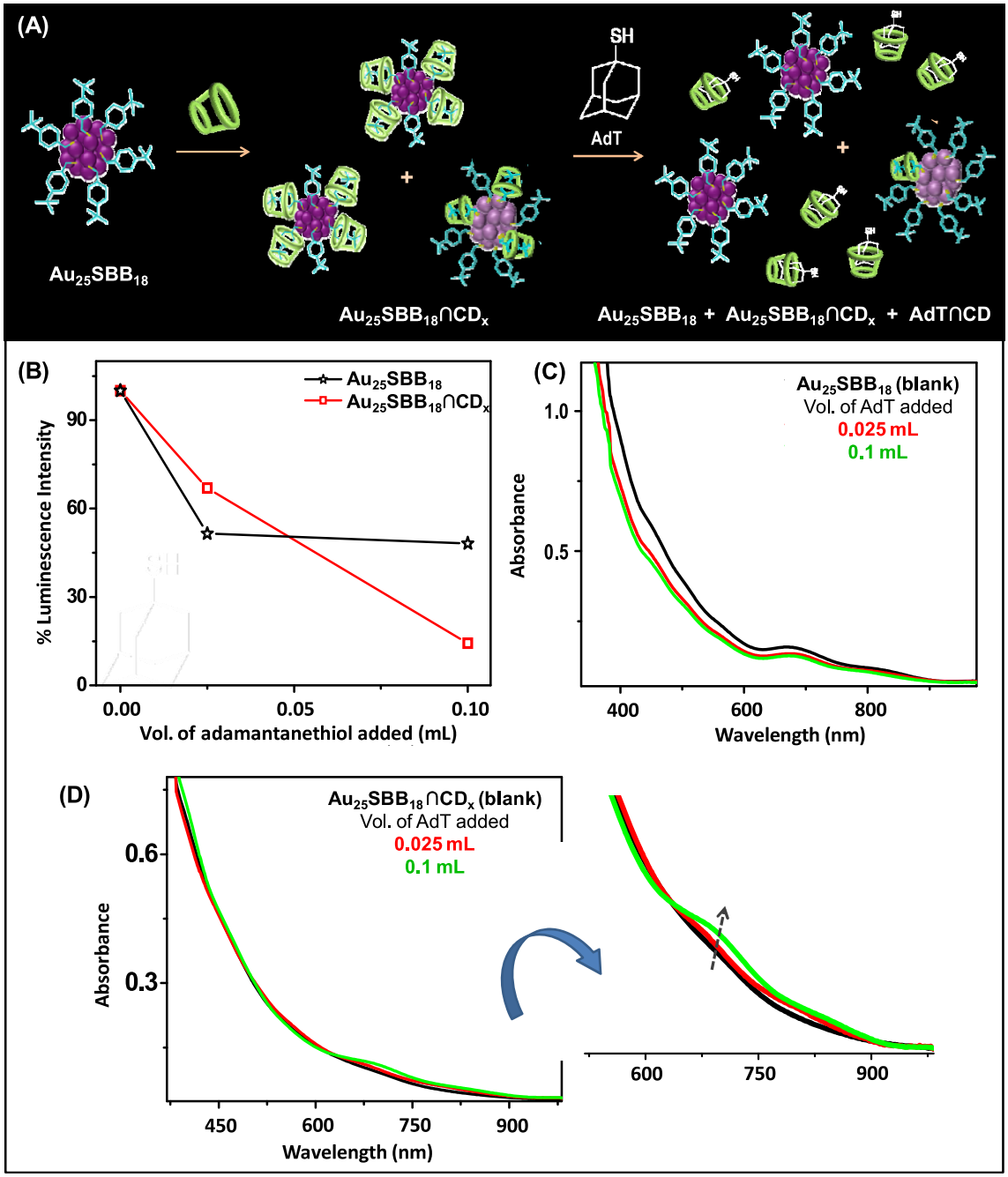

Figure S23. Effect of 1-adamantanethiol (AdT) on both $Au_{25}SBB_{18}$ and $Au_{25}SBB_{18}\cap CD_x$ was studied. Schematic of the possible events upon addition of AdT are depicted in (A). Luminescence from the QCs upon AdT addition is compared in (B). UV-vis absorption spectra of $Au_{25}SBB_{18}$ (C) and $Au_{25}SBB_{18}\cap CD_x$ (D), with addition of AdT are also shown. Re-appearence of Au_{25} absorption features with 0.1 mL of AdT (green trace, marked with an arrow) in $Au_{25}SBB_{18}\cap CD$ is observed in the expanded region of (D).

References:

1. Gaussian 09, Revision A.1. Frisch, M. J.; Trucks, G. W.; Schlegel, H. B.; Scuseria, G. E.; Robb, M. A.; Cheeseman, J. R.; Scalmani, G.; Barone, V.; Mennucci, B.; Petersson, G. *et al.* Gaussian, Inc., Wallingford CT, 2009.
2. Kleywegt, G. J., Crystallographic Refinement of Ligand Complexes. *Acta crystallographica. Section D, Biological crystallography* **2007,** *63*, 94-100.
3. http://www.chemspider.com/Chemical-Structure.2038012.html.
4. Snor, W. L. E., Weiss-Greiler P., Karpfen, A. , Viernstein, H., Wolschann, P., On the Structure of Anhydrous β-Cyclodextrin. *Chem. Phys. Lett.* **2007,** *441*, 159-162.
5. Boys, S. F.; Bernardi, F., The Calculation of Small Molecular Interactions by the Differences of Separate Total Energies. Some Procedures with Reduced Errors. *Molecular Physics* **1970,** *19*, 553-556.
6. Munoz de la Pena, A.; Ndou, T.; Zung, J. B.; Warner, I. M., Stoichiometry and Formation Constants of Pyrene Inclusion Complexes with β- and γ-Cyclodextrin. *The Journal of Physical Chemistry* **1991,** *95*, 3330-3334.
7. Wagner, B., The Use of Coumarins as Environmentally-Sensitive Fluorescent Probes of Heterogeneous Inclusion Systems. *Molecules* **2009,** *14*, 210-237

4. Patents Filed

Only list is attached

Patents

1. A method for preparing of monolayer protected silver clusters as antibacterial agents, T. Pradeep, Indranath Chakraborty, Udayabhaskararao Thumu and G. K. Deepesh, 485/CHE/2013, February 4, 2013.

2. A granulation composition for powder ingredients, T. Pradeep, A. Anil Kumar, M. Udhaya Sankar, Amrita Chaudhary, Anshup, 486/CHE/2013.

3. Water filled organic templated metal oxide/hydroxide/oxyhydroxide particle network for water purification and a device thereof, T. Pradeep, M. Udhaya Sankar, Amrita Chaudhary, A. Anil Kumar, Anshup, 525/CHE/2013.

4. Water purifier, Design application number 254443, filed on June 11, 2013.

5. AMRIT drinking water purifier, Design application number 257312, Filed on October 09, 2013.

6. Dechlorination of lindane and its removal from water using graphene nanocomposites, T. Pradeep, Soujit SenGupta, Indranath Chakraborty and Shihabudheen M. Maliyekkal, 5988/CHE/2013, filed on December 20, 2013.

7. Molecular Ionization from carbon nanotube paper, T. Pradeep, Depanjan Sarkar and Rahul Narayanan, 6137/CHE/2013 filed on December 30, 2013.

5. Technologies

AMRIT (Arsenic and heavy Metal ion Removal by Indian Technology)

Pictures are on the next pages

InnoNano Research Pvt. Ltd. has started production

Arsenic and Metal Removal by Indian Technology – AMRIT, is a drinking water purifier for communities. It is undergoing installation in arsenic affected regions of West Bengal. It was co-created by IIT Madras and InnoNano Research Private Limited, an IIT Madras incubated company.

A community unit undergoing field trials in West Bengal.

The final prototype installed in the district headquarters of Mursidabad district in West Bengal.

Enlarged Views

6. Popular Science

SUPER SCIENTIST

Perfect chemistry

The nation would remember Prof. Rao as the champion of basic science of Independent India

BY T. PRADEEP

A great teacher, intense researcher, affectionate advisor, caring mentor, careful critic, demanding disciplinarian and visionary institution builder, Prof. C.N.R. Rao, whom the nation has selected for its highest civilian honour, the Bharat Ratna, is all these and much more. I have seen him closely in all these roles for nearly 30 years and, therefore, it is difficult to look at any one of these aspects in isolation.

When I joined him as a joint PhD student (with Prof. M.S. Hegde as my other advisor), Prof. Rao was the director of the Indian Institute of Science (IISc). Though busy, he kept his doors open, whenever I wanted to meet him, which he continues for all his students even today. Once in a while, he would peep into the lab. "Are you there?" he would ask, inviting me to join him for a walk, on his way to the director's office. The walk would take us through different footpaths of the sprawling campus and he would discuss ideas, data, papers, literature, politics and many other things. Occasionally, he would catch me in the morning, while I am rushing to the lab on my bicycle. This was his method of instruction although he never considered it that way. How memorable were those days!

I remember the day I got the first signal from a photoelectron spectrometer that I constructed. Our efforts of two years breathed life into the machine. That was the best spectrum I had ever seen for argon, usually used to check the resolution of the instrument. I

ILLUSTRATION: JAIRAJ T.G.

Outstanding effort

Prof. Rao is probably the most prominent materials chemist of modern times. His most important contribution is the establishment of solid state and materials chemistry as a discipline. He started his career at a time when solid state chemistry was rather unknown. He made sustained efforts to nurture the area. The first books on solid state chemistry were written by him. Soon, his research evolved into all modern areas of materials, with deep connections to the emerging frontiers of several areas of natural science, like high-temperature superconductivity. Today, most of his contributions are in the area of nanomaterials, new forms of carbon, hybrid materials and complex oxides. He conducted the best possible science in a relatively less endowed part of the world and contributed to the development of science there and the third world at large, while being part of a larger international endeavour. For this, he nurtured institutions and organisations, both national and international.

He is credited with the isolation of the phase responsible for superconductivity in the YBaCuO system, discovery of Y-junction nanotubes, universal ferromagnetism in nanomaterials, discovery of a diverse array of novel materials such as graphene analogues of BCN [boron carbon nitride], inorganic analogues of nanotubes and graphene, electronic devices of these systems, organic framework solids and many more. Advanced gas phase spectroscopy, understanding of hydrogen bonding and expansion of computational materials science as a discipline, have all been greatly influenced by his contributions.

placed the graph on Prof. Rao's table. I could see the joy in his eyes. He stood up and fondly stroked my hair, something that he did to convey that you had done well. The second time he did that was when I finished my thesis colloquium. It was, indeed, a fascinating set of results for a PhD thesis.

As this note is about Prof. Rao's science, I must quickly move on.

Chemistry is about molecules and their transformations. For a non-specialist, describing molecular phenomena can be boring. Therefore, the discussion here will be in more general terms, although a few scientific terms may pop up occasionally.

Prof. Rao is a spectroscopist at heart. He probed chemistry through instrumentation, mostly spectroscopy. Spectroscopy is concerned with light-matter interactions. In a typical experiment, one interrogates matter with a radiation and looks at the changes in the radiation coming out of the specimen. There are diverse methods of spectroscopy which can tell the observer how matter is composed of and how it changes under a given situation.

His PhD problem at Purdue University was on the structure of molecules—how the atoms are arranged with chemical bonds—in the gas phase, using electron diffraction. Diffraction is a process by which particles or light undergo scattering from matter. He showed that the structure of some simple resonating molecules (an example would be carbon suboxide, C_3O_2) is linear, a work cited by Nobel laureate and legendary chemist Linus Pauling in his book, *The Nature of the Chemical Bond*.

Structures stayed with Prof. Rao all through his career. As he moved on from molecules to materials, structure was related strongly to the latter's properties and structure-property correlations became the central theme of his research.

Just after his PhD, Prof. Rao worked on the structure of titanium dioxide, which was his first important work in solid state chemistry. As an independent scientist in India, his early contributions of spectroscopy were to understand phenomena like hydrogen bonds, donor-acceptor interactions, phase transitions, catalysis and metal-insulator transitions. Those were the days of limited infrastructure, but

SUPER SCIENTIST

unlimited energy.

The science of Prof. Rao evolved from no-infrastructure (in the 1960s) to infrastructure-limited (in the 1980s and 90s) to infrastructure-unlimited (in the 2010s) over the past 60 years. Infrastructure is always limiting for a working scientist as thought goes far beyond, and faster than instruments. Therefore, facilities can never be enough. This change in availability of resources is reflected in his science. One of the important problems he pursued in the early days, soon after he joined the faculty of the IISc, was phase transformations, and the system was decided by the limitations of the X-ray diffractometer available. The camera of the machine could 'see' only two diffractions of titanium dioxide, but that was enough to determine the transformation. Obviously, this study would have been impossible had he chosen another chemical system. He would often stress on the need to choose the problem wisely.

For him, any material in the solid state, anything which has a structure, has been fascinating. The concept of materials itself has evolved in the course of his research life of 60 years. While they were inanimate inorganic objects then—as one would find on a road or on a barren land—today the field of materials encompasses everything that can be seen around us. We ourselves, the biological matter, are now considered part of materials science. From bricks and concrete to plastics, clay and porous catalysts to gels, nanoscale wires to molecular conductors, the field has exploded. Prof. Rao contributed to most of these evolving interfaces of the area. He has stayed at the expanding horizon of the subject. In each one of the giant explosions in this field, such as high-temperature superconductivity, fullerenes and nanotubes, nanomaterials and, recently, graphene, he has made seminal contributions so that the field itself evolved with his science. In many of the other materials, such as open framework solids, he has explored new avenues of applications. In each of them his quest has always been on the changes in properties, as change in itself is the cornerstone of chemistry.

Nation's pride: Prof. Rao with his wife after he was presented with a Mysore peta by Karnataka Chief Minister Siddaramaiah; (left) the author with Prof. Rao

In solid state materials, a big event happened in 1986 with the discovery of high-temperature superconductivity in an oxide system, $La_{2-x}Ba_xCuO_4$, belonging to a family of oxides related to perovskites [a calcium titanium oxide mineral species]. Till then, no one thought that superconductivity, generally associated with metals, is possible with oxides, which are ceramic powders. However, this indeed happened and became one of the most fascinating areas of physics, materials science and solid state chemistry.

The parent chemical system La_2CuO_4 was studied by Prof. Rao earlier. He had, in fact, shown that the system is antiferromagnetic, a property

PTI

Pinnacle of glory

Prof. Chintamani Nagesa Ramachandra Rao
Born: June 30, 1934
Chairman, Scientific Advisory Council to the Prime Minister
Education
MSc, BHU (1953)
PhD, Purdue University (1958)
DSc, Mysore University (1960)
Research interests
Solid state and materials chemistry, structural chemistry
Honorary doctorate from 51 universities
Author of nearly 1,500 research papers
Author/editor/co-editor of 48 books
Awards
Third scientist to win Bharat Ratna
Padma Shri (1974)
Padma Vibhushan (1985)
India Science Prize (2004)
Legion of Honour, France (2005)
Order of Friendship, Russia (2009)
The Queen's Medal by the Royal Society, London (2009)
Award for International Science Cooperation, China (2012)

of the oxide. However, infrastructure allowed him to pursue the properties only down to liquid nitrogen temperatures, while superconductivity was discovered at much lower temperatures. However, the Bangalore team identified the superconducting phase $YBa_2Cu_3O_7$, which showed superconductivity at liquid nitrogen temperature. This was published in *Nature* dated April 30, 1987.

The materials science wave expanded into fullerenes [a family of carbon allotropes, named after Buckminster Fuller]. They were made in Bangalore within one month of the publication of the original paper, using a new apparatus. The very first N[nitrogen]-doped fullerenes were discovered in Bangalore. The research soon expanded to carbon nanotubes, where a unique Y-junction was found by a simple reaction during the growth process, which turned out to be the smallest device to achieve rectification. The research on one-dimensional nanostructures expanded to inorganic nanotubes and several modifications of one-dimensional systems.

A natural extension of nanotubes was graphene, the planar one-atom thick sheets of carbon, which was the subject of the Nobel Prize of 2010, wherein several surprises were found in Bangalore. One such surprise was a large synergy in mechanical properties when graphene was combined with nano-diamonds.

Prof. Rao's recent interests extend to areas such as splitting of water using solar energy, problems of environmental remediation such as carbon dioxide sequestration, unusual chemical processes at nanomaterials and chemistry at interfaces.

When we observe Prof. Rao's work from a distance, it is evident that he entered into an area while it was nascent and he expanded it to an established discipline and then left it for others to explore further. Though he found several phenomena in his research career, they were not pursued for industrial exploitation, possibly because, either industry was not ready in most cases, or an application could not be made market-ready in the time normally expected by the industry. Significantly, in each of those areas, he produced a talent pool which expanded and established the subject far and wide. While infrastructure was created in his lab, he allowed the establishment of similar facilities all over the country so that advanced research could be conducted by all. As excellence disappeared in the universities, he nurtured new institutions. Prof. Rao as an individual is inseparable from the institutions he built. They remind us of the vision of the founder. While he built his own science, with equal or more passion, he built science of others through such institutions. The institutions he built were not only physical entities, they were also virtual. He also founded several professional societies and all of them are doing well.

Prof. Rao guided a large number of PhD students—155 of them in all. He has the largest number of scientific collaborators, explored the widest variety of problems and, of course, established the largest array of tools for the investigation of materials. His students built their groups and the chain continues.

The nation would remember him as the champion of basic science of Independent India.

The writer is a professor at the Indian Institute of Technology Madras.

THE HINDU

S & T

Mass spectrometry: the most important analytical tool of modern times

T. PRADEEP

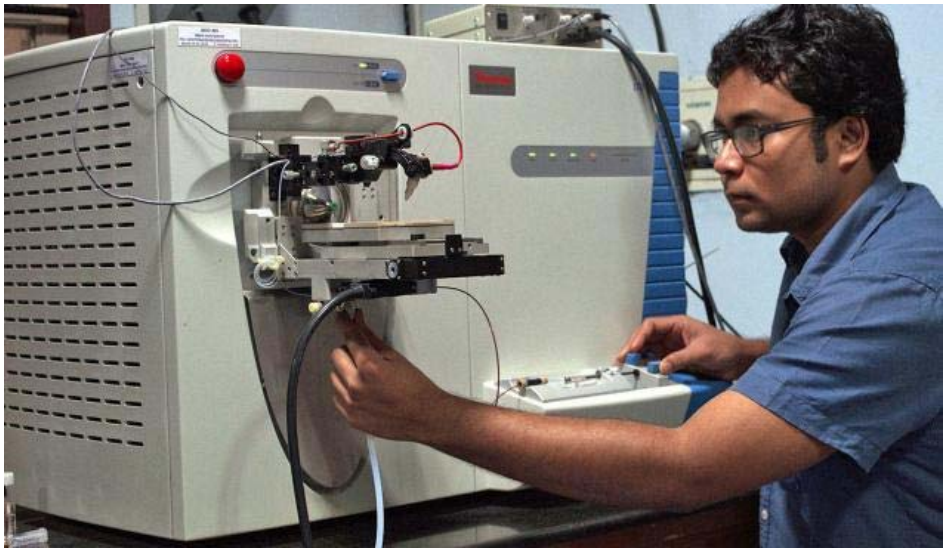

Today, there is no single area of experimental science where mass spectroscopy is not being used. *Special Arrangement*

With it, it is possible to measure the mass spectrum of complex proteins, extremely fragile molecular assemblies and even intact cells

Mass spectrometry (MS), arguably the most important analytical spectroscopic tool of modern times, is in its centenary year in 2013 along with two other celebrated discoveries of science, the Bohr atom model and the chemical bond of G. N. Lewis; both have profound connections to the first.

Sir J.J. Thomson, a Nobel Laureate, also known for the discovery of electrons, built the first rudimentary mass spectrometer in 1913 (it was built earlier, but a full description appeared in this year) which identified the existence of isotopes — atoms differing in mass but having the same atomic number and therefore occupying the same position in the periodic table ('isos' is equal and 'topos' is place, in Greek).

His student, Aston, who built more mass spectrometers, expanded the discipline, identified 212 of the 287 naturally occurring isotopes and became the first Nobel Laureate in Chemistry in the area. Five Nobel Prizes have been awarded to MS pioneers.

Mass spectrometry is a way to measure the mass of ions — electrically charged species, derived from atoms or molecules. In the preface of his celebrated book, *Rays of Positive Electricity and Their Application to Chemical Analyses* (1913) Thomson stated, "I feel sure that there are many problems in Chemistry which could be solved with far greater ease by this than by any other method. The method is surprisingly sensitive — more so even than that of Spectrum Analysis, requires an infinitesimal amount of material, and does not require this to be specially purified...". The words were prophetic. Today, there is no single area of experimental science where mass spectroscopy is not being used. There is no university or research institution in the developed world without a mass spectrometer; this may even be said about India.

The technique is used to explore the chemical constitution of molecules from this planet and beyond, e.g. the hydrocarbon "seas" of Saturn's moon Titan.

It is used to understand the fundamental atomic and molecular processes and at the same time those of immediate relevance to events within cells. As a technique, it helps to control processes in chemical and biological industries, diagnose diseases, discover new drugs, protect the environment and explore mysteries of nature.

In 100 years, it has been used to separate much of the uranium 235 used to make the Little Boy (the bomb that was dropped onto Hiroshima in 1945), led to understanding of thousands of chemical reactions, to the discovery of new molecules, to the resolution of protein structures, to solve crimes and to provide answers to complex questions of nature.

Mass spectrometers require a way to produce ions — e.g. remove or add electrons, generally one electron — to the sample, then analyse the mass of the ion formed and detect it.

In each of these areas (forming ions, analysing their mass, detecting them) innovations have led to multiple mass spectrometric techniques.

The most important developments have happened in ion formation. Years ago, it was necessary to evaporate a sample to generate vapours and bombard these with a stream of electrons in order to make ions, a process which required vacuum. This was possible only with simple molecules which can be evaporated, generally by heating. Today it is possible to measure the mass spectrum of complex proteins, extremely fragile molecular assemblies and even intact cells, none of which evaporate normally. It is now possible to measure mass spectra of ultra small volumes, as small as a single human cell.

It is possible to understand the spectrum of molecules from the surface of a rose while the plant is alive. Mass spectra of molecules — metabolites or drugs or cancer markers — can be measured on a patient's skin or in his/her blood.

Mass spectrometers may soon arrive in physicians' consulting rooms. It has been demonstrated that they can help in diagnosis during complex surgeries within the operating theatre.

Ions are enjoying a considerable following these days. The mass spectrometry community is probably the largest group of scientists working around a single tool. However, despite this large following, it is surprising that mass spectrometry is being removed gradually from our science curriculum. Mass spectrometry concerns ion chemistry and physics with an emphasis on scientific instrumentation.

However, in the past several years, paralleling the growth of applications of the method, spectrometers have become black boxes for the vast majority. Sadly, in the process, Thomson is forgotten.

Appreciation of instrumentation should be brought back to the curriculum. We must note that Thomson, after considerable work in theoretical physics, moved to experiments. The Nobel committee over many years has demonstrated its appreciation for scientific instrumentation; this is a lesson we in India cannot afford to discard.

(*The author is a Professor of Chemistry at IIT Madras*)

pradeep@iitm.ac.in

Keywords: Mass spectrometry, Sir J.J. Thomson, existence of isotopes, molecular processes

7. Media Reports

Only a selection is attached

SCIENTIFIC AMERICAN™

Sign In / Register

Subscribe | News & Features | Topics | Blogs | Videos & Podcasts | Education | Citi

Technology :: News :: May 7, 2013 :: 9 Comments :: Email :: Print

Cheap Nanotech Filter Clears Hazardous Microbes and Chemicals from Drinking Water

A $16 device could provide a family of five with clean water for an entire year

By Luciana Gravotta

About 780 million people—a tenth of the world's population—do not have access to clean drinking water. Water laced with contaminants such as bacteria, viruses, lead and arsenic claims millions of lives each

PHYS.ORG

...entists develop new kind of portable water purification

Nanoparticle Tech Could Bring Clean Water to Rural Poor

Denise Chow, LiveScience Staff Writer
Date: 06 May 2013 Time: 03:01 PM ET

A water purification system that uses nanotechnology to remove bacteria, viruses and other contaminants may be able to deliver clean drinking water to rural communities for less than $5 a year per family, according to a new study.

Researchers at the Indian Institute of Technology Madras in Chennai, India, developed a purification device that filters water through a specially crafted mixture of nanoparticles to remove harmful contaminants. Their study was published today (May 6) in the journal Proceedings of the National Academy of Sciences.

The device, which is currently being tested in communities in India, could offer an affordable way to provide small families with at least 10 liters (2.6 gallons) of safe drinking water per day, said study co-author Thalappil Pradeep, a professor in the department of chemistry at the Indian Institute of Technology Madras. [10 of the Most Polluted Places on Earth]

The Telegraph
Calcutta, India

BENGAL ARSENIC TEST FOR IIT

(Clockwise from top left) IIT team members Anshup, Kamlesh Chaudhari, Thal... Kumar, Suhejla Alimi, Mohan Udhaya Sankar and Sitthibuddheen Maliyekl

safe drinking water

'Rs 120... year's c...

Tuesday 07 May 2013

Home » National » IIT students develop low cost water filter

IIT students develop low cost water filter

Kalyan Ray, New Delhi

An inexpensive water-filter that can kill microbes ... metals may soon be a reality, thanks to a r... Technology-Madras.

The water purifier is based on comp... viruses but also scavenge toxic che...

DECCAN HERALD

materials360 online
Your premiere source for materials science news

Home > Materials News > Composite Nanomaterials Purify Drinking Water Affordably

Composite Nanomaterials Purify Drinking Water Affordably

by Rachel Nuwer
Materials Research Society | Published: 06 May 2013

Each year ... 1.6 million people die because of illness ... water, poor hygiene and unsanitary ... But most of these deaths could be prevented ... million lives could be saved ... cheap, safe means of ... water purifier ... to deliver ... the contaminants ... materials scientist at ...

1 of 11

Water hub
From Guardian Sustainable Business

The new water technologies that could save the plane

What are the new ar... business overcom...

theguardian

THE HINDU

S&T » Technology

Affordable water purification using silver nanoparticles

R. Prasad

Column Centimeter

Silver nanoparticles to purify water

The IIT Madras r... Anshup, Amrita Udhaya Sank...

HOT TOPICS: SANAULLAH RANJAY | KARNATAKA CM | NAREN...

Home News India Videos Photos Cricket Movies Sport Lifestyle Even...

Shopping

INDIA EAST | WEST | NORTH | SOUTH | NORTHEAST

India Today / India / South / Tamil Nadu / Story

DINESH C SHARMA, MAIL TODAY | MAIL TODAY | NEW DELHI, MAY 6, 2013 | UPDATED 20:53 IST

Bright lights of IIT Madras devise wonder water filter

TAGS: IIT Madras | Water filter | Nanotechnology | Water purifier

Research team (L-1st row) Amrita, Shahab, Sahaja, Udhaya, Anshup, Pradeep, Anil Kumar & Kamalesh.

RELATED

Pioneering quake study: IIT Delhi has been at the forefront of seismological research

NewScientist

Health

Home News In-Depth Articles Opinion Books & Art Galleries Topic Guides LastWord Subscribe Dating

SPACE TECH ENVIRONMENT HEALTH LIFE PHYSICS&MATH SCIENCE IN SOCIETY

Home | Health | Tech | News

Silver nanoparticles provide clean water for $2 a year

10 May 2013
Magazine issue 2916. Subscribe and save
For similar stories, visit the In Brief and Food and Drink Topic Guides

India Links
The news links of India

HOME » NEWS »

Nanotech for a glass of clean drinking water

By The India Links on May 7, 2013 3:15 am in News / no comments

1 of 13

THE HINDU

Today's Paper » NATIONAL » KERALA

A purifier that yields arsenic-free water

T. Nandakumar

IIT-Madras getting ready for its commercial launch

Scientists at the Indian Institute of Technology, Madras (IIT-M) are gearing up for commercial release of an affordable nanotechnology-based water purifier that can address the problem of arsenic contamination, a threat to drinking water sources and an emerging health hazard in several parts of the country.

The Arsenic Task Force of the West Bengal government has certified and approved the purifier developed by the IIT-M. “The pilot phase is over, and we are now preparing to take it to the market,” T. Pradeep, Professor, Department of Chemistry, who heads the research group working on water purifiers, said.

The team has incubated a company at the IIT-M to commercialise the technology, Dr. Pradeep told *The Hindu* here on the sidelines of the Nano India conference organised by the Department of Science and Technology and the National Institute for Interdisciplinary Science and Technology (NIIST) this week.

The purifier developed by the IIT-M uses iron oxyhydroxide, a nanostructured material, to remove arsenic from drinking water. It functions without electricity or piped water supply. Dr. Pradeep said it could provide arsenic-free water at an approximate cost of five paise a litre. “Over the next few years, we hope it will benefit at least 10 per cent of the people living in arsenic-contaminated areas.”

The IIT-M-incubated company will commercialise the technology with partners who can take up distribution.

The research group has also come up with a nanomaterial-based fluoride water purifier. “It will take some more work for field implementation of this purifier. We expect the technology to be ready in six months.”

Praveer Asthana, Director of the Nano Mission under the Union Department of Science and Technology, said the water purifiers developed by the IIT-M highlighted the relevance of industry-institution projects in the nanotechnology sector to deliver affordable, efficient solutions.

Dr. Pradeep said nanomaterials could play a key role in low-cost solutions to remove water contaminants. “They interact with the contaminant to remove it within a very small contact time. It is also possible to tune the chemistry of any of these materials so that they can attack a wide spectrum of contaminants.”

The IIT-M has already developed and commercialised a nano silver-based water purifier that breaks down pesticide residue.

The research team is working on an all-inclusive water purifier to address a wide spectrum of contaminants such as pesticides, mercury, cadmium, lead, fluoride, and arsenic. The group is collaborating with scientists working on other methods of water purification such as reverse osmosis, membranes, and solar and thermal technologies.

- ***A company has been incubated at IIT-M for commercialisation***
- ***IIT-M has developed nanomaterial-based fluoride water purifier***

Acknowledgements

Group 2013

Department of Science and Technology

Indian Institute of Technology Madras